



The Science Society of Thailand
Under the Patronage of His Majesty the King
and Faculty of Science, Chiang Mai University



STT50

The 50th International Congress
on Science, Technology
and Technology-based Innovation

25th – 27th November 2024

The Empress Hotel, Chiang Mai, Thailand

<https://stt50.scisoc.or.th>

Science x Creativity

Crafting
the
World

Proceeding book

TABLE OF CONTENTS

A-PHYSICS / APPLIED PHYSICS

| | |
|--|----|
| INFLUENCE OF THE GENERATION PARAMETERS ON DBD PLASMA FOR PATHOGENIC AND AIRBORNE DUST ELIMINATION | 1 |
| SIMPLE HYDROTHERMAL-MICROWAVE METHOD TO SYNTHESIZE MANGANESE PYROPHOSPHATE AND ELECTROCHEMICAL PERFORMANCE | 11 |

B-BIOLOGICAL SCIENCES

| | |
|--|-----|
| ALTERATION OF O-GLCNACYLATION AFFECTS CHEMOTHERAPY DRUG RESPONSES IN COLORECTAL CANCER CELL LINES | 18 |
| AN IN VITRO CARDIOPROTECTIVE EFFECT OF SMALL THERAPEUTIC PEPTIDES DERIVED FROM HUMAN SECRETORY LEUKOCYTE PROTEASE INHIBITOR (HSLPI) AGAINST MYOCARDIAL HYPOXIA/REPERFUSION INJURY | 26 |
| APPLICATION OF DIELECTRIC BARRIER DISCHARGE PLASMA TECHNOLOGY ON MICROBIAL INHIBITION | 36 |
| BIRD NEST SITE CHARACTERISTICS IN URBAN GREEN AREAS OF CHULALONGKORN UNIVERSITY | 44 |
| COMPARATIVE ANALYSIS OF PROKARYOTIC AND EUKARYOTIC PRODUCTION SYSTEMS FOR ANTI-GD2 TRI-SPECIFIC KILLER ENGAGER (TRIKE) | 51 |
| CYTOTOXIC AND ANTIPROLIFERATIVE EFFECTS OF ANNONA MURICATA L. EXTRACTS ON HUMAN PROMYELOCYTIC LEUKEMIA (HL-60) AND HORMONE-DEPENDENT BREAST CARCINOMA (MCF-7) CELLS | 62 |
| DETECTION OF BURKHOLDERIA PSEUDOMALLEI WITH CRISPR/CAS12A USING THE SPECIFIC MARKER ORF2 OF THE FIRST TYPE III SECRETION SYSTEM (T3SS-1) | 72 |
| DIVERSITY OF CRUSTOSE LICHEN GENUS PYRENULA (PYRENULACEAE, ASCOMYCETES) ON BOTH FROM DOI INTHANON NATIONAL PARK AND DOI SUTHEP-PUI NATIONAL PARK IN CHAING MAI PROVINCE | 81 |
| EFFECT OF NITROGEN CONCENTRATION ON BIOMASS AND LUTEIN PRODUCTION IN GREEN MICROALGA CHLOROCOCCUM HUMICOLA CULTURED IN PHOTOBIOREACTORS | 86 |
| EVALUATING CELL-FREE DNA IN SPENT CULTURE MEDIUM FOR ASSESSING BLASTOCYST QUALITY AND CHROMOSOMAL ABNORMALITIES | 92 |
| EVALUATION OF RAMBUTAN PEEL, NONI LEAF, BETEL LEAF, AND MACAO TEA EXTRACTS AS POTENTIAL ALZHEIMER'S DISEASE THERAPEUTICS: INHIBITORY EFFECTS ON ACETYLCHOLINESTERASE AND BUTYRYLCHOLINESTERASE ENZYMES | 101 |
| EXOGENOUS LOADING OF RECOMBINANT HUMAN SECRETORY LEUKOCYTES PROTEASE INHIBITOR (RHSLPI) INTO EXOSOME | 109 |
| EXPLORING THE PHYTOCHEMICAL CONSTITUENTS AND BIOLOGICAL PROPERTIES OF PIPER SARMENTOSUM LEAVES: INSIGHTS FROM CULINARY PREPARATION | 120 |
| GAMING AND SIMULATION FOR SHARE LEARNING ABOUT THE IMPORTANCE AND CO-CONSTRUCTION OF URBAN GREEN SPACE | 130 |
| INHIBITION OF STAPHYLOCOCCUS AUREUS HEMOLYTIC ACTIVITY IN A DOSE-DEPENDENT MANNER BY ENTEROCOCCUS FAECALIS R3 | 140 |

| | |
|--|-----|
| MODIFIED PACKAGING PLASMIDS FOR INTEGRASE-DEFICIENT LENTIVIRAL TRANSFECTION | 146 |
| MOLECULAR RECOGNITION OF REGULATED INTRAMEMBRANE PROTEOLYSIS (RIP) IN CELLULAR CHOLESTEROL SENSING PATHWAY | 154 |
| SPECIES DIVERSITY AND DISTRIBUTION OF THE LICHEN GENERA, HAEMATOMMA, LECANORA AND MALMIDEA IN DOI SUTHEP-PUI NATIONAL PARK, CHIANG MAI PROVINCE, THAILAND. | 161 |
| THE APPLICATION OF BARCODE DNA-HIGH RESOLUTION MELTING (BAR-HRM) ANALYSIS FOR AUTHENTICATIONC OF CLINACANTHUS NUTANS | 167 |
| THE ASSOCIATION OF CIRCADIAN RHYTHM AND DRUG SENSITIVITY IN PANCREATIC CANCER CELLS | 175 |
| THE COMBINATION TREATMENT OF ANTI-CD47 ANTIBODY AND BORTEZOMIB ENHANCES MULTIPLE MYELOMA CELL DEATH | 183 |
| THE EFFECT OF AMT2 AND DUR3 GENES IN TRANSMIGRATION PROCESS OF CRYPTOCOCCUS NEOFORMANS | 192 |
| THE EFFECT OF CORDYCEPS MILITARIS EXTRACT ON THE PROLIFERATION OF HUMAN DERMAL FIBROBLAST CELLS IN VITRO STUDY | 198 |
| THE EFFECT OF HIGH TEMPERATURE STRESS TO PHOTOSYNTHETIC EFFICACY OF LICHENS AT DOI SUTHEP-PUI NATIONAL PARK | 204 |
| THE STUDY OF FATTY ACID REDUCTASE REACTION | 209 |

C-CHEMISTRY (ANALYTICAL CHEMISTRY)

| | |
|---|-----|
| ALTERNATIVE METHOD FOR SIMULTANIOUS DETECTION OF CURCUMIN AND ALPHA-MANGOSTIN WITH VARIABLE WAVELENGTH DETECTOR | 217 |
| DETERMINATION OF GALLIC ACID AND RUTIN IN ZINGIBERACEAE USING HPLC | 226 |
| DEVELOPMENT OF A SAMPLE PREPARATION METHOD FOR ANALYZING BISPHENOL A AND DERIVATIVES BY HIGH PERFORMANCE LIQUID CHROMATOGRAPHY WITH DIODE ARRAY DETECTION | 231 |
| DEVELOPMENT OF ELECTROCHEMICAL SENSOR BASED ON MOLECULARLY IMPRINTED POLYMER FOR DETERMINATION OF ROXARSONE | 239 |
| ELECTROMEMBRANE EXTRACTION WITH FLAT SHEET MEMBRANE FOR DETERMINATION OF CHROMIUM(VI) | 249 |
| MAGNETIC LIQUID MARBLES FOR HYDROGEN SULFIDE GAS DETECTION | 255 |
| REMOVAL OF REACTIVE NAVY-BLUE DYE IN SYNTHETIC SAMPLE USING A SIMPLE LABORATORY-SCALE ELECTROCOAGULATION SYSTEM | 263 |
| SIMPLE OXALATE-SELECTIVE NAKED-EYE AND SPECTROPHOTOMETRIC DETERMINATION BASED-ON ALUMINIUM-INDICATOR COMPLEX | 270 |
| TRIPHENYL TETRAZOLIUM SALT-MEDIATED COLORIMETRIC DETECTION OF TRIAMCINOLONE ACETONIDE AND BETAMETHASONE 17-VALERATE | 277 |

C-CHEMISTRY (INORGANIC CHEMISTRY)

| | |
|---|-----|
| EFFECTS OF SULFUR SUBSTITUTION IN A NICKEL COMPLEX FEATURING A N4-SCHIFF BASE MACROCYCLE ON THE ELECTROCATALYTIC ACTIVITY TOWARDS CO ₂ REDUCTION | 283 |
|---|-----|

| | |
|--|-----|
| HYDROGEN SULFIDE ADSORPTION IN BIOGAS BY WASTE FROM PALM OIL PROCESSING | 292 |
| C-CHEMISTRY (ORGANIC & MEDICINAL CHEMISTRY) | |
| ALKYLATED 4'-AMINOCHALCONE AS NEW α -GLUCOSIDASE INHIBITORS | 298 |
| ANTIOXIDANTS ACTIVITIES OF CHINESE HERBS: HUANG QIN, HUANG LIAN, AND HUANG BAI | 305 |
| CHEMICAL MODIFICATION OF DIHYDROISOSTEVIOL | 314 |
| DETERMINATION OF ANTIOXIDANT ACTIVITY AND DEVELOPMENT OF FACIAL SERUM FORMULA CONTAINING THE CHRYSANTHEMUM INDICUM L. AND CHRYSANTHEMUM MORIFOLIUM RAMAT. LOWERS FROM THAILAND | 321 |
| DEVELOPMENT OF NOVEL FLUORESCENT CHEMOSENSORS BASED ON THIAZOLINYL QUINOLINE DERIVATIVES FOR METAL ION DETECTION. | 330 |
| EXPLORING THE α -GLUCOSIDASE INHIBITORY ACTIVITY OF N-9 ALKYL HARMINE DERIVATIVES | 339 |
| FACILE EXTRACTION AND ANTIBACTERIAL EVALUATION OF ALKALOIDS FROM THAI RED VEIN KRATOM (MITRAGYNA SPECIOSA KORTH) FOR POTENTIAL COSMETIC AND MEDICINAL APPLICATIONS | 346 |
| PHYTOCHEMICAL CONSTITUENTS FROM THE STEMS OF TILIACORA TRIANDRA | 355 |
| PREPARATION OF YELLOW LAKE FROM GARDENIA FRUIT EXTRACT. | 363 |
| SYNTHESIS AND BIOPHYSICAL PROPERTIES OF ZWITTERIONIC PYRROLIDINYL PEPTIDE NUCLEIC ACID | 369 |
| SYNTHESIS AND CHARACTERIZATION OF GREEN TEA-BASED DARK-COLORED MATERIALS | 379 |
| SYNTHESIS OF 2,3-DIOXOPYRROLIDINE DERIVATIVES AND EVALUATION OF THEIR INHIBITORY ACTIVITY AGAINST NS5 METHYLTRANSFERASE OF DENGUE VIRUS | 386 |
| SYNTHESIS OF ALKYLATED 9-O-BERBERRUBINE DERIVATIVES AS YEAST α -GLUCOSIDASE INHIBITORS | 393 |
| SYNTHESIS OF BENZO[A]PHENAZINE DERIVATIVES AND THEIR SENSOR APPLICATIONS | 401 |
| SYNTHESIS OF MOINUPIRAVIR IMPRINTED POLYMER | 409 |
| THE EXTRACTION OF THE BUDS AND CORE OF HAUYMON PINEAPPLE AND INCREASING THE STABILITY WITH ENCAPSULATION TECHNIQUE. | 416 |
| C-CHEMISTRY (PHYSICAL & THEORETICAL CHEMISTRY) | |
| APPLICATION OF THE DESIGN THINKING PROCESS IN THE DEVELOPMENT OF MAYONGCHID NAKHON NAYOK BOARD GAMES: A STUDY WITH 12TH-GRADE STUDENTS | 423 |
| DESIGNED A SERIES OF NEW COMPOUNDS OF ACETANILINDE DERIVATIVES WITH INHIBITION OF TOPOISOMERASE I AND II OF BREAST CANCER CELL | 430 |
| DEVELOPMENT OF NATURAL INDICATOR FILM BASED ON GELATIN INCORPORATED WITH ORCHID EXTRACT | 442 |

| | |
|--|-----|
| KINETICS AND ISOTHERM OF CRYSTAL VIOLET ADSORPTION USING ACTIVATED CARBON FROM COFFEE GROUNDS | 447 |
| MOLECULAR DYNAMICS ANALYSIS OF CORE PROTEIN ALLOSTERIC MODULATORS: INSIGHTS INTO HBCAG AND HBEAG INTERACTIONS FOR HEPATITIS B INHIBITION | 454 |
| D-MATHEMATICS / STATISTICS / COMPUTER SCIENCE / DATA SCIENCE / AI | |
| A GENDER EQUALITY ANALYSIS OF THE PARIS 2024 OLYMPIC GAMES | 463 |
| ADAPTIVE KALMAN FILTER FOR IMPROVED LANE TRACKING | 475 |
| ANALYTICAL SOLUTIONS OF SOME CONFORMABLE FRACTIONAL DIFFERENTIAL EQUATIONS | 476 |
| APPLICATION FOR PILL AND CAPSULE MEDICINE IDENTIFICATION BY PHYSICAL IDENTITIES | 488 |
| APPLYING MACHINE LEARNING TECHNIQUES FOR SNAKE SPECIES IDENTIFICATION | 496 |
| CARIES DETECTION IN PRIMARY TEETH USING A DEEP LEARNING-BASED CONVOLUTIONAL NEURAL NETWORK | 505 |
| NEW DELAY-DEPENDENT UNIFORM STABILITY ANALYSIS FOR THE CONFORMABLE FRACTIONAL SYSTEM WITH DELAY AND NONLINEAR PERTURBATIONS | 513 |
| NUMERICAL SOLUTION OF THE ABSOLUTE VALUE EQUATIONS USING TWO STEP ITERATIVE METHOD | 518 |
| ODD GRACEFUL LABELING OF VERTEX DUPLICATION IN PATH GRAPHS | 526 |
| OPTIMIZING THE PARAMETERS OF PROFIT-RELATIVE VIGOR INDEX STRATEGY FOR INVESTMENT IN GOLD MARKET | 532 |
| PREDICTING CHRONIC INSOMNIA USING LSTM TECHNIQUE OF MACHINE LEARNING | 546 |
| PRICING OPTION ON COMMODITY UNDER SCHWARTZ MODEL BY USING FINITE DIFFERENCE METHOD | 554 |
| QNN TRAINER : A TOOL TO SUPPORT QUANTUM NEURAL NETWORK TRAINING AND MODEL DEVELOPMENT | 574 |
| SOLUTION SETS OF SOME TWO-TERM QUADRATIC EQUATIONS INVOLVING FLOOR FUNCTIONS | 582 |
| THE CENTER COLORING OF CORONA PRODUCT OF CYCLES AND PATHS | 594 |
| E-ENERGY / ENVIRONMENTAL & EARTH SCIENCE / MATERIALS SCIENCE / CHEMICAL TECHNOLOGY | |
| ADSORPTION OF CHROMIUM BY ACID-MODIFIED DRAGON FRUIT PEEL | 603 |
| AMINE-SURFACE-MODIFIED MGO AS AN ADSORBENT FOR CO ₂ REMOVAL FROM BIOGAS | 615 |
| AN EARTHQUAKE PRECURSORY SIGN FROM GROUNDWATER LEVEL FLUCTUATION OF A DISTRICT IN CHIANG MAI PROVINCE, THAILAND | 623 |
| AN EXPERIMENT ON THE MECHANICAL PROPERTIES OF THE CIRCULAR HOLE ROCK UNDER ANISOTROPY CONDITIONS | 630 |

| | |
|--|-----|
| EFFECT OF COBALT ADDITION ON MICROSTRUCTURE AND MECHANICAL PROPERTY OF SINTERED MULTIPHASE STEELS | 639 |
| ELECTROSPUN CELLULOSE ACETATE FIBERS CONTAINING CHALCONE CRUDE EXTRACT | 649 |
| EXPERIMENTAL HEAT TREATING OF GREEN TO YELLOW APATITE FROM MADAGASCAR | 655 |
| GEOLOGICAL CHARACTERISTICS OF THE KAENG KHUT KHU RAPID AT CHIANG KHAN, LOEI PROVINCE: GEOHERITAGE SIGNIFICANCE IN THE GREATER MEKONG RIVER BASIN | 664 |
| GEOLOGICAL FEATURES INFLUENCING THE DISTRIBUTION OF METALLURGICAL SLAGS IN BAN WANG HAT, SUKHOTHAI PROVINCE: IMPLICATIONS FOR A SIGNIFICANT IRON ORE DEPOSIT | 671 |
| GREEN SYNTHESIS OF TITANIUM DIOXIDE USING BRASSICA OLERACEA LEAF EXTRACT FOR PHOTOCATALYTIC DEGRADATION OF RHODAMINE B DYE | 678 |
| HYDROGEN PRODUCTION FROM CO ₂ GASIFICATION OF BIOCHAR USING CaCO ₃ INCORPORATED WITH CATALYTIC WATER-GAS SHIFT REACTION | 687 |
| HYDROGEOCHEMICAL CHARACTERIZATION AND SALINITY PROCESSES IN GROUNDWATER OF KHOK SI SUBDISTRICT, KHON KAEN PROVINCE, THAILAND | 698 |
| MODELS FOR ESTIMATING MONTHLY AVERAGE DAILY GLOBAL SOLAR RADIATION FROM AIR TEMPERATURE: CASE STUDY SONGKHLA PROVINCE THAILAND | 707 |
| NEW DISCOVERY OF VERTEBRATE FOSSILS AT PHUWAT SITE, NONG BUA LAMPHU PROVINCE, THAILAND | 716 |
| PHASE TRANSITION AND MECHANICAL PROPERTIES OF CALCINED FLUE GAS DESULFURIZATION (FGD) WASTE AS A POTENTIAL SUBSTITUTE FOR NATURAL CALCIUM SULFATE SUBHYDRATE | 728 |
| PHYSICAL AND CHEMICAL PROPERTIES OF POTASSIUM SOAP LUBRICANTS SYNTHESIZED FROM VEGETABLE OILS OR OLEIC ACID FOR APPLICATION ON CONVEYOR BELT SYSTEMS | 735 |
| PREPARATION OF PATTANI CLAY CERAMSITE CONTANING FLY ASH FROM BIOMASS POWER PLANT AND PORE-FORMING REAGENTS | 744 |
| RECOVERY OF ALUMINIUM FROM LAMINATED PLASTIC USING SINGLE SCREW PYROLYZER | 753 |
| SYNTHESIS OF MG-MODIFIED MESOPOROUS SILICA ADSORBENT VIA SOFT TEMPLATE FOR SELECTIVE ADSORPTION OF CONGO RED DYE CONTAMINATED IN WASTEWATER | 759 |
| THE EVALUATING ECONOMIC, MEDICINAL, AND ENVIRONMENTAL BENEFITS OF MALABAR SPINACH EXTRACTS | 767 |
| TOUGHNESS ENHANCEMENT OF POLYLACTIC ACID FILLED WITH ULTRAFINE FULLY VULCANIZED NATURAL RUBBER POWDER GRAFTED WITH METHYL METHACRYLATE MONOMER | 772 |
| F-FOOD SCIENCE AND TECHNOLOGY/AGRICULTURAL SCIENCE | |
| 2 IN 1 INNOVATIVE APPARATUS FOR CHEMICAL DETECTION IN AGRICULTURAL AND ENVIRONMENTAL APPLICATIONS | 781 |
| EFFECT OF FERMENTED SOYBEAN POWDER ON METABOLIC CHANGES IN HIGH FAT DIET-TREATED RATS | 790 |

| | |
|---|-----|
| ENHANCEMENT OF HEALTH BENEFIT OF OKARA THROUGH MIX-CULTURE FERMENTATIONS FOR DEVELOPMENT INTO FUNCTIONAL FOOD PRODUCT | 796 |
| ENHANCEMENT OF OCTENYL SUCCINYLAION OF CASSAVA STARCH VIA DRY HEATING TREATMENT | 805 |
| IMPACT OF WATER AND GLUCOSE DURING STEAM-HEAT MOISTURE TREATMENT ON PHYSICOCHEMICAL PROPERTIES OF CASSAVA FLOUR | 813 |
| SCREENING OF PROTEOMICS COMPARISON ON FLOWER HONEY PRODUCTS BY USING SDS-PAGE ANALYSIS COMBINED WITH LC-MS | 822 |
| TEA PRODUCTION FROM YOUNG LEAF OF SAN PA TONG RICE VARIETY AND EVALUATION OF THE PHYTOCHEMICAL CONSTITUENTS AND ANTIOXIDATION ACTIVITIES | 829 |
| SP2-BIOMATERIALS AND MEDICAL DEVICES | |
| A CYTOPROTECTIVE EFFECTS OF NANOPARTICLES DELIVERY OF RECOMBINANT HUMAN SECRETORY LEUCOCYTE PROTEASE INHIBITORS ON BACTERIAL LIPOPOLYSACCHARIDE INDUCE CELL INJURY | 835 |
| CARDIAC CELL MEMBRANE COATED MESOPOROUS SILICA NANOPARTICLES FOR DELIVERY TO CARDIAC TARGETS | 843 |
| IMMOBILIZATION OF RECOMBINANT HUMAN SECRETORY LEUCOCYTE PROTEASE INHIBITOR (RHSLPI), BY PLASMATIZATION ON TITANIUM SURFACE, ENHANCED OSTEOBLAST CELL ADHESION | 850 |
| SP7-CEMENT AND CONCRETE: SCIENCE, TECHNOLOGY AND APPLICATIONS TOWARDS GREEN AND SUSTAINABLE FUTURE | |
| EFFECT OF PLASMA ACTIVATED WATER ON EARLY-AGE HYDRATION REACTION AND STRENGTH ACTIVITY INDEX OF FLY-ASH CEMENT PASTE | 859 |
| SP9-GENERATIVE AI: AN EMERGING AI TECHNOLOGY | |
| AUTOMATIC SEGMENTATION OF CARIES EXTENSIONS IN BITEWING RADIOGRAPHS USING YOLOV8 WITH DENTAL CROSS-SECTIONS AS GROUND TRUTH | 867 |
| SP13-HARNESSING DIGITAL SCIENCE AND ENGINEERING FOR ENVIRONMENTAL SUSTAINABILITY | |
| CARBON DIOXIDE EFFICIENCY ANALYSIS OF ADSORPTION AND DESORPTION USING K ₂ CO ₃ /AL ₂ O ₃ SORBENT UNDER VARIOUS OPERATING PARAMETERS WITH AVRAMI KINETIC MODEL | 876 |
| CELLULAR AUTOMATA BASED MODEL TO PREDICT WILDFIRE SMOKE DISPERSION | 888 |
| DEVELOPMENT OF AMINE-MODIFIED NAY ZEOLITES FROM RICE HUSK WASTE FOR EFFICIENT DIRECT AIR CO ₂ CAPTURE. | 896 |
| EXPLORING MICROWAVE-ASSISTED ZEOLITE 13X REGENERATION FOR EFFECTIVE DIRECT AIR CO ₂ CAPTURE | 905 |

A-PHYSICS / APPLIED PHYSICS



Influence of the generation parameters on DBD plasma for airborne pathogenic elimination

Thawichai Traiporm¹, Wannakan Sawatpaen¹, Nattakorn Borwornpornmetee², Worawan Bhanthumnavin³, Boonchoat Paosawatyanyong^{4*}, Chonchanok Muangnapoh⁵ and Nathaporn Promros²

¹ Program of Science for Industry, Chulalongkorn University, Bangkok, Thailand, 10330

² Department of Physics, King Mongkut's Institute of Technology Ladkrabang, Bangkok, Thailand, 10520

³ Department of Chemistry, Chulalongkorn University, Bangkok, Thailand, 10330

⁴ Department of Physics, Chulalongkorn University, Bangkok, Thailand, 10330

⁵ Department of Biology, Chulalongkorn University, Bangkok, Thailand, 10330

*e-mail: boonchoat.p@chula.ac.th

Abstract

The issue of PM 2.5 particulate matter pollution significantly impacts the quantity of pathogenic microorganisms in the air, thereby affecting human health. Managing indoor air quality to ensure safety has become crucial and necessitates technological advancements to address this problem. Cold atmospheric pressure plasma has been considered due to its capability to eliminate airborne pathogens. This study focuses on the application of dielectric barrier discharge (DBD) module as a mean to generate plasma by applying a 10 kV at 15 kHz, resulting in an electron temperature of 1.52 ± 0.051 eV and an electron density of $3.46 \pm 0.084 \times 10^{16} \text{ m}^{-3}$. Subsequently, an array of these plasma modules was integrated into a prototype air purifier equipped with a 400 – 800 CFM blower for circulating air within a 48 m³ test room over an hour test duration and yielded more than 41% for mold and 99% for antipathogenic effectiveness. The results indicate that DBD plasma effectively can reduce airborne pathogens. The effectiveness on microorganism removal originated from the direct and indirect inhibiting processes of the plasma and the appropriate airflow. This indicates that DBD module has the potential for future air pollution management products.

Keywords: Dielectric Barrier Discharge, Cold Plasma, Pathogenic Elimination, Plasma Parameter

1. Introduction

Air pollution is currently a serious problem that affects the livelihood of the population, which tends to be even more dangerous from the increasing number of airborne pathogens. With the spread of respiratory disease from these pathogens, the solution is necessary. Currently, several technologies have been applied to solve this problem, such as plasma ionizers. Within various types of plasma, dielectric barrier discharge (DBD) plasma is one of the candidates for plasma ionizers which possesses several intriguing characteristics such as the ability to generate plasma under atmospheric pressure without relying on a vacuum system or air pump, generation of free radical that can disable pathogens's growth, uncomplication design, and low-cost manufacturing.

In our previous work, N. Nanna et. al. [1] designed a miniature DBD module with $20 \times 25 \times 1 \text{ mm}^3$ dimension. The work confirmed that the plasma from DBD module exhibited glowing discharge activity then the antimicrobial test on *Escherichia Coli* under closed space proved that DBD plasma can prevent bacteria growth by 99%. However, the

module needs improvement for commercial usage. In this work, our research group aimed to employ the DBD module in the standard Thailand classroom with an area of 48 m². Hence, the module needs to be scaled up and the plasma parameters also need to be optimized to achieve the most effective antipathogenic capability.

From the research of J. Žigon and co-workers [2], they studied the influence of voltage on Optical Emission Spectroscopy (OES) by varying the voltage from 7 kV to 12 kV and found that the plasma intensity value increased at the voltage range of the second positive system of N₂. They also reported that the amount of ozone increased when increasing the voltage used for plasma generation. In addition, E. Timmermann and co-workers [3] observed the effect of the varying voltage in range of 10 kV - 14 kV on bacteria elimination and found that increment of the discharge voltage increased the rate of bacteria elimination more than 70% - 90% due to the rising of plasma intensity and numbers of ions that were produced from $2.5 \times 10^6 \text{ cm}^{-3}$ to $4 \times 10^6 \text{ cm}^{-3}$. The research of T. Y. Tang with research team [4] and S. Protugal and co-researcher [5] studied the influence of the frequency on the characteristics of OES spectra and found that the frequencies of 20, 40, 80 kHz resulted in insignificantly increased in intensity for OES spectra while created more ozone which has a significant role for bacteria elimination. According to the literature review, the optimization of voltage and frequency used for plasma generation is crucial for improvement of DBD module for antimicrobial application.

Therefore, this study aimed to improve the DBD module by optimizing the plasma parameters of the up-scaled module and the airflow rate when utilizing the module in conjunction with air purifier to achieve the highest efficiency in eliminating airborne pathogens for the room size of 48 square meters. The voltage and frequency used in plasma generation were altered to identify the most suitable parameters to improve the electron temperature (T_e) and electron density (n_e) of the plasma generated from DBD module. Then, the characteristics of the airflow trajectory and the airflow rate inside the chamber were varied to analyze the different amounts of microorganisms within test environments after being exposed to plasma generated from DBD module installed inside the chamber.

2. Methodology

2.1 Design of DBD Module

The design of DBD module is displayed in Figure 1. The DBD module was designed to possess the dimensions of $170 \times 100 \times 2 \text{ mm}^3$. As seen in Figure 1, the copper electrode used as the discharge area was shaped into serpentine pattern with $120 \times 50 \text{ mm}^2$ area where the line was 2 mm width with 2 mm gap from each other. The back electrode was a rectangular copper electrode with a surface area of $140 \times 70 \text{ mm}^2$. The DBD module was placed away from each other by 20 mm while the patterned electrodes turned to the same direction. The customized high-voltage DC source was connected to the electrode on each side of the DBD module. To optimize the parameter of generated plasma, the DBD module was applied with different voltages of 5 - 15 kV and frequencies of 15 - 35 kHz.

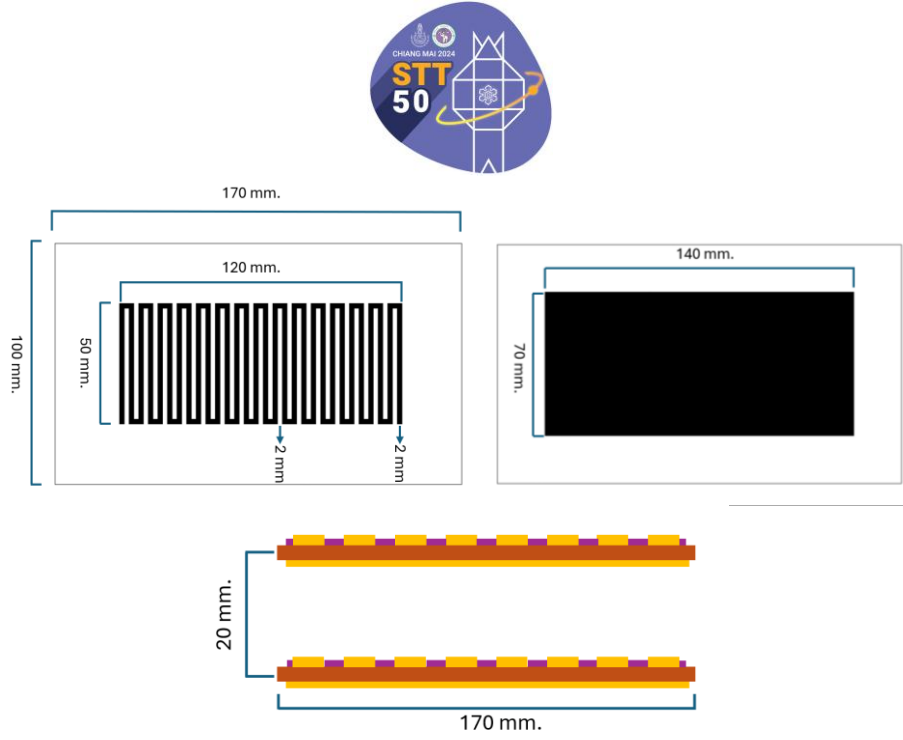


Figure 1.

Schematic of DBD module used for this study.

2.2 Investigation on Plasma Parameters of DBD Plasma

An OES apparatus (Ocean Optic, model: HR4000) was used for spectrum acquisition of glow discharge within the range of 200 - 1100 nm. Using the plot of the acquired OES spectra versus wavelength, the atomic spectra of several gases could be identified. Then, the T_e values of the plasma generated from DBD module under all variations of voltage and frequency were calculated using a two-emission line method based on Eq.(1) [6]

$$k_B T_e = \frac{E_2 - E_1}{\ln\left(\frac{I_1}{I_2}\right) - \ln\left(\frac{g_1 A_{12} \lambda_2}{g_2 A_{21} \lambda_1}\right)} \quad (1)$$

Where K_B is Boltzmann's constant $= 1.381 \times 10^{-23}$ J/K. λ is wavelength of spectral emission lines (nm). g is the statistical weight of spectral emission lines. A is transition probability. E is energy of spectral emission lines (cm^{-1}). I is intensity of spectral emission lines (arbitrary unit).

The first and second highest spectral emission lines for the observed element were picked to solve the equation. In this case, the oxygen lines were picked to observe the ionized oxygen which is related to the free radical of ambient plasma. All parameters associated with the oxygen line were cited from the NIST database.

The n_e value can also be used to discern the relative trend of ionized oxygen density which is related to the number of free radicals produced by DBD plasma. Based on Eq.(2), the n_e values were discerned using full width half maximum of the broadened peak of OES Spectra [6].

$$\Delta\lambda_{1/2} = 2\omega\left(\frac{n_e}{10^{16}}\right) \quad (2)$$

Where $\Delta\lambda_{1/2}$ is full wave half maximum. ω is electron impact width.

2.3 Study of Airflow Trajectory and Effect of Airflow Rate

The diagram of the airflow inside the prototype air purifier equipped with DBD array, comprising multiple DBD modules, designed for usage in a room with 120 m³ in volume is displayed in Figure 2. The flow trajectory was simulated in the form 3-dimensional model using Solid Edge software to analyze the airflow within the prototype. Then, the built prototype was used for the study of the effect of airflow on the rate of pathogenic elimination. The airflow rate was monitored through an anemometer (Fluke, model: 925).

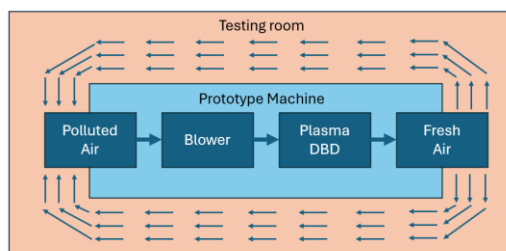


Figure 2.

Diagram of air purifier with DBD array installed.

2.4 Study on Antipathogenic Activity

Sampling of airborne pathogens was conducted through the usage of a standard impactor (SKC, model: QuickTake 30 BioStage) before the experiment. The sampled air in the testing room was fed into air purifier with DBD array inside to flow for an hour under various flow rates. Afterward, the pathogenic samples were collected and put back into the impactor after the experiment. The pathogen samples were cultured for a week on the plate to compare the amounts of pathogens colonies that appear on the plate for untreated air and air that was treated by DBD plasma under different airflow rates. In Figure 3 shows the criteria of airborne pathogens counting on the collected samples for analyzing the effectiveness of plasma using one-way ANOVA function of Minitab software with 95% confidence.



Figure 3.

Criteria of microorganisms for counting as 1 colone-forming unit (CFU).

3. Results and Discussion

3.1 Effect Frequency and Voltage on characteristic of Plasma

Plasma was generated by applying a voltage of 5 kV to 10 kV while maintaining a frequency of 15 kHz. Figure 4 which portrays a plot of the intensity of OES spectra against wavelength, reveals that DBD plasma generation primarily produces spectral lines of nitrogen ions and oxygen ions. Nitrogen was detected at wavelengths of 334.28, 354.55, 401.97, and 421.74 nm [7]. Additionally, oxygen was found at wavelengths of 777.4 and 842.45 nm [8],



along with hydroxyl (OH) at a wavelength of 314.14 nm. The OH and NO play a significant role for the inactivation of the pathogenic process [9]. The results of the analysis for T_e and n_e presented in Table 1 reveals typical value range for atmospheric DBD plasma's discharge [10-12]. The result indicates that the concentration varies with changes in voltage. This is because of the electron acceleration under influence of electric field and the ion collision with the atom of working gas and leads to generation of new free electron and positive ion resulting in an increase in n_e [13]. At fixed voltage of 10 kV while varying the frequency from 15 kHz to 35 kHz, an increase in the frequency used to generate plasma did not lead to a corresponding increase in intensity. In an inversion, frequency can affect the stability of the generated plasma, as electrons generated by the plasma bulk are trapped between two different electrodes due to the rapidly oscillating electric field of the applied voltage. This causes the accumulation of charge, which is subsequently released in the form of a spark. [14] Hence, the plasma generated at 10 kV and 15 kHz is the optimum for plasma generation of the current DBD module.

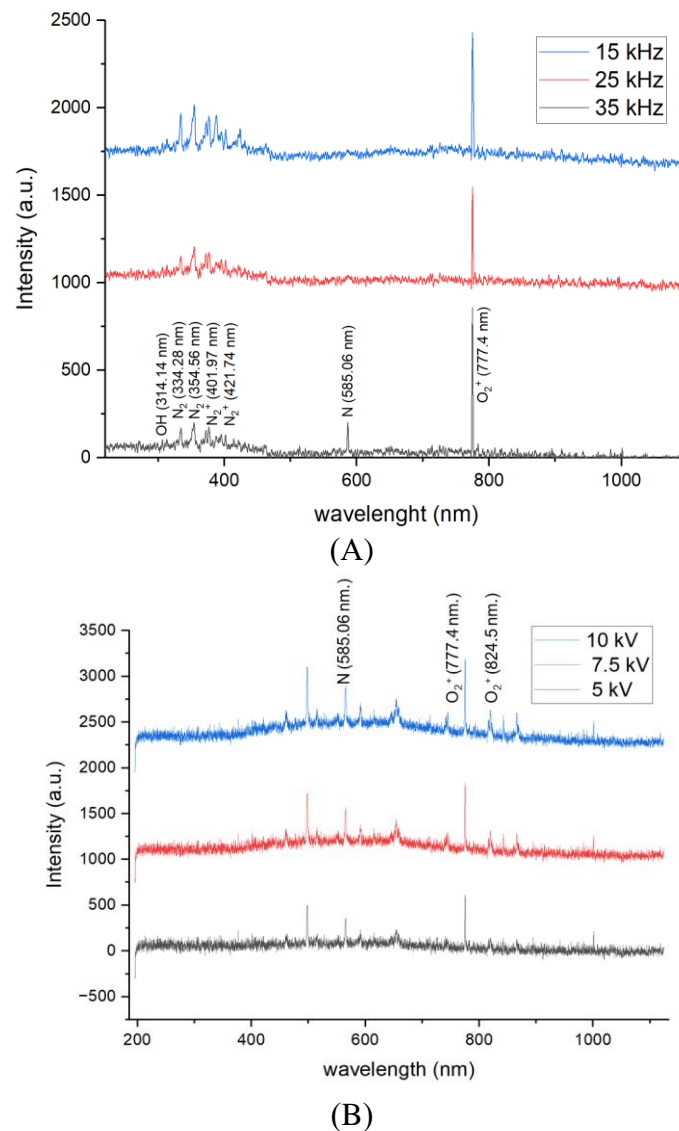


Figure 4.

Plots of OES spectra in board wavelength comparing OES spectra of the DBD plasma at (A) varying frequencies and (B) varying voltages.

Table 1
The plasma parameter at varying voltages and frequencies.

| Voltage (kV) | Frequency (kHz) | T_e (eV) | n_e (10^{16} m^{-3}) |
|-----------------|--------------------|------------------|---------------------------------------|
| 5 | 35 | 1.48 ± 0.054 | 1.97 ± 0.074 |
| 7.5 | 35 | 1.51 ± 0.035 | 2.45 ± 0.054 |
| 10 | 35 | 1.54 ± 0.047 | 3.76 ± 0.064 |
| 10 | 15 | 1.52 ± 0.051 | 3.46 ± 0.084 |
| 10 | 25 | 1.54 ± 0.037 | 3.54 ± 0.087 |

3.2 Design and Analyze of Airflow

The design of the prototype air purifier with DBD array is illustrated in Figure 5. A pair of blowers with controllable speeds ranging from 0 - 1000 RPM was installed along with 3 sets of DBD modules in front of each outlet channel. Each DBD module was vertically stacked up on top of each other with a 20 mm gap along the outlet channel. The air purifier was designed to operate with a blower to draw the air into the device and then passes through the DBD array. According to the trajectory simulation result in Figure 6, the air drawn into the device circulates due to the blower's turbulence and then compresses within the unit, resulting in the directed flow of air toward the outlet where DBD array was positioned. The air was then expelled through an outlet. The test environments had a volume of 120 m^3 , equivalent to 4237.76 ft^3 . To determine the optimal airflow velocity for full air circulation throughout the room within 10 minutes, the simulation indicated that an airflow rate of 423.76 CFM was required.

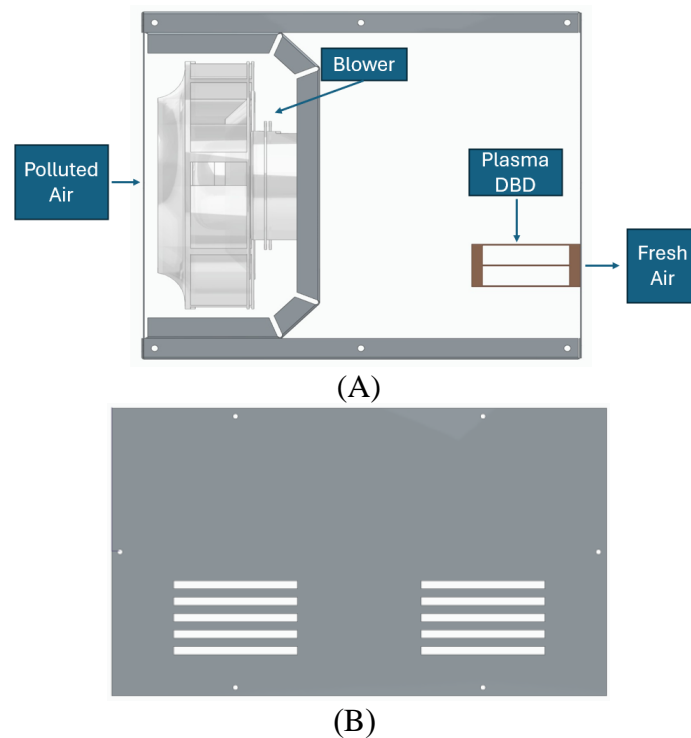


Figure 5.

The structure of the air purifier integrated with the DBD array on (A) side view and (B) outlet in front panel of air purifier.

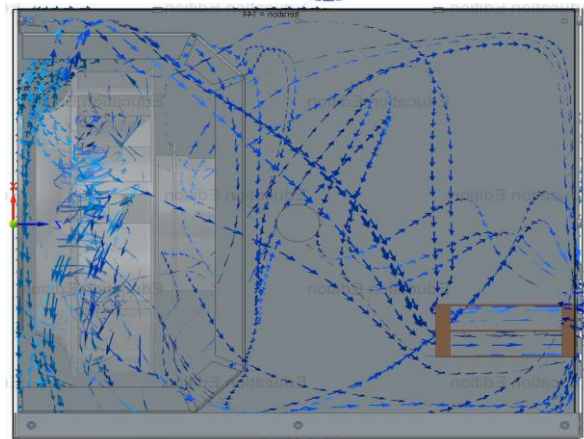


Figure 6.

The airflow patterns obtained from the trajectory simulation results.

3.3 Effect of Airflow Rate on Plasma Parameter

The airflow rates of the air brought by the blower inside the air purifier were varied at 400, 600, and 800 CFM to observe the OES spectra of the DBD plasma generated during the blower operation. In Figure 7, the result presents the spectral line of plasma which is used for calculation of T_e and n_e . The results of the calculation shown in table 2 reveal that the variations airflow rates do not affect the plasma parameters as the atmospheric plasma tends to require a high-power source and strong gas flow relative to its aperture for the flow rate to be taken into consideration like in the case of plasma jet [15]. Hence, the DBD plasma array situated inside the large chamber with several outlets could not accumulate particles to take advantage of airflow. However, the airflow rate can play a significant role in terms of air circulation rate which affects the contact time of plasma's product and pathogens.

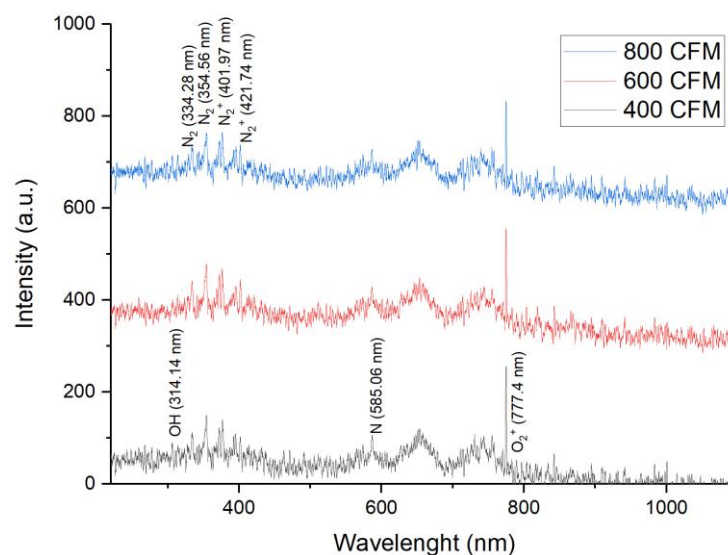


Figure 7.

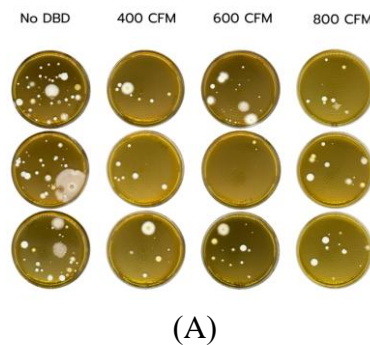
A comparative graph of the plasma spectral lines at different airflow rates.

Table 2
The properties of plasma at different airflow rates.

| CFM | T_e (eV) | n_e (10^{16} m^{-3}) |
|-----|------------------|---------------------------------------|
| 400 | 1.46 ± 0.031 | 3.47 ± 0.051 |
| 600 | 1.51 ± 0.035 | 3.41 ± 0.072 |
| 800 | 1.54 ± 0.024 | 3.35 ± 0.043 |

3.4 Antibacterial Activity

An indoor room measuring up to $8 \text{ m} \times 6 \text{ m} \times 2.5 \text{ m}$ was used as a test environment for 1 hour during the activation of the air purifier equipped with a DBD array, operating at 10 kV, 15 kHz, and 480 W. The variations of the airflow rates of 400, 600, and 800 CFM were used to assess the impact of the plasma generated by the up-scaled DBD module on the elimination of airborne pathogens in 48 m^2 room. Results presented in Figure 8 show the amount of mold and bacteria counted in CFU under different conditions. Without DBD plasma treatment, the counts for mold were 30, 22, and 17 CFU, while bacterial counts were 14, 8, and 10 CFU. With DBD plasma treatment at 400 CFM, mold counts decreased to 8, 7, and 7 CFU, while bacterial counts reduced to 0 CFU across all measurements. At 600 CFM, counts of mold were recorded as 24, 2, and 13 CFU and bacterial counts remained at 0 CFU. Under the 800 CFM airflow rate, mold counts were 9, 11, and 9 CFU, and bacterial counts were 0, 1, and 1 CFU. These reduction is equated to 41% and 99% decrease in pathogenic counts for mold and bacteria, respectively. The significance of the comparison between the unsanitized and DBD plasma-sanitized airborne pathogenic samples can be summarized in table 3. For the mold comparison, the reduction of mold is significant because the P-value of each condition in comparison to untreated control samples are 0.012, 0.014, and 0.04 for DBD treated samples under 400, 600, and 800 CFM flow rate in order, which lower than 0.05 with 95% confidence. In terms of Bacteria, it shows that the P-value of each pair of untreated control samples against DBD treated samples under 400, 600, and 800 CFM flow rates are 0.00014, 0.00014 and 0.0023 in order, which are extremely significant difference. This reduction is attributed to the products of DBD plasma like reactive oxygen species and reactive nitrogen species, including ozone, hydroxyl radicals, hydrogen peroxide [17], as well as UV emissions, which contribute to the pathogen inactivation through the extraction of protein from pathogens cell membrane [17]. The higher antipathogenic effectiveness at a lower airflow rate can be attributed to longer contact time between DBD plasma's byproduct and airborne pathogens, hence a higher chance for pathogens membrane and free radicals. Meanwhile, the comparison between each airflow rate condition is not significantly different from each other as represented by their P-values which are significantly higher than 0.05.



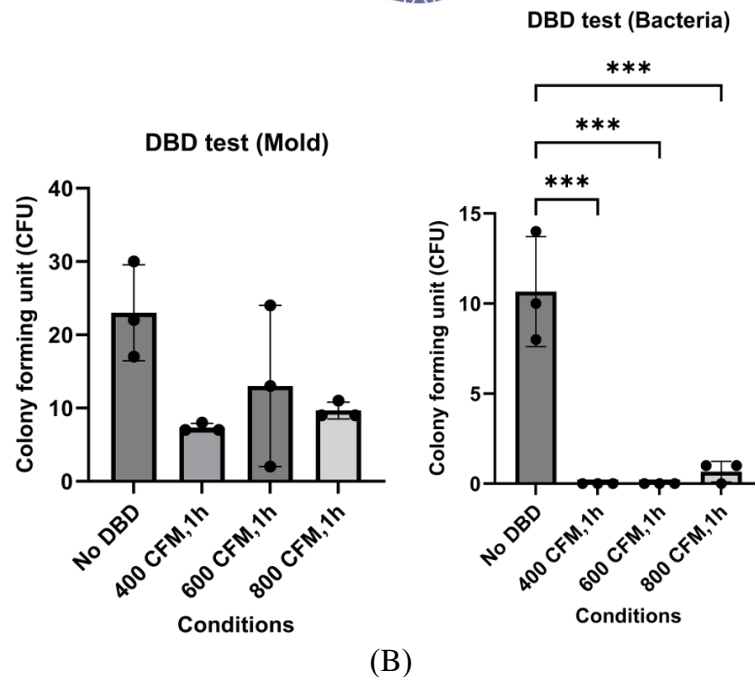


Figure 8.

(A) Culture result of airborne pathogens along with (B) ANOVA plots for effect of DBD plasma under various airflow rate on airborne pathogens.

Table 3.

Tukey Simultaneous Tests for Difference of means of Mold and Bacteria.

| Comparison condition | P-value (Mold) | P-value (Bacteria) |
|--------------------------|----------------|--------------------|
| 400 CFM – No DBD | 0.012 | 0.00014 |
| 600 CFM – No DBD | 0.014 | 0.00014 |
| 800 CFM – No DBD | 0.040 | 0.00023 |
| 600 CFM – 400 CFM | 0.999 | 1 |
| 800 CFM – 400 CFM | 0.798 | 0.95 |
| <u>800 CFM – 600 CFM</u> | <u>0.869</u> | <u>0.95</u> |

4. Conclusion

This research was a study about the optimization of DBD plasma's parameters for usage in the classroom through variations of voltage and frequency as well as the effect of different airflow rates on the antimicrobial activity of DBD plasma. The DBD plasma module was able to operate at atmospheric pressure and exhibited a glow discharge. Increment of the voltage led to a rise in both T_e and n_e . When the input of 10 kV voltage and 15 kHz frequency was applied, the T_e was found to be 1.52 ± 0.051 eV, and the n_e was $3.46 \pm 0.084 \times 10^{16} \text{ m}^{-3}$. In contrast, increasing the plasma frequency did not significantly affect T_e and n_e . However, the increasing frequency could impact plasma stability by increasing the potential of sparking.

Hence, the input of 10 kV voltage and 15 kHz frequency is the most suitable parameter. Additionally, the DBD array was installed into a prototype air purifier and tested in 48 m² room for its antipathogenic effectiveness. The controlled airborne pathogenic samples had mold counts of 30, 22, and 17 CFU and bacterial counts of 14, 8, and 10 CFU. After plasma treatment under conditions of 400 CFM flow rate, mold counts decreased to the least amount of 8, 7, and 7 CFU while bacterial counts dropped to roughly 0 for all different airflow rate cases, achieving a reduction of mold and bacteria by 41% and 99%, respectively. These findings showed promising potential for air purification applications by effectively reducing pathogenic microorganisms indicating the potential for the development of DBD modules into industrial-scale production and household air purifiers in the future.

Acknowledgements

This research was supported by Bitwise (Thailand) Co., Ltd., and Higher Education for Industry Consortium (Hi-FI) Under Experiential Learning Program, Office of The Permanent Secretary (OPS), Ministry of Higher Education, Science, Research and Innovation

Reference

1. Nanna N, Laosuk T, Borowrnpornmetee N, Promros N, Paosawatyanong B. Proceeding of the 5th CRU-NCST. 2022;342-347.
2. Žigon J, Petrič M, Dahle S, Ayata Ü, Zaplotnik R. Proceeding of In 3rd Niedersächsisches Symposium Materialtechnik, Clausthal. 2019;14:559-1–559-14
3. Timmermann E, Prehn F, Schmidt M, Höft H, Brandenburg R, Kettlitz M. J Phys D Appl Phys. 2018;51:164003-1–164003-10
4. Tang T.Y, Kim H.S, Kim G.H, Lee B, Lee H.J. AIP Adv. 2020;10:125218-1–125218-12.
5. Portugal S, Roy S, Lin J. Sci Rep. 2017;7:6388-1–6388-11.
6. Masruroh, Santjojo D.J.D.H, Abdurrouf, Abdillah M.A, Padaga M.C, Sakti S.P. Mater. Sci. Eng. 2019;515:012061-1–012061-9.
7. Teli M.D, Samanta K. K, Pandit P, Basak S, Chattopadhyay S. K. Fibers Polym. 2015;16:2375–2383.
8. Rezaei F, Abbasi-Firouzjah M, Shokri B. J Phys D Appl Phys. 2014;47:085401-1–085401-10.
9. Priya Arjunan K, Morss Clyne A. Plasma Process Polym. 2011;8:1154–1164.
10. Sabah Mazhir N, Khalaf Mohammed K, Taha Sarah K, Mohsin Hussein K. IJERT. 2018;7:1177–1180.
11. Choi E. H, Kaushik N. K, Hong Y. J, Lim Jun S, Choi Jin S, Han I. J. Korean Phys. Soc. 2022;80:817–851.
12. Offerhaus B, Kogelheide Friederike, Jalat Delawar, Bibinov N, Schulze Julian, Stapelmann Katharina, Awakowicz Peter. J. Appl. Phys. 2019;126:193301-1–193301-9.
13. Porjai P, Wattanawikkam C, Barnthip N, Pavasupree S, Jitjing P, Boonyawan D, Kachayut K, Suranaree J. Sci. Technol. 2023;30:2-12.
14. Deng X. T, Kong M. G. IEEE Trans. Plasma Sci. 2004;32:1709-1715.
15. Aadim Kadhim A, Mazhir Sabah N, Abdalameer Nisreen Kh, Ali Alyaa H. IOP Conf. Ser.: Mater. Sci. Eng. 2018;987:012020-1–012020-10.
16. Kostov K.G, Rocha V, Koga-Ito C.Y, Matos B.M, Algatti M.A, Honda R.Y, Kayama, M.E, Mota R.P. Surf. Coat. Technol. 2010;204:2954–2959.
17. Moisan M, Barbeau J, Crevie M.-C, Pelletier J, Philip N, Saoudi B. Pure Appl. Chem. 2002;74:349-358.



SIMPLE HYDROTHERMAL-MICROWAVE METHOD TO SYNTHESIZE MANGANESE PYROPHOSPHATE AND ELECTROCHEMICAL PERFORMANCE

Ratchadaporn Puntharod^{1,*}, Pattraporn Surin¹, Weerinrada Tapala¹, Nattapol Laorodphan²

¹Department of Chemistry, Faculty of Science, Mae Jo University, Chiangmai, 50290, Thailand

²Department of Innovation of Industrial Chemistry, Faculty of Science, Mae Jo University, Chiangmai, 50290, Thailand

*e-mail: ratchadaporn_p@mju.ac.th

Abstract:

Manganese pyrophosphate as chemical formula $\text{Mn}_2\text{P}_2\text{O}_7$, was synthesized by hydrothermal-microwave method at 400, 600 and 800 watt for 5 and 10 min. The powders were calcined at 500 °C for 5 hr. The starting materials were Na_2HPO_4 and MnSO_4 with deionized water as solvent and without any surfactant and without acid or base. The watt and heating time affected the morphology and particle size. Fourier transform infrared spectroscopy was analyzed the stretching vibration of P–O of $(\text{P}_2\text{O}_7)^{4-}$. The X-ray diffraction was confirmed the phase of manganese pyrophosphate as monoclinic. The manganese pyrophosphate with smallest particle and agglomerate show the highest electrochemical properties with specific capacitance was 47 F.g^{-1} .

Introduction:

The chemical formula of metal pyrophosphate is $\text{M}_2\text{P}_2\text{O}_7$ (where M = Mg, Ca, Mn, Co, Ni, Zr). Normally, the oxidation state of the metal is +2. Metal pyrophosphates have great advantages such as inexpensive and naturally abundant starting materials, easy synthesis, extensive working potential, and abundant crystal chemistry¹. The applications of pyrophosphates include use as a catalyst, such as vanadyl pyrophosphate $(\text{VO})_2\text{P}_2\text{O}_7$ ², an adsorbent like zirconyl pyrophosphate (ZrP_2O_7) , antiferromagnetic materials such as $\text{Mn}_2\text{P}_2\text{O}_7$ ³, and as anode material in lithium batteries, similar to MnP_2O_7 with initial reversible capacities of 440-330 mAh.g^{-1} ⁴. Metal pyrophosphates have been synthesized using various methods and precursor compounds. Amorphous $\text{Ni}_2\text{P}_2\text{O}_7$ microstructures were synthesized by stirring nickel acetate and ammonium phosphate to obtain $\text{NH}_4\text{Ni}(\text{PO})_4 \cdot 6\text{H}_2\text{O}$. The $\text{NH}_4\text{Ni}(\text{PO})_4 \cdot 6\text{H}_2\text{O}$ microstructure was then calcined at 700°C⁵. Porous $\text{Ni}_2\text{P}_2\text{O}_7$ nanowires were prepared by calcining precursors of $\text{NiNH}_4\text{PO}_4 \cdot \text{H}_2\text{O}$ nanowires at 600 °C⁶.

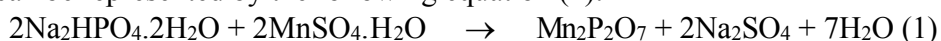
The method used to synthesize the particles was a parameter influencing the morphology and particle size of the metal oxide. The morphology of the particles was a parameter influencing the properties of manganese oxide, such as its electrochemical properties as a lithium cathode battery and anode battery. $\text{Mn}_2\text{P}_2\text{O}_7 \cdot 2\text{H}_2\text{O}$ was synthesized by dissolving manganese chloride and sodium pyrophosphate in sulfur dioxide and bubbling carbon dioxide through the solution. The microcrystals were under 2 μm , and the prismatic crystals were 0.1 mm in length⁷. Porous $\text{Mn}_2\text{P}_2\text{O}_7$ structure was prepared by thermal treatment of $\text{MnPO}_4 \cdot \text{H}_2\text{O}$ at 600 °C. The particles were agglomerated with small particles in the range of 30-50 nm⁸. $\text{Mn}_2\text{P}_2\text{O}_7$ polyhedral was synthesized using manganese nitrate hydrate and phosphoric acid in nitric acid, followed by calcination at 800 °C for 3 hours. The small and large particles were in the range of 100-200 nm and > 200-500 nm, respectively⁹. Porous $\text{Mn}_2\text{P}_2\text{O}_7$ nanoplate was obtained by calcining $\text{NH}_4\text{Mn}_2\text{PO}_4 \cdot \text{H}_2\text{O}$ nanoplates at 500°C. The crystal structure was cubic $\text{Mn}_2\text{P}_2\text{O}_7$ (JCPDF card No: 29-0891)¹⁰. In all reports, the crystal structure of $\text{Mn}_2\text{P}_2\text{O}_7$ was observed to be monoclinic and cubic. It can be noticed that

the particle size of $\text{Mn}_2\text{P}_2\text{O}_7$ was in the nanometer range except using manganese chloride and sodium pyrophosphate dissolved with sulfur dioxide, which provided particle sizes in the micron range. The annealing MnH_2PO_4 at 700 °C for 2 hours in an argon-filled tube furnace and transform into $\text{Mn}_2\text{P}_2\text{O}_7$ nanoparticle¹¹.

The findings of the simple method to synthesize manganese pyrophosphate were studied. Additionally, the results could provide ideas to researchers for synthesizing manganese pyrophosphate and their electrochemical performance. This research aimed to synthesize manganese pyrophosphate using the hydrothermal-microwave method followed by calcination without surfactant and without acid or base. The crystalline powder was identified through Fourier transform infrared spectroscopy, which revealed its vibrational characteristic. X-ray diffraction confirmed the phase of manganese pyrophosphate. The morphology of the particles was analyzed using scanning electron microscopy combined with electron dispersive spectroscopy. Also, the electrochemical performance was presented in term of specific capacitance analyzed by cyclic voltammetry technique.

Methodology:

Manganese pyrophosphate, $\text{Mn}_2\text{P}_2\text{O}_7$, was synthesized using the hydrothermal-microwave method. The raw materials used were manganese sulfate monohydrate ($\text{MnSO}_4 \cdot \text{H}_2\text{O}$, Ajax Finechem) and sodium hydrogen phosphate (Na_2HPO_4 , RCI Labscan). Firstly, 1.69 g of $\text{MnSO}_4 \cdot \text{H}_2\text{O}$ was dissolved in 10 mL of deionized water, and then 1.78 g of Na_2HPO_4 was added to another 10 mL of deionized water. The two solutions were mixed and transferred to a 100 mL Teflon tube, which was then sealed and placed in a microwave oven. The heating power varied at 400, 600, and 800 watts for 5 and 10 minutes. The precipitate obtained was filtered and washed with 10 mL of ethanol and 10 mL of deionized water, followed by drying in air and subsequent calcination at 500 °C for 5 hours. The resulting pale pink powder was analyzed for vibrational bonds using a Fourier transform infrared spectrometer (Spectrum RXI, Perkin Elmer) with a KBr pellet, at a resolution of 4 cm^{-1} and 32 scans. X-ray diffraction (D2 Phase, Bruker) confirmed the phase of manganese pyrophosphate. The morphology of the particles was analyzed using a scanning electron microscope/energy dispersive spectrometer (TESCAN Model VEGA 3, Czech Republic). The reaction can be represented by the following equation (1):



The electrochemical performance was evaluated utilizing cyclic voltammeter (PGSTAT128N, USA). The working electrode was nickel foam substrate in size of 1×2 cm and weighed. The 32 mg of active material ($\text{Mn}_2\text{P}_2\text{O}_7$), 4 mg of carbon black and 4 mg of polyvinylidene difluoride were mixed with 400 μL of N-methyl-2-pyrrolidone. After mixing, 70 μL of prepared solution was dropped onto the nickel foam and dried at 70 °C overnight. The prepared electrode was pressed at 10 MPa and recorded the weight of working electrode. The electrolyte solution was 1 M of potassium hydroxide (KOH, Ajax Finechem). The specific capacitance can be calculated with equation (2) by Yan *et.al*¹².

$$C = \frac{\int IdV}{vmV} \quad (2)$$

Where C is the specific capacitance (F g^{-1})
 I is the response current density (A cm^{-2})
 V is the potential (V)
 v is the potential scan rate (mV s^{-1}),
 and m is the mass of the electroactive materials in the electrodes (g)



Results and Discussion:

The starting materials were sodium hydrogen phosphate and manganese phosphate in a mole ratio of 1:1, heated by microwave at 400, 600, and 800 watts for 5 and 10 minutes. The pH of the mixed solutions before and after heating was 9. After calcination at 500°C for 5 hours, the resulting pale pink powder was analyzed for crystal structure using a powder X-ray diffractometer. The XRD patterns of the synthetic powder at 400-800 watts for 5 and 10 minutes are shown in Figures 1 and 2, respectively. XRD results exhibited the products as manganese pyrophosphate ($\text{Mn}_2\text{P}_2\text{O}_7$, PDF#00-029-0891). The crystal structure is monoclinic, with crystal parameters: $a=6.6360 \text{ \AA}$, $b=8.5840 \text{ \AA}$, $c=4.5457 \text{ \AA}$, $\alpha=90.0000^\circ$, $\beta=102.7800^\circ$, and $\gamma=90.0000^\circ$. Heating for 10 minutes provided sharper XRD peaks due to increased crystallinity, and the presence of sodium sulfate (Na_2SO_4 , PDF#01-075-0914) as a byproduct was observed, as shown in reaction (1). Its presence was likely due to improper washing.

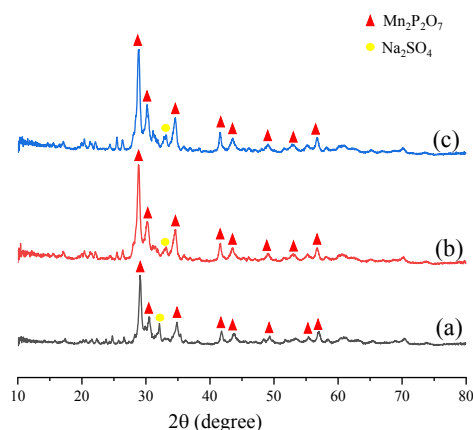


Figure 1. XRD of $\text{Mn}_2\text{P}_2\text{O}_7$ heating for 5 min at (a) 400 (b) 600 (c) 800 watt

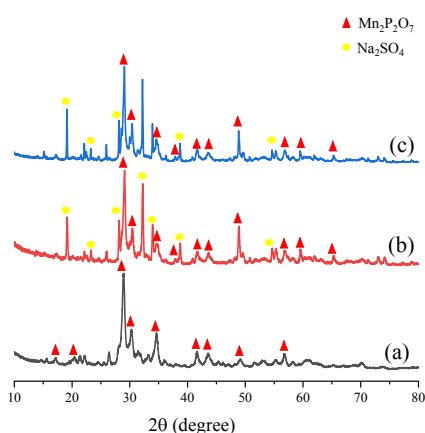


Figure 2. XRD of $\text{Mn}_2\text{P}_2\text{O}_7$ heating for 10 min at (a) 400 (b) 600 (c) 800 watt

The FTIR results of the synthetic powder at 400-800 watts for 5 and 10 minutes are shown in Figures 3 and 4, respectively. The broad vibrational band at $1,085\text{-}1,020 \text{ cm}^{-1}$ was assigned to the stretching vibration of O–P–O of $\text{Mn}_2\text{P}_2\text{O}_7$. The split peak in the region of $754\text{-}705 \text{ cm}^{-1}$ was assigned to the stretching vibration of the P–O–P bridge^{13,14}. The band in the region of $745\text{-}702 \text{ cm}^{-1}$ represented the deformation vibrations of $\text{P}_2\text{O}_7^{4-}$ ¹⁵.

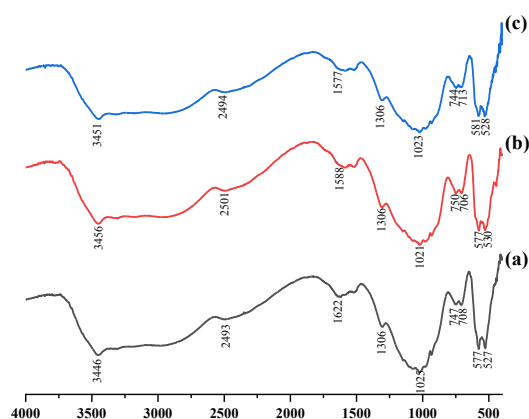


Figure 3. FTIR spectra of $\text{Mn}_2\text{P}_2\text{O}_7$ heating for 5 min at (a) 400 (b) 600 (c) 800 watt

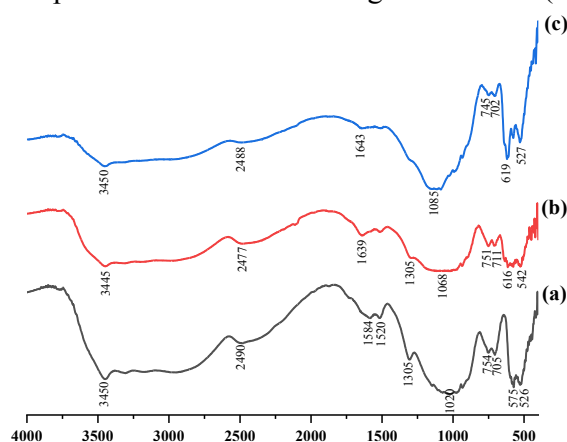


Figure 4. FTIR spectra of $\text{Mn}_2\text{P}_2\text{O}_7$ heating for 10 min at (a) 400 (b) 600 (c) 800 watt

SEM image of $\text{Mn}_2\text{P}_2\text{O}_7$ heated at 400-800 watts for 5 minutes in Figure 5. The morphology of $\text{Mn}_2\text{P}_2\text{O}_7$ resembled hexagonal prisms with a length of 5 μm . The particle grains were quite dispersed. In Figure 6(a), heating at 400 watts for 10 minutes resulted in $\text{Mn}_2\text{P}_2\text{O}_7$ with a morphology similar to hexagonal prisms, with a length of 4 μm . However, in Figure 6(b) and (c), heating at 600 and 800 watts for 10 minutes led to particle grain accumulation, with a particle size of 2 μm . As the heating time increased, the particle size decreased due to increased microwave absorption¹⁶. Under all conditions, $\text{Mn}_2\text{P}_2\text{O}_7$ was synthesized by hydrothermal-microwave methods and calcined at 500°C, resulting in particle sizes in the microstructure range. In contrast, previous research on $\text{Mn}_2\text{P}_2\text{O}_7$, synthesized using Mn metal powder and P_2S_5 in ethylene glycol by solvothermal methods at 190-220 °C, revealed nanostructured materials. The morphology of the products included flower-like microspheres with diameters of about 2-5 μm and aggregation of many nanoparticles with thicknesses of 20-40 nm, exhibiting a monoclinic crystal structure⁴. This suggests that the hydrothermal-microwave method without surfactant and alkali base affects the shape and size of particles but does not affect the crystal structure.

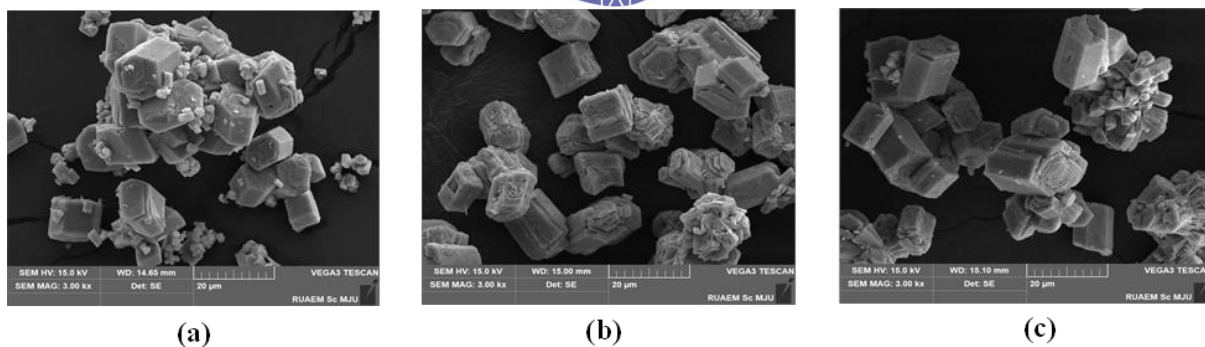


Figure 5. SEM of $\text{Mn}_2\text{P}_2\text{O}_7$ heating for 5 min at (a) 400 (b) 600 (c) 800 watt

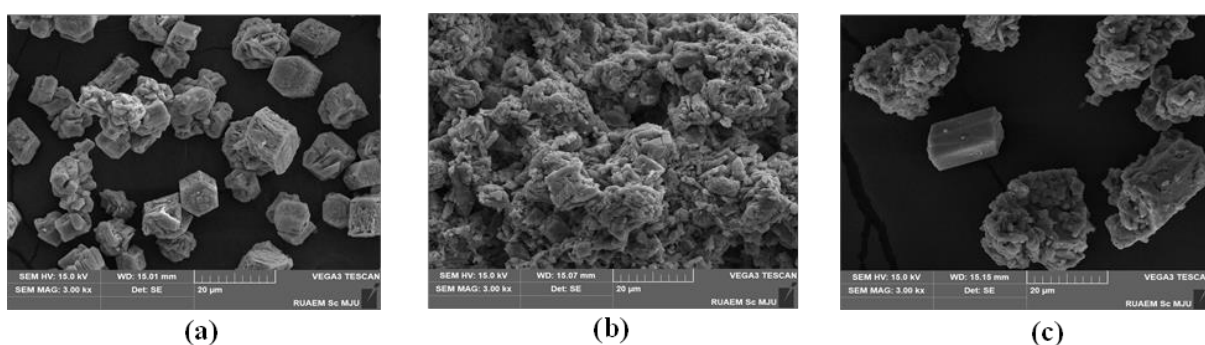


Figure 6. SEM of $\text{Mn}_2\text{P}_2\text{O}_7$ heating for 10 min at (a) 400 (b) 600 (c) 800 watt

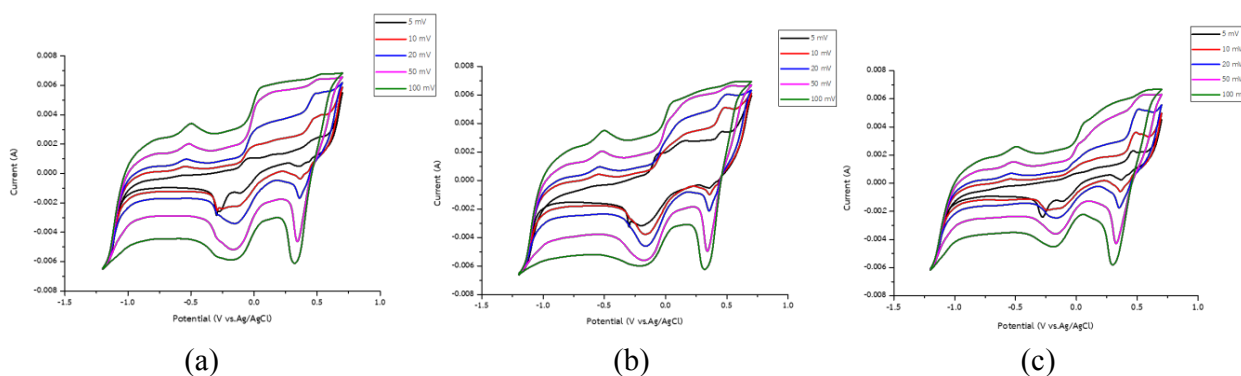


Figure 7. Cyclic voltammograms of $\text{Mn}_2\text{P}_2\text{O}_7$ heating for 10 min at (a) 400 (b) 600 (c) 800 watt

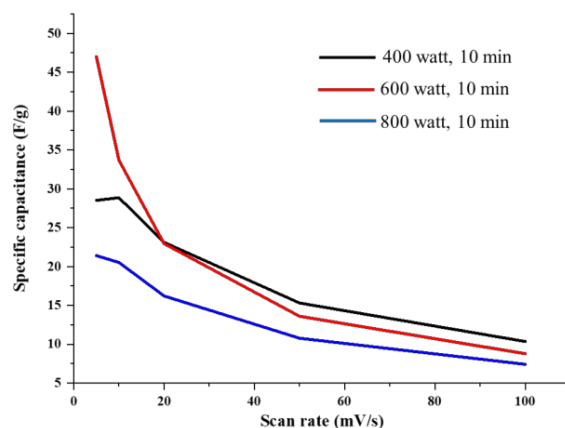


Figure 8 Scan rate of $\text{Mn}_2\text{P}_2\text{O}_7$ heating for 10 min at 400, 600 and 800 watts

Referring to XRD results and morphology of $\text{Mn}_2\text{P}_2\text{O}_7$, under heating for 10 minutes could provide more purity and crystallinity of $\text{Mn}_2\text{P}_2\text{O}_7$ including the smaller of particle size the heating for 5 minutes. Those products heating for 10 minutes were selected to analyze the electrochemical performance utilizing cyclic voltammetry shown in Figure 7. The scan rate of CV curves was from 5 to 100 mV s^{-1} . The scan rate of 5 mV s^{-1} of each $\text{Mn}_2\text{P}_2\text{O}_7$ were the highest specific capacitance shown in Figure 8. Except $\text{Mn}_2\text{P}_2\text{O}_7$ heating for 400 watt, the scan rate 5 and 10 are very closely specific capacitance. The specific capacitance of $\text{Mn}_2\text{P}_2\text{O}_7$ heating at 400, 600 and 800 watts were 28.52, 47.01 and 21.40 F g^{-1} , respectively. The particle size of $\text{Mn}_2\text{P}_2\text{O}_7$ at 600 watts show the smallest particle size. Also, it has more porous which could effectively promote the transport of electrons and ions¹⁷. It is reasonable that $\text{Mn}_2\text{P}_2\text{O}_7$ heating at 600 watt for 10 minutes performs the highest specific capacitance. Comparing the specific capacitance of $\text{Mn}_2\text{P}_2\text{O}_7$ synthesized by hydrothermal process and chemical polymerization was 64 F g^{-1} ¹⁸. Although, the specific capacitance of $\text{Mn}_2\text{P}_2\text{O}_7$ of this work is quite minimal value. The advanced point is the method to synthesize is simple, environmental friendly and less consuming the precursors.

Conclusion:

Manganese pyrophosphate, $\text{Mn}_2\text{P}_2\text{O}_7$, was successfully synthesized via simple method namely the hydrothermal-microwave method without surfactant and alkali base and followed by calcination at 500°C. The resulting pale pink $\text{Mn}_2\text{P}_2\text{O}_7$ was determined, through XRD analysis, to possess a monoclinic crystal structure. Vibrational bands observed in FTIR spectra confirmed the presence of P–O bonds characteristic of pyrophosphate. SEM analysis revealed a hexagonal prismatic morphology with varying degrees of agglomeration depending on the microwave synthesis wattage. $\text{Mn}_2\text{P}_2\text{O}_7$ heating at 600 watt for 10 minutes performs the highest the specific capacitance was 47.01 F g^{-1} .

Acknowledgements: The authors would like to thank Department of Chemistry, Faculty of Science, Mae Jo University for the laboratory facilities.

References:

1. Kulkarni A.A., Savekar V.A., Bhat T.S., Patil P.S., Energy Storage, 2022, 52, 104986.
2. Tabanelli T., Mari M., Folco F., Tanganelli F., Puzzo F., Setti L., Cavani F., Appl. Catal. A: Gen., 2021, 619, 118139.
3. Fowles D.C., Stager C.V., Can. J. Phys., 1972, 50, 2681-2687.
4. Wang S., Jiang X., Du G., Guo Z., Jang J., Kim S., Mater. Lett., 2011, 65, 3265-3268.



5. Pang H., Zhang Y., Run Z., Lai W., Huang W., *Nano Energy*, 2015, 17, 339-347.
6. Zhou Y., Liu C., Li X., Sun L., Wu D., Li J., Huo P., Wang H., *J. Alloys Compd.*, 2019, 790, 36-41.
7. Schneider S., Collin R.L., *Inorg. Chem.*, 1973, 12(9), 2136-2139.
8. Boonchom B., Youngme S., Maensiri S., Danvirutai C., *J. Alloys Compd.*, 2008, 454, 78-82.
9. Boonchom B., Baitahe R., *Mater. Lett.*, 2009, 63, 2218-2220.
10. Pang H., Yan Z., Wang W., Wei Y., Li X., Li J., Chen J., Zhang J., Zheng H., *Int. J. Electrochem. Sci.*, 2012, 7, 12340-12353.
11. Yang Y., Wang B., Zhu J., Zhou J., Xu Z., Fan L., Zhu J., Podila R., Rao A.M., Lu B., *ACS Nano*, 2016, 10, 5516-5524.
12. Yan J., Wei T., Qiao W., Shao B., Zhao Q., Zhang L., Fan Z., *Electrochim. Acta.*, 2010, 55 (23), 6973-6978.
13. Danvirutai C., Noisong P., *J. Therm. Anal. Calorim.*, 2010, 100, 117-124.
14. Noisong P., Danvirutai C., *Spectrochim. Acta A Mol. Biomol. Spectrosc.*, 2010, 77(4), 890-894.
15. Maarouf I., Oulmekki A., Toyir J., Lefebvre F., Harrach A., Ijjaali M., *JMES*, 2017, 8(8), 2722-2728.
16. Crane C.A., Pantoya M.I., Weeks B.L., Saed M., *Powder Technol.*, 2014, 256, 113-117.
17. Toghan A., Khairy M., Kamar E.M., Mousa M.A., *JMR&T*, 2022, 19, 3521-3535.
18. Boopathiraja R., Vadivel S., Parthibavarman M., Prabhu S., Ramesh R., *Surfaces and Interfaces*, 2021, 26, 101409.

B-BIOLOGICAL SCIENCES



Alteration of O-GlcNAcylation affects chemotherapy drug responses in colorectal cancer cell lines

Thirasak Bunsuk,¹ Penchatr Diskul Na Ayudthaya,² Photsathorn Mutapat², Juthamard Chantaraamporn², Jisnusun Svasti^{1,2}, Voraratt Champattanachai^{1,2} *

¹Applied Biological Sciences: Environmental Health Program, Chulabhorn Graduate Institute, Bangkok 10210, Thailand

²Laboratory of Biochemistry, Chulabhorn Research Institute, Bangkok 10210, Thailand

*e-mail: voraratt@cri.or.th

Abstract:

Colorectal cancer (CRC) is a leading cause of cancer-related morbidity and mortality. O-GlcNAcylation, a post-translational modification of N-acetylglucosamine (GlcNAc) at serine/threonine residues of cytoplasmic and nuclear proteins, has been shown to be up-regulated and associated with tumor progression in various cancers. However, the contribution of O-GlcNAcylation related to chemotherapy drug responses in cancer especially in CRC is rarely investigated. This study aimed to investigate the role of O-GlcNAcylation in modulating the efficacy of oxaliplatin (OXA), a first-line chemotherapy drug for CRC using a SW620 cell line as an *in vitro* model. SW620 cells were treated with various concentrations of OXA to evaluate its impact on O-GlcNAcylation and cell viability. OXA led to a reduction of cell viability with IC₅₀ of 10 μ M. Interestingly, treatment of OXA resulted in an increase of O-GlcNAcylation level up to 10 μ M in a dose- and time-dependent manner. To reduce O-GlcNAcylation level, RNA interference against O-GlcNAc transferase (OGT), the enzyme responsible for O-GlcNAcylation, was introduced in SW620 cells. OGT Knockdown sensitized SW620 cells to OXA treatment, enhancing cytotoxicity. Conversely, addition of Thiamet-G (TMG), an inhibitor to block O-GlcNAcase (OGA) resulting in an increase of O-GlcNAcylation level, revealed higher resistance of OXA treatment. These findings suggest that the modulation of O-GlcNAcylation can influence CRC cellular responses to chemotherapy, highlighting a potential strategy for improving treatment efficacy by targeting the O-GlcNAcylation in combination of chemotherapy drugs.

Introduction:

Colorectal cancer (CRC) is the third rank of diagnosed cancers, following lung and female breast cancer, and the second rank leading cause of cancer-related deaths, after lung cancer (1). It primarily affects the elderly, with most cases occurring in people over 50 years of age (2). CRC development takes over a decade and it is driven by the accumulation of numerous mutations in cells within intestinal tissues, resulting in uncontrollable cell expansion and transformation into malignant tumor. Once cancer cells are formed at the primary site, they can invade to neighbor cells and metastasize to distant (secondary) sites such as the liver, brain (3).

Changes in glucose metabolism in cancer affect several metabolic pathways, including the hexosamine biosynthesis pathway (HBP) (4). The end product of HBP is N-acetylglucosamine (GlcNAc) which is a substrate for both classical glycosylation and O-GlcNAcylation. Unlike classical glycosylation, which occurs in endoplasmic reticulum and Golgi apparatus, O-GlcNAcylation involves attachment of a single GlcNAc to serine and threonine residues of cytoplasmic and nuclear proteins (5). This modification is regulated by two key enzymes; O-GlcNAc transferase (OGT) and O-GlcNAcase (OGA), which are responsible for adding and removing sugar donors, respectively. Previously, our group and

others showed that the levels of OGT and O-GlcNAcylation were increased in CRC tissues compared to those of normal tissues (6, 7). In addition, our group also reported that O-GlcNAcylation and OGT levels were elevated in two CRC cell lines, SW480 (non-metastatic clone) and SW620 (metastatic clone) which are derived from the same patient, in comparison to those of normal colon epithelial cells, CCD841 CoN (8). Moreover, OGT knockdown revealed more dramatically reduce cancer colony formation of SW620 when compared to that of SW480, indicating that O-GlcNAcylation and OGT may play important roles in cancer progression, especially in the metastatic phenotype.

Several lines of evidence demonstrate that chemotherapy treatments enhanced the global O-GlcNAcylation and this augmentation may associate with stress responses (9). Therefore, the aim of this research is to test our hypothesis whether oxaliplatin, the first-line chemotherapy drug used for CRC patients, can activate O-GlcNAylation. In addition, we ask to determine whether altering O-GlcNAcylation level (both up and down) has any synergistic effect when combined with OXA treatment using in SW620 as an *in vitro* model study.

Methodology:

Cell culture

SW620 cells were purchased from the American Type Culture Collection (ATCC, USA), and cultured in completed RPMI 1640 (Thermo Fisher Scientific, USA), supplemented with 10% Fetal bovine serum (HyClone, USA), and 1% Antibiotic-Antimycotic (Thermo Fisher Scientific, USA). Cells were cultivated in 5% CO₂ at 37°C humidified incubator and sub-cultured by trypsinization when reached 70-80% confluency.

Cell viability assay

Cell viability was assessed using the CellTiter 96® AQueous One Solution MTS assay [3-(4,5-dimethylthiazol-2-yl)-5-(3-carboxymethoxyphenyl)-2-(4-sulfophenyl)-2H-tetrazolium], purchased from Promega, USA. This assay is based on the reduction of the MTS tetrazolium compound by metabolically active cells into a colored formazan product, which is soluble in the culture medium. Briefly, SW620 cells (5,000 cells/well) were seeded in 96-well microplates. After 24 h of culturing, cells were treated with oxaliplatin (OXA; MedChemExpress, USA) at various concentrations (0.01, 0.1, 1, 10, and 100 µM) for 48 h. For time-course studies, cells were treated with 10 µM OXA and harvested at 6, 12, 24, 48, and 72 h. Following treatment, MTS reagent (20 µL) was added to each well and incubated for 2 h at 37°C. Absorbance was measured at 490 and 650 nm using a microplate reader. Absorbance values were normalized to those of untreated controls to determine relative cell viability.

Evaluation of OGT and O-GlcNAcylation levels

The levels of OGT and O-GlcNAcylation were determined by immunoblotting as previously described (8). Briefly, cells (300,000 cells/well) were cultured in 6-well cell culture plates. At the end of treatments, cells were lysed using RIPA buffer containing 1% protease inhibitor cocktail (Sigma-Aldrich, USA). Protein concentration was measured by Bradford assay (Bio-Rad, USA). Protein samples (15-20 µg) were separated on 7.8% SDS-PAGE and transferred to PVDF membranes (Millipore, USA). Membranes were then blocked with 1% casein blocking buffer (Bio-Rad, USA). Primary antibodies; anti-O-linked N-Acetyl glucosamine antibody (RL2; 1:1,000 Abcam, UK), anti-N-Acetylglucosamine transferase antibody (OGT; 1: 1,000, Abcam, UK) and anti-β-actin (1: 20,000, Cell Signaling Technology, USA) were incubated overnight at 4°C. Immunoblots were developed with WesternBright ECL (Advansta, USA). The signals were captured and measured by an image analysis program ImageQuant LAS4000 (GE healthcare, USA). The level of O-GlcNAc modified proteins was



detected from all O-GlcNAc bands appeared from the immunoblots as previously mentioned (8). β -actin was used to compare protein loading of each sample.

Reduction of O-GlcNAcylation and OGT levels and combination treatments

To investigate the effect of O-GlcNAcylation and OGT reduction, SW620 cells were transfected with RNA interference against OGT gene as previously described (8). siOGT oligonucleotide of OGT (sense, 5'-UAAUCAUUUCAAUACUGCUUCUGC-3' and antisense, 5'-GCAGAAGCAGUUAUUGAAAUGAUUA-3'. and scramble negative control medium GC duplexes transfection were purchased from Invitrogen, USA. After one day of culturing, siRNA was transfected into SW620 cells using Lipofectamine™ 3000 Transfection Reagent (Invitrogen, USA) with manufacturer's instructions (Invitrogen, USA). Then, cells were incubated with the transfection mixtures and continually cultured for 48 h prior to treat with or without OXA for additional 48 h. At the end of time treatment, cell cytotoxicity and immunoblotting were examined as above mentioned.

Augmentation of O-GlcNAcylation level and combination treatments

To increase O-GlcNAcylation level, thiamet-G (TMG; MedChemExpress, USA), a potent inhibitor of OGA, was used. After one day of culturing, SW620 cells were pretreated with TMG at 10 and 50 μ M for 6 hours. Subsequently, cells were treated with or without OXA for additional 48 h. At the end of time treatment, cell cytotoxicity and immunoblotting were examined as above mentioned.

Statistical analysis

The statistical analysis was conducted using student t-test of Excel program. The statistical significance was defined as $P < 0.05$ and $P < 0.01$.

Results and Discussion:

Treatment of OXA in SW620 cells

SW620 cells were treated with various concentrations of OXA (0.01, 0.1, 1, 10, and 100 μ M) for 48 hours. The MTS assay demonstrated a dose-dependent decrease of OXA in cell viability, as shown in Figure 1A. This result indicates the cytotoxic nature of OXA, with greater cell death observed at higher concentrations. The IC_{50} value for OXA, which represents the concentration required to reduce cell viability by 50%, was approximately 10 μ M. To investigate the effects of OXA on O-GlcNAcylation level in SW620 cells, immunoblotting of O-GlcNAc (RL2) was performed. The analysis revealed a relative dose-dependent increase in O-GlcNAcylation level with OXA concentrations up to 10 μ M as shown in Figure 1B and 1C. This finding implies that OXA treatment induces an increase in O-GlcNAcylation, potentially as part of a cellular stress response. Previous studies have reported increased O-GlcNAcylation in response to numerous stresses, including chemotherapeutic drugs (10). In addition, a time-course study was conducted where SW620 cells were treated with 10 μ M OXA and harvested at different time points (6, 12, 24, 48, and 72 hours). The results showed a progressive increase in O-GlcNAcylation level with prolonged exposure to OXA as shown in Figure 1D and 1E. This indicates that continuous OXA treatment leads to an accumulation of cellular stress as well as O-GlcNAcylation level.

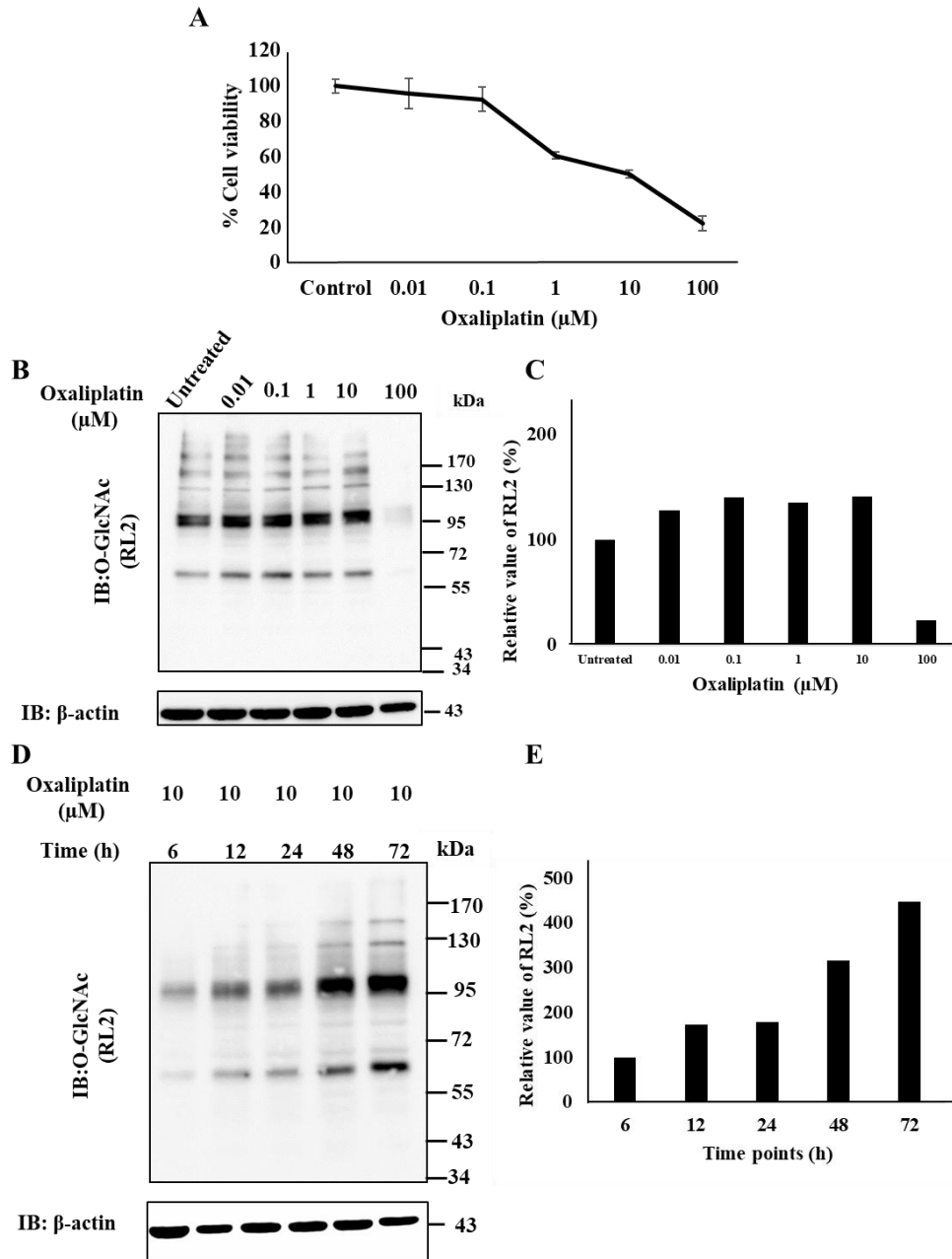


Figure 1: Cellular cytotoxicity and O-GlcNAcylation level of SW620 cells treated with OXA. (A) A graph demonstrated the cytotoxic effects of OXA in SW620 cells. Cells were treated with OXA at concentrations of 0, 0.01, 0.1, 1, 10, and 100 μM for 48 h. Cell viability was measured using the MTS assay, which assesses metabolic activity as an indicator of cell viability. Representative immunoblots (IB) of O-GlcNAc modified proteins detected by RL2 antibody and β -actin of (B) cells were treated with OXA at concentrations of 0, 0.01, 0.1, 1, 10, and 100 μM for 48 h and (D) cells treated with 10 μM OXA for 6, 12, 24, 48 and 72 h. Protein samples (20 μg) were separated by SDS-PAGE, transferred to a PVDF membrane, and probed with antibodies specific for O-GlcNAc (RL2) and β -actin used as a loading control. (C) and (E) Bar graphs represent the relative value of RL2 (%) of dose- and time-dependent experiments, respectively. The relative level of O-GlcNAc modified proteins was analyzed by normalization of the intensity of all O-GlcNAc bands divided by that of β -actin in each lane.



Reduced OGT expression using siOGT and OXA treatment in SW620 cells

To assess the effects of reduced O-GlcNAcylation level on cellular sensitivity to chemotherapy, SW620 cells were transfected with siOGT to knockdown OGT expression. Immunoblotting analysis confirmed a dramatic decrease in both OGT and O-GlcNAcylation levels in siOGT-transfected cells compared to siScramble cells as shown in Figure 2A and 2B. Furthermore, treatment with siOGT alone significantly reduce cell viability compared to that of the siScramble control group ($P < 0.001$). Interestingly, combining treatment of siOGT and 1 μM OXA treatment also significantly reduced cell viability compared to OXA treatment alone ($P < 0.01$) as shown in Figure 2C. These findings suggest that targeting O-GlcNAcylation may enhance chemotherapy efficacy by decreasing cancer cell resistance to chemotherapeutic agents, offering a potential strategy for improving treatment outcomes of CRC. A previous report also showed that reducing O-GlcNAcylation level in breast cancer led to inhibition of tumor growth both *in vitro* and *in vivo* (11). In addition, other research groups reported that chemotherapy can sensitize cancer cells to O-GlcNAcylation targeting through OGT inhibition or similar mechanisms. For instance, studies using RNA interference against OGT or OGT inhibitors to decrease O-GlcNAcylation have demonstrated decreased cell survival and enhanced therapeutic efficacy in response to various chemotherapeutic drugs (10, 12).

Increased O-GlcNAcylation level by TMG and OXA treatment in SW620 cells

To investigate the impacts of increased O-GlcNAcylation level on cell viability and cellular stress responses, SW620 cells were pretreated with 10 μM TMG for 6 h, followed by treatment with OXA at 1 μM for an additional 48 h. Immunoblotting analysis showed that TMG treatment increased O-GlcNAcylation levels as shown in Figure 3A and 3B, which may be associated with the observed increase in cell viability. SW620 cells were then treated with 10 μM TMG, as well as the combination of TMG with OXA, resulting in a statistically significant increase cell viability ($P < 0.01$). Notice that 10 μM TMG alone had no effect on cell viability when compared to the untreated control as shown in Figure 3C, indicating a potential protective effect of increased O-GlcNAcylation. This protective effect is likely due to the role of O-GlcNAcylation in enhancing cellular stress responses and promoting cell survival under adverse conditions. Previous studies have shown that increased O-GlcNAcylation enables cancer cells to better withstand oxidative stress and avoid apoptosis (11, 13). Therefore, targeting the O-GlcNAcylation pathway could help reduce cancer cell resistance to chemotherapy and improve treatment efficacy.

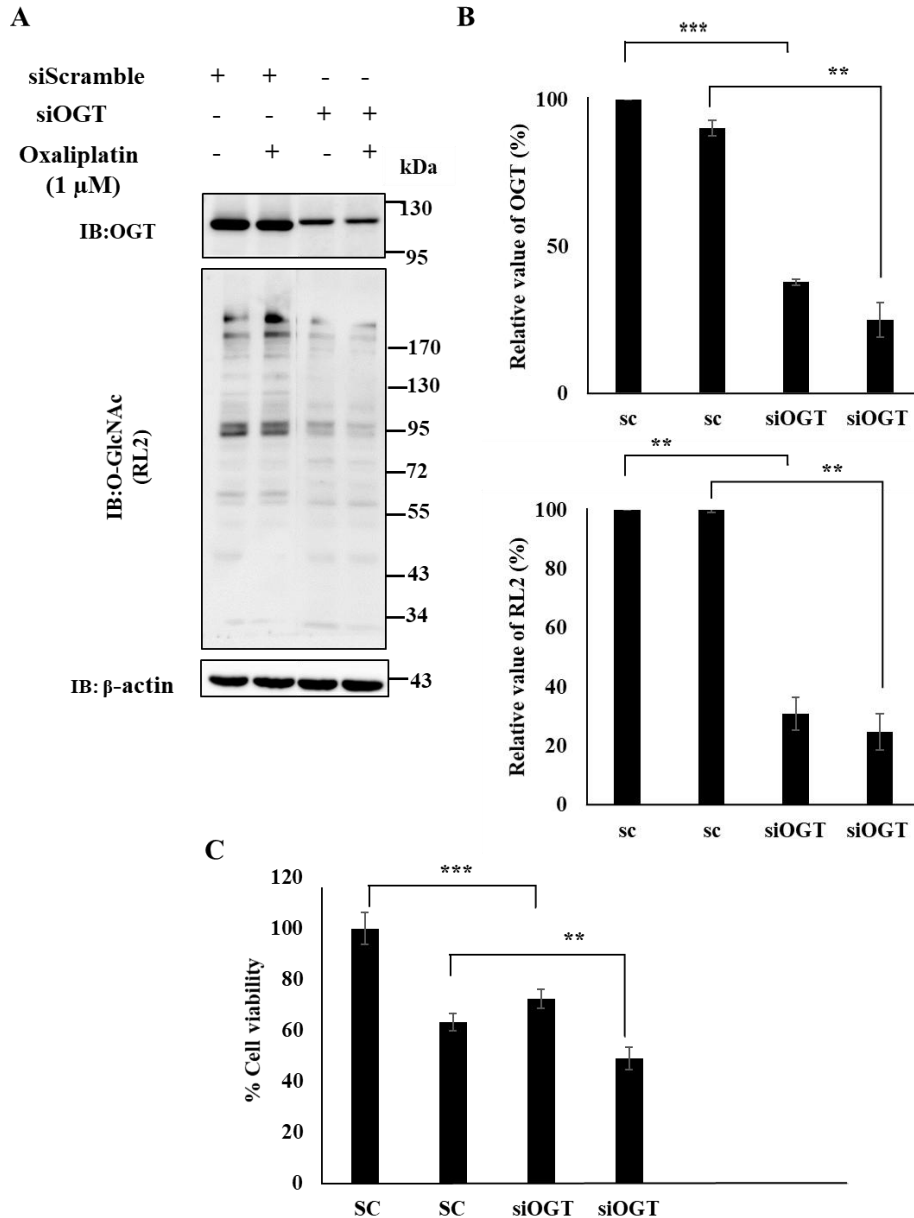


Figure 2: Effects of siOGT on O-GlcNAcylation and chemotherapy sensitivity of SW620 cells. (A) Representative immunoblots (IB) of OGT, O-GlcNAc modified proteins (RL2), and β -actin. (B) Bar graphs represent the relative value of OGT and RL2 (%) normalized to siScramble control group, respectively. SW620 cells were transfected with siOGT or siScramble (sc) with and without 1 μ M OXA for 48 h. Protein samples (20 μ g) were separated by SDS-PAGE, transferred to a PVDF membrane, and probed with the indicated antibodies. OGT and O-GlcNAcylation levels (relative values bar graph) were analyzed by normalization of the band intensity of OGT and O-GlcNAc to that of β -actin in each lane. (C) A bar graph demonstrated the cytotoxic effects of 1 μ M OXA in SW620 cells transfected with siOGT or siScramble. Cell viability was measured using MTS assay following the indicated treatments. Data represents the mean \pm standard deviation (SD) from at least two independent experiments. All data were performed at least two independent experiments. **, *** represent statistically analysis of $P < 0.01$ and $P < 0.001$, respectively.

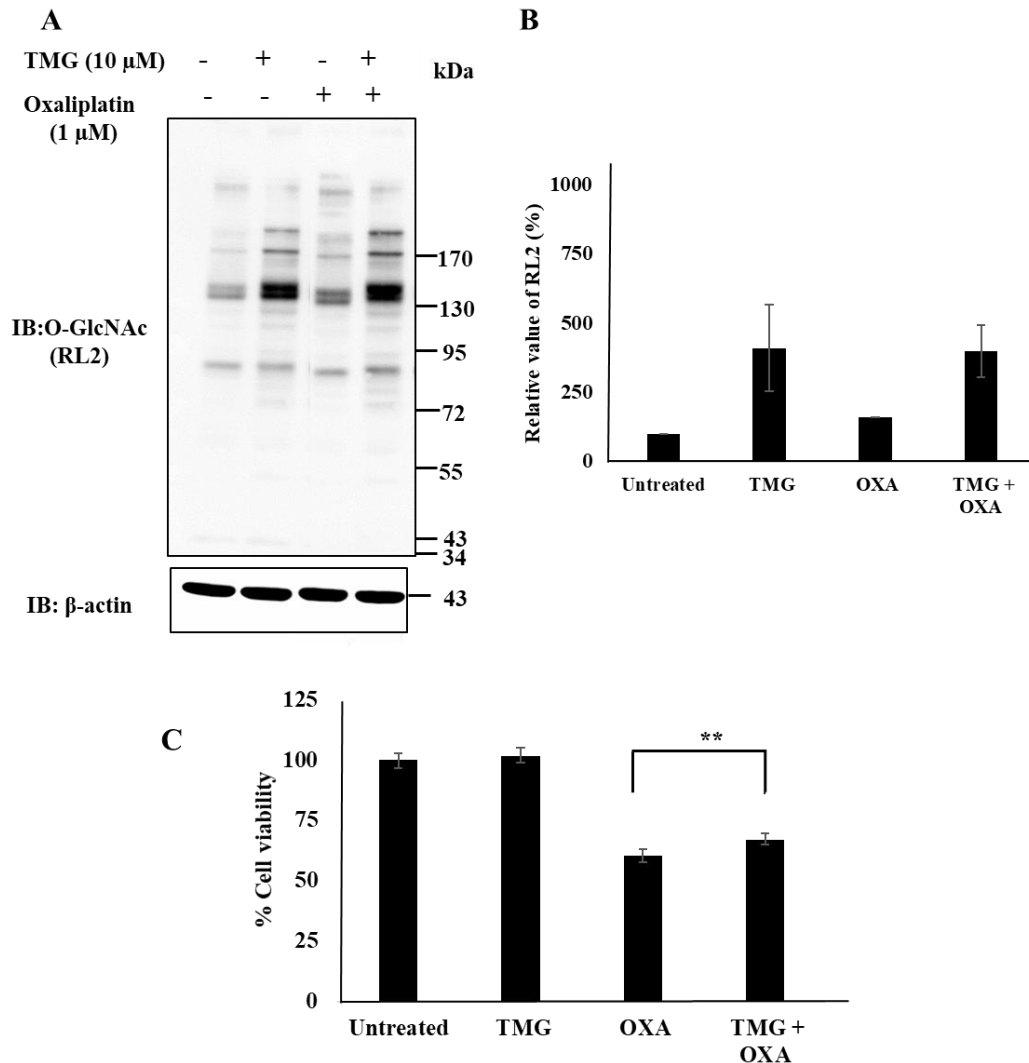


Figure 3: Effects of TMG on O-GlcNAcylation and cell viability. (A) Representative immunoblots (IB) of O-GlcNAc modified proteins (RL2), and β -actin. (B) A bar graph represents the relative value of RL2 (%) normalized to untreated group. SW620 cells were pretreated with 10 μ M TMG for 6 h, followed by treatment with 1 μ M OXA for an additional 48 h. Protein samples (20 μ g) were separated by SDS-PAGE, transferred to a PVDF membrane, and probed with antibodies specific for O-GlcNAc (RL2) and β -actin. (C) A bar graph represents cell viability following TMG and OXA treatment assessed by MTS assay. Cell viability, (%) was normalized to untreated group. Data represents the mean \pm standard deviation (SD) from at least two independent experiments. Relative values bar graph was analyzed by normalization of the intensity of all O-GlcNAc bands divided by that of β -actin in each lane. ** represent of statistically analysis of $P < 0.01$.

Conclusion:

In conclusion, our study highlights the significant role of O-GlcNAcylation in modulating the response of SW620 cells to OXA. The observed increase in O-GlcNAcylation

following OXA treatment suggests that this post-translational modification may act as a stress response mechanism, potentially contributing to chemotherapy drug resistance. Interestingly, reducing O-GlcNAcylation by targeting OGT with siOGT enhanced the sensitivity of SW620 cells to OXA, supporting the hypothesis that lowering O-GlcNAcylation level can improve chemotherapy efficacy. On the other hand, increasing O-GlcNAcylation with TMG was associated with higher cell viability, which could be attributed to enhanced cellular stress responses. These findings suggest that combining strategies to reduce O-GlcNAcylation with chemotherapy could effectively inhibit CRC cells *in vitro*. To improve cancer chemotherapy outcomes, future research is needed to focus on the precise mechanisms underlying these stress responses and identifying O-GlcNAc-modified proteins that contribute to the malignant development and progression of CRC.

Acknowledgements:

This research was supported by Chulabhorn Graduate Institute, and Thailand Science Research and Innovation (TSRI), Chulabhorn Research Institute (Grant No. 48291/4691919).

References:

1. Bray F, Laversanne M, Sung H, Ferlay J, Siegel RL, Soerjomataram I, et al. Global cancer statistics 2022: GLOBOCAN estimates of incidence and mortality worldwide for 36 cancers in 185 countries. *CA Cancer J Clin*. 2024;74(3):229-63.
2. Jung KU, Kim HO, Kim H. Epidemiology, Risk Factors, and Prevention of Colorectal Cancer-An English Version. *Journal of the Anus, Rectum and Colon*. 2022;6(4):231-8.
3. Hossain MS, Karuniawati H, Jairoun AA, Urbi Z, Ooi DJ, John A, et al. Colorectal Cancer: A Review of Carcinogenesis, Global Epidemiology, Current Challenges, Risk Factors, Preventive and Treatment Strategies. *Cancers*. 2022;14(7):1732.
4. Chiaradonna F, Ricciardiello F, Palorini R. The Nutrient-Sensing Hexosamine Biosynthetic Pathway as the Hub of Cancer Metabolic Rewiring. *Cells*. 2018;7(6).
5. Jiang M, Xu B, Li X, Shang Y, Chu Y, Wang W, et al. O-GlcNAcylation promotes colorectal cancer metastasis via the miR-101-O-GlcNAc/EZH2 regulatory feedback circuit. *Oncogene*. 2019;38(3):301-16.
6. Mi W, Gu Y, Han C, Liu H, Fan Q, Zhang X, et al. O-GlcNAcylation is a novel regulator of lung and colon cancer malignancy. *Biochim Biophys Acta*. 2011;1812(4):514-9.
7. Phueaouan T, Chaiyawat P, Netsirisawan P, Chokchaichamnankit D, Punyarit P, Srisomsap C, et al. Aberrant O-GlcNAc-modified proteins expressed in primary colorectal cancer. *Oncol Rep*. 2013;30(6):2929-36.
8. Netsirisawan P, Chaiyawat P, Chokchaichamnankit D, Lirdprapamongkol K, Srisomsap C, Svasti J, et al. Decreasing O-GlcNAcylation affects the malignant transformation of MCF-7 cells via Hsp27 expression and its O-GlcNAc modification. *Oncology Reports*. 2018;40(4):2193-205.
9. Very N, El Yazidi-Belkoura I. Targeting O-GlcNAcylation to overcome resistance to anti-cancer therapies. *Frontiers in Oncology*. 2022;12:960312.
10. Liu Y, Yao RZ, Lian S, Liu P, Hu YJ, Shi HZ, et al. O-GlcNAcylation: the "stress and nutrition receptor" in cell stress response. *Cell Stress Chaperones*. 2021;26(2):297-309.
11. Caldwell SA, Jackson SR, Shahriari KS, Lynch TP, Sethi G, Walker S, et al. Nutrient sensor O-GlcNAc transferase regulates breast cancer tumorigenesis through targeting of the oncogenic transcription factor FoxM1. *Oncogene*. 2010;29(19):2831-42.
12. Very N, El Yazidi-Belkoura I. Targeting O-GlcNAcylation to overcome resistance to anti-cancer therapies. *Frontiers in Oncology*. 2022;12.
13. Ciraku L, Esquea EM, Reginato MJ. O-GlcNAcylation regulation of cellular signaling in cancer. *Cellular Signalling*. 2022;90:110201.



AN *IN VITRO* CARDIOPROTECTIVE EFFECT OF SMALL THERAPEUTIC PEPTIDES DERIVED FROM HUMAN SECRETORY LEUKOCYTE PROTEASE INHIBITOR (hSLPI) AGAINST MYOCARDIAL HYPOXIA/REPERFUSION INJURY

Onnicha Srisopar^{1,2}, Sittiruk Roytrakul³, Sarawut Kumphune^{1, 2*}

¹ Biomedical Engineering Institute (BMEI), Chiang Mai University, Chiang Mai, 50200 Thailand

² Biomedical Engineering and Innovation Research Centre, Chiang Mai University, Chiang Mai, 50200 Thailand

³ National Centre for Genetic Engineering and Biotechnology (BIOTEC), National Science and Technology Development Agency, Pathum Thani, 12120 Thailand

*e-mail: sarawut.kumphune@cmu.ac.th

Abstract:

The ischemic heart disease (IHD) is the leading cause of global death. The only effective treatment is 'reperfusion therapy', which can also cause cellular injury. While over 80 therapeutic peptides have been identified, only a limited number have been investigated for their potential use in IHD. A secretory leukocyte protease inhibitor (SLPI) has been reported to provide cardioprotection against myocardial ischemia/reperfusion (I/R) injury. Despite the proven cardioprotective properties of SLPI, its circulation life span is short. Low-molecular-weight bioactive protein fragments are an intriguing class of medicinal compounds, due to their efficiency, decreased renal clearance, great membrane permeability, and target selectivity. Therefore, improving the stability and efficiency of SLPI by alternatively using hSLPI-derived small peptides (SDSPs) could become a novel therapeutic agent. This study investigated the cardioprotective effect of SDSPs in human ventricular myocytes subjected to an *in vitro* hypoxia/reperfusion (H/R) injury. An *in-silico* peptide digestion by pepsin was performed on full-length human SLPI peptide sequences and there are 7 SDSPs fragment candidates (P1-7). Only 5 water-soluble SDSPs (P1, P2, P3, P5, and P6) were used for assessing cardioprotection. Then, the SDSPs were synthesized and tested for their cytotoxicity and evaluated for cardioprotective effect against the H/R injury. Optimization of H/R injury showed that 6 hours of hypoxia followed by 6 hours of reperfusion (H6R6) in serum-free medium (SFM) was the optimum condition to give 50% of human cardiomyocytes death. The results showed that all 5 SDSPs fragments showed non-cytotoxicity and enhanced cell viability. Treatment of P1, P3, P5, and P6 at the onset of reperfusion could significantly reduce H/R-induced cardiac cell death. In conclusion, the SDSPs showed cardioprotection against H/R injury and should be further investigated for their potential to be a novel therapeutic agent for IHD.

Introduction:

In 2030, it is anticipated that ischemic heart disease (IHD) will be the leading cause of mortality globally.¹ This tendency appears to occur not just in developed countries but all around the world.² According to epidemiological data from Thailand, ischemic heart disease is now one of the leading causes of death for Thai people.³ Ischemic heart disease, also known as coronary artery disease (CAD) or coronary heart disease, refers to heart disorders induced by the death of heart muscle cells due to constricted coronary arteries.⁴ The survivors of myocardial infarction can subsequently suffer from heart failure.⁵ Ischemia is the

fundamental pathophysiology of IHD, and the only effective treatment is 'reperfusion therapy', which can also cause cellular injury.⁶

Therapeutic peptides are biological mediators that exhibit great therapeutic potency, selectivity, and low toxicity.^{7, 8} Moreover, small peptides have greater stability and cellular membrane penetration than larger peptides.⁹ Bioactive short peptides, or small peptides, are low-molecular-weight protein fragments of 2–20 amino acid residues that are a potent pharmaceutical drug of the future.¹⁰ While over 80 therapeutic peptides have been identified to treat several kinds of diseases, only a limited number have been investigated for their potential use in cardiovascular applications, predominantly in heart failure¹¹, with none specifically researched for ischemic heart disease (IHD).

Secretory leukocyte protease inhibitor (SLPI) is a 14.326 kDa (132 amino acid) cationic protein that is part of the serine protease inhibitor family.¹² Previous studies demonstrated that giving human SLPI (hSLPI) provided cardioprotective effects against I/R injury both in an *in vitro*^{13, 14}, *ex vivo*¹⁴, and *in vivo*¹⁵ study model. Moreover, the cardioprotection of SLPI does not depend on its anti-protease activity, suggesting a direct effect of the SLPI protein.^{16, 17} Even though the cardioprotective property of SLPI has been proven, one of the clinical limitations associated with the use of recombinant human SLPI as a therapeutic drug is its short half-life within the circulatory system.¹⁸

Since SLPI showed potential cardioprotective effects against myocardial ischemia/reperfusion (I/R) injury but had a short half-life. In addition, the small therapeutic peptides that provide cardioprotection for myocardial I/R injury have not been intensively investigated and have become one of the most challenging research questions. Therefore, this study examined the potential cardioprotective effect of human secretory leukocyte protease inhibitor (hSLPI)-derived small peptides (SDSPs) using a hypoxia/reperfusion (H/R) model. In this study, a human secretory leukocyte protease inhibitor (hSLPI), which was cut by the *in silico* porcine pepsin enzyme, was synthesized and used to determine the cytotoxicity and cardioprotective effect (**Figure 1**).

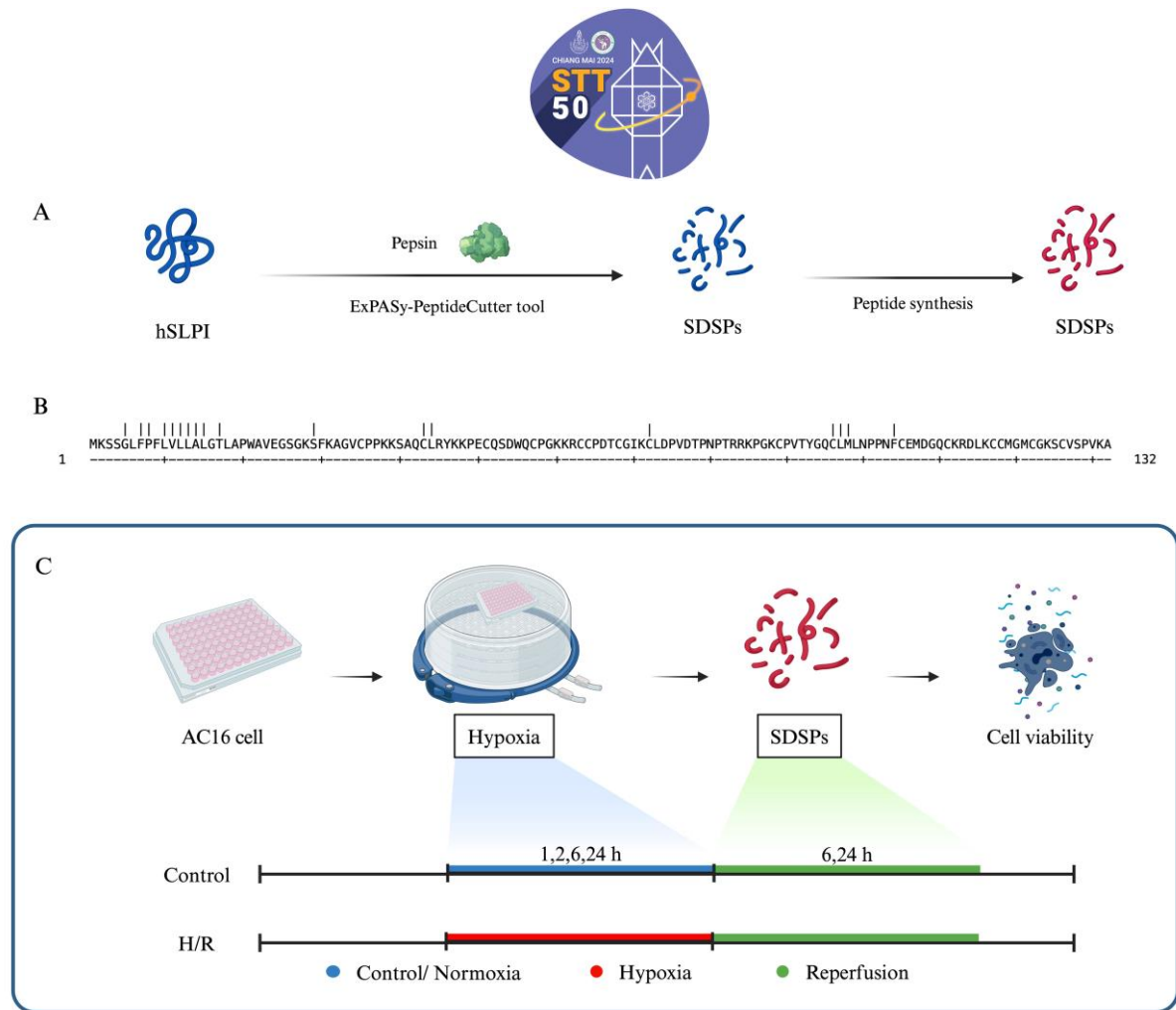


Figure 1. A schematic diagram of the study protocol.

(A) A schematic diagram of *in-silico* peptide digestion of human secretory leukocyte protease inhibitor (hSLPI) to generate the SLPI derived small peptides (SDSPs), (B) the digestion pattern of pepsin enzyme on hSLPI, and (C) A schematic diagram of study protocols to elucidate the cardioprotective effect of SDSPs against an *in vitro* hypoxia/reperfusion (H/R) injury in human cardiomyocyte (AC16) cells.

Methodology:

Chemical and reagents

Dulbecco's modified Eagle's medium (DMEM), fetal bovine serum (FBS), penicillin, streptomycin, trypsin-EDTA, and other chemicals were purchased from Gibco® (Gibco BRL; Life Technologies Inc. New York, USA).

Generation of small peptides derived from hSLPI

To hydrolyze human secretory leukocyte protease inhibitor (hSLPI) *in silico* using porcine pepsin, the ExPASy-PeptideCutter tool (SIB Swiss Institute of Bioinformatics, Lausanne, Switzerland) was used. The *in-silico* digestion obtained the human secretory leukocyte protease inhibitor (hSLPI)-derived small peptides (SDSPs) for 19 pieces. In this study, we selected the peptide fragments with 5 amino acids or longer peptides. So, there were 7 SDSPs fragments were selected and synthesized, namely P1-P7. The Fmoc-solid phase synthetic method (GL Biochem, Shanghai, People's Republic of China) was used to synthesize SDSPs in preparation for additional *in vitro* testing. Subsequently, the manufactured lyophilized SDSPs were dissolved in solvents, DMSO or water, and stored in a

freezer at a concentration of 1 mg/mL at -80 °C. In this study, 5 SDSPs fragments that dissolved in water were tested, including P1, P2, P3, P5, and P6.

Cell type and cell culture

The human cardiomyocyte cell line, AC16 cell line (ATCC®, CRL-3568™), was purchased from American Type Cell Culture and maintained in DMEM supplemented with 10% heat-inactivated FBS, 100 units/mL of penicillin, and 100 µg/mL streptomycin. The AC16 cells were maintained at 37 °C, 5% CO₂ + 95% O₂, until they reached 80% confluence.¹⁹ The media was renewed every 2 to 3 days.

The culture media was aspirated from the cell culture flask, and the cells were washed three times with 5 mL of pre-warmed phosphate-buffered saline (PBS). Next, 2 mL of pre-warmed trypsin-EDTA (Gibco®) was added and incubated at 37 °C for approximately 2 min, or until approximately 50% of the cells had detached from the flask surface as observed under a microscope. The trypsin activity will then be terminated by adding 8 mL of completed, pre-warmed DMEM. Transfer the cell suspension to a 15 mL sterile tube and centrifuge at 125 x g for 5 min. The supernatant was discarded, and the cell particle was resuspended in 1 mL of finished DMEM. The cells were transferred into a new cell culture flask to which at least 8 mL of completed DMEM was added. After that, the cells were incubated at 37 °C, 5% CO₂ + 95% O₂.

Optimization of an in vitro hypoxia/reperfusion (H/R)

H/R was optimized to identify the time point at which 50% of cells die relative to the control. AC16 cells were seeded in 96-well plates at density 1×10^4 cells/well. For hypoxia, the cells were induced by treatment with complete DMEM medium (CM), serum-free DMEM medium (SFM), and serum-glucose-free DMEM medium (SGFM) at 200 µl/well in the hypoxic chamber by adjusting the regulator valve control to a flow rate of 20 L/min, which completely purges the chamber in 4 minutes.²⁰ The cells were incubated in the hypoxic chamber at 37°C for 1, 2, 6, and 24 hours. For the control condition, CM was used and incubated at 37°C, 5% CO₂. After that, the media was discarded, and 200 µl/well of CM was added for reperfusion for 6, and 24 hours at 37°C, 5% CO₂. After that, the cell viability was measured. Condition of H/R that provide 50% of cardiac cell death was used in following experiments.

Determination for cardioprotective effect of SDSPs treatment against hypoxia/reperfusion (H/R) injury

The AC16 cells were seeded in a 96-well plate at a density 1×10^4 cells/well. Stocked SDSPs were thawed and diluted to 0.1, 1, and 10 µg/mL in prewarmed-DMEM. In the hypoxia condition, the cells were induced by treatment with CM, SFM, and SGFM at 200 µl/well in the hypoxic chamber by adjusting the regulator valve control to a flow rate of 20 L/min, which completely purges the chamber in 4 minutes. The optimized time that makes 50% of cells die relative to the control was used. For the control condition, CM was used and incubated at 37°C, 5% CO₂. After that, the media was discarded and 200 µl/well of CM or dilutions of SDSPs were added for reperfusion at 37°C, 5% CO₂ for the optimized reperfusion time. After that, the cell viability was measured at the end.

Determination of cell viability by MTT viability assay

The MTT reagent, also known as 3-(4,5-dimethylthiazol-2-yl)-2,5-diphenyl-2H-tetrazolium bromide, was obtained from Ameresco (Solon, Ohio, USA). The MTT solution was prepared at 0.5 mg/mL. The AC16 cells were treated with the MTT solution 100 µl/well for 2 hours and incubated at 37°C, 5% CO₂ after the H/R protocol. Subsequently, after the



MTT solution was removed, DMSO was added to each well and mixed to dissolve formazan crystals. Then, the absorbance was measured at 570 nm to determine the cell viability.

Statistical Analysis

All experiments were performed in triplicate. Data was processed using GraphPad Prism version 10.0 and reported as mean \pm standard error. The p value < 0.05 was considered significant.

Results and Discussion:

Optimization of an in vitro hypoxia/reperfusion (H/R) injury

The hypoxia/reperfusion model was optimized by varying the hypoxia and the reperfusion time with several types of culture media, such as complete DMEM medium (CM), serum-free DMEM medium (SFM), and serum-glucose-free DMEM medium (SGFM). The media types were considered in order to model the hypoxia reperfusion injury. In hypoxic conditions, the CM provides a deficiency of oxygen but still contains nutrients. The SFM induces cellular depletion of oxygen and essential proteins obtained from serum, while the SGFM induces cells exhibiting low glucose levels, starved of serum and oxygen. The percentage of relative cell viability with varied types of media at different time points of AC16 in H/R injury is shown in **Figure 2**. The results showed that the percentage of relative cell viability of hypoxia 1 hour with SFM (H-SFM), and SGFM (H-SGFM) was significantly decreased when compared to that of the control group with CM (C-CM) (**Figure 2A and 2E**), whereas the percentage of relative cell viability of hypoxia 2 and 6 hours with CM, SFM, and SGFM was significantly decreased when compared to that of the control group (**Figure 2B, 2C, 2F, and 2G**), and the percentage of relative cell viability of hypoxia 24 hours with CM was significantly decreased when compared to that of the control group (**Figure 2D and 2F**).

The cell viability of AC16 cells after hypoxia for 1 hour showed no difference in CM (H-CM) but was significantly decreasing in both media (H-SFM and H-SGFM) for 6 (**Figure 2A**) and 24 hours of reperfusion (**Figure 2E**). The condition might not have enough time to induce cell injury from hypoxia. For hypoxia 2 and 6 hours, the cell viability was significantly decreased in every type of media and both reperfusion times, but not down to 50% cell viability compared to their control group, except in the H6R6 condition (**Figure 2C**). After exposure to 24 hours of hypoxia, the cell viability showed a contrast with hypoxia for 1 hour. There were not significantly different with the control group when reperfused with SFM and SGFM in both time points but showed cell viability near to 50% in H-CM. Myocardial reperfusion followed by non-lethal hypoxia protected the cells from major myocardial damage.²¹ Serum and serum-glucose starvation could accelerate the cell metabolism, which made the cell survive after being exposed to hypoxia for 24 hours.^{22, 23} In addition, the optimized time point that obtained around 50% of cell death relative to the control was H6R6 with SFM (52.98 ± 4.132 %), H24R6 with CM (36.01 ± 2.621 %), and H24R24 with CM (46.32 ± 15.70 %). Therefore, the H6R6 with SFM was considered as the optimum condition and was used for determining the cardioprotective effect of SDSPs.

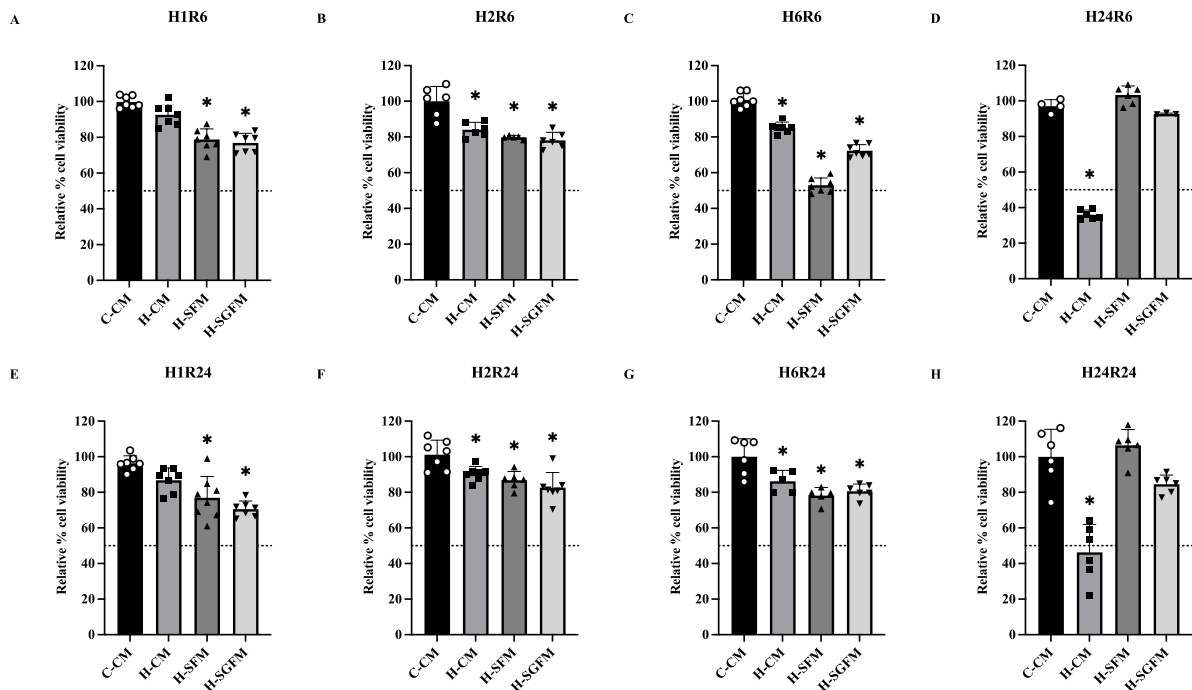


Figure 2. Optimization of H/R injury depend on time point.

The human cardiomyocyte (AC16) was optimized for H/R injury in (A) H1R6, (B) H2R6, (C) H6R6, (D) H24R6, (E) H1R24, (F) H2R24, (G) H6R24, and (H) H24R24 with varied types of culture media during hypoxia. * $p < 0.05$ vs. control (ANOVA).

The influence of culture medium condition during hypoxia and reperfusion injury model was also analyzed. The results showed that H/R injury using complete DMEM medium (CM) gave a significant reduction in cell viability in H2R6, H24R6, and H24R24 condition. However, H24R6, and H24R24 showed cell viability approximately 50% (**Figure 3A**). The serum-free DMEM medium (SFM) showed a significant reduction in cell viability, when exposed to H1R6, H1R24, H2R6, H6R6, and H6R24. Among these H/R condition, H6R6 gave approximately 50% of cell viability (**Figure 3B**). The H/R with serum-glucose-free DMEM medium (SGFM) conditions including H1R6, H1R24, H2R6, H2R24, H6R6, and H6R24 also showed a significant reduction in cell viability. However, none of these conditions gave a 50% cell death (**Figure 3C**).

The difference types of culture media did not provide the same pattern of cell injury under hypoxia/reperfusion condition. Prolonged hypoxia resulted in reduced cell viability in CM. Meanwhile, the H/R with SFM condition showed the lowest cell viability after hypoxia for 6 hours, and increasing of cell viability was found after hypoxia for 24 hours. However, using SGFM to model of H/R offered significantly decreased of cell viability with hypoxia 1,2, and 6 hours, but showed no different with the control after hypoxia 24 hours. In this study, the optimum condition that used for investigation the cardioprotective effects of SDSPs is the shortest H/R period that could provide 50% of cell death. Therefore, in this study H6R6 in SFM was selected as the optimum H/R condition.

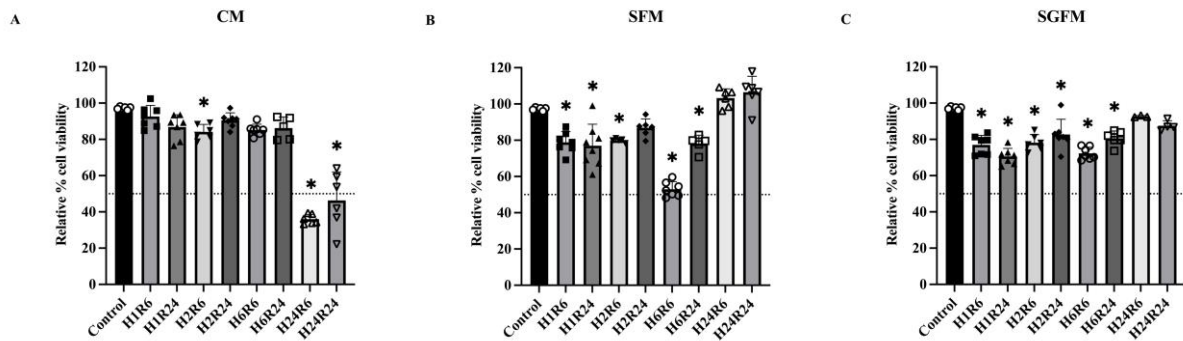


Figure 3. Optimization of H/R injury depend on types of media.

The human cardiomyocyte (AC16) was optimized for H/R injury in (A) CM, (B) SFM, and (C) SGFM with varied time point of hypoxia and reperfusion. * $p < 0.05$ vs. control (ANOVA).

The cytotoxicity of SDSPs on human ventricular myocytes

The cytotoxicity of the hSLPI-derived small peptides (SDSPs) was performed by incubating the SDSPs with AC16 cells for 24 hours, followed by evaluation of the cell viability using the MTT viability assay. Various concentrations of SDSPs were prepared by a 10-fold dilution from 0 to 10 $\mu\text{g/mL}$ and treated with the cells for 24 hours to determine cytotoxicity. The results showed that there was a significant increase in cell viability when cells were exposed to P1 (**Figure 4A**), P3 (**Figure 4C**), P5 (**Figure 4D**), and P6 (**Figure 4E**) in comparison to those of the control group. However, the results showed no significant difference in cell viability of cells treated with P2 (**Figure 4B**) in every concentration compared to the control group.

Almost all of the SDSPs showed non-toxicity to the cells, such as P1, P2, P3, P5, and P6. The SDSPs, including P1, P3, P5, and P6, could enhance cell proliferation. From the previous study, full-length SLPI was able to upregulate the cyclin D1 signaling pathway, resulting in stimulating cell proliferation.²⁴ Thus, SDSPs might contain a cyclin D1 signaling pathway.

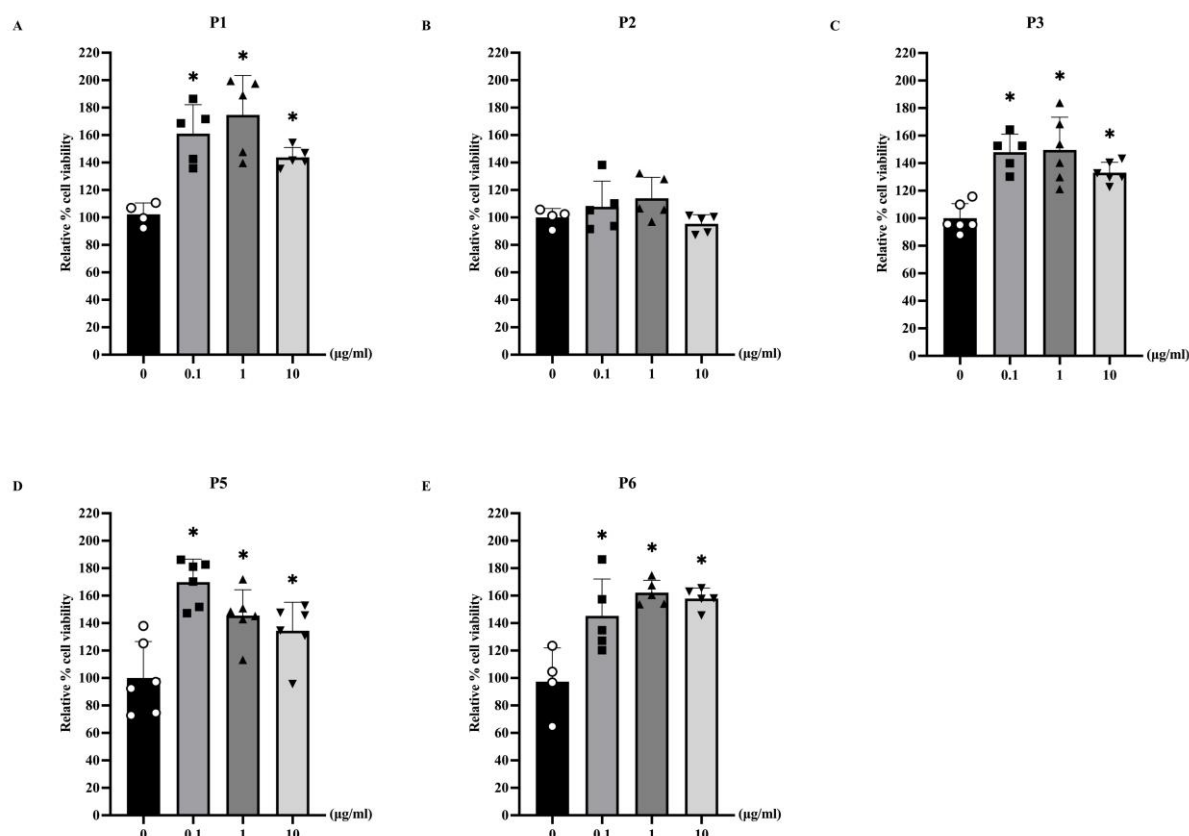


Figure 4. The cytotoxicity of SDSPs.

The varied concentrations of SDSPs such as (A) P1, (B) P2, (C) P3, (D) P5, and (E) P6 were used to identify the cytotoxicity on the AC16 cells. * $p < 0.05$ vs. control 0 µg/mL (ANOVA).

The in vitro cardioprotective effect of SDSPs against H/R injury

An *in vitro* cardioprotective effect of SDSPs was performed against H/R injury. The H6R6 with SFM condition was used to determine the cardioprotective effect of the SDSPs. The results showed that the cell viability of AC16 cells was significantly reduced approximately 50% in untreated cells with H/R when compared to those of the control group (non-H/R) group (**Figure 5A – 5D**). Various concentrations of SDSPs, including 0.1, 1, and 10 µg/mL, were treated at reperfusion, and the results showed that cell viability was significantly improved when treated SDSPs at concentrations of 0.1, 1, and 10 µg/mL of P1 (**Figure 5A**), P3 (**Figure 5C**), P5 (**Figure 5D**), and P6 (**Figure 5E**) when compared with the non-treated group. The P1, P3, P5, and P6 SDSPs improved the cell viability from the mean of each non-treated group for 34.79 - 81.15 %, 24.49 - 44.97 %, 32.1 - 51.05 %, and 40.29 - 42.09 %, respectively. The SDSPs that most promoted cell viability was P1 peptide at a concentration of 1 µg/mL, resulting in a 135 % cell viability. However, the results showed no significant difference in cell viability of cells treated with P2 (**Figure 5B**) in all concentrations compared to the non-treated group.

Similar to the results of cytotoxicity, the cell viability of AC16 cells after being treated with concentrations of SDSPs in the reperfusion process was significantly enhanced in all concentrations compared to the non-treated group, which are P1, P3, P5, and P6. This might be an effect of the small peptides that contain the essential region of the survival signaling pathway, the PI3K (phosphoinositide 3 kinase) pathway, leading to increased expression of Akt.²⁵ However, the results showed no significant difference in cell viability



between cells treated with P2. The small peptide might not contain any of the essential regions of the survival signaling pathway.

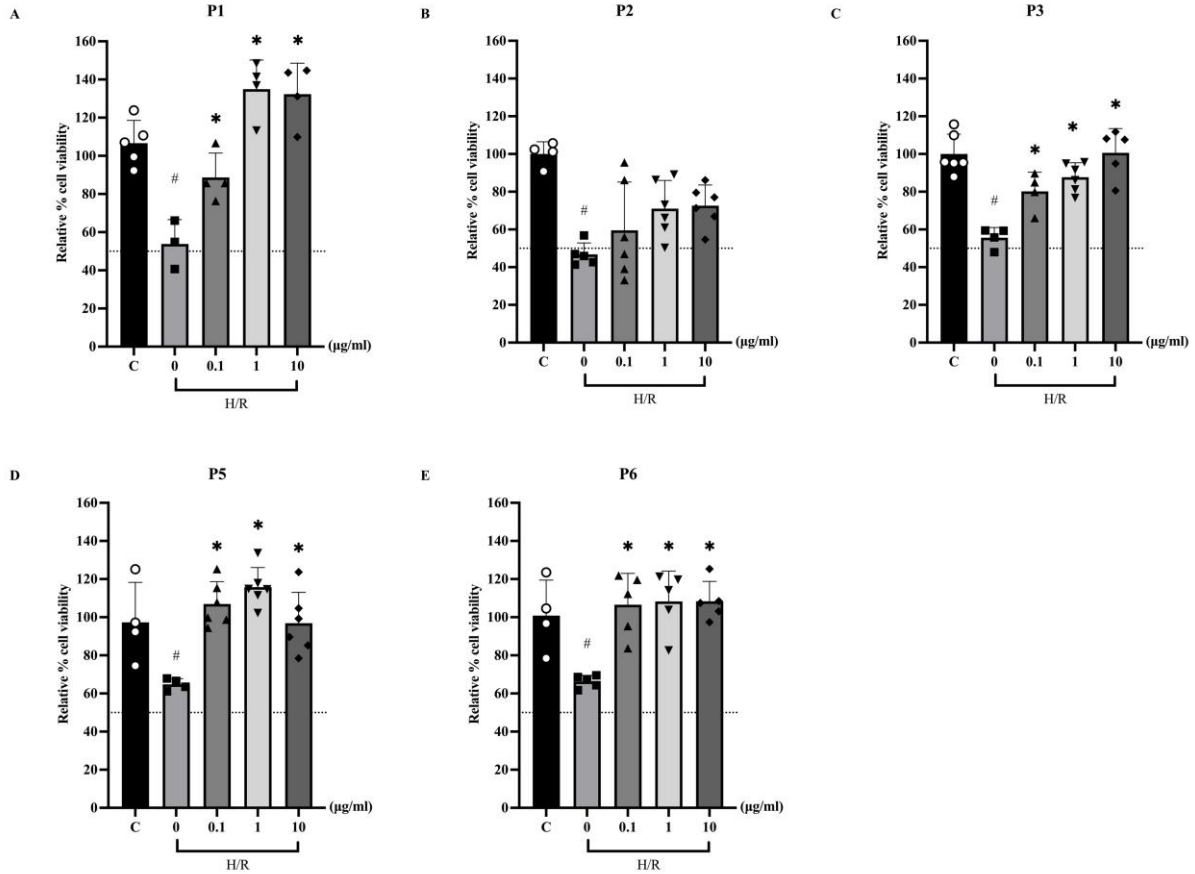


Figure 5. The cardioprotective effect of SDSPs for H/R injury.

The varied concentrations of SDSPs such as (A) P1, (B) P2, (C) P3, (D) P5, and (E) P6 were used to identify the cardioprotective effect on the AC16 cells in H/R injury.

#p < 0.05 vs. control, and *p < 0.05 vs. H/R of SDSPs at 0 µg/mL (ANOVA).

There were some limitations in this current study. This study was only screening the cardioprotective effect of SDSPs by using the MTT viability assay. The mechanisms of SDSPs against cellular apoptosis, intracellular ROS production, MAPKs phosphorylation, and signaling proteins involved in apoptosis still need to be further investigated. Moreover, an *in vitro* finding from this study might not provide sufficient information for further clinical applications, determining the cardioprotection in tissue level, such as in an *ex vivo* heart perfusion model of I/R injury or an *in vivo* model of left anterior descending (LAD) coronary artery ligation, is required to provide both physiological and biochemical explanations of the cardioprotective effects of SDSPs.

Conclusion:

In conclusion, hypoxia for 6 hours followed by reperfusion for 6 hours (H6R6) with serum-free DMEM medium (SFM) was the best condition for the hypoxia/reperfusion (H/R) model of this study. The cardioprotective effect was shown on P1, P3, P5, and P6. The cell viability following H/R was most enhanced by P1 peptide at a concentration of 1 µg/mL.

Accordingly, the SDSPs have a cardioprotective effect by reducing cardiac cell injury against I/R injury.

Acknowledgements:

The present study was supported by the CMU Presidential Scholarship 2023 from Multidisciplinary and Interdisciplinary School, Chiang Mai University for OS. We would like to acknowledge Biomedical Engineering Institute (BMEI), Chiang Mai University for travel grant to attend STT50. This research was supported by the National Research Council of Thailand (NRCT) and Chiang Mai University: N42A650305, for S.K.

References:

1. Nawsherwan, Bin W, Le Z, Mubarik S, Fu G, Wang Y. *Front Nutr.* 2022;9:898-978.
2. Wu P, Yu S, Wang J, Zou S, Yao DS, Xiaochen Y. *Front Cardiovasc Med.* 2023;10:1-7.
3. Sakboonyarat B, Rangsin R. *BMC Res Notes.* 2024;17:142-8.
4. Severino P, D'Amato A, Pucci M, Infusino F, Adamo F, Birtolo LI, et al. *Int J Mol Sci.* 2020;21.
5. Jenca D, Melenovsky V, Stehlik J, Stanek V, Kettner J, Kautzner J, et al. *ESC Heart Fail.* 2021;8:222-37.
6. Buja LM. *Cardiol Rev.* 2023;31:252-64.
7. Marqus S, Pirogova E, Piva TJ. *J Biomed Sci.* 2017;24:21.
8. Wang L, Wang N, Zhang W, Cheng X, Yan Z, Shao G, et al. *Signal Transduct Target Ther.* 2022;7:48.
9. Al Musaimi O, Lombardi L, Williams DR, Albericio F. *Pharmaceuticals (Basel).* 2022;15.
10. Purohit K, Reddy N, Sunna A. *Int J Mol Sci.* 2024;25.
11. Rossino G, Marchese E, Galli G, Verde F, Finizio M, Serra M, et al. *Molecules.* 2023;28.
12. Thompson RC, Ohlsson K. *Proc Natl Acad Sci U S A.* 1986;83:6692-6.
13. Prompunt E, Nernpermpisooth N, Sanit J, Kumphune S. *Biomol Concepts.* 2018;9:17-32.
14. Prompunt E, Sanit J, Barrere-Lemaire S, Nargeot J, Noordali H, Madhani M, et al. *Exp Ther Med.* 2018;15:5231-42.
15. Mongkolpathumrat P, Kijawornrat A, Prompunt E, Panya A, Chattipakorn N, Barrere-Lemaire S, et al. *Biomedicines.* 2021;9.
16. McGarry N, Greene CM, McElvaney NG, Weldon S, Taggart CC. *J Immunol Res.* 2015;2015:507315.
17. Yang J, Zhu J, Sun D, Ding A. *Biochim Biophys Acta.* 2005;1745:310-7.
18. Bergenfeldt M, Bjork P, Ohlsson K. *Scand J Clin Lab Invest.* 1990;50:729-37.
19. Yu Z, Ren Q, Yu S, Gao X. *Biosci Rep.* 2020;40.
20. Li Z, Zhao J, Li H, Li Y, Lin C. *J Biochem Mol Toxicol.* 2022;36:e23034.
21. Della Rocca Y, Fonticoli L, Rajan TS, Trubiani O, Caputi S, Diomedea F, et al. *J Physiol Biochem.* 2022;78:739-52.
22. Lorenz M, Fritsche-Guenther R, Bartsch C, Vietzke A, Eisenberger A, Stangl K, et al. *Int J Mol Sci.* 2023;24.
23. Nagelkerke A, Bussink J, Mujcic H, Wouters BG, Lehmann S, Sweep FC, et al. *Breast Cancer Res.* 2013;15:R2.
24. Mueller AM, Pedre X, Stempf T, Kleiter I, Couillard-Despres S, Aigner L, et al. *J Neuroinflammation.* 2008;5:20.
25. Nernpermpisooth N, Prompunt E, Kumphune S. *Exp Ther Med.* 2017;14:5793-800.



APPLICATION OF DIELECTRIC BARRIER DISCHARGE PLASMA TECHNOLOGY ON MICROBIAL INHIBITION

Wannakan Sawaspaen,¹ Thawichai Traiporm,¹ Tanapat Palaga² and Chonchanok Muangnapoh^{2*}

¹Program of Science for Industry, Faculty of Science, Chulalongkorn University, Bangkok, Thailand

²Department of Microbiology, Faculty of Science, Chulalongkorn University, Bangkok, Thailand

*e-mail: chonchanok.m@chula.ac.th

Abstract:

Dielectric barrier discharge (DBD) plasma is the electrical discharge that occurs between two electrodes separated by an insulating barrier. Since DBD plasma commonly produces a variety of reactive species, including reactive nitrogen species (RNS), reactive oxygen species (ROS), it is utilized for microbial elimination to improve indoor air quality. This study therefore aimed to test the efficacy of a DBD plasma generator that uses square electrodes and flame retardant-4 dielectric materials in the elimination of potential indoor air pathogens, including *Pseudomonas aeruginosa*, *Staphylococcus aureus*, *Aspergillus niger*, and Enterovirus-71 (EV-71). Additionally, the effects of DBD plasma on human lung cells and skin cells were evaluated. Results showed that the reduction rates of tested microorganisms are dependent on microbial species and DBD exposure time. *P. aeruginosa* and *S. aureus* exhibited elimination times of 5 minutes while *A. niger* requires 25 minutes. Significant viral reduction of EV-71 was observed at 10 minutes of DBD exposure time. Human cell culture assay demonstrated that the survival rate of PSVK1 keratinocyte and WI38 lung cells was less than 80% after 20 minutes of DBD plasma exposure. Results from this study demonstrated that DBD plasma is effective for eliminating potential pathogens, however the effective dose and exposure time should be compromised with biosafety considerations for applications involving human activity.

Introduction:

Gas discharge plasmas, also known as low-temperature plasmas, have gained significant interest in recent years due to their important role in various technological developments¹. Plasma methods are currently widely used in air cleaning systems and for the sterilization of food containers, fruits, meat, vegetables, fabrics, and medical devices². The dielectric barrier discharge (DBD) is one of the most cost-effective nonthermal plasma sources. This discharge has been shown to be effective in initiating chemical and physical processes in gases³. The dielectric barrier discharge plasma generator applies the accumulation-discharging principle to dielectric material with a high potential difference alternating current at atmospheric pressure. Dielectric discharges are generated between two electrodes, and to limit the discharge current, the device covers at least one of the electrodes with dielectric material⁴. Discharge may be linear, glowing and is determined by a variety of factors, including the electric potential difference, the type of dielectric plate, the distance between parallel plates, the type of gas, and the pressure⁵.

The plasma contains many ions, electrons, radicals, UV photons, and chemicals. These influential particles may rapidly destroy biological structures or macromolecules, resulting in fast sterilization⁶. Consequently, plasma generators were previously applied for

the elimination of microorganisms. These ions will react with air, which consists mainly of nitrogen and oxygen gasses, which contributing to the generation of free radicals, including reactive oxygen species (ROS) and reactive nitrogen species (RNS), such as hydroxyl ions (OH^\cdot) and hydrogen peroxide (H_2O_2), ozone (O_3), atomic oxygen (O), superoxide anions (O_2^\cdot), nitrogen gas (N_2), nitric oxide (NO), and peroxyxynitrite anion (ONOO^-)⁷. Previous studies mostly elucidated the effects of plasmas on bacteria for preventing food and water treatment^{8,9,10}. However, the microbial effects and biosafety of using DBD plasma for air sterilization are very limited. The application of DBD plasma technology in air purifiers necessitates microbial and biosafety assessments, particularly regarding human exposure. Therefore, the purpose of this study was to evaluate the efficacy of the generated DBD plasma ionizer in eliminating potential pathogens in indoor air, including *Pseudomonas aeruginosa*, *Staphylococcus aureus*, *Aspergillus niger*, and the hand foot and mouth disease causing virus Enterovirus (EV-71). In addition, biosafety assays of human cell lines involving the direct contact and inhalation of DBD plasma (i.e. skin and lung cells) were evaluated to consider in the application of DBD plasma in air purifier.

Methodology:

Equipment for DBD plasma generator

Install a DBD plasma generator, driven by a 120 Hz high-voltage power supply, with an electrode size of 13 x 7 centimeters and dielectric material Fr-4, attached to an acrylic box with dimensions of 30 x 40 x 15 centimeters, and a 12-centimeter gap between the electrode and the Petri dish (**Figure 1a and b**).

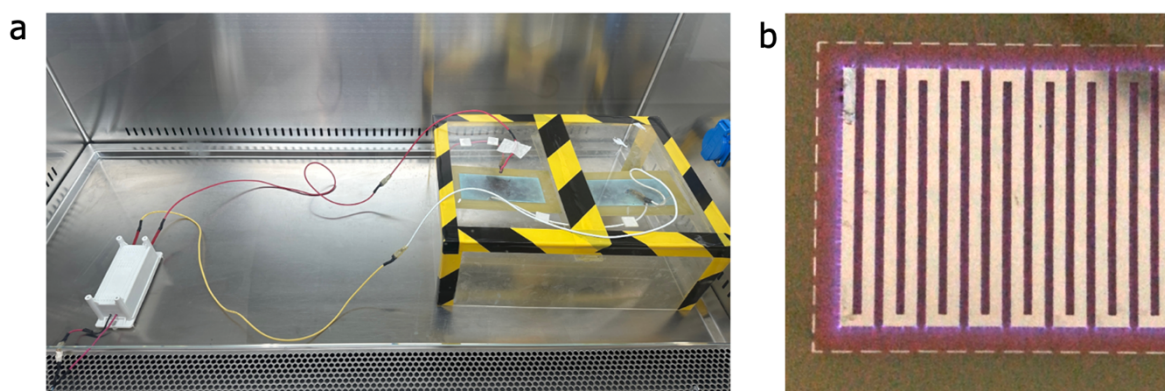


Figure 1. Equipment for DBD plasma generator (a) DBD plate (b)

Effect of DBD plasma on bacterial inhibition

The Gram-negative bacterium *P. aeruginosa* ATCC9027 and Gram-positive bacterium *S. aureus* ATCC6538 were grown in nutrient broth (NB) (Himedia, India) liquid medium at 37°C and 200 rpm for 4 hours until the optical density at 600 nm (OD600) up to 0.90 - 1.00. A ten-folded dilution of bacterial culture was prepared in 0.85% sodium chloride solution. Then, 100 microliters of the 10^{-6} dilution of bacterial culture were spread onto NA plate and exposed to DBD plasma for 1, 5, 10, 15, 20, 25, and 30 minutes. The plates were incubated at 37°C for 18 hours. The number of colonies (CFU/ml) on the plates after incubation was compared with the control group without exposure to the DBD plasma.



Effect of DBD plasma on fungal inhibition

A. niger ATCC10864 was cultivated on potato dextrose agar (PDA) (Himedia, India) at 30°C for 5 days, and spores were collected in the mix of 0.85% sodium chloride solution and Tween20. The fungal culture was ten-fold diluted in 0.85% sodium chloride solution. Then, 100 microliters of the 10⁻⁶ dilution of fungal culture were spread onto PDA plates and exposed to DBD plasma for 1, 5, 10, 15, 20, 25, and 30 minutes. The plates were incubated at 30°C for 3-5 days. The number of colonies (CFU/ml) on the plates after incubation was compared with the control group without exposure to DBD plasma.

Effect of DBD plasma on viral inhibition

Vero cells (approximately 2 × 10⁵ cells per well) were grown as a monolayer in a standard 12-well plate, with 1 ml of growth medium (DMEM, 10% FBS) per well. After forming the cell, the growth medium was carefully removed. The 250 µl of EV-71 strains, namely BrCr, that had been exposed to DBD plasma for 1, 5, 10, 15, 20, 25, 30, 40, 50, and 60 minutes was added to the 12-well plates containing the cell lines and incubated at 37°C with gentle shaking every 15 minutes for 1 hour. After that, the virus was discarded, and the cells were rinsed with 1X phosphate buffered saline (PBS). The cells were then overlaid with 0.3% agarose in DMEM/2% FBS and incubated for 3 days at 37°C with 5% CO₂. After 3 days, the plates were fixed with 10% formalin and stained with 1.25% crystal violet solution to each well and the cell were left to stand for 15 minutes, followed by washing the well with water and allowing the plates to dry at room temperature. The number of plaques was counted in PFU/ml.

Effect of DBD plasma on human cell

PSVK1 Human keratinocyte cells (JCRB1093) and WI38 lung cells (ATCC CCL-75) were grown in 100 µl keratinocyte media and 10% fetal bovine serum (FBS) Eagle's minimum essential medium (EMEM), respectively, in 96-well plates. The plates were incubated at 37°C with 5% CO₂ for 24 hours. The cells were formed a monolayer and exposed to DBD plasma for 1, 5, 10, 15, 20, 25, 30, 40, 50, and 60 minutes. Subsequently, 10 µl MTT labeling reagent was added with the final concentration of 0.5 mg/ml to each well and incubated at 37°C with 5% CO₂ for 4 hours. After that, 200 µl dimethyl sulfoxide (DMSO) was added into each well and mixed. Cell viability was measured at a wavelength of 540 nm by spectrophotometer (Bio-rad Laboratories, USA).

Results and Discussion:

The number of *P. aeruginosa* colonies on the NA plates after being exposed to DBD plasma was compared to those on the control group. It was found that no colonies grew on the plates after 5 minutes of exposure (**Figure 2**). This indicated that DBD plasma can eliminate more than 99.99% of *P. aeruginosa* within 5 minutes. For *S. aureus*, results showed that no colonies were observed on the NA plate after 5 minutes of exposure, indicating that DBD plasma effectively kills more than 99.99% of *S. aureus* within 5 minutes (**Figure 3**). However, following one minute of exposure to DBD plasma, a comparison between *P. aeruginosa* and *S. aureus* showed that *S. aureus* had more colonies on the Petri dishes than *P. aeruginosa* (**Table 1**). This difference is because Gram-positive bacteria have a thicker cell wall due to more stacked peptidoglycan layer than Gram-negative bacteria¹¹. The mechanism for killing bacteria is due to DBD plasma causing reactive oxygen and nitrogen species

(RONS), which damage cell walls and cell membranes, leading to cytoplasm leakage that makes the bacteria unable to survive¹².

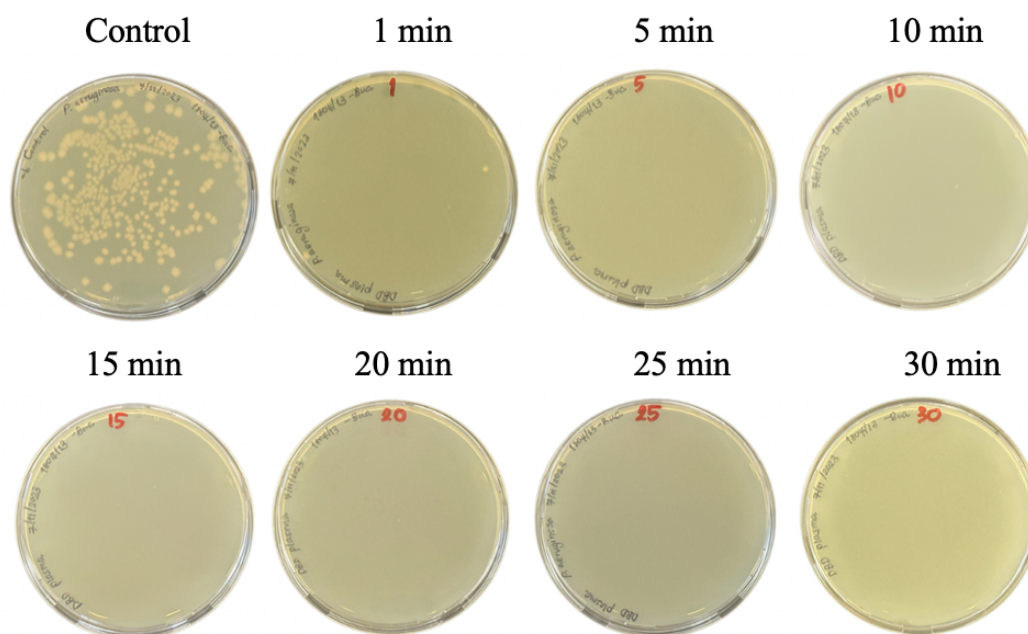


Figure 2. Colonies of *P. aeruginosa* on the NA plate after exposure to DBD plasma for 1, 5, 10, 15, 20, 25, and 30 minutes.

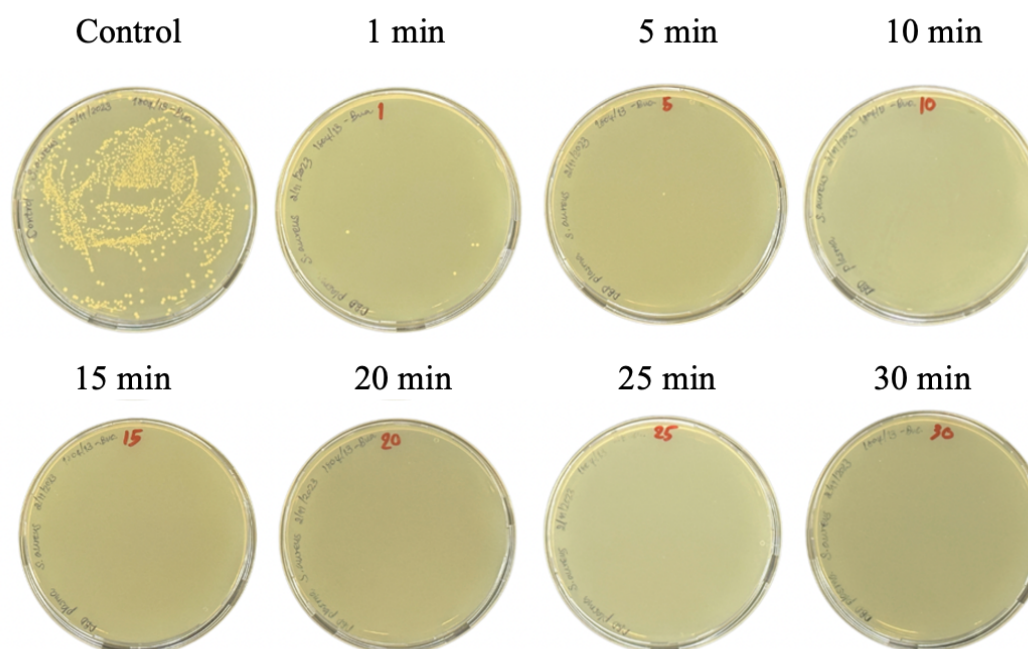


Figure 3. Colonies of *S. aureus* on the NA plate after exposure to DBD plasma for 1, 5, 10, 15, 20, 25, and 30 minutes.



Exposure of *A. niger* to DBD plasma showed that fungal colonies decreased as exposure time increased, and there were no hyphae were observed after 25 minutes of exposure (**Figure 4**). Since fungal spores have rodlets, which are structures that prevent water loss, and the cell walls of the spore are thicker than vegetative cells¹³, *A. niger* could tolerate DBD plasma better than bacterial cells (**Table 1**).

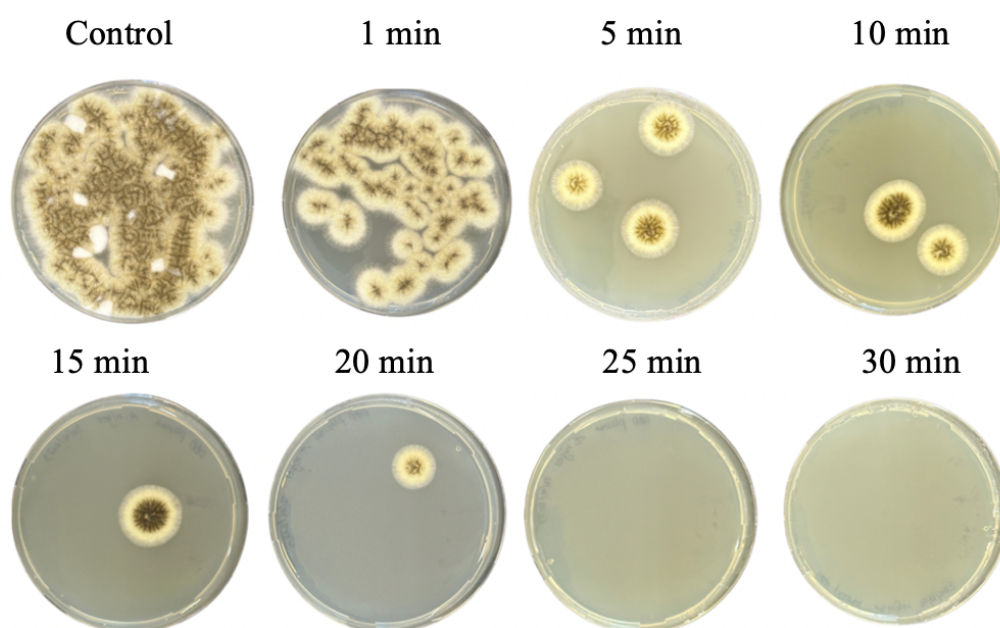


Figure 4. Colonies of *A. niger* on the NA plate after exposure to DBD plasma for 1, 5, 10, 15, 20, 25, and 30 minutes.

Table 1. Microbial colonies count (CFU/ml) after exposure to DBD plasma for 1, 5, 10, 15, 20, 25, 30, 40, 50, and 60 minutes.

| Microorganism | Exposure (min) | | | | | | | |
|----------------------|-----------------------|-------------------|-----------------|-----------------|-----------------|-----------------|----|----|
| | 0 | 1 | 5 | 10 | 15 | 20 | 25 | 30 |
| <i>P. aeruginosa</i> | 1.94×10^{11} | 2×10^7 | 0 | 0 | 0 | 0 | 0 | 0 |
| <i>S. aureus</i> | 2.92×10^{11} | 4×10^7 | 0 | 0 | 0 | 0 | 0 | 0 |
| <i>A. niger</i> | 7.2×10^8 | 3.5×10^8 | 3×10^7 | 2×10^7 | 1×10^7 | 1×10^7 | 0 | 0 |

Exposure of DBD plasma to EV-71 showed that the viral plaques decrease when the exposing time increases. Significant viral reductions were observed at 10 minutes, with plaque counts reducing to 1 PFU/ml by 60 minutes compared to the control group (**Figure 5**). DBD plasma could eliminate more than 99% of viruses at 40 minutes of exposure time. It is feasible that when microorganisms are directly exposed to plasma, the sterilizing process occurs through both chemical etching of the cells by RONS and physical damage to membrane proteins and DNA produced by charged particles¹⁴.

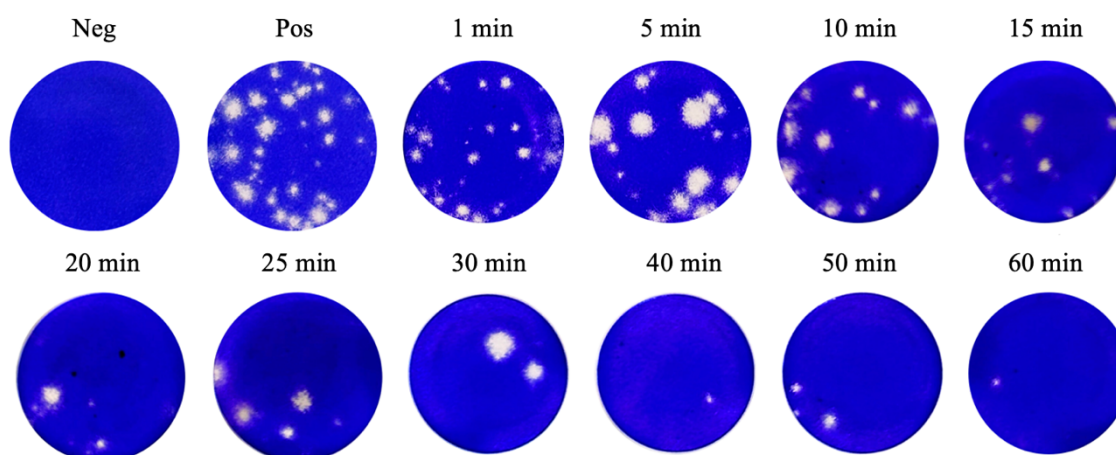


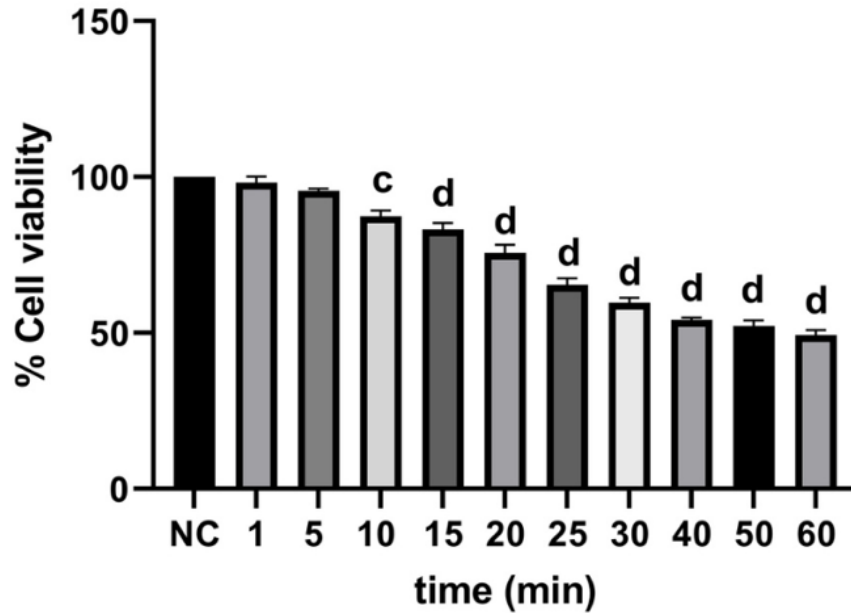
Figure 5. Plaques morphology of EV-71 after exposure to DBD plasma for 1, 5, 10, 15, 20, 25, 30, 40, 50, and 60 minutes.

The cell viabilities were measured by the absorbance values of each group. According to ISO 10993-5, a percentage of cell viability above 80% is considered non-cytotoxicity; 80% to 60% for weak cytotoxicity; 60% to 40% for moderate cytotoxicity; and less than 40% indicates strong cytotoxicity¹⁵. PSVK1 human keratinocyte cells and WI38 human lung cells had a survival rate of less than 80% when exposed for longer than 20 minutes. **(Figure 6a and b)**. At 25 minutes of exposure time, the cell viability of PSVK1 and WI38 was observed at 65.44% and 76.43%, respectively ($p < 0.0001$), indicating weak cytotoxicity. Observations at 60 minutes of exposure time showed that the cell viability of PSVK1 and WI38 further decreased to 49.31% and 50.22%, respectively, indicating moderate cytotoxicity. These outcomes were possibly caused by the generation of RONS in the DBD plasma system, which can induce cell apoptosis¹⁶. However, cell viability may vary depending on the type of cell. Previous studies examined the vitality of MRC5 and L132 lung cells, as well as H460 and HCC1588 lung cancer cells, after they were exposed to DBD plasma for 1 minute. The findings revealed that lung cancer cells were dramatically reduced, but normal lung cells were not¹⁷. Our results demonstrated that the DBD plasma could eliminate potential pathogens in indoor air, leading to air quality improvement. However, the application of DBD plasma in air purifiers should be optimized with biosafety considerations for human users.



a

PSVK1



b

WI38

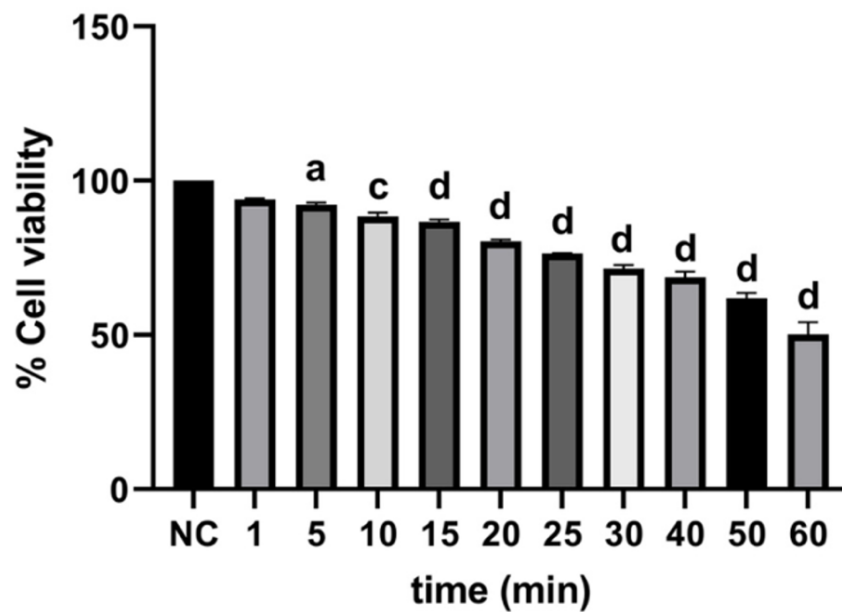


Figure 6. Cell viability of PSVK1 (a) and WI38 (b), after exposure to DBD plasma for 1, 5, 10, 15, 20, 25, 30, 40, 50, and 60 minutes.

$p < 0.05$ (a), $p < 0.01$ (b), $p < 0.001$ (c), $p < 0.0001$ (d)

Conclusion:

DBD plasma could eliminate more than 99.99% of *P. aeruginosa* and *S. aureus* within 5 minutes, while it took 25 minutes to eliminate *A. niger*. The virus EV-71 showed significant reductions at 10 minutes of exposure and decreased to more than 99% from 40 minutes onwards. The cell viability of the PSVK1 and WI38 after 25 minutes of exposure time was lower than 80%. The findings suggested that exposure of DBD plasma for 25 minutes can effectively inhibit the growth of potential pathogens, however it requires further optimization to minimize cell stress.

Acknowledgements:

Higher Education for Industry Consortium (Hi-FI) collaboration with the Bitwise (Thailand) co. ltd

References:

1. Kogelschatz U, Eliasson B, Egli W. Pure Appl. Chem. 1999;71(10):1828
2. Fridman G, Friedman G, Gutsol A *et al.* Plasma process polym. 2008;5(6):503-533
3. Borcia G, Anderson C. A., Brown N. M. D. Plasma Sources Sci Technol. 2003;12:335-344
4. Bárdos L, Baránková H. Thin Solid Films. 2010;1518(23):6705–6713
5. Kim J, Kim S, Lee Y *et al.* Applied Sciences. 2018; 8(8):1294
6. Gadri R. B., Roth J, Montie T. C. *et al.* Surf Coat Technol. 2000;131(1-3):528-541
7. Kasa R. A., Juswono U. P., Santjojo, D. J. D. H. JPPIPA. 2022;8(4):2371-2377
8. Chen J, Wang S.Z., Chen J.Y. *et al.* J. Sci Food Agric. 2019;99:39-46
9. Tappi S, Gozzi G, Vannini L *et al.* IFSET. 2016;33:225-233
10. Zhao L, Sun Y, Qiu R *et al.* J. Water Process Eng. 2022;50:103231
11. Pasquina-Lemonche L, Burns J, Turner R *et al.* Nature. 2020;582(7811):294–297
12. Wang H, Zhang L, Luo H, *et al.* Appl. Environ. Microbiol. 2019;86(1): 01907-19
13. Beever R. E., Dempsey G. P. Nature. 1978;272(5654):608-610
14. Smith J, Doe A. J. Plasma Res. 2020;45(2):123-134
15. ISO. (2009). Biological evaluation of medical devices — Part 5: Tests for in vitro cytotoxicity (ISO Standard No. 10993-5:2009). International Organization for Standardization
16. Sersenová D, Machala Z, Repiská V *et al.* Mol. 2021;26(14):4254
17. Panngom K, Baik K, Kyung Min *et al.* Cell Death Dis. 2013;4:642



BIRD NEST SITE CHARACTERISTICS IN URBAN GREEN AREAS OF CHULALONGKORN UNIVERSITY

Euakarn Thongchot,¹ Pongchai Dumrongrojwattana,² Nipada Ruankaew Disyatat^{2,*}

¹M.Sc. Program in Zoology, Department of Biology, Faculty of Science, Chulalongkorn University, Bangkok 10330, Thailand

² Department of Biology, Faculty of Science, Chulalongkorn University, Bangkok 10330, Thailand

*e-mail: Nipada.R@chula.ac.th

Abstract:

The decline of natural green spaces in urban areas negatively affect urban wildlife, especially birds, that use green spaces for living and breeding. The presence of bird nests indicates the capacity and capability of the urban green space for sustaining biodiversity. This study aims to study ecological factors determining nest site selection by native birds in Chulalongkorn University campus, one of urban green spaces in the Bangkok Metropolis. Bird nests were surveyed, and ecological characteristics of the nests and trees were measured. The study found that 160 trees of 16 species hosted 237 bird nests in the green areas of Chulalongkorn University. Four nest types were observed: platform, cavity, globular and cavity adopter nests. Platform nests were the most common nest type (52.3%). Rain trees *Samanea saman* were the species supporting the highest proportion of nests. The knowledge gained will be beneficial for appropriate conservation management of urban green spaces.

Introduction:

Loss of green spaces due to urbanization is a significant problem that impacts habitats and nesting grounds for various species^{1,2,3}, leading to biodiversity loss⁴. According to the Living Planet Report 2022, global biodiversity has declined by as much as 69% from 1997 to 2020⁵. This has prompted numerous countries to collaborate on addressing these issues, such as the strategic Plan for Biodiversity (2011-2020) and the Aichi Biodiversity Targets⁶, aimed at conserving and restoring biodiversity to ensure ecosystem services by 2050. Additionally, policies promoting the expansion of green spaces to enhance biodiversity diversity include Sustainable Development Goals (SDGs).

Thailand and Bangkok have made efforts to conserve biodiversity and green spaces by implementing various policies such as Master Plan for Integrated Biodiversity Management B.E. 2558 – 2564 (2015-2021)⁶, and ONEP Sustainable urban green space management practices phase 2 (2023-2027)⁷. Urban green spaces, defined as areas covered with diverse vegetation⁸, are currently of great interest across multiple sectors because they enhance biodiversity, provide human benefits as natural educational sites, recreational areas, and reduce urban pollution. Urban green area also benefits wildlife by serving as habitats, food sources and nesting sites^{9,10,11,12}

Similar to other wildlife, some birds can adapt to city conditions and utilize urban green spaces for survival and reproduction. Bird nests are common sights in city environment, showing evidence of successful adaptation by some birds to survive in urban green areas. The diversity of bird species and the occurrence of bird nests can indicate the environmental quality of habitat areas¹³. Birds have important roles in ecosystems, including pest control, seed dispersal, and providing cultural benefits to humans, such as recreation and stress relief. However, urbanization and the management of green spaces in the city may influence selection of nesting sites by urban birds.

Nests are constructed and used by most birds for roosting, protecting eggs, and hatchlings. Bird nests can be categorized into various types based on their shapes, including platform nests, cup nests, cavity nests, cavity adopter nests, retort nests, domed nests, and globular nests¹⁴. Human impacts have caused birds to adapt their nesting behaviors. Some bird species that have adapted to urban environments, such as *Passer montanus*, often choose to build their nests on man-made structures¹⁵. However, many bird species that have not adapted to urban areas still rely on vegetation in urban green spaces for nesting. Birds that build platform nests, such as *Nycticorax nycticorax*, need tall trees¹⁶. Birds that construct cup nests need trees with wide canopies. Species that create cavity nests, such as *Psilopogon haemacephalus*, need tall trees with dead branches¹⁷. Birds that are cavity adopters, such as *Athene brama*, depend on large natural tree cavities. Both retort and globular nests require tall trees^{18,19}. Therefore, scientific understanding on bird nesting site selection is necessary for the effective management of urban green spaces to support bird conservation in urban ecosystems.

However, studies on the impact of urbanization and green space management on bird nesting are still inadequate in Thailand. This research aims to study the ecological factors influencing birds nest site selection in urban green spaces, using Chulalongkorn University as the study site. Specifically, this study investigates the characteristics of nest sites in green spaces in Chulalongkorn University as well as the characteristics of the trees selected by birds for nesting. As the university with policies supporting the expansion of green areas and biodiversity conservation²⁰, the knowledge regarding bird nesting would be beneficial for landscape planning and management of green areas.

Methodology:

Study site

Chulalongkorn University is located in the center of Bangkok, with a campus area of 637 rai or 0.97 km², 33% of which is green areas consisting of perennial trees (approximately 4,500 trees²¹), shrubs, lawns, green roofs, and water sources. While birds can be seen nesting on all types of green areas, the current study focused mainly on bird nests on trees in the green areas of the university. The survey of bird nests and trees was conducted between April to May 2024.

Bird nest and tree characteristics

Bird nests were searched, usually with binoculars, on trees in the green areas of Chulalongkorn University. When a nest was found, it was classified into one of the following nest types: platform nests, cup nests, cavity nests, cavity adopter nests, retort nests, domed nests, and globular nests. Then nest height above the ground was measured using a NIKON Forestry Pro laser rangefinder and recorded. Subsequently, the locations of trees hosting bird nests were recorded with a Real-time Kinematics (RTK) GNSS receiver, Stonex s900a. Then the trees were identified to species using the Plants in Chulalongkorn University guidebook²², and measured for the following data: tree height, diameter at breast height (DBH), canopy cover (length of the canopy projection on the ground).

Data analysis

Descriptive statistics was used to calculate the mean and standard deviation of bird nest and tree data, including height of bird nests; height, DBH and canopy cover of trees with bird nests. The analyses were performed from two perspectives, namely bird nests categorized by nest types and trees with bird nests.



Results and Discussion:

The study found a total of 237 bird nests on 160 trees of 16 species within Chulalongkorn University's green areas. On average, 1.5 nests per tree were found, with the range between 1 to 5 nests per tree. Four types of bird nests were found: platform nest, cavity nest, globular nest, and cavity adopter nest (Figure 1).

The most common nest type was the platform nest, with 124 nests (52.3% of all nests), followed by cavity nests, globular nests and cavity adopter nests (Table 1). Overall, the platform nests were located at a higher height (15.1 ± 2.5 m above the ground) than other nest types (approximately 8-10 m above the ground). Accordingly, the trees that platform nests were located on were taller and larger in DBH and canopy cover than the trees with nests of the other types (Table 1).

Table 1.

Characteristics of bird nests and trees that the nests were found on in the green area of Chulalongkorn University

| Nest type | Nest characteristics | | Trees with bird nests | | |
|---------------------|----------------------|-----------------|-----------------------|-----------------|------------------|
| | Number of nests | Nest height (m) | Tree height (m) | Tree DBH (cm) | Canopy cover (m) |
| Platform nest | 124 | 15.1 ± 2.5 | 16.4 ± 2.0 | 93.3 ± 38.0 | 16.4 ± 5.1 |
| Cavity nest | 68 | 9.6 ± 3.7 | 13.5 ± 2.9 | 66.3 ± 32.0 | 11.4 ± 5.7 |
| Globular nest | 36 | 8.6 ± 3.0 | 10.9 ± 2.8 | 40.3 ± 17.3 | 8.7 ± 2.6 |
| Cavity adopter nest | 9 | 9.0 ± 3.4 | 14.0 ± 2.4 | 68.5 ± 26.1 | 11.1 ± 3.1 |

Notes: values are reported as average \pm standard deviation



Figure 1.

Examples of bird nests found in the green areas of Chulalongkorn University; a. platform nest; b. cavity nest; c. globular nest; and d. cavity adopter nest

More than half of the bird nests were observed on rain trees *Samanea saman* (132 nests; 55.7%), followed by *Tabebuia rosea* (24 nests) and *Pterocarpus* sp. (20 nests), respectively. Even though found on 7 tree species, 84.7% of the platform nests were observed on *S. saman*. Six tree species supported cavity nests, with more than a third of the nests on *S. saman*. Globular nests were observed on 11 tree species, including *Pterocarpus* sp. Cavity adopter nests were seen on only four tree species, with four nests on *Peltophorum pterocarpum* (Table 3).

Of the total of 16 hosting tree species, 13 were identified to species, with three unidentified taxa. The highest number of nests was found on *S. saman* (132 nests on 92 trees, with an average of 1.4 nests per tree). *P. pterocarpum*, *Pterocarpus* sp., *T. rosea*, and

Terminalia catappa also hosted bird nests, with more than one nest per each tree (Table 2). These common trees hosting bird nests tend to be tall and trees, with height greater than 15 m and DBH approaching 100 cm in some species. Smaller-sized trees such as *Lagerstroemia loudonii*, *Terminalia ivorensis*, and *Ficus* sp. could also host bird nests in their canopy.

Table 2.

Tree species hosting bird nests in the green area of Chulalongkorn University and selected ecological characteristics

| Tree species | No. of nests | No. of trees | No. of nests/tree | Nest height (m) | Tree height (m) | Tree DBH (cm) | Tree canopy cover (m) |
|--|--------------|--------------|-------------------|-----------------|-----------------|---------------|-----------------------|
| <i>Samanea saman</i> | 132 | 92 | 1.4 | 14.5 ± 3.0 | 15.9 ± 2.3 | 96.8 ± 36.8 | 17.3 ± 4.3 |
| <i>Peltophorum pterocarpum</i> | 18 | 12 | 1.5 | 11.2 ± 4.3 | 14.5 ± 2.7 | 76.3 ± 13.7 | 9.2 ± 2.1 |
| <i>Pterocarpus</i> sp. | 20 | 12 | 1.7 | 7.4 ± 4.5 | 10.1 ± 3.1 | 34.1 ± 20.0 | 5.5 ± 3.9 |
| <i>Tabebuia rosea</i> | 24 | 12 | 2.0 | 10.1 ± 2.0 | 14.6 ± 1.8 | 45.8 ± 12.0 | 7.5 ± 1.5 |
| <i>Terminalia catappa</i> | 15 | 7 | 2.1 | 12.5 ± 3.6 | 16.2 ± 2.0 | 75.6 ± 7.5 | 14.5 ± 1.2 |
| <i>Lagerstroemia loudonii</i> | 4 | 4 | 1.0 | 7.9 ± 0.8 | 8.5 ± 0.5 | 24.4 ± 2.8 | 6.1 ± 2.4 |
| <i>Terminalia ivorensis</i> | 4 | 4 | 1.0 | 11.4 ± 1.1 | 12.6 ± 0.8 | 54.5 ± 15.1 | 12.6 ± 2.8 |
| <i>Ficus</i> sp. | 3 | 3 | 1.0 | 7.2 ± 2.0 | 8.0 ± 2.8 | 42.5 ± 25.8 | 9.0 ± 0.0 |
| <i>Calophyllum inophyllum</i> | 5 | 2 | 2.5 | 5.2 ± 0.4 | 9.2 ± 0.0 | 39.7 ± 0.0 | 13.0 ± 0.0 |
| <i>Cassia fistula</i> x <i>Cassia javanica</i> | 2 | 2 | 1.0 | 6.0 ± 0.0 | 10.6 ± 0.0 | 24.8 ± 0.0 | 11.5 ± 0.0 |
| <i>Mangifera indica</i> | 2 | 2 | 1.0 | 9.0 ± 0.0 | 14.0 ± 4.2 | 52.0 ± 0.0 | 8.0 ± 0.0 |
| <i>Millingtonia hortensis</i> | 2 | 2 | 1.0 | 10.8 ± 0.0 | 15.0 ± 0.0 | 32.0 ± 0.0 | 7.3 ± 0.0 |
| Unidentified 1 | 2 | 2 | 1.0 | 9.0 ± 0.0 | 10.0 ± 0.0 | 25.0 ± 0.0 | 6.5 ± 0.0 |
| Unidentified 2 | 2 | 2 | 1.0 | 5.2 ± 0.0 | 10.6 ± 0.0 | 42.3 ± 0.0 | 6.3 ± 0.0 |
| <i>Tamarindus indica</i> | 1 | 1 | 1.0 | 8.0 ± 0.0 | 15.0 ± 0.0 | 57.2 ± 0.0 | 11.0 ± 0.0 |
| Unidentified 3 | 1 | 1 | 1.0 | 6.2 ± 0.0 | 8.4 ± 0.0 | 18.0 ± 0.0 | 8.3 ± 0.0 |

Notes: values are reported as average ± standard deviation

The majority of the platform nests (79%) were found on *S. saman* while cavity nests were distributed more evenly on *S. saman*, *Pterocarpus* sp., *T. rosea* and *T. catappa* (Table 3). About a quarter of the globular nests were found on *Pterocarpus* sp. and the rest were distributed among the other 10 tree species. Almost half of the cavity adopter nests were located on *P. pterocarpum*. Additionally, trees from a single species could host nests of more than one type.

**Table 3.**

Distribution of various bird nest types on hosting tree species in the green area of Chulalongkorn University

| Tree species | Number of nests | Platform nest | Cavity nest | Globular nest | Cavity adopter nest |
|--|-----------------|---------------|-------------|---------------|---------------------|
| <i>Samanea saman</i> | 132 | 105 | 25 | 0 | 2 |
| <i>Tabebuia rosea</i> | 24 | 2 | 16 | 4 | 2 |
| <i>Pterocarpus</i> sp. | 20 | 0 | 12 | 8 | 0 |
| <i>Peltophorum pterocarpum</i> | 18 | 10 | 0 | 4 | 4 |
| <i>Terminalia catappa</i> | 15 | 2 | 12 | 0 | 1 |
| <i>Calophyllum inophyllum</i> | 5 | 0 | 1 | 4 | 0 |
| <i>Lagerstroemia loudonii</i> | 4 | 0 | 0 | 4 | 0 |
| <i>Terminalia ivorensis</i> | 4 | 1 | 0 | 3 | 0 |
| <i>Ficus</i> sp. | 3 | 0 | 0 | 3 | 0 |
| Unidentified 1 | 2 | 0 | 0 | 2 | 0 |
| Unidentified 2 | 2 | 0 | 2 | 0 | 0 |
| <i>Millingtonia hortensis</i> | 2 | 2 | 0 | 0 | 0 |
| <i>Mangifera indica</i> | 2 | 2 | 0 | 0 | 0 |
| <i>Cassia fistula</i> x <i>Cassia javanica</i> | 2 | 0 | 0 | 2 | 0 |
| Unidentified 3 | 1 | 0 | 0 | 1 | 0 |
| <i>Tamarindus indica</i> | 1 | 0 | 0 | 1 | 0 |
| All | 237 | 124 | 68 | 36 | 9 |

Various tree species are planted and maintained within the green areas of Chulalongkorn University, including *S. saman*, the iconic tree of the university, as well as *P. pterocarpum*, *T. rosea*, and *Pterocarpus* sp.; all of which are trees with large trunk and branches, and a broad canopy, making them some of the most preferred species by landscape designers and managers²⁶. These suitable attributes also allow medium to large birds, such as *Corvus macrorhynchos* and *Butorides striata*, to nest and build platform nests on the tree canopy, especially the open top canopy of *S. saman*. Conversely, globular nests are typically constructed by smaller species, such as *Gracupica floweri* and *G. nigricollis*, which need denser leafy surroundings to avoid predators²⁷. Cavity nests are prevalently associated with the soft wood characteristic of some trees found on the campus, such as *S. saman* and *T. rosea*. These trees with large trunks and branches are ideal for cavity-nesting species, which prefer dead branches to construct the cavity¹⁷.

The composition of tree species in urban green spaces generally differ from that of natural forests because tree species were selected for purposes such as shading and aesthetics. In addition, management and maintenance practices for specific shape and size of trees would also influence tree community structures as well as physical environment. Even though the pool of available trees might be limited in a city landscape, common bird species could adapt and successfully nest in the urban environments, selecting sites that offer resources while minimizing stresses such as high human density and pollution²³. Additionally, urbanization might change the composition and abundance of predators, which may respond differently to the vegetation characters around bird nests²⁴.

Even though this study only captured the two-month snapshot of bird nest distribution on trees in the green areas of Chulalongkorn University, the results showed a potential of the trees in an urban ecosystem to function as a breeding habitat for various birds that may have adapted to the city conditions. The distribution and abundance of bird nests will definitely vary across seasons due to their varying breeding periods and nest-building behaviors throughout the year. For example, *P. haemacephalus*, one of common bird species in Chulalongkorn University, which typically breeds from January to March¹⁷, was seen in some

of the cavity nests during this study. The number of nests in urban habitats can vary greatly because of availability of suitable substrates for nest construction and environmental stressors. Furthermore, the review of literature showed that the number of nests in urban habitats could vary widely depending on the methodology and focal groups of birds or nest types. For example, 340 nests built by 16 bird species were observed in 300-ha urban landscape in China²³. In yet another case, approximately 16 cavity nests per 50 trees were observed in cemeteries and parks in Chicago, USA³⁰. Urban expansion may reduce predation rates by urban predators, leading to increased opportunities for nest building of birds adapted to city conditions²⁵. Furthermore, some nests may last longer than the actual breeding period of birds. For instance, platform nests, which consist of a complex arrangement of overlapping twigs, are strong enough to support the weight and size of birds, allowing abandoned nests to remain visible¹⁴.

Additionally, variation in resources may determine nest site selection, including floral nectar and fruits provided by tree species in the urban landscape. The abundance of food supports the nesting of some bird species that breed during the rainy season¹⁴. Other ecological characteristics, such as quality of the trees, as well as disturbance from human activities, may be determining factors for tree selection for nesting by birds in urban environments²⁸. Obtaining information on habitat preferences for nest building can be useful in management of urban green space for various purposes ranging from bird population control to conservation of bird species. For example, planting less suitable trees and tree pruning were suggested as strategies to manage the population size of birds such as House crow *Corvus splendens*²⁹. Besides, certain habitats within the urban landscape can potentially support bird nests and appropriate management is required so that sufficient nest sites to conserve bird species. For instance, cemeteries and parks retain large trees with cavities that support cavity-nesting birds, such as woodpeckers and owls³⁰. Therefore, further study is recommended to obtain complete information regarding the birds and their preferences for substrates suitable for nesting and living in urban ecosystems.

Conclusion:

The present study demonstrated that trees in urban green areas could support the nesting behavior of birds and that certain tree characteristics could provide inputs into the management of the urban ecosystems for the conservation of biodiversity and consequently provision of ecosystem services. Rain trees *S. saman* was the most preferred tree species by birds constructing nests, especially the platform nests. Other tree species could support cavity nests and other types. The knowledge gained would help in planning landscape management and biodiversity conservation in urban green spaces.

Acknowledgements:

We thank the Development and Promotion of Science and Technology Talents Project (DPST) for the financial support to E.T. We thank various research assistants for their help in carrying out the survey. We also thank the Department of Biology, Faculty of Science, Chulalongkorn University, for logistics and support.

References:

1. McKinney ML. BioScience. 2002;52:883–890.
2. Vlahov D, Galea S. Journal of Urban Health. 2002;79:s1–s12.
3. Fuller RA, Tratalos J, and Gaston KJ. Diversity and Distributions. 2009;15:328–337.
4. McKinney ML. Urban Ecosystems. 2008;11:161–176.
5. World Wide Fund for Nature. Living Planet Report 2022-Building a nature-positive society. Gland(CH): WWF. 2022.



6. Office of natural resource and environmental Policy and Planning (ONEP). Ministry of Natural Resources and Environment. 2015: 1–82.
7. Office of natural resource and environmental Policy and Planning (ONEP). Ministry of Natural Resources and Environment. 2022: 1–40.
8. De Haas W, Hassink J, and Stuiver M. *Frontiers in Environmental Science*. 2021;9:1–11.
9. McDonnell MJ, and Pickett STA. *Ecology*. 1990;71:1232–1237.
10. Fernández-Juricic E, and Jokimäki J. *Biodiversity and Conservation*. 2001;10:2023–2043.
11. Rojas-Rueda D, Nieuwenhuijsen MJ, Gascon M, Perez-Leon D, and Mudu P. *Lancet Planet Health*. 2019;3:e469–e477.
12. Kwon OH, Hong I, Yang J, Wohn DY, Jung WS, and Cha M. *EPJ Data Science*. 2021;10:1–13.
13. Sanesi G, Padoa-Schioppa E, Lorusso L, Bottoni L, and Laforteza R. *Arboriculture and Urban Forestry*. 2009;35:80–86.
14. Lovette IJ, and Fitzpatrick JW. *Cornell Lab of Ornithology's handbook of bird biology* 3rd ed. Chichester(UK): John Wiley & Sons, Ltd; 2016.
15. Lee JH, Kim SY, and Sung HC. *Animal Taxonomy and Ecology*. 2024;70:46–60.
16. Fournier AMV, Lancaster JD, Yetter AP, Hine CS, Beckerman T, Figge J, et al. *Avian Conservation and Ecology*. 2021;16:1–12.
17. Meckvichai W. *Natural History Bulletin of the Siam Society*. 1998; 46:55–62.
18. Bhattacharyya M, and Das A. *International Journal of Research and Analytical Reviews* 2020;7:97–107.
19. Ding Z, Guo A, Lian M, Wang Y, Ying W, Jiang H, et al. *Frontiers in Ecology and Evolution*. 2023;11:1–10.
20. Chief Transformation and Strategic Office. *Chulalongkorn University Strategic Plan 2021 – 2024*. Bangkok: Chulalongkorn university; 2020.
21. Wongpakdee S. *Carbon sequestration potential in aboveground biomass of trees in Chulalongkorn University*. Bangkok: Chulalongkorn Univ.; 2013
22. Boonkerd T, Klinratana P, and Yannawat S. *Plant of Chulalongkorn University*. Bangkok: Chula book center; 2013.
23. Han Y, Bai J, Zhang Z, Wu T, Chen P, Sun G, et al. *Science of the Total Environment*. 2019;690:748–759.
24. Phringphroh M, Khamcha D, Sankamethawee W, Powell LA, Angkaew R, Pierce AJ, et al. *Ornithology*, 2024;141:1–12.
25. Møller AP. *Behavioral Ecology*, 2012;23:1033 –1035.
26. Staples G, and Elevitch C. *Samanea saman* (rain tree) Species profiles for Pacific Island Agroforestry. Holualoa(USA): Permanent Agriculture Resources (PAR). 2006.
27. Martin TE. *BioScience*. 1993;43:523–532.
28. Reynolds SJ, Ibáñez-Álamo JD, Sumasgutner P, and Mainwaring MC. *Journal of Ornithology*. 2019; 160:841–860.
29. Soh MCK, Sodhi NS, Seoh RKH, and Brook BW. *Landscape and Urban Planning*. 2002;59:217–226.
30. Bovyn RA, Lordon MC, Grecco AE, Leeper AC, and LaMontagne JM. *Journal of Urban Ecology*. 2019;5:1–9.



Comparative Analysis of Prokaryotic and Eukaryotic Production Systems for Anti-GD2 Tri-specific killer engager (TriKE)

Natthanan Khankham^{1,2}, Chutipa Chiawpanit^{1,3}, Pachara Sattayawat^{1,3}, Yingmanee Tragoolpua^{1,3}, Aussara Panya^{1,3*}

¹Cell Engineering for Cancer Therapy Research Group, Chiang Mai University, Chiang Mai 50200, Thailand.

²Graduate Master's Degree Program in Applied Microbiology, Department of Biology, Faculty of Science, Chiang Mai University, Chiang Mai 50200, Thailand.

³Department of Biology, Faculty of Science, Chiang Mai University, Chiang Mai 50200, Thailand.

*e-mail: aussara.pan@cmu.ac.th

Abstract:

Immunotherapy is an alternative cancer treatment that effectively enhances cytotoxicity of immune cells and provides more safety profile against various cancers. Natural killer (NK) cells, a critical component of the innate immune system, play a vital role in targeting and eliminating abnormal and cancerous cells. However, reduced NK cell levels in cancer patients are often associated with poor outcomes in cancer treatments. To address this, a tri-specific killer engager (TriKE) has emerged as a promising strategy. TriKEs not only enhance the killing activity of NK cells but also increase their numbers, potentially leading to improved therapeutic outcomes. A TriKE molecule consists of three components: a single-chain variable fragment (ScFv) that targets tumor-associated antigens on cancer cells, human interleukin 15 to promote NK cell proliferation, and a single-domain antibody that binds to CD16 on NK cells. These components are connected by a linker domain. Although TriKEs have garnered significant attention for their potential in immunotherapy, large-scale production remains a challenge. This study aims to compare two commonly used systems for TriKE-based immunotherapy development: prokaryotic and eukaryotic expression systems. We designed and constructed a TriKE targeting disialoganglioside GD2 expressed on cancer cells. To produce this TriKE, we used *E. coli* strain BL21(DE3) with the pET-22b expression vector for prokaryotic production and HEK293T cells for eukaryotic production following lentiviral transduction and the establishment of stable cell lines. Our findings revealed that the anti-GD2 TriKE produced in the prokaryotic system was not secreted into the culture media, necessitating additional steps for isolation and recovery. In contrast, the eukaryotic system allowed efficient secretion of the TriKE into the culture media. These results provide valuable insights into production strategies for TriKEs, highlighting the advantages of eukaryotic systems for scalable and effective immunotherapy development.

Introduction:

Immune surveillance comprises two parts : innate and adaptive immunity that are working together to detect and eliminate cancer cell (Abbott and Ustoyev, 2019). The innate immunity is a first-line detection and subsequently activates the adaptive immunity (Olszanski, 2015). Natural killer (NK) cells are one of innate immunity which play a central role on anti-cancer cells response without prior activation (Abbott and Ustoyev, 2019). The cytotoxicity of NK cells mainly occurs via conjugation of CD16 and its ligand to mediate antibody-dependent cellular cytotoxicity (ADCC), resulting in target cell death (Meazza *et al.*, 2011). However, cancer cells can adapt themselves to escape immune cells (Oiseth and Aziz, 2017). For instance, the immune suppressive cytokine such as interleukin 10 (IL-10)

and transforming growth factor- β (TGF- β) secretion leading to disrupt recognition and activation of NK cells (Terrén *et al.*, 2019). Moreover, chemotherapy can decrease number of the NK cells (Braun and Harris, 1986). Thus, improving both of quality and quantity of the NK cells is an important strategy to enhance survival rate of cancer patients.

Immunotherapy is an alternative cancer treatment that improves the specificity and killing efficiency of immune cells against various cancers, including blood cancers such as lymphoma (Shanbhag and Ambinder, 2018), leukemia (Huang *et al.*, 2023) and solid tumors such as non-small cell lung cancer (Alexander *et al.*, 2020), neuroblastoma (Nguyen and Thiele, 2021), and liver cancer (Donne and Lujambio, 2023) etc. A tri-specific killer engager (TriKE)-based immunotherapy composing with three parts: a single-chain variable fragment (ScFv) that targets tumor-associated antigens on cancer cells, human interleukin 15 to promote NK cell proliferation, and a single-domain antibody that binds to CD16 on NK cells. This molecule potentially bridges between the NK cells and cancer cells (Vallera *et al.*, 2016). Recent clinical applications of TriKEs have been reported for various cancers, including leukemia (Schubert *et al.*, 2011), lymphomas (Felices *et al.*, 2019), breast cancer (Xie *et al.*, 2003), ovarian cancer (Vallera *et al.*, 2021), and lung cancer (Kennedy *et al.*, 2023). These studies demonstrate that TriKEs can effectively promote NK cell proliferation and enhance their cytotoxicity against cancer cells. Notably, the GTB-3550 TriKE has recently been approved by the Food and Drug Administration (FDA) and is currently undergoing Phase 1 clinical trials for the treatment of CD33-positive leukemia.

TriKEs are generally produced using two types of expression systems: prokaryotic and eukaryotic. In prokaryotic systems, such as those utilizing *Escherichia coli* strain BL21(DE3), TriKE production occurs through transcription and translation in the cytoplasm (Bill and von der Haar, 2015). For example, the CD19-targeting 161519 TriKE was successfully produced and isolated from *E. coli* BL21(DE3), demonstrating enhanced specificity and improved killing efficiency of NK cells against CD19-expressing Burkitt's lymphoma cell lines (Felices *et al.*, 2019). In contrast, eukaryotic systems, often using the HEK293 cell line, offer post-translational modifications that are advantageous for the functional activity of the TriKEs (Midgett and Madden, 2007). For instance, the anti-CLEC12A TriKE, when transfected into HEK293 cells, was able to induce NK cell proliferation and was specific to enhance NK cell activation against acute myeloid leukemia (AML) cell lines (Arvindam *et al.*, 2021). While there are notable differences between these production systems, a detailed comparison of their respective advantages and disadvantages is essential for guiding large-scale TriKE production.

This study aimed to compare prokaryotic and eukaryotic production systems for TriKEs. We designed and constructed a TriKE targeting disialoganglioside GD2, a well-known tumor antigen overexpressed in various solid cancers, including neuroblastoma (Mujoo *et al.*, 1987), lung cancer (Reppel *et al.*, 2022), and melanoma (Cheresh and Klier, 1986). GD2 has been reported to promote the proliferation and migration of cancer cells (Yoshida *et al.*, 2001). However, the monoclonal antibody targeting GD2, Dinutuximab, has shown limited efficacy in solid tumors due to constraints imposed by the tumor microenvironment (Ahmed and Cheung, 2014). Thus, GD2 remains a promising target for immunotherapy development in solid cancers. In this study, we utilized *E. coli* strain BL21(DE3) with the pET-22b expression vector for prokaryotic expression and HEK293T cells for eukaryotic expression following lentiviral transduction and the establishment of stable cell lines. Recombinant anti-GD2 TriKE was produced in both systems, and its expression was confirmed through SDS-PAGE and Western blot analysis. We compared the pros and cons of each system, including production steps, protein quality, and production costs, to provide valuable insights for large-scale protein production in the future.



Methodology:

Construction of anti-GD2 TriKE

The Anti-GD2 TriKE construct was designed and composed of a signal protein (SP), an anti-CD16 single domain antibody, Interleukin-15 (IL-15), and a single chain variable fragment (ScFv) from an approved human 3F8 anti-GD2 monoclonal antibody (Kushner *et al.*, 2018) (Figure 1A, 1B). Each domain was linked with a linker (L). Moreover, the molecule of anti-GD2 TriKE was tagged with a 6X HIS tag for monitoring protein expression.

Table 1. List of primers for positive clone selection

| Primer name | sequence |
|---------------------------------|----------------------------------|
| F-BamHI-antiGD2-TriKE (pET-22b) | 5'AAGGATCCGGAAGTTCAACTTGT3' |
| R-NotI-anti-GD2 TriKE (pET-22b) | 5'AAAGCGGCCGCTTTAATTTCCAG3' |
| Cloning-F (pCDH) | 5'GAATTCGGATCCATGGGATGGAGCTGTA3' |
| Cloning-R (pCDH) | 5'ATTTGCGGCCGCTCAGTGGTGATGGTGA3' |

Prokaryotic system

The anti-GD2 TriKE construct was cloned into pET-22b vector at specific restriction sites, *Bam*HI and *Not*I. After the anti-GD2 TriKE was inserted into pET-22b, the anti-GD2 TriKE in pET-22b was transformed into *E. coli* BL21(DE3), and positive clones were screened by colony PCR with specific primers as indicated in Table 1 and their sequences were analyzed.

Eukaryotic system

The anti-GD2 TriKE was inserted into the pCDH vector at the *Eco*RI and *Not*I restriction sites, which also has a red fluorescence protein (RFP) to visualize positive cells (Figure 1D). After the cloning step, successfully ligated positive clones into the pCDH vector were screened using specific primers as indicated in Table 1 and their sequences were analyzed.

Generation of the stable cell secreting anti-GD2 TriKE

Prokaryote

After the positive clone selection, *E. coli* BL21(DE3) containing a recombinant plasmid of anti-GD2 TriKE was inoculated into LB broth supplemented with 100 µg/ml of ampicillin with continuous shaking at 250 rpm for 16-18 hours at 37°C. After that, *E. coli* BL21(DE3) was subsequently inoculated into fresh LB broth supplemented with 100 µg/ml of ampicillin and grown until log phase. To express anti-GD2 TriKE, the *E. coli* BL21(DE3) was induced with 1 mM IPTG and incubated with shaking (250 rpm) at 37°C for 18-20 hours. Finally, induced *E. coli* BL21(DE3) was determined expression of anti-GD2 TriKE with 6X HIS tag via western blot analysis. In addition, the *E. coli* BL21(DE3) positively expressed anti-GD2 TriKE was prepared as glycerol stock and stored at -80°C for further uses.

Eukaryote

To determine the expression of anti-GD2 TriKE in eukaryotic cells, the recombinant plasmid was transfected into HEK293T cell lines with lipofectamine (Invitrogen, Life Technologies, Carlsbad, CA, USA) and HEK293T cells that positively expressed anti-GD2 TriKE were first observed by visualization of a red fluorescence signal under an inverted fluorescence microscope (Nikon Instrument, Inc., Melville, NY, USA). Moreover, western blot analysis was performed to observe the expression of anti-GD2 TriKE via mouse anti-His monoclonal antibody (Invitrogen, Life Technologies, Carlsbad, CA, USA).

To generate HEK293T stable cells that permanently secrete anti-GD2 TriKE, lentivirus containing anti-GD2 TriKE recombinant plasmid was generated and transduced into HEK293T cells. After transduction step, positive cells expressing RFP were selected with puromycin (1 µg/ml) until a homogenous RFP-positive population was observed. The HEK293T stable cells were subsequently stored at -80°C in freezing media (fetal bovine serum (FBS) supplemented with 10% DMSO) for further uses.

Production of anti-GD2 TriKE

Prokaryote

A positive clone of *E. coli* BL21 (DE3) containing anti-GD2 TriKE was incubated into LB medium supplemented with 100 µg/ml ampicillin. For negative control, competent cells of *E. coli* BL21 (DE3) were inoculated into plain LB medium (without ampicillin), and then incubated overnight with constant shaking (250 rpm) at 37°C. After that, the bacterial cultures were then inoculated into a fresh LB medium at a dilution of 1:100 and incubated at 37°C for 4 hours. Then the bacterial cells were collected by centrifugation at 16°C, 5,000 rpm for 15 minutes, and fresh LB medium containing 1 mM IPTG, and 100 µg/ml ampicillin was then replaced and incubated at 37°C, overnight. To collect *E. coli* BL21 (DE3) expressing anti-GD2 TriKE, centrifugation at 8,000 rpm for 15 minutes, 4°C was performed. Then the cell pellets were sonicated on ice using a sonication probe at 20% amplitude 15 sec on/ 15 sec off for 10 minutes. After that, centrifugation at 14,000 x g for 10 minutes at 4°C was subsequently demonstrated. Finally, the supernatant and pellet cell were collected to detect expression of anti-GD2 TriKE by western blot analysis (Figure 3A).

Eukaryote

To produce anti-GD2 TriKE in HEK293T cells, the HEK293T stable cells secreting anti-GD2 TriKE were cultured with DMEM medium (Gibco; Thermo Fisher Scientific, Waltham, MA, USA) supplemented with 10% FBS (Gibco; Thermo Fisher Scientific, Waltham, MA, USA) in a T75 cell culture flask (Nest Biotechnology, China) and then incubated at 37°C with 5% CO₂ for overnight. After that, the culture medium was replaced with serum-free Optimem (Gibco; Thermo Fisher Scientific, Waltham, MA, USA) cell culture medium, and the cells were continuously cultured for 72 hours. The secreted anti-GD2 TriKE was collected from the culture medium and the expression of the anti-GD2 TriKE was observed by western blot analysis (Figure 3B).

Results and Discussion:

Construction and expression of anti-GD2 TriKE

The recombinant anti-GD2 TriKE was designed to induce the NK cell proliferation and bridge the NK cells to cancer cells resulting in enhanced NK cell cytotoxicity (Figure 1A and 1B). The construction of the anti-GD2 TriKE was performed using cloning techniques. The anti-GD2 TriKE was successfully cloned into both the pET-22b (Figure 1C) and pCDH (Figure 1D) vectors. In the prokaryotic system, only one colony of the positive clone was able to grow on LB agar supplemented with 100 µg/ml of ampicillin. Positive clone identification was performed by colony PCR, and a PCR product of the positive clone was observed at 1,518 base pairs (bp) in size (Figure 2A). Additionally, the anti-GD2 TriKE was successfully ligated into the pCDH vector, with 13 clones identified by 732 bp PCR products (Figure 2B).

The positive clone of *E. coli* BL21(DE3) containing the anti-GD2 TriKE was cultured and induced to express the anti-GD2 TriKE. The protein had an expected molecular weight of 59.15 kDa (pI=5.71) according to the ExPASy Server calculation (https://web.expasy.org/compute_pi/). According to the results shown in Figure 2C, the anti-



GD2 TriKE was predominantly expressed in *E. coli* BL21(DE3), as observed by Western blot analysis with a size approximately of 63 kDa. In the eukaryotic system, the anti-GD2 TriKE clone number 4 was highly expressed in HEK293T cells at the same size as in the prokaryotic system (Figure 2D).

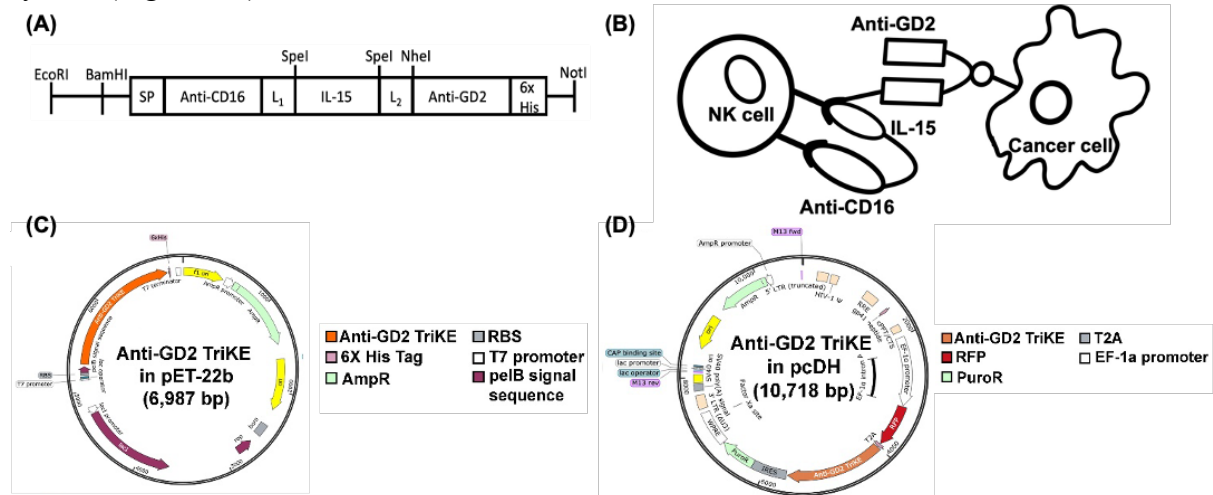


Figure 1. Construct of anti-GD2 TriKE

(A) Anti-GD2 TriKE construct, 1,518 bp in size. (B) The mechanism of anti-GD2 TriKE: Anti-CD16 recognizes the CD16 receptor on NK cells, Interleukin-15 (IL-15) promotes NK cell proliferation, and Anti-GD2 scFv recognizes GD2 on cancer cells. (C) Anti-GD2 TriKE in the pET-22b plasmid for the prokaryotic system. (D) Anti-GD2 TriKE in the pCDH plasmid for the eukaryotic system.

According to the results, the production of TriKEs is commonly performed using both prokaryotic (Sørensen and Mortensen, 2005) and eukaryotic (Jäger *et al.*, 2013) systems. In prokaryotic systems, the pET vector is frequently used for bacterial expression in *E. coli* BL21(DE3) cells under the inducible lac promoter to enhance protein expression (Dilworth *et al.*, 2018). In this study, IPTG stimulation was used to induce protein expression. In contrast, various vectors are commonly used in eukaryotic expression systems, including pTT5, pcDNA3, and pCDH vectors (Jäger *et al.*, 2013). Among these, the pCDH vector has proven to be the most effective for TriKE production (Felices *et al.*, 2016).

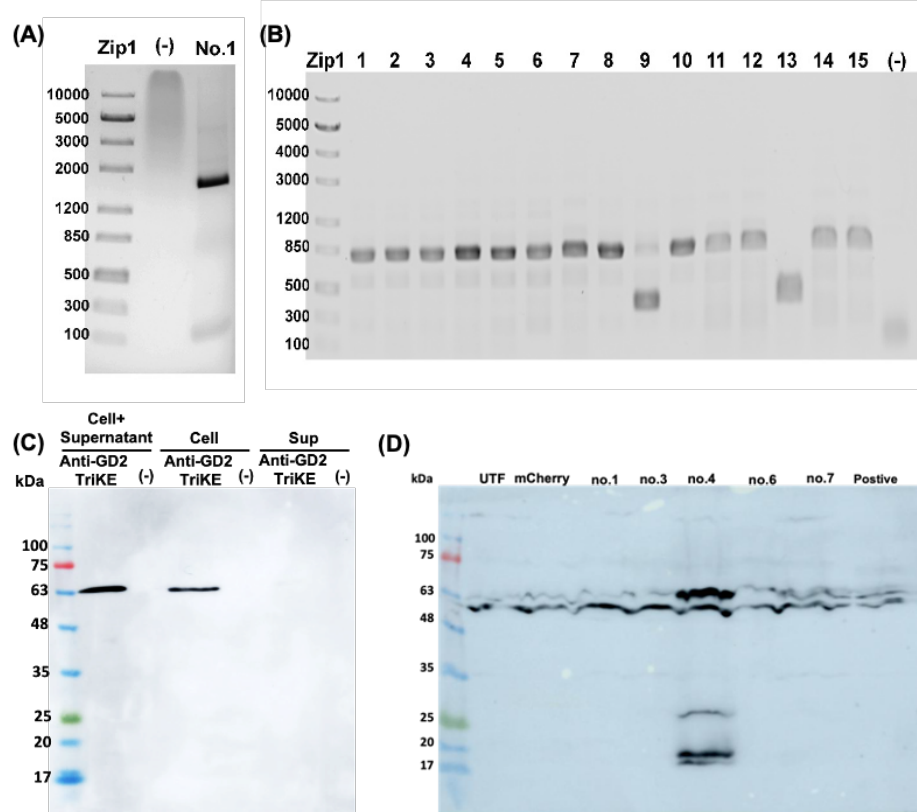


Figure 2. Positive clones and expression of anti-GD2 TriKE

(A) A positive clone from the prokaryotic system. (B) Positive clones from the eukaryotic system. (C) Expression of anti-GD2 TriKE in the prokaryotic system, Lane 1: Cell and supernatant of *E. coli* strain BL21(DE3) containing anti-GD2 TriKE, Lane 2: Cell and supernatant of negative control, Lane 3: Cell of *E. coli* strain BL21(DE3) containing anti-GD2 TriKE, Lane 4: Cell of negative control, Lane 5: Supernatant of *E. coli* strain BL21(DE3) containing anti-GD2 TriKE and Lane 6: Supernatant of negative control. (D) Expression of anti-GD2 TriKE in the eukaryotic system, Lane 1: Untransfected cell (UTF), Lane 2: mCherry, Lane 3: Positive clone number 1, Lane 4: Positive clone number 3, Lane 5: Positive clone number 4, Lane 6: Positive clone number 6, Lane 7: Positive clone number 7 and Lane 8: Positive control.

Production of Anti-GD2 TriKE

In the prokaryotic system, the anti-GD2 TriKE was produced and obtained within 24 hours (Figure 3A), whereas secretion of the anti-GD2 TriKE in the eukaryotic system required 4 days (Figure 3B). For prokaryotic production, isolation of the anti-GD2 TriKE necessitated sonication, as previously mentioned. The optimal conditions for isolating the anti-GD2 TriKE were determined to be 20% amplitude for 10 minutes (Figure 3C). Despite this, anti-GD2 TriKE was predominantly found in inclusion bodies (Figure 3C). Longer sonication times risked degrading the anti-GD2 TriKE due to heat, leading to lower protein yields from degradation. In the eukaryotic system, a homogeneous population of HEK293T stable cells secreting anti-GD2 TriKE was observed after puromycin selection (Figure 3D). The anti-GD2 TriKE was successfully secreted into the culture medium, in contrast to normal HEK293T cell lines (Figure 3E). Additionally, the secreted anti-GD2 TriKE was detected by Western blot analysis (approximately 75 kDa) (Figure 3E).



To summarize the comparison of prokaryotic and eukaryotic systems for TriKE production, the relevant data from this study are compiled and presented in Table 2

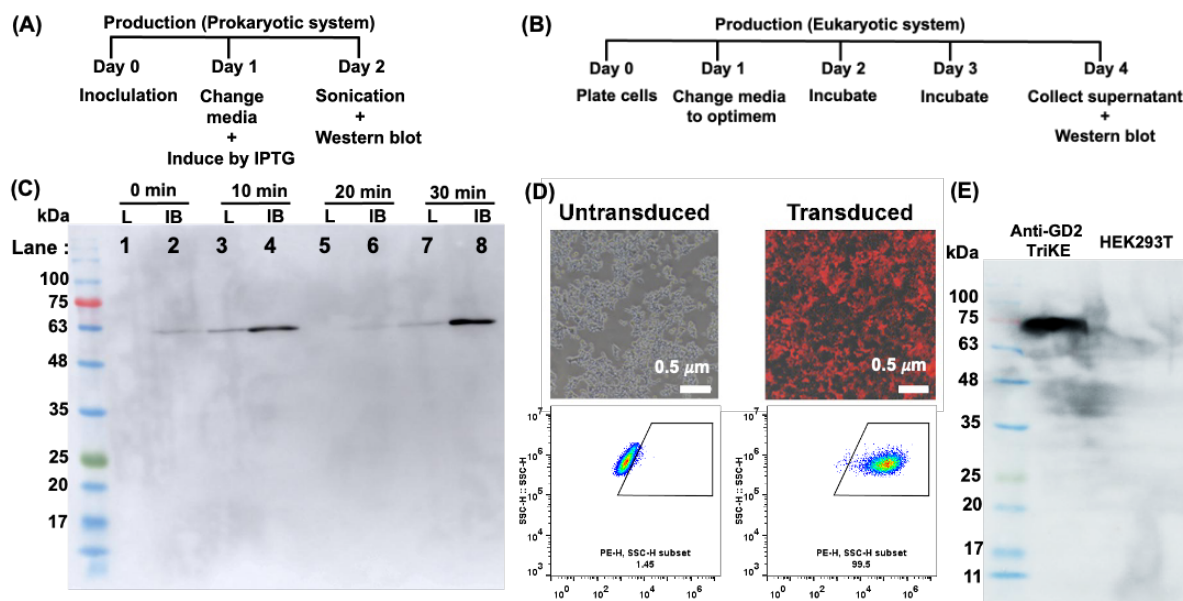


Figure 3. Production of anti-GD2 TriKE

(A) Diagram of anti-GD2 TriKE production in the prokaryotic system. (B) Diagram of anti-GD2 TriKE production in the eukaryotic system. (C) Optimization of sonication conditions by varied times; 0, 10, 20 and 30 minutes compared at 20% amplitude. Lysate (L) and Inclusion body (IB); Lane 1: lysate (no sonication), Lane 2 inclusion body (no sonication), Lane 3: lysate (10-minute sonication), Lane 4: inclusion body (10-minute sonication), Lane 5: lysate (20-minute sonication), Lane 6: inclusion body (20-minute sonication), Lane 7: lysate (30-minute sonication) and Lane 8: inclusion body (30-minute sonication). (D) Anti-GD2 TriKE expression from transduction into HEK293T under inverted fluorescence microscope compared with untransduced (negative control) and confirm expression level by Flow cytometry. (E) Western blot analysis of anti-GD2 TriKE was secreted from HEK293T cell lines into media compared with HEK293T negative.

In our experiment, the anti-GD2 TriKE could not be secreted into the culture supernatant (Figure 2C). This issue arises because the pET-22b vector contains a pelB signal sequence that directs the protein to be secreted into the periplasm rather than the culture supernatant (Low *et al.*, 2013). Consequently, isolation of the TriKE from bacterial cells requires additional procedures such as sonication, osmotic shock, detergent treatment, or high-pressure homogenization (Jalalirad, 2013; Middelberg, 2008; Nossal and Heppel, 1966). The sonication technique was used to isolate the anti-GD2 TriKE due to its rapid and simple ability to disrupt membranes for recombinant protein extraction (Kim *et al.*, 2011). Other approaches were used to isolate the TriKE molecule from bacterial cells including a homogenizer cell disruption technique (Schmohl *et al.*, 2017) and a solution containing Triton X-100 (Felices *et al.*, 2019).

Our TriKE produced in the prokaryotic system was found to be in the form of non-soluble inclusion bodies. Recombinant proteins expressed in prokaryotic systems often aggregate into insoluble inclusion bodies and may be inactive (Rosano and Ceccarelli, 2014).

Consequently, additional processing is required to recover the recombinant protein (Yamaguchi and Miyazaki, 2014). Following recovery, a lower yield and reduced binding activity of the recombinant protein have been reported (Clark, 2001). In contrast, TriKEs produced in the eukaryotic system are directly secreted into the culture medium, eliminating the need for refolding methods. However, a significant limitation of the eukaryotic system is its higher production cost, with a notable increase in cost per liter of culture (Table 2). In summary, while both prokaryotic and eukaryotic systems offer distinct advantages, the optimal system depends on the specific requirements and considerations of the application, particularly in the context of immunotherapy development.

Table 2. Comparison of prokaryotic and eukaryotic protein production systems

| Properties | Prokaryotic system | Eukaryotic system |
|------------------------------|------------------------------|---|
| Vector | pET-22b | pCDH |
| Selection process | do not require | selection with puromycin |
| Inducer | IPTG | do not require |
| Production time | 24 h* | 72 h** |
| Protein isolation process | sonication | do not require |
| Protein formation | insoluble | soluble |
| Relative yield | require refolding | do not require refolding process |
| Protein modifications | do not require | post-transcription and post-translation |
| Cost productivity (cost / L) | Low medium cost (112 Bath/L) | High medium cost (2,465 Bath/L) |
| Large-scale production | easy to up scale | difficult to up scale |

Note: * Indicates the time period from inoculation to expression, ** Indicates the time period from the change of culture media to the collection of supernatant.

Conclusion:

In this study, the production of anti-GD2 TriKE recombinant protein was successfully developed using both prokaryotic and eukaryotic systems. While each production system has its own advantages and disadvantages, the comparative analysis presented in this study provides valuable insights. This information serves as a useful guide for TriKE development and other immunotherapy platforms, particularly for large-scale or industrial production.

Acknowledgements:

This project was supported by National Research Council of Thailand (NRCT) (grant number N42A670181). We would like to thank Department of Biology, Faculty of Science, Chiang Mai University for their partial support.

References:

1. Abbott, M., and Ustoyev, Y. (2019). Cancer and the Immune System: The History and Background of Immunotherapy. *Semin Oncol Nurs*, 35(5), 150923.
2. Ahmed, M., and Cheung, N. K. (2014). Engineering anti-GD2 monoclonal antibodies for cancer immunotherapy. *FEBS Lett*, 588(2), 288-297.
3. Alexander, M., Kim, S. Y., and Cheng, H. (2020). Update 2020: Management of Non-Small Cell Lung Cancer. *Lung*, 198(6), 897-907.



4. Arvindam, U. S., van Hauten, P. M. M., Schirm, D., Schaap, N., Hobo, W., Blazar, B. R., Vallera, D. A., Dolstra, H., Felices, M., and Miller, J. S. (2021). A trispecific killer engager molecule against CLEC12A effectively induces NK-cell mediated killing of AML cells. *Leukemia*, 35(6), 1586-1596.
5. Bill, R. M., and von der Haar, T. (2015). Hijacked then lost in translation: the plight of the recombinant host cell in membrane protein structural biology projects. *Curr Opin Struct Biol*, 32, 147-155.
6. Braun, D. P., and Harris, J. E. (1986). Effect of chemotherapy on NK function in the peripheral blood of cancer patients. *Cancer Immunol Immunother*, 21(3), 240-245.
7. Cheresch, D. A., and Klier, F. G. (1986). Disialoganglioside GD2 distributes preferentially into substrate-associated microprocesses on human melanoma cells during their attachment to fibronectin. *J Cell Biol*, 102(5), 1887-1897.
8. Clark, E. D. (2001). Protein refolding for industrial processes. *Curr Opin Biotechnol*, 12(2), 202-207.
9. Dilworth, M. V., Piel, M. S., Bettaney, K. E., Ma, P., Luo, J., Sharples, D., Poyner, D. R., Gross, S. R., Moncoq, K., Henderson, P. J. F., Miroux, B., and Bill, R. M. (2018). Microbial expression systems for membrane proteins. *Methods*, 147, 3-39.
10. Donne, R., and Lujambio, A. (2023). The liver cancer immune microenvironment: Therapeutic implications for hepatocellular carcinoma. *Hepatology*, 77(5), 1773-1796.
11. Felices, M., Kodal, B., Hinderlie, P., Kaminski, M. F., Cooley, S., Weisdorf, D. J., Vallera, D. A., Miller, J. S., and Bachanova, V. (2019). Novel CD19-targeted TriKE restores NK cell function and proliferative capacity in CLL. *Blood Adv*, 3(6), 897-907.
12. Felices, M., Lenvik, T. R., Davis, Z. B., Miller, J. S., and Vallera, D. A. (2016). Generation of BiKEs and TriKEs to Improve NK Cell-Mediated Targeting of Tumor Cells. *Methods Mol Biol*, 1441, 333-346.
13. Huang, Y. H., Wan, C. L., Dai, H. P., and Xue, S. L. (2023). Targeted therapy and immunotherapy for T cell acute lymphoblastic leukemia/lymphoma. *Ann Hematol*, 102(8), 2001-2013.
14. Jäger, V., Büssow, K., Wagner, A., Weber, S., Hust, M., Frenzel, A., and Schirrmann, T. (2013). High level transient production of recombinant antibodies and antibody fusion proteins in HEK293 cells. *BMC Biotechnol*, 13, 52.
15. Jalalirad, R. (2013). Selective and efficient extraction of recombinant proteins from the periplasm of Escherichia coli using low concentrations of chemicals. *J Ind Microbiol Biotechnol*, 40(10), 1117-1129.
16. Kennedy, P. R., Vallera, D. A., Ettestad, B., Hallstrom, C., Kodal, B., Todhunter, D. A., Bendzick, L., Hinderlie, P., Walker, J. T., Pulkrabek, B., Pastan, I., Kratzke, R. A., Fujioka, N., Miller, J. S., and Felices, M. (2023). A tri-specific killer engager against mesothelin targets NK cells towards lung cancer. *Front Immunol*, 14, 1060905.
17. Kim, Y., Babnigg, G., Jedrzejczak, R., Eschenfeldt, W. H., Li, H., Maltseva, N., Hatzos-Skintges, C., Gu, M., Makowska-Grzyska, M., Wu, R., An, H., Chhor, G., and Joachimiak, A. (2011). High-throughput protein purification and quality assessment for crystallization. *Methods*, 55(1), 12-28.
18. Kushner, B. H., Cheung, I. Y., Modak, S., Basu, E. M., Roberts, S. S., and Cheung, N. K. (2018). Humanized 3F8 Anti-GD2 Monoclonal Antibody Dosing With Granulocyte-Macrophage Colony-Stimulating Factor in Patients With Resistant Neuroblastoma: A Phase 1 Clinical Trial. *JAMA Oncol*, 4(12), 1729-1735.

19. Meazza, R., Azzarone, B., Orengo, A. M., and Ferrini, S. (2011). Role of common-gamma chain cytokines in NK cell development and function: perspectives for immunotherapy. *J Biomed Biotechnol*, 2011, 861920.
20. Middelberg, A. (2008). 2 Microbial Cell Disruption by High-Pressure Homogenization. In (pp. 11-21).
21. Midgett, C. R., and Madden, D. R. (2007). Breaking the bottleneck: eukaryotic membrane protein expression for high-resolution structural studies. *J Struct Biol*, 160(3), 265-274.
22. Mujoo, K., Cheresh, D. A., Yang, H. M., and Reisfeld, R. A. (1987). Disialoganglioside GD2 on human neuroblastoma cells: target antigen for monoclonal antibody-mediated cytotoxicity and suppression of tumor growth. *Cancer Res*, 47(4), 1098-1104.
23. Nguyen, R., and Thiele, C. J. (2021). Immunotherapy approaches targeting neuroblastoma. *Curr Opin Pediatr*, 33(1), 19-25.
24. Nossal, N. G., and Heppel, L. A. (1966). The release of enzymes by osmotic shock from *Escherichia coli* in exponential phase. *J Biol Chem*, 241(13), 3055-3062.
25. Oiseth, S. J., and Aziz, M. S. (2017). Cancer immunotherapy: a brief review of the history, possibilities, and challenges ahead. *Journal of Cancer Metastasis and Treatment*, 3, 250-261.
26. Olszanski, A. J. (2015). Principles of immunotherapy. *J Natl Compr Canc Netw*, 13(5 Suppl), 670-672.
27. Reppel, L., Tsahouridis, O., Akulian, J., Davis, I. J., Lee, H., Fucà, G., Weiss, J., Dotti, G., Pecot, C. V., and Savoldo, B. (2022). Targeting disialoganglioside GD2 with chimeric antigen receptor-redirected T cells in lung cancer. *J Immunother Cancer*, 10(1).
28. Rosano, G. L., and Ceccarelli, E. A. (2014). Recombinant protein expression in *Escherichia coli*: advances and challenges. *Front Microbiol*, 5, 172.
29. Schmohl, J. U., Felices, M., Oh, F., Lenvik, A. J., Lebeau, A. M., Panyam, J., Miller, J. S., and Vallera, D. A. (2017). Engineering of Anti-CD133 Trispecific Molecule Capable of Inducing NK Expansion and Driving Antibody-Dependent Cell-Mediated Cytotoxicity. *Cancer Res Treat*, 49(4), 1140-1152.
30. Schubert, I., Kellner, C., Stein, C., Kügler, M., Schwenkert, M., Saul, D., Mentz, K., Singer, H., Stockmeyer, B., Hillen, W., Mackensen, A., and Fey, G. H. (2011). A single-chain triplebody with specificity for CD19 and CD33 mediates effective lysis of mixed lineage leukemia cells by dual targeting. *MAbs*, 3(1), 21-30.
31. Shanbhag, S., and Ambinder, R. F. (2018). Hodgkin lymphoma: A review and update on recent progress. *CA Cancer J Clin*, 68(2), 116-132.
32. Sørensen, H. P., and Mortensen, K. K. (2005). Advanced genetic strategies for recombinant protein expression in *Escherichia coli*. *J Biotechnol*, 115(2), 113-128.
33. Terrén, I., Orrantia, A., Vitallé, J., Zenarruzabeitia, O., and Borrego, F. (2019). NK Cell Metabolism and Tumor Microenvironment. *Front Immunol*, 10, 2278.
34. Vallera, D. A., Felices, M., McElmurry, R., McCullar, V., Zhou, X., Schmohl, J. U., Zhang, B., Lenvik, A. J., Panoskaltsis-Mortari, A., Verneris, M. R., Tolar, J., Cooley, S., Weisdorf, D. J., Blazar, B. R., and Miller, J. S. (2016). IL15 Trispecific Killer Engagers (TriKE) Make Natural Killer Cells Specific to CD33+ Targets While Also Inducing Persistence, In Vivo Expansion, and Enhanced Function. *Clin Cancer Res*, 22(14), 3440-3450.
35. Vallera, D. A., Oh, F., Kodali, B., Hinderlie, P., Geller, M. A., Miller, J. S., and Felices, M. (2021). A HER2 Tri-Specific NK Cell Engager Mediates Efficient Targeting of Human Ovarian Cancer. *Cancers (Basel)*, 13(16).



36. Xie, Z., Shi, M., Feng, J., Yu, M., Sun, Y., Shen, B., and Guo, N. (2003). A trivalent anti-erbB2/anti-CD16 bispecific antibody retargeting NK cells against human breast cancer cells. *Biochem Biophys Res Commun*, 311(2), 307-312.
37. Yamaguchi, H., and Miyazaki, M. (2014). Refolding techniques for recovering biologically active recombinant proteins from inclusion bodies. *Biomolecules*, 4(1), 235-251.
38. Yoshida, S., Fukumoto, S., Kawaguchi, H., Sato, S., Ueda, R., and Furukawa, K. (2001). Ganglioside G(D2) in small cell lung cancer cell lines: enhancement of cell proliferation and mediation of apoptosis. *Cancer Res*, 61(10), 4244-4252.



CYTOTOXIC AND ANTIPROLIFERATIVE EFFECTS OF ETHANOL AND METHANOL EXTRACTS FROM *Annona muricata* L. LEAVES AND SEEDS ON HUMAN PROMYELOCYTIC LEUKEMIA (HL-60) AND HORMONE-DEPENDENT BREAST CARCINOMA (MCF-7) CELLS

Cherlynn van Beem*

Department of Biological Science, Faculty of Science and Digital Innovation, Thaksin University, Phatthalung 93210, Thailand

*e-mail: cherlynn@tsu.ac.th

Abstract:

The LC₅₀ values of *Annona muricata* L. extracts (20, 40, 60, 80, and 100 mg/mL), determined from brine shrimp cytotoxicity tests and MTT assays on HL-60 and MCF-7 cells, exhibited a significant correlation with the total phenolic and flavonoid content of the extracts ($p < 0.05$). The cytotoxicity of the extracts increased in proportion to their phenolic and flavonoid concentrations, indicating a dose-dependent response. Apoptosis was induced in a concentration-dependent manner, with a marked increase in apoptotic cell populations corresponding to higher extract doses. After 24 hours of treatment, the early apoptotic cell percentage in HL-60 cells rose to $50.15 \pm 0.70\%$ following exposure to the seed extract (S/e), while in MCF-7 cells, early apoptosis reached $55.23 \pm 0.71\%$ after treatment with the methanolic seed extract (S/m). The highest early apoptotic rates were recorded in HL-60 cells ($63.13 \pm 0.64\%$) and MCF-7 cells ($55.23 \pm 0.71\%$) under S/m treatment, while the late apoptotic stages were observed at $16.52 \pm 0.52\%$ and $13.98 \pm 0.67\%$, respectively. Additionally, all extracts induced a time-dependent increase in the protein expression of apoptotic markers, including caspase-3, caspase-8, and p53, while significantly downregulating Bcl-2 expression, highlighting the apoptotic pathway activation.

Introduction:

Plants have long been central to pharmacological research due to their rich diversity of bioactive metabolites, which provide a wide spectrum of therapeutic properties. Between 1981 and 2012, natural products contributed to the development of nearly 60% of all therapeutic agents, with the figure rising to approximately 75% for anticancer drugs. Despite these advances, many plant species remain underexplored, requiring detailed scientific investigations. Species with extensive traditional use are especially promising for yielding new active compounds for treating various diseases, highlighting the need to validate traditional applications and elucidate underlying mechanisms to develop new pharmaceuticals^{1,2,3}.

Annona muricata L., commonly known as soursop or graviola, is a tropical tree from the Annonaceae family. It is widely recognized in ethnobotanical practices for treating various ailments, including fever, pain, asthma, and skin conditions. Notably, *A. muricata* has garnered attention for its potential anticancer properties, earning the title "cancer killer"^{4,19} due to its cytotoxicity against a wide range of cancer cell lines. Traditional uses of *A. muricata* leaves and seeds in South America and Africa, particularly Nigeria, for cancer treatment have spurred scientific interest in understanding its anticancer mechanisms^{5,6}. However, the detailed effects of *A. muricata* extracts on specific cancer cell lines, such as human promyelocytic leukemia (HL-60) and hormone-dependent breast carcinoma (MCF-7), remain inadequately explored.

Extensive chemical investigations of *A. muricata* leaves and seeds have identified a broad range of bioactive compounds, including acetogenins, alkaloids, and essential oils.

Acetogenins, in particular, are notable for their potent antitumor, cytotoxic, and antiparasitic activities. Over 50 mono-THF acetogenins have been isolated from *A. muricata* seeds and leaves, with compounds such as epomuricenins-A and B, montecristin, and muridienins showing potential as key intermediates in acetogenin biosynthesis. Recent studies have also identified sabadelin, a novel compound that may serve as a precursor to other bioactive acetogenins^{7,8}.

In addition to its anticancer properties, soursop is recognized for its complex aroma, with over 114 volatile compounds, predominantly esters, contributing to its unique profile. Comprehensive analyses using gas chromatography and mass spectrometry have identified key volatile compounds, including esters, alcohols, terpenes, acids, and ketones, which play a role in the fruit's sensory characteristics. Furthermore, soursop seed meal contains (S)-oxynitrilase, an enzyme with promising biocatalytic properties^{17,18,19}.

Given the promising preliminary findings on the bioactive compounds of *A. muricata* and its traditional uses, this study aims to investigate the cytotoxic and antiproliferative effects of *A. muricata* leaves and seed extracts on HL-60 and MCF-7 cancer cell lines. Specifically, the research seeks to correlate the cytotoxic effects with the total phenolic and flavonoid content of the extracts and explore the apoptotic pathways activated by these compounds. By providing deeper insights into the mechanisms of action of *A. muricata*, this study aims to contribute to the potential development of new anticancer therapies based on natural products.

Methodology:

Plant Material

Fresh leaves and ripe fruit seeds of *A. muricata* L. (four years old) were collected in November 2012 from the botanical garden at Thaksin University, Thailand. The plant samples were identified, and voucher specimens were deposited in the herbarium of the Department of Biology, Faculty of Science and Digital Innovation, TSU with the voucher number TSU-260315.

Sample Preparation

The collected leaves and seeds of *A. muricata* L., each weighing 1 kg, were cleaned and air-dried at room temperature. The dried plant parts were then ground into a fine powder. A total of 200 g of the ground leaves and seeds were separately soaked and macerated in 500 ml of 70% ethanol and 100% methanol, each in triplicate, at room temperature for 24 hours. The extracts were filtered using Whatman No. 1 filter paper (Whatman Inc., Hillsboro, OR, USA) and concentrated under reduced pressure at 50°C using a rotary evaporator. The crude extracts were freeze-dried and stored at -20°C. For experimentation, the dried extracts were weighed and stored at 4°C without further purification.

Cytotoxicity Effect by Brine Shrimp Lethality Test (BSLT)

Dried brine shrimp (*Artemia* sp.) cysts were hatched in artificial seawater (3.8% NaCl, w/v) at room temperature (25°C). To ensure that mortality observed during the bioassay was due to bioactive compounds, the larvae were not fed. After hatching, the nauplii were transferred to a 24-well plate for treatment. Ten nauplii in 200 µL of suspension were added to each well containing 50 µL of ethanolic and methanolic extracts at various concentrations (20, 40, 60, 80, and 100 mg/mL). The plates were covered and incubated at room temperature for 24 hours. Dead (non-motile) and live brine shrimp were then counted⁴. Six replicates were performed for each treatment, and the corrected mortality was calculated using Abbott's formula. Finney's probit analysis was used to determine the lethal concentration to half of the test organisms (LC₅₀) and to obtain nonlinear regression data.



Cell Culture

The human promyelocytic leukemia cell line (HL-60) was obtained from the European Collection of Cell Cultures (ECCC, Sigma-Aldrich, India) and cultured in RPMI-1640 medium. The hormone-dependent human breast carcinoma cell line (MCF-7) was purchased from the American Type Culture Collection (ATCC, Sigma-Aldrich, USA) and maintained in DMEM medium. Both cell lines were supplemented with 10% fetal bovine serum (FBS) and 1% penicillin-streptomycin (10,000 U/mL penicillin G sodium and 104 µg/mL streptomycin sulfate in 0.85% saline). Cells were seeded at a density of 5×10^5 cells/mL in 75 cm² cell culture flasks (BD Falcon, BD Biosciences, San Jose, CA, USA) with 10 mL of fresh medium and incubated in a 5% CO₂ atmosphere at 37°C with 95% humidity. Cell viability was monitored using trypan blue staining, and exponentially growing cells (1×10^6 cells/mL) were harvested, counted, and used for further assays.

Antiproliferative Effects on Cultured Cell Lines by MTT Assay

The MTT assay is a colorimetric test based on the conversion of yellow tetrazolium bromide (MTT) into purple formazan by mitochondrial succinate dehydrogenase in viable cells. HL-60 and MCF-7 cells were seeded in 96-well plates (Nunc, Denmark) at a density of 1×10^5 cells/well in 100 µL of medium and incubated for 24 hours in a 5% CO₂ atmosphere at 37°C. Test extracts, diluted to final concentrations of 20, 40, 60, 80, and 100 mg/mL, were added (100 µL/well), and the plates were incubated for another 24 hours at 37°C. Subsequently, 50 µL of MTT reagent (5 mg/mL in phosphate-buffered saline, pH 7.4) was added to each well and incubated for an additional 4 hours. After removing the MTT, the cells were washed with $1 \times$ PBS, and 200 µL of DMSO was added to dissolve the formazan precipitate. The optical density was measured using an ELISA reader (LX-800) at 540 nm, with DMSO serving as a blank. The absorbance was plotted against sample concentrations to calculate the IC₅₀ (the concentration required to reduce the absorbance of MTT by 50%) using nonlinear regression.

Observation of Apoptotic Cell Morphology

HL-60 and MCF-7 cells in the log-phase of growth were transferred from 25 cm² cell culture flasks to sterilized 24-well plates (1×10^6 cells/2 mL/well) and cultured at 37°C under a humidified atmosphere of 5% CO₂. The cells were treated with extracts (100 µL) at concentrations of 20, 40, 60, 80, and 100 mg/mL and incubated for 24 hours under the same conditions. After incubation, the cells were harvested, washed twice with cold $1 \times$ PBS (pH 7.4), and fixed with 500 µL of 10% formaldehyde (v/v) for 5-10 minutes. The cells were then washed with $1 \times$ PBS and stained with 0.2 µg/mL Hoechst 33342 in PBS for 15 minutes. Morphological changes were observed and photographed using a digital microscope camera (DP50 + View Finder Lite Programme, Olympus). LC₅₀ was calculated using nonlinear regression.

DNA Fragmentation

HL-60 and MCF-7 cells were cultured, washed, and harvested before DNA extraction and electrophoresis. Briefly, log-phase cells were transferred from 25 cm² cell culture flasks to sterilized 24-well plates (1×10^6 cells/2 mL/well) and incubated at 37°C in a humidified atmosphere of 5% CO₂. Cells were treated with various concentrations of extracts (20, 40, 60, 80, and 100 mg/mL) and incubated for 24 hours. After treatment, the cells were harvested, washed with cold PBS (pH 7.4), and lysed with lysis buffer (pH 7.5) containing 0.5% SDS, 25 mM Tris-HCl, 0.5% proteinase K, and 5 mM EDTA at 55°C for 1 hour. Proteins were precipitated using phenol-chloroform-isoamyl acetate (25:24:1), and DNA was

isolated with 3 M sodium acetate (pH 5.2) and absolute ethanol. The DNA was washed, dried, and resuspended in Tris-EDTA (TE) buffer containing 100 µg/mL RNase A at 37°C for 30 minutes. Approximately 15 µg of DNA was electrophoresed on a 1.5% agarose gel, stained with ethidium bromide, and visualized under UV light to observe the DNA ladder.

Annexin V-FITC Assay

The early and late apoptosis of HL-60 and MCF-7 cells was assessed using the Annexin-V/PI staining assay. Cells (1×10^6) were plated in culture dishes and treated with sample extracts (20 mg/mL) for 24 hours. After treatment, the cells were harvested, washed twice with 1× PBS, and stained with Annexin-V/PI following the manufacturer's protocol. Early and late apoptosis of the HL-60 and MCF-7 cells was then analyzed by flow cytometry (BD FACSCanto™ II, San Jose, CA, USA). PI was used to detect late apoptosis and necrosis, while Annexin-V was used for early and late apoptosis. RNase A (10 mg/mL) was applied to limit the ability of PI to bind exclusively to DNA molecules. The cells were then centrifuged at $12,000 \times g$ for 20 minutes. The resulting lysates were stored at -80°C for subsequent analysis.

Preparation of Protein Lysate

During log-phase growth, sub-cultured cells (1×10^6 cells/2 mL/mL) were transferred from 25 cm² cell culture flasks to sterile 24-well plates and incubated at 37°C in a humidified atmosphere of 5% CO₂. The cells were treated with extracts (100 µL) at a concentration of 20 mg/mL for 3, 6, 9, 12, and 24 hours. After treatment, the cells were washed once in cold 1× PBS and suspended in 100 µL of lysis buffer containing 50 mM Tris-HCl (pH 7.4), 150 mM HCl, 1% NP-40, 0.5% DOC, 0.1% SDS, and 1 mM PMSF for 40 minutes.

Determination of Protein Concentration

Protein concentrations were measured in triplicate using the Bradford assay.⁵ A 10 µL aliquot of the lysate was mixed with 100 µL of diluted dye reagent (1:5 dilution), and the reaction mixture was incubated at 37°C for 30 minutes. Absorbance was measured at 595 nm, using bovine serum albumin (BSA) as the standard protein.

SDS-PAGE Gel Electrophoresis and Western Blot

To evaluate the impact of the sample extracts on HL-60 and MCF-7 cell lines, Western blot analysis was performed over a 24-hour period. Denaturing polyacrylamide gel electrophoresis (SDS-PAGE) was conducted. Protein samples (100 µg) were mixed with 4 parts of 5× SDS-gel loading buffer, containing 2.5 M Tris-base, 10% SDS, 0.5% bromophenol blue, 50% glycerol, and 20% mercaptoethanol, boiled for 5 minutes, and loaded onto a 12% SDS polyacrylamide gel. The gel was electrophoresed at 100 V for 45 minutes, and the separated proteins were electrotransferred onto Immobilon-P PVDF transfer membranes at 70 V for 1.5 hours at 4°C. Amido Black staining was used to verify protein transfer efficiency, and the gels were stained with Coomassie blue for confirmation.

The blotted membranes were blocked with 0.1% Tween-20 in Tris-buffered saline (TBST) containing 5% nonfat dry milk for 20 minutes at room temperature. The blots were then incubated with primary antibodies against caspase-3, caspase-8, p53, or Bcl-2 (diluted 1:1000) for 1 hour at room temperature, followed by washing in TBST (3 × 5 minutes). The membranes were then incubated with horseradish peroxidase (HRP)-conjugated goat anti-mouse secondary antibody (diluted 1:2000) for 1 hour and washed again in TBST (3 × 5 minutes). Tetramethylbenzidine (TMB) substrate was added in the dark to visualize the HRP-substrate reaction, forming a blue precipitate at the sites of HRP activity. The developed



bands were photographed, with actin used as a loading control and 0.1% fetal calf serum (FCS) as a positive control in SDS-PAGE.

After the initial analysis, the blots were stripped using stripping buffer containing 0.2 M glycine (pH 2.2), 150 mM NaCl, and 0.1% Tween-20 for 30 minutes at 50°C. The membranes were re-blocked with 0.1% Tween-20 in TBST containing 5% nonfat dry milk for 20 minutes and washed with TBST (3 × 5 minutes). The blots were then re-probed with antibodies against actin, followed by incubation with HRP and TMB solution as per the above protocol. The final blots were photographed to confirm the presence of apoptotic proteins.

Statistical Analyses

Statistical analysis was performed using Student's t-test and one-way analysis of variance (ANOVA). A p-value of less than 0.05 was considered statistically significant. Data were presented as means ± standard deviation (SD). The analyses were conducted using the SAS Statistical Software Package (release 8.02; SAS Institute Inc., Cary, NC, USA).

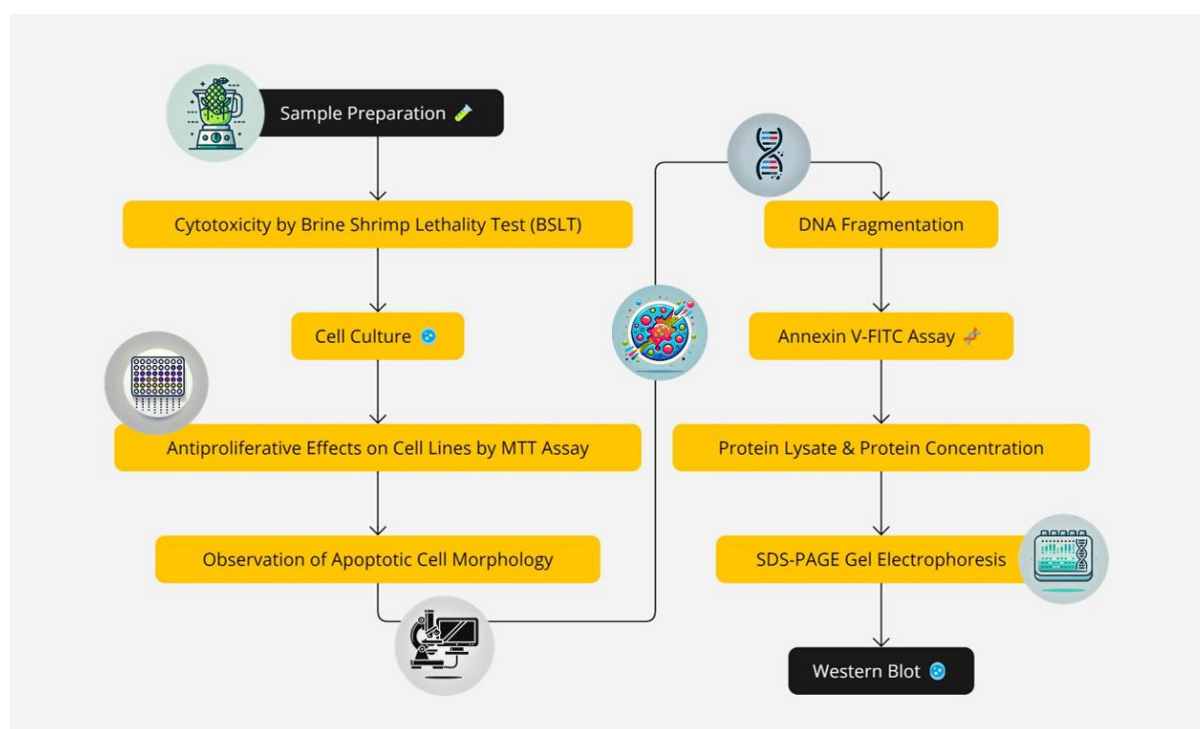


Figure 1.

Methodology for cytotoxic and antiproliferative effects of *Annona muricata* L. extracts on HL-60 and MCF-7 Cells

Results and Discussion:

The brine shrimp lethality test (BSLT) is a commonly employed bioassay for detecting a wide range of bioactivities in crude extracts. This method is cost-efficient, simple to learn, and requires only a small amount of test material. Importantly, BSLT shows a strong correlation with cytotoxic activity, making it a reliable predictor of plant toxicity. However, unlike mammalian systems, brine shrimp lack the Cytochrome P-450 enzymes necessary for metabolizing or detoxifying certain chemicals and exhibit different purine metabolism^{1,2,15}.

Despite these differences, brine shrimp bioassays have been successfully used to identify biologically active compounds that inhibit protein synthesis in mammalian cells by affecting RNA polymerase and ATPase systems. The mortality response of 24-hour-old brine shrimp larvae exposed to five different concentrations (20-100 mg/mL) of *A. muricata* L. extracts over 24 hours. Among the extracts, S/m was the most toxic, while L/e showed the highest LC₅₀. The LC₅₀ values ranked the extracts as S/m > S/e > L/m > L/e, with values of 24.14 ± 0.20 , 38.75 ± 0.29 , 67.27 ± 0.32 , and 85.11 ± 0.25 mg/mL, respectively. The cytotoxic effects of these extracts were correlated with their total phenolic and flavonoid content. The BSLT has been widely used as an initial screen for assessing the bioactivity of crude plant extracts.

In this study, *A. muricata* L. extracts showed a range of toxicities, with the methanolic seed extract (S/m) being the most potent and the ethanolic leaf extract (L/e) displaying the highest LC₅₀ value. This is consistent with studies that have demonstrated the strong cytotoxic properties of acetogenins, particularly those found in *A. muricata* seeds. Acetogenins, such as annonacin, inhibit mitochondrial complex I, leading to ATP depletion and apoptosis, a mechanism supported by the high toxicity observed in seed extracts^{3,18,19}. The ranking of LC₅₀ values in this study (S/m > S/e > L/m > L/e) corresponds to the findings of other studies that emphasize the higher potency of seed-based extracts.

The cytotoxic properties of *A. muricata* L. extracts were tested by assessing their effects on the proliferation of the human promyelocytic leukemia cell line (HL-60) and the hormone-dependent human breast carcinoma cell line (MCF-7) using the MTT assay. This assay uses a yellow, water-soluble tetrazolium salt, which is converted by metabolically active cells into a water-insoluble dark blue formazan through the reductive cleavage of the tetrazolium ring (Hansen, Nielsen, and Berg, 1989). HL-60 and MCF-7 cells were treated with varying concentrations of the extracts (20-100 mg/mL) for 24 hours at 37°C, after which cell viability was determined. Interestingly, the methanolic seed extract showed significant potency against both cell lines. The LC₅₀ values for HL-60 and MCF-7 cells treated with the S/m extract were 25.04 ± 0.32 mg/mL and 38.22 ± 0.21 mg/mL, respectively. These LC₅₀ values were correlated with the total phenolic and flavonoid content of the *A. muricata* L. extracts. When evaluating the cytotoxic effects on HL-60 and MCF-7 cancer cell lines, the methanolic seed extract (S/m) was most effective, with LC₅₀ values of 25.04 mg/mL for HL-60 cells and 38.22 mg/mL for MCF-7 cells. These results align with previous research that highlights the anticancer potential of *A. muricata* due to its acetogenins and flavonoids, where acetogenins from *A. muricata* disrupted mitochondrial functions in cancer cells, leading to apoptosis^{1,2,3}. Moreover, the correlation between the cytotoxicity and the phenolic and flavonoid content of the extracts further supports these compounds' roles in the anticancer activity observed in various studies^{10,17,18}.

Further investigation into the effects of *A. muricata* L. extracts on nuclear changes in HL-60 and MCF-7 cell lines was conducted using the Hoechst 33258 staining test at concentrations ranging from 20 to 100 mg/mL over 24 hours. Hoechst 33258 is a blue fluorescent dye that stains cell nuclei and is membrane-permeable. After 3 hours of treatment, significant nuclear morphological changes were observed. Treated cells showed fragmented nuclei with a blebbing appearance, while untreated control cells displayed normal nuclear morphology. These results suggest that the methanolic and ethanolic extracts from the leaves and seeds of *A. muricata* L. induced apoptosis in a dose-dependent manner, with an increase in the number of apoptotic cells correlating with the extract concentration.

As apoptosis progresses, characteristic changes in cellular and nuclear morphology occur, including the fragmentation of chromosomal DNA into small pieces. These DNA fragments are typically observed as a DNA ladder on a 1.5% agarose gel, reflecting DNA fragmentation due to the activation of an endogenous endonuclease. After 24 hours, a dose-dependent increase in the number of cancer cell nuclei with condensed and fragmented



morphology was noted. Agarose-gel electrophoresis of DNA from treated cells revealed a ladder-like pattern, which was dose-dependent when compared with the control. The nuclear morphology changes characteristic of apoptosis were accompanied by a biochemical event: the endonuclease-mediated cleavage of nuclear DNA, leading to the formation of dense, crescent-shaped chromatin aggregates along the nuclear membrane^{3,10}.

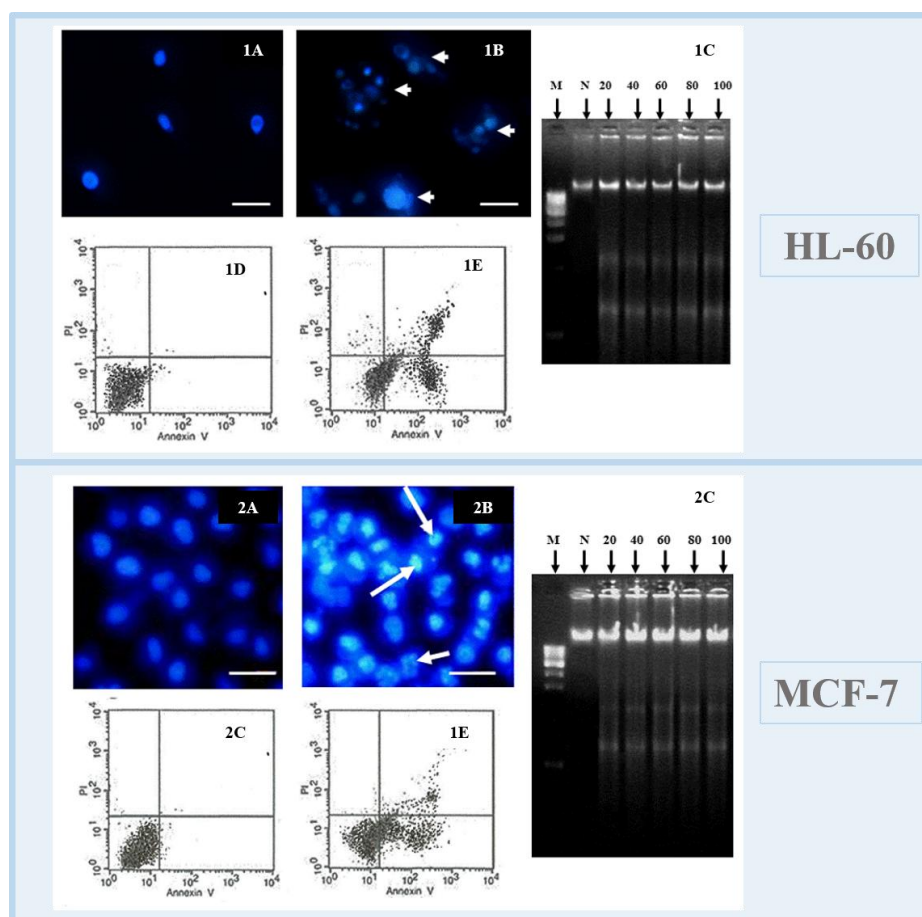


Figure 2.

The apoptotic rate (%) of HL-60 (1A-1E) and MCF-7 (2A-2E) cells after 24 hours of treatment with *A. muricata* L. extracts. 1A-2A: Untreated cells; 1B-2B: Cells treated with 100 mg/mL of methanolic seed extract (arrows indicate apoptotic fragmented cells, scale bar = 100 μ m); 1C-2C: DNA fragmentation in cells treated with 20-100 mg/mL of methanolic seed extract (M = marker; C = untreated cells); 1D-2D-1E-2E: Detection of apoptosis in cells using the Annexin V-FITC assay after incubation with 20 mg/mL of methanolic seed extract (D = viable untreated cells; E = early and late apoptotic cells).

In this study, low molecular mass DNA fragments (<200 bp) were analyzed on a 1.5% agarose gel and compared with a 1 Kb DNA standard marker. Hansen et al. (1989) noted that the formation of DNA fragments of oligonucleosomal size (180-200 bp) is a hallmark of apoptosis in many cell types. The characteristics of DNA cleavage, identifying three types that differentiate apoptosis from necrosis: internucleosomal DNA cleavage (180-200 bp), large DNA fragments (50-300 bp), and single-strand cleavage. During early apoptosis, pyknosis is a key feature, followed by late apoptosis, characterized by cell membrane blebbing and the formation of apoptotic bodies. The effects of *A. muricata* L. extracts (20 mg/mL) on early and

late apoptosis in HL-60 and MCF-7 cells were observed using the Annexin-V/PI staining assay via flow cytometry. Propidium iodide (PI) was used to detect late apoptosis and necrosis, while Annexin-V was used to identify both early and late apoptosis. RNase A was employed to restrict PI binding to DNA molecules. After 24 hours of treatment, the percentage of early apoptotic HL-60 cells increased to $50.15 \pm 0.70\%$ with S/e extract exposure, and to $55.23 \pm 0.71\%$ in MCF-7 cells with S/m extract. The highest rates of early apoptosis were observed with S/m treatment, reaching $63.13 \pm 0.64\%$ in HL-60 cells and $55.23 \pm 0.71\%$ in MCF-7 cells, while late apoptotic stages showed rates of $16.52 \pm 0.52\%$ and $13.98 \pm 0.67\%$, respectively. Apoptosis is a tightly regulated process, resulting in distinct cellular changes such as cell compaction, chromatin condensation, DNA degradation, membrane blebbing, and the formation of apoptotic bodies. These morphological changes, including chromatin condensation and nuclear shrinkage, can be observed under fluorescence microscopy after staining with DNA-specific fluorochromes^{12,13}. Lower levels of apoptosis may be due to defective apoptotic pathways in tumor cells, where overexpression of inhibitor proteins suppresses apoptotic activators. HL-60 and MCF-7 cells were used to evaluate the expression of key apoptotic proteins, including caspase-3, caspase-8, Bcl-2, and p53. The cells were treated with 20 mg/mL extracts for 3, 6, 9, 12, and 24 hours. Western blot analysis revealed that the expression of caspase-3 (17 kDa), caspase-8 (20 kDa), and p53 (53 kDa) proteins increased significantly in a time-dependent manner, while Bcl-2 (26 kDa) expression was significantly downregulated. The relative density of apoptotic protein expression over time in HL-60 and MCF-7 cells. These findings suggest that methanolic and ethanolic extracts from *A. muricata* L. leaves and seeds may disrupt apoptotic protein expression in the tested cells (Figure 3).

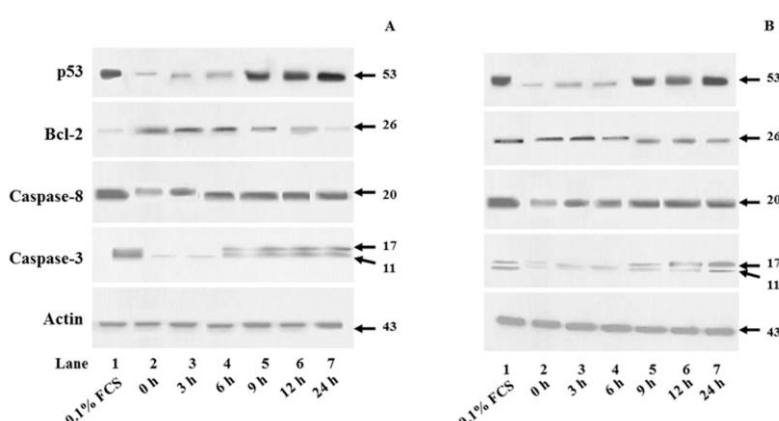


Figure 3.

Effect of methanolic seed extract of *A. muricata* L. on the expression of p53, Bcl-2, Caspase-8, and Caspase-3 proteins in HL-60 (A) and MCF-7 (B) cells. Cells were treated with the extract (20 mg/mL) for 0 to 24 hours. The blots were re-probed with an anti- α -actin antibody to confirm equal protein loading, with 0.1% FCS serving as a positive control. Protein lysates were separated on 12% SDS-PAGE, electrotransferred onto a PVDF membrane. The membrane was blocked with 0.1% (v/v) Tween-20 in Tris-buffered saline (TBST) containing 5% (w/v) nonfat dry milk for 20 minutes, then subjected to immunoblotting with anti-caspase-3, caspase-8, Bcl-2, and p53 antibodies, followed by incubation with goat anti-mouse IgG-HRP and developed with Tetramethylbenzidine (TMB) substrate.

Apoptosis plays a crucial role in development, tissue homeostasis, and the elimination of damaged cells in multicellular organisms. Dysregulation of apoptosis is observed in many types of tumors^{14,17,18}. The results of this study demonstrated that *A. muricata* L. extracts



induced apoptosis in HL-60 and MCF-7 cells, as evidenced by loss of cell viability, chromatin condensation, DNA fragmentation, and the detection of apoptotic proteins (caspase-3, caspase-8, p53, and Bcl-2). The prevention of apoptosis is often associated with the upregulation of Bcl-2 and downregulation of Bax. Mutations in the Bcl-2 gene contribute to cancers by compromising normal cell death mechanisms, weakening the anti-apoptotic influence of Bcl-2. This research showed that *A. muricata* L. extracts significantly downregulated anti-apoptotic Bcl-2 protein in a time-dependent manner. It was confirmed that Bcl-2 protein originates within the nucleus when DNA is damaged, potentially relating to the upregulation of pro-apoptotic Bax protein, which forms pores in the outer mitochondrial membrane to release cytochrome c. The apoptotic induction observed in both cell lines was characterized by nuclear morphological changes, including chromatin condensation, DNA fragmentation, and the formation of apoptotic bodies. These findings were confirmed by Hoechst staining and DNA fragmentation assays, consistent with previous studies that reported similar apoptotic mechanisms. *A. muricata* extracts trigger apoptosis through caspase activation, with increased expression of p53 and downregulation of anti-apoptotic proteins like Bcl-2^{15,17,18} which is in line with result observations of caspase-3 and caspase-8 activation and Bcl-2 downregulation.

Apoptosis, a crucial process in development and tissue homeostasis, involves changes in the expression of specific genes and can be triggered by various internal and external signals. Central to this process are the caspases, a family of 14 cysteine proteases that cleave cellular proteins at aspartic acid residues. Caspases are synthesized as inactive zymogens and are activated through a hierarchical pathway involving both intrinsic and extrinsic mechanisms, converging at caspase-3. The activation of caspase-3 leads to the execution phase of apoptosis, where “executioner” caspases are triggered. During apoptosis, cells exhibit elevated levels of cytochrome c in the cytosol due to its release from mitochondria, which activates caspase-3 by proteolytic cleavage, forming an active heterodimer. Active caspase-3 degrades poly (ADP ribose) polymerase (PARP), thereby disabling DNA repair and triggering further caspase activation.

Western blot analysis of treated HL-60 and MCF-7 cells reveals time-dependent increases in p53 and caspase expression, indicating induced apoptosis, while Bcl-2 expression decreases, supporting the activation of apoptotic pathways. Apoptotic signals from death receptors activate the Death Inducing Signaling Complex (DISC), which in turn activates caspase-8, initiating a cascade that processes effector caspases leading to apoptosis. Caspase-8 bridges both extrinsic and intrinsic apoptotic pathways. Intracellular apoptotic signals often originate in the nucleus due to DNA damage, which activates p53, a tumor suppressor that promotes pro-apoptotic Bcl-2 family members while suppressing anti-apoptotic proteins like Bcl-2 and Bcl-XL^{15,18}. Bcl-2, an anti-apoptotic protein, promotes cell survival by stabilizing the mitochondrial membrane and preventing cytochrome c release. In contrast, Bax, a pro-apoptotic protein and p53 target, promotes apoptosis by increasing mitochondrial membrane permeability, leading to cytochrome c release and subsequent caspase activation¹⁶.

The DNA fragmentation and caspase activation results in study, as revealed by agarose-gel electrophoresis and Western blot analysis, align with the apoptotic mechanisms reported in other cancer studies involving *A. muricata*. Findings of time-dependent increases in p53, caspase-3, and caspase-8, alongside the downregulation of Bcl-2, are consistent with the literatures^{17,18}, where *A. muricata* extracts were shown to induce apoptosis via intrinsic and extrinsic pathways. Overall, the findings from this study are strongly supported by existing literature on the bioactivity of *A. muricata* L., reinforcing the potential of its extracts,

particularly those from the seeds, as promising anticancer agents. The consistency results with the cytotoxicity and apoptotic mechanisms identified strengthens the evidence for *A. muricata*'s therapeutic applications in cancer treatment.

Conclusion:

In conclusion, the LC₅₀ values of *A. muricata* L. extracts, determined through brine shrimp cytotoxicity tests and MTT assays on HL-60 and MCF-7 cells, revealed a strong correlation with their total phenolic and flavonoid content. The extracts exhibited a dose-dependent induction of apoptosis, with higher concentrations significantly increasing the number of apoptotic cells. Early apoptotic responses were notably evident in both cell lines, especially with the S/m extract. Furthermore, the extracts led to a time-dependent increase in the levels of caspase-3, caspase-8, and p53 proteins, while reducing Bcl-2 expression, thereby emphasizing the activation of apoptotic pathways. These findings underscore the potential of *A. muricata* L. as a valuable source of anticancer compounds. However, the study's limitations, such as the lack of in vivo testing and mechanistic studies, should be addressed in future research to fully validate these promising results.

Acknowledgements:

This research was funded by grants from the Faculty of Science and Digital Innovation and the Research and Development Institute at Thaksin University, with equipment provided by the Department of Biological Science.

References:

1. Mishra S, Ahmad S, Kumar N, Sharma BK. Global J Pharmaceut Res. 2013;2:1613-1618.
2. Abdul Wahab SM, Jantan I, Haque MA, Arshad L. Front Pharmacol. 2018;9:661.
3. van Beem C, Salaeh A, Wichcha J NSTRU. 2024;43(1):66-79.
4. Solis PN, Wright CW, Anderson MM, Gupta MP, Phillipson JD. J Med Plant Res. 1993;59:250-252.
5. Bradford MM. Anal Biochem. 1976;72:248-254.
6. Gossiau A, Chen KY. Nutr J. 2004;20: 95-102.
7. Adewole SO, Caxton MEA. Afr J Biomed Res. 2006;9:173-187.
8. Moghadamtousi SZ, Kadir HA, Paydar M, Rouhollahi E, Karimian H. BMC Complement Altern Med. 2014;14:29.
9. Potter JD. Cancer Lett. 1997;114:7-9.
10. Naik AV, Sellappan K. Advances in Traditional Medicine. 2021;21:779-789
11. Cohen JJ. Immunol Today. 1993;14:126-130.
12. Crompton M. Curr Opin Cell Biol. 2000;12:414-419.
13. Fofana S, Ziyaev R, Abdusamatov A, Zakirov SK. Chem Nat Compd. 2011;47:321-321.
14. Häcker G. Cell Tissue Res. 2000;301:5-17.
15. Kerr JF, Wylie AH, Currie AR. Br J Cancer. 1972;26:239-257.
16. Kossouh C, Moudachirou M, Adjakidje V, Chalchat JC, Figuérédo G. J Essent Oil Res. 2007;19:307-309.
17. Mishra S, Ahmad S, Kumar N, Sharma BK. Glob J Pharm Res. 2013;2:1613-1618.
18. Gavamukulya Y, Wamunyokoli F, El-Shemy HA. Asian Pac J Trop Med. 2017;10:835-848.
19. Mutakin M, Fauziati R, Fadhilah FN, Zuhrotun A, Amalia R, Hadisaputri YE. Molecules. 2022;27:1201.



DETECTION OF *Burkholderia pseudomallei* WITH CRISPR/CAS12A USING THE SPECIFIC MARKER *ORF2* OF THE FIRST TYPE III SECRETION SYSTEM (T3SS-1)

Pimpaka Rongkratok,¹ Mantana Jamklang,² Pawana Panomket⁵, Chamnan Mongkonsaen⁶, Theeraya Simawaranon³, Watsana Penkhru², Pishyaporn Sritangos², Sirilak Chumkiew⁴, Thunyarat Surasiang², Nanthanat Pansuksan², Chompunoot Wangboon^{2,*}

¹Non Sung Medical Laboratory, Non Sung Hospital, Nakhon Ratchasima, Thailand

²School of Preclinical Sciences, Institute of Science, Suranaree University of Technology, Nakhon Ratchasima, Thailand

³School of Pathology, Institute of medicine, Suranaree University of Technology, Nakhon Ratchasima, Thailand

⁴School of Biology, Institute of Science, Suranaree University of Technology, Nakhon Ratchasima, Thailand

⁵College of Medicine and Public Health, Ubon Ratchathani University, Ubon Ratchathani, Thailand

⁶Chaophraya Abhaibhubejhr Hospital, Prachinburi, Thailand

*e-mail: Chompunoot.wang@sut.ac.th

Abstract:

In this study, we developed a method for detection of *Burkholderia pseudomallei*, the etiologic pathogen of a severe infectious disease known as melioidosis, using CRISPR/Cas12a. The detection depends on the nonspecific endonuclease activity of Cas12a which is binding to a specific target DNA via programmable guide RNA (gRNA). The specific marker, open reading frames: *orf2*, from T3SS-1 gene cluster of *B. pseudomallei* was selected for gRNA design. The DNA of *B. pseudomallei* was extracted from the colony suspension by boiling method. The results revealed that the digestion reaction involving the gRNA specific for *orf2* generated DNA fragments. This finding suggested that the newly designed gRNA was specific to the target DNA sequence leading to the digestion activity by Cas12a enzyme. Additionally, the target-activated CRISPR/Cas12a cleavage activity was verified based on signal amplification of signal of single stranded DNA fluorophore-quencher (ssDNA-FQ) reporter. The result revealed that an increased generation of fluorescence signal, which was observed in the wild type *B. pseudomallei* strain K96243 and *B. pseudomallei* isolated from clinical sample but not in *B. thailandensis*. This concludes that the newly designed gRNA of *orf2* could specifically detect *B. pseudomallei*, but not other pathogens and can be used for the development of a rapid diagnostic tool for melioidosis, such as recombinase polymerase amplification lateral flow dipstick.

Introduction:

Melioidosis is a serious infectious disease with a high mortality rate caused by *B. pseudomallei*, an environmental aerobic Gram-negative bacillus. The disease in humans ranges from asymptomatic to focal infections and can be life-threatening due to rapid fatal septicemia.^{4,9} An early diagnosis of the disease could decrease the fatal rate of the patients. Identification of *B. pseudomallei* from clinical specimens in a hospital laboratory is typically done through laboratory tests followed by biochemical identification. Although this technique is specific and relatively inexpensive, definitive identification of *B. pseudomallei* requires

expertise and can be time-consuming (5 to 7 days). Conventional culture method is the routine gold standard for diagnosis melioidosis. However, this method has a limited diagnostic sensitivity, because of the low *B. pseudomallei* numbers in clinical samples or the presence of unculturable forms of the organism that have been associated with previous antibiotic treatment in some patients. Many cases have been underdiagnosed or misdiagnosed as a *Pseudomonas* species because of similar colony morphology in blood agar, Gram staining and biochemical tests such as positive oxidase test. The detection of *B. pseudomallei* is difficult in routine culture media because it mimics contaminants, and the overgrowth of normal flora is observed.⁷

Recently, nucleic acid detection technology based on clustered regularly interspaced short palindromic repeats (CRISPR)/CRISPR-associated protein12a (Cas12a) (CRISPR/Cas12a) has been developed and demonstrate high sensitivity, specificity and reliability. The detection relies on the target-activated nonspecific endonuclease activity of Cas12a after binding to a specific target DNA via programmable guide RNAs (gRNA). By combining the programmable specificity of Cas12a with a reporter molecule that is activated upon target recognition, these enzymes result in specific and sensitive indications of the presence or quantity of nucleic acid.³

Hence, the objective of this study was to develop a diagnostic tool based on a molecular detection system for *B. pseudomallei* using CRISPR-CAS12a technology. In this study, we selected open reading frames: *orf2* from T3SS-1 gene clusters of T3SSs. The T3SS-1 gene cluster is present only in *B. pseudomallei* and not in avirulent *B. thailandensis*. Furthermore, *orf2* was found to be present in *B. pseudomallei* and not in the related *B. mallei* or *B. thailandensis*.⁸

Methodology:

Bacterial Strains and DNA extraction

The clinical isolates of *B. pseudomallei* were obtained from Chaophaya Abhaibhubejhr Hospital. The wild-type *B. pseudomallei* strain K96243 and *B. thailandensis* were obtained from the Faculty of Medicine, Khon Kean University. The isolates of *B. pseudomallei*, *B. pseudomallei* strain K96243 and *B. thailandensis* were inoculated on blood agar and incubated at 37 °C for 48 h. The bacterial colonies from the medium culture were used for DNA extraction by modified boiling method.¹

Selection of specific B. pseudomallei genes and gRNA design

The specific gene for *B. pseudomallei* was selected for a guided RNA design. The open reading frames: *orf2* from T3SS-1 was reported as specific markers for *B. pseudomallei* that was used in this study.^{2,6,8} The sequence of *orf2* was obtained from the completed *B. pseudomallei* K96243 genome sequence at the GenBank accession number AF074878 deposited by Winstanley et al.¹⁰ Sequence specificity was checked by BLAST searches for nearly exact matches via the site <http://www.ncbi.nlm.nih.gov/BLAST/>. Single nucleotide gRNA for *orf2* was designed to be complementary to the target site as well as a 5' TTTV protospacer adjacent motif (PAM) on the DNA strand opposite the target as shown in Table 1.

Table 1 The sequence of specific gRNA of *orf2* from T3SS-1 of *B. pseudomallei*.

| Target site | Sequence of gRNA | Size of bp |
|-------------|-----------------------|------------|
| <i>orf2</i> | GAUAUCCAUAAGGAUCGUCGC | 20 |

Detection of *orf2* of *B. pseudomallei* by polymerase chain reaction (PCR) amplification

PCR reactions were performed to detect *orf2* of *B. pseudomallei* situated within the gene cluster encoding T3SS-1. The primers were designed from the published sequence of strain K96243 at the GenBank accession number AF074878 by using The Primer-BLAST software, NCBI. The primers used in this study are shown in Table 2. Briefly, in each PCR reaction, the total volume of 50 µl contained 25 µl of GoTaq® Hot Start Colorless Master Mix (Promega, Madison, WI, USA), 2 µl of genomic DNA as template, and 10 µM of each forward and reverse primer. The BIO-RAD T100 thermal Cycler obtained from ICON@IBP Tower, Singapore is the instrument used to amplify DNA. Initially, the samples were subjected to gradient PCR (55–65 °C) to optimize the annealing temperature for each primer. The amplification steps were 1 cycle of initial denaturation at 95 °C for 2 min, 30 amplification cycles with denaturation at 95 °C for 30 s, annealing at 61.4 °C for 45 s and elongation at 72 °C for 20 s, and the last step was followed by a final extension at 72 °C for 5 min. Nuclease-free water was used as a negative control for PCR. The PCR products were electrophoresed through 2% agarose gel containing ViSafe Green Gel Stain (Vivantis, Malaysia) using 1X TBE buffer at 100 Volt (V) for 45 min. Finally, the gel was visualized and photographed under ultraviolet light by Gel Doc Vilber, France.

Table 2 Forward and reverse primers used for detection of *orf2* gene of *B. pseudomallei* and PCR product size

| Target site | Oligonucleotide sequence (5' → 3') | PCR product size (bp) |
|-------------|---|-----------------------|
| <i>orf2</i> | Forward: CTCACTTCGAAGCCGAACC Reverse: AGTCCGAACATCTCGCTCTC | 250 bp |

In vitro digestion activity of *Lba Cas12a* (*Cpf1*) on *B. pseudomallei* DNA target

For testing the specificity of the designed gRNA to *B. pseudomallei* DNA target, this study used EnGen® *Lba Cas12a* (*Cpf1*) (New England BioLabs, USA) for digestion reaction. All components were pre-incubated at room temperature (RT) for 10 min prior to adding the PCR product of *orf2* at the concentration of 439 ng/ µl. Briefly, the digestion reaction was performed in the total volume of 20 µl mixed with the following components: 439 ng/µl of *orf2* PCR product of *B. pseudomallei* containing the target sequence, 6 µl of 300 nM gRNA containing the target sequence in the region of interest, 2 µl of 1 µM *Cas12a*, 2 µl of 10X reaction buffer, and nuclease-free water. The two control samples consisted of all components without DNA and another sample containing all components except gRNA. After that, the mixture was incubated at 37 °C for 30 min and the digestion results were electrophoresed through 2.5 % agarose gel containing ViSafe Green Gel Stain (Vivantis, Malaysia) using 1X TBE buffer at 100 V for 45 min. Finally, the gel was visualized and photographed under ultraviolet light by Gel Doc (Vilber, France).

Measurement the signal of single stranded DNA fluorophore-quencher (ssDNA-FQ reporter) of *FAM-BHQ1* in CRISPR/*Cas12a* system

The digestion reaction from CRISPR/*Cas12a* system at the DNA target of *B. pseudomallei* was detected using ssDNA-FQ reporter molecules. The ssDNA-FQ reporter was synthesized with a fluorescein reporter molecule attached at 5' end and black hole quencher 1 on the 3' end as shown in Table 3. The following reaction of CRISPR/*Cas12a* system with ssDNA-FQ reporter was performed in the total volume of 80 µl containing 8,000 ng of DNA template from PCR product of *orf2* containing the target sequence, 6 µl of gRNA (300 nM), 1 µl of *Cas12a* (1 µM), 8 µl of 10X reaction buffer, 0.5 µl of ssDNA-FQ (10 µM)

reporter and nuclease-free water. The control samples consisted of nuclease-free water containing ssDNA-FQ and another sample containing all components except DNA. The FAM displays excitation and emission spectrum peak wavelengths of 495 nm and 520 nm, respectively. The signals of fluorescence of cleavage products were measured every single min until 2 h at RT by fluorescence plate reader (Thermo varioskans LUX) as well as the control samples. The positive signal of fluorescence indicates that CRISPR/Cas12a specifically reacted with *B. pseudomallei* DNA target as well as collateral cleavage nearby ssDNA-FQ reporters.

Table 3 The sequence of ssDNA-FQ reporter used in CRISPR/Cas12a system.

| Reporter | Sequence (5' → 3') |
|----------|--------------------|
| ssDNA-FQ | FAM-TTATTATT-BHQ1 |

Determination the specificity of selected target site orf2 of B. pseudomallei with another Gram-negative bacilli (B. thailandensis)

Another closely related Gram-negative bacilli of *B. pseudomallei*, *B. thailandensis* was used to determine the specificity of the test condition. The isolates of *B. thailandensis* were obtained from the Faculty of Medicine, Khon Kean University, and kept in 40% sterile glycerol at -80 °C before proceeding to determine the specificity of *orf2*. The bacterial stock was cultured on blood agar or MacConkey agar, and incubated at 37 °C for 48 h. Subsequently, the bacterial colonies were used for genomic DNA extraction by boiling method as described previously and then the extracted DNA was used for detection of *orf2* by PCR technique. The PCR products were electrophoresed through 2.0% agarose gel containing ViSafe Green Gel Stain (Vivantis, Malaysia) using 1X TBE buffer at 100 V for 45 min. Finally, the gel was visualized and photographed under ultraviolet light by Gel Doc (Vilber, France). The specificity of the designed gRNA in CRISPR/Cas12a system as well as the measurement signals of ssDNA-FQ reporter using FAM-BHQ1 were also investigated following the PCR technique.

Results and Discussion:

Detection of orf2 of B. pseudomallei by polymerase chain reaction (PCR) amplification

In the present study, both the wild type *B. pseudomallei* strain K96243 and clinical isolates of *B. pseudomallei* exhibited identical PCR products of *orf2* which was detected at 250 bp as shown in the Figure1. The results suggest that the primers designed for *orf2* in this study could be useful for investigation *B. pseudomallei* strain found in clinical samples.

Furthermore, the results of this study demonstrated that DNA extracted by boiling method without ethanol precipitation appeared as a clear single band in the agarose gel similar to DNA extracted by boiling method with ethanol precipitation and DNA extracted by boiling method with ethanol precipitation and incubated overnight at -20 °C, which indicates that DNA was not degraded and provided the sufficient DNA yield. Hence, the boiling method offers a rapid, easy and cost-effective approach for high-yield DNA isolation from gram-negative bacteria.

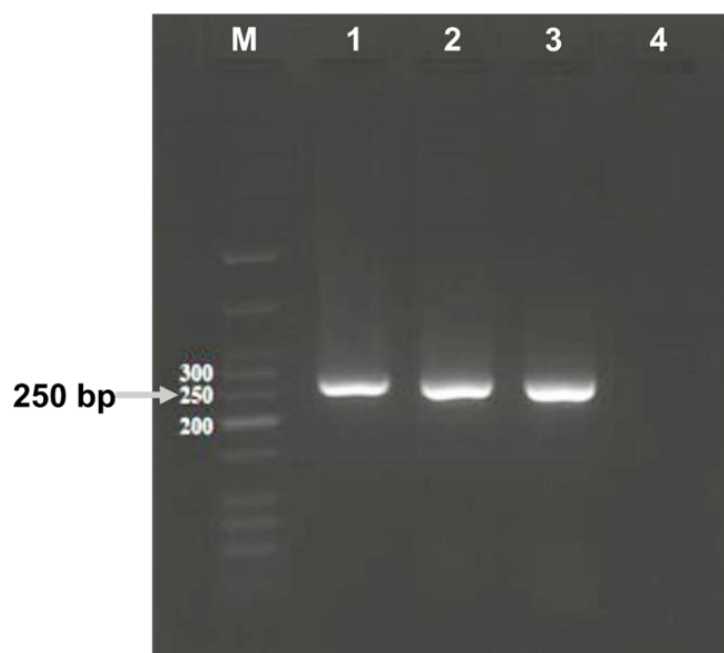


Figure 1 The PCR products of *orf2* from T3SS-1 of clinical isolate *B. pseudomallei* exhibited 250 bp using 2% agarose gel electrophoresis. Lane 1: DNA extracted by boiling method with ethanol precipitation, Lane 2: DNA extracted by boiling method without ethanol precipitation, Lane 3: DNA extracted by boiling method with ethanol precipitation and incubated overnight at -20 °C, Lane 4: negative control Lane M: 25-bp DNA ladder.

In vitro digestion activity of *Lba* Cas12a (*Cpf1*) on *B. pseudomallei* DNA target

The specificity of the designed gRNA to *B. pseudomallei* DNA target was tested using the PCR product of *orf2* containing the target sequence. The designed gRNA of this study binding to target sequences of *orf2* was illustrated in Figure 2. According to previous studies, Cas12a quickly recognized and cleaved the DNA target site under the guidance of its specific gRNA.⁵ In our study, the *in vitro* digestion activity of RNA-guided enzyme Cas12a or CRISPR/Cas12a on target sites was investigated by 2.5% agarose gel electrophoresis. The results showed that the DNA fragments of *orf2* from both the wild type *B. pseudomallei* strain K96243 and the clinical isolate *B. pseudomallei* exhibited a larger size (350 bp) than its PCR product (250 bp) which were used as a control after adding gRNA and Cas12a into the reaction. Additionally, a smaller fragment of more than 50 bp was also observed (Figure 3). In theory, if the digestion occurs in the reaction involving the gRNA and Cas12a enzyme, it should have generated small sizes of the DNA fragments. However, in our study the *orf2* reaction showed 3 distinct bands, one of which showed a larger size of fragment band. This could be explained by the presence of tightly bound proteins (endonuclease enzyme) and nucleic acid (DNA) which form stable complexes during gel electrophoresis. However, the PCR product of *orf2* containing the target sequence was subsequently tested in CRISPR/Cas12a system with ssDNA-FQ reporter to determine the specificity of the designed gRNA used in this study.

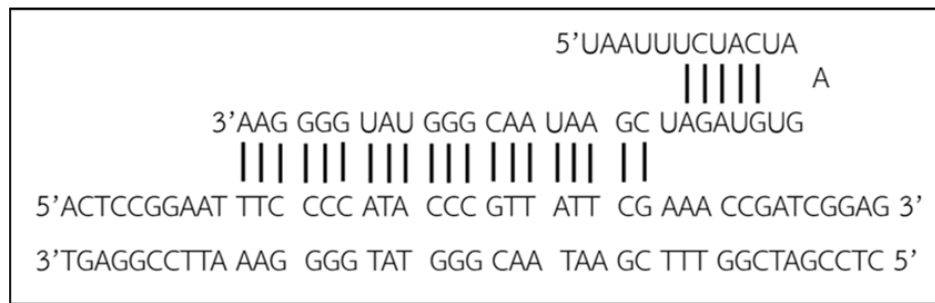


Figure 2 The gRNA binding to target sequences of *orf2* from T3SS-1 of *B. pseudomallei*

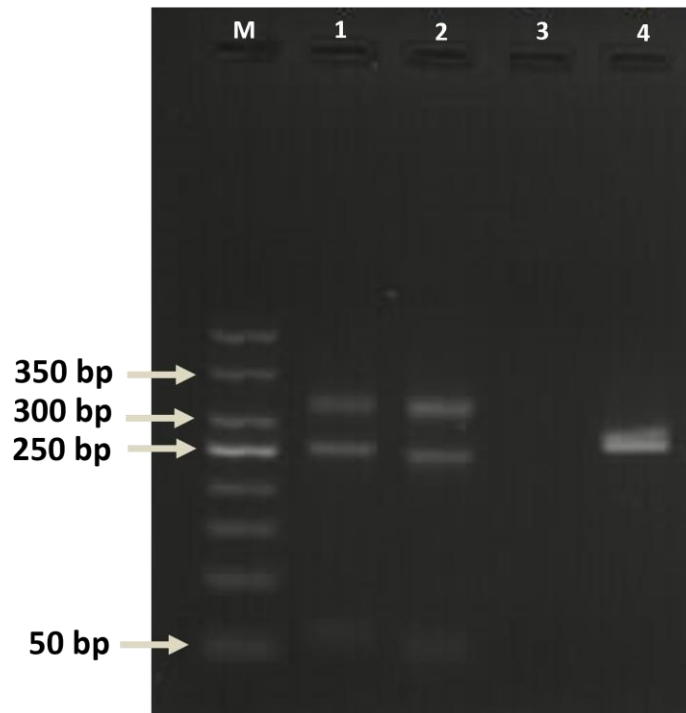


Figure 3 *In vitro* digestion activity of RNA-guided enzyme Cas12a or CRISPR/Cas12a on target sites of *orf2* PCR product using electrophoresis with 2.5% agarose gel. Lane 1 and Lane 2: PCR product of *orf2* exhibited different fragment sizes of 250, 350 and >50 bp, Lane 3: gRNA and Cas12a without PCR product, Lane 4: PCR product and Cas12a except gRNA, Lane M: 50-bp DNA ladder.

Measurement the signal of single stranded DNA fluorophore-quencher (ssDNA-FQ reporter) of FAM-BHQ1 in CRISPR/Cas12a system

The output of fluorescence signal and its intensity are directly related to the presence and concentration of the activated Cas12a in the reaction system. In our study, the target-activated CRISPR/Cas12a cleavage activity was verified based on signal amplification of ssDNA-FQ reporter. The result revealed that an increase of collateral cleavage activity of the FAM fluorophore from its quencher, leading to an increased generation of fluorescence signal, which was observed in the wild type *B. pseudomallei* strain K96243 and *B. pseudomallei* isolated from clinical sample but not in *B. thailandensis* and control samples (Figure 4). Although, the finding of slightly intense *orf2* fragment of *B. thailandensis* on the agarose gel by PCR, further analysis using the CRISPR/Cas12a system with ssDNA-FQ reporter demonstrated that the designed gRNA for *orf2* from T3SS-1 of *B. pseudomallei* of this study was specific for detecting *B. pseudomallei*.

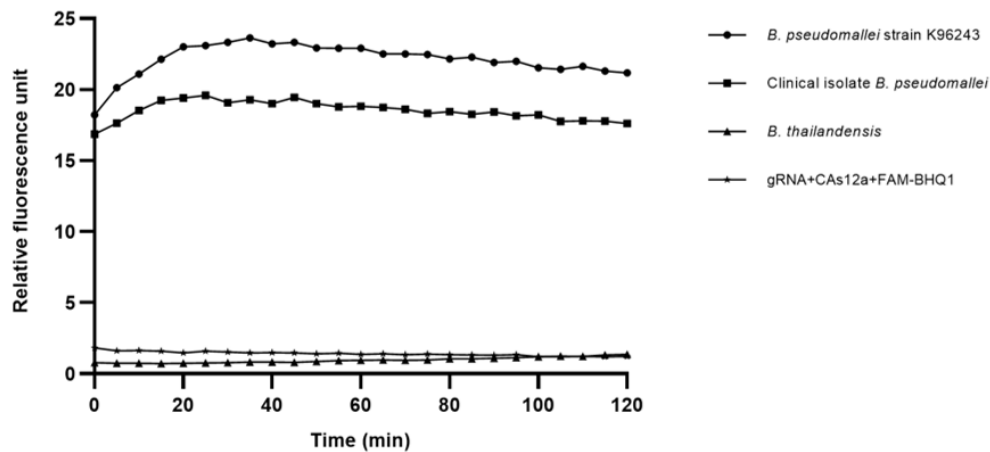


Figure 4 The signal of FAM fluorophore of cleavage products of *orf2* from T3SS-1 of *B. pseudomallei* comparing with the fluorescence signals of *B. thailandensis* and control groups.

Determination of the specificity of selected target site orf2 of B. pseudomallei with another Gram-negative bacilli

The result revealed that a slightly intense DNA fragment of *B. thailandensis* was observed on the agarose gel. However, it exhibited a different fragment length from that of *B. pseudomallei* (250 bp), which was used as a positive control as shown in Figure 5. The finding of *orf2* fragment of *B. thailandensis* on the agarose gel should be improved by sequencing. However, the primers designed of *orf2* in this study was able to detected *B. pseudomallei* at the DNA fragment length of 250 bp. Subsequently, the PCR product of *orf2* from *B. thailandensis* was tested in CRISPR/Cas12a system to determine the specificity of the designed gRNA used in this study. The further analysis using the CRISPR/Cas12a system with ssDNA-FQ reporter revealed that no fluorescence signal of *B. thailandensis* was observed (Figure 4). This indicated that the designed gRNA of this study was specific for detecting *B. pseudomallei*.

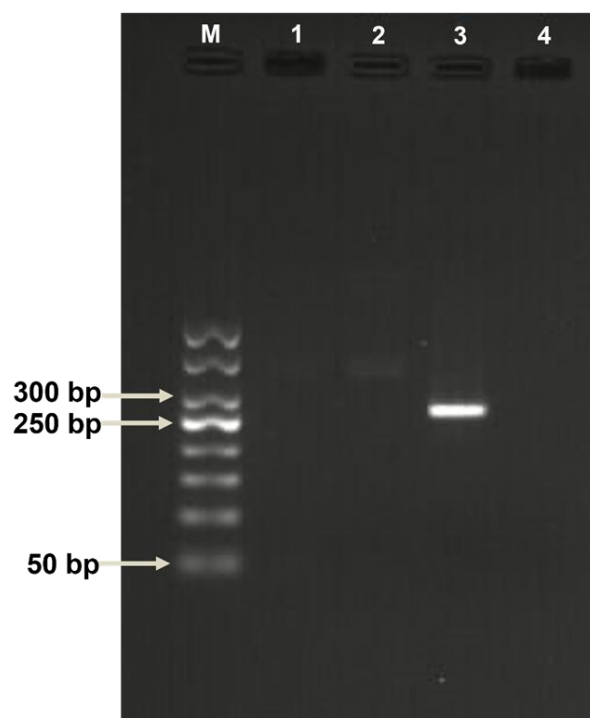


Figure 5 The PCR result of amplifying *orf2* from *B. thailandensis* using by 2% agarose gel electrophoresis to determine the specificity of *orf2* from T3SS-1 of *B. pseudomallei*. Lane 1 and Lane 2: DNA of *B. thailandensis*, Lane 3: DNA of *B. pseudomallei* as a positive control (250 bp), Lane 4: negative control Lane M: 50-bp DNA ladder.

Conclusion:

In this study, we developed a new methodology for detection of *B. pseudomallei* using CRISPR-Cas12a technology. The DNA of *B. pseudomallei* was extracted from the colony suspension by the boiling method without DNA precipitation gave the quickest and simplest methodology for DNA extraction. The newly designed gRNA was shown to be specific for *orf2* and generated digested DNA fragments with larger and smaller sizes. This indicates that the newly designed gRNA was specific for this bacterial pathogen illustrating the endonuclease activity. Furthermore, to visualize the digestion activity, a ssDNA-FQ reporter was used for simple readouts of the target-activated CRISPR/Cas12a cleavage activity. The output fluorescence signal and its intensity are directly related to the presence and concentration of the activated Cas12a in the reaction system. In our study, we observed an increase in collateral cleavage activity of the FAM fluorophore from its quencher, according to an increased generation of fluorescence signal, in the wild-type *B. pseudomallei* strain K96243 and *B. pseudomallei* isolated from clinical samples, but not in *B. thailandensis* and control samples. Although, the finding of slightly intense *orf2* fragment of *B. thailandensis* on the agarose gel by PCR was observed. This indicated that gRNA of *orf2* designed in this study could specifically detect *B. pseudomallei*, but not other pathogens. As the results, the newly designed gRNA can be used for the development of a rapid diagnostic tool for melioidosis. This could facilitate a clinical microbiological laboratory in small community hospitals to detect and interpret the infection from *B. pseudomallei* more efficiently. For the future direction, we will focus on validating this technology in clinical samples and applying to practical applications, such as recombinase polymerase amplification lateral flow dipstick.

Acknowledgements:

This research was supported by New Generation Development Researcher Fund from Suranaree University of Technology and the Center of Excellence in Microbial Technology for Agricultural Industry, Suranaree University of Technology. We would like to express our gratitude to the center for Scientific and Technological Equipment Suranaree University of Technology, School of Preclinical Sciences Suranaree University of Technology, Faculty of Medicine, Khon Kaen University, Chaophaya Abhaibhubejhr Hospital, Medical Laboratory Non Sung Hospital and College of Medicine and Public Health, Ubon Ratchathani University.

References:

1. Ahmed O, Dablood A. *Int. J. Bioassays*. 2017. 6, 5347-5349.
2. Chantratita N, Meumann E, Thanwisai A, Limmathurotsakul D, Wuthiekanun V, Wannapasni S, Tumapa S, Day NP, Peacock SJ. *J. Clin. Microbiol.* 2008. 2, 568-573.
3. Jolany vangah S, Katalani C, Boone HA, Hajizade A, Sijercic A, Ahmadian G. *Biol. Proced. Online*. 2020.1, 22.
4. Karunanayake P. *J. Clin. Med.– London*. 2022. 1, 6-8.
5. Mao Z, Chen R, Wang X, Zhou Z, Peng S, Han D, Li S, Wang Y, Han T, Liang J, Ren S, Gao Z. *Trends Food Sci.* 2022. 122, 211-222.
6. Novak RT, Glass MB, Gee JE, Gal D, Mayo MJ, Currie BJ, Wilkins PP. *J. Clin. Microbiol.* 2006. 1, 85-90.
7. Selvam K, Khalid MF, Mustaffa KMF, Harun A, Aziah I. *Microorganisms*. 2021. 4, 711.
8. Thibault FM, Valade E, Vidal DR. *J. Clin. Microbiol.* 2004. 12, 5871-5874.
9. Wiersinga WJ, van der Poll T, White NJ, Day, NP, Peacock SJ. *Nat. Rev. Microbiol.* 2006. 4, 272-282.
10. Winstanley C, Hales BA, Hart CA. *J. Med. Microbiol.* 1999. 7, 649-656.



Diversity of crustose lichen genus *Pyrenula* (Pyrenulaceae, Ascomycetes) on both from Doi Inthanon National Park and Doi Suthep-Pui National Park in Chaing Mai Province

Supattara Phokaeo,^{1*} Sanya Meesim,¹ Watchalaya matjank,¹ Samak Sangjun,¹ Nichapat Wisuttipranee,¹ Kawinnat Buaruang,² and Wetchasat Polyaim²

¹ Department of Biology, Faculty of Science, King Mongkut's Institute of Technology Ladkrabang, Bangkok, 10520

² Lichen Research Unit, Department of Biology, Faculty of Science, Ramkhamhaeng University Bangkok, 10240

*E-mail: supattara.ph@kmitl.ac.th

Abstract

The objective of this study is to investigate the diversity of lichens genus *Pyrenula* Ach. (Pyrenulaceae) is a group of crustose lichens that typically grow on smooth, shaded bark and produce sexual reproductive structures called perithecia (ascomata), which contain greyish brown to brown ascospores. Lichen specimens were collected from Doi Suthep-Pui National Park and the Inthanon Lady's Slipper Orchid Conservation Project in Doi Inthanon National Park, Chiang Mai Province, from August 2023 to March 2024. A total of ninety specimens were collected from across various forest types, including deciduous forest, dry dipterocarp forest, and hill evergreen forest. Based on morphological characteristics and chemical traits, the taxonomic identification of all samples revealed twelve species. The forest with the highest lichen diversity was the Hill Evergreen Forest (HEF) in Doi Suthep-Pui National Park, which harbored nine species. Additionally, *Pyrenula immissa* was commonly found in all forest types. The most lichens were found Doi Suthep-Pui National Park. To provide a more complete database and examination of lichen species in Thailand, this study expands on the known diversity and distribution of Chiang Mai Province and provides information for the conservation and sustainable utilization of biodiversity resources in Thailand.

Keyword Genus *Pyrenula*, Inthanon National Park, Doi Suthep-Pui National Park, Chaing Mai Province.

Introduction

Chiang Mai is located on northern Thailand, known for its mountains, diverse forest types and access to many natural areas. This includes the highest mountain in Thailand Doi Inthanon, and Doi Suthep-Pui the mountain adjacent to Chiang Mai city. Both mountains are National Parks and have provided many new botanical species and records and lichens together with and Lichen has been studied very little in Chiang Mai, especially in the national park. The first lichenological exploration of Doi Suthep dates to 1904 when Hosseus conducted research (with species later reported by Vainio in 1921). More recently, Aptroot and colleagues (2007) documented around 300 lichen species in the area. Notably, crustose lichens, primarily from the genus *Pyrenula*, were found to comprise 16 taxa. However, despite the rich biodiversity, lichenologists in Chiang Mai Province have relatively limited records of tropical monsoon region lichens, especially corticolous crustose lichens like *Pyrenula*. *Pyrenula*, a genus within the family Pyrenulaceae, thrives in tropical, subtropical, and Neotropical regions. The collected lichens form produces a reproductive structure called perithecium, a fruiting body which is rounded or flask-shaped, and which opens by a narrow pore at the apex, and exhibit UV– or UV+ yellow thalli. Some may have pseudocyphellae, while others contain lichexanthone or anthraquinones. Their perithecioid ascomata, occasional inspersed hamathecia, unbranched filaments, and various types of ascospores contribute to their diversity. Globally, there are 238 recognized *Pyrenula* species, with

Thailand hosting ninety-nine of them (Buaruang et al., 2017; Phokaeo et al., 2019). In this study, we focus on the biodiversity of the *Pyrenula* genus within the Inthanon Lady's Slipper Orchid Conservation Project, Doi Inthanon National Park, and Doi Suthep-Pui National Park. Our research builds upon previous studies, and we anticipate uncovering even greater lichen species diversity within this fascinating genus.

Methodology

Survey and collect lichen samples on plants from 3 types of forest comprised of deciduous forest (DC), dry dipterocarp forest (DDF) and hill evergreen forest (HEF) on both Doi Suthep-Pui National Park (Site A) and Inthanon Lady's Slipper Orchid Conservation Project, Doi Inthanon National Park (Site B) in Chaing Mai province (Figure 1) during 2022-2024. The lichen species were classified based on taxonomic principles, including the study of morphology, anatomy, and basic chemical composition through spot tests and ultraviolet (UV) light examination. Species identification followed the taxonomy proposed by Aptroot et al. (2008), Aptroot (2012), and Awasthi (1991).



Figure 1 A: Map of Thailand (from “Thai Plants names” by Tem Smitinand, 2001, Bangkok: Royal Forest Department), B: (DC) deciduous forest; C: (DDF) dry dipterocarp forest; D: (HEF) hill evergreen forest in Doi Suthep-Pui National Park; E: (HEF) hill evergreen forest in Inthanon Lady's Slipper Orchid Conservation Project, Doi Inthanon National Park).

Results and Discussion

From the survey and collection of lichen of the genus *Pyrenula* from Inthanon Lady's Slipper Orchid Conservation Project, Doi Inthanon National Park and Doi Suthep-Pui National Park in Chaing Mai province. All of 90 specimens in various three forest types including deciduous forest (DC), dry dipterocarp forest (DDF), hill evergreen forest HEF (Figure 1). Ninety collected samples were identified into 12 species (Figure 2) and the common lichens found in all forest conditions is *Pyrenula immissa* (Table 1). These lichen as follow some characteristics of species thallus UV-, with or without pseudocyphellae, ascomata single or with stromata black, irregularly size 0.3-2 mm., immersed to emergent, hymenium colorless with or without oil droplet, fusiform to ellipsoidal, grey brown to brown, transversely to (sub)



muriform, with 8 ascospore per ascus, Terminal lumina cell separated or directly from the exospore wall by endospore thickening (Kansri Boonpragob & Kawinnat Buaruang., 2007). The common lichens found in all forest conditions is *P. immissa*. Since it was a study of two areas, it was found that diversity of lichen in Doi Suthep-Pui National Park it has three different types of forest. This results in a great diversity of plant species, the forest with the greatest distribution of lichen is the hill evergreen forest at Doi Suthep, which has the most 9 species of lichen. Most of the plant species found have smooth shade bark, allowing the lichen to adhere and grow well, while the hill evergreen forest at Doi Inthanon has only three species. Since most of the plants are conifers, the bark is easily peeled off, lichen does not adhere well, and the weather is cool all year round, with little sunlight, there is less lichen to be found. Previous studies of this lichen genus in Chiang Mai Province, especially Doi Suthep and Doi Inthanon found a total of eight species. This study found ten more species, which had never been reported before after a study in 2007 (Aptroot et al., 2007; Buaruang et al., 2017), However, Doi Suthep and Doi Inthanon were only studied in some areas of the park, so the forest conditions were not very diverse, including the relatively humid climate. This group of lichens is found in abundance in hot, humid areas where sunlight can reach them.

Table 1. Number of lichen samples in genus *Pyrenula* and the species names collected from three forest types on both from Doi Suthep-Pui National Park and Inthanon Lady's Slipper Orchid Conservation Project, Doi Inthanon National Park in Chaing Mai province.

| Lichen species | Site A | | | Site B | Total |
|----------------------------------|-------------|-----|-----|--------|-------|
| | Forest type | | | HEF | |
| | DC | DDF | HEF | | |
| 1. <i>Pyrenula anomala</i> | 9 | 5 | 2 | | 16 |
| 2. <i>Pyrenula aspistea</i> | | 1 | 5 | | 6 |
| 3. <i>Pyrenula brunnea</i> | | | 1 | | 1 |
| 4. <i>Pyrenula cayennensis</i> | | 1 | 5 | | 6 |
| 5. <i>Pyrenula fetivica</i> | | | 12 | 20 | 32 |
| 6. <i>Pyrenula immissa</i> | 6 | 4 | 7 | 1 | 18 |
| 7. <i>Pyrenula leucostoma</i> | | | 2 | | 2 |
| 8. <i>Pyrenula mamillana</i> | | | 1 | | 1 |
| 9. <i>Pyrenula massariospora</i> | | | 2 | | 2 |
| 10. <i>Pyrenula quassiicola</i> | | 2 | | | 2 |
| 11. <i>Pyrenula thailandica</i> | | | | 2 | 2 |
| 12. <i>Pyrenula thelomorpha</i> | | 1 | | | 1 |
| Number species | 2 | 6 | 9 | 3 | |
| Total specimens | 15 | 14 | 37 | 23 | 90 |

DC: Deciduous Forest; DDF: Dry Dipterocarp Forest; HEF: Hill Evergreen Forest

Site A: Doi Suthep-Pui National Park, Site B: Inthanon Lady's Slipper Orchid Conservation Project

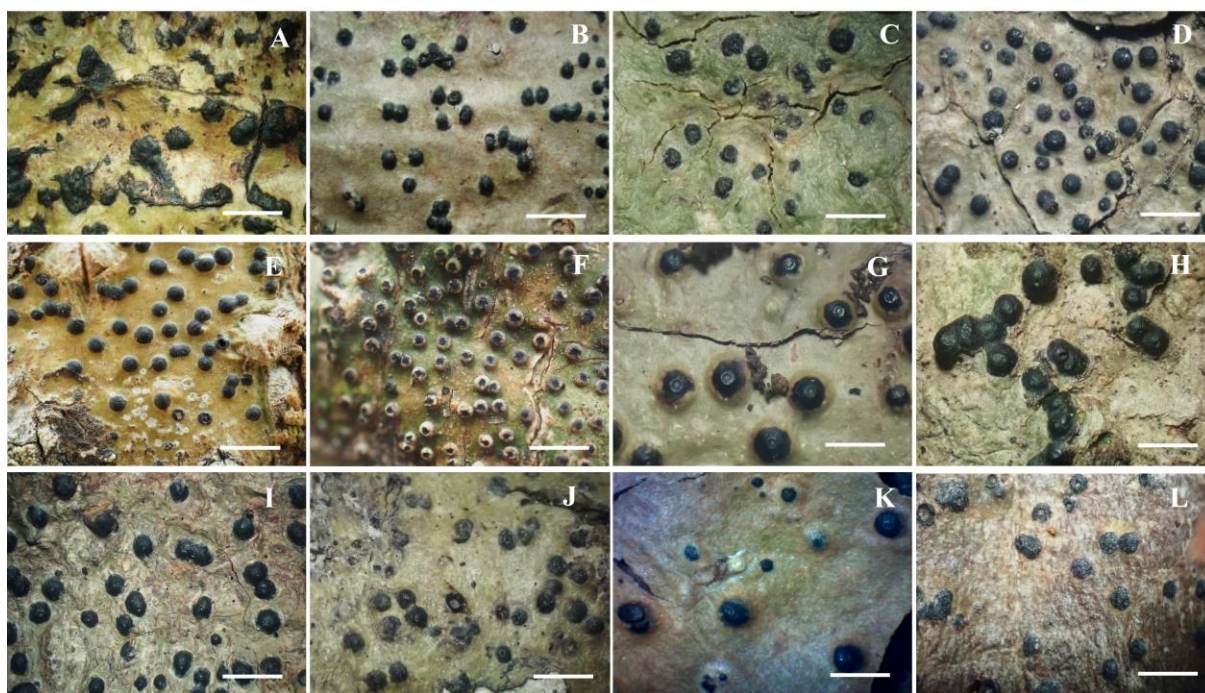


Figure 2 Thallus of perithecia lichen genus *Pyrenula* species on both from Doi Suthep-Pui National Park and Inthanon Lady's Slipper Orchid Conservation Project, Doi Inthanon National Park in Chaing Mai province; **A.** *P. anomala*, **B.** *P. aspistea*, **C.** *P. brunnea*, **D.** *P. cayennensis*, **E.** *P. fetivica*, **F.** *P. immissa*, **G.** *P. leucostoma*, **H.** *P. mamillana*, **I.** *P. massariospora*, **J.** *P. quassiicola*, **K.** *P. thailandica* and **L.** *P. thelomorpha* (scale-1 cm).

Conclusion

Ninety crustose lichen specimens of the genus *Pyrenula* were collected from Deciduous Forest (DC), Dry Dipterocarp Forest (DDF), and Hill Evergreen Forest (HEF) in both Doi Suthep-Pui National Park and the Inthanon Lady's Slipper Orchid Conservation Project within Doi Inthanon National Park. Taxonomic identification revealed twelve distinct taxa, with *Pyrenula immissa* being the common lichen found across all forest conditions. Notably, the HEF at Doi Suthep-Pui National Park exhibited the highest lichen diversity, hosting a total of nine species. Further studies may require more comprehensive sampling in other forest types in Chiang Mai Province, which may reveal more lichen species and provide a more complete database and investigation of lichen species in Thailand.

Acknowledgements

This research project is financially supported by the National Research Council of Thailand (NRCT). We extend our heartfelt gratitude to the officials involved and our dedicated colleagues in the Lichen Research Unit at the Department of Biology, Faculty of Science, Ramkhamhaeng University. Their generous assistance in utilizing laboratory equipment and facilities has been invaluable to our work.

References

1. Awasthi, D.D. A key to the microlichens of India, Nepal and Sri Lanka. *Bibliotheca Lichenologica* 1991; 40: 1-360.
2. Aptroot, A. Pyrenulaceae. In P. M. McCarthy (Ed.), *Flora of Australia* 2009; 57: 449-480.
3. Aptroot, A. A world key to the species of *Anthracotheicum* and *Pyrenula*. *The lichenologist* 2012; 44(1): 5-53.



4. Aptroot, A., Lücking, R., Sipman, K. J. M., Umaña, L., & Chaves, J. L. Pyrenocarpous lichens with bitunicate asci a first assessment of the lichen biodiversity inventory in Costa Rica. *Bibliotheca Lichenologica* 2008; 97: 1-162.
5. Aptroot, A., Saipunkaew, W., Sipman, H. J. M., Sparrius, L. B., and Wolseley, P. A. New lichens from Thailand, mainly microlichens from Chiang Mai. *Fungal Diversity* 2007; 24: 75-134.
6. Buaruang, K., Boonpragob, K., Mongkolsuk, P., Sangvichien, E., Vongshewarat, K., Polyiam, W., Rangsiruji, A., Saipunkaew, W., Naksuwankul, K., Kalb, J., Parnmen, S., Kraichak, E., Phraphuchamnong, P., Meesim, S., Luangsaphabool, T., Nirongbut, P., Poengsungnoen, V., Duangphui, N., Sodamuk, M., Phokaeo, S., Molsil, M., Aptroot, A., Kalb, K., Lücking, R., Lumbsch, H. T. A new checklist of lichenized fungi occurring in Thailand. *Myckeys* 2017; 23: 1–91.
7. Kansri Boonpragob, & Kawinnat Buaruang. Biodiversity of the lichen on Koh Samaesan, Chon Buri Province. Bangkok: Ramkhamhaeng University 2007.
8. Phokaeo, S., Buaruang, K., Mongkolsuk, P. and Boonprakob, K. The crustose lichen genus *Pyrenula* Family Pyrenulaceae on Islands in the Gulf of Thailand and Andaman Sea. National conference on Current Development and Next Generation Lichenology. *Indian Lichenological Society* 2018: 69.



EFFECT OF NITROGEN CONCENTRATION ON BIOMASS AND LUTEIN PRODUCTION IN GREEN MICROALGA *Chlorococcum humicola* CULTURED IN PHOTOBIOREACTORS

Pakhapol Triserikij,¹ Yosita Suankaew,¹ Sorawit Powtongsook^{2,3}, Kasidit Nootong^{1,*}

¹Department of Chemical Engineering, Faculty of Engineering, Chulalongkorn University, Bangkok, Thailand

²National Center of Genetic Engineering and Biotechnology, National Science and Technology Development Agency, Khlong Luang, Pathum Thani 12120, Thailand

*e-mail: kasidit.n@chula.ac.th

Abstract:

This preliminary work reports the effect of nitrogen concentration on growth and lutein production by green microalgal *Chlorococcum humicola*. Batch cultivation showed that microalgae cultured with 50% NaNO₃ in BG-11 growth medium yielded the highest biomass concentration of 630 ± 131 mg/L. In contrast, the maximum lutein content, measured at 1.33 ± 0.63 mg/g, was obtained when NaNO₃ in BG-11 growth medium was reduced to 25% of the original amount (25% NaNO₃). Lutein production observed in this study seemed to incline towards nitrogen limitation, which contrasted with the general trend that preferred nitrogen sufficient environment. This evidence suggests that optimization of lutein depends on microalgal species and requires further investigation.

Introduction:

Microalgae are unicellular organisms that are capable of photosynthesis. Microalgae are natural sources of carotenoids, which are natural pigments employed in different applications including supplementary diets, animal feed additives, cosmetics, and pharmaceuticals. One of the most important carotenoids in microalgae is lutein. Lutein, yellow color carotenoid, plays an important role in light-energy harvesting to increase the efficiency of photosynthesis and protecting microalgae from photooxidation under high-light intensity conditions.¹ Lutein production from microalgae possesses several advantages compared to conventional process (i.e., extraction from marigold), namely, higher productivity due to higher microalgal growth rate than terrestrial plants, ability to operate in photobioreactors where soil fertility is irrelevant and environmental parameters can be effectively controlled, and ability to utilize waste products such as carbon dioxide and wastewater containing nitrogen and phosphorus.^{2,3} The previous study by Powtongsook and Nootong reported the accumulation of lutein in green microalga *Chlorococcum humicola* from 25% to 40% of the total carotenoids in biomass.⁴ Other advantages of this particular strain include ability to grow in wide range of temperature, pH and carbon dioxide concentration, and its tendency to form cell clusters that allows algal biomass to be harvested by conventional methods such as filtration and sedimentation.^{5,6} Adjusting nitrogen concentration has been reported as one of the strategies to enhance growth and carotenoid accumulation in many microalgal species. Although significant progress has been accomplished to the level of commercialization for carotenoids such as astaxanthin and beta-carotene, limited progress is noted for lutein especially in *C. humicola*. Therefore, this preliminary study aims to examine the effect of varying nitrogen

concentration in the growth medium on biomass and lutein production in *C. humicola* cultured in photobioreactors.

Methodology:

Chlorococcum humicola TISTR 8266 was used in this study. Inoculum of *C. humicola* (100 mL) was mixed with sterile BG-11 growth medium (900 mL) in stirred tank photobioreactor. Liquid mixing in photobioreactor was achieved by using a magnetic stirrer at 900 rpm. The composition of BG-11 growth medium is displayed in Table 1. The photobioreactor was placed under room temperature (25 °C) and subject to continuous lighting at 134 $\mu\text{mol photons/m}^2\cdot\text{s}$ at the surface of photobioreactor. Aeration rate was maintained at 0.8 L/min for the entire cultivation. In this study, nitrate concentration, as the nitrogen source in the growth medium, was chosen as an experimental variable, adjusting to 0%, 25%, 50%, 100%, 125%, and 150% of the amount in the BG-11 growth medium. The cultivation at each nitrogen concentration was performed in triplicate ($n = 3$ photobioreactors). The cultivation proceeded until the stationary phase was established. Culture liquid sample (30 mL) from photobioreactors was obtained daily and analyzed for dry weight based on the method in APHA (1998).⁷ Chlorophyll concentration was analyzed according to Strickland and Parsons (1972).⁸ Nitrate concentration in the culture medium was analyzed according to APHA method 4500-NO₃-B.⁷ Lutein concentration was analyzed using high-performance liquid chromatography with a photo diode array detector by injecting 20 μL of the extracted carotenoid liquid sample into a C-18 column with the carrier phase being a mixture of distilled water, methanol, acetonitrile, and dichloromethane in the ratio of 1:10:79:10, respectively, at a flow rate of 1 mL/min, for a total analysis time of 30 min. Data from each treatment were statistically compared by one-way ANOVA with Tukey HSD post hoc test with the significance level of 0.05.⁹

Table 1.
Composition of BG-11 growth medium⁶

| Component | Concentration (g/L) |
|--|---------------------|
| NaNO ₃ | 1.500 |
| K ₂ HPO ₄ ·3H ₂ O | 0.040 |
| MgSO ₄ ·7H ₂ O | 0.075 |
| CaCl ₂ ·2H ₂ O | 0.036 |
| Na ₂ CO ₃ | 0.020 |
| Citric acid | 0.006 |
| Ferric ammonium citrate | 0.006 |
| EDTA | 0.001 |
| Trace metal mix A ₅ | 1 mL |

Table 2.
Composition of Trace metal mix A₅⁶

| Component | Concentration (g/L) |
|--|---------------------|
| H ₃ BO ₃ | 2.860 |
| MnCl ₂ | 1.810 |
| Na ₂ MoO ₄ ·2H ₂ O | 0.390 |
| ZnSO ₄ ·7H ₂ O | 0.222 |
| CuSO ₄ ·5H ₂ O | 0.079 |
| Co(NO ₃) ₂ ·6H ₂ O | 0.050 |



Results and Discussion:

Nitrogen is an essential macronutrient required for biosynthesis of protein, enzymes, nucleic acids, and chlorophyll during cell growth.¹⁰ Thus, availability of nitrogen in the growth medium should be one of the key factors influencing the biomass production of *C. humicola*. Biomass concentration, measured as dry weight, increased in all treatments except the cultivation supplied with the growth medium without nitrogen source (NaNO_3). At the end of the experiment, the cultivation supplied with 50% NaNO_3 yielded the highest biomass concentration at 630 ± 131 mg/L, which corresponded to the biomass productivity of 73.1 ± 16.35 mg/L-day. The maximum biomass concentration was insignificant difference ($p > 0.05$) compared to the cultivation subject to 100% NaNO_3 , 125% NaNO_3 and 150% NaNO_3 , which produced the final biomass concentration at 565 ± 229 , 545 ± 201 , and 555 ± 100 mg/L, respectively. Biomass production was less effective when nitrogen content in growth medium was reduced to 25%, as indicated by significantly lower biomass concentration at 435 ± 78 mg/L. The influence of nitrogen supply on biomass production was clearly related to the results of nitrate measurement (Figure 2). With the remaining nitrogen in the growth medium exceeding 150 mg N/L, it was apparent that nitrogen was not the limiting factor for cell growth in the cultivation supplied with 50% NaNO_3 and higher. This is in contrast to the cultivation supplied with 25% NaNO_3 that observed the remaining nitrate concentration less than 30 mg N/L (Figure 2). Chlorophyll is another parameter commonly used to track growth in green microalgae. Results of chlorophyll analysis were consistent with biomass production, with the highest chlorophyll concentration (50.6 ± 22.42 mg/L) obtained from the cultivation supplied with 50% NaNO_3 in the growth medium (Figure 1).

Previous studies have shown that nitrogen plays an important role in microalgal biosynthesis of lutein.¹¹ Unlike biomass production, the highest lutein content (1.33 ± 0.63 mg/g) was associated with the cultivation supplied with 25% NaNO_3 in the growth medium (Figure 3). The magnitude of lutein content in this study was significantly lower than the previous works, which reported lutein content in range 5 to 15 mg/g.¹⁰ The likely explanation could be related to the cultivation under sub-optimal conditions as compared to the previous works. Important environmental inputs affecting growth and lutein production such as light intensity, photoperiod, light wavelength, and types of photobioreactor were not optimized during the experiment.¹⁰ The results obtained were also in line with past researches that demonstrated nitrogen limitation can induce stress response in some microalgal species (e.g., *Scenedesmus Obliquus*, *Muriellopsis* sp.), leading to increased lutein accumulation as means to protect photosynthesis apparatus from oxidation stress.^{12,13} Nonetheless, the general trend of lutein biosynthesis in microalgae seems to incline toward nitrogen sufficient condition.¹⁰ Thus, the finding from this study is the clear evidence that optimization of lutein and other biochemicals is species specific and requires further investigation. By adopting lutein productivity as the main criteria, the suitable nitrogen concentration in growth medium was 25% NaNO_3 , leading to the highest lutein productivity of 0.07 mg/L-day (Table 3).

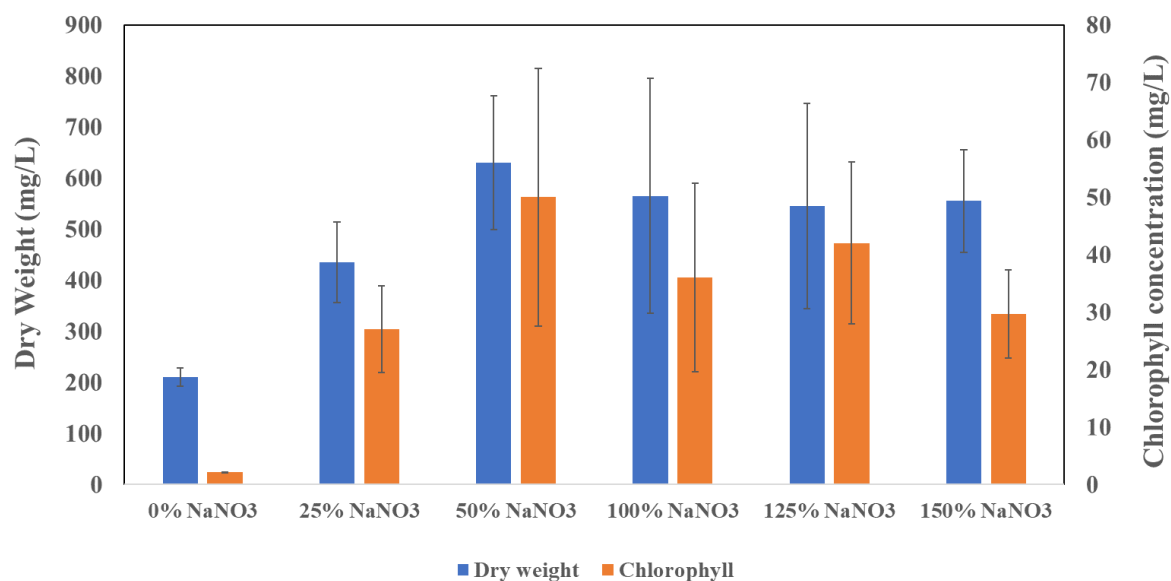


Figure 1.

Dry weight (biomass) and chlorophyll concentration at the end of the cultivation (8th day) of *Chlorococcum humicola* in BG-11 growth medium with different NaNO₃ concentration (0% - 150% of the amount in standard BG-11 growth medium i.e., 100% NaNO₃).

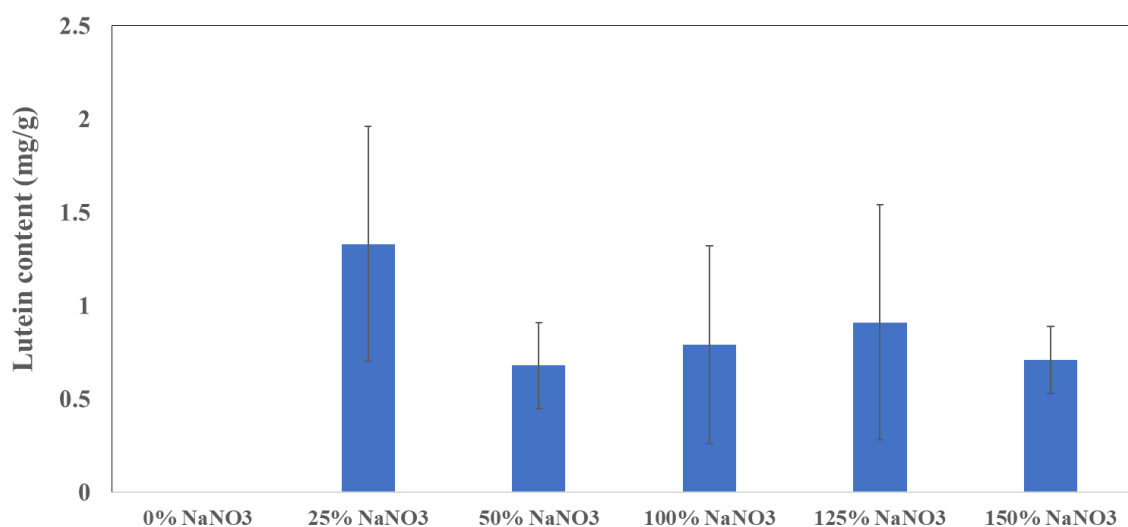


Figure 2.

Nitrate concentration at the start and the end (8th day) of the cultivation of *Chlorococcum humicola* in BG-11 growth medium with different NaNO₃ concentration (0% - 150% of the amount in standard BG-11 growth medium i.e., 100% NaNO₃).

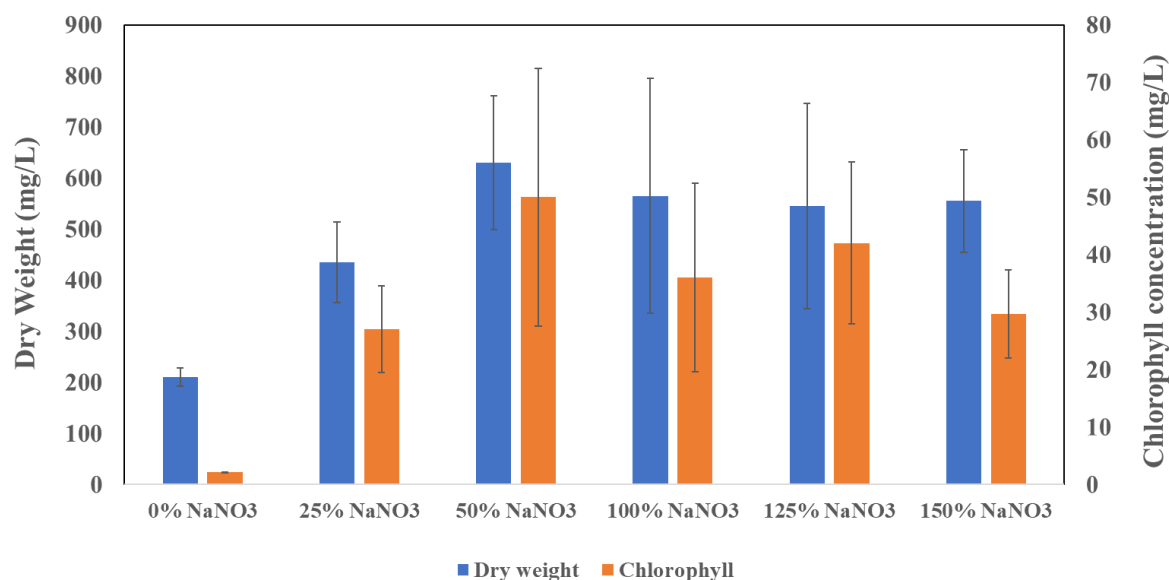


Figure 3.

Lutein content at the end of the cultivation (8th day) of *Chlorococcum humicola* in BG-11 growth medium with different NaNO₃ concentration (0% - 150% of the amount in standard BG-11 growth medium i.e., 100% NaNO₃).

Table 3.

Biomass and lutein production rate from cultivation of *Chlorococcum humicola* in BG-11 growth medium with different NaNO₃ concentration (0% - 150% of the amount in standard BG-11 growth medium i.e., 100% NaNO₃).

| NaNO ₃ concentration | Biomass productivity (mg/L·day) | Lutein productivity (mg/L·day) |
|---------------------------------|---------------------------------|--------------------------------|
| 0% | 17.29 ± 1.44 | ND |
| 25% | 39.17 ± 14.28 | 0.07 ± 0.02 |
| 50% | 73.13 ± 16.35 | 0.05 ± 0.01 |
| 100% | 55.79 ± 29.05 | 0.05 ± 0.03 |
| 125% | 55.35 ± 23.37 | 0.06 ± 0.03 |
| 150% | 56.25 ± 10.44 | 0.04 ± 0.04 |

ND = Non-detectable

Conclusion:

This preliminary work focused on the effect of adjusting nitrogen concentration on biomass and lutein production in *C. humicola*. Nitrogen availability clearly affected growth and lutein production in *C. humicola*, with maximum biomass concentration and maximum lutein content obtained when supplying 50% NaNO₃ and 25% NaNO₃ in the growth medium, respectively. Contrasting outcomes with the general trends suggested that lutein optimization is species specific. Additionally, further optimization of culture condition and improving photobioreactor design are essential for increasing lutein productivity.

References:

1. Ma R, Zhang Z, Ho S, Ruan C, Li J, Xie Y, Shi X, Liu L, Chen J, Two-stage bioprocess for hyper-production of lutein from microalga *Chlorella sorokiniana* FZU60: Effects of temperature, light intensity, and operation strategies. *Algal Research*. 2020;52.
2. Sánchez J.F., Fernández J.M., Acien F.G., Rueda A., Pérez-Parra J., Molina E., Influence of culture conditions on the productivity and lutein content of the new strain *Scenedesmus almeriensis*. *Process Biochemistry*, 2008;43(4):398-405.
3. Del Campo J.A., Rodríguez H, Moreno J, Vargas M.A., Rivas J, Guerrero M.G., Lutein production by *Muriellopsis* sp. in an outdoor tubular photobioreactor. *Journal of Biotechnology*, 2001;85(3):289-295.
4. Powtongsook, S., Nootong K., Photoautotrophic cultivation of *Chlorococcum humicola* in stirred tank and airlift photobioreactors under different light settings and light supplying strategies for biomass and carotenoid production. *Journal of Chemical Technology & Biotechnology*, 2019;94(10):3084-3092.
5. Zhang, D.-H. and Lee Y.-K., Ketocarotenoid production by a mutant of *Chlorococcum* sp. in an outdoor tubular photobioreactor. *Biotechnology Letters*, 1999;21(1):7-10.
6. Wannachod, T., Wannasutthiwat S., Powtongsook, S., Nootong K., Photoautotrophic cultivating options of freshwater green microalgal *Chlorococcum humicola* for biomass and carotenoid production. *Preparative Biochemistry and Biotechnology*, 2018;48(4):335-342.
7. Standard Methods for the Examination of Water and Wastewater. 20th ed. 1998, Washington DC: American Public Health Association.
8. Strickland J.D.H., Parsons T.R., A practical Handbook of Seawater Analysis. 2nd ed. 1972, Ottawa: Supply and Services Canada.
9. Montgomery D.C., Runger G.C., Applied Statistics and Probability for Engineers, 3rd ed., John Wiley & Sons, New York, 2002;1-706.
10. Yunlei Fu, Yinan Wang, Lanbo Yi, Jin Liu, Shufang Yang, Bin Liu, Feng Chen, Han Sun, Lutein production from microalgae: A review, *Bioresource Technology*, 2023;376:128875.
11. Youping Xie, Jun Li, Ruijuan Ma, Shih-Hsin Ho, Xinguo Shi, Lemian Liu, Jianfeng Chen, Bioprocess operation strategies with mixotrophy/photoinduction to enhance lutein production of microalga *Chlorella sorokiniana* FZU60, *Bioresource Technology*, 2019;290:121798.
12. Shih-Hsin Ho, Youping Xie, Ming-Chang Chan, Chen-Chun Liu, Chun-Yen Chen, Duu-Jong Lee, Chieh-Chen Huang, Jo-Shu Chang, Effects of nitrogen source availability and bioreactor operating strategies on lutein production with *Scenedesmus obliquus* FSP-3, *Bioresource Technology*, 2015;184:131-138.
13. José A Del Campo, José Moreno, Herminia Rodríguez, M Angeles Vargas, Joaquín Rivas, Miguel G Guerrero, Carotenoid content of chlorophycean microalgae: factors determining lutein accumulation in *Muriellopsis* sp. (Chlorophyta), *Journal of Biotechnology*, 2000;76(1):51-59.



Evaluating Cell-Free DNA in Spent Culture Medium for Assessing Blastocyst Quality and Chromosomal Abnormalities

Sasipat Teerawongsuwan,¹ Amarin Nakwichian,² Kodchakorn Wiangwised,³ Nattapavee Ngampiyakul,³ Nitid Wanikorn,³ Panida Boonnithipaisit,³ Panyada Khiuhok,³ Phanthitra Aekudompong⁴ and Ruttachuk Rungsiwiwut^{1,*}

¹Department of Anatomy, Faculty of Medicine, Srinakharinwirot University, Bangkok, Thailand

²Department of Obstetrics and Gynecology, Faculty of Medicine, Srinakharinwirot University, Nakhonnayok, Thailand

³Faculty of Medicine, Srinakharinwirot University, Bangkok, Thailand

⁴Paragon fertility clinic, Huai Khwang, Bangkok

*e-mail: ruttachuk@g.swu.ac.th

Abstract:

The study aimed to explore the relationship between cell-free DNA (cfDNA) quantity in spent culture medium and the morphology and chromosomal abnormalities of human embryos. 39 zygotes were cultured to the blastocyst stage, with morphological grading conducted on Days 5-6. The embryos underwent biopsy for preimplantation genetic testing for aneuploidy (PGT-A), and cfDNA was extracted and quantified from the spent medium. The study compared cfDNA levels between blastocysts of good and poor morphology, as well as between euploid and aneuploid blastocysts, using the Mann-Whitney statistical analysis at a significance level of 0.05. The results showed no statistically significant difference in cfDNA quantities between moderate and poor morphology embryos ($p=0.274$) or between euploid and aneuploid groups ($p=0.406$). The study concludes that cfDNA levels in spent culture medium are unsuitable for indicating blastocyst morphology or chromosomal abnormalities.

Introduction:

Infertility refers to a condition in which married couples, despite living together and having regular unprotected sex for one year, are unable to conceive¹. One of the infertility treatments is assisted reproductive technology (ART). Common ART methods include *in vitro* fertilization and embryo transfer (IVF and ET), intracytoplasmic sperm injection (ICSI), and frozen embryo transfer (FET). The choice of treatment depends on the underlying cause of infertility. However, societal trends toward later marriages often delay the discovery and initiation of infertility treatment. As a result, even with the use of ART, the likelihood of a successful pregnancy decreases as the mother's age increases. This decline in success rates may be due to a reduced number of oocytes or the presence of chromosomal abnormalities in reproductive cells²⁻³.

To overcome this challenge, a critical step in ART involves selecting good-quality embryos that have the highest chance of successful implantation. This selection can be guided by evaluating the morphology of the embryo under a microscope and assessing criteria related to pregnancy outcome. Additionally, preimplantation genetic testing for aneuploidy (PGT-A) can be used to identify embryos with chromosomal abnormalities. Aneuploid embryos are one of the causes of implantation failure, and if implantation does occur, they can lead to congenital disorders. Therefore, PGT-A plays a crucial role in improving the chances of a successful and healthy pregnancy⁴.

The PGT-A is used to detect chromosomal abnormalities of the embryo by analyzing the number of chromosomes using next-generation sequencing (NGS) techniques. The results are presented as copy number variation (CNV), indicating whether any of the 23 pairs of chromosomes exhibit an insertion or deletion in chromosome number. The embryonic sample used for PGT-A testing consists of 3-5 trophectoderm cells, biopsied from the embryo. However, this method is invasive and may pose a risk to the embryo. Additionally, biopsy technique requires highly skilled embryologists. As a result, non-invasive techniques for assessing embryo quality have been developed, which do not require direct intervention with the embryo.

One of the interesting non-invasive methods involves using spent culture medium as a specimen for analysis. The spent medium contains cell-free DNA (cfDNA), RNA, miRNA, and various proteins, which can serve as indicators of embryo anomalies and quality. In this study, we focus on cfDNA. cfDNA refers to genetic material that is freely floating in the spent medium. The average quantity of this genetic material is approximately 3 ng, with a size of around 400 base pairs⁵. The secretion of cfDNA into the embryonic solution is thought to be linked to apoptosis, a form of programmed cell death. Apoptosis is a highly regulated process in which cells undergo controlled death, leading to the fragmentation of cellular components, including DNA. Several studies support this hypothesis. For instance, Rule et al.⁶ research found cfDNA in blastocoel fluid, which was associated with embryonic morphology. Additionally, it has been shown that a portion of the cfDNA present originates from the intracellular contents of embryonic cells undergoing apoptosis. Stigliani et al.⁷ study observed embryos with 5% fragmentation, which was associated with both apoptosis and secondary necrosis. Singla et al.⁸ research demonstrated that the apoptotic pathway is involved in eliminating aneuploid cells in developing mosaic embryos in a mouse model. This leads to the hypothesis that poor-grade blastocysts, which tend to exhibit higher rates of apoptosis, will release a greater quantity of cfDNA into the medium. Therefore, the objective of this research is to explore the relationship between cell-free DNA (cfDNA) quantity in spent culture medium and the blastocyst grading and the results of chromosomal abnormalities number of human embryos.

Methodology:

Ethical Approval

The protocol of the present study was ethically approved by the Institutional Review Board of Srinakharinwirot University (IRB; SWUEC-M-079/2565E). The embryo culture media was obtained after receiving informed consent from the patients.

Participant enrollment

Twelve couples undergoing infertility treatment using the ICSI technique at Paragon Fertility Clinic, Thailand, aged between 25 and 45 years, who did not have chronic conditions such as diabetes, endocrine disorders, blood disorders, or autoimmune diseases, and who provided informed consent, participated in the research study.

Embryo culture and morphological evaluation

Following ICSI, 39 zygotes were cultured in 20 µL drops of continuous spent culture medium (Life Global, Denmark) for 5–6 days until they reached the blastocyst stage. Embryonic development was monitored using an Olympus IX73 inverted microscope. Images were captured daily for 6 days, with the embryo maintained in an IVF working chamber at 37°C, 5% CO₂, and 5% O₂ (Pulse Science, Denmark). On Days 5 and 6 post-ICSI, embryo quality at the blastocyst stage was assessed based on the morphological characteristics of the trophectoderm (TE) and Inner cell mass (ICM), using the Gardner grading system⁹ as detailed in **Table 1**. Based on this evaluation, we categorized blastocyst morphology into three groups: good morphology (AA, AB, or BA), moderate morphology



(BB), and poor morphology (AC, BC, CB, or CC). After 5–6 days of culture, embryos that developed into the blastocyst stage underwent trophectoderm biopsy, where 3–5 cells were excised for preimplantation genetic testing for aneuploidy (PGT-A) at a Next Generation Genomic laboratory, Thailand. The biopsied embryos were then cryopreserved for future transfer.

Table 1.
Gardner grading system for blastocyst-stage embryos

| <i>Grade</i> | <i>ICM Description</i> | <i>TE Description</i> |
|--------------|--|--|
| A | Large ICM, many compacted cells, tightly packed | Many cells forming a cohesive epithelium |
| B | Smaller size, fewer loosely adherent cells, less compacted | Few cells forming a loose epithelium |
| C | Very few cells visible, may be loose, difficult to distinguish from TE | very few large cells |

Spent culture medium collection

Spent culture medium, each with a volume of 20 μ l per embryo, were collected after embryo freezing. These samples were stored in tubes specifically designed to maintain DNAase- and RNAase-free conditions. The tubes were frozen at -20°C until the DNA extraction process.

Total DNA extraction

Total DNA was extracted from the spent culture medium using the DNeasy Blood & Tissue Kit (Qiagen, Germany), following the manufacturer's protocol. DNA quantity was measured using a NanoDrop 2000 spectrophotometer (Thermo Fisher Scientific, United States) and reported in ng/ μ l. Measurements were performed in triplicate, with the Elution Buffer from the DNeasy Blood & Tissue Kit used as the blank control.

Statistical analysis

To investigate the association between cfDNA quantity and blastocyst grading and PGT-A results from embryo biopsy, the Mann-Whitney U test was employed, at a confidence level of 95%.

Results and Discussion:

In this experiment, cfDNA was extracted from spent medium samples of 34 blastocysts, 5 arrested embryo and 3 negative control samples (fresh culture medium). The cfDNA concentrations were measured. The results of cfDNA concentrations were summarized in **Table 2**.

Table 2.
cfDNA concentrations

| <i>Sample name</i> | <i>Concentration (ng/μl)</i> |
|--------------------|---|
| 1 | 2.55 |
| 2 | 2.60 |

| | |
|------------|------|
| 3 | 2.60 |
| 4 | 2.70 |
| 5 | 2.70 |
| 6 | 2.70 |
| 7 | 2.70 |
| 8 | 2.70 |
| 9 | 2.80 |
| 10 | 2.80 |
| 11 | 2.90 |
| 12 | 3.00 |
| 13 | 3.00 |
| 14 | 3.00 |
| 15 | 3.10 |
| 16 | 3.20 |
| 17 | 3.30 |
| 18 | 3.40 |
| 19 | 3.40 |
| 20 | 3.45 |
| 21 | 3.50 |
| 22 | 3.70 |
| 23 | 3.80 |
| 24 | 3.80 |
| 25 | 3.90 |
| 26 | 4.30 |
| 27 | 4.40 |
| 28 | 4.50 |
| 29 | 4.90 |
| 30 | 4.90 |
| 31 | 5.00 |
| 32 | 5.70 |
| 33 | 5.90 |
| 34 | 5.90 |
| Arrested1 | 2.70 |
| Arrested2 | 3.20 |
| Arrested3 | 3.40 |
| Arrested4 | 3.20 |
| Arrested5 | 2.80 |
| Negative1 | 2.60 |
| Negative 2 | 2.55 |
| Negative 3 | 2.45 |

Morphology grading is a crucial factor in selecting high-quality embryos for transfer. Blastocyst quality evaluation involves two key components: the ICM and TE. In this study, no spent culture medium was obtained from blastocysts with TE or ICM graded as A; therefore, these were excluded from the analysis. Consequently, statistical comparisons were conducted only on embryos graded as B and C. An example of each blastocyst grade is presented in **Figure 1**. To assess whether cfDNA secretion into the spent culture medium varies with blastocyst grade and cell type, a comparative analysis of cfDNA levels across different grades within each cell type was conducted. The analysis revealed that in ICM, the median cfDNA concentration was 3.00 ng/μl for Grade B (n=19) and 3.45 ng/μl for Grade C



(n=15). In TE cells, the median cfDNA concentration was 3.15 ng/ μ l for Grade B (n=20) and 3.70 ng/ μ l for Grade C (n=13). Statistical analysis showed no significant difference in cfDNA levels between Grades B and C within the same cell type (ICM; $p=0.430$, TE; $p=0.494$), as shown in **Figure 2a** and **Figure 2b**. These results indicate that each cell type secretes similar amounts of cfDNA. When evaluating cfDNA levels based on a group of blastocyst morphology, the median value for moderate morphology was 3.00 ng/ μ l, whereas the median for poor morphology was 3.48 ng/ μ l. Although the median cfDNA concentration was higher in the poor morphology group, statistical analysis revealed no significant difference between the two morphology groups ($p=0.274$), as shown in **Figure 2c**. The analysis results indicate that the quantity of cfDNA does not correlate with the blastocyst morphology. This finding aligns with Kuznyetsov et al.¹⁰ research, which showed that the amount of cfDNA obtained from blastocoel fluid, combined with cfDNA from the embryo's spent medium, was not related to blastocyst grading. The lack of correlation may be due to the mechanism of cfDNA release into the embryonic medium, suggesting that apoptosis may not be the only mechanism. Extracellular vesicles (EVs) may also contribute to the release of cfDNA into the embryonic medium, as it has been discovered that embryos at both the cleavage and blastocyst stages release EVs to communicate with maternal cells¹¹. Research supports this concept by identifying EVs that carry detectable amounts of genomic DNA using array-based comparative genomic hybridization (aCGH)¹².

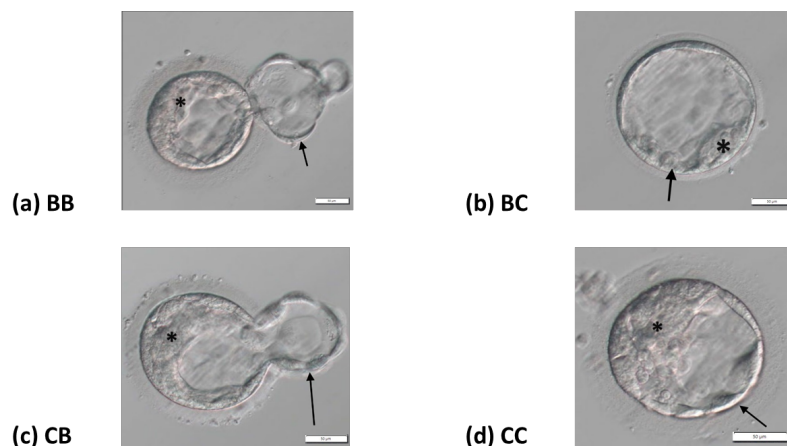


Figure 1.

Blastocyst-stage embryos were graded by two embryologists using inverted microscopy at 20x magnification, where the TE and ICM were identified. The TE is indicated by the black arrow, while the ICM is indicated by the star (*). The grading categories are as follows: (a) ICM: B TE: B, (b) ICM: B TE: C, (c) ICM: C TE: B, and (d) ICM: C TE: C.

Scale bar = 50 μ m

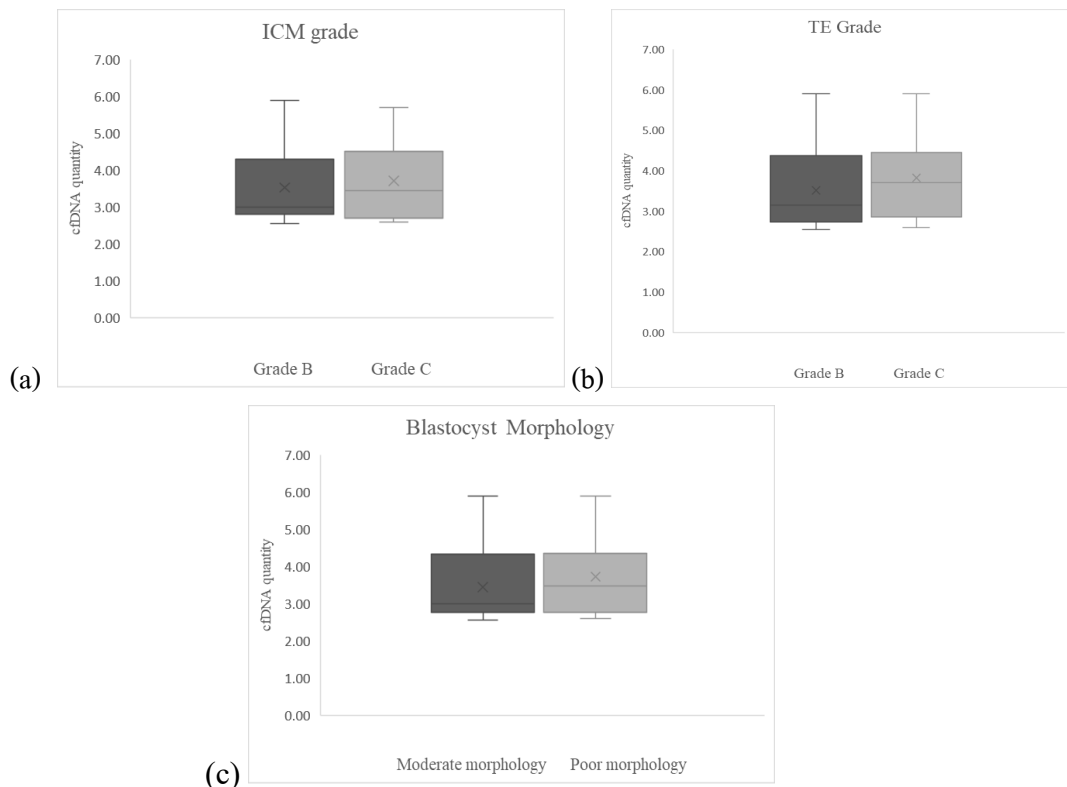


Figure 2.

A bar graph comparing cfDNA quantity in spent culture medium with (a) the blastocyst ICM grade, (b) the blastocyst TE grade (c) the blastocyst morphology employing the Man-Whitney U test. The data are presented as median and IQR, with a significant level set at a p-value of 0.05. The experiments were performed in triplicate.

Another critical factor in selecting high-quality embryos for transfer is the detection of chromosomal abnormalities through PGT-A testing, as these abnormalities can significantly impact embryo implantation. The mechanism by which an embryo eliminates abnormal cells, typically through apoptosis, may contribute to the presence of cfDNA in the culture medium¹³. To explore the relationship between cfDNA levels in spent culture medium and PGT-A results, this study categorized embryos into two groups based on PGT-A outcomes: one with a normal chromosomal count (euploid) and another with chromosomal abnormalities (aneuploid). The analysis revealed that the median cfDNA level was 2.95 ng/ μ l in the euploid group (n=14) and 3.40 ng/ μ l in the aneuploid group (n=20). Although the group with chromosomal abnormalities exhibited higher cfDNA levels, statistical analysis found no significant difference ($p = 0.406$), as shown in **Figure 3**. This lack of significance may be attributed to the small sample size, which could have limited the ability to detect differences. Additionally, the release of cfDNA into the spent culture medium may not be solely due to apoptosis, as discussed earlier. To investigate this hypothesis, we quantified the amount of cfDNA in arrested embryos.

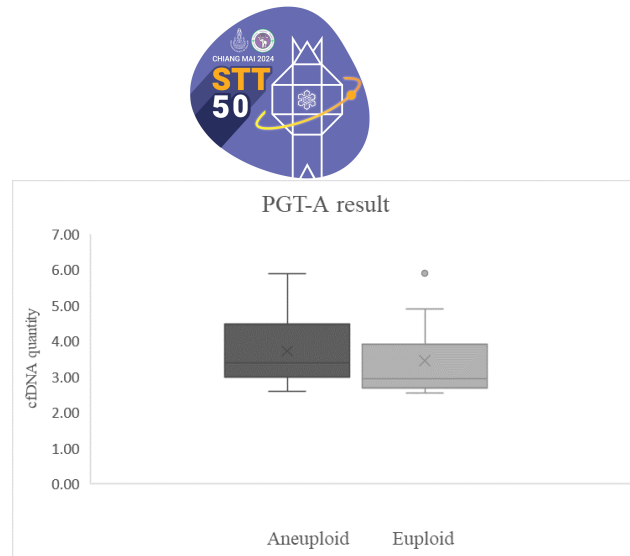


Figure 3.

A bar graph comparing cfDNA quantity in spent culture medium and results of pre-implantation genetic testing for aneuploidy is generated, utilizing the Mann-Whitney U test. The data are presented as median and IQR, with a significant level set at a p-value of 0.05. The experiments were performed in triplicate.

Embryo arrest refers to the cessation of embryonic development before reaching the blastocyst stage, as shown in **Figure 4**. This can result from various factors, including inadequate culture conditions, metabolic dysfunction, or DNA damage¹⁴. However, when comparing the cfDNA levels between arrested embryos and viable embryos, it was found that arrested embryos had a median cfDNA value of 3.20 ng/μl, while viable embryos had a median value of 3.35 ng/μl. This difference was not statistically significant ($p=0.378$) as shown in **Figure 5**. These results align with findings by Handayani¹³, who proposed an alternative theory for the release of cfDNA into the embryonic culture medium. In addition to apoptosis, cfDNA may be released through extracellular vesicles during embryonic development.

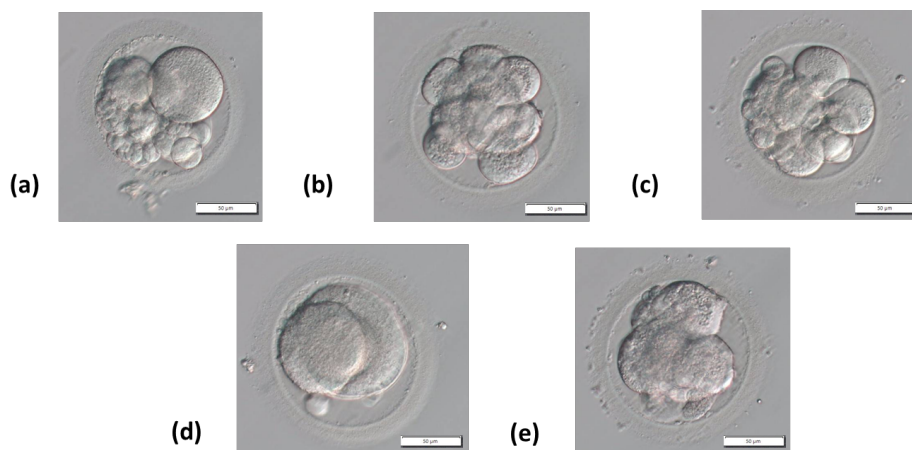


Figure 4.

The images of embryos that arrested on Day 3 post-ICSI at various developmental stages were captured using an inverted microscope at 20x magnification. (a) shows an embryo that arrested at the 4-cell stage, (b) an embryo arrested at the 8-cell stage, (c) another embryo arrested at the 8-cell stage, (d) an embryo arrested at the 3-cell stage, and (e) an embryo arrested at the 6-cell stage. Scale bar = 50 μm

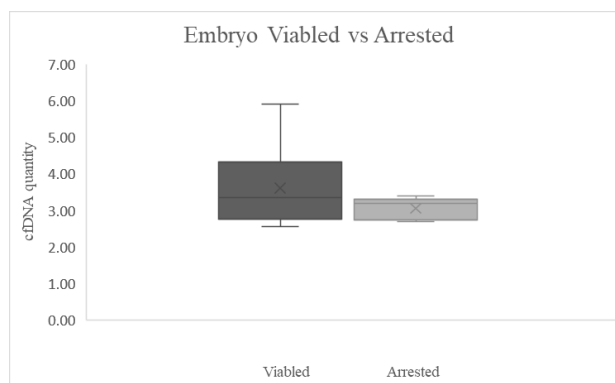


Figure 5.

A bar graph comparing cfDNA quantity in spent culture medium and embryo viability employing the Man-Whitney U test. The data are presented as median and IQR, with a significant level set at a p-value of 0.05. The experiments were performed in triplicate.

The amount of cfDNA detected in the spent culture medium ranges from 6 pg to 4 ng¹⁵, the use of a Nanodrop for measurement may lack the required sensitivity. Consequently, future studies should consider employing more advanced techniques, such as digital PCR, to accurately quantify cfDNA, particularly in samples with very low concentrations in the spent culture medium.

A key finding from this study is the detection of cfDNA in the spent culture medium not used for embryo culture. The negative control group exhibited a median cfDNA level of 2.5 ng/μL. However, when compared to the spent culture medium that had been incubated with embryos, a statistically significant difference was observed ($p=0.001$), as shown in **Figure 6**. This suggests that the source of cfDNA in the spent culture medium is not only from the embryos but may also originate from the culture medium itself. This finding is consistent with the results of Vera-Rodriguez et al.¹⁵ and Hammond, who also detected cfDNA in their negative control groups. However, while Vera-Rodriguez et al.¹⁵ and Hammond et al.¹⁶ detected cfDNA in the spent culture medium, it was present at much lower levels (approximately 1.6 pg) and differed significantly from solutions that had been in contact with embryos. The variation in cfDNA levels between studies is likely attributable to differences in the brands of culture solutions used, which may affect the concentration of protein supplements, such as human serum albumin, a component of the spent culture medium¹⁷.

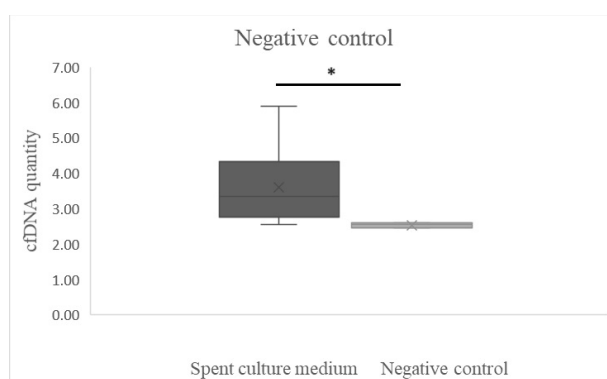


Figure 6.

A bar graph comparing cfDNA quantity in spent culture medium and negative control is generated, utilizing the Mann-Whitney U test. The data are presented as median and IQR, with a significant level set at a p-value of 0.05, * = $p \leq 0.001$. The experiments were performed in triplicate.



Conclusion:

The study found that cfDNA quantities are not associated with blastocyst morphology or chromosome abnormality results. Therefore, the study concludes that cfDNA levels in the spent culture medium are not suitable for indicators of blastocyst grading or chromosomal abnormalities.

Acknowledgements:

The authors would like to extend sincere gratitude to the Faculty of Medicine at Srinakharinwirot University for financial assistance through the research grant provided (MED-RES-200; 265/2565) (MED-RES-200;266/2565). The authors would also like to thank the embryologist and staff from Paragon Fertility Clinic for providing spent culture medium for this research.

References:

1. Vander Borcht M, Wyns C. Clin Biochem. 2018;62:2-10.
2. Cimadomo D, Fabozzi G, Vaiarelli A, Ubaldi N, Ubaldi FM, Rienzi L. Front Endocrinol (Lausanne). 2018;9:327.
3. Humm KC, Sakkas D. Fertil Steril. 2013;99(1):30-6.
4. Forman Eric J, Franasiak Jason M, Goodman Linnea R, Juneau Caroline R, Morin Scott J, Neal Shelby A, et al. Fertil Steril. 2018;110(5): 896–904.
5. Brouillet S, Martinez G, Coutton C, Hamamah S. Reprod Biomed Online. 2020;40(6):779-96.
6. Rule K, Chosed R.J, Arthur Chang, T, David Wininger J, Roudebush WE. J Assist Reprod Genet. 2018;35:1497–1501.
7. Stigliani S, Anserini P, Venturini PL, Scaruffi P. Hum Reprod. 2013;28(10):2652-60.
8. Singla S, Iwamoto-Stohl LK, Zhu M, Zernicka-Goetz M. Nat Commun . 2020;11:2958
9. Gardner DK, Lane M, Stevens J, Schlenker T, Schoolcraft WB. Fertil Steril. 2000;73(6):1155-8.
10. Kuznyetsov V, Madjunkova S, Abramov R, Antes R, Ibarrientos Z, Motamedi G, Zaman A, Kuznyetsova I, Librach CL. Sci Rep. 2020;10(1):7244.
11. Giacomini E, Vago R, Sanchez AM, Podini P, Zarovni N, Murdica V, Rizzo R, Bortolotti D, Candiani M, Viganò P. Sci Rep. 2017;7(1):5210.
12. Veraguas D, Aguilera C, Henriquez C, Velasquez AE, Melo-Baez B, Silva-Ibañez P, Castro FO, Rodriguez-Alvarez L. Zygote. 2021;29(2):138-149.
13. Handayani N, Aubry D, Boediono A, Wiweko B, Sirait B, Sini I, Polim AA, Dwiranti A, Bowolaksono A. J Assist Reprod Genet. 2023;40(6):1231-1242.
14. Orvieto R, Jonish-Grossman A, Maydan SA, Noach-Hirsh M, Dratviman-Storobinsky O, Aizer A. Reprod Biol Endocrinol. 2022;20(1):52.
15. Vera-Rodriguez M, Diez-Juan A, Jimenez-Almazan J, Martinez S, Navarro R, Peinado V, Mercader A, Meseguer M, Blesa D, Moreno I, Valbuena D, Rubio C, Simon C. Hum Reprod. 2018;33(4):745-756.
16. Hammond ER, McGillivray BC, Wicker SM, Peek JC, Shelling AN, Stone P, Chamley LW, Cree LM. Fertil Steril. 2017;107(1):220-228.e5.
17. Desai N, Yao M, Richards EG, Goldberg JM. Fertil Steril. 2020;114(6):1207-1215.



EVALUATION OF RAMBUTAN PEEL, NONI LEAF, BETEL LEAF, AND MACAO TEA EXTRACTS AS POTENTIAL ALZHEIMER'S DISEASE THERAPEUTICS: INHIBITORY EFFECTS ON ACETYLCHOLINESTERASE AND BUTYRYLCHOLINESTERASE ENZYMES

Kittisak Sangthongchin,^{1,2} Netnapa Chana,^{2,3,*}

¹Department of Chemistry, Faculty of Science and Digital Innovation, Thaksin University, Phatthalung Campus, Phatthalung, 93210, Thailand

²Innovative Material Chemistry for Environment Center, Department of Chemistry, Faculty of Science and Digital Innovation, Thaksin University, Phatthalung campus, Phatthalung, 93210, Thailand

³Department of Biological Sciences, Faculty of Science and Digital Innovation, Thaksin University, Phatthalung Campus, Phatthalung, 93210, Thailand

*e-mail: netnapa@tsu.ac.th

Abstract:

Alzheimer's disease (AD), a progressive neurodegenerative disorder, affects millions worldwide. One potential treatment approach involves inhibiting acetylcholinesterase (AChE) and butyrylcholinesterase (BChE), which degrade acetylcholine, to alleviate cognitive symptoms by increasing brain acetylcholine levels. *Nephelium lappaceum* Linn. (rambutan peel), *Morinda citrifolia* Linn. (noni leaves), *Piper betle* Linn. (betel leaves), and *Scoparia dulcis* Linn. (macao tea) possess various medicinal properties, including antioxidant, anti-inflammatory, antibacterial, and wound-healing effects. However, their potential to inhibit AChE and BChE enzymes in the cholinergic pathway remains unexplored. This study utilized ultrasound-assisted ethanol extraction to obtain extracts from these four plant species. After solvent evaporation using a rotary evaporator, viscous green crude extracts were produced from noni leaves, betel leaves, and macao tea. In contrast, the rambutan peel extract exhibited a brown color. Yield percentages ranged from 4.05-11.04% (w/w). The AChE inhibitory activity of these extracts was investigated. The concentrations required to inhibit 50% of AChE activity (IC_{50}) for rambutan peel, noni leaves, betel leaves, and macao tea were 238.25 ± 12.74 , 245.30 ± 1.89 , 203.21 ± 8.52 , and 218.67 ± 13.83 $\mu\text{g/mL}$, respectively. Betel leaf extract demonstrated the highest AChE inhibition potential, followed by macao tea, rambutan peel, and noni leaf extracts, with significant differences observed among all extracts ($p < 0.05$). BChE inhibition was also examined, with IC_{50} values of 498.92 ± 49.74 , 472.08 ± 15.21 , 306.83 ± 37.56 , and 345.60 ± 12.37 $\mu\text{g/mL}$ for the respective extracts. Betel leaf extract showed the highest BChE inhibition potential, followed by macao tea, noni leaf, and rambutan peel extracts. In conclusion, betel leaf extract demonstrates promising potential for AD treatment through its dual inhibition of AChE and BChE enzymes, presenting a possible natural alternative to synthetic compounds.

Introduction:

Alzheimer's disease (AD) is a progressive neurodegenerative disorder that significantly impacts millions of lives worldwide. As the global population ages, the prevalence of AD is expected to rise dramatically, creating an urgent need for effective therapeutic interventions.¹ Current treatment strategies for AD are limited in their efficacy and often associated with adverse side effects, highlighting the critical importance of exploring novel therapeutic approaches. One promising avenue of research focuses on the inhibition of cholinesterase enzymes, particularly acetylcholinesterase (AChE) and butyrylcholinesterase (BChE). These enzymes play a crucial role in the breakdown of acetylcholine, a neurotransmitter essential

for cognitive function and memory. By inhibiting AChE and BChE, it may be possible to increase acetylcholine levels in the brain, potentially alleviating some of the cognitive symptoms associated with AD.²

In recent years, there has been growing interest in the potential of natural products as sources of cholinesterase inhibitors. Plant-based compounds often offer the advantage of lower toxicity and fewer side effects compared to synthetic drugs.³ This study aims to evaluate the cholinesterase inhibitory effects of extracts from four plant sources: rambutan peel (*Nephelium lappaceum* Linn.), noni leaf (*Morinda citrifolia* Linn.), betel leaf (*Piper betle* Linn.), and macao tea (*Scoparia dulcis* Linn.). These plants were selected based on their traditional use in various cultures for cognitive enhancement and their known pharmacological properties. Rambutan peel has demonstrated antioxidant and anti-inflammatory properties in previous studies.⁴ Noni leaf has been used in traditional medicine for its potential neuroprotective effects.⁵ Betel leaf is known for its diverse bioactive compounds and potential cognitive benefits.⁶ Macao tea has shown promise in protecting against oxidative stress, which is implicated in AD pathogenesis.⁷ This study seeks to identify potential candidates for the development of novel AD therapeutics through AChE and BChE inhibitory activities.

The findings of this study could contribute to the growing body of knowledge on natural product-based AD treatments and potentially lead to the development of new therapeutic strategies. Moreover, this research may provide valuable insights into the traditional uses of these plants and offer scientific validation for their potential cognitive benefits.

Methodology:

Materials

Rambutan peel (*Nephelium lappaceum* Linn.), noni leaf (*Morinda citrifolia* Linn.), betel leaf (*Piper betle* Linn.), and macao tea (*Scoparia dulcis* Linn.) were collected from Songkhla province, Thailand. The following chemicals were procured from Sigma–Aldrich (Sigma-Aldrich™, Burlington, MA, USA): acetylcholinesterase (AChE) from *Electrophorus electricus*, 5,5'-dithiobis (2-nitrobenzoic acid) (DTNB), butyrylcholinesterase (BChE), butyrylthiocholine iodide (BTCI), and standards of galantamine. All chemicals were of analytical reagent grade.

Extraction of plant samples

The plant extraction process began with thoroughly washing the samples and then drying them at 50°C until completely dry. The dried samples were then finely ground and extracted with 95% ethanol at a sample-to-solvent ratio of 1:10 (w/v). Ultrasound waves via a 200-watt sonicator were applied for 1 hour at room temperature during the extraction. The resulting mixture underwent filtration, and the solvent was evaporated using a rotary evaporator. The extraction yield percentage was calculated using the following formula:

$$\% \text{ Yield} = (\text{mass of the extract} / \text{mass of the dry plant sample}) \times 100 \quad (1)$$

Finally, the extract should be stored at a temperature of 4 °C.

Acetylcholinesterase (AChE) activity assay

This study assessed the acetylcholinesterase (AChE) inhibition capabilities of four plant extracts: rambutan peel, noni leaf, betel leaf, and macao tea. The investigation employed a modified version of the colorimetric method developed by Balkrishna *et al.*⁸ The assay is based on the enzymatic hydrolysis of acetylthiocholine by AChE, resulting in the formation of thiocholine. This product subsequently reacts with 5,5'-dithiobis-(2-nitrobenzoic acid) (DTNB), generating a yellow compound, 5-thio-2-nitrobenzoate, which can be quantified spectrophotometrically at 412 nm. Fifty microliter of test compound (or control) with 25 µL of AChE solution and incubate at 37°C for 15 minutes. Add 125 µL of a reaction mixture



containing acetylthiocholine iodide and DTNB, then monitor absorbance at 412 nm. The percentage inhibition of AChE activity was calculated using the following equation:

$$\text{Inhibition (\%)} = [(A_{\text{control}} - A_{\text{sample}}) / A_{\text{control}}] \times 100 \quad (2)$$

Where: A_{control} = Absorbance of the reaction mixture without extract

A_{sample} = Absorbance of the reaction mixture with extract

The half-maximal inhibitory concentration (IC_{50}) was determined by plotting a graph of extract concentration (x-axis) versus percent inhibition (y-axis), and using linear regression analysis to calculate the IC_{50} value. The IC_{50} represents the extract concentration required to inhibit 50% of AChE activity. Galantamine was used as a positive control, while 10% ethanol served as a negative control.

Butyrylcholinesterase (BChE) activity assay

The method utilizes butyrylthiocholine as a substrate, which BChE hydrolyzes to produce thiocholine. The liberated thiocholine reacts with 5,5'-dithiobis-(2-nitrobenzoic acid) (DTNB), generating a yellow product detectable at 412 nm. In a 96-well microplate, combine 50 μ L of test compound (or control) with 25 μ L of BChE solution and incubate at 37°C for 15 minutes. Add 125 μ L of a reaction mixture containing butyrylthiocholine iodide and DTNB, then monitor absorbance at 412 nm. Plot inhibition percentage against compound concentration to calculate IC_{50} values. Perform all assays in triplicate.

Statistical analysis

Data analysis was performed using SPSS Statistics version 17.0. The results were presented as mean \pm standard deviation. One-way analysis of variance (ANOVA) followed by Tukey's multiple-range test was conducted. Statistical significance was established at a p -value less than 0.05.

Results and Discussion:

The study evaluated the acetylcholinesterase (AChE) and butyrylcholinesterase (BChE) inhibitory activities of ultrasound-assisted ethanol extracts from four plant species: rambutan peel, noni leaves, betel leaves, and macao tea.

Percentage yields of plant extraction

In this experiment, rambutan peel, noni leaf, betel leaf, and macao tea were extracted using ethanol as the solvent via ultrasound-assisted extraction. Ethanol was selected due to its ability to extract a wide range of compounds, safety profile, efficiency in penetrating plant cells, preservative properties, ease of removal, and regulatory acceptance. Subsequently, the solvent was evaporated using a rotary evaporator. The extraction process yielded viscous green crude extracts for noni leaf, betel leaf, and macao tea, while rambutan peel produced a brown-colored extract (**Figure 1**). Extraction yields ranged from 4.04% to 11.04% (w/w) as presented in **Table 1**. Noni leaf (*Morinda citrifolia* Linn.) exhibited the highest extraction yield at 11.04%, followed by rambutan peel (*Nephelium lappaceum* Linn.) at 6.86%, macao tea (*Scoparia dulcis* Linn.) at 6.36%, and betel leaf (*Piper betle* Linn.) with the lowest yield at 4.04%. The high yield of noni leaf extract suggests a greater presence of ethanol-soluble compounds, potentially indicating a higher concentration of bioactive constituents.⁹ Rambutan peel and macao tea, with moderate yields, may have a balanced composition of soluble and insoluble compounds. Betel leaf, with the lowest yield, could be due to fewer ethanol-soluble constituents or structural characteristics limiting extraction efficiency.

Inhibition of acetylcholinesterase

The acetylcholinesterase (AChE) inhibitory activity of extracts from rambutan peel, noni leaf, betel leaf, and macao tea was evaluated at concentrations between 100-400 $\mu\text{g/mL}$ (**Figure 2**). The IC_{50} values, representing the concentration required to inhibit 50% of AChE activity, were determined for each extract.

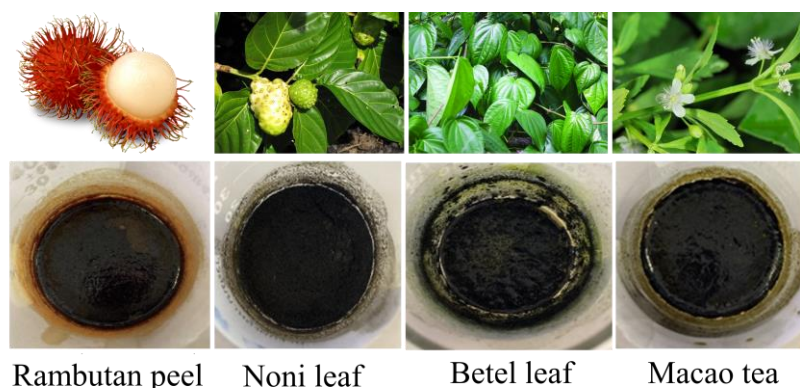


Figure 1.

Physical characteristics of fresh plants and plant extracts.

Table 1. Percentage of yield and characteristics of the plant extracts.

| Samples | Yield (w/w, %) | Physical characteristics |
|--|----------------|-----------------------------|
| Rambutan peel (<i>Nephelium lappaceum</i> Linn.) | 6.86 | brown coloration viscous |
| Noni leaf (<i>Morinda citrifolia</i> Linn.) | 11.04 | dark green viscous |
| Betel leaf (<i>Piper betle</i> Linn.) | 4.04 | dark green viscous |
| Macao tea (<i>Scoparia dulcis</i> Linn.) | 6.36 | dark green viscous |

Betel leaf extract exhibited the strongest inhibition with an IC_{50} of 203.21 ± 8.52 $\mu\text{g/mL}$, followed by macao tea (218.67 ± 13.83 $\mu\text{g/mL}$), rambutan peel (238.25 ± 12.74 $\mu\text{g/mL}$), and noni leaf (245.30 ± 1.89 $\mu\text{g/mL}$). These results, detailed in **Table 2**, indicate that betel leaf extract possesses the highest potential for AChE inhibition among the tested samples. These findings suggest that betel leaf extract may be a promising candidate for further investigation in the development of treatments for conditions associated with cholinergic dysfunction in AD.

Inhibition of butyrylcholinesterase

The butyrylcholinesterase (BChE) inhibitory activity of the same crude extracts was also evaluated at concentrations ranging from 100-400 $\mu\text{g/mL}$ (**Figure 3**). The results, expressed as IC_{50} values, revealed varying degrees of inhibition among the extracts. Betel leaf extract demonstrated the strongest BChE inhibition with an IC_{50} of 306.83 ± 37.56 $\mu\text{g/mL}$, followed closely by macao tea extract with an IC_{50} of 345.60 ± 12.37 $\mu\text{g/mL}$. Noni



leaf extract showed moderate inhibition with an IC_{50} of $472.08 \pm 15.21 \mu\text{g/mL}$, while rambutan peel extract exhibited the least potent BChE inhibition with an IC_{50} of $498.92 \pm 49.74 \mu\text{g/mL}$. Based on these results, the order of BChE inhibitory potency for the extracts can be summarized as: betel leaf > macao tea > noni leaf > rambutan peel.

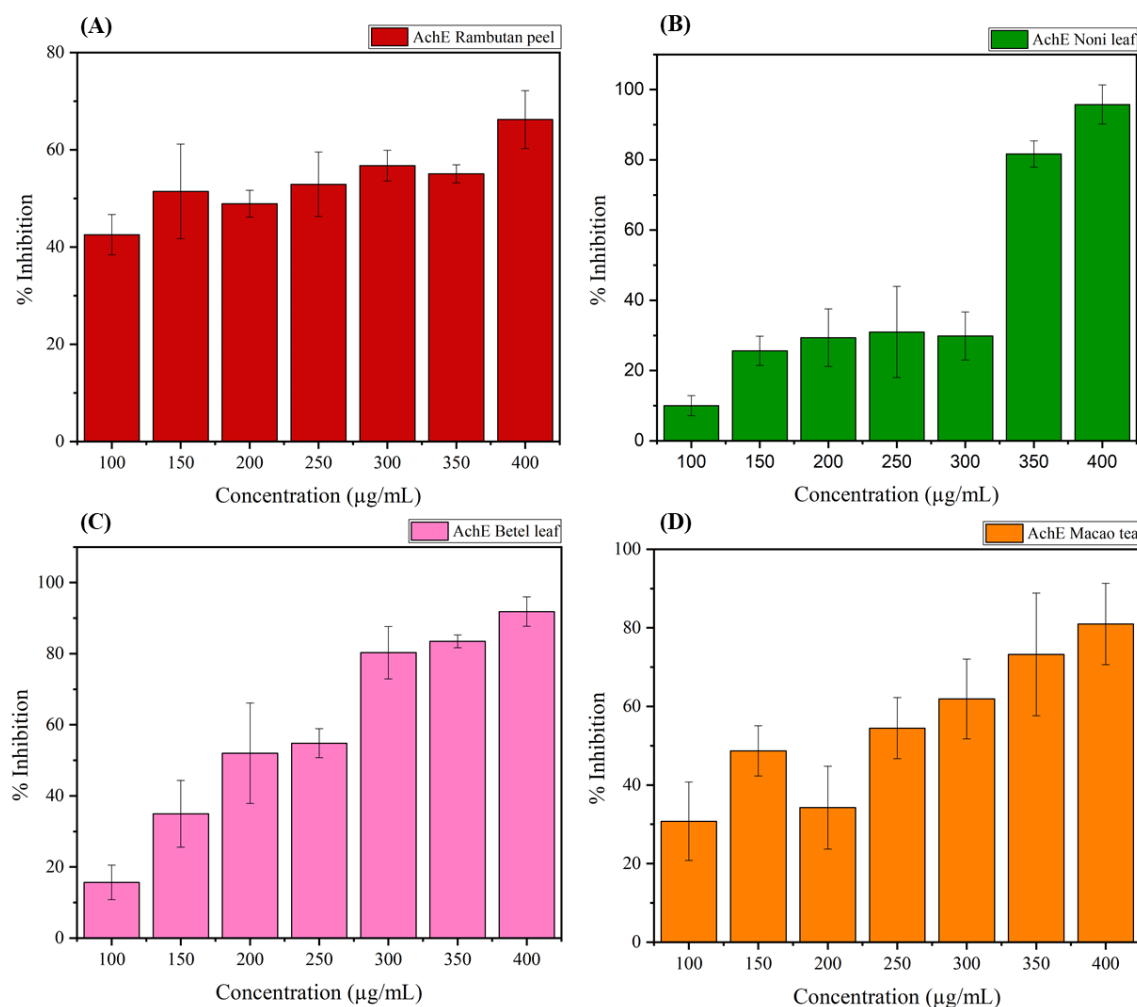


Figure 2.

The effect of ethanolic plant extract concentration on AChE inhibition in the (A) rambutan peel, (B) noni leaves, (C) betel leaves, (D) macao tea. Data are mean values of three measurements with standard deviation.

The comparative inhibitory effects of these extracts on AChE and BChE are visually represented in **Table 2**. Interestingly, betel leaf extract showed the strongest inhibitory activity against both AChE and BChE, suggesting its potential as a dual cholinesterase inhibitor. Macao tea extract consistently ranked second in inhibitory potency for both enzymes, further highlighting its promise in cholinesterase inhibition. The dual inhibitory action on both AChE and BChE could potentially provide a more comprehensive approach to managing AD treatment. Dual inhibitory action could potentially lead to increased acetylcholine levels in the brain, which may help alleviate cognitive symptoms associated with AD. The varying inhibitory potencies observed among the extracts likely reflect

differences in their phytochemical compositions. The active compounds responsible for the observed effects warrant further investigation and isolation. It is worth noting that while these extracts show promise, their IC_{50} values are higher than those typically observed for synthetic drugs galantamine (IC_{50} : 12.63 $\mu\text{g/mL}$), indicating that further purification or concentration might be necessary to achieve therapeutic efficacy.

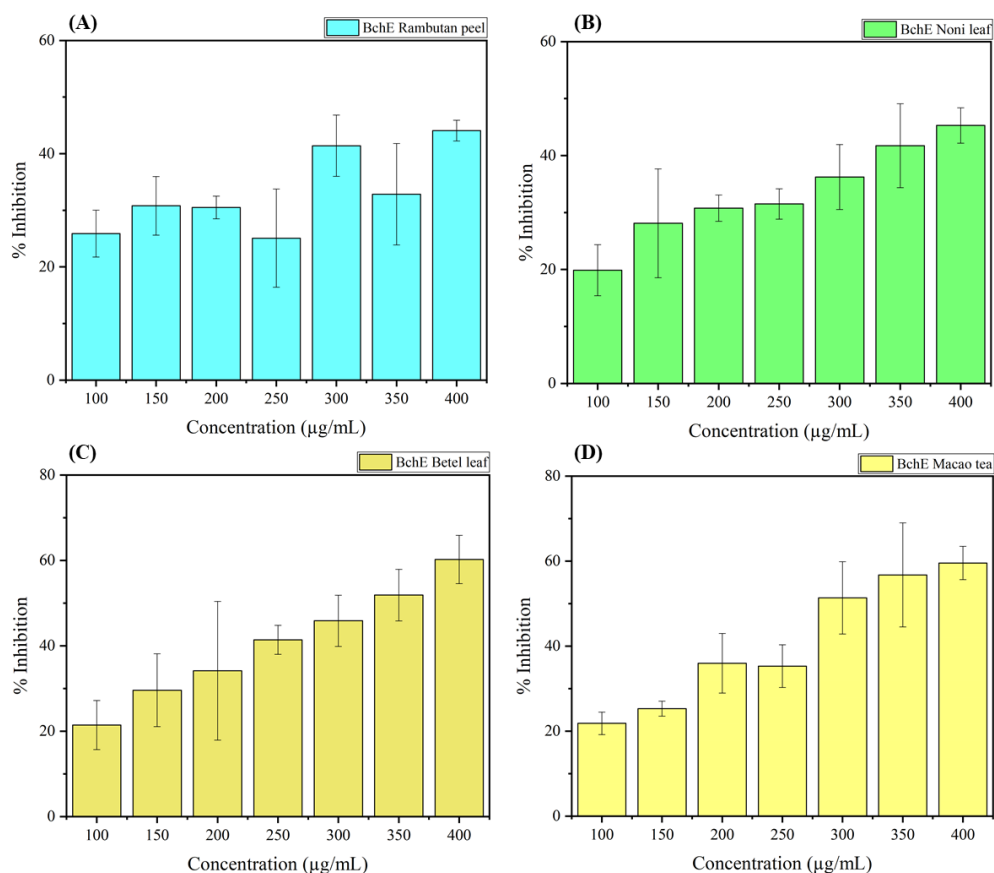


Figure 3.

Concentration-dependent inhibition of butyrylcholinesterase (BChE) by ethanolic extracts of (A) rambutan peel, (B) noni leaves, (C) betel leaves, and (D) macao tea. Data points represent mean \pm SD ($n=3$).

Betel leaf (*Piper betle* Linn.) exhibit potent inhibitory effects on both AChE and BChE through a complex interplay of phytochemical constituents and their interactions with these enzymes. The betel leaf contains a rich array of bioactive compounds, including phenols, terpenes, alkaloids, and flavonoids, with hydroxychavicol, eugenol, chavibetol, and allylpyrocatechol being particularly noteworthy.^{10,11} The inhibition mechanism primarily involves the interaction of phenolic compounds, especially hydroxychavicol, with the active sites of AChE and BChE. These interactions include the formation of hydrogen bonds and hydrophobic interactions with amino acid residues in the catalytic triads of enzyme, leading to competitive inhibition for AChE and a mix of competitive and non-competitive inhibition for BChE.¹² Eugenol, another major component, has demonstrated significant anticholinesterase properties. Additionally, flavonoids such as chavibetol and allylpyrocatechol have shown potential for enzyme inhibition. Piperol B, a phenolic compound, and beta-sitosterol, a phytosterol, have also been reported to possess mild AChE inhibitory activities.¹³ The diversity of phytochemicals in betel leaf contributes to a synergistic effect, enhancing the overall inhibitory potency against both enzymes.¹⁴ Beyond



direct enzyme inhibition, the strong antioxidant properties of betel leaf compounds, particularly flavonoids, play a supportive role by reducing oxidative stress-induced enzyme activation.¹⁵ Additionally, some compounds in betel leaf demonstrates neuroprotective effects, which may further contribute to their impact on cholinergic function.¹⁶

Macao tea (*Scoparia dulcis* Linn.) extract exhibits moderate AChE inhibitory activity, attributed to its diverse phytochemicals including flavonoids, terpenoids, and phenolic compounds. The inhibition likely involves multiple mechanisms such as competitive binding, allosteric modulation, metal chelation, and antioxidant effects.⁷ Key compounds, including scoparic acids A and D, and scopadulcic acid B, may significantly contribute to this activity. The complex phytochemical profiles of these plants not only provide effective cholinesterase inhibition but also offer a broader spectrum of beneficial effects on neurological health. Future studies should focus on isolating and characterizing the bioactive compounds, elucidating their specific mechanisms of action, and exploring their potential for therapeutic applications in cholinergic system modulation and neuroprotection.

Table 2. IC₅₀ values for AChE and BChE inhibition by plant extracts

| Samples | AChE IC ₅₀ (μg/mL) | BChE IC ₅₀ (μg/mL) |
|---------------|----------------------------------|----------------------------------|
| Rambutan peel | 238.25 ± 12.74 ^{cd} | 498.92 ± 49.74 ^b |
| Noni leaves | 245.30 ± 12.74 ^d | 472.08 ± 15.21 ^b |
| Betel leaves | 203.21 ± 8.52 ^b | 306.83 ± 37.56 ^a |
| Macao tea | 218.67 ± 13.83 ^{bc} | 345.60 ± 12.37 ^a |
| Galantamine | 12.63 ± 0.07 ^a | - |

IC₅₀ represents the concentration of samples required for 50% inhibition. Data are expressed as mean ± SD (*n* = 3). Identical letters indicate statistically insignificant differences (*p* > 0.05) within the same column.

Conclusion:

This study demonstrates the superior cholinesterase inhibitory properties of betel leaf (*Piper betle* Linn.) extract among the investigated plant samples. Notably, betel leaf extract consistently exhibited the most potent inhibitory effects against both acetylcholinesterase (AChE) and butyrylcholinesterase (BChE). This dual inhibitory capacity underscores its potential significance in neurodegenerative disorder research, particularly in relation to AD where cholinergic dysfunction is a key factor. The findings suggest promising applications in developing new therapies, cognitive enhancement strategies, early screening tools, and natural pesticides, as well as uses in agriculture and food preservation.

Acknowledgements:

This work was supported by National Higher Education, Science, Research and Innovation Policy Council, Thaksin University (Fundamental Research Fund; FF-2567A10512026 Fiscal Year 2024). The authors would like to thank the Department of Chemistry, Faculty of Science and Digital Innovation, Thaksin University, for providing research facilities, software packages and computing times.

References:

1. Breijyeh Z.,Karaman, R.Molecules. 2020;25:5789.
2. Gajendra K ,Pratap G, Poornima D, Shantaram M, Ranjita G, European Journal of Medicinal Chemistry Reports.2024;11:100154.
3. Tamfu A, Kucukaydin S, Yeskaliyeva B, Ozturk M, Dinica RM .Molecules. 2021;26(18):5582.
4. N Chana, A Muengpoon, S Pethkaew, N Kulsin, A Mahasuk, S Srirat. Songklanakarin Journal of Science & Technology.2022;44(4):1067-1074.
5. Shakti P, Santoshkumar T, Kiran K, PV erma, Chandishwar N, Kashif H, Rakesh S, J Saxena, Anil D. Journal of Ethnopharmacology.2012;139(1):34-41.
6. Madhumita M, Guha P, Nag A. Phytother Res. 2020;34(10):2609-2627.
7. N Chana, T Aiebchun, P Pinwanit, A Hiranrat. Trends in Sciences.2022;19(2):2050.
8. Balkrishna A, Pokhrel S, Tomer M, Verma S, Kumar A, Nain P, Gupta A, Varshney A. Molecules. 2019;24(22):4175.
9. Setyani W, Setyowati H, Utami, W.Jurnal Farmasi Sains dan Komunitas.2016;13(1):44-51.
10. Ferreres F., Oliveira A. P., Gil-Izquierdo A., Valentão P, Andrade P. B. *Phytochem.Anal.*2014; 25(5)453–460.
11. Nayaka NMDMW, Sasadara MMV, Sanjaya DA, Yuda PESK, Dewi NLKAA, Cahyaningsih E, Hartati R. Molecules. 2021;26(8):2321
12. Ingkaninan K, Temkitthawon P, Chuenchom K, Yuyaem T, Thongnoi W. J Ethnopharmacol. 2003;89(2):261.
13. Pandey A, Bani S.J Neuroimmunol. 2010;14(12):48-58.
14. S. Jaiswal, M. Patel, D. Saxena, S. Naik.Journal of Biores Engg Technol.2014;2(2):12-20.
15. Alam MB, Park NH, Song BR, Lee SH. Antioxidants (Basel). 2023;12(2):374.
16. Biswas P, Anand U, Saha S, Kant N, Mishra T, Masih H, Bar A, Pandey D, Jha N, Majumder M, Das N, Gadekar V, Shekhawat MS, Kumar M, Radha, Proćków J, Lastra JMP. J Cell Mol Med. 2022;26(11):3083-3119.



EXOGENOUS LOADING OF RECOMBINANT HUMAN SECRETORY LEUKOCYTES PROTEASE INHIBITOR (rhSLPI) INTO EXOSOME

Chayanisa Phutiyothin,^{1,2} Surasak Tangkamonsri,^{1,2} Phornsawat Baipaywad,^{1,2} Hathaitip Sritanaudomchai,³ Anyapat Atipimonpat,⁴ Kovit Pattanapanyasat,⁵ Sarawut Kumphune^{1,2, *}

¹Biomedical Engineering Institute, Chiang Mai University, Chiang Mai 50200, Thailand

²Biomedical Engineering and Innovation Research Center, Chiang Mai University, Mueang Chiang Mai District, Chiang Mai, 50200 Thailand

³Department of Oral Biology, Faculty of Dentistry, Mahidol University, Bangkok, 10700, Thailand

⁴Department of Biochemistry, Faculty of Medical Science, Naresuan University, Phitsanulok, 65000, Thailand

⁵Center of Excellence for Microparticle and Exosome in Diseases, Department of Research and Development, Faculty of Medicine Siriraj Hospital, Mahidol University, Bangkok, 10700, Thailand

*e-mail: sarawut.kumphune@cmu.ac.th

Abstract:

Secretory leukocyte protease inhibitor (SLPI) is a serine protease inhibitor with various therapeutic potential. Over the last decade, several studies have reported that SLPI provides cardio-protective effects against myocardial ischemia/reperfusion (I/R) injury. However, circulating enzymes may degrade SLPI, leading to a short circulation half-life and limiting its clinical applications. To overcome the limitations of SLPI, researchers are interested in the use of exosomes as carriers to deliver therapeutic substances, and exogenous biomolecules from donor cells to target cells. Previous studies have demonstrated that exosome treatment can protect the heart by reducing I/R-induced apoptosis through the activation of survival signaling pathways. However, the exogenous loading of SLPI into exosomes has never been reported. In this study, we performed the exogenous loading of recombinant human SLPI (rhSLPI) into exosomes via electroporation. The morphology of SLPI-loaded exosomes was verified by transmission electron microscopy (TEM). Both blank and SLPI-loaded exosomes (SLPI-Ex) are spherical, with a cup-like shape and few clumps. ImageJ and nanoparticle tracking analysis (NTA) were performed on the size of exosomes. The results showed that the diameters of blank and SLPI-Ex ranged from 30 to 100 nm. After loading the rhSLPI, the zeta potential was reduced. Moreover, SLPI-Ex exhibited an SLPI encapsulation efficiency of 0.019%. The results demonstrated successful cellular uptake of SLPI-Ex by the human cardiomyocyte cell line (AC16). In summary, this work is the first to examine the introduction of rhSLPI into exosomes for targeted delivery to cardiac cells. This finding has potential for future research in the context of an ischemia/reperfusion paradigm.

Keywords: Secretory leukocyte protease inhibitor (SLPI); Bioengineering; Extracellular vesicle; Exosome; Exogenous loading; Electroporation

Introduction:

Secretory leukocyte protease inhibitor (SLPI)¹, a member of the cationic-whey acidic protein family, has been demonstrated to protect host cells against the detrimental effects of proteolytic enzymes generated during inflammatory processes. SLPI selectively inhibits

serine proteases, such as elastase and cathepsin G from neutrophils, chymotrypsin and trypsin from pancreatic acinar cells, and mast cell chymase.² Our previous studies reported that SLPI provided cardioprotection³⁻⁶ and vasculoprotection⁷⁻⁹ against I/R injury. Since the SLPI protein is unstable and inefficient in entering target cells^{3,7,8}, using nanoparticles to deliver recombinant human SLPI (rhSLPI) could enhance intracellular drug delivery efficiency.

In multicellular organisms, cells communicate through direct contact or by releasing secreted molecules, which are taken up by other cells. The principal classes of cell-to-cell communication are distinguished by the distance between the originating and recipient cells. Autocrine signaling involves molecules acting on the same cell that produced them. while paracrine signaling involves molecules affecting nearby cells. Endocrine signaling involves molecules secreted into the bloodstream, and carried by the blood and tissue fluid to distant target cells.¹⁰ Recent studies have demonstrated that cells communicate by releasing extracellular vehicles (EVs), a heterogeneous group of membrane-bound vesicles originating from nearly all cell types. These vesicles are released under normal physiological conditions as well as in response to cellular activation, senescence, and apoptosis.

EVs is a generic term that refers to various secreted vesicle subtypes, including exosomes, microvesicles, ectosomes, oncosomes, and apoptotic bodies.¹¹ EVs play a crucial role as cargo carriers capable of exchanging intercellular messages composed of various soluble and non-soluble cell-derived bioactive molecules such as proteins, mRNAs, microRNAs (miRNAs), lipids, and metabolites.¹² When these bioactive component-rich EVs are transferred to selectively responsive recipient cells to trigger cellular activation, phenotypic changes, and reprogramming of gene expression and function.^{13,14} The identification of EVs as carriers of biological signals facilitates functional communication networks among cells highlighting the relevance of EVs in health and diseases.

Among the EV family, there is growing clinical interest in “exosomes”, Exosomes are not only promising biomarkers with potential clinical value¹⁵, but also as alternative therapeutic agents, and drug delivery vehicles.¹⁶ Previous reports have indicated the role of exosomes in the pathogenesis of several diseases and their therapeutic potential in cardiovascular diseases.¹⁷ Several diseases are inadequately treated due to the challenges associated with delivering medicinal compounds effectively to the target area. Nanoparticle delivery methods are utilized as drug vehicles to provide regulated release, target specific regions of the body, ensure biocompatible, biodegradable, and non-toxic¹⁸, and provide protection to overcome the limitations of rhSLPI.¹⁹ However, the use of biological nanoparticles, especially exosomes for delivering rhSLPI to target tissues has not been reported. In this study, we are interested in using exosomes as a carrier for rhSLPI to treat cardiac cells subjected to ischemia/reperfusion injury. One of the interesting technical issues is the fabrication of an exosome carrying rhSLPI. Several methods of introducing biomolecules to exosomes have been reported.¹⁶ However, there is no report on the exogenous loading of rhSLPI into exosome (SLPI-Ex). Therefore, this study aims to fabricate SLPI-Ex using the exogenous loading method (i.e., electroporation) of rhSLPI and investigate the characteristics of the particles, and the internalization of the SLPI-Ex. The results of this study will provide valuable insights for the further preparation of SLPI-Ex for use in the myocardial I/R model.

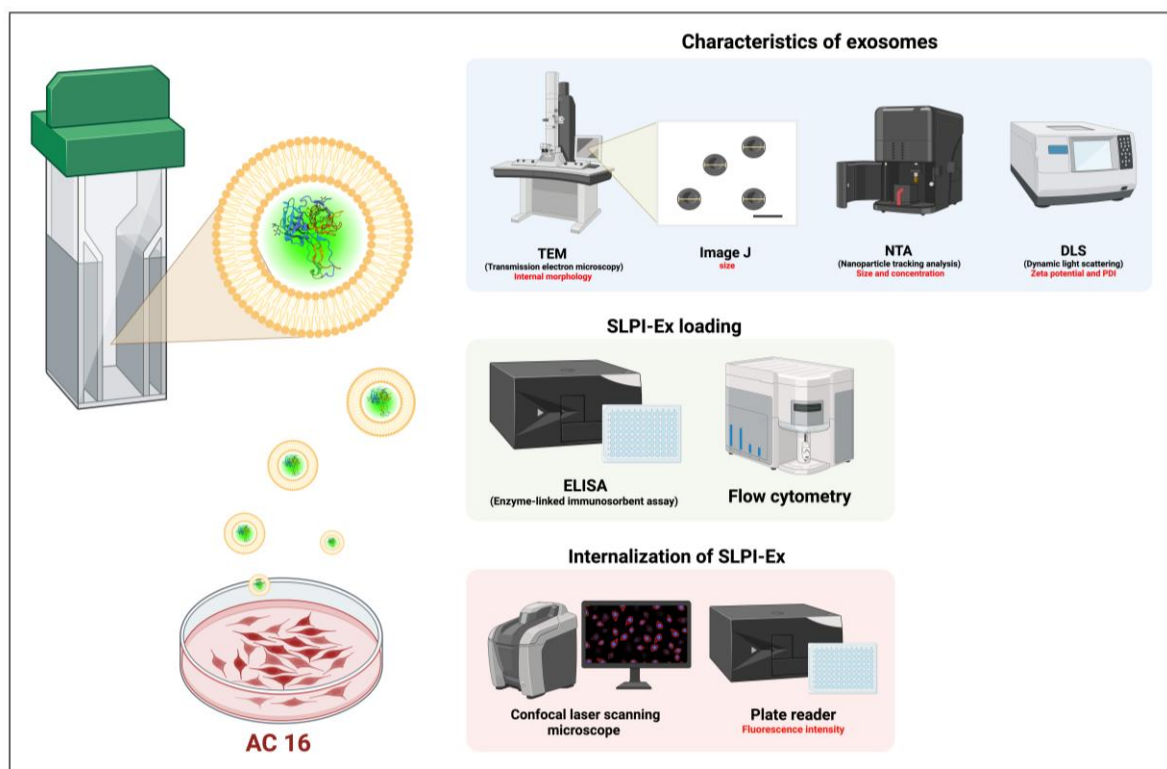


Figure 1.
Preparation and analysis of SLPI-Ex

Methodology:

Chemical and Reagent

Recombinant human SLPI (rhSLPI) was purchased from Sino Biology Inc. (Beijing, China), Dulbecco's modified Eagle's medium (DMEM), fetal bovine serum (FBS), trypsin-EDTA, and penicillin/streptomycin were purchased from Gibco (Gibco BRL, Life Technologies, Inc., NY, USA). Enzyme-linked immunosorbent assay (ELISA) was purchased from Abcam (Cambridge, UK). Other chemicals were purchased from Sigma-Aldrich® (Merck KGaA, Darmstadt, Germany).

Labelling recombinant human SLPI (rhSLPI)

The rhSLPI labelling was performed using the Alexa Fluor® 488 Protein Labelling Kit (Thermo Fisher Scientific Inc., Waltham, MA, USA). 2 mg/mL of rhSLPI 500 μ L was mixed with 1 M sodium bicarbonate 50 μ L and then dyed by transferring the mixture into a reactive dye vial, followed by stirring the reaction mixture for 1 hour at room temperature, protected from light. After that, purify the labelled protein by adding the rhSLPI labelling to the column, and periodically rinse with \sim 100 μ L of elution buffer. The rhSLPI labelling was observed under UV light, divided into 2 bands: the first band is the rhSLPI labelling and the second is a free dye. Collect the band into each collection tube and measure the absorbance at λ 280 and λ 494, followed by calculating the concentration of protein in the sample (1):

$$\text{Protein concentration (M)} = \frac{(A_{280} - (A_{494} - 0.11)) \times \text{dilution factor}}{\text{molar extinction coefficient}} \quad (1)$$

SLPI-Ex loading

In this study, we received an isolated exosome from Naresuan University, which was stem cells from human exfoliated teeth (SHED) (COE.No.MU-DT/PY -IRB 2022/0 13.2502). To prepare SLPI-Ex loading, the 0.04 µg/µL of isolated exosome was mixed with 0.2 µg/µL of dye-labeled rhSLPI protein to reach a mixture final volume of 400 µL by adjusting the volume with PBS. The mixture was added into 0.2 cm-gap Gene Pulser/MicroPulser Electroporation Cuvettes Invitrogen electroporation cuvettes (Bio-Rad Laboratories, Inc., Hercules, CA, USA) and electroporated in a Gene Pulser Xcell Electroporation System (Bio-Rad Laboratories, Inc., Hercules, CA, USA) at 140 V and 25 pulses.²⁰

After that, exosomes containing rhSLPI protein (SLPI-EV) were purified by adding 400 µL of Ni-NTA agarose resin (Qiagen)²¹, incubated with shaking at 4 °C for 24 h, and then centrifuged at 14,000 x g for 30 s. The supernatant was collected (SLPI-EV) and the precipitated Ni-NTA agarose was resuspended with PBS.²² Next, the load and non-loading rhSLPI in exosomes were determined by flow cytometry (CytoFLEX S, Beckman Coulter, United States).

Transmission Electron Microscopy (TEM)

The morphological characterization of an exosome was determined by transmission electron microscopy (TEM, JEM-2100Plus, JEOL, Germany). The exosome was fixed by 2.5% glutaraldehyde at a ratio of 1:1 and then incubated at room temperature for 30 min. Place one drop (approximately 10 µL) of fixative exosomes on a parafilm, invert a 400-mesh copper grid (Ted Pella, Redding, CA, USA) onto the sample for one minute at room temperature, and then blot the excess liquid with filter paper. After that the grid was washed with 100 µL ultrapure water 2 times before staining the sample with 30 µL of 3% phosphotungstic acid (PTA) for 15 s, kept in a desiccator for drying overnight, and observed by TEM under an acceleration voltage of 100 kV. The sizes of nanoparticles (at least 100 particles) were measured manually and calculated using ImageJ software (National Institute of Health).²³

Nanoparticle Tracking Analysis (NTA)

Nanoparticle tracking analysis (NTA) measured the size and concentration of exosomes with a NanoSight NS-1300 (Malvern Instruments, Ltd., UK). Every measurement was conducted at a consistent temperature of 25 ± 1 °C to maintain a uniform viscosity of the fluid. The dilutions used in this experiment varied from 1:100 to 1:1000 and were prepared in sterile filtered (0.22 µm) phosphate-buffered saline.

Polydispersity index (PDI) and zeta potential

The zeta potential of exosomes and the polydispersity index (PDI) were measured by using a Malvern Zetasizer (UK) at the Biomedical Engineering Institute, Chiang Mai University. The polydispersity index (PDI) of the 1 mL of exosomes was determined using the disposable plastic micro-cuvette (ZEN0040). The zeta potential of the 1 mL of exosomes was determined using the foldable capillary cell (DTS1070).

Encapsulation efficiency



To determine the encapsulated SLPI level, exosome needs to be ruptured. The exosome sample was mixed with RIPA buffer at a ratio of 1:1, then sonicated for 5 min, followed by vortex, and then repeated 3 times. Following that, a 1:10000 dilution of the sample with PBS was used to find the concentration of rhSLPI using an enzyme-linked immunosorbent assay (ELISA) and to figure out the percentage of encapsulation efficiency (%EE) equation (2).⁷

$$\% \text{Encapsulation efficiency (\%EE)} = \frac{\text{The amount of rhSLPI encapsulation}}{\text{The total amount of rhSLPI}} \times 100 \quad (2)$$

Cell and cell culture

The human cardiomyocyte cell line (AC16) (ATCC-CRL3568) was cultured in Dulbecco's modified eagle medium (DMEM) supplemented with 10 percent heat-inactivated fetal bovine serum (FBS) (ATCC 30-2020) and 5000 units/mL of penicillin/streptomycin. The cells were maintained at a temperature of 37 °C in a humidified atmosphere consisting of 95% air and 5% CO₂ until they reached a confluency of 70 to 80% before conducting any experiments.

The internalization of SLPI-Ex

The human cardiomyocyte cell line (AC16) was cultured in an 8-chamber slide by adding 200 µL of a cell solution containing 5×10^5 cells/mL and incubated for 24 hours until the cells reached about 80% confluence. Next, cells were pre-treated with labelled-SLPI-loaded exosomes at concentrations of 1 µg/mL and incubated for 24 hours at a temperature of 37 °C, with an atmosphere consisting of 95 percent air and 5 percent CO₂. The chamber slide was washed twice with 200 µL of PBS. Then fixed cells with 4% paraformaldehyde for 20 minutes at room temperature and washed twice before staining with 200 µL of FITC-phalloidin conjugate (Sigma-Aldrich; Merck KGaA) for 1 h at room temperature with protective light followed by washing twice. Subsequently, nuclear staining with 200 µL of DAPI (4',6-diamidino-2-phenylindole) (Sigma-Aldrich; Merck KGaA) for 20 min, washing twice. Then 20 µL of 50% glycerol was added, sealed with a cover slide and nail polish, and kept at 4 °C in the dark moist box until used. The internalization of SLPI-Ex was observed under a confocal laser scanning microscope (Stellaris 5, Leica, Germany)

The AC16 was cultured in a 96-well plate by adding 200 µL of a cell solution containing 1×10^4 cells/mL and incubated for 24 h until the cells reached about 80% confluence. Then, treated cells with labeled SLPI-loaded exosomes at concentrations of 0.0005 µg/µL at a temperature of 37 °C in an atmosphere consisting of 95 percent air and 5 percent CO₂. After 2, 6, and 24 h, the wells were washed three times with 100 µL of PBS. Then fixed cells with 4% paraformaldehyde for 20 min at room temperature and protected from light. Subsequently, the fluorescence intensity was measured in a microplate reader excitation/emission at 485/528 nm.²⁰

Statistical analysis

The statistical analysis in this work was conducted using commercially accessible software (GraphPad Prism version 10, San Diego, CA, USA). The data were presented as the mean ± standard deviation (SD). The significance of all comparisons was assessed using an unpaired t-test or ANOVA, followed by the Tukey-Kramer test, when appropriate. A significance level of 0.05 was employed to determine statistical significance

Results and Discussion:

Characteristics of Exosomes

This study investigated the characteristics of exosomes using TEM, DLS, NTA, flow cytometry, and ELISA. The transmission electron microscopy revealed all exosomes (blank and SLPI-Ex) to be spherical, with a cup-shaped structure and slight clumping (**Figure 2A and 2B**). Exosome size was measured by ImageJ and NTA. According to ImageJ, the average diameters of blank and SLPI-Ex were 44.4 ± 5.5 nm and 41.4 ± 9.6 nm, respectively, based on a few randomly selected samples from TEM images (**Figure 2E**). In contrast, NTA measurements showed the sizes of blank and SLPI-Ex to be 94.8 ± 1.8 nm and 66 ± 4.6 nm, respectively (**Figure 2C and 2D**).

The results indicate that the exosome sizes measured by ImageJ (TEM) and NTA may be attributed to differences in measurement techniques and sample preparation. For TEM imaging, samples of fixation, dehydration, and staining processes, can lead to size alterations due to shrinkage, potentially resulting in inaccurate measurements.²⁴ The TEM may not accurately represent the actual size of exosomes. Thus, NTA seemed to be more accurate in sizing exosomes than ImageJ (TEM).²⁵ Furthermore, the measurements of the blank (SHED-Ex) from NTA match those from the previous study.²⁶ NTA measures exosomes by tracking their Brownian motion in a liquid suspension, which can better reflect the actual size of exosomes.²⁷ Furthermore, the size of SLPI-Ex in NTA was lower than the blank, most of the blanks in the graph have a size similar to SLPI-Ex, but some parts of them have larger sizes, possibly due to exosomes clumping when compared with the TEM image, resulting in an average size of the blank that is higher than SLPI-Ex. The concentration of exosomes before and after loading rhSLPI was $5.43 \times 10^{11} \pm 4.88 \times 10^{10}$ and $1.39 \times 10^{11} \pm 6.59 \times 10^9$ (mean particles per mL \pm standard error), respectively (**Figure 2C and 2D**).

The polydispersity index (PDI) of exosomes was measured by Zetasizer, and the PDI values for blank and SLPI-Ex were 0.592 ± 0.07 and 0.583 ± 0.1 , respectively (**Figure 2F**). The PDI is a measure of the uniformity of a nanoparticle distribution in the solution.²⁸ The PDI of the blank was similar to the SLPI-Ex. The PDI ranging from 0.05 to 0.7 is used for determining the size distribution of particles.²⁹ A PDI value less than 0.05 indicates high uniformity dispersity, whereas a PDI value greater than 0.7 indicates low uniformity dispersity.²⁹ As a result, the PDI of all subtypes of nanoparticles was close to 0.7, suggesting that the nanoparticles exhibited low uniformity in dispersity. This could be attributed to the aggregation of nanoparticles or the presence of a wide range of particle sizes within the samples.

The zeta potential of blank and SLPI-Ex measured by DLS was -23.5 ± 5.9 mV and -13.1 ± 0.6 mV, respectively (**Figure 2H**). The zeta potential of SLPI-Ex is significantly greater than blank, possibly due to the positive charge of the rhSLPI protein², which reduces the overall negative charge of the exosome upon loading.³⁰ These findings demonstrate that exosomes can encapsulate rhSLPI.

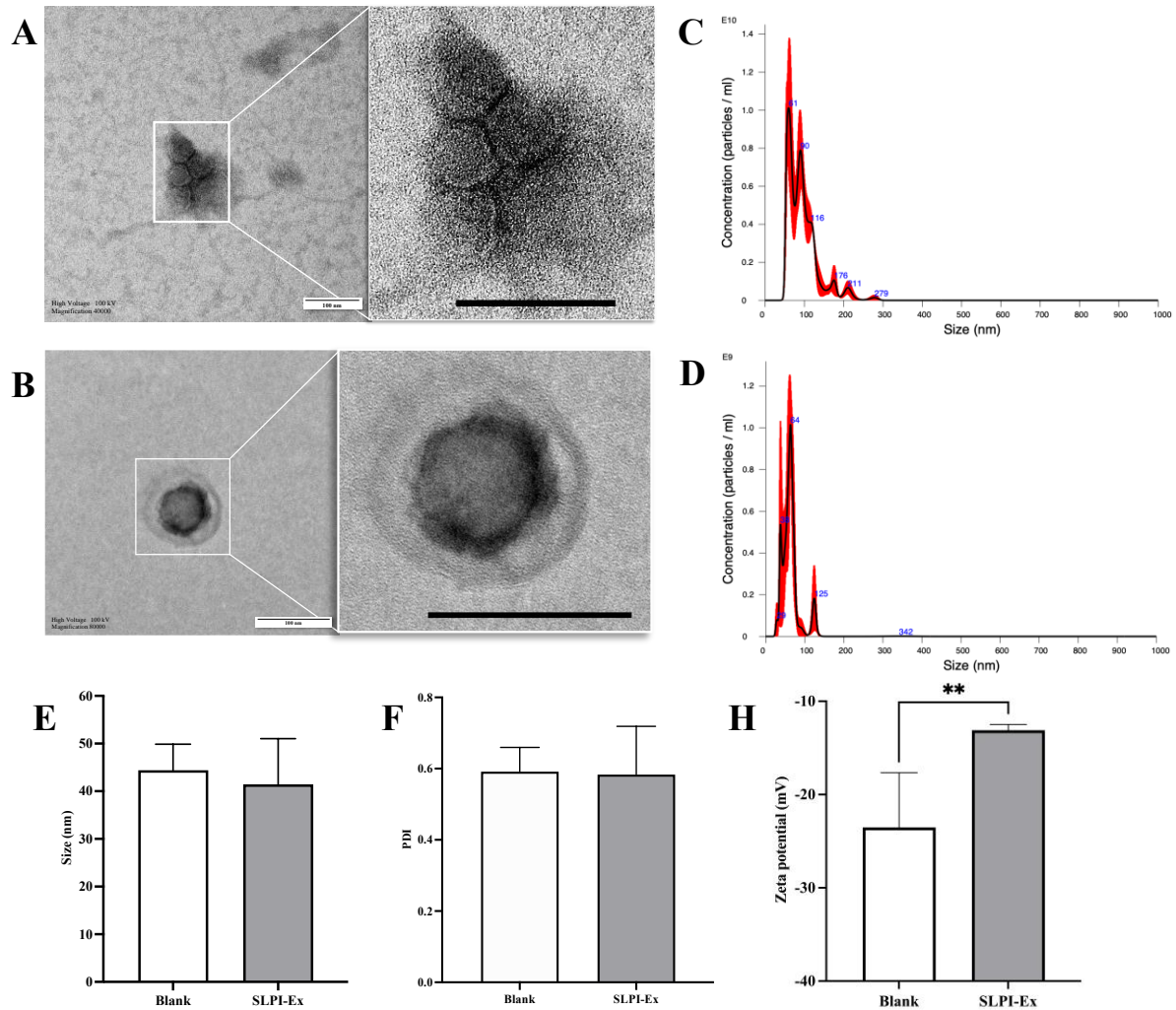


Figure 2.

The physical characteristics of exosomes using the transmission electron microscopy image of (A) Blank and (B) SLPI-Ex; nanoparticle tracking analysis of (C) Blank and (D) SLPI-Ex, (E) size from ImageJ; (F) PDI; (H) zeta potential compared with blank $**p < 0.001$ (unpaired t-test).

SLPI-Ex loading

The initial concentration of rhSLPI was $2 \mu\text{g}/\mu\text{L}$, which was used for labeling with the Alexa Fluor® 488 Protein Labelling Kit. After the labeling process, the concentration of the labeled rhSLPI was $0.212 \mu\text{g}/\mu\text{L}$. The experimental procedures resulted in a substantial loss of rhSLPI protein, approximately tenfold, as the post-labeling concentration was lower than the initial concentration, possibly due to purification steps to remove excess dye or the excessive amount of rhSLPI protein compared with dye. Therefore, to minimize this loss, the purification process should be optimized, and adjustment of the dye-to-protein ratio or the incubation should be considered.

The encapsulation efficiency percentage (EE%) was calculated based on the actual amounts of SLPI incorporated into SLPI-Ex. Starting with $0.212 \mu\text{g}/\mu\text{L}$ of labeled rhSLPI, $378 \mu\text{L}$ was used totaling $75.6 \mu\text{g}$ of initial SLPI. After fabricating SLPI-Ex, the concentration of SLPI-Ex obtained was $316,444 \text{ pg/mL}$, when $50 \mu\text{L}$ of SLPI-Ex was added to an ELISA containing with $0.015 \mu\text{g}$ of SLPI-Ex. The results showed that the rhSLPI

loading efficiency of SLPI-Ex was 0.019%. The concentration of rhSLPI protein encapsulated in exosomes was measured using the ELISA technique. The results demonstrated that the concentration of rhSLPI protein in SLPI-Ex was significantly higher than in blank ($316,444 \pm 28,240$ pg/mL compared to 0.00 ± 0.00 pg/mL, *** $p < 0.0001$), indicating that that exosome effectively encapsulated the rhSLPI protein (**Figure 3A**).

However, the encapsulation efficiency percentage of rhSLPI in SLPI-Ex was very low compared to the initial value of rhSLPI. This might be due to the addition of an excessive amount of rhSLPI protein, which results in the exosome being unable to encapsulate all the rhSLPI protein, or the electrophoresis process may not be sufficiently effective in loading rhSLPI into exosomes alone. To improve the encapsulation efficiency of rhSLPI in exosomes, adjustments to the loading process could be considered, such as optimizing the ratio of exosomes to rhSLPI, extending the incubation period, or incorporating additional exogenous loading steps. These strategies could potentially enhance the encapsulation efficiency of rhSLPI into exosomes. Even though our results showed a low percentage of encapsulation efficiency (about 316,444 pg/mL), a previous study found that a concentration of rhSLPI between 0.05 and 0.5 pg/mL is enough to treat ischemia/reperfusion (I/R).³¹ This suggests that the rhSLPI concentration in our study is sufficient to exert therapeutic effects on myocardial ischemia/reperfusion (I/R) injury or other vascular-related diseases. Nevertheless, further optimization and adjustments to the concentration may be necessary to achieve a higher encapsulation efficiency of SLPI-Ex in future studies.

To verify the success of exogenous loading of rhSLPI into exosomes, we analyzed the population of loaded and unloaded rhSLPI into exosomes by flow cytometry. The rhSLPI was labeled with a fluorescence dye Alexa flour 488 loaded into exosomes. Our results revealed 2 populations: unloaded exosomes and rhSLPI-labeled exosomes, with 14.95% and 49.17% of the particles, respectively. Among the detectable events, the percentage of fluorescence-positive particles was detected at approximately 56% compared with un-loaded SLPI-labeled, confirming the existence of SLPI-labeled. These findings demonstrate that the exogenous loading of rhSLPI into the exosome was successful (**Figure 3B**).

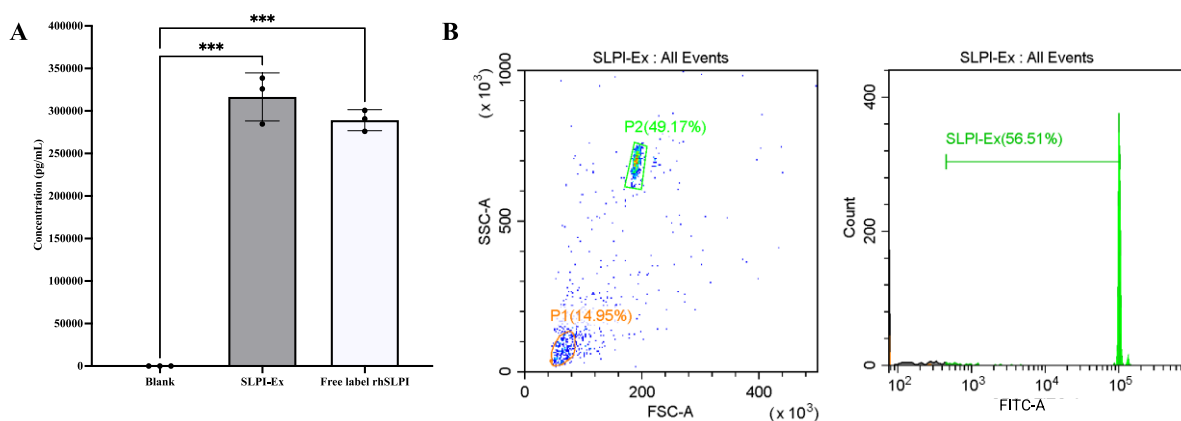


Figure 3.

(A) The concentration of rhSLPI in SLPI-Ex compared with blank by ELISA *** $p < 0.0001$ (unpaired t-test); (B) flow cytometry (left) the population of unloaded and loaded of SLPI-Ex (right) the percentage of SLPI-labeled loaded exosomes

Internalization of SLPI-Ex

Confocal laser scanning microscopy revealed that SLPI-Ex accumulated in the cytoplasm after 24 h (**Figure 4A**). The fluorescence intensity of SLPI-Ex was measured at 2,



6, and 24 h with values of 97.7 ± 1.53 , 99.7 ± 1.53 , and 4.33 ± 0.57 , respectively (**Figure 4B**). As a result, the fluorescence intensity after 24 h was shown to be significantly lower than the fluorescence intensity at 2 and 6 h, indicating that exosomes were capable of uptake into the cells (AC16) after incubating for 24 h.

Future research needs to address several limitations of this study. Specifically, the cytotoxicity effects, *in vitro* release profile, and stability of SLPI-Ex (Secretory Leukocyte Protease Inhibitor-Exosome) must be thoroughly evaluated. Additionally, employing *in vitro*, *ex vivo*, and *in vivo* models will be essential to validate the efficacy of SLPI-Ex and enhance its clinical relevance. For successful clinical application, exosomes must be engineered to effectively target specific cells or tissues of interest.

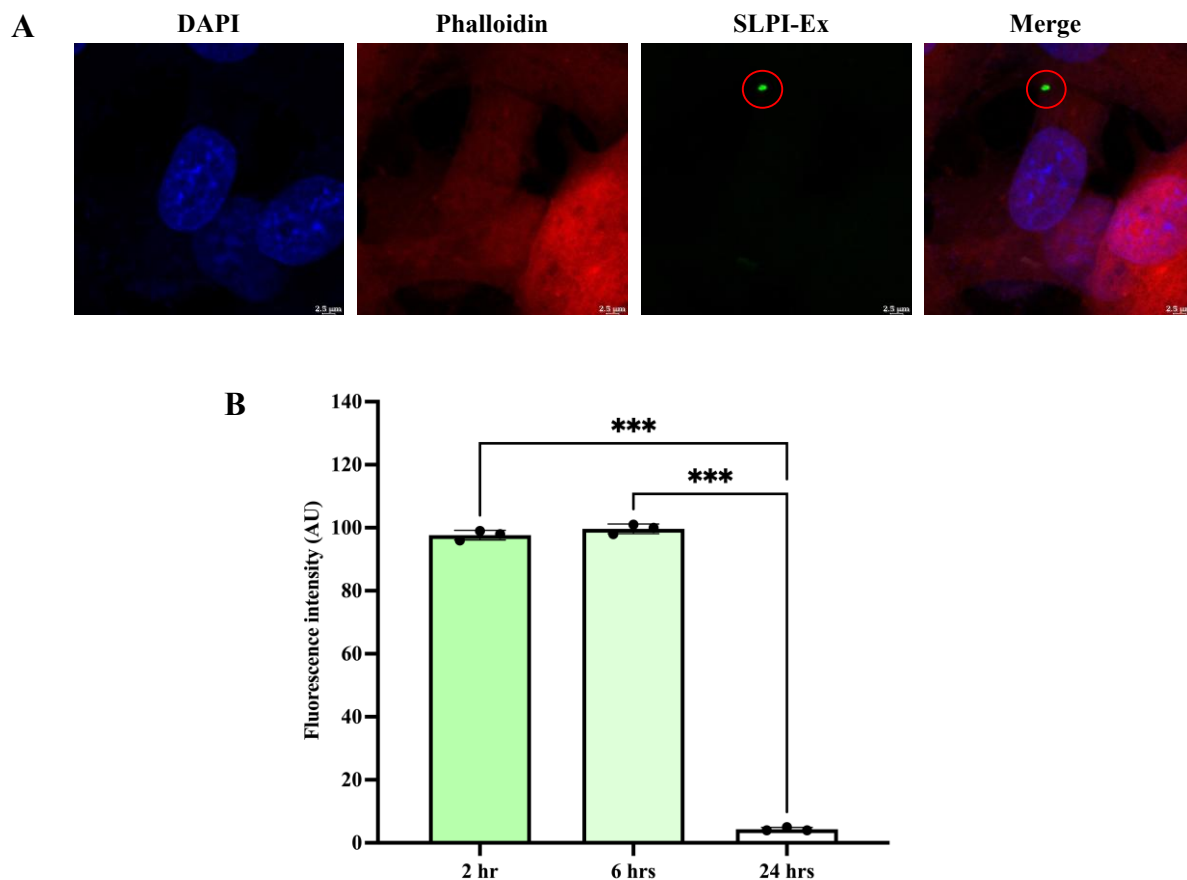


Figure 4.

The internalization of SLPI-Ex (A) Confocal laser scanning images (B) The fluorescence intensity at 2, 6, and 24 h *** $p < 0.0001$ versus each other group (unpaired t-test).

Conclusion:

Our study is the first to demonstrate that the recombinant human secretory leukocyte protease inhibitor (rhSLPI) can be successfully loaded exogenously into exosomes and effectively taken up by the human cardiomyocyte cell line (AC16). The results of this study will provide valuable insights for the future development of SLPI-Ex for investigation in myocardial I/R models.

Acknowledgements:

This project is funded by National Research Council of Thailand (NRCT): High-Potential Research Team Grant Program Contract no. N42A650870, and the TA&RA Scholarship 2023 from Multidisciplinary and Interdisciplinary School, Chiang Mai University for CP. The authors would like to acknowledge Biomedical Engineering Institute (BMEI), Chiang Mai University for a travel grant to attend STT50. Finally, the authors would like to thank The Graduate school, Biomedical Engineering Institute, Faculty of Science, Chiang Mai University for providing the valuable instruments, and the Faculty of Medical Science from Naresuan University for providing the isolated exosome for this research project.

References:

1. Bouchard D, Morisset D, Bourbonnais Y, Tremblay GM. *The Lancet Oncology*. 2006;7:167-74.
2. Majchrzak-Gorecka M, Majewski P, Grygier B, Murzyn K, Cichy J. *Cytokine Growth Factor Rev*. 2016;28:79-93.
3. Mongkolpathumrat P, Kijawornrat A, Prompant E, Panya A, Chattipakorn N, Barrere-Lemaire S, et al. *Biomedicines*. 2021;9.
4. Prompant E, Sanit J, Barrere-Lemaire S, Nargeot J, Noordali H, Madhani M, et al. *Exp Ther Med*. 2018;15:5231-42.
5. Prompant E, Nernpermpisooth N, Sanit J, Kumphune S. *Biomol Concepts*. 2018;9:17-32.
6. Paiyabhroma NN, N. Kumphune, S. *Journal of Applied Pharmaceutical Science*. 2018;8:156-62.
7. Kongpol K, Nernpermpisooth N, Prompant E, Kumphune S. *Biomolecules*. 2019;9.
8. Kantapich K, Rungrueang Y, Nitirut N, Sarawut K. *Journal of Applied Pharmaceutical Science*. 2020.
9. Nernpermpisooth N, Prompant E, Kumphune S. *Exp Ther Med*. 2017;14:5793-800.
10. Tkach M, Kowal J, Thery C. *Philos Trans R Soc Lond B Biol Sci*. 2018;373.
11. Yokoi A, Ochiya T. *Semin Cancer Biol*. 2021;74:79-91.
12. Uddin MJ, Mohite P, Munde S, Ade N, Oladosu TA, Chidrawar VR, et al. *Intelligent Pharmacy*. 2024;2:312-28.
13. Kowal J, Arras G, Colombo M, Jouve M, Morath JP, Primdal-Bengtson B, et al. *Proc Natl Acad Sci U S A*. 2016;113:E968-77.
14. Yanez-Mo M, Siljander PR, Andreu Z, Zavec AB, Borrás FE, Buzas EI, et al. *J Extracell Vesicles*. 2015;4:27066.
15. Zhou E, Li Y, Wu F, Guo M, Xu J, Wang S, et al. *EBioMedicine*. 2021;67:103365.
16. Zeng H, Guo S, Ren X, Wu Z, Liu S, Yao X. *Cells*. 2023;12.



17. Reiss AB, Ahmed S, Johnson M, Saeedullah U, De Leon J. *Metabolites*. 2023;13.
18. Kianfar E. *J Nanobiotechnology*. 2021;19:159.
19. Patra JK, Das G, Fraceto LF, Campos EVR, Rodriguez-Torres MDP, Acosta-Torres LS, et al. *J Nanobiotechnology*. 2018;16:71.
20. Rodriguez-Morales B, Antunes-Ricardo M, Gonzalez-Valdez J. *Pharmaceutics*. 2021;13.
21. Breyne K, Ughetto S, Rufino-Ramos D, Mahjoum S, Grandell EA, de Almeida LP, et al. *Commun Biol*. 2022;5:485.
22. Lasser C, Eldh M, Lotvall J. *J Vis Exp*. 2012:e3037.
23. Choi JS, Meghani N. *Colloids Surf B Biointerfaces*. 2016;145:653-61.
24. Malenica M, Vukomanovic M, Kurtjak M, Masciotti V, Dal Zilio S, Greco S, et al. *Biomedicines*. 2021;9.
25. Bachurski D, Schuldner M, Nguyen PH, Malz A, Reiners KS, Grenzi PC, et al. *J Extracell Vesicles*. 2019;8:1596016.
26. Xie Y, Yu L, Cheng Z, Peng Y, Cao Z, Chen B, et al. *J Nanobiotechnology*. 2022;20:239.
27. Comfort N CK, Bloomquist TR, Strait MD, Ferrante AW Jr, Baccarelli AA. . *J Vis Exp*. 2021;10:3791/62447.
28. Danaei M, Dehghankhold M, Ataei S, Hasanzadeh Davarani F, Javanmard R, Dokhani A, et al. *Pharmaceutics*. 2018;10.
29. Rao S, Song Y, Peddie F, Evans AM. *Int J Nanomedicine*. 2011;6:1245-51.
30. Beit-Yannai E, Tabak S, Stamer WD. *J Cell Mol Med*. 2018;22:2001-6.
31. Phutiyothin C, Chouyratchakarn W, Pikwong F, Jantrawut P, Baipaywad P, Kumphune S. *Materials Today: Proceedings*. 2023.



EXPLORING THE PHYTOCHEMICAL CONSTITUENTS AND BIOLOGICAL PROPERTIES OF *Piper sarmentosum* LEAVES: INSIGHTS FROM CULINARY PREPARATION

Nichakarn Sanguankaew,¹ Sirinya Taya,² Rawiwan Wongpoomchai,¹ Orawan Khantamat^{1,*}

¹Department of Biochemistry, Faculty of Medicine, Chiang Mai University, Chiang Mai, Thailand

²Functional Food Research Unit, Multidisciplinary Research Institute, Chiang Mai University, Chiang Mai 50200, Thailand

*E-mail: orawan.kh@cmu.ac.th

Abstract:

Piper sarmentosum Roxb., also known as "Cha-plu" in Thailand, is a traditional herb valued for its phytochemical content. Its leaves are widely used in cooking, but their bioactive potential after cooking has not been fully studied. This research examines the phytochemical content, antioxidant activity, and mutagenicity of *P. sarmentosum* leaf extracts prepared using traditional culinary methods to assess potential health benefits.

Fresh *P. sarmentosum* leaves were extracted using two methods that mimic cooking practices. Boiling the leaves created a hot water extract (PHWE) similar to curry broth, while ethanolic extraction of the boiled leaves (PREE) represented the leftover vegetable residue. The chemical composition, antioxidant activity, and mutagenic potential of both extracts were then evaluated. PHWE and PREE exhibited distinct chemical profiles. PREE, with higher amounts of phenolics and flavonoids, had stronger antioxidant activity in both ABTS and FRAP assays. PHWE, however, contained more condensed tannins, indicating better extraction of water-soluble compounds. Neither extract showed mutagenic activity in the *Salmonella* assay, suggesting they are safe for therapeutic or dietary use.

These findings suggest that *P. sarmentosum* leaves maintain strong antioxidant properties even after culinary preparation. This highlights their potential as a functional food ingredient with promising health benefits. Further research is warranted to explore their broader therapeutic potential, particularly in conditions where antioxidant properties are beneficial.

Introduction:

Piper sarmentosum Roxb. (Piperaceae), commonly known as "wild betel" or "Cha-plu" in Thai, is a perennial creeping herb with white blooms, widely distributed across Southeast Asia. It is not only an integral part of traditional medicine but also a popular culinary ingredient (1, 2), particularly in Lanna and Thai cuisine. The leaves are consumed both raw, as in the wrap snack Miang Kham, and cooked in curry like Kaeng Khua.

P. sarmentosum is a rich source of health-promoting phytochemicals, including phenolic compounds, xanthophylls, tannins, and essential oils (3), which exhibit a broad spectrum of biological activities such as antimicrobial, anti-inflammatory, antioxidant, and anticancer effects (4-6). Among its various parts, the leaves are particularly abundant in natural antioxidants, primarily due to their high content of flavonoids and other bioactive compounds (7, 8). Notable flavonoids identified in *P. sarmentosum* leaves include quercetin, naringenin, myricetin, and apigenin (9), all of which are known to exert anticancer effects through multiple molecular pathways, including apoptotic, autophagy, NF- κ B, JAK/STAT, and tumor suppressor pathways (10).

The potent bioactive compounds and antioxidant properties of *P. sarmentosum* leaves contribute to a range of other therapeutic effects, including anti-inflammatory, antimicrobial, and cardioprotective activities (5, 11-13). For instance, methanolic extracts of *P. sarmentosum* leaves have been shown to prevent stress-induced gastric ulcers by modulating oxidative stress and inflammation (14), while aqueous extracts have demonstrated *in vivo* anti-nociceptive and anti-inflammatory activities (15), along with *in vitro* cytoprotective effects against oxidative stress (16). Importantly, the aqueous extracts have also been reported to be non-mutagenic, supporting the safety of using *P. sarmentosum* as a medication or dietary supplement (17).

Given the growing interest in natural antioxidants, *P. sarmentosum* leaves hold significant promise as a resource for developing novel functional foods and therapeutic agents. This plant is commonly consumed in Thailand, particularly in curries and soups, where the leaves are typically boiled for 15–30 minutes. However, there remains limited understanding of the phytochemical profile, content, and biological activities of *P. sarmentosum* leaves following culinary preparation.

Polyphenols, key antioxidants in plants, are often considered heat-labile, with total phenolic content typically highest at moderate extraction temperatures of 60–80°C. Nonetheless, some studies report that water extraction at temperatures as high as 100°C or above can yield substantial amounts of phenolic compounds and antioxidant activity (18). Despite the general perception that high temperatures degrade bioactive compounds, *P. sarmentosum* leaves are hypothesized to maintain considerable antioxidant activity even after undergoing typical cooking processes.

To address this gap, we simulated the extraction of *P. sarmentosum* leaves using methods that mimic traditional cooking practices, resulting in two extracts: PHWE (broth of the curry) and PREE (residue of the vegetable in the curry). This study aims to explore the phytochemical profile, content, antioxidant activity, and mutagenicity of these extracts, which will provide valuable insights for the future standardization and consumption of *P. sarmentosum* leaves as functional food ingredients.

Methodology:

Preparation of P. sarmentosum extracts

The fresh leaves of *P. sarmentosum* were obtained from Terdwalai farm, Chiang Mai province, Thailand, and collected at the Faculty of Pharmacy, Chiang Mai University, with voucher specimen No. 0023333. Briefly, fresh leaves were added to hot water (100°C) and boiled for 15 minutes to mimic culinary preparation, as in curries or soups where the vegetables are typically boiled for 15–30 minutes. The extract was filtered using a filter cloth, then centrifuged at 9,000 rpm at 4°C for 10 minutes. The supernatant was dried using a lyophilizer, yielding the hot water extract of *P. sarmentosum* leaves (PHWE).

The residue from the hot water extract was dried in a hot air oven at 60°C for 24 hours, as previous findings showed that drying *P. sarmentosum* leaves in a hot air oven at 40–60°C did not significantly alter total tannin content or phytochemicals (19). The dried residue was then ground into a powder and extracted twice with 70% ethanol, with a 2-day soaking period and 4 hours of stirring each day. After this period, the extract was filtered using vacuum pumps and the resulting ethanolic extract of residue was evaporated and dried with a lyophilizer, yielding the residue ethanolic extract (PREE). The extracts of *P. sarmentosum* leaves (PSLEs), comprising PHWE and PREE, were stored at -20 °C until analysis.

Determination of chemical constituents in PSLEs

Total phenolics determination



The content of total phenolic compounds was measured using the Folin-Ciocalteu colorimetric method with minor modifications (20). The PSLEs were mixed with Folin-Ciocalteu reagent and incubated at 45 °C for 15 minutes. The absorbance was measured at 765 nm using a UV-visible spectrophotometer. The total phenolic content was calculated with the calibration curve of gallic acid and expressed as mg of gallic acid equivalent per g of the extract (mg GAE/g extract).

Total flavonoids determination

The content of total flavonoid was measured using the aluminum chloride colorimetric method with minor modifications (21). The PSLEs were mixed with NaNO₂ and AlCl₃•6H₂O and then incubated at 45 °C for 20 minutes. After that, NaOH was added to the mixture. The absorbance was measured at 520 nm. Catechin was used as a standard for the calibration curve and expressed as mg catechin equivalents per g of the extract (mg CE/g extract).

Chlorophyll and carotenoid determination

The content of total chlorophyll and carotenoid were evaluated using spectrophotometry with minor modifications (22). The PSLEs were homogenized with 80% acetone and incubated for 3 hours at 4 °C. The solution was centrifuged at 9,000 rpm for 5 minutes. The absorbance of the solution was measured at 480, 510, 645, and 663 nm. The concentrations of total chlorophyll and carotenoid were calculated using the following equations (23, 24), and then express in mg per gram of extract (mg/g extract).

$$\text{Total chlorophyll (mg/L)} = 20.2(A_{645}) + 8.02(A_{663})$$

$$\text{Total carotenoids (mg/L)} = 7.6(A_{480}) - 1.49(A_{510})$$

Tannin determination

The content of hydrolysable tannins was used to evaluate the gallotannin and ellagitannin content with minor modifications (25). The PSLEs were mixed with H₂SO₄ and then incubated at 85 °C for 20 hours. The solution was centrifuged at 3,000 xg, and the supernatant was collected. After that, ethanolamine and ammonium acetate were added to the solution and, adjusted the pH to 5.5. The mixture was incubated at 4 °C for 48 hours. Next, KIO₃ was added to the solution to produce methyl gallate. The solution was measured at 525 nm. Methyl gallate was used as a standard for the calibration curve, expressed as mg methyl gallate equivalents per gram of extract (mg methyl gallate/g extract).

The content of condensed tannins was measured using the vanillin method with minor modifications (26). The PSLEs were mixed with vanillin reagent, which contains concentrated HCl and vanillin in methanol, and then incubated at 30°C for 20 minutes. The solution was measured at 550 nm, and catechin was used as a standard for the calibration curve, expressed as mg of catechin equivalents per gram of extract (mg CE/g extract).

HPLC analysis

The HPLC analysis was performed to observe the phenolic compounds and flavonoids fingerprints using the system of Agilent Technologies (Santa Clara, CA, USA) with Zorbax Eclipse XDB-C18 column and photodiode array detector (27). To observe the phenolic compounds in the extracts, a gradient mobile phase consisted of 3% acetic acid in water and methanol was used and UV-Visible spectra of the extracts were detected at 260, 280, 320 and 360 nm.

The flavonoids fingerprint of the extracts was observed by using a mobile phase system consisting of acetonitrile and 0.2% formic acid in water under gradient conditions, followed by conducted UV-Vis spectra at wavelengths of 270 and 340 nm.

Determination of antioxidant activity in PSLEs

ABTS assay

The ABTS assay was used to evaluate the relative ability of antioxidants to scavenge the ABTS radical as described in previous study (28). The PSLEs were added to the working ABTS radical solution and incubated for 6 minutes in the dark. The reaction mixture was measured at wavelength 734 nm, and the antioxidant capacity was expressed as % ABTS radical scavenging using Trolox as a positive control.

FRAP assay

The FRAP assay is the rapid reduction of ferric-tripyridyltriazine (Fe^{III} -TPTZ) by antioxidants present in the samples, resulting in ferrous-tripyridyltriazine (Fe^{II} -TPTZ), a blue-coloured product (29). The FRAP reagent containing 2,4,6-tripyridyl-s-triazine (TPTZ) and 20 mM ferric chloride (FeCl_3) in sodium acetate buffer (pH 3.6) was mixed with PSLEs and incubated at 37°C for 4 minutes. The absorbance was estimated at 593 nm. Ferrous sulphate (FeSO_4) was used to create a standard curve, and the antioxidant activity of PSLEs was expressed as milligram of ferrous sulphate per gram of extract (mg FeSO_4 /g).

Mutagenicity test using Salmonella mutation assay

The mutagenicity of PSLEs was tested using *S. typhimurium* strains TA98 and TA100 in the presence and absence of metabolic activation. PSLEs were mixed with the S9 mixture (+S9), the mixture of S9 fraction and cofactors, and a sodium phosphate buffer (-S9). After that, a bacterial culture was added and incubated at 37 °C for 20 minutes in a water bath shaker. Then, a top agar solution containing L-histidine and D-biotin was added, and the mixture was poured on a minimal glucose agar plate. The plate was incubated at 37 °C for 48 hours. DMSO were used as negative control for all mutagens and PREE, while DW were used as negative control for PHWE. Positive control of TA98 and TA100 in the presence metabolic activation condition (+S9) is 2-aminoanthracene (2-AA), and in the absence metabolic activation condition (-S9) is 2-(2-furyl)-3-(5-nitro-2-furyl)-acrylamide (AF-2). Mutagenicity was expressed as the mutagenic index (MI). The MI is a value that indicates the mutagenic potential of the test substance. When the MI is higher than two, indicating mutagenicity of the test substance (30).

Statistical Analysis

The data are reported as mean \pm SD (n=3), except for the results obtained from the *Salmonella* mutation assay, which was expressed as mean \pm SEM values and performed in two independent experiments. The statistical significance of differences between groups was analyzed by one-way analysis of variance (ANOVA) using *GraphPad Prism* software version 9.5.1 (GraphPad Software, CA, USA), and $p < 0.05$ was considered significant.

Results and Discussion:

Physical appearance, extraction yield, and HPLC profile of PSLEs

The physical appearance and extraction yield of *P. sarmentosum* leaf extracts are summarized in Table 1. The PHWE extract appeared as a black powder, while the PREE extract exhibited a dark brown powder form. The extraction yields, calculated as the percentage of dry extract per kilogram of fresh leaves, were different between the two methods. PHWE yielded 32.64%, approximately double that of PREE, which yielded 18.07%. This notable difference suggests



that hot water extraction (PHWE) is more efficient for extracting soluble components from *P. sarmentosum* leaves compared to ethanol extraction (PREE).

The HPLC chromatograms of PHWE and PREE, shown in Figure 1, revealed key differences in their chemical profiles. Both extracts exhibited prominent peaks at retention times around 30.2, 44.4, 48.8, and 49.6 minutes. The similar peak absorptions at retention times of 30.2 and 44.4 minutes suggest that both extracts contain comparable amounts of certain hydrophilic analytes. However, at the retention times of 48.8 and 49.6 minutes, PREE showed a higher absorption than PHWE, indicating a higher concentration of hydrophobic compounds in the ethanol extract.

These findings are consistent with the solvent properties used in the extraction processes. Water, being a polar solvent, predominantly extracts hydrophilic compounds, whereas ethanol, with both polar and non-polar characteristics, can solubilize a broader range of compounds, including more hydrophobic substances. Consequently, the higher retention time and greater absorption observed in PREE reflect its enriched content of hydrophobic compounds compared to PHWE.

Table 1. Physical appearances and percentage yield of PSLEs

| Extracts | Physical appearances | %Yield/kg fresh weight of leaves |
|----------|----------------------------|----------------------------------|
| PHWE | Powdered, back color | 32.64 ± 10.3 |
| PREE | Powdered, dark brown color | 18.07 ± 4.2 |

Values are expressed as mean ± SD.

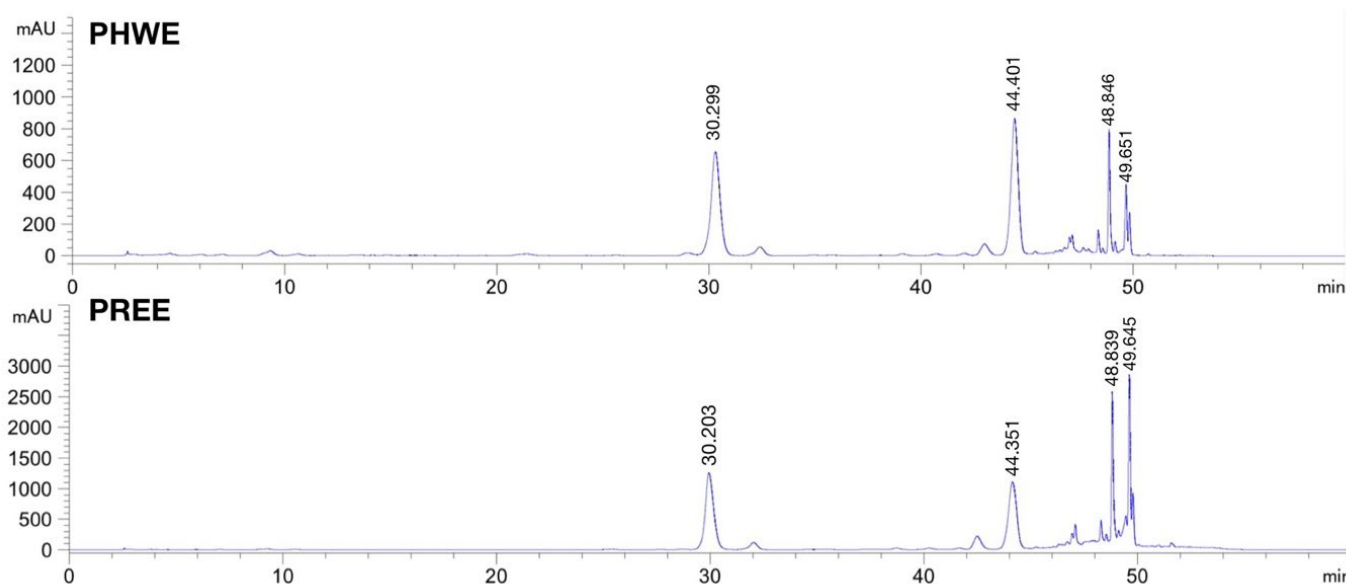


Figure 1. HPLC chromatograms of PSLEs

Chemical constituents in PSLEs

The chemical composition of PSLEs is presented in Figure 2. The PREE extract contained higher levels of most phytochemicals compared to PHWE, except for condensed tannins. Specifically, the total phenolic content in PREE was 48.1±6.2 mg GAE/g extract, slightly higher than the 41.1±7.6 mg GAE/g extract found in PHWE. Moreover, the total flavonoid content in PREE (12.3±2.1 mg CE/g extract) was approximately three times greater than that in PHWE (4.1±0.4 mg CE/g extract). Phenolics and flavonoids are well-known for their biological and antioxidant

activities, primarily due to the presence of functional hydroxyl groups that enable them to scavenge free radicals and chelate metal ions (31).

Previous reports have shown that *P. sarmentosum* leaves contain a variety of phenolics and flavonoids. Purba *et al.* demonstrated that *P. sarmentosum* leaves contain phenolic acids such as caffeic acid, syringic acid, *p*-coumaric acid, and ferulic acid, while flavonoids such as catechin, rutin, myricetin, quercetin, apigenin, and kaempferol are also present (19). The higher phenolic and flavonoid content found in PREE suggests potentially greater biological activity compared to PHWE.

In addition, PREE exhibited significantly higher levels of total chlorophyll (11.3 ± 0.7 mg/g extract) compared to PHWE (0.3 ± 0.0 mg/g extract). The carotenoid content followed a similar trend, with PREE containing 3.6 ± 0.3 mg/g extract, far exceeding the 0.2 ± 0.0 mg/g extract observed in PHWE. Chlorophylls and carotenoids are essential pigments in plants, playing crucial roles in photosynthesis. Previous studies have highlighted the presence of antioxidants such as vitamins C and E, carotenes, xanthophylls, tannins, and phenolic compounds in *P. sarmentosum* leaf extracts (3). Among the carotenoids, xanthophylls are the most abundant (32), particularly lutein, which contributes to light harvesting, photoprotection, and the assembly of light-harvesting antenna complexes (33).

Regarding tannin content, both PHWE and PREE showed similarly low levels of total hydrolysable tannins, with 0.22 ± 0.3 and 1.33 ± 0.6 mg methyl gallate/g extract, respectively. However, PHWE contained a significantly higher concentration of total condensed tannins at 126.7 ± 12.6 mg CE/g extract, compared to 39.5 ± 3.7 mg CE/g extract in PREE. This difference is likely due to the water-soluble nature of condensed tannins, which are more efficiently extracted by the hot water method used for PHWE.

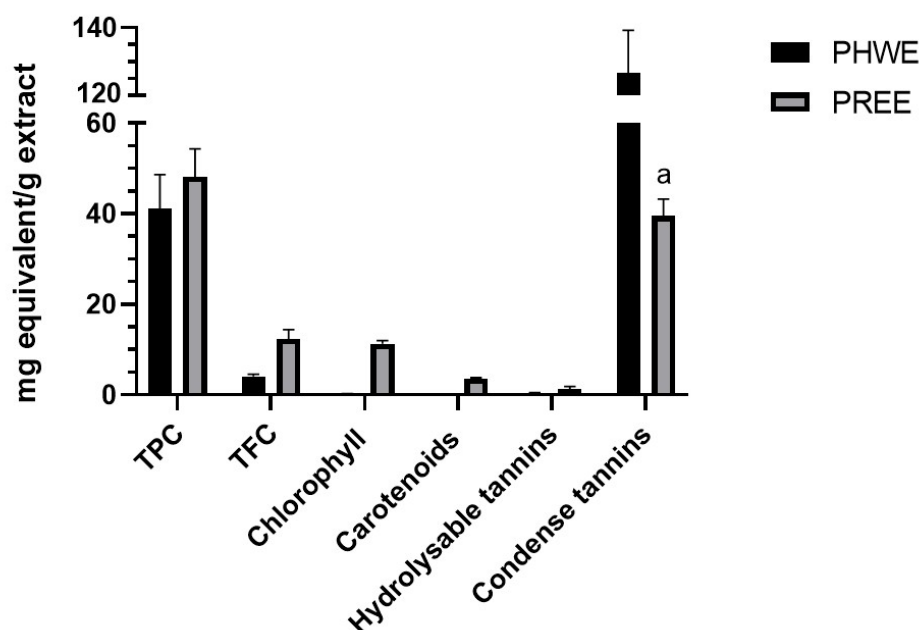


Figure 2. The contents of TPC, TFC, chlorophylls, carotenoids, and tannins in PSLEs.

a indicate statistical differences from PHWE at $p < 0.0001$.

TPC: Total phenolic content; TFC: total flavonoid content.

Antioxidant activity in PSLEs

The antioxidant activity of PSLEs was evaluated using the ABTS radical cation scavenging assay and the FRAP assay, with Trolox serving as the positive control at concentrations of 0.5 mg/ml for ABTS and 0.05 mg/ml for FRAP. As shown in Figure 3A, Trolox at 0.5 mg/ml achieved a 72% ABTS radical scavenging activity. Both PHWE and PREE exhibited a dose-



dependent inhibition of ABTS radicals across a concentration range of 5-50 mg/ml, with PREE demonstrating a stronger scavenging effect than PHWE.

Similarly, the FRAP assay, which measures the ferric ion-reducing capacity, showed that Trolox at 0.05 mg/ml reduced ferric ions, forming 0.14 mg FeSO₄/ml, as presented in Figure 3B. Both PHWE and PREE, within a concentration range of 1-5 mg/ml, exhibited antioxidant activity by reducing ferric ions in a dose-dependent manner. Notably, PREE consistently showed higher antioxidant activity than PHWE in both assays, which correlates with its higher phenolic and flavonoid content.

These findings are consistent with previous research indicating that *P. sarmentosum* possesses significant antioxidant properties, largely attributed to its rich content of bioactive compounds such as polyphenols and flavonoids, which are known to contribute to antioxidant activity (7).

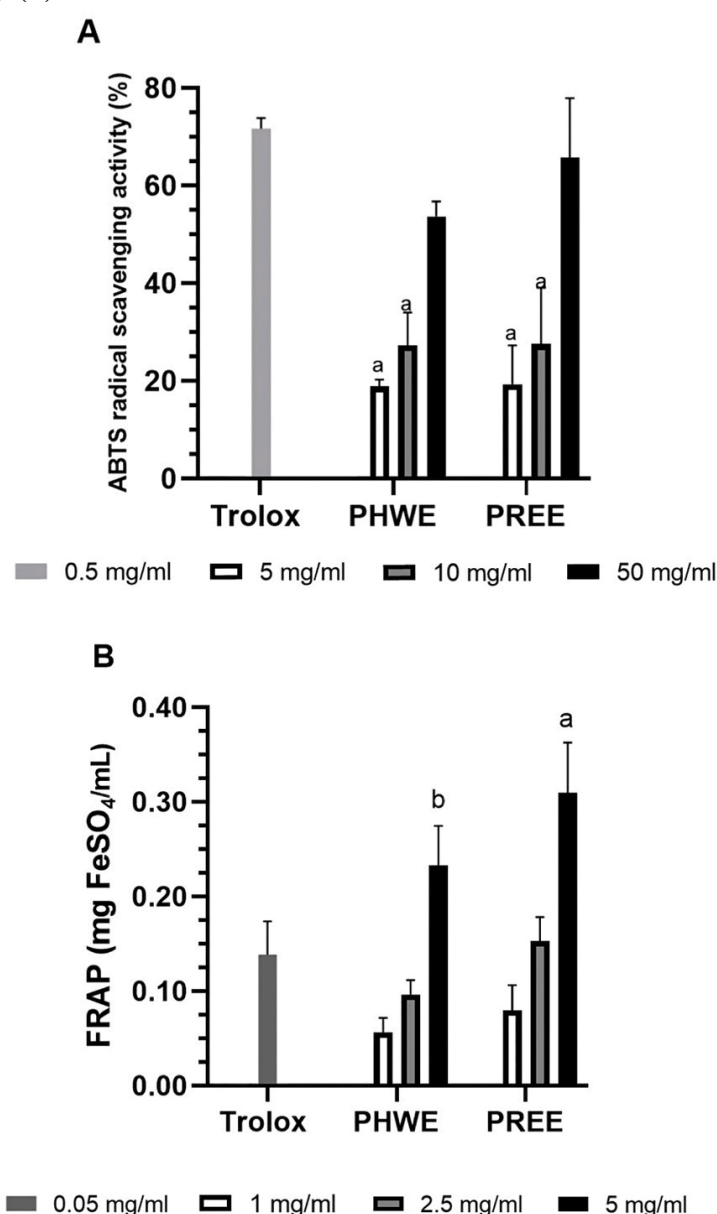


Figure 3. Antioxidant activity of PSLEs. (A) ABTS assay (B) FRAP assay. a and b indicate statistical differences from Trolox at $p < 0.0001$ and $p < 0.01$, respectively.

Mutagenicity of PSLEs in *Salmonella* Mutation Assay

The *Salmonella* mutation assay, a widely used method for assessing potential mutagenic effects, was employed to evaluate the mutagenicity of PSLEs. The results, summarized in Table 2, indicate that all tested concentrations of PSLEs had no significant effect on the number of revertant colonies in *S. typhimurium* strains TA98 and TA100, both in the presence and absence of metabolic activation, when compared to the vehicle control. Additionally, PSLEs did not exhibit a mutagenic index greater than 2.0 in either strain, further supporting the absence of mutagenic activity.

Previous research indicates that the water extract of *P. sarmentosum* has neither direct nor indirect genotoxic effects and shows no significant mutagenic activity. This was demonstrated by the lack of genotoxic effects, measured by micronucleus formation, both with and without S9 metabolic activation (17). These findings are consistent with our results, further suggesting that PSLEs are non-mutagenic and non-toxic under the conditions tested, highlighting their potential safety for use in therapeutic and dietary applications.

However, the limitations of our study include the need for further investigation using animal models and clinical trials to gather more comprehensive information on the potential toxicity of *P. sarmentosum*.

Table 2. Mutagenicity of PSLEs in *S. typhimurium* strains TA98 and TA100 in the presence and absence of metabolic activation

| Extracts | Concentration (per plate) | Number of His ⁺ revertant colonies (Mutagenic Index) | | | |
|----------|---------------------------|---|---------------------|----------------------|---------------------|
| | | TA98 | | TA100 | |
| | | +S9 | -S9 | +S9 | -S9 |
| DW | - | 24.8 ± 3.3 (1.0) | 28.2 ± 4.2 (1.0) | 84.3 ± 0.3 (1.0) | 85.0 ± 4.7 (1.0) |
| DMSO | - | 23.5 ± 0.5 (1.0) | 20.0 ± 1.0 (1.0) | 80.5 ± 2.8 (1.0) | 88.5 ± 6.5 (1.0) |
| 2AA | 0.50 µg | 1339.2 ± 391.0 (57.0) | - | 1157.8 ± 44.6 (14.4) | - |
| AF-2 | 0.10 µg | - | 307.7 ± 13.0 (15.4) | - | - |
| AF-2 | 0.01 µg | - | - | - | 1203.5 ± 9.9 (13.6) |
| PHWE | 200 µg | 33.8 ± 7.8 (1.4) | 31.7 ± 8.7 (1.1) | 77.8 ± 7.9 (0.9) | 86.1 ± 0.4 (1.0) |
| | 1000 µg | 31.8 ± 2.8 (1.3) | 28.7 ± 6.7 (1.0) | 87.7 ± 1.0 (1.0) | 79.5 ± 7.9 (0.9) |
| | 5000 µg | 20.0 ± 6.7 (0.8) | 33.1 ± 7.6 (1.2) | 81.3 ± 8.0 (1.0) | 84.2 ± 4.2 (1.0) |
| PREE | 200 µg | 28.5 ± 1.8 (1.2) | 22.0 ± 0.0 (1.1) | 94.0 ± 4.0 (1.2) | 87.7 ± 4.7 (1.0) |
| | 1000 µg | 27.1 ± 4.4 (1.2) | 25.2 ± 0.2 (1.3) | 88.0 ± 4.0 (1.1) | 86.7 ± 5.0 (1.0) |
| | 5000 µg | 34.5 ± 4.5 (1.5) | 30.8 ± 7.5 (1.5) | 84.3 ± 6.0 (1.1) | 96.3 ± 0.7 (1.1) |

Values are expressed as mean ± SEM. 2AA: 2-Aminoanthracene; AF-2: 2-(2-furyl)-3-(5-nitro-2-furyl)-acrylamide; DMSO: dimethyl sulfoxide; DW: distilled water.

Conclusion:

This study provides a comprehensive evaluation of the chemical composition, antioxidant activity, and mutagenicity of *P. sarmentosum* leaf extracts (PSLEs), specifically focusing on the broth (PHWE) and residue (PREE) derived from culinary preparation methods that mimic traditional Thai curry-making. Our findings indicate that both PHWE and PREE extracts possess significant antioxidant properties, with PREE showing a higher concentration of phenolic compounds, flavonoids, chlorophylls, and carotenoids compared to PHWE. This suggests that the ethanolic extraction of the residue (PREE) after boiling the leaves yields a more potent extract with enhanced bioactive properties, likely due to its higher content of hydrophobic compounds.

The antioxidant assays (ABTS and FRAP) further corroborated the superior efficacy of PREE in scavenging free radicals and reducing ferric ions, highlighting its potential as a robust source of natural antioxidants. Additionally, the *Salmonella* mutation assay demonstrated that



both PHWE and PREE are non-mutagenic under the conditions tested, confirming their safety for consumption and potential use in therapeutic applications.

These findings underscore the importance of understanding the effects of culinary preparation on the phytochemical profile and biological activity of *P. sarmentosum* leaves. The residue left after boiling retains significant bioactive compounds that could be utilized in the development of functional foods or natural health products. Furthermore, the broth resulting from the hot water extraction, although containing fewer bioactive compounds than the residue, still offers substantial antioxidant benefits. This study highlights the potential of both components, encouraging the full utilization of *P. sarmentosum* leaves in both culinary and medicinal contexts.

Acknowledgements:

We would like to thank Research Center for Development of Local Lanna Rice and Rice Products, Chiang Mai University, Thailand. This research work was partially supported by Chiang Mai University, Thailand.

References:

1. Burkill IH. *Nature*. 1936;137:255.
2. Sim KM, Mak CN, Ho LP. *J Asian Nat Prod Res*. 2009;11:757-60.
3. Chanwitheesuk A, Teerawutgulrag A, Rakariyatham N. *Food Chem*. 2005;92:491-7.
4. Sanusi NA, Umar RA, Zahary MN, Rohin MAK, Pauzi MR, Ismail S. *IOSR J Dent Med Sci*. 2017;16:62-5.
5. Yeo ETY, Wong KWL, See ML, Wong KY, Gan SY, Chan EWL. *J Ethnopharmacol*. 2018;217:187-94.
6. Ghazali NF, Mohd MA, Ibrahim MA, Muhammad TST. *Malay Nat J*. 2018;70:195-202.
7. Nguyen N, Nguyen V, Van N, Vo T. *IOP Conf. Ser.: Mater. Sci. Eng.* 2020;991:12028.
8. Ismail SM, Chua KH, Aminuddin A, Ugusman A. *Sains Malays*. 2018;47:2359-68.
9. Sun X, Chen W, Dai W, Xin H, Rahmand K, Wang Y, Zhang J, Zhang S, Xu L, Han T. *J Ethnopharmacol*. 2020;263:112897.
10. Liao CY, Lee CC, Tsai CC, Hsueh CW, Wang CC, Chen I. *BioMed Res Int*. 2015;2015:840542.
11. Chanprapai P, Chavasiri W. *J Integr Agric*. 2017;16:2513-24.
12. Ware I, Franke K, Dube M, Enshasy H, Wessjohann LA. *Int J Mol Sci*. 2023;24:1328.
13. Md Salleh M, Aminuddin A, Hamid AA, Salamt N, Japar Sidik FZ, Ugusman A. *Front Pharmacol*. 2021;12:667102.
14. Akmal MN, Abdel Aziz I, Nur Azlina MF. *Front Pharmacol*. 2022;13:971443.
15. Zakaria ZA, Patahuddin H, Mohamad AS, Israf DA, Sulaiman MR. *J Ethnopharmacol*. 2010;128:42-8.
16. Ugusman A, Zakaria Z, Hui CK, Nordin NA, Mahdy ZA. *EXCLI J*. 2012;11:705-14.
17. Tammasakchai A, Peungvicha P, Tamsiririrkkul R, Siripong P, Puchadapirom P. *Songklanakarin J Sci Technol*. 2021;43:203-9.
18. Antony A, Farid M. *Appl Sci*. 2022;12:2107.
19. Purba RAP, Paengkoum S, Paengkoum P. *Separations*. 2021;8:152.
20. Gong Y, Liu X, He WH, Xu HG, Yuan F, Gao YX. *Fitoterapia*. 2012;83:481-9.
21. Zhishen J, Mengcheng T, Jianming W. *Food Chem*. 1999;64:555-9.
22. Kalaji HM, Dąbrowski P, Cetner MD, Samborska IA, Łukasik I, Brestic M. *J Plant Nutr*. 2017;40:1024-34.
23. Arnon DI. *Plant Physiol*. 1949;24:1.

24. Momin R, Ahire P, Kadam V. *J Phytol.* 2011;3:52-4
25. Hartzfeld PW, Forkner R, Hunter MD, Hagerman AE. *J Agric Food Chem.* 2002;50:1785-90.
26. Butler LG, Price ML, Brotherton JE. *J Agric Food Chem.* 1982;30:1087-9.
27. Suttisansanee U, Thiyajai P, Chalermchaiwat P, Wongwathanarat K, Pruesapan K, Charoenkiatkul S. *Plants.* 2021;10:1563.
28. Tantipaiboonwong P, Pintha K, Chaiwangyen W, Suttajit M, Khanaree C, Khantamat O. *Plants.* 2023;12:2210.
29. Benzie IF, Strain JJ. *Anal Biochem.* 1996;239:70-6.
30. Silva VA, Gonçalves GF, Pereira MS, Gomes IF, Freitas AF, Diniz MF, Pessôa HL. *Rev bras farmacogn.* 2013;23:329-34.
31. Kumar S, Pandey AK. *Sci World J.* 2013;2013:162750.
32. Rukachaisirikul T, Siri wattanakit P, Sukcharoenphol K, Wongvein C, Ruttanaweang P, Wongwattana vuch P. *J Ethnopharmacol.* 2004;93:173-6.
33. Izadpanah F, Frede K, Soltani F, Baldermann S. *Hortic Plant J.* 2024;10:743-54.



GAMING AND SIMULATION FOR SHARE LEARNING ABOUT THE IMPORTANCE AND CO-CONSTRUCTION OF URBAN GREEN SPACE

Satayu Panjinda,¹ Suthinee Onuam,¹ Montathip Sommeechai,² Wirongrong Duangjai,² Jamroon Srichaichana,³ Thanawat Jinjaruk,⁴ Pongchai Dumrongrojwattana^{5,*}

¹ M.Sc. Interdisciplinary Program in Environmental Science, Graduate School, Chulalongkorn University, Bangkok 10330, Thailand

² Department of Silviculture, Faculty of Forestry, Kasetsart University, Bangkok 10900, Thailand

³ Faculty of Humanities and Social Sciences, Thaksin University, Songkhla 90000, Thailand

⁴ Research and Innovation for Sustainability Center (RISC) by Magnolia Quality Development Corporation Limited (MQDC), Samut Prakan 10540, Thailand

⁵ Department of Biology, Faculty of Science, Chulalongkorn University, Bangkok 10330, Thailand

*e-mail: pongchai.d@chula.ac.th

Abstract:

The loss of green space causes various impacts to wildlife and humans. In response, governmental agencies have implemented policies aimed at expanding green spaces. However, current initiatives predominantly emphasize quantitative targets and lack sufficient public participation, resulting in a lack of sustainability. To foster participatory green space expansion, it is necessary to promote stakeholders' understanding, particularly among local communities, regarding the typologies and co-benefits of green spaces. Moreover, facilitating dialogue is important for them to exchange ideas on determining the benefits that the community and government agencies will receive in order to create joint ownership and sustainable green space management. To enhance such knowledge and understanding, this research created a gaming and simulation tool in the form of a board game. The game incorporates six green space types and illustrates the co-benefits for humans and other living organisms. Additionally, it simulates various scenarios that may influence the establishment and maintenance of green spaces. Preliminary testing results with 9 university students indicated that the created game effectively fulfills its intended purpose. Subsequent research will focus on refining the game to optimize its efficacy and implementing it in participatory field workshops with representatives from local stakeholders in the Bang Kachao area and Laem Chabang municipality. These workshops aim to facilitate knowledge exchange and collectively identify feasible strategies for green space expansion.

Introduction:

Green space degradation and loss due to the expansion of agricultural and urban areas has caused various problems for both living organisms and humans, such as loss of biodiversity¹, air pollution from particulate matter², urban heat island³, and mental health of urban inhabitants⁴. If the green space is insufficient for the population, it will affect human health, well-being, and economics⁵. Due to the mentioned problems, numerous international organizations and countries have implemented policies to increase green space and conserve biodiversity, such as the FAO Green Cities Initiative, and the Aichi Biodiversity Targets⁶. Thailand, in particular, has established a 20-year National Strategy, which has set a target to increase green areas (both natural forests, economic forests, and green spaces in urban areas) to 55% nationwide by 2036. Various policies have also been created and implemented, such as the National Economic and Social Development Plan, the Integrated Biodiversity Master

Plan, and the National Forestry Policy, and Guidelines for Promoting Sustainable Green Space management⁵.

Unfortunately, it was found that most policies focus on increasing green space in quantity rather than quality and pay little attention in public participation to sustain public green space^{6,7}. They set numerical or percentage targets and encourage government agencies to increase the green area to achieve the target, such as planting trees on various important occasions. They also lack public participation, particularly co-design⁷, causing the newly created green space to be damaged or neglected because it does not align with local needs and lacks a sense of community ownership. For instance, trees planted in industrial zones may obstruct transportation, leading to unauthorized removal.

To achieve sustainable green space expansion, it is necessary to foster a comprehensive understanding of green space typologies and the benefits they offer to both governmental and local stakeholders. Integrative and participatory approach must be implemented, starting from selecting site for green space creation or improvement, co-designing green space that considers the co-benefits of all stakeholders, as well as collaborative planning and monitoring to ensure sustainable management of green space.

Addressing complex natural resource management issues requires tools that can provide a common representation of current and future scenarios, illustrating both positive and negative impacts of decisions at individual and community levels⁸. Such tools should facilitate dialogue and support collective decision-making among diverse stakeholders. Previous research has shown that gaming and simulation is an effective tool for knowledge sharing in various natural resource management contexts, such as terrestrial and mangrove forests^{9,10,11,12}. However, their application to participatory green space expansion is still limited, most of them were specific to green roof and urban park^{13,14,15}. This research therefore aims to create gaming and simulation that can be used to facilitate shared learning about green space typologies, co-benefits, and participatory green space creation. By employing these innovative approaches, we can bridge the gap between policy objectives and practical implementation, ensuring that green space initiatives are not only quantitatively successful but also qualitatively meaningful and sustainable for local communities.

Methodology:

Gaming and simulation construction

The following steps were carried out to create a gaming and simulation:

1) Review the literature on green spaces: Related documents were reviewed, including types of green spaces, appropriate management of green spaces, ecosystem services and co-benefits provided by green spaces, etc.

2) Determine the objectives: The created game intended to be used as a learning model about green space typologies, co-benefits obtained from green spaces, and participatory design of green spaces. The game emphasized the concepts of visualization¹⁶ adapting to various forms of green spaces, as well as interactions and cooperation between players to achieve common goals in the game.

3) Create a conceptual model and collect relevant data: Unified Modeling Language (UML) diagram was used to represent important components of green spaces and their properties and interactions in the system, as well as define possible scenarios to be explored to make users aware of the adaptive management of green space¹⁷.

4) Construct gaming and simulation tool in the form of board game: The UML was used as a guide to construct a game that will be used to create a shared and support decision making among players. The game was set for approximately 8-10 players to use simultaneously within 2 hours. Gameboard and artifacts were prepared, as well as excel spread sheet to show the results during the gaming session.



5) Create pre- and posttests: To assess participants' learning, pretest and posttest were created. The posttest also included the satisfaction assessment questions¹⁸. The results and suggestions will be useful for further improvement of the game.

6) Create detailed description of the created game: The instructions and description of the game were prepared. It will be used in workshops and disseminated.

Gaming and simulation testing

A preliminary game testing session was carried out with 9 Chulalongkorn University students from different backgrounds but related to the education and environment, such as education, biology, and environmental sciences. After completing the testing, a brainstorming session was conducted to share testers' feelings, idea and suggestions to improve the game, both feature and process. The suggestion will be used to improve the game before using it again with representatives from local administration organizations and local communities at Kung Bang Kachao, Phra Padaeng district and Laem Chabang Municipality under the enhancing Thailand's urban and suburban green space project carried out by the research team.

Results and Discussion:

Description of the "Coco green space: Co-design for co-benefits" game

Design Concept: This game integrated diverse ecological and socio-economic concepts, including ecosystem services, co-benefits, biodiversity conservation, and system visualization and scenario explorations. Companion Modeling approach¹¹, which focuses on the creation of a shared representation of a system and support decision-making with stakeholders, was used to design and create the game. Therefore, the game format is characterized by mutual agreement to determine the co-benefits of green space to be constructed in the community. At the same time, players must perform various activities to achieve personal goals. These individual and collective goals will stimulate participants to learn about trade-off or win-win situations on green space creation or improvement.

Objective: This game is created to 1) facilitate shared learning among participants about 6 types of green space based on their characteristics and uses (i.e. private green space, institutional green space, public utility green space, striped green space along public utility lines, community economic green space, natural green space, and unused or undeveloped green space), 2) support learning about the co-benefits that will be gained from the green spaces in community, and 3) support discussions among players leading to co-design and planning to increase green space in reality.

Game components:

1) Game board: It consists of 200 squares (6 cm x 6 cm) for placing different types of pictograms (Figure 1).

2) Player tokens: This game is designed for 9 players, each assuming a role numbered from 1 to 9 as follows: Teacher, Student, Local Government Organization, Private Factory, Sub-district Health Promotion Hospital, Farmer, Monk, Bird, and Environmentalist (symbols representing each role are shown in Figure 1). The purpose of assigning these roles is to foster learning about the importance of green spaces and how each role can participate in planning and management.

3) Pictograms (6 cm x 6 cm): There are two main categories, green space and other land-use/land-cover pictograms. The green space consists of 6 types as mentioned above. The

other pictograms represent man-made structures, including roads, schools, factories, local administrative organizations, hospitals, houses, temples, offices, and bared land (Figure 2)

4) Data Recording Sheets: These allow players to track the goals of each role (the Environmentalist will have an additional biodiversity recording sheet to document the living organisms found in the constructed green spaces). There is also an order form to record decisions made when purchasing pictograms.

5) Scenario cards: There are 5 scenarios developed from the possible situations found in the study sites by research team:

- Normal condition: Uses in the first round for players to focus on learning about game materials and steps.
- Tourist visiting for bird watching: Demonstrates the importance of green space for biodiversity conservation (represented by birds) and the economic benefits from bird-watching tourism.
- Global warming: Shows environmental and socio-economic impacts from recent climate change problem, resulting in reduced community income.
- PM (particulate matter) 2.5: Highlights importance of green spaces on environmental and socio-economic aspects, and showing how air pollution affects well-being, leading to healthcare costs and necessitating training for adaptive management.
- Private sector funding: Demonstrates the green space development funding from external sources.

6) Co-benefit cards: There are 16 types, including biodiversity, carbon storage, air quality monitoring, temperature reduction, education, non-timber forest products, water retention areas, exercise spaces, event organizing spaces, recreation activities, job creation, and tourism activities (Figure 3). These are used for participants to select their common co-benefits to be obtained from the green space.

7) Bird settlement condition card: This represents emerging property when green space is large enough. One water bird needs 2 connected water spaces, and one non-water bird requires 4 adjacent green spaces vertically, horizontally, or diagonally.

8) Excel File: It is used to record players' purchasing decisions, calculates income, and displays decision outcomes. It is used for the debriefing session.

9) Other materials: They are activity cards, knowledge card (players read for knowledge sharing), fish tokens, non-timber forest product tokens, bird tokens, orange beads (represent carbon dioxide emitted from human activities), and 4 types of certificate (players obtained after joining the activity; training on green space types and benefits, training on health care under global warming, training on good conservation practices for fish release, and participating on wetland field trip for water quality measurement) (Figure 1)

10) Assessment Forms: Pretest and posttest are prepared for knowledge assessment and satisfaction survey (Figure 4).

Instructions to play a game

This game is designed for 5 rounds and can be played simultaneously by 2 groups to compare decision-making results and to enhance the learning experience. Game playing steps are:

1. Prepare 2 sets of materials for 2 groups (2 game boards and a bank with materials)
2. Divide players into two groups of 9 each



Figure 1.
Game board and supporting components



Figure 2.
Pictograms; a. green space pictograms; b. other land-use/land-cover pictograms



Figure 3.
Co-benefit cards for players to co-design before starting the game

| แบบทดสอบก่อนทำกิจกรรม | | แบบทดสอบหลังทำกิจกรรม | |
|---|---|---|--|
| <p>วัตถุประสงค์ 1. สำคัญงานนโยบายและแผนทรัพยากรธรรมชาติและสิ่งแวดล้อม (สน.) ให้ความหมายของ "พื้นที่สีเขียว" ไว้ว่า เป็น..... ปกคลุมด้วยพืชพรรณเป็นองค์ประกอบหลัก ก. พื้นที่รวมชาติ หรือพื้นที่ที่มีมนุษย์สร้างขึ้นหรือกำหนดขึ้นในเมืองหรือชุมชน ข. พื้นที่มนุษย์สร้างขึ้น ค. พื้นที่รวมชาติในเมืองหรือชุมชน ง. พื้นที่ป่าเพื่อการพัฒนา</p> <p>2. สน. ได้กำหนดพื้นที่สีเขียวออกเป็นกี่ประเภท? ก. 5 ข. 6 ค. 8 ง. 10</p> <p>3. ประเทศไทยได้ประกาศเป้าหมายว่าจะเป็นกลางทางคาร์บอน (carbon neutrality) ในปีใด ก. ค.ศ. 2040 (พ.ศ. 2583) ข. ค.ศ. 2050 (พ.ศ. 2593) ค. ค.ศ. 2055 (พ.ศ. 2598) ง. ค.ศ. 2060 (พ.ศ. 2573)</p> <p>4. ประเทศไทยตั้งเป้าหมายว่าต้องเพิ่มพื้นที่สีเขียวต่อพื้นที่เมืองให้ได้ไม่น้อยกว่าร้อยละเท่าใดภายในปี พ.ศ. 2570? ก. 5 ข. 10 ค. 15 ง. 30</p> <p>5. พื้นที่สีเขียวมีประโยชน์ต่อมนุษย์เท่านั้น? ก. ใช่ ข. ไม่ใช่ ค. ไม่แน่</p> <p>6. ข้อใดไม่ใช่ประโยชน์ของพื้นที่สีเขียว? ก. ช่วยลดมลพิษทางอากาศ ข. เพิ่มความร่มเย็นในเมือง ค. สร้างรายได้ให้ชุมชน ง. เพิ่มความร่มเย็นในเมือง</p> | <p>7. พื้นที่สีเขียวสำคัญต่อสุขภาพจิตของมนุษย์อย่างไร? ก. เป็นพื้นที่พักผ่อนเรียนรู้ ข. ช่วยลดความเครียดและความวิตกกังวล ค. เพิ่มความเมตตา ง. ไม่มีผลต่อสุขภาพจิต</p> <p>8. ข้อใดคือประโยชน์ด้านสังคมของพื้นที่สีเขียว? ก. เป็นพื้นที่ในการทำกิจกรรมร่วมกัน ข. เป็นพื้นที่สร้างรายได้ เช่น ขายของฝาก ค. ลดค่าใช้จ่ายของโรคภัยไข้เจ็บ ง. ไม่มีข้อใดที่เป็นประโยชน์ด้านสังคม</p> <p>9. การจัดการพื้นที่สีเขียวในเมืองควรทำอย่างไร? ก. ปลูกต้นไม้ขนาดใหญ่ให้มากที่สุด ข. ปลูกต้นไม้และพืชพรรณที่เหมาะสม ค. สร้างสิ่งปลูกสร้างในพื้นที่สีเขียว ง. ใช้พื้นที่สีเขียวเป็นที่จอดรถ</p> <p>10. การเพิ่มพื้นที่สีเขียว ควรเป็นหน้าที่ของใคร? ก. หน่วยงานภาครัฐ ข. ชาวบ้านในท้องถิ่น ค. ภาคเอกชนที่มีเงินลงทุน ง. ทุกคนควรช่วยกัน</p> <p>11. โปรดระบุประโยชน์ของพื้นที่สีเขียวเพิ่มเติม </p> <p>12. (ให้คะแนนตัวเอง) ท่านคิดว่าท่านมีความรู้เกี่ยวกับประเภทและประโยชน์ของพื้นที่สีเขียว ในระดับใด / 10 คะแนน</p> | <p>วัตถุประสงค์ 1. สำคัญงานนโยบายและแผนทรัพยากรธรรมชาติและสิ่งแวดล้อม (สน.) ให้ความหมายของ "พื้นที่สีเขียว" ไว้ว่า เป็น..... ปกคลุมด้วยพืชพรรณเป็นองค์ประกอบหลัก ก. พื้นที่รวมชาติ หรือพื้นที่ที่มีมนุษย์สร้างขึ้นหรือกำหนดขึ้นในเมืองหรือชุมชน ข. พื้นที่มนุษย์สร้างขึ้น ค. พื้นที่รวมชาติในเมืองหรือชุมชน ง. พื้นที่ป่าเพื่อการพัฒนา</p> <p>2. สน. ได้กำหนดพื้นที่สีเขียวออกเป็นกี่ประเภท? ก. 5 ข. 6 ค. 8 ง. 10</p> <p>3. ประเทศไทยได้ประกาศเป้าหมายว่าจะเป็นกลางทางคาร์บอน (carbon neutrality) ในปีใด ก. ค.ศ. 2040 ข. ค.ศ. 2050 ค. ค.ศ. 2055 ง. ค.ศ. 2060</p> <p>4. ประเทศไทยตั้งเป้าหมายว่าต้องเพิ่มพื้นที่สีเขียวต่อพื้นที่เมืองให้ได้ไม่น้อยกว่าร้อยละเท่าใดภายในปี พ.ศ. 2570? ก. 5 ข. 10 ค. 15 ง. 30</p> <p>5. พื้นที่สีเขียวมีประโยชน์ต่อมนุษย์เท่านั้น? ก. ใช่ ข. ไม่ใช่ ค. ไม่แน่</p> <p>6. ข้อใดไม่ใช่ประโยชน์ของพื้นที่สีเขียว? ก. ช่วยลดมลพิษทางอากาศ ข. เพิ่มความร่มเย็นในเมือง ค. สร้างรายได้ให้ชุมชน ง. เพิ่มความร่มเย็นในเมือง</p> <p>7. พื้นที่สีเขียวสำคัญต่อสุขภาพจิตของมนุษย์อย่างไร? ก. เป็นพื้นที่พักผ่อนเรียนรู้ ข. ช่วยลดความเครียดและความวิตกกังวล ค. เพิ่มความเมตตา ง. ไม่มีผลต่อสุขภาพจิต</p> <p>8. ข้อใดคือประโยชน์ด้านสังคมของพื้นที่สีเขียว? ก. เป็นพื้นที่ในการทำกิจกรรมร่วมกัน ข. เป็นพื้นที่สร้างรายได้ เช่น ขายของฝาก ค. ลดค่าใช้จ่ายของโรคภัยไข้เจ็บ ง. ไม่มีข้อใดที่เป็นประโยชน์ด้านสังคม</p> <p>9. การจัดการพื้นที่สีเขียวในเมืองควรทำอย่างไร? ก. ปลูกต้นไม้ขนาดใหญ่ให้มากที่สุด ข. ปลูกต้นไม้และพืชพรรณที่เหมาะสม ค. สร้างสิ่งปลูกสร้างในพื้นที่สีเขียว ง. ใช้พื้นที่สีเขียวเป็นที่จอดรถ</p> <p>10. การเพิ่มพื้นที่สีเขียว ควรเป็นหน้าที่ของใคร? ก. หน่วยงานภาครัฐ ข. ชาวบ้านในท้องถิ่น ค. ภาคเอกชนที่มีเงินลงทุน ง. ทุกคนควรช่วยกัน</p> <p>11. พื้นที่สีเขียว ช่วยลดต้นทุนในการควบคุมและเฝ้าระวังทางคาร์บอนได้อย่างไร? ก. สร้างรายได้ให้กับคนในท้องถิ่น ข. ลดค่าใช้จ่ายในการดูแลสุขภาพของเมือง ค. ลดค่าใช้จ่ายในการดูแลสุขภาพของเมือง ง. ลดต้นทุนในการดูแลสุขภาพของเมือง</p> <p>12. โปรดระบุประโยชน์ของพื้นที่สีเขียวเพิ่มเติม </p> | <p>1. ข้อใดคือประโยชน์ด้านสังคมของพื้นที่สีเขียว? ก. เป็นพื้นที่ในการทำกิจกรรมร่วมกัน ข. เป็นพื้นที่สร้างรายได้ เช่น ขายของฝาก ค. ลดค่าใช้จ่ายของโรคภัยไข้เจ็บ ง. ไม่มีข้อใดที่เป็นประโยชน์ด้านสังคม</p> <p>2. ข้อใดคือประโยชน์ด้านสังคมของพื้นที่สีเขียว? ก. เป็นพื้นที่ในการทำกิจกรรมร่วมกัน ข. เป็นพื้นที่สร้างรายได้ เช่น ขายของฝาก ค. ลดค่าใช้จ่ายของโรคภัยไข้เจ็บ ง. ไม่มีข้อใดที่เป็นประโยชน์ด้านสังคม</p> <p>3. ข้อใดคือประโยชน์ด้านสังคมของพื้นที่สีเขียว? ก. เป็นพื้นที่ในการทำกิจกรรมร่วมกัน ข. เป็นพื้นที่สร้างรายได้ เช่น ขายของฝาก ค. ลดค่าใช้จ่ายของโรคภัยไข้เจ็บ ง. ไม่มีข้อใดที่เป็นประโยชน์ด้านสังคม</p> <p>4. ข้อใดคือประโยชน์ด้านสังคมของพื้นที่สีเขียว? ก. เป็นพื้นที่ในการทำกิจกรรมร่วมกัน ข. เป็นพื้นที่สร้างรายได้ เช่น ขายของฝาก ค. ลดค่าใช้จ่ายของโรคภัยไข้เจ็บ ง. ไม่มีข้อใดที่เป็นประโยชน์ด้านสังคม</p> <p>5. ข้อใดคือประโยชน์ด้านสังคมของพื้นที่สีเขียว? ก. เป็นพื้นที่ในการทำกิจกรรมร่วมกัน ข. เป็นพื้นที่สร้างรายได้ เช่น ขายของฝาก ค. ลดค่าใช้จ่ายของโรคภัยไข้เจ็บ ง. ไม่มีข้อใดที่เป็นประโยชน์ด้านสังคม</p> <p>6. ข้อใดคือประโยชน์ด้านสังคมของพื้นที่สีเขียว? ก. เป็นพื้นที่ในการทำกิจกรรมร่วมกัน ข. เป็นพื้นที่สร้างรายได้ เช่น ขายของฝาก ค. ลดค่าใช้จ่ายของโรคภัยไข้เจ็บ ง. ไม่มีข้อใดที่เป็นประโยชน์ด้านสังคม</p> <p>7. ข้อใดคือประโยชน์ด้านสังคมของพื้นที่สีเขียว? ก. เป็นพื้นที่ในการทำกิจกรรมร่วมกัน ข. เป็นพื้นที่สร้างรายได้ เช่น ขายของฝาก ค. ลดค่าใช้จ่ายของโรคภัยไข้เจ็บ ง. ไม่มีข้อใดที่เป็นประโยชน์ด้านสังคม</p> <p>8. ข้อใดคือประโยชน์ด้านสังคมของพื้นที่สีเขียว? ก. เป็นพื้นที่ในการทำกิจกรรมร่วมกัน ข. เป็นพื้นที่สร้างรายได้ เช่น ขายของฝาก ค. ลดค่าใช้จ่ายของโรคภัยไข้เจ็บ ง. ไม่มีข้อใดที่เป็นประโยชน์ด้านสังคม</p> <p>9. ข้อใดคือประโยชน์ด้านสังคมของพื้นที่สีเขียว? ก. เป็นพื้นที่ในการทำกิจกรรมร่วมกัน ข. เป็นพื้นที่สร้างรายได้ เช่น ขายของฝาก ค. ลดค่าใช้จ่ายของโรคภัยไข้เจ็บ ง. ไม่มีข้อใดที่เป็นประโยชน์ด้านสังคม</p> <p>10. ข้อใดคือประโยชน์ด้านสังคมของพื้นที่สีเขียว? ก. เป็นพื้นที่ในการทำกิจกรรมร่วมกัน ข. เป็นพื้นที่สร้างรายได้ เช่น ขายของฝาก ค. ลดค่าใช้จ่ายของโรคภัยไข้เจ็บ ง. ไม่มีข้อใดที่เป็นประโยชน์ด้านสังคม</p> <p>11. ข้อใดคือประโยชน์ด้านสังคมของพื้นที่สีเขียว? ก. เป็นพื้นที่ในการทำกิจกรรมร่วมกัน ข. เป็นพื้นที่สร้างรายได้ เช่น ขายของฝาก ค. ลดค่าใช้จ่ายของโรคภัยไข้เจ็บ ง. ไม่มีข้อใดที่เป็นประโยชน์ด้านสังคม</p> <p>12. ข้อใดคือประโยชน์ด้านสังคมของพื้นที่สีเขียว? ก. เป็นพื้นที่ในการทำกิจกรรมร่วมกัน ข. เป็นพื้นที่สร้างรายได้ เช่น ขายของฝาก ค. ลดค่าใช้จ่ายของโรคภัยไข้เจ็บ ง. ไม่มีข้อใดที่เป็นประโยชน์ด้านสังคม</p> |

Figure 4.

Assessment forms; left. pretest; right. posttest

- Assign player numbers 1-9 based on seating order. Distribute player code tags A and B, along with writing boards and data recording sheets



4. Complete a 5-minute pretest, then distribute game material set to each player
5. The game leader explains materials, rules, individual and community goals, and game steps. Allow time for questions
6. Players agree on three desired co-benefits from green spaces by selecting three co-benefit cards
7. Begin Round 1 under normal scenario
8. Allow 3 minutes for players to plan green space purchases (fill out order forms) and discuss collaborative development strategies
9. Player 1 (Teacher) submits the order form to the bank, purchases green space pictograms, and places them on the game board. Players 2-7 follow in order
10. Player 8 (Bird) places bird tokens on green spaces according to birds' condition card.
11. Player 9 (Environmentalism) records bird names and their benefits on the record sheet
12. Players consult to organize two activities. Participants pay a cost of 1,000 and place their players' tokens on the organizing area. Organizers read knowledge cards and provide certificates to participants who attend the activities
13. Game leader takes photos of the board from different dimensions for further analysis.
14. Players return their representative tokens to their own areas
15. Players place carbon beads on green spaces to represent carbon absorption by green space. Game leader takes photos again
16. The bank (a gaming assistant) distributes income to each player, ending Round 1
17. Start Round 2 by pouring carbon beads into a clear container to show carbon emission and accumulation in the atmosphere. This will be used for debriefing again
18. Game leader announces second and third scenarios
19. Distribute new carbon beads to represent emissions and place non-timber forest products in community forests
20. Repeat steps 6-14 to complete Round 2. Continue Round 3 with another 2 scenarios, if time is available
21. Pour carbon beads into another clear container to show Round 2 emissions.
22. Players complete the posttest within 5 minutes
23. Game leader conducts a debriefing session to summarize learnings, including:
 - Allowing players to observe the other group's game board, highlighting differences in green space construction and their decision-making strategies to achieve the individual and collective goals
 - Summarize carbon dioxide emission by displaying containers accumulated with orange beads from different rounds. Show temperature change graphs from the Excel file, reflecting the relationship between carbon emissions and the community's green space absorption capacity. Explain that effective green space management helps reduce atmospheric carbon
 - Summarize biodiversity outcomes, emphasizing that birds in this game serve as indicators of green space health. Explain that degraded or insufficient green spaces negatively impact bird habitats, leading to reduced biodiversity
24. Game leader conducts a group discussion and question/answer sessions to ensure the achievement of gaming goals. Moreover, a brainstorming session will be conducted to collectively determine the desired co-benefits from the greenspace to be established in the community and to co-design a pilot site to support green space creation.

Preliminary testing results

The preliminary results revealed that after the game leader explained the objectives, materials, and individual and collective goals, players understood various components,

including green space representative pictograms, information sheets, pictogram ordering form, and usage of data recording sheet. Players were able to play the game, but some assistance between players was observed due to varying details between players, with some grasping concepts slower than others. Nevertheless, players successfully collaborated to create green spaces, achieving both community and personal goals. The atmosphere and game results are shown in Figure 5. Many players interested to invest in “community economic,” “striped”, and “public utility” green space types, respectively because of their provided co-benefits can support the common goals.

The suggestion to improve had emerged from the group discussion session as follows:

1. The game board and green space image sizes were appropriate for 9-10 players. The representative pictograms and text detailing green spaces were adequately sized.
2. The green space detail tables and order forms were suitably sized, but suggestions were made to improve the method of inputting numbers and calculating total costs to expedite player calculations.
3. The information sheets providing knowledge to players were too lengthy, potentially distracting villagers, who are actual players, from reading. Therefore, content should be reduced, and methods to stimulate interest among other players should be devised.
4. Computer-based income calculation was a time-consuming step, as data from all players needed to be collected. For actual use, additional assistants should be employed to share data entry tasks, and online forms should be created to distribute data input.
5. Playing three rounds (3 scenarios: normal, tourist influx, and global warming) took approximately 2 hours. For actual use, steps for explaining details may need to be condensed if time is really limited.
6. The debriefing phase is crucial for gaming and simulation session¹⁹, as players may not have time to digest all the information during gameplay. This game used various Excel graphs for debriefing, which provided clear visuals but may lack the content continuity as prepared slides. Therefore, a checklist of debriefing topics should be created to ensure comprehensive coverage.



Figure 5.

The atmosphere and examples of game results

Conclusion:

This research aims to create a gaming and simulation tool to facilitate shared learning among players about green space types and co-benefits provided by green spaces, as well as to support participatory design and planning to increase public green spaces. The “Coco green space: Co-design for co-benefits” game was created with supporting materials. From the testing session, it was found that the game can be used according to the intended objectives. The next step of the research, the researcher will take into account the suggestion from students to improve the “Coco green space: Co-design for co-benefits” game features, such as improve record sheet details for easier cost calculation, reduce information in the knowledge sheet, improve computer input steps, and prepare debriefing slides for time controlling. After improving, the game will be used with representatives from Khung Bang Kachao community (consisting of 6 sub-districts: Song Kanong, Bang Krasob, Bang Kobua, Bang Kachao, Bang Nam Phueng, and Bang Yo, which are relatively high-quality green spaces), and the Laem Chabang Municipality, which is an industrial area where it is difficult to increase green spaces. The aims are to facilitate local participants to understand the co-benefits provided by greenspaces and co-identify a pilot site to establish or improve a good quality and quantity green space. If we can make government officials and community members understand the importance of green spaces and agree upon the increasing of green spaces in the area, it will create a learning tool about green spaces that can be applied in other areas and can be applied in teaching and learning in related subjects.

Acknowledgements: The authors extend their gratitude to participants from Kung Bang Kachao and Laem Chabang Municipality for essential data to design the game. Additionally, the authors acknowledge the gaming assistants for their time and suggestions. This research is supported by the Deutsche Gesellschaft für Internationale Zusammenarbeit (GIZ) GmbH, and Center of Learning Network for the Region, Chulalongkorn University.

References:

1. McKinney ML. *Urban Ecosyst.* 2008;11:161–176.
2. Junior DPM, Bueno C, and da Silva CM. *Bull Environ Contam Toxicol.* 2022;108:108:1–7.
3. Cui L, and Shi J. *Urban Clim.* 2012;2:1–15.
4. Zhou H, Liu Y, and He M. *Int J Environ Res Public Health.* 2022;19:10360.
5. Office of the National Economic and Social Development Council (NESDC). *20 Years National Strategy 2018 - 2037.* 2018;1–68.
6. Office of Natural Resource and Environmental Policy and Planning (ONEP). Ministry of Natural Resources and Environment. 2015;1–82.
7. Zhang Y, Van den Berg AE, Van Dijk T, and Weitzkamp G. *Int J Environ Res Public Health.* 2017;14:535.
8. Chambers JM, Wyborn C, Ryan ME, Reid RS, Riechers M, Serban A, ... and Pickering T. *Sustainability.* 2021;4:983–996.
9. Tan CKW, and Nurul-Asna H. *Integr Conserv.* 2023;2:19–42.
10. Voinov A, Jenni K, Gray S, Kolagani N, Glynn PD, Bommel P, ... and Smajgl A. *Environ Model Softw.* 2018;109:232–255.
11. Etienne M. *Companion modelling: A participatory approach to support sustainable development.* Avignon (France): Quæ and Springer;2014.
12. Crookall D, and Thorngate W. *Simul Gaming.* 2009;40:8–26.
13. Phoomirat R, Akkapihat J, and Dumrongrojwattana P. *Transl Syst Sci.* 2019;191–199.
14. Menconi ME, Tasso S, Santinelli M, and Grohmann D. *Eval Program Plann.* 2020;79:101741.
15. Pombo L, Marques MM, Carlos V, Guerra C, Lucas M, and Loureiro MJ. *Smart Innov Syst Technol.* 2017;90–100.
16. Kornhauser D, Wilensky U, and Rand W. *J Artif Soc Soc Simul.* 2009;12:1.
17. Williams BK. *J Environ Manage.* 2011;92:1346–1353.
18. Lee N. *Encyclopedia of Computer Graphics and Games.* Los Angeles(USA): Springer International Publishing;2018.
19. Crookall D. *Simul Gaming.* 2010;41:898–920.



INHIBITION OF *Staphylococcus aureus* HEMOLYTIC ACTIVITY IN A DOSE-DEPENDENT MANNER BY *Enterococcus faecalis* R3

Natchaya Pakdeesiriwong¹, Sainamthip Rangdist¹, Ekkasit Kanklang¹, Chompunoot Wangboon¹, Watsana Penkhruue¹, Sirilak Chumkiew², Mantana Jamklang^{1,*}

¹School of Preclinical Sciences, Institute of Science, Suranaree University of Technology, Nakhon Ratchasima 30000, Thailand

²School of Biology, Institute of Science, Suranaree University of Technology, Nakhon Ratchasima 30000, Thailand

*e-mail: mjamklang@sut.ac.th

Abstract:

Various virulence factors that contribute to *S. aureus* infection and its virulence have been a topic of increasing attention. This pathogen can cause cell lysis and tissue damage through alpha-hemolysin (α -hemolysin). Targeting its virulence factors can be an effective strategy to combat infections and provide novel alternatives to conventional antibiotics. Our previous studies found that *Enterococcus faecalis* strain R3 exhibited a positive result in the reverse-CAMP test, demonstrating attenuation of *S. aureus* hemolysis. The aim of this study was to investigate the influence of the supernatant of *E. faecalis* strain R3 (EFR3) on factors contributing to the pathogenicity of *S. aureus*, including hemolysis and cytotoxicity. The co-culture method was used to confirm the activity of enterococcal effector molecules. The results demonstrated that EFR3, in the presence of *S. aureus* supernatants at a concentration of 1:10, most significantly reduced hemolytic activity, indicating that the attenuation of *S. aureus* hemolysin occurs in a dose-dependent manner. Then, the effects of *S. aureus* supernatant from *S. aureus* culture on OUMS-36 cell viability were investigated after treatment with EFR3. The survival rate of fibroblast cells infected with *S. aureus* did not significantly differ when EFR3 was added to the fibroblast cell cultures. Accordingly, *E. faecalis* strain R3 will be further examined as a potential effective inhibitor of hemolysin. Future investigations will assess whether the attenuation of *S. aureus* hemolytic activity by enterococcal effector molecules correlates with a reduction in α -hemolysin gene (*Hla*) expression. Our research aims to contribute to the development of antivirulence medications for *S. aureus* infections.

Introduction:

Staphylococcus aureus (*S. aureus*), a Gram-positive coccus bacterium that forms clusters, can exhibit both pathogenic and non-pathogenic behavior. It commonly inhabits the skin and mucous membranes of humans and other mammals, facilitating its transmission and contributing to a range of skin and soft tissue infections due to its widespread presence¹. Infections caused by pathogenic *S. aureus* often lead to the formation of abscesses, localized pus-producing lesions, and the production of various toxins. These virulence factors enable the development of a range of infections, from superficial skin conditions to severe, life-threatening diseases². The bacterial exoproducts released by *S. aureus* include several toxins and enzymes, such as Toxic Shock Syndrome Toxin (TSST), which functions as a superantigen to activate complex molecular pathways; enterotoxins, which are a major concern for food-borne illnesses and hemolysins, which lyse red blood cells (RBCs) and cause hemolysis³. Among these exotoxins, polypeptides that damage the host cell plasma membrane, such as pore-forming toxins like α -hemolysin, are particularly significant. Alpha-

hemolysin is a major cytotoxin of *S. aureus*, contributing to severe infections by destroying host cells, including RBCs, and causing hemolysis. This toxin is crucial as it leads to disturbances in hemostasis, thrombocytopenia, and pulmonary lesions. Non-pathogenic strains of *Enterococcus* spp., which are Gram-positive cocci arranged in chains, have been effectively utilized as probiotics to promote health in both humans and animals. These bacteria are commonly found in various environments, including the human gastrointestinal tract⁵. *Enterococcus* species produce and secrete compounds that facilitate cell communication and inhibit competitive bacteria within ecological niches such as the gut and oral cavity. One notable type of compound is bacteriocins, which are antimicrobial peptides that help suppress the growth of other bacteria⁶.

Our previous research, using a reverse CAMP test, identified that *E. faecalis* strain R3 can inhibit the hemolytic activity of *S. aureus*. In this study, we aimed to further investigate the efficacy of *E. faecalis* strain R3 in reducing hemolytic activity through co-culture experiments with various concentrations of *S. aureus* supernatant. Additionally, we evaluated the ability of EFR3 to mitigate the cytotoxic effects of *S. aureus* supernatants on normal cells using cytotoxicity assays. The findings from our study validated the properties of the effector molecules produced by *E. faecalis* strain R3. These molecules have the potential to be developed into therapeutic agents for mitigating the severity of both systemic and localized infections caused by *S. aureus*.

Methodology:

Bacterial strains and cell lines

The bacterial strains used in this study include *S. aureus* ATCC 25923, sourced from the American Type Culture Collection (ATCC, USA), as well as *E. faecium* and *E. faecalis* strain R3, which were obtained from our previous research. The bacterial isolates were cultured in tryptic soy broth at 37°C for 18-24 hours before conducting all experiments.

In this experiment, we utilized the human fibroblast cell line OUMS-36, purchased from the Japanese Collection of Research Bioresources (JCRB, Japan) provided by Assoc. Prof. Dr. Pathanin Chantree (Thammasat University, Thailand). The cell lines were maintained in Dulbecco's Modified Eagle's Medium (DMEM) supplemented with 10% fetal bovine serum (FBS) (Gibco, NY, USA) and 1% penicillin/streptomycin (Gibco, NY, USA).

Microorganism culture for bacterial supernatants

The bacterial strains (*S. aureus* ATCC 25923, *E. faecium*, and *E. faecalis* strain R3) were initially cultured from -80°C glycerol stocks on tryptic soy agar (TSA). Fresh single colonies were inoculated into tryptic soy broth (TSB) and cultured at 37°C with aeration, achieved by incubating in tubes or flasks with a capacity at least four times the volume of the medium, and vigorous shaking at 200 rpm on an orbital shaker. Overnight cultures were diluted 1:100 in fresh TSB and incubated until reaching the post-exponential growth phase (OD₆₀₀ of 2.5) for all experiments. After incubation, cells were harvested by centrifugation, and the supernatants containing the effector molecules were isolated by filtration through a 0.2 µm filter (MilliporeSigma, Germany).

Screening of EFR3 for anti-hemolytic activity using the co-incubation method

The ability to inhibit hemolysis was assessed using a hemolysis assay. Supernatants from *E. faecium*, *E. faecalis* strain R3, and *S. aureus* were prepared, as effector molecules may be secreted into the culture media. After harvesting the bacterial cells by centrifugation and filtering the supernatants, *S. aureus* supernatants were diluted 10-fold to achieve concentrations of 1, 1:10, 1:100, and 1:1000. Subsequently, 500 µL of *E. faecium* supernatants (EFC) and EFR3 were combined with 500 µL of each concentration of *S. aureus*



supernatants. Red blood cells, prepared by centrifugation and washing three times in phosphate-buffered saline (PBS), were mixed with 30 μ L of the supernatant solutions and incubated at 37°C for 1 hour. After incubation, the mixtures were centrifuged, and the supernatants were collected for analysis of red blood cell lysis. Hemolysis was quantified by measuring the OD₅₄₃ of the supernatants using a spectrophotometer and compared to the positive control (*S. aureus* supernatants alone).

Cytotoxicity evaluation of EFR3 with OUMS-36 cells by S. aureus supernatant infection

The MTT assay was employed to evaluate the impact of EFR3 on the survival of fibroblast cells exposed to *S. aureus*-induced injury. This assay relies on the activity of NAD(P)H-dependent oxidoreductase enzymes in viable cells, which reduce the yellow tetrazolium salt, 3-(4,5-dimethylthiazol-2-yl)-2,5-diphenyltetrazolium bromide (MTT), to a purple formazan product. Initially, *S. aureus* was cultured to the post-exponential growth phase (OD₆₀₀ of 2.5) in TSB. Following centrifugation of the bacterial culture, the supernatants were combined with EFR3 solutions to achieve final concentrations of 50%. Fibroblast cells were cultured until they reached 80% confluence. The fibroblast cells were washed three times with PBS and then seeded into 96-well plates, followed by incubation for 24 hours. The cell medium was subsequently replaced with DMEM containing either *S. aureus* supernatants alone, a combination of *S. aureus* supernatants with previously prepared EFR3, or medium without *S. aureus* supernatants, with TSB serving as a control. Cell viability at 48 hours post-treatment was assessed using the MTT assay. MTT solution (0.5 mg/mL) was added to each well and incubated for 3 hours. Following incubation, the medium was removed, and formazan crystals were dissolved in dimethyl sulfoxide (DMSO). Absorbance at 562 nm was measured using a microplate reader (Thermo Scientific, USA). The percentage of cell viability was calculated by normalizing the absorbance data to that of untreated control cells, which were considered to have 100% viability. Statistical significance between groups was determined using a paired t-test.

Results and Discussion:

Staphylococcus aureus (*S. aureus*) is an opportunistic pathogen that primarily colonizes the mucous membranes of the human nasopharynx and skin. It can either persist as a part of the normal flora or exist transiently in these environments¹. Infections usually spread through direct contact with the skin and its surrounding structures. Skin infections caused by *S. aureus* often start with the invasion of the hair follicle, epidermis, and dermis. If the infection progresses and spreads to nearby areas, it can extend into deeper muscle tissues, leading to pyomyositis. The virulence factors associated with *S. aureus* infection and its overall virulence have been a major focus of research. This pathogen can cause cell lysis and tissue damage, such as lysing red blood cells and inducing hemolysis, with α -hemolysin directly disrupting the membranes of host cells.

Our previous study discovered that only the *E. faecalis* species isolated from human feces demonstrated a species-specific ability to reduce the hemolysis caused by *S. aureus*, as shown using the reverse CAMP test. In this study, we used a co-incubation method to further investigate the effect of the *E. faecalis* strain R3 on blood hemolysis, focusing on its impact on the hemolysins secreted by *S. aureus*. The *S. aureus* supernatants were co-cultured with red blood cells in the presence of either *E. faecalis* strain R3 supernatants (EFR3) or *E. faecium* supernatants (EFC) for 1 hour. The resulting blood hemolysis was then compared to the hemolysis induced by each concentration of *S. aureus* supernatants alone. This is illustrated in **Figure 1**, which shows that the supernatant from *S. aureus* induces a dose-

dependent lysis of red blood cells, resulting in the release of hemoglobin, as evidenced by the red color of the hemoglobin in the supernatant. *S. aureus* supernatants alone served as positive controls to determine if the red blood cells were already affected. However, at a concentration of 1:10, EFR3 was effective in interfering with the hemolysin secreted by *S. aureus* (**Figure 1D**). The absorbance of hemoglobin released into the supernatant was measured using a spectrophotometer. Quantitative analysis revealed that treatment with EFR3 in the presence of *S. aureus* supernatants at a concentration of 1:10 most significantly reduced hemolytic activity, as shown in **Figure 2**. This result is attributed to EFR3's ability to reduce red blood cell lysis, as evidenced by the lower color intensity of hemoglobin when red blood cells were incubated with *S. aureus* supernatant alone. This finding is consistent with previous observations that *E. faecalis* MN1 supernatant can inhibit the superantigen toxic shock syndrome toxin-1 produced by *S. aureus*⁷.

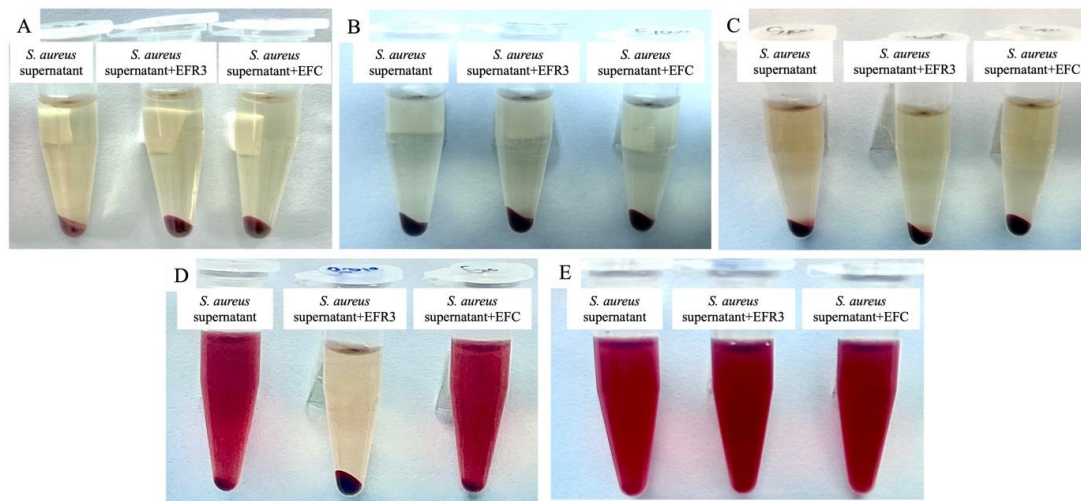


Figure 1 Treatment of red blood cells with EFR3 and various concentrations of *S. aureus* supernatant resulted in a reduction of blood hemolysis at the following concentrations: 0 (A), 1:1000 (B), 1:100 (C), 1:10 (D), and 1 (E).

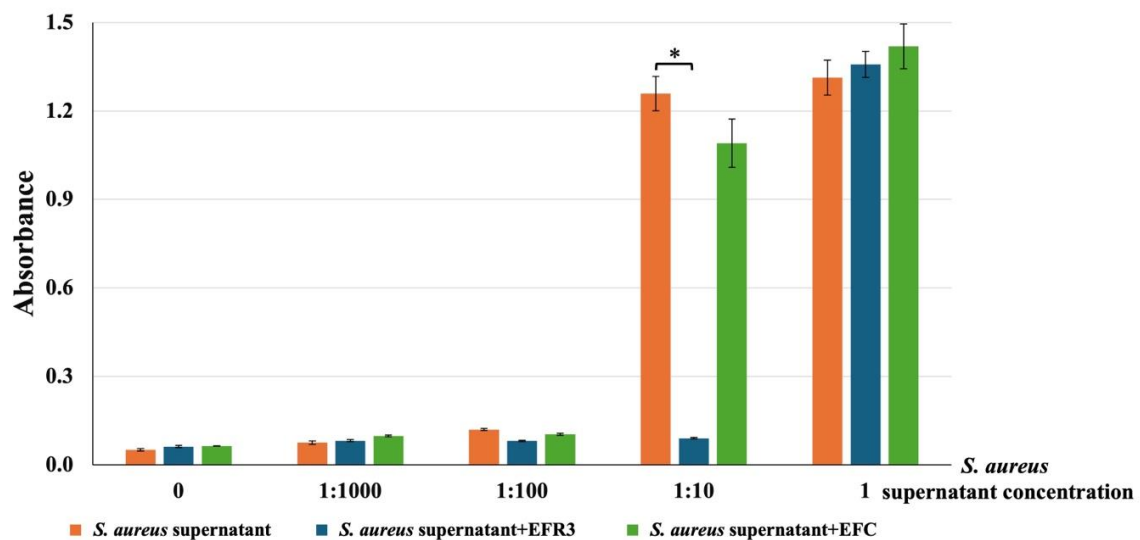


Figure 2 The effect of EFR3 in reducing the hemolytic activity of *S. aureus* was evident, as indicated by the attenuated release of hemoglobin in the supernatant, as measured by the



spectrophotometer. The data are represented as mean \pm SD. *Statistically significant differences between the two groups, $p < 0.05$, compared to the effect induced by each concentration of *S. aureus* supernatant.

This suggests that *E. faecalis* secretes exoproduct molecules, specifically EFR3, which have the capability to interfere with *S. aureus* infection. To examine EFR3's capability to mitigate the effect of *S. aureus* supernatant on normal cells, a cytotoxicity test was conducted. In our study, we used OUMS-36, a fibroblast cell line, as the normal cell control. The effects of *S. aureus* supernatant from *S. aureus* culture on OUMS-36 cell viability were investigated after treatment with EFR3 for 48 hours at 37°C. Cytotoxicity was analyzed by measuring absorption at 562 nm in the MTT assay (**Figure 3**).

Cell viability was significantly reduced in OUMS-36 cells exposed to *S. aureus* supernatant ($p < 0.05$), indicating that *S. aureus* supernatant inhibits cell viability. However, there was no significant difference ($p > 0.05$) in cell viability between EFR3-treated and untreated cells, suggesting that EFR3 did not alter the effect of *S. aureus* supernatant on cell viability. The cell viability of OUMS-36 cells was $77.59 \pm 3.3\%$ when exposed to *S. aureus* supernatant and $81.27 \pm 2.2\%$ when treated with EFR3 in the presence of *S. aureus* supernatant. These results indicate that the reduction in hemolytic activity observed with EFR3 was not attributable to damage to OUMS-36 cells, even at a 50% concentration of EFR3.

Similar findings were reported by Zhu Cheng in 2013⁸, which demonstrated that experimental groups treated with higher concentrations of methicillin-resistant *S. aureus* (MRSA) supernatant consistently had a lower number of cells compared to groups treated with equivalent or lower concentrations. This observation was statistically significant, demonstrating a dose-dependent effect of MRSA supernatant on cell numbers. It suggests that lower concentrations of *S. aureus* supernatant may affect cell viability differently than EFR3 supernatant. Additionally, a previous study by Brosnahan et al., (2013)⁷ reported that *E. faecalis* MN1 supernatant, concentrated 480-fold relative to the original culture, inhibits interleukin-8 production induced by superantigen toxic shock syndrome toxin-1. This indicates that higher concentrations of EFR3 might also influence cell viability in comparison to *S. aureus* supernatant. Consequently, further research into varying concentrations of EFR3 and *S. aureus* supernatant could shed light on their differential effects on cell viability differential effects on the viability of OUMS-36 cells.

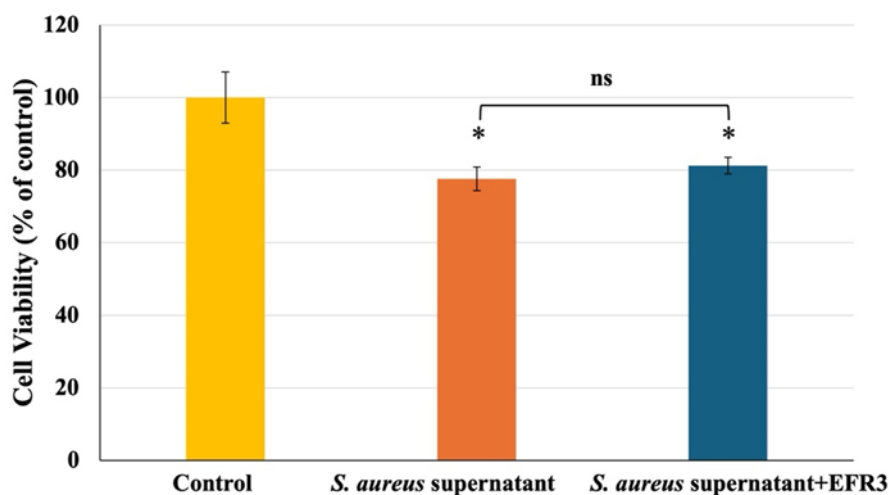


Figure 3 The effect of EFR3 on enhancing the viability of OUMS-36 cells infected with *S. aureus* supernatant is comparable to the effect observed with treatment using *S. aureus* supernatant alone. Data are presented as means \pm SD, with "ns" indicating not significant ($p > 0.05$), whereas an asterisk (*) indicates statistically significant differences compared to the control (untreated cells) ($p < 0.05$).

Conclusion:

In this study, the cell-free supernatant produced by *Enterococcus faecalis* strain R3 (EFR3) demonstrated the capacity to inhibit *S. aureus* hemolysin. The results indicate that the presence of *S. aureus* supernatant at a concentration of 1:10 significantly reduced hemolytic activity. However, when evaluating the cytotoxic effects of *S. aureus* supernatant on OUMS-36 cells after treatment with EFR3, no significant difference in cell damage was observed at a 50% concentration of EFR3. Further investigation should examine the role of EFR3 in the expression of the virulence gene *Hla*, which encodes alpha-hemolysin.

Acknowledgements:

This work was supported by the Center of Excellence (CoE) in Advanced Functional Materials, Suranaree University of Technology. We heartily thank Assoc. Prof. Dr. Pathanin Chantree for providing the human fibroblast cell line OUMS-36. We also wish to express our gratitude to the School of Preclinical Sciences at Suranaree University of Technology, Thailand, for offering the necessary research facilities. Lastly, I am deeply grateful for the generous support from the Development and Promotion of Science and Technology Talents Project (DPST) Scholarship.

References:

1. Linz MS, Mattappallil A, Finkel D, and Parker, D. Antibiotics. 2023;12(3), 557.
2. Balasubramanian D, Harper L, Shopsin B, Torres VJ. Pathog Dis. 2017; 75(1).
3. Otto, M. (2014). Staphylococcus aureus toxins. Curr. Opin. Microbiol. 17, 32–37.
4. Ortines RV, Liu H, Cheng LI, Cohen TS, Lawlor H, Gami A, Miller LS. Antimicrob Agents Chemother. 2018; 62(3), e02288-17.
5. Riaz A, Noureen S, Qamar MF, Liaqat I, Arshad M, Arsha NJ Pak Vet J. 2018; 10
6. Franz CM, Huch M, Abriouel H, Holzapfel W, Gálvez AJ. Int J Food Microbiol. 2011;151(2): 125-140.
7. Brosnahan AJ, Merriman JA, Salgado-Pabón W, Ford B, Schlievert PM. PLoS One. 2013; 8(4), e61255.
8. Zhu C, Qin, H, Cheng T, Tan HL, Guo YY, Shi SF, Zhang XL. Int J Mol Med. 2013;31(6), 1484-1494.



MODIFIED PACKAGING PLASMIDS FOR INTEGRASE-DEFICIENT LENTIVIRAL TRANSFECTION.

Rachan Pangnuchar¹, Suparat K Lithanatudom², Natnapa Jaitan¹, Pathrapol Lithanatudom^{1*}

¹Department of Biology, Faculty of Science, Chiang Mai University, Chiang Mai, Thailand

²Program in Genetics, Faculty of Science, Maejo University, Chiang Mai, Thailand

*e-mail: pathrapol.l@cmu.ac.th

Abstract:

Genetic engineering techniques have been used as tools for studying various cellular processes. Introducing foreign DNA into host cells using plasmids can be accomplished through various methods, such as lipofection, electroporation, nucleofection, and viral transduction. While transduction *via* viral particles can be more efficient than other physical methods, there are significant concerns, particularly the risk of viral DNA integrating into the host genome, which could lead to mutations and the development of diseases.

In this project, we aimed to develop a packaging plasmid with integrase defects for viral transfection, including mutations in the *Pol* gene that result in the inability to integrate viral DNA into the host genome. The psPAX2 plasmid was mutated at aspartic acid 116 (D116) in the integrase sequence to reduce the integration activity of the lentiviral system. Interestingly, nine positive clones were successfully constructed, and sequencing results showed that two clones contained only the D116N mutation site as designed, while the other seven clones had D116N and additional missense mutations at various locations on the integrase sequence. The recombinant plasmid constructed in this project will be further used to evaluate integrase defects using various techniques. The non-integrating lentiviral system may lead to promising methods for safer gene therapy, avoiding the risks of insertional mutagenesis in the future.

Introduction:

Gene therapy involves the modification or correction of mutated genes to cure or prevent diseases without relying on drugs or surgery. This approach shows promise for treating various conditions caused by inherited genetic disorders, such as hemophilia, muscular dystrophy, thalassemia, and sickle cell anemia, as well as acquired genetic diseases such as cancer and certain viral infections [1, 2]. Gene delivery systems, which introduce selected genes into target cells, are crucial for effective gene therapy, as a reliable gene delivery system is essential for success [3]. The process of introducing foreign nucleic acids into eukaryotic cells is called transfection. Transfection methods can generally be categorized into viral-based and non-viral-based method. Ongoing efforts are focused on developing more efficient and safer gene delivery systems for advanced gene therapy [4, 5].

Viral-based transfection uses viral vectors as vehicles to deliver genetic information into the target cells. Research and development efforts have focused on creating vectors with high efficiency, low genotoxicity, and minimal immunogenicity. Among these, adeno-associated virus (AAV) and lentivirus-based vectors have gained significant attention due to their promising clinical outcomes. AAV vectors offer strong potential for *in vivo* genetic information delivery because they integrate into host genome at low-level. However, AAV vectors have relatively low efficiency. Whereas lentiviral vectors are more efficiency, but there are concerns about their ability to integrate into the host genome [6]. Lentiviral vectors have been developed since 1980s [7]. Based on HIV-1, the most widely used lentiviral vectors

have been developed for three generations. After years of development to improve safety, the third-generation plasmid was created by removing *Rev* gene from the transfer plasmid and replacing it on a fourth plasmid, as well as eliminating U3 on the 3' LTR to create a self-inactivating transfer vector [8, 9]. To produce a viral vector, three types of plasmids are required: 1) a packaging plasmid that codes for all necessary viral proteins for viral particle formation and delivery of the transgene into target cells, 2) an envelope plasmid that codes for a glycoprotein, enabling target cells recognition, and 3) a transfer vector plasmid that carries the transgene of interest. The packaging plasmid codes for all necessary viral proteins for particle formation and transgene delivery, including the Gag polyprotein (a structural protein) and Pol polyprotein (an enzymatic protein). Pol includes viral protease, which cleaves polyproteins to allow viral particle maturation, and reverse transcriptase (RT), which reverse transcribes the RNA genome into double-stranded DNA. This genetic material can then be integrated into the target cell genome by the viral integrase protein [10].

Duo to the risk of insertional mutagenesis with viral vectors, efforts have been made to mitigate this effect, leading to the development of integrase-defective lentiviral vector through various methods [11]. Several approaches can impair the integration ability of lentiviral vector, with one of the most effective being the generation of mutated virus strains, such as replacing the standard *Gag/Pol* packaging plasmid with an integrase-mutant (*IN*-mutant). There are many studies that have introduced specific mutations in the amino acids of integrase to produce strains with integrase-defective capabilities. These mutants enhance biosafety, allowing for advanced clinical applications, as they have very low genomic integration frequencies and pose a much lower risk of insertional mutagenesis and replication-competent retrovirus (RCR) generation than integrating lentivectors [12]. However, it is important to note that integration-deficient lentiviral vectors can still integrate into the host genome, despite being at a very low frequency. Thus, further development of integrase-defective lentiviral vectors that can further reduce or eliminate integration is necessary.

The aim of this project is to create and construct a novel integrase-defective lentiviral vector by developing psPAX2 (Addgene, No. 12260), the packaging plasmid for viral transfection, by introducing mutation at different sites of the integrase protein on the *Pol* gene that disables the insertion of viral DNA into the host genome [11]. The integrase-defective lentiviral vector constructed from this project will be further used to for lentiviral-based gene transfer, offering benefits for therapeutic use and expanding potential clinical applications. This could potentially lead more efficient and safer gene therapy techniques in the future.

Methodology:

Designing of Modified psPAX2 Plasmid.

The plasmid modification design process was completed using Benchling [Biology Software] (2022). Retrieved from <https://benchling.com>. The sequence of the psPAX2 plasmid was downloaded from addgene.com (No.12260) and imported into Benchling. The integrase gene in the HIV-I pol sequence of the psPAX2 plasmid was targeted at aspartic acid (D) at amino acid position 116. The target was designed to alter GAC (aspartic acid; D) to AAC (asparagine; N) by ligating two modified integrase fragments. The first fragment was amplified with a modified primer at the 3' end, and the second fragment was amplified with a modified primer at the 5' end. These fragments were named PAX-F and PAX-L, respectively. The final ligation product of the two amplified fragments contained the recognition sites for the *Swa*I and *Afl*III restriction enzymes, which flank the aspartic acid (D) at amino acid position 116 of the *Pol* gene in the psPAX2 plasmid.

Plasmid extraction.



The plasmid used for this study was extracted using GF-1 Plasmid DNA Extraction Kit (Vivantis Technologies), following the manufacturer's instructions. Bacteria containing plasmids were cultured in 5 ml of LB medium with 100 µg/ml of ampicillin antibiotic and incubated in shaking incubator at 37°C, 250 rpm for 16-18 hours. A 3 - 4.5 ml aliquot of the culture was harvested in 1.5 ml centrifuge tube by centrifuging at 6,000 g for 2 minutes. The pellet was resuspended by adding 250 µl of resuspend buffer containing RNase, and mixed by vortexing. The resuspended pellet was lysed by adding 250 µl of lysis buffer, gently mixed, and left to stand for 4 minutes at room temperature. The lysate was neutralized by adding 400 µl of neutralization buffer, gently mixed, and centrifuged at 10,000 g for 10 minutes. After the precipitate was spun down, the supernatant was transferred to a column and centrifuged at 10,000 g for 1 minute; the remaining buffer in the column was discarded. The column was washed by adding 650 µl of wash buffer and centrifuged at 10,000 g for 1 minute; the remaining buffer was discarded. The column was centrifuged again at 10,000 g for 1 minute to remove any remaining wash buffer. Then, the column was transferred to a new 1.5 ml microcentrifuge tube, and 50-100 µl of the elution buffer was added. The column was left to stand for 1 minute at room temperature. Finally, the column was centrifuged at 10,000 g for 1 minute then removed from 1.5 ml microcentrifuge tube. The eluted plasmids were evaluated for quantity using spectrophotometers (NanodropTM) and stored at 4°C.

Gene amplification using polymerase chain reaction (PCR).

After acquisition of primer from Benchling, each gene fragment was amplified using the polymerase chain reaction (PCR) method. The amplicons are generated by mixing a master mix containing 1 unit of DNA polymerase, up to 5 ng of template (purified plasmid psPAX2), 0.5 µM of each primer, 5 mM of MgCl₂, 1X of the buffer (as per the polymerase manufacturer's instruction), 100 µM of dNTPs, and the addition of H₂O until the final volume are 50 µl. The reactions were carried out using a thermal cycler. The temperature and elongation time for each primer pair were adjusted based on the size of the amplicon and the melting temperature (T_m) of the primers. The size of each amplicon was verified by using gel electrophoresis with 1-1.5 % agarose gel containing SYBR® Safe DNA Gel Stain and observed the result on the chemical documentation imaging system.

Digestion and Purification of the amplicon and plasmid.

The amplicons containing modified overhangs were digested using *Swa*I and *Afl*III restriction enzymes. The amplicons and plasmids were digested by mixing a master mix containing 1 unit of digestive enzyme, up to 1000 ng of template, 1X of the buffer (according to the digestive enzyme manufacturer's instructions), and H₂O to a final volume are 50 µl. The reactions were performed using thermal cycler. The digested amplicons and plasmids were purified using GF-1 Nucleic Acid Extraction Kits (Vivantis Technologies) following the manufacturer's instructions. The digested product was transferred to the column and centrifuged at 10,000 g for 1 minute, and the remaining buffer was discarded. Each column was washed by adding 650 µl of wash buffer and centrifuged at 10,000 g for 1 minute, the remaining buffer was discarded. The column was centrifuged again at 10,000 g for 1 minute to remove any residual wash buffer. Each column was then transferred to a new 1.5 ml microcentrifuge tube, and 30-50 µl of the elution buffer was added. After allowed the column to stand for 1 minute at room temperature, it was centrifuged at 10,000 g for 1 minute. The purified product was then evaluated for quantity by using spectrophotometers (NanodropTM) and stored at 4°C.

Ligation of the digested product and Transformation

The fragments for ligation were calculated, and the volume of each template and insert fragment was adjusted according to the calculation. The ligation reaction was contained 100 ng of vector, insert in the appropriate proportion, 5% PEG4000, 1X of ligation buffer, 2.5 units of ligation enzyme, and H₂O to a final volume of 50 µl. The reaction was incubated at 16°C for 16 hours. Chemically competent cells (*E. coli* strain Stbl3) stored at -80 °C were thawed on ice for 30 minutes. After thawing, the ligation reaction was added to the competent cells and incubated on ice for 30 minutes. Following this, the competent cells were subjected to a heat shock at 42°C for 90 seconds, then incubated on ice for 5 minutes. LB medium was added to the competent cells, and the mixture was incubated at 37°C for 1 hour in a shaking incubator. After incubation, the transformed cells were spread onto LB agar plate contained 100 µg/ml of ampicillin, and the plates were incubated at 37 °C for 16-18 hours.

Verification of plasmids through colony PCR technique and sequencing

After incubation the transformed competent cells on LB agar plates containing ampicillin, each colony was picked and propagated on the master plates. The master plates were LB agar plates containing ampicillin, each labeled to correspond with a colony on a grid drawn on the plate (approximately 5X5 squares). Each picked colony was cultured within it assigned name and space on the master plates. Once all colonies were picked, the master plates were incubated at 37 °C for 16-18 hours. Verification of each colony on the master plate was performed using colony PCR technique. Firstly, each colony was picked and transferred to a PCR tube containing 5 µl of H₂O. Then, each tube was vortexed for 2 minutes in order to tear the cells wall and release the plasmid. The master mix for the PCR reaction contained 0.5 µM of each primer, 1X polymerase master mix, and H₂O to a final volume of 10 µl. The reactions were carried out using thermal cycler. The temperature and elongation times for each primer pair were adjusted based on the size of amplicon and the T_m of the primers. The size of each amplicon was verified using gel electrophoresis with 1-1.5% of agarose gel containing the SYBR® Safe DNA Gel Stain, and the results were observed using a gel documentation imaging system. The amplification results from the colony PCR were confirmed by sequencing using Sanger method. The sequencing results were imported into BioEdit software [13] for alignment and comparison with the expected sequence.

Results and Discussion:

The psPAX2 plasmid was mutated at aspartic acid 116 (D116) in the integrase sequence to reduce the integration activity of the lentiviral system. Aspartic acid at position 116 is part of the catalytic triad of the integrase protein; thus, changing it from aspartic acid to asparagine (D116N) results in integrase deficiency [14]. This mutation was introduced by altering the bases at two sticky ends, which was achieved through amplification, ligation, and reintroduction of the mutated fragment into the plasmid (Figure 1).

The integrase gene in the HIV-I pol sequence within the psPAX2 plasmid was targeted at aspartic acid (D) at amino acid position 116. The target was designed to alter GAC (aspartic acid; D) to AAC (asparagine; N) by ligating two modified integrase fragments. The first fragment was amplified with a modified primer at the 3' end, and the second fragment was amplified with a modified primer at the 5' end. These fragments were named PAX-F and PAX-L, respectively. The psPAX2-*Swa*I-F and D116N-R primer pair (T_m 55.8 and 51.5 °C, respectively), and the D116N-F and psPAX2-*A*/II-R primer pair (T_m 52.4 and 55.7 °C, respectively) were designed for the amplification of PAX-F and PAX-L, respectively (Table 1). The results from gel electrophoresis showed a major positive band in both PAX-F and PAX-L amplifications, with approximate sizes of 900 bp and 200 bp, respectively (Figure 2A). The optimal conditions for PCR amplification of each primer pair were tested using the



thermostable *Taq* DNA polymerase (HOTFIREPol®) to generate the expected PCR product, while *pfu* DNA polymerase was used for generated the fragment for the ligation reaction. The *pfu* DNA polymerase possesses 3' to 5' exonuclease proofreading activity, preventing mutation in the nucleotide sequence of PCR product at locations other than the D116N site. The PCR amplification successfully produced the target fragment as designed, allowing them to be used in the next step of recombinant plasmid construction.

The transformation of the recombinant plasmid into *Stbl3* competent cells was performed using the heat shock method. Positive clones were selected using ampicillin antibiotics plates, and each colony was propagated individually. Bacterial colony growing on LB plate contained ampicillin antibiotic represent bacteria that successfully transformed the psPAX2 plasmid. Colony PCR was conducted to confirm the insertion of each clone using the psPAX2-*SwaI*-F and psPAX2-*AflIII*-R primer pair (flanking the insert fragment). Gel electrophoresis results from the colony PCR revealed that 9 clones—A1, A3, E1, E3, BA2, BA3, EA2, EB2, and EC3—contained the integrase gene after ligation, producing a PCR product of approximately 1,000 bp (Figure 2B).

Subsequently, recombinant plasmids were extracted from the 9 clones, and the success of recombinant plasmid construction was confirmed by *SwaI* and *AflIII* digestion. The results showed that all 9 clones contained an insert fragment of approximately 1,000 bp (Figure 2C). Sequencing analysis was performed on all 9 positive clones to check for the base substitution at the D116N position in *Pol* gene. Sequencing alignment revealed that 2 of the 9 positive clones (BA2 and EA2) had the expected change from aspartic acid to asparagine at position 116 (D116N), resulting in integrase deficiency as designed. In the remaining 7 positive clones, several missense mutations were detected at various sites, including the D116N site (Figure 3).

In this study we used *pfu* DNA polymerase to amplify the designed insert fragment due to its 3' to 5' exonuclease proofreading activity, which reduces the mutation rate during PCR amplification. Although *Pfu* DNA polymerase exhibits high PCR fidelity, previous studied have shown that thermostable DNA polymerases still generate an average error rate of 1.3×10^{-6} mutation frequency/bp/duplication [15], which explains the mutations detected in 7 of the positive clones. However, we successfully constructed two recombinant plasmids in this study, which will be further used to evaluate the effects of the D116N mutation and other missense mutation sites on integrase activity, using assays such as the reverse transcriptase assay, colorimetric assay, or HIV-1 p24 ELISA. This result may provide new information on the level of integrase activity between the psPAX2 containing only the D116N mutation and those containing the D116N mutation along with other mutations.

The recombinant plasmid constructed in this project will be further used as the packing plasmid, combined with other plasmids required for viral vector production. This can be applied in various viral-based gene transfer applications such as cell biological research, gene editing technologies (e.g., CRISPR/Cas9) and gene therapy [16, 17].

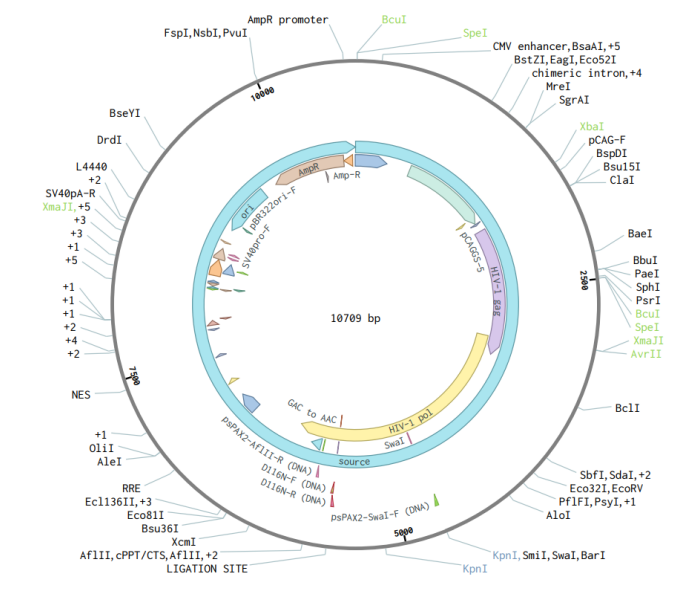


Figure 1.
Plasmid map of the integrase-defective packaging plasmid for the lentiviral vector.

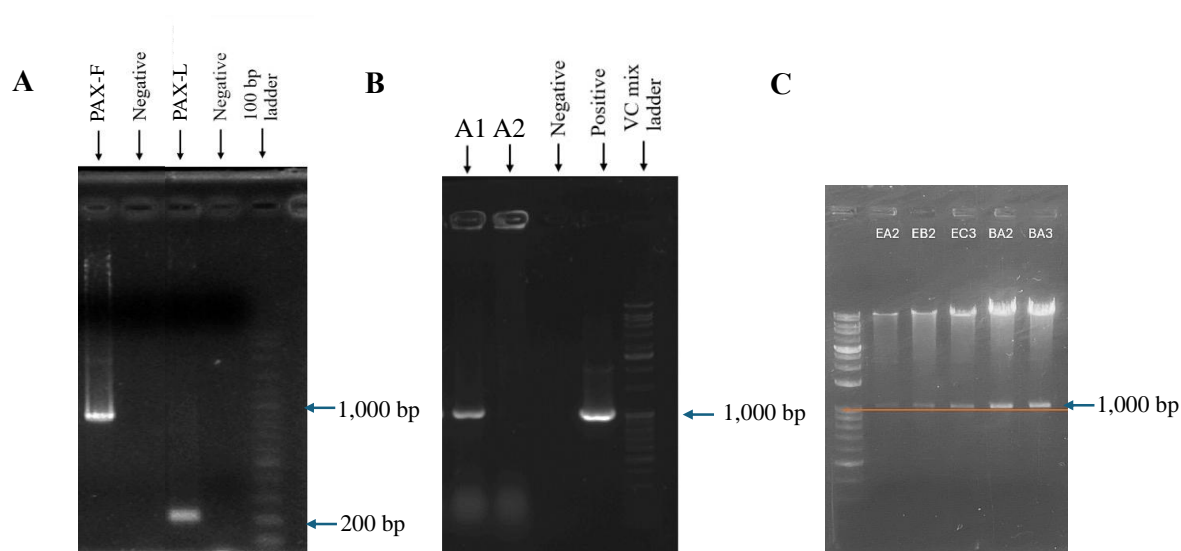


Figure 2.
Gel electrophoresis results from (A) PCR product of PAX-F and PAX-L, (B) colony PCR on psPAX-D116N clone A1 and A1, and (C) *Swa*I and *A*/III restriction enzyme cut check.

**Table 1.**

| Primer name | Sequence (5' to 3') | Product size (bp) | Annealing temperature (°C) |
|----------------|---------------------------------------|-------------------|----------------------------|
| psPAX2-SwaI-F | GGGGAAAGACTCCTAAATTTAAATTACCC | 893 | 55.88 |
| D116N-R | ATCGACGTCTCCGTTTGTATGTACTGTTTTTAC TGG | | 51.5 |
| D116N-F | ATCGACGTCTCCAAACAATGGCAGCAATTTTC | 192 | 52.4 |
| psPAX2-A/III-R | GCTGTCTTAAGATGTTTCAGCCTG | | 55.73 |

In this project, we successfully constructed two psPAX2 plasmid with the D116N mutation and seven psPAX2 plasmids containing the D116N mutation along with various other mutation sites on the integrase sequence. These recombinant plasmids will be further used to evaluate the impact of the D116N mutation and other missense mutations on integrase deficiency within the lentiviral transfection system. The non-integrating lentiviral system will offer advantages for widening clinical applications by reducing the risks of insertional mutagenesis, potentially leading to promising methods for safer gene therapy in the future.

This project would not have been possible without the support from my adviser, Asst. Prof. Pathrapol Lathanutudom and Asst. Prof. Suparat Lathanatudom who supporting me educationally and mentally throughout my years of research. The PL Lab members include Dr. Mattapong Kulaphisit and Dr. Kumpanat Pomlok who taught me the laboratory practices.

This project was funded by Chiang Mai University and Development and Promotion of Science and Technology Talents Project (DPST) Scholarship, Royal Government of Thailand.

References:

1. Sayed, N., et al., *Gene therapy: Comprehensive overview and therapeutic applications*. Life Sci, 2022. 294: p. 120375.
2. Wang, C., et al., *Emerging non-viral vectors for gene delivery*. Journal of Nanobiotechnology, 2023. 21(1): p. 272.
3. Shahryari, A., et al., *Engineering Gene Therapy: Advances and Barriers*. Advanced Therapeutics, 2021. 4(9): p. 2100040.
4. Chong, Z.X., S.K. Yeap, and W.Y. Ho, *Transfection types, methods and strategies: a technical review*. PeerJ, 2021. 9: p. e11165.
5. Sung, Y.K. and S.W. Kim, *Recent advances in the development of gene delivery systems*. Biomaterials Research, 2019. 23(1): p. 8.
6. Kotterman, M.A., T.W. Chalberg, and D.V. Schaffer, *Viral Vectors for Gene Therapy: Translational and Clinical Outlook*. Annu Rev Biomed Eng, 2015. 17: p. 63-89.
7. Mann, R., R.C. Mulligan, and D. Baltimore, *Construction of a retrovirus packaging mutant and its use to produce helper-free defective retrovirus*. Cell, 1983. 33(1): p. 153-9.
8. Durand, S. and A. Cimorelli, *The inside out of lentiviral vectors*. Viruses, 2011. 3(2): p. 132-159.
9. Sakuma, T., M.A. Barry, and Y. Ikeda, *Lentiviral vectors: basic to translational*. Biochem J, 2012. 443(3): p. 603-18.
10. Ginter, E.K., *[Gene therapy of hereditary diseases]*. Vopr Med Khim, 2000. 46(3): p. 265-78.
11. Luis, A., *The Old and the New: Prospects for Non-Integrating Lentiviral Vector Technology*. Viruses, 2020. 12(10).
12. Wanisch, K. and R.J. Yáñez-Muñoz, *Integration-deficient lentiviral vectors: a slow coming of age*. Mol Ther, 2009. 17(8): p. 1316-32.
13. Hall, T.A. *BIOEDIT: A User-friendly biological sequence alignment editor and analysis program for WINDOWS 95/98/ NT*. 1999.
14. Shaw, A.M., et al., *Differences in vector-genome processing and illegitimate integration of non-integrating lentiviral vectors*. Gene Ther, 2017. 24(1): p. 12-20.
15. Cline, J., J.C. Braman, and H.H. Hogrefe, *PCR Fidelity of Pfu DNA Polymerase and Other Thermostable DNA Polymerases*. Nucleic Acids Research, 1996. 24(18): p. 3546-3551.
16. Zhao, Z., A.C. Anselmo, and S. Mitragotri, *Viral vector-based gene therapies in the clinic*. Bioengineering & Translational Medicine, 2022. 7(1): p. e10258.
17. Ghosh, S., et al., *Viral Vector Systems for Gene Therapy: A Comprehensive Literature Review of Progress and Biosafety Challenges*. Applied Biosafety, 2020. 25(1): p. 7-18.



MOLECULAR RECOGNITION OF REGULATED INTRAMEMBRANE PROTEOLYSIS (RIP) IN CELLULAR CHOLESTEROL SENSING PATHWAY

Charal Khiewdee¹, Atchara Sripanya², Puey Ounjai^{1,*}

¹ Department of Biology, Faculty of Science, Mahidol University, Bangkok 10400

² Department of Biochemistry, Faculty of Science, Mahidol University, Bangkok 10400

*e-mail: puey.oun@mahidol.edu

Abstract:

The sterol regulatory-element (SRE) binding protein-2 (SREBP-2) is a key protein in the SREBP pathway, containing the transcription factor of the cholesterol homeostasis operon (SRE promoter). The transcription factor on SREBP-2 is cleaved by regulated intramembrane proteolysis (RIP) of S1P and S2P in the Golgi apparatus membrane. Even though the nuclear magnetic resonance (NMR) structure of SREBP-2 was studied, the structural mechanism underlying the RIP process on the SREBP-2 remains unclear. Therefore, we conducted atomistic (AT) molecular dynamics (MD) simulations to investigate the RIP process regarding different lipid environments (DLPC, POPC, DPPC, and LMPG) on SREBP-2. Interestingly, we found that the different lipid environments modulated the transmembrane (TM) and luminal (LM) domains of SREBP-2. Moreover, we also found that the thicker lipid membrane affected the SREBP-2 structure by stretching the NP motif at the N-terminus transmembrane α -helix (ca. $\sim 132^\circ$ of the NP-angle in POPC system). Our studies highlight that the thicker membrane environment plays a role in a stretch of NP motif leading to an initiation of RIP process, correlating the translocation of SREBP-2 from the endoplasmic reticulum (ER) to the Golgi apparatus membrane. Together, this study highlights unique insights into lipid environmental factors' effect on SREBP-2 which possibly addresses the molecular mechanism of the RIP process on SREBP-2 in cholesterol homeostasis. This will be beneficial in the therapeutic development targeting the RIP process and NP motif movement for the diseases that occur due to the malfunction of the cholesterol regulation.

Introduction:

Cholesterol is one of the essential lipids constituting approximately 30% of the overall mammalian cell membrane¹⁻³. It plays a significant role in regulating membrane permeability and steroid biosynthesis, such as progesterone and estrogen^{4,5}. Notably, cellular cholesterol level modulation is crucial as dysregulated cholesterol homeostasis as excessive and deficient cholesterol levels can cause heart disease and mental disorders, respectively⁶⁻⁹. One of the cholesterol homeostasis mechanisms is the SREBP pathway on the endoplasmic reticulum (ER) membrane, consisting of sterol regulatory-element binding protein (SREBP), SREBP cleavage-activating protein (SCAP), and insulin-induced gene protein (INSIG)¹⁰. The SREBP pathway is launched after the cholesterol level is dropped below 5 mol% of the total lipids in the ER membrane, sensed by the sterol-sensing domain (SSD) of SCAP¹¹. Then, SREBP is translocated into the Golgi apparatus membrane and cleaved by the regulated intramembrane proteolysis (RIP) process^{10,12}. The RIP process cleaves the basic helix-loop-helix leucine zipper (hLHL-Zip) at the N-terminus of SREBP by site-1 protease (SP1) and site-2 protease (SP2), on the luminal loop and the N-terminus transmembrane α -helix, respectively¹³. After, the bHLH-Zip activates the transcription of proteins underlying the sterol regulatory element (SRE) promoter leading to an increase in cholesterol levels¹⁴. Oppositely, INSIG will dimerize

with SCAP when the cholesterol level rises above 5 mol% resulting in an absence of the SREBP translocation and a decrease in cholesterol level¹⁵.

According to a crucial of the bHLH-Zip in cholesterol homeostasis, the RIP process was then studied to understand a key mechanism that occurs on SREBPs. Thus, the NMR structure of SREBP-1, an isomer of the SREBPs family involved in lipid regulation, was solved in an LMPG detergent micelle¹⁶. The obtained structure was then studied using atomistic (AT) molecular dynamic (MD) simulation by conducting in 2 different lipid environments, DLPC and POPC, for 1 μ s. The study reveals the N-terminus transmembrane α -helix responded to the change in membrane thickness, resulting in a wider angle on the asparagine-proline (NP) motif (residue 501-502). Moreover, this wider confirmation on the NP motif of SREBP-1 allowed an S2P docking at the scissile bond¹⁶⁻¹⁷. However, there is a lack of knowledge on the effect of lipid environment in other compositions on the SREBP-2 which plays a role in cholesterol homeostasis. Besides, the differences in lipid saturation influencing the RIP process on SREBPs remain unclear, only 2 lipid species (DLPC and POPC) were studied. The understanding of the insights of lipid environments including thickness and lipid saturation potentially elucidates the lipid-driven molecular mechanisms of the RIP process.

Here, we aimed to study the effect of lipid environments on the SREBP-2, another isomer of the SREBP family regulating cholesterol homeostasis, using AT-MD simulations. Our work highlights different conformations and stabilities of the transmembrane domains of SREBP-2 in saturated (DLPC and DPPC), unsaturated (POPC) and detergent (LMPG) lipid environments. Besides, our work potentially describes the RIP process which relates with the change of lipid thickness between organisms, ER and Golgi apparatus membranes, within the SREBP pathway leading to benefit the future treatment of abnormal cholesterol homeostasis.

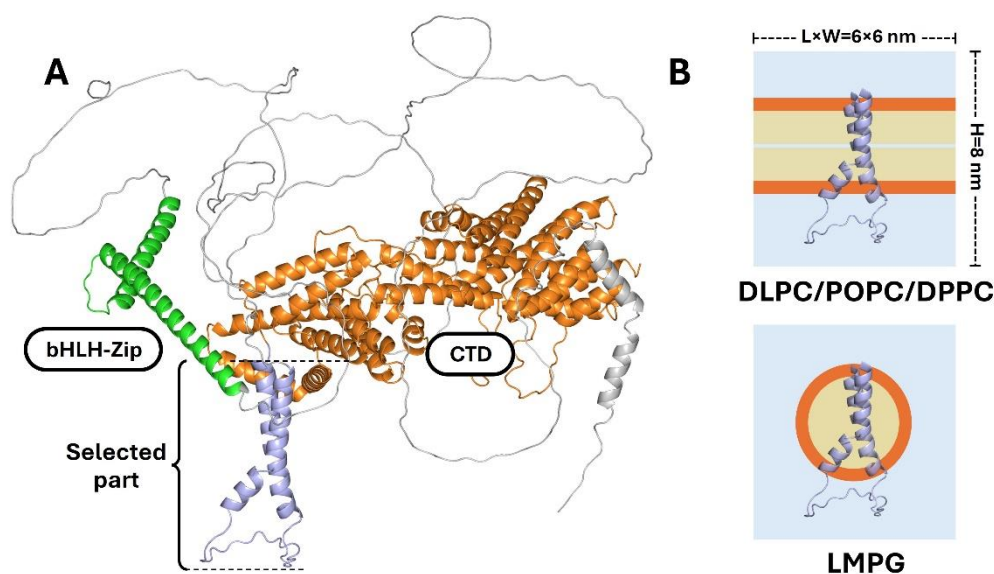


Figure 1. Molecular modelling of SREBP-2 and the construction of simulation systems

(A) The SREBP-2 structure was obtained from the AlphaFold protein database. Only the selected part (light blue) was used for the study. The cytosolic domains, bHLH-Zip, and CTD, are shown in green and orange, respectively. The disordered part is shown in grey. (B) The simulation boxes of PC lipids (top) and LMPG detergent (bottom) were constructed with a size of $6 \times 6 \times 8 \text{ nm}^3$. The head groups of each lipid are shown in orange, while the tails are shown in light orange. The light blue within each system represents a solvent (0.15M NaCl in water). L, length; W, width; H, height.

Methodology:



Molecular modeling of SREBP-2 structure

The structure of SREBP-2 was obtained from the AlphaFold protein database (UniProt entry: Q12772). According to the previous NMR structure of SREBP-1, the obtained structure was modified by removing the cytosolic domains, the bHLH-Zip, and the C-terminus regulatory domain (CTD), using PyMOL software. The remaining transmembrane (TM) domain with a luminal (LM) loop (residue 475-559) was then selected for the RIP process study (Figure 1A).

Atomistic simulations of SREBP-2 in different lipid environments

The phosphatidylcholine (PC) lipid species were selected to study because of the major lipid ratio in the ER and Golgi apparatus membrane¹⁸. The DLPC and DPPC lipids were selected to imitate a thin and thick saturated lipid environment, respectively. The thin lipid environment was used to represent the ER membrane, while the thicker one represented the Golgi apparatus membrane²⁵. The POPC lipid was picked to imitate an unsaturated lipid environment which has a similar thickness to DPPC. Lastly, the LMPG detergent was picked to simulate the environment of SREBP-2 as in the micelle the previous NMR structure of SREBP-1¹⁶. The LMPG system was observed to explain the effect of detergent micelle comparing with other lipid systems.

The systems of SREBP-2 in DLPC, POPC, DPPC, and LMPG membranes were generated using CHARMM-GUI with CHARMM36m forcefield^{19,20}. Each simulation system was constructed in $6 \times 6 \times 8 \text{ nm}^3$ size with TIP3P water and 0.15 M NaCl²¹ (Figure 1B). Then, each system was independently energy minimized using the steepest-descent algorithm with restrains on C_α atoms at 1000 kJ/mol/nm^2 with 2 fs timesteps for 5 ns. The DLPC, POPC, and DPPC systems were equilibrated for 100 ns with a semi-isotropic Berendsen barostat for equilibration. Otherwise, the LMPG system was equilibrated for 100 ns with isotropic Berendsen barostat²². After, all systems were simulated for 250 ns (3 repeats independently in each system) using a semi-isotropic Parrinello-Rahman barostat, while the LMPG system was simulated with an isotropic Parrinello-Rahman barostat²³. All simulations, excluding the energy minimization, were maintained temperature at 310 K with V-rescale temperature coupling and 1 bar of pressure coupling, and were performed by using GROMACS version 2021.3²⁴.

Analyses of the lipid environments affecting the structure of SREBP-2

Our analyses used 3 criteria; root means square fluctuation (RMSF), root means square deviation (RMSD), and the angle on NP motif of SREBP-2 (residue 495-496). In the RMSD analysis, all simulations were calculated an overall change in the SREBP-2 structure compared with the first frame of each system. Next, the RMSF analysis, every C_α atom of SREBP-2 in all systems were observed fluctuations in different lipid environments. Another, the angle analysis, we defined 3 residues, S480, N495, and W503, as the NP-angle reference. All analyses were performed by using GROMACS version 2021.3²⁴.

Results and Discussion:

The fluctuation of the SREBP-2 structure in different lipid environments

After the simulations, all systems were analyzed for the fluctuation of the C_α of the SREBP-2 structure. The results showed that the SREBP-2 structure, in terms of the TM domain, has a slightly different corresponding to the length of each lipid type (Figure 2B). On the TM1 of SREBP-2 structure, the LMPG micelle potentially influences the fluctuation of the TM1 more than the others ($\text{RMSF} \approx 0.18\text{-}0.34 \text{ nm}$). The DLPC membrane effects slightly lower than the LMPG ($\text{RMSF} \approx 1.2\text{-}2.2 \text{ \AA}$), but still more than the DPPC and POPC membrane at residue 490-500 on the TM1 ($\text{RMSF} \approx 0.8\text{-}1.7 \text{ \AA}$). Interestingly, the higher fluctuations on TM1

of LMPG and DLPC systems covered the area of NP motif which previously described as a motile part of SREBPs (Figure 2A). However, an overall fluctuation on TM2 exists correlatedly with the TM1 that the fluctuation occurred mostly in the LMPG system. Another, the LM loop existed in the highest fluctuation on the DLPC (max RMSF \approx 7.8 Å), while the other systems presented in non-significant differences (max RMSF \approx 5.8 Å).

Our results denote the effects of a lipid construction, and thickness according to the length of PC lipids. In the case of the LMPG micelle, the detergent was constructed in a spherical shape around the TM domains of SREBP-2, mimicking the protein isolation process of NMR in the previous study¹⁶. This probably allows a movement of TM domains more than the bilayers construction of DLPC, DPPC, and POPC, especially in the NP motif. Another, the thickness of each system potentially plays a role in a partial change of the SREBP-2 structure. Due to a DLPC lipid tail consisting of 12 carbon atoms that was the shortest among lipids in the study, the covering area of DLPC therefore took a thinner thickness than the others. This shorter covering area may allow the PC headgroup to interact with residues surrounding the NP motif, resulting in a higher fluctuation index. Besides, according to the simulations, the thinner membrane of the DLPC lipid increases distances between the LM loop and the PC head groups on the membrane leading to the lower chance of interaction and a higher fluctuation index. Surprisingly, the translocation of the SREBP-SCAP complex moves from the thinner to a thicker membrane, from the ER to Golgi apparatus membrane^{12,25}. This suggests that the thicker membrane may be involved in the RIP process in terms of the protein stabilization.

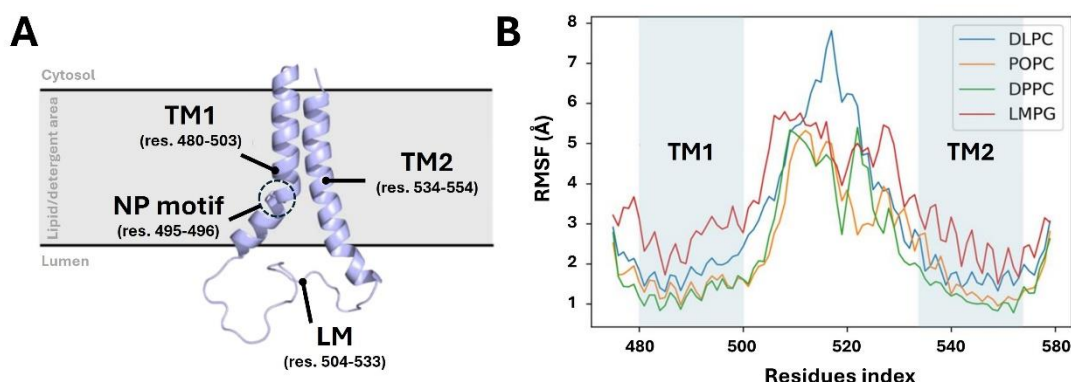


Figure 2. An overall structure of SREBP-2 in each system and the RMSF analysis

(A) The details of the SREBP-2 structure within the covering area of PC lipids or LMPG detergent. The transmembrane (TM) domain, luminal (LM) loop, and the NP motif are shown within the figure with residues (res.). (B) The results of the RMSF analysis represent the fluctuation of C α atoms of SREBP-2 in each system, the labels are shown in the upper-right box. The light blue areas represent the TM domain of SREBP-2.

The movement of SREBP-2 in the different lipid environments

From the RMSF analysis, the thicker membrane (DPPC and POPC) resulted in a better stability of the SREBP-2 structure. We hypothesized that a fluctuation of the SREBP-2 structure should play a role in the activation of the RIP process on the Golgi apparatus membrane. We then shed light on the conformational change in different lipid environments. All systems were analyzed for the change in the overall SREBP-2 structure by calculating the RMSD throughout each simulation. The results showed that all systems result in an average range of \sim 2-6 Å (Figure 3A). In detail, the LMPG system showed an unstable altering of the SREBP-2 structure along the simulation (ca. 2-6 Å). For the rest of the systems, the DLPC and DPPC systems resulted in a non-significant difference (ca. 2-4 Å), while one repeat of POPC systems resulted in a high RMSD (ca. 2-6 Å). This may be caused by a movement on the TM2



that was bent transiently in the simulation (Figure 3B). An unsaturated oleoyl chain of the POPC potentially influences SREBP-2 to be more flexible than the saturated chains in DPPC and DLPC (Figure 3B). However, the change in a structure must be further analyzed for more insights of the effects of lipid environments.

Therefore, we additionally study the movement of the TM domain of SREBP-2. The angle analysis was used to observe the change in the referenced angle (NP-angle), consisting of S480, N495, and W503, on the NP motif (Figure 3C). The results showed that the NP-angle of the POPC system is the widest angle (average= $\sim 132^\circ$). In the DPPC system, the NP-angle is slightly lower than that in the POPC system (average= $\sim 130^\circ$). The DLPC and LMPG systems showed the lowest NP-angle (average= $\sim 127^\circ$ and $\sim 119^\circ$, respectively) (Figure 3D).

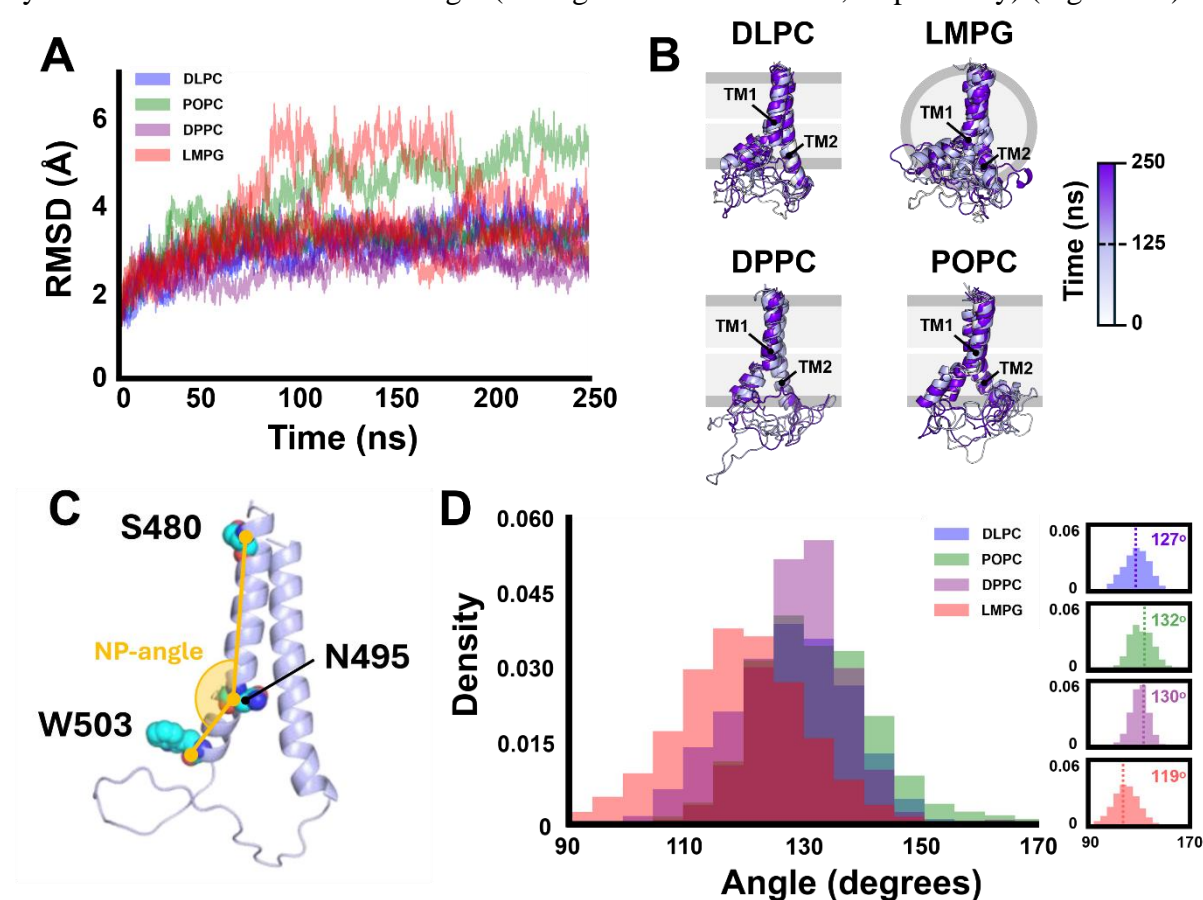


Figure 3. The movement of the SREBP-2 structure in different lipid environments

(A) The RMSD results of each system represent the change of overall SREBP-2 structure throughout the 250 ns simulation ($n=3$ of each system). The flexible region (LM domain) was excluded from the analysis due to the instability. (B) The movement of the SREBP-2 structure within each system. The different colors of the SREBP-2 structure represent different time frames: 0 ns (white), 125 ns (light blue), and 250 ns (purple blue). The dark grey boxes (lipid head groups) and the light grey region (lipid tails) represent the covering area of PC lipids and LMPG detergent. (C) The reference residues represent the NP-angle (yellow) of the angle analysis. Each reference residue, with side chain, is shown in sphere, with carbon atoms (cyan), positively charged atoms (blue), and negatively charged atoms (red). (D) The distribution histograms of the angle analysis results of each system represent the change in the NP-angle throughout the 250 ns simulation ($n=3$ of each system). The right boxes represent angle distribution and averaged angle in each system.

Even though the POPC and DPPC lipid environment are different from each other by the saturated lipid tail, the NP-angle within each system showed a non-significant difference. This may be caused by the thickness dependency of the SREBPs. However, the study of lipid saturation environment is needed to explain some transient movement of TM2 within the POPC system and the wider-angle distribution on the NP-angle (Figure 3A-B&D).

Our angle analysis highlights more essential information on the SREBP-2 structure in the different lipid environments. The wider NP-angle represents the stretching conformation around the NP motif, which was originally described as a crucial role in the S2P access^{17,26}. Together with the stability study, the thicker membrane tends to affect the SREBP-2 structure and benefits the RIP process of the SP2 in the Golgi apparatus membrane. In the LMPG system, the system was constructed to mimic the NMR structure. The spherical construction of the LMPG micelle acts as the DLPC system in the lifting of the NP motif. This bending hinge-like NP motif potentially be an obstruction of the S2P binding¹⁶ (Figure 4). Our finding also proposes the potential role of the RIP process on the NP-motif of SREBPs which is important for the regulation of genes under controlled the SRE promoter, the bHLH-zipper's target. For instance, a mutation on the NP motif causes a loss of S2P cleavage resulting in a cholesterol deficient condition which leads to a mental disorder, such as depression⁶. However, the deeper understanding of the lipid-driven molecular mechanism of the NP motif movement is needed.

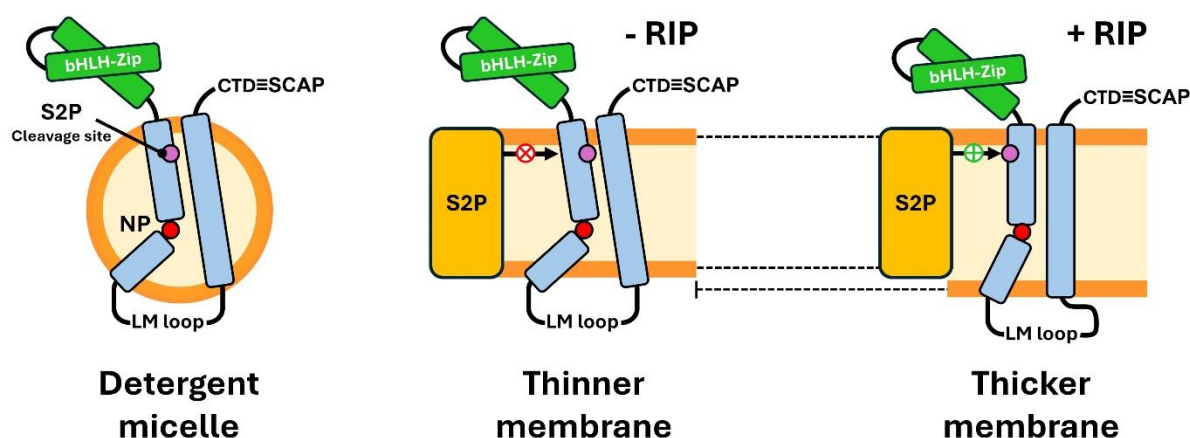


Figure 4. The schematic diagram of the NP motif movement affecting the RIP process in different lipid environments

The detergent micelle (LMPG) and thinner membrane (DLPC) environments represent a similar configuration of SREBP-2, where the RIP process is blocked by the bending of NP motif (red spot). The thicker membrane (POPC and DPPC) represents the potential consequences of stretching/opening of the NP motif. Therefore, S2P probably accesses the S2P cleavage site (purple spot) allowing the RIP process to take place.

Conclusion:

In conclusion, the different lipid environments influence the conformational change of the SREBP-2 structure. The lipid construction and membrane thickness could alter the NP motif on the TM1 of the SREBP-2. The movement of the NP motif essentially involves the RIP process in terms of the S2P binding. In the POPC system, the TM1 was stretched leading to the wider NP-angle, which serves as an accessible path to the cleavage site. Conversely, in the LMPG system, the NP angle resulted in the sharpest angle leading to the bending of the NP motif, which potentially avoids access to S2P. This also suggests that the translocation of the SREBP-SCAP complex from ER to the Golgi apparatus membrane is reasonable to allow the



RIP process. Besides, the lipid saturation may have a role in processes on SREBPs because of the movement of TM2 within the POPC system, while no obvious signal in the DPPC system. For further study, we suggest that the study of SREBPs in other lipid compositions is needed for a better understanding of the RIP process, especially in the mocked-up Golgi apparatus membrane using various types of lipids and cholesterol. This may elucidate more insight into the shadowed lipid-driven molecular mechanisms between RIP process and SREBPs. Moreover, this will benefit the drug design or therapeutic development to tackle diseases caused by mutations in the RIP-related regions on SREBPs.

References:

1. Harayama T, Riezman H. *Nat Rev Mol Cell Biol.* 2018;19:281-296.
2. van Meer G, Voelker D R, Feigenson G W. *Nat Rev Mol Cell Biol.* 2008;9:112-124 .
3. Zhang J, et al. *Cell Commun Signal.* 2019;17:15.
4. Olżyńska A, et al. *Langmuir.* 2020;36:10438-10447.
5. Raffy S, Teissié J. *Biophys J.* 1999;76:2072-2080.
6. Carson J A S, et al. *Circulation.* 2020;141:e39-e53.
7. Cheon S Y. *Exp Neurobiol.* 2023;32:57-67.
8. Lin C J, et al. *Biomedicine (Taipei).* 2015;5:7
9. Paukner K, Králová Lesná I, Poledne R. *Int J Mol Sci* 2022;23.
10. Sokolov A, Radhakrishnan A. *J Biol Chem.* 2010;285:29480-29490.
11. Radhakrishnan A, Sun L P, Kwon H J, Brown M S, Goldstein J L. *Mol Cell.* 2004;15: 259-268.
12. Luo J, Yang H, Song B L. *Nat Rev Mol Cell Biol.* 2020;21:225-245.
13. Brown M S, Goldstein J L. *Cell.* 1997;89:331-340.
14. Brown M S, Goldstein J L, *Proc Natl Acad Sci USA.* 1999;96:11041-11048.
15. Gao Y, Zhou Y, Goldstein J L, Brown M S, Radhakrishnan A. *J Biol Chem.* 2017;292:8729-8737.
16. Linser R, et al. *Proceedings of the National Academy of Sci.* 2015;112:12390-12395.
17. Ye J, Davé U P, Grishin N V, Goldstein J L, Brown M S. *Proceedings of the National Academy of Sci.* 2000;97:5123-5128.
18. Casares D, Escribá P V, Rosselló C A. *Int J Mol Sci.* 2019;20:2167.
19. Huang J, MacKerell A D. *J Com Chem.* 2013;34:2135 - 2145.
20. Lee J, et al. *J Chem The & Com.* 2019;15:775-786.
21. Wu Z, Newstead S, Biggin P C. *Sci Rep.* 2020;10:16903.
22. Berendsen H J C, Postma J P M, Gunsteren W F v, DiNola A, Haak J R. *J Chem Phy.* 1984;81:3684-3690.
23. Parrinello M, Rahman A. *J App Phy.* 1981;52:7182-7190.
24. Abraham M J, et al. *SoftwareX.* 2015;1:19-25.
25. Mitra K, Ubarretxena-Belandia I, Taguchi T, Warren G, Engelman D M. *Proc Natl Acad Sci USA.* 2004;101:4083-4088.
26. Feng L, et al. *Science* 2007;318:1608-1612.



SPECIES DIVERSITY AND DISTRIBUTION OF THE LICHEN GENERA, *HAEMATOMMA*, *LECANORA* AND *MALMIDEA* IN DOI SUTHEP-PUI NATIONAL PARK, CHIANG MAI PROVINCE, THAILAND.

Phimpisa Phrapphuchamnong¹, Kawinnat Buaruang, Mongkol Pangpet, Vasun Poengsungnoen Sanya Meesim² and Wetchasart Polyiam*,

¹Lichen Research Unit, Department of Biology, Faculty of Science, Ramkhamhaeng University, Huamark, Bangkok, Bangkok 10240, Thailand.

*e-mail: e-mail: wetchasart1p@gmail.com

²Scientific Instruments center, School of Science of Technology Ladkrabang, Bangkok 10520, Thailand

Abstract:

A survey and collection of three lichen genera *Haematomma*, *Lecanora*, and *Malmidea* was conducted in Doi Suthep-Pui National Park, Chiang Mai Province, Thailand, between February 2023 and March 2024. A total of 264 specimens were collected from 23 phorophytes across two forest types and were taxonomically cataloged. The catalog includes six species from the genus *Haematomma*, and nine species each from the genera *Lecanora* and *Malmidea*. The highest species diversity was observed in the Lower Montane Forest (LMF) at 1,600 meters above sea level (masl), while it was lower in the Dry Dipterocarp Forest (DDF) at 400 masl. The common species found distributed across four elevations in two forest types include *Malmidea aurigera*, *Lecanora helva*, *Lecanora argentata*, and *Haematomma rufidulum*. The unknown tree species can be referred to as the favorite phorophyte of the most diverse lichens, followed by *Castanopsis* sp. and *Shorea obtusa*, respectively. Our research has shown that at higher altitudes, temperatures decrease, and humidity levels rise, leading to a significant increase in the variety of lichen species. This study has improved our understanding of the diversity and distribution patterns of these three lichen genera, providing valuable insights for future conservation efforts.

Introduction:

Doi Suthep-Pui National Park is a mountainous area located in Chiang Mai Province, Thailand (approx. latitude: 18° 48' 34" N, longitude: 98° 54' 57" E). Elevations range from 330 to 1,685 meters above sea level. The park area is 261 square kilometers covering three districts consist of Mueang Chiang Mai, Mae Rim, and Hang Dong.¹ The park experiences cool-dry season, hot-dry season and rainy season.² Temperatures averaged from 2-23°C. The annual rainfall ranges between 1,350 and 2,500 millimeters, and the relative humidity averages about 70-80%.¹ The three lichen genera, *Haematomma*, *Lecanora* and *Malmidea* in this study are referred to the crustose growth form with disc-like apothecia. The apothecial disc may be exposed, flat, convex, or concave and normally upraised on the thallus. The two types of apothecia were found, the lecanorine apothecia with the margin of an apothecia can be concolorous. It is characterized by having photobiont cell (algae) incorporated with the exciple, the lichen with these types of apothecia includes *Haematomma* and *Lecanora*. Another type of apothecia is lecideine or biatorine apothecia, this apothecium lacks photobiont cells incorporated within the margin. This type of apothecia is found in lichen *Malmidea*. All three lichen genera produced colourless ascospores and contained within clavate asci. They exhibit a variety of ascospore types including simple, trans-septate, sub-muriform, or muriform, depending on the lichen genus.⁴ The phorophyte, the plant on which the epiphyte grows, provides an important growth host for lichens.³

This study aims to assess the species diversity of three lichen genera: *Haematomma*, *Lecanora*, and *Malmidea*, and their relationship to environmental factors.

Methodology:

Samples of three lichen genera, along with temperature and relative humidity data (recorded using an Elitech, RC-51H datalogger, USA), were collected from Doi Suthep-Pui National Park in Chiang Mai Province between February 2023 and March 2024. The study covered four altitudes: 400, 800, 1,200, and 1,600 meters above sea level. The collection sites included Huay Tung Tao checkpoint and Wat Padhammachart (400 masl), as well as Chaloem Phrakiat pavilion viewpoint and Sirindhorn Observatory Chiang Mai (800 masl). These study sites are located within Dry Dipterocarp Forest (DDF). At higher altitudes, between 1,200 and 1,600 meters above sea level, such as Bann Khun Chang Khian, Doi Suthep viewpoint, San Ku (1,200 masl), Doi Hua Moo and Doi Pui peak (1,600 masl), the areas are covered by Lower Montane Forest (LMF).

All lichen specimens were identified based on their thallus morphology and anatomy.^{5,6,7,8,9} Lichen substances were clarified using spot test and Thin Layer Chromatography (TLC) techniques.¹⁰

Results and Discussion:

Two hundred and sixty-four specimens of three lichen genera which were found on twenty-three phorophytes. The most diverse taxa were *Lecanora* and *Malmidea* (9 species each), followed by *Haematomma* (6 species) respectively (see Table 1). It was shown that lichen species in this area have high species diversity at higher elevations in Lower Montane Forest at altitudes around 1,600 meters, but lower diversity in Dry Dipterocarp Forest (DDF) at altitudes around 400 meters. The temperature and humidity are key environmental factors that strongly influence lichen diversity and distribution. Lower temperatures and higher humidity tend to create favorable conditions for a wider range of lichen species (see Table 1). This may indicate that most lichen species of the three genera prefer high-altitude habitats. The suitable habitats for these lichens are likely cool and humid forests. However, their colonization is also influenced by vegetation and environmental factors such as air ventilation, light direction, and the acidic, smooth bark of dominant phorophytes.¹¹ In table 1., *Malmidea aurigera* shows high frequency and adaptability across different forest types (see figure 1.D), such as DDF and LMF, suggest that it is well-suited to varying environmental conditions in the national park. Its ability to thrive in multiple habitats makes it a strong indicator species for the resilience of lichen communities. The presence of other species like *Haematomma rufudulum*, *Lecanora argentata*, and *L. helva* (see figure 1.) across all study sites also highlights their ecological flexibility, but *Malmidea aurigera* abundance points to its particularly adaptive nature in this environment.^{12, 13}

The phorophyte, or host tree, is indeed a critical factor influencing lichen distribution. In our study, the highest lichen species diversity was observed on an unknown tree with 21 species, followed by *Castanopsis* sp., which supports 11 species and is dominant in LMF, and *Shorea obtusa*, which supports 9 species and is dominant in DDF (see Table 2). These three phorophytes collectively support over half of the lichen species in the area, highlighting the significant role of phorophyte specificity in shaping the diversity and distribution of tropical lichen communities.



Table1.
Lichen species and distribution in altitude habitats (meters above sea level) at Doi Suthep-Pui National Park, Chiang Mai Province.

| Lichen taxa | | Altitude/Forest types | | | | Total no. of specimens |
|------------------------|----------------------------|-----------------------|--------------|----------------|----------------|------------------------|
| | | 400 (DDF) | 800 (DDF) | 1,200 (LMF) | 1,600 (LMF) | |
| Haematomataceae | <i>Haematomma collatum</i> | 1 | 4 | 4 | | 9 |
| | <i>H. parda</i> | | | | 4 | 4 |
| | <i>H. persoonii</i> | | 13 | 6 | | 19 |
| | <i>H. puniceum</i> | | 1 | | 2 | 3 |
| | <i>H. rufidulum</i> | 9 | 3 | 1 | 2 | <u>15</u> |
| | <i>H. wattii</i> | | | 4 | 1 | 5 |
| Lecanoraceae | <i>Lecanora achroa</i> | | 2 | | 3 | 5 |
| | <i>L. allophana</i> | | | | 4 | 4 |
| | <i>L. argentata</i> | 3 | 14 | 1 | 3 | <u>21</u> |
| | <i>L. arthothelinella</i> | | | | 1 | 1 |
| | <i>L. caesiorubella</i> | | | | 4 | 4 |
| | <i>L. helva</i> | 3 | 8 | 10 | 3 | <u>24</u> |
| | <i>L. kansriai</i> | | | 1 | 2 | 3 |
| | <i>L. tropica</i> | 7 | 11 | 1 | | 19 |
| | <i>L. pseudagentata</i> | 16 | | | | 16 |
| Malmideaceae | <i>Malmidea aurigera</i> | 1 | 1 | 38 | 11 | <u>51</u> |
| | <i>M. bakeri</i> | | | 1 | | 1 |
| | <i>M. ceylanica</i> | 6 | 1 | | | 7 |
| | <i>M. chrysostigma</i> | | | 16 | 1 | 17 |
| | <i>M. granifera</i> | | | 5 | 1 | 6 |
| | <i>M. infrata</i> | | | 1 | 1 | 2 |
| | <i>M. perplexa</i> | | 1 | 1 | | 2 |
| | <i>M. piaie</i> | 11 | | | | 11 |
| | <i>M. subaurigera</i> | | | 13 | 2 | 15 |
| Total no. of specimens | | 57 | 59 | 103 | 45 | 264 |
| Total no. of species | | 9 | 11 | 15 | 16 | 24 |
| Average Temperature | | 24.9 | 31.1 | 20.4 | 18.4 | |
| Average Humidity | | 73.2 | 75.0 | 77.6 | 79.4 | |

Note: Dry Dipterocarp Forest (DDF), Lower Montane Forest, (LMF).

Table 2.
List of lichen-taxa on phorophytes at Doi Suthep-Pui National Park, Chiang Mai Province.

| Lichen taxa | Phorophyte number. | | | | | | | | | | | | | | | | | | | | | | | Total no. of specimens |
|----------------------------|--------------------|----|----|----|----|---|---|---|---|----|----|----|----|----|----|----|----|----|----|----|----|----|----|---------------------------|
| | 1 | 2 | 3 | 4 | 5 | 6 | 7 | 8 | 9 | 10 | 11 | 12 | 13 | 14 | 15 | 16 | 17 | 18 | 19 | 20 | 21 | 22 | 23 | |
| <i>Haematomma collatum</i> | 5 | 1 | | 1 | | 2 | | | | | | | | | | | | | | | | | | 9 |
| <i>H. parda</i> | 2 | 2 | | | | | | | | | | | | | | | | | | | | | | 4 |
| <i>H. persoonii</i> | 4 | 4 | 3 | | 1 | 2 | 2 | | | 1 | | | | | | 2 | | | | | | | | 19 |
| <i>H. puniceum</i> | 2 | 1 | | | | | | | | | | | | | | | | | | | | | | 3 |
| <i>H. rufidulum</i> | 11 | | | 3 | | 1 | | | | | | | | | | | | | | | | | | 15 |
| <i>H. wattii</i> | 2 | | | | | | 3 | | | | | | | | | | | | | | | | | 5 |
| <i>Lecanora achroa</i> | 3 | | 1 | | | | | | | | | | | | | | | | | | | 1 | | 5 |
| <i>L. allophana</i> | 2 | | | 1 | | | | 1 | | | | | | | | | | | | | | | | 4 |
| <i>L. argentata</i> | 8 | 2 | 2 | 1 | 2 | 1 | | 1 | 2 | | | | | 1 | | | | | | | 1 | | | 21 |
| <i>L. arthothelinella</i> | | | | | | | 1 | | | | | | | | | | | | | | | | | 1 |
| <i>L. caesiorubella</i> | 2 | | | 1 | | | | | | | | | | | | | | | | | 1 | | | 4 |
| <i>L. helva</i> | 5 | 5 | 2 | 1 | 2 | 1 | 2 | 2 | | | | | 3 | | | | | 1 | | | | | | 24 |
| <i>L. kansriae</i> | 2 | 1 | | | | | | | | | | | | | | | | | | | | | | 3 |
| <i>L. tropica</i> | 1 | 2 | 2 | | 8 | 1 | | | 1 | 1 | | 3 | | | | | | | | | | | | 19 |
| <i>L. pseudagentata</i> | | | 11 | | 3 | | | | | 1 | | | | | 1 | | | | | | | | | 16 |
| <i>Malmidea aurigera</i> | 27 | 9 | | 4 | 1 | 1 | | | | | 7 | | 2 | | | | | | | | | | | 51 |
| <i>M. bakeri</i> | 1 | | | | | | | | | | | | | | | | | | | | | | | 1 |
| <i>M. ceylanica</i> | 1 | | 1 | | | | | | 1 | | | 2 | | 1 | | | | | 1 | | | | | 7 |
| <i>M. chrysostigma</i> | 9 | 8 | | | | | | | | | | | | | | | | | | | | | | 17 |
| <i>M. granifera</i> | 5 | | | | | | | | | | | | | | | | | | | | | 1 | | 6 |
| <i>M. infrata</i> | 2 | | | | | | | | | | | | | | | | | | | | | | | 2 |
| <i>M. perplexa</i> | | | 1 | | | | | | | | 1 | | | | | | | | | | | | | 2 |
| <i>M. piaie</i> | 3 | | 3 | 2 | 1 | | | | | | | | | | 1 | | 1 | | | | | | | 11 |
| <i>M. subaurigera</i> | 7 | 7 | | | | | 1 | | | | | | | | | | | | | | | | | 15 |
| Total no. of specimens | 104 | 42 | 26 | 14 | 18 | 9 | 9 | 4 | 4 | 3 | 8 | 5 | 5 | 2 | 2 | 2 | 1 | 1 | 1 | 1 | 1 | 1 | 1 | 264 |
| Total no. of species | 21 | 11 | 9 | 8 | 7 | 7 | 5 | 3 | 3 | 3 | 2 | 2 | 2 | 2 | 2 | 1 | 1 | 1 | 1 | 1 | 1 | 1 | 1 | |

Note: 1= Unknown tree, 2= *Castanopsis* sp., 3= *Shorea obtusa*, 4= Vine, 5= *Shorea siamensis*, 6= *Castanopsis diversifolia*, 7= *Castanopsis acuminatissima*, 8= *Gardenia sootepensis*, 9= *Strychnos nux-vomica*, 10= *Dipterocarpus tuberculatus*, 11= *Schima wallichii*, 12= *Buchanania lanzan*, 13= *Lannea coromandelica*, 14= *Gluta usitata*, 15= *Quercus kerrii*, 16= *Xylia xylocarpa*, 17= *Afgekia sericea*, 18= *Dipterocarpus intricatus*, 19= *Dipterocarpus obtusifolius*, 20= *Engelhardia spicata*, 21= *Juniperus chinensis*, 22= *Phyllanthus emblica*, 23= *Rhododendron moulmeinense*.

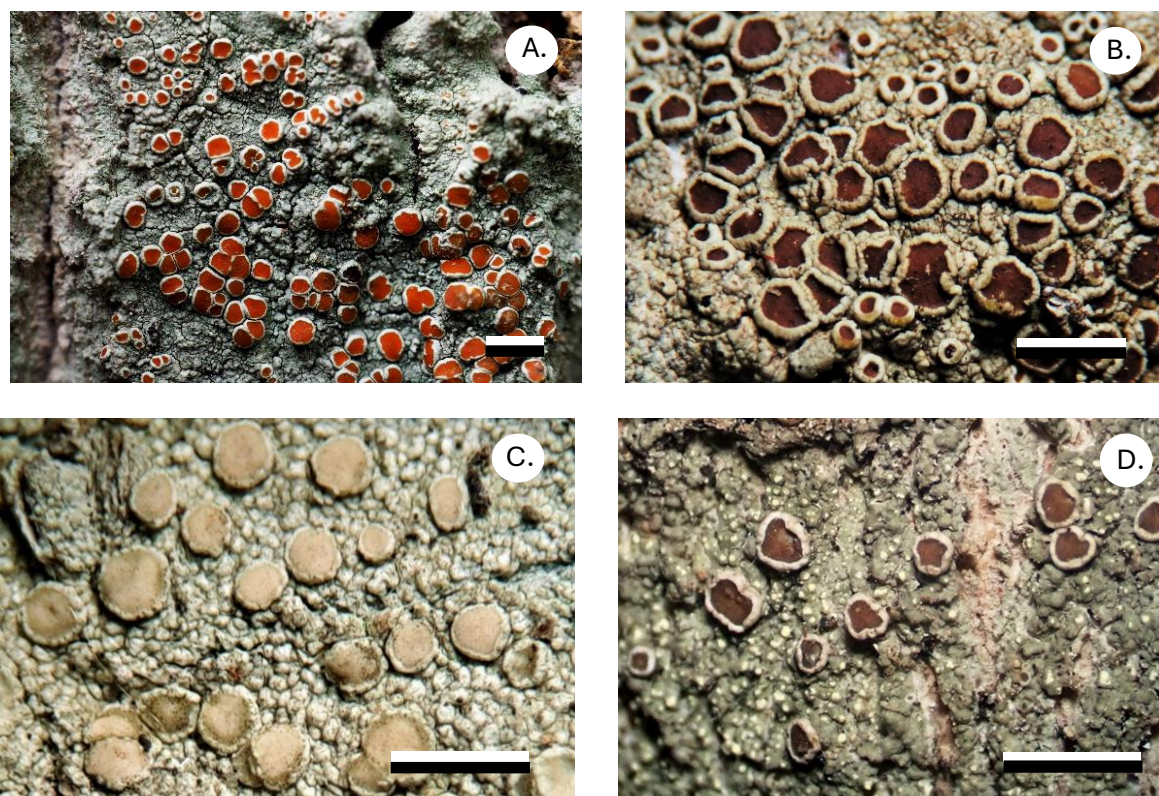


Figure 1.

The common lichen observed from study sites. A) = *Haematomma persoonii*, B) = *Leanora argentata*, C) = *Lecanora helva* and D) = *Malmidea aurigera*, Scale bar = 1 mm.

Conclusion:

The distribution of three lichen genera (*Haematomma*, *Lecanora* and *Malmidea*) was studied across twenty-three phorophytes. The highest species diversity of lichen was found in the Lower Montane Forest, indicating that most lichen taxa adapt well to cool and humid conditions. The dominant species, such as *Malmidea aurigera* were found in all four forest types. This lichen species may be considered widely distributed within the national park and plays a crucial role in maintaining the important species composition of the lichen community. Epiphytic lichens observed on the phorophytes indicated that suitable habitats include the unknown tree and *Castanopsis* sp. Those trees are the most important phorophyte for lichen diversity. Conservation efforts to maintain these tree species may help preserve a high diversity of lichen composition in Doi Suthep-Pui National Park. Studying lichen communities and individual species in relation to environmental factors would be an interesting approach to further understanding the patterns of lichen diversity and distribution.

Acknowledgements:

We are grateful to the lichen team from the Biology Department, Faculty of Science, Ramkhamhaeng University, and the officers of Doi Suthep-Pui National Park for their assistance with fieldwork and specimen collection. This work was financially supported by the National Research Council of Thailand (NRCT).

References:

1. Department of National Park, Wildlife and Plant Conservation (DNP), Thai. Accessed July 29, 2024.
<https://portal.dnp.go.th/Content/nationalpark?contentId=34707>
2. ReddotExplorer. "Chiang Mai Weather Guide: Seasonal Insights for Your Perfect Trip" Trip.com. Accessed December 7, 2023.
<https://sg.trip.com/guide/info/chiang-mai-weather.html>
3. Wikipedia, the free encyclopedia. Accessed July 29, 2024.
<https://en.wikipedia.org/wiki/Phorophyte>
4. Kalb, K., Rivas Plata, E., Lücking, R., Lumbsch, HT. *Biblo. Lichen.* 2011; 106: 13-163.
5. Awasthi DD. *Biblo. Lichen.* 1991; 40: 66-75.
6. Brodo JM, Culberson WL, Culberson CF. *Bryologist.* 2008; 111 (3): 363-423.
7. Elix JA, *Lichenologist.* 2007; 38 (2): 135-141.
8. Lumbsch HT. *Flora of Australia.* 2004; 56A:11-62.
9. Rambold, G. *Biblo. Lichen.* 1989; 34: 10-69.
10. White et al, *Anim. Feed Sci. Technol.*, 2002; 99 (1-4): 45-64.
11. Lugo AE, Snedarker SC. *Annual Review of Ecology and Systematics.* 1974; 5: 39-64.
12. Aptroot, A. *Bibliotheca Lichenologica.* 1997; 68: 203-213.
13. Boonpragob, K., and Polyiam, W. *Biblo. Lichen.* 2007; 96: 25-48.
14. Aptroot, A., Saipunkaew, W., Sipman, H. J. M., Sparrius, L. B., & Wolseley, P. A. *Fungal Diversity.* 2007; 24: 75-134.
15. Kantvilas G, Papong K, Lumbsch HT. *Lichenologist.* 2010; 42 (5): 557-561.
16. Nash, T.H., Ryan, B.D., Gries, C., Bungartz, F., (eds.), *Lichen Flora of the Greater Sonoran Desert Region.* 2004; 2.
17. Papong K, Lumbsch HT. *Lichenologist.* 2011; 43: 299-320.



THE APPLICATION OF BARCODE DNA-HIGH RESOLUTION MELTING (BAR-HRM) ANALYSIS FOR AUTHENTICATION OF *Clinacanthus nutans*

Nattawat Angkuljarernpon,¹ Aussara Panya,² Pattarasuda Chayapakdee^{2,*}

¹ Master of Science Program in Biology, Faculty of Science, Chiang Mai University, Chiang Mai 50200, Thailand

² Department of Biology, Faculty of Science, Chiang Mai University, Chiang Mai 50200, Thailand

*e-mail: pattarasuda.c@cmu.ac.th

Abstract:

Clinacanthus nutans, a medicinal plant from Acanthaceae family, is included in Thailand's essential medicinal plant list for treating diabetes, skin rashes, insects and snake bites, and inflammation from Herpes simplex virus infection. This plant has very similar morphological features to another Acanthaceae species, namely *Clinacanthus siamensis*. Also, they share local names across regions leading to confusion of plant identification. For effective use of medicine derived from the plants, raw plant materials should be accurately authenticated. However, the identification of these plants from dried leaves or herbal powder is challenging, therefore, application of molecular biology technique is necessitated. This research aimed to analyze potential genes to create molecular markers and develop Bar-HRM (Barcode DNA-High Resolution Melting) system for discrimination of *C. nutans* from other closely related plant species. Two highly conserved chloroplast genes, *rbcL* and *trnH-psbA* were selected for Bar-HRM analysis. The results showed that the *rbcL* gene with 95.97 - 97.98% identity could distinguish each species in this family but could not separate *C. nutans* from *C. siamensis* by Bar-HRM analysis. While the *trnH-psbA* gene has higher variation with 56.06 – 80.45% identity of DNA sequences could clearly separate the two plants. The Bar-HRM system from this study will be useful for the plant authentication, purity verification of medicinal plants in local markets, and can be used as a raw materials quality control in the plant-derived medicine industry.

Introduction:

Clinacanthus nutans (Burm.f) Lindau, known in Thai as "Phaya Yo," is a prominent medicinal plant in Thailand. It is used to treat skin rashes, insect and snake bites, inflammation from Herpes virus infection, diabetes, and gout in Thailand, Malaysia, Indonesia, and China. Chemical analyses have identified various bioactive compounds in *C. nutans*¹, such as flavonoids, glycosides, glycolipids, cerebrosides, and monoacyl-monogalatosylglycerol, which possess anti-inflammatory, antioxidant, and anti-diabetes properties.^{2,3,4,5,6} These plant extracts are non-toxic⁷, making them suitable for developing therapeutic treatments. However, quality control of the raw materials is crucial to ensure the efficacy and safety of these herbal medicines. In Thailand, more in-depth research is needed to harness the full potential of *C. nutans* extracts and develop high-value products.

Due to similar morphological characteristics and varying local names within the Acanthaceae family, confusion can arise. For example, "Male Sled Pang Pohn" refers to both *Clinacanthus siamensis* and *Barleria lupulina*. *C. siamensis* closely resembles *C. nutans*, to the extent that they were once classified as the same species.⁸ Despite their similar appearance, these plants have distinct pharmacological properties, indicating they are separate species.⁹ Therefore, accurately distinguishing *C. nutans* from other morphologically similar plants, especially in dried powder form, is challenging. This necessitates the development of molecular

biology techniques for precise plant identification and species discrimination more accurately than morphological separation to ensure the authenticity of herbal raw materials and analyze market products, including fresh, dried, and powdered samples.

Genetic variations can be used in plant species discrimination through gene sequencing or DNA fingerprinting. However, these methods are often time-consuming, expensive, and require expert analysis.¹⁰ To overcome these challenges, the Bar-HRM (Barcode DNA-High Resolution Melting) technique has proven effective. The Bar-HRM uses real-time PCR (Polymerase Chain Reaction) combined with DNA melting temperature curves to analyze variations in the DNA sequence of a specific gene region and measures subtle differences in the melting curve. If the target gene has sufficient sequence variations, this technique can effectively differentiate closely related plant species, even in powdered form.¹¹

Chloroplast genes are widely used to study plant diversity and DNA barcoding.^{12,13} For example, the *rbcL* gene was successfully used to separate three species within the Acanthaceae family using the Bar-HRM technique.¹¹ Meanwhile, the *ITS2* gene demonstrated the ability to discriminate several Acanthaceae species but could not separate *C. nutans* from *C. siamensis*.¹⁴ Additionally, the *trnH-psbA* gene can be used as a DNA marker to separate *C. nutans* and *C. siamensis* from other species in the Acanthaceae family.¹⁵

This study aims to analyze genes with potential to create molecular markers for discrimination of medicinal plants in the Acanthaceae family and to develop a Bar-HRM system for the identification and authentication of *C. nutans* and *C. siamensis*. This method is intended to serve as a quality assurance tool for herbal raw materials in the development of medicinal products from *C. nutans*. In addition, the system will be benefit for authentication of other herbal products available in the market.

Methodology:

Plant materials and DNA isolation

Clinacanthus nutans (Phaya Yo) plant samples were collected from ten diverse cultivation sources across Thailand along with three other plant species in the Acanthaceae family with similar characteristics. These species included *Andrographis paniculata* (Fah Talai Jone), *Barleria lupulina* (Male Sled Pang Pohn), and *Clinacanthus siamensis* (Phaya Plong Thong). The plant sample locations were listed in Table 2. The Queen Sirikit Botanic Garden's (QSBG) taxonomist has verified the identification of the plant species.

DNA was isolated from both fresh and dried leaf samples using liquid nitrogen for sample grinding, followed by a Genomic Plant DNA Purification Kit (PureLink™, USA). DNA quality and quantity were evaluated using an agarose gel electrophoresis and a NanoDrop microvolume spectrophotometer. The best extraction method yielding the highest quality DNA was used for further analysis.

Data mining & Genes analysis

Plastid DNA regions suitable for DNA barcoding, such as *trnH-psbA*, *rbcL*, and *matK* genes from selected medicinal plants in the Acanthaceae family were extracted from the GenBank database (NCBI; National Center for Biotechnology Information). These sequences were undergoing critical evaluation via multiple alignments using Bioedit software (version 7.2). Variable characters were calculated to design specific primer for high-resolution melting (HRM) analysis. The suitable genes should contain conserved region within species collected from diverse areas, while showing enough variation among different species.

Specific primers design

Primers specific to the target gene were designed considering gene positions, gene length, GC base composition, and percentage of base sequence variations using Primer3Plus



and MEGA11. Two criteria were ensured successful HRM analysis: 1) primer pairs should amplify a PCR product less than 300 bp, and 2) primers should cover enough variable sites to distinguish among the tested species.¹⁶ Candidate primer pairs were tested by amplifying the target gene using PCR and gel electrophoresis.

Optimization of real-time PCR condition

Real-time PCR was performed using HOT FIREPol® EvaGreen® HRM Mix (Solis Biodyne, Tartu, Estonia) in CFX Opus 96 Real-Time PCR System (Bio-RAD, California, USA) to increase DNA quantity. Primer concentrations and real-time PCR conditions were optimized. The thermocycling reactions was conducted in a 96-well plate with an initial denaturation step at 95 °C for 2 minutes, followed by 40 cycles of denaturation at 95°C for 10 seconds, annealing at 57°C for 30 seconds and extension at 72°C for 30 seconds. Fluorescent data was acquired at the end of each extension step during the PCR. After that, products were denatured at 95°C for 30 seconds, annealed at 60°C for 60 seconds to form heteroduplexes, and then melted gradually from 60°C to 95°C. Fluorescence data were collected every 0.2°C by Bio-Rad CFX Maestro programs. After that, Bio-Rad Precision Melt Analysis program was used to generate normalized and differential melting curves for characterization of DNA melting temperature (T_m) from each sample, and to distinguish different medicinal plants from DNA melting curves. The Precision Melt Analysis was conducted on each species, including DNA derived from fresh and dried samples to develop the Bar-HRM system.

Results and Discussion:

From previous research, Bar-HRM analysis has been used to authenticate some plant species in Acanthaceae family. The *rbcL* gene has been successfully used for discrimination of three Acanthaceae species: *Rhinacanthus nasutus*, *Acanthus ebracteatus*, and *Andrographis paniculata*.¹¹ While the *ITS2* gene was used to distinguish several Acanthaceae species except *C. nutans* and *C. siamensis*.¹⁴ In addition, the *trnH-psbA* gene was reported to have more variation among these two species.¹⁵ Therefore, the *rbcL* and *trnH-psbA* genes were further analyzed in this study.

Specific primer design

The sequences of two genes, *rbcL* and *trnH-psbA*, were extracted from the NCBI GenBank database to design specific primers. However, the sequence for *C. siamensis* is not available in the database. Therefore, sequences from other two close species, *B. lupulina* and *A. paniculata* have been used together with *C. nutans* for primer design. The reference accession number of these three species were NC_070082.1, NC_022451.2, and NC_042162.1, respectively. The specific primers were designed based on the previous study^{15,11} and sequence alignment. The sequence of specific primers was shown in Table 1.

DNA isolation and primer evaluation

Total DNA extracted from leaves of 17 plant samples were subjected to evaluation of quality and quantity (Table 2). Samples 1-11 were *C. nutans* collected from various planting areas across Thailand, while samples 12-17 were closely related Acanthaceae species. The extracted DNA samples had high quality and concentration ranged from 7.0 – 545.9 ng/μL which is good enough to be used as DNA templates. All extracted DNA samples were subjected to DNA amplification by PCR using the specific primers designed for this study.

Table 1. Specific primer sequences designed for DNA amplification of the *rbcL* and *trnH-psbA* gene and the PCR product sizes from each plant species

| Primer | Sequence | PCR product (bp) | | |
|---------|----------------------------------|------------------|--------------------|----------------------|
| | | <i>C. nutans</i> | <i>B. lupulina</i> | <i>A. paniculata</i> |
| rbcL1_F | 5'-CACAAACAGAGACTAAAGCAAGTGTT-3' | 247 | 247 | 247 |
| rbcL1_R | 5'-GTAGCATCGCCCTTTGTAACG-3' | | | |
| rbcL2_F | 5'-GCGTTGGAGAGATCGTTTCTTATT-3' | 191 | 192 | 192 |
| rbcL2_R | 5'-GCAGTGAATCCTCCTGTAAAGTAG-3' | | | |
| psbA1_F | 5'-GCCTTGATCCACTTGGCTACAT-3' | 311 | 527 | 303 |
| psbA1_R | 5'-GRTCCAACAAATGGATAAGACTTG-3' | | | |
| psbA2_F | 5'-CGCATGGTGGATTCAACAATC-3' | 392 | 608 | 384 |
| psbA2_R | 5'-GAAGTTATGCATGAACGTAATGCTC-3' | | | |

The PCR products amplified by *rbcL1* and *rbcL2* primers were the same size among four plant species, 247 bp and 192 bp, respectively (Figure 1A, 1B, Table 1). While the PCR products amplified by *trnH-psbA1* and *trnH-psbA2* primers ranged from 303 – 527 bp and 384 – 608 bp, respectively (Figure 1C, 1D, Table 1). The results suggest that there are more genetic variations in *trnH-psbA* gene than that of *rbcL* gene. Similar results were found in previous study ¹⁵, indicating that *trnH-psbA* gene would be a better candidate for developing of genetic markers.

Table 2. Locations of plant samples and concentrations of DNA extracted from leaf samples

| No. | Species | Location | Sample Code | DNA Conc. (ng/μL) |
|-----|--------------------------------|-------------------------|--------------------|-------------------|
| 1 | <i>Clinacanthus nutans</i> | Bangkok | C. nut BKK - Fresh | 368.1 |
| 2 | <i>Clinacanthus nutans</i> | QSBG, Chiang Mai | C. nut CM1 - Fresh | 18.2 |
| 3 | <i>Clinacanthus nutans</i> | QSBG, Chiang Mai | C. nut CM1 - Dried | 128.7 |
| 4 | <i>Clinacanthus nutans</i> | Mueang, Chiang Mai | C. nut CM2 - Fresh | 336.5 |
| 5 | <i>Clinacanthus nutans</i> | San Pa Tong, Chiang Mai | C. nut CM3 - Fresh | 545.9 |
| 6 | <i>Clinacanthus nutans</i> | Loei | C. nut LEI - Fresh | 93.7 |
| 7 | <i>Clinacanthus nutans</i> | Lampang | C. nut LP - Fresh | 128.6 |
| 8 | <i>Clinacanthus nutans</i> | Nonthaburi | C. nut NB - Fresh | 194.5 |
| 9 | <i>Clinacanthus nutans</i> | Nakhon Si Thammarat | C. nut NST - Fresh | 114.3 |
| 10 | <i>Clinacanthus nutans</i> | Samut Prakan | C. nut SPK - Fresh | 328.3 |
| 11 | <i>Clinacanthus nutans</i> | Ubon Ratchathani | C. nut UBN - Fresh | 358.0 |
| 12 | <i>Clinacanthus siamensis</i> | QSBG, Chiang Mai | C. siam CM – Fresh | 7.6 |
| 13 | <i>Clinacanthus siamensis</i> | QSBG, Chiang Mai | C. siam CM – Dried | 7.0 |
| 14 | <i>Barleria lupulina</i> | QSBG, Chiang Mai | B. lupu CM – Fresh | 87.1 |
| 15 | <i>Barleria lupulina</i> | QSBG, Chiang Mai | B. lupu CM – Dried | 46.0 |
| 16 | <i>Andrographis paniculata</i> | QSBG, Chiang Mai | A. pani CM – Fresh | 16.0 |
| 17 | <i>Andrographis paniculata</i> | QSBG, Chiang Mai | A. pani CM – Dried | 9.3 |

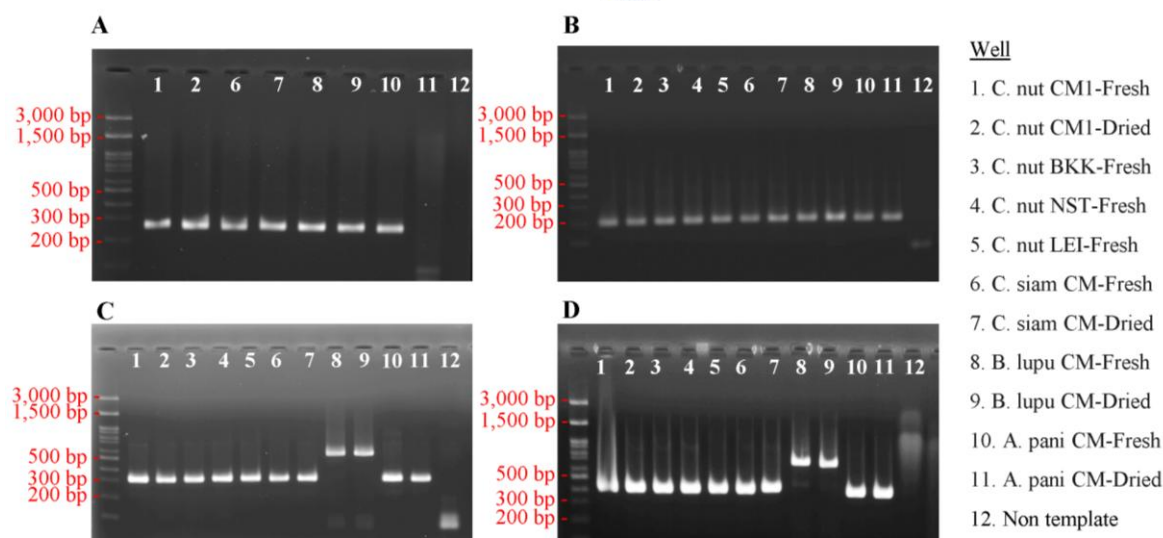


Figure 1. The PCR products amplified by each primer pairs with DNA templates extracted from four medicinal plants including fresh and dried leaf samples. A) *rbcL1* primer B) *rbcL2* primer C) *trnH-psbA1* primer D) *trnH-psbA2* primer.

HRM profile validation

To develop Bar-HRM system, the real-time PCR was performed, and DNA melting curves were analyzed in four plant species using each specific primer pairs. The results demonstrated same pattern of DNA melting curves of *rbcL* and *trnH-psbA* genes in the same species collected from different region of Thailand. Additionally, the melt curves from DNA extracted from both fresh and dried samples of the same species yielded consistent results (Figure 2), indicating that these two genes were quite conserved and HRM analysis was very accurate. The PCR products amplified by *rbcL1* primers revealed three patterns of meting curves from four species (Figure 2A, 2C), suggesting that this primer pair could distinguish *Clinacanthus* genus from other genus. However, *C. nutans* (red lines) and *C. siamensis* (green lines) could not be separated by this gene. We expected the same results for *rbcL2* primers; therefore, they were not further analyzed for HRM.

On the other hand, the PCR products from *trnH-psbA1* primers showed distinct four patterns of melting curves from four different plant species (Figure 2B, 2D). This indicates that the *trnH-psbA1* primer could effectively discriminate four species including *C. nutans* and *C. siamensis*. The *trnH-psbA2* primers showed potential for distinguishing the four plants (data not show), however, the melting curves were quite fluctuated and not as distinct as those obtained with *trnH-psbA1* primers. It probably because the size of PCR products amplified by this primer pair were larger than 600 base pairs, which may reduce accuracy of the analysis.¹⁴

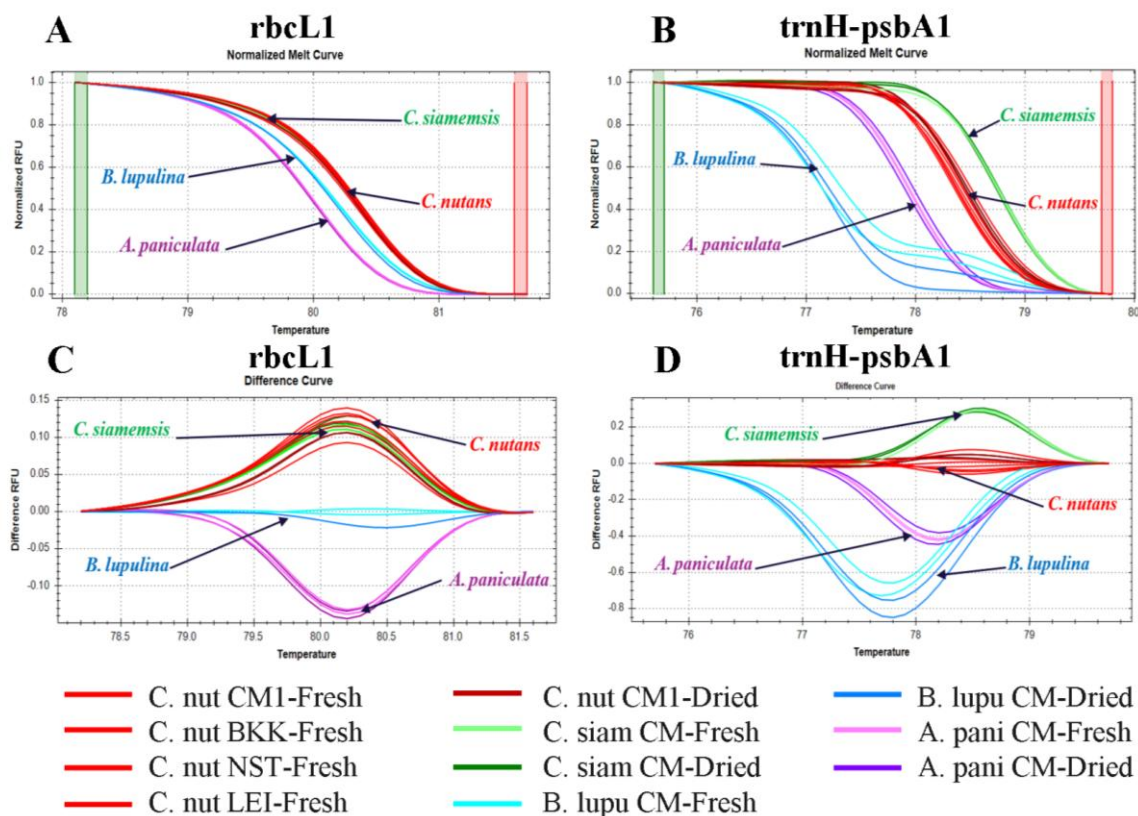


Figure 2. The normalized curves of melting temperature (T_m) of PCR products derived from A) *rbcL1* primer, B) *trnH-psbA1* primer, and adjusted difference curves of C) *rbcL1* primer, D) *trnH-psbA1* primer using a reference species in HRM analysis. The DNA templates were extracted from fresh and dried leaves of four medicinal plants. The real-time PCR reaction was conducted twice for each samples.

The pairwise analysis revealed that PCR products from *rbcL1* primer have % identity range from 95.97% - 97.98% (Table 3A), suggesting that this gene is highly conserved among different species. Hence, the inability to distinguish between *C. nutans* and *C. siamensis* may cause by the sequences are very similar¹⁴

. The DNA sequences from *rbcL2* primers showed similar range of % identity, 95.83% - 96.88% (Table 3B), therefore HRM analysis of this primer was not continued. On the other hand, the *trnH-psbA1* primer could clearly separate all four species, probably because DNA sequences from this primer have more diversity with % identity range from 56.06% - 80.45% (Table 3C). To characterize sequence difference between *C. nutans* and *C. siamensis*, the gene sequencing should be further examined.

Conclusion:

The Bar-HRM system developed with specific primers for *rbcL* gene can be used to classify some plants in Acanthaceae family, but cannot distinguish *C. nutans* and *C. siamensis*, while *trnH-psbA* gene is more effective for discrimination of these two species. This study demonstrated the potential of Bar-HRM technique as an essential tool for medicinal plants authentication and purity verification of raw herbal materials in plant-derived medicine industry in the future.



Table 3. Pairwise analysis showing percent identity (%) of the DNA sequences derived from four primer pairs in three plant species. The numbers in brackets refer number of nucleotide difference.

A) The rbcL1 primer

| Species | <i>C. nutans</i> | <i>B. lupulina</i> | <i>A. paniculata</i> |
|----------------------|------------------|--------------------|----------------------|
| <i>C. nutans</i> | 100% (0) | 97.18% (7) | 95.97% (10) |
| <i>B. lupulina</i> | | 100% (0) | 97.98% (5) |
| <i>A. paniculata</i> | | | 100% (0) |

B) The rbcL2 primer

| Species | <i>C. nutans</i> | <i>B. lupulina</i> | <i>A. paniculata</i> |
|----------------------|------------------|--------------------|----------------------|
| <i>C. nutans</i> | 100% (0) | 96.88% (6) | 95.83% (8) |
| <i>B. lupulina</i> | | 100% (0) | 95.83% (8) |
| <i>A. paniculata</i> | | | 100% (0) |

C) The trnH-psbA1 primer

| Species | <i>C. nutans</i> | <i>B. lupulina</i> | <i>A. paniculata</i> |
|----------------------|------------------|--------------------|----------------------|
| <i>C. nutans</i> | 100% (0) | 56.06% (>10) | 80.45% (>10) |
| <i>B. lupulina</i> | | 100% (0) | 57.96% (>10) |
| <i>A. paniculata</i> | | | 100% (0) |

D) The trnH-psbA2 primer

| Species | <i>C. nutans</i> | <i>B. lupulina</i> | <i>A. paniculata</i> |
|----------------------|------------------|--------------------|----------------------|
| <i>C. nutans</i> | 100% (0) | 56.13% (>10) | 80.50% (>10) |
| <i>B. lupulina</i> | | 100% (0) | 58.03% (>10) |
| <i>A. paniculata</i> | | | 100% (0) |

References:

1. Tuntiwachwuttikul P, Pootaeng-On Y, Phansa P, Taylor WC. Chemical and Pharmaceutical Bulletin. 2004; 52: 27–32.
2. Pannangpetch P, Laupattarakasem P, Kukongviriyapan V, Kukongviriyapan U, Kongyingyoes B, Aromdee C. Songklanakarin Journal of Science and Technology. 2007; 29: 1–9.
3. Thongyim S, Chiangchin S, Pandith H, Tragoolpua Y, Jangsutthivorawat S, Panya A. Antibiotics. 2023; 12: 549.
4. Wanikiat P, Panthong A, Sujayanon P, Yoosook C, Rossi AG, Reutrakul V. Journal of Ethnopharmacology. 2008; 116: 234–244.
5. Yong YK, Tan JJ, Teh SS, Mah SH, Ee GCL, Chiong HS, Ahmad Z. Evidence-based Complementary and Alternative Medicine. 2013; 1-8.
6. Ong WY, Herr DR, Sun GY, Lin TN. Molecules. 2022; 27: 1–16.
7. Chelyn JL, Omar MH, MohdYousof NSA, Ranggasamy R, Wasiman MI, Ismail Z. TheScientific World Journal. 2014; 1-6.
8. Alam A, Ferdosh S, Ghafoor K, Hakim A, et al. Asian Pacific Journal of Tropical Medicine. 2016; 9(4): 402–409.
9. Kunsorn P, Ruangrunsi N, Lipipun V, Khanboon A, Rungsihirunrat K. Asian Pacific Journal of Tropical Biomedicine. 2013; 3: 284-290.
10. Boonsom T. EAU HERITAGE JOURNAL Science and Technology. 2017; 11(2): 1-13.
11. Osathanunkul M, Madesis P, Hugo de Boer. PLoS ONE. 2015; 10: 1–11.

12. Huang S, Ge X, Cano A, Salazar BGM, Deng Y. Peerj. 2020; 1-24.
13. CBOL Plant Working Group. PNAS. 2009; 106: 12794-12797.
14. Suesatpanit T, Osathanunkul K, Madesis P, Osathanunkul M. BMC Complementary and Alternative Medicine. 2017; 17: 1–10.
15. Ismail NZ, Arsad H, Samian MR, Hamdan MR, Othman AS. 3 Biotech. 2018; 8:1-8.
16. Madesis P, Ganopoulos I, Anagnostis A, Tsaftaris A. Food Control. 2012; 25:576–582.



THE ASSOCIATION OF CIRCADIAN RHYTHM AND DRUG SENSITIVITY IN PANCREATIC CANCER CELLS

Pakjira Rattanabuntur¹, Kittipong Prajanpol², Waratchaya Naksiang², Pagkapol Y. Pongsawakul², Thaned Kangsamaksin^{1, *}

¹ Department of Biochemistry, Faculty of Science, Mahidol University, Bangkok, Thailand

² Department of Biology, Faculty of Science, Mahidol University, Bangkok, Thailand

*E-mail: thaned.kan@mahidol.edu

Abstract:

The circadian clock is an internal timekeeper that regulates daily cellular, physiological and behavioral functions including cell cycle, proliferation, and apoptosis. In mammals, core clock proteins CLOCK:BMAL1 as activators and PER:CRY as repressors drive rhythmic expression of *PER*, *CRY*, and many other clock-controlled genes via transcription-translation feedback loops. Disruptions in the circadian rhythm of clock genes are linked to various cancers, including pancreatic cancer, which is aggressive and challenging to treat due to its rapid progression and resistance to chemotherapy. Many chemotherapeutic drugs have targets that are rhythmic in cancer cells, suggesting that treatment timing could affect drug efficacy. However, the circadian gene expression in cancer cells varies by tissue type and individuals, which complicates treatment optimization. This study explores whether pancreatic cancer cell lines, PANC-1 and MIA PaCa-2, exhibit circadian rhythms that could inform more effective drug treatment timing. Representative gene expression of core circadian clock components *PER2* and *BMAL1* was measured using qRT-PCR. Cells were treated with chemotherapy at times of peak and trough expression of these genes, and the cell viability was assessed by an MTT assay. Our findings indicate that PANC-1 and MIA PaCa-2 cells do have circadian rhythms. Treatment with the chemotherapeutic drug oxaliplatin at the peak of *PER2* expression (28 hours post-synchronization) showed an increased drug sensitivity compared to that of the trough of *PER2* (16 or 40 hours post-synchronization). Thus, timing of the chemotherapy treatment with the cellular circadian rhythms could improve treatment outcomes for pancreatic cancer leading to potential cancer chronotherapeutic practices for pancreatic cancer patients in clinical settings.

Introduction:

The circadian clock is an endogenous oscillator that drives rhythmic physiological and behavioral processes with a period of approximately 24 hours such as the sleep-wake cycle, hormone secretion, metabolic processes, biochemical processes, and molecular processes¹. Circadian rhythms can be synchronized with external environmental factors that change daily such as the light-dark cycle, temperature, and food intake¹. In mammals, circadian clocks are present in almost every tissue. They are essential for controlling almost rhythmic pathways in humans, such as cell cycle, cell proliferation, apoptosis, and DNA repair². The mammalian circadian system is composed of a central clock, which resides in the SCN of the hypothalamus. SCN neurons receive the timing light signals from the retinohypothalamic tract³; and the peripheral clocks outside of the SCN such as liver, colon, and pancreas that receive the timing signals from the SCN and other cues such as hormones and nutrients. Both of these works together to maintain cyclical homeostasis in the body². At

the cellular level, the circadian clock is regulated by many genes and protein activities. The eukaryotic circadian molecular mechanism works as transcription-translation negative feedback loops. In the mammalian system, the core clock genes are *CLOCK* and *BMAL1*, which encode transcriptional activators, and *PERIOD* (*PER1*, *PER2*, *PER3*) and *CRYPTOCHROME* (*CRY1* and *CRY2*) genes, which encode transcriptional repressors. After translation, PER and CRY proteins repress the activity of CLOCK/BMAL1⁴. Many studies have suggested that circadian disrupted lifestyles such as shift work increase risks of many pathogenic diseases such as sleep disorders, obesity, diabetes, mental disorders, and cancer⁵. Irregularity of the circadian clock can affect cellular processes, especially with the development of cancer. Several circadian clock genes exert tight control of several hallmarks of cancer including cell cycle, proliferation, immune response, and DNA damage response, and directly control many cancer-related genes such as *p53*, *Xpa*, and *c-Myc*⁶. Many types of human cancer show altered expression of clock genes including colorectal cancer, breast cancer, and pancreatic cancer.

Pancreatic cancer is one of the most aggressive cancers with poor survival rates. The initial symptoms are often not expressed. Early diagnosis is difficult, and the later stages are often different and obscure. Treatments are also quite difficult due to the emergence of resistance to conventional chemotherapy and radiotherapy⁷. One of the problems with cancer chemotherapeutic drugs is poor targeting efficiency and severe side effects⁸. Interestingly, some anticancer drugs have targets that vary at different cell cycle phases and those targets also have rhythmic drug metabolism, which is under the circadian clock regulation⁸. In addition, the healthy and malignant cells may have different expression patterns of circadian rhythm that may affect the different efficiency of drug administration and toxicity of anticancer agents⁹.

Chronotherapy or treatment that depends on circadian timing is a promising new approach to cancer treatments. The optimal timing to treat anticancer drugs can help maximize drug efficiency and minimize side effects⁸. Clinically, there are many chronotherapy studies with cancer patients, for example, colorectal cancer shows a better response in cancer patients and increase complete surgical when treated with the chemotherapy depending on the time¹⁰. However, these treatment approaches depend on the time specific to individual patients and the phase of circadian rhythm, which is tissue-specific and dependent on the stages of cancer. Therefore, this study aims to investigate the presence of circadian clock in pancreatic cancer cells by measuring clock gene expression and the differential responses and sensitivity of chemotherapeutic drug at different circadian times based on the rhythmic patterns of clock gene expression.

Methodology:

Cell culture

PANC-1 and MIA PaCa-2 were used as representative pancreatic cancer cells. PANC-1 was isolated from a pancreatic carcinoma of ductal cell origin. MIA PaCa-2 is an epithelial cell line that is established from tumor tissue of the pancreas. They were obtained from the American Type Culture Collection (ATCC, Manassas, VA, USA). These cells were maintained in culture media, which consists of Dulbecco's Modified Essential Medium (DMEM) with high glucose supplemented with 1% Penicillin-Streptomycin (Gibco, USA) and 10% fetal bovine serum, FBS (Cytiva, USA) at 37°C under 5% CO₂. Medium was replaced every 2 days while the cells were subcultured with 1:3 ratio.



Cell synchronization and collection

PANC-1 and MIA PaCa-2 were seeded into 6-well plates at 6×10^5 cells/well in 1 ml complete DMEM for 18 hours to allow cell attachment. Then, the culture media was replaced with 1 mM dexamethasone (MedChemExpress, USA) to reset and synchronize the cells, in complete DMEM media for 2 hours. Post dexamethasone treatment, the cells were maintained in complete DMEM and harvested for RNA extraction every 4 hours for a total of 48 hours.

RNA extraction and cDNA synthesis

Cell pellets were processed to isolate the total RNA by using GENEzol™ Reagent (Geneaid Biotech Ltd, Taiwan) and chloroform. RNA was then precipitated with isopropanol and washed with cold 70% ethanol. RNase-free water was used to serve as the elution buffer. RNA concentrations were determined using a nanodrop 2000 UV-Vis spectrophotometer at OD 260 nm. Subsequently, RNA at a concentration of 1 µg/µL was converted to cDNA using 5x iScript™ Reverse Transcription Supermix (Bio-Rad, USA) according to the manufacturer's protocol. The cDNA from each cell line was stored at -80°C.

Quantitative Reverse Transcription Polymerase Chain Reaction (qRT-PCR) assay

Following RNA extraction and cDNA conversion, the relative gene expression of *BMAL1* and *PER2* was assessed using qRT-PCR. The primers were employed for qRT-PCR (Table 1), and each sample was conducted in triplicate. Each qRT-PCR reaction consisted of Luna® Universal qPCR Master Mix (Biolabs), 10 µM of forward and reverse primers, and 1 µg of cDNA. In brief, the qPCR protocol included 40 cycles with initial denaturation at 95°C for 15 seconds, followed by annealing at 60°C for 30 seconds and extension at 55°C. Relative gene expression levels were determined using comparative quantification and normalized against the housekeeping gene *ACTB* that codes for β-actin.

Table 1. The list of primer sequences for qRT-PCR

| Gene | Primer sequence |
|-----------------------------|------------------------------|
| Housekeeping gene | |
| <i>ACTB</i> -f | 5'-CGAGGCCCCAGAGCAAGAGAG-3' |
| <i>ACTB</i> -r | 5'-CTCGTAGATGGGCACAGTGTG-3' |
| Circadian clock gene | |
| <i>PER2</i> -f | 5'-AGTTGGCCTGCAAGAACCAG-3' |
| <i>PER2</i> -r | 5'-ACTCGCATTTCCTCTTCAGGG-3' |
| <i>BMAL1</i> -f | 5'-GCCCATTGAACATCACGAGTAC-3' |
| <i>BMAL1</i> -r | 5'-CCTGAGCCTGGCCTGATAGTAG-3' |

Rhythmicity analysis

The rhythmicity of PDAC cells was analyzed from the expression of *PER2* and *BMAL1*. Cosinor Analysis (<https://cosinor.online/app/cosinor.php>) was used for non-linear regression of the expression of *PER2* and *BMAL1*.

Chemotherapeutic drug treatment and cell viability assay

After analysis of the gene expression, results showed patterns of rhythmicity, time points that *PER2* and *BMAL1* genes expressed the highest and the lowest were chosen for treatment with oxaliplatin, a chemotherapeutic drug for cancer treatment. The cells were seeded in each 24-well plate at 1×10^4 cells/well in 500 μ L culture DMEM at 37°C under 5% CO₂ for 18 hours to allow cell attachment. Then, the cells were synchronized by using 1 mM dexamethasone in 500 μ L culture DMEM for 2 hours. After cell synchronization, the cells were maintained with 500 μ L culture DMEM until the chosen time points. The cells were treated with oxaliplatin at 0, 1, 10, 100, 1000 μ M for PANC-1 and 0, 0.1, 1, 10, 100 μ M for MIA PaCa-2 and incubated for 48 hours at 37°C under 5% CO₂ prior to the MTT assay. Cell viability was determined by using the MTT assay with 0.5 mg/ml MTT solution. Fifty microliters of 5 mg/mL of the MTT solution were added per well and then incubated for 3 hours. The resulting crystal formazan was later dissolved by DMSO, and the absorbance at 540 nm of the resulting solution was measured using a microplate reader. The half-maximal inhibitory concentration (IC₅₀) was calculated from the absorbance data of each time point.

Statistical analysis

The quantitative data were shown as the mean \pm standard deviation (SD). The statistical significance was calculated using the student's t-test or one-way analysis of variance (ANOVA). The *P-value* that is less than 0.05 was determined as a statistically significant difference.

Results and Discussion:

Pancreatic cancer cell lines exhibit circadian rhythms

To investigate the circadian rhythm in pancreatic cancer cell lines, PANC-1 and MIA PaCa-2 were used as representatives for pancreatic cancer. After the cancer cell lines were reset and synchronized by dexamethasone to initiate the same phase of the circadian rhythm, a 48-hour time course cell collection and RT-qPCR measurement were performed (Figure 1). The expression of *PER2* and *BMAL1* that represented core clock genes were observed. According to our data and the Cosinor Analysis, PANC-1 and MIA PaCa-2 showed circadian oscillation. In PANC-1, *BMAL1* and *PER2* are expressed with circadian rhythmic and anti-phasic oscillation (*PER2* has a *P-value* = 0.00732; *BMAL1* has a *P-value* = 0.36536) (Figure 2A). Similarly, in MIA PaCa-2, *BMAL1* and *PER2* were expressed with circadian rhythms and exhibited anti-phasic oscillation (*PER2* has *P-value* = 0.10868, *BMAL1* has *P-value* = 0.16951), but *BMAL1* exhibited early phase approximately 4 hours compare with *PER2* phase (Figure 2B). Thus, PANC-1 and MIA PaCa-2 express the circadian rhythms. These suggest that the circadian clock exist in the pancreatic cancer cells *in vitro* and may regulate many intact cellular processes such as cell cycle events, cell proliferation, DNA repair, and metabolism processes found in the pancreas¹¹.

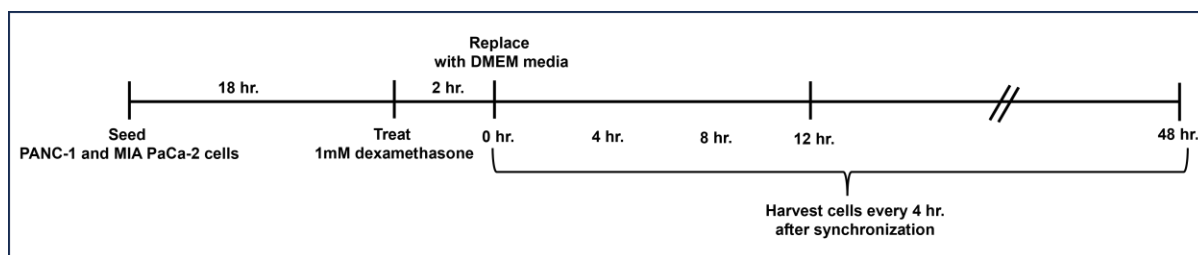


Figure 1. Diagram of experiment showing the protocol for preparing the sample to investigate the circadian rhythm in PDAC cell lines. The cells were collected every 4 hours until 48 hours after synchronization with 1 mM dexamethasone to analyse *PER2* and *BMAL1* expression by qRT-PCR.

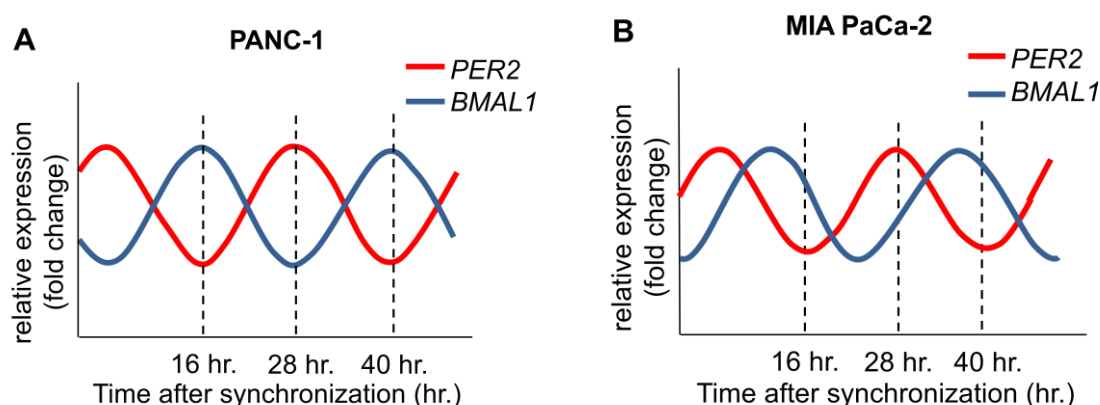


Figure 2. Expression of circadian clock genes in PANC-1 and MIA PaCa-2 from a 48-hour time course RT-qPCR. (A) *PER2* and *BMAL1* gene expression of PANC-1 and (B) *PER2* and *BMAL1* gene expression of MIA PaCa-2. The redrawn trace of *PER2* and *BMAL1* genes expression is shown as red and blue lines, respectively. These non-linear regression graphs were retrieved by Cosinor analysis.

Different timing of the drug treatment affects the drug sensitivity

According to the rhythmicity present in PANC-1 and MIA PaCa-2, the effects of different timing to the chemotherapeutic drugs sensitivity of pancreatic cancer cells were investigated. According to the data from Figure 2, the time points that expressed the highest and lowest of *PER2* expression were selected for the chemotherapeutic drug treatment. PANC-1 and MIA PaCa-2 exhibited the circadian rhythm of which *PER2* and *BMAL1* expressed the rhythmicity that varies at different time. In both cell lines, *PER2* has the highest expression at 28 hours and the lowest expression at 16 hours and 40 hours post synchronization, respectively. The cells at 16 hours, 28 hours, and 40 hours after synchronization were then treated with oxaliplatin, and the cell viability was assessed by the MTT assay (Figure 3). We found that the IC₅₀ at 28 hours was significantly decreased more

than 5-fold compared with IC_{50} at 16 hours in PANC-1 (Figure 4A). Similarly, in MIA PaCa-2, the IC_{50} at 28 hours was significantly decreased more than 2-fold compared with the IC_{50} at 16 hours (Figure 4B). The time point that coincides with the highest expression of *PER2* exhibited more sensitivity of the drug than the time point with the lowest expression of *PER2*. This finding indicates that different timing of drug treatment affects drug sensitivity.

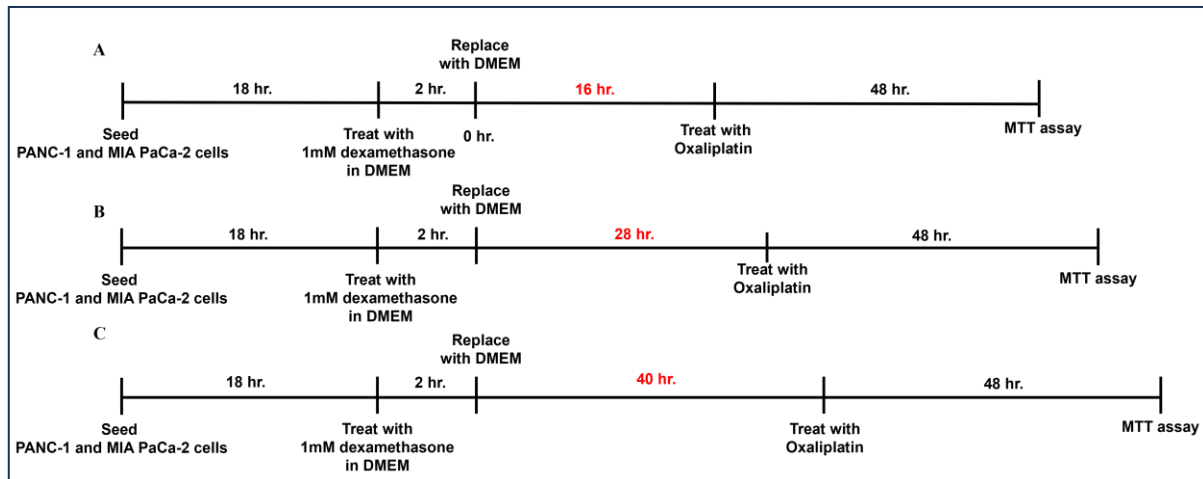


Figure 3. Diagram showing the experimental protocol for investigating the effect of different time treatments on drug sensitivity. Following the expression of *PER2* and *BMAL1*, the cells were treated with oxaliplatin at 16 hours (A), 28 hours (B), and 40 hours (C) after dexamethasone synchronization. The MTT assay was used for cell viability measurement.

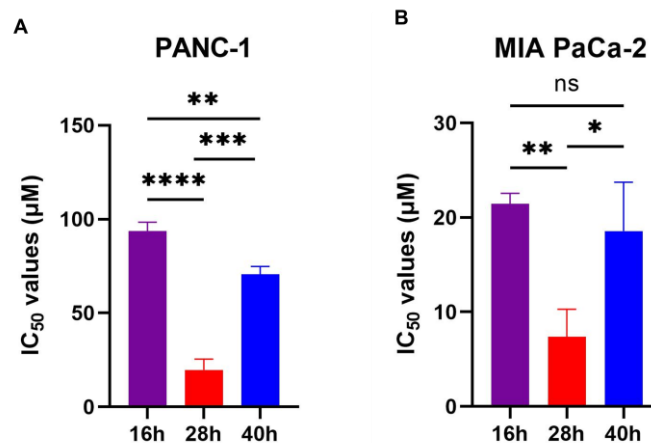


Figure 4. Different timing of drug treatment affects drug sensitivity. IC_{50} values of oxaliplatin between timepoint 16 hours (violet), 28 hours (red), and 40 hours (blue) after dexamethasone synchronization in PANC-1 (A) and in MIA PaCa-2 (B). The statistical analysis was tested by student's t-test. The error bar represented the mean \pm standard deviation (SD) of three independent experiments. * $P < 0.05$, ** $P < 0.01$, *** $P < 0.001$, and **** $P < 0.0001$ indicated statistically significant and ns indicated not significant.



The sensitivity of the chemotherapy drug, oxaliplatin, to pancreatic cancer cell lines increases at the phase with the highest expression of *PER2* (and the lowest of *BMAL1*) compared with the time point at the lowest expression of *PER2* (and the highest of *BMAL1*). Our work has suggested that anticancer drug sensitivity varies with the cellular circadian time and the expression of clock genes that is in agreement with previous reports that many pharmaceutical and anticancer drugs have cellular targets that are circadian-controlled^{12,13}. When *PER2* expression peaks, CRY protein is expressed at the lowest and may affect other genes that involve cell survival, cell cycle, or cell proliferation in decreased efficiency, resulting in more response to the drug treatment. A recent report has shown that pharmacological inhibition of CRY can improve cellular responses in cisplatin-treated osteosarcoma *in vitro*¹⁴. On the other hand, there is a report in colorectal cancer cells that *BMAL1* overexpression can inhibit cell proliferation and increase the sensitivity of cancer cells to oxaliplatin⁹. Taken together, several lines of evidence have shown that the response of cancer cells to the chemotherapy drug is specific and dependent upon types of cancer and the mechanisms of which chemotherapeutic drugs target. Therefore, thorough investigations of timing of chemotherapy and pharmacological modulation of circadian clock targets may provide optimal conditions that improve tissue tolerance and tumor toxicity for cancer treatment.

Conclusion:

In this study, PANC-1 and MIA PaCa-2 exhibit circadian rhythmicity after synchronization *in vitro*, which was observed by the rhythmic expression of clock genes *PER2* and *BMAL1*. Expression of *PER2* showed the highest expression at 28 hours and the lowest expression at 16 hours and 40 hours post synchronization by dexamethasone treatment. After the cells were treated with oxaliplatin and measured by the MTT assay, IC₅₀ values of timepoint at 28 hours was statistically decreased when compared with those of 16 hours and 40 hours in both cell lines. Our results show that the cellular circadian rhythms affect chemotherapeutic drug sensitivity suggesting that the anticancer drug sensitivity can be timely modulated as a result of molecular processes of the circadian clock. Therefore, modulation of circadian clock gene expression and protein activity may represent an alternative approach to chronotherapy for treating pancreatic cancer.

References:

1. Yao, J.; He, C.; Zhao, W.; Hu, N.; Long, D. *Acta Histochem* 2021, 123 (8), 151816.
2. Garcia-Costela, M.; Escudero-Feliu, J.; Puentes-Pardo, J. D.; San Juan, S. M.; Morales-Santana, S.; Rios-Arrabal, S.; Carazo, A.; Leon, J. *Front Endocrinol (Lausanne)* 2020, 11, 638.
3. Tsuchiya, Y.; Umemura, Y.; Yagita, K. *Int J Urol* 2020, 27 (6), 518-524.
4. Cox, K. H.; Takahashi, J. S. *J Mol Endocrinol* 2019, 63 (4), R93-r102.
5. Lee, Y. *Exp Mol Med* 2021, 53 (10), 1529-1538.
6. Sulli, G.; Lam, M. T. Y.; Panda, S. *Trends Cancer* 2019, 5 (8), 475-494.
7. Society., C. s. C. P. C. *Pancreatic Cancer Overview*.
<https://www.craigscase.ca/learn#Learn-Overview-pancreatic-cancer> (accessed 2020 14/12).
8. Fu, L.; Lee, C. C. *Nat Rev Cancer* 2003, 3 (5), 350-361.
9. Ozturk, N.; Ozturk, D.; Kavakli, I. H.; Okyar, A. *Int J Mol Sci* 2017, 18 (10).
10. Eriguchi, M.; Levi, F.; Hisa, T.; Yanagie, H.; Nonaka, Y.; Takeda, Y. *Biomed Pharmacother* 2003, 57 Suppl 1, 92s-95s.
11. Chan, K.; Wong, F. S.; Pearson, J. A. *Front Endocrinol (Lausanne)* 2022, 13, 920261.

12. Zhang, R.; Lahens, N. F.; Ballance, H. I.; Hughes, M. E.; Hogenesch, J. B. *Proc Natl Acad Sci U S A* 2014, *111* (45), 16219-16224.
13. Lee, Y.; Fong, S. Y.; Shon, J.; Zhang, S. L.; Brooks, R.; Lahens, N. F.; Chen, D.; Dang, C. V.; Field, J. M.; Sehgal, A. *Sci Adv* 2021, *7* (7).
14. Anabtawi, N.; Cvammen, W.; Kemp, M. G. *Sci Rep* 2021, *11* (1), 17997.



THE COMBINATION TREATMENT OF ANTI-CD47 ANTIBODY AND BORTEZOMIB ENHANCES MULTIPLE MYELOMA CELL DEATH

Ratchaneewan Sumankan^{1,2}, Chutipai Chiawpanit^{1,3}, Nunghathai Sawasdee^{4,5}, Yupanun Wutti-in^{1,6}, Pa-thai Yenchitsomanus^{4,5}, Seiji Okada⁷, Aussara Panya^{1,*}

¹ Cell Engineering for Cancer Therapy Research Group, Chiang Mai University, Chiang Mai 50200, Thailand.

² Graduate Master's Degree Program in Biology, Faculty of Science, Chiang Mai University, Chiang Mai 50200, Thailand.

³ Office of Research Administration, Chiang Mai University, Chiang Mai 50200, Thailand.

⁴ Siriraj Center of Research Excellence for Cancer Immunotherapy (SiCORE-CIT), Faculty of Medicine Siriraj Hospital, Mahidol University, Bangkok 10700, Thailand

⁵ Division of Molecular Medicine, Research Department, Faculty of Medicine Siriraj Hospital, Mahidol University, Bangkok 10700, Thailand

⁶ Department of Medical Technology, Faculty of Associated Medical Sciences, Chiang Mai University, Chiang Mai 50200, Thailand.

⁷ Division of Hematopoiesis, Joint Research Center for Human Retrovirus Infection, Kumamoto University, 2-2-1 Honjo, Chuo-ku, Kumamoto 860-0811, Japan

*e-mail: aussara.pan@cmu.ac.th

Abstract:

Multiple myeloma (MM) is a hematological malignancy that is characterized by uncontrolled clonal proliferation, which can cause the failure of bone marrow, causing other relevant organ dysfunctions. Bortezomib is the treatment for first-line therapy but nowadays some patients are resistant to bortezomib leading to relapse and becoming refractory to the treatments. A previous study showed that MM patients, who are resistant to bortezomib, have CD47 overexpression, resulting in inhibition and suppression of the anti-tumor activity of immune responses. Hence, blocking the CD47 signaling pathway has been proposed for cancer immunotherapy. Thus, this study aims to determine CD47 expression on MM.1S which is the cell line in MM, and to investigate the effect of the combination treatment of anti-CD47 antibody (magrolimab) and bortezomib enhances its anti-cancer effect against MM cells. Firstly, the CD47 expression of MM.1S is $97.4 \pm 1.87\%$ when compared with the isotype control. Thus, our result revealed that MM.1S has a high-level expression of CD47. Secondly, the cytotoxicity of bortezomib to MM.1S was investigated to obtain the appropriate concentration. The CC_{50} is equal to 7.426 and 3.714 nM for 24 and 48 hours after the treatment. Furthermore, the effect of the combination treatment was determined. The combination treatment of 34.25- μ M magrolimab and 3.125-nM bortezomib dramatically decreased MM.1S cell viability to $4.81 \pm 62.30\%$ compared to the non-treatment control (100%), bortezomib alone ($89.47 \pm 3.49\%$), and magrolimab alone ($94.45 \pm 8.27\%$). Moreover, the combination treatments can enhance MM cell death by sensitizing MM.1S cells to the effect of bortezomib, suggesting that magrolimab has a chemosensitization effect. In conclusion, our findings supported that the combination treatment of anti-CD47 antibody and bortezomib could be an effective alternative cancer treatment for MM patients.

Introduction:

Multiple myeloma (MM) is a hematological malignancy that is characterized by the uncontrolled clonal proliferation of malignant plasma cells in the bone marrow. The

malignant plasma cells secrete abnormal antibodies called monoclonal proteins (M-proteins) which can be detected in the blood and urine of patients with multiple myeloma. In addition, M-proteins can inhibit the production of normal blood cells and antibodies. Multiple myeloma can cause bone marrow failure or osteolytic lesions leading to other organ dysfunctions for instance hypercalcemia, renal failure, anemia, and immune paresis with resulting infection. [1] However, the cause of multiple myeloma has not been clearly studied. Many countries in Asia, particularly China, Japan, South Korea, Taiwan, and Thailand, have higher incidences than other regions. [2] Especially, the incidence of MM in Thailand ranks third among hematologic malignancies. [3] Currently, there are various therapeutics for patients with multiple myeloma such as standard chemotherapy, proteasome inhibitors (PIs), immunomodulatory drugs (IMiDs), and autologous transplantation, which aim to improve the outcomes and expand overall survival [4]. Bortezomib is a member of proteasome inhibitors, which is the first-line therapy that has been shown to improve the outcomes of the patients, however the acquired resistant to bortezomib has been increasingly reported resulting in relapse and becoming refractory to the standard treatments [5].

Interestingly, the previous report has shown that MM patients who are resistant to bortezomib have Cluster of Differentiation 47 (CD47) overexpression on the cell surface of cancer cells. [6] However, neither an underlying mechanism of CD47 overexpression in those patients nor the direct effect of bortezomib on CD47 expression has been reported currently. CD47, an integrin-associated protein (IAP), plays an important role in the immune escape mechanism of cancer cells by binding to signal regulatory protein- α (SIRP α) which is expressed on macrophages resulting in the activation of the “don’t eat me” signal. The binding causes the inhibition of cancer cell death and suppression of the phagocytosis activity of macrophages leading to the inability to engulf and kill cancer cells. [7] Thus, blocking the CD47 signaling pathway has been proposed as the target for tumor immunotherapy to enhance the anti-tumor activity.

Immunotherapy is an alternative treatment that can improve the efficacy and specificity to extend the overall survival of patients. The monoclonal antibodies (mAbs) are typically used in cancer patients. There are many mAbs for treatment with MM patients by targeting the specific proteins on MM cells. Hu5F9-G4 or Magrolimab, a humanized IgG4 antibody targeting CD47 expression, was the first used in humans (Phase I clinical trial). In preclinical *in vivo* models, magrolimab has shown potent antitumor activity in MM patients and can inhibit tumor cell growth in human tumor xenograft models. [8] In this study, we hypothesized that myeloma cells have high CD47 expression levels. So, the blockade of the CD47 signaling pathway by anti-CD47 antibody may enhance the anti-tumor activity against myeloma cells when combined with bortezomib. The expression level of CD47 on MM.1S cancer cell surface was investigated and tested whether the combination treatment of anti-CD47 antibody (magrolimab) and bortezomib could provide the synergistic effects to enhance MM cell death. Our findings support the combination treatment as a promising therapeutic strategy for MM treatment.

Methodology:

Cell line and cell culture condition

MM.1S, a multiple myeloma cell line was used in this study which was kindly acquired from Prof. Seiji Okada, Division of Hematopoiesis, Joint Research Center for Human Retrovirus Infection, Kumamoto University. The cell was cultured in RPMI-1640 media supplemented with 10% fetal bovine serum (10% FBS) (Gibco, Thermo Fisher Scientific, MA, USA), 2 nM of L-glutamine (Gibco, Thermo Fisher Scientific, MA, USA), and penicillin-streptomycin (Gibco, Thermo Fisher Scientific, MA, USA). The cell was



cultured at 37°C, 5% CO₂ incubator, and sub-cultures at every 3-day interval or when it reached 80-90% confluence. The MM.1S characteristic is represented in Table 1.

Table 1. The characteristics of MM.1S.

| Cell line | Phenotypes |
|-----------|---|
| MM.1S | B lymphoblast cell that was isolated from the peripheral blood of a Black, 42-year-old, female patient with immunoglobulin A lambda myeloma. (ATCC) |

Determination of CD47 expression on MM.1S

Flow cytometry was performed to obtain CD47 expression on MM.1S. The cells were harvested approximately 10⁵ cells per reaction. CD47 protein expression was detected by staining with anti-Human CD47 (eBioscience, California, USA) and IgG₁ (ImmunoTools, Friesoythe, Germany) as an isotype control at the dilution of 1:50 with 2% FBS in 1X of phosphate-buffered saline (1X PBS) and incubated on ice for 30 minutes in the dark environment. The stained cells were washed twice with 2% FBS in 1X PBS and subsequently analyzed by CytoFLEX flow cytometry. (Beckman Coulter, CA, USA)

Determination of the cytotoxicity of bortezomib on MM.1S

To determine the cytotoxicity of Bortezomib (Selleckchem, Japan) to MM.1S. The cells were seeded into 96-well plates (2x10⁴ cells per well) with RPMI-1640 media supplemented with 10% FBS, 2 nM of L-Glutamine, and penicillin streptomycin. Then, bortezomib in different concentrations (1.56, 3.125, 6.25, 12.5, 25, and 50 nM) was added and incubated for 24 and 48 hours, at 37°C, 5% CO₂ incubator. After the indicated times, Prestoblue™ reagent 10 µL per well was added to strain viable cells. The changes of the reagent color were measured at the absorbance of 570 and 595 nM by using a microplate reader. The percentage of cell viability was calculated and compared with the untreated control (set as 100%). Then, the half-maximal cytotoxicity concentration (CC₅₀) of each cell was analyzed using linear regression.

$$\% \text{ Cell viability} = [(\text{OD}_{570}-\text{OD}_{595})_{\text{test}} - (\text{OD}_{570}-\text{OD}_{595})_{\text{control}}] \times 100$$

Investigation of the anti-tumor activity of the combination treatment of anti-CD47 antibody and bortezomib against MM cell line

MM.1S was plated into 96-well plates with approximately 2x10⁴ cells per well with complete-RPMI-1640 media. The conditions of treatment were added and incubated for 24 hours at 37°C, 5% CO₂ incubator. After the indicated time, the percentage of cell viability was analyzed by Prestoblue™ reagent as aforementioned. The treatment conditions consist of two parts including a single treatment which is 34.25 µM of magrolimab (Selleckchem, Japan) or 3.125 nM of bortezomib. The second treatment is a combination treatment which is 34.25 µM of magrolimab combined with 3.125 nM of bortezomib.

Statistical analysis

All statistical analyses were conducted using GraphPad Prism5 software (GraphPad Software, Inc., San Diego, CA, USA) and Scikit (Python). Each experiment in this study was conducted in three independent experiments (n=3) and the data were expressed as mean ±

standard error of the mean (SEM). The independent-sample t-test (performed in comparing CD47 expression on MM.1S) and one-way ANOVA with post hoc Tukey-HSD test (performed in comparing the %cell viability in the control and the combination treatment) were used to analyze the statistical comparison of the data. All bar graphs show the error bars of the standard error of the mean (SEM). A p-value less than 0.05 was considered statistically significant.

Results and Discussion:

CD47 expression on MM.1S

To investigate CD47 expression on MM.1S. The cells were collected and stained with the antibody as aforementioned in the material and method. Flow cytometry was performed to determine the level expression of CD47 and the flow cytometry gating strategy shown in Figure A. The results are represented in the histogram (Figure 1A) and the bar graph (Figure 1B) demonstrating $97.4 \pm 1.87\%$ of MM.1S were CD47 positive cells. Thus, the results indicated that MM.1S has a high-level expression of CD47 similar to the previous report that showed the CD47 expression on MM.1S is higher than other cell lines such as H929 and U266 [9]. Indeed, CD47 is a potential prognosis marker based on its correlation with the disease progression and aggressiveness of MM which leads to unfavorable prognoses and worse clinical outcomes. [10] The previous report represented that MM patients with high CD47 expression had shorter progression-free survival and overall survival than those with low expression of CD47. [11] Hence, CD47 is an interesting target and the blockade of CD47 could be a potential therapeutic.

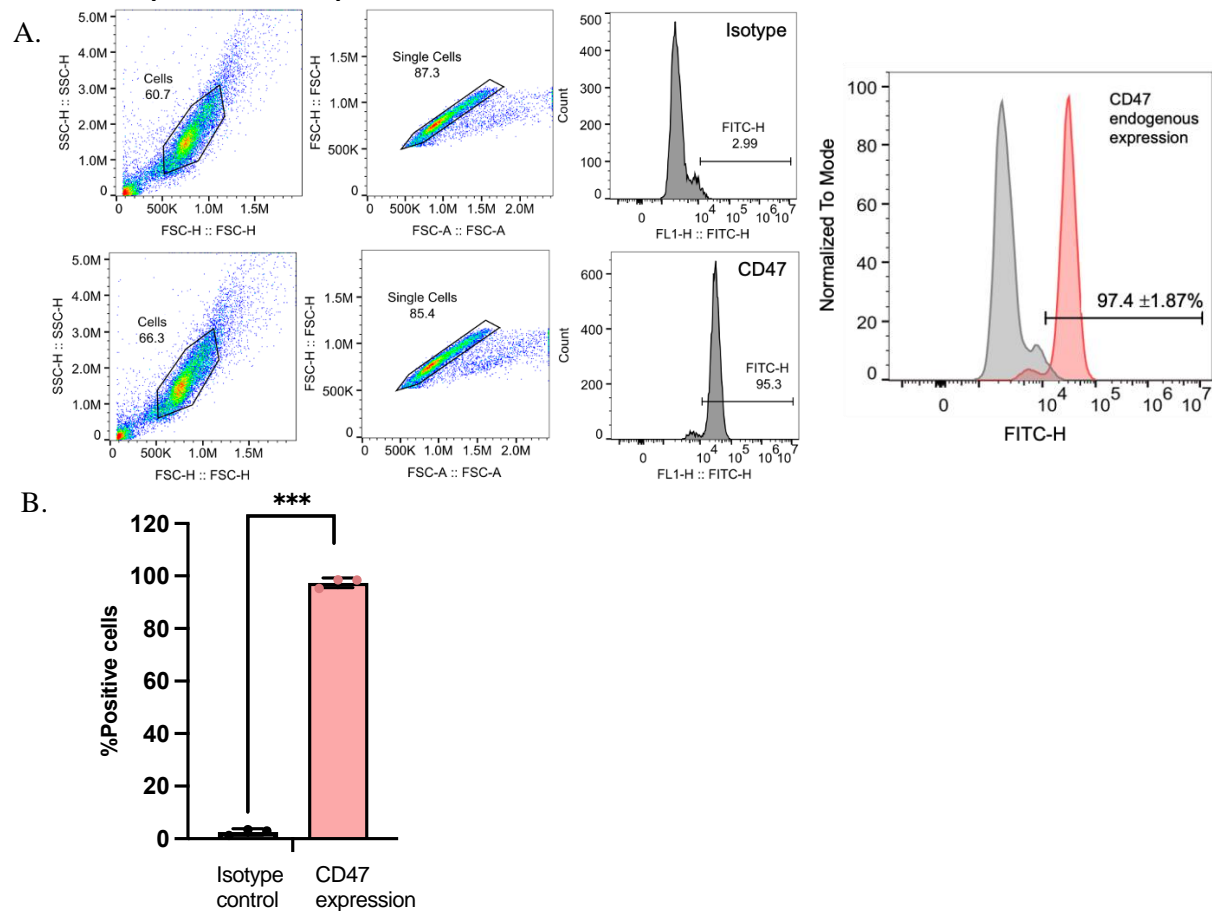


Figure 1. MM.1S has a high level of CD47 expression was represented as %positive cells in the histogram (A) and the bar graph (B) by flow cytometry when compared with the isotype control (IgG₁). (***) indicates $p < 0.001$ obtained from independent-sample-t-test)



Bortezomib cytotoxicity to MM.1S

MM.1S cells were treated with various concentrations of bortezomib including 1.56, 3.125, 6.25, 12.5, 25, and 50 nM, and incubated for 24 and 48 hours. After the indicated times, the cell viability was monitored and calculated to the percentage of cell viability (%cell viability) relative to non-treatment control (cells treated with drug diluent, DMSO). The results have demonstrated that the %cell viability of MM.1S decreased in a dose and time-dependent manner. (Figure 2A) The half-maximal cytotoxic concentration (CC_{50}) was analyzed by non-linear regression. The results revealed the CC_{50} of bortezomib for 24 and 48 hours are 7.426 and 3.714 nM, respectively. Thus, our study demonstrated that bortezomib can affect MM.1S cell death. Bortezomib is a proteasome inhibitor so it can cause cancer cell death by its ability to bind at the proteasome subunit 5 ($\beta 5$) for inhibition of proteasome activity leading to misfolded protein accumulated in the endoplasmic reticulum (ER) and then ER stress [5]. Consequently, interrupting the cell cycle leads to the accumulation of proapoptotic signals which triggers the apoptotic signaling pathway. In addition, it can also inhibit transcription factor nuclear factor- κB (NF- κB) pathway activation. [12] The previous studies reported that bortezomib resistance can develop in MM patients after receiving bortezomib for a while, also known as acquired resistance, and frequently occurs in MM. It is strongly associated with relapsed and refractory. [5]

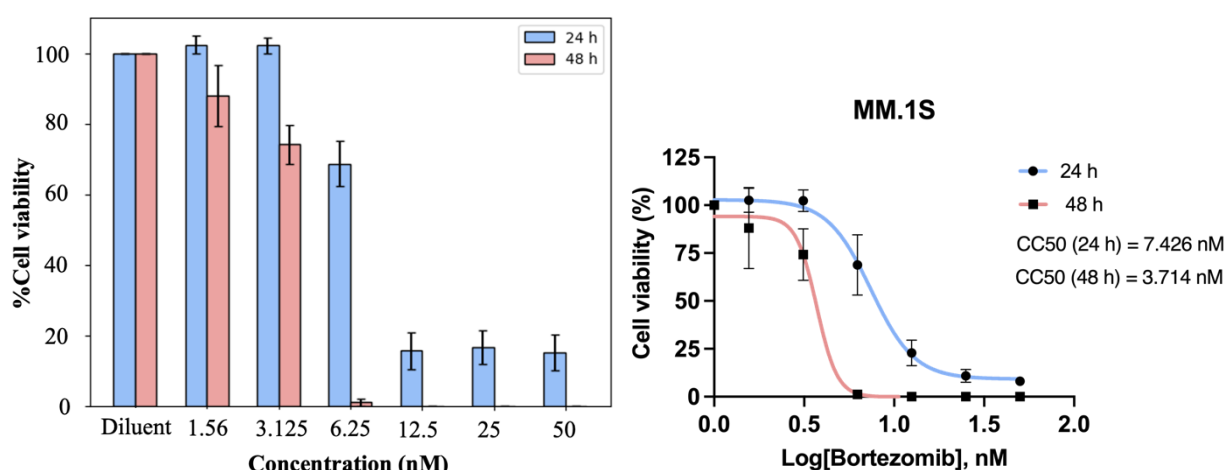


Figure 2. The cytotoxicity of bortezomib on MM.1S is determined by PrestobluTM reagent. The percentage of cell viability was calculated relative to the diluent control (DMSO), %cell viability was decreased in a dose and time-dependent manner. (Figure 2A) Moreover, the half-maximal cytotoxic concentration (CC_{50}) values using non-linear regression represented that CC_{50} equals 7.426 and 3.714 nM for 24 and 48 hours, respectively. (Figure 2B)

The combination treatment of anti-CD47 antibody and bortezomib to eliminate MM.1S

Due to CD47 overexpression is frequently found in MM patients who are resistant to bortezomib. Therefore, we hypothesized that the combination treatment of bortezomib with anti-CD47 antibody (magrolimab) would provide the synergistic effect. MM.1S cells were treated with four conditions of treatment including the diluent alone (DMSO), single treatment of 34.25 μM of magrolimab or 3.125 nM of bortezomib, and a combination

treatment of 34.25 μ M of magrolimab combined with 3.125 nM of bortezomib. The results revealed that the combination treatment had the most potential effect to reduce the % cell viability of MM.1S to $4.81 \pm 62.30\%$ which is higher than that of the bortezomib alone ($89.47 \pm 3.49\%$) and magrolimab alone ($94.45 \pm 8.27\%$) (Figure 3) Hence, our study demonstrated the synergistic effect of the combination treatment of anti-CD47 antibody and bortezomib to enhance MM.1S cell death.

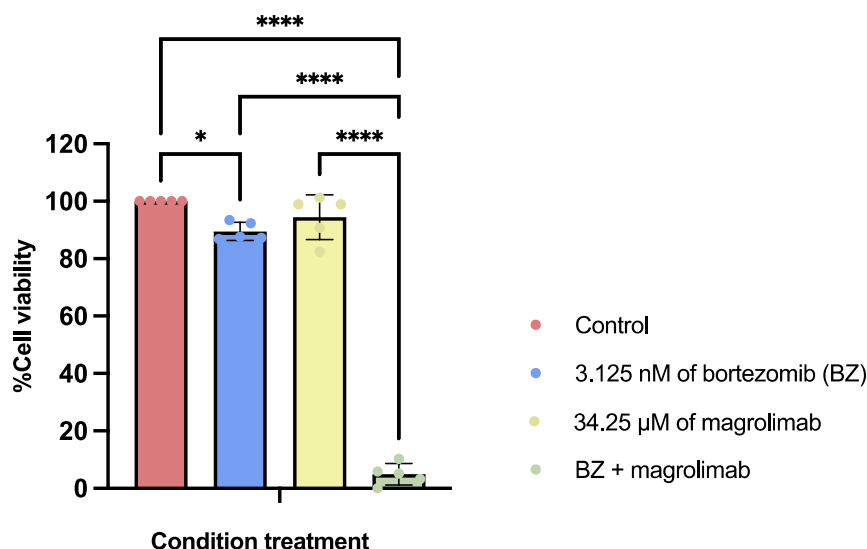
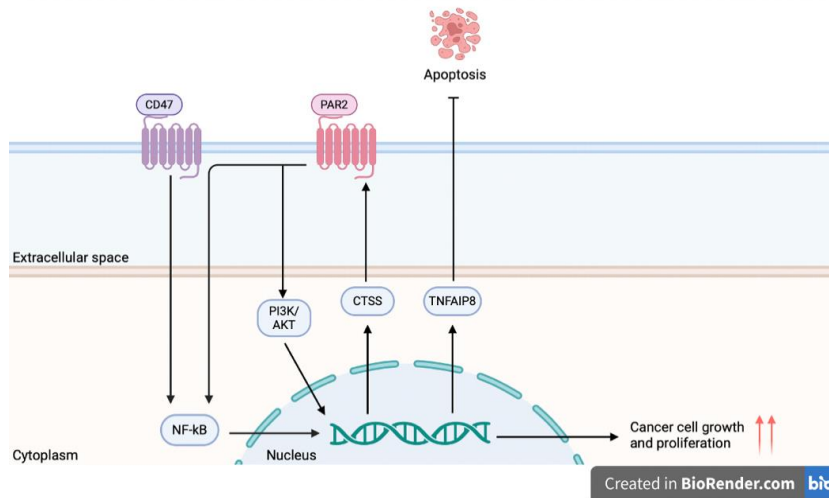


Figure 3. The combination of anti-CD47 antibody and bortezomib can enhance MM.1S cell death by sensitizing MM.1S cells to the effect of bortezomib via CTSS/PAR2 signaling pathway suggesting that magrolimab has a chemosensitization effect. (* and **** indicates $p < 0.05$ and $p < 0.0001$, respectively obtained from one-way ANOVA with post hoc Tukey-HSD test).

In accompanied with the previous report, the combination of anti-CD47 monoclonal antibody (B6H12) at 10 μ g/ml and the chemotherapeutic drugs doxorubicin or cisplatin significantly improved the anti-tumor effect on inhibiting the growth of hepatocellular carcinoma cells (HCC) [13]. Moreover, they found that this sensitization effect was independent on the macrophage phagocytosis role in CD47 and suggested that it was involved in the anti-CD47 antibody that inhibited the growth of HCC by chemosensitization effect via blocking of CTSS/PAR2 signaling pathway which is associated with the activation of cancer cell death. [13] [14] CD47 role in promoting tumor growth has been reported via two main mechanisms. Firstly, they activated the antiapoptotic activity of TNF- α -inducible protein 8 (TNFAIP8) leading to inhibiting caspase-8 and of caspase-3 activation. [15] Secondly, NF- κ B activation induces the cathepsin S (CTSS), a proteasome and a ligand for protease-activated receptor 2 (PAR2), resulting in the activation of PAR2. Additionally, PAR2 promotes tumor-initiating cells (TICs) which can be highly self-renewable and chemoresistance resulting in high development of cancer cell growth via activation PI3K/AKT. (Figure 4A) [16] [17] [18]. Hence, the blockade of CD47 activity by anti-CD47 antibody leads to the reduction of the NF- κ B and TNFAIP8 activations resulting in enhancing the cancer cell apoptosis. Accordingly, the combination treatment of anti-CD47 antibody and bortezomib might improve the sensitivity of myeloma cells to bortezomib via CD47 blockade which disturbed the anti-apoptotic activity. This could enhance bortezomib effect on promoting ER stress, suppressing NF- κ B activity by stabilizing the inhibition I κ B [19] resulting in the suppression of cancer cell growth and proliferation. Therefore, the combination treatment showed more anti-tumor effects than the single treatment which is anti-CD47 alone or bortezomib alone. (Figure 4B)



A



B

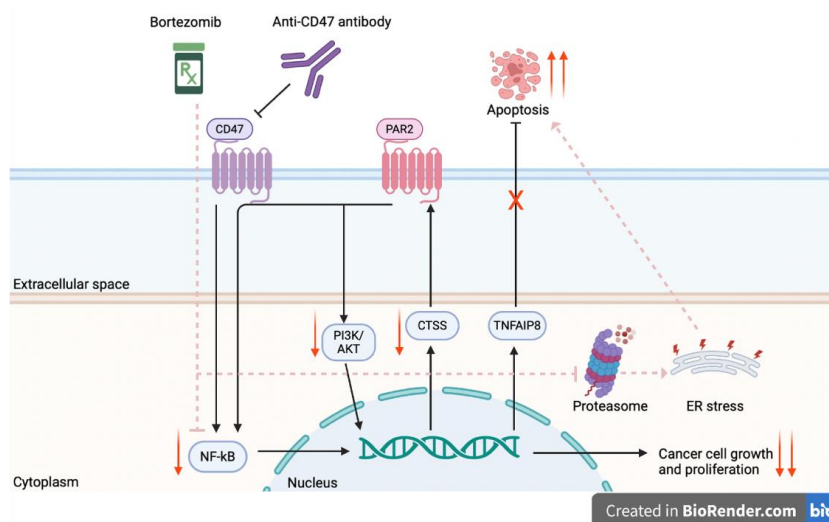


Figure 4. The schematic represents the mechanism of the combination treatment to enhance myeloma cell death. Normally, cancer cells/drug-resistant cells have CD47 overexpression leading to the activation of the NF- κ B signaling pathway resulting in the induction of two pathways which are CTSS/PAR2 and TNFAIP8 to increase the growth of the tumors and drug resistance. So, bortezomib cannot affect the cancer cell death. (Figure 4A) In addition, the combination treatment enhanced MM cell death by anti-CD47 antibody block CD47 signaling pathway leading to reduce the NF- κ B, CTSS/PAR2 and TNFAIP8 signaling pathway. Consequently, MM cell death was increased by the effect of bortezomib via the inhibition of the proteasome activity. (Figure 4B)

Conclusion:

This study demonstrated that the potential of combination treatment of an anti-CD47 antibody (magrolimab) and bortezomib on enhancing myeloma cell death. Our findings supported the use of the bortezomib-based combinational therapy with the anti-CD47 antibody which may be an alternative treatment for MM patients to improve the outcomes and expand the survival rate of the patients.

Acknowledgements:

This study was supported by Cell Engineering for Cancer Therapy Research Group, Chiang Mai University. We would like to express gratitude to the Development and Promotion of Science and Technology (DPST) and also sincerely thank the Siriraj Center of Research Excellence for Cancer Immunotherapy (SiCORE-CIT), Faculty of Medicine Siriraj Hospital, Mahidol University and Department of Medical Technology, Faculty of Associated Medical Sciences, Chiang Mai University, and Division of Hematopoiesis, Joint Research Center for Human Retrovirus Infection, Kumamoto University for the access of facilities and the equipment.

References:

1. Bird, S. A., & Boyd, K. (2019). Multiple myeloma: an overview of management. *Palliat Care Soc Pract*, 13, 1178224219868235.
2. Kumar, S. K., Rajkumar, V., Kyle, R. A., van Duin, M., Sonneveld, P., Mateos, M.-V., Gay, F., & Anderson, K. C. (2017). Multiple myeloma. *Nature Reviews Disease Primers*, 3(1), 17046.
3. Jirabanditsakul, C., Dakeng, S., Kunacheewa, C., Y, U. P., & Owattanapanich, W. (2022). Comparison of Clinical Characteristics and Genetic Aberrations of Plasma Cell Disorders in Thailand Population. *Technol Cancer Res Treat*, 21, 15330338221111228.
4. Rajkumar, S. V., & Kumar, S. (2020). Multiple myeloma current treatment algorithms. *Blood Cancer Journal*, 10(9), 94.
5. Kozalak, G., Bütün, İ., Toyran, E., & Koşar, A. (2023). Review on Bortezomib Resistance in Multiple Myeloma and Potential Role of Emerging Technologies. *Pharmaceuticals (Basel)*, 16(1).
6. Yue, Y., Cao, Y., Wang, F., Zhang, N., Qi, Z., Mao, X., Guo, S., Li, F., Guo, Y., Lin, Y., Dong, W., Huang, Y., & Gu, W. (2022). Bortezomib-resistant multiple myeloma patient-derived xenograft is sensitive to anti-CD47 therapy. *Leuk Res*, 122, 106949. [6]
7. Maute, R., Xu, J., & Weissman, I. L. (2022). CD47-SIRP α -targeted therapeutics: status and prospects. *Immunooncol Technol*, 13, 100070.
8. Sikic, B. I., Lakhani, N., Patnaik, A., Shah, S. A., Chandana, S. R., Rasco, D., Colevas, A. D., O'Rourke, T., Narayanan, S., Papadopoulos, K., Fisher, G. A., Villalobos, V., Prohaska, S. S., Howard, M., Beeram, M., Chao, M. P., Agoram, B., Chen, J. Y., Huang, J., . . . Padda, S. K. (2019). First-in-Human, First-in-Class Phase I Trial of the Anti-CD47 Antibody Hu5F9-G4 in Patients With Advanced Cancers. *J Clin Oncol*, 37(12), 946-953.
9. Sun, J., Muz, B., Alhallak, K., Markovic, M., Gurley, S., Wang, Z., Guenther, N., Wasden, K., Fiala, M., King, J., Kohnen, D., Salama, N. N., Vij, R., & Azab, A. K. (2020). Targeting CD47 as a Novel Immunotherapy for Multiple Myeloma. *Cancers (Basel)*, 12(2).
10. Muz, B., Azab, F., de la Puente, P., Landesman, Y., & Azab, A. K. (2017). Selinexor Overcomes Hypoxia-Induced Drug Resistance in Multiple Myeloma. *Transl Oncol*, 10(4), 632-640.
11. Rastgoo, N., Wu, J., Liu, A., Pourabdollah, M., Atenafu, E. G., Reece, D., Chen, W., & Chang, H. (2020). Targeting CD47/TNFAIP8 by miR-155 overcomes drug resistance and inhibits tumor growth through induction of phagocytosis and apoptosis in multiple myeloma. *Haematologica*, 105(12), 2813-2823.
12. Ito, S. (2020). Proteasome Inhibitors for the Treatment of Multiple Myeloma. *Cancers*, 12(2), 265.



13. Kozalak, G., Bütün, İ., Toyran, E., & Koşar, A. (2023). Review on Bortezomib Resistance in Multiple Myeloma and Potential Role of Emerging Technologies. *Pharmaceuticals (Basel)*, 16(1).
14. Lee, T. K., Cheung, V. C., Lu, P., Lau, E. Y., Ma, S., Tang, K. H., Tong, M., Lo, J., & Ng, I. O. (2014). Blockade of CD47-mediated cathepsin S/protease-activated receptor 2 signaling provides a therapeutic target for hepatocellular carcinoma. *Hepatology*, 60(1), 179-191.
15. Rastgoo, N., Wu, J., Liu, A., Pourabdollah, M., Atenafu, E. G., Reece, D., Chen, W., & Chang, H. (2020). Targeting CD47/TNFAIP8 by miR-155 overcomes drug resistance and inhibits tumor growth through induction of phagocytosis and apoptosis in multiple myeloma. *Haematologica*, 105(12), 2813-2823.
16. Lo, J., Lau, E. Y., So, F. T., Lu, P., Chan, V. S., Cheung, V. C., Ching, R. H., Cheng, B. Y., Ma, M. K., Ng, I. O., & Lee, T. K. (2016). Anti-CD47 antibody suppresses tumour growth and augments the effect of chemotherapy treatment in hepatocellular carcinoma. *Liver Int*, 36(5), 737-745.
17. Smyth, P., Sasiwachirangkul, J., Williams, R., & Scott, C. J. (2022). Cathepsin S (CTSS) activity in health and disease - A treasure trove of untapped clinical potential. *Molecular Aspects of Medicine*, 88, 101106.
18. Hua, J., Zhuang, G., & Qi, Z. (2021). Current research status of TNFAIP8 in tumours and other inflammatory conditions (Review). *Int J Oncol*, 59(1), 46.
19. Hideshima, T., Richardson, P., Chauhan, D., Palombella, V. J., Elliott, P. J., Adams, J., & Anderson, K. C. (2001). The proteasome inhibitor PS-341 inhibits growth, induces apoptosis, and overcomes drug resistance in human multiple myeloma cells. *Cancer Res*, 61(7), 3071-3076.



THE EFFECT OF *Amt2* AND *Dur3* GENES IN TRANSMIGRATION PROCESS OF *Cryptococcus neoformans*

Sainamthip Rangdist¹, Natchaya Pakdeesiriwong¹, Ekkasit Kanklang¹, Chompunoot Wangboon¹, Watsana Penkhrue¹, Angela gelli², Mantana Jamklang^{1*}

¹School of Preclinical Sciences, Institute of Science, Suranaree University of Technology, Nakhon Ratchasima 30000, Thailand

²Department of Medical Pharmacology and Toxicology, University of California, California 95616-8635, United States of America

*e-mail: mjamklang@sut.ac.th

Abstract:

Cryptococcus neoformans (*Cn*) is an encapsulated yeast that causes serious central nervous system infection in immunocompromised individuals, particularly cryptococcal meningitis (CM). This condition suggests that the fungus is capable of crossing the blood-brain barrier (BBB). Nitrogen sources are crucial for fungal pathogenicity, as they support both survival under adverse conditions and the development of processes necessary for disease, such as promoting transmigration. Our preliminary results indicated high expression levels of ammonium and urea transporter genes during transmigration, prompting a focus on these genes in this study which aimed to evaluate the BBB transmigration capability of *Cn* strains deficient in the ammonium transporter gene (*amt2Δ* mutant) and the urea transporter gene (*dur3Δ* mutant) using an *in vitro* model. Results showed that the absence of the *Amt2* gene significantly decreased the transmigration ability, while the absence of the *Dur3* gene did not affect *Cryptococcus neoformans*'s ability to cross the brain compared to the wild-type strain (H99). In conclusion, the *Amt2* gene likely plays a crucial role in the transmigration of *Cn* across the BBB. This gene may be essential for obtaining the nutrients needed for the fungus to survive and move through human brain endothelial cells. On the other hand, the *Dur3* gene does not appear to be directly involved in the transmigration process. Nonetheless, both genes are important for the overall virulence and adaptability of *Cn*, affecting its ability to cause infections in the central nervous system (CNS).

Introduction:

Opportunistic invasive fungal infections are becoming a problem of concern for the national health systems worldwide, especially in the patients with HIV/AIDS, cancer patients, or organ transplant recipients¹. Human fungal pathogens, including *Candida*, *Aspergillus*, and *Cryptococcus*, can cause mortality rates up to 90% in immunocompromised patients². In 2022, the World Health Organization (WHO) Fungal Priority Pathogens List (FPPL) identified *Cryptococcus neoformans* as the top fungal pathogen in the critical priority group. This pathogen is associated with a mortality rate ranging from 41% to 61% in cases of cryptococcosis³. Globally approximately 1 million cases of cryptococcosis are reported each year resulting in 625,000 deaths⁴. *Cryptococcus* spp. is commonly found in the environment such as soil, pigeon dropping and, in the trunks of eucalyptus trees⁵. Cryptococcal infections start with the inhalation of desiccated yeasts or basidiospores, which then enter the lungs and cause pulmonary cryptococcosis. The infection can disseminate and invade the CNS, leading to cryptococcal meningitis (CM)⁶. CM occurs when *Cryptococcus neoformans* (*Cn*) uses a specific strategy to traverse host barrier or BBB which plays an important role to transport nutrients and prevent the uptake of neurotoxins or pathogens into the brain⁷. There are three mechanisms that *Cn* can transigrate across the BBB including paracellular, transcellular and Trojan horse mechanism⁸. In 2010, Shi et al. reported that *Cn* can alter its morphology to an

ovoid shape when it becomes trapped in the brain capillaries during a mouse brain infection⁹. The morphological change of *Cn* is induced by nutrient sensing as nitrogen source which plays an important role in regulating fungal dimorphism leading pseudohyphae¹⁰.

Our preliminary RNA sequencing data of *Cn* during hCMEC/D3 infection showed that the ammonium transporter gene and the urea transporter gene were upregulated by 1.98-fold and 1.47-fold, respectively, during *Cn* transmigration. First, the ammonium transporter gene is regulated by a family of proteins that includes Amt (ammonium permeases), Mep (methyl-ammonium permeases), and Rh (human Rhesus proteins)¹¹. This protein family regulates morphological changes and is primarily found in pathogenic fungi, including *Saccharomyces cerevisiae*, *Candida albicans*, and *Cn*¹². The Mep2 protein in *Saccharomyces cerevisiae* has been identified as a crucial sensor for the development of filamentous structures¹³. Evidence shows that strains of *Cn* lacking *Amt1* and *Amt2* genes do not exhibit invasive growth and fail to develop pseudohyphae¹⁴. For the urea transporter, is a key protein involved in the transport of urea with a dual transport mechanism including active and passive transport¹⁵. Urea induces the dimorphism of *Candida albicans* through *Dur1*, *Dur2*, and *Dur3*, which are crucial for resisting innate host immunity, although the exact mechanism remains unclear.¹⁶ Moreover, several studies have shown that the *Ure1* gene, which encodes urease in *Cn*, facilitates trapping, transmigration, and replication within the brain¹⁷⁻¹⁸. However, these genes are crucial in determining the physiological and virulence characteristics of *Cn*. Consequently, they influence its ability to transmigrate through the brain and contribute to the development of cryptococcosis. Therefore, this study aimed to investigate how the deletion of the *Amt2* and *Dur3* genes in *Cn* affects their transmigration in an in vitro model.

Methodology:

Yeast strains and cell lines

The *C. neoformans* strains were used in this study including strains H99 (serotype A, wild-type), *dur3Δ* mutant (07448; Urea transporter) and the *amt2Δ* mutant (04758; Ammonium transporter). *Cryptococcus* strains have been constructed in the Hiten Madhani lab (UCSF, USA). All strains were kept at -80°C, cultured on YPD (Yeast Extract-Peptone-Dextrose) agar and incubated at 30°C for 72 h.

In the in vitro model of the BBB, the immobilized human cerebral microvascular endothelial cell line (hCMEC/D3) line was used for BBB model. The cells were purchased from the American Type Culture Collection (ATCC) and provided from Asst. Prof. Dr. Oratai Weeranantanapan (Suranaree University of Technology, Thailand). The hCMEC/D3 cells were seeded on a collagen-coated culture flask until the cell were grown to confluence in EBM-2 medium with growth factors and antibiotic (gentamicin and amphotericin B) at 37°C in an atmosphere of 5% CO₂.

Yeast culture media

Yeast Extract-Peptone-Dextrose broth (YEPD broth) medium and Potato Dextrose agar (PDA) medium (Himedia, India) were sterilized using an autoclave, at 121°C for 15 minutes (at a pressure of 15 psi).

Cell culture media

Endothelial cell basal medium-2 (EBM-2) and growth factors were purchased from Lonza (Walkersville, MD, USA). The complete growth medium was prepared by adding growth factors (25 mL of Fetal bovine serum (FBS), 0.2 mL of hydrocortisone, 2 mL of Human fibroblastic growth factor-basic (hFGF-B), 0.5 mL of vascular endothelial growth factor (VEGF), 0.5 mL of Recombinant long R insulin-like growth factor-1 (R3IGF-1), 0.5



mL of ascorbic acid, 0.5 mL of Human epidermal growth factor (hEGF), and 0.5 mL of Gentamicin Sulfate-Amphotericin-B (GA-1,000)) into 500 mL of basal medium as 1X EBM-2. The complete medium was stored at 4°C before being used in the experiments.

Transcytosis assay in the in vitro model of the BBB

The hCMEC/D3 was used for the transcytosis assay with the passage of less than 35. The *in vitro* static monolayer model consisted of a transwell apparatus with the lower chamber (abluminal side) and the upper chamber (luminal side) separated by a porous membrane with a collagen-coated (8 µm; Corning). 1×10^4 cells of hCMEC/D3 were added on the upper chamber and were cultured for approximately 2 weeks at 37°C and 5% CO₂. During the incubation, the medium was changed from 1 to 0.5 and 0.25 strength every 3-4 days before the assay. The lower-strength medium containing growth factors was reduced for the cells to differentiate, and the tight junction proteins were completely formed. Before the transcytosis assay, the integrity of the monolayer was measured as the trans-endothelial electrical resistance measurement (TEER) value by an endothelial meter. The cryptococcal cells (1×10^6 cells) were added to the upper chamber and incubated for 24 h before collecting the migrated cryptococcal cells from the bottom chamber for CFU determination.

Results and Discussion:

Preliminary data from RNA sequence at the overall transcriptome of Cn

The overall transcriptome analysis of *Cn* during hCMEC/D3 infection revealed that the expression of certain genes is upregulated. The differentially expressed protein include SLC39; Solute Carrier Family39, NDC80; Kinetochore Protein NDC80, IDH2 ; L-iditol 2-dehydrogenase, FRD; Fumarate reductase, TauD; Taurine catabolism dioxygenase TauD, UraP; Uracil permease, ACOX; Acyl-CoA Oxidase, UreaT; Urea transporter, PI; Plant-inducible, TRPT; tRNA 2'-phosphotransferase, ICL; Isocitrate Lyase, NCS2; Nucleoside Transporter Family Member2, CB5; Cytochrome b5, SLC25 ; Solute Carrier Family25, PTEF or PTS; Phosphotransferase enzyme family, AMT; amt family ammonium transporter and OxR; Oxidoreductase. The amt family ammonium transporter gene and the urea transporter gene were emphasized in this study due to they are involved in the morphological changes of *Cn*. The transcriptome analysis of these two genes revealed a 1.98-fold upregulation of the ammonium transporter gene and a 1.47-fold upregulation of the urea transporter gene (**Figure 1**). The involvement of these genes in morphological changes may be linked to the transmigration process, during which *Cn* undergoes morphological transformations to pass through the endothelial cells and achieve the brain

The transmigration of C. neoformans across through the in vitro BBB model

The colony-forming units (CFUs) were counted to quantify and compare the ability of *Cn* to cross the blood-brain barrier (BBB) model. In this study, the cryptococcal free cells of the wild-type strain were measured at $8.36 \times 10^5 \pm 1.71$ CFU/mL. In contrast, the *amt2Δ* and *dur3Δ* mutant strains showed reduced transmigration through the brain side, with counts decreasing to $2.26 \times 10^5 \pm 0.94$ CFU/mL and $5.1 \times 10^5 \pm 1.2$ CFU/mL, respectively (**Figure 2**). In addition, the *amt2Δ* mutant strain showed a significant reduction in its ability to pass through the brain, while the *dur3Δ* mutant strain did not exhibit a significant decrease when compared to the wild-type strain (H99), as determined by an unpaired t-test (Mean \pm SEM, n = 3, **p* < 0.05) (GraphPad Prism). The disruption of *Dur3* gene, however, decreased the ability to transmigrate through the brain. This result revealed that *Amt2* gene affects the

transmigration process of *Cn* while *Dur3* gene may not be directly responsible for transmigration process.

Previous study reported that the *Amt* gene related with the ammonium signal that regulates fungal morphology by downstream signal transduction pathway¹⁰. There are *Amt1* and *Amt2* gene that regulate the pseudohyphae generating but the *amt2Δ* mutant strains did not form invasive growth under the low ammonium conditions¹⁹. The *Amt1* and *Amt2* transporters import the ammonia molecules into intracellular for growth and development. This ammonia act as a signaling molecule in nitrogen metabolism and play a crucial role in inducing capsule production of *Cn*²⁰. While evidence linking specific nitrogen source to enhance transmigration through the BBB is limited, it is known that nitrogen molecules can influence the virulence factor of *Cn*, helping the fungus evade the host immune system and facilitating its penetration of the CNS⁸. Furthermore, Shi et al reported that *Cn* enable change morphological during direct transcytosis. Additionally, *Dur3* is a urea transporter associated with yeast dimorphism, although its exact mechanism remains unclear¹⁶. Several studies have directly deleted genes related to the urease system, such as *Ure1* and its three accessory proteins *Ure4*, *Ure6*, and *Ure7*. These deletions have been found to impact the efficiency of brain invasion. Therefore, the *Dur3* gene, which is a urea transporter, is directly involved in the urea metabolism of yeast cells. For pathogenic microorganisms, urease hydrolyzes urea into ammonia and carbon dioxide, a critical virulence factor that neutralizes the acidic microenvironment. This process helps pathogens survive the harsh pH conditions within phagolysosome²². It has been reported that urease produces ammonia, which is toxic to mammalian cells and weakens the endothelial vessel walls. This weakening facilitates the fungal traversal of epithelial barriers and enhances the fungus's ability to invade the CNS²³⁻²⁴. However, this does not result in trapping within capillaries or growth within the CNS. Currently, the urease mechanism that introduce *Cn* to transmigrate into brain is still unknown, but it could involve the ammonia production or other nitrogenous products present in host plasma that increases the expression of adhesins on the endothelial cells and affect astrocytes leading to opening the tight junctions and weakening the integrity of the BBB²⁵. These results suggest that the absence of the *Amt2* gene affects the ammonium signaling that directly influences the morphological changes of *Cn*. In addition, the deletion of *Dur3* gene is crucial for reducing the fungus's ability to transmigrate, which may impact other virulence mechanisms and consequently influence the transmigration process.



The gene expression of *Cn* response to hCMEC/D3 cell

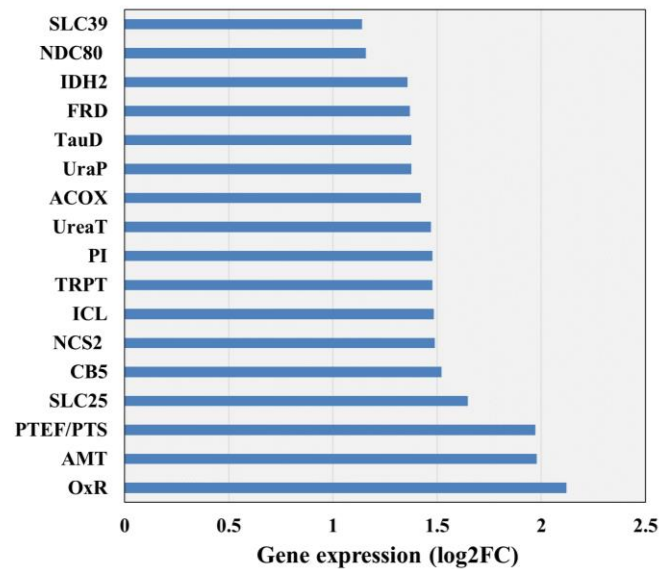


Figure 1 The gene expression of *Cn* response to Human Brain Endothelial cells (D3).

Transcytosis assay

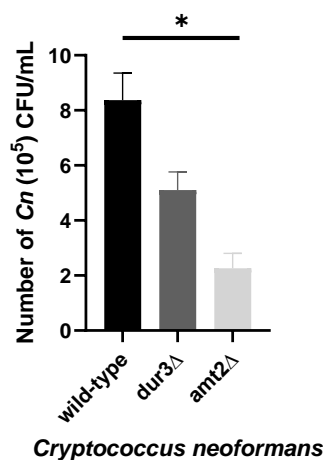


Figure 2 CFU counting of cryptococcal cells in the *in vitro* model.

Conclusion:

This study demonstrated that a deficiency in the *Amt2* gene significantly reduces *C. neoformans*'s ability to transmigrate through the brain, whereas a deficiency in the *Dur3* gene does not have a similar effect. Future research will investigate the mechanisms by which *C. neoformans* traverses the brain and explore how the deletion of the *Amt2* and *Dur3* genes may affect virulence factors in mutant strains.

Acknowledgements:

This research was supported by grants from the Office of the Ministry of Higher Education, Science, Research and Innovation under the Research Grant for New Scholars. We sincerely thank Asst. Prof. Dr. Oratai Weeranantanapan for providing the immobilized human cerebral microvascular endothelial cell line (hCMEC/D3). We also appreciate the

support from the School of Preclinical Sciences, Institute of Science, Suranaree University of Technology, Thailand, for providing the facilities necessary for this research.

References:

1. Dixon DM, McNeil M M, Cohen M L, Gellin B G, Montagne JRL. *Public Health Rep.*1996; 111(3): 226–235.
2. Rathore SS, Sathiyamoorthy J, Lalitha C, Ramakrishnan J. *Microb. Pathog.* 2022;166:1055211996
3. World Health Organization. WHO fungal priority pathogens list to guide research, development and public health action 2022
4. Park BJ, Wannemuehler KA, Marston BJ, Govender N, Pappas PG, Chiller TM. *AIDS.* 2009;23(4): 525-530.
5. Ellis D., Pfeiffer T. J. *Clin. Microbiol.* 1990;28(7): 1642-1644.
6. Maziarz EK, Perfect JR. *Infect. Dis. Clin. North. Am.* 2016;30(1): 179-206
7. Abbott NJ, Atabendige AA, Dolman DE, Yusof SR, Begley DJ. *Neurobiol. Dis.* 2010;37(1): 13-25.
8. Tseng HK, Huang TY, Wu AY, Chen HH, Liu CP, Jong A. *Future Microbiol.* 2015; 10(10):1669-1682.
9. Shi M, Li SS, Zheng C, Jones GJ, Kim KS, Zhou H, Mody CH. *mBio.* 2010;4(3).
10. Berg BVD, Lister S, Rutherford JC. *PLoS Pathog.* 2019; 15(11): e1008059.
11. Bizior A, Williamson G, Harris T, Hoskisson PA, Javelle A. *Microbial.* 169(7): 001360.
12. Smith DG, Garcia-Pedrajas MD, Gold SD, Perlin MH. *Mol. Microbiol.* 2003;50(1): 256-275.
13. Lorenz MC, Heitman J. *EMBO J.* 1998 ;17:1236–1247.
14. Lee SC, Phadke S, Sun S, Heitman J. *Eukaryotic cell* 2012;11(11): 1391-1398.
15. Frazzitta AE, Vora H, Price MS, Tenor JL, Betancourt-Quiroz M, Toffaletti DL, Cheng N., Perfect JR. *Eukaryot Cell.* 2013;12(11):1439–1450.
16. Navarathna DHMLP, Das A, Morschhauser J, Nickerson KW, Roberts DD. *Microbiol.* 2011;157, 270–279.
17. Olszewski MA, Noverr MC, Chen GH, Perfect JR, Huffnagle GB. *Am. J. Pathol.*, 2004;Vol.164, No. 5.
18. Shi M, Li SS, Zheng C, Jones GJ, Kim KS, Zhou H, Mody CH. *J Clin Invest.* 2010;120(5), 1683-1693.
19. Rutherford JC, Lin X, Nielsen K., Heitman J. *Eukaryotic cell* 2008;7(2): 237-246. (19)
20. Frazzitta AE, Vora H, Price MS, Tenor JL, Betancourt-Quiroz M, Toffaletti DL, Cheng N, Perfect JR. *Eukaryot Cell.* 2013;12(11):1439-50.
21. Singh A, Panting RJ, Varma A, Saijo T, Waldron KJ, Jong A, Ngamskulrungrroj P, Chang YC, Rutherford JC, Kwon-Chung KJ. *Adv. Appl. Microbiol.* 2013;87:1-41.
22. Feder V, Kmetzsch L, Staats CC, Vidal-Figueiredo N, Ligabue-Braun R, Carlini CR, Vainstein MH. *FEBS J.* 2015;282(8):1406-1418.
23. Liu TB, Perlin DS, Xue C. *Virulence.* 2014; 3(2): 173-181.
24. May RC, Stone NR, Wiesner DL, Bicanic T, Nielsen K. *Nat. Rev. Microbiol.* 2016;14(2): 106-117.
25. Olszewski MA, Noverr MC, Chen GH, Perfect JR, Huffnagle GB. *Am. J. Pathol.* 2004;164(5).



THE EFFECT OF *Cordyceps militaris* EXTRACT ON THE PROLIFERATION OF HUMAN DERMAL FIBROBLAST CELLS *in vitro* STUDY

Kanjana Soodpakdee,^{1,2} Yin Quan Tang,³ Suttichai Krisanaprakornkit,⁴ Anupong Makeudom,⁴ Sunita Chamyuang^{1,2*}

¹School of Science, Mae Fah Luang University, Chaing Rai, Thailand, 57100

²Microbial Products and Innovation Research Group, School of Science, Mae Fah Luang University, Chaing Rai, Thailand, 57100

³School of Biosciences, Faculty of Health & Medical Sciences, Taylor's University, 47500 Selangor, Malaysia

⁴School of Dentistry, Mae Fah Luang University, Chiang Rai 57100, Thailand

*e-mail: sunita@mfu.ac.th

Abstract:

Human dermal fibroblasts (HDFs) are crucial cells located within the dermis layer of the skin. They play essential roles in epidermal proliferation, differentiation, and the formation of the cellular matrix by secreting various growth factors and cytokines, which are vital for maintaining skin health and function. *Cordyceps militaris* mycelium extract (CME) is widely used in both traditional and modern medicine due to its diverse therapeutic effects. However, the specific impact of CME, which contains adenosine and cordycepin, on the proliferation of human dermal fibroblast cells has not been fully clarified. In this study, we optimized the concentrations of CME, commercial adenosine, commercial cordycepin, and a mixture of adenosine and cordycepin (1:5 ratio) to proliferate HDFs cells without toxicity. We found that CME concentrations of 0.156 and 0.313 μM significantly increased HDFs cell proliferation by approximately 60% compared to untreated cells ($p < 0.001$). Our research suggests that CME has potential as a therapeutic agent for wound healing and angiogenesis. Its ability to enhance cell proliferation and promote vascular development makes it a promising candidate for future medical applications.

Keywords: *Cordyceps militaris*, Adenosine, Cordycepin, Human dermal fibroblasts

Introduction:

According to the World Health Organization (WHO), approximately 75% of people worldwide rely on herbs and various traditional medical practices for treating diseases and maintaining health. The study of bioactive compounds in the past decades has enabled the extraction of substances from medicinal fungi, which are used as medications or as building blocks for several important pharmaceuticals still in use today¹. *Cordyceps militaris* is one of the medical fungi that contains bioactive compounds in both its mycelium and fruiting bodies, including adenosine, cordycepin, and polysaccharides². These compounds have shown potential therapeutic applications in modern medicine, such as anticancer properties³, immune system enhancement, aging delay, resistance to viral and bacterial infections, energy-boosting, and wound healing properties^{4,5}. Cordycepin, primarily present in *C. militaris*, has significant interest in recent years due to its exceptional health and therapeutic properties, particularly in cancer treatment⁶, and a new class anti-inflammatory agents⁷. Adenosine has been reported to enhance endothelial cell migration, tissue remodeling during the healing process, and proliferation, which is essential in the process of creating new blood vessels, also known as angiogenesis⁸. Furthermore, adenosine significantly aids in the complex process of new blood vessel formation by interacting with critical growth factors such as fibroblast growth factor-2 (FGF-2) and vascular endothelial growth factor-A (VEGF-

A)⁹. In contrast to the pro-angiogenic effects of adenosine, numerous studies have demonstrated the anti-angiogenic properties of cordycepin and the mechanisms behind these effects¹⁰. Nevertheless, the impact of crude extracts from *C. militaris*, which contain both adenosine and cordycepin, on promoting or enhancing cell proliferation has not been explored in normal cells, such as primary human dermal fibroblast cells (HDFs). Fibroblasts are the most prevalent cell type in connective tissues throughout the body and are widely used in studies related to wound healing, tissue engineering, and regeneration. They play crucial roles in various biological processes, including acting as mediators during inflammatory responses and angiogenesis¹¹. Despite the potential of crude extracts from *C. militaris* containing adenosine and high amounts of cordycepin to induce HDFs cell proliferation, this effect remains unknown. Thus, this study aimed to investigate the effect of crude extracts from *C. militaris* on enhancing human dermal fibroblast cell viability and proliferation without toxicity.

Methodology:

Cordyceps militaris cultivation

Cordyceps militaris strain SH01 which obtained from Shanghai, China were used in the present experiments. The fungal mycelium was maintain in potato dextrose agar (PDA) at 20°C for 21 days prior transferred into the culture medium which modified from Shih et al., (2007)¹². Five of active mycelia disc (5 mm. in diameter) were placed in 300 mL of seed culture medium and incubated at 25°C in darkness on a on a rotary shaker (at 110 rpm) for 7 days and kept in static condition until 14 days. The mycelium part was collected via filter glass vacuum using nylon filter pore size 45 µm and freeze-drying prior extraction to determine adenosine and cordycepin content.

Extraction and chemical analysis of Cordyceps militaris mycelium

The dried mycelium was extracted with distilled water and quantified of adenosine and cordycepin followed the protocol of ChokeUmnay & Owatworakit., (2021)¹³. In brief, 20 mL of deionized water was mixed with one gram of dried sample and incubated at 60°C for 3 hrs., filtered through a nylon filter membrane (0.2 µm pore size). The filtrate was analyzed by using High-performance liquid chromatography (HPLC) was quantified by creating a plot of peak area against concentration. The 1 µL of the crude extract was analyzed using Waters HPLC system (Waters Corporation, Milford, USA) and separation was carried out using C₁₈ column, 4.6 × 250 mm, 5 µm. The analysis was conducted at a flow rate of 0.2 mL/min and a temperature of 30°C. The chromatographic condition was isocratic, with a 95:5 ratio of 0.2% formic acid in deionized water (A) and methanol (B). Both adenosine and cordycepin were monitored at a wavelength of 260 nm.

Human dermal fibroblast cells culture

Human dermal fibroblast cells (HDFs) were purchased from American Type Culture Collection (ATCC, PCS-201-010TM). HDFs were cultured in fibroblast basal medium (ATCC, PCS-201-030TM) supplemented with a fibroblast growth kit-low serum (ATCC, PCS-201-041TM) and 1% antibiotic-antimycotic (100X) solution containing 10,000 units/mL of penicillin, 10,000 µg/mL of streptomycin, and 25 µg/mL of amphotericin (GibcoTM, Cat. No. 15240062). HDFs were maintained in a humidified atmosphere with 5% CO₂ at 37°C, and the complete media was replaced every two days. The cultures were washed with phosphate-buffered saline (PBS, pH 7.4, Gibco, Cat. No. 10010023) and passaged with 0.25% Trypsin-EDTA solution (Gibco, Cat. No. 25200072) when the cells reached approximately 80% confluence. HDFs cells were passaged 2-5 times before being used in the subsequent experiments.



MTT assay

The MTT (3-[4,5-dimethylthiazol-2-yl]-2,5 diphenyl tetrazolium bromide) powder was purchased from Sigma–Aldrich, USA. MTT is a colorimetric assay for assessing cellular metabolic activity that was used to determine cell viability and proliferation.

Cell viability

HDFs cells (1×10^4 cell/well) were seeded in 96-well plates (NuncTM) and incubated at 37°C with 5% CO₂ in a humidified atmosphere for 24 hrs. The samples used included *C. militaris* mycelium extract (CME), adenosine standard (Sigma, USA), cordycepin standard (Sigma, USA), and a mixture of adenosine and cordycepin standard in the same ratio in CME. Each sample was initially prepared as stock solutions at a concentration of 20 µM. These solutions were subsequently diluted to a range of concentrations from 10 µM to 0.078 µM using a two-fold dilution method. A total of 100 µL of each sample were added to the wells and incubated for 24 hours. After incubation, the samples were removed, and 0.5 mg/mL of MTT solvent was added. The plate was then incubated at 37°C with 5% CO₂ for 3 hours. The absorbance at 570 nm was recorded for each well using a microplate reader (Envision, PerkinElmer, MA, USA). The results were interpreted and compared with the control (untreated). The percentage of cell viability was calculated using Equation 1 below, and the minimal non-toxic dose (MNTD) was evaluated accordingly.

$$\% \text{ Cells viability} = \frac{\text{Absorbance of sample}}{\text{Absorbance of control}} \times 100 \quad (1)$$

Cell proliferation

HDFs cells (1×10^4 cell/well) were placed in each well of 96-well plates before incubated at 37°C with 5% CO₂ in a humidified atmosphere for 24 hours. The concentration of each sample was followed MNTD value that shown the best potential for induced cell proliferation without toxic including commercial adenosine (0.156 µM), commercial cordycepin (0.625 µM), mixture of commercial adenosine and cordycepin (5 µM) and CME (0.156 and 0.313 µM). HDFs cells was pre-explosion with one hundred microliters of samples by incubated at 37°C with 5% CO₂ in humidified atmosphere for 5, 15, 30, 60, 180 mins and 24 hours as a positive control. The solution was removed and added 0.5 mg/mL of MTT and then incubated for 3 hrs. before measured the absorbance at 570 nm. using microplate reader. The results were interpreted and compared with negative control (untreated). The percentage of cell viability was calculated by following equation 1.

Statistical analysis

All data are presented as the mean \pm standard deviation and were performed using SPSS 20.0 software (SPSS Inc., Chicago, IL, USA). One-way analysis of variance (ANOVA) followed by post-hoc multiple comparison. Duncan test was carried out for determination the significantly Differences with $p < 0.05$, and $p < 0.001$ were considered to indicate significance differences.

Results and Discussion:

High-performance liquid chromatography (HPLC) determines the amount of adenosine and cordycepin in C. militaris extract

High-Performance Liquid Chromatography (HPLC) analysis revealed that the concentrations of adenosine and cordycepin in CME were 1.382 ± 0.161 mg/g and 6.544 ± 1.109 mg/g respectively. Interestingly, cordycepin was presented in the CME at 4.7 times higher than adenosine. *C. militaris* is known to have a significantly higher cordycepin concentration compared to other species especially under static culture conditions¹². After determining the quantity of these in CME, we proceed to observe their efficacy in enhancing human skin cells proliferation without serious effect.

Determination of the optimal concentration of CME on proliferation of human dermal fibroblast cells (HDFs)

In this part of the study, we aimed to determine the optimal concentrations of CME that would most effectively promote the proliferation of human dermal fibroblast cells (HDFs) compared to pure standard adenosine, cordycepin, and a mixture of adenosine and cordycepin (ratio 1:5). We examined various CME concentrations (0.078, 0.156, 0.313, 0.625, 1.250, 2.50, 5, and 10 μ M, alongside controls including standard adenosine, standard cordycepin, and a mixture of both in the same ratio as found in CME (1:5), over a period of 24 hours. Our findings, illustrated in **Figure 1**, indicated a significant increase in HDFs cell viability by up to 60% when treated with 0.313 and 0.156 μ M of CME, compared to untreated cells. Additional treatments involving adenosine (0.156 μ M), cordycepin (0.625 μ M), and a standard mixture (1:5 ratio at 5 μ M) yielded increases in HDFs viability by approximately 54%, 53%, and 56%, respectively, relative to untreated cells. According to the previous research, *C. militaris* may promote cell proliferation and provide protection against oxidative stress-induced premature aging¹⁴. Based on these results, we established the minimal non-toxic dose (MNTD) for each sample within the tested range, which proved to be conducive for HDFs treatment, as they did not significantly reduce cell viability while demonstrating the highest potential for cell proliferation.

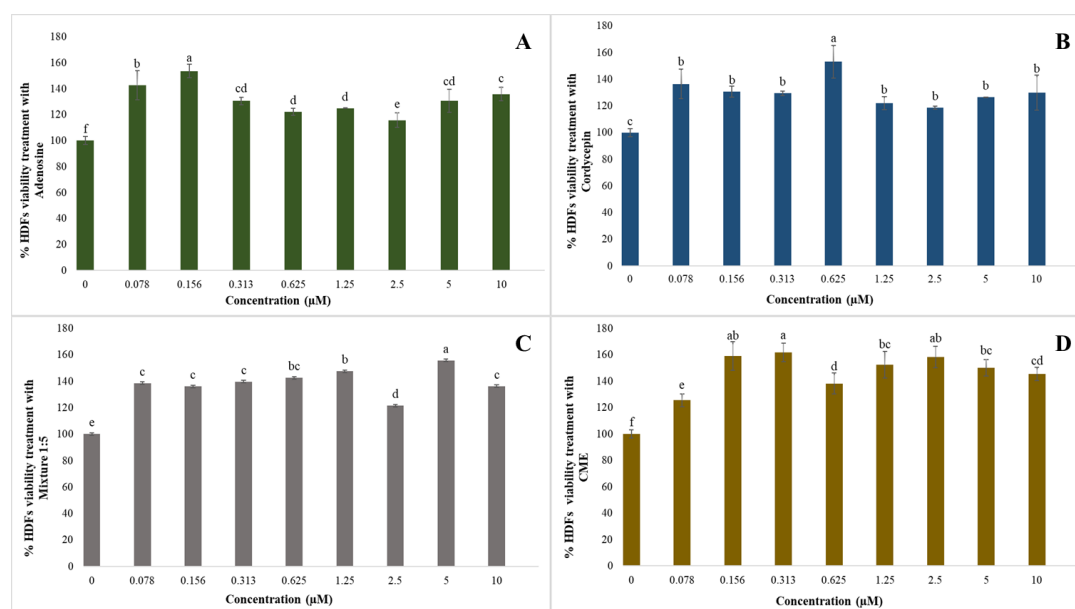


Figure 1. The percentage of HDFs cells viability after treatment 24 hrs. was determined through MTT assay. The effects of various concentrations of adenosine standard (4.1A), cordycepin standard (4.1B) and mixture of adenosine and cordycepin standard in ratio 1:5 (4.1C) and CME (4.1D), on HDFs cells viability were examined by compared with untreated. Duncan's multiple range tests, $p < 0.001$.



HDFs cell proliferation after treated with CME

After identifying the Minimal Non-Toxic Dosage (MNTD), the MTT assay was established to assess the proliferation potential of human dermal fibroblast cells (HDFs) post-treatment with each sample's MNTD compared to the untreated control group. Remarkably, within fifteen minutes, all treatments facilitated more than 50% proliferation in HDFs cells relative to the control. Notably, a CME concentration of 0.156 μ M propelled HDFs cell proliferation to 80%, outperforming both adenosine and cordycepin standards, as showed in **Table 1**. Treatment with a mixture of adenosine and cordycepin (ratio 1:5) yielded a proliferative effect almost as high as that of CME and commercial adenosine. Furthermore, HDFs cells maintained their capacity for proliferation up to one-hour post-treatment. Within one-hour, standard cordycepin alone significantly diminished the proliferation rate of HDFs cells. Our findings corroborate the research by Radhi et al. (2021), which demonstrated that cordycepin consistently inhibits cell proliferation, migration, and inflammation, particularly in cancerous cells¹⁵. Notably, a decline in cell proliferation across all treatments was observed at the three-hour mark. This suggests that HDFs cells may undergo cell cycle arrest and prepare for the transition to mitosis (G2/M phase) post-treatment. During the G2 phase, cells continue to grow, synthesize proteins and organelles, and reorganize their contents in anticipation of mitosis—a process lasting approximately 3-4 hours as described by Israels & Israels¹⁶.

Table 1. The results of proliferation rate without toxicity in human dermal fibroblast cells (HDFs) (n=3).

| Treatments | Pre-explosion time | | | | | |
|---------------------|--------------------------------|----------------------------------|---------------------------------|---------------------------------|--------------------------------|---------------------------------|
| | 5 mins | 15 mins | 30 mins | 60 mins | 180 mins | 24 hrs. |
| Adenosine | 177.78 \pm 6.97 ^d | 242.32 \pm 10.92 ^{bc} | 293.30 \pm 8.91 ^a | 297.86 \pm 8.46 ^a | 223.48 \pm 5.76 ^c | 260.68 \pm 14.70 ^b |
| Cordycepin | 249.85 \pm 6.60 ^a | 271.37 \pm 13.25 ^a | 258.12 \pm 11.19 ^a | 211.27 \pm 16.19 ^b | 183.79 \pm 1.64 ^c | 250.85 \pm 11.90 ^a |
| Mixture 1:5 | 208.12 \pm 7.42 ^d | 248.52 \pm 5.72 ^c | 294.06 \pm 10.49 ^a | 299.95 \pm 7.35 ^a | 242.49 \pm 4.41 ^c | 265.21 \pm 7.13 ^b |
| CME (0.156 μ M) | 221.00 \pm 5.68 ^c | 263.25 \pm 8.78 ^b | 286.97 \pm 6.62 ^a | 284.41 \pm 1.08 ^a | 221.00 \pm 8.07 ^c | 278.94 \pm 17.6 ^{ab} |
| CME (0.313 μ M) | 215.47 \pm 3.58 ^c | 254.71 \pm 6.97 ^c | 249.15 \pm 3.19 ^c | 282.65 \pm 2.44 ^a | 245.81 \pm 4.61 ^c | 269.00 \pm 8.91 ^b |

Data represents the mean \pm standard deviation. The different superscript letters (a–c) indicate not significant differences of each treatment in difference pre-explosion time ($p > 0.05$).

Conclusion:

In conclusion, our research successfully cultivated and extracted adenosine and cordycepin from *Cordyceps militaris* (SH01), demonstrating significant therapeutic potential in modulating cell proliferation which is essential in tissue repair, and angiogenesis process. The crude extract of *C. militaris* mycelium (CME) underwent the quantification of adenosine and cordycepin content using HPLC analysis. Subsequent application of CME to Human Dermal Fibroblast cells (HDFs) key mediators in tissue repair during wound healing process as well as angiogenesis revealed its efficacy in comparison to standard adenosine, standard cordycepin, and their mixture in a 1:5 ratio, as found in CME. Around 60% increased of HDFs cells viability after treatment with CME was determined through MTT assay, which also helped establish the minimal non-toxic dose (MNTD). Following the MNTD value, CME was induced the increasing the proliferation rate of HDFs cells more than sixty percents

during 30 mins to 1 hr. The study's findings indicated that CME, with its high cordycepin content, is not only non-toxic but also significantly enhances HDFs proliferation compared to untreated cells. Collectively, these results position CME as a promising therapeutic agent, offering substantial benefits for wound healing and angiogenesis, and highlighting its potential for medical applications in enhancing cell proliferation and vascular development in the future.

Acknowledgements:

The authors thank the Scientific and Technological Instruments Centre for providing laboratory space and equipment, and the Global Relations Division and the Office of Postgraduate Studies at Mae Fah Luang University, Chiang Rai, Thailand for supporting travel expenses for this research.

References:

1. Das SK, Masuda M, Sakurai A, Sakakibara M. *Fitoterapia*. (2010);81:961-8.
2. Lin Q, Long L, Wu L, Zhang F, Wu S, Zhang W, Sun X. *J Sci Food Agric*. (2017);97:3476-3480.
3. Shrestha B, Zhang W, Zhang Y, Liu X. *Mycol Prog*. (2012);11:599-614.
4. Choi E, Oh J, Sung G-H. *Mycobiology*. (2020);48:512-517.
5. Phull AR, Ahmed M, Park HJ. *Microorganisms*. (2022);10
6. Tuli HS, Sharma AK, Sandhu SS, Kashyap D. *Life Sci*. (2013);93:863-869.
7. Tan L, Song X, Ren Y, Wang M, Guo C, Guo D, Gu Y, Li Y, Cao Z, Deng Y. *Phytother Res*. (2021);35:1284-1297.
8. Clark AN, Youkey R, Liu X, Jia L, Blatt R, Day Y-J, Sullivan GW, Linden J, Tucker AL. *Circ Res*. (2007);101:1130-1138.
9. Auchampach JA. *Circ Res*. (2007);101:1075-7.
10. Tuli HS, Sandhu S, Sharma AK, Gandhi P. *Int J Pharm Pharm Sci*. (2014);6:581-583.
11. Kendall RT, Feghali-Bostwick CA. *Front Pharmacol*. (2014);5:91491.
12. Shih L, Tsai K-L, Hsieh C. *Biochem Eng J*. (2007);33:193-201.
13. Chokeumnuay N, Owatworakit A. *Kasetsart J: Nat Sci*. (2021);55:537–546-537–546.
14. Park JM, Lee JS, Lee KR, Ha S-J, Hong EK. *Nutrients*. (2014);6:3711-3726.
15. Radhi M, Ashraf S, Lawrence S, Tranholm AA, Wellham PAD, Hafeez A, Khamis AS, Thomas R, McWilliams D, De Moor CH. *Molecules*. (2021);26:5886.
16. Israels E, Israels L. *J Oncol*. (2000);5:510-513.



THE EFFECT OF HIGH TEMPERATURE STRESS TO PHOTOSYNTHETIC EFFICACY OF LICHENS AT DOI SUTHEP-PUI NATIONAL PARK

Mongkol Phaengphech,* Vasun Poengsungnoen, Kawinnat Buaruang, Kajonsak Vongshewarat, Wetchasart Polyiam,

Lichen research unit, Department of Biology, Faculty of Science, Ramkhamhaeng University, Bangkok, 10240.

*e-mail: mongkolpp@gmail.com

Abstract:

Climate change induced high temperature stress is expected to significantly impact lichens by damaging their photosynthetic activity. This study aims to investigate how different temperatures affect the photosynthetic efficiency of the lichens *Parmotrema tinctorum*, *Usnea baileyi*, and *Ramalina calicaris*. We observed heat stress and damage to the photosynthetic apparatus of lichens after incubating them at temperatures of 25, 30, 35, 40, 45, and 50°C for one hour. The maximum quantum yield (Fv/Fm value) and net photosynthetic rate (Pn) of photosystem II were measured to examine the effects on lichens. According to our research, lichens exposed to temperatures between 30 and 35°C have a considerable reduction in their capacity to undertake photosynthesis. Lichens decrease 60% of their capacity of photosynthesis when stored in incubators exceeding 40°C. Based on our studies, *P. tinctorum* has a temperature damage to photosynthetic efficacy (T_{dp}) of 25°C, while *U. baileyi* and *R. calicaris* have a T_{dp} of around 30°C. This suggests that rising temperatures may influence the physiology of lichens in their natural habitats, particularly in the hot season as well as during periods of high humidity and precipitation. Lichens that grow in humid environments are more susceptible to temperature increases in their photosynthesis. They will therefore probably react significantly to any future climate change.

Keywords: Climate change, Heat stress, Lichens, Photosynthesis, Photosystem II.

Introduction:

The impact of climate change is significant in altering species composition and biological communities of both plants and animals. Lichens are poikilohydric organism, able to conserve and obtain water from the environment. As a result, they can withstand water loss without damage to physiological processes. Although lichens can tolerate high temperatures and adapt to harsh environments, they can grow in dry conditions at temperatures as high as 35-46°C. Some species can even survive and withstand temperatures at up to 50-70°C.¹ Global warming affects lichens because they can only tolerate temperatures of 35-46°C when wet, which can happen in direct sunlight.² This thermal effect can damage the donor side of photosystem II (PSII), reducing photosynthesis and increasing respiration rates,³ resulting in increased carbon loss in lichens and decreased growth rate.⁴ However, the heat stress impacts on lichens can be assessed by measuring chlorophyll a fluorescence and CO₂ gas exchange. The maximum quantum yield of photosystem II (Fv/Fm) is a commonly used measure that reflects the actual physiological states of the organism during photosynthesis. After being incubated at high air temperatures that cause heat stress, the decrease in Fv/Fm is related to a reduction in CO₂ assimilation.⁵ Thus, this study aims to investigate how lichen photosynthesis responds to short-term

temperatures ranging from 25°C to 50°C in wet conditions. Understanding this relationship is important because it can reveal the effect of the growth rate of lichens within natural habitat conditions.

Methodology:

Studies area and lichens: Thallus of lichens *P. tinctorum*, *U. baileyi*, and *R. calicaris* (Figure 1a-c) were collected on September 28, 2023, from the lower montane forest of Doi Suthep-Pui National Park in Chiang Mai, Thailand, at an altitude approximately 1,600 m.a.s.l. Before testing the lichens in a temperature-controlled chamber, all lichen thalli were prepared by being cleaned, cut into small pieces (approximately 3-5 cm² in size), and weighing the dry thallus before physiological change measurements.

Photosynthetic efficacy measurement: We measured the photosynthesis processes by two techniques. (1) CO₂ gas exchange measuring, or net photosynthesis rate measurement detected the decrease in carbon dioxide concentration as a function of time. (2) The chlorophyll fluorescence technique using the Fv/Fm value indicates the donor side efficiency in photosystem II (PSII). Thallus of all lichens were sprayed with distilled water and incubated in dark conditions for 12 hours and 6 hours under light intensity (PAR) at 100 $\mu\text{mol m}^{-2}\text{s}^{-1}$. Then, the net photosynthetic rate (Pn) measured by the infra-red gas analyzer (Li-Cor 6400 Portable Photosynthesis system, Li-Cor, Lincoln, Nebraska, USA)⁶ with closed system conditions, and the maximum quantum efficiency of PSII (Fv/Fm) measured by a Chlorophyll Fluorescence model Mini-PAM; Photosynthesis Yield Analyzer (Heinz Walz GmbH; Germany). Both measurements were made for all thallus before being incubated at a specified temperature and then repeated the measurement afterward.

The incubation of lichens under various temperatures and measurement of the photosynthesis: The lichens was sprayed with water and kept inside a clear plastic box to maintain humidity of approximately 90-100%. Then, the lichens were incubated at different temperatures (20, 25, 30, 35, 40, 45, and 50°C) for one hour at each temperature, under a light intensity of 100 $\mu\text{mol m}^{-2}\text{s}^{-1}$. After incubation, those thalli were sprayed with distilled water and measured to the net photosynthesis rate. Then, they were kept for 30 minutes in the dark to detect the maximum quantum yield of PSII or Fv/Fm value and used to indicate the maximum light efficiency of PSII of lichen.

Data analysis: The proportion of photosynthesis efficiency was calculated from the net photosynthetic rate and Fv/Fm value and used to evaluate the response of lichens to different temperature points. These results are presented as a graph and a nonlinear model (Equation: Sigmoidal, Sigmoid 5 Parameters) for extrapolating the temperature damage to photosynthetic efficacy (T_{dp}) made using Sigmaplot 14 software (Inpixon HQ; Palo Alto, USA).



Figure 1.

The thallus of the lichens *Parmotrema tinctorum* (a), *Usnea baileyi* (b) and *Ramalina calicaris* (c) were collected from Doi Suthep-Pui National Park, Chiang Mai province, Thailand.



Results and Discussion:

The photosynthesis efficiency of three lichens, *P. tinctorum*, *U. baileyi* and *R. calicaris* are responded to a raising of the air temperature under an environmental control chamber. Our results found that the photosynthesis efficiency of lichens *P. tinctorum* will begin to decline at a temperature of 25.1°C (Figure 2a). While lichens *U. baileyi* and *R. calicaris* showed that photosynthesis efficiency declined at higher temperature around 29.5 and 29.6 °C, respectively (Figure 2b-c).

Lichens that incubated at a temperature of 30°C showed different photosynthesis efficiency, *P. tinctorum* was reduced by about -7%, while *U. baileyi* and *R. calicaris* were unaffected by this temperature level. When incubated at 35°C, the photosynthetic efficiency of *P. tinctorum* decreased to -30% while *U. baileyi* and *R. calicaris* decreased by more than -44%. Lichens *U. baileyi* and *R. calicaris* have a fruticose growth form, characterized by a coral or shrubby-like, which can respond to high temperatures faster than foliose growth form of *P. tinctorum*. According to Table 1, the average net photosynthesis rate (Pn) of *U. baileyi* and *R. calicaris* decreased by -59 and -65%, respectively, while Fv/Fm values decreased -28 and -25 % respectively, which both values decreased more than *P. tinctorum*. Our study found that the Pn of lichens is more reduced at temperatures of 30-35°C, although this temperature is at the optimal range for most algae of 25–35 °C. Lichens were incubated at 40°C, the lowest photosynthetic efficiency was found with *P. tinctorum*, which was reduced to -71% (Figure 2a). However, our data in Table 1 shows the Pn and Fv/Fm values of *P. tinctorum* the most reduced to -63 and -79%, respectively, and *U. baileyi* and *R. calicaris* showed similar pattern of photosynthetic efficiency declining (Figure 2b-c). At 45-50°C after incubation, the photosynthesis efficiency of lichens decreased almost 80-90 % in average for all lichens, especially *P. tinctorum* and *U. baileyi* showed the lowest photosynthetic efficiency about 90% at 45°C.

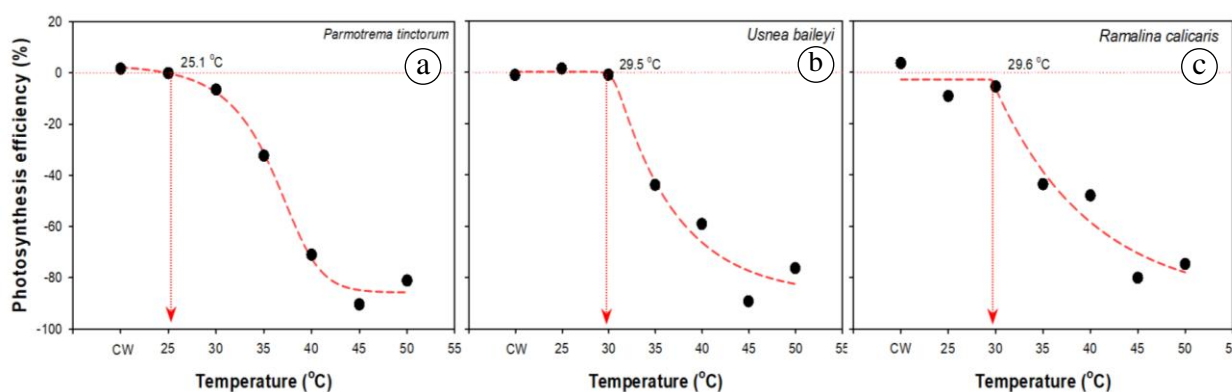


Figure 2.

The percentage of photosynthetic efficiency exhibited by three lichens *Parmotrema tinctorum* (a), *Usnea baileyi* (b) and *Ramalina calicaris* (c), when subjected to varying temperatures of 25, 30, 35, 40, 45, and 50 °C. The control group (CW) was composed of lichens stored at room temperature 25°C (n=3).

Table 1.

The comparison of the photosynthesis rate and the maximum quantum efficiency of PSII (Fv/Fm) before and after exposure to temperatures of 25, 30, 35, 40, 45, and 50°C (n=3) for 1 hour of 3 lichens, which collected from Doi Suthep-Pui National Park, Chiang Mai province, Thailand.

| Lichens | Temp. treatments | Photosynthesis rate; Pn | | Damage of Pn (%) | Fv/Fm | | Damage of PSII (%) |
|-----------------------------|---------------------|---|--------------|---------------------|----------------|----------------|--------------------------|
| | | (μmol CO ₂ g ⁻¹ S ⁻¹) | | | | | |
| | | Before | After | | Before | After | |
| <i>Parmotrema tinctorum</i> | Control | 35.8 (±14.1) | 35.4 (±11.5) | -1.0 | 0.691 (±0.028) | 0.708 (±0.020) | 2.4 |
| | 25 | 27.7 (±3.1) | 26.8 (±4.4) | -3.2 | 0.685 (±0.016) | 0.706 (±0.020) | 3.1 |
| | 30 | 25.2 (±3.2) | 21.8 (±2.9) | -13.5 | 0.699 (±0.000) | 0.703 (±0.009) | 0.5 |
| | 35 | 33.0 (±2.8) | 17.9 (±11.0) | -45.7 | 0.685 (±0.013) | 0.563 (±0.060) | -17.9 |
| | 40 | 38.5 (±3.3) | 14.3 (±5.7) | -63.0 | 0.689 (±0.006) | 0.145 (±0.019) | -78.9 |
| | 45 | 33.3 (±4.5) | 6.1 (±0.2) | -81.8 | 0.636 (±0.052) | 0.005 (±0.002) | -99.2 |
| | 50 | 39.0 (±11.3) | 14.9 (±5.3) | -62.0 | 0.699 (±0.018) | 0.002 (±0.002) | -99.8 |
| <i>Usnea baileyi</i> | Control | 27.2 (±2.5) | 25.4(±4.2) | -6.5 | 0.666 (±0.013) | 0.686 (±0.032) | 3.1 |
| | 25 | 20.6 (±4.4) | 21.3(±4.2) | 3.3 | 0.681 (±0.033) | 0.678 (±0.038) | -0.5 |
| | 30 | 29.7 (±5.1) | 28.9(±4.4) | -2.5 | 0.646 (±0.027) | 0.648 (±0.034) | 0.3 |
| | 35 | 41.0 (±10.2) | 16.7(±5.5) | -59.2 | 0.665 (±0.033) | 0.480 (±0.094) | -27.9 |
| | 40 | 28.1 (±0.7) | 19.3(±4.6) | -31.4 | 0.613 (±0.046) | 0.082 (±0.020) | -86.6 |
| | 45 | 35.7 (±11.8) | 6.2(±6.7) | -82.6 | 0.632 (±0.032) | 0.003 (±0.003) | -99.5 |
| | 50 | 37.6 (±7.5) | 18.2(±8.4) | -51.6 | 0.627 (±0.047) | 0.003 (±0.004) | -99.5 |
| <i>Ramalina calicaris</i> | Control | 27.4 (±6.1) | 28.3 (±6.3) | 3.3 | 0.583 (±0.072) | 0.553 (±0.049) | -5.1 |
| | 25 | 27.5 (±2.7) | 25.0 (±5.5) | -9.2 | 0.582 (±0.148) | 0.546 (±0.200) | -6.3 |
| | 30 | 23.5 (±3.6) | 19.5 (±2.3) | -17.0 | 0.521 (±0.025) | 0.550 (±0.053) | 5.6 |
| | 35 | 28.2 (±5.8) | 9.9 (±5.8) | -64.8 | 0.617 (±0.016) | 0.464 (±0.015) | -24.7 |
| | 40 | 26.9 (±2.9) | 19.5 (±4.0) | -27.4 | 0.591 (±0.034) | 0.187 (±0.004) | -68.3 |
| | 45 | 25.3 (±6.0) | 8.0 (±3.2) | -68.6 | 0.587 (±0.029) | 0.048 (±0.051) | -91.9 |
| | 50 | 33.6 (±10.8) | 15.8 (±4.4) | -53.0 | 0.362 (±0.079) | 0.010 (±0.016) | -97.1 |

To model for the temperature damage to photosynthetic efficacy (T_{dp}), the trend lines of three lichens were assessed (red dotted line in Figure 2), which will begin to decrease in the temperature range of 25-30°C. According to the optimal temperature range for most algae is 25–35°C.⁷ When air temperatures are higher than T_{dp} , it will cause lichens to become stressed by those temperatures. Thus, lichens grow in natural habitats, where they are exposed to higher temperatures than T_{dp} for a long time, which can cause the photosynthetic process to decrease and the growth of lichens to slow.⁸ Therefore, in natural habitats, it is harmful to lichens that are exposed to high air temperatures during a wet state. This situation could occur after rain, wherever there is high humidity and high intensity of sunlight, or in some areas that have high temperatures (such as Dry Dipterocarp forests). If lichen is exposed to a temperature of 35-40°C, its photosynthetic efficiency is reduced by more than half. Especially, the photosystem II is affected by more than 70%.¹ We know that temperature increases will directly affect photosynthesis and respiration. In metabolically active wet lichens, the lethal temperatures for photosynthesis in photobionts usually range between 30 and 44°C.⁴ However, in dry states, lichens can be exposed to air temperatures up to 40°C, which can resist a high temperature and have no effect on the photosynthetic process during inactive periods.¹ In addition, this study can predict the impact of global warming that may decrease photosynthesis efficiency of lichens. This may cause the disappearance of lichens that inhabit an uncontrol habitat because of the raised temperature.



Conclusion:

This study assessed the effect of temperature on lichen photosynthetic efficiency under control conditions. We found that the T_{dp} of fruticose lichen was about 30°C, while foliose lichen was found at 25°C. A temperature above this point causes heat stress in lichens, resulting in injury on the donor side of photosystem II. These results lead to a reduction in Fv/Fm and a decrease in photosynthesis rate. During incubation at 35-40°C, photosynthetic efficiency decreases significantly. Temperatures exceeding 45-50 °C inhibited photosynthetic efficiency by over 90%. This study revealed that tropical lichens are more sensitive to high temperatures in wet conditions. That could predict the effect of current global warming.

Acknowledgements:

We would like to express our gratitude to the staff members of Doi Suthep-Pui National Park for their valuable assistance during our fieldwork, as well as to our colleagues at the Lichen Research Unit, Ramkhamhaeng University for their laboratory support. This study was funded by the National Research Council of Thailand (NRCT).

References:

1. Pisani T, Paoli L, Gaggi C, Pirintsos S A, Loppi S. *Plant Biosystems*. 2007; 141(2), 164-169.
2. Gauslaa Y. *J Exp Bot*. 1999; 50: 697-705.
3. Kvíderová J, Kumar D. *Protoplasma*, 2020; 257(1), 61-73.
4. Oukarroum A, Strasser R J, Schansker G. *Photosynth Res*. 2012; 111(3), 303-314.
5. Molina-Bravo R, Arellano C, Sosinski B, Fernandez G. *Sci Hort-Amsterdam*. 2011; 130, 524-530.
6. Boonpeng C, Boonpragob K, Homsud K. *Thai Journal of Botany*. 2014; 6, 67-76.
7. Stanton, D. E., Ormond, A., Koch, N. M., & Colesie, C. *American Journal of Botany*, (2023);110(2), e16131.
8. Marín C, Barták M, Palfner G, Vergara-Barros P, Fernandez F, Hájek J, Casanova-Katny A. (2022). *Plants*. 2022; 11(19), 2463.



THE STUDY OF FATTY ACID REDUCTASE REACTION

Atchara Sripanya,¹ Autchara Wongsathep¹, Ruchanok Tinikul^{1,*}

¹Department of Biochemistry and Center for Excellence in Protein and Enzyme Technology, Faculty of Science, Mahidol University, Bangkok, Thailand.

*e-mail: ruchanok.tin@mahidol.edu

Abstract:

A significant number of syntheses in various industries, especially cosmetic and pharmaceutical, rely on the presence of a reactive aldehyde functional group, which is obtained by reducing the carboxylic group. While there are several chemical techniques available to create aldehydes, these procedures typically involve the use of hazardous and costly chemicals and generally lack the ability to selectively target certain chemical groups. Enzyme-based reduction provides a technique that is both environmentally safe and chemospecific. Carboxylic acid reductase (CAR) and fatty acid reductase (i.e., LuxCE multienzyme reductase) enzymes have the ability to facilitate the reduction of carboxylic groups to form matching aldehydes. While the CAR reaction has been thoroughly researched, the information on the LuxCE reaction and its use is still very limited. Hence, this work aims to express and examine the biochemical properties and reactions of LuxCE reductase in aldehydes production. The LuxC and LuxE overexpression conditions in *Escherichia coli* (*E. coli*) BL21 (DE3) were optimized for each protein and the result showed that both LuxC and LuxE could overexpress under the same conditions at 20 °C with 1 mM IPTG inducer in Luria-Bertain (LB) media. However, the optimal LuxE soluble expression required the co-transformation with pTF16 chaperone. The purified recombinant enzyme could yield 45.36 mg/L for LuxC (~55 kDa) and 3.85 mg/L for LuxE (~43 kDa). The bioluminescence-based assay was successfully established to detect aldehyde product from LuxCE reaction. With the employed assay condition, light output was dependent on the LuxCE concentration from 4-8 μ M, indicating that the coupling compositions was not the limiting factor. The increase in the LuxE to LuxC ratio has the potential to enhance enzyme activity, indicating that in an Acyl-AMP intermediate formation by LuxE reaction determines the aldehyde production. Furthermore, investigations on substrate specificity have verified that the LuxCE reaction was specific to aliphatic long chain acids, particularly myristic acid (C14), rather than medium and aromatic acids. The findings of this work will provide valuable foundational knowledge for the implementation of LuxCE in biocatalysis, which will primarily impact the use of aldehydes in the cosmetic and pharmaceutical industries via the sustainable method of enzyme usage.

Introduction:

Aldehydes play a crucial role in a wide range of chemical syntheses and are also important components in the creation of flavor and fragrance compounds¹. They also act as reactive moiety of important intermediates for the preparation of several high-value alcohol and amine compounds. Carboxylic acids are highly desirable for the synthesis of aldehydes because of their plentiful, naturally occurring nature and stability in laboratory conditions. This makes them essential for reliable and efficient synthetic pathways¹. Although there are several chemical techniques available to create aldehydes from acid functional group. The poor chemo-selectivity of chemical catalysts makes the process to be relatively difficult as requiring appropriate protection/deprotection steps with hazardous reagents. Due to the ability to selectively reduce carboxylic acids to aldehydes, biocatalyst offers a promising alternative way to conventional chemical strategies^{1,2}.

Carboxylic acid reductase (CAR) refers to the enzymes that have ability to generate aldehyde from carboxylic acid functional group. Typically, they catalyze the reduction of carboxylic acid using ATP and NADPH. The CAR is a single protein with multidomain enzymes (A, PCP and R domains), which utilizes a peptidyl carrier protein (PCP domain) to bind to carboxylic acids. The first acyl-AMP intermediate is formed in A-domain, stimulating the production of pyrophosphate as a byproduct. By transferring the acyl group to a phosphopantetheine 'arm' that is attached to the PCP-domain, an enzyme-bound thioester is formed. Following delivery to the R-domain, this thioester is reduced by NADPH to produce the aldehyde product³. CAR is attractive to apply for aldehyde synthesis because it uses ATP as an activating agent and NADPH as a reducing agent in water, both of which are environmentally friendly¹. Thus, there are extensive studies in catalytic mechanism, engineering and application of CAR for aldehyde synthesis. However, aldehyde synthesis by CAR is limited to aromatic and short-chain acid substrates due to active site architecture⁴.

Another enzyme capable to generate aldehyde from carboxylic acid is a multienzyme fatty acid reductase or LuxCE. The LuxC and LuxE are encoded by separated *luxC* and *luxE* genes commonly found in *lux* operon of luminous bacteria^{5, 6}. To generate light, LuxCE functions to generate fatty aldehyde that acts as a substrate for bioluminescence reaction catalyzed by LuxAB bacterial luciferase. The LuxCE enzyme facilitates the conversion of fatty acids into fatty aldehydes by utilizing ATP and NADPH as CAR, but the reactions of AMP acylation and reduction happen in different proteins^{4, 7}. The reaction mechanism is proposed to start with free fatty acids interacting with LuxE synthetase. The LuxE uses ATP to activate the fatty acid into acyl-AMP intermediate, which then forms a second step covalently attached to Cys362. This intermediate is proposed to be delivered directly to the LuxC reductase's active site to form a thioester adduct with Cys286 of LuxC. This intermediate is then reduced by NADPH, resulting in aldehyde formation⁵. Although the catalytic mechanism of LuxCE resembles the CAR reaction, its protein sequences and structure are very diverse from CAR. Currently, there is a limited understanding of the LuxCE multicomplex formation, enzyme reaction and substrate specificity to generate aldehydes. Therefore, the goal of this work is to produce active recombinant LuxC and LuxE for investigating the aldehyde production reaction and to establish bioluminescence-based assay to detect aldehyde generation. Additionally, we studied the ratio of LuxC to LuxE to explore the significance of each enzyme subunit in aldehyde generation to achieve optimal aldehyde production. In the final part, various substrates were investigated to confirm inconclusive information about substrate specificity. The knowledge obtained from this study will provide an in-depth mechanism of LuxCE for aldehyde production and pave the way for further application of LuxCE in the generation of aldehydes in various industries, especially cosmetics and pharmaceuticals, which are growing trends globally with sustainable aldehyde production via LuxCE multienzymes.

Methodology:

Construction – pET24b-*luxE* with C-terminus hexa-histidine tagged, *luxE* gene was subcloned into pET24b plasmid at *NdeI* and *XhoI* cut sites to create His-tagged *luxE*. Primers (Forward primer: CATTTCATATGGACGTACTTTCAGCGGT and Reverse primer: CCGCTCGAGTCAG TTGCCTCCTTCAT TCTTAGC) were used to amplify *V. campbellii luxE* gene from pET17b-*VluxE*. A 50 µL PCR reaction consisted of 0.5 µM primers, 200 µM dNTPs, and 0.025 units of *Pfu* DNA polymerase. The PCR reaction began with 2 minutes of heating at 95 °C, followed by 30 cycles of denaturing, annealing, and extension at 95, 70, and 72°C for 30 seconds, 30 seconds, and 2 minutes, respectively, and followed by a final extension at 72 for 5 minutes. PCR product was evaluated by agarose gel electrophoresis (1% w/v) and purified using FavorPrep Gel/PCR Purification Mini Kit (Favogen). Then cut



pET24b plasmid and *luxE* gene were ligated at 25°C for overnight, before transformed into competent *E. coli* XL1 blue using heat-shock method. The cells harboring plasmid were selected by spreading on LB agar containing 34 µg/µl kanamycin. Recombinant plasmids were screened by alkaline lysis then digested with *NdeI* restriction enzyme. Sanger sequencing was used to verify the correctness of pET24b-*luxE* sequence. Clustal Omega from EMBL-EBI evaluated nucleotide and amino acid sequences.

Expression of *LuxE* and *LuxC* – The plasmids pTF16, which encoded a chaperone, was co-transformed into the *E. coli* BL21 (DE3) strain with pET24b-*luxE* to enhance soluble protein production. The cells were spread on LB agar containing 34 µg/µl of kanamycin and 34 µg/µl of chloramphenicol. A single colony was picked and inoculated into a 50 ml LB medium containing the same antibiotics and cultivation was carried out at 37 °C, 220 rpm for 16 hours. Then 1% inoculation was proceeded in 4-L LB medium with 17 µg/µl of kanamycin and 17 µg/µl of chloramphenicol. Once the OD₆₀₀ reached a range of 0.6 to 0.8, 1 mM IPTG was introduced to allow the protein expression at 20 °C for 16 hours. Cells were harvested by centrifugation at 8,000 rpm at 4 °C for 10 minutes, prior to being stored cell paste at a of -80 °C. pET17b-*luxC* was previously constructed by our colleague. The *LuxC* from *V. campbellii* was expressed in *E. coli* BL21 (DE3) with 4-L of LB media using the same methods of *LuxE*, but without the pTF16 plasmid. The expression was induced at an OD₆₀₀ of 0.6-0.8 with 1 mM IPTG at 20 °C for a further 16 hours. The cells were harvested by centrifugation at 8,000 rpm at 4 °C for 10 minutes. The cell pellet was collected and weighed before being kept at -80 °C.

Purification of *LuxE* – A Ni-NTA affinity chromatography column was used for purifying *LuxE* with an N-terminal hexa-histidine tag. Cell paste was lysed in 50 mM sodium phosphate buffer at pH 7.0 containing 200 mM NaCl buffer using sonication before the crude extract was obtained by centrifugation at 15,000 rpm at 4 °C for 1 hour. The column was pre-equilibrated with 50 mM sodium phosphate, pH 7.0 containing 200 mM NaCl prior to loading of crude extract. A 50 mM sodium phosphate buffer at pH 7.0 containing 200 mM NaCl and 20 mM imidazole was a wash buffer. To elute the protein, a linear gradient of 20 to 200 mM imidazole in 50 mM sodium phosphate buffer pH 7.0 containing 200 mM NaCl was used. The elution fractions were collected by employing a Biorad automated fraction collector. Based on SDS-PAGE and 280 nm absorbance analysis, enzyme containing fractions of *LuxE* (~43 kDa) were pooled before overnight dialysis against 50 mM sodium phosphate pH 7.0 containing 1 mM DTT. An ultrafiltration membrane with a 10 kDa cutoff was used to concentrate the enzyme. The extinction coefficient (ϵ_{280}) of 14,625 M⁻¹cm⁻¹ obtained from ExPASy analysis was utilized for calculating the protein concentration. The enzyme was stored in 50 mM sodium phosphate pH 7.0 with 1 mM DTT and 10% (v/v) glycerol at -80 °C.

Purification of *LuxC* - The *LuxC* purification procedure involved with the first precipitating with 1 % (v/v) polyethyleneimine. The precipitated protein was then dialyzed against the dialysis buffer (50 mM sodium phosphate buffer pH 7.0, containing 1 mM DTT) at 4°C for 16 hours, before clarified and applied onto Diethylaminoethanol (DEAE)-Sephacrose column. The column was pre-equilibrated and washed with 50 mM sodium phosphate buffer pH 7.0 containing 30 mM NaCl and 1 mM DTT. The protein was eluted using linear gradient 30 to 300 mM NaCl in 50 mM sodium phosphate buffer pH 7.0 containing 1 mM DTT and the fractions were collected and evaluated using absorbance at 280 nm and SDS-PAGE. The fractions with the anticipated molecular weight of *LuxC* (~55 kDa) were combined and concentrated before going through gel filtration (G-25) column chromatography to remove salt using 50 mM sodium phosphate buffer pH 7.0 with 1 mM

DTT. The purified LuxC enzyme was concentrated and quantified using extinction coefficient (ϵ_{280}) of $16,125 \text{ M}^{-1}\text{cm}^{-1}$.

Activity assay – LuxCE activity was assessed using a bioluminescent coupling assay, in which LuxCE catalyzed the reduction of long chain fatty acids to corresponding aldehydes using ATP and NADPH as co-substrates. The aldehyde product was then employed as a substrate by LuxAB luciferase to produce a light signal. Thus, the measured light signal corresponded to the presence of fatty aldehyde and represented LuxCE activity (Figure 1). The LuxCE *in vitro* reaction consisted of two mixtures: mixture A contained 20 mM Hepes (pH 7.5), 150 mM NaCl, 5% Glycerol, 1 mM MgCl_2 , 2 mM DTT, 20 μM FMN, 1 mM ATP, 10 μM LuxAB, and 2 μM C1, and mixture B contained 4 mM NADPH, 4 mM NADH, 8 μM LuxC, 8 μM LuxE, and 20 μM myristic acid. The reaction was initiated by combining the two-solution mixtures, and the bioluminescent signal was measured for 30 minutes using a luminometer (ATTO-AB-2770 Octa) kinetics measurement mode, followed by the display of the luminescence signal via integrated signal. The positive control reaction utilized decanal aldehyde instead of myristic acid, whereas the negative control was the reaction without LuxCE. The trace of light emission was recorded, and the light underneath the trace reflected the overall light output. Subsequently, the effect of LuxCE concentration was investigated by varying the concentration of LuxCE in the same mixtures. The effect of LuxC:LuxE ratio was also examined by varying ratios to 1:1, 1:2, 2:1, 1:4, and 4:1. In addition, the specificity of LuxCE was evaluated by varying the chain length of the fatty acid. Then, the result of the integrated signal of luminescence was performed statistically with the one-way ANOVA method.

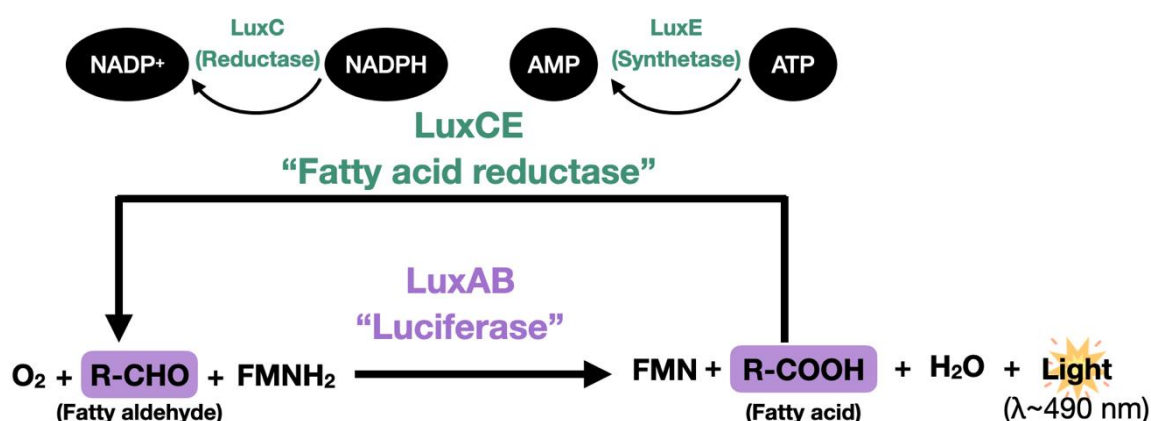


Figure 1. The reaction of LuxAB and LuxCE to generate the luminescence signal.

Results and Discussion:

Construction and expression – The expression plasmids of pET24b-LuxE was successfully constructed to express LuxE with an N-terminus hexa-histidine tag. We could success to express LuxC with reasonable amount in optimized expression condition in LB medium with 1 mM IPTG at 20°C for 16 hours. However, most LuxE expressed as an inclusion body. We then tried to improve LuxE folding using chaperones. Each of chaperone, including pGro7, pKJE7 and pTF16 were co-transformed with pET24b-LuxE using IPTG and L-arabinose, as LuxE and chaperone inducers, respectively. The SDS-PAGE results in Figure 2A showed a 43-kDa protein soluble band corresponding to LuxE protein in all circumstances. Among tested chaperones, the co-transforming of pET24b-LuxE with pTF16 provided the highest improved amount of soluble LuxE. The improvement of LuxE folding by pTF16 chaperone was confirmed as the results shown in Figure 2B. Therefore, the condition of LB medium with 1 mM IPTG at 20°C and the pTF16 chaperone was used to



produce LuxE protein. Approximately 20 g cell pastes/4-L culture were obtained for both LuxC and LuxE expression.

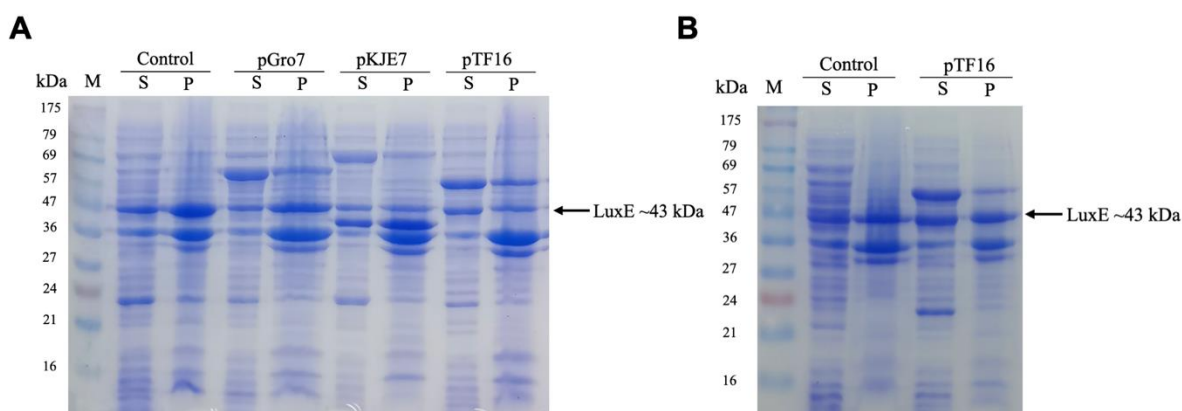


Figure 2. Improvement of LuxE expression by using chaperone proteins. **(A)** Each of chaperone expression plasmid (pGro7, pKJE7, and pTF16) was co-transformed with pET24b-LuxE in *E. coli* strain BL21 (DE3) in LB medium with 1 mM IPTG and 0.5 mg/ml L-arabinose inducers at 20 °C. **(B)** Expression of LuxE with pTF16 chaperone and L-arabinose was introduced during inoculation. A 20 µg of crude extract or pellet were examined using 15% SDS-PAGE. Lane M: protein markers; Lane P: pellet; Lane S: crude extract.

Purification – LuxC was purified through a two-step protocol that included PEI precipitation and DEAE Sepharose chromatography (Figure 3A). The LuxC purification yielded around 45.36 mg/L culture. Notably, during LuxC purification and storage, it is important to keep all steps to be reducing condition by adding 1 mM DTT to preserve active form of LuxC⁸. This is due to the reductase activity of LuxC requires reactive cysteine residue. The N-terminus hexahistidine tagged LuxE was purified using an imidazole gradient elution on a Ni-NTA (nickel-nitrilotriacetic acid) affinity chromatography column. The SDS-PAGE analysis (Figure 3B) showed that after pass through affinity column, we could obtain purified LuxE and yielded of 3.85 mg/L culture. However, both purified enzymes still appeared some impurity bonds remaining. Another column chromatography method, such as ion-exchange and hydrophobic column, can further be implemented to enhance purity. Nevertheless, the objective of this study is to examine the production of aldehyde using LuxC and LuxE enzymes, the proteins with this purity are desired.

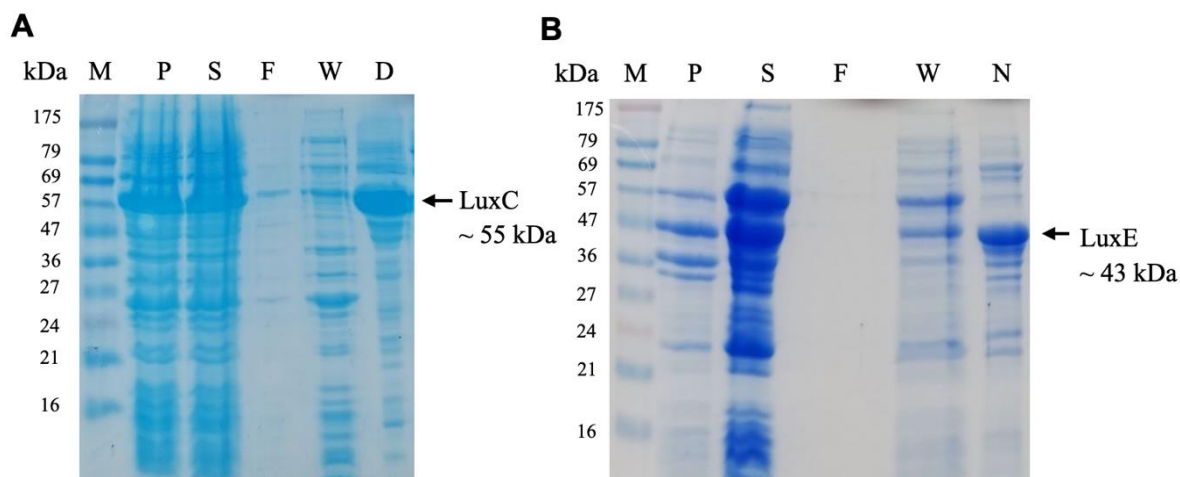


Figure 3. Purification of LuxC and LuxE. SDS-PAGE analysis of purified LuxC (A) and LuxE (B). A 20- μ g protein was analyzed by 15% SDS-PAGE. Lane M; protein marker, Lane P; pellet crude extract protein, Lane S; supernatant crude extract protein, Lane F; flow through of protein after loading to Ni-NTA column, Lane W; wash step, Lane D; protein after purified by DEAE, Lane N; protein after purified by Ni-NTA column.

Activity assay – The activity of LuxCE was investigated by detecting the luminescence signal resulting from LuxAB reaction using luminometer (AB-2270 Luminescencer Octa, ATTO). In this experiment, we hypothesized that LuxCE has activity to convert fatty acid (myristic acid) to fatty aldehyde. The aldehyde product will be further used as a substrate for LuxAB to generate the luminescence signal. As we employed excess amount of LuxAB in the system, the light signal detected by luminometer as a total luminescence signal in RLU (Relative Light Units) can represent the LuxCE activity. The investigation of the luminescence signal for the positive control using fatty aldehyde (C12 aldehyde) revealed the highest signal (Figure 4). While the reaction containing LuxCE proteins provided the bioluminescence signal significantly higher than the negative control reactions (p values <0.0001). This indicates that the LuxCE enzymes can actively convert fatty acid to fatty aldehyde, subsequently utilized by LuxAB. Furthermore, LuxCE reactions provide a significantly higher luminescence signal than only LuxC or LuxE (p values <0.0001); this suggests that reaction to convert fatty acid to fatty aldehyde requires both LuxC and LuxE.

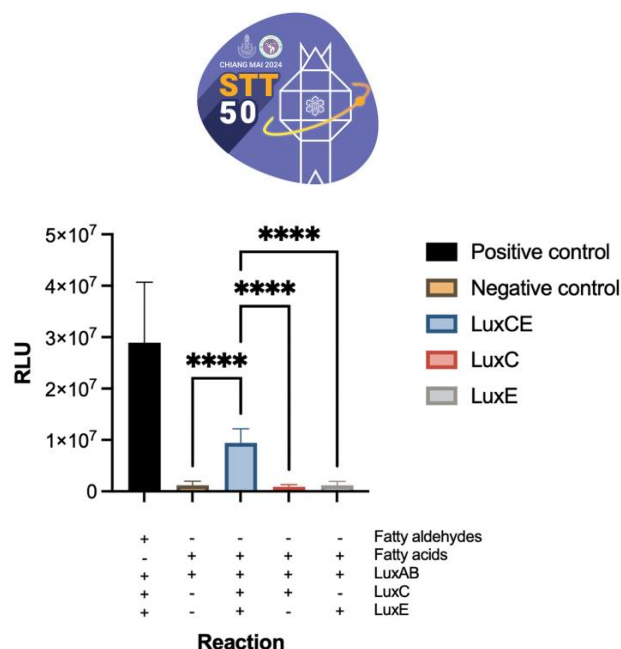


Figure 4. The luminescent signal produced by the LuxAB and LuxCE reactions. The LuxAB coupling assay was employed to measure LuxCE activity using myristic acid as a substrate. The negative control is the reaction without LuxCE enzymes, while the positive control utilized dodecanal as a substrate.

To investigate the effect of LuxCE concentration on light signal, the concentration of LuxCE was varied and carried out using the same mixture condition. The results (Figure 5A) indicated that detected light signal was dependent on LuxCE concentration and increase of LuxCE from 4 μ M to 8 μ M could result the higher light signal. However, an increase in concentration further from 8 μ M to 12 μ M, provided in a higher signal, but this difference was not statistically significant according to one-way ANOVA (Figure 5B). These results indicated that the increment amount of LuxCE in 4-8 μ M range can generate more fatty aldehyde available for LuxAB to generate light and at this condition LuxAB and other components are not limitative agents. However, beyond this LuxCE concentration, light was not significant increase, and this might be limited by LuxAB activity and other assay components. Thus, with the employed condition, LuxCE concentration should not excess than 8 μ M. As LuxCE was previously proposed to function as heterooctameric composing 4LuxC:4LuxE⁷, in this section, the effect of LuxC:LuxE ratio was investigated by varying in the following ratios: 1:1, 1:2, 2:1, 1:4, and 4:1. The results in Figure 5C indicate that an increase in the ratio of LuxE led to an increase in the signal. This could be attributed by the slow reaction of LuxE enzyme, which function to activate fatty acid substrate by generating acyl-AMP intermediates prior to transferring to the LuxC active site⁵. Higher amount of LuxE in the system can lead to generate more acyl-AMP intermediates. On the other hand, when the ratio of LuxC:LuxE increases to 2:1, the signal exhibits a similarity to the 1:1 ratio, and exhibited negative effect when the ratio reached to 4:1. This may be caused an improper oligomerization of LuxC and LuxE, resulting in a conformational change of the multienzyme complex and a decrease in signal. Therefore, it is necessary to investigate and confirm the presence of polymerized multicomplex enzymes.

In addition, the substrate specificity of LuxCE to convert aldehydes was evaluated (Figure 5D). The results indicated that myristic acid (C14) exhibited the highest light signal among the fatty acid substrates, while lauric acid (C12) and palmitic acid (C16) did not significantly differ in their signals. On the other hand, hexanoic acid (C8), decanoic acid (C10) and aromatic substrate benzoic acid (C6) showed significantly decreasing signals when compared with myristic acid. This suggests that myristic acid (a long-chain fatty acid) might

best accommodate to LuxCE active site. While the LuxCE active site might not be suitable for short-chain fatty acids and aromatic substrates. This is consistent to the previous study indicating specificity to aliphatic long chain acids⁵.

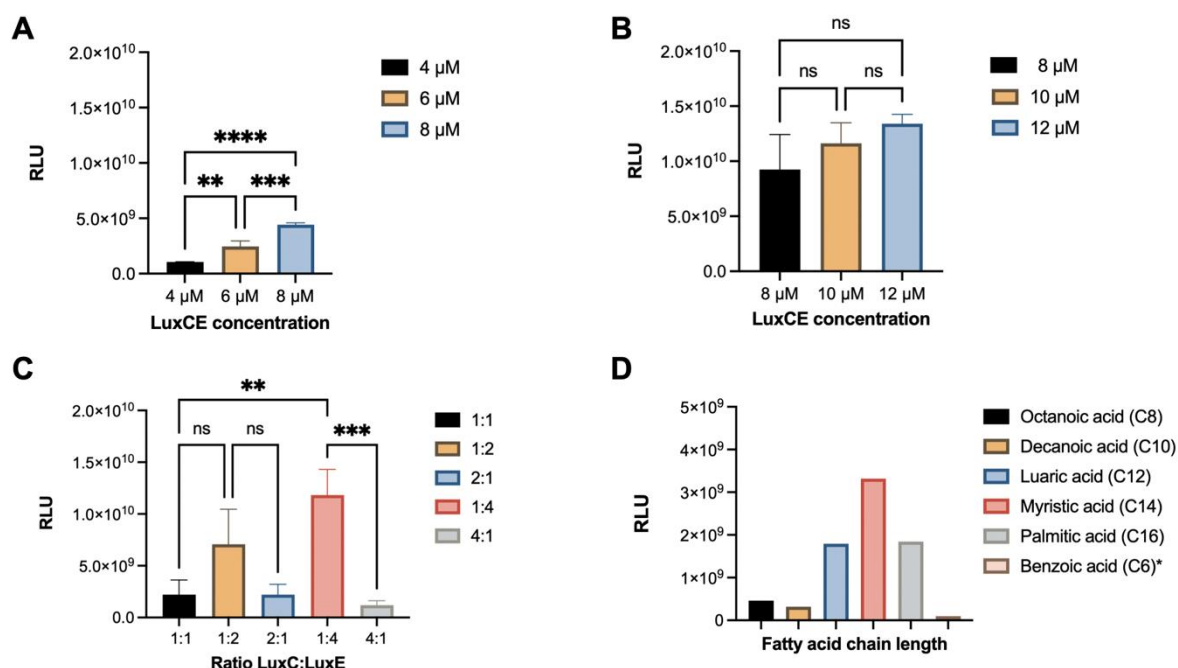


Figure 5. Bioluminescent based determination of LuxCE activity. (A) and (B) The effect of LuxCE concentration. (C) The effect of LuxC:LuxE ratio and (D) The effect of acid substrates on aldehyde generation by LuxCE. *aromatic fatty acid

Conclusion:

In summary, we succeeded to express and purify fatty acid reductase, LuxCE and established the bioluminescence-based assay for LuxCE. The enzyme could actively function to convert fatty acid to aldehydes and specific toward aliphatic and long-chain fatty acids. The increase of LuxE ratio relative to LuxC resulted to enhance substrate conversion activity.

References:

1. Derrington, S. R.; Turner, N. J.; France, S. P. *Journal of Biotechnology* 2019, 304, 78-88.
2. Devine, P. N.; Howard, R. M.; Kumar, R.; Thompson, M. P.; Truppo, M. D.; Turner, N. J. *Nature Reviews Chemistry* 2018, 2 (12), 409-421.
3. Finnigan, W.; Thomas, A.; Cromar, H.; Gough, B.; Snajdrova, R.; Adams, J. P.; Littlechild, J. A.; Harmer, N. J. *ChemCatChem* 2017, 9 (6), 1005-1017.
4. Hu, Y.; Zhu, Z.; Gradischnig, D.; Winkler, M.; Nielsen, J.; Siewers, V. *Proceedings of the National Academy of Sciences* 2020, 117 (37), 22974-22983.
5. Brodl, E.; Winkler, A.; Macheroux, P. *Computational and Structural Biotechnology Journal* 2018, 16, 551-564.
6. Riendeau, D.; Meighen, E. *Journal of Biological Chemistry* 1979, 254 (16), 7488-7490.
7. Tian, Q.; Wu, J.; Xu, H.; Hu, Z.; Huo, Y.; Wang, L. *Journal of Biological Chemistry* 2022, 298 (6), 102006.
8. Vankemmelbeke, M.; Healy, B.; Moore, G. R.; Kleanthous, C.; Penfold, C. N.; James, R. *J Bacteriol* 2005, 187 (14), 4900-4907.

C-CHEMISTRY (ANALYTICAL CHEMISTRY)



ALTERNATIVE METHOD FOR SIMULTANEOUS DETECTION OF CURCUMIN AND ALPHA-MANGOSTIN WITH VARIABLE WAVELENGTH DETECTOR

Songsuda Promthong, Watchara Kaewsuan*

Office of Scientific Instrument and Testing, Prince of Songkla University, Hat Yai Campus, Songkhla, 90110, Thailand

*e-mail: watchara.kae@psu.ac.th

Abstract:

The aim of this study was to develop the alternative method for simultaneous detection of curcumin and alpha-mangostin in oil sample using HPLC-VWD. The chromatographic system for the quantification of curcumin and alpha-mangostin was carried out using a Hypersil ODS C18 column (4.0 x 250 mm, 5 μ m particle size) at 25°C with gradient elution of a mobile phase consisting of methanol, 2% formic acid in water, and acetonitrile at a flow rate of 1.0 mL/min. The absorption wavelengths for curcumin and alpha-mangostin were monitored at 425 nm and 320 nm, respectively, (gradient wavelength). Under the optimal HPLC-VWD conditions, linearity was achieved in the concentration range of 0.01-10 mg/g for both analytes. The LODs of curcumin and alpha-mangostin were 0.0025 mg/g, and the LOQs were 0.0050 mg/g, the accuracies of curcumin and alpha-mangostin were $92.93 \pm 0.79\%$ and $95.37 \pm 0.99\%$ recovery, respectively, and the repeatability precisions were 0.46% and 0.94% RSD, respectively, with all values meeting the acceptable criteria according to AOAC. The developed method not only simplicities of the extraction process, but also short analysis time, good accuracy and repeatability precision. Moreover, the alternative method for simultaneous detection of curcumin and alpha-mangostin with HPLC-VWD was successfully and can be applied the queue in lab-booking to increase the hour of self-service instrument at the Office of Scientific Instrument and Testing, Prince of Songkla University, Songkhla, Thailand.

Introduction:

Curcumin (Figure 1.A) is a natural product isolated as a main active ingredient in turmeric (*Curcuma longa*). It is native to Southeast Asia but is popular around the world. Claims about the health benefits of curcumin abound. Traditionally, it has been used in Asian countries as a medical herb due to its antioxidant, anti-inflammatory, antimutagenic, antimicrobial, and anticancer properties.^{6,10} Alpha-mangostin (Figure 1.B) is the major component and bioactive compound, and it has been widely used as a traditional medicine for treatment of abdominal pain, diarrhea, dysentery, infected wound, suppuration, chronic ulcer,⁹ anti-inflammatory, antibacterial, and anticancer effects.⁵ So, the customer interested and required the quantitative analysis of curcumin and alpha-mangostin using HPLC technique.

Consequently, from the customer data and literature reviews, curcumin^{1,3,6} and alpha-mangostin^{2,5,9} can be detected by HPLC technique, but it has not yet been reported for simultaneous detection. Moreover, the maximum absorption wavelength of each compound was different. So, the suitable detectors of HPLC used for the detection are diode array detector (DAD) and variable wavelength detector (VWD) to provide a high sensitivity, good resolution and precision.^{7,8} In case of DAD, the scientist and customer a lot of booking the HPLC-DAD queue, this causes customers to wait long times to test sample. Thus, the aim of this study was to develop an analytical method and sample preparation technique for simultaneous detection of curcumin and alpha-mangostin in oil sample.

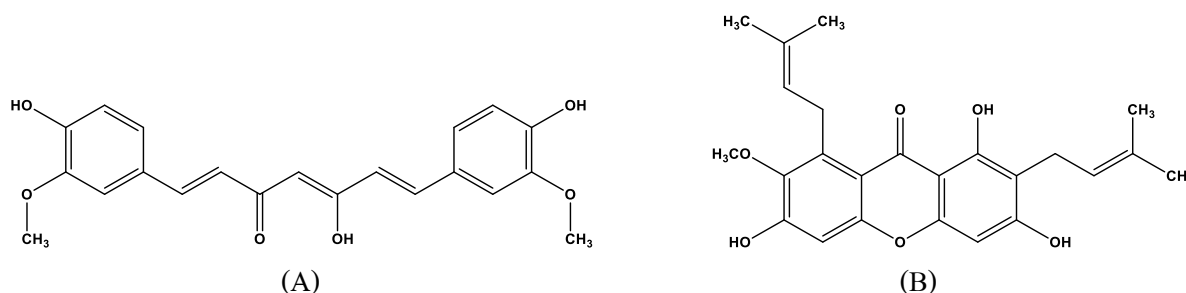


Figure 1. The molecular structure of curcumin (A) and alpha-mangostin (B).

In addition, a sample preparation technique was important and required prior to instrumental analysis. In this work, to develop a sample preparation for the extraction process of curcumin and alpha-mangostin in oil sample as shown in Figure 2.

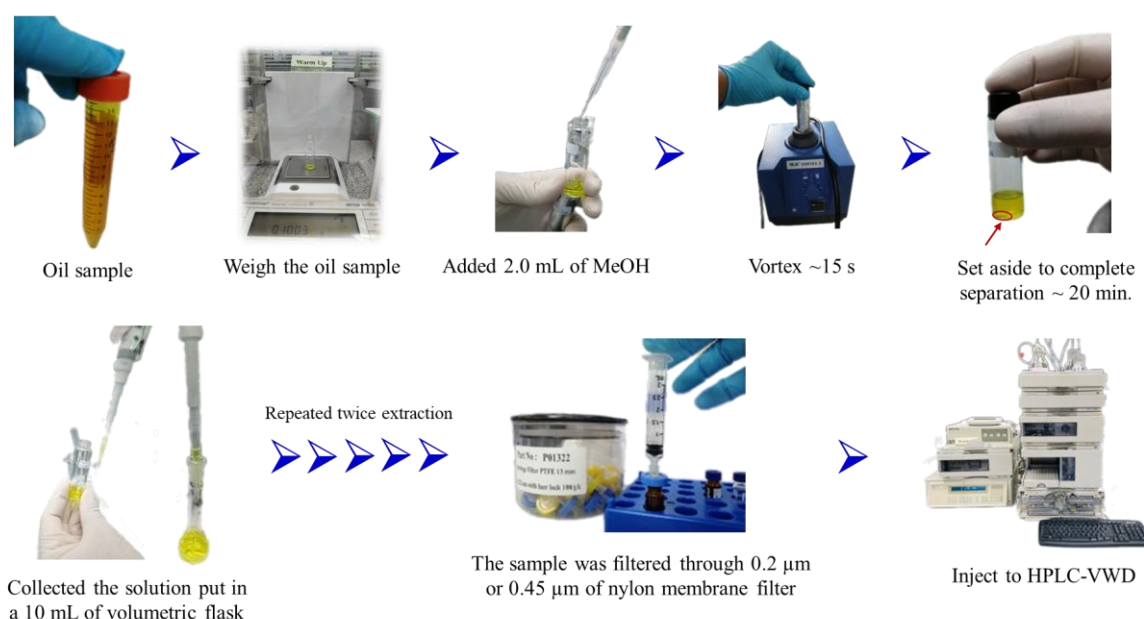


Figure 2. The extraction process of curcumin and alpha-mangostin in oil sample.

Methodology:

Chemical and standard: Curcumin (purity $\geq 98\%$) and Alpha-mangostin (purity $> 98\%$) were purchased from Axxo Chemicals and Services Co.,Ltd. Methanol and Acetonitrile (HPLC grade, RCI Labscan Limited, Bangkok, Thailand) were purchased from High Science Limited Partnership. Formic acid (98-100%, Merck, Darmstadt, Germany) was purchased from A & A Reagent Limited Partnership. Water Purification System, Human Corporation, Zeneer navi UP 900, Korea.

Instruments: High Performance Liquid Chromatograph-Variable Wavelength Detector (HPLC-VWD), Agilent Technologies, 1100 series, Germany. High Performance Liquid Chromatograph-Diode Array Detector (HPLC-DAD), Agilent Technologies, 1200 series, Germany. Hypersil ODS C18 column (4.0 x 250 mm, 5 µm particle size), Agilent Technologies. Analytical balance 5 digits, Mettler Toledo XP205, Switzerland. Centrifuge, Eppendorf, 5430 R, Germany. Ultrasonic Cleaners, Elma sonic e30H, United States. Vortex Mixer Genie 2, Scientific Industries, G560E, United States.

Mobile phase preparations: Methanol (HPLC grade), 2% formic acid in water and acetonitrile (HPLC grade) were filtered through 0.45 µm of nylon membrane filter and degassed by ultrasonication before use. A 2% formic acid in water should be freshly prepared.



Preparation of stock standard and working standard: 10 mg of curcumin and alpha-mangostin were dissolved with methanol in 10 mL of volumetric flask to obtain a stock standard and kept in freeze ($-20\text{ }^{\circ}\text{C}$). Diluted a stock standard with methanol to achieve the working standard in the concentration range of 0.1-100 mg/L

Oil sample preparation: Weighed the oil sample 0.1 g approximately in bottle and protected the light with aluminium foil, added 2.0 mL of methanol, vortex 15 seconds and set aside to complete separation about 20 min., then collected the sample solution put in a 10 mL of volumetric flask. The extraction process was repeated twice and adjusted final volume with methanol. The extracted sample solution was filtered through $0.45\text{ }\mu\text{m}$ of nylon membrane filter before injecting to HPLC-VWD or HPLC-DAD system.

Analytical performances: The analytical performances of the developed method were based on AOAC method (AOAC, 2016)⁴ including,

Linearity: The linearity of curcumin and alpha-mangostin were investigated, the calibration curves were plotted between the peak area and the concentration of each standard to obtain the linear range; it was determined by considering the correlation coefficient (r) greater than 0.995.

Limit of detection (LOD): The LOD is generally determined at the lowest concentration of the standard that can be distinguished between signal response and baseline noise to establish the minimum concentration that gave the signal to noise ratio greater than or equal to 3 ($S/N \geq 3$).

Limit of quantitation (LOQ): The LOQ is generally performed by comparing the signal response and baseline noise to establish the minimum concentration that gave the signal to noise ratio greater than or equal to 10 ($S/N \geq 10$).

Accuracy: The accuracy of the developed method was investigated in terms of %recovery. Oil sample extract was spiked with the curcumin and alpha-mangostin standard to obtain the final concentration of 2.00 mg/g.

Repeatability precision: The precision of the developed method was also investigated by considering the percent relative standard deviation (%RSD) within ten replicates ($n=10$).

Results and Discussion:

Preliminary test of HPLC-DAD

Generally, the HPLC-DAD, Agilent Technologies, 1200 series, was used to preliminary studies can be set the different wavelength for each standard up to 8 wavelengths at the same time. The preliminary experiment checks the chromatogram of the standard when using the DAD as a detector. The result as shown in Figure 3., the chromatogram of each standard was separated window channel according to the wavelength set (DAD channel A, 320 nm for alpha-mangostin) and (DAD channel B, 425 nm for curcumin), this makes it difficult to interpret the results. In addition, to increase the challenge of the work, develop an analytical method for simultaneous detection of curcumin and alpha-mangostin under gradient wavelength using HPLC-VWD instead.

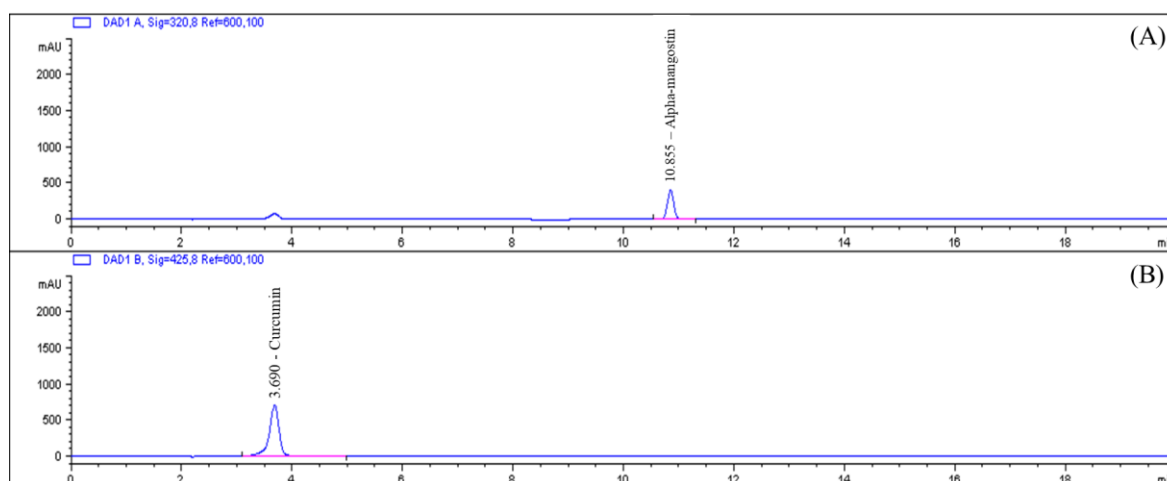


Figure 3. The HPLC-DAD chromatogram in the separate window channel of curcumin (A) and alpha-mangostin (B) standard (25 mg/L).

Preliminary test of HPLC-VWD

To resolve the problem from HPLC-DAD, the HPLC-VWD, Agilent Technologies, 1100 series was also used to preliminary studies for the determination of curcumin and alpha-mangostin under the gradient elution. However, it has set only a single wavelength for each injection at 425 nm for curcumin and 320 nm for alpha-mangostin (Figure 4.), that causes waste time for analysis.

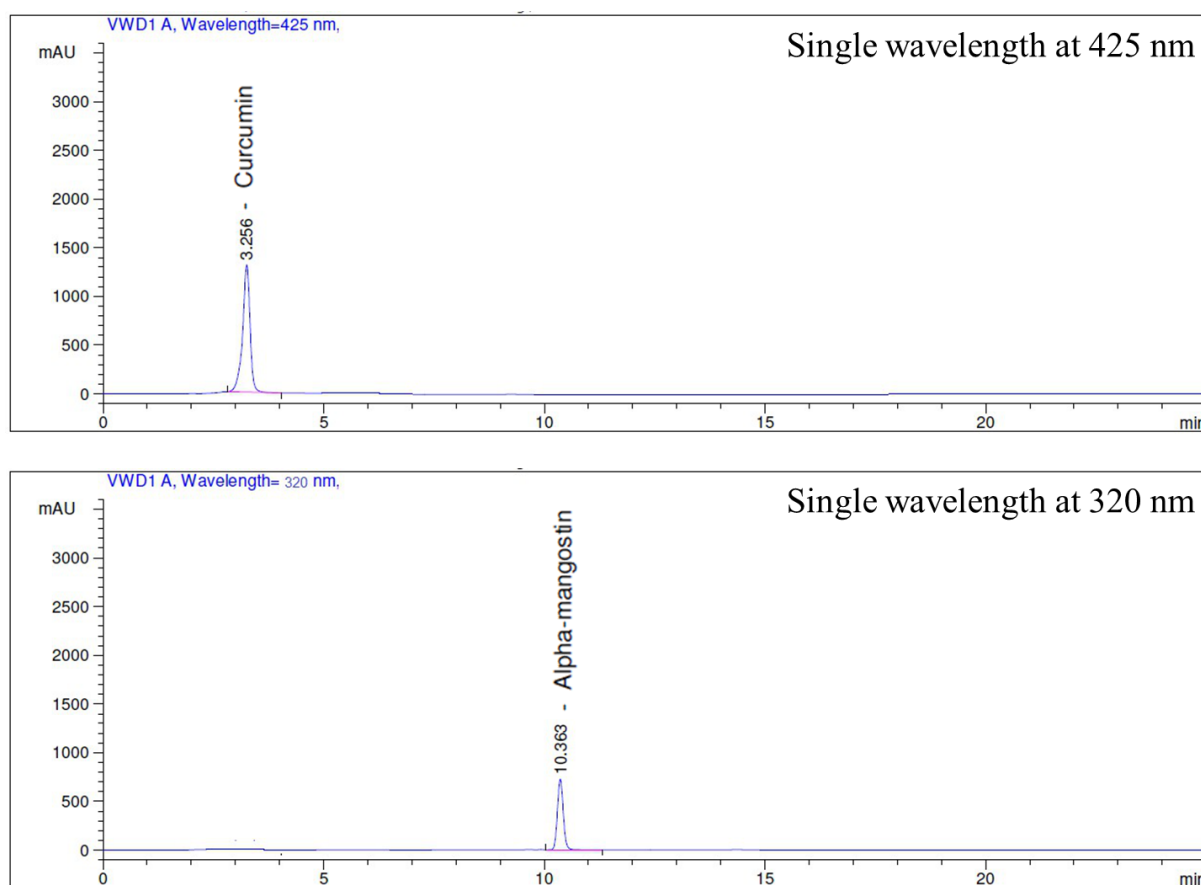


Figure 4. The HPLC-VWD chromatogram of curcumin and alpha-mangostin.



Optimization of HPLC conditions under gradient elution and gradient wavelength

The optimal HPLC conditions for simultaneous detection of curcumin and alpha-mangostin as shown in Table 1.

Table 1. The optimal HPLC-VWD conditions for the simultaneous detection of curcumin and alpha-mangostin.

| High Performance Liquid Chromatograph (HPLC-VWD conditions) | | | | |
|---|---|-----------------|-----------------------------|------------------|
| - Column: | Hypersil ODS C18 column (4.0 x 250 mm, 5 μ m particle size) | | | |
| - Column temperature: | 25 $^{\circ}$ C | | | |
| - Flow rate: | 1.0 mL/min | | | |
| - Mobile phase: | Mobile phase compositions (Gradient elution program) | | | |
| | Time (min) | Methanol (%) | 2% formic acid in water (%) | Acetonitrile (%) |
| | 0 | 80 | 20 | 0 |
| | 5 | 80 | 20 | 0 |
| | 6 | 0 | 20 | 80 |
| | 15 | 0 | 10 | 90 |
| | 20 | 80 | 20 | 0 |
| - Detector: | Variable wavelength detector (Gradient wavelength program) | | | |
| | Time (min) | Wavelength (nm) | | Compound name |
| | 0 - 6 | 425 | | Curcumin |
| | 7 - 20 | 320 | | Alpha-mangostin |

Under the optimal HPLC-VWD conditions, the chromatogram of curcumin and alpha-mangostin exhibited sharp peak, good resolution, short analysis time and simultaneous detection (Figure 5).

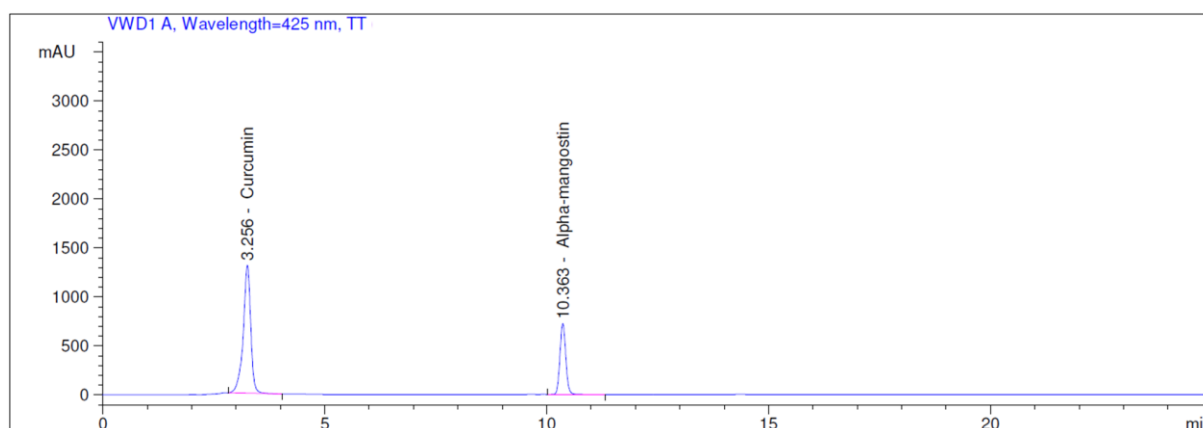


Figure 5. The HPLC-VWD chromatogram in the same window channel under gradient wavelength of curcumin and alpha-mangostin standard (100 mg/L).

Analytical performances

Linearity: The linear range of the developed method was obtained in the concentration range of 0.01-10 mg/g with correlation coefficient (r) of 0.99988 and 0.99991 for curcumin and alpha-mangostin, respectively.

Limit of detection (LOD): The LOD of the developed method based on $S/N \geq 3$ was obtained at 0.0025 mg/g.

Limit of quantitation (LOQ): The LOQ of the developed method based on $S/N \geq 10$ was obtained at 0.0050 mg/g.

Accuracy: The accuracy of the developed method was evaluated in terms of %recoveries were shown in Table 2.** Satisfactory recoveries were achieved $92.93 \pm 0.79\%$ and $95.37 \pm 0.99\%$ for curcumin and alpha-mangostin, respectively, with final concentration 20 mg/L (2.00 mg/g at sample weight 10 mg approximately) for both analytes, which acceptable recovery criteria of AOAC, 2016.⁴

Repeatability precision: The repeatability precision of the developed method was considered by the percent relative standard deviation (%RSD) in oil samples were shown in Table 2.* The %RSD of the developed method were obtained 0.46% and 0.94% for curcumin and alpha-mangostin, respectively, which acceptable repeatability precision criteria of AOAC, 2016.⁴

Table 2. The accuracy and repeatability precision of the developed method.

| Replicate no. | Amount in oil sample (mg/g)* | | Accuracy (%recovery)** | |
|---------------|------------------------------|-----------------|------------------------|-----------------|
| | Curcumin | Alpha-mangostin | Curcumin | Alpha-mangostin |
| 1 | 2.41 | 1.96 | 92.40 | 96.71 |
| 2 | 2.41 | 1.96 | 92.35 | 96.24 |
| 3 | 2.40 | 1.96 | 93.77 | 96.53 |
| 4 | 2.41 | 1.96 | 93.54 | 96.44 |
| 5 | 2.44 | 2.00 | 92.34 | 94.54 |
| 6 | 2.42 | 1.99 | 93.65 | 94.98 |
| 7 | 2.43 | 2.00 | 92.01 | 94.18 |
| 8 | 2.42 | 1.99 | 93.30 | 94.78 |
| 9 | 2.43 | 2.00 | 91.95 | 94.47 |
| 10 | 2.42 | 2.00 | 93.97 | 94.84 |
| Mean** | 2.42 | 1.98 | 92.93 | 95.37 |
| SD | 0.01 | 0.02 | 0.79 | 0.99 |
| %RSD* | 0.46 | 0.94 | 0.85 | 1.03 |

**The accuracy (%recovery) of the developed method in oil sample (n=10).

*The repeatability precision (%RSD) of the developed method in oil sample (n=10).



Under the optimal HPLC-VWD conditions, the analytical performances of the developed method are summarized in Table 3.

Table 3. Summary the analytical performances of the developed method.

| Parameters | Optimal conditions | |
|--|-----------------------------|----------------------------|
| | Curcumin | Alpha-mangostin |
| - Regression equation | $y = 164.74932x + 48.36004$ | $y = 61.81520x + 18.20486$ |
| - Correlation coefficient (r) | 0.99988 | 0.99991 |
| - Linearity, mg/g | 0.01-10 | 0.01-10 |
| - Limit of detection (LOD), mg/g | 0.0025 | 0.0025 |
| - Limit of quantitation (LOQ), mg/g | 0.0050 | 0.0050 |
| - Accuracy (%recovery), (n=10) | 92.93 | 95.37 |
| - Repeatability precision (%RSD), (n=10) | 0.46 | 0.94 |

Oil sample analysis: The developed a sample preparation technique for the extraction process were successfully and could be applied for simultaneous detection of curcumin and alpha-mangostin, the results are shown in Table 4. Recoveries of curcumin and alpha-mangostin in oil samples were obtained in the range of 98.48-101.00% and 91.41-107.61%, respectively, with acceptable criteria of AOAC.⁴ Under the optimal conditions, the peak of curcumin and alpha-mangostin in oil sample could be separated from the others matrix (Figure 6).

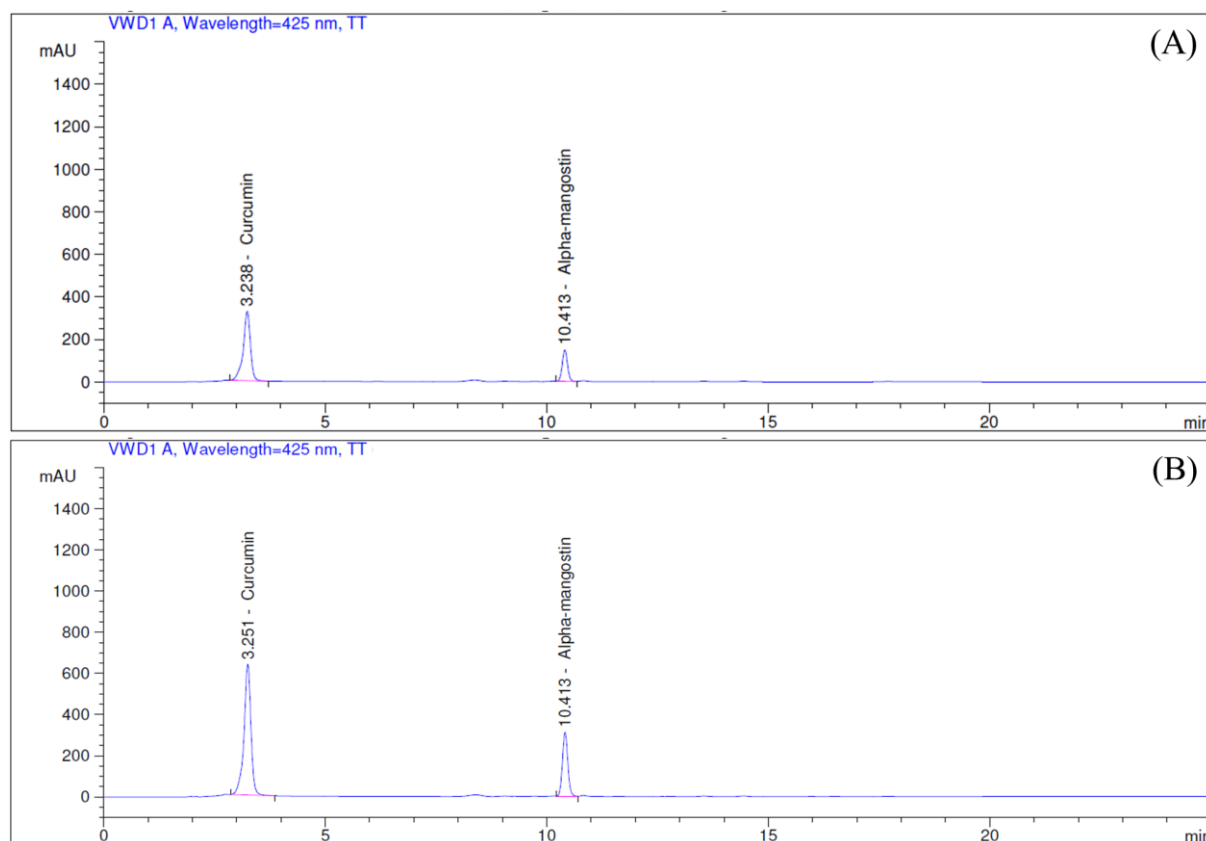


Figure 6. The chromatogram of curcumin and alpha-mangostin in oil sample (A) and standard spiked in oil sample extracted (B).

Table 4. The %recoveries of curcumin and alpha-mangostin in oil sample.

| Sample No. | Amount in oil sample \pm SD* (mg/g) | | Standard spiked (mg/g) | Final content \pm SD* (mg/g) | | %Recovery | |
|------------|---------------------------------------|------------------|------------------------|--------------------------------|------------------|-----------|-----------------|
| | Curcumin | Alpha-mangostin | | Curcumin | Alpha-mangostin | Curcumin | Alpha-mangostin |
| No.1 | 1.46 \pm 0.02 | 1.08 \pm 0.01 | 2.00 | 3.45 \pm 0.01 | 3.06 \pm 0.003 | 99.50 | 99.00 |
| No.2 | 1.73 \pm 0.13 | 1.10 \pm 0.09 | 2.00 | 3.75 \pm 0.005 | 3.17 \pm 0.002 | 101.00 | 103.50 |
| No.3 | 2.24 \pm 0.01 | 1.77 \pm 0.01 | 1.97 | 4.18 \pm 0.01 | 3.89 \pm 0.01 | 98.48 | 107.61 |
| No.4 | 1.02 \pm 0.01 | 0.92 \pm 0.004 | 1.97 | 2.97 \pm 0.004 | 2.99 \pm 0.01 | 98.98 | 105.08 |
| No.5 | 2.02 \pm 0.03 | 1.32 \pm 0.01 | 1.98 | 3.97 \pm 0.01 | 3.13 \pm 0.01 | 98.48 | 91.41 |

*SD: The standard deviation (n=2)

Conclusion:

The developed alternative method and sample preparation were successfully established for the simultaneous detection of curcumin and alpha-mangostin in oil sample. It has several advantages including simplicity of extraction process, good accuracy and precision. The linearity was obtained 0.01-10 mg/g, the LODs of curcumin and alpha-mangostin were obtained 0.0025 mg/g, the LOQs of curcumin and alpha-mangostin were obtained 0.0050 mg/g, the accuracy was obtained $92.93 \pm 0.79\%$ and $95.37 \pm 0.99\%$ recovery for curcumin and alpha-mangostin, respectively, and the repeatability precision was obtained 0.46% and 0.94% RSD for curcumin and alpha-mangostin, respectively, with the acceptable criteria according to AOAC. Moreover, the developed method and sample extraction process were applied to the new service at the Office of Scientific Instrument and Testing, Prince of Songkla University (OSIT-PSU), Songkhla, Thailand.

Acknowledgements:

The authors would like to thank the Office of Scientific Instrument and Testing, Prince of Songkla University (OSIT-PSU) for financial support. We also thank the Executive Board and Kaizen Team of the Office of Scientific Instrument and Testing for a consultant and supporting the personnel to develop the knowledge and idea from kaizen to research refer to kaizen award code no. 52/63 (Gradient Wavelength) and code no. 66/64 (Timeline of Curcumin and Alpha-mangostin) in kaizen program (<https://192.168.53.5/new/kaizen/>).

References:

1. Jayaprakasha G. K, Jagan Mohan Rao L, Sakariah K. K. J. Agric. Food Chem. 2002;50:3668-3672.
2. Muchtaridi M, Nadia A. P, Tiana M, Ida M. J. Appl. Pharm. Sci. 2017;7:125-130.
3. Bruno F. S, Maria P. D. G, Marlus C. Arab. J. Chem. 2017;10:1029-1037.
4. Guidelines for Standard Method Performance Requirements, AOAC Official Methods of Analysis. 2016:1-18.
5. Sukit Y, Anusak S, Chatchai W. J. Chromatogr. Sci. 2009;47:185-189.
6. Dewi S, Yosua A. S, Yustina S. H, Yosi B. M, Wouter L.J. H, Christine P. Heliyon. 2021;7:1-8.
7. Rashmi P, Vandana J. J. Chromatogr. Sci. 2021;59:191-203.



8. Mrinalini D, Namrata G. Int. j. pharm. res. scholars. 2016;5:47-53.
9. Werayut P, Wandee K. Thai J. Agric. Sci. 2009;42:7-12.
10. Elizabeth M. M, Paula N. B, Catherine A. R, Melissa M. P. J. AOAC Int. 2020;103:1625-1632.



DETERMINATION OF GALLIC ACID AND RUTIN IN ZINGIBERACEAE USING HPLC

Sirirat Phaisansuthichol*, Nicharat Akephaisarnpong and Manoch Thanomwat

Department of Chemistry, Faculty of Science, Maejo University, Chiang Mai 50290, Thailand

*Corresponding author e-mail: phaisansuthichol@gmail.com

Abstract:

Zingiberaceae is another type of herbal plant commonly consumed. They have a special characteristic: all parts of the plant emit the fragrance of essential oils, making them useful as spices. Additionally, they possess antioxidant properties. Most of the antioxidant compounds found in these herbs include polyphenolic compounds such as gallic acid and flavonoids such as rutin. The objective of this research is to simultaneously analyze the amount of gallic acid and rutin in methanol extracts from plants in the ginger family, including ginger, turmeric, cardamom, and zedoary, using high-performance liquid chromatography (HPLC). The optimal conditions for the analysis are as follows: use of a C18 column (4.0 mm × 250 mm), elution with acetonitrile and 0.10% formic acid (80:20 by volume) in isocratic mode at a flow rate of 1.20 mL min⁻¹, and detection with a photodiode array at a wavelength of 268 nm. The results showed that zedoary contained the highest amounts of gallic acid and rutin, measuring 416.56 ± 0.04 and 58.42 ± 0.25 mg kg⁻¹, respectively, followed by cardamom, turmeric, and ginger. These results demonstrate that HPLC is an effective technique for analyzing gallic acid and rutin in ginger family plant samples.

Keywords: Zingiberaceae, HPLC, Gallic acid, Rutin

Introduction:

Consumers today are increasingly health-conscious, leading to the development of various herbal products such as supplements, cosmetics, beverages, and health tonics. Among these, plants from the Zingiberaceae are particularly popular. These plants are notable for their aromatic essential oils present in all parts of the plant, making them a common choice for spices. Extensive research has been conducted on the diversity of Zingiberaceae plants, including studies on their antioxidant properties using DPPH¹ techniques and total phenolic content². The ginger family plants studied in this research include ginger, turmeric, cardamom, and zedoary. Most antioxidant substances found in herbs include polyphenolic compounds, flavonoids, and various vitamins. Rutin³⁻⁴ is a type of phytochemical naturally occurring as a flavonoid, classified within the bioflavonoid group. It possesses notable antioxidant properties and is effective against inflammation, viruses, and microorganisms. This compound has garnered significant interest from researchers worldwide, particularly since the onset of the COVID-19 pandemic, for its potential in inhibiting the COVID-19 virus. The chemical structure is shown in Figure 1.

Gallic acid⁵, a compound classified under polyphenols, features hydroxyl groups in its chemical structure, as shown in Figure 1. This structure allows it to donate electrons to other molecules effectively, functioning as an antioxidant. It helps protect cells from oxidative reactions and age-related stress, thereby reducing the risk of heart disease and cancer in the elderly.

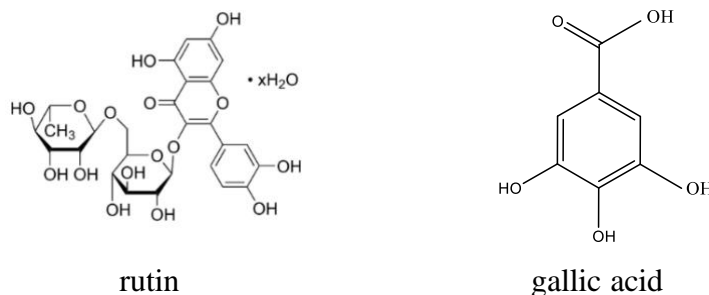


Figure 1.

The structure formulas of rutin and gallic acid.

The aim of this study was to quantitatively analyze the rutin and gallic acid contents in the Zingiberaceae samples using high performance liquid chromatography (HPLC)⁶⁻⁸ technique.

2. Materials and Methods

2.1 Materials

The Zingiberaceae samples were collected from Maejo market, located in Chiang Mai, Thailand. Rutin and gallic acid standards were purchased from Sigma-Aldrich (Sigma-Aldrich Company, St. Louis, MO, USA). Chemicals including methanol, acetonitrile, formic acid and other solvents and reagents used in the HPLC analysis were purchased from Merck (Darmstadt, Germany). All chemicals and reagents used in the study were of an analytical grade. Ultrapure water was obtained by a Milli-Q purification system (Millipore, Billerica, MA, USA).

2.2 Sample preparation

First, clean the herbal samples and cut them into small pieces. Next, dry the pieces at 60 degrees Celsius for 72 hours. After drying, grind the material into a fine powder using a mortar and pestle. Measure 3.000 grams of each powdered herbal sample and transfer them into a 25 mL Erlenmeyer flask. Immerse the samples in 10.00 mL of methanol solution, then seal the flask with aluminum foil and fasten it securely with a rubber band. Place the flask in a temperature-controlled shaker set at 25 degrees Celsius for 24 hours. After this period, filter the mixture using No. 1 filter paper, then evaporate the solution at 60 degrees Celsius until it is nearly dry. Allow the residue to cool. Dissolve the residue by adding a small amount of methanol solution, then transfer it into a 25 mL volumetric flask. Adjust the volume to 10 mL with methanol and filter the solution through a 0.22-micron filter. Analyze the prepared solution using high-performance liquid chromatography (HPLC).

2.3 Validation and quantification

The method for rutin and gallic acid analyses were validated by HPLC¹¹ including linearity, limit of detection (LOD), limit of quantification (LOQ), precision and accuracy. LOD and LOQ were determined on signal-to-noise ratios by 3 and 10, respectively. The accuracy was assessed by calculating recovery from samples spiked with mixed standards and calculated. The precision was expressed as the RSD. The precision of analyses was investigated by determining five times on the same day and five times on 3 different days.



2.4 Determination of rutin and gallic acid

The HPLC (Hewlett Packard Series 1100, Waldbronn, Germany) system was equipped with hypersil ODS C₁₈ (250 × 4 mm I.D., 5 µm particle). The isocratic mobile phase consists of solvent A (acetonitrile) and solvent B (0.1% formic acid)⁹ at ratio 80:20 (v/v) at flow rate of 1.20 mL min⁻¹. The concentrations of rutin and gallic acid were calculated based on the absorbance at 268 nm using photodiode array detector, which is like previous work by Idaresit *et al.*¹⁰ The concentrations of rutin and gallic acid standards were in the range of 0.01-10.00 mg L⁻¹.

3. Results & Discussion

The retention times for gallic acid and rutin were 3.32 and 8.09 minutes, respectively. Figure 2 shows the chromatograms for the rutin and gallic acid standards and samples. The results indicated a linear calibration curve between peak areas and concentrations (mg L⁻¹) of gallic acid and rutin in the range of 0.10-10.00 and 0.50-10.00 mg L⁻¹ with correlation coefficients of 0.9979 and 0.9994, respectively. The limit of detection (LOD) and limit of quantification (LOQ) for gallic acid were 0.020 mg L⁻¹ and 0.067 mg L⁻¹, respectively, while for rutin they were 0.130 mg L⁻¹ and 0.434 mg L⁻¹. The calibration curve presented in Figure 3. The recovery rates of rutin and gallic acid in spiked herbs at concentrations of 3 and 5 mg L⁻¹ ranged from 98% to 105%. The relative standard deviation was 1.36% for rutin and 0.99% for gallic acid (n=12). Results of the method validation are presented in Table 1.

Table 1.

Results of the method validation for the determination of gallic acid and rutin in Zingiberaceae samples using HPLC.

| Analytes | Linear range (mg L ⁻¹) | Calibration curve | R ² | LOD (mg L ⁻¹) | LOQ (mg L ⁻¹) |
|-------------|------------------------------------|-------------------|----------------|---------------------------|---------------------------|
| Gallic acid | 0.10-10.00 | Y=15.429x+9.269 | 0.9979 | 0.020 | 0.067 |
| Rutin | 0.50-10.00 | Y=8.4057x+2.5571 | 0.9994 | 0.130 | 0.434 |

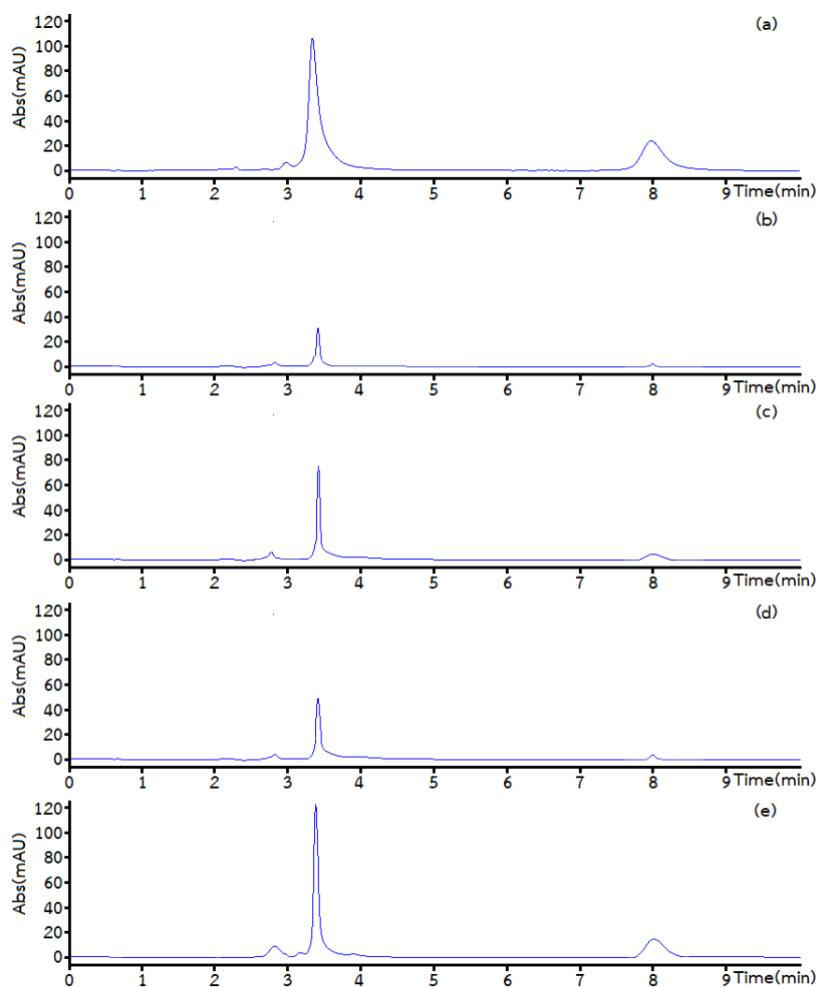


Figure 2.

The chromatograms of gallic acid and rutin in a standard solution (a), ginger (b), turmeric (c), cardamom (d), and zedoary (e). When 6.00 mg L⁻¹ of rutin and gallic acid were used in the standard solution.

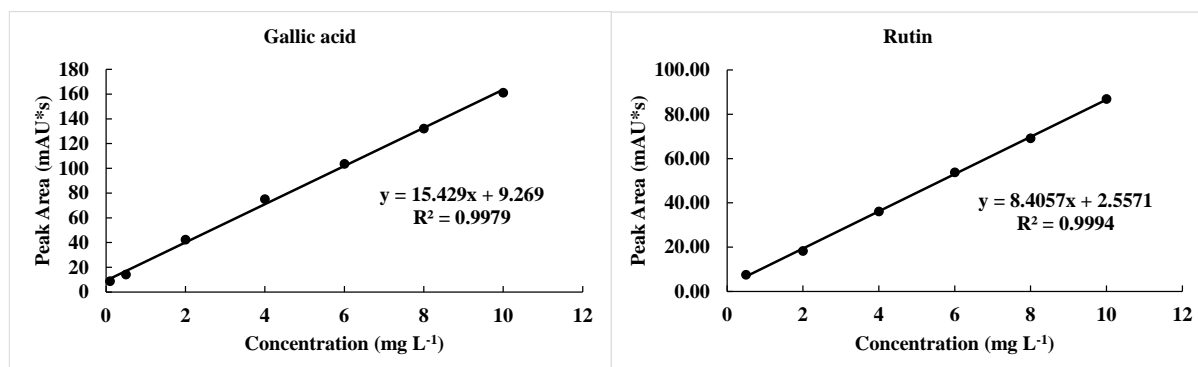


Figure 3.

The standard calibration curves of gallic acid and rutin.



The measured concentrations of rutin and gallic acid are shown in Table 2. The rutin content in the four samples ranged from 4.40 ± 0.10 to 58.42 ± 0.25 mg kg⁻¹, while the gallic acid content ranged from 13.76 ± 0.04 to 416.56 ± 0.40 mg kg⁻¹. Zedoary had the highest concentration of rutin among the samples, whereas ginger had the lowest. Similarly, zedoary exhibited the highest concentration of gallic acid, and ginger had the lowest.

Table 2.

The concentration of rutin and gallic acid in the Zingiberaceae samples.

| Sample | Concentration (mg kg ⁻¹) \pm SD ^a | | | |
|----------|--|------|------------------|------|
| | Gallic acid | %RSD | Rutin | %RSD |
| Ginger | 13.76 ± 0.04 | 0.29 | 4.40 ± 0.10 | 2.27 |
| Turmeric | 200.34 ± 0.08 | 0.04 | 5.40 ± 0.04 | 0.74 |
| Cardamom | 92.39 ± 0.04 | 0.04 | 4.48 ± 0.04 | 0.89 |
| Zedoary | 416.56 ± 0.40 | 0.10 | 58.42 ± 0.25 | 0.43 |

^a Standard deviation from triplicate measurements

4. Conclusion

In this study, HPLC was utilized as a simple and rapid method for the simultaneous determination of rutin and gallic acid in Zingiberaceae samples. The optimized HPLC conditions ensured excellent selectivity and specificity in the separation of rutin and gallic acid within these samples.

Acknowledgements

This work was financially supported by Program in Chemistry, Faculty of Science, Maejo University.

References (In ACS style)

- [1] Otmani A, Amessis-Ouchemoukh N, Birinci C, Yahiaoui S, Kolayli S, Rodríguez-Flores MS, Escuredo O, Seijo MC, Ouchemoukh S. Food Biosci. 2021;42:101070.
- [2] Carrasco-Sandoval J, Falcó I, Sánchez G, Fabra MJ, López-Rubio A, Rodriguez A, Henríquez-Aedo K, Aranda M. J. Appl. Res. Med. Aromat. Plants. 2022;28100356.
- [3] Zhang H, Zhao Q, Qiu J, Wang Z, Yang X. J. Chromatogr. B. 2023;1214:123492.
- [4] Dramou P, Wang F, Sun Y, Zhang J, Yang P, Liu D, He H. Appl. Clay Sci. 2022;217:106397.
- [5] Shukla S, Singh B, Singh A, Singh C. Phytomedicine Plus. 2022;2:100369.
- [6] Lazuo LH, Takashi FT, Yasuji KY. J. Chromatogr. B. 2001;759:161-168.
- [7] Hasan T, Jahan E, Ahmed KS, Hossain H, Siam SMM, Nahid N, Mazumder T, Shuvo MSR, Daula AFMSU. Biomed. Pharmacother. 2022;148:112774.
- [8] Xu X, Huang L, Wu Y, Yang L, Huang L. J. Chromatogr. B. 2021;1168:122589.
- [9] Kebal L, Pokajewicz K, Djebli N, Mostefa N, Poliwoda A, Wieczorek PP. Biomedicine & Pharmacotherapy. 2022;155:113738.
- [10] Ekaette I, Saldaña MDA. Food Chemistry. 2021;344:128629.
- [11] Jaicharoensub J, Sakpakdeejaroen I., Panthong S. Talanta Open. 2023;7:100227.

DEVELOPMENT OF A SAMPLE PREPARATION METHOD FOR ANALYZING BISPHENOL A AND DERIVATIVES BY HIGH PERFORMANCE LIQUID CHROMATOGRAPHY WITH DIODE ARRAY DETECTION

Tuangrat Senmad^{1,2,3}, Fonthip Makkliang⁴, Proespichaya Kanatharana^{1,2,3}, Panote Thavarungkul^{1,2,3} and Chongdee Thammakhet-Buranachai^{1,2,3} *

¹Center of Excellence for Trace Analysis and Biosensor and Division of Physical Science, Faculty of Science, Prince of Songkla University, Hat Yai, Songkla 90110, Thailand

²Division of Physical Science, Faculty of Science, Prince of Songkla University, Hat Yai, Songkla 90110, Thailand

³Center of Excellence for Innovation in Chemistry, Faculty of Science, Prince of Songkla University, Hat Yai, Songkla 90110, Thailand

⁴School of Language and General Education, Walailak University, Thasala, Nakhon Si Thammarat, 80160, Thailand

*email: chongdee.t@psu.ac.th

Abstract:

Bisphenol A and its derivatives are commonly used as additives in plastics and epoxy resin production. Exposure to these contaminants may cause toxicity to the endocrine and genetic systems. A polypyrrole-coated luffa fibers sorbent was developed for the extraction of bisphenol A and derivatives and analysis by high-performance liquid chromatography with a diode array detector. Under the optimum conditions, good linearity in the range of 0.05 to 100 mg L⁻¹ for bisphenol A and derivatives was achieved. The limits of detection were 0.05, 0.05, and 0.50 mg L⁻¹, and the limits of quantitation were 0.50, 0.50 and 0.50 mg L⁻¹ for bisphenol A (2,3-dihydroxypropyl) ether (BADGE.2H₂O), bisphenol A (BPA), and bisphenol A (2,3-dihydroxypropyl) glycidyl ether (BADGE.H₂O), respectively. The developed sorbent can extract the analytes within 15 minutes from the spiked solution at a concentration of 0.5 mg L⁻¹. The method provided good extraction recovery of 40.11%, 57.85%, and 45.59% for BADGE.2H₂O, BPA and BADGE.H₂O, respectively. The sorbent preparation and extraction are simple, easy, and low-cost. Moreover, the developed sorbent has potential application for extracting analytes from the real sample.

Introduction:

Bisphenol A (BPA) is a chemical widely used in certain industries, particularly in synthetic polymers and thermal paper. It is commonly found in products such as plastic containers, toys, tableware, medical devices, and polycarbonate bottles, among others, which can release BPA at room temperature ¹. BPA is an estrogenic substance that is toxic to living organisms and can cause genetic and cellular toxicity, mutations, and carcinogenic effects. BPA may cause various health issues in humans, such as obesity, diabetes, and heart disease ². Humans are typically exposed to BPA through food, but it can also come from contaminated water and air ³. The United States Environmental Protection Agency (US EPA) estimated a reference dose of 50 µg kg⁻¹ bw day⁻¹ for BPA ⁴. For this reason, analytical methods for the determination of trace bisphenol A and derivatives are necessary.

Based on the study of research analyzing bisphenol A, it was found that adsorbents used include polypyrrole and nanosilica coated on steel wires ⁵. Therefore, the researcher became interested in and developed an adsorbent by coating polypyrrole onto natural fibers to analyze bisphenol A and its derivatives. Analytical methods that have been developed to determine bisphenol A and derivatives are generally based on chromatographic techniques such as gas chromatography (GC) and liquid chromatography (LC). However, GC requires a derivatization procedure to improve the limit of detection and LC provides low sensitivity as

well as it need to couple with a sensitive detector ⁶. High-performance liquid chromatography with diode array detection (HPLC-DAD) was used in this study as this technique provide high sensitivity and high selectivity.

In this study, luffa (LF) fibers were coated with polypyrrole to enhance the adsorption efficiency for bisphenol A and its derivatives. Among various alternative adsorbents, *Luffa cylindrica* (LF) is a subtropical plant in the Cucurbitaceae family. Due to its environmentally friendly properties, structure, and morphology (e.g., naturally occurring, biodegradable, non-toxic, low cost, highly porous, tough, strong, lightweight, and rigid) ⁷, luffa fibers gained attention for being used as an adsorbent. Luffa fibers consist of 60% cellulose, 30% hemicellulose, and 10% lignin. This lignocellulosic material has a micro sponge structure with 200–500 microcellular fibers, making it a promising adsorbent material ⁸. Polypyrrole (PPy) is a conductive polymer characterized by properties such as high electrical conductivity, good environmental and chemical stability, high porosity, ease of synthesis, non-toxicity, and low cost ⁹. This polymer is often used in adsorption studies because it can reversibly switch between charged and neutral states, enabling it to adsorb various types of contaminants ¹⁰.

Prior to instrumental analysis, sample preparation is always required due to the complexity of food and environmental samples. The conventional sample preparation techniques are labor-intensive and require sequential steps to improve the accuracy of the analysis. Thus, solid phase extraction (SPE) is the most desire technique, which has the ability to provide a high extraction efficiency for BPA ¹¹. However, there is still a requirement to develop the technique to be simple to prepare, easy for extraction, and environmentally friendly. Based on the properties of luffa fibers and mainly on the properties of PPy, it is expected that PPy-coated luffa fibers may enhance its capacity to adsorb analyte from real sample.

Therefore, this work focuses on developing PPy-coated luffa fibers sorbent for determination bisphenol A and derivatives, and their using HPLC-DAD.

Materials and Methods:

(a) Materials

BPA (99 % purity) was purchased from Sigma-Aldrich Chemie (St. Louise, USA), BADGE.2H₂O (95%) and BADGE.H₂O (97%) were purchased from Sigma-Aldrich Chemie (St. Louise, Switzerland). Acetonitrile, ethanol, methanol, acetone and isopropyl alcohol were purchased from RCI Labscan (Bangkok, Thailand). Ferric chloride anhydrous (FeCl₃) solid (99%) was purchased from LOBA Chemie (Mumbai, India). Pyrrole (98%) was purchased from Sigma-Aldrich Chemie (St. Louis, China).

(b) Instrument

The HPLC analysis was carried out using an Agilent HPLC 1200 system equipped with diode array detector (DAD). A reversed-phase VertiSepTM UPS C18 column (4.6×150 mm, 5μm, protected by VertiSepTM UPS C18 guard column (4.6×50 mm, 5μm, Vertical Chromatography, Thailand), was used for the separation. The mobile phase is composed of 43% acetonitrile and 57% water. The flow rate of the mobile phase was set at 0.80 mL min⁻¹. The sample injection volume and the column temperature of the HPLC-DAD system were fixed at 10 μL and 25 °C, respectively. The detection wavelength for bisphenol A and derivatives analysis was set at 230 nm.

A magnetic stirrer (IKA, U.P.V Service Co., LTD) and hot air oven (Memmert, Germany) were used for the sorbent cleaning and drying. A vortex mixer (Vortex G560E, Scientific Industries, USA) and ultrasonic cleaner (ELMA Model S100H, Germany) were

used in the extraction and desorption process. Rotary evaporator (Heidolph, Germany) was applied to dry organic solvent.

(c) Optimization of HPLC-DAD

Various parameters of the HPLC-DAD, i.e., mobile phase composition, flow rate and detection wavelength were optimized. The optimization was done with three replications of the analysis of 0.5 mg L^{-1} of bisphenol A and derivatives by varying one parameter, while keeping other parameters constant. The optimum conditions were determined by considering the good separation, the highest response and the shortest analysis time.

(d) Preparation of LF/Polypyrrole

The summary of the preparation of sorbent is shown in **Figure 1**. Firstly, a raw luffa sponge was cut into small pieces and put it in the blender. After that, the luffa fibers were thoroughly washed with an ethanol-water solution (70:30 v/v) three times, and oven-dried at 50°C for 24 h. In the second step, the luffa fibers were coated with polypyrrole (PPy). Three grams of clean luffa fiber were placed into a beaker; 300 mL of isopropyl alcohol and 50 mL of 0.1 mol L^{-1} FeCl_3 solution were then added and kept under vigorous stirring for 30 min. A pyrrole solution of 3 mL was gently added into the beaker and then was cooled down to 4°C using an ice bath. The mixture was kept stirring overnight to ensure an adequate polymerization of polypyrrole on the luffa fibers. Finally, the excess solution was decanted, and PPy-coated luffa fibers were washed with isopropyl alcohol and distilled water and oven-dried at 50°C for 24 h.

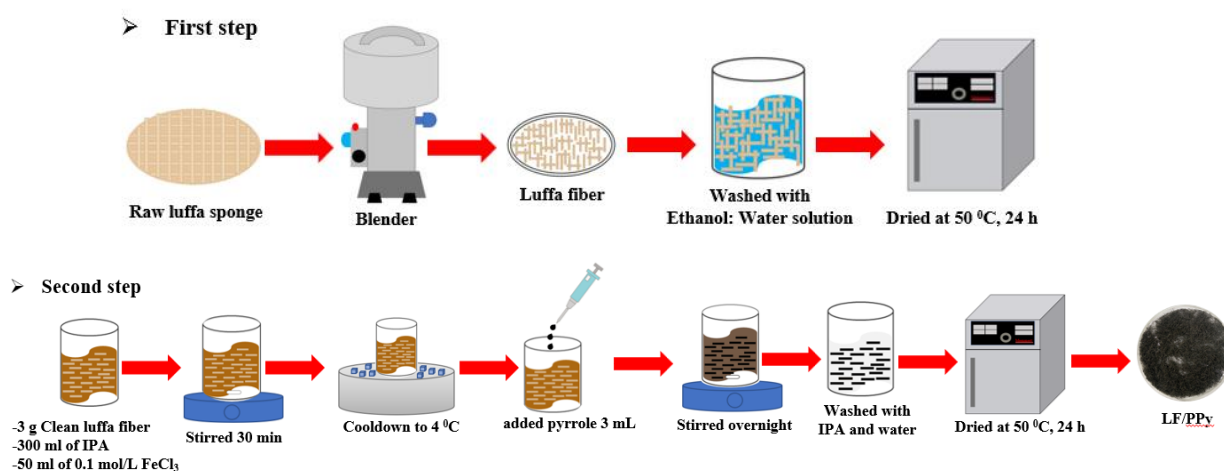


Figure 1. Schematic presentation of the preparation of LF/Polypyrrole

(e) Extraction and desorption procedure

The extraction and desorption were performed by immersing 0.02g of polypyrrole-coated luffa fibers sorbent in a glass vial containing 2.0 mL of spiked standard solution of bisphenol A and derivatives (0.5 mg L^{-1}). Then, the extraction was carried out by vortexing at 1400 rpm for 2.5 min. After extraction, the supernatant was decanted and 2.5 mL of desorption solvent was added to a vial, and the analytes were desorbed by sonication for 15 min. The desorption solvent (to determine the desorbed amount) and water after extraction (to determine the remaining analyte in water after adsorption) were evaporated to dryness before re-dissolving with 1 mL of acetonitrile-water solution (43:57 v/v). The solution was filtered into an autosampler vial with a syringe filter and was injected into the HPLC-DAD system for analysis. The process was schematically described in **Figure 2**.

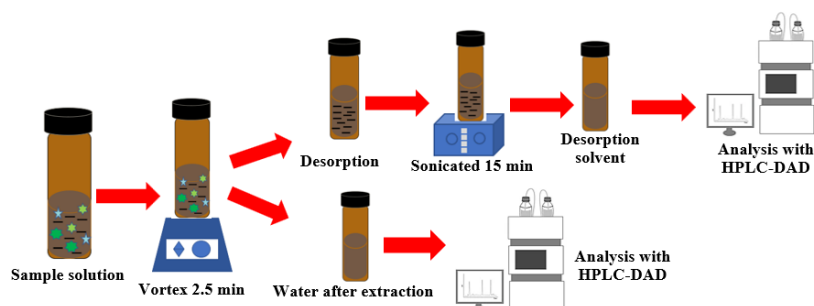


Figure 2. The extraction and desorption procedure of PPy-coated luffa fibers sorbent for extraction of bisphenol A and derivatives

Results and Discussion:

(a) Optimization of the HPLC-DAD conditions

The optimum conditions of HPLC-DAD for the analysis of bisphenol and derivatives are summarized in Table 1. The mobile phase composition was studied by varying the volume of acetonitrile and ultrapure water. The ratio of 43% of acetonitrile and 57% of ultrapure water provided a symmetric peak and can be separated all three analytes with the shortest analysis time. Therefore, it was chosen as the optimum mobile phase composition. The flow rate of the mobile phase was investigated from 0.4 to 1.0 mL min⁻¹. Flow rate at 0.8 mL min⁻¹ was found to be good separation with a total analysis time of 15 min. Thus, the maximum flow rate was fixed at 0.8 mL min⁻¹. Detection wavelength was the main factor affecting the response (peak area) of the analytes. It varied from 200 to 235 nm. The maximum peak area was obtained at the detection wavelength of 230 nm, and therefore it was the optimum detection wavelength. The chromatogram under optimum conditions is shown in **Figure 3**.

The analytical performances of HPLC-DAD for the analysis of bisphenol A and derivatives were summarized in **Table 2**. The linearity for BADGE.2H₂O, BPA, and BADGE.H₂O were obtained in the range of 0.05 to 100 mg L⁻¹ with a good coefficient of determination, $R^2 = 0.9995$, 0.9999 and 0.9996, respectively as shown in **Figure 4**. The limit of detection (LOD) and limit of quantitation (LOQ) were evaluated by the IUPAC guidelines. The limit of detection (LOD) was calculated by a signal-to-noise ratio of 3:1 ($S/N \geq 3$). The limit of quantitation (LOQ) was determined by a signal-to-noise ratio of 10:1 ($S/N \geq 10$). The linearity, LOD and LOQ are shown in **Table 2**.

Table 1. Optimum conditions of HPLC-DAD

| HPLC-DAD parameter | Investigated conditions | Optimum condition |
|--|-------------------------------|-------------------|
| Ratio of mobile phase (% ACN: %H ₂ O) | 40:60, 43:57, 45:55 and 50:50 | 43:57 |
| Flow rate (mL min ⁻¹) | 0.4, 0.6, 0.8 and 1.0 | 0.8 |
| Detection wavelength (nm) | 220, 225, 230 and 230 | 230 |

Table 2. Analytical performance of HPLC-DAD for the analysis of bisphenol A and derivatives

| Analyte | Linear range (mg L ⁻¹) | LOD (mg L ⁻¹) | LOQ (mg L ⁻¹) |
|-------------------------|------------------------------------|---------------------------|---------------------------|
| BADGE.2H ₂ O | 0.05-100 | 0.05 | 0.10 |
| BPA | 0.05-100 | 0.10 | 0.50 |
| BADGE.H ₂ O | 0.05-100 | 0.50 | 0.50 |

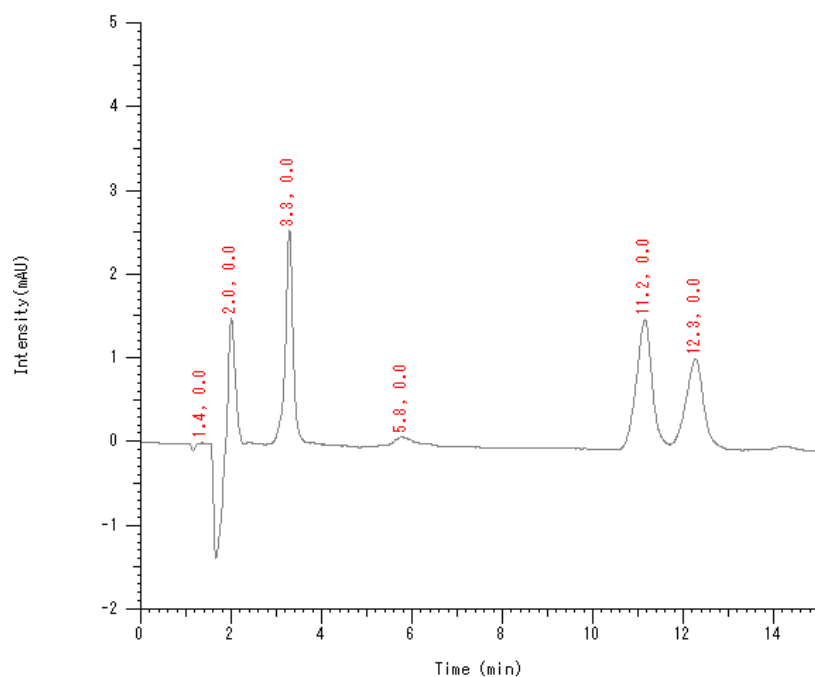
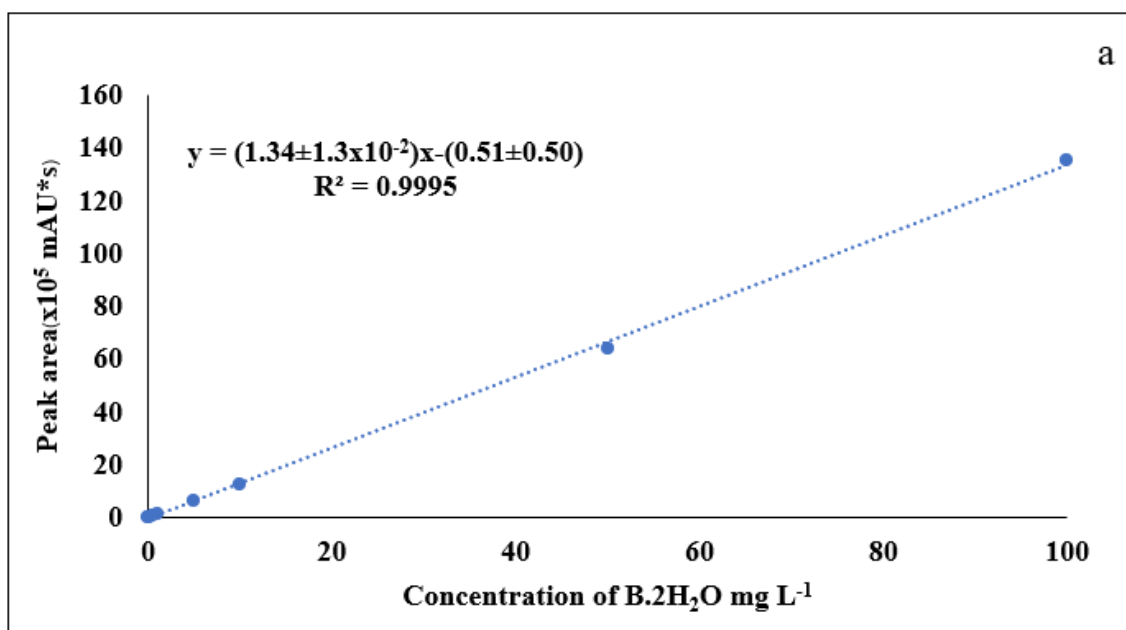


Figure 3. The chromatogram under optimum conditions at concentration 1.0 mg L⁻¹, BADGE.2H₂O (t_R =3.3 min), BPA (t_R =11.2 min) and BADGE.H₂O (t_R =12.3 min), respectively



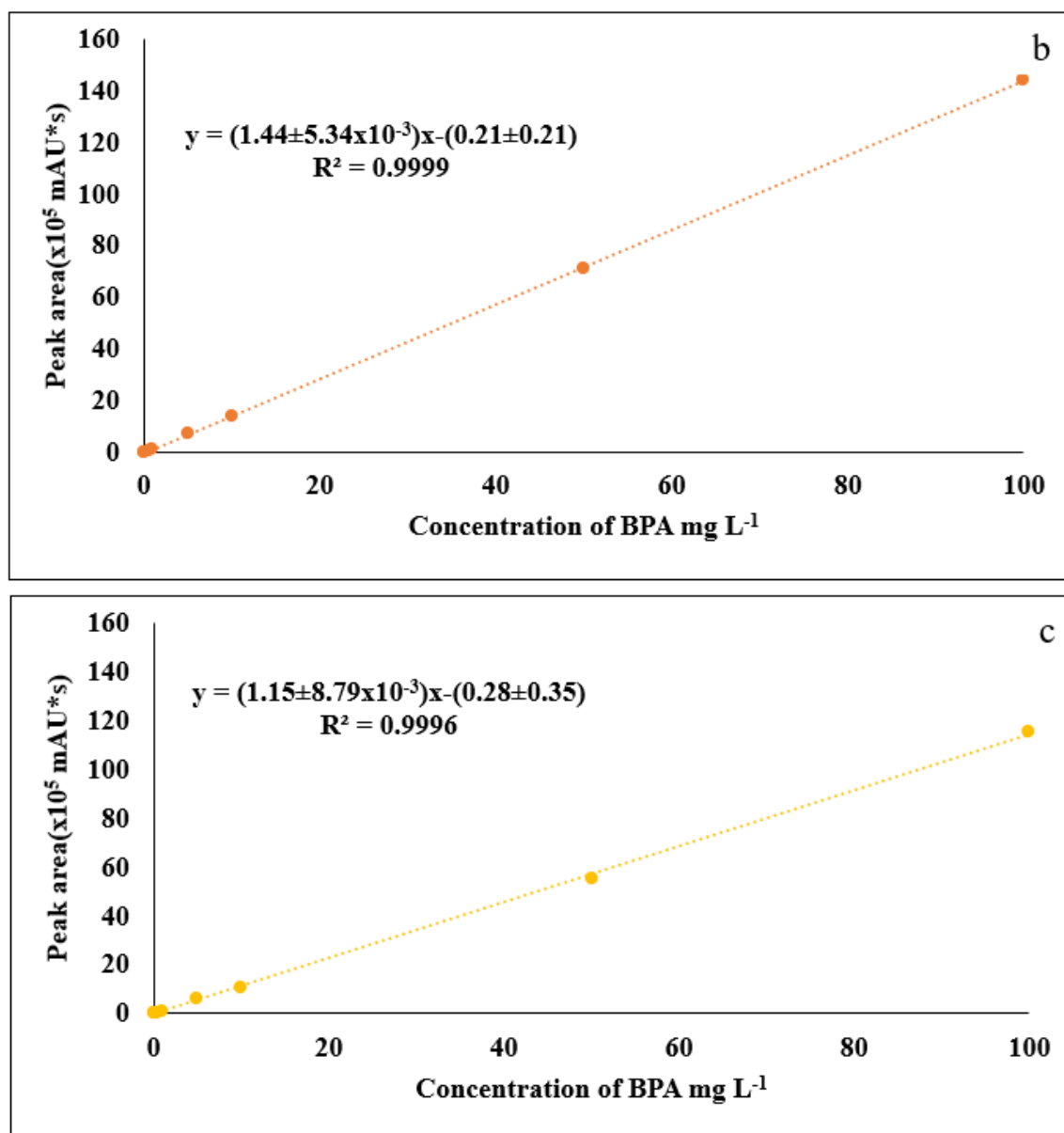


Figure 4. Linearity of target analytes under optimum conditions, BADGE.2H₂O (a) BPA (b) and BADGE.H₂O (c)

(b) Optimization of desorption procedure

The type of desorption solvent plays a crucial role in the elution of analytes from the sorbent. In the developed method, the desorption efficiency of target analyte varies depending on the polarity of organic solvent used. In the desorption step, four organic solvents, including methanol, acetone, ethanol and acetonitrile, were studied. The polarities of methanol and acetone were 5.1, 5.2 for ethanol, and 5.8 for acetonitrile, respectively. The results in (**Figure 5a**) showed that acetonitrile provided good desorption recoveries of 40.11%, 57.85% and 45.59% for BADGE.2H₂O, A BPA and BADGE.H₂O, respectively. This might be due to the highly polar nature of acetonitrile, can interact with target analytes via hydrogen bonding, hydrophobic interaction, π -lone pair interaction and π - π interaction. Thus, it can elute the analyte from the adsorbent more effectively than methanol, ethanol and acetone. Acetonitrile, therefore, was selected as the suitable desorption solvent for subsequent studies.

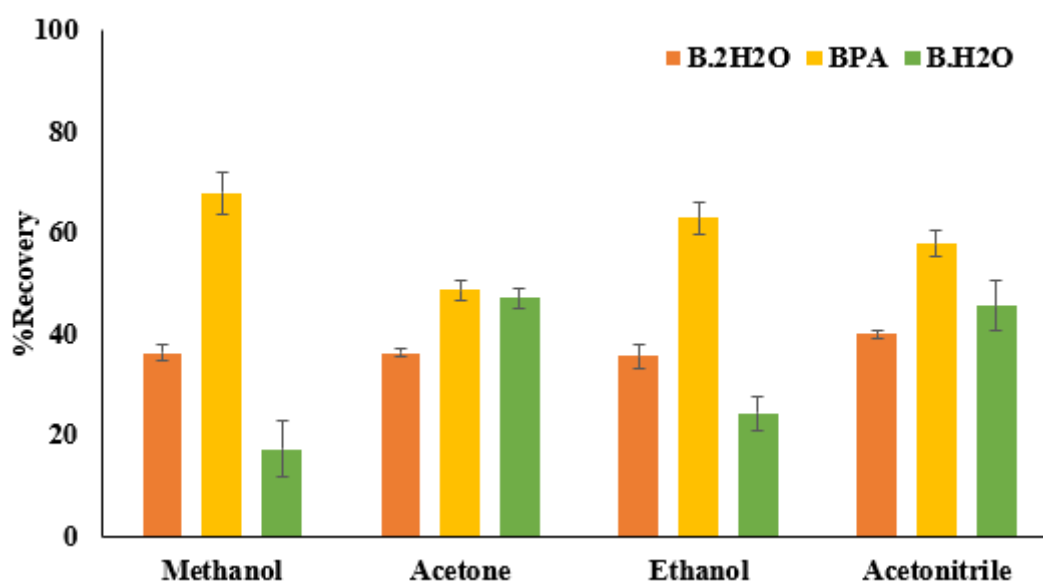


Figure 5. Effect of desorption solvents on percent of adsorption

Conclusion:

The developed PPy-coated luffa fibers showed the possibility and capability of being used as a sorbent in vortex-assisted solid-phase extraction of bisphenol A and derivatives. Under the optimum conditions, good linearity in the range of 0.05 to 100 mg L⁻¹ for bisphenol A and derivatives was achieved. The limits of detection were 0.05, 0.05, and 0.50 mg L⁻¹, and the limits of quantitation were 0.50, 0.50 and 0.50 mg L⁻¹ for bisphenol A (2,3-dihydroxypropyl) ether (BADGE.2H₂O), bisphenol A (BPA), and bisphenol A (2,3-dihydroxypropyl) glycidyl ether (BADGE.H₂O), respectively. The developed sorbent can extract the analytes within 15 minutes from the spiked solution at a concentration of 0.5 mg L⁻¹. The method provided good extraction recovery of 40.11%, 57.85%, and 45.59% for BADGE.2H₂O, BPA and BADGE.H₂O, respectively. However, further adjustment for the parameters that affect the extraction and desorption conditions will be needed to achieve more accurate results.

Acknowledgements:

This project was supported by the Center of Excellence for Trace Analysis and Biosensor (TAB-CoE); Division of Physical Science and Graduate school, Prince of Songkla University, Hatyai, Thailand.

References:

1. Tarafdar, A.; Sirohi, R.; Balakumaran, P. A.; Reshmy, R.; Madhavan, A.; Sindhu, R.; Binod, P.; Kumar, Y.; Kumar, D.; Sim, S. J. The hazardous threat of Bisphenol A: Toxicity, detection and remediation. *Journal of Hazardous Materials* 2022, 423, 127097.
2. Michałowicz, J. Bisphenol A – Sources, toxicity and biotransformation. *Environmental Toxicology and Pharmacology* 2014, 37 (2), 738-758.
3. Ruan, T.; Liang, D.; Song, S.; Song, M.; Wang, H.; Jiang, G. Evaluation of the in vitro estrogenicity of emerging bisphenol analogs and their respective estrogenic contributions in municipal sewage sludge in China. *Chemosphere* 2015, 124, 150-155.
4. USEPA. Bisphenol A Action Plan (CASRN 80-05-7). 2010.
5. Ansari Dogaheh, M.; Behzadi, M. Preparation of polypyrrole/nanosilica composite for solid-phase microextraction of bisphenol and phthalates migrated from containers to eye drops and injection solutions. *Journal of Pharmaceutical Analysis* 2019, 9 (3), 185-192.
6. Rozaini, M. N. H.; Yahaya, N.; Saad, B.; Kamaruzaman, S.; Hanapi, N. S. M. Rapid ultrasound assisted emulsification micro-solid phase extraction based on molecularly imprinted polymer for HPLC-DAD determination of bisphenol A in aqueous matrices. *Talanta* 2017, 171, 242-249.
7. Khadir, A.; Motamedi, M.; Pakzad, E.; Sillanpää, M.; Mahajan, S. The prospective utilization of Luffa fibres as a lignocellulosic bio-material for environmental remediation of aqueous media: A review. *Journal of Environmental Chemical Engineering* 2021, 9 (1), 104691.
8. Adeniyi, A.; Abdulkareem, S.; Adeyanju, C.; Abdulkareem, M.; Odimayomi, K.; Iwuozor, K.; Amoloye, M.; Belgore, R. Production and properties of the fibrillated plastic composite from recycled polystyrene and Luffa cylindrica. *Polymer Bulletin* 2022, 80.
9. Cui, Y.; Chen, X.; Liang, J.; Liu, Z.; Yang, G.; Zhang, Q.; Fan, H.; Peng, F.; Duan, X. Boosting pseudocapacitive sodium storage while restraining the shuttle effect of polysulfides in holey nickel disulfide nanoplatelets by a polypyrrole-coating strategy. *Applied Surface Science* 2024, 669, 160524.
10. da Costa, J. S.; Fajardo, A. R. Polypyrrole/stearic acid-coated Luffa cylindrica for enhanced removal of sodium diclofenac from water: Batch and continuous adsorption studies. *Journal of Cleaner Production* 2023, 389, 136084.
11. Jing, -. X.; Bing, -. S.; XiaoYan, -. W.; XiaoJie, -. S.; YongNing, -. W. - A Study on Bisphenol A, Nonylphenol, and Octylphenol in Human Urine Samples Detected by SPE-UPLC-MS. - *Biomedical and Environmental Sciences* 2011, - 24 (- 1), - 40.



DEVELOPMENT OF ELECTROCHEMICAL SENSOR BASED ON MOLECULARLY IMPRINTED POLYMER FOR DETERMINATION OF ROXARSONE

Pitranan Kunthanasap¹, Wilai Siriwatcharapiboon², and Janjira Panchompoo^{1,*}

¹ Electrochemistry and Optical Spectroscopy Center of Excellence, Department of Chemistry, Faculty of Science, Chulalongkorn University

² Department of Chemistry, Faculty of Science, Kasetsart University

*Corresponding author, Email: janjira.p@chula.ac.th

Abstract:

Roxarsone (ROX), a growth enhancer in poultry and swine, has the potential to improve weight gain and prevent coccidiosis. Excessive use of ROX may lead to its accumulation in animal tissues, potentially contaminating food products and posing health risks to humans through consumption. This research aims to develop an electrochemical sensor based on a magnetic screen-printed graphene electrode (mSPGE) modified with a highly selective molecularly imprinted polymer (MIP) for the determination of ROX with enhanced sensitivity and selectivity. Typically, an applied magnetic field at the mSPGE could accelerate mass transport at the electrode surface through the magnetohydrodynamic (MHD) effect, leading to improved electrochemical responses and consequently increased sensitivity in the detection. The mSPGE was subsequently modified with MIP *via* electropolymerization using cyclic voltammetry (CV), with *o*-phenylenediamine (*o*-PD) serving as the functional monomer and ROX as the template. All experimental parameters related to the electrode modification with MIP were thoroughly investigated to achieve optimal sensitivity and selectivity for detection. The analytical performance of the resulting MIP/mSPGE sensor towards ROX oxidation was then evaluated using differential pulse voltammetry (DPV). Under optimal conditions, the sensor exhibited high sensitivity and good selectivity for the determination of ROX with a linear range of 0.03 to 0.1 mM. Limits of detection (LOD) and quantification (LOQ) were found to be 0.015 mM and 0.051 mM, respectively.

Introduction:

Roxarsone (ROX), also identified as 3-nitro-4-hydroxyphenylarsonic acid, depicted in **Figure 1**, is an organoarsenic compound extensively used in the poultry and swine industries to treat coccidiosis, a disease caused by enteric parasites (1). ROX has also been widely employed as a growth promotor to stimulate weight gain in animals and birds (2). However, more than 90% of ROX is not metabolized and is excreted unchanged in animal's waste, which may eventually be present in the environment in the form of water-soluble toxic arsenicals. Literally, the permissible limit for total arsenic concentration in soil is 15 mg/kg (3). Nevertheless, the biodegradation of ROX in the environment, leading to the formation of toxic arsenic species, may result in a total arsenic concentration to reach 50 mg/kg, significantly exceeding the established safety limit (3). This has raised concerns regarding its environmental impact and potential human health risks (4). Consequently, ROX has been banned in several countries, including Australia, Canada, China, the EU, Malaysia, and the US (2). Additionally, the use of ROX has been associated with various health problems in humans, including an increased risk of bladder, lung, and skin cancers, cardiovascular diseases, diabetes, and cognitive deficits (3). Due to these risks, it is crucial to develop sensitive and reliable analytical devices for the ongoing monitoring of ROX contamination in the environment and animal products. As reported in the literature, ROX could be determined by several methods, such as fluorescence spectroscopy (5), high-performance liquid

chromatography (HPLC) (6), gas chromatography (GC) (7), and UV-Vis spectroscopy (8). However, these methods have some limitations, including high equipment costs, large instrumentation, extended detection times, and the requirement for trained personnel.

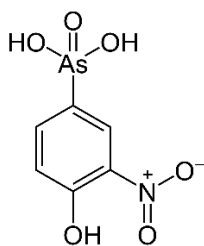


Figure 1.
Chemical structure of ROX (1).

Typically, ROX contains two functional groups that can undergo electrochemical reactions. The presence of the nitro group ($-\text{NO}_2$) and the hydroxyl group ($-\text{OH}$) can facilitate electron transfer reactions, enabling the electrochemical detection of ROX. Basically, these electrochemical techniques utilize changes in current or potential resulting from the oxidation or reduction of functional groups in the target molecule, thereby providing a means of detection and analysis (2). Moreover, electrochemical methods have garnered considerable attention due to their low cost, simplicity, high sensitivity, rapid detection, potential for miniaturization, and the capability to enhance detection sensitivity and selectivity through modification of the electrode surface (9).

Currently, molecularly imprinted polymers (MIPs) have been extensively employed in electrochemical sensors to enhance their selectivity. Typically, MIPs are synthetic polymers that selectively recognize target molecules based on their shape, size, and functional groups (10, 11). They consist of three components: template molecule, functional monomer, and crosslinker (12). MIPs can be formed using the electrochemical polymerization technique, offering control over the thickness of the polymeric film. Therefore, the resulting uniform and stable film thickness makes MIPs widely employed in electrochemical sensors, thereby enhancing selectivity in detection (13). *o*-Phenylenediamine (*o*-PD) is a type of monomer that can easily undergo electropolymerization on various conductive materials. Importantly, *o*-PD contains two amino groups ($-\text{NH}_2$) that can form hydrogen bonds with template molecules during the electropolymerization process, leading to the formation of a highly stable MIP film with excellent mechanical and chemical stability (14).

However, sensors developed with MIPs often exhibit low conductivity and poor adsorption capacity, resulting in relatively low sensitivity in the electrochemical response. Therefore, magnetoelectrochemistry has recently emerged as an attractive approach to enhance overall electrocatalytic performance (15). When a magnetic field (B) is applied to an electrochemical cell, it interacts with the charged species and the current density (j), generating the Lorentz force (F_L), as described by the equation:

$$F_L = B \times j$$

The magnitude of F_L depends on the magnitudes of B and j , as well as the angle θ between them. When B and j are perpendicular to each other, the magnitude of F_L reaches its maximum value. Under experimental conditions, B is typically perpendicular to the electrode surface, which can result in a nonuniform current density, particularly at the edges of the electrode. This nonuniformity can lead to rim flow caused by the Lorentz force. Additionally, bulges and trapped bubbles may also contribute to rim flow. Both of these phenomena arise from magnetohydrodynamic (MHD) effect (15, 16). This effect induces convection in the electrolyte, leading to a reduction in the diffusion layer thickness and an increase in mass



transport. As the current-limited diffusion-controlled system improves, the sensitivity of the sensor also increases (15, 16).

This research aims to thoroughly investigate the electrochemical behavior of the functional groups present in ROX to assess its electrochemical properties. Additionally, the study seeks to develop an electrochemical sensor based on a magnetic screen-printed graphene electrode (mSPGE) modified with a highly selective molecularly imprinted polymer (MIP) for the determination of ROX with enhanced sensitivity and selectivity.

Methodology:

Apparatus and materials

All chemicals used were of analytical grade, and all solutions were prepared using Milli-Q water. Graphene and silver/silver chloride conductive inks used for the fabrication of the screen-printed graphene electrodes (SPGEs) were purchased from Sun Chemical (UK). ROX, *o*-nitrophenol, nitrobenzene, and phenol were obtained from Sigma-Aldrich (USA). All solvents, including acetone and ethanol, were bought from RCL Labscan group (Thailand) and Merck (USA). The phosphate buffer solution (PBS) was prepared using sodium phosphate monobasic and di-sodium hydrogen phosphate 7-hydrate, which were purchased from CARLO ERBA (France) and Panreac AppliChem (Germany), respectively. The pH of PBS was adjusted to the desired value using a pH meter at 25 °C.

All electrochemical measurements were implemented with PGSTAT302N (Autolab, the Netherlands) with NOVA software. All electrochemical experiments were conducted at room temperature using a three-electrode system based on the fabricated SPGEs.

Design and fabrication of the SPGEs for electrochemical analysis

The SPGEs are composed of three electrodes: a 3 mm diameter graphene working electrode (WE), a graphene counter electrode (CE), and an Ag/AgCl reference electrode (RE), all screen-printed onto a PVC substrate. The production of the SPGEs began with the fabrication of RE by screen-printing Ag/AgCl ink onto a PVC sheet using a dedicated RE block. Subsequently, the resulting PVC sheet was baked at 55°C for 30 min to remove solvent. Following this, the same PVC sheet was employed to screen-print graphene ink using another block, resulting in the fabrication of WE and CE segments. These electrodes were then baked at 55°C for 1 h to remove solvent and were stored in a desiccator when not in use.

Investigation of electrochemical behavior of ROX

The electrochemical behavior of ROX was thoroughly investigated using the SPGEs. The results were then compared with those of molecules sharing similar functional groups, specifically nitrobenzene, *o*-nitrophenol, and phenol. The oxidation reactions of the studied substances were examined using cyclic voltammetry (CV) by first scanning the potential towards more positive values, ranging from 0.0 V to +1.2 V (*vs.* Ag/AgCl).

Fabrication of the MIP-modified mSPGE

The bare SPGE was firmly attached to an external magnet with a diameter of 9 mm, ensuring that the magnet is positioned underneath all three electrodes. This setup resulted in the formation of the magnetic screen-printed graphene electrode (mSPGE). Next, the mSPGE was modified with MIP by electropolymerization. This modification was initially performed by drop-casting 100 μ L of a solution containing 0.5 mM *o*-PD monomer and 1.0 mM ROX template in 0.1 M PBS (pH = 7.0) onto the surface of the mSPGE, covering all three electrodes. Next, CV was carried out in a potential range of 0.0 V to +1.20 V (*vs.* Ag/AgCl) at a scan rate of 50 mV/s for 5 cycles, resulting in the formation of MIP. Afterward, the template was removed using an electrochemical method as follows: 100 μ L of 0.1 M PBS

(pH = 7.0) was drop-cast onto the surface of the modified mSPGE, covering all three electrodes. Next, CV was scanned in a potential range of +0.70 to +1.50 V (*vs.* Ag/AgCl) at a scan rate of 50 mV/s for 5 cycles. Over-oxidation during this process triggered the release of the template during elution (17). After that, the PBS droplet was wiped off, and the modified electrode was rinsed with Milli-Q water and dried at 55 °C for 2 min to obtain the MIP/mSPGE sensor. A non-molecularly imprinted polymer (NIP) was also prepared in the same manner, except that no ROX template was added.

Optimization for polymerization and template removal of MIP

The experimental parameters for MIP electropolymerization and template removal were optimized by CV using the modified mSPGEs. Within similar optimization procedures, both the MIP/mSPGE and the NIP/mSPGE obtained were characterized by detecting 1.0 mM ROX *via* oxidation, and the resulting anodic peak currents were recorded. The difference in anodic peak current (ΔI) between the MIP/mSPGE and the NIP/mSPGE was then measured. This ΔI value was used to evaluate the binding capability of the MIP film prepared for the detection of ROX. Typically, a larger ΔI indicates a higher binding capability of the MIP.

Study of analytical performance of the MIP/mSPGE sensor

The linear range and limit of detection (LOD) for the determination of ROX by the developed MIP/mSPGE sensor were studied under optimal conditions using differential pulse voltammetry (DPV). All DPV measurements were conducted within a potential window of +0.5 V to +1.2 V (*vs.* Ag/AgCl), with a modulation amplitude of 0.2 V, a modulation time of 0.01 s, a step potential of 0.01 V, and an interval time of 0.5 s.

Study of the anti-interference ability of the MIP/mSPGE for ROX detection

A 0.1 mM ROX solution was mixed with various common interferents found in animal waste and food products, including nitrobenzene, chloramphenicol (CAP), and uric acid, each at a concentration of 0.1 mM in 0.1 PBS (pH = 7.0). Electrochemical responses were recorded using DPV to assess the effects of these interfering substances on the detection of ROX. The anodic peak currents of the mixed solutions were compared to the peak current of ROX alone, which was set at 100%, to evaluate the degree of interference and the selectivity of the MIP/mSPGE sensor.

Results and Discussion:

Electrochemical behavior of ROX at the SPGEs

The CV analysis of 0.5 mM ROX in 0.1 M PBS (pH = 7.0) was first conducted over a potential range of +0.0 V to +1.2 V (*vs.* Ag/AgCl) at a scan rate of 50 mV/s, where the oxidation of ROX occurred. An anodic peak corresponding to ROX oxidation could be clearly observed at *ca.* +0.9 V (*vs.* Ag/AgCl), as shown in **Figure 2(A)**. This voltammetric response was potentially attributed to the oxidation of the hydroxyl group in ROX. Note that no such voltammetric behavior was observed in a blank solution.

To verify whether the observed anodic peak of ROX was indeed associated with the oxidation of the hydroxyl group in ROX, the electrochemical responses of molecules with similar functional groups (namely nitrobenzene, *o*-nitrophenol, and phenol) were thoroughly investigated and compared. The measurements were conducted using CV within the same scanning potential range, and the resulting voltammograms are presented in **Figure 2(B)**. The results showed that phenol and *o*-nitrophenol, both of which contain a hydroxyl group, exhibited well-defined anodic peaks at *ca.* +0.53 V and +0.68 V (*vs.* Ag/AgCl), respectively. These anodic peaks typically corresponded to the oxidation of the hydroxyl group to the quinone group, consistent with reports in the literature (2). In contrast, no oxidative response could be observed for nitrobenzene, which lacks a hydroxyl group. These findings confirm that the observed electrochemical response of ROX in the oxidation region likely arises from



the oxidation of the hydroxyl group within ROX. Consequently, ROX could be detected electrochemically through this oxidation reaction.

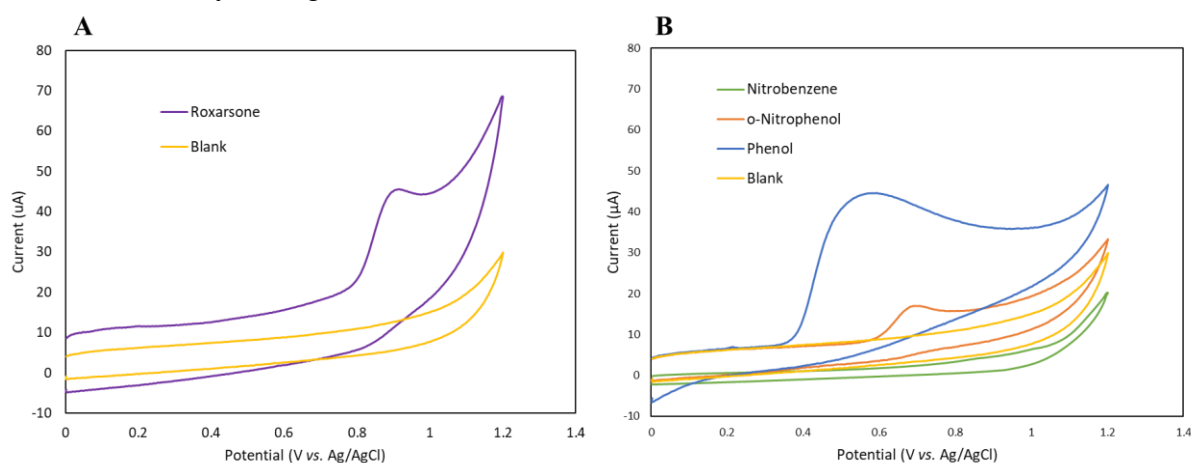


Figure 2.

CVs recorded at the SPGEs in 0.1 M PBS (pH = 7.0) containing (A) 0.5 mM ROX, and (B) 0.5 mM each of nitrobenzene (green), *o*-nitrophenol (orange), and phenol (blue). These measurements were also compared with those from a blank solution (yellow).

Oxidative electrochemical responses of ROX at the modified SPGEs

The electrochemical responses of ROX during oxidation were examined and compared among the bare SPGE, the MIP/SPGE, and the MIP/mSPGE. The experiments were performed using CV, with a potential range of +0.0 V to +1.2 V (vs. Ag/AgCl) at a scan rate of 50 mV/s, in 0.1 M PBS (pH = 7.0) containing 1.0 mM ROX. The resulting voltammograms and the plots of anodic peak currents are illustrated in Figure 3. As shown in Figure 3(A), anodic peaks corresponding to the oxidation of ROX could be observed at *ca.* +0.90 V (vs. Ag/AgCl) across all three types of electrodes. When the anodic peak currents were measured and compared, as shown in Figure 3(B), the MIP/mSPGE exhibited the highest voltammetric response relative to both the bare SPGE and the MIP/SPGE.

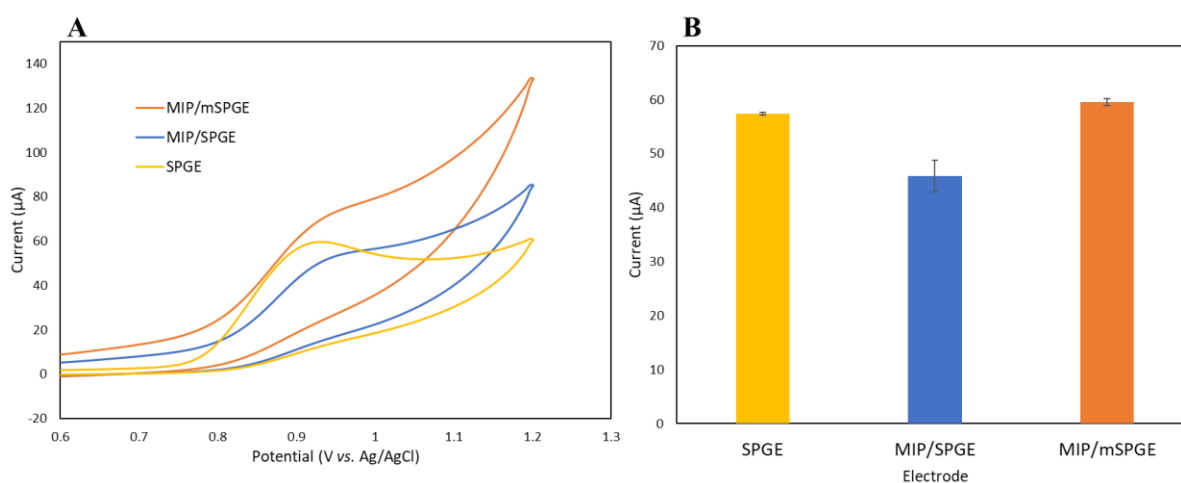


Figure 3.

(A) CVs in 0.1 M PBS (pH = 7.0) containing 1.0 mM ROX, recorded using the SPGE (yellow), the MIP/SPGE (blue), and the MIP/mSPGE (orange). (B) Plots of anodic peak currents of ROX measured at the SPGE, the MIP/SPGE, and the MIP/mSPGE.

This enhancement is attributed to the application of an external magnet to the SPGE, resulting in the formation of the mSPGE. The magnet-induced magnetohydrodynamic (MHD) effect generated convection in the electrolyte, reducing the diffusion layer thickness and increasing mass transport. Consequently, this led to improved detection efficiency for ROX with increased sensitivity at the modified mSPGE. Note that, in the absence of the MHD effect, the anodic peak current of ROX decreased after modifying the surface of the SPGE with MIP, due to the formation of an insulating polymeric film that obstructed electron transfer at the electrode surface (*cf.* the SPGE *vs.* the MIP/SPGE).

Comparative electrochemical responses of ROX at the MIP/mSPGE and the NIP/mSPGE

The electrochemical responses of ROX at the MIP/mSPGE were examined and compared with those obtained at the NIP/mSPGE. The studies were performed using CV in 0.1 M PBS (pH = 7.0) containing 1.0 mM ROX, both before and after template removal during the MIP modification process. The results obtained from the MIP were subsequently compared with those from the NIP synthesized under the same conditions, as presented in **Figure 4**. As seen from the CVs, after the electropolymerization process and prior to the template removal step, neither the MIP nor the NIP exhibited any oxidation behavior for ROX. This is due to the absence of specific sites or cavities for recognizing target molecules in the MIP, as well as the presence of a non-conductive polymeric film in the NIP, resulting in the passivation of the electrode surface.

Following template removal *via* electrochemical elution using CV, the resulting MIP displayed a distinct anodic response for ROX, confirming the successful imprinting of the MIP with specific recognition sites for ROX. However, the NIP, after undergoing the same electrochemical elution, also exhibited a voltammetric response for ROX, with a lower signal compared to the MIP. This indicates that some polymeric regions of the NIP were also leached out, leading to non-specific binding of ROX to the NIP electrode surface. Consequently, further optimization of the electropolymerization and electrochemical elution processes during the modification of the MIP onto the mSPGE is required to establish the optimal conditions for effective ROX detection.

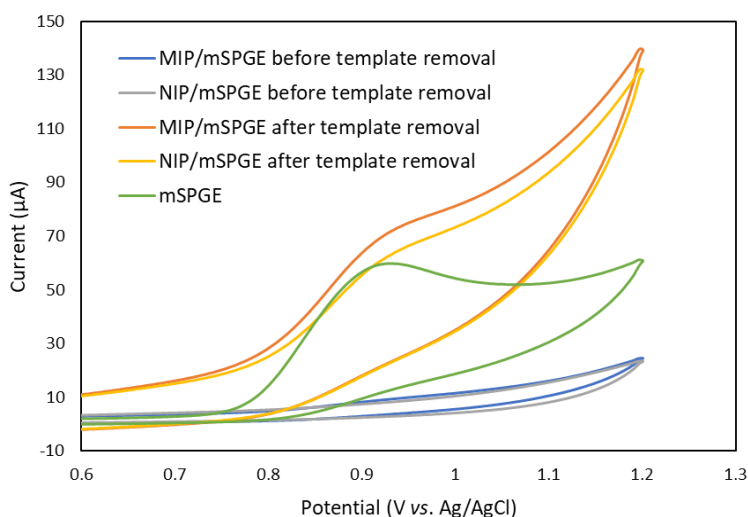


Figure 4.

CVs of different modified electrodes in 1.0 mM ROX in 0.1 M PBS (pH = 7): the MIP/mSPGE before template removal (blue), the NIP/mSPGE before template removal (gray), the MIP/mSPGE after template removal (orange), the NIP/mSPGE after template removal (yellow), and the unmodified mSPGE (green).



Optimization for polymerization and template removal of MIP

The experimental parameters related to the modification of MIP onto the mSPGE by electropolymerization, as well as the subsequent template removal by electrochemical elution, were thoroughly investigated and optimized. These parameters included the concentration ratio of monomer to template, the potential range used for template removal, and the number of scan cycles employed during the template removal process. The resulting MIP/mSPGEs, optimized through these parameters, were characterized by the detection of ROX. The results were then compared with those obtained from the NIP/mSPGEs fabricated under the same experimental conditions. Typically, the electrochemical analysis was conducted by CV in 0.1 M PBS (pH = 7.0) containing 1.0 mM ROX, and the anodic peak current corresponding to the oxidation of ROX was measured. The difference in anodic peak current (ΔI) between the MIP/mSPGE and the NIP/mSPGE, obtained under similar experimental conditions, was subsequently calculated. These ΔI values reflected the binding capability of the MIP film for ROX detection, with a larger ΔI indicating a higher binding capability of the MIP.

Initially, the effect of the concentration ratios of monomer to template was examined at ratios of 1:1, 1:2, and 1:4, with an optimal constant concentration of ROX template set at 1.0 mM. The results obtained from the MIP/mSPGE and the NIP/mSPGE are presented in **Figure 5(A)**, and the ΔI values were subsequently calculated and compared. As shown in the plot, the 1:2 monomer-to-template ratio exhibited the highest ΔI , indicating that this ratio produced the most optimal MIP with the best binding capability for the analyte. Deviations from this ratio resulted in poorer voltammetric responses, as well as an increase in non-specific binding of the sensor, as indicated by the smaller ΔI values, which was undesirable. Therefore, the monomer-to-template ratio of 1:2 was selected as the optimal condition for use in electropolymerization for electrode modification with MIP.

After the MIP is electropolymerized onto the mSPGE, the MIP/mSPGE would undergo template removal by electrochemical elution. This was achieved by performing CV at a higher oxidation potential than that used during polymerization, in a 0.1 M PBS (pH = 7.0) blank solution. The elution process electrochemically removed the template molecules, creating specific recognition sites within the polymer matrix. This approach is known as a non-chemical-based template removal strategy (17). Therefore, the effect of the potential range used for template removal during the electrochemical elution process was systematically optimized. Generally, the electrochemical elution for template removal was conducted over two potential ranges: +0.7 V to +1.5 V and +0.8 V to +1.5 V (vs. Ag/AgCl) for 10 cycles. The resulting oxidation peak currents of ROX obtained from the MIP/mSPGE and the NIP/mSPGE are shown in **Figure 5(B)**. The ΔI values were also calculated and plotted for comparison. The results indicate that the potential range of +0.7 V to +1.5 V (vs. Ag/AgCl) is the most suitable potential window for template removal, based on the highest ΔI observed. It should be noted that using a wider potential window of +0.8 V to +1.5 V (vs. Ag/AgCl) not only removed the template but also potentially leached out the polymeric film, thereby reducing the efficiency of the MIP. Consequently, the potential region of +0.7 V to +1.5 V (vs. Ag/AgCl) was selected as the optimal condition for the template removal procedure.

Next, the effect of the number of scan cycles during template removal was investigated using CV over the optimal potential window of +0.7 V to +1.5 V (vs. Ag/AgCl) for 5, 10, and 15 cycles. The results are shown in **Figure 5(C)**. It can be seen that as the number of CV cycles was increased up to 10 scans, the ΔI values also increased, indicating

successful template removal and effective formation of the MIP. However, the ΔI decreased when the number of CV scans was extended to 15 cycles, possibly due to the leaching out of the polymeric film, which resulted in a reduction in the efficiency of the synthesized MIP. Therefore, 10 CV cycles were selected as the optimal condition for template removal by electrochemical elution.

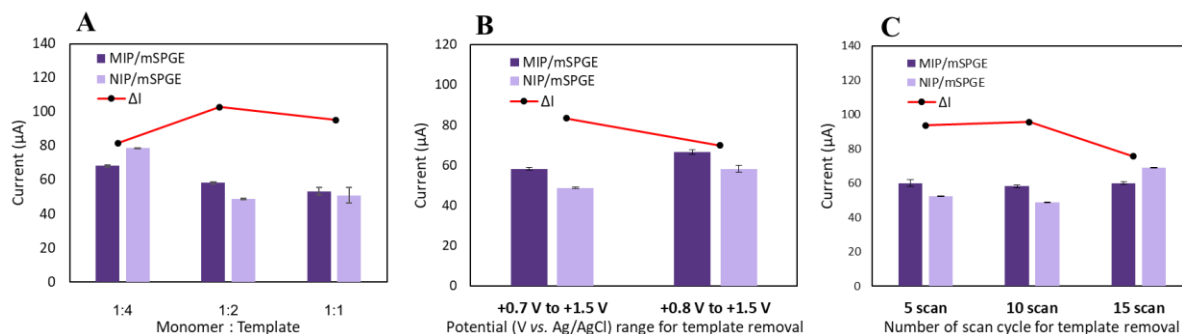


Figure 5.

Effects of (A) concentration ratio of *o*-PD monomer to ROX template, (B) potential range, and (C) number of CV scan cycles for template removal by electrochemical elution. All measurements were conducted using both the MIP/mSPGE and the NIP/mSPGE.

Analytical performance of the developed sensor

The MIP/mSPGE sensor was ultimately evaluated for its analytical performance in the determination of ROX using DPV under optimal experimental parameters. The resulting DPV voltammograms and the corresponding plot of anodic peak current vs. ROX concentration are displayed in **Figure 6(A)** and **6(B)**, respectively. A calibration plot of anodic peak current vs. ROX concentration, shown in **Figure 6(B)**, demonstrates a good linear response over the ROX concentration range of 0.03 to 0.1 mM with the regression equation: $I_{pa}(\mu A) = 49.727C(mM) - 0.5806$ and an R^2 value of 0.9824. The limits of detection (LOD) and quantification (LOQ) were found to be 0.015 and 0.051 mM, calculated based upon 3σ and 10σ , respectively.

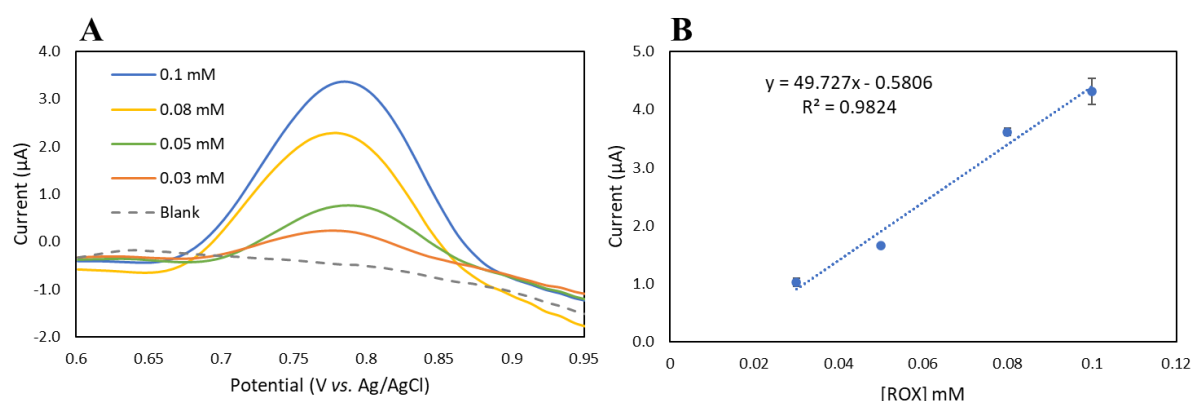


Figure 6.

(A) DPV voltammograms (with baseline correction) of 0.1 M PBS (pH = 7.0) containing varying ROX concentrations of 0.03 mM to 0.1 mM. (B) Calibration plot with ROX concentrations ranging from 0.03 mM to 0.1 mM.



Anti-interference ability of the MIP/mSPGE for ROX detection

The anti-interference capability of the proposed sensor was evaluated by examining its response to various potential interferences, including nitrobenzene, chloramphenicol (CAP), and uric acid, using DPV. **Figure 7(A)** presents the resulting DPV voltammograms of 0.1 mM ROX in the absence and presence of these three interferences, each at the same concentration (0.1 mM). **Figure 7(B)** illustrates the corresponding plot showing the relative current of ROX in the presence of the interferences, compared to the current of ROX alone, which was set to 100%. The results clearly indicate that the presence of these interfering compounds has little to no impact on the electrochemical response of ROX. This generally demonstrates the exceptional anti-interference performance of the MIP/mSPGE sensor for detecting ROX with high selectivity.

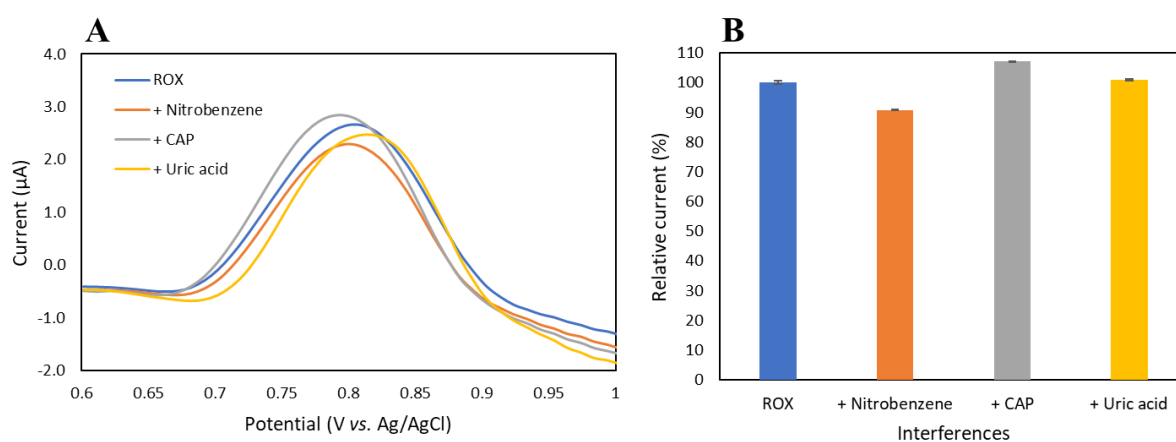


Figure 7.

(A) DPV voltammograms of 0.1 mM ROX in the absence and presence of interferences, each at a concentration of 0.1 mM. (B) The corresponding plot showing the relative current of ROX in the absence and presence of interferences, each at a concentration of 0.1 mM.

Conclusion:

The MIP/mSPGE sensor was successfully developed for the determination of ROX with enhanced sensitivity and selectivity. Initially, the electrochemical behavior of ROX was investigated using CV and compared with molecules having similar functional groups, confirming that ROX could be detected electrochemically through the oxidation of its hydroxyl group. This oxidative response of ROX was significantly enhanced by the mSPGE through the magnetohydrodynamic (MHD) effect of an applied external magnet, which improved mass transport *via* convection and thereby increased sensor sensitivity. Moreover, the MIP modified onto the mSPGE through electropolymerization demonstrated improved selectivity for ROX detection. Under optimal conditions, the MIP/mSPGE sensor exhibited high sensitivity, good selectivity, and excellent linearity, with detection and quantification limits (LOD and LOQ) of 0.015 mM and 0.051 mM, respectively, effectively covering the permissible limit for total arsenic concentration in the environment.

Acknowledgement:

This research project has been funded by National Research Council of Thailand (NRCT): N41A640073, and by the Electrochemical and Optical Spectroscopy Center of Excellence (EOSCE), Chulalongkorn university.

References:

1. Govindasamy M, Wang S-F, Jothiramalingam R, Noora Ibrahim S, Al-Lohedan HA. *Microchimica Acta*. 2019;186:1-10.
2. Ferreira LM, Martins PR, Silva CG, Marcolino-Junior LH, Bergamini MF, Vicentini FC. *Food Chemistry*. 2024;437:137698.
3. Nascimento ALA, Figueiredo IM, Botero WG, Santos JCC. *Chemosphere*. 2023;339:139688.
4. Wen Z, Chen R, Zhang G, Li S, Zhang Y, Liao X, et al. *Journal of Cleaner Production*. 2023;423:138801.
5. Li F, Gao J, Wu H, Li Y, He X, Chen L. *Nanomaterials*. 2022;12(17):2997.
6. Eom HY, Yang D-H, Suh JH, Kim U, Kim J, Cho H-D, et al. *Journal of Chromatography B*. 2015;1006:151-7.
7. Qadah DT, Aldstadt III JH. *Analytical Letters*. 2018;51(9):1321-34.
8. Li Z-Y, Zhang H-X, He T-S, Jiang H-X, Liu X-W, Zhu L-N, et al. *Inorganica Chimica Acta*. 2023;547:121334.
9. Kokulnathan T, Rajagopal V, Wang T-J, Huang S-J, Ahmed F. *Inorganic Chemistry*. 2021;60(23):17986-96.
10. He S, Zhang L, Bai S, Yang H, Cui Z, Zhang X, et al. *European Polymer Journal*. 2021;143:110179.
11. Ozcelikay G, Kurbanoglu S, Yarman A, Scheller FW, Ozkan SA. *Sensors and Actuators B: Chemical*. 2020;320:128285.
12. Cetinkaya A, Yıldız E, Kaya SI, Çorman ME, Uzun L, Ozkan SA. *Green Analytical Chemistry*. 2022;2:100017.
13. Lu H, Liu M, Cui H, Huang Y, Li L, Ding Y. *Electrochimica Acta*. 2022;427:140858.
14. Dong J, Zhang H, Ding Z, Li J, Xu L, Kong Y, et al. *Analytical Biochemistry*. 2024;691:115551.
15. Luo S, Elouarzaki K, Xu ZJ. *Angewandte Chemie International Edition*. 2022;61(27):e202203564.
16. Monzon LM, Coey JMD. A mini-review. *Electrochemistry Communications*. 2014;42:38-41.
17. Garg M, Pamme N. *TrAC Trends in Analytical Chemistry*. 2023;117437.



ELECTROMEMBRANE EXTRACTION WITH FLAT SHEET MEMBRANE FOR DETERMINATION OF CHROMIUM(VI)

Preenapa Saengaroorn, Pakorn Varanusupakul*

Department of Chemistry, Faculty of Science, Chulalongkorn University

*e-mail: pakorn.v@chula.ac.th

Abstract:

An electromembrane extraction with a flat sheet membrane platform and colorimetric detection of chromium (VI) was developed. This study designed an electromembrane extraction device using a simple flat sheet membrane with an open area to reduce the effect of gas generation from the electrolysis reaction of hollow fiber liquid phase microextraction, (HF-LPME). In this system, a 1,5-Diphenylcarbazine (DPC) colorimetric reagent for Cr(VI) was introduced into the acceptor phase. When a voltage was applied, the analytes were extracted and transferred from the sample solution (donor phase) to the acceptor phase. The analytes then simultaneously reacted with the colorimetric reagents inside the acceptor phase, producing a pink-violet color Cr-DPC complex. This color was measured by using ImageJ program to analyzing color intensity in green color mode. Parameters that affected extraction efficiency were evaluated and optimized. A 1% (w/v) DPC in HCl (pH3) was used as the acceptor phase. Cr(VI) was extracted at an applied voltage of 30 V and an extraction time of 10 min. Under the optimized conditions, the developed systems provided linear responses within 10 min for Cr(VI) concentrations ranging from 50 to 800 $\mu\text{g L}^{-1}$, with a detection limit of 34 $\mu\text{g L}^{-1}$ and enrichment factor was 62. This system is simple, uses small amounts of organic solvents, and does not require the synthesis of sorbents, complicated microfluidic chips.

Introduction:

Nowadays, the miniaturization of analytical instrumentation, including sample preparation, has seen significant development. Micropreparative techniques like hollow fiber liquid phase extraction (HF-LPME), single drop microextraction (SDME), and solid phase microextraction (SPME) have been developed to extract analytes from complex matrices. These techniques offer better performance than traditional methods, such as liquid-liquid and solid phase extraction, due to their compatibility with raw complex matrices, high extraction efficiency, low solvent consumption, and instrumental simplicity. [1,2]. However, they have drawbacks, such as expensive commercial microfibers in SPME, organic drop instability in SDME, and long extraction times in HF-LPME. [3].

EME has gained great popularity in the last decade [4]. In 2006, Pedersen-Bjergaard et al. developed the EME technique for extracting ions from the donor phase to the acceptor phase through a supported liquid membrane (SLM) accelerated or driven by an electric field [5]. EME offers high mass transfer efficiency and high concentration after extraction (enrichment factor, EF) in a short time compared to conventional HF-LPME extraction. HF-EME uses a hollow fiber membrane, containing a solvent impregnated in the porous wall of the membrane as SLM and an acceptor phase inside the membrane lumen. Typically, the donor and acceptor phases are aqueous solutions. When a high electric potential (>30 V) is applied, water electrolysis can occur generating gas bubbles at both phases. The gas bubbles could affect the acceptor phase more critically due to the small volume and small diameter of the lumen. This could cause the loss of the acceptor phase leading to irreproducible results and sometimes an uncollectible acceptor phase.

In 2008, Li Xu developed EME using a flat sheet membrane to extract a nerve agent [6]. The process involved sealing two polypropylene membranes together and closing them by heating the membrane where the acceptor phase solution was contained. The extraction time was 30 minutes, the volume was 20 μL , and the electric potential was 300 V. This design reduced the loss of the acceptor due to gas generation during extraction, making it more collectible.

Nickolaj Jacob Petersen et al. developed a flat sheet membrane EME for drug extraction from human plasma and urine samples [7]. The donor phase is placed on an aluminum plate with small holes, covered by a flat sheet of polymer membrane. The sample solution is dropped into the aluminum channel, followed by the SLM section above the sample drop. The acceptor phase is then dropped, and the platinum electrode is submerged in the acceptor phase. The extraction recoveries were 33% and 47%, respectively, with an electric potential of 15 V and a 5-min extraction time.

In 2020, Zarghampour et al. developed EME equipment using a polypropylene sheet membrane combined with solid phase extraction for the determination of Cr (VI) [8]. Cr (VI) was determined by colorimetric analysis based on the reaction between Cr (VI) and 1,5-diphenylcarbazide, or DPC. In this work, the device design was called spiral style, a popular style for sheet membranes, which provided a large contact surface area between DP and AP. Extraction was performed using an electric potential of 30 V. The extraction time was 33 minutes, and the EF value was 19.

The majority of EME equipment is designed based on spiral or sandwich-shaped flow cell types to maximize mass transfer due to the large contact surface area between DP and AP resulting in a high enrichment factor. However, these specialized designs require advanced instruments for fabrication. This research aims to develop a simple EME device using a flat sheet membrane with an open area to reduce the effect of gas generation due to electrolysis and apply it to the extraction of Cr(VI). The method compensates for the limited contact area between DP and AP by using the reaction of Cr-DPC in the acceptor phase to improve the mass transfer of Cr(VI) and maintain a high enrichment factor.

Methodology:

Materials

All chemicals used in this study were of analytical reagent grade, and solutions were prepared in Milli-Q water (Millipore, USA). Potassium dichromate, 1-Octanol, sodium hydroxide (NaOH), and hydrochloric acid (HCl) were obtained from Merck (Germany). 1,5-Diphenylcarbazide (DPC) was obtained from Himedia (India).

Apparatus and detection system

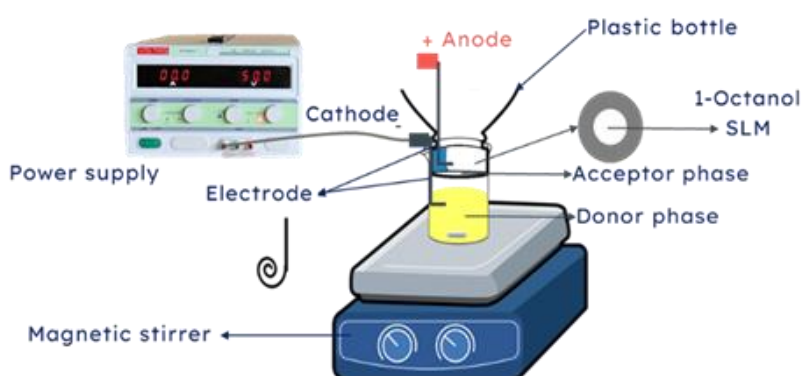
For the detection and extraction systems, GPR11H30D benchtop DC power supply (GwInstek, China) with adjustable voltage within the range of 0–110 V. A platinum wire (0.02 mm diameter) was obtained from Sigma-Aldrich (St. Louis, MO, USA).

EME device with a flat sheet membrane and colorimetric detection of Cr(VI)

Scheme 1 represents the setup of an EME device with a flat sheet membrane. A bottle cap with a 1.5 cm diameter hole is used as a flat sheet membrane supporter and a container for the acceptor phase. The flat sheet membrane with the same diameter (ca. 1.5 cm) was situated to cover the hole of the cap and sealed with the screwed-cut bottle mouth. A 20 mL of sample or standard solution ($10 \mu\text{g L}^{-1}$ Cr(VI)) was placed in the beaker. Then, the flat sheet EME device was put facing the open hole down touching the surface of the sample. A 300 μL of the acceptor phase (optimized volume) was added to cover the other side of the membrane. The cathode (-) and the anode (+) platinum electrodes connected to a DC power



supply were placed in the donor phase and acceptor phase, respectively. The extraction was carried out for 10 min. The pink-violet color of the Cr-DPC complex was observed. A 10 μL of the colored acceptor phase was withdrawn and placed onto a piece of paper for taking a picture in a light-controlled box. The color image was analyzed by the ImageJ software to measure the color intensity. The calibration curve for Cr(VI) detection was subsequently constructed using Microsoft Excel. Specifically, the color intensity in the green channel ($G_0 - G$) was plotted against Cr(VI) concentration, where G and G_0 are color intensities in the green channel in the presence and absence of Cr(VI), respectively. This difference was directly correlated with the Cr(VI) concentrations. To obtain the best results, parameters that could affect the extraction efficiency were examined, including the diameter of the membrane, the pH of the acceptor and donor phases, applied voltage, extraction time, and acceptor phase volume.



Scheme 1 The schematic of EME device with a flat sheet membrane.

Results and Discussion:

According to the proposed method, the external electric potential causes Cr(VI) to migrate from the sample solution/matrix toward the acceptor phase, then reacts with the DPC reagents and produces pink-violet color of the Cr-DPC complex

Effect of the applied voltage

Cr(VI) was transferred across the membrane from the donor to the acceptor solutions, mostly driven by electrical potential. Therefore, the extraction voltages ranging from 10 to 50 V were studied in order to identify the most effective voltage. The extraction increased significantly when the applied voltage was increased from 10 to 30 V shown in figure 1. This was caused by an improvement in the analyte flow and an increase in the driving force between the electrodes. Based on these results, a voltage of 30 V was chosen to be set between the acceptor and donor solutions.

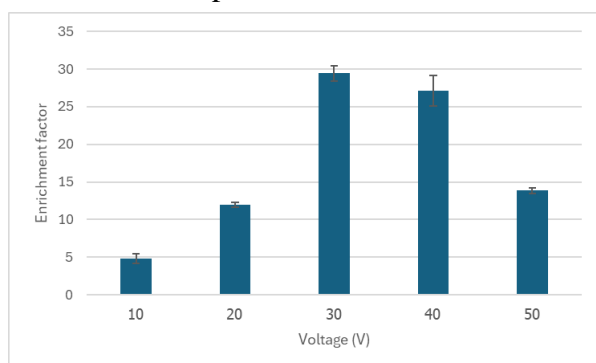


Figure 1. Applied voltage result: acceptor phase : DPC 1% (w/v) 100 μL , donor phase : $\text{Cr}_2\text{O}_7^{2-}$ 10 ppb 20 mL

Effect of extraction time

The sensitivity of the developed technique can be affected by extraction time, which is an important parameter that establishes the total amount of analytes transported from the donor phase to the acceptor phase. Various extraction times between 5 and 20 min were studied shown in figure 2. The extraction efficiency increased as increased extraction time up to 10 min and slightly decreased for longer extraction time because Cr-DPC has a positive charge. As time increases, Cr-DPC moves to the cathode in the donor phase, resulting in a decrease in extraction efficiency. Hence, the extraction time of 10 min was selected as the optimum value.

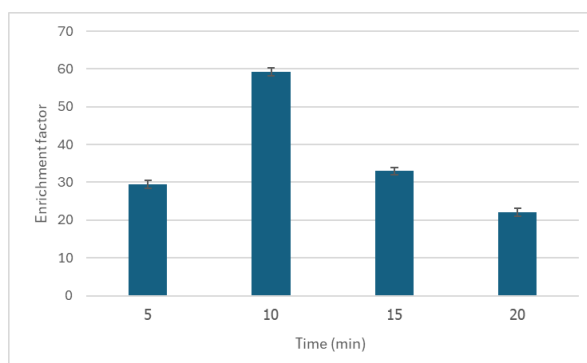


Figure 2. Applied time result: acceptor phase : DPC 1% (w/v) 100 μ L, donor phase : $\text{Cr}_2\text{O}_7^{2-}$ 10 ppb 20 mL, voltage 30 V

Effect of pH of donor phase and acceptor phase

In EME systems, analytes should be converted to their suitable ionic forms for efficient extraction under the application of an external voltage. To obtain maximum extraction for Cr(VI), in this experiment, the pH of the donor phase and acceptor phase between 1.0 and 5.0 was investigated the result shown in figure 3. NaOH and HCl solutions (0.1 M) were used for the pH adjustments of the donor and acceptor phases. In these experiments, when the pH of the donor phase increased from pH 1.0 to 4.0, the extraction efficiency increased. Therefore, the donor pH of 4.0 was used. When the pH of the acceptor phase increased from pH 1.0 to 3.0, the extraction efficiency increased. Therefore, the acceptor pH of 3.0 was used.

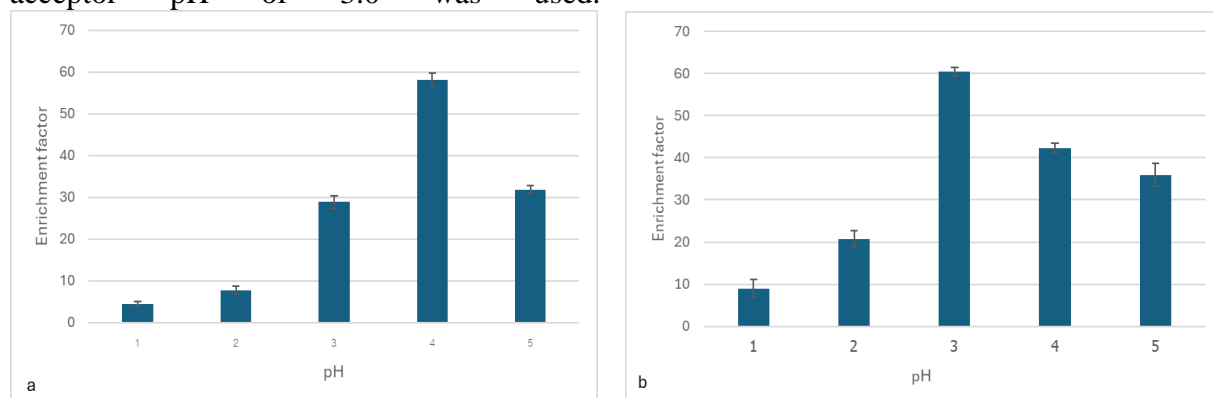


Figure 3. Applied pH result, a) donor phase, b) acceptor phase: acceptor phase : DPC 1% (w/v) 100 μ L, donor phase : $\text{Cr}_2\text{O}_7^{2-}$ 10 ppb 20 mL, voltage 30, V 10 min



Effect of the surface area of the membrane and the volume of the acceptor phase

After obtaining the appropriate conditions above, the surface area of the membrane and the volume of the acceptor phase are studied shown in figure 4. A larger membrane surface area provides more contact area, facilitating the transfer of analytes across the membrane. The volume of the acceptor phase is important, and it could affect the enrichment factor of the method. A smaller volume of the acceptor phase results in a higher concentration after extraction (enrichment factor). The highest enrichment factor was reached at a membrane diameter of 1.50 cm and a volume of the acceptor phase of 300 μL .

Under the optimized conditions, the developed systems provided linear responses within 10 min for Cr(VI) concentrations ranging from 50 to 800 $\mu\text{g L}^{-1}$, with a detection limit of 34 $\mu\text{g L}^{-1}$ and an enrichment factor of 62.

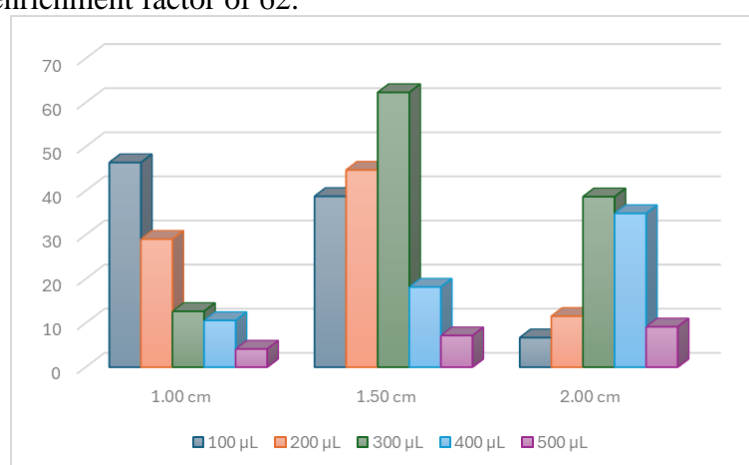


Figure 3. Applied the surface area of the membrane and the volume of the acceptor phase result : acceptor phase : DPC 1% (w/v), donor phase : $\text{Cr}_2\text{O}_7^{2-}$ 10 ppb 20 mL, voltage 30, V 10 min

Conclusion:

The flat sheet design deals with important issues associated with hollow fiber systems, including gas production during electrolysis, which may affect extraction efficiency and precision. This technique uses an open-area flat sheet membrane to reduce the impacts of gas production, resulting in more stable and dependable performance. The flat sheet configuration's simplicity also helps to reduce system complexity by eliminating the requirement for specialized microfluidic chips. The designed device can accommodate a flat sheet membrane and be used for the EME of Cr(VI). Various parameters affecting the extraction efficiency of the EME with a flat sheet membrane were investigated and optimized. The method was applied for the extraction and determination of Cr(VI) giving an enrichment factor of 62. Our method is simple, uses small amounts of organic solvents, and does not require the synthesis of sorbents, complicated microfluidic chips.

Acknowledgements:

This research project is supported by the Development and Promotion of Science and Technology Talents Project (DPST), Chulalongkorn University.

References:

1. Krishna Marothu, V.; Gorrepati, M.; Vusa, R. Electromembrane Extraction A Novel Extraction Technique for Pharmaceutical, Chemical, Clinical and Environmental Analysis. *J. Chromatogr. Sci.* 2013, *51*, 619–631.
2. Ocaña-González, J. A.; Aranda-Merino, N.; Pérez-Bernal, J. L.; Ramos-Payán, M. Solid Supports and Supported Liquid Membranes for Different Liquid Phase Microextraction and Electromembrane Extraction Configurations. A Review. *J. Chromatogr. A* 2023, *1691*, 463825.
3. Drouin, N.; Kubán, P.; Rudaz, S.; Pedersen-Bjergaard, S.; Schappler, J. Electromembrane Extraction: Overview of the Last Decade. *TrAC Trends in Analytical Chemistry* 2019, *113*, 357–363.
4. Bavlovič Piskáčková, H.; Øiestad, E. L.; Váňová, N.; Lengvarská, J.; Štěrbová-Kovářiková, P.; Pedersen-Bjergaard, S. Electromembrane Extraction of Anthracyclines from Plasma: Comparison with Conventional Extraction Techniques. *Talanta* 2021, *223*, 121748.
5. Pedersen-Bjergaard, S.; Rasmussen, K. E. Electrokinetic Migration across Artificial Liquid Membranes. *J. Chromatogr. A* 2006, *1109* (2), 183–190.
6. Xu, L.; Hauser, P. C.; Lee, H. K. Electro Membrane Isolation of Nerve Agent Degradation Products across a Supported Liquid Membrane Followed by Capillary Electrophoresis with Contactless Conductivity Detection. *J. Chromatogr. A* 2008, *1214* (1–2), 17–22.
7. Petersen, N. J.; Jensen, H.; Hansen, S. H.; Rasmussen, K. E.; Pedersen-Bjergaard, S. Drop-to-Drop Microextraction across a Supported Liquid Membrane by an Electrical Field under Stagnant Conditions. *J. Chromatogr. A* 2009, *1216* (9), 1496–1502.
8. Zarghampour, F.; Yamini, Y.; Baharfar, M.; Javadian, G.; Faraji, M. On-Chip Electromembrane Extraction Followed by Sensitive Digital Image-Based Colorimetry for Determination of Trace Amounts of Cr(VI). *Analytical Methods* 2020, *12* (4), 483–490



MAGNETIC LIQUID MARBLES FOR HYDROGEN SULFIDE GAS DETECTION

Cinta Nur Ihya and Apichat Imyim*

Department of Chemistry, Faculty of Science, Chulalongkorn University, Bangkok, Thailand

*e-mail: apichat.i@chula.ac.th

Abstract:

Liquid Marbles (LMs) are droplets coated with hydrophobic particles, creating a non-wetting, stable structure with unique properties suitable for various applications. In this research, we explored the fabrication of magnetic liquid marbles (MLMs) and their application for H_2S gas detection. The Fe_3O_4 particles were synthesized via co-precipitation of FeCl_3 and $\text{FeSO}_4 \cdot 7\text{H}_2\text{O}$ in the presence of NaOH , with controlled pH levels. When the pH was maintained at or close to 11, black marbles (B-MLMs) were formed, whereas red marbles (R-MLMs) were created when the pH exceeded 11. The pH control during synthesis resulted in variations in particle size and content, as evidenced by the color differences. Stability testing demonstrated that B-MLMs were significantly more stable than R-MLMs, maintaining their structure for over 5 minutes on water, compared to just 11 seconds for R-MLMs. Additionally, B-MLMs exhibited a superior evaporation resistance of up to 1 hour, while R-MLMs collapsed within 30 minutes. For H_2S detection, *N,N*-dimethyl-1,4-phenylenediamine (DMPD) solution at a concentration of 0.01 M was encapsulated within the B-MLMs. Upon exposure to H_2S gas at concentrations of 60 mg/L, the DMPD solution underwent a color change from pinkish-brown to blue, indicating the formation of methylene blue. The B-MLMs demonstrated their potential as efficient and affordable sensors for real-time H_2S monitoring. Their magnetic properties and enhanced stability made B-MLMs particularly suitable for environmental applications, including the detection of hazardous gases.

Introduction:

Liquid marbles (LMs) are intriguing droplets composed of a water-based core coated with hydrophobic micro or nanoscale particles, which prevent the droplets from contacting and wetting surfaces¹. These particles adhere to the droplet's surface as marble rolls, forming a protective coating that can vary from a single thick layer to multiple thin layers. Common materials used for this hydrophobic coating include polytetrafluoroethylene (PTFE), polyvinylidene fluoride (PVDF), and other fluorinated compounds². These materials are selected for their ability to repel water while maintaining adhesion to the liquid core, effectively isolating the internal liquid from the external environment³.

The unique structure of LMs provides them with non-stick properties and allows manipulation of their movement, shape, structure, and stability through external factors such as pH, temperature, light, and organic solvents¹. This versatility has made LMs valuable in various research fields, particularly in applications where precise control over these factors is crucial⁴.

Recent studies have highlighted the growing popularity and versatility of liquid marbles as micro-laboratories for a range of applications, including gas detection⁵. Magnetic liquid marbles (MLMs), which incorporate magnetic particles into the coating, are particularly noteworthy for their ability to be controlled remotely, enabling manipulation without direct contact⁶. This feature is especially useful in environments where safety and precision are paramount⁷.

The stability of LMs is a critical factor that influences their functionality, particularly in applications such as chemical sensing or controlled drug release. Asaumi et al. have shown that the size of the stabilizing particles plays a significant role in the behavior and adaptability of liquid marbles⁸. Their findings demonstrate how particle size affects the formation, stability, and responsiveness of LMs to external stimuli, which is crucial for ensuring the reliability and effectiveness of LMs in practical applications. Additionally, studies by Tosun and Erbil have explored the evaporation dynamics of LMs, emphasizing how factors like temperature and humidity impact their stability and, consequently, their performance in applications where long-term reliability is essential⁹.

In this study, we focus on the creation of Fe₃O₄ modified with stearic acid (SA) magnetic liquid marbles, which have shown remarkable stability under various conditions and effective responsiveness to magnetic control¹⁰. This research aims to explore the potential of these MLMs in detecting hydrogen sulfide (H₂S) gas, a substance known for its hazardous properties and significant role in environmental and industrial safety concerns¹¹. For the detection process, *N,N*-dimethyl-1,4-phenylenediamine (DMPD) is encapsulated within the MLMs. When exposed to H₂S gas, DMPD undergoes a chemical reaction forming methylene blue, a clear indicator of H₂S presence¹². This reaction can be represented as¹⁴:

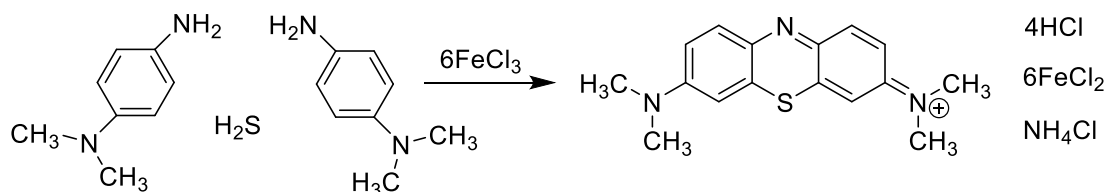


Figure 1. Reaction between H₂S, DMPD, and FeCl₃ forming methylene blue, a visual indicator for H₂S¹⁴.

We synthesized two types of MLMs by adjusting the pH during the Fe₃O₄ synthesis process, which resulted in different particle sizes and corresponding color variations. Previous research has indicated that particle size and pH control are crucial for achieving the desired stability and functionality of MLMs¹².

Given the importance of stability in gas detection applications, our study investigates the use of these MLMs for H₂S detection, focusing on their ability to provide reliable, real-time monitoring of this toxic gas¹³. H₂S is a dangerous gas with significant environmental and industrial implications, making the development of effective detection methods a critical area of research⁴. Our findings suggest that the magnetic liquid marbles we have developed are well-suited for this purpose, offering a promising approach to enhancing safety and environmental monitoring through improved gas detection capabilities¹⁴.

Methodology:

Materials

The following chemicals were used in this study: iron(II) sulfate heptahydrate (UNIVAR, analytical grade), iron(III) chloride (Merck Schuchardt OHG, anhydrous, for synthesis), *N,N*-dimethyl-1,4-phenylenediamine (DMPD, Chemenu), sodium hydroxide (Sigma-Aldrich, analytical grade), potassium hydroxide (Sigma-Aldrich, analytical grade), stearic acid (Daejung), hydrochloric acid (Sigma-Aldrich, analytical grade), and sodium sulfide nonahydrate (Carlo Erba, ACS for analysis grade). All reagents were of analytical grade and used without further purification. Milli-Q water was used for all solution preparations.



Instruments

The characterization of the Fe_3O_4 particles and magnetic liquid marbles (MLMs) was performed using the following instruments available at Chulalongkorn University: X-ray diffraction (XRD) was carried out using a Rigaku SmartLab diffractometer. Scanning Electron Microscopy (SEM) was conducted with a JEOL IT-100 instrument. The contact angle measurements were performed using a goniometer from the Angiometer series.

Preparation of Fe_3O_4 particles and modified with Stearic Acid (SA)

The Fe_3O_4 particles were synthesized via the co-precipitation method using 3 M NaOH as the precipitating agent. Initially, $\text{FeSO}_4 \cdot 7\text{H}_2\text{O}$ was dissolved in deionized water, and FeCl_3 was dissolved in ethanol. These two solutions were then mixed, followed by the addition of NaOH to precipitate Fe_3O_4 particles. The resulting precipitate was thoroughly washed with deionized water and collected by filtration. These Fe_3O_4 particles were then modified with stearic acid to enhance their hydrophobicity. Specifically, stearic acid was dissolved in ethanol and added to the Fe_3O_4 dispersion in ethanol. The mixture was sonicated and stirred for 1 hour to ensure uniform coating. The modified Fe_3O_4 -SA particles were separated using an external magnet, washed 10 times with water and once with ethanol, and then air-dried.

Preparation of Liquid Core

The liquid core used for the magnetic liquid marbles was prepared by mixing a 0.01 M DMPD solution in 0.9 M HCl. This preparation ensured that the liquid core had an appropriate pH and concentration for effective H_2S detection.

Preparation of Magnetic Liquid Marbles (MLMs)

To form the MLMs, a 20 μL droplet of the prepared liquid core was carefully placed onto a bed of Fe_3O_4 -SA particles spread on a watch glass. The droplet was gently rolled over the particles for approximately one minute until it was completely coated, forming a stable liquid marble.

Application of Liquid Marbles for Gas Sensing

To accurately determine the concentration of H_2S gas in our experiments, we utilized a stoichiometric approach based on the reaction between Na_2S and HCl as¹⁴: $\text{Na}_2\text{S} + 2\text{HCl} \rightarrow \text{H}_2\text{S} + 2\text{NaCl}$. This approach allowed us to calculate the theoretical concentration of H_2S gas based on the assumption that this reaction proceeded completely. The magnetic liquid marbles were exposed to H_2S gas (60 mg/L), which was generated by reacting 704 μL of 0.1 M Na_2S with 24 μL of 6 M HCl in a 40 mL acrylic chamber. Upon exposure to the H_2S , the DMPD solution in the MLMs underwent a distinct color change from pinkish-brown to blue, confirming the formation of methylene blue and enabling visual detection with the aid of a capillary tube.

Results and Discussion:

Synthesis and Characterization of Fe_3O_4 -SA particles

The Fe_3O_4 particles synthesized through the co-precipitation method exhibited a uniform size distribution with an average diameter of approximately 50 nm, as confirmed by scanning electron microscopy (SEM) images (Figure 2a). SEM analysis (Figure 2b) revealed that the red Fe_3O_4 -SA particles are larger, with an irregular and aggregated surface structure, averaging around 10 μm . In contrast, the black Fe_3O_4 -SA particles exhibited a more uniform

and smaller size distribution, averaging around 6 μm , contributing to their enhanced stability and hydrophobic properties.

(Leave a blank line before and after Figures.)

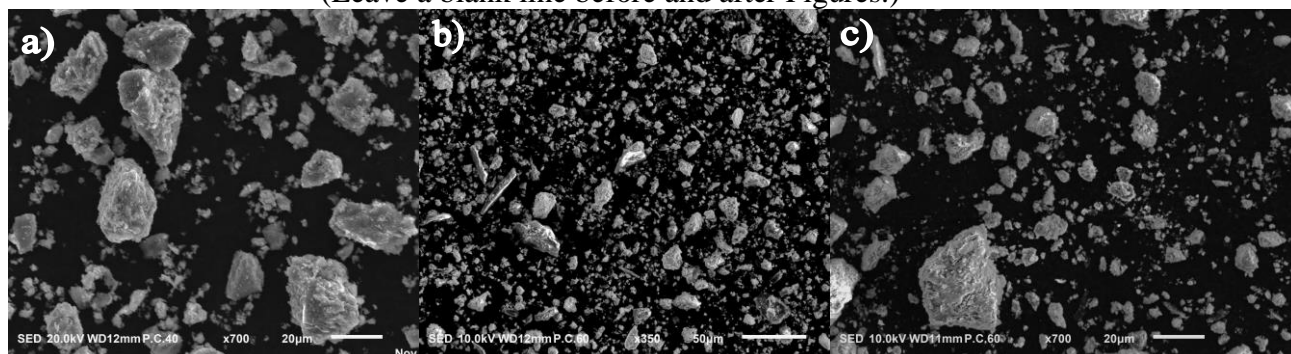


Figure 2. SEM image for (a) Fe_3O_4 , after modifying with stearic acid, (b) red powder, and (c) black powder.

X-ray diffraction (XRD) analysis was conducted to confirm the crystalline structure and phase purity of the synthesized Fe_3O_4 and Fe_3O_4 -SA particles. The XRD patterns of the samples were compared against the standard Joint Committee on Powder Diffraction Standards (JCPDS) card for Fe_3O_4 (JCPDS 00-019-0629). Characteristic peaks at 2θ values of 30.05° , 35.42° , 43.05° , 53.40° , 56.94° , and 62.52° corresponded to the (220), (311), (400), (422), (511), and (440) planes, confirming the successful synthesis of Fe_3O_4 in both the red and black samples.

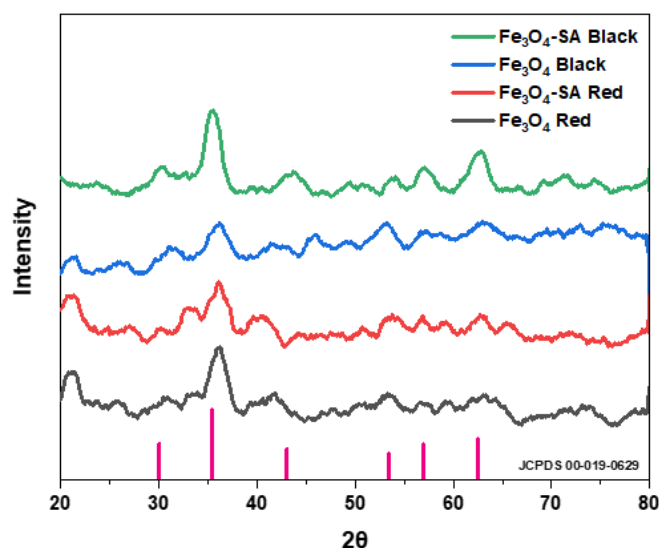


Figure 3. XRD patterns of Fe_3O_4 and Fe_3O_4 -SA particles.

The XRD patterns (Figure 3), show that the black Fe_3O_4 -SA sample (green line) exhibits the most intense and sharp peaks, indicating a higher degree of crystallinity and possibly smaller crystallite size compared to the other samples. The black Fe_3O_4 sample (blue line) shows a slightly lower peak intensity, potentially due to the absence of stearic acid modification, which might influence crystallinity and surface properties. On the other hand, the red Fe_3O_4 -SA sample (red line) and unmodified red Fe_3O_4 (black line) exhibit broader, less intense peaks, suggesting larger crystallite sizes or reduced crystallinity, likely due to different synthesis conditions, such as higher pH levels during particle formation. The broader peaks also indicate a less ordered crystalline structure, which could influence the



magnetic properties and stability of the particles in applications such as liquid marbles or gas sensing.

The comparison between the red and black samples highlights the influence of pH control during synthesis. The black samples, synthesized under controlled pH conditions, have more defined crystalline structures, as evidenced by sharper peaks in the XRD patterns. In contrast, the red samples, synthesized without strict pH control, show lower crystallinity, which could affect their performance in practical applications, such as magnetic responsiveness and structural stability when used in liquid marbles.

Contact Angle Measurements

The contact angle measurements demonstrated that the black $\text{Fe}_3\text{O}_4\text{-SA}$ exhibited significantly higher hydrophobicity compared to the red $\text{Fe}_3\text{O}_4\text{-SA}$. Specifically, the average contact angle for black $\text{Fe}_3\text{O}_4\text{-SA}$ was calculated to be $94.3 \pm 3.3^\circ$, while red $\text{Fe}_3\text{O}_4\text{-SA}$ had a lower contact angle of $86.1 \pm 4.5^\circ$ (Figure 4). This indicates that the black $\text{Fe}_3\text{O}_4\text{-SA}$ are more hydrophobic, contributing to their enhanced stability on water surfaces.

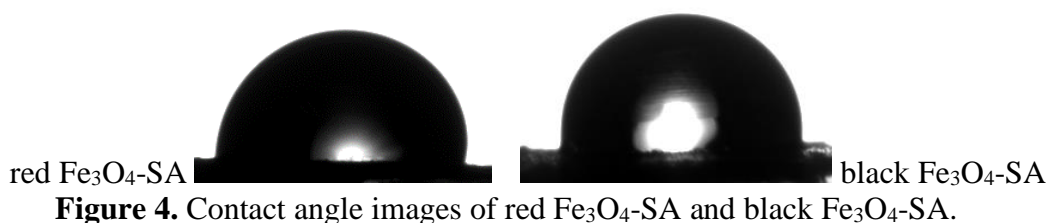


Figure 4. Contact angle images of red $\text{Fe}_3\text{O}_4\text{-SA}$ and black $\text{Fe}_3\text{O}_4\text{-SA}$.

Formation and Stability of Magnetic Liquid Marbles (MLMs)

The successful synthesis of hydrophobic $\text{Fe}_3\text{O}_4\text{-SA}$ particles was confirmed through contact angle measurements, which demonstrated their hydrophobic nature. This hydrophobicity was crucial for forming stable magnetic liquid marbles (MLMs). As shown in Figure 5, 20 μL droplets were effectively encapsulated by the $\text{Fe}_3\text{O}_4\text{-SA}$ particles, leading to the formation of both red (R-MLMs) and black (B-MLMs) marbles, illustrating the effectiveness of these particles in stabilizing MLMs.



Figure 5. Formation of Magnetic Liquid Marbles (MLMs). The upper row shows red MLMs (R-MLMs), while the lower row shows black MLMs (B-MLMs).

The stability of these MLMs was assessed under different conditions. R-MLMs demonstrated limited stability, collapsing on the water surface within 11 seconds (Figure 6a).

In contrast, B-MLMs exhibited significantly greater stability, withstanding over 5 minutes before collapsing (Figure 6b). This enhanced stability is directly correlated to the more uniform and smaller particle size distribution of the B-MLMs, as confirmed by SEM images.

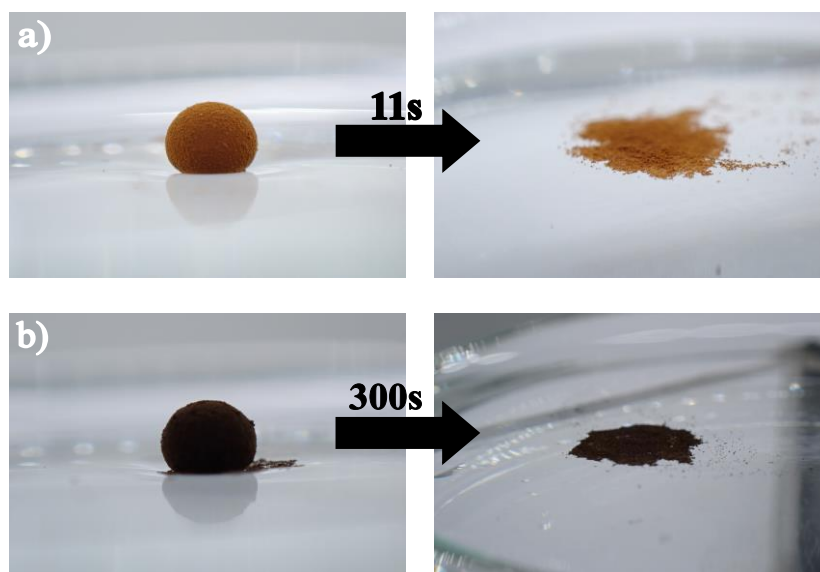


Figure 6. (a) Red magnetic liquid marble (R-MLM) collapsing on water within 11 seconds. b) Black magnetic liquid marble (B-MLM) demonstrating significantly enhanced stability on water, remaining intact for over 5 minutes before collapsing.

The instability observed in the R-MLMs is likely due to several factors, primarily related to the synthesis conditions. The red coloration suggests the possible presence of Fe_2O_3 (hematite) alongside Fe_3O_4 (magnetite) in the particle composition. Hematite, which is typically red-brown, is less magnetic and has different surface properties compared to magnetite⁶. This composition difference may lead to weaker hydrophobic interactions and less effective stabilization of the liquid marbles. Additionally, the non-controlled pH conditions during the synthesis of R-MLMs might have resulted in a broader range of particle sizes, leading to increased aggregation and uneven coating of the liquid droplets, creating weak spots that allow water to pass through, thus causing the marbles to collapse quickly. In contrast, the B-MLMs, synthesized under controlled pH conditions, exhibit more uniform particle sizes and a consistent Fe_3O_4 phase, resulting in stronger hydrophobic properties and significantly greater stability. These observations align with the SEM images and stability tests, providing a coherent explanation for the differences in the performance of R-MLMs and B-MLMs.

Demonstration of H_2S Gas Detection by B-MLMs

The B-MLMs were demonstrated for their ability to detect hydrogen sulfide (H_2S) gas in a controlled environment. During the 10-minute exposure period within a chamber containing H_2S gas at a concentration of 60 mg/L, the DMPD solution inside the B-MLMs initially displayed a pinkish-brown hue. Upon exposure to the gas, the solution within the B-MLMs underwent a distinct color change to blue (Figure 7), indicating the successful formation of methylene blue¹¹, which serves as a qualitative marker for the presence of H_2S . This color change was observed in the liquid inside the MLMs, which was visualized using a capillary tube (Figure 7). The capillary tube's narrow diameter and transparency enhanced the sensitivity and accuracy of the color observation. The observed change confirms the effectiveness of the B-MLMs in detecting H_2S . This research shows the potential application



of our new MLMs with remote controllability, allowing safe operation away from toxic gases. The quantitative analysis is undergoing based on digital image colorimetry (DIC).



Figure 7. The color change in the DMPD solution inside B-MLMs before and after exposure to H_2S gas (60 mg/L).

Conclusion:

This research demonstrates the successful synthesis of stable magnetic liquid marbles for hydrogen sulfide gas detection. The pH-controlled synthesis of Fe_3O_4 -SA particles resulted in black MLMs with enhanced stability and responsiveness compared to red MLMs. The black MLMs exhibited a distinct color change upon exposure to H_2S gas. The magnetic properties of B-MLMs allow for easy manipulation and recovery, making them suitable for various environmental applications. These findings pave the way for the development of efficient, cost-effective sensors for real-time monitoring of hazardous gases.

Acknowledgements:

Cinta Nur Ihya is grateful to ASEAN and NON-ASEAN Scholarship 2023-2024, Chulalongkorn University for providing financial support.

References:

1. Nguyen NK, Ooi CH, Singha P, Jin J, Sreejith KR, Phan HP, Nguyen NT. *Processes*. 2020;8:793.
2. Zhu R, Liu M, Hou Y, Zhang L, Li M, Wang D, Fu S. *ACS Appl Mater Interfaces*. 2020;12:17004-17017.
3. Zhao Y, Xu Z, Niu H, Wang X, Lin T. *Adv Funct Mater*. 2014;25:437-444.
4. Nguyen NK, Singha P, Zhang J, Phan HP, Nguyen NT, Ooi CH. *ChemPhysChem*. 2021;22:99-105.
5. Tyowua AT, Ahor F, Yiase SG, Binks BP. *SN Appl Sci*. 2020;2:345.
6. Sun Y, Zheng Y, Liu C, Zhang Y, Wen S, Song L, Zhao M. *RSC Adv*. 2022;12:15296-15315.
7. Zhao Y, Xu Z, Niu H, Wang X, Lin T. *Adv Mater*. 2010;22:707-710.
8. Asaumi Y, Rey M, Oyama K, Vogel N, Hirai T, Nakamura Y, Fujii S. *Langmuir*. 2020;36:13274-13284.
9. Tosun A, Erbil HY. *J Colloid Interface Sci*. 2009;333:419-424.
10. Zuluaga-Parra JD, Sánchez-Valdés S, Ramos-deValle LF, Beltrán-Ramírez FI, da-Silva L, Ramírez-Vargas E, Vázquez-Rodríguez S, Flores-Gallardo S, Méndez-Nonell J, Valera-Zaragoza M, Cabrera-Álvarez EN. *J Magn Magn Mater*. 2020;514:167169.
11. Su L, Xu Y, Tian J, Song J. *Anal Chim Acta*. 2010;675:1-5.
12. Ba A, Singh M, Ahmed S. *Adv Mater*. 2013;25:4572-4577.

13. Tian J, Hu W, Chen X, Zhang Z. Chem Commun. 2010;46:4734-4736.
14. Pla-Tolós J, Moliner-Martínez Y, Verdú-Andrés J, Casanova-Chafer J, Molins-Legua C, Campíns-Falcó P. Talanta. 2016;156-157:79-86.



REMOVAL OF REACTIVE NAVY-BLUE DYE IN SYNTHETIC SAMPLE USING A SIMPLE LABORATORY-SCALE ELECTROCOAGULATION SYSTEM

Chawinroj Kritsunankul,¹ Yanapat Thongthawee,¹ Phansiri Seniwong Na Ayuthaya,¹ Chanyud Kritsunankul,² Orawan Kritsunankul^{3,*}

¹Naresuan University Secondary Demonstration School, Phitsanulok 65000, Thailand

²Department of Natural Resources and Environment, Faculty of Agriculture Natural Resources and Environment, Naresuan University, Phitsanulok 65000, Thailand

³Department of Chemistry, Faculty of Science, Naresuan University, Phitsanulok 65000, Thailand

*e-mail: orawant@nu.ac.th

Abstract:

This research investigates the efficiency of a simple laboratory-scale electrocoagulation (EC) system for removing reactive navy-blue (rNB) dye from synthetic samples. The process was conducted in a plastic reactor containing 500 mL of 400 mg/L rNB dye and utilized four iron plate electrodes arranged in different configurations and at two interelectrode distances. Applied voltages of 6, 12, 18, and 24 V were tested, with removal times measured until the absorbance reached zero. Under optimal conditions, a parallel electrode connection, a 3 cm interelectrode distance, and an applied voltage of 24 V were selected. The results showed 100% removal of rNB dye within 20 minutes, with a current consumption of 1.05 A, a reactor temperature of 45.0 °C, a total electrode weight loss of 0.13%, sludge production of 1.9994 g/L, a color measurement of 32 ADMI, and a pH value of 11. This process was successfully applied to rNB synthetic samples. The system demonstrated high removal efficiency, rapid color removal, simplicity of operation, reduced chemical usage, and safety in equipment use. It also effectively removed commercial reactive blue, reactive indigo, direct navy-blue dyes, and their mixed blue tone colors.

Introduction:

Reactive dyes are a class of highly colored organic substances primarily used for dyeing textiles. They generally consist of four components: solubilizing, chromophoric, bridging, and reactive groups. ^[1] These dyes are termed "reactive" because their reactive group forms a covalent bond with the fiber molecules during the dyeing process, which differs from most other dyes that simply adhere to the surface of the fiber. Reactive dyes are extensively used for dyeing cellulosic fibers in the textile industry due to their favorable properties, including water solubility, ease and variety of applications, availability in different shades, brightness of colors, and excellent wash and light fastness. ^[2] High concentrations of dyes in wastewater from the textile industry are often discharged as effluent into aquatic environments, causing significant color pollution in water sources. In Thailand, the Ministry of Industry regulates wastewater quality by setting a color discharge limit of less than 300 American Dye Manufacturers Institute (ADMI) units. Untreated wastewater can have significant negative impacts on living organisms, including humans. Therefore, it is crucial to treat dye-containing wastewater effectively using eco-friendly methods. ^[3]

Various technologies and methodologies have been reported for the treatment of textile dye-containing wastewater, particularly reactive dyes. These processes involve physical, biological, and chemical systems. ^[2, 4-8] However, many of these technologies have disadvantages, such as lower efficiency, complexity, and high chemical consumption. Electrocoagulation (EC) overcomes these disadvantages and is also economically attractive. EC is an electrochemical water treatment process that uses electrical currents to remove

contaminants from water. The process involves the generation of coagulant agents in situ by the electrolytic oxidation of a sacrificial anode, usually made of iron or aluminum, when an electric current is passed through the water. [9-11]

In this work, a simple laboratory-scale EC system was investigated for the color reduction of reactive navy-blue (rNB) dye from synthetic samples, with a focus on its removal efficiency. The investigation aimed to ensure that this EC system was easy to operate, safe to use, required minimal chemicals, and provided rapid results.

Methodology:

A stock solution of 5000 mg/L reactive navy-blue dye (referred to as rNB, color code: C.I. Reactive Blue 194, INDAFIX, KTB Textile Co., Ltd.) was prepared in distilled water. Working standard solutions were freshly prepared by diluting the stock solution with distilled water.

A simple laboratory-scale EC system (an example of a parallel connection is shown in Figure 1) consisted of a plastic box (8.7 cm width × 12.0 cm length × 8.7 cm height, containing 500 mL of rNB solution), four iron-sheet electrodes arranged in different configurations, a thermometer, a switching DC power supply (KPS3010D, Wanptek), a magnetic bar, and a magnetic stirrer. Each iron sheet was fixed at a constant interelectrode distance. This system was designed by Chanyud Kritsunankul. The DC power supply was used to apply constant voltage values. A UV-Visible spectrophotometer (Specord 200 Plus, Analytik Jena) was employed to study the absorption spectra and the linear range of the calibration graph. A UV-Visible spectrophotometer (Genesys 30, Thermo Scientific) was used to measure absorbance and analyze dye removal.

The main parameters affecting dye removal efficiency (% dye removal), such as electrode connections, interelectrode distances, applied voltages, and removal times, were optimized. Various parameters were measured during the operation, including absorbance values (at 580 nm), applied voltages (V), current consumption (amperes; A), temperatures (°C), pH values, total weight loss of the electrode (%), sludge production (g/L), and color measurement values (ADMI). The dye color removal efficiency (% dye removal) was calculated using the following equation:

$$\text{Dye removal (\%)} = [(C_o - C_t)/C_o] \times 100$$

Where C_o and C_t represent the dye color concentrations before and after the removal process, respectively.

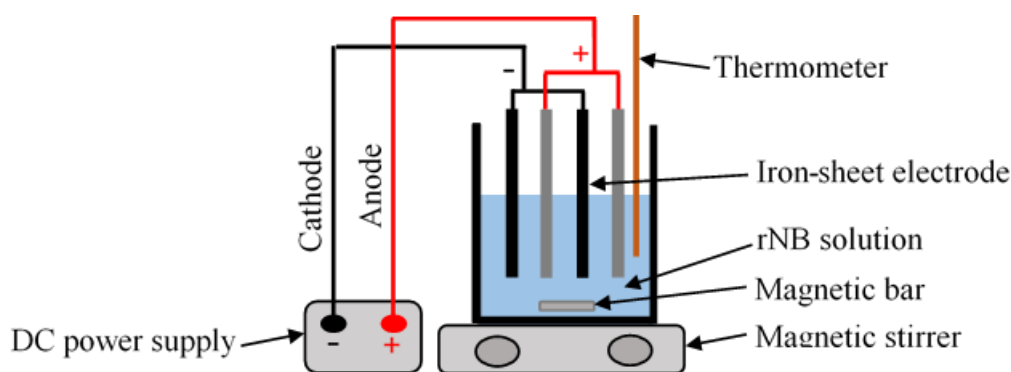


Figure 1 A simple laboratory-scale EC system with a parallel electrode connection.



Results and Discussion:

The absorption spectra of standard solutions containing 10, 20, 40, 60, 80, 100, 200, 400, 600, 800, and 1000 mg/L of rNB dye were recorded at wavelengths ranging from 200 to 800 nm, with a scan rate of 50 nm/s. The maximum absorption for rNB dye was found to occur at 580 nm (Figure 2(a)). A linear calibration graph was established for the concentration range of 10-400 mg/L ($y = 0.0046x + 0.0763$, $R^2 = 0.9951$) (Figure 2(b)), with a limit of detection (LOD) of 0.23 mg/L (calculated as $LOD = 3S_0$, where S_0 represents the standard deviation of the y-intercept).

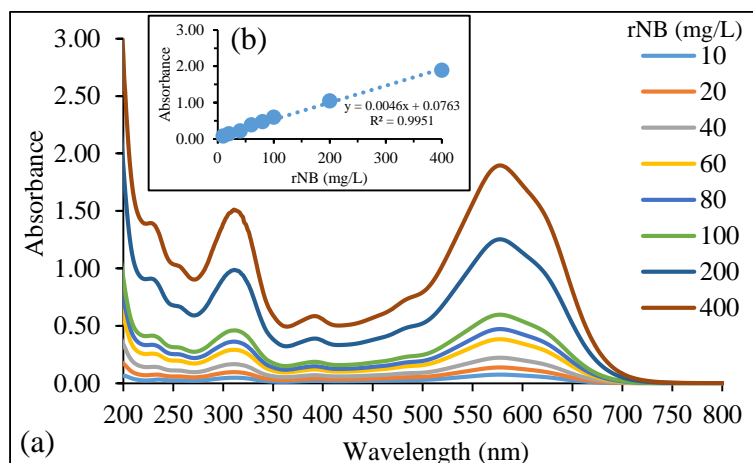


Figure 2. (a) Absorption spectra and (b) calibration graph for 10-400 mg/L of rNB dye.

To enhance and evaluate removal efficiency, the effects of electrode connection types (parallel, series, and bipolar), interelectrode distances (2 and 3 cm), applied voltages (6, 12, 18, and 24 V), and removal times were investigated. For this investigation, a 500 mL solution of 400 mg/L rNB dye (with an initial color measurement value of 3067 ADMI) was used throughout the experiment.

In Figure 3(a), after the treatment process (with constant applied voltage of 12 V and interelectrode distance of 2 cm), it was observed that the dye color reduction with the parallel electrode connection was more efficient and faster compared to the series and bipolar electrode connections. With the parallel connection, the dye removal efficiency for rNB reached 100% within 40 minutes. In comparison, the series and bipolar connections achieved dye removal efficiencies of over 85% (within 115 minutes) and over 87% (within 120 minutes), respectively. Although the parallel connection had higher current consumption and sludge production (ranging from 0.30-0.34 A and 1.48 g/L), compared to the series (ranging from 0.04-0.05 A and 0.75 g/L) and bipolar connections (ranging from 0.04-0.05 A and 0.85 g/L), it was also noted that the reactor temperature was higher for the parallel connection (ranging from 33.5 to 35.7°C) compared to the series (ranging from 31.0 to 32.5°C) and bipolar connections (ranging from 31.0 to 32.0°C) (Figure 3(b) and Figure 3(c)). The results indicate that the current density across all electrodes in the parallel connection was higher than in the series and bipolar configurations. Higher current density increases the production of Fe^{2+} ions at the anode and OH^- ions along with H_2 gas at the cathode. Consequently, the parallel connection enhances the rate of electrochemical reactions, improving the performance of electrocoagulation processes for removing rNB dye. Based on these findings, the parallel electrode configuration was selected for further experiments.

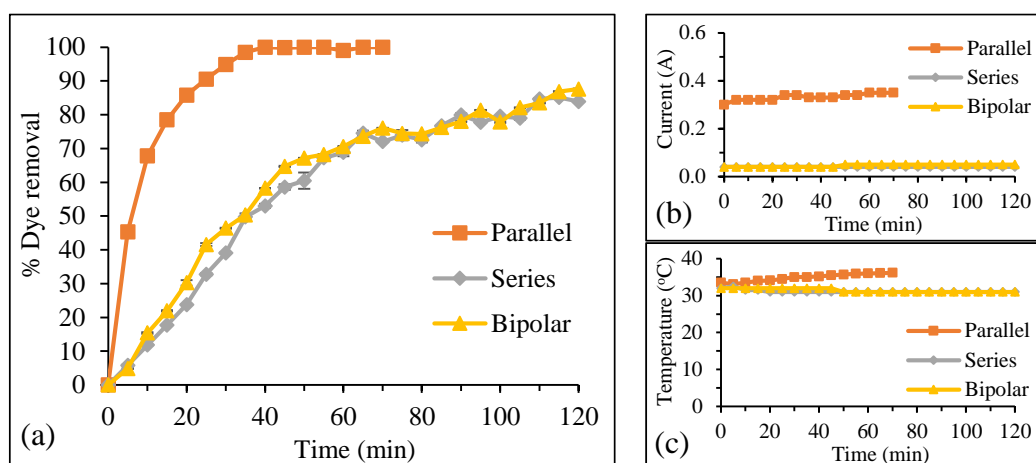


Figure 3. Effect of the electrode connections on (a) dye removal efficiency (%), (b) current consumption (A), and (c) reactor temperature (°C).

In Figure 4(a), after the removal process (with a constant parallel connection and 12 V applied voltage), it was found that dye color reduction at interelectrode distances of 2 cm and 3 cm yielded similar results, with 100% dye removal achieved within 40 minutes. The current consumption ranged from 0.30-0.34 A at 2 cm and 0.31-0.37 A at 3 cm (Figure 4(b)), while the reactor temperature ranged from 32.0-35.7°C at 2 cm and 32.0-35.1°C at 3 cm (Figure 4(c)). Sludge production was 1.48 g/L at 2 cm and 1.50 g/L at 3 cm. Though during the first 30 minutes of the removal process, the 2 cm interelectrode distance achieved slightly faster dye removal than the 3 cm distance, due to a stronger electric field and more efficient ion migration. Based on these results and considering the operational convenience for solution collection at each reaction time, a 3 cm interelectrode distance was selected for further experiments.

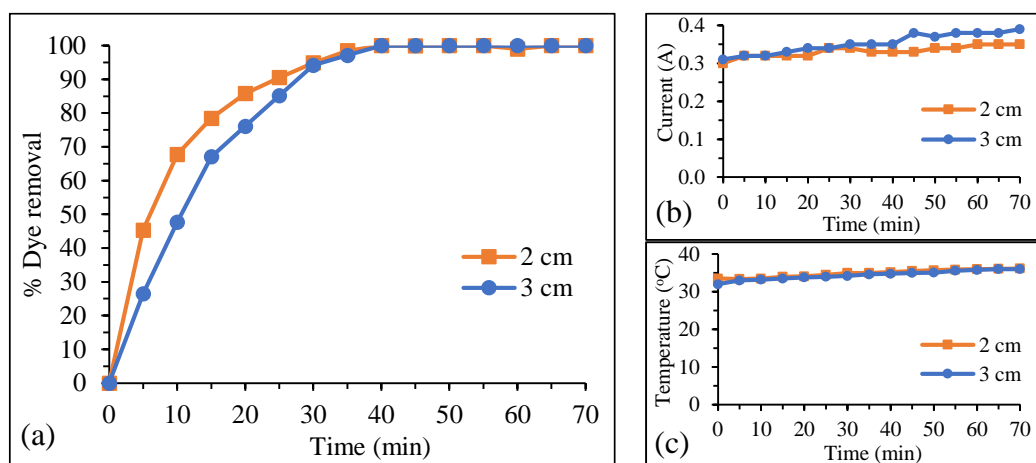


Figure 4. Effect of interelectrode distances in the parallel electrode connection on (a) dye removal efficiency (%), (b) current consumption (A), and (c) reactor temperature (°C).

In Figure 5(a), after the removal process (with constant parallel connection and 3 cm interelectrode distance), it was found that dye color reduction at 24 V applied voltage was more efficient and faster compared to 18, 12, and 6 V. At 24 V, the dye removal efficiency for rNB reached 100% within 20 minutes. In comparison, at 18 V, 12 V, and 6 V, the



efficiencies were 100% within 25 minutes, 100% within 40 minutes, and over 92% within 100 minutes, respectively. Moreover, 24 V resulted in higher current consumption (A) (Figure 5(b)), higher reactor temperature ($^{\circ}\text{C}$) (Figure 5(c)), higher sludge production (g/L), greater total weight loss of the electrode (%), and higher ADMI values compared to 18, 12, and 6 V. All efficiency results are summarized in Table 1. At 24 V with a current consumption of 1.05 A, a removal time of 20 minutes, and a dye volume of 500 mL, the electrical energy consumption was 16.8 kWh/m³, with an estimated cost of 67.2 baht/m³.

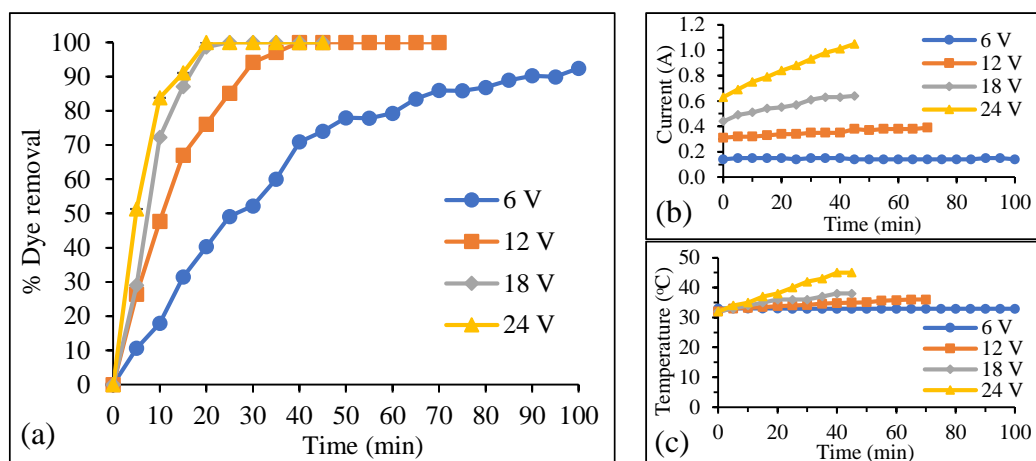


Figure 5. Effect of the applied voltages of parallel electrode connection on the; (a) the dye removal efficiency (%), (b) the current consumption (A) and (c) the reactor temperature ($^{\circ}\text{C}$).

Table 1. Summary of efficiency results for rNB color reduction using the simple laboratory-scale EC system (with varying applied voltages, a constant parallel connection, and a 3 cm interelectrode distance).

| Parameters | Applied voltages (V) | | | |
|---|----------------------|-----------|-----------|-----------|
| | 6 | 12 | 18 | 24 |
| Dye removal efficiency (%): | > 92 | 100 | 100 | 100 |
| Removal time (minutes): | 100 | 40 | 25 | 20 |
| Current consumption (A): | 0.14/0.15 | 0.31/0.39 | 0.44/0.64 | 0.63/1.05 |
| (before/after of removal process) | | | | |
| Reactor temperature ($^{\circ}\text{C}$): | 32.0/33.0 | 32.0/36.0 | 32.0/38.0 | 32.0/45.0 |
| (before/after of removal process) | | | | |
| Total weight loss of the electrode (%) ^a : | 0.10 | 0.10 | 0.11 | 0.13 |
| (before/after of removal process) | | | | |
| Sludge production (g/L) ^b : | 0.7904 | 1.4992 | 1.8302 | 1.9994 |
| (after of removal process) | | | | |
| Color measurement (ADMI): | 3067/166 | 3067/32 | 3067/32 | 3067/32 |
| (before/after of removal process) | | | | |
| pH values: | 9/10 | 9/10 | 9/11 | 9/11 |
| (before/after of removal process) | | | | |

^a Total weight loss of the electrode (%) = [(Total initial weight (g) – Total final weight (g)) x 100] / (Total initial weight (g)).

^b Sludge production (g/L) = (Sludge weight (g) x 500 mL) / (1000 mL).

Under the conditions of the highest % dye removal, the parallel electrode connection at 24 V applied voltage and 3 cm interelectrode distance was used for the blue tone color removal from four synthetic dye-wastewater samples. These samples included a 400 mg/L reactive blue dye (INDAFIX brand) and a 400 mg/L reactive indigo dye (from Cha Craft Studio, Ban Tunghong, Phare, without a brand name), both prepared in distilled water, as well as a 400 mg/L direct navy-blue dye (Sampoaw brand). Another sample, prepared in tap water, contained a mixed color of three dyes (100 mg/L of each). Results were compared with a 400 mg/L reactive navy-blue dye (INDAFIX) in distilled water and are shown in Figure 6. For the reactive blue dye (detected at 670 nm), the dye removal was 100% within 20 minutes (43 ADMI after color removal). For the reactive indigo dye (detected at 690 nm), the dye removal was 99.68% within 80 minutes (29 ADMI after color removal). For the direct navy-blue dye (detected at 542 nm), the dye removal was 99.70% within 15 minutes (85 ADMI after color removal). For the mixed blue tone dye (detected at 610 nm), the dye removal was 99.68% within 80 minutes (87 ADMI after color removal). The differences in removal times may be attributed to the molecular structure of each dye.

The EC system using the parallel electrode connection can operate until one pair of iron-sheet electrodes fails or becomes less efficient. Although the EC system can continue operating with the remaining electrodes, a new pair of iron-sheet electrodes will need to be replaced to meet efficiency requirements.

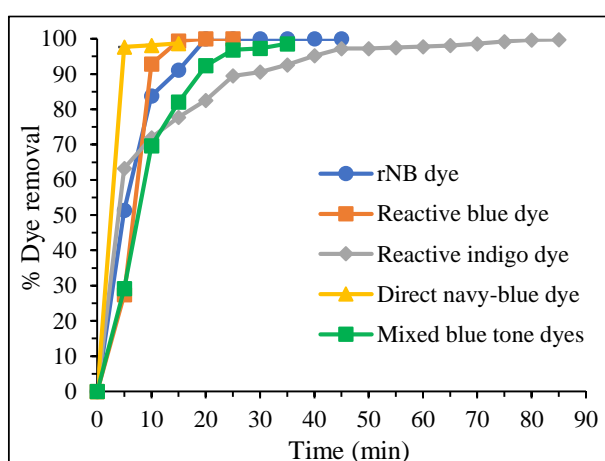


Figure 6. Application of the proposed EC system for the removal of synthetic samples of reactive navy-blue dye (rNB), reactive blue dye, reactive indigo dye, direct navy-blue dye, and mixed blue-tone dye.

Conclusion:

This research aimed to investigate the electrocoagulation process using a simple laboratory-scale system for removing color from a 400 mg/L reactive navy-blue dye (rNB) in a synthetic sample. The results indicate that this system, utilizing a parallel electrode connection, a 3 cm interelectrode distance, and an applied voltage of 24 V, achieved the highest removal efficiency (100% dye removal), rapid color removal (within 20 minutes), and offered benefits such as simplicity of operation, reduced chemical usage, and safety in equipment use. After the removal process, the system produced less sludge, consumed fewer electrodes, and resulted in a lower color value (32 ADMI). This system also successfully removed commercial reactive blue, reactive indigo, direct navy-blue dyes, and their mixed blue tone



colors. It could serve as an alternative method for removing blue tone dyes in community enterprises involved in dyeing blue clothes.

Acknowledgements:

The author would like to thank the Department of Chemistry, Faculty of Science, and the Department of Natural Resources and Environment, Faculty of Agriculture, Natural Resources and Environment, Naresuan University, for providing the instruments and facilities. Special thanks also go to Naresuan University Secondary Demonstration School for their partial support of this research.

References:

1. Śmigiel-Kamińska D, Wąs-Gubała J, Stepnowski P, Kumirska J. *Molecules*. 2020; 25:5435.
2. Nachiyar CV, Rakshi AD, Sandhya S, Jebasta NBD, Nellore J. *CSCEE*. 2023;7:100339.
3. Al-Tohamy R, Ali SS, Li F, Okasha KM, Mahmoud YA-G, Elsamahy T, Jiao H, Fu Y, Sun J. *Ecotoxicol. Environ. Saf.* 2022;231:113160.
4. Aksu Z. *Process Biochem.* 2005;40:997-1026.
5. Gül UD. *Water SA*. 2013;39:593-598.
6. Xu XR, Li HB, Wang WH, Gu JD. *Chemosphere*. 2005;59:893-898.
7. Bilgi S, Demir C. *Dyes Pigm.* 2005;66:69-76.
8. Rezaee A, Ghaneian MT, Khavanin A, Hashemian SJ, Moussavi G, Ghanizadeh G, Hajizadeh E. *Iran J Environ. Health. Sci. Eng.* 2008;5:95-100.
9. Hakizimana JN, Chafi BGM, Stiriba Y, Vial C, Drogui P, Naja J. *Desalination*. 2017;404:1–21.
10. Mohammed AS, El-Gendi A, El-Khatib KM, Hassan SH. *Wat. Ener. Food. Env. J.* 2021;2:41- 53.
11. Gasmi A, Ibrahim S, Elboughdiri N, Tekaya MA, Ghernaout D, Hannachi A, Mesloub A, Ayadi B, Kolsi L. *ACS Omega*. 2022;7:22456–22476.



SIMPLE OXALATE-SELECTIVE NAKED-EYE AND SPECTROPHOTOMETRIC DETERMINATION BASED ON ALUMINIUM-INDICATOR COMPLEX

Phetlada Kunthadee*, Rattikon Yong, Jiraporn Kitikul

Program in Chemistry, Faculty of Science, Maejo University, Chiang Mai 50290, Thailand

*e-mail: phetlada@mju.ac.th

Abstract:

Indirect determination of anion by indicator displacement in a complex between aluminium(III) and xylenol orange (XO) has been carried out using the naked-eye detection along with UV-Visible spectroscopy. A red-pink complex solution of Al_2XO was observed at pH 3 which absorb the light at the maximum wavelength of 554 nm for studying anion selectivity and the linear range of target anion. The most selective anions were found to be oxalate and pyrophosphate, considering from the decreasing concentration of Al_2XO together with the return of yellow solution of XO free ligand at 436 nm in the absorption spectra. However, in case of pyrophosphate, it took longer than 2 hours to process the color change at low concentrations. The narrow linear range of pyrophosphate was also observed and not suitable for the quantitative determination. The working concentration range of oxalate was obtained in the range of 8.0×10^{-6} – 7.0×10^{-5} M after 30 minutes of indicator substitution. The limit of detection (LOD) was 6.6×10^{-6} M and the limit of quantitation (LOQ) was 1.5×10^{-5} M of oxalate. Stoichiometric ratio of Al(III) : oxalate was 2 : 3 after the indicator displacement. Moreover, repeatability and reproducibility confirmed a good precision of oxalate analysis with 0.159% and 0.322% RSD, respectively. The proposed method was then applied for the determination of oxalate in 7 water samples and beverages. Oxalate content was expectedly not detected in drinking water, ultrapure water, and also tap water, whereas mineral water, kombucha tea, guava juice and carrot juice contained the concentrations of oxalate with the percentage recoveries in acceptable range of 80.5–91.5%.

Introduction:

It is of great interest to develop a rapid, simple, cost-friendly and sensitive method for various anions. Recently, more attention has been paid to indicator displacement assays (IDAs) due to the good selectivity, high sensitivity and visibility.^{1,2} IDA approaches can detect anions, amino acids, and other functional group molecules²⁻⁶ and have been considered as an alternative technique besides the developed methods such as ion chromatography (IC)⁷, high performance liquid chromatography (HPLC)^{8,9}, gas chromatography (GC)^{10,11}, chemiluminescence¹², fluorescent detection¹³⁻¹⁵, and enzyme assays^{16,17}, etc. Xylenol orange (XO) is one of metallochromic indicator, most commonly used as a tetrasodium salt which appears between yellow (in acid) and purple (in base) depending on the pK_a value.^{18,19} It was reported from the previous work that Al^{3+} could bind strongly to XO and introduce a regulated change in color and UV-Visible absorption spectrum shift at pH 3.²⁰⁻²² Therefore, we herein report a rapid naked-eye and spectrophotometric method for the quantitatively determination of target anion using the mixed solution of Al^{3+} and XO in pH 3 via IDA process as proposed in Figure 1.²³

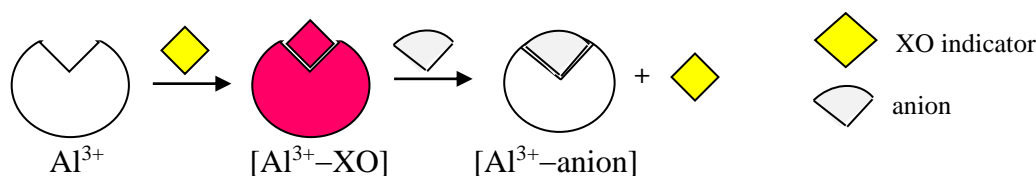


Figure 1. IDA mechanism for the detection of selective anion.

Methodology:

Materials

The chemicals used were of analytical reagent grade. All solutions were made with ultrapure water (Milli Pore/Milli-Di 18.2 MΩ·cm). The stock solution of xylenol orange (XO) indicator were 0.01 M and then adjusting the pH to 3.0 by adding HCl. The stock solution of $\text{Al}_2(\text{SO}_4)_3 \cdot 18\text{H}_2\text{O}$ were 0.01 M. The stock solutions of tested anion; Cl^- , Br^- , I^- , NO_2^- , NO_3^- , SO_3^{2-} , SO_4^{2-} , HCO_3^- , CH_3COO^- , $\text{C}_2\text{O}_4^{2-}$, H_2PO_4^- and $\text{P}_2\text{O}_7^{4-}$ were 0.01 M. The working solutions of all these reagents were diluted from the stock solutions with ultrapure water.

Equipments

pH determinations were performed using a Metrohm-913 pH meter. UV-Visible absorption spectra were recorded on Hitachi-UH5300 spectrophotometer.

Measurement procedure

The pH 3.0 containing 25 μL of 0.01 M XO and 25 μL of 0.01 M $\text{Al}_2(\text{SO}_4)_3$ solution was initial examined using naked-eye detection and UV-vis spectrophotometric measurements in the range of 350-700 nm wavelength, then 200 μL of 0.01 M tested anions were added separately for 30, 60, and 120 mins to investigate the most selective anion and response time.

The control Al_2XO complex solution containing 0.5 mM XO (pH 3.0) and 0.5 mM $\text{Al}_2(\text{SO}_4)_3$ at the equal volume were prepared, followed by adding the solution of 0.5 and 1.0 mM of target anion to make the concentration range of 5.0×10^{-7} to 3.0×10^{-4} M for linearity test. The naked-eye detection was carried out after the solutions had been mixed and left for 30-60 mins to reach the equilibrium of reaction and then UV-vis spectra were recorded. Stoichiometric molar ratio of Al^{3+} : target anion was also investigated by adding different volumes of 0.5 mM target anion into the Al_2XO complex solution at pH 3.0 in order to predict the indicator displacement mechanism. The limit of detection (LOD) and limit of quantitation (LOQ) were studied by preparing at least 7 replicates of the mixed solution between 0.5 mM XO and 0.5 mM $\text{Al}_2(\text{SO}_4)_3$ as the blank solution. LOD (mean of sample blank value+3SD) and LOQ (mean of sample blank value+10SD) were then calculated using the calibration curve of target anion. Repeatability and reproducibility were examined in 12 replicates by preparing the Al_2XO complex solution in the presence of 5.0×10^{-5} M of target anion to ensure the precision of method.

Real samples analysis was carried out by preparing the control Al_2XO complex solution and then adding 7 water samples and beverages as follows; drinking water, ultrapure water, tap water, mineral water, kombucha tea, guava juice and carrot juice (Notes; fruit juices were obtained by blending, centrifuging, and filtering through Whatman paper), to determine the target anion content and percentage recovery was calculated in triplicates by using the spiking method. The 1.0×10^{-5} M of standard target anion was spiked into the mixed solution of Al_2XO complex and 200 μL of real sample.



Results and Discussion:

Figure 1 shows the change in color of the solution from yellow to red-pink due to the complex formation between XO and Al^{3+} at pH 3.0. The maximum absorption at 436 nm of free XO indicator was shifted to 554 nm when the $\text{Al}_2(\text{SO}_4)_3$ solution was added into the pH 3.0 containing XO solution, indicating the presence of Al_2XO complex.

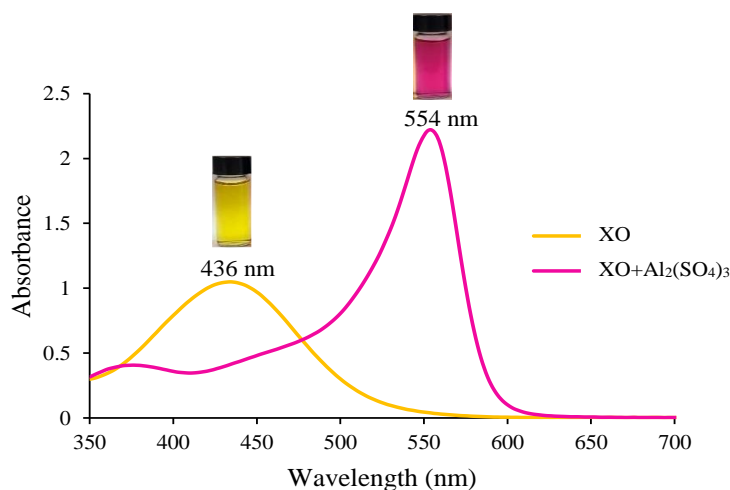


Figure 1. Color and UV-vis spectra of XO free ligand (yellow) and Al_2XO complex (red-pink) solutions.

When adding 0.01 M of tested anions; Cl^- , Br^- , I^- , NO_2^- , NO_3^- , SO_3^{2-} , SO_4^{2-} , HCO_3^- , CH_3COO^- , $\text{C}_2\text{O}_4^{2-}$, H_2PO_4^- and $\text{P}_2\text{O}_7^{4-}$. The most selective anions were found to be pyrophosphate ($\text{P}_2\text{O}_7^{4-}$) and oxalate ($\text{C}_2\text{O}_4^{2-}$), considering from the disappearance of Al_2XO red-pink color along with the return of yellow solution of XO free ligand (Figure 2).

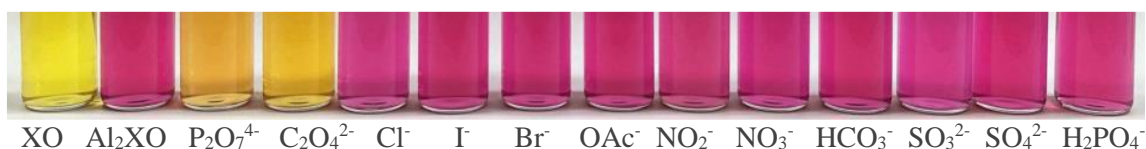


Figure 2. Color photograph of the XO free ligand, Al_2XO complex, and the mixture of Al_2XO with various anions at pH 3.

However, oxalate ($\text{C}_2\text{O}_4^{2-}$) exhibited the good response time to complete the indicator displacement process compare to pyrophosphate ($\text{P}_2\text{O}_7^{4-}$). The quick return of yellow solution indicated the selectivity of $\text{C}_2\text{O}_4^{2-}$ to substitute XO ligand and bind to Al^{3+} effectively.



Figure 3. Effect of time on the indicator displacement process.

The linearity of $\text{P}_2\text{O}_7^{4-}$ and $\text{C}_2\text{O}_4^{2-}$ were further investigated in the concentration range of 5.0×10^{-7} to 3.0×10^{-4} M of target anions. Figure 4a shows the narrow linear range of $\text{P}_2\text{O}_7^{4-}$ in the UV-vis spectra and therefore not suitable for the quantitative determination. The addition of $\text{C}_2\text{O}_4^{2-}$ into the complex solution led to the gradually decrease in red-pink color and absorbance at 554 nm, as increasing the concentration of $\text{C}_2\text{O}_4^{2-}$. The blue shift from 554 to nearly 436 nm illustrated in Figure 4b indicating the return of free XO after the indicator displacement by $\text{C}_2\text{O}_4^{2-}$ into the original complex.²⁰ The linear concentration range of oxalate was 8.0×10^{-6} – 7.0×10^{-5} M (Figure 5) with the calculated limit of detection of 6.6×10^{-6} M and the limit of quantitation of 1.5×10^{-5} M.

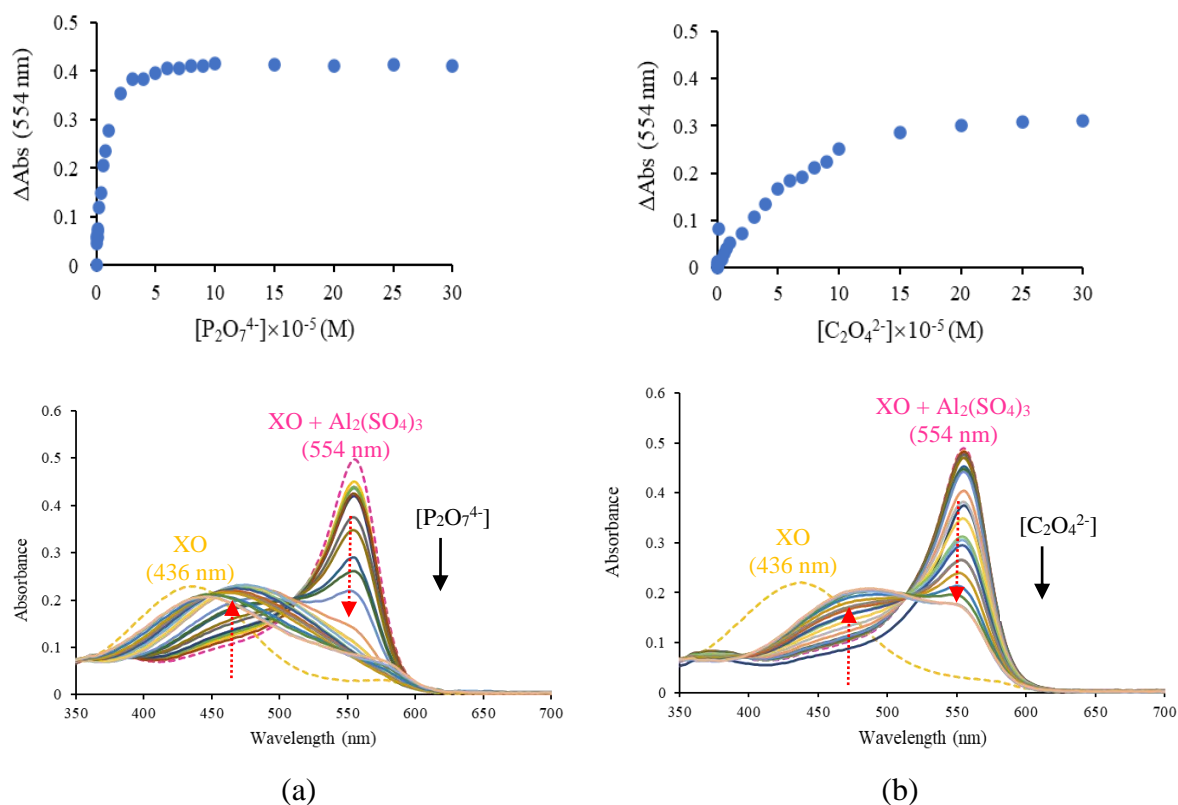


Figure 4. Linearity and UV-vis spectra of Al_2XO complex in the presence of different concentrations of (a) $\text{P}_2\text{O}_7^{4-}$ and (b) $\text{C}_2\text{O}_4^{2-}$

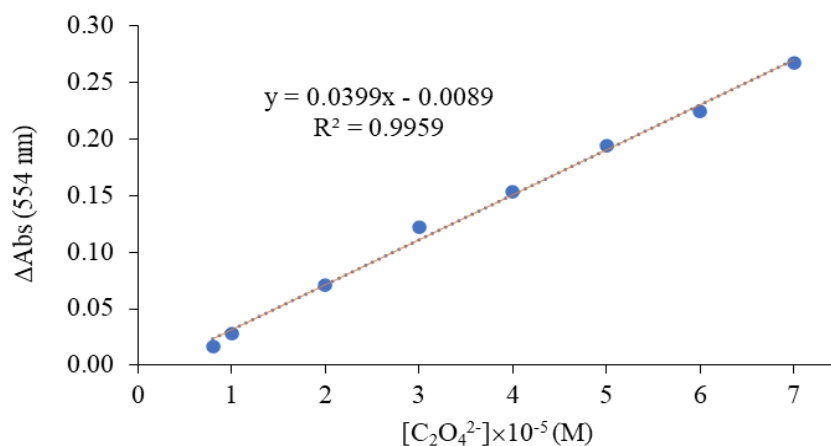


Figure 5. Calibration curve of oxalate ($\text{C}_2\text{O}_4^{2-}$)



Stoichiometric ratio of $\text{Al}^{3+} : \text{C}_2\text{O}_4^{2-}$ was 2 : 3 as presented in Figure 6 due to the chelation of stronger bidentate $\text{C}_2\text{O}_4^{2-}$ ligand¹⁹⁻²⁰, leading to the indicator displacement in Al_2XO complex.

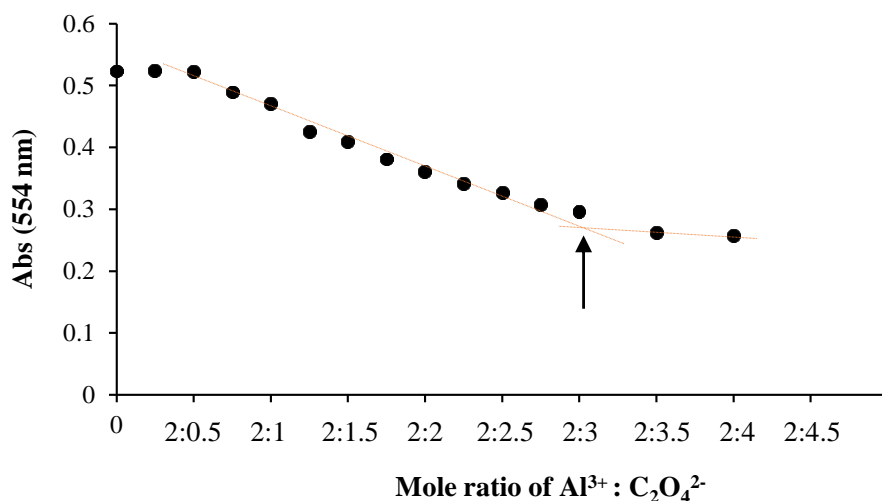


Figure 6. Stoichiometric ratio of $\text{Al}^{3+}:\text{C}_2\text{O}_4^{2-}$

Repeatability and reproducibility confirmed a good precision of oxalate analysis with 0.159% and 0.322%RSD, respectively. The proposed method was furthered applied for the determination of oxalate in real water samples and beverages. The low volume of filtered sample was added into the control Al_2XO complex. The naked-eye detection of real samples illustrated in Figure 7 that the original color of tea and juice samples did not affect the determination of oxalate.

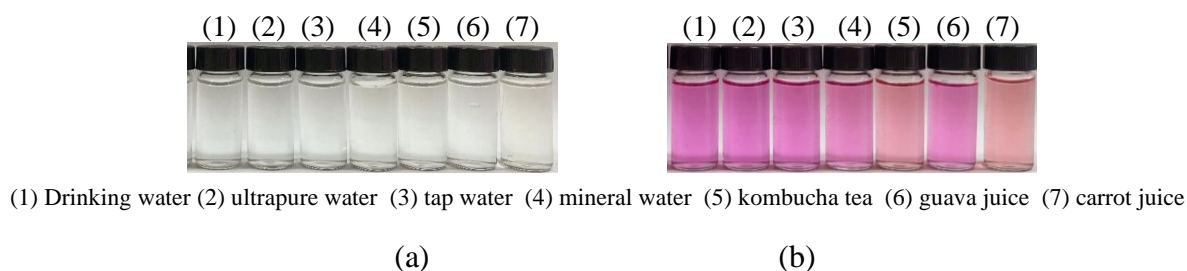


Figure 7. Color photograph of (a) water samples and beverages and (b) the mixture of Al_2XO complex with the samples at pH 3.

Table 1 shows the concentrations of $\text{C}_2\text{O}_4^{2-}$ found in mineral water, kombucha tea, guava juice and carrot juice, while not detected in drinking water, ultrapure water, and tap water. The percentage recoveries in acceptable range of 80.5–91.5% were obtained using the developed method after triplicate measurements.

Table 1. Analysis of oxalate ($\text{C}_2\text{O}_4^{2-}$) in real samples by the proposed method*.

| Samples | $\text{C}_2\text{O}_4^{2-}$ added ($\times 10^{-5}$ M) | $\text{C}_2\text{O}_4^{2-}$ found ($\times 10^{-5}$ M \pm SD) | Recovery (%) |
|-----------------|--|---|-----------------|
| Drinking water | - | 0.38 ± 0.02 | ND** |
| Ultrapure water | - | 0.46 ± 0.03 | |
| Tap water | - | 0.45 ± 0.02 | |
| Mineral water | - | 2.33 ± 0.02 | 80.56 |
| | 1.0 | 3.14 ± 0.04 | |
| Kombucha tea | - | 6.44 ± 0.02 | 91.54 |
| | 1.0 | 7.35 ± 0.01 | |
| Guava juice | - | 2.17 ± 0.01 | 88.69 |
| | 1.0 | 3.06 ± 0.01 | |
| Carrot juice | - | 7.41 ± 0.02 | 91.56 |
| | 1.0 | 8.33 ± 0.01 | |

*Triplicate experiments (n = 3).

Not Detected ($\text{C}_2\text{O}_4^{2-}$ found lower than LOD)Conclusion:**

Indirect determination of oxalate ($\text{C}_2\text{O}_4^{2-}$) anion by indicator displacement in a complex between Al^{3+} and XO indicator has been proposed in this work and studied using the naked-eye detection and UV-Visible spectroscopic method. $\text{C}_2\text{O}_4^{2-}$ could replace and bind effectively to Al^{3+} with a response time of 30 minutes, leading to the decrease in absorbance of Al_2XO complex, changing in color from red-pink (554 nm) to yellow (436 nm) as increasing of the concentration of oxalate. The working concentration range were 8.0×10^{-6} – 7.0×10^{-5} M with the calculated LOD of 6.6×10^{-6} M and LOQ of 1.5×10^{-5} M. The simple proposed method could be applied in real water samples and beverages with the satisfying percentage recoveries.

Acknowledgements:

This work was supported in part from the Faculty of Science, Maejo University, Chiang Mai, Thailand.

References:

1. Nguyen BT, Anslyn EV. Coordination Chemistry Reviews. 2006;250(2):3118–3127.
2. Liu X, Ngo HT, Ge Z, Butler SJ, Jolliffe KA. Chemical Science. 2013;4:1680–1686.
3. Qian S, Lin H. Analytical Bioanalytical Chemistry. 2014;406:1903–1908.
4. Watchasit S. Burapha Science Journal. 2017;22(3):464-480.
5. Zepeda DLM, González BM, Hernández MLÁ, Rodríguez IJB, Néstor ARV, Guzmán FC, Espinosa RMG, García JV, González AD. Dyes and Pigments. 2021;188:109239.
6. Lu L, Shao X, Lin X, Ding L, Song B, Sun J. Tb3+-xylenol orange complex-based colorimetric and luminometric dual-readout sensing platform for dipicolinic acid and metal ions. Chinese Chemical Letters. 2023, 34, 107203.
7. Nozal MJD, Bernal JL, Diego JC, Gómez LA, Ruiz JM, Higes M. Journal of Chromatography A. 2000;881:629-638.
8. David TAN, Skotty R. Journal of Chromatography B. 1995;665:27–36.
9. Skotty DR, Lee WY, Nieman TA. Analytical Chemistry. 1996;68:1530-1535.
10. Li HH, Chai XS, Martini ND, Zhan HY, Fu SY. Journal of Chromatography A. 2008;1192:208–211.



11. Chai XS, Samp J, Song HN, Zhu HX. *Journal of Chromatography A*, 2006;1122:209–214.
12. Ruiz TP, Lozano CM, Tomas VJF. *Analytical Chimica Acta*. 2005;552:147–151.
13. Liu SY, Fang L, He YB, Chan WH, Yeung KT, Cheng YK, Yang RH. *Organic Letters*. 2005;7:5825–5828.
14. Raker J, Glass TE. *Journal of Organic Chemistry*. 2002;67:6113–6116.
15. Wu JL, He YB, Zeng ZY, Wei LH, Meng LJ, Yang TX. *Tetrahedron*. 2004;60:4309–4314.
16. Fiorito PA, Torresi SICD. *Talanta*. 2004;62:649–654.
17. Elizabeth FP, Graciliano DON, Lauro TK. *Sensors and Actuators B*. 2001;72:80–85.
18. Bishop E. *Indicators*. UK: Elsevier Science. 2013;231–235.
19. Gholivand MB, Bamdad F, Ghasemi J. *Talanta*. 1998;46:875–884.
20. Namkanya N, Kunthadee P. *Proceeding in the 8th PSRU Conference*. Phitsanulok. 2023;682–690.
21. Zolgharnein J, Shahrjerdi A, Azimi G, Ghasemi J. *Analytical Sciences*. 2009;25:1249–1253.
22. Dwyer FP, Mellor DP. *Chelating Agents and Metal Chelates*. USA: Elsevier Science. 2012;98–99.
23. Su J, Sun YQ, Huo FJ, Yanga YT, Yin CX. *The Royal Society of Chemistry*. 2010;135:2918–2923.



TRIPHENYL TETRAZOLIUM SALT-MEDIATED COLORIMETRIC DETECTION OF TRIAMCINOLONE ACETONIDE AND BETAMETHASONE 17-VALERATE

Jakrin Lohanawakul,^{1,2} Atchara Lomae,² Proespichaya Kanatharana,^{1,2,3} Panote Thavarungkul,^{1,2,3} Chongdee Thammakhet-Buranachai^{1,2,3*}

¹Division of Physical Science, Faculty of Science, Prince of Songkla University, Hat Yai, Songkhla 90110, Thailand

²Center of Excellence of Trace Analysis and Biosensor, Prince of Songkla University, Hat Yai, Songkhla 90110, Thailand

³Center of Excellence for Innovation in Chemistry, Faculty of Science, Prince of Songkla University, Hat Yai, Songkhla 90110, Thailand

*e-mail: chongdee.t@psu.ac.th

Abstract:

Corticosteroids are synthetic steroids used to treat inflammatory diseases and are commonly applied in dermatological treatments. Moreover, they can also cause the depigmenting of melanocytes. Due to this effect, corticosteroids are misused for skin whitening purposes. Misuse of corticosteroids can lead to serious side effects such as Cushing's syndrome, diabetes mellitus, and skin atrophy. Thus, this study presents a simple colorimetric reaction for monitoring the corticosteroids, including triamcinolone acetonide (TMA) and betamethasone-17 valerate (BMT). The colorimetric reaction is based on the oxidation reaction of corticosteroids with triphenyl tetrazolium salt in the presence of tetramethyl ammonium hydroxide, resulting in red-colored products monitored by UV-visible spectrophotometer. Under optimal conditions, TMA and BMT induce a rapid color change within 15 minutes with good linearity ranging from 10.0 – 250.0 mg L⁻¹ for TMA and 50.0 – 250.0 mg L⁻¹ for BMT. Additionally, this proposed colorimetry demonstrates good efficiency with the detection limit of 3.3 for TMA and 11.9 mg L⁻¹ for BMT and the quantification limits of 10.9 mg L⁻¹ for TMA and 35.9 mg L⁻¹ for BMT. This study highlights the simple and rapid colorimetric detection of TMA and BMT, which could be developed as the alternative approach for screening the misuse of these corticosteroids.

Introduction:

Corticosteroids are synthetic steroids structurally similar to natural corticoid hormones produced by the adrenal gland cortex, such as cortisol and corticosterone¹. Corticosteroids are well-known drugs primarily used to treat inflammatory diseases. Additionally, they are commonly applied in dermatological treatments such as psoriasis, dermatoses, and eczema. Corticosteroids are classified into seven groups due to their potency². However, prolonged use of corticosteroids can lead to adverse effects, including skin atrophy, cutaneous reactivity, systematic side effects, hypertension, diabetes mellitus, osteoporosis, allergic contact dermatitis, and Cushing's syndrome³. Therefore, corticosteroids must be used only for medical treatment purposes. Additionally, these corticosteroids can decrease the number of melanocytes by inhibiting cytokine or prostaglandin activity, leading to depigmentation^{4,5}. This effect has resulted in the illegal use of corticosteroids, particularly betamethasone valerate (medium potency), and triamcinolone acetonide (medium potency) in whitening cosmetic products⁶⁻⁸, despite EU regulations prohibiting their use in cosmetic products^{9,10}. Therefore, there is an urgent need for rapid and accurate methods to monitor and control these illegal uses.

Several methods for determining corticosteroids have been reported, including liquid chromatography coupled with a tandem mass spectrometer (LC-MS/MS), reverse phase-high

performance liquid chromatography with ultraviolet detection (RP-HPLC-UV) and thin-layer chromatography. LC-MS/MS can determine 10 corticosteroid targets with the detection limit ranging from 0.085-0.109 mg kg⁻¹. RP-HPLC-UV can quantify 8 corticosteroid targets with the limit of quantification between (9.0-31.3 ng mL⁻¹)¹¹. Thin-layer chromatography can detect a single corticosteroid with a detection limit of 0.061 µg spot⁻¹¹². Although these techniques offer high accuracy and sensitivity, they still have notable drawbacks, such as high costs and complicated sample preparation.

Herein, the UV-visible technique, which is simple, inexpensive, and easy to operate, has been employed for detecting corticosteroids. Several reagents such as sulfuric acid, prussian blue and triphenyl tetrazolium salt can be used to determine corticosteroids indirectly¹³. Among these, triphenyl tetrazolium salt offers rapid analysis and better sensitivity than others¹³. Therefore, this study utilized the triphenyl tetrazolium salt reagent to detect triamcinolone acetonide (TMA) and betamethasone-17 valerate (BMT). The colorimetric reaction relies on the redox reaction of corticosteroids and triphenyl tetrazolium salt, producing the triphenylformazan derivative (reduced form), which generates the red color. This proposed colorimetry exhibits good efficiency with limits of detection of 3.3 and 11.9 mg L⁻¹ for TMA and BMT, respectively.

Methodology:

Materials

Triamcinolone acetonide (TMA) and betamethasone-17 valerate (BMT) were purchased from LGC Standard Ltd. (Teddington, United Kingdom). Triphenyl tetrazolium chloride (TTZ) and tetramethyl ammonium hydroxide (TMAH) were from Sigma-Aldrich CO, Ltd. (Massachusetts, United States of America). Spectrostar Nano UV-visible spectrophotometer was obtained from BMG LabTech Ltd. (Offenburg, Germany).

Standard preparation

To prepare the corticosteroids standard, 1 mg of TMA and BMT were each dissolved in 1 mL of methanol to obtain the stock standard of 1000 mg L⁻¹. For the color reagent, triphenyl tetrazolium chloride of 334.8 mg was dissolved in 2 mL of methanol to obtain the stock standard of 500 mM. Note that the color reagent should be freshly prepared before measurement.

Colorimetric reaction

The color reagent, consisting of triphenyl tetrazolium chloride (TTZ) and tetramethyl ammonium hydroxide (TMAH), was added for 7.0 and 32.0 µL to a 96-well plate to achieve a final concentration of 80.0 mM and 40.0 mM, respectively. Then, each corticosteroid standard of 20.0 µL was added to the solution to reach a final concentration of 100.0 mg L⁻¹, and the volume was adjusted to 200.0 µL by methanol. After the reaction time reaches 15 minutes, the reaction results in a color change from colorless to red, which can be monitored by UV-Vis spectrometry with maximum absorbance at the wavelength of 480 nm.

Results and Discussion:

The colorimetric detection of TMA and BMT using TTZ as a color reagent was initially studied in 96-well plates to achieve the highest sensitivity. This color reaction is based on the redox reaction between the TTZ reagent and corticosteroid analyte in the presence of TMAH. TMAH first acts as a catalyst by deprotonating α-carbonyl of C-21 of corticosteroids, activating them for the subsequent oxidation reaction with TTZ¹⁴. TTZ, acting as an oxidizing agent, oxidizes the alcohol (-CH₂OH) functional group of corticosteroids at the C-21 position to the aldehyde (-CHO) functional group. Meanwhile, the TTZ occurs the reduction, generating its reduced form called triphenylformazan (red product), which exhibits a maximum absorbance at 480 nm^{15,16}, as illustrated in Figure 1.



Thus, the absorbance is proportional to the concentration of the corticosteroid analytes (TMA and BMT).

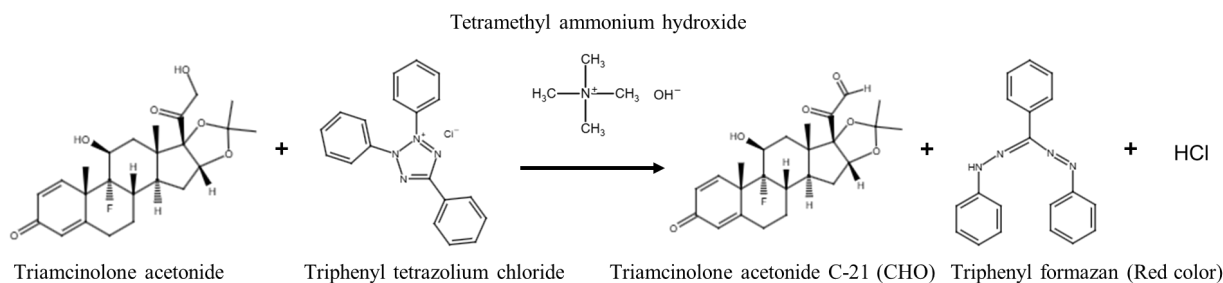


Figure 1. Illustration of the colorimetric reaction between triamcinolone acetonide (TMA), representing a corticosteroid analyte, and triphenyl tetrazolium chloride (TTZ) in the presence of the tetramethyl ammonium hydroxide (TMAH).

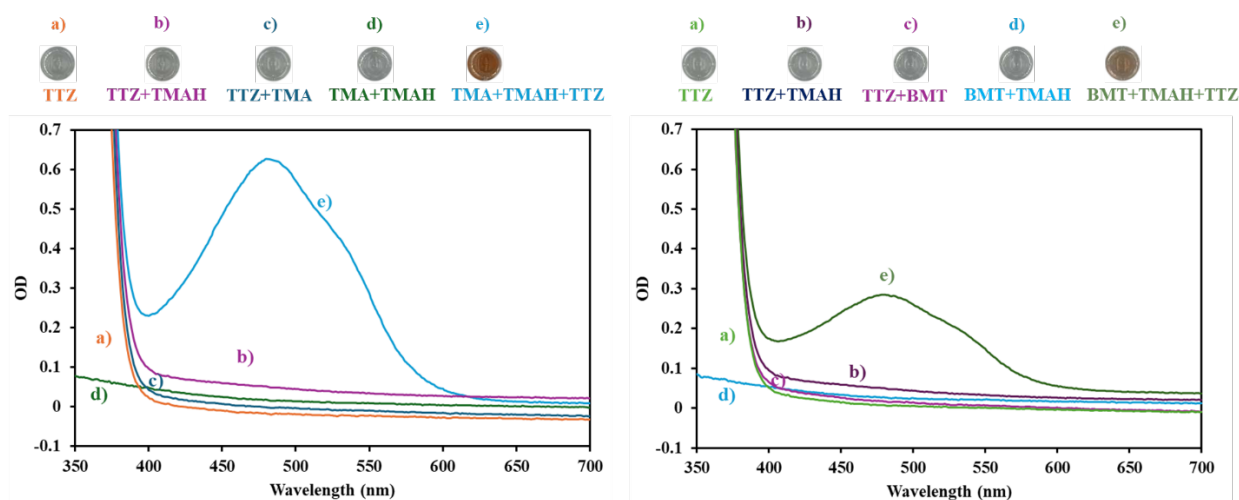


Figure 2. The UV-Vis absorption spectra of colorimetry reagent (50 mM of TTZ) and catalyst (50 mM of TMAH) in the presence of 200.0 mg L⁻¹ (A) TMA and (B) BMT were measured over the wavelength ranging from 350–700 nm.

In order to characterize the role of reagents in detecting corticosteroids, the absorption spectrum of each reagent and corticosteroid was measured to confirm their function. As shown in Figure 2, the reagent solution of TTZ (Figure 2A(a) and Figure 2B(a)) and TTZ mixed with TMAH (Figure 2A(b) and Figure 2B(b)), remained colorless, indicating no reaction occurred. Similarly, the mixture of corticosteroid analytes with only TTZ reagent, as shown in Figure 2A(c) and Figure 2B (c), also remained colorless. This result demonstrates that TTZ cannot oxidize corticosteroid analytes in the absence of catalyst TMAH due to the inactivated form of corticosteroid analytes¹⁴. Likewise, the mixture of corticosteroid analytes with only TMAH catalyst, as shown in Figure 2A(d) and Figure 2B(d), remained colorless. Although TMAH can activate the corticosteroid analytes, the absence of an oxidizing agent makes it unable to cause their oxidation reaction. Therefore, under these conditions, triphenylformazan is not produced, resulting in no absorbance at 480 nm. However, in the presence of TTZ, TMAH and corticosteroid analytes, the red color was observed with high absorbance at 480 nm, indicating the redox reaction occurring and producing triphenylformazan¹⁷.

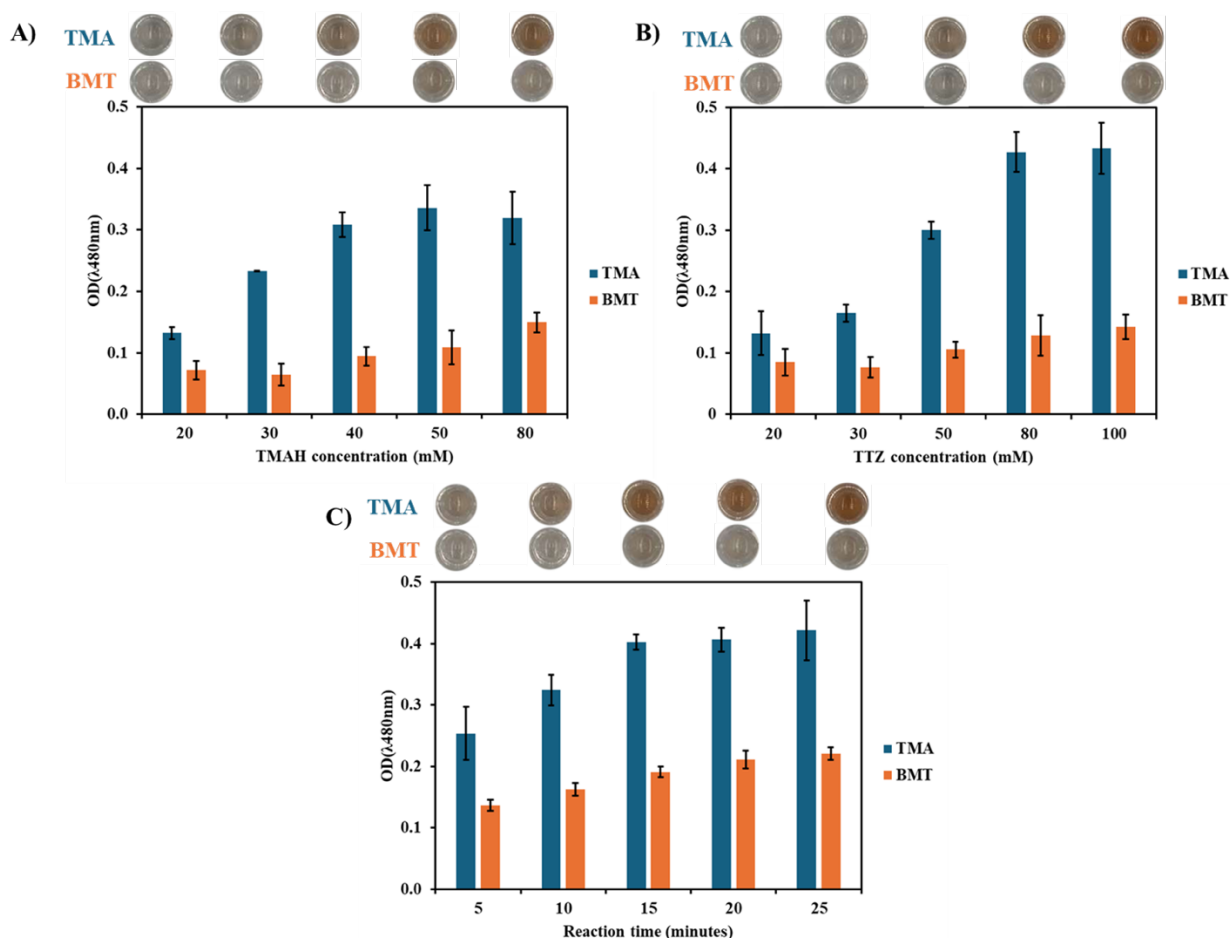


Figure 3. Optimization of key parameters affecting the colorimetry detection of TMA and BMT. Effect of (A) TMAH concentration, (B) TTZ concentration, and (C) reaction time. The blue and orange bars represent TMA and BMT analytes, respectively. The error bars indicate the standard deviation obtained from three replications.

To achieve high efficiency from the proposed colorimetry for detecting TMA and BMT, the critical parameters affecting the detection were investigated. The optimal TMAH concentration was first studied due to its role in activating the TMA and BMT analyte. The concentrations of TMA ranging from 20.0 to 80.0 mM were studied, while the concentration of TMAH and the corticosteroid analytes (TMA and BMT) was fixed at 50.0 mM and 100.0 mg mL⁻¹, respectively, with reaction time of 15 minutes. As shown in Figure 3A., the absorbance at 480 nm for both TMA and BMT analytes increased with increasing TMAH concentration up to 40.0 mM and plateaued over 40.0 mM. This result might be attributed to the limited amount of TMA and BMT available to react with TMAH. Therefore, 40.0 mM of TMAH was selected as the optimal concentration for further experiments.

Next, the TTZ concentration was investigated, ranging from 20.0 to 100.0 mM, while maintaining the TMAH and the corticosteroid analytes concentrations at 40.0 mM and 100.0 mg L⁻¹, respectively, with reaction time of 15 minutes. As demonstrated in Figure 3B, the absorbance of both analytes increased with increasing TTZ concentration to 80 mM and remained constant beyond this concentration. Thus, 80.0 mM of TTZ was selected as the optimal concentration for further study.

Finally, the reaction time was evaluated from 5 to 20 minutes with the concentration of TMAH, TTZ, and the corticosteroid analytes fixed at 40.0 mM, 80.0 mM, and 100.0 mg L⁻¹.



¹. As shown in Figure 3C, the absorbance increased to reach the maximum absorbance at 15 minutes and then plateaued over 15 minutes, indicating that the redox reaction had completed. Considering the high absorbance and rapid analysis, the reaction time of 15 minutes was chosen as the optimal condition. Moreover, these results were consistent with the visualized detection, suggesting that this method could serve as an alternative screening method for TMA and BMT via naked-eye observations.

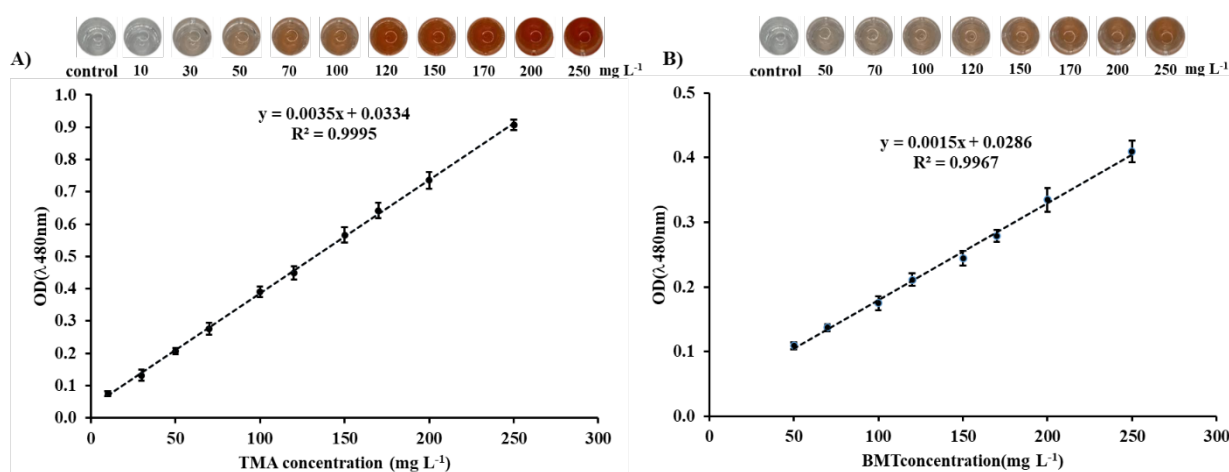


Figure 4. The calibration curve of BMT (A) and TMA (B) under the optimal condition. The error bars indicate the standard deviation obtained from three replications.

Under the optimal conditions, the analytical performance of TMA and BMT was evaluated using standard solutions at various concentrations. The results shown in Figure 4A and 4B, the absorbance at 480 nm increased with the increase in the concentration of BMT and TMA. The absorbance was directly proportional to the TMA concentration in the range of 10.0-250.0 mg L⁻¹ and the BMT concentration in the range of 50.0-250.0 mg L⁻¹. The detection limits, calculated using $3.3\sigma/\text{slope}$ (where σ is the standard deviation of intercept of a calibration curve, and the slope is the slope of the calibration curve), were found to be 3.3 and 11.9 mg L⁻¹ for TMA and BMT, respectively. The quantification limits ($10\sigma/\text{slope}$) of TMA and BMT were found to be 10.9 and 35.9 mg L⁻¹, respectively. These absorbance results were consistent with the red color intensity observed visually, suggesting that this method could be used for screening TMA and BMT using the naked eye.

Conclusion:

The detection of the triamcinolone acetonide (TMA) and betamethasone-17 valerate (BMT) using UV-visible spectroscopy has been successfully achieved through redox reaction via the triphenyl tetrazolium chloride reagent. This reaction produces formazan products with a red color that shows the maximum absorption at 480 nm. This proposed method enabled rapid analysis within 15 minutes and demonstrated good analytical performance with the detection limits of 3.3 and 11.9 mg L⁻¹ for TMA and BMT, respectively. Further experiments will investigate the method's selectivity and application to real samples. Additionally, the red color intensity which was visually proportional to the concentration of both TMA and BMT, suggests the potential for developing a screening test.

Acknowledgments:

We express our gratitude to the Talent Management Project of Prince of Songkla University, the Ministry of Higher Education, Science, Research and Innovation. The authors

acknowledge assistance from the Development and Promotion of Science and Technology Talents (DPST) Project, Center of Excellence for Trace Analysis and Biosensors (TAB-CoE), Division of Physical Science, Faculty of Science and Graduate School, Prince of Songkla University, Hat Yai, Songkhla, Thailand.

References:

1. Burford NG, Webster NA, Cruz-Topete D. Hypothalamic-Pituitary-Adrenal Axis Modulation of Glucocorticoids in the Cardiovascular System. *Int J Mol Sci.* 2017;18(10). doi:10.3390/ijms18102150
2. Ference JD, Last AR. Choosing topical corticosteroids. *Am Fam Physician.* 2009;79(2):135-140.
3. Katzung G SBM and AJT. *Basic & Clinic Pharmacology.*; 2012.
4. Arnold J, Anthonioz P, Marchand JP. Depigmenting action of corticosteroids. Experimental study on guinea pigs. *Dermatologica.* 1975;151(5):274-280. <https://www.ncbi.nlm.nih.gov/pubmed/1225665>
5. Venkatesan P, Fangman WL. Linear hypopigmentation and cutaneous atrophy following intra-articular steroid injections for de Quervain's tendonitis. *J Drugs Dermatol.* 2009;8(5):492-493. <https://www.ncbi.nlm.nih.gov/pubmed/19537375>
6. Merck & Co I. Relative potency of selected topical corticosteroids. Merck & Co, Inc. Accessed May 5, 2024. <https://www.msmanuals.com/professional/multimedia/table/relative-potency-of-selected-topical-corticosteroids>
7. THAI FDA. THAI FDA Press release. 2022. Accessed May 5, 2024. https://oryor.com/media/newsUpdate/media_news/2220?ref=search
8. THAI FDA. THAI FDA Press release. 2024. Accessed May 5, 2024. https://oryor.com/media/newsUpdate/media_news/2689?ref=search
9. Chemistry inspection & regulation service. EU Cosmetics Regulations and Registration. 2009. Accessed May 5, 2024. https://www.cirs-reach.com/Cosmetics_Registration/eu_cosmetics_directive_cosmetics_registration.html
10. THE EUROPEAN PARLIAMENT AND THE COUNCIL OF THE EUROPEAN UNION. REGULATION (EC) No 1223/2009 OF THE EUROPEAN PARLIAMENT AND OF THE COUNCIL on cosmetic products. Published online 2009.
11. Ivkovic B, Crevar M, Cvetanović A, Ubavkić K, Marković B. Development and validation of RP-HPLC method for quantification of trace levels of topical corticosteroids in ambiphilic cream. *Acta Chromatogr.* 2022;35. doi:10.1556/1326.2021.00998
12. Dolowy M, Kozik V, Bak A, et al. A Rapid and Simple TLC-Densitometric Method for Assay of Clobetasol Propionate in Topical Solution. *Molecules.* 2017;22:1888. doi:10.3390/molecules22111888
13. Tu E, Pearlmutter P, Tiangco M, Derosé G, Begdache L, Koh A. Comparison of Colorimetric Analyses to Determine Cortisol in Human Sweat. *ACS Omega.* 2020;5(14):8211-8218. doi:10.1021/acsomega.0c00498
14. Guttman DE. Analysis of Steroids in Mixtures Using the Kinetics of Blue Tetrazolium Reduction. *J Pharm Sci.* 1966;55(9):919-922. doi:https://doi.org/10.1002/jps.2600550910
15. Ashutosh Kar. *PHARMACEUTICAL DRUG ANALYSIS.* Second Edition.; 2001.
16. Sefid-Sefidehkhani Y, Jouyban A, Khoshkam M, Amiri M, Rahimpour E. A mini review on materials used for the colorimetric detection of corticosteroids. *Chemical Papers.* 2022;76(8):4627-4643. doi:10.1007/s11696-022-02233-w
17. Oteiza RM, Wooten RS, Kenner CT, Graham RE, Biehl ER. Kinetics and Mechanism of Blue Tetrazolium Reaction with Corticosteroids. *J Pharm Sci.* 1977;66(10):1385-1388. doi:https://doi.org/10.1002/jps.2600661008

C-CHEMISTRY (INORGANIC CHEMISTRY)



EFFECTS OF SULFUR SUBSTITUTION IN A NICKEL COMPLEX FEATURING A N₄-SCHIFF BASE MACROCYCLE ON THE ELECTROCATALYTIC ACTIVITY TOWARDS CO₂ REDUCTION

M. Rofif Nurfaizi,¹ Michael S. Bennington,^{2,3} Patchanita Thamyongkit,¹ Thawatchai Tuntulani,¹ Sally Brooker,^{2,3} Pannee Leeladee,^{1,*}

¹Department of Chemistry, Faculty of Science, Chulalongkorn University, Thailand.

²Department of Chemistry, University of Otago, Dunedin, 9016, New Zealand

³The MacDiarmid Institute for Advanced Materials and Nanotechnology, New Zealand

*e-mail: pannee.l@chula.ac.th

Abstract:

The electrochemical reduction of carbon dioxide (CO₂RR) presents a promising approach to mitigating CO₂ emissions while producing valuable chemical products. Nickel complexes have gained attention as molecular catalysts due to their tunability and diverse redox properties. In this study, a new Schiff base macrocyclic nickel complex, Ni-N₃S, was synthesized with sulfur incorporation, aiming to investigate the effect of this sulfur donor in comparison with that of the nitrogen counterpart (Ni-N₃NH) on its electrochemical and catalytic properties for CO₂ reduction. The nickel complex (Ni-N₃S) was prepared through Ni-templated condensation of 2,2'-iminobisbenzaldehyde and 2,2'-thiobis(ethylamine) and characterized using UV-vis spectroscopy, mass spectrometry, and ¹H NMR spectroscopy. The UV-vis results revealed a red shift in the absorption spectrum compared to its nitrogen counterpart, indicating altered electronic properties due to sulfur substitution. Mass spectrometry confirmed the molecular formula, with the molecular ion peak [Ni-N₃S]⁺ observed at $m/z = 366.05823$. ¹H NMR data indicated that Ni-N₃S is diamagnetic, consistent with the anticipated d⁸ electronic configuration and square planar geometry, though some dynamic behavior due to sulfur coordination was evident. Electrochemical studies using cyclic voltammetry demonstrated a reversible redox process corresponding to the Ni^I/Ni^{II} couple at -1.456 V versus Fc/Fc⁺, which was more cathodic compared to the previously reported Ni-N₃NH complex (-1.864 V). However, under a CO₂ atmosphere, it was revealed that Ni-N₃S exhibited lower CO₂RR activity compared to the Ni-N₃NH. This reduction in catalytic activity is attributed to either the shift in redox potential, or the absence of the N-H moiety, which can be crucial for stabilizing CO₂ intermediates in solution, as seen previous studies. Further investigation will focus on immobilizing the complex onto carbon supports to evaluate its potential in heterogeneous electrocatalysis.

Introduction:

The carbon dioxide reduction reaction (CO₂RR) to fuels and chemicals powered by renewable electricity, offers a path for addressing both carbon dioxide emissions and challenges associated with renewable energy storage.^{1, 2} Subsequently, electrochemical conversion of CO₂ to its reduced forms such as CO, methanol, formate, etc., is thermodynamically uphill due to the natural inertness of CO₂ with an initial C=O bond energy of 806 kJ mol⁻¹.³ For conversion to occur at appropriate rates, considerably more negative potentials than the thermodynamic values are required.⁴ Hence, catalysts are necessary to accelerate reaction rates. Notably, the hydrogen evolution reaction (HER) can emerge a competitive reaction for electrochemical CO₂ reduction (ECR). As HER consumes protons and electrons at comparatively lower voltages, it significantly reduces the faradaic efficiency for CO₂RR.⁵

The appeal of molecular catalysts for electrochemical CO₂ reduction has been drawing considerable interest, largely owing to their tunability and well-defined active site structures.^{4, 6} Nickel complexes are notably intriguing due to their rich redox properties and diverse coordination geometries, which enable the rational design of ligand frameworks.⁷ Among the well-established ligand frameworks, aza-macrocyclic ligands such as cyclam, porphyrins, and phthalocyanine have been widely reported. These ligands have demonstrated exceptional activity and selectivity towards CO₂ reduction.^{6, 8, 9} Notably, [Ni(cyclam)]²⁺ (**Figure 1**) efficiently converts CO₂ to CO in water with 96% FE, demonstrating the suitability of tetraazamacrocycles ligand structures to facilitate ECR. Additionally, the existence of π -contributing units in catalytic systems, like porphyrins and phthalocyanines, are crucial for ECR. They enable efficient electron transfer to the catalytic center,¹⁰ allowing these catalysts to operate effectively in aqueous environments.

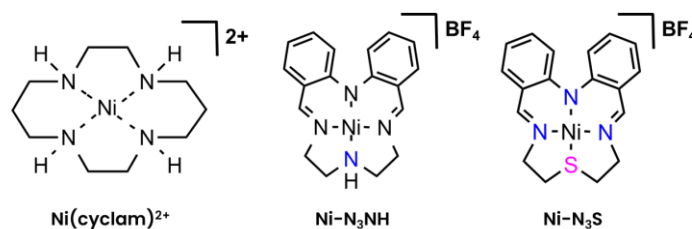


Figure 1. Chemical structure of [Ni(cyclam)]²⁺, Ni-N₃NH, and Ni-N₃S

In addition to the well-established ligand frameworks mentioned previously, recent studies have explored the potential of metal complexes containing Schiff-base ligands as catalysts for ECR.¹¹ In particular, Brooker and co-workers have reported metal complexes of porphyrin-like N₄-Schiff base macrocycles in their works¹²⁻¹⁶, including 1-Ni.¹⁷ Recently, our research group reported that 1-Ni and its derivatives exhibited ECR activity and selectively convert CO₂ into CO. Especially, the hybrid catalyst based on molecularly dispersed nickel complex on N-doped graphene (1-Ni@NG) showed high performance of CO production with FE_{CO} of 82% in aqueous media.¹⁸ This complex is notably interesting because 1-Ni has the structural motif similar to that of cyclam and features a conjugated system which allow the immobilization onto carbon supports *via* non-covalent interactions as shown in **Figure 1** (In this paper, to enhance clarity and accurately convey the structural and compositional details of the complex, the designation 1-Ni will be replaced with Ni-N₃NH in the Results and Discussion sections).

Ligand modification of the metal complex can be made to study the effects on overall catalyst performance.¹⁹ For example, nature inspired substitutions of Ni(isocyclam)²⁺ have been conducted by Gerschel and co-workers.^{19, 20} Despite lost in the selectivity, the sulfur incorporated complex Ni-L^S was able to facilitate CO₂RR at 0.3 V lower potential compared with the original Ni-L^N, which led to reduction in energy demand. In other work by Kojima and co-workers, a Ni(II) complex inspired by the active site of carbon monoxide dehydrogenase (CODH), Ni^{II}-N₂S₂, has shown a photocatalytic reduction activity of CO₂ with a high selectivity (>99%) and a turnover number (TON) of 713 for the formation of CO (see **Figure 2**).²¹

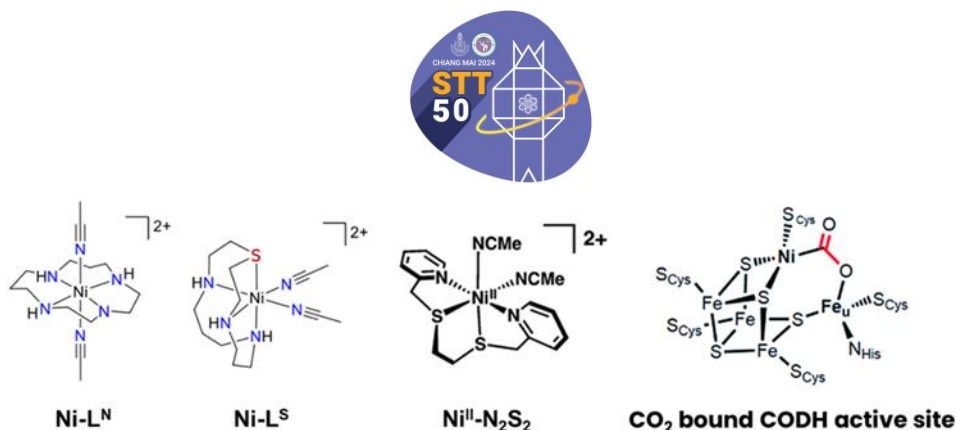


Figure 2. Ni complexes from previous studies.^{19, 21, 22}

Here, we synthesize a new compound, Ni-N₃S (**Figure 1**), a derivative of 1-Ni (Ni-N₃NH) by incorporating sulfur into the ligand framework. This ligand modification aims to investigate the impact on electrochemical behavior, catalytic activity, and selectivity of the catalyst towards CO₂RR.

Methodology:

Materials and instrumentations

All the chemicals were used as received without further purification. 2,2'-Iminodibenzoic acid (HN(C₆H₄CO₂H)₂, 95%) and tetrabutylammonium hexafluorophosphate (NBu₄PF₆, >99%) were obtained from Sigma-Aldrich. Nickel(II) tetrafluoroborate hexahydrate (Ni(BF₄)₂·6H₂O, 99%) was purchased from fisher scientific and 2,2'-thiobis(ethylamine) (S(C₂H₄NH₂)₂, >98%) was purchased from Tokyo Chemical Industry. Milli-Q water (18.2 MΩ cm) was used in this work.

¹H NMR spectra were recorded on a JEOL 500 MHz spectrometer and Bruker 400 MHz spectrometer. Mass spectra were collected by high-resolution electrospray ionization mass spectroscopy (HR-ESI-MS) using a Bruker MicroTOF-Q spectrometer. UV-vis adsorption spectra were obtained with a Varian Cary 50 Probe using a quartz cuvette with the optical path length of 1 cm. Cyclic voltammetry (CV) was performed on a Metrohm Autolab PGSTAT101 model.

Synthesis and characterization of the nickel complex (Ni-N₃S)

Ni-N₃S was synthesized through a modified method referring to a published literature.¹⁷ Three steps of synthesis were conducted to obtain the ligand precursor, 2,2'-iminobisbenzaldehyde, from 2,2'-iminodibenzoic acid as a starting material. The literature synthetic route to the ligand precursor^{23, 24} is summarized in **Figure 3**. For the first step (esterification), 1 gram of 2,2'-iminodibenzoic acid was dissolved in 40 mL of methanol, then 1 mL of concentrated H₂SO₄ was slowly added to catalyze the reaction. The mixture was refluxed for 5 hours followed by extraction with dichloromethane and evaporation to afford the pale-yellow solid of ester compound, 2,2'-iminobis(methyl benzoate), as the desired product (86% yield). ¹H NMR (500 MHz, CDCl₃, 298 K): δ_{N-H} (ppm) = 11.05 (s).

The ester compound then was reduced to the alcohol compound (2,2'-iminobis(hydroxymethyl benzene)) using LiAlH₄ (4 equivalents) as the reducing agent. The mixture was stirred overnight and then quenched with Milli-Q water. After filtration and washing with dichloromethane, then the solvent (diethylether) was removed under reduced pressure, yielding a crude off-white solid, which was purified by precipitation in a CH₂Cl₂/Hexane mixture to obtain the white solid (75% yield). ¹H NMR (500 MHz, CDCl₃, 298 K): δ_{N-H} (ppm) = 7.40 (s).

The final step of ligand preparation is oxidation of 2,2'-iminobis(hydroxymethyl benzene) to form 2,2'-iminobisbenzaldehyde. A colorless solution of 2,2'-iminobis(hydroxymethyl benzene) in dry Et₂O (30 mL) was treated with activated MnO₂ (20 equivalents). The resulting black suspension was stirred for 72 hours at room temperature. Afterward, the MnO₂ was filtered off and the filtrate was concentrated to yield a crude yellow solid, which was then purified by chromatography in silica gel using 1:4 EtOAc/Hexane, resulting in the product as a bright yellow solid (58% yield). ¹H NMR (500 MHz, CDCl₃, 298 K): δ_{N-H} (ppm) = 11.36 (s).

The nickel complex then was prepared through Ni-templated condensation using Ni(BF₄)₂·6H₂O as Ni(II) precursor, the obtained 2,2'-iminobisbenzaldehyde and 2,2'-thiobis(ethylamine) as the peripheral unit for Ni-N₃S (see **Figure 4**). To a bright yellow solution of 2,2'-iminobisbenzaldehyde (102 mg, 0.45 mmol) in 20 mL of acetonitrile (MeCN) under reflux, a solution of nickel(II) tetrafluoroborate hexahydrate (159 mg, 0.45 mmol) in 10 mL of MeCN was added. Subsequently, a solution of 2,2'-thiobis(ethylamine) (54 mg, 0.45 mmol) in 15 mL of MeCN was added dropwise. The resulting dark red solution was then refluxed at 90 °C for 18 hours. After refluxing, the solvent was removed under reduced pressure, yielding a dark green solid, which was subsequently recrystallized using layer diffusion of acetonitrile and diethyl ether of diethyl ether over a green acetonitrile solution (60% yield). ESI(+) MS(*m/z*) (MeCN): [Ni-N₃S]⁺ calculated 366.05749, found 366.05823. UV-vis (MeCN): λ_{max}/nm (ε) = 311 (10731), 421 (3306), 480 (9065), 642 (1042).

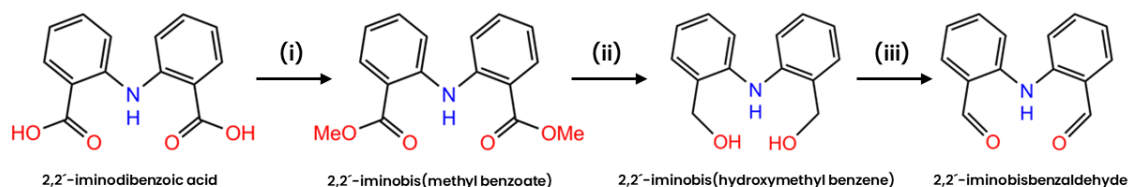


Figure 3. Synthetic route of the ligand precursor. (i) conc. H₂SO₄, MeOH. (ii) LiAlH₄, Et₂O. (iii) MnO₂, Et₂O.

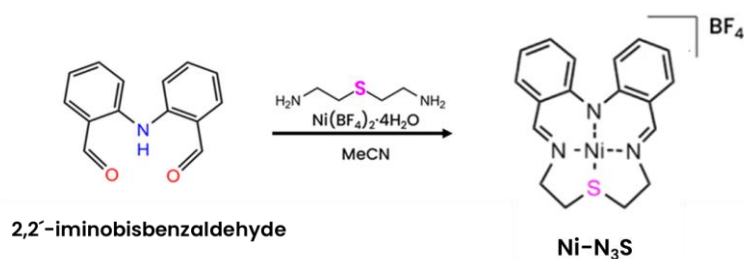


Figure 4. Ni-templated condensation to form Ni-N₃S

Electrochemical study

Cyclic voltammetry (CV) was performed to investigate the redox activity of Ni-N₃S in CH₃CN solutions (1 mM) with 0.1 M NBu₄PF₆ as the supporting electrolyte. As the working electrode, a glassy carbon electrode was used after being polished with alumina suspension and rinsed with deionized water. A platinum wire and a 0.01 M AgNO₃/Ag electrode were used as the counter electrode and the reference electrode respectively, whereas the results were externally calibrated to the Fc/Fc⁺ couple (*E*_{Fc/Fc⁺} = 0.09 V ± 0.01 V, Δ*E*_p = 65 mV). CV experiments were performed first in N₂ atmosphere to study the electrochemical properties of the complex. After that, another CV was performed in CO₂ atmosphere to investigate the catalytic activity of the complex.

Results and Discussion:



The Ni-N₃S complex has been successfully synthesized using the previously described method. The UV-vis absorption spectrum of Ni-N₃S in acetonitrile exhibits a pattern somewhat similar to that of Ni-N₃NH by showing signals at around 311 nm, 480 nm, and 642 nm as shown in **Figure 5**. In the region above 500 nm, while Ni-N₃NH shows absorption signal at 554 nm, Ni-N₃S exhibits a higher wavelength absorption signal at 642 nm. This significant shift is reflected in the color of the Ni-N₃S solution, which appears green, in contrast to the maroon color of Ni-N₃NH. By comparing their absorption peaks (see **Table 1**), the sulfur derivative showed significant red shifts which confirm that a new compound was successfully obtained. This result also confirms the notion that by substituting the donor atom, the electronic property of the complex is altered which most likely due to the different donating character of nitrogen and sulfur.

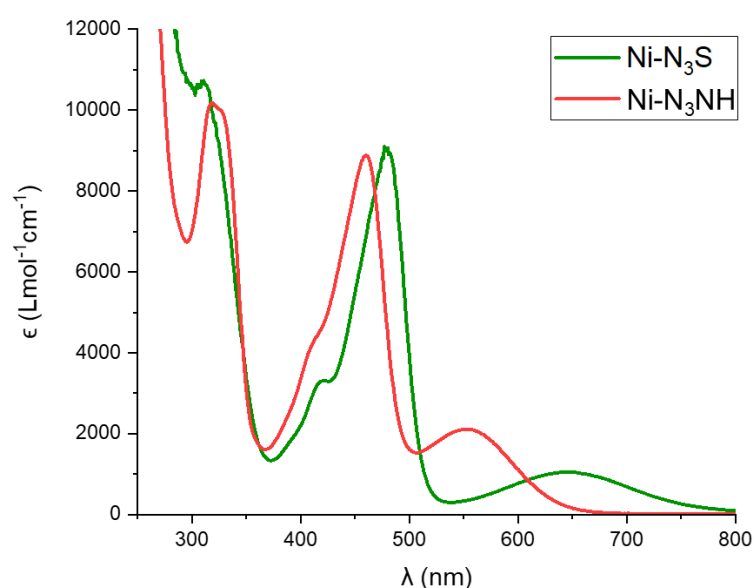


Figure 5. UV-vis absorption spectra in acetonitrile of Ni-N₃S (green line) and Ni-N₃NH (red line)

The molecular mass of the synthesized compound was confirmed using electrospray ionization mass spectrometry (ESI-MS). As shown in **Figure 6**, the mass spectrum of Ni-N₃S showed a prominent molecular ion peak at $m/z = 366.05823$, which corresponds to the [Ni-N₃S]⁺ species. This data aligns with the calculated exact molecular mass of the complex (366.05749 Da) and molecular formula [C₁₈H₁₈N₃SNi]⁺. This result confirms that the desired Ni-N₃S complex was successfully synthesized.

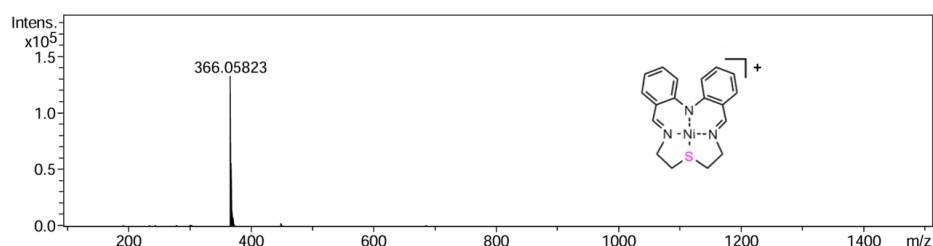


Figure 6. Mass spectrum of Ni-N₃S

The structure of the synthesized nickel complex was further characterized by ^1H NMR spectroscopy at room temperature. The integration of the proton signals corresponds well with the proposed structure, indicating the correct stoichiometry of the complex (see **Figure 7**). In addition, ^1H NMR spectrum of Ni-N₃S was recorded to gain insight into the electronic and structural properties of the complex. The spectrum reveals important features that inform both the coordination environment and potential dynamic behavior of the complex. The presence of a well-defined yet slightly broadened signals in the ^1H NMR spectrum suggests that the Ni-N₃S complex is mostly diamagnetic. This is consistent with a low-spin d^8 nickel(II) center, commonly associated with square planar geometries. Furthermore, the slight broadening of several peaks ($\delta=8.0$ ppm; $\delta=7.5$ ppm; $\delta=3.5$ - 4.0 ppm) suggests that some dynamic behavior may be occurring. Even though the complex is most likely adopting a square planar geometry, the incorporation of sulfur could introduce some degree of flexibility in the coordination sphere, resulting in dynamic behavior.²⁵ This fluctuation could account for the observed peak broadening, and further investigation is needed to fully understand the extent of this behavior. Notably, no evidence of axial ligand coordination (e.g., solvent molecules) is observed in the spectrum, further supporting a primarily square planar structure.

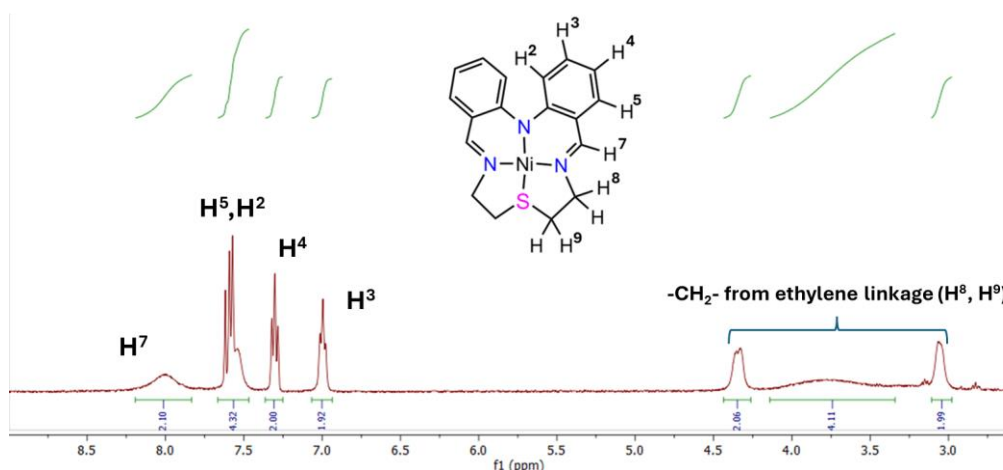


Figure 7. ^1H NMR spectrum of Ni-N₃S in CD_3CN

After confirming the successful synthesis by several techniques, electrochemical properties of Ni-N₃S were analyzed by conducting cyclic voltammetry (CV) experiments. The redox activity of Ni-N₃S was investigated in solutions with NBu_4PF_6 as the electrolyte and acetonitrile as the solvent. From the CV results shown in **Figure 8**, the complex showed a reversible redox process that corresponds to $\text{Ni}^{\text{I}}/\text{Ni}^{\text{II}}$ redox couple at -1.456 V versus Fc/Fc^+ . Interestingly, this peak appeared at more cathodic potential compared to the original Ni-N₃NH from the previous work¹⁸ with the difference of 408 mV as detailed in **Table 1**.

Then to investigate the catalytic activity of Ni-N₃S, experiments were conducted in CO_2 atmosphere. When purging CO_2 to the solution, Ni-N₃S showed almost no current enhancement, however a slight enhancement was observed upon an addition of water as proton source. Furthermore, in the presence of water, the Ni-N₃S showed higher enhancement in CO_2 atmosphere than in N_2 (see **Figure 8a**). This result indicates the lower reactivity of Ni-N₃S towards CO_2RR in homogeneous system compared to Ni-N₃NH which possibly due to the absence of N-H moiety in the structures. Without the N-H group, the complex may struggle to stabilize the CO_2 intermediate, resulting in reduced efficiency in the CO_2 reduction reaction. Previous work from our research group on Ni-N₃NH, 2-Ni, and its methyl derivative supports this conclusion.¹⁸ The methyl derivative $[2\text{-Ni}]^{\text{Me}}$, which lacks the N-H moiety, demonstrated lower catalytic activity in homogeneous systems compared to Ni-



N₃NH and 2-Ni. This is consistent with our findings for Ni-N₃S, where the absence of an N-H moiety similarly hinders the stabilization of the CO₂ intermediate. Interestingly, when both 2-Ni and its methyl derivative were immobilized onto carbon supports and used in a heterogeneous aqueous system, they exhibited similar catalytic performance. This suggests that immobilization onto carbon supports can mitigate the effects of the missing N-H moiety, possibly by providing additional stabilization from the aqueous solution. Therefore, although Ni-N₃S shows low activity in a homogeneous system, it is still our interest to explore its performance in a heterogeneous catalysis, particularly by immobilizing the complex onto carbon supports, where it may perform more effectively.

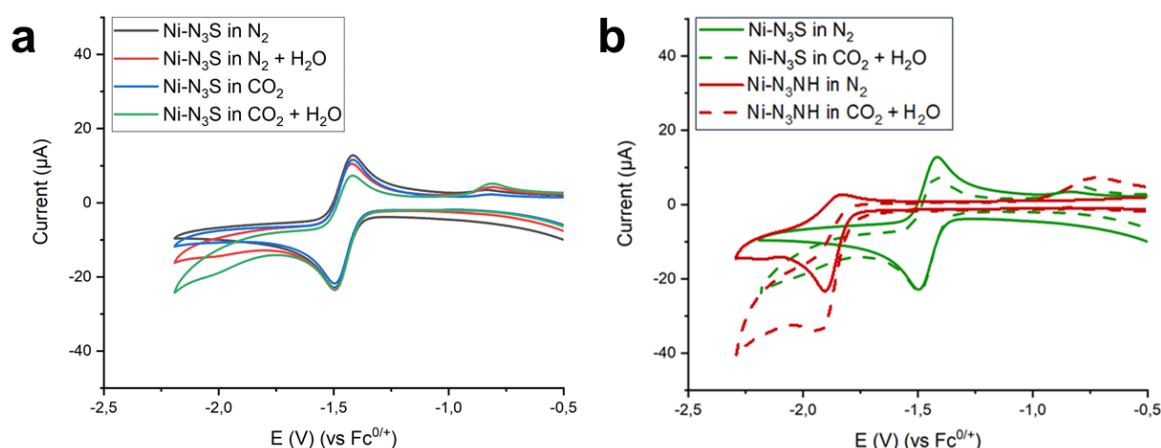


Figure 8. CV of (a) Ni-N₃S in CO₂ atmosphere and (b) comparison to Ni-N₃NH

Table 1. Electrochemical comparison between Ni-N₃S and Ni-N₃NH

| Complex | E _{pc} (V) | E _{pa} (V) | ΔE (V) | E _{1/2} vs Fc/Fc ⁺ (V) |
|----------------------|---------------------|---------------------|--------|--|
| Ni-N ₃ NH | -1.902 | -1.826 | 0.076 | -1.864 |
| Ni-N ₃ S | -1.499 | -1.413 | 0.086 | -1.456 |

Conclusion:

In summary, we successfully incorporated a sulfur donor into a new macrocyclic nickel complex. It was prepared by Ni-templated condensation, then characterized and homogeneous electrochemical studies were carried out. UV-vis measurements revealed a red shift in the absorption spectrum of Ni-N₃S, confirming altered electronic properties due to the different donating characteristics of sulfur compared to nitrogen. Mass spectrometry also helps to confirm the successful synthesis of the complex, Ni-N₃S, with a single strong peak observed at $m/z = 366.05823$, which matched with the calculated mass for the complex minus the BF₄ anion. Additionally, ¹H NMR spectroscopy demonstrated that Ni-N₃S is diamagnetic, consistent with the expected d⁸ electronic configuration and likely square planar geometry. The slight broadening of some peaks indicates potential dynamic behavior, likely caused by fluctuations in the sulfur-nickel coordination. Finally, electrochemical studies using cyclic voltammetry revealed that Ni-N₃S has a redox activity at a significantly more cathodic potential and exhibits lower activity toward CO₂ reduction (CO₂RR) in a homogeneous system compared to its nitrogen counterpart, Ni-N₃NH. This difference may be due to the significant shift in redox potential observed or could underscore a crucial role of the N-H moiety in stabilizing CO₂ intermediates during homogeneous CO₂RR, consistent with previous studies. However, this result suggests that further investigation is needed in a

heterogeneous system, where the absence of the N-H moiety may have less impact on catalytic performance. Future work will focus on immobilizing Ni-N₃S onto carbon supports to evaluate its potential in heterogeneous electrocatalysis.

Acknowledgements:

M. R. N. gratefully acknowledge the Asean & Non-Asean Scholarship of Chulalongkorn University. M. S. B. and S. B. thank the University of Otago, the MacDiarmid Institute and He Honoka Hauwai for their support.

References:

1. D H Nam, P De Luna, A Rosas-Hernandez, A Thevenon, F Li, T Agapie, J C Peters, O Shekhah, M Eddaoudi and E H Sargent(s). *Nat Mater.* 2020;19:266-276.
2. T N Nguyen, M Salehi, Q V Le, A Seifitokaldani and C T Dinh(s). *ACS Catalysis.* 2020;10:10068-10095.
3. E E Benson, C P Kubiak, A J Sathrum and J M Smieja(s). *Chem Soc Rev.* 2009;38:89-99.
4. S Zhang, Q Fan, R Xia and T J Meyer(s). *Acc Chem Res.* 2020;53:255-264.
5. S Zhao, R Jin and R Jin(s). *ACS Energy Letters.* 2018;3:452-462.
6. Y Wu, Y Liang and H Wang(s). *Acc Chem Res.* 2021;
7. J-W Wang, W-J Liu, D-C Zhong and T-B Lu(s). *Coordination Chemistry Reviews.* 2019;378:237-261.
8. J D Froehlich and C P Kubiak(s). *Inorg Chem.* 2012;51:3932-3934.
9. S Gu, A N Marianov, T Lu and J Zhong(s). *Chemical Engineering Journal.* 2023;470:
10. P Kang, S Zhang, T J Meyer and M Brookhart(s). *Angew Chem Int Ed Engl.* 2014;53:8709-8713.
11. S Sengupta, S Khan, B Naath Mongal, W Lewis, M Fleck, S K Chattopadhyay and S Naskar(s). *Polyhedron.* 2020;191:114798.
12. R W Hogue, O Schott, G S Hanan and S Brooker(s). *Chemistry.* 2018;24:9820-9832.
13. A M Abudayyeh, O Schott, H L C Feltham, G S Hanan and S Brooker(s). *Inorganic Chemistry Frontiers.* 2021;8:1015-1029.
14. S Rodriguez-Jimenez, M S Bennington, A Akbarinejad, E J Tay, E W C Chan, Z Wan, A M Abudayyeh, P Baek, H L C Feltham, D Barker, K C Gordon, J Trivas-Sejdic and S Brooker(s). *ACS Appl Mater Interfaces.* 2021;13:1301-1313.
15. V Singh, A M Abudayyeh, M G Robb and S Brooker(s). *Dalton Trans.* 2022;51:4166-4172.
16. A M Abudayyeh, M S Bennington, J Hamonnet, A T Marshall and S Brooker(s). *Dalton Trans.* 2024;53:6207-6214.
17. R K Wilson and S Brooker(s). *Dalton Trans.* 2013;42:7913-7923.



18. M Juthathan, T Chantarojsiri, K Chainok, T Butburee, P Thamyongkit, T Tuntulani and P Leeladee(s). Dalton Trans. 2023;
19. P Gerschel, B Battistella, D Siegmund, K Ray and U-P Apfel(s). Organometallics. 2020;39:1497-1510.
20. P Gerschel, K Warm, E R Farquhar, U Englert, M L Reback, D Siegmund, K Ray and U P Apfel(s). Dalton Trans. 2019;48:5923-5932.
21. D Hong, Y Tsukakoshi, H Kotani, T Ishizuka and T Kojima(s). J Am Chem Soc. 2017;139:6538-6541.
22. W Lubitz, H Ogata, O Rudiger and E Reijerse(s). Chem Rev. 2014;114:4081-4148.
23. D Black and N Rothnie(s). Australian Journal of Chemistry. 1983;36:2395-2406.
24. E D Bergmann, M Rabinovitz and I Agranat(s). Bulletin of the Research Council of Israel, Section A: Chemistry. 1962;11:149.
25. S Brooker, G S Dunbar and G B Jameson(s). Polyhedron. 1999;18:679-688.



Hydrogen sulfide adsorption in biogas by waste from palm oil processing

Nattiya Khongkuea^{1,*} and Niramol Juntarachat^{2,*}

¹Department of Chemistry, Faculty of Science and Digital Innovation, Thaksin University, Phatthalung Campus, Phatthalung, 93210, Thailand

²Innovative Material Chemistry for Environment Center, Department of Chemistry, Faculty of Science and Digital Innovation, Thaksin University, Phatthalung campus, Phatthalung, 93210, Thailand

*e-mail: niramol@tsu.ac.th

Abstract:

In this work, the removal of hydrogen sulfide from biogas by palm oil processed sorbent was studied. which is oil palm bunch and oil palm shell. The first step was to study the physical and chemical properties of the adsorbent. To assess the adsorption capacity, it was found that The moisture contents of the oil palm bunch charcoal were 9.28 and 9.37 respectively, and the pH values of the charcoal sorbents were 9.36 and 9.22 g/l solution, respectively, and FTIR value of charcoal oil palm bunch and oil palm shell scouring adsorbent scouring second step Comparison of adsorption of three sorbent sizes with spherical shapes. It has a diameter of 0.5 1.0 and 1.5 cm. The biogas components (CH_4 , CO_2 and H_2S) were measured before and after adsorption in a 30 cm long column and 3.5 cm diameter fabric using a gas chromatography apparatus. The adsorption efficiency of the three adsorbents showed that the adsorbent size of 0.5 cm was better at adsorbing H_2S than the adsorber size of 1.0 and 1.5 cm respectively.

Keywords: Biogas, hydrogen sulfide, adsorbent, oil palm bunch, oil palm shell.

Introduction:

Alternative renewable sources of energy are today seen as potential solutions to the problems of growing energy demand, progressive depletion, and negative environmental impact of fossil fuel resources. Biogas, one of potential renewable energies, is a mixture of different gases produced by the biological decomposition of organic matters in the absence of oxygen. Biogas mainly consist of methane (CH_4), carbon dioxide (CO_2), and a trace amount of other gases such as hydrogen sulfide (H_2S), ammonia (NH_3), hydrogen (H_2), nitrogen (N_2), and carbon monoxide (CO). The composition of the biogas varies based on the substrate feedstock, temperature, and pressure of each process. The presence of elevated concentrations of H_2S in biogas is problematic because of its highly corrosiveness and toxicity. and serious environmental concerns due to their oxidation to sulfur dioxide (SO_2) and sulfuric acid (H_2SO_4)³. Several physicochemical processes have been studied in order to remove H_2S from biogas such as the absorption process, catalytic process, biological process and hydrate formation. However, these technologies required a high-cost operation as well as technical complication, preventing its application for small-scale users.

The adsorption process is a promising technology to remove H_2S contained in biogas for small-scale users, especially in household owning to its low-cost operation and uncomplicated utilization and maintenance. Adsorbent type is an important factor effecting on the efficiency of such a process. Activated carbon is one of the most suitable adsorbent materials. But, its cost acts as a barrier to the take up of biogas technology. Biochar, a carbon-rich material obtained by a thermal decomposition of biomass under oxygen limiting conditions, is currently attractive for the new low-cost alternative adsorbents. In comparison with an activated carbon, the manufacturing of biochar required less energy and no pre- and pros-activation processes.

This research is therefore interested in developing palm bunches and palm shell. It is an organic material obtained from palm oil mills. It is the part of the bunch that has been removed from the oil palm. Currently, palm bunch it is being used as an alternative fuel, biomass type, for use in agriculture, such as as a material for making compost. It has the properties of plant nutrients consists of 0.8% nitrogen, 0.08% phosphorus and 2.41% potassium. Palm shells have the property of providing a high calorific value per unit of energy, so they are popularly used as biomass fuel. Substitute for mainstream fuels. The developpement of palm bunch and palm shells into biochar increase the efficiency of the adsorbent.

Methodology:

1. Preparation of biochar

Palm bunch and palm shell samples were collected from Hua Sai District, Nakhon Si Thammarat Province and dried in the sun for a period of 24 hours. Sample was passed through a pyrolysis process at the temperature of 350 °C for 4 hours. Biochar was stored in a heat-proof jar for further analysis of physical and chemical properties and adsorption efficiency.



Figure 1.

Palm bunch biochar adsorbent (a) and Palm shell biochar adsorbent (b)

2. Chemical and physical properties of adsorbent

The physical and chemical properties of palm bunch studied in this work were moisture content, volatile compound content, ash content, fixed carbon content, pH and BET surface. Moisture content analysis was performed according to ASTM D 3173 standard procedure by heating 1 g of biochar at 105-110 °C for 180 minutes. Volatile matter content was determined according to ASTM D 3175 standard procedure by heating 1 g of charcoal at 900 °C for 30 minutes. The percentage of ash content was determined, according to ASTM-D 2866-94 standard procedure, Three experiments were performed for each property, Fixed carbon content (%) was calculated by $100 - (\text{moisture content (\%)} + \text{volatile matter content (\%)} + \text{ash content (\%)})$. pH measurement was performed by taking 1 g of biochar and mixed with 10 ml of distilled water. A mixture was agitated during 30 minutes for equilibrium and filtrated to separate biochar and solution. Solution was taken to measure the pH using a pH meter. The experiment was repeated 3 times. The functional group of selected biochar palm bunch was analyzed before adsorption process, through FTIR transmission spectra.

3. Absorption efficiency.

The efficiency adsorption of hydrogen sulfide contaminants in biogas was studied using palm bunch biochar as an adsorbent. In the first step, the effect of pallet sizes (0.5,1.0



and 1.5 cm of diameter) of adsorbent on adsorption capacity was studied. Experiment was carried out using 10 g of palm bunch biochar in the packed-column with an internal diameter of 2.50 cm and the length of 40.00 cm, initial concentration of hydrogen sulfide of 1000 ppm and a flowrate of 1.0 L/min. The adsorption system is installed with the biogas production system as shown in Figure 2. Composition to biogas was analyzed by GC every 5 min for 120 minutes

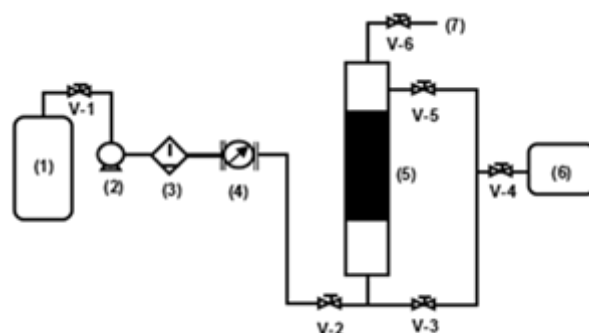


Figure 2.

Schematic diagram of the adsorption system experiment

The adsorption percentage was calculated using the following equation (1).

$$\text{adsorption percentage (\%)} = \frac{(C_0 - C_t)}{C_0} \times 100$$

Where C_t is the concentration of adsorbate at time t , C_0 is the initial concentration of the adsorbate, t is time, Q_f is flowrate of biogas and m_c is mass of ash adsorbent. A breakthrough curve was established from C/C_0 and time. A comparison of H_2S breakthrough curve (C/C_0 versus time) at different conditions of adsorption provides information about the optimal adsorption condition. The breakthrough capacity at 5% was calculated using the following equation (2).

$$q_t = \left(1 - \frac{c_t}{c_0}\right) \frac{Q_f t_f y_f}{m_c}$$

Results and Discussion:

1. Chemical properties and physical properties of biochar adsorbent

Physical and chemical properties of palm bunch biochar and palm shell biochar was determined and are shown in Table 1.

Table 1.

| physical and chemical properties palm bunch biochar and palm shell biochar | | |
|--|--------------------|--------------------|
| Feature | Palm bunch biochar | Palm shell biochar |
| Moisture content (%) | 9.88 ± 0.88 | 9.37 ± 0.08 |
| Volatile compound content (%) | 36.34 ± 0.63 | 55.12 ± 0.98 |
| Ash content (%) | 28.18 ± 3.46 | 20.12 ± 8.38 |
| Fixed carbon content (%) | 25.90 | 15.32 |
| pH | 9.36 | 9.22 |
| BET surface | 53.68 | 218.22 |

The moisture content in palm bunch biochar was found to be $9.28 \pm 0.88\%$ and palm shell biochar was $9.37 \pm 0.08\%$ which was consistent with that found in the investigation of [1] who study of H_2S removal with biochar, sewage sediment and pig biochar. They reported that increasing moisture content increases the ability to eliminate H_2S of biochar. Volatile compound content was found to be in palm bunch biochar $36.34 \pm 0.63\%$ and palm shell biochar was $55.12 \pm 0.98\%$. Biochar with low volatile compounds provides higher absorption capacity. The ash content of palm bunch biochar was $28.18 \pm 3.46\%$ and palm shell biochar was $20.12 \pm 8.38\%$. The fixed carbon content of biochar from the palm bunch was 25.90% and palm shell biochar was 15.32% . Biochar with higher fixed carbon will have higher adsorption capacity. According to [6] The pH value of palm bunch biochar was 9.36 and palm shell biochar was 9.22. According to [7], the pH values greater than 7.0 make the alkaline surface which is conducive to H_2S adsorption since H_2S is an acidic gas.

2. FTIR analysis and morphological properties

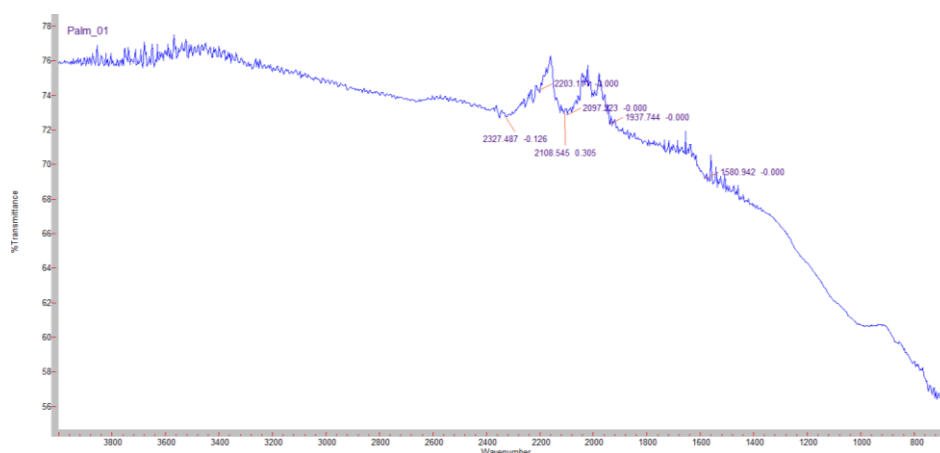


Figure 3.

FTIR spectra of the palm bunch biochar before the adsorption process

The important peaks were characterized. The peak at $890\text{--}600\text{ cm}^{-1}$ was associated with C–H. The peak at $1820\text{--}1760\text{ cm}^{-1}$ corresponded to C=O stretching vibration in aromatic ring. The spectra between $2260\text{--}2100\text{ cm}^{-1}$ broad characteristics revealed C=C stretching induced by alkyne bonding.



Figure 3.

FTIR spectra of the palm shell biochar before the adsorption process



The important peaks were characterized. The peak at $2250\text{--}2225\text{ cm}^{-1}$ was associated with $\text{C}\equiv\text{N}$. The peak at $1820\text{--}1760\text{ cm}^{-1}$ corresponded to $\text{C}=\text{O}$ stretching vibration in aromatic ring. The spectra between $2260\text{--}2100\text{ cm}^{-1}$ broad characteristics revealed $\text{C}\equiv\text{C}$ stretching induced by alkyne bonding.

3. Hydrogen sulfide (H_2S) adsorption.

Efficiency adsorption of H_2S was studied using palm bunch biochar and palm shell biochar as the adsorbent. In the first step, the effect of pallet sizes of adsorbent on the adsorption capacity as evaluated using initial concentration of H_2S of 1000 ppm. Figure 5 represents palm bunch biochar H_2S breakthrough curves of adsorbent with diameters of 0.5, 1.0 and 1.5 cm. Figure 6 represents palm shell biochar H_2S breakthrough curves of adsorbent with diameters of 0.5, 1.0 and 1.5 cm. It can be seen that palm bunch biochar and palm shell biochar with the pallet size of 0.5 cm. had better adsorption efficiency than that with the pallet size of 1.0 and 1.5 cm. This can be explained by a greater and consistent adsorption area. Our experimental results agree well with the investigations of [7]

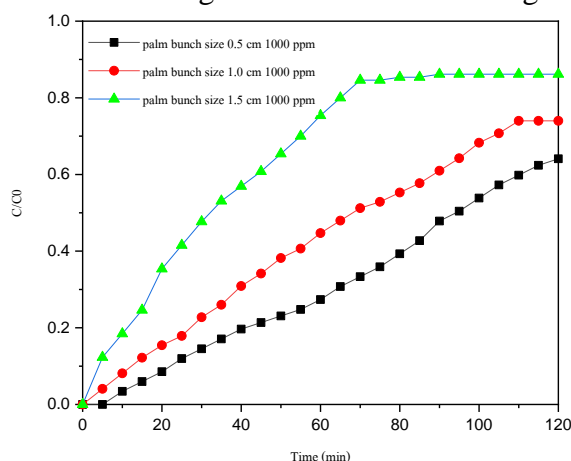


Figure 5.

H_2S breakthrough curves of adsorbent of the palm bunch biochar with diameters of 0.5, 1.0 and 1.5 cm

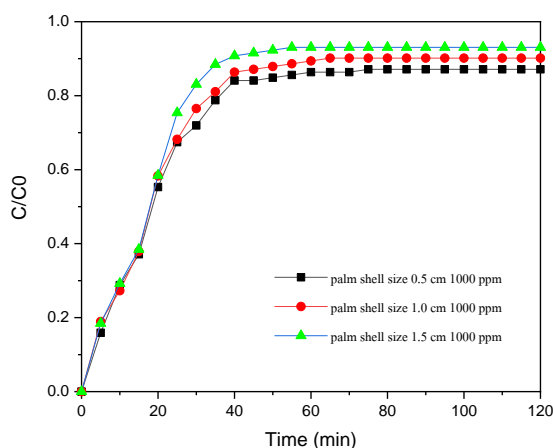


Figure 6.

H_2S breakthrough curves of adsorbent of the palm shell with diameters of 0.5, 1.0 and 1.5 cm

Conclusion:

The removal efficiency of H₂S from biogas using palm bunch biochar and palm shell biochar as an adsorbent was studied. Physical and chemical properties of biochar: moisture content, volatile matter content, ash content, and fixed carbon content were determined and found to palm bunch biochar be 9.88% ,36.34% ,28.18% and 25.90% respectively and found to palm shell biochar be 9.37% ,55.12% ,20.12% and 15.32% respectively . An appropriate amount of moisture can increase the adsorption capacity of adsorbent but the high ash content can decrease such a capacity. The pH value of palm bunch biochar and palm shell biochar was 9.36 and 9.22 , making the alkaline surface of adsorbent and leading to be conducive for removing H₂S. Then, the H₂S removal efficiency of palm bunch biochar and palm shell biochar adsorbent was investigated at different pellet sizes: 0.5,1.0 and 1.5 cm with initial concentration of H₂S at 1000 ppm . The results showed that a small pellet size increases surface area of adsorbent.

References:

- [1] Sun Q, Li H, Yan J, Liu L, Yu Z, Yu X. Renewable and Sustainable Energy Reviews. 2015; 51: 521–532.
- [2] Manmeen A, Kongjan P, Palamanit A , Jariyaboon R, Biomass and Bioenergy, 2023; 174. doi:10.1016/j.biombioe.2023.106816.
- [3] Manmeen A, Jariyaboon R, Doctor of Philosophy (Energy Technology), 2023; 219.
- [4] Sahota S,Vijay VK, Subbarao PMV, Chandra R, Ghosh P, Shah G, Kapoor R, Vijay V, Koutu V, Thakur IS. Biores. Tech. 2018; 250: 635–641.
- [5] Kanjanarong J, Giri BS, Jaisi DP, Oliveira FR, Boonsawang P, Chaiprapat S, Singh RS, Balakrishna A, Khanal SK. Biores Technol. 2016; 234:115–121
- [6] Juntarachat, N, Onthong U.Biomass Conversion and Biorefinery. 2022 doi.org/10.1007/s13399-022-03430-z
- [7] Shang G, Shen G, Liu L, Chen Q, Xu Z, Biores. Tech. 2016; 133: 495-499

C-CHEMISTRY (ORGANIC & MEDICINAL CHEMISTRY)



ALKYLATED 4'-AMINOCHALCONE AS NEW α -GLUCOSIDASE INHIBITORS

Emmanuel Sunday Idoko, Warinthorn Chavasiri*

Center of Excellence in Natural Products Chemistry, Department of Chemistry, Faculty of Science, Chulalongkorn University, Bangkok 10330, Thailand

*e-mail: warinthorn.c@chula.ac.th

Abstract:

Diabetes mellitus, one of the most predominant health problems worldwide characterized by hyperglycemia, has attracted the attention of medicinal chemists. Although several therapeutic drugs have been developed and used clinically, diabetes continues to pose a growing threat to public health. One of the promising approaches for the treatment of type 2 diabetes involves reducing the rate of carbohydrate hydrolysis by inhibiting the action of α -glucosidase. In this study, twelve novel derivatives of 4'-aminochalcone (**2a-2l**) were synthesized *via* one-pot reductive amination with substituted benzaldehyde, and their anti-hyperglycemic inhibitory activity was evaluated against α -glucosidase. Compounds **2c**, **2f**, **2i**, and **2k** exhibited moderate activities with IC_{50} values ranging from 1.52 to 0.06 μ M compared to the positive control, acarbose (IC_{50} 836.00 μ M). The structure-activity relationship was established by considering the parent skeleton and different substitution on aryl ring. The most potent compound, **2k** (IC_{50} 0.15) was also subjected to enzyme kinetic studies and displayed an uncompetitive mode of inhibition.

Introduction:

Diabetes mellitus is a chronic metabolic disease that is predominant globally both in developed and developing countries and continues to increase at an alarming rate.¹ It is characterized by an abnormally elevated blood glucose level caused by impaired insulin secretion and insulin resistance.^{2,3} Prolonged hyperglycemia can have devastating effects including retinopathy, nephropathy, neuropathy, and other complications.^{4,5} Type 2 diabetes mellitus (T2DM) accounts for more than 90% of all types of diabetes. The use of hyperglycemic drugs can impede glucose absorption by inhibiting α -glucosidase thereby controlling post-prandial hyperglycemia in patients with T2DM.⁶ Currently, α -glucosidase inhibitors such as acarbose, miglitol, and voglibose are used clinically to treat T2DM. Nevertheless, the long-term administration of these drugs have adverse side effects and limitations such as stomach ache, diarrhea, and flatulence.⁷ It is thus essential to discover novel drug candidates with fewer side effects for the treatment of T2DM.

Chalcones are natural products found in plants and have been found to possess numerous biological and therapeutic properties including anticancer, antitumor, antimalarial, antiviral, and antituberculosis.⁸ The 1,3-diphenylpropen-1-one is produced as an intermediate in the biosynthesis of flavonoids. Hence, they are considered precursors of open-chain flavonoids. They can be synthesized chemically *via* Claisen-Schmidt condensation reaction under basic conditions.⁹ Aminated chalcone derivatives have recently been reported to have the potential to act as a new class of α -glucosidase inhibitors.¹⁰ Moreover, sulfonylurea-sulfonamide hybridized compounds have also shown excellent antidiabetic activity.¹¹ Molecular docking has revealed that the NH moiety of these compounds is important for interacting with the desired target through hydrogen bonding.¹²

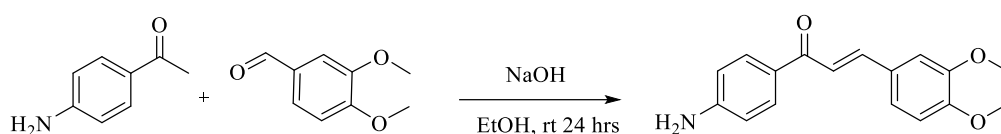
Reductive amination plays an important role in medicinal chemistry due to its synthetic merits in C-N bond formation and the abundant presence of amines among biologically active compounds.¹³ In this paper, alkylated aminochalcone have been synthesized *via* a one-pot reductive amination reaction of 4'-aminochalcone and substituted

benzaldehydes derivatives and evaluated for their α -glucosidase inhibitory activity. The interaction mechanism between the desired compound and the targeted enzyme was investigated by kinetic study.

Methodology:

The general procedure for the synthesis of 4'-aminochalcone

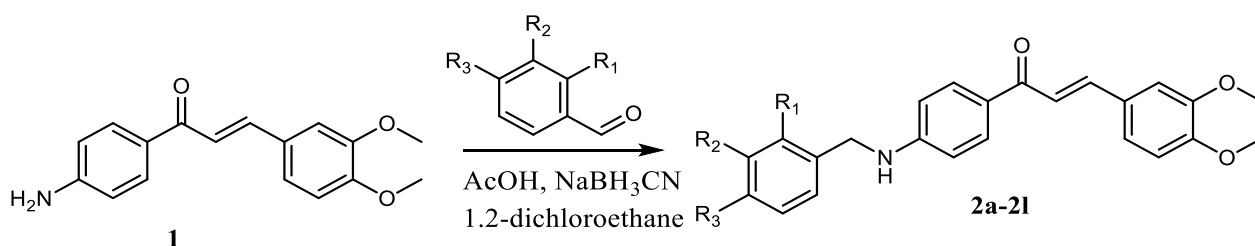
4'-Aminochalcone (**1**) was synthesized *via* Claisen–Schmidt condensation under basic condition (**Scheme 1**). A mixture of *p*-aminoacetophenone 270 mg (2 mmol) and veratraldehyde 415 mg (2.5 mmol) was stirred in EtOH (10 mL) and then drops of 40% aqueous NaOH were added. The resulting mixture was stirred for 24 hrs and then poured into crushed ice.¹⁴ Furthermore, 10% HCl was added to adjust the pH to 5-4. The organic layer was extracted using EtOAc, dried over anhydrous Na₂SO₄, and separated by silica gel chromatography using hexane:EtOAc to obtain a yellowish compound **1**. Yield 75 %



Scheme 1: Synthesis of 4'-aminochalcone **1**

Synthesis of alkylated 4'-aminochalcone derivatives

The alkylated derivatives of 4'-aminochalcone were synthesized *via* reductive amination reaction as shown in **Scheme 2**. To a stirred mixture of **1** 57 mg (0.2 mmol), substituted benzaldehyde (0.6 mmol), and glacial acetic acid in DCM was added NaBH₃CN (0.4 mmol) at room temperature overnight. After the completion of the reaction monitored by TLC, saturated NaHCO₃ solution was added to adjust the pH to 7–8, DCM was added for extraction, and the organic phase was collected. The target compound was obtained by column chromatography using hexane: EtOAc. All the compounds were obtained as yellow powders with yield ranging from 67 to 82%



2a: R₁ = R₂ = R₃ = H

2b: R₁ = R₂ = H, R₃ = CH₃

2c: R₁ = R₂ = H, R₃ = OCH₃

2d: R₁ = R₂ = H, R₃ = F,

2e: R₁ = R₂ = H, R₃ = CH₂CH₃

2f: R₁ = OCH₃, R₂ = R₃ = H

2g: R₁ = R₃ = H, R₂ = OCH₃

2h: R₁ = H, R₂ = R₃ = OCH₃

2i: R₂ = H, R₁ = R₃ = OCH₃

2j: R₁ = R₂ = H, R₃ = NO₂

2k: R₁ = R₂ = H, R₃ = OH

2l: R₁ = R₂ = H, R₃ = OCH₂CH₂CH₂CH₃

Scheme 2: Synthesis of alkylated 4'-aminochalcone derivatives

(*E*)-1-(4-(Benzylamino) phenyl)-3-(3,4-dimethoxyphenyl) prop-2-en-1-one (**2a**) yield 67% ¹H NMR (500 MHz, CDCl₃) δ_{H} (ppm) 7.86, 7.84, 7.64, 7.61, 7.32, 7.29, 7.25, 7.21,



7.20, 7.19, 7.19, 7.18, 7.12, 7.12, 7.10, 7.10, 7.05, 7.05, 6.79, 6.78, 6.60, 6.58, 4.33, 3.84, 3.82. 7.27 – 7.17 (m, 5H), 7.11 (dd, $J = 8.2, 2.1$ Hz, 1H), 7.05 (d, $J = 2.0$ Hz, 1H), 6.79 (d, $J = 8.4$ Hz, 1H), 6.59 (d, $J = 8.8$ Hz, 2H), 4.33 (s, 2H), 3.84 (s, 3H), and 3.82 (s, 3H). ^{13}C NMR (126 MHz, CDCl_3) δ_{C} (ppm) 187.8, 151.1, 150.8, 149.0, 142.9, 137.7, 130.8, 128.6, 128.2, 127.5, 127.4, 122.6, 119.8, 112.2, 110.9, 109.8, 55.8, 55.8, and 47.8. HRMS (ESI) m/z calcd for $\text{C}_{24}\text{H}_{23}\text{NO}_3$ $[\text{M}+\text{H}]^+$ 374.1720, found 374.1750.

(*E*)-3-(3,4-Dimethoxyphenyl)-1-(4-((4-methylbenzyl)amino)phenyl)prop-2-en-1-one (**2b**) yield 70% ^1H NMR (500 MHz, CDCl_3) δ_{H} (ppm) 7.97 (d, $J = 8.6$ Hz, 2H), 7.75 (d, $J = 15.5$ Hz, 1H), 7.42 (d, $J = 15.8$ Hz, 1H), 7.29 – 7.22 (m, 4H), 7.20 – 7.15 (m, 3H), 6.91 (d, $J = 8.3$ Hz, 1H), 6.73 (d, $J = 8.4$ Hz, 2H), 4.40 (s, 2H), 3.97 (s, 3H), 3.95 (s, 3H), and 2.36 (s, 3H). ^{13}C NMR (126 MHz, CDCl_3) δ_{C} (ppm) 187.9, 150.8, 149.0, 143.1, 137.4, 130.8, 129.4, 128.1, 127.5, 122.6, 119.8, 110.8, 109.8, 55.8, 55.8, 47.8, and 21.1. HRMS (ESI) m/z calcd for $\text{C}_{25}\text{H}_{25}\text{NO}_3$ $[\text{M}+\text{H}]^+$ 388.188, found 388.1907.

(*E*)-3-(3,4-Dimethoxyphenyl)-1-(4-((4-methoxybenzyl)amino)phenyl)prop-2-en-1-one (**2c**) Yield 68%, ^1H NMR (500 MHz, CDCl_3) δ_{H} (ppm) 7.95 (d, $J = 8.9$ Hz, 2H), 7.72 (d, $J = 15.5$ Hz, 1H), 7.41 (d, $J = 15.5$ Hz, 1H), 7.27 (d, $J = 8.6$ Hz, 2H), 7.20 (dd, $J = 8.3, 2.0$ Hz, 1H), 7.14 (d, $J = 2.0$ Hz, 1H), 6.90 – 6.87 (m, 3H), 6.66 (d, $J = 6.9$ Hz, 2H), 4.34 (s, 2H), 3.94 (s, 3H), 3.91 (s, 3H), and 3.79 (s, 3H). ^{13}C NMR (126 MHz, CDCl_3) δ_{C} (ppm) 188.3, 158.6, 152.9, 151.3, 149.5, 143.4, 131.3, 130.3, 129.2, 128.7, 128.4, 123.1, 120.8, 114.5, 112.5, 111.5, 110.4, 57.0, 56.7, 55.7, and 47.7. HRMS (ESI) m/z calcd for $\text{C}_{25}\text{H}_{25}\text{NO}_4$ $[\text{M}+\text{H}]^+$ 404.1865, found 404.1857.

(*E*)-3-(3,4-Dimethoxyphenyl)-1-(4-((4-fluorobenzyl)amino)phenyl)prop-2-en-1-one (**2d**) Yield 65% ^1H NMR (500 MHz, CDCl_3) δ_{H} (ppm) 7.95 (d, $J = 8.6$ Hz, 2H), 7.73 (d, $J = 15.5$ Hz, 1H), 7.40 (d, $J = 15.5$ Hz, 1H), 7.32 (dd, $J = 8.7, 5.3$ Hz, 2H), 7.21 (dd, $J = 8.2, 2.1$ Hz, 1H), 7.14 (d, $J = 2.0$ Hz, 1H), 7.03 (t, $J = 8.7$ Hz, 2H), 6.88 (d, $J = 8.3$ Hz, 1H), 6.67 (d, $J = 8.9$ Hz, 2H), 4.39 (s, 2H), 3.94 (s, 3H), and 3.92 (s, 3H). ^{13}C NMR (126 MHz, CDCl_3) δ_{C} (ppm) 187.9, 150.9, 149.0, 143.1, 130.8, 129.0, 128.1, 122.7, 119.7, 115.6, 115.5, 112.2, 110.9, 109.8, 55.8, and 47.1. HRMS (ESI) m/z calcd for $\text{C}_{24}\text{H}_{22}\text{FNO}_3$ $[\text{M}+\text{H}]^+$ 392.1663, found 392.1655.

(*E*)-3-(3,4-Dimethoxyphenyl)-1-(4-((4-ethylbenzyl)amino)phenyl)prop-2-en-1-one (**2e**) Yield 76% ^1H NMR (500 MHz, CDCl_3) δ_{H} (ppm) 7.93 (d, $J = 8.9$ Hz, 2H), 7.71 (d, $J = 15.6$ Hz, 1H), 7.39 (d, $J = 15.6$ Hz, 1H), 7.24 (d, $J = 2.1$ Hz, 1H), 7.20 (d, $J = 2.1$ Hz, 1H), 7.18 (s, 2H), 7.16 (s, 1H), 7.13 (d, $J = 2.0$ Hz, 1H), 6.86 (d, $J = 8.4$ Hz, 1H), 6.65 (d, $J = 8.9$ Hz, 2H), 4.36 (s, 2H), 3.92 (s, 3H), 3.90 (s, 3H), 2.62 (q, $J = 7.6$ Hz, 2H), and 1.21 (t, $J = 7.7$ Hz, 3H). ^{13}C NMR (126 MHz, CDCl_3) δ_{C} (ppm) 188.0, 152.0, 151.0, 149.2, 143.8, 143.1, 135.5, 131.1, 128.5, 128.4, 127.8, 127.6, 122.8, 120.1, 111.9, 111.5, 110.1, 77.4, 77.1, 76.9, 56.1, 56.0, 47.5, 28.6, and 15.7. HRMS (ESI) m/z calcd for $\text{C}_{26}\text{H}_{27}\text{NO}_3$ $[\text{M}+\text{H}]^+$ 402.2062, found 402.2051.

(*E*)-3-(3,4-Dimethoxyphenyl)-1-(4-((2-methoxybenzyl)amino)phenyl)prop-2-en-1-one (**2f**) Yield 66 % ^1H NMR (500 MHz, CDCl_3) δ_{H} (ppm) 7.92 (d, $J = 6.9$ Hz, 2H), 7.70 (d, $J = 13.7$ Hz, 1H), 7.38 (d, $J = 17.2$ Hz, 1H), 7.24 (d, $J = 1.7$ Hz, 3H), 7.20 – 7.10 (m, 2H), 6.94 – 6.82 (m, 3H), 6.67 (d, $J = 6.9$ Hz, 2H), 4.40 (s, 2H), 3.92 (s, 3H), 3.90 (s, 3H), and 3.85 (s, 3H). ^{13}C NMR (126 MHz, CDCl_3) δ_{C} (ppm) 188.1, 157.5, 150.7, 149.3, 143.1, 131.1, 129.0, 125.9, 122.8, 120.7, 120.2, 112.5, 111.2, 110.5, 110.2, 56.1, 55.5, and 43.4. HRMS (ESI) m/z calcd for $\text{C}_{25}\text{H}_{25}\text{NO}_4$ $[\text{M}+\text{H}]^+$ 404.1867, found 404.1854.

(*E*)-3-(3,4-Dimethoxyphenyl)-1-(4-((3-methoxybenzyl)amino)phenyl)prop-2-en-1-one (**2g**) Yield 69 % ^1H NMR (500 MHz, CDCl_3) δ_{H} (ppm) 7.95 (d, $J = 8.9$ Hz, 2H), 7.73 (d, $J = 15.5$ Hz, 1H), 7.41 (d, $J = 15.5$ Hz, 1H), 7.30 – 7.25 (m, 1H), 7.21 (dd, $J = 8.3, 2.0$ Hz,

1H), 7.15 (d, $J = 2.0$ Hz, 1H), 6.94 (d, $J = 7.4$ Hz, 1H), 6.91 – 6.87 (m, 2H), 6.83 (dd, $J = 7.4$, 2.9 Hz, 1H), 6.65 (d, $J = 8.6$ Hz, 2H), 4.40 (d, $J = 4.9$ Hz, 2H), 3.94 (s, 3H), 3.92 (s, 3H), and 3.79 (s, 3H). ^{13}C NMR (126 MHz, CDCl_3) δ_{C} (ppm) 187.8, 159.9, 151.7, 150.8, 149.0, 142.9, 139.8, 130.9, 129.7, 128.2, 127.7, 122.6, 119.9, 119.4, 112.9, 112.7, 111.7, 110.9, 109.8, 55.8, 55.8, 55.1, and 47.5. HRMS (ESI) m/z calcd for $\text{C}_{25}\text{H}_{25}\text{NO}_4$ $[\text{M}+\text{H}]^+$ 404.1867, found 404.1853.

(*E*)-1-(4-((3,4-Dimethoxybenzyl)amino)phenyl)-3-(3,4-dimethoxyphenyl)prop-2-en-1-one (**2h**) Yield 73 % ^1H NMR (500 MHz, CDCl_3) δ_{H} (ppm) 7.96 (d, $J = 8.9$ Hz, 2H), 7.73 (d, $J = 15.5$ Hz, 1H), 7.42 (d, $J = 15.5$ Hz, 1H), 7.21 (dd, $J = 8.3$, 2.0 Hz, 1H), 7.15 (d, $J = 2.0$ Hz, 1H), 6.93 – 6.81 (m, 4H), 6.66 (d, $J = 8.9$ Hz, 2H), 4.35 (s, 2H), 3.94 (s, 3H), 3.92 (s, 3H), 3.88 (s, 3H), 3.87 (s, 3H). ^{13}C NMR (126 MHz, CDCl_3) δ_{C} (ppm) 187.8, 151.8, 150.8, 149.1, 148.4, 142.9, 130.9, 130.5, 128.3, 127.6, 122.6, 119.8, 119.6, 111.7, 111.1, 110.9, 110.5, 109.9, 55.8, and 47.4. HRMS (ESI) m/z calcd for $\text{C}_{26}\text{H}_{27}\text{NO}_5$ $[\text{M}+\text{H}]^+$ 434.1968, found 434.1965.

(*E*)-1-(4-((2,4-Dimethoxybenzyl)amino)phenyl)-3-(3,4-dimethoxyphenyl)prop-2-en-1-one (**2i**) Yield 65% ^1H NMR (500 MHz, CDCl_3) δ_{H} (ppm) δ 7.94, 7.92, 7.73, 7.70, 7.42, 7.38, 7.21, 7.21, 7.20, 7.19, 7.18, 7.16, 7.14, 7.14, 6.89, 6.87, 6.69, 6.67, 6.47, 6.47, 6.44, 6.43, 6.42, 6.41, 4.33, 3.94, 3.91, 3.83, 3.79. ^{13}C NMR (126 MHz, CDCl_3) δ_{C} (ppm) 187.8, 159.8, 156.8, 155.1, 149.4, 147.9, 140.9, 131.5, 128.3, 127.6, 123.4, 121.8, 112.6, 111.7, 111.1, 110.9, 110.5, 109.9, 56.2, 55.8 and 46.4. HRMS (ESI) m/z calcd for $\text{C}_{26}\text{H}_{27}\text{NO}_5$ $[\text{M}+\text{H}]^+$ 434.1968, found 434.1951.

(*E*)-3-(3,4-Dimethoxyphenyl)-1-(4-((4-nitrobenzyl)amino)phenyl)prop-2-en-1-one (**2j**) Yield 82 % ^1H NMR (500 MHz, CDCl_3) δ_{H} (ppm) 8.19 (d, $J = 8.9$ Hz, 2H), 7.93 (d, $J = 8.9$ Hz, 2H), 7.72 (d, $J = 15.5$ Hz, 1H), 7.51 (d, $J = 8.9$ Hz, 2H), 7.38 (d, $J = 15.5$ Hz, 1H), 7.20 (dd, $J = 8.3$, 2.0 Hz, 1H), 7.13 (d, $J = 2.3$ Hz, 1H), 6.88 (d, $J = 8.3$ Hz, 1H), 6.62 (d, $J = 8.6$ Hz, 2H), 4.56 (s, 2H), 3.93 (s, 3H), and 3.91 (s, 3H) ^{13}C NMR (126 MHz, CDCl_3) δ_{C} (ppm) 188.0, 150.9, 149.0, 147.2, 146.0, 143.3, 130.9, 128.4, 128.0, 127.5, 123.9, 122.7, 119.6, 112.0, 110.9, 109.8, 77.2, 76.9, 76.7, 55.8, and 46.9. HRMS (ESI) m/z calcd for $\text{C}_{24}\text{H}_{22}\text{N}_2\text{O}_5$ $[\text{M}+\text{H}]^+$ 419.1601, found 419.1606.

(*E*)-3-(3,4-Dimethoxyphenyl)-1-(4-((4-hydroxybenzyl)amino)phenyl)prop-2-en-1-one (**2k**) Yield 69 % ^1H NMR (500 MHz, CDCl_3) δ_{H} (ppm) δ 7.95 (d, $J = 8.9$ Hz, 2H), 7.74 (d, $J = 15.5$ Hz, 1H), 7.42 (d, $J = 15.5$ Hz, 1H), 7.21 (d, $J = 8.3$ Hz, 3H), 7.14 (d, $J = 2.3$ Hz, 1H), 6.89 (d, $J = 8.3$ Hz, 1H), 6.84 (d, $J = 8.6$ Hz, 2H), 6.64 (d, $J = 8.6$ Hz, 2H), 4.33 (s, 2H), 3.94 (s, 3H), and 3.92 (s, 3H). ^{13}C NMR (126 MHz, CDCl_3) δ_{C} (ppm) 188.1, 155.3, 151.9, 150.9, 149.0, 143.1, 131.0, 130.0, 128.8, 128.2, 127.5, 122.7, 119.8, 115.6, 113.8, 111.7, 111.0, 109.9, 77.2, 76.9, 76.7, 55.9, 55.8, and 47.0. HRMS (ESI) m/z calcd for $\text{C}_{24}\text{H}_{23}\text{NO}_4$ $[\text{M}+\text{H}]^+$ 390.1706, found 390.1702.

(*E*)-1-(4-((4-Butoxybenzyl)amino)phenyl)-3-(3,4-dimethoxyphenyl)prop-2-en-1-one (**2l**) yield 77% ^1H NMR (500 MHz, CDCl_3) δ_{H} (ppm) δ 7.95 (d, $J = 8.6$ Hz, 2H), 7.73 (d, $J = 15.5$ Hz, 1H), 7.41 (d, $J = 15.5$ Hz, 1H), 7.26 (d, $J = 8.6$ Hz, 2H), 7.21 (dd, $J = 8.2$, 2.1 Hz, 1H), 7.15 (d, $J = 2.0$ Hz, 1H), 6.88 (dd, $J = 8.6$, 3.2 Hz, 3H), 6.66 (d, $J = 8.9$ Hz, 2H), 4.34 (s, 2H), 3.95 (s, 5H), 3.92 (s, 3H), 1.80 – 1.73 (m, 2H), 1.49 (dq, $J = 14.9$, 7.4 Hz, 2H), and 0.97 (t, $J = 7.4$ Hz, 3H). ^{13}C NMR (126 MHz, CDCl_3) δ_{C} (ppm) 187.8, 158.6, 150.8, 149.0, 142.9, 130.9, 129.6, 128.7, 128.2, 122.6, 119.9, 114.6, 111.8, 110.9, 109.8, 67.6, 55.9, 55.8, 47.2, 31.2, 19.1, and 13.7. HRMS (ESI) m/z calcd for $\text{C}_{28}\text{H}_{31}\text{NO}_4$ $[\text{M}+\text{H}]^+$ 446.2332, found 446.2325.

α -Glucosidase inhibitory assay

The synthesized compounds **2a-2l** were assayed for *in vitro* glucosidase inhibition. The α -glucosidase inhibitory assay was carried out by based on the procedure reported by

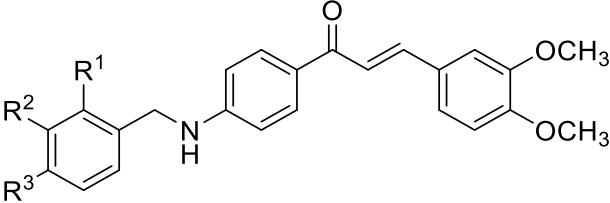


Ramadhan and coworkers with little modification.¹⁵ α -Glucosidase (0.4 U/mL) was prepared using 0.1 M, buffer (pH 6.9), and substrate (3 mM *p*-nitrophenyl- α -D-glucopyranoside) was dissolved in 0.1 M phosphate buffer (pH 6.9). The stock sample was prepared by dissolving 4 mM of the compound in DMSO. Furthermore, 1 mM of the loading sample was prepared from this solution. 10 μ L of the loading sample was pipetted into the 96 well plate followed by adding 40 μ L of α -glucosidase and then incubated at 37 °C for 10 min. Subsequently, 50 μ L substrate solution was added to the reaction mixture and incubated for another 20 min at 37° C. The reaction was terminated by adding 100 μ L of 1 M Na₂CO₃ solution. The absorbance was measured at 405 nm (ALLSHENG AMR-100 microplate reader) to analyze the enzymatic activity. The percentage inhibition was calculated using the formula: % Inhibition = [(A₀-A₁)/A₀] x 100, where A₀ is the absorbance without the sample and A₁ is the absorbance with the sample. The IC₅₀ value was deduced from the plot of % inhibition vs concentration of the tested sample. The experiment was performed in triplicate and acarbose was used as a positive control.

Results and discussion:

Twelve new (**2a–2l**) alkylated 4'-aminochalcone derivatives were successfully synthesized, characterized, and screened for their *in vitro* glucosidase activity. As shown in **Table 1**, compounds **2c**, **2f**, **2i**, and **2k** revealed potent inhibitory activity against the tested enzyme with IC₅₀ values ranging from 1.5 to 0.15 μ M.

Table 1. *In vitro* α -glucosidase inhibitory activity of alkylated 4'-aminochalcones **2a–2l**

|  | | | | | |
|--|------------------|------------------|--|----------------------------|-----------------------------|
| Compounds | R ¹ | R ² | R ³ | % inhibition at 50 μ M | IC ₅₀ (μ M) |
| 2a | H | H | H | 57.17 \pm 9.70 | - |
| 2b | H | H | CH ₃ | 58.64 \pm 2.56 | - |
| 2c | H | H | OCH ₃ | 82.51 \pm 4.30 | 0.65 \pm 0.15 |
| 2d | H | H | F | 65.11 \pm 1.88 | - |
| 2e | H | H | CH ₂ CH ₃ | 37.52 \pm 1.94 | - |
| 2f | OCH ₃ | H | H | 98.92 \pm 0.47 | 0.33 \pm 0.12 |
| 2g | H | OCH ₃ | H | 62.90 \pm 3.19 | - |
| 2h | H | OCH ₃ | OCH ₃ | 50.43 \pm 4.97 | - |
| 2i | OCH ₃ | H | OCH ₃ | 83.33 \pm 6.12 | 1.52 \pm 0.23 |
| 2j | H | H | NO ₂ | 57.05 \pm 3.90 | - |
| 2k | H | H | OH | 95.13 \pm 3.40 | 0.15 \pm 0.02 |
| 2l | H | H | OCH ₂ CH ₂ CH ₂ CH ₃ | 53.40 \pm 6.81 | - |
| Acarbose | | | | - | 836.00 \pm 47.19 |

^aIC₅₀ value was evaluated as mean \pm SD from the three independent experiments.

^bIC₅₀ value was not tested if the inhibition rate was less than 70% at 50 μ M.

Considering the effect of substitution on the aromatic aldehyde against α -glucosidase, the derivatives with stronger electron donating group at the *ortho/para* position increased the inhibitory activity compared to the unsubstituted compound, **2a**. Compound **2c** ($IC_{50} = 0.65 \mu\text{M}$) and **2f** ($IC_{50} = 0.33 \mu\text{M}$) with OMe at the *para* and *ortho* position respectively as well as compound **2i** ($IC_{50} = 1.5 \mu\text{M}$) with dimethoxy groups at both *ortho* and *para* position exhibited better activity than compound **2g** and **2h** with OMe group at the *meta* position.

Interestingly, compound **2l** bearing hydroxyl group at the *para* position was the most potent derivative with IC_{50} value of $0.15 \mu\text{M}$. This may be due to the stronger electron-donating effect of the hydroxyl group and its ability to form hydrogen bonding with the enzyme.

Moreover, comparing the %inhibition of compounds **2k**, **2c**, and **2l** as 95, 82, and 53%, respectively revealed that an increase in the hydrophobic character such as an increase in the length of the carbon chain on R^3 , decreased the α -glucosidase inhibitory activity.

α -glucosidase inhibitory kinetics

The mode of action of alkylated 4-aminochalcones was evaluated using the Lineweaver-Burk plot. The X-axis showed $1/(\text{PNPG})$ and $1/V$ values were plotted on the Y-axis. The activity was examined at different concentrations of *p*-nitrophenyl- α -D-glucopyranoside at 0.750, 0.375, 0.187, 0.093, and 0.046 mM in the presence or absence of the active compound.

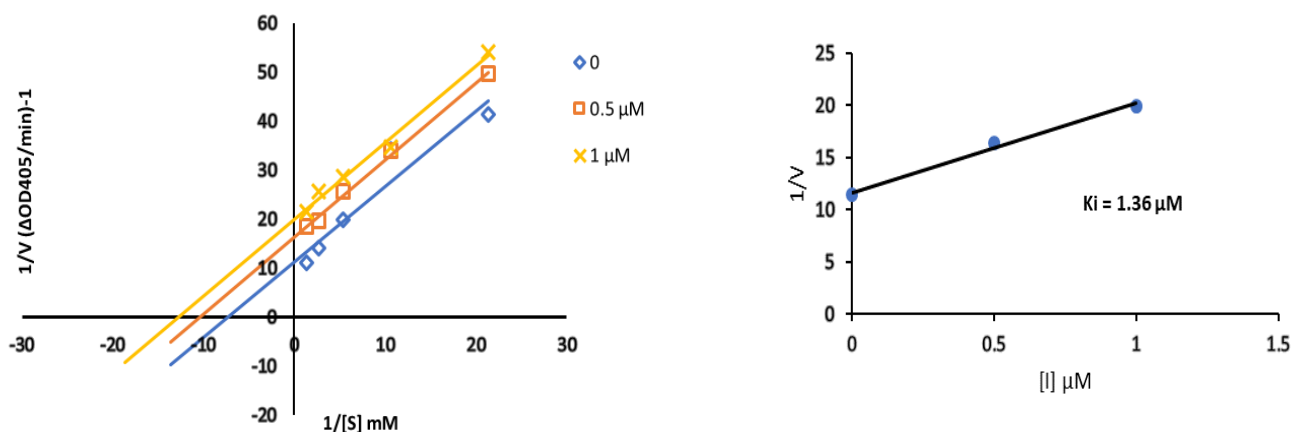


Figure 1. Kinetic study of **2k** and plots of slope against different concentrations **2k**

As shown in **Figure 1**, K_m and V_{max} values decreased which is typical of an uncompetitive inhibitor. The K_i of $1.36 \mu\text{M}$ was calculated using a secondary replot of the Lineweaver-Burk plot against the varying concentrations of the inhibitors at 0, 0.5, and $1 \mu\text{M}$.

Conclusion:

Twelve novel alkylated 4'-aminochalcone derivatives were successfully synthesized, characterized, and evaluated for α -glucosidase inhibition activity. Four compounds showed potential inhibitory activity with IC_{50} values ranging from 0.15 to $0.65 \mu\text{M}$ which is better than the positive control. The SAR indicates that strong electron-donating groups such as alkoxy and hydroxyl substitutions enhance the activity of the compound.



Acknowledgements:

ASEAN and Non-ASEAN scholarship under the Chulalongkorn University graduate program.

Reference

1. World Health Organization: Geneva: WHO. 2019;6–8.
2. Tan S.Y., Joyce L.M., Yan J.S., Wong S.S., Mohamed A.S., Sean H.T., Grace P.L., *et al.* Clin. Res. & Rev. 2019;13:364–372.
3. Yukako T., Akiko M., Kei A., Nao S., Naomi M., Yuko O., Yoshihiro M., Satoshi I., Takayoshi O. *Diabetes Res. Clin. Pract.* 2018;135:11–17.
4. Khalil H. Clin. Res. & Rev. 2017;11:133–139.
5. Skamagas M., Breen T., LeRoith D. Oral dis. 2008;14:105–114.
6. Faiza S., Kanwal, Khalid M., Sridevi C., Mehwish S., Appala R., Maria M., Zaheer U., Muhammad T. Bioorg. Chem. 2021;106:104489–104507.
7. Meiyang F., Wei Y., Zhiyun P., Yan H., Guangcheng W. Bioorg. Chem. 2023;31:106276–106287
8. Verma S., Srivastava K., Pandey P. PharmaTutor 2018;6(2):22–39
9. Sahu N.K., Balbhadra S.S., Choudhary J., Kohli D.V. Curr. Med. Chem. 2012;19:209–225.
10. Seo W.D., Jin H.K. Bioorg. Med. Chem. Lett. 2005;15:5514–5516.
11. Tanveer A., Tariq M., Muhammad S., Adnan A., Muhammad A.R., Muhammad Z., Munawar A.M. Pakistan J. Zool. 2020;52(3): 857-862.
12. Bharatham K., Nagakumar B., Ki Hun P., Keun W. J. Mol. Graphics Modell. 2008;26:1202–1212
13. Afanasyev O., Ekaterina K., Dmitry L., Denis C. Chem. Rev. 2019;119:11857–11911
14. Bahekar S.P., Hande S.V., Agrawal N.R., Chandak H.S., Bhoj P.S., Goswami K., Reddy M.V.R. Eur. J. Med. Chem. 2016;124:262–269
15. Ramadhan R., Phuwapraisirisan P. Bioorg. Med. Chem. Lett. 2015;25:4529–4533.



ANTIOXIDANT ACTIVITIES OF CHINESE HERBS: HUANG QIN, HUANG LIAN, AND HUANG BAI

Saloem Salot,¹ Santi Phosri,^{1,3} Mayuramas Wilai,^{1,2,*}

¹School of Cosmetic Science, Mae Fah Luang University, Chiang Rai, Thailand

²Phytocosmetics and Cosmeceuticals Research Group, Mae Fah Luang University, Chiang Rai, Thailand

³Department of Chemical Engineering, Faculty of Engineering, Burapha University, Chonburi, Thailand

*e-mail: mayuramas@mfu.ac.th

Abstract:

Huang Qin (HQ), Huang Lian (HL), and Huang Bai (HB) are herbal combinations used in traditional Chinese medicine (TMC) for the treatment of various heat-related diseases. In addition, phytochemicals found in these herbs, such as phenolic, flavonoid, and alkaloid compounds, act as antioxidant agents that scavenge free radicals and reactive oxygen species (ROS), helping to combat oxidative stress and damage. This study aims to compare the antioxidant activities of paired and triple combinations of HQ, HL, and HB with those of individual extracts. This investigation was conducted to estimate the total phenols, flavonoid content, and total alkaloids in paired and triple combinations of HQ, HL, and HB, compared to the individual extracts. The antioxidant experiments were conducted using *in vitro* assays, including DPPH, ABTS, and FRAP. The result indicated that the combination of HQ: HL: HB showed the highest antioxidant activities based to DPPH and ABTS scavenging assays, with IC₅₀ of 168.79±21.31 µg/ml and 210.34±9.14 µg/ml, respectively. Furthermore, the combination of HQ: HL: HB also exhibited the highest antioxidant activity in the FRAP assay, with a value of 307.31±6.07 mg TE/ g extract. However, all the combination showed underscore which had antagonistic effect. The outcome of this study suggests that the combination did not enhance the antioxidant properties compared to the single extract.

Introduction:

Skin is the initial line of defense between the human body and its surroundings, or the barrier between the internal and exterior aggressions. Numerous environmental variables, including visible and ultraviolet radiation from the sun, particulate matter, and ozone pollution, including the oxidative metabolism in the skin mitochondria raise the skin's generation of reactive oxygen species (ROS)^{1,2} which affect the skin microbiota composition.^{3,4} Furthermore, by reducing the antioxidant defenses, long-term psychological stress can also cause oxidative stress in the skin,⁵ which contributes to many diseases such as cardiovascular diseases, degenerative diseases, diabetes, inflammation,⁶ cancer, anemia, and ischemia.⁷ The skin's oxidative stress leads to wrinkles, sagging, dryness, roughness, and aging.⁸

Numerous novel cosmeceuticals and formulas have been discovered to help the skin repair wrinkles, resulting in a younger, healthier-looking face with glowing skin. The most promising topical therapies contain vitamins, minerals, estrogen, and antioxidants. It is known to scavenge free radicals and to cause irreversible damage to cell structure and function, which accelerates the natural aging process.⁹

Herbal products are used in a variety of ways to treat and prevent aging skin. These include their potential as antioxidants,¹⁰ antiphotaging agent,^{11,12} anti-inflammatory activity,¹³ promoters of skin cell proliferation¹⁴ or inhibitor of the synthesis of melanin.¹⁵

Many botanical medications are typically used in a Traditional Chinese Medicine (TCM) recipe, and each botanical drug has variety of chemical components.¹⁶ These elements are the TCM formula's material basis for both effect and mechanism of action (MOA). The pharmacological mechanism of the TCM formula can be better understood by examining the chemical composition and variation in formula compatibility effectiveness.¹⁷ The *vivo* and *vitro* assays are the conventional methods to investigate the pharmacological effects of one or more TCM components.

It is commonly known that the water decoction of Chinese medicinal formulas that contain *Radix Scutellariae*, called Huang Qin *Rhizoma Coptidis*, called Huang Lian, or/and *Cortex Phellodendri*, called Huang Bai. It is well-known combinative usage as a "medicine couple" Huang Qin and Huang Lian are frequently prescribed in Chinese medicinal formulae such as "Shigao Tang", Huanglian Jiedu Tang", "Huanglian Ejiao Tang", and "Gegen Qinlian Tang" because of the thought that their combined use enhances therapeutic effect. Additionally, this "medicine couple" is frequently utilized in "herbal tea", which Southern Chinese people regularly drink.¹⁸ It has been used for detoxifying and eliminating heat.¹⁹ Because different components of the herbal combination can hit several sites at once and conduct synergistic therapeutic activities, it is thought to be superior to single herbal. Huang Qin (HQ), which is prepared by decoction which is used in treatment such as diarrhea, dysentery, hypertension, hemorrhaging, insomnia, inflammation, and respiratory infection in TCM.²⁰ The major bioactive compounds found in HQ are flavones such as baicalin, wogonoside, and their aglycone baicalein which are responsible for anti-viral, anti-bacteria, antioxidant, anti-inflammatory, hepatoprotective, and neuroprotective activities.²¹ Antioxidant and anti-inflammation effects have been shown in many diseases' models, such as diabetes, cardiovascular disease, inflammatory bowel disease, gout, rheumatoid arthritis, asthma, neurodegenerative diseases, liver and kidney disease, cerebrospinal inflammation, and cancer.²² In addition, the study of the effectiveness of baicalein and wogonin isolated from *Scutellaria baicalensis* roots on skin damage found that wogonin and baicalein can inhibit irradiation-induced skin damage in hairless mice that are irradiated by UVB.²³ Huang Lian (HL), is widely used in food and pharmacological applications. The dried root was often prepared by decoction in TCM. In TCM, it is often used for clearing heat, eliminating dampness, purring fire, and detoxification.^{24,25} The main components found in *Coptis chinensis* Franch were alkaloids, such as magnolia, berberine, coptisine, jatrorrhizine, and palmatine which have potential anti-carcinogen, anti-microbial, anti-inflammation, and antioxidant.^{26,27} Huang Bai (HB), the dried bark of *Phellodendron chinense* Scheid.²⁸ The cortex part of HB is frequently prepared in TCM use in treatment of diarrhea, jaundice, leucorrhea, stranguries, and knee swelling.²⁹ In pharmacological activities, it is used in treatment such as inflammation, anti-diarrhea, anti-tumor, anti-viral, and pneumonia.³⁰ The main bioactive compounds that are found in cortex of HB are alkaloids such as berberine, palmatine, and phellodendron which are known as anti-inflammatory agents are used in pharmacological in anticancer, antimicrobial, and neuroprotective activities.^{31,32}

However, the research on the comparison between single and combination herbal has not been performed yet. Because different components of the herbal combination can hit several sites at once and conduct synergistic therapeutic activities. The purpose of this study aimed to determine single (HQ, HL, and HB) and combinations (HQ:HL, HQ:HB, HL:HB, and HQ:HL:HB) extracts on antioxidant properties *in vitro*.



Methodology:

Plant materials

The plants of HQ, HL, and HB were purchased from Hua Chiew Traditional Chinese Medicine Hospital in Bangkok, Thailand.

Preparation of plant extract

The plant extract was prepared using a Hermetic decoction apparatus: one kilogram of each plant is soaked in 8 liters of deionized water for one hour at room temperature before extract. The soaked sample of each plant was extracted at 120 degrees Celsius under pressure (1300 watts) for one hour (YJ13B-G, Donghuayuan Medical, China). The extract was filtered, evaporated, freeze-dried, and stored under 4 degrees Celsius before further experiment.

Determination of total phenolic content (TPC)

The total phenolic contents (TPC) of each plant extract and the combinations were determined using Folin-Ciocalteu following the method of Silva et al.³³ with slight modification. In brief, 20 μ l of diluted sample was mixed with 20 μ l of Folin-Ciocalteu reagent, and then 100 μ l of 7.5% (w/v) Na_2CO_3 solution was inserted into a 96-well microplate. The mixture was incubated at room temperature for 30 mins under dark conditions. The absorbance of the mixture was determined at 760 nm by microplate reader (BMG LABTECH, SPECTRO star Nano, Germany). Using gallic acid as a standard, the outcome was described as mg of gallic acid equivalent (GAE) per gram sample.

Determination of total flavonoid content (TFC)

The total of flavonoid contents (TFC) was described according to Fattahi et al.³⁴ After mixing 40 μ l of the diluted test sample with 15 μ l of 5% NaNO_2 , the mixture was placed in the dark for 5 mins. Then, add 15 μ l of 10% AlCl_3 and kept in the dark at room temperature for 6 mins. The solution was mixed with 100 μ l of 1M NaOH solution and kept in the dark for 10 mins. Using quercetin as the standard, the outcome was described as mg of quercetin equivalent (QE) per gram of sample. The absorbance of mixture was read at 510 nm by microplate reader (BMG LABTECH, SPECTRO star Nano, Germany).

Determination of total alkaloid content (TAC)

The total alkaloid was determined following method of Jain et al.³⁵ To determine the total alkaloids in medicine plants, a spectrophotometric technique according to the response with bromocresol green (BCG) has been devised. At pH 4.7, a yellow complex occurs that is readily extracted with chloroform.

Preparation of the solution: 69.8 mg of bromocresol green, 3 ml of 2 N NaOH, and 5 ml of distilled water were added, the mixture was well dissolved, and 1000 ml of distilled water was added to make bromocresol green solution (1×10^{-4}). To make phosphate buffer solution (pH 4.7), 2 M sodium phosphate was adjusted to pH 4.7 using 0.2 M citric acid. 1 milligram of pure atropine was dissolved in 10 ml of distilled water to create an atropine standard solution.

Preparation of standard curve: determine the exact volume of atropine standard solution in aliquots (0.6, 0.8, 1, 1.2, and 1.5 ml) and transfer each to a separate separatory funnel. Then, add 5ml of pH 4.7 phosphate buffer and 5 ml of BCG solution. Agitate a solution with 1, 2, 3, and 4 ml of chloroform solution with vigorous mixing. The extracts were gathered into a 10 ml volumetric flask, and chloroform was then added to regulate the volume. At 470 nm by UV-vis spectrophotometer (Libra S80, Biochrom), the complex's absorbance in chloroform was evaluated in comparison to a blank that was similar but without atropine.

Plant extract: after dissolving 100 mg of plant extract in 2 N HCl, the mixture was filtered. This solution was poured into a separatory funnel, and 1 ml was rinsed three times with 10 ml of chloroform. This solution's pH was brought to neutral using 0.1 N NaOH. Next, this solution was mixed with 5 ml of phosphate buffer and 5 ml of BCG. After giving the mixture a good shake, the solution was extracted using 1, 2, 3, and 4 ml of chloroform. After being collected into a 10 ml volumetric flask, the extracts were diluted to volume using chloroform. At 470 nm, the complex's absorbance in chloroform was determined.

The DPPH assay

The DPPH (2,2-diphenyl-1-picrylhydrazyl) scavenging capacities were determined according to the method of Kantangkul et al.³⁶ with some modifications. Absolute ethanol was used to dissolve the DPPH reagent. Briefly, 50 µl of the different concentrations of the test sample was added into 50 µl of 0.89 mM DPPH solution and incubated for 30 mins in the dark condition at room temperature. The absorbance was determined at 517 nm by microplate reader (BMG LABTECH, SPECTRO star Nano, Germany). Ascorbic acid was used as the standard. The ability of the test sample to scavenge radicals was assessed by measuring the reduction in DPPH absorbance and calculating it using the following equation: Inhibition (%) = $[(A_{\text{control}} - A_{\text{sample}})/A_{\text{control}}] \times 100$

The result was demonstrated as IC₅₀ and calculated by graphing the reminding percentage of DPPH against the sample concentrations to obtain the quantity of antioxidant required to reduce the initial DPPH concentration by 50%. The lower value of IC₅₀ denotes greater antioxidant activity.

The ABTS assay

The ABTS^{•+} (2,2'-azinobis (3-ethylbenzothiazoline-6-sulphonic acid)) radical scavenging assay was evaluated according to Polbuppha et al.³⁷ ABTS^{•+} was produced by reacting of 7 mM ABTS stock solution with 2.45 mM potassium persulfate (K₂S₂O₈) with the ratio of 1:1 and incubated for 16 hrs. in the dark at room temperature before use. The working solution was prepared by mixing with deionized water with the ratio of 1:10. Briefly, 10 µl of different concentration of test samples was added into 100 µl of ABTS^{•+} solution and incubated for 30 mins in the dark. The absorbance was established at 734 nm by microplate reader (BMG LABTECH, SPECTRO star Nano, Germany). Ascorbic acid was used as standard. The radical scavenging activity was calculated following: Inhibition (%) = $[(A_{\text{control}} - A_{\text{sample}})/A_{\text{control}}] \times 100$

The FRAP assay

Ferric reducing antioxidant power assay (FRAP) was determined according to method of Phosri et al with some modification.³⁸ The FRAP reagent stock was produced by combining 30 mM acetate buffer (pH 3.6), 10 mM TPTZ (2,4,6-tri(2-pyridyl)- s-triazine) in 40 mM HCl, and 20 mM FeCl₃·6H₂O in a 10:1:1 ratio. The FRAP solution was made immediately prior to its usage. 10 µl of different concentration of test sample was added into 200 µl of the fresh FRAP solution and kept in the room temperature for 4 mins. The absorbance was determined at 593 nm using microplate reader (BMG LABTECH, SPECTRO star Nano, Germany). The result was calculated and expressed as FRAP value indicated as mg of trolox equivalent (TE) per gram sample.

The data was described as the means value ± SD value. One-way ANOVA was performed. SPSS software was used to calculate the significant difference ($p < 0.05$) between mean values.

The synergistic scavenging effect of the compounds on DPPH and ABTS radicals

The synergistic effect of the combination was determined as the ratio of the oxidation reaction's experimental antioxidant capacity versus its theoretical antioxidant capacity. The experimental scavenging capacity of DPPH (%ESC_{DPPH}) was determined.³⁹

$$\% \text{ESC}_{\text{DPPH}} = 100 - \{ [A_{\text{sample}} - A_{\text{blank}}] / A_{\text{control}} \}$$



A_{sample} = The absorbance value of the sample, (antioxidant (s) and DPPH solution)

A_{blank} = The absorbance value of the blank, (antioxidant (s) and ethanol)

A_{control} = The absorbance value of the control, (DPPH solution and ethanol)

The theoretical scavenging capacity of DPPH (%TSC_{DPPH}) is the total of the scavenging capacities of each antioxidant, determined using the individual scavenging capacity according to method of Fuhrman et al.⁴⁰

$$\%TSC_{DPPH} = 100 - \{ [(100 - ESC_1)/100] * [(100 - ESC_2)/100] * [(100 - ESC_3)/100] \}$$

ESC₁₋₃ = The percentage ESC of the individual antioxidant

$$SE(DPPH) = ESC_{DPPH} / TSC_{DPPH}$$

Whereby synergism was evident when SE greater than 1 (SE>1).

The theoretical scavenging capacity of ABTS (%TSC_{ABTS}) is the total of the scavenging capacities of each antioxidant, determined using the individual scavenging capacity following method of Fuhrman et al.⁴⁰

$$\%TSC_{ABTS} = 100 - \{ [(100 - ESC_1)/100] * [(100 - ESC_2)/100] * [(100 - ESC_3)/100] \}$$

ESC₁₋₃ = The percentage ESC of the individual antioxidant

$$SE(ABTS) = ESC_{DPPH} / TSC_{DPPH}$$

Whereby synergism was evident when SE greater than 1 (SE>1).

Statistical analysis, all the data were conducted triplicate. One-way ANOVA was performed for comparison. SPSS software was used to determine the significant difference ($p < 0.05$) between mean value.

Results and Discussion:

The quantification of phytoconstituents of plant extract, total phenol, total flavonoid contents, and total alkaloid content is shown in Table 1.

Table 1. Total phenol, total flavonoid, and total alkaloid content of single, pairs, and three combinations of HQ, HL, and HB in 1 g plant extract.

| Sample or standard | TPC (mg GAE/ g extract) | TFC (mg QE/ g extract) | TAC (mg AE/ g extract) |
|---------------------------|----------------------------|---------------------------|---------------------------|
| HQ | 193.00±9.77 ^c | 122.53±16.60 ^c | ND |
| HL | 74.81±3.74 ^f | 26.30±11.10 ^d | 15.82±0.46 ^a |
| HB | 138.85±2.76 ^d | 43.16±1.33 ^d | 9.89±0.06 ^c |
| HQ: HL (1:1, v/v) | 268.57±10.61 ^b | 223.23±9.06 ^b | 8.52±0.06 ^e |
| HQ: HB (1:1, v/v) | 286.56±16.15 ^a | 141.94±11.53 ^c | 5.31±0.08 ^f |
| HL: HB (1:1, v/v) | 257.81±4.88 ^b | 280.84±9.47 ^a | 13.26±0.10 ^b |
| HQ: HL: HB (1:1:1, v/v/v) | 292.07±10.92 ^a | 263.55±28.28 ^a | 9.48±0.11 ^d |

The data are presented as mean ± S.D. of triplicate determinations (n=3). Different letters within each column indicate statistically significant difference ($p < 0.05$). ND means not detected.

The TPC and TFC were determined in comparison with the standard gallic acid plot equivalent per gram of crude extract (mg GAE/ g crude extract) and quercetin plot equivalent per gram of crude extract (mg QE/ g crude extract). The gallic acid calibration curve was plotted of different concentrations of gallic acid (15.625, 31.25, 62.5, 125, 250, 500 µg/ml, y

= 0.0031x -0.0549, $R^2 = 0.9976$) and the quercetin calibration curve was plotted of different concentrations (62.5, 125, 250, 500, and 1000 $\mu\text{g/ml}$, $y = 0.0006x - 0.0081$, $R^2 = 0.9955$). The combination of HQ:HL:HB had the highest TPC and TFC, as 292.07 ± 10.92 mg GAE/ g extract not significant different with HQ:HB 286.56 ± 16.15 mg GAE/ g extract and 263.55 ± 28.28 mg QE/ g extract not significant different with HL:HB 280.84 ± 9.47 mg QE/ g extract, respectively. All the combinations had more quantities of TPC and TFC compared to the single extract. The total of alkaloid content (TAC) was calculated by the calibration curve regression equation ($y = 0.003x - 0.0086$, $R^2 = 0.9904$) and represented in atropine equivalent (AE). HL showed the highest amount of TAC, 15.82 ± 0.46 mg AE/ g extract. The pair combination of HL:HB had the second highest TAC, 13.26 mg AE/ g extract. However, TAC was not detectable in HQ.

Radical scavenging is important because free radicals can cause harm to biological systems and typically involved the transfer of hydrogen atoms or the donation of electron.⁴¹ This assay used different types radical scavenging activity, DPPH and ABTS to demonstrate the antioxidant activity of the plant extract. The antioxidant assays were shown in Table 2.

Table 2. Antioxidants activities, DPPH, ABTS, and FRAP of single, pairs, and three combinations of HQ, HL, and HB.

| Sample or standard | DPPH IC ₅₀ ($\mu\text{g/ml}$) | ABTS IC ₅₀ ($\mu\text{g/ml}$) | FRAP (mg TE/ g extract) |
|--------------------------|---|---|----------------------------|
| HQ | 366.99 ± 17.83^c | 598.60 ± 32.15^b | 149.95 ± 2.09^e |
| HL | 655.86 ± 17.64^e | 808.73 ± 24.81^d | 127.51 ± 5.22^f |
| HB | 567.56 ± 23.74^d | 654.65 ± 15.24^c | 135.58 ± 4.02^f |
| HQ: HL (1:1,v/v) | 289.73 ± 5.49^b | 228.16 ± 12.61^a | 265.04 ± 4.56^c |
| HQ: HB (1:1,v/v) | 303.86 ± 12.24^b | 222.54 ± 7.11^a | 289.92 ± 6.91^b |
| HL: HB (1:1,v/v) | 299.55 ± 22.16^b | 223.62 ± 9.02^a | 249.28 ± 4.91^d |
| HQ: HL: HB (1:1:1,v/v/v) | 168.79 ± 21.31^a | 210.34 ± 9.14^a | 307.37 ± 6.07^a |
| Ascorbic acid | 33.02 ± 2.85 | 54.02 ± 9.28 | - |

The data are presented as mean \pm S.D. of triplicate determinations (n=3). Different letters within each column indicate statistically significant difference means that do not share a letter in a column are significant different ($p < 0.05$).

DPPH and ABTS radical scavenging activities assay were used to determine the efficacy of an antioxidant molecule in eliminating the DPPH[•] and ABTS[•] radicals. The three combinations, HQ: HL: HB had the highest antioxidant activities both DPPH and ABTS assay with IC₅₀ of 168.79 ± 21.31 ($\mu\text{g/ml}$) and 210.34 ± 9.14 ($\mu\text{g/ml}$), respectively. It was significant different ($p < 0.05$) with others extract in DPPH assay; however, it was not significant different obtained by ABTS assay with the pair of HL: HB, HQ: HL, and HQ: HB. The result of antioxidant obtained by FRAP was used to determined reducing ability of compound that donates the electron to the ferric ions ($[\text{Fe(III)} (\text{TPTZ})_2]^{3+}$) and transforms to ferrous iron ($[\text{Fe(II)} (\text{TPTZ})_2]^{2+}$). Trolox calibration curve was plotted of different concentrations of gallic acid (7.8125, 15.625, 31.25, 62.5, 125, 250 $\mu\text{g/ml}$, $y = 0.0051x + 0.0651$, $R^2 = 0.9997$). According to the result, the combination of HQ: HL: HB exhibited the highest antioxidant activity of any extracts, 307.37 ± 6.07 mg TE/ g extract. These test results may be predicted to be based on the properties of the well-known single compound (flavonoids; baicalin, wogonoside, and alkaloid; berberine) found in HQ, HL, and HB which also indicating significant role of the formation of the complex in the bioavailability enhancement of the pharmacologically active constituents.⁴²⁻⁴⁴ The flavonoids, revealing that double bonds and phenolic hydroxyls on rings A and B are augmentors, and sugar moiety is



an attenuator influencing antioxidant abilities in scavenging DPPH[•], ABTS^{•+}, and FRAP.^{45,46} While the berberine play an important role in the scavenging a variety of free radicals may follow either of the typical mechanisms of (i) formal hydrogen transfer, (ii) single electron transfer- proton transfer, and (iii) sequential proton-loss electron transfer or/and radical adduct formation. It depends on the hydroxy group substituent at the C-9 and C-12 positions of the berberine backbone's structure.^{47,48}

It is commonly known that the TCM formula is a complex system and that by using herb-herb synergy, combinations can improve further use such as active ingredients in cosmetics. Furthermore, compared to berberine alone, the combination had superior anti-inflammation, antibacterial, and antioxidant properties according to a metabolomics study. The ability of the three combinations to restore the whole disturbing metabolism of model rats was greater than that of berberine used alone.⁴⁹ There are different approaches developed to evaluate the interaction of the compounds in combination therapies.⁵⁰ The synergism effect and selection of the ratio of the combination is one of the factors affecting the synergism quantification.⁵¹ This may be the reason to support that why all of combinations (HQ, HL, HB) from these studies exhibited $SE < 1$, hence exhibiting an antagonistic effect.

Table 3. The SE_{DPPH} and SE_{ABTS} value of pair and three mixtures of HQ, HL, and HB.

| Sample | SE_{DPPH} | SE_{ABTS} |
|-------------------|-------------|-------------|
| SEHQ:HL | 0.57±0.01 | 0.538±0.01 |
| SEHQ:HB | 0.59±0.01 | 0.565±0.01 |
| SEHL:HB | 0.57±0.01 | 0.578±0.01 |
| SEHQ:HL:HB | 0.62±0.04 | 0.545±0.01 |

$SE > 1$: Synergistic effect found, $SE < 1$: antagonism effect found, and $SE = 1$: indicating an additive interaction. The data showed as mean \pm SD (n=3).

Conclusion:

This study indicates that *in vitro* bioactivity of the plant extract from HQ, HL, and HB is associated with their active substances. The experiments show that the paired, and triple combinations contained higher quantities of phenolic and flavonoid compounds. However, the total alkaloid content (TAC) of the combination is lower than that of HL. The antioxidant properties reveal the paired, and triple combinations of HQ, HL, and HB demonstrate high antioxidant potential, as evidenced by the percentage of %IC₅₀ value in the DPPH and ABTS assays. Moreover, the reducing ability of the compounds, as measured by the FRAP assay, shows that do the combination has greater potency in donating electron to ferric ions. Specially, the combination of HQ:HL:HB exhibited the lowest %IC₅₀ values in both DPPH and ABTS assays, and the highest value in FRAP assay. Nevertheless, the study showed that the combination presents significant antagonistic activity, indicating that not all combinations influence antioxidant ability. The limitation of this study is that it is based solely on *in vitro* assays; therefore, further investigation into the cytotoxic effects on skin cells is required to assess safety for use in skincare and pharmaceutical products.

Acknowledgements:

The author would like to acknowledge to the faculty of Cosmetic, Mae Fah Luang University for their financial support, and provision of facilities for the study.

References:

1. Liebel F, Kaur S, Ruvolo E, Kollias N, Southall M. *J Invest Dermatol*. 2012;132:1901–1907.
2. Jurkiewicz B, Buettner G. *J Photochem Photobiol A Chem*. 1996;64:918–922.
3. Leung M, Tong X, Bastien P, Guinot F, Tenenhaus A, Appenzeller B, Betts R, Mezzache S, Li J, Bourokba N, Breton L. *Microbiome*. 2020;8:1–7.
4. Patra V, Byrne S, Wolf P. *Front Microbiol*. 2016;7:1235.
5. Dunn J, Koo J. *Dermatol. Online J*. 2013;19.
6. Simpson D, Oliver P. *Antioxidants*. 2020;9:1–27.
7. Jomova K, Raptova R, Alomar S, Alwasel S, Nepovimova E, Kuca K, Valko M. *Arch. Toxicol*. 2023;97:2499–2574.
8. Clatici V, Racocanu D, Dalle C, Voicu C, Tomas L, Marron S, Wollina U. *Maedica*. 2017;12:191.
9. Mukherjee P, Maity N, Nema N, Sarkar B. *Phytomedicine*. 2011;19:64–73.
10. Pérez-Sánchez A, Barrajón-Catalán E, Herranz-López M, Micol V. *Nutrients*. 2018;10:403.
11. Almeida I, Pinto A, Monteiro C, Monteiro H, Belo L, Fernandes J, Bento A, Duarte T, Garrido J, Bahia M, Lobo J. *J Photochem Photobiol B*. 2015;144:28–34.
12. Bulla M, Hernandez L, Baesso M, Nogueira A, Bento A, Bortoluzzi B, Serra L, Cortez D. *Photochem. Photobiol*. 2015;91:558–566.
13. Shin S, Jung E, Kim S, Kim E, Lee J, Park D. *PLoS One*. 2013;8.
14. Dudonné S, Poupard P, Coutière P, Woillez M, Richard T, Merillion J, Vitrac X. *J Agric Food Chem*. 2011;59:4527–4536.
15. Chao H, Najjaa H, Villareal M, Ksouri R, Han J, Neffati M, Isoda H. *Exp. Dermatol*. 2013;22:131–136.
16. Jia W, Gao W, Yan Y, Wang J, Xu Z, Zheng W, Xiao P. *Phytother Res*. 2004;18:681–686.
17. Wang K, Gao Y, Gong W, Ye X, Fan L, Wang C, Gao X, Gao L, Du G, Qin X, Lu A. *Front Pharmacol*. 2020;11.
18. Wang J, Tanaka T, Zhang H, Kouno I, Jiang Z. *Chem Pharm Bull*. 2012;60:706–711.
19. Qi Y, Zhang Q, Zhu H. *Chin. Med*. 2019;14:1–22.
20. Zhou X, Choi P, Yang J, Or P, Hoi P, Lee S, Leung G, Ngai S, Kong S, Ho H, Wong M. *Springerplus*. 2016;5.
21. Wang Z, Wang S, Kuang Y, Hu Z, Qiao X, Ye M. *Pharm Biol*. 2018;56:465–484.
22. Liao H, Ye J, Gao L, Liu Y. *Biomed Pharmacother*. 2021;133.
23. Kimura Y, Sumiyoshi M. *Eur J Pharmacol*. 2011;661:124–132.
24. Li X, Motwani M, Tong W, Bornmann W, Schwartz G. *Mol. Pharmacol*. 2000;58:1287–1293.
25. Pan H, Wang T, Che Y, Li X, Cui y, Chen Q, Wu Z, Yi J, Wang B. *Infect Drug Resist*. 2023;16:7071–7095.
26. Han L, Wang R, Zhang X, Yu X, Zhuo L, Song T, Deng X, Zhang Y, Zhang L, Bai C. *J AOAC Int*. 2019;102:699–707.
27. Wang T, Pan H, Che Y, Fu Q, Chen Q, Li X, Cui Y, Chen Q, Wu Z, Li R, Liu M. *Res Sq*. 2022.
28. Ryuk J, Zheng M, Lee M, Seo C, Li Y, Lee S, Moon D, Lee H, Lee J, Park J, Son J. *Arch Pharm Res*. 2012;35:1045–1054.
29. Lee S, Lee H, Lee S, Kim Y, Lee D, Chun J, Lee JY, Kim H, Chang G. *Chin. Med*. 2018;13:1–9.
30. Lin P, Hsu K, Shiu M, Liu W. *Sci Rep*. 2017;7:9009.



31. Cao X, Sun L, Li D, You G, Wang M, Ren X. *Molecules*. 2018;23:2307.
32. Jung H, Jin G, Kim S, Kim Y, Park Y. *Cell Biol. Int.* 2009;33:957–963.
33. Silva A, Rocha B, Moreira M, Delerue M, Neves J, Rodrigues F. *Int J Mol Sci.* 2024;25:2478.
34. Fattahi S, Zabihi E, Abedian Z, Pourbagher R, Ardekani A, Monstafazadeh A, Akhavan H. *Int J Mol Sci.* 2024;3:102.
35. Jain K, Tabasum S, Khare S. *Asian J Pharm Clin Res.* 2016;9.
36. Kantangkul T, Siripongvutikorn S, Sae-Wong. *Int. Food Res. J.* 2015;12:1073–1076.
37. Polbuppha I, Maneerat W, Sripisut T, Limthaeakul T, Cheenpracha S, Phyne S, Muanprasat C, Seemakhan S, Borwornpinyo S, Laphookhieo S. *Nat Prod Commun.* 2017;12:1073–1076.
38. Phosri S, Kiattisin K, Intharuksa A, Janon R, Na Nongkhai T, Theansungnoen T. *Cosmetics.* 2022;9.
39. Mensor L, Menezes F, Leitão G, et al. *Phytother Res.* 2001;15:127–130.
40. Fuhrman B, Volkova N, Rosenblat M, Aviram M. *Antioxid Redox Signal.* 2000;2:491–506.
41. Niki E and Noriko N. *IUBMB Life.* 2000;50:323–329.
42. Wang J, Tanaka T, Zhang H, Kouno I, Jiang Z. *Chem Pharm Bull.* 2012;60:706–711.
43. Fu X, Wang J, Liao S, Lv Y, Xu D, Yang M, Kong L. *Front Pharmacol.* 2019;10:337.
44. Qi Y, Zhang Q, Zhu H. *Chin. Med.* 2019;14:1–22.
45. Li K, Fan H, Yin P, Yang L, Xue Q, Li X, Sun L, Liu Y. *Arab. J. Chem.* 2018;11:159–170.
46. Gao Z, Yang X, Huang K, Xu H. *Appl. Magn. Reason.* 2000;19:35–44.
47. Nam P, Trung N, Hoa N, Bich HN, Manh TD, Quang DT, Mechler A, Vo QV. *RSC Adv.* 2022;12:9738–9743.
48. Liu Y, Long S, Zhang S, Tan Y, Wang t, Wu Y, Jiang T, Liu X, Peng D, Liu Z. *RSC Adv.* 2021;11:17611–17621.
49. Lv Y, Wang J, Xu D, Liao S, Li P, Zhang Q, Yang M, Kong L. *J Pharm Biomed Anal.* 2017;145:794–804.
50. Duarte D, Vale N. *Curr. Res. Pharmacol. Drug Discov.* 2022;3.
51. Gao Z, Li Z, Yan J, Wang P. *Drug Des Devel Ther.* 2017;11:2595–2604.



CHEMICAL MODIFICATION OF DIHYDROISOSTEVIOL

Daorueang Auppachai, Waraluck Chaichompoo, Wachirachai Pabuprapap,* Apichart Suksamrarn

Department of Chemistry and Center of Excellence for Innovation in Chemistry, Faculty of Science, Ramkhamhaeng University, Bangkok 10240, Thailand

*e-mail: wachirachai.p@ru.ac.th

Abstract:

Isosteviol (**2**), the hydrolyzed analog of stevioside (**1**), has been reported to exhibit vasorelaxant activity. In order to enhance the bioactivity of this compound, chemical modification of **2** to the dihydro analog (**3**) was undertaken. Compound **3** was then converted to the corresponding ester analogs (**4a–4h**). These analogs were prepared in yields between 20% and 81%, and their structures were elucidated using spectroscopic analyses.

Introduction:

Natural products have long been a cornerstone of drug discovery and development, providing a rich source of bioactive compounds with diverse chemical structures and biological activities.^{1,2} Despite their therapeutic potential, many natural products face limitations that can hinder their direct use as drugs, including suboptimal pharmacokinetic properties, low bioavailability and undesirable side effects.³ To overcome these challenges and enhance the efficacy, safety, and specificity of natural products, structural modification has emerged as a crucial strategy.⁴

Isosteviol (**2**) is a naturally derived diterpenoid compound obtained through the acid hydrolysis of stevioside (**1**), a well-known sweetener from the leaves of *Stevia rebaudiana*.⁵ This compound has gained considerable attention due to its diverse chemical properties and promising biological activities.⁶ Structurally, isosteviol features a tetracyclic framework with a carboxylic acid group, making it a versatile molecule for chemical modifications.⁷ Over the years, researchers have explored its potential in various therapeutic areas, including anti-inflammatory, anticancer, vasodilation, reduce blood pressure, and exhibit cardioprotective effects.^{8–10} In addition, a previous study by our group reported that compound **2** exhibits moderate vasorelaxant activity, while its analog, dihydroisosteviol (**3**), showed better vasorelaxant activity.¹¹ It was of particular interest to investigate whether modifying the structure of compound **3** could result in analogs with significantly enhanced biological activities. This study focuses on the chemical modification of dihydroisosteviol (**3**) to produce analogs **4a–4h** (Scheme 1).

Methodology:

1. General

Optical rotations were measured on a JASCO-1020 polarimeter. ¹H and ¹³C NMR spectra were recorded on a Bruker ASCEND 400 FT-NMR spectrometer, operating at 400 MHz and 100 MHz for ¹H and ¹³C NMR, respectively. HR-TOFMS spectra were measured with a Bruker micrOTOF-QII mass spectrometer, using electrospray ionization (ESI) as the ionization technique. Column chromatography was carried out using Merck silica gel 60 (particle sizes < 0.063 mm). For thin-layer chromatography (TLC), Merck pre-coated silica gel 60 F₂₅₄ plates were used. TLC spots were detected under UV light and by spraying with anisaldehyde-H₂SO₄ reagent, followed by heating. Stevioside was purchased from Thai-China Flavors and

Fragrances Industry Company, Limited. Other chemicals and solvents were of analytical grade and obtained from local distributors.

2. Acid hydrolysis of stevioside (**1**)

Stevioside (10.0 g) was hydrolyzed with 25% H₂SO₄ (200 mL) at 80 °C for 2 h. The precipitate was separated by filtration, washed with *n*-hexane and air-dried to afford compound **2**. The spectroscopic data were consistent with the reported values.¹¹ Yield 95%; [α]_D²⁵ –104.8 (*c* 0.45, MeOH); ¹H NMR (CDCl₃, 400 MHz): δ 0.76 (*s*, 3H, 20-CH₃), 0.88 (*td*, *J* = 13.2, 4.1 Hz, 1H, H-1 β), 0.95 (*s*, 3H, 17-CH₃), 1.00 (*td*, *J* = 13.5, 4.1 Hz, 1H, H-3 α), 1.11–1.19 (*m*, 1H, H-11 α), 1.12 (*dd*, *J* = 11.9, 2.2 Hz, 1H, H-5 β), 1.17–1.20 (*m*, 1H, H-9 β), 1.23 (*s*, 3H, 18-CH₃), 1.32–1.39 (*m*, 1H, H-2 α), 1.32–1.43 (*m*, 3H, H-7 β , H-12 α , H-14 α), 1.45 (*ddd*, *J* = 13.5, 4.0 Hz, 1H, H-7 α), 1.52 (*dd*, *J* = 11.5, 2.6 Hz, 1H, H-14 β), 1.59 (*brdd*, *J* = 14.5, 2.7 Hz, 1H, H-12 β), 1.67–1.74 (*m*, 1H, H-11 β), 1.71–1.77 (*m*, 1H, H-1 α), 1.74–1.79 (*m*, 1H, H-6 α), 1.75–1.82 (*m*, 1H, H-15 β), 1.81–1.87 (*m*, 1H, H-6 β), 1.82–1.90 (*m*, 1H, H-2 β), 2.14 (*brd*, *J* = 13.5 Hz, 1H, H-3 β), 2.61 (*dd*, *J* = 18.6, 3.7 Hz, 1H, H-15 α); ¹³C NMR (CDCl₃, 100 MHz): δ 13.2 (CH₃, C-20), 18.8 (CH₂, C-2), 19.8 (CH₃, C-17), 20.4 (CH₂, C-11), 21.5 (CH₂, C-6), 28.9 (CH₃, C-18), 37.2 (CH₂, C-12), 37.6 (CH₂, C-3), 38.1 (C, C-10), 39.4 (C, C-13), 39.6 (CH₂, C-1), 41.3 (CH₂, C-7), 43.6 (C, C-4), 48.4 (CH₂, C-15), 48.7 (C, C-8), 54.2 (CH₂, C-14), 54.6 (CH, C-9), 56.9 (CH, C-5), 183.5 (C, C-19), 231.1 (C, C-16); HR-TOFMS (ESI⁺): *m/z* 659.4283 [2M + Na]⁺ (calcd for C₄₀H₆₀NaO₆, 659.4282).

3. Synthesis of dihydroisosteviol (**3**)

Compound **3** was synthesized according to the published literature and its spectroscopic characterization data were consistent with reported values.¹¹ Yield 84%; [α]_D²⁵ –61.6 (*c* 1.00, MeOH); ¹H NMR (CD₃OD, 400 MHz): δ 0.85 (*s*, 3H, 20-CH₃), 0.89 (*s*, 3H, 17-CH₃), 0.94 (*td*, *J* = 13.3, 4.1 Hz, 1H, H-1 β), 0.96 (*brd*, *J* = 12.8 Hz, 1H, H-9 β), 0.99 (*ddd*, *J* = 13.2, 8.7, 4.2 Hz, 1H, H-3 α), 1.06 (*dd*, *J* = 11.8, 2.1 Hz, 1H, H-5 β), 1.12–1.20 (*m*, 1H, H-12 α), 1.16 (*s*, 3H, 18-CH₃), 1.28 (*dd*, *J* = 11.6, 2.6 Hz, 2H, H-14), 1.33 (*ddd*, *J* = 13.2, 13.1, 7.1 Hz, 1H, H-7 β), 1.32–1.39 (*m*, 1H, H-2 α), 1.50 (*ddd*, *J* = 13.1, 3.6, 2.7 Hz, 1H, H-7 α), 1.51–1.59 (*m*, 1H, H-11 α), 1.61–1.70 (*m*, 1H, H-11 β), 1.66–1.70 (partially overlapping signal, 1H, H-15 β), 1.70–1.76 (partially overlapping signal, 1H, H-1 α), 1.72–1.87 (partially overlapping signal, 1H, H-6), 1.75–1.79 (partially overlapping signal, 1H, H-12 β), 1.82–1.90 (partially overlapping signal, 1H, H-2 β), 1.83–1.87 (partially overlapping signal, 1H, H-15 α), 2.11 (*brd*, *J* = 13.2 Hz, 1H, H-3 β), 3.79 (*dd*, *J* = 10.8, 4.6 Hz, 1H, H-16 β); ¹³C NMR (CD₃OD, 100 MHz): δ 14.4 (CH₃, C-20), 20.6 (CH₂, C-2), 21.9 (CH₂, C-11), 23.5 (CH₂, C-6), 25.9 (CH₃, C-17), 30.1 (CH₃, C-18), 35.4 (CH₂, C-12), 39.6 (CH₂, C-3), 39.8 (C, C-10), 41.7 (CH₂, C-1), 43.5 (CH₂, C-7), 43.5 (C, C-8), 43.7 (C, C-13), 44.0 (CH₂, C-15), 45.1 (C, C-4), 57.0 (CH₂, C-14), 57.9 (CH, C-9), 58.9 (CH, C-5), 81.5 (CH, C-16), 182.2 (C, C-19); HR-TOFMS (ESI⁺): *m/z* 343.2242 [M + Na]⁺ (calcd for C₂₀H₃₂NaO₃, 343.2243).

4. General procedure for the synthesis of compounds **4a–4h**

A mixture of compound **3** (20 mg, 0.06 mmol), corresponding alcohol (5 mL, excess) and concentrated H₂SO₄ (20 μ L) were dissolved in benzene (5 mL) and the solution was stirred under reflux using a Dean-Stark apparatus to remove water from the reagents. After 1 h, the resulting mixture was diluted with water and extracted with EtOAc. Then, the organic layer was dried with anhydrous Na₂SO₄ and evaporated under reduced pressure, followed by column chromatography to afford compounds **4a–4h**.

4.1 Dihydroisosteviol-19-methyl ester (**4a**)

Yield 50%; ¹H NMR (CDCl₃, 400 MHz): δ 0.72 (*s*, 3H, 20-CH₃), 0.84 (*td*, *J* = 13.0, 3.9 Hz, 1H, H-1 β), 0.88 (*s*, 3H, 17-CH₃), 0.95 (*dd*, *J* = 13.2, 3.0 Hz, 1H, H-9 β), 0.96–1.00 (*m*,



1H, H-3a), 1.01 (*dd*, $J = 11.5, 2.8$ Hz, 1H, H-5 β), 1.14 (*s*, 3H, 18-CH₃), 1.15–1.24 (*m*, 1H, H-12a), 1.24 (*dd*, $J = 11.6, 3.2$ Hz, 2H, H-14), 1.24–1.29 (*m*, 1H, H-15 α), 1.32 (*ddd*, $J = 12.0, 11.2, 3.5$ Hz, 1H, H-7 β), 1.33–1.39 (*m*, 1H, H-2a), 1.44–1.52 (*m*, 1H, H-11a), 1.50 (*dd*, $J = 11.8, 10.5$ Hz, 1H, H-15 β), 1.54–1.60 (*m*, 1H, H-6a), 1.65–1.72 (partially overlapping signal, 1H, H-11b), 1.67–1.75 (overlapping signal, 1H, H-1 α), 1.69–1.75 (overlapping signal, 1H, H-12b), 1.73 (*brdd*, $J = 12.0, 4.5$ Hz, 1H, H-7 α), 1.74–1.79 (partially overlapping signal, 1H, H-6b), 1.76–1.80 (*m*, 1H, H-2b), 2.12 (*brd*, $J = 13.2$ Hz, 1H, H-3b), 3.60 (*s*, 3H, 1'-OCH₃), 3.83 (*dd*, $J = 10.5, 4.8$ Hz, 1H, H-16 β); ¹³C NMR (CDCl₃, 100 MHz): δ 13.1 (CH₃, C-20), 18.9 (CH₂, C-2), 20.4 (CH₂, C-11), 21.7 (CH₂, C-6), 24.8 (CH₃, C-17), 28.8 (CH₃, C-18), 33.6 (CH₂, C-12), 38.0 (CH₂, C-3), 38.0 (C, C-10), 39.8 (CH₂, C-1), 41.6 (C, C-13), 41.8 (CH₂, C-15), 42.0 (C, C-8), 42.8 (CH₂, C-7), 43.7 (C, C-4), 51.1 (CH₃, C-1'), 55.2 (CH₂, C-14), 55.7 (CH, C-9), 57.1 (CH, C-5), 80.6 (CH, C-16), 178.1 (C, C-19); HR-TOFMS (ESI⁺): m/z 335.2515 [M + H]⁺ (calcd for C₂₁H₃₅O₃, 335.2508). The NMR spectral data were in agreement with those of the reported values.¹²

4.2 Dihydroisosteviol-19-ethyl ester (**4b**)

Yield 81%; ¹H NMR (CDCl₃, 400 MHz): δ 0.72 (*s*, 3H, 20-CH₃), 0.84 (*td*, $J = 13.0, 3.9$ Hz, 1H, H-1 β), 0.88 (*s*, 3H, 17-CH₃), 0.91–0.98 (*m*, 1H, H-3a), 0.92 (*dd*, $J = 13.6, 3.2$ Hz, 1H, H-9 β), 1.00 (*dd*, $J = 11.1, 2.9$ Hz, 1H, H-5 β), 1.13 (*s*, 3H, 18-CH₃), 1.15–1.24 (partially overlapping signal, 1H, H-12a), 1.22 (*t*, $J = 7.1$ Hz, 3H, 2'-CH₃), 1.26 (*dd*, $J = 11.8, 4.8$ Hz, 1H, H-15 α), 1.27 (*dd*, $J = 11.8, 3.2$ Hz, 2H, H-14), 1.32 (*ddd*, $J = 13.7, 11.3, 3.8$ Hz, 1H, H-7 β), 1.33–1.40 (*m*, 1H, H-2a), 1.45–1.53 (*m*, 1H, H-11a), 1.51 (*dd*, $J = 11.8, 10.6$ Hz, 1H, H-15 β), 1.56–1.62 (*m*, 1H, H-6a), 1.66–1.73 (partially overlapping signal, 1H, H-11b), 1.68–1.76 (partially overlapping signal, 1H, H-1 α), 1.70–1.76 (overlapping signal, 1H, H-12b), 1.72 (*brdd*, $J = 13.7, 4.7$ Hz, 1H, H-7 α), 1.75–1.80 (*m*, 1H, H-6b), 1.79–1.83 (*m*, 1H, H-2b), 2.13 (*brd*, $J = 13.4$ Hz, 1H, H-3b), 3.83 (*dd*, $J = 10.6, 4.8$ Hz, 1H, H-16 β), 4.06 (*q*, $J = 7.1$ Hz, 2H, H-1'); ¹³C NMR (CDCl₃, 100 MHz): δ 13.3 (CH₃, C-20), 14.0 (CH₃, C-2'), 18.9 (CH₂, C-2), 20.4 (CH₂, C-11), 21.7 (CH₂, C-6), 24.8 (CH₃, C-17), 28.9 (CH₃, C-18), 33.6 (CH₂, C-12), 38.0 (CH₂, C-3), 38.0 (C, C-10), 39.9 (CH₂, C-1), 41.7 (C, C-13), 42.0 (C, C-8), 42.0 (CH₂, C-15), 42.7 (CH₂, C-7), 43.6 (C, C-4), 55.2 (CH₂, C-14), 55.7 (CH, C-9), 57.1 (CH, C-5), 59.9 (CH₂, C-1'), 80.5 (CH, C-16), 177.5 (C, C-19); HR-TOFMS (ESI⁺): m/z 349.2743 [M + H]⁺ (calcd for C₂₂H₃₇O₃, 349.2737).

4.3 Dihydroisosteviol-19-propyl ester (**4c**)

Yield 52%; ¹H NMR (CDCl₃, 400 MHz): δ 0.72 (*s*, 3H, 20-CH₃), 0.85 (*td*, $J = 13.1, 4.3$ Hz, 1H, H-1 β), 0.88 (*s*, 3H, 17-CH₃), 0.94 (*t*, 3H, 3'-CH₃), 0.95–1.00 (*m*, 1H, H-3a), 0.98 (*dd*, $J = 9.0, 2.5$ Hz, 1H, H-9 β), 1.01 (*dd*, $J = 11.7, 2.6$ Hz, 1H, H-5 β), 1.14 (*s*, 3H, 18-CH₃), 1.19 (*ddd*, $J = 12.5, 12.4, 5.7$ Hz, 1H, H-12a), 1.26 (*dd*, $J = 13.9, 5.2$ Hz, 1H, H-15 α), 1.27 (*dd*, $J = 11.8, 2.5$ Hz, 2H, H-14), 1.32 (*ddd*, $J = 13.5, 13.0, 3.8$ Hz, 1H, H-7 β), 1.34–1.42 (*m*, 1H, H-2a), 1.45–1.53 (*m*, 1H, H-11a), 1.51 (*dd*, $J = 13.9, 10.3$ Hz, 1H, H-15 β), 1.53–1.58 (partially overlapping signal, 1H, H-6a), 1.58–1.67 (*m*, 2H, H-2'), 1.66–1.73 (partially overlapping signal, 1H, H-11b), 1.69 (*brdd*, $J = 13.1, 3.5$ Hz, 1H, H-1 α), 1.70–1.76 (partially overlapping signal, 1H, H-12b), 1.72 (*brdd*, $J = 13.5, 3.1$ Hz, 1H, H-7 α), 1.75–1.80 (overlapping signal, 1H, H-6b), 1.79–1.83 (*m*, 1H, H-2b), 2.14 (*brd*, $J = 13.2$ Hz, 1H, H-3b), 3.83 (*dd*, $J = 10.3, 5.2$ Hz, 1H, H-16 β), 3.90–4.00 (*m*, 2H, H-1'); ¹³C NMR (CDCl₃, 100 MHz): δ 10.7 (CH₃, C-3'), 13.3 (CH₃, C-20), 18.9 (CH₂, C-2), 20.4 (CH₂, C-11), 21.7 (CH₂, C-6), 21.8 (CH₂, C-2'), 24.8 (CH₃, C-17), 29.0 (CH₃, C-18), 33.7 (CH₂, C-12), 38.0 (CH₂, C-3), 38.0

(C, C-10), 39.9 (CH₂, C-1), 41.7 (C, C-13), 42.0 (C, C-8), 42.0 (CH₂, C-15), 42.7 (CH₂, C-7), 43.8 (C, C-4), 55.2 (CH₂, C-14), 55.7 (CH, C-9), 57.1 (CH, C-5), 65.7 (CH₂, C-1'), 80.6 (CH, C-16), 177.7 (C, C-19); HR-TOFMS (ESI⁺): m/z 363.2893 [M + H]⁺ (calcd for C₂₃H₃₉O₃, 363.2894).

4.4 Dihydroisosteviol-19-butyl ester (**4d**)

Yield 20%; ¹H NMR (CDCl₃, 400 MHz): δ 0.72 (*s*, 3H, 20-CH₃), 0.85 (*td*, $J = 13.0$, 4.2 Hz, 1H, H-1 β), 0.88 (*s*, 3H, 17-CH₃), 0.91 (*t*, $J = 7.4$ Hz, 3H, 4'-CH₃), 0.92–0.98 (*m*, 1H, H-3a), 0.98 (*dd*, $J = 9.8$, 3.2 Hz, 1H, H-9 β), 1.01 (*dd*, $J = 11.4$, 2.0 Hz, 1H, H-5 β), 1.14 (*s*, 3H, 18-CH₃), 1.19 (*ddd*, $J = 12.7$, 12.6, 5.9 Hz, 1H, H-12a), 1.26 (*dd*, $J = 11.2$, 4.8 Hz, 1H, H-15 α), 1.27 (*dd*, $J = 11.2$, 3.2 Hz, 1H, H-14), 1.32 (*ddd*, $J = 14.4$, 13.8, 2.5 Hz, 1H, H-7 β), 1.33–1.42 (*m*, 2H, H-3'), 1.35–1.42 (*m*, 1H, H-2a), 1.45–1.53 (*m*, 1H, H-11a), 1.50 (*dd*, $J = 11.2$, 10.5 Hz, 1H, H-15 β), 1.53–1.59 (*m*, 2H, H-2'), 1.57–1.64 (*m*, 1H, H-6a), 1.66–1.73 (partially overlapping signal, 1H, H-11b), 1.69 (*br dd*, $J = 13.0$, 2.5 Hz, 1H, H-1 α), 1.70–1.76 (partially overlapping signal, 1H, H-12b), 1.73 (*br dd*, $J = 13.8$, 3.2 Hz, 1H, H-7 α), 1.75–1.80 (*m*, 1H, H-6b), 1.79–1.83 (*m*, 1H, H-2b), 2.14 (*brd*, $J = 13.2$ Hz, 1H, H-3b), 3.83 (*dd*, $J = 10.5$, 4.8 Hz, 1H, H-16 β), 3.94–4.05 (*m*, 2H, H-1'); ¹³C NMR (CDCl₃, 100 MHz): δ 13.3 (CH₃, C-20), 13.6 (CH₃, C-4'), 18.9 (CH₂, C-2), 19.3 (CH₂, C-3'), 20.4 (CH₂, C-11), 21.7 (CH₂, C-6), 24.8 (CH₃, C-17), 29.0 (CH₃, C-18), 30.5 (CH₂, C-2'), 33.6 (CH₂, C-12), 38.0 (CH₂, C-3), 38.0 (C, C-10), 39.9 (CH₂, C-1), 41.7 (C, C-13), 42.0 (CH₂, C-15), 42.7 (C, C-8), 43.8 (CH₂, C-7), 43.9 (C, C-4), 55.2 (CH₂, C-14), 55.7 (CH, C-9), 57.1 (CH, C-5), 63.9 (CH₂, C-1'), 80.6 (CH, C-16), 177.6 (C, C-19); HR-TOFMS (ESI⁺): m/z 377.3049 [M + H]⁺ (calcd for C₂₄H₄₁O₃, 377.3050).

4.5 Dihydroisosteviol-19-pentyl ester (**4e**)

Yield 32%; ¹H NMR (CDCl₃, 400 MHz): δ 0.72 (*s*, 3H, 20-CH₃), 0.85 (*td*, $J = 13.1$, 4.2 Hz, 1H, H-1 β), 0.88 (*s*, 3H, 17-CH₃), 0.89 (*t*, $J = 7.9$, 3H, 5'-CH₃), 0.92–0.98 (*m*, 1H, H-3a), 0.98 (*dd*, $J = 9.8$, 3.2 Hz, 1H, H-9 β), 1.01 (*dd*, $J = 11.2$, 3.2 Hz, 1H, H-5 β), 1.14 (*s*, 3H, 18-CH₃), 1.19 (*ddd*, $J = 12.6$, 12.4, 5.7 Hz, 1H, H-12a), 1.26 (*dd*, $J = 12.0$, 5.0 Hz, 1H, H-15 α), 1.27 (*dd*, $J = 12.0$, 3.2 Hz, 2H, H-14), 1.28–1.36 (partially overlapping signal, 1H, H-7 β), 1.30–1.36 (*m*, each 2H, H-3' and H-4'), 1.37–1.43 (*m*, 1H, H-2a), 1.48–1.56 (*m*, 1H, H-11a), 1.50 (*dd*, $J = 12.0$, 10.4 Hz, 1H, H-15 β), 1.56–1.62 (*m*, 2H, H-2'), 1.57–1.64 (*m*, 1H, H-6a), 1.66–1.73 (*m*, 1H, H-11b), 1.69 (*brdd*, $J = 13.1$, 3.8 Hz, 1H, H-1 α), 1.70–1.76 (partially overlapping signal, 1H, H-12b), 1.73 (*brdd*, $J = 13.2$, 2.5 Hz, 1H, H-7 α), 1.75–1.80 (*m*, 1H, H-6b), 1.79–1.83 (*m*, 1H, H-2b), 2.13 (*br d*, $J = 13.5$ Hz, 1H, H-3b), 3.83 (*dd*, $J = 10.4$, 5.0 Hz, 1H, H-16 β), 3.92–4.04 (*m*, 2H, H-1'); ¹³C NMR (CDCl₃, 100 MHz): δ 13.3 (CH₃, C-20), 13.9 (CH₃, C-5'), 18.9 (CH₂, C-2), 20.4 (CH₂, C-11), 21.7 (CH₂, C-6), 22.2 (CH₂, C-4'), 24.8 (CH₃, C-17), 28.1 (CH₂, C-2'), 28.3 (CH₂, C-3'), 29.0 (CH₃, C-18), 33.7 (CH₂, C-12), 38.0 (CH₂, C-3), 38.0 (C, C-10), 39.9 (CH₂, C-1), 41.7 (C, C-13), 42.0 (C, C-8), 42.0 (CH₂, C-15), 42.7 (CH₂, C-7), 43.8 (C, C-4), 55.2 (CH₂, C-14), 55.7 (CH, C-9), 57.1 (CH, C-5), 64.2 (CH₂, C-1'), 80.6 (CH, C-16), 177.6 (C, C-19); HR-TOFMS (ESI⁺): m/z 391.3206 [M + H]⁺ (calcd for C₂₅H₄₃O₃, 391.3207).

4.6 Dihydroisosteviol-19-isobutyl ester (**4f**)

Yield 54%; ¹H NMR (CDCl₃, 400 MHz): δ 0.72 (*s*, 3H, 20-CH₃), 0.84 (*td*, $J = 13.0$, 4.3 Hz, 1H, H-1 β), 0.88 (*s*, 3H, 17-CH₃), 0.89 (*d*, $J = 1.6$, 3H, 5'-CH₃), 0.90 (*d*, $J = 1.6$, 3H, 4'-CH₃), 0.92–0.98 (*m*, 1H, H-3a), 0.98 (*dd*, $J = 9.9$, 3.2 Hz, 1H, H-9 β), 1.01 (*dd*, $J = 11.6$, 2.3 Hz, 1H, H-5 β), 1.14 (*s*, 3H, 18-CH₃), 1.19 (*ddd*, $J = 12.5$, 12.2, 5.7 Hz, 1H, H-12a), 1.26 (*dd*, $J = 11.9$, 2.7 Hz, 1H, H-15 α), 1.27 (*dd*, $J = 11.9$, 3.2 Hz, 2H, H-14), 1.32 (*ddd*, $J = 13.9$, 10.1, 3.8 Hz, 1H, H-7 β), 1.35–1.45 (*m*, 1H, H-2a), 1.45–1.53 (*m*, 1H, H-11a), 1.46–1.54 (*m*, 2H, H-



2'), 1.48–1.55 (partially overlapping signal, 1H, H-15 β), 1.53–1.62 (*m*, 1H, H-6a), 1.62–1.69 (*m*, 1H, H-3'), 1.68–1.73 (partially overlapping signal, 1H, H-11b), 1.69 (*brdd*, *J* = 13.0, 3.1 Hz, 1H, H-1 α), 1.70–1.76 (partially overlapping signal, 1H, H-12b), 1.73 (*brdd*, *J* = 13.9, 2.5 Hz, 1H, H-7 α), 1.75–1.80 (*m*, 1H, H-6b), 1.79–1.83 (*m*, 1H, H-2b), 2.13 (*brd*, *J* = 13.2 Hz, 1H, H-3b), 3.83 (*brd*, *J* = 10.5 Hz, 1H, H-16 β), 3.96–4.08 (*m*, 2H, H-1'); ^{13}C NMR (CDCl_3 , 100 MHz): δ 13.3 (CH_3 , C-20), 18.9 (CH_2 , C-2), 20.4 (CH_2 , C-11), 21.7 (CH_2 , C-6), 22.4 (CH_3 , C-5'), 22.4 (CH_3 , C-4'), 24.8 (CH_3 , C-17), 25.2 (CH , C-3'), 28.9 (CH_3 , C-18), 33.7 (CH_2 , C-12), 37.2 (CH_2 , C-2'), 38.0 (CH_2 , C-3), 38.0 (C , C-10), 39.9 (CH_2 , C-1), 41.7 (C , C-13), 42.0 (C , C-8), 42.0 (CH_2 , C-15), 42.7 (CH_2 , C-7), 43.7 (C , C-4), 55.2 (CH_2 , C-14), 55.7 (CH , C-9), 57.1 (CH , C-5), 62.7 (CH_2 , C-1'), 80.6 (CH , C-16), 177.6 (C , C-19); HR-TOFMS (ESI^+): m/z 391.3205 [$\text{M} + \text{H}$] $^+$ (calcd for $\text{C}_{25}\text{H}_{43}\text{O}_3$, 391.3206).

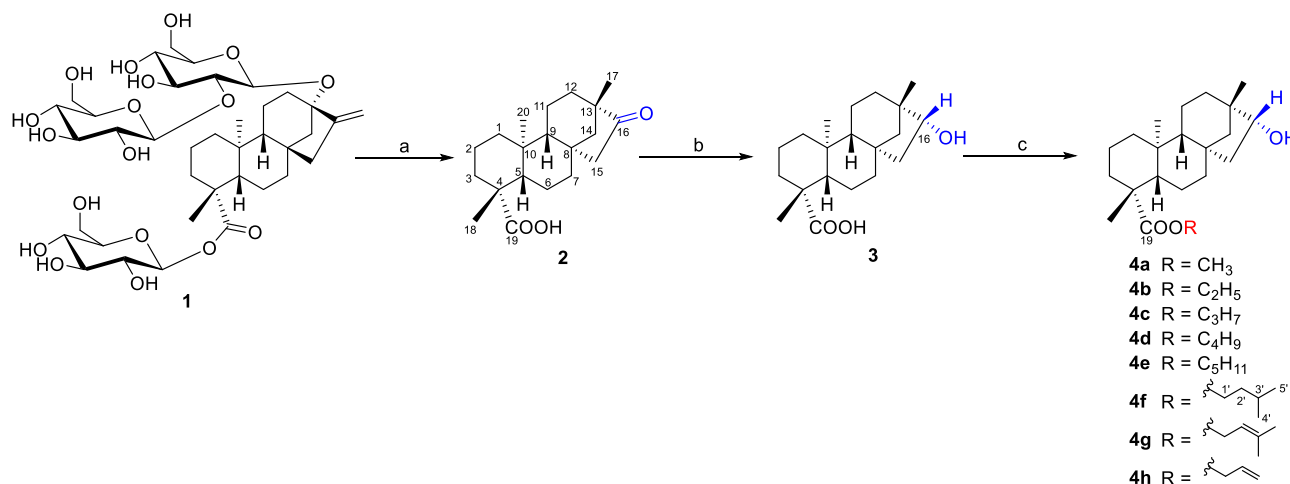
4.7 23-Methyl-19-butenyldihydroisosteviol (**4g**)

Yield 63%; ^1H NMR (CDCl_3 , 400 MHz): δ 0.70 (*s*, 3H, 20- CH_3), 0.83 (*td*, *J* = 13.4, 3.7 Hz, 1H, H-1 β), 0.88 (*s*, 3H, 17- CH_3), 0.90–0.99 (*m*, 1H, H-3a), 0.96 (*dd*, *J* = 11.5, 1.9 Hz, 1H, H-9 β), 1.00 (*brd*, *J* = 12.8 Hz, 1H, H-5 β), 1.13 (*s*, 3H, 18- CH_3), 1.18 (*ddd*, *J* = 12.7, 12.5, 5.9 Hz, 1H, H-12a), 1.26 (*dd*, *J* = 13.4, 4.8 Hz, 1H, H-15 α), 1.27 (*dd*, *J* = 11.6, 1.9 Hz, 2H, H-14), 1.32 (*ddd*, *J* = 12.5, 11.1, 3.9 Hz, 1H, H-7 β), 1.32–1.40 (*m*, 1H, H-2a), 1.45–1.53 (*m*, 1H, H-11a), 1.48 (*dd*, *J* = 13.4, 10.5 Hz, 1H, H-15 β), 1.53–1.62 (*m*, 1H, H-6a), 1.67 (*s*, 3H, 5'- CH_3), 1.67–1.74 (partially overlapping signal, 1H, H-1 α), 1.68–1.73 (partially overlapping signal, 1H, H-11b), 1.70–1.75 (partially overlapping signal, 1H, H-7 α), 1.70–1.76 (partially overlapping signal, 1H, H-12b), 1.72 (*s*, 3H, 4'- CH_3), 1.75–1.80 (*m*, 1H, H-6b), 1.79–1.83 (*m*, 1H, H-2b), 2.13 (*brd*, *J* = 13.1 Hz, 1H, H-3b), 3.82 (*dd*, *J* = 10.5, 4.8 Hz, 1H, H-16 β), 4.40–4.54 (*m*, 2H, H-1'), 5.28–5.33 (*m*, 1H, H-2'); ^{13}C NMR (CDCl_3 , 100 MHz): δ 13.2 (CH_3 , C-20), 18.0 (CH_3 , C-4'), 18.9 (CH_2 , C-2), 20.4 (CH_2 , C-11), 21.7 (CH_2 , C-6), 24.8 (CH_3 , C-17), 25.6 (CH_3 , C-5'), 28.9 (CH_3 , C-18), 33.6 (CH_2 , C-12), 38.0 (CH_2 , C-3), 38.0 (C , C-10), 39.9 (CH_2 , C-1), 41.7 (C , C-13), 41.9 (CH_2 , C-15), 42.0 (C , C-8), 42.7 (CH_2 , C-7), 43.7 (C , C-4), 55.2 (CH_2 , C-14), 55.7 (CH , C-9), 57.2 (CH , C-5), 60.8 (CH_2 , C-1'), 80.6 (CH , C-16), 118.7 (CH , C-2'), 138.3 (C , C-3'), 177.4 (C , C-19); HR-TOFMS (ESI^+): m/z 411.2856 [$\text{M} + \text{Na}$] $^+$ (calcd for $\text{C}_{25}\text{H}_{40}\text{NaO}_3$, 411.2869).

4.8 19-Propenyldihydroisosteviol (**4h**)

Yield 68%; ^1H NMR (CDCl_3 , 400 MHz): δ 0.72 (*s*, 3H, 20- CH_3), 0.85 (*td*, *J* = 13.0, 4.2 Hz, 1H, H-1 β), 0.88 (*s*, 3H, 17- CH_3), 0.93–1.01 (*m*, 1H, H-3a), 0.99 (*dd*, *J* = 11.6, 2.0 Hz, 1H, H-9 β), 1.03 (*dd*, *J* = 12.0, 1.6 Hz, 1H, H-5 β), 1.15–1.23 (*m*, 1H, H-12a), 1.16 (*s*, 3H, 18- CH_3), 1.26 (*dd*, *J* = 13.5, 4.8 Hz, 1H, H-15 α), 1.27 (*dd*, *J* = 12.8, 2.0 Hz, 2H, H-14), 1.32 (*ddd*, *J* = 14.0, 13.5, 3.9 Hz, 1H, H-7 β), 1.35–1.42 (*m*, 1H, H-2a), 1.45–1.53 (*m*, 1H, H-11a), 1.50 (*dd*, *J* = 13.5, 10.5 Hz, 1H, H-15 β), 1.53–1.62 (*m*, 1H, H-6a), 1.66–1.73 (partially overlapping signal, 1H, H-11b), 1.69 (*brdd*, *J* = 13.0, 3.6 Hz, 1H, H-1 α), 1.70–1.76 (partially overlapping signal, 1H, H-12b), 1.71 (*brdd*, 14.0, 3.7 Hz, 1H, H-7 α), 1.75–1.80 (*m*, 1H, H-6b), 1.79–1.83 (*m*, 1H, H-2b), 2.15 (*brd*, *J* = 13.3 Hz, 1H, H-3b), 3.83 (*dd*, *J* = 10.5, 4.8 Hz, 1H, H-16 β), 4.45–4.56 (*m*, 2H, H-1'), 5.19 (*brdd*, *J* = 10.4, 1.2 Hz, 1H, H-3'a), 5.30 (*brdd*, *J* = 17.2, 1.2 Hz, 1H, H-3'b), 5.80–5.93 (*m*, 2H, H-2'); ^{13}C NMR (CDCl_3 , 100 MHz): δ 13.3 (CH_3 , C-20), 18.9 (CH_2 , C-2), 20.4 (CH_2 , C-11), 21.7 (CH_2 , C-6), 24.8 (CH_3 , C-17), 28.9 (CH_3 , C-18), 33.6 (CH_2 , C-12), 38.0 (CH_2 , C-3), 38.0 (C , C-10), 39.9 (CH_2 , C-1), 41.7 (C , C-13), 42.0 (C , C-8), 42.0 (CH_2 , C-15), 42.7 (CH_2 , C-7), 43.8 (C , C-4), 55.1 (CH_2 , C-14), 55.7 (CH , C-9),

57.1 (CH, C-5), 64.8 (CH₂, C-1'), 80.5 (CH, C-16), 117.9 (CH₂, C-3'), 132.3 (CH₂, C-2'), 177.2 (C, C-19); HR-TOFMS (ESI⁺): m/z 361.2727 [M + H]⁺ (calcd for C₂₃H₃₇O₃, 361.2737).



Scheme 1. Reagents and conditions: (a) 25% H₂SO₄, 80 °C, 2 h; (b) NaBH₄, THF, rt, 2 h; (c) ROH, benzene, conc. H₂SO₄, reflux, 1 h.

Results and Discussion:

The acid hydrolysis of stevioside (**1**) yielded isosteviol (**2**) in 95% yields. Reduction of **2** with NaBH₄ gave the dihydro analog **3** in 84%. The reduction occurred exclusively from the β -face of the molecule, as indicated by the chemical shifts of H-15 β (δ_H 1.75–1.82) and H-15 α (δ_H 2.61), which were consistent with β -selective reduction. The absence of any significant shifts or additional coupling constants for other positions suggests that the reduction occurred exclusively at the C-16 keto group. Dihydroisosteviol (**3**) was chosen as the parent compound for structural modification to its analogs. We aimed to modify the carboxylic functional group at the 19-position to the corresponding ester analogs. The preparation of dihydroisosteviol esters **4a–4h** was achieved through esterification of dihydroisosteviol (**3**), the corresponding alcohol and concentrated H₂SO₄ in refluxing benzene using Dean-Stark apparatus to remove water from the condensation reaction (see Scheme 1). The dihydroisosteviol analogs **4a–4h** were obtained in moderate to good yields ranging from 20% to 81%. The structures of the ester analogs were confirmed by a combination of ¹H NMR, ¹³C NMR, and HR-TOFMS data. For example, in the ¹H NMR spectrum, the methyl ester group in **4a** is observed as a singlet at δ_H 3.60, while in the ¹³C NMR, the ester carbonyl carbon (C-19) is clearly visible at δ_C 178.1, confirming the successful esterification at the carboxyl group. A notable upfield shift in the chemical shift of the C-19 carbonyl group (compared to the parent dihydroisosteviol) further confirmed the formation of the ester linkage. This upfield shift is consistent with the introduction of electron-donating alkyl groups, which reduce the deshielding effect on the carbonyl carbon.

Conclusion:

In summary, this study successfully demonstrated the synthesis and structural modification of isosteviol (**2**) and its dihydro analog (**3**) through a series of chemical reactions. Through esterification at the 19-position carboxylic group, a series of dihydroisosteviol esters were synthesized. These analogs provide a collection of analogs with isosteviol scaffold for further study of their biological activities.



Acknowledgements:

This work was supported by Department of Chemistry, Faculty of Science, Ramkhamhaeng University. DA acknowledges a scholarship from the Center of Excellence for Innovation in Chemistry (PERCH-CIC), Ministry of Higher Education, Science, Research and Innovation.

References:

1. Newman DJ, Cragg GM. *J Nat Prod.* 2020;83:770–803.
2. Harvey AL, Edrada-Ebel R, Quinn RJ. *Nat Rev Drug Discov.* 2015;14:111–129.
3. Atanasov AG, Zotchev SB, Dirsch VM. *Nat Rev Drug Discov.* 2021;20:200–216.
4. Patridge E, Gareiss P, Kinch MS, Hoyer D. *Drug Discov Today.* 2016;21:204–207.
5. Chatsudthipong V, Muanprasat C. *Pharmacol Ther.* 2009;121:41–54.
6. Chen J, Wang J, Xie Y. *Life Sci.* 2010;86:935–942.
7. Jayaraman S, Manoharan MS, Illanchezian S. *J Med Plants Res.* 2011;5:4485–4493.
8. Chang CF, Hsieh MS, Chou TC. *Neurochem Int.* 2013;62:521–531.
9. Liu JC, Kao PF, Chan P. *Eur J Pharmacol.* 2011;660:532–539.
10. Wong KH, Lai CK, Cheng LK. *Eur J Pharmacol.* 2013;714:365–373.
11. Wonganan O, Tocharus C, Puedsing C, Homvisasevongsa S, Sukcharoen O, Suksamrarn A. *Eur J Med Chem.* 2013;62:771–776.
12. Trinh AD, Holth, MA, Walters OEH, Gunda IG. *ACS Comb Sci.* 2020;22:150–155.



DETERMINATION OF ANTIOXIDANT ACTIVITY AND DEVELOPMENT OF FACIAL SERUM FORMULA CONTAINING THE *Chrysanthemum indicum* L. AND *Chrysanthemum morifolium* Ramat. LOWERS FROM THAILAND

Nattanan Aekvitayavetchanukul¹, Warisararak Chimfueng¹, Wilai. Mayuramas.^{1,2*}

¹School of Cosmetic Science, Mae Fah Luang University, Chiang Rai 57100, Thailand

²Phytocosmetics and Cosmeceuticals Research Group, Mae Fah Luang University, Chiang Rai, Thailand

*e-mail: mayuramas@mfu.ac.th

Abstract:

In this study, *Chrysanthemum indicum* L. and *Chrysanthemum morifolium* Ramat. flowers were extracted using two different techniques maceration and ultrasonic techniques. The quantitative study was a UV-Vis spectroscopy and Fourier-transform infrared spectroscopy (FTIR). The total phenolic contents analysis and DPPH radical scavenging activity were performed using an atomic absorption spectrophotometer. In addition, the extracts obtained from different techniques were developed for the facial serum formulas. The physicochemical properties of all formulas were performed including organoleptic test, homogeneity, pH, and viscosity. In conclusion, the Fourier-transform infrared (FTIR) and UV-vis spectrophotometer analyses showed that all extracts displayed similar characteristics related to the phenolic compounds. The *C. indicum* L. extracted using the maceration technique showed the highest percentage yield at 21.66. The highest total phenolic contents were found in the *C. morifolium* Ramat. extracted by maceration technique at $76.39 \pm 0.07 \mu\text{g GAE/mg}$ of the extract. The high inhibitory activity on DPPH radical scavenging activity was found in the *C. morifolium* Ramat. extract obtained from an ultrasonic technique at $\text{IC}_{50} = 0.069 \text{ mg/mL}$. All extracts exhibited stability through centrifugation, pH and viscosity, and colorimetric testing when used as an active ingredient in the serum formulas.

Keyword: *Chrysanthemum morifolium* Ramat, *Chrysanthemum indicum* L., Maceration, Ultrasonic, DPPH radical scavenging activity

Introduction:

Chrysanthemum morifolium Ramat. (CM) and *C. indicum* L. (CI) are two closely related plant species with similar morphological characteristics in edible and medicinal purpose.¹ These two plants belong to the family Asteraceae which found in Asia, mainly in Mongolia, China, Japan, and Eastern Europe. In China, the chrysanthemum flowers are categorized as the cool/acrid herbs which used to treat the early stages of diseases that affect the upper respiratory tract, the eyes, the ears, the nose, the throat, or the skin.² The flowers of these plants regularly consumed and widely used in many countries as food supplements, herbal teas, and health foods. The chemical constituent investigation of these plants led to the identification of many bioactive secondary metabolites represented mainly by flavonoids, phenolic and terpenoids compounds.³ *C. morifolium* Ramat. is an ideal source of natural flavonoids with significant antioxidant and anti-inflammatory activities. The *C. morifolium* Ramat. flowers isolated by 85% ethanol displayed strong antioxidant in DPPH scavenging activity. The isolated compounds from *C. morifolium* Ramat. included quercetin, isorhamnetin 3-O- β -D-glucoside, eriodictyol, pyracanthoside, apigenin, apigetrin, acacetin, acacipetalin, luteolin, diosmetin, spinacetin, axillarin, bonanzin, cirsiliol, chrysosplenol D and artemetin were characterized by detailed spectroscopic analysis.⁴ The volatile components of

essential oils from *C. indicum* L. was isolated which are 1,8-cineole, o-cymene, camphor, pinocarvone, chrysanthenyl acetate, bornyl acetate, *trans*-caryophyllene, terpinen-4-ol, umbellulone, *trans*-pinocarveol, *cis*-verbenol, borneol, α -terpineol, caryophylleneoxide, and thymol.⁵ The modern pharmacological studies indicate that the flower extracts of both flowers possess various bioactivities including anti-inflammation, antioxidation, cardiovascular protection, anticancer and antibacterial activities.^{1,6,7} Moreover, the review reported from Nguyen (2020)⁸ indicated that the bioactive compounds isolated from *Chrysanthemum* potent in dermatologic applications such as hyperpigmentation, skin rejuvenation and UV protection which may possess in cosmetic field. In this study, we evaluated the *C. indicum* L. and *C. morifolium* Ramat. crude extracts from maceration and ultrasonic techniques to compare the effectiveness and predicted functional group that contain in the compounds by using Fourier-transform infrared spectroscopy (FTIR) and UV-vis spectroscopy and were developed into a facial serum.

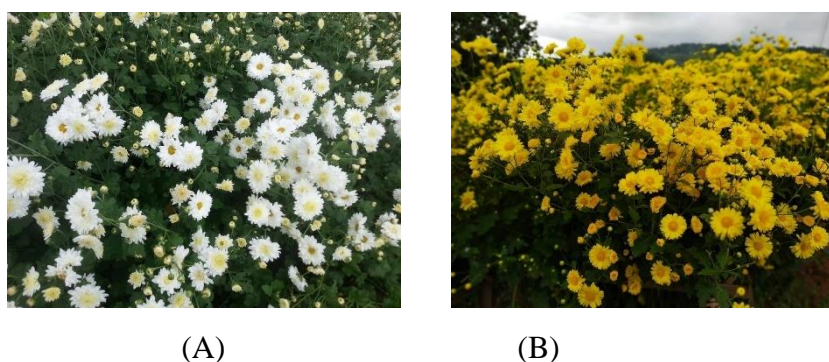


Figure 1. shows the figure of *Chrysanthemum morifolium* Ramat (A) and *Chrysanthemum indicum* L. (B). Photographed by Miss Supharat Intanam from Wang Lao Dried Plant Community Enterprise, Doi Sango, Chiang Sean, Chiang Rai, Thailand in November 2022.

Methodology:

Chemicals, solvents, reagents

Ethanol was purchased from Northern Chemicals and Glasswares. Tween-80 was purchased from Micromaster laboratories (CAS No. 9005-65-6). Sodium hyaluronic acid was purchased from Myskinrecipes (CAS No. 9067-32-7). PEG-12 Dimethicone was purchased from Dow Chemical Thailand (CAS No. 68937-54-2). Aristoflex velvet was purchased from Clariant (CAS No. 1355508-95-0). Provitamin B5 and Triethanolamine were purchased from Chemipan corporation CAS No. 81-13-0 and 102-71-6). Aloe Vera extract was purchased from Veda oils (CAS No. 85507-69-3). EDTA Tetrasodium was purchased from Eastern Petroleum Private Limited (CAS No. 10378-23-1). Hydroxyethylcellulose was purchased from MakingCosmetics (CAS No. 9004-62-0).

Plant material collection and preparation

The dried flowers of *C. morifolium* Ramat and *C. indicum* L. were collected from Wang Lao Dried Plant Community Enterprise, Doi Sango, Chiang Sean, Chiang Rai, Thailand (November 2022). Each flower was grinded to obtain the desired size and stored at 4 °C before used.

The extraction was performed using maceration and ultrasonic techniques. The 95% ethanol was used as solvent in the ration between dried plant: solvent (1:5 w/v).

For maceration extraction, *C. morifolium* Ramat. and *C. indicum* L. flowers were obtained by soaking in 95% ethanol at room temperature for 3 days, while the crude extracts



from ultrasonic techniques were obtained by ultrasonicated in 95% ethanol for 30 min at room temperature.

The extract solutions were filtered through filter paper (Whatman No.4), the residue was re-extracted twice, and then the combined extracts were evaporated by using rotary evaporator (Eyela/CCA-1110) and dried using a freezer dryer (LABCONCO/7960032). The obtained dry extracts were stored in a dark place at 4 °C until further analysis.

UV-Vis Spectroscopy

The *C. indicum* L. and *C. morifolium* Ramat. extracts were prepared at concentration 0.1 and 0.05 mg/mL. The *C. indicum* L. and *C. morifolium* Ramat. sample solutions were scanned at a wavelength of 200-800 nm (Biochrom Libra S80 UV-vis spectrophotometer). Methanol was used as a solvent.

Determination of Total Phenolic Content by Folin-Ciocalteu Assay

Total phenolic content of the extracts was determined by Folin-ciocalteu assay. The extract was prepared in two-fold dilution series and then incubated with Folin-ciocalteu reagent and 7.5% sodium carbonate in dark condition for 30 min. The absorbance was measured by a spectrophotometer at 750 nm (Biochrom Libra S80 UV-vis spectrophotometer). Gallic acid was used as a standard and the result shown as mg/g Gallic acid equivalent, GAE.⁹

Determination of Antioxidant Activity by DPPH Radical Scavenging Method

The antioxidant activity of the extracts was evaluated by the free radical DPPH (1, 1-diphenyl-2-picrylhydrazyl) assay.¹⁰ Two-fold dilution series of the extract was mixed individually with 0.2 mM DPPH. The reactions were incubated in dark area for 30 min, and then measured at 517 nm by a spectrophotometer (Biochrom Libra S80 UV-Vis spectrophotometer). One hundred microliters of the extract mixed in DPPH solution was used as a control, and ascorbic acid was used as a standard.

Formulation

The components of the 5 formulas are presented in Table1. Percentage of extract referred from Choi (2015).¹¹

Table 1. The formulation for serum products

| Phase | Ingredients | Formula (%w/w) | | | | | Function |
|-------|---|----------------|-------|-------|-------|-------|-------------------|
| | | 1 | 2 | 3 | 4 | 5 | |
| A | Distilled Water | 86.76 | 86.65 | 86.65 | 86.65 | 86.65 | Diluent |
| | Polyacrylate | 0.6 | 0.6 | 0.6 | 0.6 | 0.6 | Thickener |
| | Crosspolymer-11 | | | | | | |
| | Hydroxyethylcellulose | 0.1 | 0.1 | 0.1 | 0.1 | 0.1 | Thickener |
| | EDTA (tetrasodium ethylenediaminetetraacetic acid tetrasodium salt) | 0.1 | 0.1 | 0.1 | 0.1 | 0.1 | Stabilizer |
| B | dl-panthenol | 1 | 1 | 1 | 1 | 1 | Humectant |
| C | Sodium hyaluronic acid | 0.2 | 0.2 | 0.2 | 0.2 | 0.2 | Humectant |
| D | PEG-12 Dimethicone | 2.5 | 2.5 | 2.5 | 2.5 | 2.5 | Solubilizer |
| E | Aloe Vera extract | 3 | 3 | 3 | 3 | 3 | Humectant |
| F | Polysorbate 80 | 4.5 | 4.5 | 4.5 | 4.5 | 4.5 | Solvent |
| | Extract* | - | 0.5 | 0.5 | 0.5 | 0.5 | Active ingredient |

Table 1. The formulation for serum products (Continue)

| Phase | Ingredients | Formula (%w/w)* | | | | | Function |
|-------|-----------------|-----------------|------|------|------|------|----------------|
| | | 1 | 2 | 3 | 4 | 5 | |
| G | Phenoxyethanol | 0.8 | 0.8 | 0.8 | 0.8 | 0.8 | Preservative |
| H | Triethanolamine | 0.05 | 0.05 | 0.05 | 0.05 | 0.05 | pH Adjuster |
| I | CI42090 | 0.09 | - | - | - | - | Coloring agent |
| | CI17200 | 0.28 | - | - | - | - | Coloring agent |

*Extracts.

Formula 1: Base formula, Formula 2: *C. morifolium* Ramat. by maceration technique, Formula 3: *C. morifolium* Ramat. by ultrasonic extraction, Formula 4: *C. indicum* L. by maceration technique, Formula 5: *C. indicum* L. by ultrasonic extraction.

Preparation

An aqueous phase was prepared by dispersing the hydorxyethylcellulose and polyacrylate crosspolymer-11 into distilled water and continuously stirring in a water bath at 70 °C until homogenization. Subsequently, add the dl-panthenol, sodium hyaluronic acid, and PEG-12 dimethicone when it cools down at 50 °C with continuous stirring until homogenization. The aloe vera and Chrysanthemum extracts were suspended in polysorbate 80, and phenoxyethanol was added to the mixture when the system was cooled down at 45 °C with continuous stirring until homogenization. Finally, adjust the pH to 5.5 by using triethanolamine. The formula's color was adjusted using CI47005 and CI42090, respectively.

Stability test

Physical analysis

The obtained emulsions: the serum formulas and serum based, were submitted to determine of organoleptic (homogeneity, color, odor, spread ability) and physical (phase separation and creaming) analysis.¹²

Centrifugation tests

The centrifugation tests were performed by placing 1 gram of sample in the centrifugal tube under the conditions at 5000 rpm and 25 °C for 20 minutes. The samples were tested directly after preparation, and repeated after 1 day 7 days, 14 days, 21 days and 28 days of storage.¹²

Cycle testing

The six cycles between refrigerator temperature (4 °C) and accelerated temperature (40 °C) with storage at each temperature for 24 hours and were evaluated for physical parameters like color, odor, pH, consistency and spread ability.¹²

pH determination

The pH value of cosmetic formulations stored at different conditions was determined using a digital pH Meter. The pH tests were repeated for multiple cosmetic formulations.¹²

Colorimetric analysis

The observation of the color change of the emulsion was carried out using the reflection principle. From a colorimeter (HunterLab/UltraScan) based on CIE, which has the following parameters: L* indicates the brightness index in grayscale between black and white is in the range 0-100, the color coordinate was a* b*, where the parameter a* takes positive values for red and negative values for green, while parameter b* uses positive values for yellow and negative values for blue.¹³



Preference test

The preference was tested based on sensory evaluation such as color, smell, texture, ability to absorb, spread ability, moisture, feeling during use and feeling after use for 5 min. All 5 formulas were presented to the panelists, a total of 34 people, to assess the satisfaction with the product in the specified parameters. The level of preference was collected using numerical scale as follow: 5 = extremely like, 4 = like, 3 = neutral, 2 = dislike, 1 = extremely dislike.¹⁴

Statistics analysis

DPPH radical scavenging activity assay was performed in triplicate. The results are expressed as the mean \pm standard deviation (SD). The statistical analysis was performed by using pair t-test to determine difference of the test sample at before and after of observation and at all storage conditions. Statistically, a significant difference was considered at a p value of less than 0.05.

Results and Discussion:

UV-Vis spectrophotometer

The UV-vis spectrophotometer was used to determine the spectrum profile of all extracts. The spectrum of chrysanthemum extracts was recorded in a range of 200 - 800 nm. The analysis showed that both extraction methods had a spectra curve over the same wavelength range as shown in Figure 2. All extracts showed maximum peaks at UV range in between 216-224 nm and 321-333 nm which indicated the characteristic of phenolic and terpenoids compounds.^{15,16}

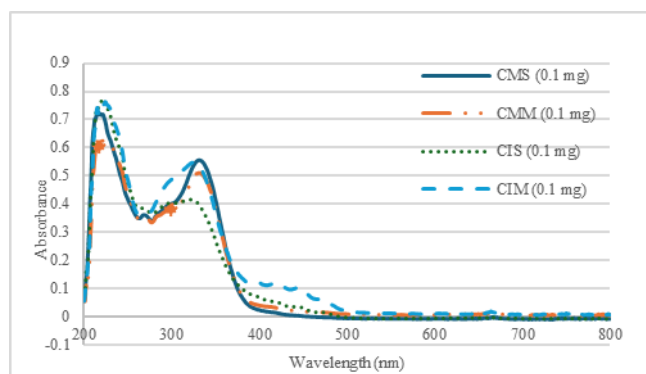


Figure 2. The UV-vis spectra of *C. indicum* L. extracted by maceration (CIM) and ultrasonic (CIS) and *C. morifolium* Ramat. extracted by maceration (CMC) and ultrasonic (CMS).

FTIR analysis

The FTIR results from *C. morifolium* Ramat. and *C. indicum* L. extract are shown in Figure 3. The absorption spectrum of all 4 extracts (*C. indicum* L. and *C. morifolium* Ramat. extracted by maceration, and *C. morifolium* Ramat. and *C. indicum* L. extracted by ultrasonic techniques) consisted of C-O-C group were indicated by the presence of a strong absorption bands at 1049, 1046, 1051 and 1048 cm^{-1} . The peak at 3358, 3350, 3332 and 3342 cm^{-1} resulted from the presence of hydroxyl compound. The peak between 2923-2924, 2853-2855 and 776-817 cm^{-1} resulted from presence of methyl group. The peak at 1732, 1730, 1729 and 1731 cm^{-1} resulted from the presence of carbonyl compounds. The peak between 1604-1634 cm^{-1} resulted from the presence of diketone. The peak between 1451-1458 cm^{-1} resulted from presence of phenol ring (aromatic ring). The peak at 1375, 1376, 1376 and 1374 cm^{-1} resulted

from presence of C-O bending. The halogen compound attributed the bands between 494.27-717.03 cm^{-1} .¹⁷

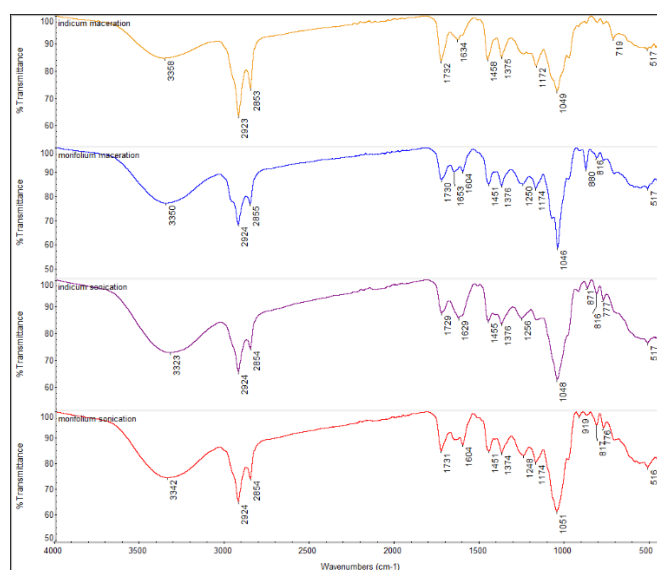


Figure 3. The absorption spectrum of *C. indicum* L. extract by maceration (top line), *C. morifolium* Ramat. extract by maceration (2nd from top line), *C. morifolium* Ramat. extract by ultrasonic (3rd from top line), and *C. indicum* L. extract by ultrasonic techniques (bottom line).

Extraction yield, total phenolic content and antioxidant activity by DPPH assay

The percentage yield of chrysanthemum extracted by maceration and ultrasonic were given in Table 2.

Table 2. Extraction yield, total phenolic content and DPPH radical scavenging activity of *C. morifolium* Ramat. and *C. indicum* L. as extracted by different extraction techniques.

| Plant Materials | Extraction methods | Extraction yield (%) | Total Phenolic Content $\mu\text{g GAE/ mg sample } (\pm\text{S.D.})$ | DPPH Radical Scavenging Activity (IC_{50}) (mg/mL) |
|-----------------------------|--------------------|----------------------|--|--|
| <i>C. morifolium</i> Ramat. | Maceration | 15.05 | 76.39 \pm 0.07 | 0.128 |
| <i>C. morifolium</i> Ramat. | Ultrasonic | 19.37 | 54.97 \pm 0.07 | 0.069 |
| <i>C. indicum</i> L. | Maceration | 21.66 | 59.22 \pm 0.04 | 0.111 |
| <i>C. indicum</i> L. | Ultrasonic | 16.47 | 68.36 \pm 0.06 | 0.103 |
| Ascorbic acid | - | - | - | 0.028 |

The percentage yield of *C. morifolium* Ramat. extracted by maceration technique and ultrasonic technique were found to be 15.05% and 19.37, respectively. The percentage yield of *C. indicum* L. extracted by maceration technique and ultrasonic technique were found to be 21.66 and 16.47% respectively. The research found that *C. morifolium* Ramat. and extracted by maceration and ultrasonic techniques were 76.39 \pm 0.07 and 54.97 \pm 0.07 $\mu\text{g GAE/mg}$ sample of total phenolic content, respectively. The *C. indicum* L. extracted *C. indicum* L. 59.22 \pm 0.04 and 68.36 \pm 0.0607 $\mu\text{g GAE/mg}$ sample of total phenolic content,



respectively. The gallic acid was used as standard phenolic compound ($y = 110.28x + 0.0044$, $R^2 = 0.9998$). The free radical scavenging activities were assayed by using the stable DPPH radical. The ascorbic acid ($IC_{50} = 0.028$ mg/mL) was used as the reference antioxidant compound ($y = 1587.2x + 6.3002$, $R^2 = 0.9994$). The observed IC_{50} values of *C. morifolium* Ramat. and *C. morifolium* Ramat. extracted by maceration and ultrasonic techniques were 0.128, 0.069, 0.111, and 0.103, respectively.

Accelerated Stability evaluation

Physical stability test included measurement of pH, color, viscosity, and separation of products. These characteristics were observed at 4 ± 2 °C and 40 ± 2 °C for 12 days or 6 cycles.

The accelerated stability centrifugation was test under the conditions at 5000 rpm and 25 °C for 20 minutes. No phase separation after centrifugation was found in the tested formulations kept neither at 4 ± 2 °C and 40 ± 2 °C, during the entire period of study, which means that all formulas are stable.

Table 3. Results of L^* a^* b^* color space parameters determination before and after an accelerated stability studies.

| Formulas* | Before | | | After | | | ΔE |
|-----------|--------|-------|-------|-------|-------|-------|------------|
| | L^* | a^* | b^* | L^* | a^* | b^* | |
| Formula 1 | 21.58 | -0.21 | 1.11 | 21.56 | -0.21 | 1.10 | 0.96 |
| Formula 2 | 19.71 | -0.41 | 0.80 | 19.74 | -0.41 | 0.80 | 1.12 |
| Formula 3 | 19.22 | -0.33 | 0.25 | 19.21 | -0.33 | 0.24 | 0.24 |
| Formula 4 | 17.64 | -0.37 | 1.52 | 17.62 | -0.37 | 1.54 | 0.95 |
| Formula 5 | 18.87 | -0.47 | 1.76 | 18.85 | -0.46 | 1.77 | 1.64 |

*Formula 1: Base formula, Formula 2: *C. morifolium* Ramat. by maceration technique, Formula 3: *C. morifolium* Ramat. by ultrasonic extraction, Formula 4: *C. indicum* L. by maceration technique, Formula 5: *C. indicum* L. by ultrasonic extraction.

Colorimetry evaluation

Color was evaluated with a colorimeter and results were expressed according to the color space CIE $L^*a^*b^*$. The three coordinates represent the lightness of the color (L^*), its position between red and green (a^*), its position between yellow and blue (b^*), and ΔE represents the color difference of L^* , a^* and b^* before and after the period. After 6 cycles: formulas 1-5 exhibited significant change in lightness ($p < 0.05$); formulas 1, 2, and 4 did not show statistically significant change in green color (a^*) ($p > 0.05$) while formulas 3 and 5 significantly change in the green color (a^*) ($p < 0.05$); the formulas 1, 3, and 4 did not show statistically significant change in the yellow color (b^*) ($p > 0.05$) while formulas 2 and 5 significantly change in yellow color (b^*) ($p < 0.05$). The ΔE values of the serum contained the extracts of *C. morifolium* Ramat. ($\Delta E = 1.12$) from maceration technique and of the *C. indicum* L. from ultrasonic technique ($\Delta E = 1.64$) indicated that only an experienced observer can notice the difference between these two serum products.¹⁸

pH determination

The pH was determined using a digital pH meter. All formulas 1-5 had pH values in the range between 4.75 - 5.00 and did not show statistically significant change after 6 cycles ($p > 0.05$) except formula 3 exhibited a pH value of significant change after 6 cycles ($p < 0.05$). The pH value of formula 3 represents an acceptable range indicating that the skin serum should be in the range of 4.1-6.7.^{19,20} Therefore, all formulas 1-5 exhibited stability after accelerated test 6 cycles.

Viscosity evaluation

Viscosity determinations were performed using a spindle number 4, at shear rate 200 rpm. Temperature was kept constant at 25 °C. All serums were equilibrated at room temperature on the plate for 15 seconds prior to viscosity measurement. The result showed that base formula had highest viscosity, and the serum formula contained extracts (1-5) shown lower viscosity than base formula. All serum formulas exhibited significantly change viscosity with time after 6 cycles ($p < 0.05$).

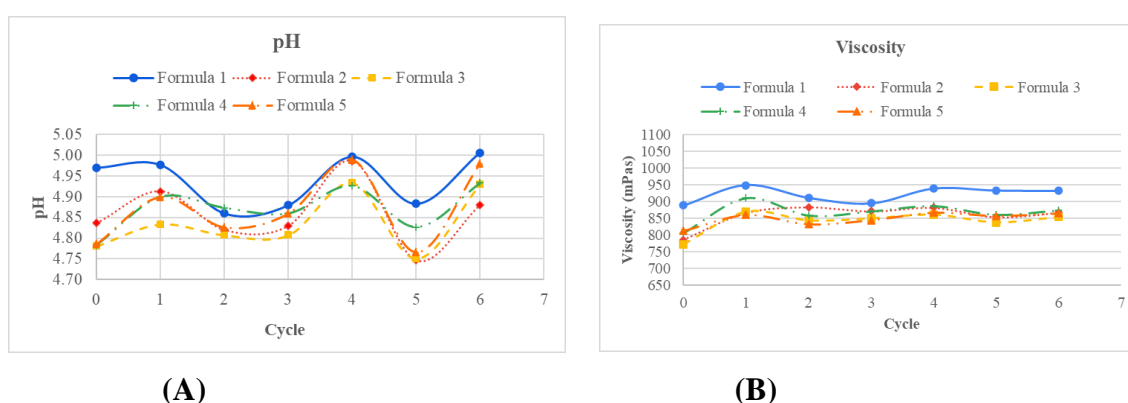


Figure 4. pH value of formulas 1-5 (A) and rheological behavior of formulas 1-5 (B).

Preference test

The evaluation was based on questionnaires regarding the sensory characteristics such as color, smell, texture, drying time, spread ability, moisture feeling after test, feeling after use, where each property had a defined hedonic scale, and each number corresponded to a specific descriptor. The satisfaction analysis of the five formulations performed by 34 volunteers was summarized in Figure 5.

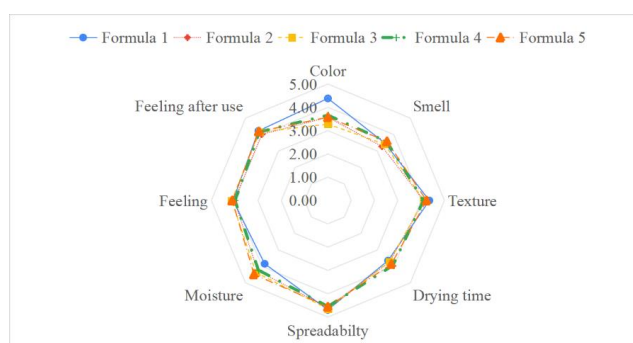


Figure 5. The satisfaction of formulas 1-5.

Formula 1 received the highest score regarding color, texture, spread ability, and feeling after use. Formula 3 had the highest score in terms of feeling during use. Formula 4 received the highest score for time of drying, and Formula 5 received the highest score for smell and moisture. The overall scoring of 5 formulas, all formulas exhibited in good condition except the color of the formula 2-5 according to the color of extracts.



Conclusions:

The results showed that the different extraction methods and species provide the results differently. The maceration technique showed an extraction yield higher than the ultrasonic technique for all extracts. Both *C. indiche um* L. and *C. morifolium* Ramat. extracted by maceration exhibited the highest total phenolic content. The *C. morifolium* Ramat. extracted by ultrasonic exhibited the highest inhibition activity of DPPH radical scavenging activity. All formulas 2-5 contained the extracts CMM, MS, CIM, and CIS exhibited stability when determined under accelerated test. These studies suggest that all extracts could be used as active ingredients. A further suggestion is to study the safety and efficacy of these ingredients using volunteers.

Acknowledgements:

The authors would like to acknowledge Scientific Technological Instrument Center, Mae Fah Luang University for providing the facilities of the research work.

References

1. He J, Zhang Q, Ma C, Giancaspro G, Bi K, & Li Q. *Front. Pharmacol.* 2021; 12, 1-11.
2. Shahrajabian MH, Sun W, Zandi P, & Cheng Q. *Appl. Ecol. Env. Res.* 2019; 17(6), 13355- 13369.
3. Youssef FS, Eid SY, Alshammari E, Ashour ML, Wink M, El-Readi MZ. *Foods*, 2020; 9(1460):1-18.
4. Hu J, Ma W, Li N, Wang K. *J. Mex. Chem. Soc.* 2017;61(4):282-289.
5. Lee BH, Nam TG, Park WJ, Kang H, Heo HJ, Dae KC, Kjm GH, Kim DO. *Food Sci. Biotechnol.* 2015;24:717-723.
6. Jiang S, Wang M, Jiang Z, Zafar S, Xie Q, Yang Y, Liu Y, Huan H, Jian Y, Wang W. *Mol.* 2021;26(10):3038.
7. Liang WL, Gong D, Zhang WK. *STEMedicine.* 2020;2(5):1-7.
8. Nguyen JK, Masub N, Jagdeo J. *J. Cosmet. Dermatol.* 2020;19(17):1555-1569.
9. Srimoon R, Niyomwan S. *BSJ.* 2021;26(1):378-398.
10. Obeng E, Kpodo FM, Tettey CO, Essuman EK, Adzinyo OA. *Sci. Afr.* 2020;7:e00227.
11. Choi KT, Kim JH, Cho HT, Lim SS, Kwak SS, Kim YJ. *Cosmet. Dermatol.* 2016;15:162-168.
12. Smaoui S, Hlima HB, Chobba IB, Kadri A. *Arab. J. Chem.* 2017;10:S1216-S1222.
13. Devillers C, Piérard-Franchimont C, Schraeder A, Docquier V, Piérard, G E. 2010. *Int. J. Cosmet. Sci.* 2010;32:241-245.
14. Sripanidkulchai B, Chaiittianan R, Suttanut K. Songklanakarin J. *Sci. Tech.* 2020;42(2):305-313.
15. Parlinska-Wojtan M, Kus-Liskiewicz M, Depciuch J & SadikO. *Bioprocess Biostyst. Eng.* 2016;39:1213-1223.
16. Kowalski R and Wolski T. 2003. *EJPAU.* 2003;6(1):1-10.
17. Lingegowda DC, Kumar JK, Prasad AD G, Zarei M, Gopal S. *Rom. J. Biophys.* 2013; 22:137-143.
18. Mokrzycki W and Tatol M. *MG&V.* 2021;20(4):383-411.
19. Udupurkar P, and Sanap AS. *IJCRT.Org.* 2023;11(6):a833-a845.
20. Shejul TS, and Kudale K. *IJPRA.* 2023;8(2):680-692.



DEVELOPMENT OF NOVEL FLUORESCENT CHEMOSENSORS BASED ON THIAZOLINYL QUINOLINE DERIVATIVES FOR METAL ION DETECTION.

Kavisara Srithadindang,¹ Waroton Paisuwan,^{1,2} Anawat Ajavakom^{1,*}

¹ Department of Chemistry, Faculty of Science, Chulalongkorn University, Bangkok, Thailand

² Futuristic Science Research Center, School of Science, Walailak University, Thasala, Nakhon Si Thammarat 80160, Thailand

*e-mail: anawat.a@chula.ac.th

Abstract:

Heavy metals can cause harm to the human body when exposed in excess doses through the skin, inhalation, or digestion. Among various metal ion detection techniques, fluorescent sensors are reliable for measuring metal ions. Quinoline is a heterocyclic compound that has the ability to bind to specific metal ions like Zn^{2+} , Cd^{2+} , Co^{2+} , etc., and at the same time can also serve as a practical fluorophore unit. The thiazoline unit, in particular, has been noted for its specific binding to Hg^{2+} , resulting in turn-on type sensing. Therefore, our project aims to design, synthesize, and evaluate fluorescent sensor, **8-TQ1**, by incorporating an aminoquinoline derivative with a thiazoline unit. **8-QT1** was successfully synthesized by $\text{S}_{\text{N}}2$ alkylation with 2-bromoethanol followed by Mitsunobu reaction with 2-thiazoline-2-thiol unit. Interestingly, **8-TQ1** selectively exhibits instantaneous fluorescence quenching by Cu^{2+} with an emissive change from bright yellow to arctic blue under UV light irradiation (365 nm). We propose that the probe could be useful in applications for heavy metal detection in the environment. Detailed results such as the photophysical properties, interference experiment, mechanistic studies, and tests with real samples, etc., will be presented.

Introduction:

Contamination by metal ions has become a pressing environmental concern, posing significant threats to ecosystems and human health over the past century. These metal ions, known for their toxicity and non-biodegradability, can infiltrate the human body through air, food, water, or skin absorption, disrupting normal concentrations of essential minerals such as Zn, Mg, Ca, and Cu, and adversely affecting organ system function.¹ The harmful impact of metal ions stems from their capacity for binding with protein sites, displacing essential metals, accumulating in the body, and ultimately causing harm. The resulting detrimental effects, particularly beyond biologically safe concentrations, often target the nervous system, kidney/liver functions, and hard tissues such as bones and teeth.^{2,3,4}

To accurately assess metal ion contamination in drinking water, traditionally, large, sophisticated, and costly lab-based techniques such as atomic absorption spectrometry (AAS)⁵, mass spectrometry (MS)⁶, inductively coupled plasma MS (ICP-MS)⁷, atomic emission spectrometry (AES)⁸, and X-ray fluorescence (XRF)⁹ are required for trace metal analysis. However, among these methods, fluorescent chemosensors offer a standout solution, providing a convenient, affordable, and reliable approach for determining metal ions even at very low concentrations.

Quinoline, belonging to the class of heterocyclic compounds, forms fluorescent complexes with metal ions and is particularly intriguing. It serves as a standard green emissive material for Organic Light-Emitting Diodes (devices) or OLEDs, with its derivatives being vital fluorescent sensors for detecting metal ions. Quinoline derivatives

have been synthetically developed for the detection of various metal ions in our lab^{10, 11, 12}, and also widely applied as a heavy metal sensing such as Zn^{2+} , Cd^{2+} , Co^{2+} , etc.,^{13, 14, 15}

The thiazoline unit, in particular, has been noted for its specific binding to Hg^{2+} , resulting in turn-on type sensing.¹⁶ In 2019, Wang and colleagues reported the selective copper(II) ion thiazolyl pyrene sensor, as fluorescence response to Cu^{2+} has revealed the selective “Turn-on” sensing.¹⁷ Therefore, our project aims to synthesize a new fluorescent probe by incorporating an aminoquinoline derivative with a thiazoline unit. We anticipate that the heteroatoms within the thiazoline unit, especially sulfur atoms, will confer selectivity to metal ions.

Methodology:

1. Materials and instruments

Reagents were purchased from Sigma-Aldrich Company, Merck Company, Tokyo Chemical Industry, and these were used without further purification: 8-aminoquinoline, 2-thiazoline-2-thiol, pyridine, 1,1'-(azodicarbonyl)dipiperidine (ADDP), 2-Bromoethanol, tributylphosphine (PBU_3), potassium carbonate (K_2CO_3), potassium iodide (KI), anhydrous sodium sulfate, sodium chloride, ammonium chloride, Anhydrous solvents used in the synthesis process of all compounds include tetrahydrofuran (THF), and acetonitrile (MeCN). Commercial-grade solvents used for extraction and chromatography include chloroform (CHCl_3), dichloromethane (CH_2Cl_2), ethyl acetate (EtOAc), and hexane (Hex). Deionized water was used in all extraction procedures. Column chromatography was executed on Wakogel[®] silica gel C-200 for a glass column, and on Biotage[®] Sfar silica High Capacity Duo for an auto column. Solvents used for the study of photophysical properties include Milli-Q water, MeCN, THF, ethanol (EtOH), and dimethyl sulfoxide (DMSO). Milli-Q water was used to prepare the stock metal ions for UV–Vis and fluorescence experiments. The stock solutions of all ligands were prepared in DMSO. Metal ions were prepared from their commercially available nitrate salts; exceptions to this procedure include potassium, magnesium, iron(II), mercury(II), and lead(II), which were in the form of acetate salts in deionized water (Milli-Q). The ^1H and ^{13}C NMR spectra were carried out by a 500 MHz NMR spectrometer (JEOL Company) at 500 MHz and 126 MHz, respectively. The UV–vis and fluorescence spectra were recorded on a UV-2250 UV–vis spectrophotometer (SHIMADZU) and a Cary Eclipse fluorescence spectrophotometer (Agilent Technologies) in a quart cell with 1 cm path length at 25 °C, respectively. High-resolution mass spectra were obtained from a JEOL AccuTof LC-plus (JMS-T100LP) spectrometer.

2. Synthesis

2.1 Synthesis of **8-QH**

8-Aminoquinoline (500 mg, 3.47 mmol), 2-bromoethanol (1230 μL , 17.4 mmol), KI (58.1 mg, 0.35 mmol) and K_2CO_3 (1,439 mg, 10.4 mmol) were mixed in MeCN (10 mL). Then, the mixture was stirred at reflux temperature for 48 h. The mixture was filtered to remove K_2CO_3 and concentrated under reduced pressure. The obtained residue was redissolved in CH_2Cl_2 and extracted 3 times with saturated NH_4Cl . The organic fraction was combined and dried over anhydrous Na_2SO_4 . The resulting solution was then concentrated under reduced pressure. The column chromatography was conducted with gradient eluent from 0-60% EtOAc/hexanes to afford a brown oil of **8-QH** in 40% yield.

2-(Quinolin-8-ylamino)ethan-1-ol (8-QH);

^1H NMR (500 MHz, CDCl_3) δ 8.7 (dd, $J = 4.3, 1.7$ Hz, 1H), 8.1 (dd, $J = 8.3, 1.7$ Hz, 1H), 7.4 – 7.3 (m, 2H), 7.1 (d, $J = 8.3$ Hz, 1H), 6.7 (d, $J = 7.7$ Hz, 1H), 4.0 (t, $J = 5.3$ Hz, 2H), 3.5 (t, $J = 5.3$ Hz, 2H).



2.2 Synthesis of **8-TQ1**

PBu₃ (262 μ L, 1.07 mmol) and ADDP (268 mg, 1.07 mmol) were dispersed in THF (5 mL). Then, **8-QH** (100 mg, 0.53 mmol) and 2-thiazoline-2-thiol (126 mg, 1.07 mmol) were added, and the solution was refluxed for 2 days. After the reaction was completed, the reaction solution was evaporated to remove the solvent. The obtained residue was redissolved in CHCl₃ and washed with saturated NH₄Cl. The organic phase was dried over anhydrous Na₂SO₄ and evaporated under a vacuum. The crude product was purified by column chromatography to afford **8-TQ1** as a yellow solid with a 66% yield.

N-(2-((4,5-Dihydrothiazol-2-yl)thio)ethyl)quinolin-8-amine (8-TQ1);

¹H NMR (500 MHz, CDCl₃) δ 8.7 (dd, J = 4.3, 1.7 Hz, 1H), 8.1 (dd, J = 8.3, 2.0 Hz, 1H), 7.5 – 7.4 (m, 2H), 7.1 (d, J = 7.2 Hz, 1H), 6.8 (d, J = 7.4 Hz, 1H), 4.3 (t, J = 8.0 Hz, 2H), 3.7 (t, J = 6.7 Hz, 2H), 3.5 – 3.4 (m, 4H).

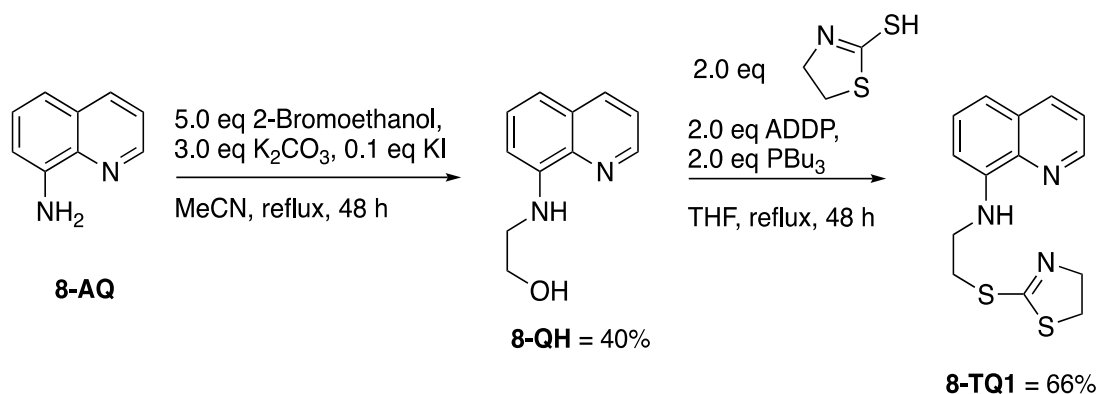
3. Preparing stock solutions of **8-TQ1**, and metal ions

Dimethyl sulfoxide (DMSO) was used to dissolve **8-TQ1** probes for the preparation of each 10 mM stock solution. There were 20 types of stock metal ions consisting of Li⁺, Na⁺, Ca²⁺, Sr²⁺, Ba²⁺, Al³⁺, Fe³⁺, Cr³⁺, Zn²⁺, Cd²⁺, Co²⁺, Cu²⁺, Ni²⁺, Mn²⁺, and Ag⁺ in the form of their nitrate salts: also, K⁺, Mg²⁺, Fe²⁺, Pb²⁺, and Hg²⁺. All salts were dissolved in Milli-Q water to produce 10 mM metal ion stock solutions.

Results and Discussion:

1. Synthesis of target probe (**8-TQ1**)

In the synthesis of the **8-TQ1** probe, 8-aminoquinoline was initially reacted with 2-bromoethanol to afford **8-QH** in a 40% yield. The hydroxyl group in **8-QH** was then substituted by a 2-thiazoline-2-thiol unit under Mitsunobu conditions (**Scheme 1**) furnishing **8-TQ1** with a 66% yield.



Scheme 1. The synthetic scheme of **8-TQ1**

2. Spectroscopic properties of **8-TQ1**

The photophysical properties of **8-TQ1** measured in five different solvents: THF, MeCN, DMSO, EtOH, and Milli-Q water, are summarized in **Table 1** and **Figure 1**. The UV–Vis absorption spectra in each solvent showed peaks with maximum absorption wavelengths (λ_{ab}) that ranged from 361 to 367 nm. The emission bands in all solvents were revealed in similar shapes with maximum emission wavelengths (λ_{em}) that ranged from 467 to 486 nm.

Table 1. Photophysical properties of **8-TQ1**

| Solvent | λ_{ab} (nm) | λ_{em} (nm) | Stoke shift* (nm) |
|---------------|--------------------------------|---------------------|-------------------|
| THF | 361 (log ϵ = 3.52) | 468 | 107 |
| ACN | 361 | 480 | 119 |
| EtOH | 361 | 467 | 106 |
| DMSO | 367 | 486 | 119 |
| Milli-Q water | 361 | 469 | 108 |

*Stoke shift comparison between the longer λ_{ab} and λ_{em}

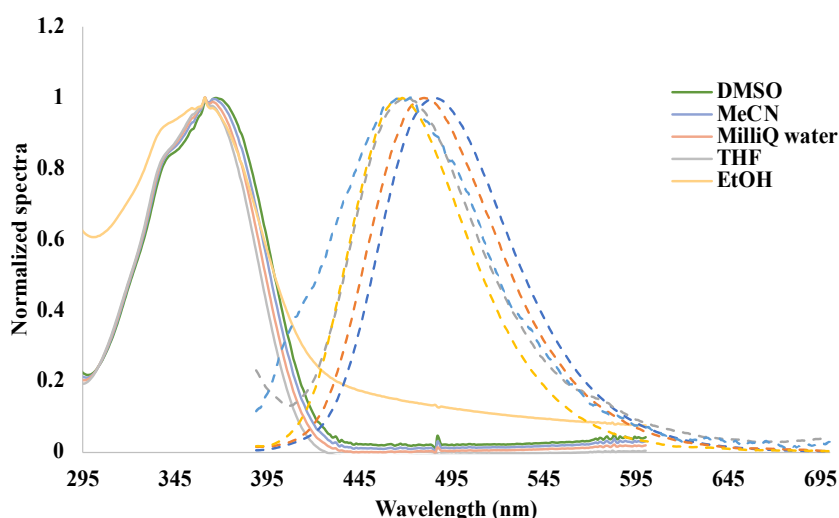


Figure 1. The normalized absorption and emission spectra of **8-TQ1** in various solvents at the concentration of 50 μ M.

3. Optical responses to Cu^{2+}

Using a standard transilluminator under UV light irradiation at 365 nm, the sensing properties of **8-TQ1** were initially screened using only the naked eye for 20 metal ions in five types of media: THF, MeCN, DMSO, EtOH, and Milli-Q water (**Figure 2**). **8-TQ1**, on the other hand, showed selective fluorescence quenching with Cu^{2+} in DMSO and THF. The Cu^{2+} sensing was further optimized in THF, due to the much higher I_0/I value than in DMSO (**Figure 3**). To utilize this Cu^{2+} probe for applications in aqueous media, the influence of the water fraction was examined at 1, 3, 5, 10, and 20 % (v/v) in THF (**Figure 4a**). The fluorescence responses of **8-TQ1** in the presence of Cu^{2+} revealed that the emission intensity was decreased with increases in the water content. The reduction of fluorescence intensity was probably due to the ICT state formed after binding with Cu^{2+} . Based on the results of the quenching ratio (I_0/I) shown in **Figure 4b**, 1% water was chosen to be the optimal water fraction for this sensing system, because the fluorescence change could not be seen by the naked eye at a higher aqueous ratio.

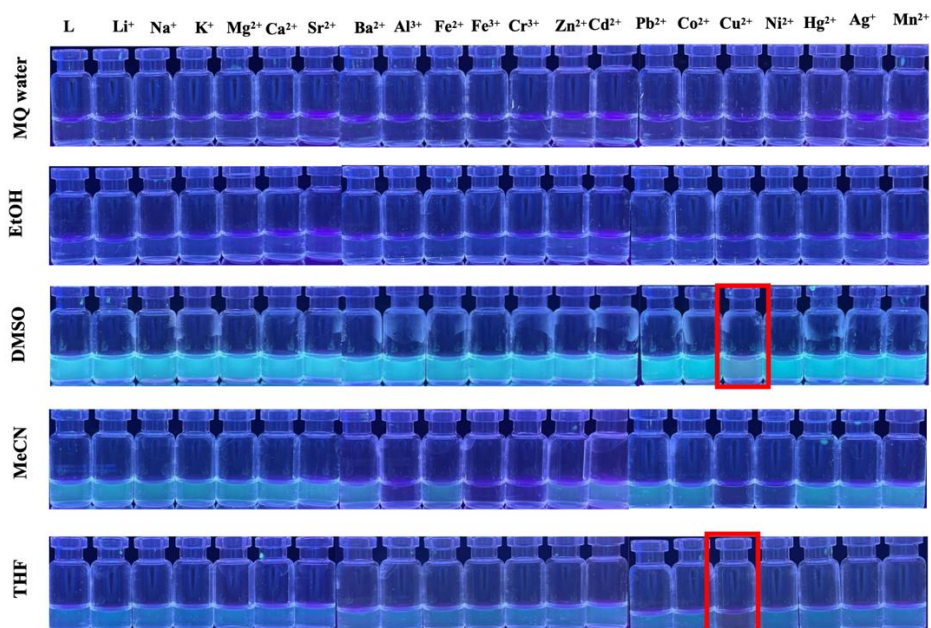


Figure 2. 10 μM **8-TQ1** in the presence of 100 μM metal ion in various solvents



Figure 3. The quenching ratio of **8-TQ1**+ Cu^{2+} in DMSO (486 nm) and THF (468 nm)

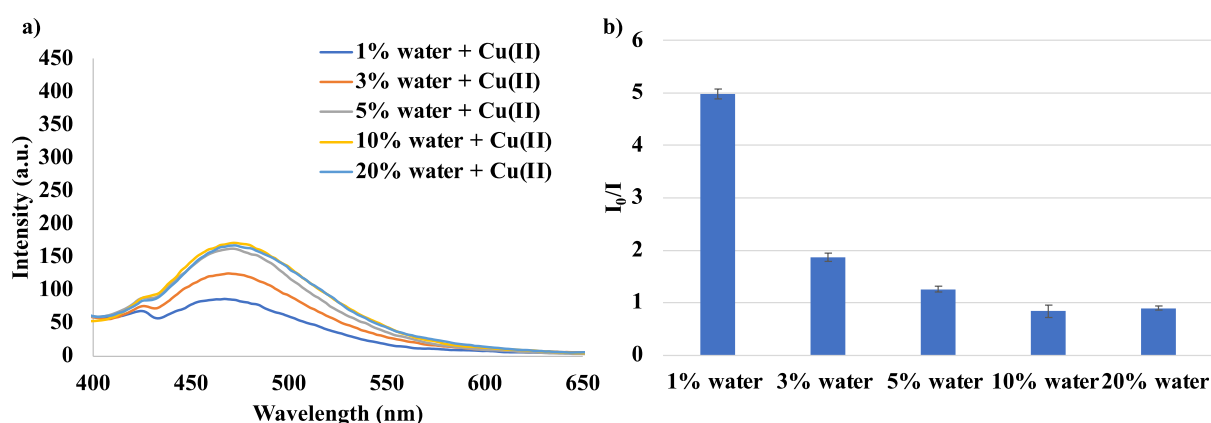


Figure 4. (a) fluorescence spectra of **8-TQ1** + Cu^{2+} and (b) the quenching ratio (I_0/I) in THF at various water fractions in the range of 0-20% (v/v).

The selectivity studies of **8-TQ1** with various metal ions were carried out under these optimized conditions. The extreme fluorescence quenching of **8-TQ1** with Cu^{2+} was

selectively observed at 468 nm (**Figure 5a**) with the quenching ratio (I_0/I) around 5 folds (**Figure 4b**) along with a complete fading of the bright green fluorescence (**Figure 5b**).

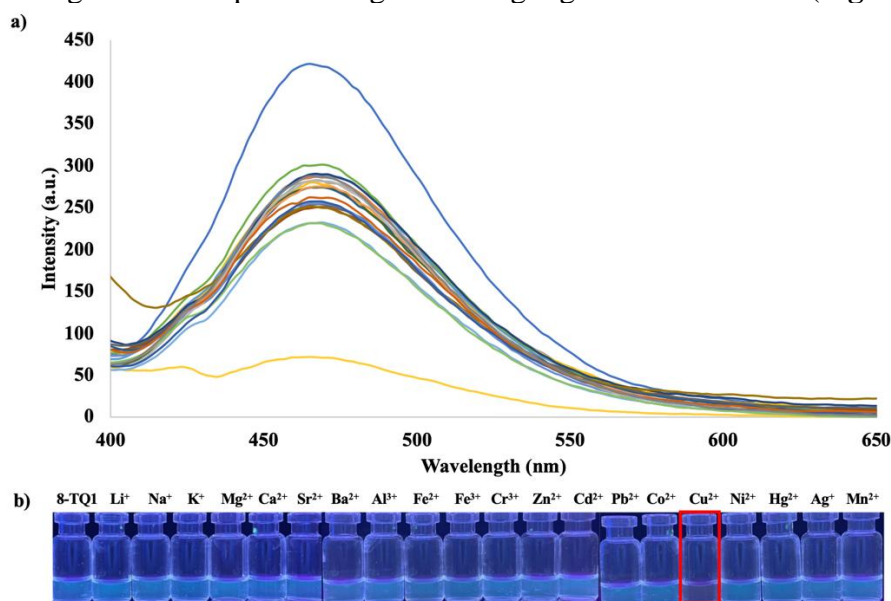


Figure 5. (a) Fluorescence responses of **8-TQ1** (10 μM) in the presence of various metal ions (100 μM) in THF : Milli-Q water (99 : 1) ($\lambda_{\text{ex}} = 365$ nm). (b) The photograph shows a fluorescence appearance under blacklight

The effects of the presence of other metal ions on the efficiency of Cu^{2+} detection by **8-TQ1** were investigated using metal ions: Li^+ , Na^+ , K^+ , Mg^{2+} , Ca^{2+} , Sr^{2+} , Ba^{2+} , Al^{3+} , Fe^{2+} , Fe^{3+} , Cr^{3+} , Zn^{2+} , Cd^{2+} , Pb^{2+} , Co^{2+} , Ni^{2+} , Hg^{2+} , Ag^+ , and Mn^{2+} (**Figure 6**). The presence of additional metal ions did not significantly affect the fluorescence quenching of **8-TQ1** by Cu^{2+} , except for Cr^{3+} and Mn^{2+} . It can be assumed that these 2 metal ions are also capable of binding with **8-TQ1** but probably with a lower association constant. Therefore, the existence of their complexes in this sensing system could competitively disturb the Cu^{2+} detection resulting in the acceleration of the quenching effect.

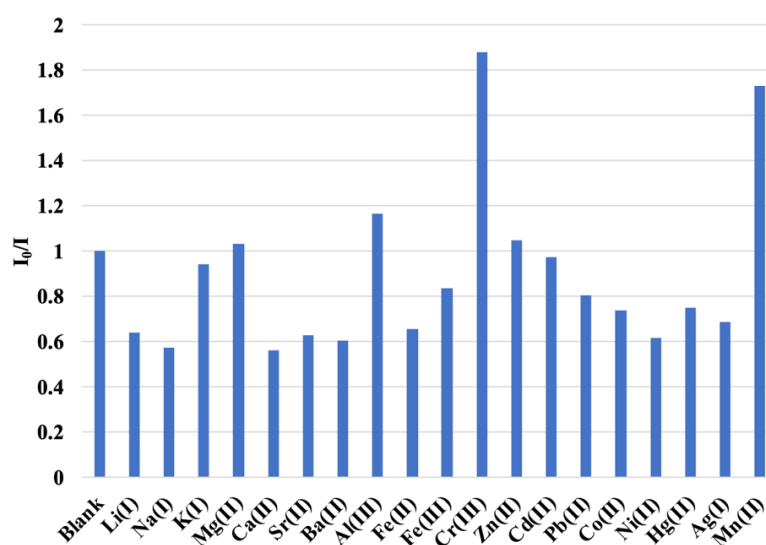


Figure 6. Fluorescence responses of a mixture of **8-TQ1** (10 μM) and Cu^{2+} (10 μM) in the presence of other metal ions (10 μM).



4. Sensing mechanism

The UV–Vis titration of **8-TQ1** with various amounts of Cu^{2+} (**Figure 7**) showed that the absorption band at 361 nm gradually decreased, while the new band at 295 nm and 435 nm gradually increased. An increase in Cu^{2+} concentration resulted in the fluorescent quenching of **8-TQ1** with two isosbestic points at 345 and 405 nm, suggesting a complex formation between **8-TQ1** and Cu^{2+} . The band at 295 nm is, therefore, concluded to correspond to the characteristic absorption property of the **8-TQ1** Cu^{2+} complex. Conversely, the typical absorption band of the quinoline probe at 361 nm decreased.

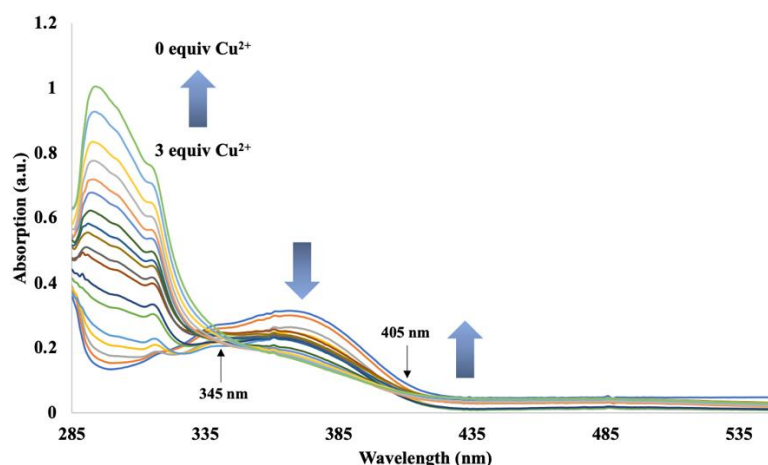


Figure 7. Absorption titration of **8-TQ1** (100 μM) with Cu^{2+} (0 – 3 equiv)

3.4. Quantitative analysis of Cu^{2+}

The fluorescence titration of **8-TQ1** with various concentrations of Cu^{2+} was performed to obtain a calibration curve for quantitative analysis. The emission spectra of **8-TQ1** were immediately recorded after the addition of Cu^{2+} and the decrease in fluorescence intensity was relatively dependent upon the increase in Cu^{2+} (**Figure 8a**).

The plot of I_0/I against the Cu^{2+} concentrations provided a linear correlation in a range of from 0 to 5 μM with an $R^2 = 0.9929$ (**Figure 8b**). The limit of detection (LOD) for this Cu^{2+} sensing system was calculated to be 2.706 μM based on the $3\sigma/K$ equation (where σ is a 3-fold standard deviation of the blank and K is the slope of the plot).

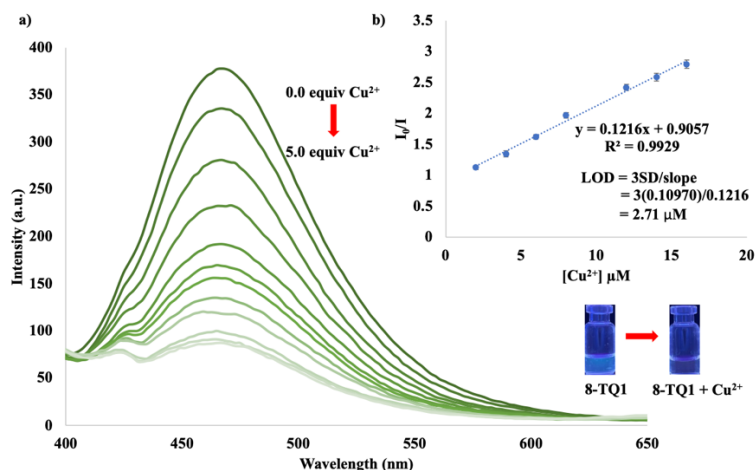


Figure 8. a) fluorescence titration of **8-TQ1** (10 μM) after the addition of 0 – 5.0 μM of Cu^{2+} in 99:1 THF : Milli-Q water; and b) Calibration curve of I_0/I plotted against Cu^{2+} concentrations.

Conclusion:

The novel fluorometric probe **8-TQ1**, based on a thiazolynyl-quinoline structure, was successfully synthesized and demonstrated high selectivity for Cu^{2+} detection, with a fluorescence quenching response visible under UV light. The probe showed optimal performance in THF with 1% water, achieving a detection limit of 2.706 μM and a linear response up to 5 μM . Interference studies with various metal ions confirmed that **8-TQ1** remained highly selective for Cu^{2+} , with only interference from Cr^{3+} and Mn^{2+} . These findings indicate that **8-TQ1** is a promising tool for practical applications in detecting copper contamination in environmental samples.

Acknowledgements:

We would like to express our sincere gratitude to DPST (Development and Promotion of Science and Technology Talents Project, Thai government scholarship) and the National Research Council of Thailand (NRCT, N42A661000), which have contributed to this project.

References:

1. Rubino A, Queirós R. *Talanta Open*. 2023;7:100203.
2. Qian X, Xu Z. *Chemical Society Reviews*. 2015;44(14):4487-4493.
3. Järup L. *Br Med Bull*. 2003;68:167-182.
4. Jaishankar M, Tseten T, Anbalagan N, Mathew B. B, Beeregowda K. N. *Interdiscip Toxicol*. 2014;7(2):60-72.
5. Nikolovska-Coleska Z, Xu L, Hu Z, Tomita Y, Li P, Roller P. P, Wang R, Fang X, Guo R, Zhang M, et al. *Journal of Medicinal Chemistry*. 2004;47(10):2430-2440.
6. Pohl P. *TrAC Trends in Analytical Chemistry*. 2009;28(1):117-128.
7. Gasparik J, Vladarova D, Capcarova M, Smehyl P, Slamecka J, Garaj P, Stawarz R, Massanyi P. *J Environ Sci Health A Tox Hazard Subst Environ Eng*. 2010;45(7):818-823.
8. Flamini R, Panighel A. *Mass Spectrom Rev*. 2006;25(5):741-774.
9. O'Meara J. M, Chettle D. R, McNeill F. E, Webber C. E. *Appl Radiat Isot*. 1998;49(5-6): 713-715.



10. Hojitsiriyant J, Chaibuth P, Boonkitpatarakul K, Ruangpornvisuti V, Palaga T, Chainok K, Sukwattanasinitt M. *Journal of Photochemistry and Photobiology A: Chemistry*. 2021;415:113307.
11. Paisuwan W, Srithadindang K, Kodama T, Sukwattanasinitt M, Tobisu M, Ajavakom A. *Spectrochimica Acta Part A: Molecular and Biomolecular Spectroscopy*. 2024;322:124706.
12. Boonkitpatarakul K, Smata A, Kongnukool K, Srisurichan S, Chainok K, Sukwattanasinitt M. *Journal of Luminescence*. 2018; 198.
13. Musikavanhu B, Muthusamy S, Zhu D, Xue Z, Yu Q, Chiyumba C. N, Mack J, Nyokong T, Wang S, Zhao L. *Spectrochimica Acta Part A: Molecular and Biomolecular Spectroscopy*. 2022;264:120338.
14. Anand T, Sivaraman G, Mahesh A, Chellappa D. *Analytica Chimica Acta*. 2015;853:596-601.
15. Kamal A, Raj R, Kumar V, Mahajan R. K. *Electrochimica Acta*. 2015;166:17-25.
16. Erdemir S, Oguz M, Malkondu S. *Analytica Chimica Acta*. 2022;1192:339353.
17. Wang J, Liang J, Liu X, Xiao H, Dong F, Wang Y, Shu X, Huang F, Liu H.-B. *Spectrochimica Acta Part A: Molecular and Biomolecular Spectroscopy*. 2019;215:260-265.



EXPLORING THE α -GLUCOSIDASE INHIBITORY ACTIVITY OF N-9 ALKYL HARMINE DERIVATIVES

Fayaz Ahmad, The Thanh Ngo, Warinthorn Chavasiri*

Center of Excellence in Natural Products Chemistry, Department of Chemistry, Faculty of Science, Chulalongkorn University, Pathumwan, Bangkok 10330, Thailand

*e-mail: warinthorn.c@chula.ac.th

Abstract:

Treatment of type 2 diabetes involves limiting postprandial hyperglycemia by reducing glucose uptake through the inhibition of α -glucosidase. However, many drugs with this target cause side effects. Harmine, a compound from *Peganum harmala*, was considered for its medicinal and health benefits. Fourteen alkyl derivatives of harmine (**1-14**) were synthesized, characterized by spectroscopic means, and evaluated for their yeast α -glucosidase inhibitory activity at 50 μ M. Certain derivatives revealed the remarkable activity in comparison to harmine. Compounds **9** and **14** exhibited IC_{50} 13.8 and 12.1 μ M, respectively regarding that of acarbose, the standard drug, with IC_{50} 836.0 μ M. The kinetic study of these compounds was conducted further to investigate the interaction mechanism which revealed that both compounds were competitive inhibitors. This suggests that the derivatives bind to the active sites of enzyme and enhance its inhibitory activity, which might apply to diabetes treatment in the future.

Introduction:

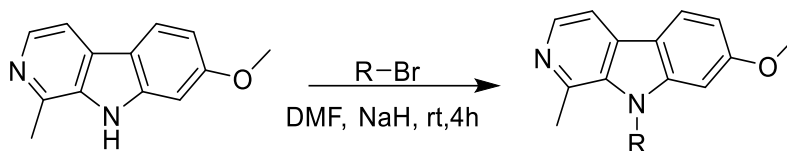
Diabetes mellitus is a chronic disease marked by high blood sugar levels due to irregularities in glucose, lipid, and protein metabolism.¹ α -Glucosidase in the small intestine converts carbohydrates into energy. Inhibitors can delay carbohydrate digestion, lowering blood glucose and insulin levels.² However, acarbose, miglitol, and voglibose are the best commercial α -glucosidase inhibitors, but they have many side effects.³ Therefore, providing more potent, less toxic α -glucosidase inhibitors is required.

Harmine is one of the major constituents of *Peganum harmala*, a plant grown in Central America, Asia, and Africa, Asian native people use it for psychological effects, pharmaceutical values, and as a dye.⁴ Harmine and its derivatives have been reported as bioactive compounds against acetylcholinesterase, lipoxygenase, and cancer. They are also used as antibacterial, antiviral, anti-Alzheimer, and various pharmacological activities including cell cycle arrest, apoptosis induction, and inhibition of *Plasmodium falciparum* heat shock protein 90 (pHsp90).⁵ This study aims to explore α -glucosidase activity of harmine and its derivatives.

Methodology:

The general procedure for the synthesis of alkyl derivatives of harmine.

The synthetic route for alkyl derivatives of harmine **1-14** is shown in **Scheme 1** with their structures displaying in **Table 1**. A mixture of harmine (1 mmol) and halo-alkane (1 mmol) in DMF (10 mL) was stirred at room temperature.⁶ Thin-layer chromatography (TLC) was used to monitor the progress of the reaction. After the reaction was complete, water was added to the reaction mixture and extracted with EtOAc. The organic layer was dried over anhydrous Na_2SO_4 , and the residue was chromatographed on silica gel column by a mixture of *n*-hexane and EtOAc to obtain desirable products. The structures of these compounds were characterized by using 1H and ^{13}C NMR.



Scheme 1 General procedure for the synthesis of alkyl derivatives of harmine

α -Glucosidase inhibition assay

This activity was performed by the method described by Ramadhan and coworkers.⁷ Briefly, α -glucosidase (0.1 U/mL) and substrate (1 mM *p*-nitrophenyl- α -D-glucopyranoside) were dissolved in 0.1 M phosphate buffer (pH 6.9). A 10 μ L test sample was pre-incubated with α -glucosidase (40 μ L) at 37° C for 10 min. A substrate solution (50 μ L) was then added to the reaction mixture, incubated at 37° C for 20 min, and terminated by adding 1 M Na₂CO₃ solution (100 μ L). Enzymatic activity was quantified by measuring the absorbance at 405 nm (ALLSHENG AMR-100 microplate reader). The percentage inhibition was calculated as follows: % Inhibition = [(A₀-A₁)/A₀] x 100, where: A₀ is the absorbance without the sample; A₁ is the absorbance with the sample. The IC₅₀ value was deduced from the plot of %inhibition *versus* concentration of the test sample. Acarbose was used as standard control, and the experiment was performed in triplicate.

Results and Discussion:

Isolation of harmine from harmal seeds

The isolation of harmine from *Peganum harmala* seeds was performed using an acid-base extraction method. Initially, from 200 g of harmal seeds, 2 g of harmine was obtained and its identity was confirmed from ¹H and ¹³C spectra.

Harmine: 7-methoxy-1-methyl-9H-pyrido[3,4-b]indole

¹H NMR (500 MHz, CD₃OD): δ_{H} 8.07 (d, J = 5.4 Hz, 1H), 7.95 (d, J = 8.9 Hz, 1H), 7.77 (d, J = 5.5 Hz, 1H), 7.01 (d, J = 2.3 Hz, 1H), 6.83 (dd, J = 8.6, 2.3 Hz, 1H), 3.88 (s, 3H), 2.74 (s, 3H). ¹³C NMR (126 MHz, CD₃OD): δ_{C} 161.2, 136.7, 122.1, 120.3, 117.1, 111.9, 111.0, 109.5, 94.0, 93.9, 54.5, 46.9, 22.9, 19.0.

The synthesis of harmine derivatives

Compound 1: 7-methoxy-1,9-dimethyl-9H-pyrido[3,4-b]indole

¹H NMR (500 MHz, CD₃OD): δ_{H} 8.25 (d, J = 5.4 Hz, 1H), 7.97 (d, J = 8.6 Hz, 1H), 7.74 (d, J = 5.4 Hz, 1H), 6.90 (dd, J = 8.6, 2.3 Hz, 1H), 6.84 (d, J = 2.3 Hz, 1H), 4.09 (s, 4H), 3.95 (s, 4H), 3.09 (s, 4H). ¹³C NMR (126 MHz, CD₃OD): δ_{C} 161.4, 144.2, 140.4, 137.0, 135.8, 129.8, 122.6, 114.7, 112.5, 109.5, 92.9, 55.8, 32.4, 22.7. Isolated yield: 70%

Compound 2: 9-ethyl-7-methoxy-1-methyl-9H-pyrido[3,4-b]indole

¹H NMR (500 MHz, CDCl₃): δ_{H} 8.27 (d, J = 5.2 Hz, 1H), 7.98 (d, J = 8.6 Hz, 1H), 7.75 (d, J = 5.2 Hz, 1H), 6.90 (dd, J = 8.6, 2.0 Hz, 1H), 6.86 (d, J = 2.0 Hz, 1H), 4.55 (q, J = 7.2 Hz, 1H), 3.95 (s, 3H), 3.05 (s, 2H), 1.45 (t, J = 7.3 Hz, 2H). ¹³C NMR (126 MHz, CDCl₃): δ_{C} 161.2, 143.0, 140.2, 137.5, 135.0, 129.8, 122.6, 115.2, 112.5, 109.1, 93.1, 55.8, 39.6, 22.7, 15.6. Isolated yield: 72%

Compound 3: 9-butyl-7-methoxy-1-methyl-9H-pyrido[3,4-b]indole

¹H NMR (500 MHz, CDCl₃): δ_{H} 8.27 (d, J = 5.3 Hz, 1H), 7.98 (d, J = 8.6 Hz, 1H), 7.75 (d, J = 5.3 Hz, 1H), 6.89 (dd, J = 8.6, 2.1 Hz, 1H), 6.86 (d, J = 2.1 Hz, 1H), 4.50 – 4.42 (m, 1H), 3.95 (s, 4H), 3.04 (s, 3H), 1.86 – 1.76 (m, 1H), 1.46 (dt, J = 15.2, 7.5 Hz, 1H), 0.98 (t, J = 7.4 Hz, 3H). ¹³C NMR (126 MHz, CDCl₃): δ_{C} 161.1, 143.4, 140.3, 137.5, 135.3, 129.7, 122.5, 115.1, 112.4, 108.9, 93.5, 55.8, 44.8, 32.8, 22.9, 20.2, 14.2. Isolated yield: 68%



Compound 4: 9-hexyl-7-methoxy-1-methyl-9H-pyrido[3,4-b]indole

^1H NMR (500 MHz, CDCl_3): δ_{H} 8.27 (d, $J = 5.2$ Hz, 1H), 7.97 (d, $J = 8.5$ Hz, 1H), 7.73 (d, $J = 5.2$ Hz, 1H), 6.88 (dd, $J = 8.5, 2.1$ Hz, 1H), 6.85 (d, $J = 2.1$ Hz, 1H), 4.54 – 4.38 (m, 1H), 3.95 (s, 2H), 3.01 (s, 2H), 1.82 (p, $J = 7.7$ Hz, 2H), 1.43 (tt, $J = 11.6, 6.3$ Hz, 2H), 1.38 – 1.28 (m, 3H), 0.89 (t, $J = 6.8$ Hz, 2H). ^{13}C NMR (126 MHz, CDCl_3): δ_{C} 160.9, 143.1, 140.6, 138.2, 135.4, 129.4, 122.4, 115.3, 112.3, 108.6, 93.5, 55.7, 45.0, 31.6, 30.6, 26.6, 23.4, 22.6, 14.0. Isolated yield: 75%

Compound 5: 7-methoxy-1-methyl-9-octyl-9H-pyrido[3,4-b]indole

^1H NMR (500 MHz, CDCl_3): δ 8.26 (d, $J = 5.2$ Hz, 1H), 7.96 (d, $J = 8.5$ Hz, 1H), 7.72 (d, $J = 5.2$ Hz, 1H), 6.87 (dd, $J = 8.6, 2.3$ Hz, 1H), 6.84 (d, $J = 2.2$ Hz, 1H), 4.49 – 4.38 (m, 2H), 3.94 (s, 3H), 3.00 (s, 3H), 1.89 – 1.77 (m, 3H), 1.48 – 1.29 (m, 5H), 1.24 (s, 13H), 0.86 (t, $J = 6.9$ Hz, 3H). ^{13}C NMR (126 MHz, CDCl_3): δ_{C} 160.7, 142.9, 140.4, 137.9, 135.1, 129.2, 122.2, 115.0, 112.1, 108.4, 93.3, 55.5, 44.8, 31.6, 30.4, 29.2, 29.0, 26.7, 23.1, 22.4, 13.9. Isolated yield: 77%

Compound 6: 9-dodecyl-7-methoxy-1-methyl-9H-pyrido[3,4-b]indole

^1H NMR (500 MHz, CDCl_3): δ_{H} 8.26 (d, $J = 5.2$ Hz, 1H), 7.96 (d, $J = 8.5$ Hz, 1H), 7.72 (d, $J = 5.2$ Hz, 1H), 6.87 (dd, $J = 8.6, 2.3$ Hz, 1H), 6.84 (d, $J = 2.2$ Hz, 1H), 4.47 – 4.41 (m, 2H), 3.94 (s, 3H), 3.00 (s, 3H), 1.86 – 1.77 (m, 3H), 1.45 – 1.31 (m, 4H), 1.24 (s, 14H), 0.86 (t, $J = 6.9$ Hz, 3H). ^{13}C NMR (126 MHz, CDCl_3): δ_{C} 160.9, 143.1, 140.6, 138.2, 135.4, 129.4, 122.4, 115.3, 112.3, 108.6, 93.5, 55.7, 45.0, 31.9, 30.6, 29.7, 29.6, 29.6, 29.4, 29.4, 27.0, 23.4, 22.7, 14.2. Isolated yield: 65%

Compound 7: 9-hexadecyl-7-methoxy-1-methyl-9H-pyrido[3,4-b]indole

^1H NMR (500 MHz, CDCl_3): δ_{H} 8.28 (d, $J = 5.2$ Hz, 1H), 7.98 (d, $J = 8.6$ Hz, 1H), 7.77 (d, $J = 5.4$ Hz, 1H), 6.90 (dd, $J = 8.6, 2.0$ Hz, 1H), 6.85 (d, $J = 2.0$ Hz, 1H), 4.46 – 4.42 (m, 2H), 3.95 (s, 3H), 3.05 (s, 3H), 1.82 (p, $J = 7.7$ Hz, 2H), 1.42 (p, $J = 6.9$ Hz, 2H), 1.37 – 1.32 (m, 2H), 1.24 (s, 22H), 0.87 (t, $J = 6.9$ Hz, 3H). ^{13}C NMR (126 MHz, CDCl_3): δ_{C} 160.9, 143.1, 140.6, 138.2, 135.4, 129.4, 122.4, 115.3, 112.3, 108.6, 93.5, 55.7, 45.0, 32.0, 30.6, 29.7, 29.7, 29.7, 29.6, 29.6, 29.4, 27.0, 23.4, 22.7, 14.2. Isolated yield: 78%

Compound 8: 9-(4-bromobutyl)-7-methoxy-1-methyl-9H-pyrido[3,4-b]indole

^1H NMR (500 MHz, CDCl_3) δ 8.27 (d, $J = 5.2$ Hz, 1H), 7.97 (d, $J = 8.5$ Hz, 1H), 7.73 (d, $J = 5.3$ Hz, 1H), 6.92 – 6.85 (m, 2H), 4.50 (t, $J = 7.4$ Hz, 2H), 3.95 (s, 3H), 3.42 (t, $J = 6.1$ Hz, 2H), 3.01 (s, 3H), 2.05 – 1.92 (m, 4H). ^{13}C NMR (126 MHz, CDCl_3): δ_{C} 161.1, 143.1, 140.4, 138.2, 135.2, 129.7, 122.6, 115.2, 112.4, 109.0, 93.4, 55.8, 44.0, 32.9, 29.8, 29.1, 23.3. Isolated yield: 66%

Compound 9: 9-(6-bromohexyl)-7-methoxy-1-methyl-9H-pyrido[3,4-b]indole

^1H NMR (500 MHz, CDCl_3): δ_{H} 8.27 (d, $J = 5.3, 1.2$ Hz, 1H), 7.98 (d, $J = 8.6, 1.2$ Hz, 1H), 7.75 (d, $J = 5.2$ Hz, 1H), 6.89 (dd, $J = 8.7, 1.7$ Hz, 1H), 6.84 (d, $J = 1.5$ Hz, 1H), 4.46 (t, $J = 7.8$ Hz, 2H), 3.95 (s, $J = 1.4$ Hz, 3H), 3.38 (t, $J = 6.6, 1.2$ Hz, 2H), 3.02 (s, $J = 1.1$ Hz, 3H), 1.89 – 1.78 (m, 10H), 1.55 – 1.40 (m, 4H). ^{13}C NMR (126 MHz, CDCl_3): δ_{C} 161.0, 143.2, 140.5, 138.0, 135.3, 129.6, 122.5, 115.3, 112.4, 108.8, 93.4, 55.8, 44.8, 33.4, 30.0, 29.8, 26.1, 23.2, 14.2. Isolated yield: 72%

Compound 10: 9-(8-bromooctyl)-7-methoxy-1-methyl-9H-pyrido[3,4-b]indole

^1H NMR (500 MHz, CDCl_3): δ 8.25 (d, $J = 5.2$ Hz, 1H), 7.96 (d, $J = 8.6$ Hz, 1H), 6.87 (dd, $J = 8.6, 2.2$ Hz, 1H), 6.84 (d, $J = 2.2$ Hz, 1H), 4.48 – 4.39 (m, 2H), 3.94 (s, 3H), 3.38 (t, $J = 6.8$ Hz, 2H), 3.00 (s, 3H), 1.88 – 1.75 (m, 4H), 1.46 – 1.21 (m, 7H). ^{13}C NMR (126 MHz, CDCl_3): δ_{C} 161.0, 143.2, 140.5, 138.0, 135.3, 129.6, 122.5, 115.3, 112.4, 108.8, 93.4, 55.8, 44.8, 33.4, 30.0, 29.8, 26.1, 23.2, 14.2. Isolated yield: 78%

Compound 11: 9-benzyl-7-methoxy-9H-pyrido[3,4-b]indole

^1H NMR (500 MHz, CDCl_3): δ_{H} 8.31 (d, $J = 5.3$ Hz, 1H), 8.03 (d, $J = 8.6$ Hz, 1H), 7.81 (d, $J = 5.3$ Hz, 1H), 7.28 (dd, $J = 13.2, 5.7$ Hz, 3H), 7.00 (d, $J = 6.5$ Hz, 2H), 6.92 (dd, $J = 8.7, 2.1$ Hz, 1H), 6.77 (d, $J = 2.3$ Hz, 1H), 5.73 (s, 2H), 2.86 (s, 3H). ^{13}C NMR (126 MHz, CDCl_3): δ_{C} 161.4, 143.9, 140.7, 137.9, 137.8, 135.7, 129.9, 129.1, 127.7, 125.5, 122.6, 115.1, 112.5, 109.7, 93.4, 55.7, 48.3, 22.5. Isolated yield: 69%

Compound 12: 7-methoxy-9-phenethyl-9H-pyrido[3,4-b]indole

^1H NMR (500 MHz, CDCl_3): δ_{H} 8.29 (s, 1H), 7.98 (d, $J = 8.6$ Hz, 2H), 7.76 (d, $J = 5.3$ Hz, 2H), 7.30 – 7.26 (m, 4H), 7.26 – 7.22 (m, 1H), 7.16 – 7.12 (m, 3H), 6.89 (dd, $J = 8.7, 2.2$ Hz, 1H), 6.74 (d, $J = 2.2$ Hz, 2H), 4.74 – 4.68 (t, 3H), 3.89 (s, 5H), 3.15 – 3.06 (t, 3H), 3.03 (s, 5H). ^{13}C NMR (126 MHz, CDCl_3): δ_{C} 161.0, 143.1, 140.5, 138.0, 135.3, 129.7, 128.8, 127.0, 122.5, 115.2, 112.48, 109.1, 93.4, 55.7, 46.6, 36.9, 23.2. Isolated yield: 70%

Compound 13: 7-methoxy-9-(3-phenylpropyl)-9H-pyrido[3,4-b]indole

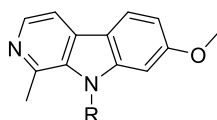
^1H NMR (500 MHz, CDCl_3): δ_{H} 8.27 (d, $J = 5.2$ Hz, 1H), 7.95 (d, $J = 8.6$ Hz, 1H), 7.72 (d, $J = 5.2$ Hz, 1H), 7.36 – 7.27 (m, 1H), 7.22 (dt, $J = 8.0, 1.8$ Hz, 2H), 6.86 (dd, $J = 8.6, 2.2$ Hz, 1H), 6.64 (d, $J = 2.1$ Hz, 1H), 4.50 – 4.38 (m, 2H), 3.85 (s, 3H), 2.90 (s, 3H), 2.77 (t, $J = 7.3$ Hz, 2H), 2.32 – 2.09 (m, 2H). ^{13}C NMR (126 MHz, CDCl_3): δ_{C} 160.9, 143.0, 140.7, 140.6, 138.2, 135.3, 129.5, 128.7, 128.4, 126.4, 122.4, 115.2, 112.3, 109.1, 93.0, 55.7, 44.1, 33.0, 31.8, 23.1. Isolated yield: 76%

Compound 14: 7-methoxy-9-(4-phenylbutyl)-9H-pyrido[3,4-b]indole

^1H NMR (500 MHz, CDCl_3): δ_{H} 8.27 (d, $J = 5.2$ Hz, 1H), 7.97 (d, $J = 8.5$ Hz, 1H), 7.73 (d, $J = 5.3$ Hz, 1H), 7.32 – 7.22 (m, 2H), 7.22 – 7.11 (m, 3H), 6.88 (dd, $J = 8.6, 2.2$ Hz, 1H), 6.81 (d, $J = 2.2$ Hz, 1H), 4.50 – 4.42 (m, 2H), 3.92 (s, 2H), 2.97 (s, 2H), 2.66 (t, $J = 7.5$ Hz, 2H), 1.93 – 1.79 (m, 4H), 1.76 (ddd, $J = 8.8, 6.5, 1.6$ Hz, 1H). ^{13}C NMR (126 MHz, CDCl_3): δ_{C} 160.9, 143.1, 141.6, 140.6, 138.2, 135.3, 129.4, 128.5, 128.4, 126.1, 122.4, 115.2, 112.3, 108.7, 93.4, 55.8, 44.8, 35.5, 30.1, 28.5, 23.4. Isolated yield: 71%

 α -Glucosidase inhibitory activity

As shown in **Table 1**, among alkyl derivatives of harmine (**1-7**), the inhibitory activity increased with the carbon chain length, it reached a maximum value at eight carbons, whereas the activity did not change even when the carbon chain reached twelve or sixteen. For compounds **8-9** with bromine at terminal, when the carbon chain increased from four to six the inhibition increased; however when the carbon chain increased up to eight in compound **10**, the activity dropped. Besides, compounds **11-14** containing the phenyl group at the terminal increased the activity, as the carbon chain increased. Compound **14** with a four-carbon chain showed effective inhibition at 50 μM with IC_{50} value of 12.2 μM . These results aligned with the prior investigation by Rita *et al.* for synthesized chrysin alkyl derivatives.⁸ With the increase in the carbon chain, the activity also increased. With six-carbon chain containing bromine at terminal, the inhibition achieved the highest inhibition at 96.22%. **Table 1** indicates that varying carbon chain lengths showed a clear trend in the inhibitory activity reaching an optimal point with an eight-carbon chain. This suggested the hydrophobic interaction between the enzyme and the alkyl chain. The introduction of bromine at the terminal position in compounds **8-10** further enhanced the activity of compound **9** with a six-carbon chain and bromine at the terminal position significantly increased the activity indicating that bromine, being a heavier and more electronegative atom increased the interaction of the compound with the active sites. The addition of the phenyl at the terminal position in compounds **11-14** could also further increase the activity in which compound **14** showed better activity due to the ability of the phenyl group to engage in π - π interactions with the enzyme.



- | | |
|--|---|
| (1) R = CH ₃ | (8) R = CH ₂ (CH ₂) ₂ CH ₂ Br |
| (2) R = CH ₂ CH ₃ | (9) R = CH ₂ (CH ₂) ₄ CH ₂ Br |
| (3) R = CH ₂ (CH ₂) ₂ CH ₃ | (10) R = CH ₂ (CH ₂) ₆ CH ₂ Br |
| (4) R = CH ₂ (CH ₂) ₄ CH ₃ | (11) R = CH ₂ Ph |
| (5) R = CH ₂ (CH ₂) ₆ CH ₃ | (12) R = CH ₂ CH ₂ Ph |
| (6) R = CH ₂ (CH ₂) ₁₀ CH ₃ | (13) R = CH ₂ CH ₂ CH ₂ Ph |
| (7) R = CH ₂ (CH ₂) ₁₄ CH ₃ | (14) R = CH ₂ (CH ₂) ₂ CH ₂ Ph |

Table 1 α -Glucosidase inhibitory activity of alkyl derivatives of harmine.

| Compound | % inhibition at 50 μ M | IC ₅₀ ^a |
|----------|----------------------------|-------------------------------|
| 1 | 0 | – ^b |
| 2 | 0 | – |
| 3 | 0 | – |
| 4 | 49.76 | – |
| 5 | 60.00 | – |
| 6 | 62.05 | – |
| 7 | 60.80 | – |
| 8 | 44.29 | – |
| 9 | 96.22 | 13.78 \pm 0.87 |
| 10 | 70.14 | – |
| 11 | 0 | – |
| 12 | 0 | – |
| 13 | 63.30 | – |
| 14 | 98.34 | 12.20 \pm 1.12 |
| Harmine | 0 | – |
| Acarbose | | 817.38 \pm 6.3 |

^aIC₅₀ value was expressed as mean \pm SD from three independent experiments.

^bIC₅₀ value was not tested if the inhibition rate was less than 50% at 50 μ M.

Kinetic Analysis of α -Glucosidase Inhibition by Harmine Derivatives

Compounds **9** and **14** were explored for their mode of action in inhibiting α -glucosidase through kinetic analysis. The type of inhibition was determined using Lineweaver-Burk plots, as shown in **Figure 1**. The resulting plots for 1/V vs 1/[S] resulted in a group of straight lines that intersected the vertical axis. In addition, competitive inhibition was indicated by the constant V_{\max} and increased K_m for **9** and **14**. This demonstrated that all compounds could bind to the active site of α -glucosidase. The equilibrium constants (K_i) for both inhibitors were 27.65 and 34.37 μ M, respectively.

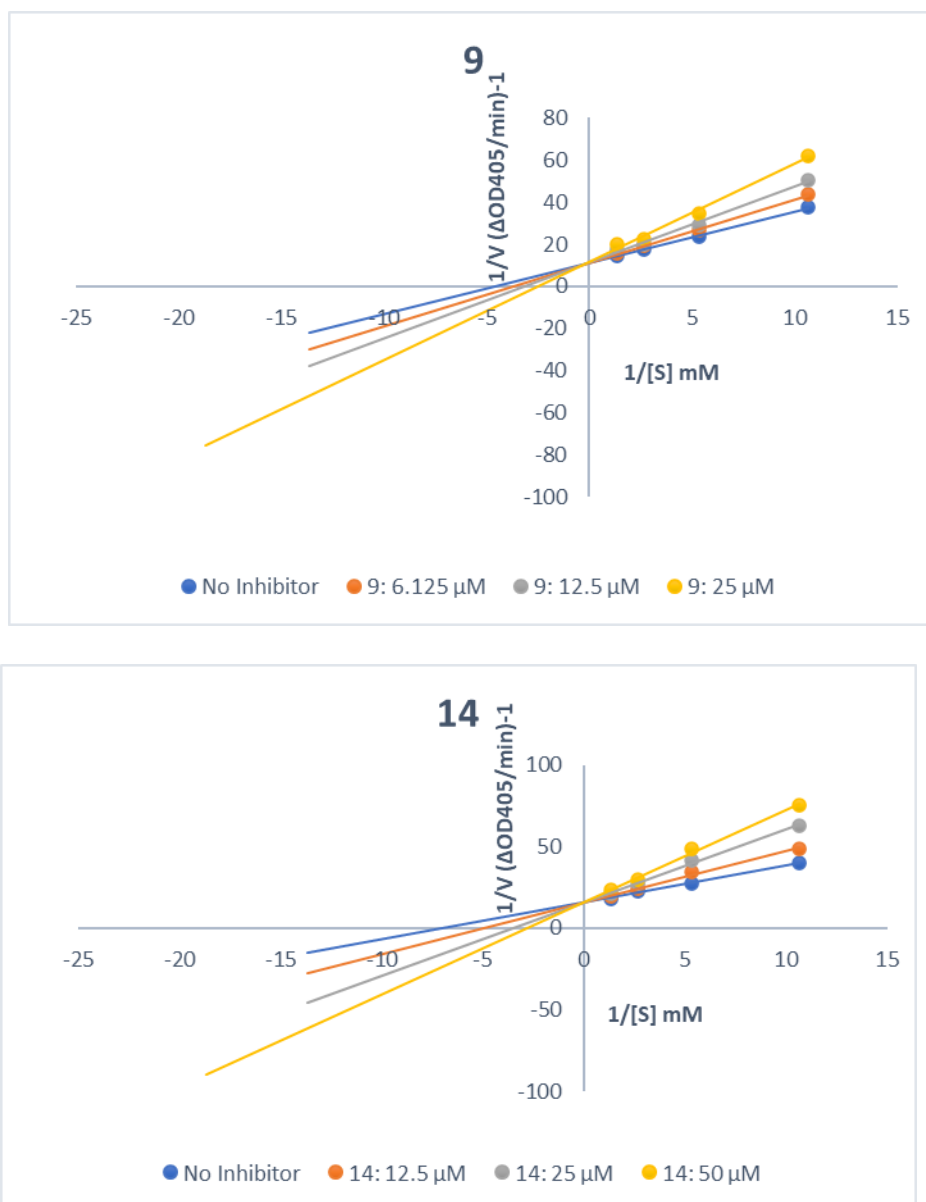


Figure 1 Double reciprocal plot of inhibition kinetics of yeast α -glucosidase by compounds **9** and **14**

Conclusion:

Fourteen harmine derivatives were successfully synthesized, characterized, and evaluated for α -glucosidase inhibitory activity. Increasing the carbon chain effectively increased the inhibitory activity. Compounds **9** and **14** were good α -glucosidase inhibitors with IC_{50} values of 13.8 and 12.2 μ M, respectively, which were better than inactive harmine. The kinetic study revealed that both compounds were competitive inhibitors.

Acknowledgements:

Fayaz A. is grateful thank to Chulalongkorn University's Asian non-Asian scholarship.



References:

- (1) Tanwar, A. Case Study: A Patient with Uncontrolled Type 2 Diabetes and Carbuncle in Thigh Whose Diabetes is Managed by Ayurvedic Intervention. *Research & Reviews: Journal of Herbal Science*. 2021; 10 (3): 8–13p. *A Patient with Uncontrolled Type 2*, 2.
- (2) Limpanit, R.; Chuanasa, T.; Likhitwitayawuid, K.; Jongbunprasert, V.; Sritularak, B. α -Glucosidase inhibitors from *Dendrobium tortile*. *Records of Natural Products* **2016**, 10 (5), 609.
- (3) Scheen, A. J. Is there a role for α -glucosidase inhibitors in the prevention of type 2 diabetes mellitus? *Drugs* **2003**, 63, 933-951.
- (4) Abbas, M. W.; Hussain, M.; Qamar, M.; Ali, S.; Shafiq, Z.; Wilairatana, P.; Mubarak, M. S. Antioxidant and anti-inflammatory effects of *Peganum harmala* extracts: An in vitro and in vivo study. *Molecules* **2021**, 26 (19), 6084.
- (5) Toghyani, M.; Ghasemi, A.; Tabeidian, S. The effect of different levels of seed and extract of harmal (*Peganum harmala* L.) on immune responses of broiler chicks. *International Journal of Animal and Veterinary Sciences* **2015**, 9 (1), 51-54.
- (6) Du, H.; Tian, S.; Chen, J.; Gu, H.; Li, N.; Wang, J. Synthesis and biological evaluation of N9-substituted harmine derivatives as potential anticancer agents. *Bioorganic & Medicinal Chemistry Letters* **2016**, 26 (16), 4015-4019.
- (7) Ramadhan, R.; Phuwapraisirisan, P. New arylalkanones from *Horsfieldia macrobotrys*, effective antidiabetic agents concomitantly inhibiting α -glucosidase and free radicals. *Bioorganic & medicinal chemistry letters* **2015**, 25 (20), 4529-4533.
- (8) Hairani, R.; Chavasiri, W. A new series of chrysin derivatives as potent non-saccharide α -glucosidase inhibitors. *Fitoterapia* **2022**, 163, 105301.



FACILE EXTRACTION AND ANTIBACTERIAL EVALUATION OF ALKALOIDS FROM THAI RED VEIN KRATOM (*Mitragyna speciosa* Korth) FOR POTENTIAL COSMETIC AND MEDICINAL APPLICATIONS

Ananya Panchuchird, Muhammad Niyomdechcha, Pornthip Tongying*

Department of Chemistry, Faculty of Science, Silpakorn University, Sanam Chandra Palace Campus, Nakhon Pathom 73000, Thailand

*e-mail: tongying_p@su.ac.th

Abstract:

Kratom (*Mitragyna speciosa* Korth) has been traditionally used in Thailand for its therapeutic benefits, largely attributed to its alkaloid-rich profile. Thai red vein kratom is particularly notable for its high concentrations of mitragynine (up to 66%) and 7-hydroxymitragynine (up to 2%), which are linked to its wound-healing and pain-relieving effects. This study aimed to develop an efficient extraction method to produce a cleaner crude extract and evaluate its antibacterial properties. A facile extraction process was employed, involving maceration with an ethanolic solution (25% ethanol: distilled water: 10% citric acid), followed by dichloromethane extraction and column chromatography purification. This method resulted in a purified extract containing 68.87% mitragynine, 10.40% paynantheine, 4.60% speciogynine, and a negligible amount of 7-hydroxymitragynine. Antibacterial testing of the crude extract and purified mitragynine was conducted using disk diffusion against *Escherichia coli* (Gram-negative), *Staphylococcus aureus*, and *Staphylococcus epidermidis* (Gram-positive). Mitragynine demonstrated significant antibacterial activity with inhibition indices of 1.03 ± 0.01 , 1.08 ± 0.01 , and 1.22 ± 0.02 at 10 mg/mL, respectively. In contrast, the crude extract was effective only against Gram-positive bacteria, with inhibition indices of 1.28 ± 0.03 and 1.39 ± 0.02 . This study underscores the effectiveness of the facile extraction method for obtaining mitragynine and highlights its potential as an antibacterial agent.

Introduction:

Sustainable and green chemistry is increasingly vital in chemical processes, including extraction techniques, to minimize environmental and health risks. Traditional organic solvent extraction has long been used to isolate bioactive compounds but poses significant environmental and health hazards due to the toxic solvents involved.

Kratom, native to Southeast Asia, particularly Thailand, is known for its rich alkaloid content, especially in the red vein variety.¹ Thai red vein kratom in **Figure 1** is particularly valued for its high mitragynine content, which contributes to its stimulating and therapeutic properties.² The pharmacokinetics of kratom have attracted significant interest,³ leading to studies on the isolation of over 25 alkaloids, with a focus on mitragynine and its major analogs, such as paynantheine, speciogynine, speciociliatine, corynantheidine, and 7-hydroxymitragynine in **Figure 2**.⁴

However, excessive consumption and inadequate processing of kratom can lead to adverse effects,⁵ underscoring the need for safer and more sustainable extraction methods.⁶⁻⁹ For instance, Sharma *et al.* employed an ethanolic extraction method combining ethanol and hydrochloric acid to effectively isolate key kratom alkaloids with minimal harmful solvent usage.¹⁰ Similarly, Yong *et al.* demonstrated that accelerated solvent extraction (ASE) with ethanol is a more efficient, safer, and cost-effective method, yielding high mitragynine content.¹¹

Recent studies have also explored the antibacterial properties of kratom extracts.^{2, 8, 11-13} Niyomdechcha *et al.* tested crude extracts from ethanolic extraction of Thai red vein kratom against *Staphylococcus aureus* and *Escherichia coli*, showing promising antibacterial activity.² Paankhao *et al.* found that ethanolic extracts of kratom could serve as an alternative to antibiotics for managing bacterial infections in fish.¹²

In this study, we employ a green solvent system using citric acid and ethanol for the maceration process to extract mitragynine from kratom leaves. Citric acid, a weak organic acid found in citrus fruits, is chosen for its biodegradability, non-toxicity, and cost-effectiveness. It enhances extraction by breaking down cell walls and creating an acidic environment that improves alkaloid solubility and stability.¹⁴ Ethanol, known for its low toxicity and environmental safety, dissolves both free and salt alkaloids while reducing the extraction of water-soluble impurities such as polysaccharides and proteins. This approach maximizes extraction efficiency and selectivity for mitragynine. Additionally, the study evaluates the antibacterial activity of these extracts against bacteria associated with skin diseases.



Figure 1.
Red vein kratom leaves from Thailand.

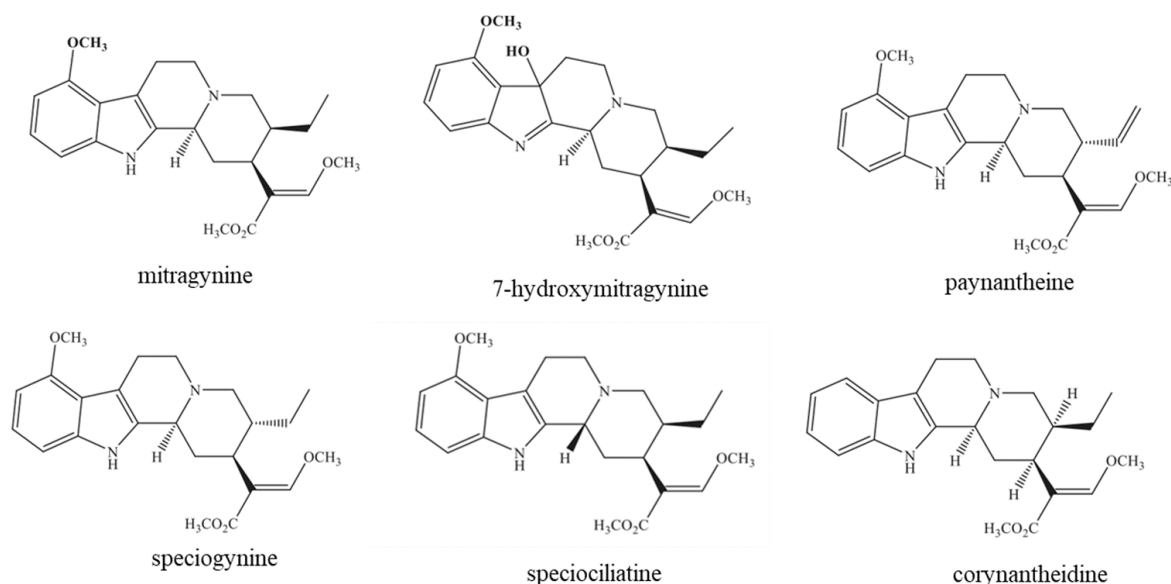


Figure 2.
Chemical structures of mitragynine and its analogs most commonly found in red vein kratom leaves.

Methodology:

Experimental materials

Dichloromethane, ethanol, and citric acid were purchased from Lab-Scan (Bangkok, Thailand). Hexane, ethyl acetate, and anhydrous sodium sulfate were purchased from Sigma-Aldrich (Saint Louis, USA). Acetone and sodium bicarbonate were purchased from Merck (Darmstadt, Germany). All solvents were purified by distillation before use. Analytical thin-layer chromatography (TLC) was performed using TLC plates from Merck (silica gel 60 F254 on an aluminum sheet). Solvents were evaporated using a rotary evaporator (Buchi Rotavapor R-114). UV-Vis spectra were recorded using a PerkinElmer Lambda 35 UV/Vis spectrophotometer. Proton (^1H) and carbon (^{13}C) nuclear magnetic resonance (NMR) spectra were recorded using a Bruker Avance-300 spectrometer.

Extraction of crude extracts and mitragynine analogs from red vein kratom leaves

The dried red vein kratom leaves from Ratchaburi province, Thailand, were weighed to approximately 100 g and extracted using the maceration method in **Figure 3** with 500 mL of a 10% w/v citric acid dissolved in 25% ethanol at room temperature for one week. The mixture was then filtered, retaining only the solution, which was divided into two fractions: one with adjusted pH and one with unadjusted pH. These fractions were compared for purity and color. Subsequently, the first fraction was made alkaline by adding a saturated sodium bicarbonate solution until the pH reached 8. The two resulting solutions were then placed into a separatory funnel and extracted with dichloromethane at least three times. The mixtures were allowed to separate, and only the organic phases were collected and dried using a rotary evaporator. The crude extracts and mitragynine constituents (four major groups of *Mitragyna speciosa* Korth) were analyzed using thin-layer chromatography (TLC). The R_f (retardation factor) values were calculated and compared with a standard mitragynine sample under UV light at 254 nm. Finally, the dried red vein kratom crude extracts were stored as a solid at room temperature. The yield of the crude extract was calculated as follows:

$$\% \text{ Yield of crude extract } (\% \text{ Yield}_{\text{C.E.}}) = (\text{mass of the extract} / \text{mass of the dried leaves}) \times 100$$

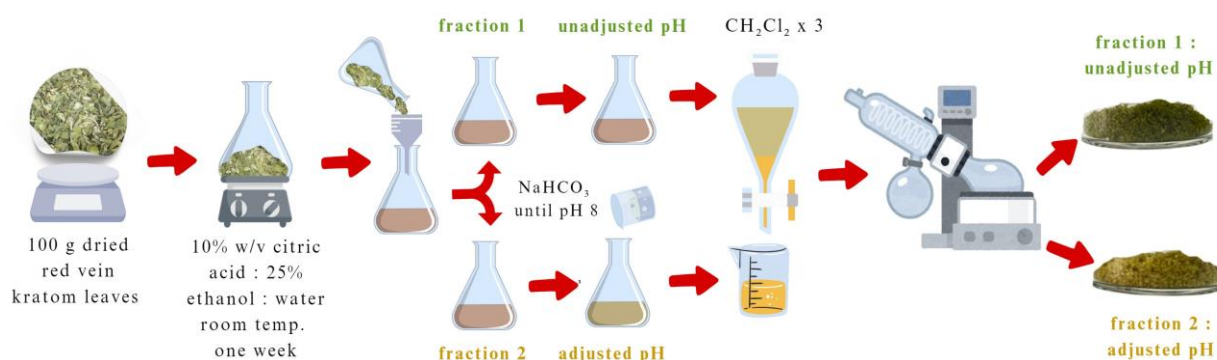


Figure 3.

Schematic: extraction of crude extracts and mitragynine analogs from red vein kratom leaves.

Purification and characterization of the crude extract and mitragynine analogs

The crude extract, in which the pH was adjusted to 8, was purified by column chromatography using silica gel 60 as the stationary phase. The mobile phase for TLC was

used to determine the R_f value of mitragynine, which was found to be 0.61 (eluted with *n*-hexane: ethyl acetate (1:1)). In the column chromatography system, the mobile phase was *n*-hexane: ethyl acetate (4:1), and the elution continued until 100 fractions were collected, with preliminary monitoring performed using TLC. Selected fractions were analyzed using UV-Vis spectrophotometry, ^1H -NMR, and ^{13}C -NMR, and compared with reference data.^{4, 15} The yield after purification was calculated as follows:

$$\% \text{Yield after purification (\% Yield}_p) = (\text{mass of the pure compound} / \text{mass of the crude extract}) \times 100$$

Antibacterial activity test

The antibacterial activity of the crude extracts was evaluated using the disc diffusion method, adapted from the Manual of Antimicrobial Susceptibility Testing (NCCLS). The test was conducted on one Gram-negative bacterium, *Escherichia coli* (TISTR 073), and two Gram-positive bacteria, *Staphylococcus aureus* (ATCC 6538) and *Staphylococcus epidermidis* (TISTR 518). Crude extracts from red vein kratom leaves and mitragynine were prepared by creating 6 mm diameter discs from Whatman No. 1 filter paper, which were sterilized before use. The crude extract and mitragynine were dissolved in a 6:4 ethanol-to-deionized water solution to achieve a concentration of 10 mg/mL. A 15 μL aliquot of this solution was placed on each disc and allowed to dry. Using a sterile cotton swab, the test pathogen culture was spread evenly over the surface of an agar plate. The prepared discs were then placed onto the inoculated agar plates using sterile forceps, ensuring they were positioned away from the edges of the Petri dish. The plates were incubated at 37 °C for 24 hours. After incubation, the diameter of the inhibition zones around each disc was measured, and the Inhibition Index was calculated (an Inhibition Index greater than 1 indicates effective antibacterial activity). Chloramphenicol and tetracycline, prepared at the same concentration as the samples, served as the controls. Each experiment was performed in triplicate, and the standard deviation was calculated.

Results and Discussion:

Crude extract yield

Crude extracts from dried red vein kratom leaves were obtained under non-pH-adjusted (acidic, pH ~4) and pH-adjusted (pH = 8) conditions and analyzed using TLC with a 1:1 ethyl acetate to *n*-hexane mobile phase. TLC analysis revealed four distinct compounds and a noticeable color difference between the pH-adjusted and non-pH-adjusted extracts. This difference is attributed to the pH adjustment, which alters the chemical forms of the compounds. At pH 8, the compounds are converted from their salt forms (present in the non-pH-adjusted extract) to their free base forms (in the pH-adjusted extract). The use of a 10% citric acid solution in 25% ethanol effectively preserves mitragynine by optimizing the solution's acidity and polarity, resulting in a distinct color, as shown in **Figure 4**. TLC analysis confirmed that both extracts exhibited comparable R_f values, as detailed in **Table 1**. Additionally, ^1H NMR (300 MHz, CDCl_3) analysis showed that the spectra of both extracts were similar, as shown in **Figure 5**. Column chromatography was employed for further purification, and based on these observations, the pH-adjusted extract was selected for continued refinement.

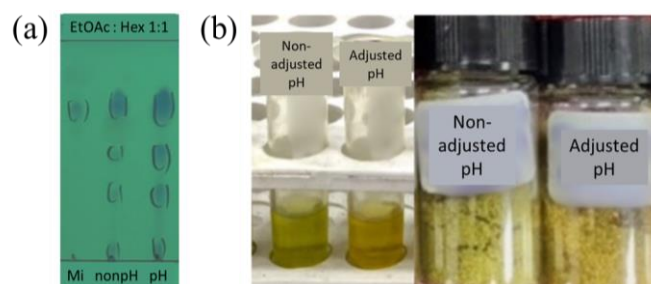


Figure 4.

(a) TLC of the crude extract from red vein kratom leaves (Mi = mitragynine; nonpH = non-adjusted pH; pH = pH-adjusted), and (b) the noticeable difference in color between the non-adjusted pH and pH-adjusted crude extracts.

Table 1. R_f values and %yield of the crude extract for pH-adjusted and non-pH-adjusted crude extracts.

| Crude extract | R_f values | Crude extract (g) | %Yield _{C.E.} |
|-----------------|------------------------|-------------------|------------------------|
| non-adjusted pH | 0.61, 0.43, 0.27, 0.03 | 1.35 | 1.4 |
| adjusted pH | 0.60, 0.42, 0.27, 0.03 | 1.56 | 1.6 |

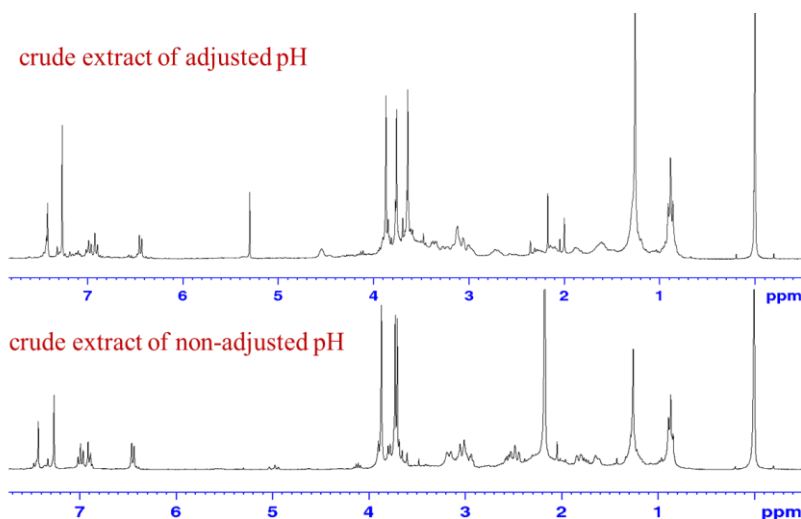


Figure 5.

^1H NMR spectra (CDCl_3 , 300 MHz) of crude extracts for pH-adjusted and non-pH-adjusted conditions.

Purification and characterization of the crude extract and mitragynine analogs

The crude extract under the pH-adjusted condition was selected for purification using column chromatography due to its higher yield, which is likely indicative of a higher mitragynine content. The system was eluted with a mixture of *n*-hexane and ethyl acetate (4:1), based on TLC results, ^1H NMR spectra, and %Yield_{C.E.}. This process successfully separated four compounds in the crude extract, as observed in TLC. After purification, each fraction yielded: 68.87% (1.0744 g) mitragynine (1); 10.40% (162.3 mg) paynantheine (2); 4.60% (71.7 mg) speciogynine (3); and a negligible amount of 7-hydroxymitragynine (4) in the last fraction, as shown in **Figure 6**. The structures of these compounds were identified by comparing them with reference data using NMR spectroscopy.^{4, 15} Although characteristic peaks were present, some fractions were not completely pure, as illustrated in **Figure 7**. Each fraction exhibited key signal characteristics for structure elucidation. The results indicated that the ^1H and ^{13}C NMR data for the four compounds matched previously reported data.⁴

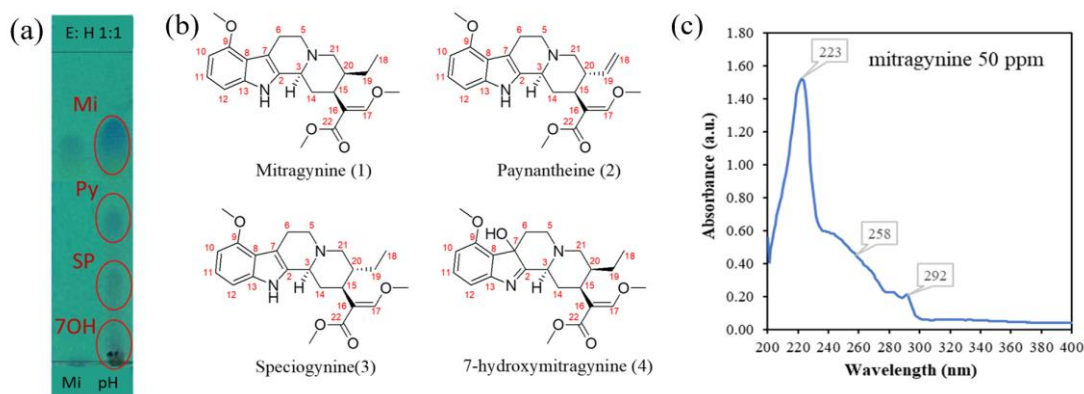


Figure 6.

(a) TLC of the four separated compounds in the crude extract (Mi = mitragynine (1), Py = paynantheine (2), SP = speciogynine (3), and 7OH = 7-hydroxymitragynine (4)); (b) the chemical structure of each compound in the crude extract; and (c) UV-Vis absorption spectrum of mitragynine (1) in a 6:4 (ethanol: D.I. water) solution.

Compound (1) was obtained as a yellow powder. The UV-Vis absorption spectrum of compound (1) exhibited characteristic peaks (λ_{\max}) at 223 nm and 292 nm in **Figure 6c**, which were similar to those found in pure mitragynine.^{2, 16} ^1H NMR (300 MHz, CDCl_3): δ (ppm) = 0.85 (t, J = 7.2 Hz, 3H, 18- CH_3), 1.12-1.18 (m, 1H), 1.62 (br-d, J = 10.1 Hz, 1H), 1.69-1.75 (m, 2H), 2.36-2.53 (m, 3H), 2.86-3.16 (m, 5H), 3.64 (s, 3H, 9- OCH_3), 3.68 (s, 3H, 17- OCH_3), 3.82 (s, 3H, 22- OCH_3), 6.41 (d, J = 7.9 Hz, 1H, 10-ArCH), 6.85 (d, J = 7.9 Hz, 1H, 12-ArCH), 6.96 (t, J = 7.8 Hz, 1H, 11-ArCH), 7.40 (s, 1H, 17-CH), 8.14 (s, 1H, 1-NH); ^{13}C NMR (75 MHz, CDCl_3): δ (ppm) = 12.8, 19.1, 24.0, 29.6, 40.0, 40.7, 51.3, 53.7, 55.2, 57.7, 61.4, 61.5, 99.6, 104.5, 107.4, 111.4, 117.5, 121.5, 133.8, 137.4, 154.4, 160.7, 169.4. Comparing with previously reported data,⁴ compound (1) was assigned as mitragynine.

Compound (2) was obtained as an orange-yellow powder. ^1H NMR (300 MHz, CDCl_3): δ (ppm) = 1.97 (dt, J = 12.1, 3.4 Hz, 1H), 2.13 (br-q, J = 12.2 Hz, 1H), 2.31 (t, J = 11.7 Hz, 1H), 2.63 (td, J = 11.7, 4.4 Hz, 1H), 2.77 (td, J = 11.7, 3.8 Hz, 1H), 2.88-3.05 (m, 4H), 3.10-3.19 (m, 1H), 3.35 (br-d, J = 10.2 Hz, 1H, 3-CH), 3.69 (s, 3H, 9- OCH_3), 3.78 (s, 3H, 17- OCH_3), 3.87 (s, 3H, 22- OCH_3), 4.97 (dd, J = 10.5, 2.0 Hz, 1H, 18- $\text{C}=\text{H}_{\text{cis}}$), 5.03 (dd, J = 18.6, 1.3 Hz, 1H, 18- $\text{C}=\text{H}_{\text{trans}}$), 5.56 (ddd, J = 17.9, 10.2, 1.8 Hz, 1H, 19- $\text{C}=\text{H}$), 6.46 (d, J = 7.7 Hz, 1H, 10-ArCH), 6.88 (d, J = 7.7 Hz, 1H, 12-ArCH), 7.00 (t, J = 7.9 Hz, 1H, 11-ArCH), 7.33 (s, 1H, 17-CH), 7.80 (s, 1H, 1-NH); ^{13}C NMR (75 MHz, CDCl_3): δ (ppm) = 23.6, 33.3, 38.5, 42.5, 51.3, 53.0, 55.3, 59.9, 61.2, 61.6, 99.8, 104.3, 107.8, 111.5, 115.6, 117.5, 122.1, 132.4, 137.4, 139.2, 154.5, 159.9, 169.0. The NMR spectra of compound (2) were similar to those of compound (1), except for the main difference: the absence of signals for the C19 ethyl moiety, which was replaced by a vinylic moiety at C19 and C18. This was consistent with the presence of a double bond, as indicated by two doublets of doublets (δ_{H} 4.97-5.03) and a doublet of doublet of doublets resembling a pentet (δ_{H} 5.44-5.66). Therefore, compound (2) was identified as paynantheine based on the spectra, the number of protons and carbons, and the R_f value, despite the presence of some impurity peaks.

Compound (3) was obtained as a pale-yellow powder. ^1H NMR (300 MHz, CDCl_3): δ (ppm) = 0.86 (m, 3H), 1.05 (m, 1H), 1.46 (m, 1H), 1.93-1.98 (m, 2H), 2.10 (td, J = 10.7, 1.1 Hz, 1H), 2.25-2.30 (m, 2H), 2.63 (td, J = 11.6, 3.9 Hz, 2H), 3.02 (br-d, J = 15.5 Hz, 1H), 3.09-3.28 (m, 3H), 3.57-3.82 (m, 6H, 9,17- OCH_3), 3.88 (s, 3H, 22- OCH_3), 6.45 (d, J = 7.5 Hz, 1H, 10-ArCH), 6.88 (d, J = 7.9 Hz, 1H, 12-ArCH), 7.00 (t, J = 7.8 Hz, 1H, 11-ArCH), 7.26

(s, 1H, 17-CH), 7.37 (s, 1H, 1-NH); ^{13}C NMR (75 MHz, CDCl_3): δ (ppm) = 11.2, 19.3, 22.7, 23.5, 24.3, 25.2, 26.5, 27.0, 27.9, 29.7, 30.6, 31.9, 33.7, 35.9, 38.0, 39.9, 45.6, 47.3, 51.4, 53.2, 55.3, 60.4, 61.7, 66.8, 99.8, 104.3, 107.7, 111.6, 112.9, 117.5, 122.0, 132.7, 137.4, 154.5, 160.0. The ^1H NMR spectrum resembled those of compound (1), but the two methoxy groups appeared as broad singlet peaks (δ_{H} 3.57-3.82) instead of two distinct singlet peaks. The analysis indicated an excessive amount of carbon, suggesting that the isolated substance is not entirely pure. Nevertheless, its structure can still be determined by comparing its spectral characteristics, which confirm that it is speciogynine (3).

Compound (4) was obtained as a yellow powder. ^1H NMR (300 MHz, CDCl_3): δ (ppm) = 0.85-0.91 (m, 3H), 1.10-1.58 (m, 1H), 1.61-1.71 (m, 7H), 1.87 (d, J = 13.1 Hz, 1H), 2.21-2.33 (m, 1H), 2.49 (d, J = 11.7 Hz, 1H), 2.64 (d, J = 12.1 Hz, 3H), 2.81 (t, J = 13.1 Hz, 3H), 3.03 (d, J = 11.8 Hz, 2H), 3.14 (d, J = 10.5 Hz, 1H), 3.67 (s, 3H, 9- OCH_3), 3.78 (s, 3H, 17- OCH_3), 3.85 (s, 3H, 22- OCH_3), 6.71 (d, J = 7.7 Hz, 1H, 10-ArCH), 7.18 (d, J = 7.5 Hz, 1H, 12-ArCH), 7.72 (t, J = 7.2 Hz, 1H, 11-ArCH), 7.43 (s, 1H, 17-CH); ^{13}C NMR (75 MHz, CDCl_3): δ (ppm) = 12.8, 14.0, 19.0, 22.7, 26.1, 29.7, 31.9, 35.7, 38.7, 40.5, 50.1, 51.2, 55.4, 58.1, 61.4, 61.7, 81.0, 109.0, 111.3, 114.1, 126.6, 128.8, 130.7, 154.9, 156.0, 169.3, 184.5. The ^1H NMR spectrum of the isolated compound (4) was not entirely pure, but its structure and the number of protons and carbons can still be determined by comparison with reference data.¹⁵ The downfield shifts observed in δ_{H} and δ_{C} are attributed to the hydroxyl group at C7, suggesting that the compound is 7-hydroxymitragynine.

Antibacterial activity test

The antibacterial activity of pH-adjusted crude extract and mitragynine (1) in a 6:4 (ethanol: D.I. water) solution was evaluated against *Escherichia coli*, *Staphylococcus aureus*, and *Staphylococcus epidermidis* at a concentration of 10 mg/mL using the disc diffusion method. The results indicate that the pH-adjusted crude extract from red vein kratom leaves was effective only against the Gram-positive bacteria (*S. aureus* and *S. epidermidis*), while mitragynine (1) was effective against all tested bacteria. The mitragynine content in the crude extract likely did not reach the effective concentration of 10 mg/mL, which may account for its ineffectiveness against *E. coli*. This is consistent with findings by Chuekwon *et al.*, where kratom leaf ethanol extracts required a concentration of 200 mg/mL to inhibit Gram-negative bacteria—20 times higher than the concentration used in this study.¹⁷ These results indicate that mitragynine concentration is crucial for activity against *E. coli*, and the mitragynine content in this study's crude extract at 10 mg/mL was insufficient. The antibacterial activity results are summarized in **Table 2**.

Table 2. Inhibition index from the agar disc diffusion method for crude extract and mitragynine at a concentration of 10 mg/mL.

| Bacteria for testing | | Inhibition Index | |
|-----------------------------------|-----------|-------------------|-------------------|
| | | No.1 ^a | No.2 ^b |
| <i>Escherichia coli</i> | TISTR 073 | NA ^c | 1.03±0.01 |
| <i>Staphylococcus aureus</i> | ATCC 6538 | 1.28±0.03 | 1.08±0.01 |
| <i>Staphylococcus epidermidis</i> | TISTR 518 | 1.39±0.02 | 1.22±0.02 |

^aNo.1 is 10 mg/mL of the adjusted pH crude extract in 6:4 (ethanol: D.I. water).

^bNo.2 is 10 mg/mL of the mitragynine in 6:4 (ethanol: D.I. water).

^cNA means No Activity.

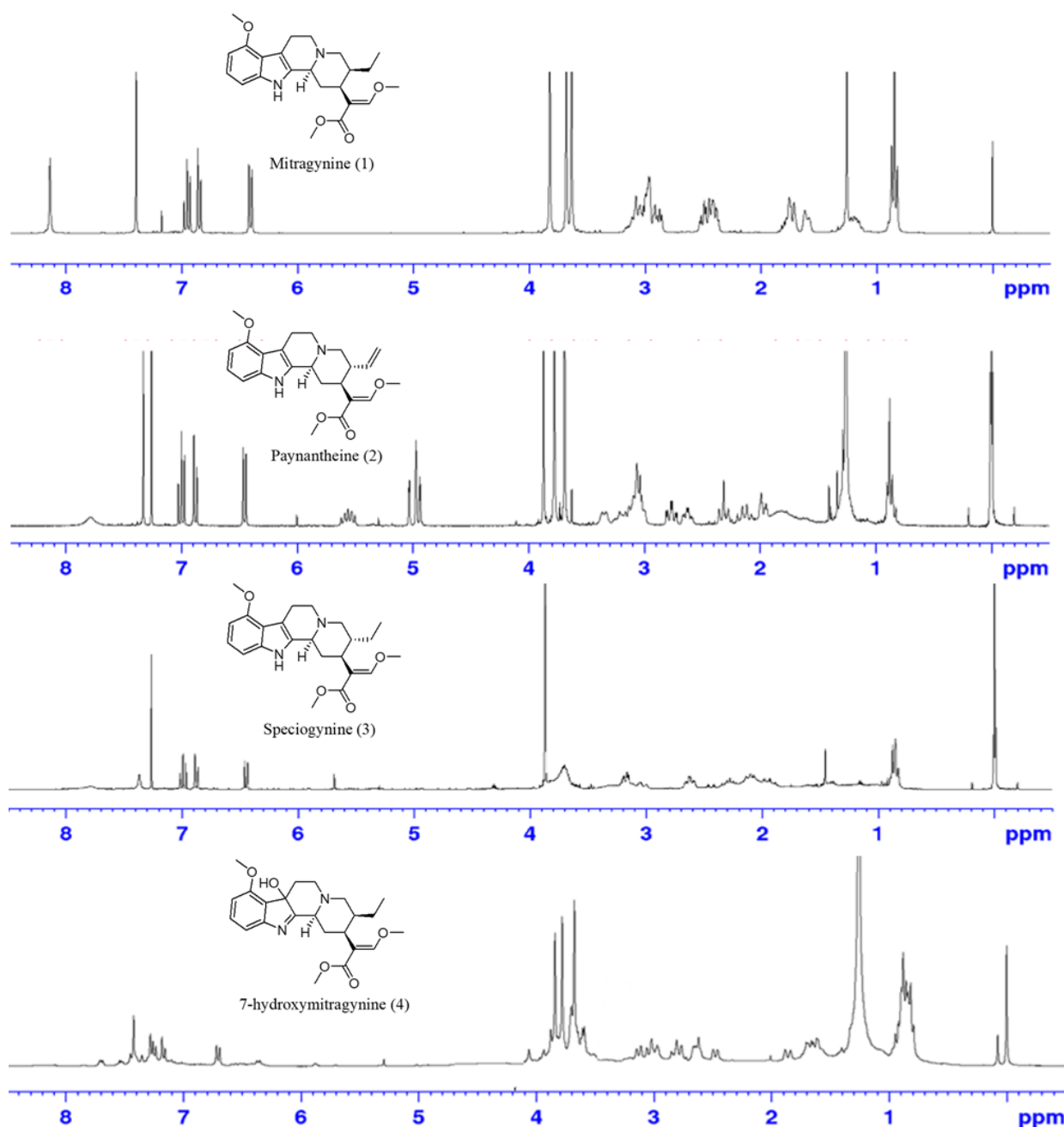


Figure 7.

^1H NMR spectra of the four compounds in the crude extract.

Conclusion:

Conventional extraction methods using organic solvents have long been established and are supported by decades of scientific data. However, as the field advances, greener methods that minimize the use of harmful solvents for more sustainable processes are expected to replace traditional techniques. In this research, we successfully developed a safe, clean, and effective method for the facile extraction of four major indole alkaloids—mitragynine (1), paynantheine (2), speciogynine (3), and 7-hydroxymitragynine (4)—from red vein kratom leaves. The process involved an ethanolic extraction with 10% citric acid using maceration, which effectively separated these compounds. The structures of the compounds in the crude extract were confirmed through NMR spectroscopy, and compared with reference spectra following column chromatography. The antibacterial activity tests revealed that the crude extract at a concentration of 10 mg/mL was effective against only

Gram-positive bacteria (*S. aureus* and *S. epidermidis*), while mitragynine at the same concentration was active against all evaluated bacteria, including *E. coli*. The kratom extraction method presented in this study is a significant step toward developing safe cosmetic and medicinal applications from natural sources, owing to its antibacterial properties and other therapeutic benefits.

Acknowledgements:

The author would like to express gratitude to the Innovation and Creativity Research Fund (grant number SRIF-JRG-2567-14) provided by the Faculty of Science, Silpakorn University, and to the Development and Promotion of Science and Technology Talents Project (DPST) for the graduate scholarship grant.

References:

1. Sengnon N, Vonghirundecha P, Chaichan W, Juengwatanatrakul T, Onthong J, Kitprasong P, Sriwiriyan S, Chittrakarn S, Limsuwanchote S, Wungsintaweekul J. *Plants* (Basel). 2023;12(4):949.
2. Niyomdecha M, Muandao K, Sanongkiet S, Jaramornburapong C. *SEHS*. 2024;18:24030002.
3. Pohanka M. *Bratisl Med J*. 2023;124(12):896-902.
4. Flores-Bocanegra L, Raja H, Graf T, Augustinovic M, Wallace E, Hematian S, Kellogg J, Todd D, Cech N, Oberlies N. *J. Nat. Prod.* 2020;83(7):2165-2177.
5. Hassan Z, Muzaimi M, Navaratnam V, Yusoff NHM, Suhaimi FW, Vadivelu R, Vicknasingam BK, Amato D, von Hörsten S, Ismail NIW, Jayabalan N, Hazim AI, Mansor SM, Müller CP. *Neurosci. Biobehav. Rev.* 2013;37(2):138-151.
6. Khamooshi F, Akinawo AS, Doraji-Bonjar S, Modarresi-Alam AR. *Chem. Afr.* 2024;7(5):2907-2920.
7. Kumar R, Methven L, Oruna-Concha MJ. *Molecules*. 2023;28(17):6405.
8. Herman H, Ibrahim A, Rahayu B, Arifuddin M, Nur Y, Prabowo W, M M, Ambarwati N, Rijai L, Ahmad I. *Phcog J*. 2021;13:1109-1115.
9. Ji Y, Yu M, Ang B, Zhang Y. *JOCPR*. 2014;6:338-345.
10. Sharma A, Kamble SH, León F, Chear NJ, King TI, Berthold EC, Ramanathan S, McCurdy CR, Avery BA. *DTA*. 2019;11(8):1162-1171.
11. Goh YS, Karunakaran T, Murugaiyah V, Santhanam R, Abu Bakar MH, Ramanathan S. *Molecules*. 2021;26(12):3704.
12. Paankhao N, Sangsawang A, Kantha P, Paankhao S, Promsee K, Soontara C, Kongsriprapan S, Srisapoome P, Kumwa B, Meachasompop P, Phrompanya P, Buncharoe W, Uchuwittayakul A. *ISFSI*. 2024;152:109771.
13. Ditthapornset S, Lerkkasemsan N, Areerat S. *ETH*. 2023;40:72-84.
14. Halee A. *JMBFS*. 2018;8:765-769.
15. Sakamoto J, Kitajima M, Ishikawa H. *Chem. Pharm. Bull.* 2022;70(9):662-668.
16. Casey C, Conley T, Heise A, Thomas T, Ayres P. *JRS*. 2015;3:1-14.
17. Chuekwon K, Choopeng P, Boonwong N. *NUJST*. 2024;21:e0210102.



PHYTOCHEMICAL CONSTITUENTS FROM THE STEMS OF *Tiliacora triandra*
 Phitchudaphorn Chulaphon, Waraluck Chaichompoo, Wachirachai Pabuprapap, Apichart Suksamrarn*

Department of Chemistry and Center of Excellence for Innovation in Chemistry, Faculty of Science, Ramkhamhaeng University, Bangkok 10240, Thailand

*e-mail: asuksamrarn@yahoo.com

Abstract:

A phytochemical investigation of the stems of *Tiliacora triandra* (Colebr.) Diels (Menispermaceae) led to the isolation of four bisbenzylisoquinoline alkaloids, including tiliacorinine (**1**), yanangcorinine (**2**), nortiliacorinine (**3**) and tiliacorinine (**4**). The structures of the isolated compounds were identified by spectroscopic data and by comparisons with those reported in the literature.

Introduction:

Tiliacora triandra (Colebr.) Diels, commonly known in Thai as Yanang, is a perennial climbing shrub belonging to the family Menispermaceae.¹ It is widely distributed in Southeast Asian countries, particularly in Thailand, Laos, Cambodia, and Vietnam.² The leaves are commonly used in Thai and Laotian cuisine, and the roots and leaves have been utilized in various folk medicines across Thailand and other Asian countries to treat various illnesses, including fever relief, hypertension, malaria, gastrointestinal diseases, inflammation, bacterial/fungal infection, alcohol intoxication and skin diseases.³⁻⁵ Recent phytochemical investigations of this plant revealed the presence of alkaloids, flavonoids, terpenoids and polyphenols. Among these, bisbenzylisoquinoline-type alkaloids were identified as the major compounds.² According to these investigations, *T. triandra* and its components exhibit a wide range of biological activities, including anti-diabetes, anti-hyperlipidemia, anti-obesity, anti-inflammation, anti-oxidant, and infective diseases.^{2,6-8} Additionally, our group has reported the antitumor activity of tiliacorinine, a major compound from the roots of this plant, in human cholangiocarcinoma cells.^{9,10} Although there are quite a few studies on the phytochemicals from various parts of this plant, the investigation of its stems has not been widely reported. In our ongoing investigation of biologically active compounds from Thai medicinal plants, we herein report the isolation and structural characterization of four bisbenzylisoquinoline alkaloids (**1–4**) from the stems of *T. triandra* (Figure 1).

Methodology:

1. General

Optical rotations were measured on a JASCO-1020 polarimeter. IR spectra were recorded in the ATR mode using a PerkinElmer FT-IR Spectrum 400 spectrophotometer. ¹H and ¹³C NMR spectra were recorded on a Bruker ASCEND 400 FT-NMR spectrometer, operating at 400 MHz and 100 MHz for ¹H and ¹³C NMR, respectively. HR-TOFMS spectra were measured with a Bruker micrOTOF-QII mass spectrometer, using electrospray ionization (ESI) as the ionization technique. Column chromatography was carried out using Merck silica gel 60 (particle sizes < 0.063 mm and 0.063–0.200 mm). The slurry method of column packing was employed. Sephadex LH-20 (GE Healthcare) was used for gel filtration chromatography. For thin-layer chromatography (TLC), Merck pre-coated silica gel 60 F₂₅₄

plates were used. TLC spots were detected under UV light and by spraying with anisaldehyde-H₂SO₄ reagent and Dragendorff's reagent, followed by heating.

2. Plant Material

The stems of *T. triandra* were collected from Namoungpet subdistrict, Sikao district, Trang, in May 2021. A voucher specimen is deposited at the Faculty of Science, Ramkhamhaeng University (Apichart Suksamrarn, No. 109).

3. Extraction and Isolation

The fresh stems of *T. triandra* (5.0 kg) were chopped into small pieces, air-dried, powdered, and macerated successively with *n*-hexane, EtOAc, and MeOH at room temperature (20 L × 3 times for each solvent). The filtered solution from each extraction was evaporated to dryness under reduced pressure at 40–45 °C to give the hexane (199.0 g), EtOAc (177.4 g), and MeOH (506.7 g) crude extracts.

The MeOH extract (500.0 g) was fractionated by column chromatography (Merck silica gel 60, particle sizes 0.063–0.200 mm) using a gradient solvent system of CH₂Cl₂, CH₂Cl₂–MeOH, MeOH and 5% H₂O–MeOH with increasing amounts of the more polar solvent. The eluates were examined by TLC, resulting in the combination of five fractions (M1–M5). Fraction M2 (65.0 g) was chromatographed on a silica gel column, eluting with a gradient solvent system of *n*-hexane–CH₂Cl₂–MeOH (1:4:0.1–1:4:0.3, v/v) to yield three subfractions (M2.1–M2.3). Subfraction M2.2 (21.0 g) was further chromatographed on a silica gel column, eluting with *n*-hexane–CH₂Cl₂–MeOH (1:4:0.15, v/v) to provide compound **1** (116.1 mg). Fraction M4 (230.0 g) was further chromatographed by a silica gel column eluting with CH₂Cl₂–MeOH (5:0.15, v/v) to afford six subfractions (M4.1–M4.6). Silica gel column chromatography of subfraction M4.2 (67.0 g), using *n*-hexane–CH₂Cl₂–MeOH (1:4:0.3, v/v) as the eluting solvent, furnished compounds **2** (19.0 mg) and **3** (26.3 mg). Subfraction M4.6 (42.0 g) was subjected to Sephadex LH-20 column chromatography, eluting with MeOH to give three subfractions (M4.6.1–M4.6.3). Subfraction M4.6.3 (17.5 g) was further subjected to column chromatography, eluting with *n*-hexane–CH₂Cl₂–MeOH (1:4:0.15, v/v) to yield compound **4** (3.2 mg).

3.1 Tiliacorinine (**1**)

Pale brownish amorphous solid; $[\alpha]_D^{25} +258.1$ (*c* 0.71, CHCl₃); IR (ATR) ν_{\max} 3343, 2929, 2841, 2790, 1586, 1500, 1436, 1359, 1272, 1234, 1115, 1050, 951, 874, 820 cm⁻¹; ¹H NMR data, see Table 1 and ¹³C NMR data, see Table 2; HR-TOFMS (ESI⁺) *m/z* 577.2688 [M + H]⁺ (calcd. for C₃₆H₃₇N₂O₅, 577.2696).

3.2 Yanangcorinine (**2**)

Pale brownish amorphous solid; $[\alpha]_D^{25} +179.5$ (*c* 0.34, CHCl₃); IR (ATR) ν_{\max} 3366, 2925, 2850, 2794, 1587, 1502, 1449, 1361, 1273, 1234, 1115, 1022, 948, 872, 820 cm⁻¹; ¹H NMR data, see Table 1 and ¹³C NMR data, see Table 2; HR-TOFMS (ESI⁺) *m/z* 577.2697 [M + H]⁺ (calcd. for C₃₆H₃₇N₂O₅, 577.2696).

3.3 Nortiliacorinine (**3**)

Pale brownish amorphous solid; $[\alpha]_D^{25} +204.5$ (*c* 0.53, CHCl₃); IR (ATR) ν_{\max} 3355, 2928, 2858, 1588, 1500, 1440, 1361, 1275, 1234, 1115, 1018, 961, 892, 823 cm⁻¹; ¹H NMR data, see Table 1 and ¹³C NMR data, see Table 2; HR-TOFMS (ESI⁺) *m/z* 563.2556 [M + H]⁺ (calcd. for C₃₅H₃₅N₂O₅, 563.2540).

3.4 Tiliacorine (**4**)

Pale brownish amorphous solid; $[\alpha]_D^{25} +191.1$ (*c* 0.14, CHCl₃); IR (ATR) ν_{\max} 3400, 2925, 2858, 1590, 1507, 1459, 1370, 1272, 1122, 1028, 959, 885, 825, 753 cm⁻¹; ¹H NMR data, see Table 1 and ¹³C NMR data, see Table 2; HR-TOFMS (ESI⁺) *m/z* 577.2669 [M + H]⁺ (calcd. for C₃₆H₃₇N₂O₅, 577.2696).

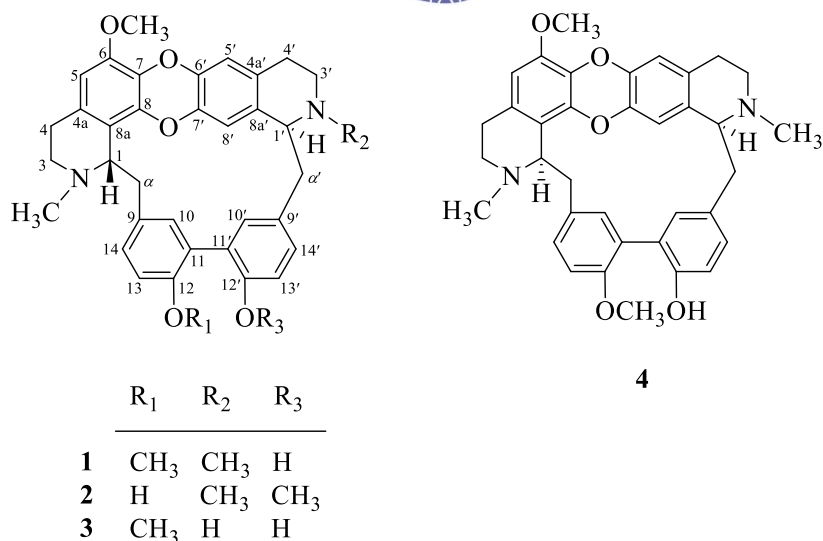


Figure 1. Chemical Structures of the Isolated Compounds **1–4**

Results and Discussion:

Compound **1** was obtained as a pale brownish amorphous solid, with a specific optical rotation of $[\alpha]_D^{25} +258.1$ (c 0.71, CHCl₃). The IR spectrum indicated the presence of a hydroxy group (3343 cm⁻¹) and an aromatic nucleus (1586 and 1500 cm⁻¹). The molecular formula was determined to be C₃₆H₃₆N₂O₅ based on HR-TOFMS (positive ion electrospray ionization, ESI⁺) at m/z 577.2688 [M + H]⁺ (calcd. for C₃₆H₃₇N₂O₅, 577.2696). The ¹H NMR data (Table 1) showed aromatic protons at δ_H 8.05 (1H, *s*, H-8'), δ_H 7.64 (H-10), 7.57 (H-10') (each *brs*, 1H), δ_H 7.33 (1H, *brd*, J = 8.4 Hz, H-14), 7.25 (1H, *brd*, J = 8.6 Hz, H-14'), 6.97 (1H, *d*, J = 8.6 Hz, H-13'), 6.94 (1H, *d*, J = 8.4 Hz, H-13), δ_H 6.62 (H-5'), 6.28 (H-5) (each *s*, 1H). Relatively downfield signals of methine protons at C-1 and C-1' at δ_H 3.69 (*brd*, J = 7.3 Hz) and 3.40 (*m*), respectively. The ¹H-NMR spectrum also showed signals of methylene protons at δ_H 2.94/3.33 (H_{ab}-3), 2.69/3.08 (H_{ab}-3'), 2.35/2.83 (H_{ab}-4), 2.52/2.94 (H_{ab}-4'), 2.80/3.35 (H_{ab}- α) and 2.92/3.34 (H_{ab}- α'). Two singlet methyl signals (δ_H 2.28 and 2.60) and two singlet methyl signals (δ_H 3.82 and 3.95) were indicative of the presence of two *N*-methyl and two methoxy groups, respectively. The locations of these singlet methyl groups were confirmed by HMBC correlations shown in Figure 2. Analysis of the ¹H–¹H COSY spectrum (Figure 2) of compound **1** revealed the spin-coupling system of H-3/H-4, H-3'/H-4', H-13/H-14 and H-13'/H-14'. The ¹³C-NMR (Table 2) and DEPT-135 spectra revealed the presence of thirty-six carbon atoms, including eleven methine (δ_C 135.7, 134.2, 130.1, 129.8, 118.4, 115.1, 114.2, 111.1, 106.2, 67.0, 62.6), six methylene (δ_C 52.9, 43.7, 40.9, 40.3, 26.6, 21.4), four methyl (δ_C 56.4, 56.2, 41.9, 41.9) and fifteen quaternary (δ_C 153.1, 152.4, 146.2, 139.9, 139.8, 137.4, 135.2, 133.7, 130.1, 129.6, 128.6, 128.6, 127.7, 126.3, 118.5) carbons. The HMBC correlations are summarized in Figure 2. The configuration of this alkaloid was supported by the NOESY experiment (see Figure 2). The spectroscopic data led to the identification of **1** as tiliacorinine. The structure of this compound was confirmed by comparison with spectroscopic data reported in the literature.¹¹

Table 1. ¹H NMR Data (400 MHz) of Compounds 1–4 (δ in ppm, J in Hz)

| Position | 1 ^a | 2 ^b | 3 ^a | 4 ^a |
|----------------------|---|--|--|--|
| 1 | 3.69 (<i>brd</i> , 7.3) | 3.60 (<i>m</i>) ^c | 3.70 (<i>m</i>) ^c | 3.69 (<i>m</i>) ^c |
| 3 | a: 2.94 (<i>m</i>) ^c b: 3.33 (<i>dd</i> , 11.8, 5.3) | a: 2.93 (<i>m</i>) ^c b: 3.36 (<i>m</i>) ^c | 3.37 (<i>m</i>) ^c | a: 2.90 (<i>m</i>) ^c b: 3.37 (<i>m</i>) ^c |
| 4 | a: 2.35 (<i>dd</i> , 15.9, 5.3) b: 2.83 (<i>m</i>) ^c | a: 2.35 (<i>m</i>) ^c b: 2.94 (<i>m</i>) ^c | a: 2.34 (<i>dd</i> , 16.5, 4.2) b: 2.92 (<i>m</i>) ^c | a: 2.35 (<i>m</i>) ^c b: 2.86 (<i>m</i>) ^c |
| 5 | 6.28 (<i>s</i>) | 6.45 (<i>s</i>) | 6.29 (<i>s</i>) | 6.28 (<i>s</i>) |
| α | a: 2.80 (<i>dd</i> , 13.9, 7.3) b: 3.35 (<i>m</i>) ^c | 2.78 (<i>m</i>) ^c | 2.77 (<i>m</i>) ^c | 2.78 (<i>m</i>) ^c |
| 10 | 7.64 (<i>brs</i>) | 7.53 (<i>d</i> , 2.0) | 7.61 (<i>d</i> , 1.8) | 7.70 (<i>brs</i>) |
| 13 | 6.94 (<i>d</i> , 8.4) | 6.94 (<i>d</i> , 8.4) | 6.94 (<i>d</i> , 8.2) | 7.01 (<i>d</i> , 8.6) |
| 14 | 7.33 (<i>brd</i> , 8.4) | 7.28 (<i>dd</i> , 8.4, 2.0) | 7.33 (<i>brd</i> , 8.2) | 7.39 (<i>brd</i> , 8.5) |
| 1' | 3.40 (<i>m</i>) ^c | 3.29 (<i>brd</i> , 7.9) | 3.93 (<i>m</i>) ^c | 3.46 (<i>m</i>) ^c |
| 3' | a: 2.69 (<i>ddd</i> , 11.8, 11.5, 2.4) b: 3.08 (<i>dd</i> , 11.8, 5.0) | a: 2.56 (<i>m</i>) ^c b: 3.04 (<i>m</i>) ^c | a: 2.94 (<i>m</i>) ^c b: 3.02 (<i>m</i>) ^c | a: 2.69 (<i>m</i>) ^c b: 3.08 (<i>m</i>) ^c |
| 4' | a: 2.52 (<i>brd</i> , 16.4) b: 2.94 (<i>ddd</i> , 16.4, 11.5, 5.0) | a: 2.53 (<i>m</i>) ^c b: 2.86 (<i>m</i>) ^c | a: 2.56 (<i>brd</i> , 16.7) b: 2.90 (<i>m</i>) ^c | a: 2.56 (<i>brd</i> , 16.8) b: 3.00 (<i>m</i>) ^c |
| 5' | 6.62 (<i>s</i>) | 6.58 (<i>s</i>) | 6.29 (<i>s</i>) | 6.65 (<i>s</i>) |
| 8' | 8.05 (<i>s</i>) | 8.04 (<i>s</i>) | 8.08 (<i>s</i>) | 8.05 (<i>s</i>) |
| α' | a: 2.92 (<i>m</i>) ^c b: 3.34 (<i>m</i>) ^c | a: 2.89 (<i>m</i>) ^c b: 3.36 (<i>m</i>) ^c | 3.18 (<i>m</i>) ^c | a: 2.95 (<i>m</i>) ^c b: 3.44 (<i>m</i>) ^c |
| 10' | 7.57 (<i>brs</i>) | 7.57 (<i>d</i> , 2.2) | 7.56 (<i>brs</i>) | 7.52 (<i>brs</i>) |
| 13' | 6.97 (<i>d</i> , 8.6) | 7.06 (<i>d</i> , 8.3) | 6.95 (<i>d</i> , 8.3) | 6.96 (<i>d</i> , 8.2) |
| 14' | 7.25 (<i>brd</i> , 8.6) | 7.34 (<i>dd</i> , 8.3, 2.2) | 7.32 (<i>brd</i> , 8.3) | 7.30 (<i>brd</i> , 8.2) |
| 2-NCH ₃ | 2.28 (<i>s</i>) | 2.23 (<i>s</i>) | 2.31 (<i>s</i>) | 2.31 (<i>s</i>) |
| 2'-NCH ₃ | 2.60 (<i>s</i>) | 2.60 (<i>s</i>) | — | 2.63 (<i>s</i>) |
| 6-OCH ₃ | 3.82 (<i>s</i>) | 3.81 (<i>s</i>) | 3.83 (<i>s</i>) | 3.85 (<i>s</i>) |
| 12-OCH ₃ | 3.95 (<i>s</i>) | — | 3.95 (<i>s</i>) | 3.91 (<i>s</i>) |
| 12'-OCH ₃ | — | 3.99 (<i>s</i>) | — | — |

^aRecorded in CDCl₃^bRecorded in acetone-*d*₆^cPartially overlapping signal

**Table 2. ^{13}C NMR Data (100 MHz) of Compounds 1–4**

| Position | 1 ^a | 2 ^b | 3 ^a | 4 ^a |
|----------------------|----------------|----------------|----------------|----------------|
| 1 | 62.6 | 63.4 | 62.5 | 62.8 |
| 3 | 40.9 | 43.9 | 43.6 | 43.8 |
| 4 | 21.4 | 21.2 | 21.3 | 21.4 |
| 4a | 128.6 | 130.0 | 129.1 | 128.9 |
| 5 | 106.2 | 107.3 | 106.3 | 106.3 |
| 6 | 146.2 | 147.1 | 146.2 | 146.2 |
| 7 | 130.1 | 140.3 | 139.6 | 130.3 |
| 8 | 139.8 | 129.6 | 128.7 | 139.9 |
| 8a | 118.5 | 118.8 | 118.6 | 118.9 |
| α | 40.3 | 40.9 | 40.6 | 40.6 |
| 9 | 137.4 | 137.6 | 137.5 | 134.6 |
| 10 | 135.7 | 135.0 | 135.7 | 135.7 |
| 11 | 126.3 | 127.0 | 127.7 | 126.6 |
| 12 | 153.1 | 153.4 | 153.2 | 153.9 |
| 13 | 111.1 | 118.3 | 111.0 | 112.0 |
| 14 | 129.8 | 130.5 | 130.7 | 130.1 |
| 1' | 67.0 | 68.1 | 58.9 | 67.0 |
| 3' | 52.9 | 53.2 | 43.8 | 52.8 |
| 4' | 26.6 | 27.6 | 27.5 | 30.0 |
| 4a' | 128.6 | 130.9 | 130.1 | 128.9 |
| 5' | 115.1 | 115.3 | 115.8 | 115.3 |
| 6' | 139.9 | 136.6 | 140.2 | 140.1 |
| 7' | 135.2 | 140.3 | 139.8 | 140.0 |
| 8' | 114.2 | 114.5 | 113.7 | 114.2 |
| 8a' | 129.6 | 130.4 | 135.7 | 135.0 |
| α' | 43.7 | 41.4 | 42.9 | 40.6 |
| 9' | 133.7 | 134.2 | 132.6 | 136.2 |
| 10' | 134.2 | 135.9 | 133.9 | 134.6 |
| 11' | 127.7 | 128.3 | 126.3 | 127.6 |
| 12' | 152.4 | 154.5 | 152.6 | 152.0 |
| 13' | 118.4 | 111.3 | 118.3 | 117.2 |
| 14' | 130.1 | 130.1 | 129.8 | 130.3 |
| 2-NCH ₃ | 41.9 | 41.8 | 42.0 | 42.0 |
| 2'-NCH ₃ | 41.9 | 42.2 | — | 42.0 |
| 6-OCH ₃ | 56.2 | 56.0 | 56.2 | 56.2 |
| 12-OCH ₃ | 56.4 | — | 56.4 | 56.3 |
| 12'-OCH ₃ | — | 56.1 | — | — |

^aRecorded in CDCl₃^bRecorded in acetone-*d*₆

Compound **2** was obtained as pale brownish amorphous solid, $[\alpha]_D^{25} +179.5$ (c 0.34, CHCl_3). The IR spectrum indicated the presence of hydroxy group (3366 cm^{-1}), and aromatic nucleus (1587 and 1502 cm^{-1}). The molecular formula was determined to be $\text{C}_{36}\text{H}_{36}\text{N}_2\text{O}_5$ based on the HR-TOFMS (positive ion electrospray ionization, ESI^+) at m/z 577.2697 $[\text{M} + \text{H}]^+$ (calcd. for $\text{C}_{36}\text{H}_{37}\text{N}_2\text{O}_5$, 577.2696). The ^1H and ^{13}C NMR spectra of compound **2** (Tables 1 and 2) exhibited spectral features closely similar to those of compound **1**. The significant difference was observed in the deshielding of aromatic protons at δ_{H} 7.06 (1H, d , $J = 8.3\text{ Hz}$, H-13') and 7.34 (1H, dd , $J = 8.3, 2.2\text{ Hz}$, H-14'), which were shifted approximately 0.09 ppm compared to those of compound **1**. These deshielding effects are consistent with the presence of a methoxy group (δ_{H} 3.99, s) at position C-12' in compound **2**, as confirmed by HMBC correlations shown in Figure 2. Furthermore, H-10 (δ_{H} 7.53, d , $J = 2.0\text{ Hz}$) and H-14 (δ_{H} 7.28, dd , $J = 8.4, 2.0\text{ Hz}$) showed the correlations with C-12 (δ_{C} 153.4) in the HMBC spectrum. The HMBC correlations of H-10' (δ_{H} 7.57, d , $J = 2.2\text{ Hz}$) and H-14' (δ_{H} 7.34, dd , $J = 8.3, 2.2\text{ Hz}$) with C-12' (δ_{C} 154.5) were also observed. Moreover, the configuration of this compound was established from the NOESY correlation between H-13' (δ_{H} 7.06, d , $J = 8.3\text{ Hz}$) and 12'- OCH_3 (see Figure 2). The spectroscopic data led to the identification of **2** as yanangcorinine. The structure of this compound was confirmed by comparison with spectroscopic data reported in the literature.¹²

The molecular formula of compound **3** was determined as $\text{C}_{35}\text{H}_{34}\text{N}_2\text{O}_5$ by the analysis of HR-TOFMS (ESI^+) at m/z 563.2556 $[\text{M} + \text{H}]^+$ (calcd. for $\text{C}_{35}\text{H}_{35}\text{N}_2\text{O}_5$, 563.2540). The IR spectrum indicated the presence of hydroxy group (3355 cm^{-1}), and aromatic nucleus (1588 and 1500 cm^{-1}). The ^1H NMR spectrum of compound **3** (Table 1) showed that most of the spectral patterns similar to those of compound **1**. The key difference was the absence of the NCH_3 signal at position N-2' in compound **3**. Instead, signals at δ_{H} 3.93 (H-1'), 2.94/3.02 ($\text{H}_{\text{ab}}\text{-3'}$), 2.56/2.90 ($\text{H}_{\text{ab}}\text{-4'}$) and 3.18 (H- α') were observed. The singlet signal for the 2- NCH_3 group appeared at δ_{H} 2.31. The methine protons at positions C-1 and C-1' were observed at δ_{H} 3.70 and 3.93, respectively. The ^{13}C -NMR spectral data (Table 2) displayed thirty-five carbon atoms, one carbon less than compound **1**, as confirmed by HR-TOFMS data. The configuration was confirmed by NOESY experiment with the same analogy to those of compounds **1** and **2** (Figure 2). The spectroscopic data led to the identification of **3** as nortiliacorinine. The structure of this compound was confirmed by comparison of spectroscopic data reported in the literature.¹³

Compound **4** had the molecular formula $\text{C}_{36}\text{H}_{36}\text{N}_2\text{O}_5$, as deduced from its HR-TOFMS (ESI^+) at m/z 577.2669 $[\text{M} + \text{H}]^+$ (calcd. for $\text{C}_{36}\text{H}_{37}\text{N}_2\text{O}_5$, 577.2696). The IR spectrum indicated the presence of hydroxy group (3400 cm^{-1}), and aromatic nucleus (1590 and 1507 cm^{-1}). The ^1H and ^{13}C NMR spectra of compound **4** (Tables 1 and 2) are closely similar to those of compound **1**. The notable difference is the configuration at position C-1, which is S -configuration in compound **1** and R -configuration in compound **4**. In addition, the chemical shifts of the aromatic proton signals in rings C and C' of compound **4** were downfield compared to those in compound **1**, as shown in Table 1. The structural assignment for compound **4** was confirmed by analyzing its NOESY spectrum (Figure 2). The NOESY correlations between H-1 (δ_{H} 3.69, m) and H-14 (δ_{H} 7.39, brd , $J = 8.5\text{ Hz}$) confirmed the R -configuration at C-1. The spectroscopic data led to the identification of **4** as tiliacorine. The NMR spectral data were in agreement with those of the reported values.¹¹

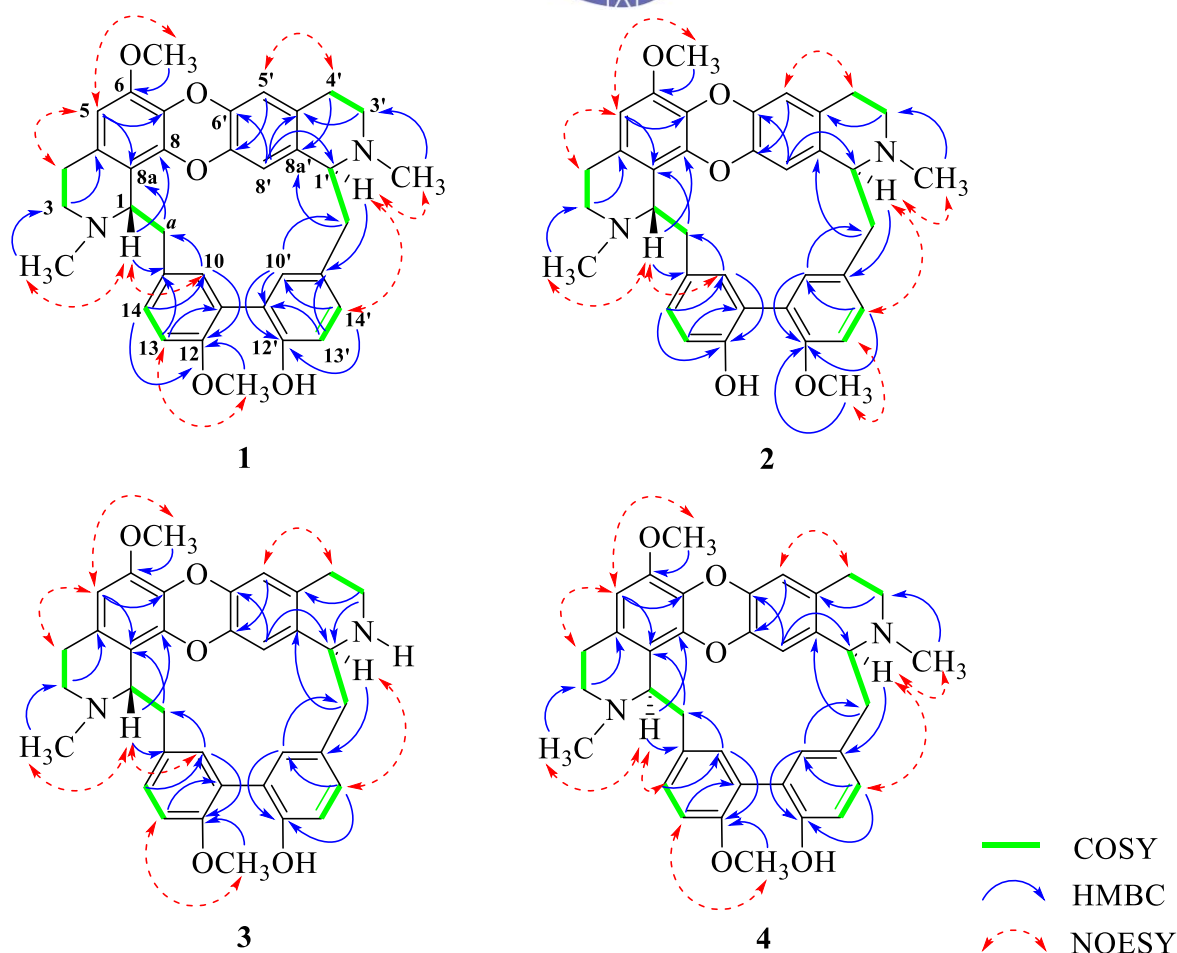


Figure 2. Selected ^1H - ^1H COSY, HMBC and NOESY Correlations of Compounds **1–4**

Conclusion:

In summary, four known bisbenzylisoquinoline alkaloids (**1–4**) have been isolated from the stems of *T. triandra*.

Acknowledgements:

This work was supported by Department of Chemistry, Faculty of Science, Ramkhamhaeng University. PC acknowledges a scholarship from the Center of Excellence for Innovation in Chemistry (PERCH-CIC), Ministry of Higher Education, Science, Research and Innovation.

References:

1. Smitinand T. Thai Plant Names. 2014. Office of the Forest Herbarium, Department of National Parks, Wildlife and Plant Conservation, Bangkok.
2. Das G, Gouda S, Kerry RG, Cortes H, Prado-Audelo MLD, Leyva-Gómez G, Tsouh FPV, Gutiérrez-Grijalva EP, Heredia JB, Shin H-S, Patra JK. J Chem. 2022;8754528:1–16.
3. Duangjai A, Saokaew S. J Complement Integr Med. 2018;16:1–8.
4. Kaewpiboon C, Assavalapsakul W, Winayanuwattikun P, Yongvanich T, Phuwapraisirisan P. Pharmacog Mag. 2014;10:S549–S556.
5. Neamsuvan O, Komonhiran P, Boonming K. J Ethnopharmacol. 2018;214:58–70.

6. Chaveerach A, Lertsatitthanakorn P, Tanee T, Puangjit N, Patarapadungkit N, Sudmoon R. *Int J Pharmacog Phytochem Res*. 2016;8:722–729.
7. Maneenoon K, Khuniad C, Teanuan Y, Saedan N, Prom-in S, Rukleng N, Kongpool W, Pinsook P, Wongwiwat W. *J Ethnobiol Ethnomed*. 2015;11:1.
8. Sureram S, Senadeera SPD, Hongmanee P, Mahidol C, Ruchirawat S, Kittakoo P. *Bioorg Med Chem Lett*. 2012;22:2902–2905.
9. Janeklang S, Nakaew A, Vaeteewoottacharn K, Seubwai W, Boonsiri P, Kismali G, Suksamrarn A, Okada S, Wongkham S. *Asian Pac J Cancer Prevent*. 2014;15:7473–7478.
10. Detarya M, Mahalapbutr P, Waenphimai O, Kidoikhammouan S, Janeklang S, Sawanyawisuth K, Vaeteewoottacharn K, Seubwai W, Saengboonmee C, Thothisong T, Pabuprapap W, Suksamrarn A, Wongkham S. *Biochim et Biophys Acta: General Subjects*. 2023;1867:130486.
11. Saiin C, Markmee S. *Kasetsart J Nat Sci*. 2003;37:47–51.
12. Pachaly P, Tan JT, Khosravian H, Klein M. *Arch Pharm*. 1986;319:126–133.
13. Patra A, Ghosh S, Mukherjee B. *Magn Reson Chem*. 2010;48:823–828.



PREPARATION OF YELLOW LAKE FROM GARDENIA FRUIT EXTRACT

Ratwalee Liangmongkolkran,¹ Pornpen Werawatganone^{2,*} Walaisiri Muangsiri,³

Department of Pharmaceutics and Industrial Pharmacy, Faculty of Pharmaceutical Sciences, Chulalongkorn University, Bangkok, 10330, Thailand.

*e-mail: Pornpen.W@chula.ac.th, walaisiri@yahoo.com

Abstract:

Lakes are obtained from chemical reactions between metal ions, alkalis, and dyes, which form insoluble compounds. It is used to fix or intensify stains in a tissue or cell preparation. The advantages of laking process are improving brightness, fastness, and providing a wide range of colors depending on the dyes used. One of natural yellow colorants comes from fruit of *Gardenia jasminoides* J. Ellis, a plant in RUBIACEAE family. *G. jasminoides* fruit contains natural dyes, primarily yellow pigments in the carotenoid group known as crocins and crocetin. The aim of this study was to prepare gardenia lakes. Our group is interested in using the yellow colorant of *G. jasminoides* in cosmetic products. In this study, gardenia lakes were prepared from yellow dye of *G. jasminoides* fruit precipitated with potassium aluminum sulfate and calcium sulfate as mordants at various conditions. Based on CIELab color system, the color parameters were measured during the storage time. The optimum condition showed the highest yellowness ($b = 63.8$) using 5% calcium sulfate.

Keywords: *Gardenia jasminoides* fruit; CIELab; yellow lakes; stability

Introduction:

Lakes are insoluble colorants commonly used in cosmetic products. Based on the chemical reaction between metal ions, alkalis, and dyes¹, lakes are metal complexes which are insoluble in water. Metal ion, known as mordant, a substance that fixes a dyestuff in or on, combines² with a dye to form an insoluble compound.

The advantages of laking process are improvement of color attributes (hue, chroma and brightness) and producing a wide variety of colorants. Once precipitated with a mordant, the dye becomes insoluble, more stable compound being better light and heat resistant when compared to the regular dye. Lakes can be used as pigments in various media such as paints, inks, plastics including cosmetic and food products. Being derived from plant sources, colorants are considered safe and environmentally friendly.^{1,3}

Gardenia Jasminoides J. Ellis is a plant in RUBIACEAE family, commonly known as gardenia or cape jasmine. The fruit of *G. jasminoides* contains natural dyes, primarily yellow pigments in the carotenoid group known as crocins and crocetin.^{4,5} Gardenia fruit has been used in traditional Chinese medicine for centuries. Records indicate its usage dates back to at least the Han dynasty (206 BCE – 220 CE). The fruit of the gardenia plant, known as "zhī zi" (栀子) in Chinese, has been utilized for its medicinal properties. *G. jasminoides* yellow colorant has been widely used in food products.^{1,6,7}

In Thailand, gardenia is also grown in northern areas such as Chiang Mai and Chiang Rai provinces. The fresh fruit was extracted and used as yellow food colorant. The NSTDA (National Science and Technology Development Agency) reported that the yellow dye from the gardenia fruit provides a unique shade of yellow.

This study focused on preparation of yellow lakes from *G. jasminoides* to promote the use in cosmetic products and enhance the value of this agricultural product.

Color attributes; hue, chroma, brightness, were monitored using CIELab color system. The CIELab system was used to evaluate colorants in three-dimensional space. The L-axis is lightness or brightness, ranging from 0 (black) to 100 (white). The values a and b illustrate the spectrum from greenness (negative value of a) to redness (positive value of a), and blueness (negative value of b) to yellowness (positive value of b), respectively. ΔE value represents information regarding color change in three dimension color system between two points (equation 1) ^{1,8,9} as following.

$\Delta E < 1$ Not noticeable difference to the human eye.

$\Delta E 1 - 2$ Noticeable difference under close observation or under optimal lighting conditions.

$\Delta E 2 - 10$ Noticeable difference.

$\Delta E > 10$ Clearly noticeable or easily distinguishable difference.

$$\Delta E_{ab} = (\Delta L^2 + \Delta a^2 + \Delta b^2)^{1/2} \quad \text{equation 1}$$

Chroma is the intensity or purity of a color (equation 2).

$$\text{Chroma (C)} \quad C = (a^2 + b^2)^{1/2} \quad \text{equation 2}$$

In this paper, we used potassium aluminum sulfate, which is the most frequently used mordant,^{1,3} and calcium sulfate as mordants at the concentration of 1%, 5%, and 10% w/w. The mordants formed complexes with the dye extracted from *G. jasminoides* fruit. Then their stabilities were evaluated using CIELab color system.

Methodology:

Preparation of Lakes from Gardenia Fruit

Dye Extraction: Maceration

Gardenia dried fruit was purchased from Saendee Pharmacy (Bangkok, Thailand) 60 grams of gardenia fruit were ground with a mortar. The ground fruit 60 grams was soaked in 600 ml of 60% ethanol for 2 hours (10 grams of gardenia fruit / 100 ml of 60% ethanol)^{10,11} with constantly stirring. *G. jasminoides* dye was extracted by soaking in 60% v/v ethanol¹⁰ to release yellow colorant. A coffee filter paper was used to get all the dye liquor. The extract was dried using a rotary evaporator under the condition: vacuum 175 mbar, 90 rpm, water bath temperature 50°C

Laking Process: Mordant Addition

Potassium aluminum sulfate, calcium sulfate, and sodium carbonate were purchased from Lab Valley (Bangkok, Thailand). A mordant, potassium aluminum sulfate or calcium sulfate, was added to the dye extract from *G. jasminoides* fruit. The concentration of mordant was varied at 1%, 5%, and 10% w/w in water. The dye extract was dissolved in the solution at concentration of 20% w/w. Sodium carbonate was added into the mixture at amount of half of the mordant. The mixture was allowed to stand until the lake precipitated out of the solution approximately for 15 hours.

Drying, and Stability Study

The precipitated lake was filtered using a Buchner funnel equipped with filter paper No.1 (Whatman International Ltd., Maidstone, England), and then let it dry for 4 days at ambient temperature. The dried sample was ground using a glass mortar to ensure a fine and uniform powder. All samples were stored in sealed amber glass bottles to avoid from light exposure. The samples were kept in two conditions ; a desiccator at ambient temperature and



an incubator at 40°C with 75 % RH. Each sample was collected and evaluated at day 4,6, and 33.

Evaluation of color parameters using CIELab system

Color change was monitored using a colorimeter (Color Reader CR-20®, Konica minolta INC., Japan). Regarding CIELab system (Commission internationale de l'éclairage or International Commission on Illumination), color parameters are reported in terms of L, a, and b. In this work, we are interested in yellowness of the samples, which corresponds to a positive value of b in CIELab.






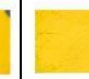







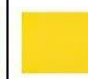

Statistical analysis

The data were collected in triplicate and expressed as a mean \pm standard deviation (SD). Statistical analysis was performed using a one-way analysis of variance (ANOVA) and T-test using SPSS software (version 29.0.2.0). A p-value < 0.05 was considered statistically significant.

Results and Discussion:

Yellow lake precipitation was obtained from potassium aluminum sulfate and calcium sulfate interacting with gandenian dye as shown in Table 1.

Table 1. Yellow lakes of *G. jasminoides* dye presenting at day 0; The experiment found that potassium aluminum sulfate at 1% w/w did not yield any lake precipitation.

| Metal ion | 1 % | | | 5 % | | | 10 % | | |
|------------------|---|---|---|---|---|---|---|---|---|
| | N1 | N2 | N3 | N1 | N2 | N3 | N1 | N2 | N3 |
| Al ³⁺ | NA | NA | NA |  |  |  |  |  |  |
| % yield | NA | | | 4.9 \pm 1.3 | | | 13.2 \pm 0.3 | | |
| Ca ²⁺ |  |  |  |  |  |  |  |  |  |
| % yield | 1.4 \pm 0.6 | | | 9.9 \pm 1.2 | | | 19.1 \pm 0.3 | | |

Al³⁺ from potassium aluminum sulfate, Ca²⁺ from calcium sulfate, NA = not available

CIELab parameters for the yellow lakes were calculated using equation 1,2. As presented in Table 2, the highest percent yield was obtained from Ca- dye complex at 10% calcium sulfate. The reason could be due to the amount of metal ion in the solution. Molecular weights of potassium aluminum sulfate and calcium sulfate are 474 and 136, respectively. At equal percent weight concentration, available metal ion obtained from calcium sulfate is more

than potassium aluminum sulfate. Higher percent yield of lake was obtained at higher concentration of metal salt.

Table 2. CIE Lab parameters of yellow lakes from *Gardenia jasminoides* fruit extract over the storage time

| Mor dant | Ambient temperature | | | | | 40 °C and 75 % RH | | | | |
|------------------------------|---------------------|-------------|------------------------|-----------------|------------------|-------------------|-------------|------------------------|-----------------|------------------|
| | b day 4 | b day 33 | ΔE day 4-33 | Chroma day 4 | Chroma day 33 | b day 4 | b day 33 | ΔE day 4-33 | Chroma day 4 | Chroma day 33 |
| ${}^3\text{Al}^{3+}$ 5 % | 58.245 | 57.539 | 0.924 | 59.540 | 58.740 | 57.328 | 54.894 | 3.815 | 58.666 | 55.730 |
| ${}^3\text{Al}^{3+}$ 10 % | 54.381 | 57.178 | 5.116 | 55.833 | 58.612 | 54.783 | 52.939 | 3.026 | 56.243 | 53.956 |
| ${}^4\text{Ca}^{2+}$ 1 % | 45.828 | 48.506 | 5.554 | 47.706 | 50.301 | NA | NA | NA | NA | NA |
| ${}^4\text{Ca}^{2+}$ 5 % | 61.211 | 63.772 | 5.500 | 62.377 | 64.868 | 60.572 | 58.233 | 3.597 | 61.673 | 59.031 |
| ${}^4\text{Ca}^{2+}$ 10 % | 57.172 | 57.711 | 5.143 | 57.718 | 58.207 | 55.944 | 49.945 | 6.615 | 56.430 | 50.211 |

³ potassium aluminum sulfate, ⁴ calcium sulfate, NA = not available

Moreover, b value and chroma of calcium lake are higher than that of aluminium lake. It is implied that Ca^{2+} ion could be able to form lake complex with gardenia dye better than Al^{3+} ion. Yellowness of the samples was changed over the storage time (Figure 1). Brownish yellow was observed when the samples were kept in 40 °C and 75 % RH. Yellowness fading was also observed.

ΔE values of most samples were in the range of 5-7 meaning that the difference was noticeable and could be seen by naked eye. ΔE was less when the samples were kept at ambient temperature. Longer storage time of stability study should be further explored.



(a)

Aluminum lake

yellowness (positive value of b)



(b)

calcium lake

yellowness (positive value of b)

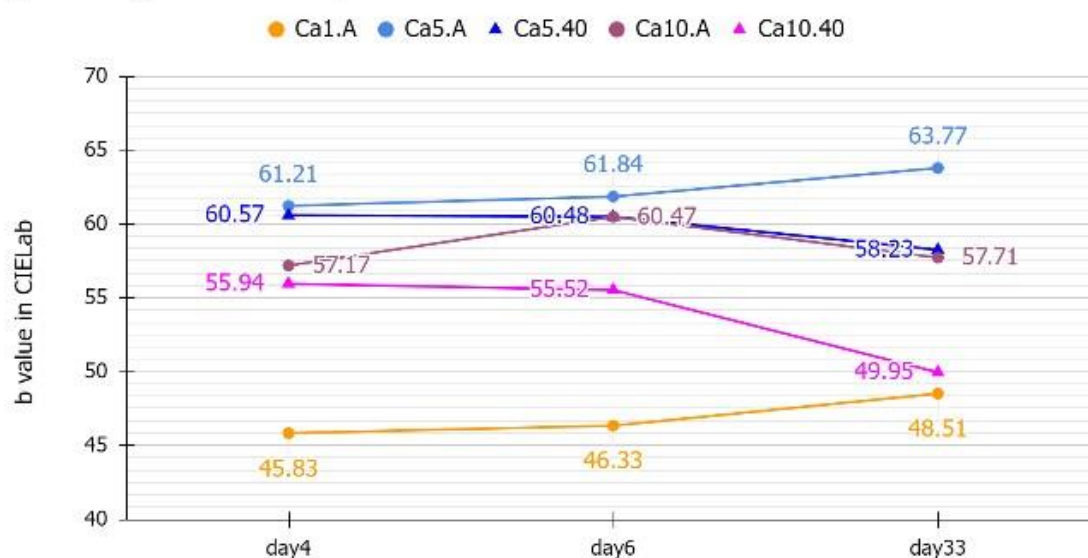


Figure 1. The graph shows the change of b value (yellowness) over storage time. (a)

aluminium lake, (b) calcium lake, ● = ambient temperature, ▲ = 40 °C and 75 % RH

Conclusion:

Yellow lakes were prepared from reaction between gardenia colorant and metal ions (Al^{3+} and Ca^{2+}). The highest percent yield was obtained from gardenia Ca lake at 10% w/w calcium sulfate. At 5% w/w calcium sulfate, the obtained gardenia-Ca lake showed the highest

color intensity (chroma and yellowness). Color change (ΔE) of gardenia Al lake and gardenia Ca lake was noticeable over the storage time in ambient temperature and stress condition.

Acknowledgements:

The authors would also like to express their gratitude for the scholarship from the Cosmetic Science Graduate Program at Chulalongkorn University.

References:

1. Handbook of Natural Colorants. 2023 : 4-5,40,94,104,465.
2. Duffus J. Pure Appl. Chem .1993:2072.
3. İşmal ÖE, Yıldırım L. The Impact and Prospects of Green Chemistry for Textile Technology; 2019:57-82.
4. Tian J, Qin S, Han J, Meng J, Liang A. J. Ethnopharmacol. 2022;289:1-45.
5. Song YN, Wang Y, Zheng YH, Liu TL, Zhang C. Fitoterapia. 2021:153-169.
6. Zhang L, Ai Y, Chen Y, Li C, Li P, Chen J, et al. Plants. 2023;12 :2209-2226.
7. Yin F, Liu J-h. Chin. Herb. Med. 2018;10 :362-370.
8. Popescu V. Elsevier; 2024:111-37.
9. . Piyarat K, Walaisiri M, Pornpen W.. Int. Food Res. J. 2014;21:325-330.
10. Hong IK, Jeon H, Lee SB.. J. Ind. Eng. Int . 2015 :326-332.
11. Thuy NM, Nhu PH, Tai NV, Minh VQ.. Horticulture. 2022;8:1199-1211.



SYNTHESIS AND BIOPHYSICAL PROPERTIES OF ZWITTERIONIC PYRROLIDINYL PEPTIDE NUCLEIC ACID

Wachiraya Pinthongnoi, Tirayut Vilaivan*

Organic Synthesis Research Unit, Department of Chemistry, Faculty of Science, Chulalongkorn University, Pathumwan, Bangkok 10330, Thailand

*e-mail: vtirayut@chula.ac.th

Abstract:

Pyrrolidinyl peptide nucleic acid (pyrrolidinyl PNA) is a DNA mimic with a conformationally constrained backbone consisting of alternating proline-cyclic β -amino acid dipeptide subunits. It exhibits excellent binding specificity towards DNA targets and high chemical and biological stability. Although pyrrolidinyl PNA offers great potential for applications in the biological field, it also has some disadvantages due to its hydrophobic structure leading to problems such as low water solubility and non-specific binding to hydrophobic molecules such as proteins, lipids, plastics, or other PNA molecules. To address these problems, the pyrrolidinyl PNA backbone was made Zwitterionic by modification with functional groups that contain an equal number of positive and negative charges within the same structure. Specifically, pyrrolidinyl PNA with a modified backbone incorporating a nitrogen atom was reacted with isopropyl ethenesulfonate or isopropyl 2-(2-oxoethoxy)ethane-1-sulfonate) through Michael addition or reductive alkylation, respectively. A preliminary investigation of the DNA binding properties revealed a decrease in binding strength compared to the unmodified PNA, while the base-pairing specificity is still preserved. The zwitterionic PNA showed good water solubility up to millimolar concentrations, but it was not yet possible to conclude the benefits of the zwitterionic modification to solubility improvement.

Introduction:

Peptide nucleic acid (PNA) is a DNA mimic consisting of a peptide backbone instead of deoxyribose and phosphate. The original PNA system, now known as aegPNA, was first reported by Nielsen et al. in 1991.¹ PNA recognizes its complementary DNA or RNA targets according to the Watson-Crick base pairing rules. Not only can PNA exhibits stronger binding affinity towards its target DNA and RNA than natural DNA or RNA² (Figure 1), but PNA also offers higher specificity as shown by the large decrease in T_m of the hybrids with DNA or RNA containing one or more mismatched bases. The uncharged PNA can form stable hybrids with DNA irrespective of salt concentrations³ and is resistant to acidic-basic conditions and enzymatic digestion (nucleases and proteases).⁴

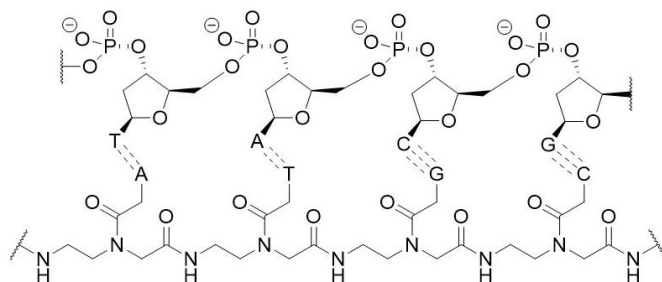


Figure 1. Structure of aegPNA pairing to its complementary DNA strand.

Although PNA exhibits several interesting properties that suggest its potential applications in the biological fields, there are limitations due to its poor water solubility and cell entry properties. Therefore, PNA must rely on other carrier molecules such as cell-penetrating peptides or nanoparticles to enhance its cell-entry capability.⁵⁻⁷ Furthermore, the conformational flexibility of aegPNA could benefit from structural modification to increase rigidity. Backbone-modified aegPNA incorporating embedded rigid structures (cyclopentane and cyclohexane)⁸ or modification at the gamma position (γ PNA) have been explored.⁹ Additionally, the pyrrolidine ring is a frequently used motif in many conformationally constrained PNA systems such as pyrrolidine oxy-PNA, pyrrolidine amide, aepPNA, and pyrrolidinyl PNA.¹⁰

A remarkable example of such conformationally constrained modified PNA systems is the pyrrolidinyl PNA developed by Vilaivan's group. It consists of a dipeptide building block deriving from a nucleobase-modified proline and a cyclic β -amino acid spacer (Figure 2).¹¹ This PNA system can be easily synthesized in a modular fashion on a solid support using the solid-phase peptide synthesis (SPPS) method. Pyrrolidinyl PNA shares similar properties to aegPNA but it binds to DNA targets more strongly and with higher specificity due to its rigid structure. However, like other PNA systems, pyrrolidinyl PNA is an uncharged molecule, which results in low water solubility and non-specific binding to molecules such as proteins, lipids, plastics, or other PNA molecules.¹²

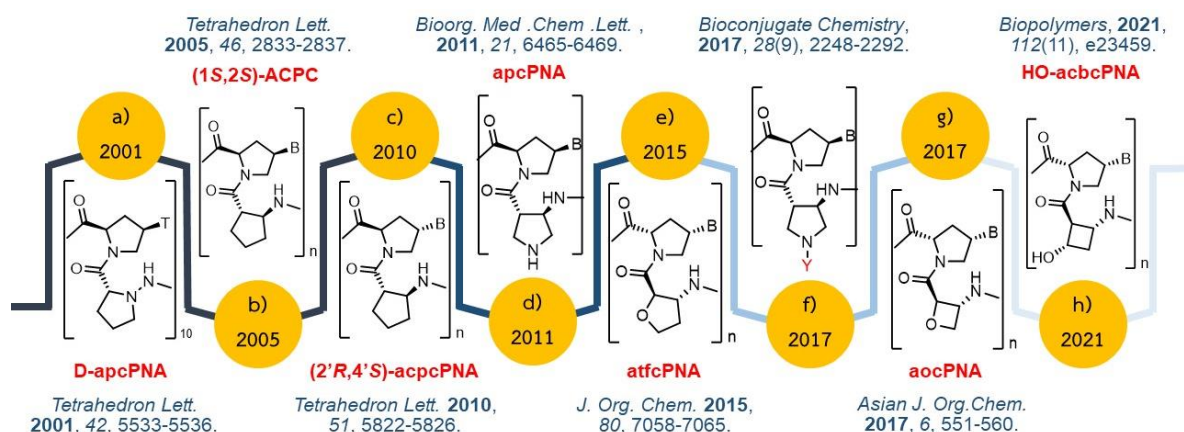


Figure 2. Evolution of pyrrolidinyl PNA structures over a period of two decades.

Zwitterions carrying both positive and negative charges within the same structure have been used to solve the problems of low water solubility and nonspecific interactions for many types of molecules. In previous work, only zwitterionic DNA was reported.¹³⁻¹⁵ These zwitterionic DNAs exhibited stronger binding with DNA or RNA targets than original DNA because the total charge of zwitterionic molecules was neutralized and the unfavorable electrostatic repulsion between phosphate groups of the original DNA was reduced. Moreover, zwitterionic polymers exhibit interesting properties, such as lowering nonspecific interactions.¹⁶⁻¹⁸ This study aims to modify the structure of the original pyrrolidinyl PNA molecules into zwitterionic pyrrolidinyl PNA to address the problem of low water solubility and nonspecific aggregation mentioned above without compromising the binding affinity and specificity towards its DNA target.



Methodology:

Materials

All organic reagents and solvents were purchased from TCI, Merck, Sigma-Aldrich, and RCI Labscan and used without further purification. Oligonucleotides were purchased from Integrated DNA Technologies, and starting materials for pyrrolidiny PNA synthesis were a gift from Synna Science. ^1H and ^{13}C NMR spectra were obtained on a JEOL JNM-ECZ500/S1 500 MHz NMR spectrometer. Thin-layer chromatography (TLC) was conducted on Merck® aluminum-backed 0.2 mm thick silica gel 60 F254 plates, Germany. The zwitterionic pyrrolidiny PNA was characterized by a JEOL JMS-S3000 SpiralTOF™-plus 3.0 mass spectrometer. Purification of the zwitterionic pyrrolidiny PNA was carried out on a Shimadzu Nexera Prep (HPLC Preparative System) and the purity of zwitterionic pyrrolidiny PNA was verified by Shimadzu Nexera high-performance liquid chromatography (HPLC). The solubility and DNA binding properties of the zwitterionic pyrrolidiny PNA were studied by Thermo Scientific NanoDrop™ 2000/2000c spectrophotometer, and Cary 100 Bio UV-vis spectrophotometer.

Synthesis of zwitterionic monomers

Synthesis of isopropyl ethenesulfonate (1)

To a solution of 2-chloroethanesulfonyl chloride (0.30 mL, 2.9 mmol) in dichloromethane (DCM) 2 mL was added isopropanol (0.20 mL, 2.6 mmol) at $-10\text{ }^{\circ}\text{C}$ and the solution of pyridine (0.4 mL, 5.0 mmol) in dichloromethane (DCM) 2 mL was added dropwise in the reaction mixture at $-10\text{ }^{\circ}\text{C}$. The reaction mixture was stirred at $-10\text{ }^{\circ}\text{C}$ for 2 h before warming to room temperature and the stirring was continued for 30 min. The reaction progress was monitored by thin-layer chromatography (10% EtOAc/Hexanes ($R_f = 0.48$; KMnO_4). After completion, the reaction was quenched with 10% HCl, extracted with water, washed with brine, and dried over anhydrous Na_2SO_4 . Then, the crude mixture was purified by column chromatography to give compound **1** as a pale-yellow oil (245.6 mg, 58%). ^1H NMR (500 MHz, CDCl_3) δ 6.55 (dd, $J = 16.6, 10.0$ Hz, 1H), 6.40 (d, $J = 16.6$ Hz, 1H), 6.07 (d, $J = 9.9$ Hz, 1H), 4.80 (sept, $J = 6.3$ Hz, 1H), 1.40 (d, $J = 6.2$ Hz, 6H). ^{13}C NMR (126 MHz, CDCl_3) δ 133.8, 129.2, 77.8, 23.1.

Synthesis of isopropyl 2-(2-hydroxyethoxy)ethane-1-sulfonate (2)

To a suspension of potassium *tert*-butoxide (60 mg, 0.5 mmol) in dry tetrahydrofuran (THF) 2 mL and dropwise the mixture of isopropyl ethenesulfonate (**1**) (377.3 mg, 2.51 mmol) and ethylene glycol (0.10 mL, 5.02 mmol) in dry tetrahydrofuran (THF) 2 mL. The reaction mixture was stirred at $0\text{ }^{\circ}\text{C}$ for 10 min before cooling to room temperature and continued stirring for 18 h. The reaction progress was monitored by thin-layer chromatography (100% EtOAc ($R_f = 0.62$; KMnO_4). After completion of the reaction, the crude mixture was concentrated *in vacuo* and purified by column chromatography to give compound **2** as a pale-yellow oil (374.3 mg, 70%). ^1H NMR (500 MHz, CDCl_3) δ 4.99 (sept, $J = 6.3$ Hz, 1H), 3.94 (t, $J = 6.1$ Hz, 2H), 3.74 (t, $J = 6.1$ Hz, 2H), 3.62 (t, $J = 6.1$ Hz, 2H), 3.37 (t, $J = 6.1$ Hz, 2H), 1.43 (d, $J = 6.3$ Hz, 6H). ^{13}C NMR (126 MHz, CDCl_3) δ 77.3, 72.6, 64.8, 61.7, 51.6, 23.3.

Synthesis of isopropyl 2-(2-oxoethoxy)ethane-1-sulfonate (3)

To a solution of 2-iodoxybenzoic acid (IBX) (197.4 mg, 0.71 mmol) in acetonitrile 1 mL, then the reaction was stirred under reflux for 10 min and added isopropyl 2-(2-hydroxyethoxy)ethane-1-sulfonate (**2**) (100 mg, 0.47 mmol) and continued stirring for 2 h.

Subsequently, the reaction mixture was followed by thin-layer chromatography (50% EtOAc/Hexanes ($R_f = 0.22$; KMnO_4 , 2,4-DNP). Then, the crude mixture was concentrated *in vacuo* to remove acetonitrile, added dichloromethane (DCM) in the crude mixture. The reaction was quenched and extracted with saturated NaHCO_3 and purified by column chromatography to give compound **3** as a pale-yellow oil (84.5 mg, 85%). ^1H NMR (500 MHz, CDCl_3) δ 9.70 (s, 1H), 5.04 – 4.93 (m, 1H), 4.19 (s, 2H), 3.99 (t, $J = 6.3$ Hz, 2H), 3.43 (t, $J = 6.3$ Hz, 2H), 1.42 (d, $J = 6.1$ Hz, 6H). ^{13}C NMR (126 MHz, CDCl_3) δ 199.2, 77.6, 76.7, 65.6, 51.4, 23.3.

Synthesis of zwitterionic pyrrolidinyl PNA (Figure 3)

The pyrrolidinyl PNA (acpcPNA) with apc modification was synthesized from the pyrrolidinyl PNA building blocks following a previously published protocol.¹⁹ The acpc space was replaced with apc at one or more specified positions by substitution Fmoc-(1*S*,2*S*)-2-aminocyclopentane carboxylic acid pentafluorophenyl ester with (3*R*,4*S*)-Fmoc-3-amino-*N*-trifluoroacetyl-pyrrolidine-4-carboxylic acid pentafluorophenyl ester.

Modification of zwitterionic pyrrolidinyl PNA

For the zwitterionic modification of pyrrolidinyl PNA, the *N*-terminal Fmoc group was removed from the PNA on the solid support followed by *N*-acetylation. The nucleobase side chain protecting group as well as the Tfa protection of the apc residue was removed by treatment of the resin-supported PNA with 1:1 aqueous ammonia:dioxane at 65 °C for 12 h. Next, the side-chain deprotected PNA was reacted with compound **1** or **3** as follows.

1) Michael reaction (compound **1**)

The resin-supported apc-modified acpcPNA (0.75 μmol) was soaked in a solution of isopropyl ethenesulfonate (**1**) (3.40 mg, 22.5 μmol) and DIEA (0.5 μL , 3 μmol) per number of apc-modified in 30 μL of anhydrous DMF at ambient temperature for 2 days.

2) Reductive alkylation (compound **3**)

The resin-supported apc-modified acpcPNA (0.75 μmol) was soaked in a solution of isopropyl 2-(2-oxoethoxy)ethane-1-sulfonate (**3**) (4.73 mg, 22.5 μmol) and acetic acid (3.0 μL , 45.0 μmol) per number of apc-modified in 30 μL of methanol at ambient temperature for 1 h. Next, sodium cyanoborohydride (NaBH_3CN) (1.4 mg, 22.5 μmol) per number of apc-modified was added in the mixture solution and the reaction was continued at ambient temperature for 2 days.

After the modification, the zwitterionic pyrrolidinyl PNA was then cleaved from the resin by treatment with trifluoroacetic acid (TFA) and precipitated by ether to give the crude zwitterionic pyrrolidinyl PNA as a white fluffy solid. This was further purified by reverse phase HPLC and characterized by MALDI-TOF MS (see Materials section).

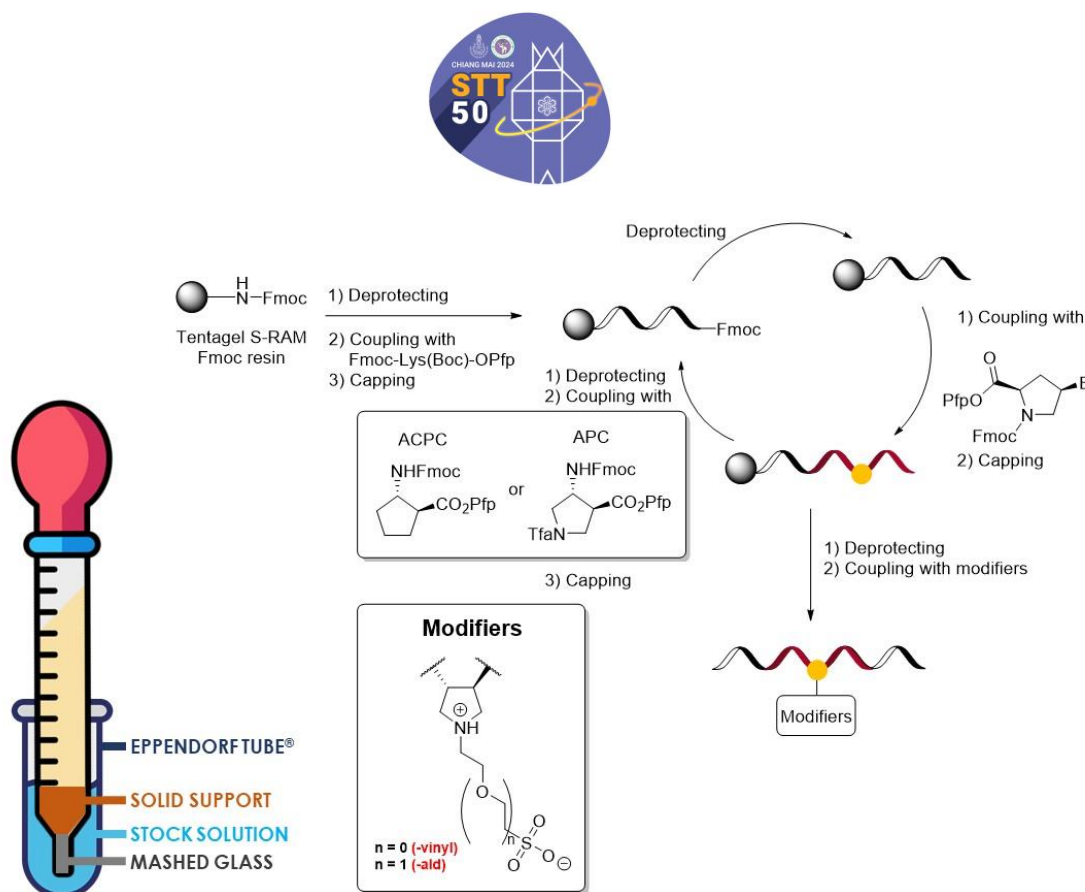


Figure 3. Synthesis of zwitterionic pyrrolidiny PNA

Results and Discussion:

We propose the aminoalkylsulfonate group as a modifier for pyrrolidiny PNA because it carries a zwitterionic group that should improve poor water solubility and reduces nonspecific interactions. To install the zwitterionic aminoalkylsulfonate group, the reactive monomers (compounds **1** and **3**) whereby the sulfonate group was protected with the isopropyl group²⁰ were first synthesized and then reacted with the pyrrolidiny PNA that had been modified by replacement of one or more 2-aminocyclopentanecarboxylic acid (acpc) spacer with the aminopyrrolidine carboxylic acid (apc) spacer.²¹ The nucleophilic nitrogen atom on the apc spacer reacted with the vinyl sulfonate (compound **1**) through Michael addition and with the aldehyde group in compound **2** through the reductive alkylation in the presence of NaBH₃CN. The modification processes were carried out while the PNA was still attached to the solid support, transforming it into zwitterionic pyrrolidiny PNA (Figure 4). It was planned to synthesize pyrrolidiny PNA sequences that were modified with one and multiple zwitterionic groups to study the effect of the number and position of the modifiers. The zwitterionic pyrrolidiny PNA was cleaved from the resin by treatment with TFA, which also resulted in the simultaneous removal of the isopropyl protecting group. All PNA sequences were purified by HPLC and characterized by MALDI-TOF MS. In all cases, the observed mass was consistent with the expected structure, and moderate or low percentage yields were obtained especially for multiple modifications possibly due to the incomplete reaction between the modifier and the PNA molecules (Table 1).

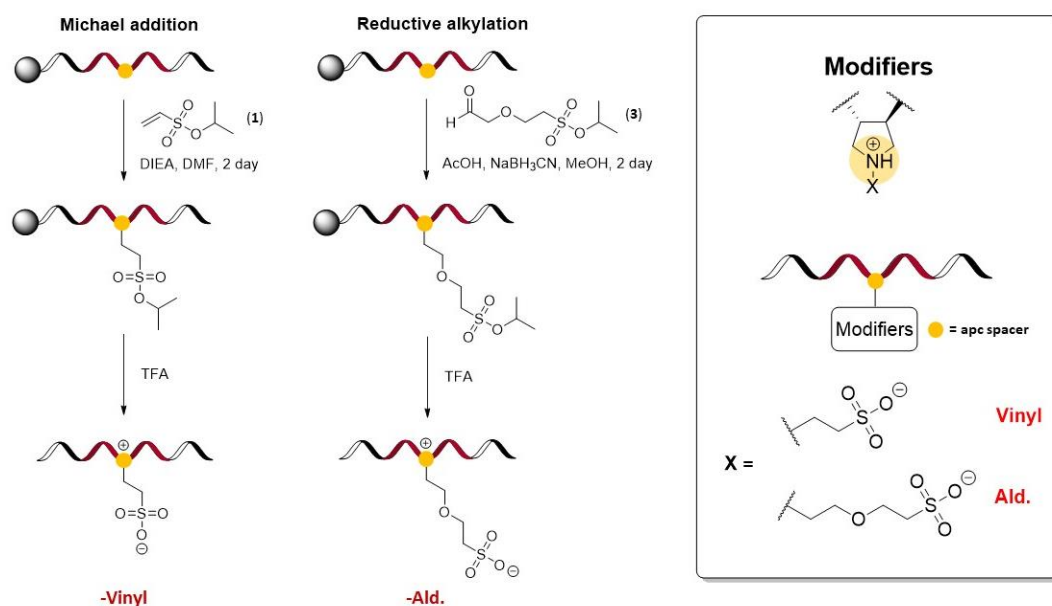


Figure 4. Attachment of the sulfonate group on the nitrogen atom of apc-modified PNA

Table 1.

Base sequence and MALDI-TOF spectrometric of zwitterionic pyrrolidiny PNA.

| PNA | Sequence (N → C) ^a | Modifier (x) | <i>m/z</i> (calcd.) ^b | <i>m/z</i> (found) ^c | %yield ^d |
|------------|---|--------------|----------------------------------|---------------------------------|---------------------|
| PNA1 | Ac-GTAGAT <u>CA</u> CT-LysNH ₂ | none | 3581.8086 | 3580.5012 | 15.8 |
| PNA1-vinyl | Ac-GTAGAT <u>CA</u> CT-LysNH ₂ | vinyl | 3706.0908 | 3710.3410 | 40.2 |
| PNA1-ald | Ac-GTAGAT <u>CA</u> CT-LysNH ₂ | ald | 3750.1438 | 3754.4217 | 6.9 |
| PNA2 | Ac-GTAGATCACT-LysNH ₂ | none | 3583.7848 | 3582.5335 | 23.3 |
| PNA2-vinyl | Ac-GTAGATCACT-LysNH ₂ | vinyl | 3885.1910 | 3884.4323 | 7.1 |
| PNA2-ald | Ac-GTAGATCACT-LysNH ₂ | ald | 4017.3500 | 4016.6003 | 1.1 |

^aThe acpc spacer at the underlined position was replaced with apc spacer.

^bAverage mass of M + H⁺ (PNA2-vinyl and PNA2-ald), M + Na⁺ (PNA1 and PNA2), and M + K⁺ (PNA1-vinyl and PNA1-ald)

^cMALDI-TOF MS

^dIsolated yield after HPLC purification, spectrophotometrically determined

Thermal denaturation experiments provided the melting temperature (T_m) value that indicated the strength of binding of the PNA with its DNA target. The higher the T_m , the more stable the PNA·DNA duplexes. PNA·DNA duplexes typically exhibit higher thermal stabilities than the corresponding DNA·DNA duplexes, which is attributed to the absence of unfavorable electrostatic repulsion between the negatively charged phosphate groups in the DNA backbones. The T_m values were determined at neutral, basic, and acidic pH as the charge in zwitterionic PNA might be sensitive to the pH change.

At pH 7.0, the unmodified apcPNAs (PNA1 and PNA2) showed large T_m values approximately 58.2 and 63.2 °C, indicating strong binding with complementary DNA. The PNA with 3x apc modifications gave higher T_m due to the favorable electrostatic interaction between the positively charged nitrogen atom on the apc residue and the negatively charged phosphate group of DNA. In contrast, the modified apcPNAs (PNA1-vinyl, PNA1-ald,



PNA2-vinyl, and PNA2-ald) bearing one or three zwitterionic aminoalkylsulfonate groups with different linker lengths (Figure 4) at the same pH showed T_m value of approximately 48.6, 48.6, 43.7, and 44.8 °C. Disappointingly, the T_m values of all zwitterionic apcPNAs were lower than those of the unmodified apcPNAs by -9.7, -9.7, -19.5, and -18.7 °C, respectively. This decrease in T_m is likely due to the repulsion between the negatively charged sulfonate groups on the modified apcPNAs and the negative charges on the DNA phosphate backbone, similar to the behavior seen in original DNA·DNA duplexes.

At low pH (pH 4.0), the hybrids between unmodified apcPNAs (PNA1 and PNA2) and DNA showed T_m values of approximately 61.2 and >90 °C, respectively, and modified apcPNAs (PNA1-vinyl, PNA1-ald, PNA2-vinyl, and PNA2-ald) have T_m values of approximately 48.6, 54.4, 48.6, and 55.4 °C, respectively. These values indicate stronger binding with complementary DNA at pH 4.0 compared to pH 7.0. This is due to the favorable electrostatic interaction between the positive charge from the protonated NH^+ groups of the apc spacer in PNA1 (one apc modification) and PNA2 (three apc modification) under acidic conditions and the negative charge of the phosphate groups in the DNA molecules. However, at pH 4.0, the sulfonate group in the zwitterionic PNAs (PNA1-vinyl, PNA1-ald, PNA2-vinyl, and PNA2-ald) may still be in the unprotonated forms due to the low pK_a of the sulfonic acid at approximately 2. Thus, some electrostatic repulsion with the phosphate groups of the DNA molecules still exists, resulting in the lower T_m values observed for modified apcPNAs compared to unmodified apcPNAs.

At high pH (pH 11.0), the results show that neither unmodified apcPNAs (PNA1 and PNA2) nor modified apcPNAs (PNA1-vinyl, PNA1-ald, PNA2-vinyl, and PNA2-ald) were able to show proper T_m values. At high pH, the Watson-Crick base pairing would have been destabilized, which adversely affects the stability of the duplexes.

Table 2.

Thermal melting (T_m) data of zwitterionic pyrrolidinyl PNA.

| PNA | Modifier (x) | T_m (°C) ^{a,c} | | | T_m (°C) ^{b,c} | | | T_m (°C) ^d |
|------------|-----------------|---------------------------|-----------|------------|---------------------------|-----------|------------|-------------------------|
| | | pH 4.0 | pH 7.0 | pH 11.0 | pH 4.0 | pH 7.0 | pH 11.0 | pH 7.0 |
| PNA1 | none | 61.2 | 58.2 | 25.4 | 51.4 | 53.4 | 27.3 | 32.1 |
| PNA1-vinyl | vinyl | 48.6 | 48.6 | 24.4 | 47.7 | 43.7 | <20 | <20 |
| PNA1-ald | ald | 54.4 | 48.6 | <20 | 47.7 | 47.7 | <20 | <20 |
| PNA2 | none | >90 | 63.2 | 34.1 | 52.5 | 54.4 | 30.2 | <20 |
| PNA2-vinyl | vinyl | 48.6 | 43.7 | <20 | 44.8 | 45.7 | 27.2 | <20 |
| PNA2-ald | ald | 55.4 | 44.8 | <20 | 47.7 | 47.7 | 29.3 | <20 |

^aCondition: 10 mM sodium phosphate buffer pH 4.0, 7.0 and 11.0, 0 mM NaCl, [PNA] = 1.0 μM and [DNA] = 1.0 μM

^bCondition: 10 mM sodium phosphate buffer pH 4.0, 7.0 and 11.0, 100 mM NaCl, [PNA] = 1.0 μM and [DNA] = 1.0 μM

^cWith complementary DNA (5'-AGTGATCTAC-3')

^dWith single mismatch DNA (5'-AGTGCTCTAC-3')

PNA generally forms a stable hybrid with its complementary DNA target regardless of salt concentrations due to the uncharged backbone. In contrast, DNA exhibits strong binding with its DNA target at high salt concentrations because the Na^+ ions from salt neutralize the negative charges on the phosphate groups of DNA, effectively reducing

repulsion. Salt concentration may therefore have a significant effect on the zwitterionic molecules, which contain both positive and negative charges within the same structure. As a result, the charges from lone pair electrons on the *N*-atom of unmodified apcPNAs (PNA1 and PNA2) at pH 7.0 are neutralized by Cl⁻ ions from salt, leading to lower T_m values of approximately -4.8 and -8.8 °C compared to the T_m values in the absence of salt. However, modified apcPNAs (PNA1-vinyl, PNA1-ald, PNA2-vinyl, and PNA-ald) with negative charges from sulfonate groups are stabilized by Na⁺ ions. Among these, the triply modified zwitterionic PNA (PNA2-vinyl and PNA2-ald) exhibit stronger binding with DNA targets, with T_m values approximately +2.0°C and +2.9°C, respectively.

Under acidic conditions, more or less the same T_m values were observed for the zwitterionic PNA. However, the T_m for unmodified apcPNAs were much lower than in the absence of salt indicating the important contribution of the electrostatic interaction that is suppressed at high salt concentrations. Interestingly, low but noticeable T_m values were also observed at high salt concentrations for both zwitterionic and unmodified PNA. The sequence specificity was also further confirmed by measuring the T_m of unmodified and modified apcPNAs with a single mismatch DNA target carrying a cytosine base in place of adenine at the middle position. We observed that both unmodified and modified apcPNAs still demonstrate excellent sequence specificity as shown by very low or total absence of measurable T_m (<20 °C) in all cases.

Table 3.
Water solubility of zwitterionic pyrrolidinyl PNA.

| PNA | Modifier (x) | Saturated concentration (mM) ^a | Saturated concentration (mg/mL) |
|------------|-----------------|--|------------------------------------|
| PNA1 | none | 3.3 ± 0.03 | 11.8 ± 0.1 |
| PNA1-vinyl | vinyl | 3.5 ± 0.03 | 12.7 ± 0.1 |
| PNA1-ald | ald | 3.7 ± 0.03 | 13.7 ± 0.1 |
| PNA2 | none | 3.6 ± 0.04 | 12.7 ± 0.2 |
| PNA2-vinyl | vinyl | 3.7 ± 0.06 | 14.4 ± 0.2 |
| PNA2-ald | ald | >1.8 ± 0.02 | >7.3 ± 0.1 |

^aSpectrophotometrically determined by Nanodrop 2000

Next, the water solubilities of unmodified and modified apcPNAs were compared by adding a minimal amount of water until reaching saturation followed by centrifugation, and the concentration was determined spectrophotometrically (Table 2).²² The saturated concentrations for all PNA were more or less the same with or without the zwitterionic modifications. However, the use of apc-modified PNA as a comparator may not be appropriate since they also contain charged groups which should also improve the solubility of the PNA. What can be concluded from the currently available data is that the zwitterionic PNA can dissolve in water to millimolar concentrations that are considered very high since most applications require PNA concentrations in the micromolar ranges or lower. Nevertheless, future studies should aim to compare the solubility of zwitterionic PNA with unmodified apcPNA and to study the impact of the modification on the reduction of non-specific interaction by other means.

In previous modifications of apcPNA, only the cationic-modified PNA backbone (-OH, -NH₂, and guanidine) was reported.²³ These cationic apcPNAs exhibit excellent binding properties with DNA target, improved water solubility approximately 10-fold compared with unmodified apcPNA, and enhanced cell permeability without carrier molecules due to increased positive charges of cationic-modified PNAs. The zwitterionic



PNA developed in this work formed less stable hybrids but still retained good specificity towards complementary DNA targets. For water solubility, the saturated concentrations of the zwitterionic PNA were somewhat lower than the cationic PNA, but the effects on reduced non-specific binding remained to be evaluated.

Conclusion:

In summary, we successfully synthesized zwitterionic acpcPNA by the reaction of apc-modified acpcPNA with sulfonate-containing modifiers including isopropyl ethenesulfonate (compound **1**) and isopropyl 2-(2-oxoethoxy)ethane-1-sulfonate (compound **3**) through Michael addition and reductive alkylation, respectively. DNA binding studies of the zwitterionic PNAs revealed that they bind strongly to the complementary DNA target at neutral or acidic pH, albeit with lower stability than the apc-modified acpcPNA without the zwitterionic modification both in the absence and presence of salt. Additionally, the zwitterionic PNAs exhibit excellent sequence specificity. Regarding water solubility, it is not yet possible to conclude that the zwitterionic PNAs show improved solubility due to the selection of inappropriate comparators.

Acknowledgements:

The authors gratefully acknowledge Synna Science Co., Ltd. for the generous supply of acpcPNA monomers and spacers.

References:

1. Nielsen P E, Egholm M, Berg R H, Buchardt O. *Science*. 1991;254:1497-1500.
2. Egholm M, Buchardt O, Christensen L, Behrens C, Freier S M, Driver D A, Berg R H, Kim S K, Norden B, Nielsen P E. *Nature*. 1993;365:566-568.
3. Nielsen P E, Egholm M, *Curr. Issues Mol. Biol.* 1999;1:89-104.
4. Shakeel S, Karim S, Ali A. J. *Chem. Technol. Biotechnol.* 2006;81:892-899.
5. McNeer N A, Chin J Y, Schleifman E B, Fields R J, Glazer P M, Saltzman W M. *Mol Ther.* 2011;19:172-180.
6. Gupta A, Bahal R, Gupta M, Glazer P M, Saltzman W M. *J Control Release.* 2016;240:302-311.
7. Swenson C S, Heemstra J M. *Chem. Commun.* 2020; ;56:1926-1935.
8. Pokorski J K, Witschi M A, Purnell B L, Appella D H. *J. Am. Chem. Soc.* 2004;126:15067-15073.
9. Sugiyama T, Kittaka A. *Molecules*. 2013;18:287-310.
10. Vilaivan T. *Acc. Chem. Res.* 2015;48:1645-1656.
11. Vilaivan T, Suparpprom C, Harnyuttanakorn P, Lowe G. *Tetrahedron Lett.* 2001;42:5533-5536.
12. Tackett A J, Corey D R, Raney K D. *Nucleic Acids Res.* 2002;30:950-957.
13. Su Y, Bayarjargal M, Hale T K, Filichev V V, Beilstein J. *Org. Chem.* 2021;17:749-761.
14. Hashimoto H, Nelson M G, Switzer C. J. *Am. Chem. Soc.* 1993;115:7128-7134.
15. Meng M, Schmidtgal B, Ducho C. *Langmuir.* 2022;38:4483-4489.
17. Lau S K, Yong W F. *ACS Appl. Polym. Mater.* 2021;3:4390-4412.
18. Liu Y, Zhang D, Ren B, Gong X, Xu L, Feng Z-Q, Chang Y, He Y, Zheng J. *J. Mater. Chem. B.* 2020;8:3814-3828.
19. Ditmangklo B, Muangkaew P, Supabowornsathit K, Vilaivan T. *Methods Mol Biol.* 2020;2105:35-60.

20. Baxter N J, Rigoreau L J M, Laws A P, Page M I. *J. Am. Chem. Soc.* 2000;122:3375-3385.
21. Reenabthue N, Boonlua C, Vilaivan C, Vilaivan T, Suparpprom C. *Bioorg. Med. Chem. Lett.* 2011;21:6465-6469.
22. Sahu B, Sacui I, Rapireddy S, Zanotti K J, Bahal R, Armitage B A, Ly D H. *J. Org. Chem.* 2011;76:5614-5627.
23. Pansuwan H, Ditmangklo B, Vilaivan C, Jiangchareon B, Pan-In P, Wanichwecharungruang S, Palaga T, Nuanyai T, Suparpprom C, Vilaivan T. *Bioconjugate Chem.* 2017;28:2284-2292.



SYNTHESIS AND CHARACTERIZATION OF GREEN TEA-BASED DARK-COLORED MATERIALS

Huzaifa Ahmad, Supason Wanichwecharungruang *

Department of Chemistry, Faculty of Science, Chulalongkorn University, Pathumwan, Bangkok, 10330, Thailand

*e-mail: Supason.P@chula.ac.th

Abstract:

Epigallocatechin-3-gallate (EGCG) is the primary component of green tea extract and is naturally unstable. It can easily convert into a dark-colored material under alkaline and high-temperature conditions. Here we focused on investigating how the pH affects the conversion of EGCG into dark-colored materials. Our UV/VIS absorption spectra of reaction mixtures showed that alkaline conditions (pH 9) gave darker materials as compared to the acidic condition (pH 3). Gel electrophoresis revealed variations in molecular sizes among products from different pH conditions. Solubility tests indicated that the dark-colored material dissolves in water and some polar organic solvents.

Introduction:

Green tea has long been used as a safe medicinal herb worldwide, and it is made from the leaves of *Camellia sinensis*¹. In green tea, the main constituents are polyphenol compounds (24-36% dry weight)². Among these polyphenols, catechins are of particular interest due to their extensive health benefits, including anticancer, antioxidant³, anti-bacterial⁴, anti-diabetic⁵, anti-radiation⁶, anti-viral⁷, and anti-tumor⁸, properties. The most abundant and biologically active catechin in green tea is (-)-epigallocatechin-3-gallate (EGCG)⁹.

Despite its therapeutic benefits, EGCG is naturally unstable, particularly in alkaline environments exposed to oxidation. This instability is caused by its hydroxyl groups at carbons 3', 4', and 5' of the B ring (3' 4' 5'-OH) and the gallate moiety of EGCG, which result in the generation of oxidized products and subsequent polymerization and the formation of the large molecule into dark-colored materials¹⁰.

The change in color of EGCG into a dark-colored material is particularly interesting due to its potential application as a natural colorant¹¹. This transformation occurs through a complex process of oxidation and polymerization, which changes the color and increases the material's stability¹².

In this study, we synthesize and characterize a dark-colored material from EGCG. We aim to understand the chemical transformation under different pH conditions.

Methodology:

Synthesis of Dark-Colored Material

The preparation of dark color material followed by the previous method with some modification¹³. 33 g of (EGCG) was dissolved in 30 ml of phosphate buffer saline (PBS, 0.1 M, pH 9). The solution was set to various pH conductions (pH 3, 7, and 9) by sodium hydroxide (NaOH). To induce auto-oxidation and polymerization, the solution was refluxed at 100°C for two weeks. Finally, the crude reaction mixtures were dried at ambient temperature under moisture control.

Spectral analysis of dark-colored material

Dark-colored material was diluted 100-fold with distilled water. Optizen POP spectrophotometer (GABTI CO., LTD. KOREA) measures the sample from 335 to 800 nm.

Solubility tests of Dark-Colored material in organic solvent

Water, dimethylformamide, dimethyl sulfoxide, methanol, ethanol, acetone, ethyl acetate, chloroform, hexane, and dichloromethane were used to test solubility at room temperature. 5 mg of dark-colored crude reaction mixture was added to each solvent and stirred at 800 rpm for 4 minutes.

Structural Elucidation of Dark-Colored material with 1D and 2D NMR

The samples were subjected to ^1H NMR, ^{13}C NMR, COSY, HSQC, and HMBC spectra were recorded with JEOL JNM-ECZ500R/S1 NMR spectrometers operating at 500 MHz for ^1H or 125 MHz for ^{13}C nuclei.

Gel Electrophoresis

Dark-colored reaction mixtures were compared by gel electrophoresis to determine molecular size. A 0.8%wt gel was obtained from 0.2 g agarose in 25 mL of 1x TAE (Tris-acetate-EDTA) buffer at pH 8.0. Agarose was dissolved in water under 100 °C and put into a gel casting tray. The gel was cooled down to room temperature for 30 minutes. 250 mg dark-colored material was dissolved in 1 ml 0.01 M PBS buffer, pH 7.4. To load each sample, 20 μL of dark-colored material solution was mixed with 60 μL glycerol and 40 μL PBS, and placed in (6x10x0.5cm) agarose gel wells.

The electrophoresis was done at ambient temperature in 0.005 M TAE buffer, pH 8.0. 25 minutes of 100 V constant voltage electrophoresis were monitored. For analysis, the gel was photographed immediately after the run.

Results and Discussion:

The synthesis and characterization of dark-colored material

Figure 1 (A, B, C) demonstrates the UV/VIS spectra of dark-colored materials synthesized from EGCG at various pH levels. The absorption profiles of dark-colored materials synthesized from EGCG at various pH levels (3, 7, and 9) exhibit variations in the UV-Vis spectrum, demonstrating the influence of pH on the polymerization process¹⁴. A broad absorption band around 400–535 nm is observed in the material at pH 3, indicative of highly conjugated polymeric structures formed through extensive auto-oxidation and polymerization under acidic conditions. A slight shift in the absorption profile towards higher wavelengths with more defined peaks at pH 7 suggests the formation of specific chromophores. This shift is attributed to a balanced environment that facilitated controlled oxidation and polymerization, resulting in a more organized polymeric structure. A higher degree of polymerization and the formation of larger conjugated structures under alkaline conditions are suggested by the darker appearance of the material at pH 9, which exhibits the most pronounced absorption with peaks further shifting towards the visible range (~490–640 nm). The significance of pH in determining the extent and nature of polymerization in EGCG is highlighted by these findings, which indicate that alkaline pH levels facilitate the formation of darker materials and more pronounced conjugation¹⁵.

Gel electrophoresis demonstrates the molecular size distribution of dark-colored materials synthesized at various pH levels (pH 3, 7, and 9) as shown in Figure 1 (D). The broad and diffuse band at pH 3 suggests the presence of larger compounds or a heterogeneous mixture of high-molecular-weight compounds, which exhibit limited migration due to their size. At pH 7, the band is more concentrated and extends further, indicating that the material is composed of smaller, more uniform compounds with a consistent molecular weight. At pH 9, the material comprises smaller compounds or a highly homogeneous low molecular weight compound when the darkest and most compact band migrates. The pH 9 material exhibits the most consistent molecular size distribution and the lowest molecular weight, indicating that higher pH levels promote the formation of smaller, more uniform molecular structures¹⁶.



The two compounds, theasinensin, and oolongtheanin (Figure 3), were identified from the crude reaction mixture of the dark-colored material. Their structures were confirmed through ^1H NMR, ^{13}C NMR, COSY, HSQC, and HMBC analyses.

The chemical shifts of the ^{13}C and ^1H atoms are presented in Table 1, with atom numbering corresponding to the structure shown in (Figure 3). The data from the NMR analysis of theasinensin and oolongtheanin allow for direct comparison with previously reported findings in the literature¹⁷, enhancing the structural interpretation of these compounds. In the HMBC analysis of oolongtheanin, key correlations were observed involving the C2-H of Ring (C) with various carbons of Ring (B), including C1 (132.1 ppm), C2 (124.1 ppm), and C6 (106.0 ppm). Additionally, another significant correlation was noted between the C2-H of Ring (C') and various carbons of Ring (B'), specifically C1 (156.7 ppm), C2 (129.3 ppm), and C5 (51.1 ppm).

The absence of the ^1H signal at position C2 of Ring (B) further supports the coupling between Rings (B) and (B'), particularly in theasinensin. Due to the repeating polymeric units in theasinensin, the chemical shifts of Ring (B') are identical to those of Ring (B), and similarly, the shifts of Rings (A', C', and D') are identical to those of Rings A, C, and D, respectively.

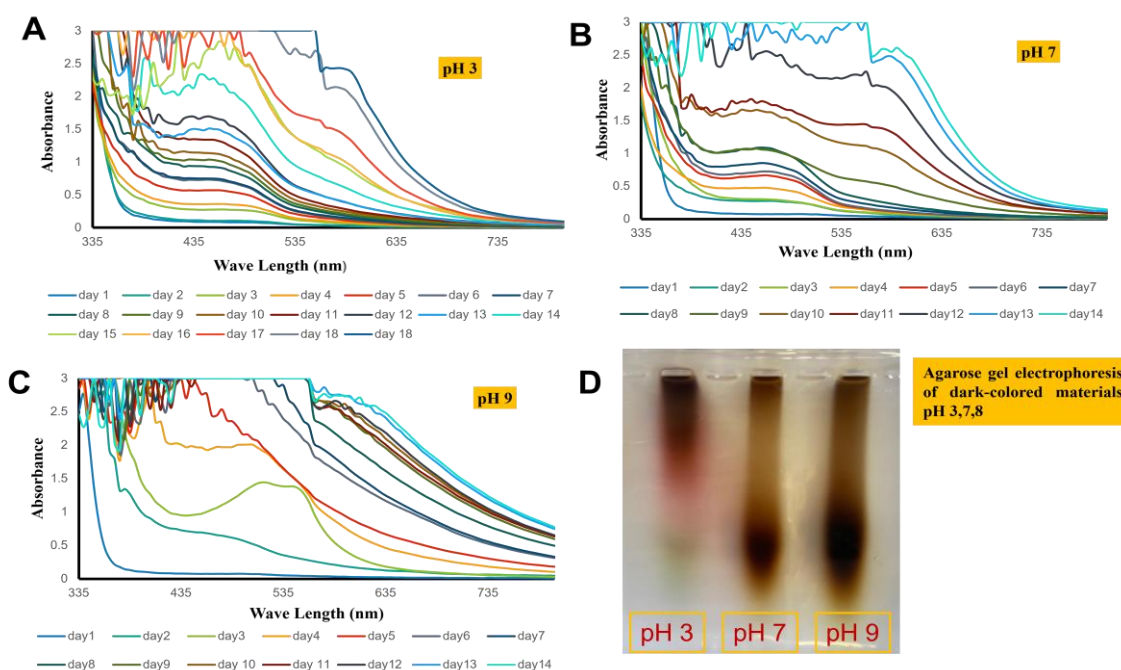


Figure 1: UV/VIS spectra of dark-colored material; (A) pH 3, (B) pH 7, (C) pH 9, and (D) indicate the gel electrophoresis of dark-colored materials synthesized at different pH levels.

Table 1: ^{13}C (125 MHz) and ^1H (500 MHz) NMR data for theasinensina and oolongtheanin in (d_6 – acetone)

| Ring system | Theasinensin | | | | Oolongtheanin | | |
|-------------|--------------|-----------------|--------------|--|-----------------|--------------|--|
| | No | ^{13}C | ^1H | HMBC (^1H to ^{13}C) | ^{13}C | ^1H | HMBC (^1H to ^{13}C) |
| Ring C | 2 | 77.7 | 5.06 | ring (C)3,4 ring (B) 1, 6, 3 | 77.7 | 5.06 | ring(C) 1,2,5,6 ring (B) 3,4 |
| | 3 | 68.8 | 5.52 | ring (C) 2, 4 | 68.8 | 5.52 | ring (C) 2,4 |
| | 4 | 27.2 | 3.02 | ring (C) 3, 2, 4a ring (A) 8a, 5 | 27.1 | 3.02 | ring (C) 3, 2, 4a ring (A) 8a, 5 |
| | 4a | 98.1 | ----- | ----- | 98.1 | ----- | ----- |
| Ring A | 5 | 157 | ----- | ----- | 157 | ----- | ----- |
| | 6 | 95.4 | 5.98 | ring (C) 4a ring (A) 5, 7, 8 | 95.4 | 5.98 | ring (C) 4a ring (A) 5, 7, 8 |
| | 7 | 157 | ----- | ----- | 157 | ----- | ----- |
| | 8 | 95.3 | 6.06 | ring (A) 6, 7, 8a | 95.3 | 6.06 | ring (A) 6, 7, 8a |
| | 8a | 156.0 | ----- | ----- | 156.0 | ----- | ----- |
| Ring B | 1 | 132.1 | ----- | ----- | 131.1 | ----- | ----- |
| | 2 | 112 | ----- | ----- | 124.1 | ----- | ----- |
| | 3 | 146.2 | ----- | ----- | 145.8 | ----- | ----- |
| | 4 | 132.3 | ----- | ----- | 132 | ----- | ----- |
| | 5 | 146.1 | ----- | ----- | 145.8 | ----- | ----- |
| | 6 | 106 | 6.63 | ring (B) 2, 3, 4, 5 | 106 | 6.63 | ring (B) 2,3,4 |
| Ring D, D' | G1 | 122 | ----- | ----- | 122 | ----- | ----- |
| | G2 | 109.3 | 7.05 | ring (D) G1, 3, 4, 5, 7 | 109.3 | 7.05 | ring (D) G1, 3, 4, 5, 7 |
| | G3 | 145 | ----- | ----- | 145 | ----- | ----- |
| | G4 | 138 | ----- | ----- | 138 | ----- | ----- |
| | G5 | 145 | ----- | ----- | 145 | ----- | ----- |
| | G6 | 109.3 | 7.05 | ring (D) G1, 2, 4, 5, 7 | 109.3 | 7.05 | ring (D)G1, 2, 4, 5, 7 |
| | G7 | 165 | ----- | ----- | 165 | ----- | ----- |
| Ring B' | 1' | | | Due to the polymeric structure and repeating unit the chemical shift of the ring B and B' is identical | 156.7 | ----- | ----- |
| | 2' | | | | 129.3 | 6.26 | ----- |
| | 3' | | | | 199 | ----- | ----- |
| | 4' | | | | 94.2 | ----- | ----- |
| | 5' | | | | 51.1 | ----- | ----- |
| Ring C' | 2' | | | Due to the polymeric structure and repeating unit the chemical shift of the ring C and C' is identical | 78.1 | 5.11 | ring (B') 1,2,5 |

Due to the polymeric structure and the repeating units being the same, the chemical shift of rings A and A' remain identical.

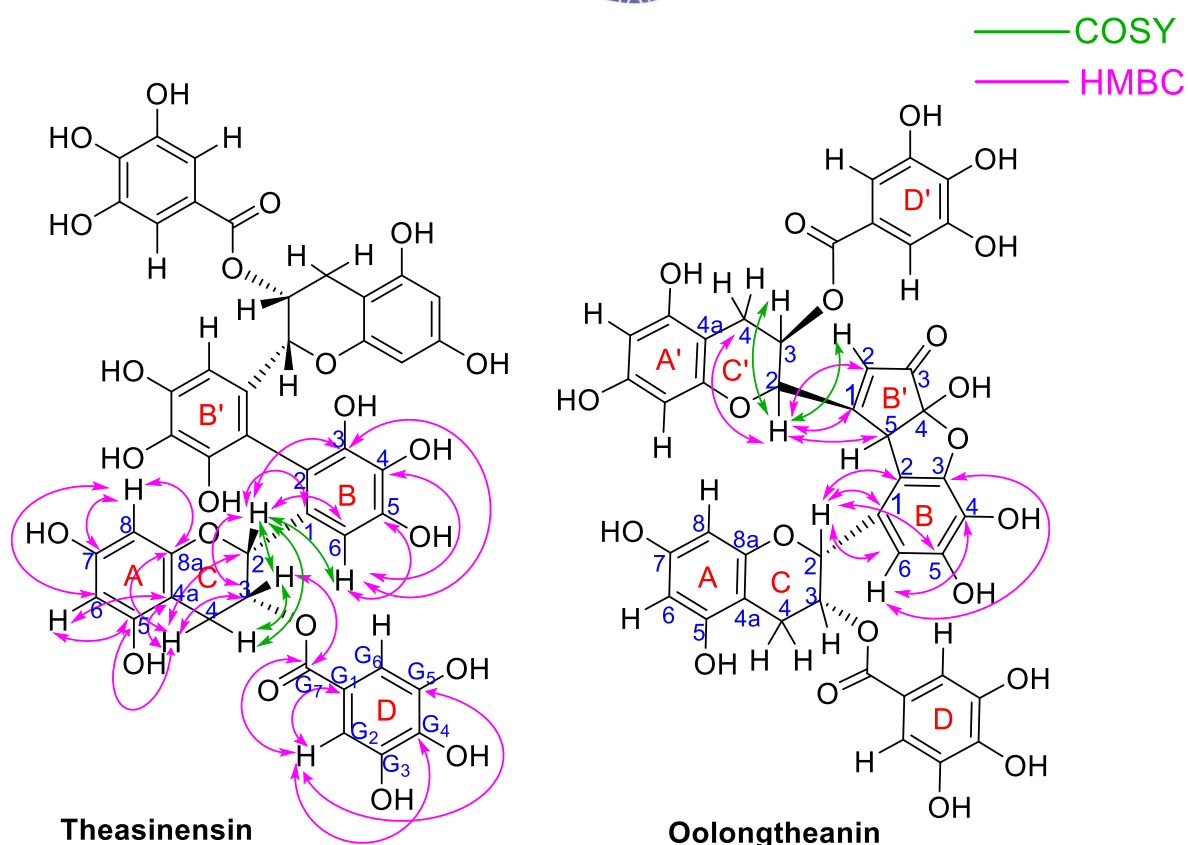


Figure 2: HMBC and COSY correlations of theasinensin and oolongtheanin

Solubility of dark-colored material

The results of the solubility test, as shown in Figure 3, demonstrate that the dark-colored material dissolves in water and polar organic solvents such as dimethylformamide, dimethyl sulfoxide, methanol, ethanol, and acetone. It is partially soluble in ethyl acetate and does not dissolve in non-polar solvents such as chloroform, hexane, and dichloromethane.



Figure 3: solubility of dark-colored material in organic solvents.

Conclusion:

In this study, the dark-colored materials were synthesized by refluxing EGCG in phosphate buffers at pH conditions 3, 7, and 9. UV absorption spectral analysis revealed that the alkaline conditions produced the darkest-colored materials. From the solubility test, the result shows that the dark-colored material was soluble in polar organic solvent. Gel electrophoresis indicates that EGCG polymerized at pH 3 to form larger molecular size compounds with light color, while at pH 7 and 9 the polymerization induced smaller molecular size with darker color. 2-D NMR analyses of the materials indicate the presence of theasniensin and oolongthanin substructure in the polymerized materials.

Acknowledgements:

Huzaifa A. is grateful to Chulalongkorn University's Asian Non-Asian scholarship.

References:

- (1) Wang, T.; Xu, H.; Wu, S.; Guo, Y.; Zhao, G.; Wang, D. Mechanisms underlying the effects of the green tea polyphenol EGCG in sarcopenia prevention and management. *Journal of Agricultural and Food Chemistry* **2023**, 71 (25), 9609-9627.
- (2) Kapoor, M. P.; Sugita, M.; Fukuzawa, Y.; Timm, D.; Ozeki, M.; Okubo, T. Green tea catechin association with ultraviolet radiation-induced erythema: A systematic review and meta-analysis. *Molecules* **2021**, 26 (12), 3702.
- (3) Zhan, C.; Chen, Y.; Tang, Y.; Wei, G. Green tea extracts EGCG and EGC display distinct mechanisms in disrupting A β 42 protofibril. *ACS chemical neuroscience* **2020**, 11 (12), 1841-1851.
- (4) Park, J.; Chi, L.; Kwon, H.-Y.; Lee, J.; Kim, S.; Hong, S. Decaffeinated green tea extract as a nature-derived antibiotic alternative: An application in antibacterial nano-thin coating on medical implants. *Food Chemistry* **2022**, 383, 132399.
- (5) Granja, A.; Frias, I.; Neves, A. R.; Pinheiro, M.; Reis, S. Therapeutic potential of epigallocatechin gallate nanodelivery systems. *BioMed Research International* **2017**, 2017 (1), 5813793.
- (6) Xie, L.-W.; Cai, S.; Zhao, T.-S.; Li, M.; Tian, Y. Green tea derivative (–)-epigallocatechin-3-gallate (EGCG) confers protection against ionizing radiation-induced intestinal epithelial cell death both in vitro and in vivo. *Free Radical Biology and Medicine* **2020**, 161, 175-186.
- (7) Falcó, I.; Randazzo, W.; Gómez-Mascaraque, L. G.; Aznar, R.; López-Rubio, A.; Sánchez, G. Fostering the antiviral activity of green tea extract for sanitizing purposes through controlled storage conditions. *Food Control* **2018**, 84, 485-492.
- (8) Sur, S.; Panda, C. K. Molecular aspects of cancer chemopreventive and therapeutic efficacies of tea and tea polyphenols. *Nutrition* **2017**, 43, 8-15.
- (9) Almatroodi, S. A.; Almatroudi, A.; Khan, A. A.; Alhumaydhi, F. A.; Alsahli, M. A.; Rahmani, A. H. Potential therapeutic targets of epigallocatechin gallate (EGCG), the most abundant catechin in green tea, and its role in the therapy of various types of cancer. *Molecules* **2020**, 25 (14), 3146.
- (10) Shi, M.; Shi, Y.-L.; Li, X.-M.; Yang, R.; Cai, Z.-Y.; Li, Q.-S.; Ma, S.-C.; Ye, J.-H.; Lu, J.-L.; Liang, Y.-R. Food-grade encapsulation systems for (–)-epigallocatechin gallate. *Molecules* **2018**, 23 (2), 445.
- (11) Mohammad, F. Natural colorants in the presence of anchors so-called mordants as promising coloring and antimicrobial agents for textile materials. *ACS Sustainable Chemistry & Engineering* **2015**, 3 (10), 2361-2375.



- (12) Huang, T.-W.; Lu, H.-T.; Ho, Y.-C.; Lu, K.-Y.; Wang, P.; Mi, F.-L. A smart and active film with tunable drug release and color change abilities for detection and inhibition of bacterial growth. *Materials Science and Engineering: C* **2021**, *118*, 111396.
- (13) Wei, Y.; Chen, P.; Ling, T.; Wang, Y.; Dong, R.; Zhang, C.; Zhang, L.; Han, M.; Wang, D.; Wan, X. Certain (–)-epigallocatechin-3-gallate (EGCG) auto-oxidation products (EAOPs) retain the cytotoxic activities of EGCG. *Food chemistry* **2016**, *204*, 218-226.
- (14) Latos-Brozio, M.; Masek, A. Natural polymeric compound based on high thermal stability catechin from green tea. *Biomolecules* **2020**, *10* (8), 1191.
- (15) Chen, S.; Peng, L.; Liu, Y.; Gao, X.; Zhang, Y.; Tang, C.; Zhai, Z.; Yang, L.; Wu, W.; He, X. Conjugated polymers based on metalla-aromatic building blocks. *Proceedings of the National Academy of Sciences* **2022**, *119* (29), e2203701119.
- (16) Bhilocha, S.; Amin, R.; Pandya, M.; Yuan, H.; Tank, M.; LoBello, J.; Shytuhina, A.; Wang, W.; Wisniewski, H.-G.; De La Motte, C. Agarose and polyacrylamide gel electrophoresis methods for molecular mass analysis of 5-to 500-kDa hyaluronan. *Analytical biochemistry* **2011**, *417* (1), 41-49.
- (17) Alfke, J.; Kampermann, U.; Kalinina, S.; Esselen, M. Isolation and structural elucidation of dimeric epigallocatechin-3-gallate autoxidation products and their antioxidant capacity. *European Food Research and Technology* **2021**, *247* (12), 2961-2975.



SYNTHESIS OF 2,3-DIOXOPYRROLIDINE DERIVATIVES AND EVALUATION OF THEIR INHIBITORY ACTIVITY AGAINST NS5 METHYLTRANSFERASE OF DENGUE VIRUS

Dini Aulia,¹ Naphat Loeanurit,² Aphinya Suroengrit², Siwaporn Boonyasuppayakorn², Tanatarn Khotavivattana^{1,*}

¹Center of Excellence in Natural Product Chemistry, Faculty of Science, Chulalongkorn University, Bangkok 10330, Thailand

²Center of Excellence in Applied Medical Virology, Department of Microbiology, Faculty of Medicine, Chulalongkorn University, Bangkok, 10330, Thailand

*e-mail: tanatarn.k@chula.ac.th

Abstract:

Dengue virus has been recognized as a significant leading cause of viral disease globally, and no anti-dengue drug has passed clinical tests. The SAM binding site in the NS5 methyltransferase (MTase) domain presents a promising target for new drug development. Previous studies identified NSC 140047 as a potent MTase inhibitor, with a 2,3-dioxopyrrolidine moiety interacting with key residues in MTase. Building on this, we designed and synthesized novel 2,3-dioxopyrrolidine derivatives with varied substitutions to explore their potential as anti-dengue agents. 2,3-Dioxopyrrolidine derivatives were synthesized through Michael addition of *tert*-butyl acrylate and amine followed by refluxing with diethyl oxalate to form the 2,3-dioxopyrrolidine carboxylate as the key intermediate. Knoevenagel condensation with variations of benzaldehydes under acidic conditions yielded the novel 2,3-dioxopyrrolidine derivatives, which were characterized using ¹H and ¹³C NMR spectroscopy. The anti-dengue activity was determined by an enzymatic assay against DENV2-MTase. Among the compounds tested, compound **2** showed the most potent activity with 95% inhibition at 50 μM. These findings indicated that the hydroxy moiety of the derivative might play an important role in their anti-dengue activity. Moreover, none of the compounds showed high toxicity to the Vero cells.

Introduction:

The Dengue virus (DENV) poses a significant global challenge due to its persistence and the substantial disease burden it imposes, with approximately 400 million people infected worldwide, resulting in several million deaths.¹ Due to the presence of five different serotypes of DENV, it becomes challenging to find the clinically antiviral medication for this disease.^{2,22} In their search to create a therapy for this disease, scientists have identified methyltransferase (MTase) as one of the potential targets. It plays an important role in the early stage of DENV replication, which catalyzes the methyl transfer from *S*-adenosyl-L-methionine, to form the caps of the mRNA at the *N*7 of guanine and the 2'-*O* of the first ribonucleotide.^{3,4} However, the presence of MTases in humans presents the most significant barrier in terms of selectivity.⁵

Several studies have reported some SAH derivatives with exceptionally low IC₅₀ values against DENV MTase, but these derivatives face several issues such as low stability, poor bioavailability, and lack of selectivity.^{6,7} Additionally, the complexity of synthesizing SAH derivatives presents a barrier to discovering new anti-dengue drugs from these analogs.⁸ To overcome these challenges, various strategies have been explored, including structure-based virtual screening. In 2010, Podvinec et al. performed a large-scale virtual screening of commercially available compounds against DENV MTase.⁹ After high throughput docking,

selected compounds were assayed against MTase, and hits with IC_{50} values of less than 10 μ M were identified. Among these, NSC 140047 (**Fig. 1**) was shown to inhibit MTase at the SAM binding site with an IC_{50} of 4.4 μ M. The structure of NSC 140047 includes a 2,3-dioxopyrrolidine moiety at its central part, which interacts similarly to dihydroxyfuran in SAM through conventional hydrogen bonding with His110 and Glu111.¹⁰ However, other studies have shown that NSC 140047 does not bind strongly enough to the NS5 protein of DENV.⁹

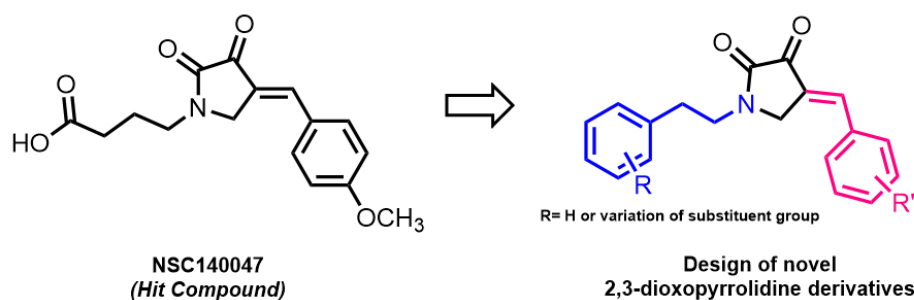


Figure 1. The structure of the hit compound and the design of novel 2,3-dioxopyrrolidine derivatives

Since no one has further explored this promising scaffold for anti-dengue drug discovery yet, we considered using the NSC140047 which contains the 2,3-dioxopyrrolidine linker as the starting point. Considering the feasibility of the synthesis process, we propose to design a novel inhibitor using the 2,3-dioxopyrrolidine in NSC 140047 as the core scaffold and vary substituents at both sides of the ring (**Fig. 1**) to enhance interactions with the SAM binding site, enabling our compound to exhibit better interactions. The synthesized novel analogs were tested for their inhibitory activities against the dengue virus and their toxicity against normal cells. The structure-activity relationship (SAR) was established, which could be key to advancing dengue virus treatment.

Methodology:

General methods

All reagents and solvents are ACS grade, and were purchased from Sigma-Aldrich (St. Louis, MO, USA), and TCI Chemicals (Tokyo, Japan). All reactions were monitored by thin layer chromatography (TLC) using aluminum Merck TLC plates coated with silica gel 60 F254 and column chromatography was performed using silica gel 60 (0.063-0.200 mm, 70-230 mesh ASTM, Merck, Darmstadt, Germany). Structural elucidation with proton, carbon, and fluorine nuclear magnetic resonance (1H , ^{13}C , and ^{19}F NMR) was conducted using Jeol JNM-ECZ500/S1 (500 MHz). The synthetic route of 2,3 dioxopyrrolidine derivatives **1-4** is shown in **Fig. 2**.

The procedure for the synthesis of intermediate compounds

Synthesis of *tert*-butyl 4,5-dioxo-1-phenethylpyrrolidine-3-carboxylate (**Int-1**)

A mixture of phenylethylamine (645 μ L, 5.0 mmol, 1.0 equiv.), and *tert*-butyl acrylate (735 μ L, 5.0 mmol, 1.0 equiv.) in EtOH (2.5 mL) was stirred at room temperature for 16 hours. Diethyl oxalate (690 μ L, 5.0 mmol, 1.0 equiv.) and 5M sodium methoxide 1 mL solution was added. The mixture was stirred under reflux conditions for 1.5 hours. The volatiles were removed *in vacuo*. The crude product was diluted with H_2O (5 mL) and the pH of the mixture was adjusted to 1 by adding concentrated HCl. The mixture was filtrated to afford **Int-1** as a white solid (1.318 g, yield 87%). 1H NMR (500 MHz, $CDCl_3$) δ_H 7.32-7.19



(m, 5H), 3.82 (d, $J = 8.7$ Hz, 1H), 3.80 (s, 2H), 3.73 (dd, $J = 8.4, 6.6$ Hz, 2H), 2.92 (dd, $J = 8.3, 6.7$ Hz, 2H), 1.52 (s, 9H).

Synthesis of *tert*-butyl 4,5-dioxo-1-(2-(3-(trifluoromethyl)phenethyl)pyrrolidine-3-carboxylate (**Int-2**)

The title compound was synthesized according to the method for **Int-1**, using 2-(3-(trifluoromethyl)phenylethylamine (160 μ L, 1.0 mmol, 1 equiv.) as the amine source. **Int-2** was obtained as a white solid (0.285 g, yield 77%). $^1\text{H NMR}$ (500 MHz, CDCl_3) δ_{H} 7.52-7.33 (m, 4H), 3.74 (s, 1H), 3.64 (t, $J = 14.3$ Hz, 2H), 2.91 (t, $J = 12.6$ Hz, 1H), 1.43 (s, 9H).

The procedure for synthesis of 2,3-dioxopyrrolidine derivatives

Synthesis of (*E*)-4-(4-methoxybenzylidene)-1-phenethylpyrrolidine-2,3-dione (**1**)

A mixture of **Int-1** (151 mg, 0.5 mmol, 1.0 equiv.), *p*-anisaldehyde (78 μ L, 0.5 mmol, 1.0 equiv.) in EtOH (0.5 mL)/ 20 % aq. HCl (2 mL) was heated at reflux for 14 h in an oil bath. After cooling down to room temperature, the reaction was extracted with EtOAc. The combined organic layers were washed with brine (3 mL) and H_2O (15 mL) and dried with anhyd. Na_2SO_4 , filtered, and the solvent was removed under reduced pressure to obtain the yellow crude. The pure product was isolated via silica gel column chromatography (eluent: 1:1 hexanes: EtOAc v/v) to obtain **1** (46 mg, 33%) as a bright yellow solid. $^1\text{H NMR}$ (500 MHz, CDCl_3) δ_{H} 7.63 (s, 1H), 7.37-7.38 (d, $J = 8.8$ Hz, 2H), 7.22-7.23 (m, 5H), 6.97 (d, $J = 8.8$ Hz, 2H), 4.32 (s, 1H), 3.86-3.89 (t, $J = 14.9$ Hz, 2H), 3.03-3.06 (t, $J = 7.5$ Hz, 2H); $^{13}\text{C NMR}$ (125 MHz, CDCl_3) δ_{C} 182.9, 166.7, 162.5, 159.4, 137.4, 133.2, 128.9, 128.7, 126.9, 124.9, 120.9, 115.1, 55.1, 48.9, 44.41, 34.1; mp. 161.1-162.8 $^{\circ}\text{C}$.

Synthesis of (*E*)-4-(3-hydroxy-4-methoxybenzylidene)-1-phenethylpyrrolidine-2,3-dione (**2**)

The title compound was synthesized according to the method for **1**, using 3-hydroxy-*p*-anisaldehyde (91 mg, 0.6 mmol, 1.0 equiv.) as the benzaldehyde source. The product was isolated via silica gel column chromatography (eluent: 3:7 hexanes: EtOAc v/v) to obtain **2** (50 mg, 25%) as an orange solid. $^1\text{H NMR}$ (500 MHz, $\text{DMSO}-d_6$) δ_{H} 6.50 (s, 1H), 6.31-6.34 (m, 5H), 6.22-6.25 (m, 1H), 6.19 (s, 1H), 6.18 (s, 1H), 5.94 (d, $J = 8.6$ Hz, 1H), 3.57 (s, 1H), 2.95 (s, 1H), 2.75-2.76 (t, $J = 9.5$ Hz, 2H), 1.98-2.01 (t, $J = 14.7$ Hz, 2H). $^{13}\text{C NMR}$ (500 MHz, $\text{DMSO}-d_6$) δ_{C} 186.9, 161.0, 151.0, 148.5, 139.2, 137.3, 129.2, 129.0, 126.9, 126.7, 125.5, 123.5, 116.7, 116.0, 56.2, 47.1, 45.2, 33.0; mp. 193.2-194.8 $^{\circ}\text{C}$.

Synthesis of (*E*)-4-(3,4-dimethoxybenzylidene)-1-phenethylpyrrolidine-2,3-dione (**3**)

The title compound was synthesized according to the method for **1**, 3-methoxy-*p*-anisaldehyde (83 mg, 0.5 mmol, 1.0 equiv.) as the benzaldehyde source. The pure product was isolated via silica gel column chromatography (eluent: 1:1 hexanes: EtOAc v/v) to obtain **3** (42 mg, 29%) as a bright yellow solid. $^1\text{H NMR}$ (500 MHz, CDCl_3) δ_{H} 7.60 (s, 1H), 7.21-7.33 (m, 5H), 7.04 (dd, $J = 8.4, 2.0$ Hz, 1H), 6.93 (d, $J = 8.4$ Hz, 1H), 6.81 (d, $J = 2.0$ Hz, 1H), 4.25 (d, $J = 2.0$ Hz, 2H), 3.95 (s, 1H), 3.89 (t, $J = 7.2$ Hz, 1H), 3.86 (s, 1H), 3.04 (t, $J = 7.2$ Hz, 1H). $^{13}\text{C NMR}$ (125 MHz, CDCl_3) δ_{C} 186.0, 161.3, 152.3, 149.4, 138.3, 138.2, 128.9, 128.7, 127.0, 126.5, 125.9, 122.8, 113.7, 111.6, 56.2, 56.1, 47.9, 45.9, 33.8; mp. 161.1-161.8 $^{\circ}\text{C}$.

Synthesis of (*E*)-4-(3,4-dimethoxybenzylidene)-1-(3-(trifluoromethyl)phenethyl)pyrrolidine-2,3-dione (**4**)

The title compound was synthesized according to the method for **1**, 3-methoxy-*p*-anisaldehyde (35 mg, 0.213 mmol, 1.0 equiv.) as the benzaldehyde source and **Int-2** (79 mg, 0.213 mmol, 1.0 equiv.) was used for this reaction. The pure product was isolated via silica gel column chromatography (eluent: 1:1 hexanes: EtOAc v/v) to obtain **4** (33 mg, 38%) as a

bright yellow solid. $^1\text{H NMR}$ (500 MHz, CDCl_3) δ_{H} 7.63 (s, 1H), 7.51-7.54 (m, 2H), 7.42-7.48 (m, 2H), 7.07 (dd, $J = 8.4, 2.1$ Hz, 1H), 6.94 (d, $J = 8.5$ Hz, 1H), 6.87 (d, $J = 2.1$ Hz, 1H), 4.36 (s, 2H), 3.95 (s, 3H), 3.89-3.91 (t, $J = 4.3$ Hz, 2H), 3.88 (s, 3H), 3.09-3.12 (t, $J = 14.5$ Hz, 2H). $^{13}\text{C NMR}$ (125 MHz, CDCl_3) δ_{C} 185.7, 161.5, 152.5, 149.5, 138.9, 138.6, 132.3 (q, $^2J_{\text{C-F}}$ 31.5 Hz), 129.4 (q, $^1J_{\text{C-F}}$ 272.2 Hz), 126.4, 125.7 (q, $^3J_{\text{C-F}}$ 2.52 Hz), 123.9, 122.6 (q, $^3J_{\text{C-F}}$ 2.52 Hz), 114.1, 111.6, 56.22, 56.2, 56.1, 47.8, 45.6, 33.5. $^{19}\text{F NMR}$ (471 MHz, CDCl_3) δ_{F} -62.4; **mp.** 201.5-203.3 °C.

Inhibition of DENV-2 MTase

DENV-2 MTase inhibition assay was carried out following the protocols outlined in earlier studies (Boonyasuppayakorn & Padmanabhan, 2014; Loeanurit, et al., 2023).^{16,21}

Anti-Viral Activity and Cytotoxicity Assay

Antiviral assay and cytotoxic screening were carried out following the protocols outlined in earlier studies (Srivarangkul et al., 2018; Suroengrit et al., 2017).^{11,12}

Results and Discussion:

Chemical Synthesis

Novel 2,3-dioxopyrrolidine derivatives (**1-4**) were synthesized according to the recently published work by Wang et al. in 2021,¹³ with some modifications (**Fig. 2**). This method involved a Michael addition between primary amines and excess *tert*-butyl acrylate in EtOH at room temperature, followed by cyclization with diethyl oxalate using NaOMe as a base, yielding 2,3-dioxopyrrolidine carboxylate intermediates, **Int-1** and **Int-2**, with yields of 77% and 87%, respectively. Finally, the modification of the C4 position of the 2,3-dioxopyrrolidine linker was achieved by performing a Knoevenagel condensation with various benzaldehydes under acidic conditions (20% HCl). This reaction produced compounds **1-4**, bearing methoxy and hydroxy groups on the phenyl ring. The reason for selecting specific substituents on benzaldehyde involves retaining the *p*-methoxy group found in the hit compound and introducing methoxy or hydroxy groups at the *meta* position to introduce more hydrogen bond donors/acceptors at the target site.

Previous studies have reported yields for this reaction ranging from 35% to 80%. However, in this work, the yields of compounds **1-4** ranged from 25-38%. We hypothesized that the concentration of hydrochloric acid might be a factor influencing the yield. For the original concentration of acid (20% HCl), we observed that some starting material remained unreacted, as confirmed by TLC analysis, even after allowing the reaction to proceed for 14 hours. When the HCl concentration was increased to 30%, the starting material was fully consumed. However, further increases in acid concentration resulted in product decomposition, as evidenced by a new spot appearing at the baseline on the TLC plate. This decomposition not only complicated the purification process but also further reduced the overall yield. These findings underscore the importance of carefully optimizing the acid concentration to achieve a balance between complete reaction and minimal decomposition.¹⁷

Additionally, the substituents on the benzaldehyde are also likely influence the yield. Electron-donating groups such as methoxy and hydroxyl groups used in this study, can reduce the reactivity of the carbonyl group, potentially lowering yields. Conversely, electron-withdrawing groups can enhance the electrophilicity of the aldehyde, typically resulting in higher yields.¹⁸ Moving forward, we plan to synthesize additional analogs with varying substituents to further explore their impact on reaction yield.

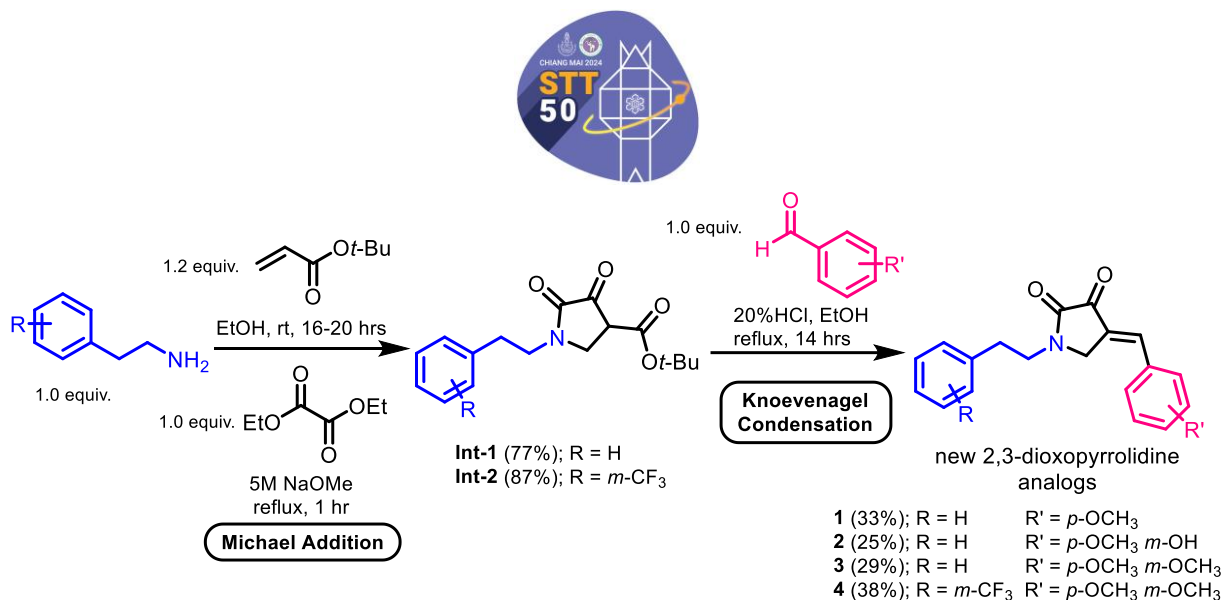


Figure 2. Synthetic scheme of 2,3-dioxopyrrolidine derivatives (**1-4**)

Inhibition against DENV-2 MTase

The four synthesized novel 2,3-dioxopyrrolidine derivatives were tested against NS5 MTase of DENV2 at 50 μ M. As shown in **Fig. 3**, sinefungin, the known inhibitor for MTase¹⁴, was used as a control in MTase enzymatic assays. Among the compounds synthesized, compound **2** shows the strongest inhibition exceeding 90%, compared to no inhibitor control. In contrast, the remaining compounds (**1**, **3-4**) did not show any inhibitory effect. The chemical structure of compound **2**, which is absent in the others, was hydroxyl group moiety at *meta* position predicted to be a key contributing factor. This specificity can be particularly important for achieving potent inhibition.

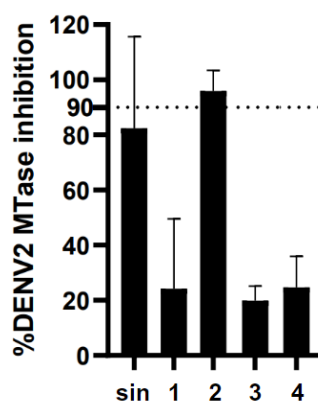


Figure 3. DENV2 MTase enzymatic assay results of the synthesized compounds at 50 μ M

Anti-Viral Activity and Cytotoxicity

A toxicity study of the final compounds was carried out using Vero cell lines (**Fig. 4**). Among the final compounds, none were detected as toxic compounds even at 50 μ M. Those final compounds give almost 100% cell viability of normal cells, implying that these compounds are relatively safe. However, the antiviral assay results (**Fig. 4**) indicated that none of the compounds tested at a concentration of 50 μ M showed significant antiviral activity against DENV2. The discrepancies were usually due to solubility or permeability issues.^{19,20}

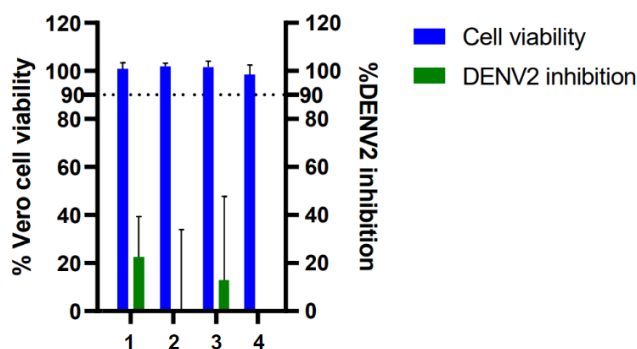


Figure 4. Cytotoxicity and DENV2 anti-viral activity of the synthesized compounds at 50 μ M

Conclusion:

We have modified and synthesized novel 2,3-dioxopyrrolidine derivatives (**1-4**) in two key steps. The cytotoxicity, antiviral activity against DENV, and enzyme inhibition activity against DENV2-MTase of the synthesized compounds were reported. All synthesized compounds exhibit non-toxic properties towards normal cells. Notably, compound **2** demonstrates the most effective inhibition of DENV2-MTase activity. However, none of the compounds have shown significant activity in inhibiting DENV2 itself. These findings provide a foundation for our further research aimed at discovering anti-dengue therapeutics.

Acknowledgements:

Dini Aulia is grateful to the Chulalongkorn University graduate scholarship for ASEAN and non-ASEAN countries that funding her Master's program. The reagent of methyltransferase assay is supported by the National Research Council of Thailand and Chulalongkorn University to SB.

References:

1. Brady OJ, Gething PW, Bhatt. PLoS Negl Trop Dis. 2012; 1:1-15.
2. Wilson ME, Chen LH. Curr Infect Dis Rep. 2015; 457:1-8.
3. Gan SJ, Leong YQ, Barhanuddin, MFH. Parasit Vectors. 2021; 14: 1-19.
4. Obi JO, Barbosa HG, Chua JV, Deredge DJ. Trop Med Infect Dis. 2021; 6: 1-19.
5. Ramanathan A, Robb GB, Chan, SH. Nucleic Acids Res. 2016; 44: 7511-7526.
6. Lim SP, Sonntag LS, Noble C, Nilar SH, Ng RH, Zou G, Monaghan, P, Chung, KY. J Biol Chem. 2011; 286: 6233-6240.
7. Fischer FR, Meidner L, Schwickert M, Weber M, Zimmermann, RA, Kersten C, Schirmeister T, Helm M, Nucleic Acids Res. 2022; 50: 4216-4245.
8. Chen H, Zhou B, Brecher M, Banavali N, Jones SA, Li Z, Zhang J, Nag D, Kramer LD, Ghosh AK, Li H. PLoS ONE. 2013; 8: 1-12.
9. Podvinec M, Lim SP, Schmidt T, Scarsi M, Wen D, Sonntag LLS, Sanschagrin P, Shenkin PS, Schwede T. J Med Chem. 2010; 53: 1483-1495.
10. Tambunan USF, Nasution, MAF, Azhima F, Parikesit AA, Toepak EP, Idrus S, Kerami D. Drug Target Insights. 2017; 11:1-14.
11. Srivarangkul P, Yuttithamnon W, Suroengrit A, Pankaew S, Hengphasatporn K, Rungrotmongkol T, Phuwapraisirisan P, Ruxrungtham K, Boonyasuppayakorn S. Antivir Res. 2018; 151: 27-28.
12. Suroengrit A, Yuttithamnon W, Srivarangkul P, Pankaew S, Kingkaew K, Chavasiri W, Boonyasuppayakorn S, Sci Rep. 2017; 7: 13696.
13. Wang H, Zeng T, Liu L, Chang W, Li J. Org Lett. 2021; 23: 3573-3577.



14. Wangikar P, Martis EAF, Ambre PK, Nandan S, Coutinho EC. *J Emerg Infect Dis.* 2016; 1: 1-10.
15. Wu M, Sirota M, Butte AJ, Chen B. *Pac Symp Biocomput.* 2015: 68-79.
16. Boonyasuppayakorn, S., Padmanabhan, R. *Methods Mol Biol.* 2014; 1138: 361-373
17. Van BK, De KS, Molendijk D, Van SJ. *Green Chem Lett Rev.* 2020; 13: 349-364.
18. Biswajit B, Dilip KM, Pradip P, Enrique C, Debajyoti G. *Inorg. Chem. Front.* 2014; 1: 414-425
19. Emilse SL, Natalia SA, Gabriela AF, Leopoldo GG, Leandro B, Maria GA, Mariela V, María EM, Alejandro HR, John AAD, María LM, Sandra MC, Cybele CG, Andrea VG, Claudio NC, Mariela B. *Eur J Med Chem.* 2019; 182 : 111628.
20. Wang QY, Patel SJ, Vangrevelinghe E, Xu HY, Rao R, Jaber D, Schul W, Gu F, Heudi O, Ma NL, Poh MK, Phong WY, Keller TH, Jacoby E, Vasudevan SG. *Antimicrob Agents Chemother.* 2009; 53: 1823-1831.
21. Loeanurit N, Tuong TL, Nguyen VK, Vibulakhaophan V, Hengphasatporn K, Shigeta Y, Ho SX, Chu JJH, Rungrotmongkol T, Chavasiri W, Boonyasuppayakorn S. *Molecules.* 2023; 28: p. 974.
22. Palanichamy KM, St John AL, Rathore APS. *Curr Treat Options Infect Dis.* 2023; 15: 27-52.



SYNTHESIS OF ALKYLATED 9-*O*-BERBERRUBINE DERIVATIVES AS YEAST α -GLUCOSIDASE INHIBITORS

Nattanit Suddee,¹ Duy Vu Nguyen,² Warinthorn Chavasiri^{1,*}

¹ Center of Excellence in Natural Products Chemistry, Department of Chemistry, Faculty of Science, Chulalongkorn University, Bangkok 10330, Thailand.

² Faculty of Environment and Labour Safety, Ton Duc Thang University, Ho Chi Minh City, Vietnam

*e-mail: warinthorn.c@chula.ac.th

Abstract:

Diabetes mellitus is a chronic disease in which the pancreas fails to produce enough insulin, leading to increasing blood sugar levels, more than 90% of diabetic patients suffer from type-2 diabetes. To treat type 2 diabetes, one strategy is to inhibit α -glucosidase, which was a crucial enzyme to hydrolyze polysaccharides into absorbable glucose. Berberrubine (BBRB) is a key active metabolite of berberine (BBR), a natural product with a wide range of pharmacological activities. It has potential benefits in the treatment of diabetes, as it can regulate glucose as an alternative option because natural products are less toxic and have fewer side effects. Sixteen 9-*O*-berberrubine derivatives with hydrophobic substituents were synthesized and well characterized by spectroscopic means. Most derivatives revealed higher antidiabetic activity than BBR, BBRB, and the positive control acarbose, based on their inhibitory activities against yeast α -glucosidase. Among the tested compounds, compounds **2f**, **2g** and **2h** with $-C_{10}$, $-C_{12}$ and $-C_{16}$ alkyl chains showed the inhibition with IC_{50} value of 0.40, 1.71 and 2.76 μ M, respectively. The results suggested that increasing hydrophobicity by addition numbers of carbon atoms, improved inhibition activity. The kinetic study was performed using the most potent derivative **2f**, the result revealed the competitive mode of action. This indicated that this series occupied the active site of α -glucosidase. Accordingly, alkylated 9-*O*-berberrubine derivatives are good candidate for diabetic drugs in the future.

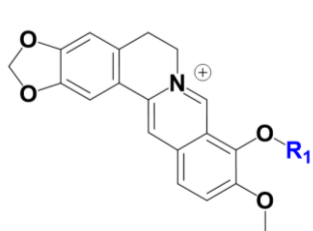


Figure 1. Core structure of alkylated 9-*O*-berberrubine derivatives

Introduction:

Diabetes mellitus is a metabolic disease that causes high blood sugar by over 90% of diabetic patients have type 2 diabetes (T2D) which is caused by two factors: insufficient insulin production from the pancreas and a poor insulin response known as insulin resistance, leading to less sugar intake by cells, causing hyperglycemia. A common strategy for controlling blood glucose levels is to reduce carbohydrate absorption. Inhibiting α -glucosidase is a key therapeutic target for lowering blood sugar levels as it reduces the hydrolysis of carbohydrates into monosaccharide units that enter the bloodstream. However, commercial inhibitors such as acarbose, miglitol and voglibose are frequently associated with gastrointestinal side effects such as nausea, diarrhea, and liver problems.¹ Therefore, the

development of inhibitors from natural products offers an alternative option for the control of hyperglycemia because traditional herbal remedies are less toxic and have fewer side effects.

BBR is one of the natural products belong to isoquinoline alkaloids found in the roots and stem barks of *Hydrastis canadensis*, *Coptis chinensis*, *Berberis aquifolium*, *Berberis vulgaris*, and *Berberis aristata*.^{2, 3} It is composed of five rings, the core structure of which is benzyl tetrahydroisoquinoline, which has key bioactive metabolite known as **BBRB**. It showed various pharmacological activities such as antiparasitic, antihyperlipidemic,⁴ anti-Alzheimer's disease,⁵ anticancer,⁶ antiobesity,⁷ antidiabetic, as well as lipid lowering agents.⁸

According to several studies in clinical research and animal studies, 9-*O*-berberrubine is easily functionalized to provide derivatives that have shown potential benefits in medicinal chemistry, particularly in drug design and development of diabetes because it could regulate glucose, lipid metabolism, and reduce insulin resistance through its effects on hyperglycemia and dyslipidemia. **BBR** and **BBRB** have been reported for anti-glucosidase in a competitive manner, according to molecular docking studies, the main interaction involved hydrophobic interactions with the enzyme. Additionally, previous research has demonstrated that adding benzoic esters to 9-*O*-**BBRB** leading molecules to enhance their anti-glucosidase inhibitory activity against yeast.⁹

The aim of this study was to investigate α -glucosidase inhibition effect by introducing various alkyl chains at the 9-*O*-position and to establish the potency of alkyl 9-*O*-**BBRB** for antidiabetic activity.

Methodology:

General procedure for the synthesis of **BBRB**

BBR chloride was heated at 190° C for 4 h. The reaction was allowed to cool to room temperature to furnish **BBRB** as red wine solid, 89% yield. ¹H NMR (500 MHz, DMSO-*d*₆) δ _H 9.08 (s, 1H), 7.99 (s, 1H), 7.61 (s, 1H), 7.22 (d, *J* = 8.0 Hz, 1H), 6.96 (s, 1H), 6.37 (d, *J* = 7.8 Hz, 1H), 6.09 (s, 2H), 4.48 (t, *J* = 6.1 Hz, 2H), 3.72 (s, 3H), 3.04 (t, *J* = 6.1 Hz, 2H). ¹³C NMR (125 MHz, DMSO-*d*₆) δ _C 166.8, 149.7, 148.4, 147.4, 145.9, 133.3, 132.1, 129.4, 121.9, 121.4, 120.0, 117.3, 108.4, 104.8, 101.7, 101.4, 55.8, 52.5, 27.5.

General procedure for the synthesis of alkyl 9-*O*-**BBRB** (**2**)

BBRB 1 mmol and alkyl halide or tosylate (2.0 equiv) were stirred in 3.00 mL of CH₃CN under refluxed for 8–16 h. After completion, the reaction mixture was allowed to cool to room temperature. The crude product was purified by column chromatography on silica gel using 10% MeOH /DCM as eluent to afford alkyl 9-*O*-**BBRB** **2**.

9-ethoxy-10-methoxy-5,6-dihydro-[1,3]dioxolo[4,5-*g*]isoquinolino[3,2-*a*]isoquinolin-7-ium (**2a**) as yellow solid, 72% yield. ¹H NMR (500 MHz, DMSO-*d*₆) δ _H 9.81 (s, 1H), 8.94 (s, 1H), 8.19 (d, *J* = 9.2 Hz, 1H), 7.99 (d, *J* = 9.1 Hz, 1H), 7.78 (s, 1H), 7.08 (s, 1H), 6.17 (s, 2H), 4.96 (t, *J* = 6.4 Hz, 2H), 4.36 (q, *J* = 7.0 Hz, 2H), 4.05 (s, 3H), 3.21 (t, *J* = 6.4 Hz, 2H), 1.45 (t, *J* = 7.0 Hz, 3H). ¹³C NMR (125 MHz, DMSO-*d*₆) δ _C 150.5, 149.9, 147.7, 145.4, 142.0, 137.5, 133.8, 133.0, 130.8, 126.6, 123.6, 121.9, 120.5, 120.3, 119.2, 108.5, 105.5, 102.1, 74.6, 57.1, 55.3, 26.7.¹⁰

9-(isopentyloxy)-10-methoxy-5,6-dihydro-[1,3]dioxolo[4,5-*g*]isoquinolino[3,2-*a*]isoquinolin-7-ium (**2b**) as yellow solid, 60% yield. ¹H NMR (500 MHz, DMSO-*d*₆) δ _H 9.74 (s, 1H), 8.93 (d, *J* = 4.5 Hz, 1H), 8.20 (d, *J* = 9.2 Hz, 1H), 7.99 (d, *J* = 9.1 Hz, 1H), 7.79 (s, 1H), 7.09 (s, 1H), 6.17 (s, 2H), 4.95 (t, *J* = 6.4 Hz, 2H), 4.32 (t, *J* = 6.8 Hz, 2H), 4.06 (s, 3H), 3.21 (t, *J* = 6.3 Hz, 2H), 1.87 (tt, *J* = 14.6, 7.4 Hz, 1H), 1.79 (q, *J* = 6.9 Hz, 2H), 0.99 (d, *J* = 6.6 Hz, 6H). ¹³C NMR (125 MHz, DMSO-*d*₆) δ _C 150.4, 149.8, 147.7, 145.3, 142.8, 137.5, 133.0, 130.7, 126.6, 123.3, 121.7, 120.5, 120.2, 108.4, 105.4, 102.1, 72.7, 57.0, 55.3, 38.2, 26.3, 24.5, 22.5 (2C). HRMS (ESI) calcd. for C₂₄H₂₆NO₄⁺ (M)⁺ : 392.1856 found 392.1851.



9-Butoxy-10-methoxy-5,6-dihydro-[1,3]dioxolo[4,5-g]isoquinolino[3,2-a]isoquinolin-7-ium (**2c**) as a yellow solid, 68% yield. ^1H NMR (500 MHz, $\text{DMSO}-d_6$) δ_{H} 9.74 (s, 1H), 8.94 (s, 1H), 8.19 (d, $J = 9.1$ Hz, 1H), 7.99 (d, $J = 9.1$ Hz, 1H), 7.79 (s, 1H), 7.09 (s, 1H), 6.17 (s, 2H), 4.95 (t, $J = 6.4$ Hz, 2H), 4.29 (t, $J = 6.8$ Hz, 2H), 4.05 (s, 3H), 3.21 (t, $J = 6.3$ Hz, 2H), 1.86 (p, $J = 6.9$ Hz, 2H), 1.51 (h, $J = 7.4$ Hz, 2H), 0.98 (t, $J = 7.4$ Hz, 3H). ^{13}C NMR (125 MHz, $\text{DMSO}-d_6$) δ_{C} 150.4, 149.8, 147.7, 145.3, 142.9, 137.5, 133.0, 130.7, 126.7, 123.3, 121.7, 120.5, 120.3, 108.5, 105.5, 102.1, 74.0, 57.1, 55.4, 31.6, 26.4, 18.6, 13.8.¹⁰

9-(Hexyloxy)-10-methoxy-5,6-dihydro-[1,3]dioxolo[4,5-g]isoquinolino[3,2-a]isoquinolin-7-ium (**2d**) as a yellow solid, 71% yield. ^1H NMR (500 MHz, $\text{DMSO}-d_6$) δ_{H} 9.75 (s, 1H), 8.94 (s, 1H), 8.20 (d, $J = 9.1$ Hz, 1H), 7.99 (d, $J = 9.1$ Hz, 1H), 7.80 (s, 1H), 7.09 (s, 1H), 6.17 (s, 2H), 4.95 (t, $J = 6.2$ Hz, 2H), 4.28 (t, $J = 6.9$ Hz, 2H), 4.05 (s, 3H), 3.20 (t, $J = 6.3$ Hz, 2H), 1.87 (p, $J = 7.1$ Hz, 2H), 1.48 (q, $J = 7.3$ Hz, 2H), 1.39 – 1.32 (m, 4H), 0.90 (t, $J = 4.5$ Hz, 3H). ^{13}C NMR (125 MHz, $\text{DMSO}-d_6$) δ_{C} 150.4, 149.8, 147.7, 145.3, 142.9, 137.4, 133.0, 130.7, 126.7, 123.4, 121.7, 120.5, 120.2, 108.5, 105.5, 102.1, 74.3, 57.1, 55.3, 31.1, 29.5, 26.4, 25.0, 22.1, 14.0.¹⁰

10-Methoxy-9-(octyloxy)-5,6-dihydro-[1,3]dioxolo[4,5-g]isoquinolino[3,2-a]isoquinolin-7-ium (**2e**) as a yellow solid, 52% yield. ^1H NMR (500 MHz, $\text{DMSO}-d_6$) δ_{H} 9.75 (s, 1H), 8.95 (s, 1H), 8.19 (d, $J = 9.1$ Hz, 1H), 7.99 (d, $J = 9.1$ Hz, 1H), 7.80 (s, 1H), 7.09 (s, 1H), 6.17 (s, 2H), 4.95 (t, $J = 6.4$ Hz, 2H), 4.27 (t, $J = 6.8$ Hz, 2H), 4.05 (s, 3H), 3.21 (t, $J = 6.3$ Hz, 2H), 1.87 (p, $J = 6.9$ Hz, 2H), 1.47 (p, $J = 8.4$ Hz, 2H), 1.41 – 1.21 (m, 8H), 0.87 (t, $J = 7.3$ Hz, 3H). ^{13}C NMR (125 MHz, $\text{DMSO}-d_6$) δ_{C} 150.4, 149.8, 147.7, 145.3, 142.9, 137.5, 133.0, 130.7, 126.7, 123.3, 121.7, 120.5, 120.2, 108.4, 105.5, 102.1, 74.3, 57.0, 55.3, 31.3, 29.5, 28.8, 28.7, 26.3, 25.3, 22.1, 14.0.¹⁰

9-(Dodecyloxy)-10-methoxy-5,6-dihydro-[1,3]dioxolo[4,5-g]isoquinolino[3,2-a]isoquinolin-7-ium (**2f**) as a yellow solid, 47% yield. ^1H NMR (500 MHz, $\text{DMSO}-d_6$) δ_{H} 9.74 (s, 1H), 8.93 (s, 1H), 8.19 (d, $J = 9.2$ Hz, 1H), 7.99 (d, $J = 9.0$ Hz, 1H), 7.79 (s, 1H), 7.09 (s, 1H), 6.17 (s, 2H), 4.94 (t, $J = 6.4$ Hz, 2H), 4.27 (t, $J = 6.8$ Hz, 2H), 4.04 (s, 3H), 3.21 (t, $J = 6.3$ Hz, 2H), 1.87 (p, $J = 7.0$ Hz, 2H), 1.47 (p, $J = 7.2$ Hz, 2H), 1.38 – 1.25 (m, 12H), 0.85 (t, $J = 6.7$ Hz, 3H). ^{13}C NMR (125 MHz, $\text{DMSO}-d_6$) δ_{C} 150.4, 149.8, 147.7, 145.3, 142.9, 137.5, 133.0, 130.7, 126.7, 123.3, 121.7, 120.5, 120.2, 108.5, 105.5, 102.1, 74.3, 57.1, 55.4, 31.3, 29.5, 29.1, 29.0, 28.9, 28.8, 26.4, 25.3, 22.2, 14.0.¹¹

9-(Dodecyloxy)-10-methoxy-5,6-dihydro-[1,3]dioxolo[4,5-g]isoquinolino[3,2-a]isoquinolin-7-ium (**2g**) as a yellow solid, 48% yield. ^1H NMR (500 MHz, $\text{DMSO}-d_6$) δ_{H} 9.71 (s, 1H), 8.90 (s, 1H), 8.16 (d, $J = 9.2$ Hz, 1H), 7.95 (d, $J = 9.2$ Hz, 1H), 7.76 (s, 1H), 7.06 (s, 1H), 6.14 (s, 2H), 4.91 (t, $J = 6.4$ Hz, 2H), 4.24 (t, $J = 6.8$ Hz, 2H), 4.01 (s, 3H), 3.17 (t, $J = 6.3$ Hz, 2H), 1.83 (p, $J = 6.9$ Hz, 2H), 1.43 (p, $J = 7.1$ Hz, 2H), 1.36 – 1.19 (m, 16H), 0.81 (t, $J = 6.7$ Hz, 3H). ^{13}C NMR (125 MHz, $\text{DMSO}-d_6$) δ_{C} 150.5, 149.9, 147.7, 145.4, 142.9, 137.5, 133.0, 130.7, 126.7, 123.3, 121.7, 108.5, 105.5, 102.1, 74.3, 57.1, 55.0, 48.6, 31.3, 30.8, 29.5, 29.1, 29.1 (2C), 28.9, 28.8, 26.4, 25.3, 22.2, 14.0.¹¹

9-(Hexadecyloxy)-10-methoxy-5,6-dihydro-[1,3]dioxolo[4,5-g]isoquinolino[3,2-a]isoquinolin-7-ium (**2h**) as a yellow solid, 41% yield. ^1H NMR (500 MHz, $\text{DMSO}-d_6$) δ_{H} 9.74 (s, 1H), 8.93 (s, 1H), 8.19 (d, $J = 9.2$ Hz, 1H), 7.99 (d, $J = 9.1$ Hz, 1H), 7.79 (s, 1H), 7.09 (s, 1H), 6.17 (s, 2H), 4.94 (t, $J = 6.4$ Hz, 2H), 4.27 (t, $J = 6.8$ Hz, 2H), 4.05 (s, 3H), 3.20 (t, $J = 6.4$ Hz, 2H), 1.87 (p, $J = 7.0$ Hz, 2H), 1.47 (p, $J = 7.1$ Hz, 2H), 1.24 (d, $J = 9.5$ Hz, 24H), 0.84 (t, $J = 6.8$ Hz, 3H). ^{13}C NMR (125 MHz, $\text{DMSO}-d_6$) δ_{C} 150.4, 149.8, 147.7, 145.3, 142.9, 137.5, 133.0, 130.7, 126.7, 123.3, 121.7, 120.5, 120.2, 108.5, 105.4, 102.1, 74.2, 57.1, 55.3, 31.3, 29.5, 29.1 (5C), 29.0 (3C), 28.9, 28.7, 26.4, 25.3, 22.1, 14.0.¹¹

(*Z*)-10-Methoxy-9-(octadec-9-en-1-yloxy)-5,6-dihydro-[1,3]dioxolo[4,5-*g*]isoquinolino[3,2-*a*]isoquinolin-7-ium (**2i**) as a yellow solid, 59% yield. ¹H NMR (500 MHz, DMSO-*d*₆) δ_H 9.75 (s, 1H), 8.93 (s, 1H), 8.19 (d, *J* = 9.2 Hz, 1H), 7.98 (d, *J* = 9.1 Hz, 1H), 7.80 (s, 1H), 7.50 – 7.43 (m, 2H), 7.14 – 7.07 (m, 2H), 5.37 – 5.27 (m, 2H), 4.94 (t, *J* = 6.5 Hz, 2H), 4.27 (t, *J* = 6.8 Hz, 2H), 4.04 (s, 3H), 3.21 (d, *J* = 6.5 Hz, 2H), 2.28 (s, 3H), 1.97 (q, *J* = 6.6 Hz, 3H), 1.87 (p, *J* = 6.9 Hz, 2H), 1.47 (p, *J* = 7.2 Hz, 2H), 1.26 (d, *J* = 34.6 Hz, 24H), 0.88 – 0.79 (m, 3H). ¹³C NMR (125 MHz, DMSO-*d*₆) δ_C 150.4, 149.8, 147.7, 145.7, 145.3, 142.8, 137.6, 137.4, 133.0, 130.7, 129.6, 128.0 (2C), 126.6, 125.5 (2C), 123.4, 121.6, 120.5, 120.2, 108.4, 105.4, 102.1, 74.2, 57.0, 55.3, 31.3, 29.5, 29.2, 29.1, 29.1, 29.0, 28.9 (2C), 28.7, 28.7, 28.6, 26.6, 26.6, 26.4, 25.3, 22.1, 20.8, 14.0. HRMS (ESI) calcd. for C₃₇H₅₀NO₄⁺ (M)⁺: 572.3734 found 572.3735.

9-(Allyloxy)-10-methoxy-5,6-dihydro-[1,3]dioxolo[4,5-*g*]isoquinolino[3,2-*a*]isoquinolin-7-ium (**2j**) as a yellow solid, 62% yield. ¹H NMR (500 MHz, DMSO-*d*₆) δ_H 9.81 (s, 1H), 8.93 (s, 1H), 8.20 (d, *J* = 9.1 Hz, 1H), 8.00 (d, *J* = 9.1 Hz, 1H), 7.80 (s, 1H), 7.09 (s, 1H), 6.26 – 6.19 (m, 1H), 6.17 (s, 2H), 5.43 (dd, *J* = 17.2, 1.7 Hz, 1H), 5.28 (dd, *J* = 10.4, 1.6 Hz, 1H), 4.94 (t, *J* = 6.3 Hz, 2H), 4.86 (dt, *J* = 6.0, 1.3 Hz, 2H), 4.06 (s, 3H), 3.21 (d, *J* = 6.3 Hz, 2H). ¹³C NMR (125 MHz, DMSO-*d*₆) δ_C 150.5, 149.9, 147.7, 145.4, 142.0, 137.5, 133.8, 133.0, 130.8, 126.6, 123.6, 121.9, 120.5, 120.3, 119.2, 108.5, 105.5, 102.1, 74.6, 57.1, 55.3, 26.4.¹²

10-Methoxy-9-(prop-2-yn-1-yloxy)-5,6-dihydro-[1,3]dioxolo[4,5-*g*]isoquinolino[3,2-*a*]isoquinolin-7-ium (**2k**) as a yellow solid, 44% yield. ¹H NMR (500 MHz, DMSO-*d*₆) δ_H 9.88 (s, 1H), 8.98 (s, 1H), 8.23 (d, *J* = 9.1 Hz, 1H), 8.06 (d, *J* = 9.0 Hz, 1H), 7.80 (s, 1H), 7.09 (s, 1H), 6.17 (s, 2H), 5.09 (d, *J* = 2.5 Hz, 2H), 4.96 (t, *J* = 6.4 Hz, 2H), 4.08 (s, 3H), 3.62 (t, *J* = 2.4 Hz, 1H), 3.21 (t, *J* = 6.5 Hz, 2H). ¹³C NMR (125 MHz, DMSO-*d*₆) δ_C 150.8, 149.9, 147.7, 145.4, 140.7, 137.7, 132.9, 130.8, 126.5, 124.3, 122.1, 120.5, 120.3, 108.5, 105.5, 102.2, 79.9, 78.8, 61.0, 57.2, 55.3, 26.4.¹³

9-((5-Carboxypentyl)oxy)-10-methoxy-5,6-dihydro-[1,3]dioxolo[4,5-*g*]isoquinolino[3,2-*a*]isoquinolin-7-ium (**2l**) as a dark yellow solid, 13% yield. ¹H NMR (500 MHz, DMSO-*d*₆) δ_H 9.74 (s, 1H), 8.94 (s, 1H), 8.19 (d, *J* = 9.1 Hz, 1H), 7.99 (d, *J* = 9.1 Hz, 1H), 7.80 (s, 1H), 7.09 (s, 1H), 6.17 (s, 2H), 4.95 (t, *J* = 6.4 Hz, 2H), 4.28 (t, *J* = 6.7 Hz, 2H), 3.21 (t, *J* = 6.3 Hz, 3H), 2.27 (t, *J* = 7.3 Hz, 2H), 1.87 (p, *J* = 7.0 Hz, 3H), 1.62 – 1.46 (m, 5H). ¹³C NMR (125 MHz, DMSO-*d*₆) δ_C 150.4, 149.8, 147.7, 145.4, 142.8, 137.4, 133.0, 130.8, 126.6, 123.3, 121.7, 120.5, 120.3, 108.5, 105.5, 102.1, 74.0, 57.0, 55.3, 29.3, 26.4, 25.1, 24.7. HRMS (ESI) calcd. for C₂₅H₂₆NO₆⁺ (H)⁺: 436.1755 found 436.1753.

10-Methoxy-9-(2-methoxy-2-oxoethoxy)-5,6-dihydro-[1,3]dioxolo[4,5-*g*]isoquinolino[3,2-*a*]isoquinolin-7-ium (**2m**) as a yellow solid, 80% yield. ¹H NMR (500 MHz, DMSO-*d*₆) δ_H 9.94 (s, 1H), 8.95 (s, 1H), 8.20 (d, *J* = 9.2 Hz, 1H), 8.00 (d, *J* = 9.2 Hz, 1H), 7.81 (s, 1H), 7.10 (s, 1H), 6.18 (s, 2H), 5.07 (s, 2H), 4.94 (t, *J* = 6.3 Hz, 2H), 4.03 (s, 3H), 3.72 (s, 3H), 3.21 (t, *J* = 6.4 Hz, 2H). ¹³C NMR (125 MHz, DMSO-*d*₆) δ_C 169.4, 149.9, 149.3, 147.8, 145.8, 141.5, 137.6, 133.0, 130.8, 126.8, 123.7, 121.2, 120.5, 120.2, 108.5, 105.5, 102.2, 69.3, 57.3, 55.5, 52.0, 26.4.¹⁴

10-Methoxy-9-(4-methoxybutoxy)-5,6-dihydro-[1,3]dioxolo[4,5-*g*]isoquinolino[3,2-*a*]isoquinolin-7-ium (**2n**) as a yellow solid, 59% yield. ¹H NMR (500 MHz, DMSO-*d*₆) δ_H 9.76 (s, 1H), 8.93 (s, 1H), 8.20 (dd, *J* = 9.2, 4.6 Hz, 1H), 7.99 (dd, *J* = 9.1, 5.9 Hz, 1H), 7.79 (s, 1H), 7.09 (d, *J* = 1.7 Hz, 1H), 6.17 (s, 2H), 4.95 (t, *J* = 6.6 Hz, 2H), 4.30 (t, *J* = 6.7 Hz, 2H), 4.05 (s, 2H), 3.42 (t, *J* = 6.3 Hz, 2H), 3.26 (s, 3H), 3.21 (t, *J* = 6.4 Hz, 3H), 1.97 – 1.82 (m, 2H), 1.78 – 1.69 (m, 2H). ¹³C NMR (125 MHz, DMSO-*d*₆) δ_C 150.4, 149.8, 147.7, 145.3, 142.8, 137.5, 133.0, 130.7, 126.7, 123.3, 121.7, 120.5, 120.2, 108.5, 105.5, 102.1, 74.1, 71.6, 57.9, 57.1, 55.3, 26.5, 26.3, 25.5. HRMS (ESI) calcd. for C₂₄H₂₆NO₅⁺ (H)⁺: 408.1805 found 408.1802.



10-Methoxy-9-(2-(2-methoxyethoxy)ethoxy)-5,6-dihydro-[1,3]dioxolo[4,5-g]isoquinolino[3,2-a]isoquinolin-7-ium (**2o**) as a yellow solid, 35% yield. ^1H NMR (500 MHz, DMSO- d_6) δ_{H} 9.76 (s, 1H), 8.94 (s, 1H), 8.20 (d, $J = 9.1$ Hz, 1H), 8.00 (d, $J = 9.1$ Hz, 1H), 7.81 (s, 1H), 7.10 (s, 1H), 6.18 (s, 2H), 4.92 (t, $J = 6.1$ Hz, 2H), 4.45 – 4.39 (m, 2H), 4.06 (s, 3H), 3.82 – 3.77 (m, 2H), 3.59 – 3.54 (m, 2H), 3.42 – 3.39 (m, 2H), 3.22 (t, $J = 6.5$ Hz, 2H), 3.14 (s, 3H). ^{13}C NMR (125 MHz, DMSO- d_6) δ_{C} 150.5, 149.8, 147.7, 145.5, 142.6, 137.4, 132.9, 130.6, 126.5, 123.6, 122.0, 120.5, 120.2, 108.5, 105.4, 102.1, 73.0, 71.3, 69.4 (2C), 58.1, 57.0, 55.4, 26.4. HRMS (ESI) calcd. for $\text{C}_{24}\text{H}_{26}\text{NO}_6^+$ (H^+): 424.1755 found 424.1754.

10-Methoxy-9-(2-(2-(2-methoxyethoxy)ethoxy)ethoxy)-5,6-dihydro-[1,3]dioxolo[4,5-g]isoquinolino[3,2-a]isoquinolin-7-ium (**2p**) as a yellow solid, 32% yield. ^1H NMR (500 MHz, DMSO- d_6) δ_{H} 9.77 (s, 1H), 8.96 (s, 1H), 8.20 (d, $J = 9.2$ Hz, 1H), 8.01 (d, $J = 9.0$ Hz, 1H), 7.80 (s, 1H), 7.10 (s, 1H), 6.17 (s, 2H), 4.93 (t, $J = 6.4$ Hz, 2H), 4.46 – 4.38 (m, 2H), 4.06 (s, 3H), 3.84 – 3.76 (m, 2H), 3.58 (dd, $J = 6.0, 3.4$ Hz, 2H), 3.51 (dd, $J = 6.0, 3.4$ Hz, 2H), 3.45 (dd, $J = 5.8, 3.6$ Hz, 2H), 3.21 (t, $J = 6.3$ Hz, 4H), 3.15 (s, 3H). ^{13}C NMR (126 MHz, DMSO- d_6) δ_{C} 150.5, 149.8, 147.7, 145.5, 142.5, 137.5, 132.9, 130.7, 126.6, 123.6, 122.0, 120.5, 120.2, 108.5, 105.4, 102.1, 73.1, 71.2, 69.8, 69.6, 69.5, 69.4, 58.0, 57.0, 55.5, 26.4. HRMS (ESI) calcd. for $\text{C}_{26}\text{H}_{30}\text{NO}_7^+$ (H^+): 468.2017 found 468.2015.

In vitro yeast α -glucosidase inhibition assay

Alkylated 9-*O*-berberrubine derivatives **2a–p** were synthesized and evaluated for their anti- α -glucosidase from *Saccharomyces cerevisiae* (Type I, Sigma-Aldrich) using *p*-nitrophenyl- α -D-glucopyranoside, *p*-NPG as a substrate (TCI Chemical). Acarbose was purchased from Sigma-Aldrich. The method was slightly modified from Supasuteekul *et al.*¹⁵ α -Glucosidase was prepared in phosphate-buffered solution pH 6.9. To measure the inhibitory activity against α -glucosidase, 10 μL of berberrubine derivatives with various concentrations were loaded to 96-well plate, followed by adding 40 μL of α -glucosidase solution (0.4 U/mL) and then pre-incubation was performed at 37° C for 10 min 500 rpm. After pre-incubation, 50 μL of 3 mM *p*-NPG was added and reacted at 37° C for 20 min 500 rpm. Then quench the reaction by adding 100 μL of 1M Na_2CO_3 . To determine the absorbance by using microplate reader at 405 nm. Acarbose was used as the control and standard drug. The percentage of enzyme inhibition was calculated as follows equation 1:

$$\% \text{ Inhibition} = [(\text{Abs}_{\text{Blank}} - \text{Abs}_{\text{Sample}}) / \text{Abs}_{\text{Blank}}] \times 100$$

where $\text{Abs}_{\text{Blank}}$ is the absorbance without sample and $\text{Abs}_{\text{Sample}}$ is the absorbance with sample. The IC_{50} will be calculated for the compound with a percentage inhibition higher than 70%. The half-maximal inhibitory concentration (IC_{50}) value was calculated by plotting sample concentrations against and the percentage of yeast α -glucosidase inhibition.

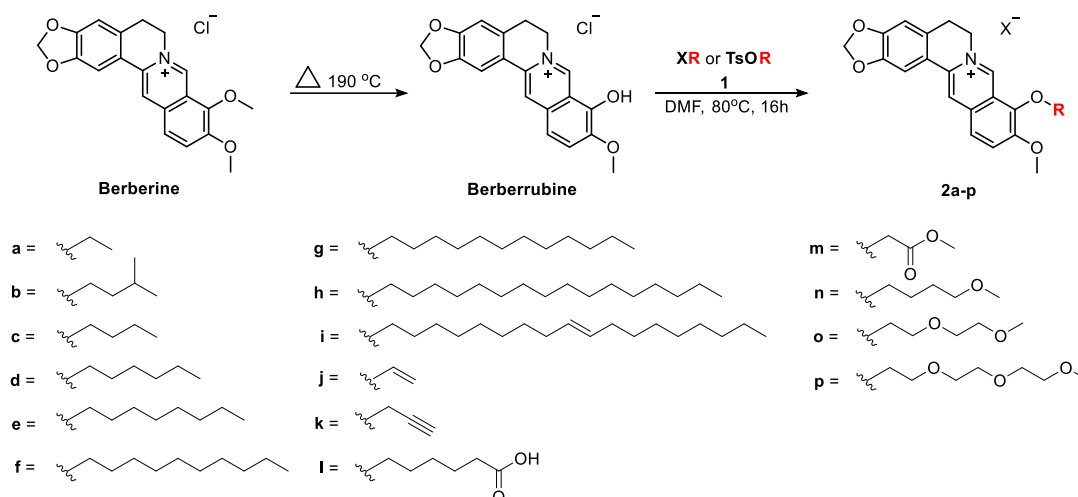
Kinetic studies

Compound **2f**, the most potent compound with the lowest IC_{50} 0.40 μM , was studied in terms of inhibitory kinetics. To investigate the type of inhibition of active compounds against α -glucosidase, a fixed concentration of α -glucosidase and various concentrations of PNPG as a substrate were tested at 37° C for 10 minutes in the absence and presence of IC_{50} concentrations. All tests were administered three times. The type of inhibition (competitive, uncompetitive, noncompetitive, or mixed) was determined through Lineweaver–Burk plot analysis of the data, which was calculated using Michaelis–Menten kinetics.

Results and Discussion:

BBRB derivatives **2a–p** were successfully synthesized as shown in Scheme 1. Initially, berberrubine prepared by demethylation of **BBR** through heated at 190° C.

Furthermore, the hydroxyl group at position 9 of **BBRB** reacted with alkyl halide or tosylate to obtain compound alkylated 9-*O*-**BBRB** **2a–p** via nucleophilic substitution. Normal alkyl chain and branched chain were used. Additionally, double bond, triple bond, carboxylic acid and ether groups were introduced within the chain to study the structures activity relationship (SAR) of different types of hydrophobic groups.



Scheme 1. Synthesis of alkylated 9-*O*-**BBRB** derivatives **2a–p**.

9-*O*-**BBRB** **2a–p** were screened for α -glucosidase inhibitory activity against yeast from *Saccharomyces cerevisiae* EC.3.2.1.20. Acarbose was used as a reference drug. **Figure 2**, depicted **BBR** and **BBRB** showed no inhibition activity toward α -glucosidase. Upon introduction of alkyl chain of 9-*O*-**BBRB**, the activity was enhanced significantly. Compounds **2b** and **2c** with the addition of four carbons slightly increased the activity. Furthermore, a series of long alkyl chain **2c–2f** demonstrated that the longer chain could elevate the inhibition. However, increasing the carbon more than twelve such as compounds **2g–2i** gradually lower the inhibition. On the other hand, introducing double bond, triple bond, carboxylic acid and ester into the chain of **2j–2p** demolished the activity. Among the tested compounds, only compounds **2f**, **2g** and **2h** exhibited % inhibition more than threshold 70%. The IC_{50} of these compounds was calculated as shown in Figure 3. Compound **2f** is the most potent with the IC_{50} value of 0.40 μ M, followed by **2g** and **2h** with IC_{50} values of 1.71 and 2.76 μ M, respectively.

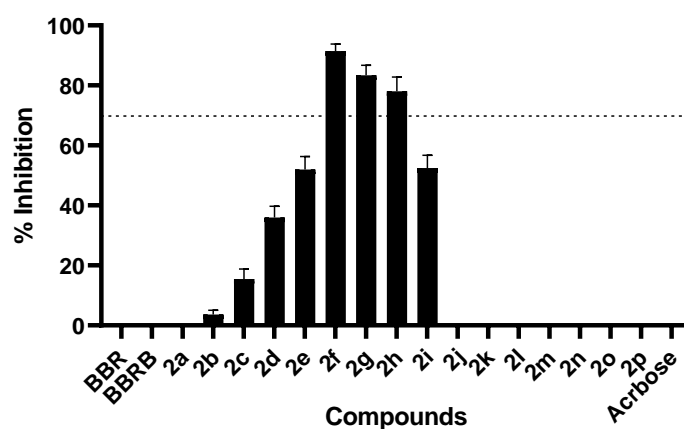


Figure 2. Percentage inhibition of α -glucosidase by alkylated 9-*O*-berberrubine derivatives **2a–p** at 10 μ M

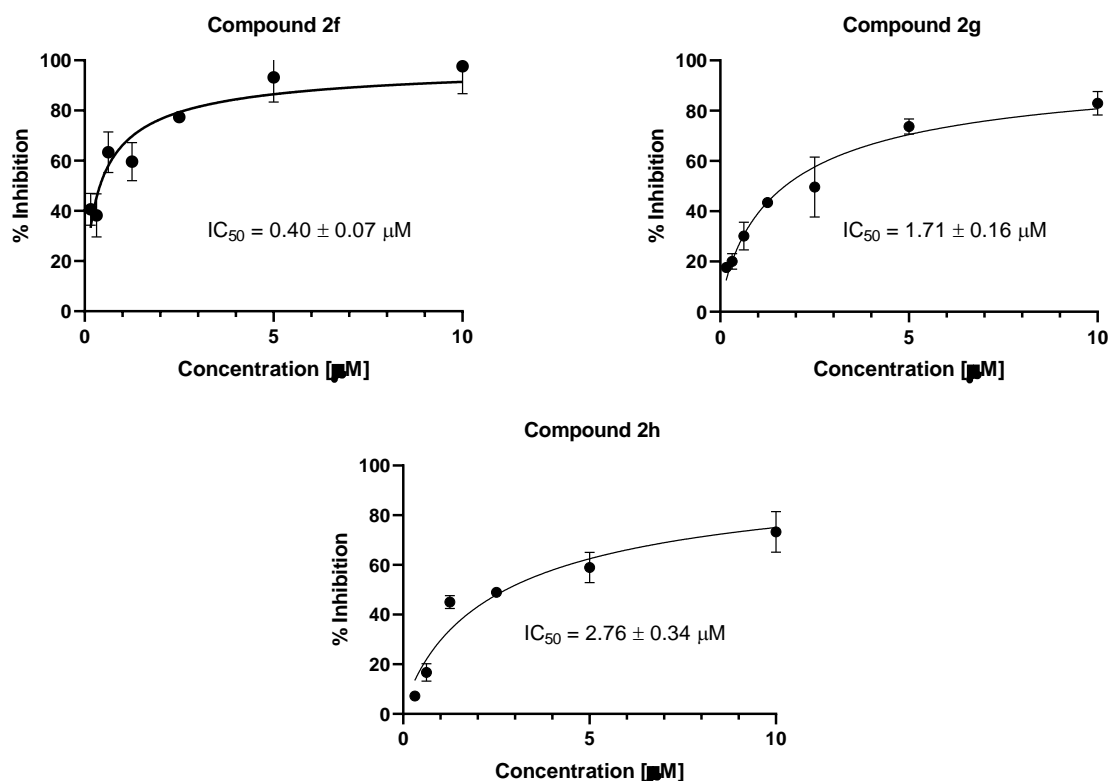


Figure 3. α -Glucosidase inhibitory effects *in vitro* of compound **2f**, **2g** and **2h**.

a)

b)

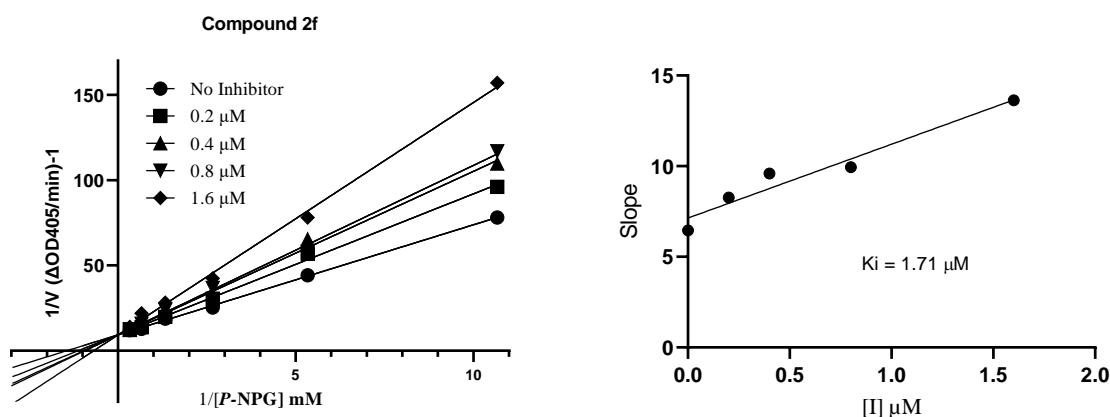


Figure 4. Kinetics of α -glucosidase inhibition by compound **2f**. (a) Lineweaver – Burk plots for α -glucosidase inhibition; (b) The secondary plot between K_m and various concentrations of compound **2f**.

To study the inhibition mechanism of 9-*O*-BBRB derivatives against α -glucosidase, a kinetic study was performed using the most potent derivative **2f**. Lineweaver–Burk plots and secondary re-plotting were used for show inhibition type and K_i . In **Figure 4a**, increasing inhibitor concentration led to an increase in K_m value but no change in V_m value. This suggests that compound **2f** is a competitive inhibitor, competing with substrate for

binding to the enzyme active site. The inhibition constants (K_i) was 1.71 μM for compound **2f** as shown in **figure 4b**.

Conclusion:

Some potent α -glucosidase inhibitors were developed as alkylated 9-*O*-BBRB derivatives. Three 9-*O*-berberrubine derivatives (**2f**, **2g**, and **2h**) inhibited α -glucosidase with IC_{50} values ranging from 0.40 – 2.76 μM , outperforming the core structure berberine and berberrubine as well as the standard inhibitor acarbose. Compound **2f** demonstrated the highest inhibitory potency, with IC_{50} of 0.40 μM . Kinetic analysis demonstrated that this compound displayed competitive inhibition.

References:

- Galasko, G. T. In Pharmacology and therapeutics for dentistry, 2017;437–445.
- Gentry, E. J.; Jampani, H. B.; Keshavarz-Shokri, A.; Morton, M. D.; Velde, D. V.; Telikepalli, H.; Mitscher, L. A. J. Nat. Prod. 1998;61:1187–1193.
- Li, C. Y.; Tsai, S. I.; Damu, A. G.; Wu, T. S. J. Pharm. Biomed. Anal. 2009;49:1272–1276.
- Ye, X.; He, K.; Zhu, X.; Zhang, B.; Chen, X.; Yi, J.; Li, X. Med. Chem. Res. 2011;21:1353–1362.
- Liang, Y.; Ye, C.; Chen, Y.; Chen, Y.; Diao, S.; Huang, M. ACS Chem. Neurosci. 2021;12:1894–1904.
- Vlavcheski, F.; O'Neill, E. J.; Gagacev, F.; Tsiani, E. Mol. 2022;27:8630.
- Abdelrahman, R.; Abdel-monsif, D.; Farghaly, E.; Abounazel, M.; Zaki, E. Egypt. J. Histol. 2021;45:1071–1034.
- Kong, Y.; Xing, Q. Q.; Tian, Y. X.; Li, L.; Yu, P.; Zhao, L. G.; Li, D. D. Nat. Prod. Res. 2023;37:3452–3460.
- Nguyen, D. V.; Hengphasatporn, K.; Danova, A.; Suroengrit, A.; Boonyasuppayakorn, S.; Fujiki, R.; Shigeta, Y.; Rungrotmongkol, T.; Chavasiri, W. Sci. Rep. 2023;13:18865.
- Wang, R.; Rostyslav, S.; Li, X.; Lin, H.; Zhang, X.; Zhang, S.; Liu, K.; Wang, L. J. Iran. Chem. Soc. 2020;17:3251–3260.
- Fu, S.; Xie, Y.; Tuo, J.; Wang, Y.; Zhu, W.; Wu, S.; Yan, G.; Hu, H. Med. Chem. Comm. 2015;6:164–173.
- Meenu, M. T.; Cherian, A. R.; Sherin, D. R.; Nair, A. R.; Manojkumar, T. K.; Radhakrishnan, K. V.; Varghese, A. Dyes Pigm. 2021;194.
- Han, L.; Sheng, W.; Li, X.; Sik, A.; Lin, H.; Liu, K.; Wang, L. Med. Chem. Comm. 2019;10:598–605.
- I. V. Nechepurenko; N. I. Komarova; V. G. Vasil'ev; N. F. Salakhutdinov. Chem. Nat. Compd. 2013;48:1047–1053.
- Supasuteekul, C.; Nonthitipong, W.; Tadtong, S.; Likhitwitayawuid, K.; Tengamnuay, P.; Sritularak, B. Rev. Bras. Farmacogn. 2016;26:312–320.



SYNTHESIS OF BENZO[*a*]PHENAZINE DERIVATIVES AND THEIR SENSOR APPLICATIONS

Thanakorn Sitthasakul, Natthapat Pitakwong, Torsak Luanphaisarnnont*

Department of Chemistry and Center of Excellence for Innovation in Chemistry, Faculty of Science, Mahidol University, Bangkok 10400, Thailand

*e-mail: torsak.lua@mahidol.ac.th

Abstract:

Development of new small molecules with useful applications is an important area in chemistry. Benzo[*a*]phenazine derivatives, a class of polycyclic aromatic compounds, have been shown to exhibit interesting photophysical properties. Although benzo[*a*]phenazines have been previously synthesized and studied, their use as a sensor was limited. This work aimed to investigate the use of benzo[*a*]phenazine derivatives as a quantitative sensor for a trace amount of water in organic solvents. 5-(2,4,6-trimethoxyphenyl)benzo[*a*]phenazine was synthesized and its photophysical and sensor properties were studied. The result showed that the compound can be used as a quantitative fluorescence sensor for a trace amount of water in acetonitrile, tetrahydrofuran, and ethanol.

Introduction:

Development of new small organic molecules for sensor applications is an ongoing challenge in chemistry. One sensor application that is important in synthetic chemistry is the quantitative detection of a trace amount of water in organic solvents. The presence of water in the solvents could pose a detrimental effect in organic synthesis because water can cause decomposition of many water-sensitive reagents, which were used prevalently in many syntheses. A trace amount of water can also affect the reproducibility of moisture-sensitive reactions.¹

Various types of sensors for a trace amount of water in organic solvents using different mechanisms have been previously reported (**Figure 1**). Selected examples of such sensors are shown hereafter. A crown ether containing a hydrazone moiety (**1**) was shown to be able to detect a water content in acetonitrile.² The fluorescence emission of the compound changed depending on the presence of water. A two-dimensional metal-organic framework [Ni₃(nic)₂(μ-Cl)₄(DMF)₄] (**2**) was reported to be an effective colorimetric water sensor.³ In the presence of water, the color of the compound changed from green to blue. Poly(1,5-diaminonaphthalene) nanofibers (**3**) were developed as a quantitative detector for water in acetonitrile.⁴ The electric current of acetonitrile solutions containing the compound were measured to determine the amount of water using cyclic voltammograms. 5-Azidopentanoic acid (**4**) was an effective sensor for water in organic solvents.⁵ The N–N–N asymmetric stretching band changed depending on the amount of the water. An aggregation-induced emission-active fluorescent polymer sensor⁶ (**5**) and a styryl pyrene probe⁷ (**6**) were also reported to detect water in organic solvents.

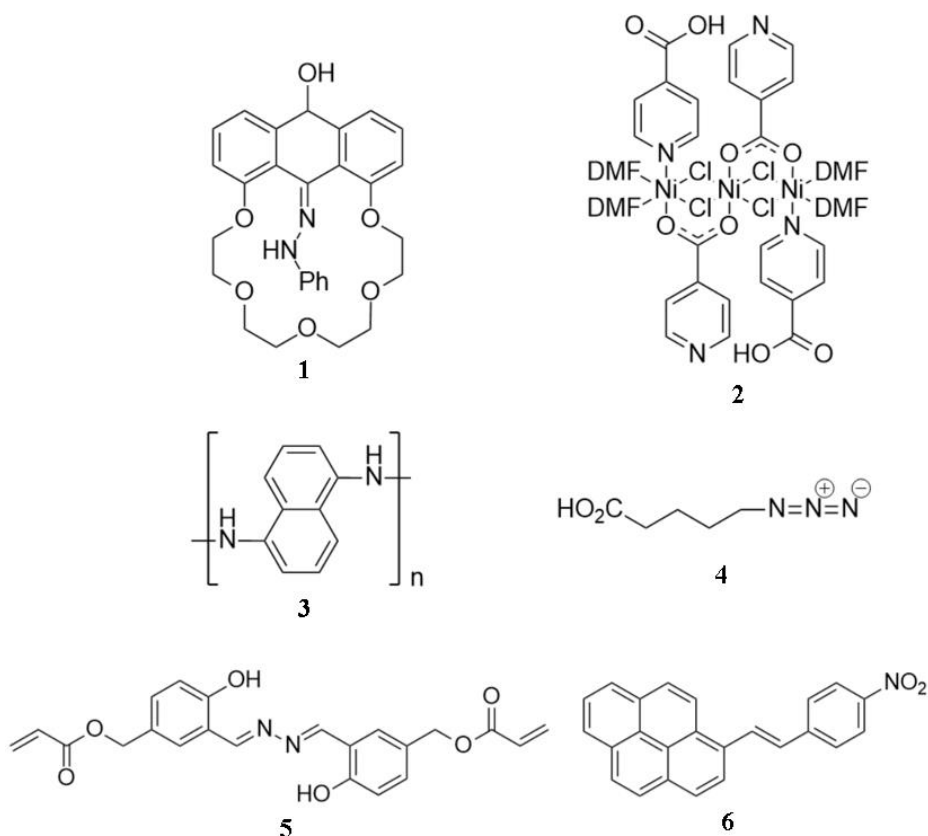


Figure 1.

Examples of sensors for a trace amount of water in organic solvents

One interesting class of compounds with interesting photophysical properties is benzo[*a*]phenazine derivatives (**Figure 2**). A general structure of benzo[*a*]phenazine (**7**) is a naphthalene ring fused with a quinoxaline ring. Various substituted benzo[*a*]phenazine derivatives have been synthesized for their photophysical properties. Selected examples are: arylamine-substituted benzo[*a*]phenazine (**8**),⁸ 1,8-dihydroxydibenzo[*a,h*]-phenazine (**9**),⁹ and morpholine-substituted benzo[*a*]phenazine (**10**).¹⁰ These compounds have been shown to exhibit solvatochromic properties in different organic solvents. Although various benzo[*a*]phenazine derivatives exhibit interesting photophysical properties, their use as a water sensor has been limited. This work aimed to study the use of benzo[*a*]phenazine derivatives as a sensor for a trace amount of water in common water-miscible organic solvents.

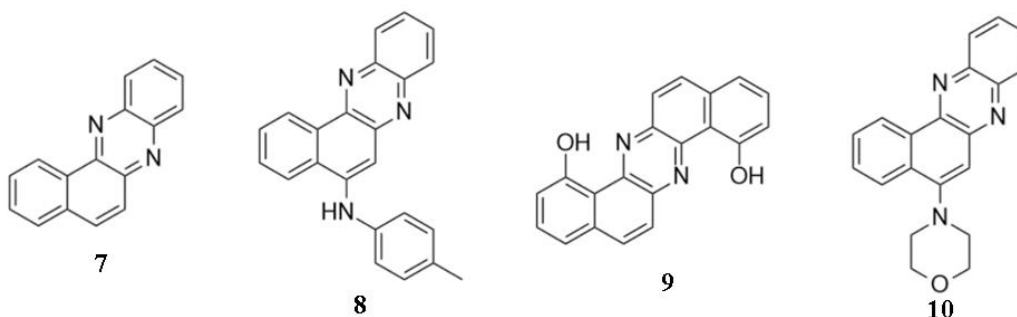


Figure 2.

A general structure of benzo[*a*]phenazine and examples of benzo[*a*]phenazine derivatives with solvatochromic properties



Methodology:

Chemicals and organic solvents were purchased from commercial sources (Sigma Aldrich, TCI, Merck, and Alfa Aesar) and were used without further purification. All reactions were performed under an ambient atmosphere in oven-dried glassware with a magnetic stirrer. 4-(2,4,6-Trimethoxyphenyl)-1,2-naphthoquinone was synthesized following the published method.¹¹ Analytical thin layer chromatography (TLC) was performed on alumina sheets pre-coated with a Merck silica gel 60 F254 plate and compounds were visualized under UV light. Flash chromatography was performed with silica gel 60 (particle size 40–60 μm) from Merck. ^1H and ^{13}C NMR spectra were recorded on a Bruker Avance 400 MHz NMR spectrometer in CDCl_3 . The chemical shifts were recorded in part per million (ppm) relative to the resonance of the residual protonated solvent (^1H : CDCl_3 , $\delta = 7.26$ ppm and ^{13}C : CDCl_3 , $\delta = 77.00$ ppm). Data are reported as following: (s = singlet, d = doublet, t = triplet, and m = multiplet; coupling constants, J in Hz, integration). Absorption and emission spectra were measured in a standard quartz cell with 1 cm path length on a Shimadzu UV-1800 spectrometer with a wavelength between 300 and 700 nm. Emission Spectra were recorded on a Fluoromax Horiba wavelength range between 400 and 700 nm. UV kinetic experiments were recorded using a Shimadzu UV-2600 spectrometer with a wavelength between 400 and 700 nm.

Synthesis of 5-(2,4,6-trimethoxyphenyl)benzo[a]phenazine (13)

To a solution of 4-(2,4,6-trimethoxyphenyl)-1,2-naphthoquinone (**11**, 0.2 mmol, 1.0 equiv.) in methanol (2 mL), was added 1,2-phenylenediamine (**12**, 0.3 mmol, 1.5 equiv.). The reaction was stirred at room temperature. After the reaction was complete (as determined by TLC), the reaction was extracted with dichloromethane (3x20 mL). The combined organic layers were washed with brine solution and dried over anhydrous Na_2SO_4 . The solvent was removed under reduced pressure. Purification using column chromatography yielded the desired product **13** in 96% as a yellow solid. The NMR spectra were identical to those in the literature.¹¹

Yellow solid; 76.2 mg (96%).

$R_f = 0.30$ (EtOAc/Hexanes, 1/3, v/v).

^1H NMR (400 MHz, CDCl_3) δ 9.49 (d, $J = 8.0$ Hz, 1H), 8.43–8.34 (m, 1H), 8.32–8.23 (m, 1H), 7.89 (s, 1H), 7.87–7.81 (m, 2H), 7.77 (td, $J = 8.0$, 1.2 Hz, 1H), 7.66 (td, $J = 8.0$, 1.2 Hz, 1H), 7.58 (dd, $J = 8.2$, 1.4 Hz 1H), 6.33 (s, 2H), 3.94 (s, 3H), 3.66 (s, 6H).

^{13}C NMR (100 MHz, CDCl_3) δ 161.6, 159.1, 143.8, 142.8, 141.9, 138.5, 133.9, 131.2, 129.7, 129.7, 129.4, 129.3, 129.2, 129.0, 127.3, 126.6, 125.3, 109.1, 90.9, 55.8, 55.4.

UV kinetic experiments

Stock solutions of 4-(2,4,6-trimethoxyphenyl)-1,2-naphthoquinone (**11**) and 1,2-phenylenediamine (**12**) were prepared as a 0.45 mM solution and a 13.5 mM solution in methanol, respectively. The sample solutions with the final concentration of **11** at 0.15 mM and various final concentrations of **12** [1.5 (10 times excess), 2.25 (15 times excess), 3 (20 times excess), 3.75 (25 times excess), and 4.5 mM (30 times excess)] were prepared from the stock solution. The UV absorption at 408 nm (the maximum absorption of the product **13**) of each solution was recorded at various times to determine the rate of the condensation reaction.

The water-sensor experiments

A method to test the water-sensor ability was developed. First, a stock solution of the model benzo[a]phenazine derivative (**13**) was prepared as a 0.5 mM solution in DMSO. The sample solutions containing the compound (at the final concentration of 2% (v/v)) and water

(at different final concentrations: 0, 0.1, 0.2, 0.4, 1, 5, 10, 15, 20, 25, 30, 35, 40, 45, 50, 60, 70, 80, 90, and 98% (v/v)) in the selected solvent (CH_3CN , THF, or EtOH) were prepared. The fluorescence spectra of the sample solutions were measured, and the data were used to determine the water sensor ability.

Results and Discussion:

To study the use of benzo[*a*]phenazine derivatives as a water-sensor, 5-(2,4,6-trimethoxyphenyl)benzo[*a*]phenazine (**13**) was selected as a model compound because the compound has an electronic push-pull effect with the trimethoxybenzene substituent as an electron donor. Compound **13** was synthesized using a condensation between 4-(2,4,6-trimethoxyphenyl)-1,2-naphthoquinone and 1,2-phenylenediamine (**12**).¹¹ The compound was obtained in 96%.

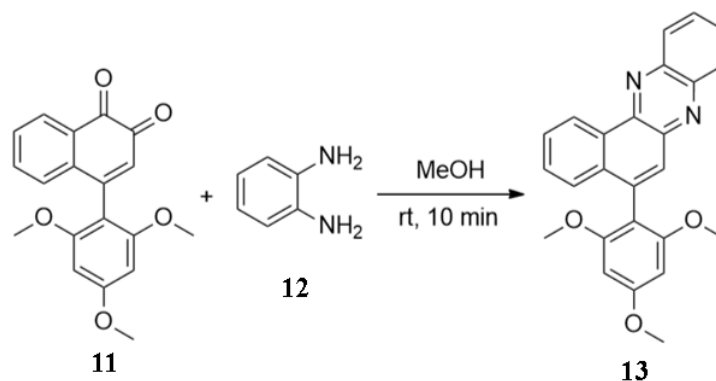


Figure 3.

Synthesis of the model benzo[*a*]phenazine derivative (**13**)

After the benzo[*a*]phenazine derivative (**13**) was synthesized, its photophysical properties were investigated. Their absorption spectrum and emission spectrum were determined using a UV-Vis spectrometer and a fluorescence spectrometer, respectively. The wavelengths for maximum absorption and maximum emission in acetonitrile were 408 and 535 nm, respectively (**Figure 4**).

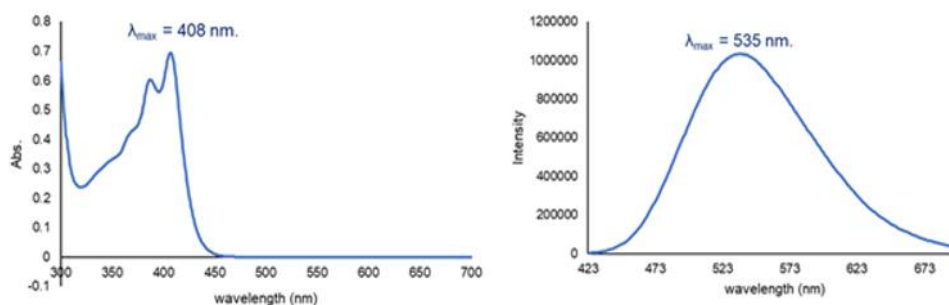


Figure 4.

The absorption and emission spectra of **13** in acetonitrile

Next, we studied the rate of the condensation reaction between 4-(2,4,6-trimethoxyphenyl)-1,2-naphthoquinone (**11**) and 1,2-phenylenediamine (**12**) using a pseudo-first-order approximation. To simplify a second order rate law to a first order rate law, 1,2-phenylenediamine (**12**) was used in large excess (the final concentrations of 1.5–4.5 mM



compared with the final concentration of 0.15 mM of naphthoquinone **11**). The concentration of the product **13** was recorded using its maximum UV absorption at 408 nm. A plot between $\ln[5-(2,4,6\text{-trimethoxyphenyl})\text{benzo}[a]\text{phenazine}]$ and time was constructed, which showed a pseudo-first-order rate constant at various concentrations of 1,2-phenylenediamine (10, 15, 20, 25, and 30 times excess). An example of the plot at 30 times excess was shown in **Figure 5a**. A plot between the pseudo-first-order rate constants and the concentrations of **12** was used to determine the absolute rate constant of the condensation reaction. The absolute rate constant was calculated to be $0.0729 \text{ M}^{-1}\text{s}^{-1}$ (**Figure 5b**).

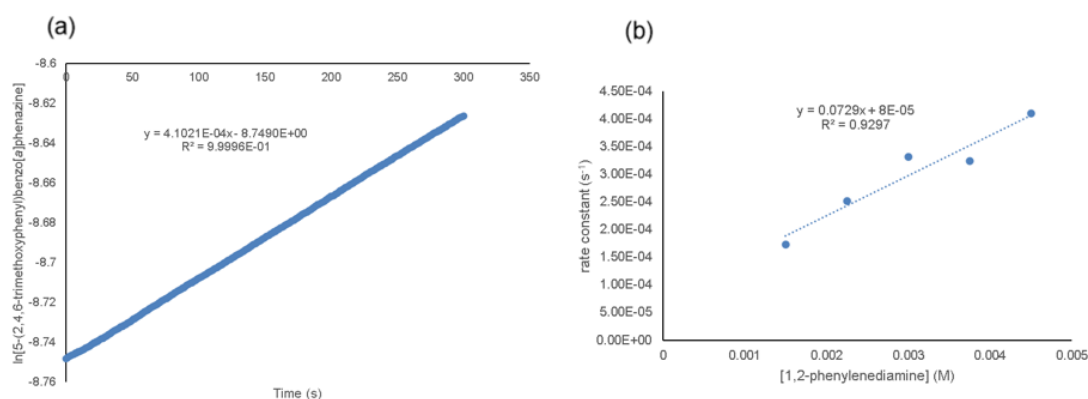


Figure 5.

(a) Example of a pseudo-first order plot between $\ln[5-(2,4,6\text{-trimethoxyphenyl})\text{benzo}[a]\text{phenazine}]$ and time (a condensation reaction with 30 times excess concentration of 1,2-phenylenediamine) (b) A plot between the pseudo-first-order rate constants and the concentration of 1,2-phenylenediamine

The model benzo[*a*]phenazine derivative (**13**) was tested for its potential utility as a sensor for detection of a trace amount of water in three organic solvents: acetonitrile (CH_3CN), tetrahydrofuran (THF), and ethanol (EtOH).

First, the water sensor ability in acetonitrile was investigated (**Figure 6**). The result showed that the fluorescence emission intensity decreased when %water increased from 0 to 80% (v/v). A plot between the ratios of the blank fluorescence intensity to the measured fluorescence intensities (F_0/F) at 535 nm and %water (% (v/v)) was constructed, and the plot showed a linear relationship in a range from 0% to 45% (v/v). The limit of detection and the limit of quantitation were determined to be 0.011% (v/v) and 0.034% (v/v), respectively.

Second, the water sensor ability in tetrahydrofuran was investigated (**Figure 7**). The result showed that the fluorescence emission intensity decreased when %water increased from 1 to 70% (v/v). A plot between the ratios of the blank fluorescence intensity to the measured fluorescence intensities (F_0/F) at 493 nm and %water (% (v/v)) was constructed, and the plot showed a linear relationship in a range from 1% to 45% (v/v). The limit of detection and the limit of quantitation were determined to be 0.074% (v/v) and 0.224% (v/v), respectively.

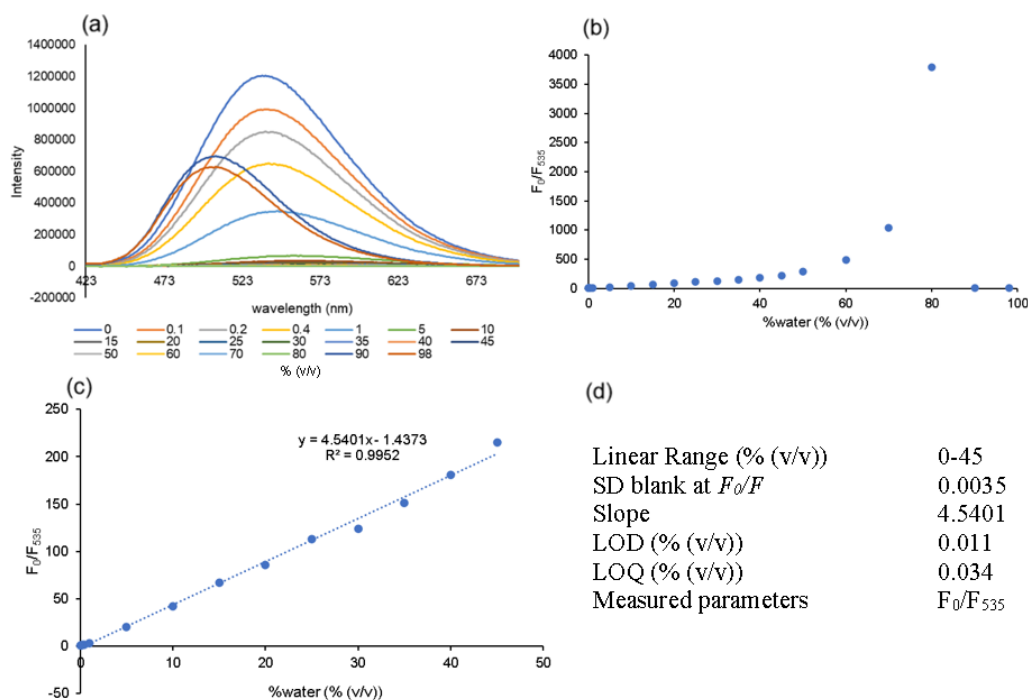


Figure 6.

(a) Fluorescence emission spectra of **13** in acetonitrile with various amounts of water (% (v/v)) (b) The plot between fluorescence intensity ratio (F_0/F_{535}) and % water (% (v/v)) (c) A linear relationship a range from 0% to 45% (v/v) (d) Summary of the key values for the water sensor ability of compound **13** in acetonitrile

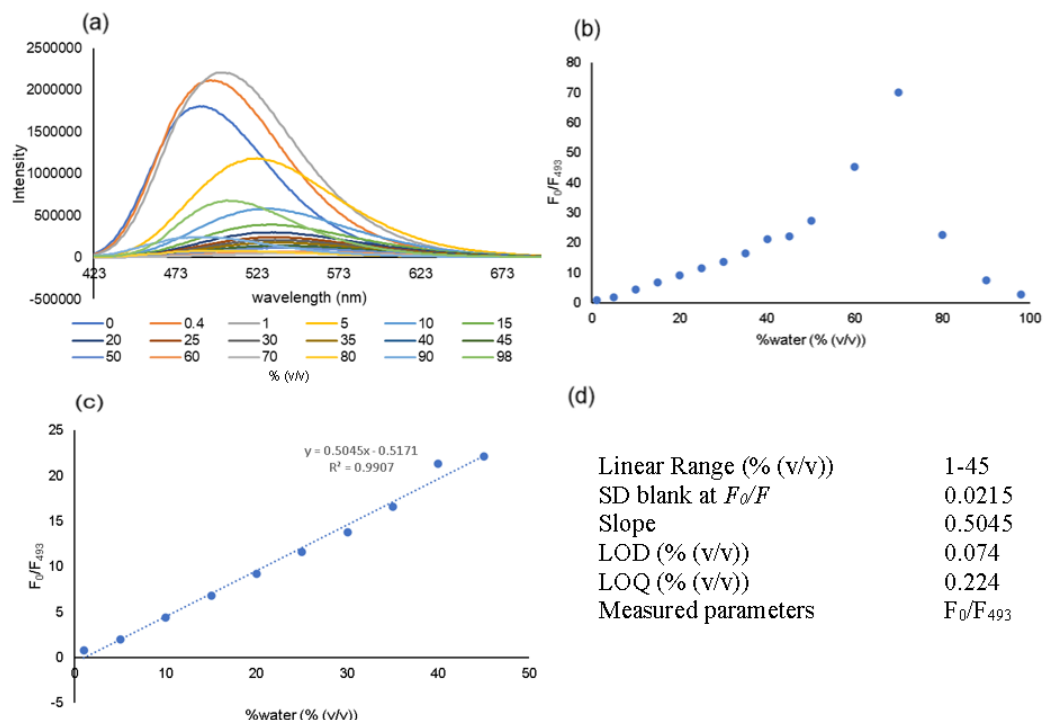


Figure 7.

(a) Fluorescence emission spectra of **13** in tetrahydrofuran with various amount of water (% (v/v)) (b) The plot between fluorescence intensity ratio (F_0/F_{493}) and % water (% (v/v)) (c) A linear relationship a range from 1% to 45% (v/v) (d) Summary of the key values for the water sensor ability of compound **13** in tetrahydrofuran



Third, the water sensor ability in ethanol was investigated (**Figure 8**). The result showed that the fluorescence emission intensity decreased when %water increased from 0 to 80% (v/v). A plot between the ratios of the blank fluorescence intensity to the measured fluorescence intensities (F_0/F) at 547 nm and %water (% (v/v)) was constructed, and the plot showed a linear relationship in a range from 0% to 40% (v/v). The limit of detection and the limit of quantitation were determined to be 0.039% (v/v) and 0.118% (v/v), respectively.

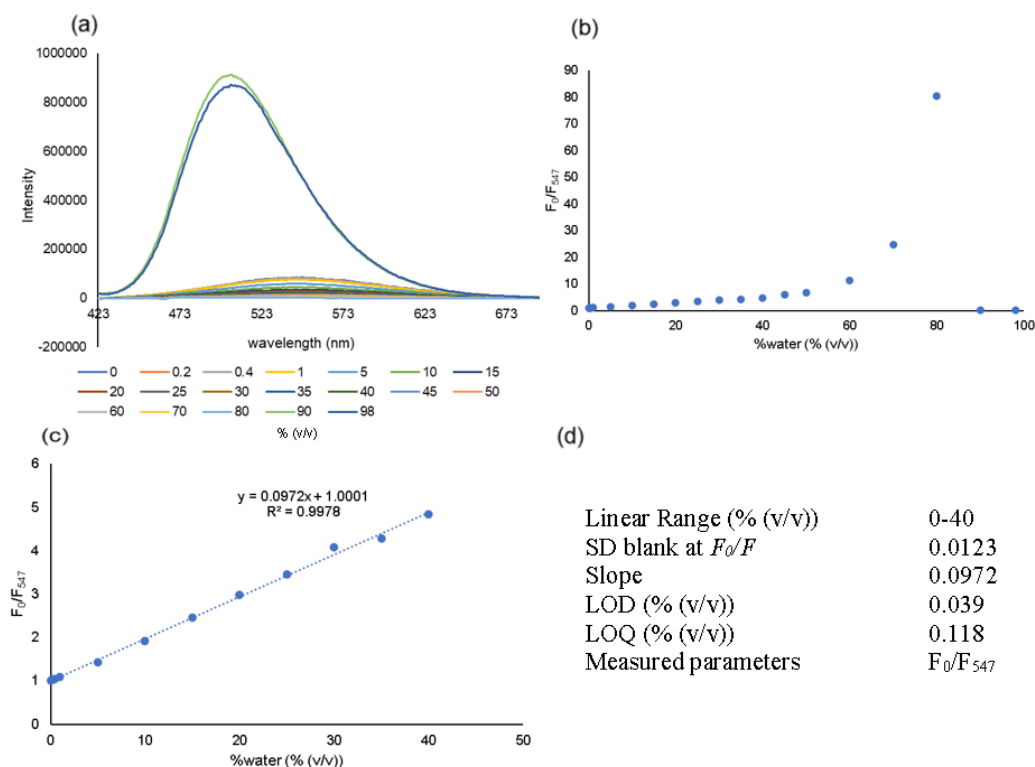


Figure 8.

- (a) Fluorescence emission spectra of **13** in ethanol with various amount of water (% (v/v)) (b) The plot between fluorescence intensity ratio (F_0/F_{547}) and %water (% (v/v)) (c) A linear relationship a range from 0% to 40% (v/v) (d) Summary of the key values for the water sensor ability of compound **13** in ethanol

The effective ranges as a water sensor in organic solvents of **13** was compared with the effective ranges of other previously reported water sensors (**Table 1**). The result showed that **13** has effective ranges for MeCN and THF similar to the previously reported sensors. Compound **13** has a better effective range for EtOH compared to other selected water sensors. This result suggested that **13** was an effective quantitative fluorescence sensor for a trace amount of water (ranging from 1 to 40 % (v/v) in various organic solvents.

Table 1.
Comparison of the effective range (% (v/v)) for the trace-water sensor property in different organic solvents of **13** and other selected water sensors

| Compound | Effective range (% (v/v)) | | |
|-----------------------|---------------------------|--------|-----------|
| | MeCN | THF | EtOH |
| 13 | 0–45 | 1–45 | 0–40 |
| 1 ² | 0–50 | - | - |
| 3 ⁴ | 0–20 | - | - |
| 4 ⁵ | - | 0–60 | - |
| 6 ⁷ | 0–39.7 | 0–34.2 | 36.8–63.6 |

Conclusion:

In summary, we synthesized 5-(2,4,6-trimethoxyphenyl)benzo[*a*]phenazine (**13**), using a condensation reaction between 4-aryl-1,2-naphthoquinones and 1,2-phenylenediamine. The kinetics of the reaction was investigated using a pseudo-first-order approximation. The absolute rate constant of the condensation was determined to be 0.0729 M⁻¹s⁻¹. The sensor properties of **13** were investigated. The compound **13** could be used as a quantitative fluorescent sensor for a trace amount of water in acetonitrile, tetrahydrofuran, and ethanol with effective ranges of 0–45, 1–45, and 0–40 % (v/v), respectively.

Acknowledgements:

This research was supported by Mahidol University (Fundament Fund: fiscal year 2024 by National Science Research and Innovation Fund, FF-067/2567). The support from the Center of Excellence for Innovation in Chemistry (PERCH-CIC) and the Department of Chemistry, Faculty of Science, Mahidol University were acknowledged. We also thank the Central Instrumental Facility (CIF) at the Faculty of Science, Mahidol University for research facilities.

References:

- Pirrung, M. C. (Ed). The Synthetic Organic Chemist's Companion; John Wiley & Sons: Hoboken. 2007.
- Mariappan K, Alaparthi M, Caple G, Balasubramanian V, Hoffman M. M, Hudspeth M, Sykes A. G. Inorg. Chem. 2014; 53:2953-2962.
- Karim S, Adhikary A, Ahmed M. E, Samanta D, Das D. ACS Sustainable Chem. Eng. 2022; 10:16657-16669.
- Rahman M. A, Won M.-S, Kwon N.-H, Yoon J.-H, Park D.-S, Shim Y.-B. Anal. Chem. 2008; 80:5307-5311.
- Wolfshorndl M. P, Baskin R, Dhawan I, Londergan C. H. J. Phys. Chem. 2012; 116:1172-1179.
- Qin H, Huang J, Liang H, Lu J. ACS Appl. Mater. Interfaces. 2021; 13:5668-5677.
- Noikham M, Sriwiphasathit C, Siri Wong K, Vilaivan T. Dyes Pigm. 2023; 208:110847.
- Singh P, Baheti A, Thomas K. R. J. J. Org. Chem. 2011; 76:6134-6145.
- Piechowska J, Virkki K, Sadowski B, Lemmetyinen H, Tkachenko N. V, Gryko D. T. J. Phys. Chem. A. 2014; 118:144-151.
- Tathe A. B, Sekar N. J. Fluoresc. 2015; 25:1403–1415.
- Prasitwatcharakorn W, Rujirasereesakul C, Luanphaisarnnont T. Results Chem. 2022; 4:100319.



SYNTHESIS OF MOLNUPIRAVIR IMPRINTED POLYMER

Suparada Surapanthanakorn,¹ Waranya Kalupae,² Daran Satjayanukun,² Wanpen Naklua,^{1*}

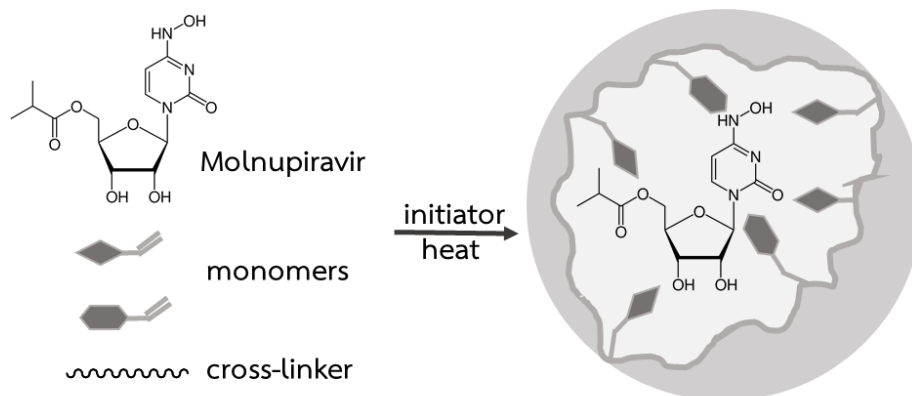
¹Faculty of Science and Technology, Prince of Songkla University, Pattani Campus, Pattani, Thailand

²Islamic Science Demonstration School, Prince of Songkla University, Pattani campus, Thailand

*e-mail: wanpen.n@psu.ac.th

Abstract:

Over the past five years, extensive research efforts have been dedicated to the development of treatments for COVID-19, encompassing approaches derived from herbal plants, chemical substances, and natural products. This work aimed to synthesize a molnupiravir imprinted polymer (MIP) based on template-guided synthesis using a self-assembly mode imprinting approach. The MIP material was successfully produced in 50% ethanol by free radical polymerization at 70 °C in the presence of molnupiravir as a template molecule together with methacrylic acid (MAA), 1-vinyl-2-pyrrolidone (VP) as functional monomers and ethylene glycol dimethacrylate (EGDMA) as a cross-linking agent with molar ratios of MAA:VP:EGDMA of 1:1:30. Additionally, FT-IR spectra of the polymers was found that both the MIP and NIP exhibited similar spectral characteristics. However, the molnupiravir imprinted polymer had numerous scattered pores with pore diameters larger than the control polymer about 1 μm , and showed an absorption capacity that was tenfold greater than that of the non-imprinted polymer (NIP). The future goal is to streamline the process of isolating desired compounds from Thai herbal crude extracts, thereby reducing both the time and costs associated with such extractions for the discovery of candidate antiviral active compounds.



The scheme for MIPs synthesis

Introduction:

COVID-19, caused by SARS-CoV-2, emerged in 2019 and rapidly spread globally. Despite vaccination efforts, the pandemic has resulted in millions of infections and deaths worldwide. Symptoms range from asymptomatic to severe, with significant impacts on healthcare systems. Antiviral drugs like molnupiravir have shown promise in treating COVID-19, particularly in reducing severe cases.^{1,2} Molnupiravir, a promising antiviral agent, has shown effectiveness against several coronaviruses, including SARS-CoV-2. Its mechanism of action involves promoting rapid viral RNA synthesis, leading to mutations that inhibit the virus's ability to replicate. Clinical data indicate that molnupiravir can reduce

COVID-19 cases by up to 50%, from mild to severe, thereby presenting a viable therapeutic option.³

Nonetheless, there remains an imperative for further research and the development of novel materials to combat COVID-19. The research team aims to investigate the synthesis of molnupiravir imprinted polymers (MIP) based on template-guided synthesis in a self-assembly mode, imprinting approach. These have advantages including easier preparation methods and higher physical/chemistry stability for a wide range of experimental conditions. Molecularly imprinted polymers have emerged as a versatile class of synthetic materials with remarkable molecular recognition properties.⁴ These polymers possess a unique ability to selectively bind to a specific template molecule, making them highly attractive for a wide range of applications in analytical chemistry, separation science, and drug delivery.⁵ The synthesis of MIPs involves co-polymerizing functional monomers around a template molecule, creating cavities within the polymer matrix that are complementary in shape, size, and functional groups to the template.⁶ Upon removal of the template, these cavities serve as highly specific binding sites for the rebinding of the template or structurally similar molecules. Moreover, the potential of MIP-based sensors was studied by comparing electropolymerization and photopolymerization techniques.⁷ The resulting MIP-based electrochemical sensor is expected to offer a rapid, sensitive, and selective method for the quantification of molnupiravir in various matrices.⁸

Unlike previous methods, our approach offers a simplified and streamlined synthesis. The MIPs represent a potential solution in the identification or isolation of compounds with antiviral properties. By imparting such properties to these imprinted polymers, they may be utilized to identify analogous compounds in herbal remedies or synthetic chemicals, potentially contributing to the suppression of SARS-CoV-2.

Methodology:

Chemicals and reagents

All reagents and chemicals were of analytical grade and commercially available, and all aqueous solutions were prepared using DI water. 1,1'-Azobis(cyclohexanecarbonitrile) (ABCN) was sourced from Sigma-Aldrich (Steinheim, Germany). Methacrylic acid (MAA), 1-vinyl-2-pyrrolidone (VP), ethylene glycol dimethacrylate (EGDMA), and ethanol were all obtained from Merck (Darmstadt, Germany). Molnupiravir was obtained from Optimus Pharma Private Limited, India, and acetic acid was supplied by QReC (Auckland, New Zealand).

Synthesis of Molnupiravir Imprinted Polymers.

The polymer was synthesized based on information from research on molecularly imprinted polymers.⁹ The synthesis was carried out using molnupiravir as the template molecule. Monomers, cross-linking agents, initiators, and solvents were prepared. The chemicals potentially suitable for synthesizing the polymer are shown in **Table 1**.

Table 1. Chemicals Used in Polymer Synthesis.

| Chemical | Function |
|---|-------------|
| Molnupiravir | Template |
| Methacrylic acid (MAA) | Monomer |
| 1-Vinyl-2-pyrrolidone (VP) | Monomer |
| Ethylene glycol dimethacrylate (EGDMA) | Crosslinker |
| 1,1'-Azobis(cyclohexanecarbonitrile) (ABCN) | Initiator |



To obtain the polymer with the highest specificity for molnupiravir, the polymer was synthesized in five experimental sets, each using different proportions of monomers as follows: Set 1 used MAA as the only monomer. Set 2 used VP as the only monomer. Set 3 used both MAA and VP as monomers in equal molar ratios. Set 4 used both MAA and VP as monomers, with the molar ratio of MAA higher than that of VP. Set 5 used both MAA and VP as monomers, with the molar ratio of VP higher than that of MAA. The ratios of template, cross-linking agent, initiator, and solvent are shown in **Table 2**.

Table 2. Shows the amount of substances used in polymer synthesis.

| Set | Sample | Molnupiravir (mol) | 50%Ethanol (ml) | MAA (mol) | VP (mol) | EGDMA (mol) | ABCN (mol) |
|-----|--------|--------------------|-----------------|-----------|----------|-------------|------------|
| 1 | NIP1 | - | 30 | 0.001 | - | 0.03 | 0.00003 |
| | MIP1 | 0.001 | 30 | 0.001 | - | 0.03 | 0.00003 |
| 2 | NIP2 | - | 30 | - | 0.001 | 0.03 | 0.00003 |
| | MIP2 | 0.001 | 30 | - | 0.001 | 0.03 | 0.00003 |
| 3 | NIP3 | - | 30 | 0.001 | 0.001 | 0.03 | 0.00003 |
| | MIP3 | 0.001 | 30 | 0.001 | 0.001 | 0.03 | 0.00003 |
| 4 | NIP4 | - | 30 | 0.002 | 0.001 | 0.03 | 0.00003 |
| | MIP4 | 0.001 | 30 | 0.002 | 0.001 | 0.03 | 0.00003 |
| 5 | NIP5 | - | 30 | 0.001 | 0.002 | 0.03 | 0.00003 |
| | MIP5 | 0.001 | 30 | 0.001 | 0.002 | 0.03 | 0.00003 |

Afterward, all round-bottom flasks were shaken in a hot water bath for 10 seconds to dissolve the solution completely and then heated at 70°C for 24 h in a hot air oven. The resulting polymer was a solid, white substance. The polymer was then ground into a fine white powder, sieved, and washed with 50% ethanol using a magnetic stirrer at room temperature for 2-3 h. This washing process was repeated three times to remove the template from the polymer.¹⁰⁻¹¹

Study of the Physical Characteristics of Molnupiravir Imprinted Polymers.

The MIP with the highest specificity for the molnupiravir was selected and analyzed for the maximum amount of the molnupiravir absorbed by the imprinted polymer. One gram of the polymer was added to 30 mL of a 0.016 M solution of the molnupiravir in three sets. These were placed on a magnetic stirrer at room temperature for 15 min and allowed to settle at room temperature for 24 h. The solution was then analyzed using a UV/Vis Spectrophotometer, Hewlett-Packard diode array spectrophotometer series 8452 (CS, USA), at a wavelength of 310 nm. A control solution of 0.016 M molnupiravir was also prepared and analyzed using a UV/Vis Spectrophotometer at the same wavelength as the solution containing the polymer. The characteristics of the polymer were further studied using Fourier Transform Infrared Spectrophotometry (FT-IR), 1720X, Perkin-Elmer, Beaconsfield, U.K., and Scanning Electron Microscopy (SEM), Quanta 400, FEI, Hillsboro, OR, USA.

Statistical Analysis

The data from all experiments were obtained from at least three repetitions and presented as the mean \pm standard deviation (S.D.).

Results and Discussion:

The imprinted polymers and corresponding non-imprinted polymers were synthesized with a thermal method involving free radical polymerization by using two functional monomers. The hydroxyl group from MAA and the amide group of VP might interact and act as hydrogen donor-acceptor interactions, with hydroxy carboxylate and/or amino groups of the molnupiravir template.¹² Previous studies have demonstrated that the function of monomers can alter the conformation of a polymer chain within the structure of MIP and that these have a strong effect on the percent yield of MIP. The resultant bulk polymer, with a soap-like appearance, was ground in a mortar and sieved through a 100-mesh sieve to obtain a coarse white powder. The yield of the product varied with the monomer ratio used in each synthesis, as shown in **Table 3**. The polymerization process incorporated MAA and VP as monomers, with various molar ratios of MAA to VP being evaluated. Notably, the formulation with a molar ratio of MAA:VP of 1:2 resulted in the highest yield of polymer.

Table 3. Percentage of Product from Synthesized Polymer.

| Set | Sample | Monomer Ratio | | Yield (%) |
|-----|--------|---------------|----|-----------|
| | | MAA | VP | |
| 1 | NIP1 | 1 | - | 0-5 |
| | MIP1 | 1 | - | 0-5 |
| 2 | NIP2 | - | 1 | 0-5 |
| | MIP2 | - | 1 | 0-5 |
| 3 | NIP3 | 1 | 1 | 59.039 |
| | MIP3 | 1 | 1 | 13.839 |
| 4 | NIP4 | 2 | 1 | 10.845 |
| | MIP4 | 2 | 1 | 13.956 |
| 5 | NIP5 | 1 | 2 | 61.868 |
| | MIP5 | 1 | 2 | 30.319 |

To investigate the selectivity of the imprinted polymer, 1 g of synthesized polymer was mixed with 30 mL of 50% ethanol. It was observed that the polymer did not dissolve in the solvent, and its physical characteristics did not change. The results of molnupiravir adsorption experiments are as follows. From the tests with molnupiravir solution, it was found that the polymer with the highest adsorption capacity for molnupiravir was set 3, specifically MIP3, which used MAA and VP as monomers in equal molar ratios. From calibration curve results for molnupiravir detection by UV/Vis Spectrophotometer at 310 nm as shown in **Figure 1**, it was determined that 1 g of the polymer could adsorb 0.0064 ± 0.0001 g of molnupiravir, as shown in **Figure 2**. The results show that the imprint cavity exhibited good selectivity for the molnupiravir.

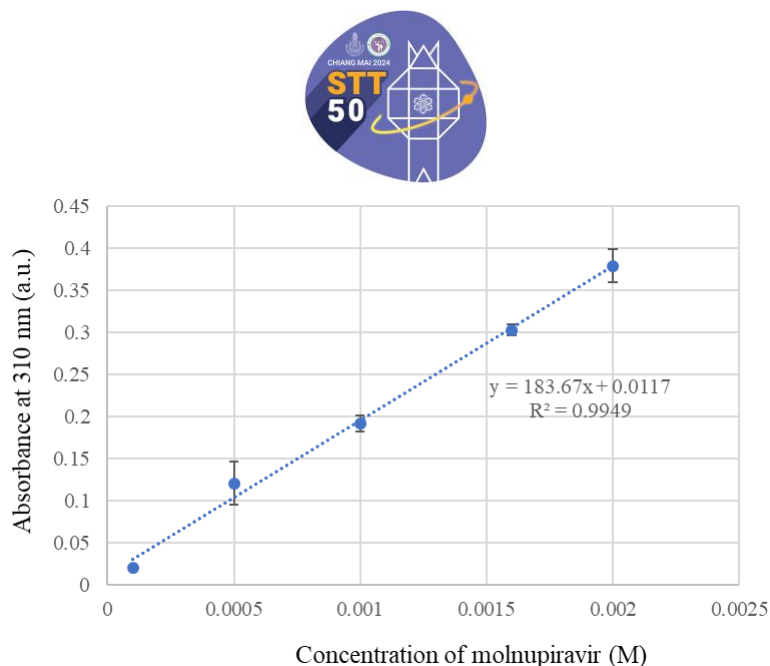


Figure 1. Molnupiravir Calibration Curve

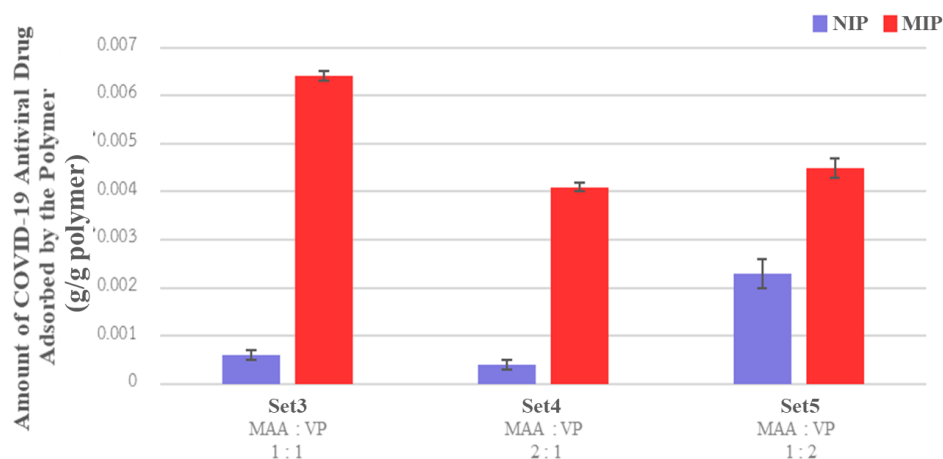


Figure 2. Amount of Molnupiravir Adsorbed by the Polymers.

Figure 3 compares the results of the FT-IR of imprinted polymer and non-imprinted polymer (NIP). It was found that both the MIP and the NIP exhibited similar spectral characteristics. In the FT-IR spectra of NIP3 and MIP3, the absorption peak of the polymer was observed at the stretching vibration of the O-H bond at a wavenumber of 3304 cm^{-1} , which is indicative of the structure of MAA. Additionally, the stretching vibration of the C-N bond from the structure of VP was observed at a wavenumber of 1120 cm^{-1} .

Furthermore, the stretching vibrations of the C-O and C=O bonds were observed at wavenumbers of 1225 cm^{-1} and 1658 cm^{-1} , respectively, indicating the structure of EGDMA. Moreover, in the spectrum range of wavenumbers from 1620 cm^{-1} to 1640 cm^{-1} , no C=C bond was observed, but the presence of the C-C bond was observed at a wavenumber of 1411 cm^{-1} . This confirms the occurrence of radical polymerization reactions in the synthesis of the polymer.

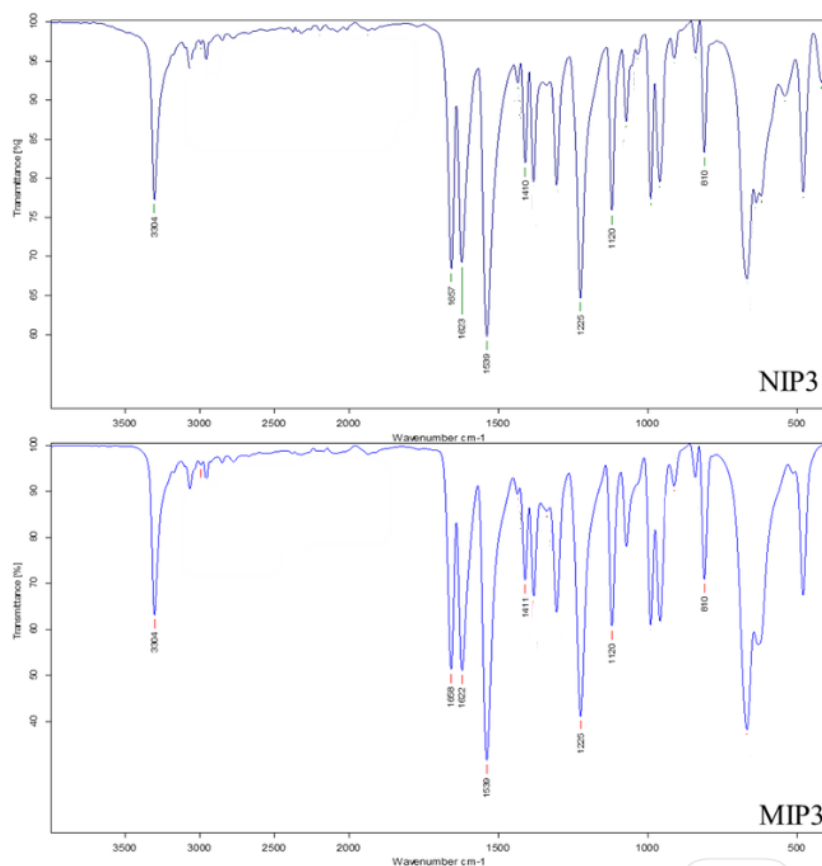


Figure 3. FT-IR spectra of NIP3 and MIP3.

Surface morphology was observed with scanning electron microscopy (SEM). From the SEM micrographs in **Figure 4**, it was found that both the NIP3 and MIP3 polymers from set 3 did not have distinct shapes due to being synthesized in a bulk polymerization manner and being ground before template washing. When observed at a magnification of 15,000 times, it was found that the surface of the synthesized polymer had numerous scattered pores with a pore diameter larger than the control polymer by about 1 μm . These pores were formed due to the template used in the polymer synthesis being the molnupiravir.

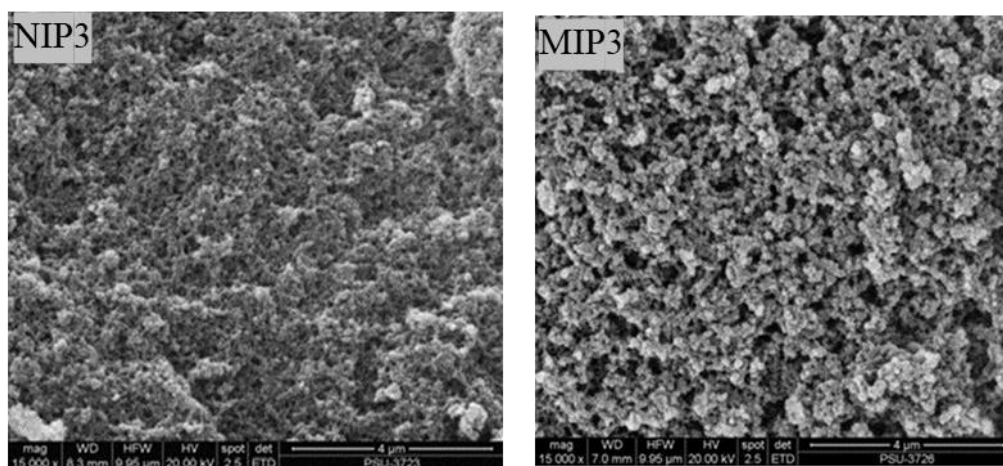


Figure 4. SEM micrographs $\times 15,000$ of NIP3 and MIP3



Conclusion:

From the synthesis, it was found that the polymer imprinted with molnupiravir, synthesized using molnupiravir as a template, methacrylic acid (MAA), and 1-vinyl-2-pyrrolidone (VP) as monomers, with ethylene glycol dimethacrylate (EGDMA) as a crosslinker, and 50% ethanol as a solvent, was achieved. 1,1'-Azobis(cyclohexanecarbonitrile) (ABCN) was used as the initiator. A total of five formulations of polymers were synthesized with varying monomer ratios, along with a control group of Non-Imprinted Polymers (NIP). It was observed that the polymer synthesized with a monomer ratio (MAA:VP) of 1:1 provided a high yield. In the drug adsorption test using UV-Vis Spectrophotometry, it was found that MIP3, which had a monomer ratio of 1:1, exhibited the highest drug adsorption capacity at 0.0064 ± 0.0001 g/g polymer, which was ten times greater than that of the control group. FT-IR spectroscopy analysis of the polymer imprinted with molnupiravir showed that both the template-removed polymer (MIP) and the control polymer (NIP) had similar spectral characteristics. This indicates that polymerization reactions occurred during the polymer synthesis. Furthermore, morphological analysis through SEM revealed significant differences in the pore diameter size and number of pores between the polymer with the imprinted molnupiravir and the control polymer.

Acknowledgements:

The authors are grateful for financial support from the Prince of Songkla University, Pattani Campus Research Fund for the fiscal year 2023, an Innovation and Creative Development Grant, Grant no. SAT6603007S. The sample analysis was supported by the Scientific Equipment Center, Prince of Songkla University.

References:

1. Siriboriruk J. and Prueksaritanond S., *Burapha Journal of Medicine*, 2020;7:89-94,
2. Booncherd C. and Anugoolpracha, S. *Journal of Health Science of Thailand*, 2024;33: 108-119.
3. Hashemian, S. M. R., M. H. Pourhanifeh, M. R. Hamblin, M. K. Shahrzad and H. Mirzaei *Biomedicine & Pharmacotherapy*, 2022;146:112517.
4. Alexander, C., Davidson, L. Hayes, W. *Tetrahedron* 2003;59:2025-2057.
5. Vasapollo, G. *Journal of Molecular Sciences* 2011;12:5908-5945.
6. Yan, H., Row, K. H. *International Journal of Molecular Sciences* 2006;7:155-178.
7. Cetinkaya, A., Ünal, M., Nazir, H., Corman, M., Uzun, L., Ozkan, S. *Microchimica Acta* 2024;191:270.
8. Sayed, R., Elmasry, M., Taha, A., Hassan, W. el nashar, R. *Journal of The Electrochemical Society* 2024;171:6.
9. Suedee, R., V. Seechamnaturakit, A. Suksuwan and B. Canyuk, *International Journal of Molecular Sciences*, 2008;9(12):2333-2356.
10. Noble, B. B. and M. L. Coote, *International Reviews in Physical Chemistry*, 2013;32(3): 467-513.
11. Cunningham, M. F., *Progress in Polymer Science*, 2008;33(4):365-398.
12. Suedee, R., Seechamnaturakit, V., Canyuk, B., Ovatlarnporn, C., Martin, G. P. *Journal of Chromatography A* 2006;1114: 239-249.



THE EXTRACTION OF THE BUDS AND CORE OF HAUYMON PINEAPPLE AND INCREASING THE STABILITY WITH ENCAPSULATION TECHNIQUE

Uthumporn Kankeaw,* Tawisa Pangsakunyanon,

Program in Chemistry, Faculty of Science, Maejo University, Chiang Mai, Thailand

*e-mail: mooeed@hotmail.com

Abstract:

Hauymon pineapple (*Ananas comosus* (L.) Merr.) is a pineapple species native to Nam pat district, Uttaradit. There are vitamins, fiber and flavonoids in pineapple which have antioxidant properties. In this research buds and cores of Hauymon pineapple were extracted with two methods maceration and soxhlet extraction. Ethanol and ethyl acetate were use as solvent to compare the results. The total phenolic content of extract was determined by Folin-Ciocalteu method. The study demonstrated that Soxhlet extraction using ethanol as a solvent express the highest percentage yield at 24.57 and exhibited the total phenolic contents of 71.85 mg GAE/g crude extract and increasing the stability with encapsulation of sodium alginate. The functional group of beads was analyzed by ATR-FTIR technique. Hydroxy group was observed at 3301 cm^{-1} and at 1594 and 1418 cm^{-1} for the aromatic group, respectively. The physical characteristics of the extracted alginate beads were studied under scanning electron microscopy (SEM). The SEM revealed that the microcapsules of extract have fewer fissures and pores than the microcapsules of alginate. Total phenolic release was analyzed at different times and the total phenolic retention efficiency. It was found that the amount of phenolics released after 24 hours being 2 mg/g of microcapsules.

Introduction:

Pineapples are monocot plants that tolerate various environmental conditions well. Once the fruit matures, it continues to develop as the buds on the stem grow into new plants. Pineapples are an important economic crop, widely cultivated in the northern provinces of Thailand. They can be processed using basic technology or advanced techniques in factories, and can be exported to both domestic and international markets. However, industrial processing generates a significant amount of waste. In the food industry, a large portion of agricultural raw materials often remains as waste. One approach to developing an eco-friendly industry is to use raw materials and waste efficiently, reducing the amount of waste or improving its reuse. Similarly, in pineapple processing, the leftover parts such as the cores and skins can be extracted to find bioactive compounds.

Pineapples from Huay Mun, grown in Huay Mun Sub-district, Nam Pad District, Uttaradit Province, are available for harvest throughout the year and can be purchased in Chiang Mai Province. Therefore, the leftover cores and skins of Huay Mun pineapples are extracted to determine the amount of active compounds, specifically the phenolic content.

Amzad Hossain M. and groups [1] studied the total phenolic content, flavonoids, and antioxidant-active compounds in pineapple flesh extracted using a maceration method with methanol, ethyl acetate, and water. The yields were as follows: methanol 21.5%, ethyl acetate 4.9%, and water 4.3%. The total phenolic content was analyzed using the Folin-Ciocalteu method and compared to caffeic acid. It was found that methanol extraction had the highest phenolic content at 51.1 ± 0.2 mg caffeic acid/g, followed by ethyl acetate at 13.8 ± 0.3 mg caffeic acid/g, and water at 2.6 ± 0.1 mg caffeic acid/g, respectively.

Moreover, Wanwisa S. [8] studied the effects of drying temperature and solvents on the active compounds and antioxidant activity of pineapple peel extract. Pineapple peels were dried at temperatures of 70, 80, and 90 degrees celsius and extracted using a soxhlet

extraction method with different solvents: ethanol, methanol, and water. The total phenolic content was analyzed using the Folin-Ciocalteu method and compared to gallic acid. At 70 degrees Celsius, methanol had the highest phenolic content at 1.44 g GAE/100 g of pineapple powder, followed by ethanol at 1.23 g GAE/100 g, and water at 0.95 g GAE/100 g. At 80 degrees Celsius, methanol again had the highest phenolic content at 1.40 g GAE/100 g, with water at 1.20 g GAE/100 g, and ethanol at 0.09 g GAE/100 g. At 90 degrees Celsius, methanol had the highest phenolic content at 0.13 g GAE/100 g, while ethanol and water had the same phenolic content at 0.12 g GAE/100 g. Therefore, the optimal conditions for extracting active compounds from pineapple peel are drying at 70 degrees Celsius and using methanol as the solvent.

From the literature review [2] [3] [4], it is evident that pineapples can be extracted using various solvents with both maceration and soxhlet extraction methods, and still yield high amounts of phenolic compounds. Therefore, exploring methods to extract bioactive compounds from pineapple by-products, such as the bud or core of the pineapple, presents a viable approach solvent. However, the extract obtained through solvent extraction is often viscous and sticky, which makes it difficult to use in further processing. Therefore, the extract is encapsulated into microcapsules to determine the optimal ratio for capsule production. Subsequently, these microcapsules will be applied in product development.

Microencapsulation is the process of enclosing certain substances, such as vitamins, pharmaceuticals, antioxidants, etc., within a thin polymeric capsule known as a microcapsule, which ranges in size from 1 to 1,000 microns. [5] This process helps in maintaining the stability of the substance throughout its use. Encasing sensitive substances that are prone to environmental factors, such as oxidation, light, temperature, and pH changes, improves their stability and extends their shelf life. Additionally, microencapsulation protects volatile substances. [7] Transforming liquid substances into microcapsules can also reduce interactions between mixed substances, make them easier to handle, and control the release of the substances to the targeted area at the appropriate time. Thus, it is beneficial in minimizing waste and optimizing the use of the substances.

In this research, a basic spherification technique will be used. This involves mixing sodium alginate directly with the liquid to be formed into spherical shapes, such as extracts. The mixture is then slowly dripped into a container containing a calcium chloride solution. When sodium alginate comes into contact with calcium, it gradually forms a gel, creating a gel bead with the liquid inside. Afterward, the properties of the encapsulation will be analyzed for further application

Methodology:

1. Preparation of Pineapple bud and Core Samples

Fresh samples of Houymon pineapples were sourced from the market around Sansai district area in Chiang Mai. The bud and core of Houymon pineapples were cut into small pieces and dried at 50 °C in oven for 2-3 days until fully dried. The sample stored in an airtight dark container prior to the extracted process.

2. Extraction

2.1 Maceration

The 200.00 grams of dried core and bud were soaked in 1000 mL of ethanol at room temperature for 3 days. Then, filter out the sediment using cheesecloth and further filter with filter paper number 1, then evaporate the solvent from the obtained extract using a rotary evaporator. Repeat the experiment with the same procedure but change the solvent to ethyl acetate.



2.2 Soxhlet extraction

The 50.00 grams of the dried sample place in a Soxhlet extractor with 250.00 mL of ethanol. The sample was extracted for 3 hours to obtain a crude extract of the pineapple core and buds. Repeat the experiment with the same procedure but use ethyl acetate as the solvent.

3. Analysis of Total Phenolic Compounds in Crude Extracts.

The phenolic content in crude extracts was analyzed by the Folin-Ciocalteu method, adapted from the method of M. Amzad Hossain[1] and comparing with the standard gallic acid.

4. Preparation of Microcapsule extracts.

The microcapsule extracts were prepared with 100 mL solution of 3% (w/v) sodium alginate and 10 mL of 90% (w/v) pineapple extract. The mixture stirred at 80 degrees Celsius and let it cool. Then, the mixture was dropped into 100 mL of 5% (w/v) calcium chloride solution, stirring continuously to prevent the gel beads from sticking together. Stir the solution and leave it to allow the gel to solidify for 30 minutes. The microcapsules were flited from the solution using filter paper number 1 and wash them with distilled water and leave the microcapsules at room temperature for 2 days. The functional groups of the obtained microcapsules were analyzed by ATR-FTIR. Moreover, the structural characteristics of the microcapsules was determined by a scanning electron microscope (SEM).

5. Analyzation of the release of total phenolic compounds from microcapsule extract.

Prepare A pH 4.5 buffer solution prepared by 100 mL of 0.4 M sodium acetate trihydrate and 100 mL of 0.4 M acetic acid. The 0.10 grams of the capsules add to 30 mL of the buffer and stirred the solution for 3 hours. Repeat the procedure by stirring the solution for 6 hours, 12 hours, and 24 hours, respectively. After each specified time, the filtered solution was analyzed total phenolic content by Folin-Ciocalteu method.

Results and Discussion:

1. Extraction of Compounds from Pineapple Crown and Core

Extraction of compounds from pineapple bud and core can be performed using several methods. In this study, we investigated the extraction of compounds from pineapple bud and core using maceration and Soxhlet extraction methods with ethanol and ethyl acetate respectively. The results of each extraction method with both solvents were compared. The physical characteristics of the extracts and the percentage yields are detailed in Table 1. From the Table1 the extraction of pineapple bud and core using both the soxhlet extraction and marceration method, it was found that the using of ethanol effort a higher percentage than the using of ethyl acetates. Therefore, it can be concluded that the desired compounds from pineapple dissolve better in more polar solvents. Hence, ethanol is selected as the solvent for extracting compounds from pineapple bud and core. The soxhlet method, as it requires less extraction time and provides a higher yield compared to the maceration.

2. Analysis of Total Phenolic Compounds in Crude Extracts.

The analysis of the phenolic content in crude extracts by using the Folin-Ciocalteu method, adapted from the method of M. Amzad Hossain and comparing with the standard gallic acid found the result in Table2.

Table 1.
Physical Characteristics of Extracts and Percentage Yields for Each Technique

| Technique | Solvent | Physical Characteristics | % yield |
|--------------------|---------------|--|---------|
| soxhlet extraction | ethanol | viscous Liquid dark brown pineapple aroma | 24.57 |
| | ethyl acetate | viscous Liquid yellowish-brown pineapple aroma | 0.72 |
| maceration | ethanol | viscous Liquid light-brown pineapple aroma | 17.04 |
| | ethyl acetate | viscous Liquid yellow pineapple aroma | 0.18 |

Table 2.
Total Phenolic Content in Milligrams of Gallic Acid per Gram of Extract.

| Technique | Solvent | Total Phenolic Content (milligrams of gallic acid per gram of extract) |
|--------------------|---------------|--|
| soxhlet extraction | ethanol | 71.85 |
| | ethyl acetate | 64.70 |
| maceration | ethanol | 67.70 |
| | ethyl acetate | 50.29 |

When considering the use of each type of solvent in Table2, it was found that ethanol extraction yielded the highest amount of total phenolic compounds, with 71.85 mg GAE/g of extract when using the soxhlet extraction method. These findings are consistent with the research of M. Amzad Hossain[1], which studied the total phenolics, flavonoids, and antioxidant compounds in pineapple flesh using solvents including methanol, ethyl acetate, and water. The study found that methanol extraction had the highest amount of phenolics, followed by ethyl acetate and water, respectively. This indicates that phenolic compounds are likely to be quite polar and dissolve well in alcohol-based solvents, leading to higher yields with alcohol extractions compared to less polar solvents like ethyl acetate. When comparing extraction methods, the differences in the amount of phenolic compounds extracted are not very significant. Therefore, the choice of extraction method may depend on convenience and extraction time. The soxhlet method has the advantage of a shorter extraction time but may lose some active compounds due to the use of heat. The maceration method has the advantage of not using heat, thus preserving some heat-sensitive compounds, but requires a longer extraction time.



3. The preparation of microcapsule with Encapsulation Technique

The preparation of microcapsules with 3% (w/v) sodium alginate and 90% (w/v) pineapple extract drop into a calcium chloride solution, to product capsule beads, as shown in the Figure1.



Figure 1.

Alginate microcapsule (left) and Pineapple extract microcapsule (right)

From **Figure 1**, it can be observed that the appearance of the capsules, when comparing alginate microcapsules and extract microcapsules, shows that both have a droplet shape. However, they differ in color: alginate microcapsules are white, while the extract microcapsules are yellowish-brown, reflecting the color of the pineapple extract mixed with alginate. Based on these physical characteristics, it can be inferred that alginate effectively encapsulates the extract. Therefore, The IR-spectroscopy (ATR-FTIR) and SEM techniques were conducted to examine the molecular and structural levels. The functional groups in the extracted microcapsules were analyzed using the ATR-FTIR technique comparing the spectra of crude extract as shown in **Figure 2**.

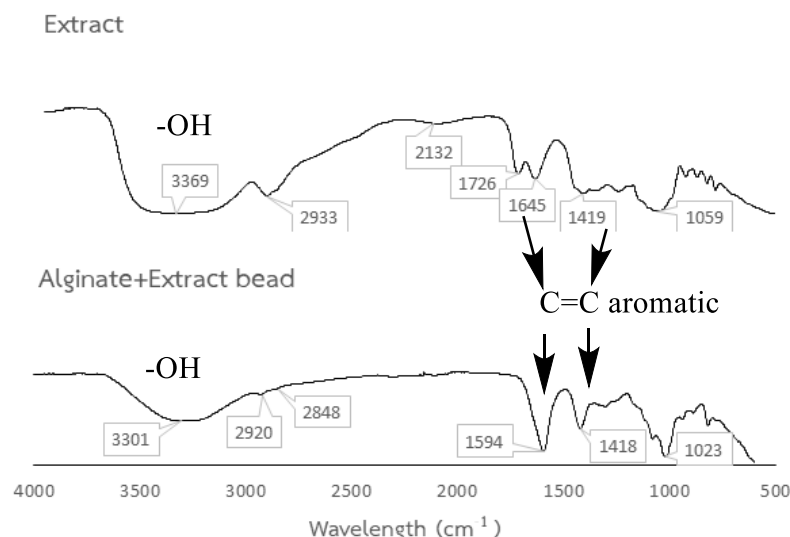


Figure 2.

ATR-FTIR spectrum of extract and extract microcapsules

From the FTIR results, the functional groups in the pineapple extract can be analyzed as phenolic compounds and other components in pineapple. The structure includes hydroxyl, aromatic, and carboxyl groups, as observed from the peaks of O-H, C-H, C=O, C=C, and C-

O stretching appearing at wavenumbers 3369, 2933, 1726, 1645, and 1419 cm^{-1} , respectively. When examining the spectrum of the extract microcapsules, the peaks for O-H stretching and C-O stretching appear at wavenumbers 3301 and 2920 cm^{-1} , respectively, while the aromatic C=C peaks are observed at 1594 and 1418 cm^{-1} . These observations are similar to those of the peak of pineapple extract, suggesting that the extract is indeed incorporated into the microcapsules.

In the study of the microstructure of extract microcapsules compare with alginate microcapsules by using a scanning electron microscope at 1000x magnification, the external characteristics of the microcapsules can be observed, as shown in **Figure 3**.



Figure 3.

SEM of alginate microcapsule (left) and SEM of pineapple extract microcapsule (right)

From the data of SEM of the microstructure of alginate microcapsules and extract microcapsules, it can be observed that alginate microcapsules have deep cracks and a high number of pores. In contrast, extract microcapsules exhibit shallower cracks and fewer pores compared to the alginate microcapsules. This indicates that the extract microcapsules are better at retaining the extract.

4. Analysis of the Release Capability of Total Phenolic Compounds in Microcapsules

The test for the ability to release the total phenolic compounds from microcapsules was conducted by preparing a mixing of the extract microcapsules and pH 4.5 buffer solution and stirring it for 3, 6, 12, and 24 hours. The phenolic compounds in the solution were then quantified using the Folin-Ciocalteu method, modified from the method of M. Amzad Hossain. The result show in **Table 3**.

Table 3.

The release capability of total phenolic compounds in extract microcapsules

| Time (hour) | Total Phenolic Content (milligrams of gallic acid per gram of extract) |
|-------------|--|
| 3 | 1.25 |
| 6 | 1.38 |
| 12 | 1.67 |
| 24 | 2.00 |



Based on the data in **Table 3**, it is evident that as the extract microcapsules are stirred for longer periods, the rate of release of phenolic compounds increases with the duration of the microcapsule immersion. This finding can be applied to cosmetic products to enhance their stability, prolong their effectiveness, improve skin penetration, and increase the efficacy of the cosmetic's desired effects.

Conclusion:

The study demonstrated that the extract of buds and cores of Hauymon pineapple with Soxhlet extraction by using ethanol as a solvent express the highest percentage yield at 24.57% and exhibited the total phenolic contents of 71.85 mg GAE/g crude extract and increasing the stability with encapsulation of sodium alginate. The functional group of beads was analysis by ATR-FTIR technique. Hydroxy group were observed at 3301 cm^{-1} and at 1594 cm^{-1} and 1418 cm^{-1} for the aromatic group, respectively. The physical characteristics of the extracted alginate beads were studied under scanning electron microscopy (SEM). The SEM revealed that the microcapsules of extract have fewer fissures and pores than the microcapsules of alginate. Total phenolic release was analyzed at different times and the total phenolic retention efficiency was analyzed. It was found that the amount of phenolics released after 24 hours being 2 milligrams per gram of microcapsules.

References:

1. Amzad Hossain M, Mizanur Rahman SM. Food Research International. 2011;44:672–676.
2. Martono Y, Novitasari F, Aminu NR. Jurnal Kimia Sains dan Aplikasi. 2020; 23:325-332.
3. Munteanu IG, Apetrei C. Analytical Methods Used in Determining Antioxidant Activity: A Review. 2021;22:3380-3385.
4. Alara OR, Abdurahman NH, Ukaegbu CI. Journal of Applied Research on Medicinal and Aromatic Plants. 2018; 11:12-17.
5. Kühbeck D, Mayr J, Häring M, Hofmann M, Quignard F, Díaz Díaz D. New Journal of Chemistry. 2015;39:2306-2315.
6. Vatcharaporn P, Pichit S. KKU Science Journal. 2017;45:531-542.
7. Timilsena YP, Haque A, Adhikari B. Food and Nutrition Science. 2020;11: 481-508.
8. Wanwisa S, Niramol P. The 9th Science research conference. 2017; May: 372-378.

C-CHEMISTRY (PHYSICAL & THEORETICAL CHEMISTRY)



APPLICATION OF THE DESIGN THINKING PROCESS IN THE DEVELOPMENT OF MAYONGCHID NAKHON NAYOK BOARD GAMES: A STUDY WITH 12TH-GRADE STUDENTS

Poom Tookammee, Sucheewin Chotiwit, Chatchadaporn Pinthong*

Department of Chemistry, Faculty of Science, Srinakharinwirot University, Bangkok 10110, Thailand

*e-mail: chatchadaporn@g.swu.ac.th

Abstract:

Mayongchid Nakhon Nayok, a geographical indication (GI) of Thailand, is predominantly cultivated in Nakhon Nayok province. Despite its significance, there is a gap in the local community's understanding of this fruit's cultivation practices and characteristics. Older farmers primarily hold this knowledge, posing a challenge in transferring this expertise to the younger generation. Our study identified the need for an effective learning tool to bridge this knowledge gap and facilitate the transmission of agricultural techniques from one generation to the next. To address this issue, we designed a series of learning activities that empowered local students to maintain and continue the agricultural heritage associated with Mayongchid Nakhon Nayok. Utilizing a five-stage design thinking process: empathize, define, ideate, prototype, and test. We implemented purposive samples of 12th-grade students from the local area. This process was integrated into each learning activity, enabling students to design and create educational board games incorporating chemistry and problem-solving concepts. The results of our study demonstrated improvements in students' problem-solving abilities; the paired-sample t-test results showed that the mean posttest score (35.13 ± 9.10) was significantly higher than the mean pretest score (21.28 ± 18.90) and overall satisfaction with the learning activities. These findings suggest that integrating design thinking into educational activities can effectively enhance student engagement and knowledge retention. This approach offers valuable insights for curriculum developers, highlighting the potential for such methods to inspire and sustain educational innovation.

Introduction:

The challenges of 21st-century learning management during the rapid development of communication technology enhance the quality of life across economic, political, social, and environmental trends. Therefore, modern teaching and learning methods should prioritize helping students achieve outcome-based learning. It is crucial to foster higher-order thinking skills like analytical thinking and synthesizing new knowledge. These skills require more complex cognitive processes for effective decision-making and problem-solving.¹ Lead students to think critically, make the right decisions, solve problems using appropriate methods, and live with others based on moral and ethical work, which is essential for advancing societal progress.²

The current chemistry curriculum of Thailand was developed by the Office of Basic Education Commission (OBEC) and the Institute for the Promotion of Teaching Science and Technology (IPST). To emphasize knowledge, scientific process skills, 21st-century skills, and scientific attitude. Science, mathematics and technology curriculum (the revised curriculum 2017) following the Basic Education Core Curriculum B.E. 2551 (2008) contained learning outcomes in an extra subject in chemistry that allow students 1) to define problems and propose solutions using their knowledge of chemistry from everyday situation, 2) to provide evidence of the integration of chemical knowledge with other fields of study

including analytical thinking, problem-solving, and creative thinking, 3) to present a piece of work from situational problem-solving or an exciting issue by using information technology, 4) to show the evidence of participation in a seminar, academic conference or in an exhibition.³ Therefore, instructors need to find instructional media for teaching and learning to encourage students to achieve explicit learning, experience, and skills for applying to further careers.

Board games are one of the effective instructional media that enhance students' attention. This method motivates students to engage actively in learning and challenges them to learn through trial and error, making strategic decisions during gameplay.⁴ Research has demonstrated the positive impact of educational board games on learning chemistry, suggesting that incorporating games as educational tools enhances students' conceptual understanding and classroom participation.⁵ Moreover, board games were used to promote student communication and perception. They discuss complex problems and reflect on game elements using their prior knowledge, which promotes sharing, understanding, and addressing communication issues.⁶ Science-themed board games have been shown to develop students' scientific concepts and creative problem-solving skills. The results showed that students perform creative problem-solving abilities by applying their chemistry knowledge to social science issues within game mechanics.⁷ Furthermore, designing and developing board games for various scenarios using a design thinking process allows students to define a problem and ideate solutions. Prototyping and testing these ideas facilitate a deeper understanding and promote effective learning outcomes.

Mayongchid (Marian plum) is an important fruit that generates income for the agricultural sector of Nakhon Nayok province. It has been registered as a geographical indication product of Thailand. Mayongchid Nakhon Nayok is characterized by its yellow-orange color, big size, oval shape, thick and firm flesh, and crispy, fragrant, sweet, and sour taste⁸. Most farmers managing Mayongchid orchards are elderly and require their children to take over these agricultural responsibilities. Young farmers will be more adaptable than older farmers in maintaining this career. Therefore, building knowledge and understanding of Mayongchid cultivation among the new generation is critical, particularly regarding its nutritional value and the growing process. Additionally, it is essential for local farmers to accurately convey information to consumers about Mayongchid, including its high-value-based pricing, health benefits, and the issue of chemical residues from planting and harvesting; that is the pain point of the moment.

Based on the problems mentioned earlier, we had an idea to develop learning activities using a board game with a design thinking process on Mayongchid Nakhon Nayok to promote students learning in chemistry and problem-solving concepts.

Methodology:

This research was conducted through a one-group pretest-posttest design. Forty 12th-grade students from a secondary school in Thailand enrolled in chemistry and problem-solving courses. The learning activities were implemented using the design thinking process and divided into three phases: seven activities, as shown in **Table 1**.

Table 1.
Learning activities with the design thinking process.

| Phases | Activities | Stage of design thinking |
|---------|--|--------------------------|
| Phase 1 | 1. Preparation of students' knowledge before learning the topic of the design thinking process to create a board game. | |
| Phase 2 | 2. Students studied problems or factors | 1. Empathy of Mayongchid |

| Phases | Activities | Stage of design thinking |
|---------|--|---|
| Phase 3 | affecting Mayongchid Nakhon Nayok using in-depth interviews with farmers and document analysis. | Nakhon Nayok's problems. |
| | 3. Students summarized information from individual sources and classified information. | 2. Define problems related to Mayongchid Nakhon Nayok. |
| | 4. Students designed a board game based on data collection about Mayongchid Nakhon Nayok, consistent with science and society issues and presentation in class. | 3. Ideate and design methods to solve Mayongchid Nakhon Nayok's problems. |
| | 5. Students made a board game prototype and checked with a teacher to develop it more efficiently. | 4. Prototype of Mayongchid Nakhon Nayok board game. |
| | 6. Students tested the board game with their classmates. A class discussion was organized, and satisfaction with the board game and an individual score was evaluated. | 5. Test of Nakhon Nayok Mayongchid board game. |
| | Students learning outcomes and the Mayongchid Nakhon Nayok board game were evaluated. | |

Results and Discussion:

Table 2 shows the summaries of students' learning outcomes according to the learning activity, which involved using the design thinking process to create a board game.

Table 2.
The students' learning outcomes with the design thinking activities.

| Activities | Students learning outcomes |
|------------|---|
| Empathy | <ul style="list-style-type: none"> - Students were able to identify problems to solve. - Students could raise questions that helped them access the interviewees' information. |
| Define | <ul style="list-style-type: none"> - Students paid attention to the activities and work in the group. - Students were able to express their opinions and discuss within the group. - Students could summarize the information and identify the problems to make others understand. |
| Ideate | <ul style="list-style-type: none"> - Students were able to analyze the information to design a board game. |
| Prototype | <ul style="list-style-type: none"> - Students were able to create a Mayongchid Nakhon Nayok board game as they designed - Students were able to write their rules for playing the game and let other people understand |
| Test | <ul style="list-style-type: none"> - Students could present their group board game, share their friends to play, and give a score to the board game of their group and the others. |

The students' learning outcomes scores with the design thinking activities were evaluated based on their five-stage performance and the effectiveness of the Mayongchid Nakhon Nayok board games. The average score for student performance and board games was more than 80%, as shown in **Table 3**. The high scores in the prototype stage demonstrate

that students have effectively developed board games that involve chemistry and problem-solving concepts. In contrast, the lower scores in the empathy stage reveal that students initially lacked an understanding of Mayongchid Nakhon Nayok, indicating the importance of providing more experiential learning opportunities to enhance their comprehension and empathy.

Table 3.

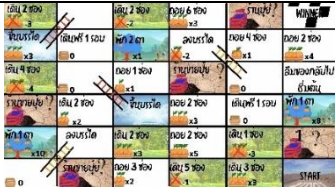

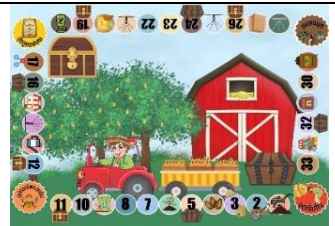
The average student performance scores and board games based on the design thinking process used to develop the Mayongchid Nakhon Nayok board game.




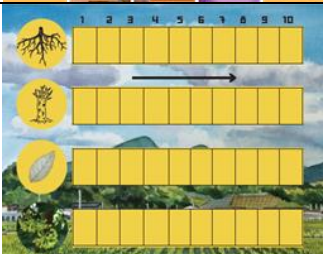

| | Student performance scores of the design thinking process | | | | | Total (25) | Board game (20) |
|------------|---|--------|--------|-----------|------|------------|-----------------|
| | Empathy | Define | Ideate | Prototype | Test | | |
| \bar{x} | 3.50 | 4.30 | 4.05 | 4.80 | 4.60 | 21.25 | 17.75 |
| S.D. | 0.51 | 0.46 | 0.68 | 0.41 | 0.50 | | |
| percentage | | | | | | 85.00 | 88.75 |

Based on the design thinking process, students can create their own board game with different characteristics of the Mayongchid Nakhon Nayok, depending on their collected data, as shown in **Table 4**. These results confirmed in **Table 3** that students had higher scores in the prototype stage.

Table 4.

The example of students' board game.

| Name | Board game | Number of players | Played Time | Theme |
|--------------------------------|---|---------------------|-------------|--|
| Explore the land of Mayongchid |  | Two persons or more | 30 minutes | Sharing ideas about the use of fertilizers in planting Mayongchid and the sale of Mayongchid |
| Mayongchid, I am here |  | 3 – 6 persons | 40 minutes | Planning and taking care of Mayongchid to get the product that makes the highest profit from the sales |
| Billion baht Mayonchid |  | 2 – 6 persons | 40 minutes | Sharing ideas about the use of fertilizers in planting Mayongchid and the sale of Mayongchid |

| | | | | |
|---------------------------------|---|---|------------|--|
| Joyful Mayongchid |  | Four persons or more | 40 minutes | Pest control and how to take care of Mayongchid trees and fruit |
| Grandma's Mayongchid Orchard |  | Four persons or more divided into two teams | 40 minutes | How to take care of an orchard of mature Mayongchid to get quality Mayongchid fruit under a limited budget |
| Where Bug |  | Five persons or more | 40 minutes | Types and structures of chemicals associated with Mayongchid |
| Sell Mayongchid and Catch a Spy |  | 6- 8 persons divided into two teams | 40 minutes | How to take care of Mayongchid roots, trunks, leaves, flowers, and fruit |
| The Finding Traitor |  | Five persons or more | 40 minutes | How to plant Mayongchid trees |

Moreover, the achievement test of problem-solving skills was determined using four open-ended questions with a total score of 48. Each question has a chemistry and problem-solving scenario, which allows students to use scientific methods to solve it. The data were then evaluated using a paired-sample t-test for dependent samples, which showed that at a 0.05 significance level, the mean score of the posttests (35.13 ± 9.10) was significantly higher than the mean score of pretests (21.28 ± 18.90) shown in **Table 5**. The findings indicate that integrating the design thinking process into the learning unit. This can encourage students to connect their knowledge to a scientific process, leading to students having problem-solving skills in the context of chemistry. For example, students know about using fertilizers to plant Mayongchid and reducing the use of pesticides, how to take care of an orchard of mature Mayongchid to get quality Mayongchid fruit under a limited budget, etc.

Table 5.
Statistical parameters for problem-solving skills test.

| Problem-solving skill test | n | Total score | \bar{x} | S.D. | t | df | p |
|-----------------------------------|----------|--------------------|-----------------------------|-------------|----------|-----------|-------------------|
| Pretest | 40 | 48 | 21.28 | 18.90 | 24.69 | 39 | .000 ^a |
| posttest | 40 | 48 | 35.13 | 9.10 | | | |

^aSignificant at the level of $p < 0.05$

The developed learning activities align with the core components of the science and technology curriculum, as revised in 2017 under the Basic Education Core Curriculum B.E. 2551 (2008), which was specific to students who learn in Nakhon Nayok province. This study highlights the effectiveness of incorporating the design thinking process into activities, particularly in developing board games that challenge students to create a game from the learning process. One notable application involved the agricultural product Mayongchid, which is significant in Nakhon Nayok. The information revealed that students had limited knowledge about Mayongchid, indicating a gap that these learning activities effectively addressed. The design thinking process motivated students to engage in deeper inquiry, prompting them to formulate questions, conduct systematic research, and discuss real problem issues. This investigative approach increased their knowledge about Mayongchid and enhanced their problem-solving skills. The activities facilitated opportunities for students to express their opinions in groups and share ideas to develop prototypes, which, consistent with Pitchaya Klaharn (2021), demonstrated learning activities based on the design thinking process and project-based learning management promoted active engagement, inquiry, observation, and interaction, contributing to knowledge to connection through peer discussions. Similarly, Sumitra Bucha (2020) found that learning activities based on design thinking and a participatory learning approach significantly enhanced student's creative thinking⁹. Students played a role in learning and working together as a collaborative, which had knowledge sharing, including working collaboratively to create a successful work as they designed.

These findings show the importance of integrating the design thinking process into the chemistry and problem-solving learning unit. This can encourage students to connect their knowledge to a scientific process, leading to more meaningful and effective learning outcomes as students have problem-solving skills in the context of chemistry and building a body of knowledge independently. Learning activities in class stimulate students to have thinking and practice abilities. Therefore, students had the highest level of satisfaction with the learning management. This is consistent with Manit Asanok (2020), who conducted a study on integrating design thinking to develop learning management innovation¹⁰. It was found that the design thinking process promotes students' learning and development skills, including creative thinking and problem-solving processes, through doing by themselves.

Design thinking learning activities allow students to demonstrate their potential through a 5-stage process, developing questioning skills, observation skills, and understanding situations and environments at that time, using their own experiences. It emphasizes students' hands-on experience in discovering and creating knowledge by themselves. Students connect their knowledge and experiences, creating works or projects and identifying issues related to longan, which are exciting and real in their immediate society. Students explore challenging problems in their communities, present ideas and methods of solving problems to users, and promote the courage to express themselves. It allows students to experiment, have self-confidence, and successfully create works or projects from students' problem-solving skills. The design thinking process can be applied to increase problem-solving skills and create innovations, effectively promoting 21st-century

learning skills. Therefore, it can be seen that design thinking has been applied to classroom learning activities for students. Students who have used design thinking in learning activities have advanced problem-solving skills that they can apply in their studies and daily lives.

Conclusion:

We successfully developed the Mayongchid Nakhon Nayok board game using a design thinking process with 12th-grade students, demonstrating this approach's effectiveness. Students could engage in the five stages of design thinking: empathize, define, ideate, prototype, and test. The results indicated that over 80% of students achieved the learning outcomes. They can apply their design thinking knowledge to create innovative board games that showcase various characteristics of Mayongchid Nakhon Nayok. These findings suggest that integrating design thinking into learning activities can significantly enhance students' problem-solving skills and foster creativity.

Acknowledgements:

This work was funded by Strategic Wisdom and Research Institute (grant numbers 381/2566) and Graduate School, Srinakharinwirot University (grant numbers 317/2565) (to C. Pinthong). We thank Dr. Wissawat Sakulsaknimitr, Kasetsart University, Sriracha campus, and Assistant Prof. Piyarat Srivilai, Srinakharinwirot University, for insightful suggestions.

References:

1. Royal Academy. Dictionary of Educational Terms Royal Academy. 2012.
2. Chantorn K. Journal of Education, Silpakorn University. 2022;1:143–158.
3. Institute for the Promotion of Teaching Science and Technology. Indicators and core learning content Science learning subject group (Revised Edition B.E. 2017) according to the core curriculum Basic Education, B.E. 2008. 2017.
4. Songsai N. E-Journal of Media Innovation and Creative Education. 2020;3:1–11.
5. Franco Mariscal A.J; Oliva-Martínez J.M, Almoraima Gil M.L.J. Chem. Educ. 2015;92 (2):278-285.
6. Eisenack K. Simulation & gaming. 2013;44:328–348.
7. Chen S.Y. Thinking Skills and Creativity. 2021;41:100921.
8. Department of Intellectual Property. Thailand's Geographical Indication Mayongchid Nakhon Nayok. 2015.
9. Bucha S. Journal of MCU Nakhondhat. 2020;7(12):210–221.
10. Asanok M. Journal of Educational Technology and Communications Faculty of Education Mahasarakham University. 2018;1(1):6–12.



DESIGNED A SERIES OF NEW COMPOUNDS OF ACETANILIDE DERIVATIVES WITH INHIBITION OF TOPOISOMERASE I AND II OF BREAST CANCER CELL

Prechakorn Yasamorn, Rachanon Thiratrakulchai,* Sutthasin Kunmongkonwut, Sirihathai Srikwanjai and Sorachai Sae-lim

Mahidol Wittayanusorn School, Phutthamonthon, Nakhon Pathom, Thailand

*e-mail: rachanon.thi_g32@mwit.ac.th

Abstract:

Breast cancer is one of the most prevalent diseases worldwide. Chemotherapy is a crucial treatment option, though it has many adverse effects. "*N*-phenylacetamide" or "Acetanilide" derivatives remain largely unexplored in anticancer research. In this study, derivatives of acetanilide compounds were meticulously crafted to assess their biological efficacy. A total of sixty-eight compounds were designed, followed by a rigorous evaluation. Employing advanced computational techniques, including ADMET analysis using SwissADME, geometry optimization via Gaussian 09, and molecular docking with Autodock Vina, physicochemical descriptors were computed, facilitating the prediction of ADME parameters, pharmacokinetic properties, drug-likeness, and medicinal chemistry friendliness of potential small molecules, thereby bolstering drug discovery endeavors. Compounds M3, M10, and M11 emerged as promising candidates with lead-like characteristics among the developed acetanilide derivatives. By demonstrating strong binding affinity to the target proteins Human Topoisomerase, I and II, as evidenced by docking scores ranging from -6.5 to -7.3 kcal/mol and -6.8 to -7.7 kcal/mol, respectively, 2-hydroxy-*N*-(4-hydroxyphenyl) propanamide (M10) exhibited superior inhibition of both topoisomerases compared to the positive controls (Melphalan: -6.6 and -5.8 kcal/mol). These *in silico* analyses suggest substantial potential for pharmacological activity *in vivo*. This research project delves into the intriguing pharmacological properties of newly synthesized compounds, presenting a promising avenue for breakthroughs in cancer research.

Introduction:

Breast cancer is one of the most common cancers affecting women worldwide. Breast cancer significantly contributes to cancer morbidity and mortality worldwide. It originates in the cells of the lungs and is among the most common types of cancer, leading to a high number of cancer-related deaths². Chemotherapy is a crucial treatment option despite its many adverse effects. "*N*-phenylacetamide" or "Acetanilide" derivatives remain largely unexplored in anticancer research (**Figure 1**).

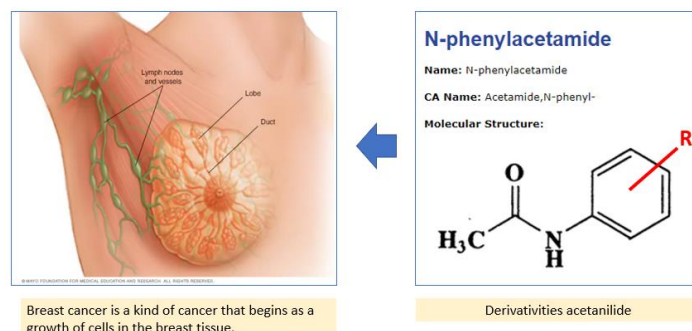


Figure 1.
Breast cancer and derivatives acetanilide.

Small-molecule drugs remain the most commonly used treatment for cancer. However, the cytostatic agents and DNA poisons initially developed for clinical use are losing their prominence. Their severe, often life-threatening, and difficult-to-manage side effects significantly degrade patients' quality of life and frequently lead to therapy discontinuation. This is due to their non-specific mechanism of action and low selectivity. Some alkylating agents are more toxic to normal cells than to malignant ones. Another common issue is the development of resistance, which may emerge after a brief positive response to therapy or even occur immediately in some patients. This resistance is also challenging in targeted therapies using novel agents like kinase inhibitors and larger therapeutics like monoclonal antibodies. Therefore, while novel small-molecule agents are still in demand, newly designed compounds must possess a specifically targeted mechanism of action and good selectivity for cancer cells over normal cells. Simple aromatic amides are attractive scaffolds for designing new drugs because they resemble biological structures and have excellent synthetic availability. Drugs used in the clinic, such as Niclosamide, Flutamide, Mebendazole, Sirtinol, and Derivative of amide A, contained a scaffold of acetanilide derivatives (**Figure 2**).

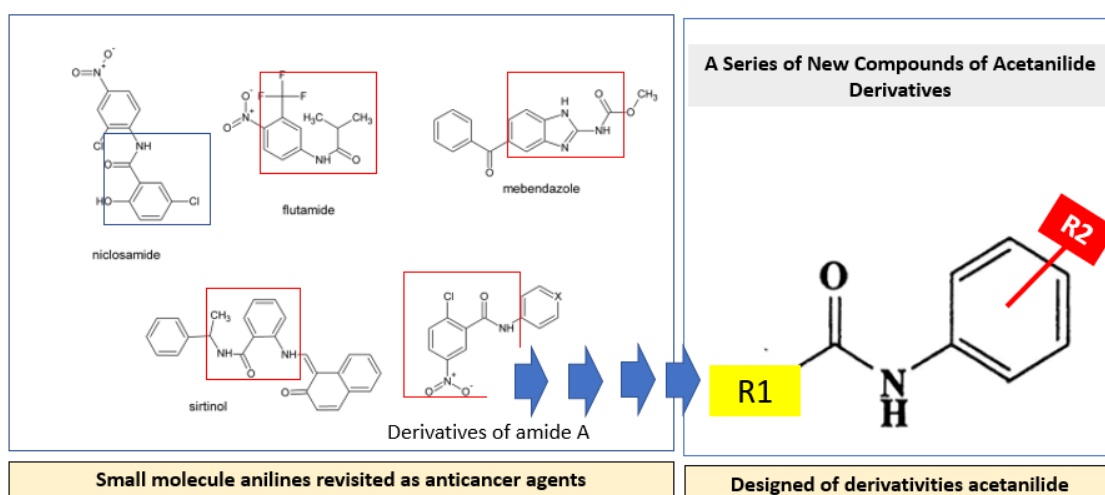


Figure 2.

Drugs used in the clinic, such as Niclosamide, Flutamide, Mebendazole, Sirtinol, and Derivative of amide A, contained a scaffold of acetanilide derivatives.

We decided to exploit the acetanilide skeleton compounds to increase its lipophilicity and affinity to DNA and the replicative enzymes for drugs anti-cancer cells by using Molecular docking, which simulates the binding between a receptor and a ligand. In our continuing search for potential drug candidates.

Methodology:

Designed the structures of Ligand

Acetanilide derivatives contain naphthalic acid (R1) and aromatic amines (R2), which showed the results in their synthetic availability. On the other hand, no specific target has yet been proposed for similar compounds and their mechanism of action appears to be multitargeted as described for niclosamide or its analogs. An overview of this approach is presented in **Figure 3**. A commercial library of building blocks can easily cover the substitution pattern in the amine moiety selected in this approach. This method seems particularly suitable for designing easily obtainable compounds with a common structural motif, as we reported for anticancers.

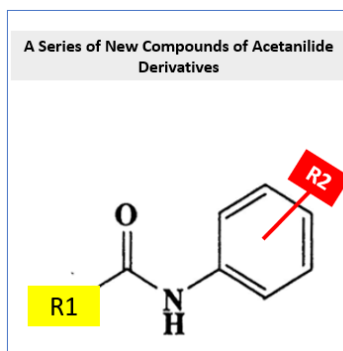


Figure 3.

Design of the target amides, naphthalic acid (R1), and aromatic amines (R2).
Compounds with an anticancer activity provided amine-derived.

Computational Methods

1. Drug-likeness Screening

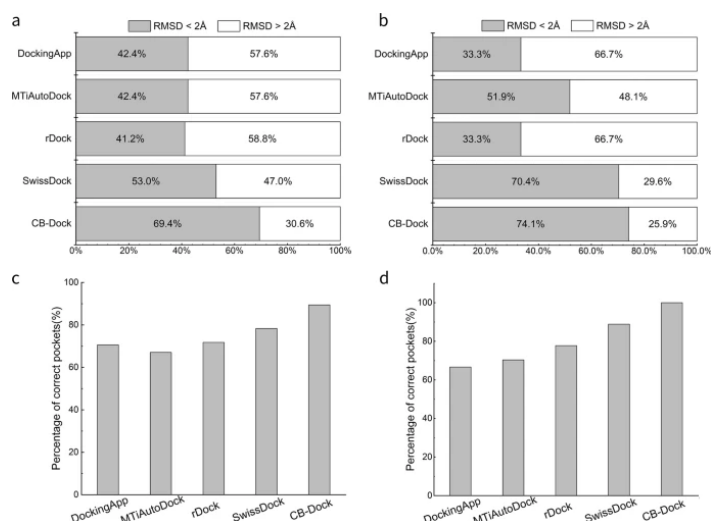
Drug-likeness of compounds acetanilide derivative compounds were determined using SwissADME (<http://www.swissadme.ch/index.php>). According to 4 criteria, no lead likeness violations (molecular weight < 350 Dalton, LogP < 3.5, number of rotatable bonds ≤ 7), no Lipinski rule of 5 violations (molecular weight < 500 Dalton, LogP < 5, number of hydrogen bond donor ≤ 5 , and number of hydrogen bond acceptor ≤ 5), TPSA (Topological Polar Surface Area) < 120 Å², and high GI absorption (Gastrointestinal absorption).

2. Absorption, Distribution, Metabolism, Excretion, and Toxicity (ADMET method)

A further ADMET study of acetanilide derivative compounds was carried out using SwissADME (<http://www.swissadme.ch/>). The ADMET properties were considered as follows: Absorption (Human Intestinal Absorption, Caco-2 Permeability, Pgp-Substrate, Pgp-Inhibitor I, Pgp-Inhibitor II, and Renal Organic Cation Transporter), Distribution (Blood-Brain Barrier and Subcellular localization), Metabolism (CYP450 2C9 Substrate, CYP450 2D6 Substrate, CYP450 3A4 Substrate, CYP450 1A2 Inhibitor, CYP450 2C9 Inhibitor, CYP450 2D6 Inhibitor, CYP450 2C19 Inhibitor, CYP450 3A4 Inhibitor), and Excretion (CYP Positively Promiscuity), and Toxicity (skin sensitization, Estrogen receptor binding, Aromatase binding, AMES Toxicity, Acute Oral Toxicity, and Carcinogens).

3. Molecular Docking Studies

Molecular docking simulates the binding between a receptor and a ligand. This method is essential in drug development using computers as a computational aid. The aim of doing Protein-Ligand molecular docking is a predicted 3D binding between receptors, which are proteins and ligands. The binding simulation randomly determines the optimal structure by calculating binding energy terms and using the scoring function as a scoring index, the Vina score, with the more significant the negative. It shows excellent protein-ligand binding capacity. The DockingApp, MTiAutoDock, rDock, SwissDock performance, and CB-Dock on Astex Diverse Set and MTiAutoDock Set websites were used to compare programs using molecular docking to determine proteins and ligands' three-dimensional (3D) structure, predicting capture position and correlation. CB-Dock websites showed the most accurate and accurate graph in **Figure 4**. Yang Cao Lab developed the CB-Dock website, which signifies the binding site of a given protein and calculates its center and size with a new curvature-based compartment detection method. It was carefully optimized and had a success rate of about 70% with a mean squared mean (RMSD). As ≤ 2 Å, which outperformed the Molecular Instruments, another docking, the researcher focused on using the CB-Dock website to study docking molecules.

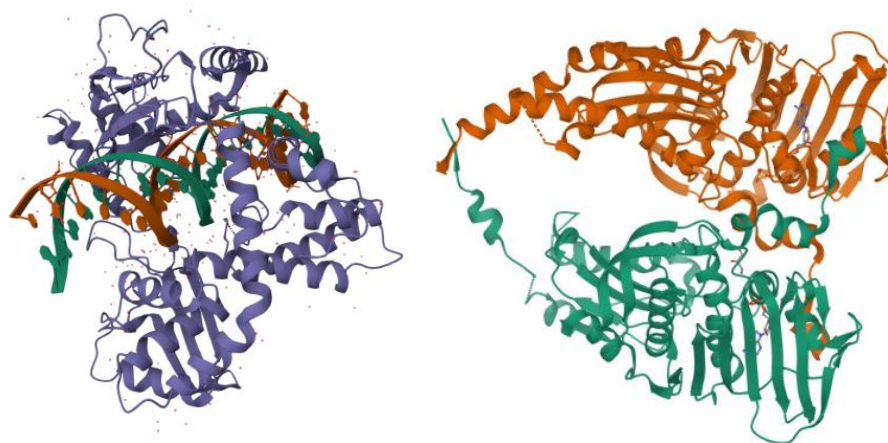
**Figure 4.**

DockingApp, MTiAutoDock, rDock, SwissDock performance, and CB-Dock on Astex Diverse Set and MTiAutoDock Set. (Yang Liu, 2019).

3.1. Protein and Ligand Preparation.

Toxicology predictions for ligands and ADMET were also made using the pkSCM and Molsoft websites with the hyperlink <https://structure.bioc.cam.ac.uk/pkscm> and <https://www.molsoft.com/>, respectively, the three-dimensional structure of the ligands was obtained from the PubChem website <https://pubchem.ncbi.nlm.nih.gov/>.

3.1.1 Protein Preparation



Topoisomerase I (PDB: 1A35) Topoisomerase II (PDB: 4FM9)

Figure 5.

Human DNA topoisomerase I and II ATPase/ADP.

3.1.2 Ligand Preparation

Acetanilide derivatives comprise naphthalic acid (R1) and aromatic amines (R2), resulting in synthetic availability. The sixty-eight compounds were obtained. The 3D structures of derivatives acetanilide were obtained from the DFT calculations using the M062X method with the 6-31g(d,p) basis set implemented in the Gaussian09W package (Frisch et al., 2009).

3.2 Preparation of the Grid area for molecular docking

Using Autodock Vina 1.1.2 for molecular docking, the grid area is determined using the receptor grid generation feature to identify the region in the system that serves as a receptor. The grid area is set using the receptor grid generation feature in the Maestro. The grid is set with the inhibitory center of topoisomerase I and II, the native ligands of PDB ID 1A35 and 4FM9, at the protein's active site. We locked a grid area with the center coordinates of both for Topoisomerase I and II as X = 25, Y = 25, and Z = 25, and the grid box center is 19x20x33 and 43x30x12 respectively. The topoisomerase I and II-DNA complex were kept rigid. Well-known amino acid residues defined the binding sites of the ligands on the receptor. Subsequently, the grid box was fixed, and the area of interest on the receptor was mapped by grid parameters, grid spacing with 1.000 Å using the Centre of the target topoisomerase I and II-DNA complex (PDB: 1A35, 4FM9) as the Centre of the grid box. The Van der Waals radius is scaled to 1 in the Ligand section, with a partial charge cutoff of 0.25.

Molecular docking uses an extra-high level of accuracy (XP) option. Using the Protein Preparation Wizard function of the Maestro program, the three-dimensional structure of proteins is prepared by attaching hydrogen atoms, eliminating water molecules that do not interact with proteins, enhancing protein structure, and optimizing hydrogen bonds in proteins.

Results and Discussion:

1. The design of structures of ligands for drug compounds to anticancer cell

Acetanilide derivatives are composed of naphthalic acid (R1) and aromatic amines (R2), resulting in synthetic availability. The sixty-eight compounds were designed, followed by a rigorous evaluation. Employing computational techniques, including ADMET analysis using SwissADME, geometry optimization via Gaussian 09, and molecular docking with Autodock Vina, physicochemical descriptors were computed. This facilitated the prediction of ADME parameters, pharmacokinetic properties, drug-likeness, and medicinal chemistry friendliness of potential small molecules, thereby bolstering drug discovery endeavors.

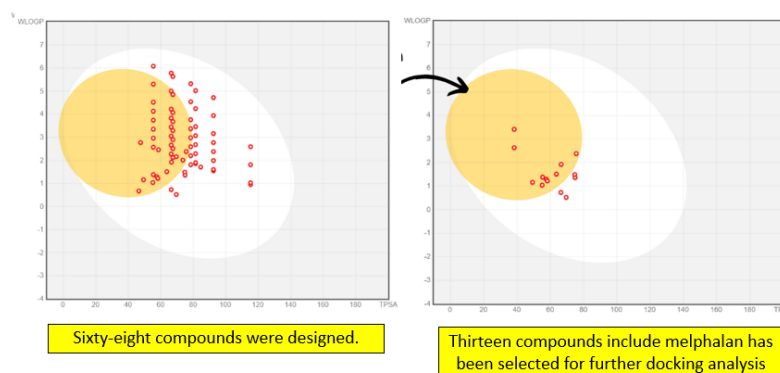


Figure 6.

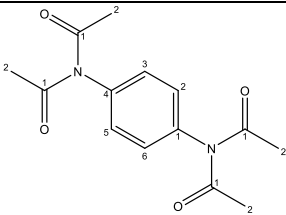
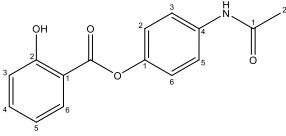
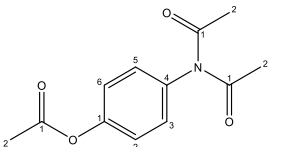
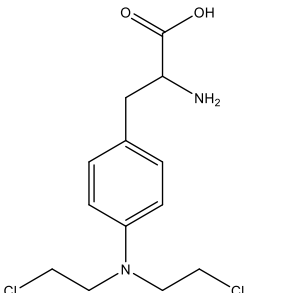
Results show that thirteen compounds were selected as drug compounds for docking.

Table 1.

The structure of molecular docking.

| No. | Structure | smile | Name |
|-----|-----------|---------------------------------|----------------------------------|
| M0 | | <chem>CC(=O)Nc1ccc(O)cc1</chem> | N-(4-hydroxyphenyl) acetamide |

| No. | Structure | smile | Name |
|-----|-----------|---|---|
| M1 | | <chem>O=C1C=C/C(C=C1)=N/C(C)=O</chem> | <i>N</i> -(4-oxocyclohexa-2,5-dien-1-ylidene)acetamide |
| M2 | | <chem>OC1=CC=C(C=C1)N(C(C)=O)C(C)=O</chem> | <i>N</i> -acetyl- <i>N</i> -(4-hydroxyphenyl)-acetamide |
| M3 | | <chem>OC1=CC=C(C=C1)NC(C(C)=O)O</chem> | 2-hydroxy- <i>N</i> -(4-hydroxyphenyl)propanamide |
| M4 | | <chem>OC1=CC=C(C=C1)NC(C(C)=O)C(=O)O</chem> | <i>N</i> -(4-hydroxyphenyl)-2-oxopropanamide |
| M5 | | <chem>CC(=O)OC1=CC=C(C=C1)NC(C)=O</chem> | 4-acetaminophenyl acetate |
| M6 | | <chem>CC(=O)Nc1ccc([N+](=O)[O-])cc1</chem> | <i>N</i> -(4-nitrophenyl)acetamide |
| M7 | | <chem>CC(=O)Nc1ccc(N)cc1</chem> | <i>N</i> -(4-aminophenyl)acetamide |
| M8 | | <chem>CC(=O)Nc1ccc(NC(C)=O)cc1</chem> | <i>N,N'</i> -(1,4-phenylene)diacetamide |

| No. | Structure | smile | Name |
|------------|---|--|--|
| M9 |  | <chem>CC(N(C(C)=O)C1=CC=C(C=C1)N(C(C)=O)C(C)=O)=O</chem> | <i>N,N'</i> -(1,4-phenylene) bis(<i>N</i> -acetylacetamide) |
| M10 |  | <chem>CC(NC1=CC=C(C=C1)OC(=O)C2=CC(=O)C=CC=C2)=O</chem> | 4-acetamidophenyl 2-hydroxybenzoate |
| M11 |  | <chem>CC(N(C(C)=O)C1=CC=C(OC(=O)C)C=C1)=O</chem> | 4-(<i>N</i> -acetylacetamido)phenyl acetate |
| Melp-halan |  | <chem>O=C(O)C(N)CC1=CC=C(N(CCCl)CCCl)C=C1</chem> | 2-amino-3-(4-(bis(2-chloroethyl)amino)phenyl)propanoic acid |

2. The predictions of drug-likeness

2.1 Lipinski's Rule of Five, Drug Likeness Score, and ADMET Prediction.

The compounds were carried out using SwissADME (<http://www.swissadme.ch/index.php>). The results of Lipinski's rule and drug-likeness scores are shown in **Table 2**, and ADMET predictions are shown in **Table 3**.

Table 2.
Drug-likeness predictions of compounds M2-M11, computed by SwissADME.

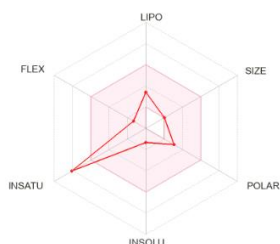
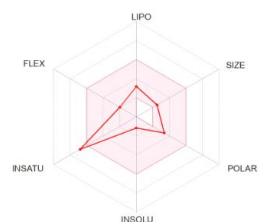
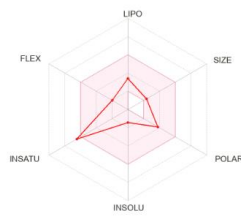
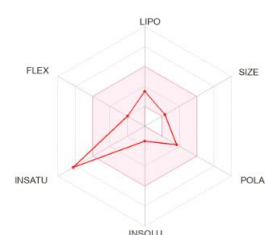
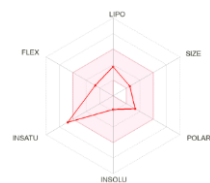
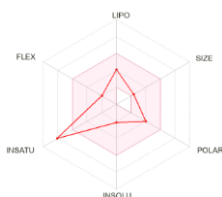
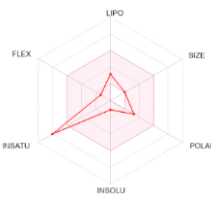
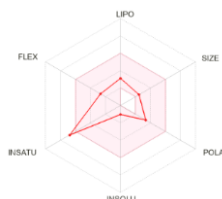
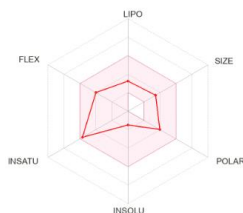
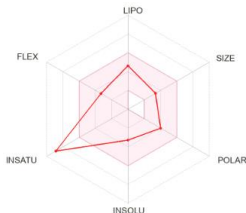
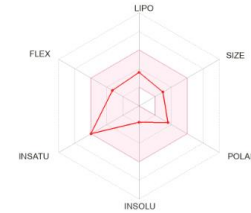
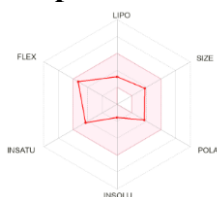
| No. | MW (g.mol ⁻¹) | TPSA (Å ²) | R.B | H.A | H.D | L.V | W Log P | Log S (ESOL) |
|-----|------------------------------|---------------------------|-----|-----|-----|-----|---------|-----------------|
| M2 | 193.20 | 49.33 | 2 | 2 | 2 | 0 | 1.16 | -1.34 |
| M3 | 181.19 | 57.61 | 3 | 3 | 1 | 0 | 1.29 | -1.18 |
| M4 | 179.17 | 69.56 | 3 | 3 | 3 | 0 | 0.52 | -1.42 |
| M5 | 193.20 | 66.4 | 3 | 3 | 2 | 0 | 0.73 | -1.49 |
| M6 | 180.16 | 55.4 | 4 | 3 | 1 | 0 | 1.38 | -1.75 |
| M7 | 150.18 | 74.92 | 3 | 3 | 1 | 0 | 1.36 | -2.15 |
| M8 | 192.21 | 55.12 | 2 | 1 | 2 | 0 | 1.04 | -1.09 |

| No. | MW (g.mol ⁻¹) | TPSA (Å ²) | R.B | H.A | H.D | L.V | W Log P | Log S (ESOL) |
|-----|------------------------------|---------------------------|-----|-----|-----|-----|---------|-----------------|
| M9 | 276.29 | 58.2 | 4 | 2 | 2 | 0 | 1.22 | -1.05 |
| M10 | 271.27 | 74.76 | 6 | 4 | 0 | 0 | 1.49 | -1.5 |
| M11 | 235.24 | 75.63 | 5 | 4 | 2 | 0 | 2.38 | -3.27 |

Table 3.

ADME predictions of compounds M2-M11, computed by SwissADME.

| No. | LogKp (cm/s) | GIA | BBB | Pgp substrate | Inhibitor interaction (SwissADME) | | | | |
|-----|-----------------|------|-----|------------------|-----------------------------------|---------|--------|--------|--------|
| | | | | | CYP1A2 | CYP2C19 | CYP2C9 | CYP2D6 | CYP3A4 |
| M2 | -6.90 | High | Yes | No | No | No | No | No | No |
| M3 | -7.45 | High | Yes | No | No | No | No | No | No |
| M4 | -7.06 | High | No | No | No | No | No | No | No |
| M5 | -6.95 | High | No | No | No | No | No | No | No |
| M6 | -6.73 | High | Yes | No | No | No | No | No | No |
| M7 | -6.22 | High | No | No | Yes | No | No | No | No |
| M8 | -7.16 | High | Yes | No | No | No | No | No | No |
| M9 | -7.52 | High | Yes | No | No | No | No | No | No |
| M10 | -7.84 | High | No | No | No | No | No | No | No |
| M11 | -6.12 | High | Yes | No | No | No | No | No | No |

M0**M2****M3****M4****M5****M6****M7****M8****M9****M10****M11****Melphalan****Figure 7.**

Radar plot of the selected ligands and phytoconstituents based on physicochemical indices ideal for oral bioavailability.

The data suggest that M2-M10 and M11 likely exhibit excellent ADMET properties (**Table 2-3** and **Figure 7**).

3. Molecular docking simulation

Molecular docking simulations were utilized to elucidate the interactions between M2-M10, M11, and Melphalan. First, the optimized structure of M2 was obtained from DFT calculations using the B3LYP method with the 6-31G(d,p) basis set implemented in Gaussian09W, and the protein crystal structure was obtained from the Protein Data Bank. Subsequently, the PDB files of the protein and the ligand were uploaded to the CB-Dock2 web server (<https://cadd.labshare.cn/cb-dock2/php/index.php>). This server allows a convenient binding cavity detection, followed by a structure-based docking with AutoDock Vina. The final results were visualized using the PyMol program. The results show that identifying the best-docked pose with a Vina score of topoisomerases I and II (**Figure 8**).

| Name | Topoisomerase I | Topoisomerase II |
|-----------|-----------------|------------------|
| M0 | -6.4 | -6.1 |
| M2 | -6.9 | -7.1 |
| M3 | -6.7 | -7.1 |
| M4 | -6.7 | -7.1 |
| M5 | -6.5 | -6.3 |
| M6 | -6.3 | -6.0 |
| M7 | -6.2 | -6.5 |
| M8 | -6.9 | -6.5 |
| M9 | -6.7 | -6.9 |
| M10 | -7.3 | -7.7 |
| M11 | -6.5 | -6.8 |
| Melphalan | -6.6 | -5.8 |

Figure 8.

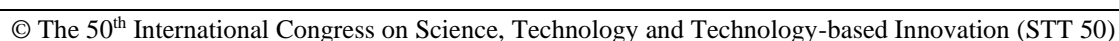
A Vina score with Topoisomerase I and II.

Consequently, the molecular docking findings support the activity observed experimentally in silico. M3, M10, and M11 showed the Vina score more than Melphalan as a positive control in topoisomerase I and II (**Figures 8-9** and **Table 4**).

Table 4.

Molecular docking scores and the corresponding residual amino acid and DNA interaction of the isolated compounds and standard drugs melphalan against Human Topoisomerase I and II.

| Compounds | Lowest binding energy (kcal/mol) | H-bonding with | Hydrophobic bonding with |
|------------------------------|----------------------------------|----------------------|---------------------------------------|
| Human Topoisomerase I | | | |
| M3 | -6.7 | Arg362, Arg364, da14 | Da13, da113, dg12, da15, dt112, dt111 |



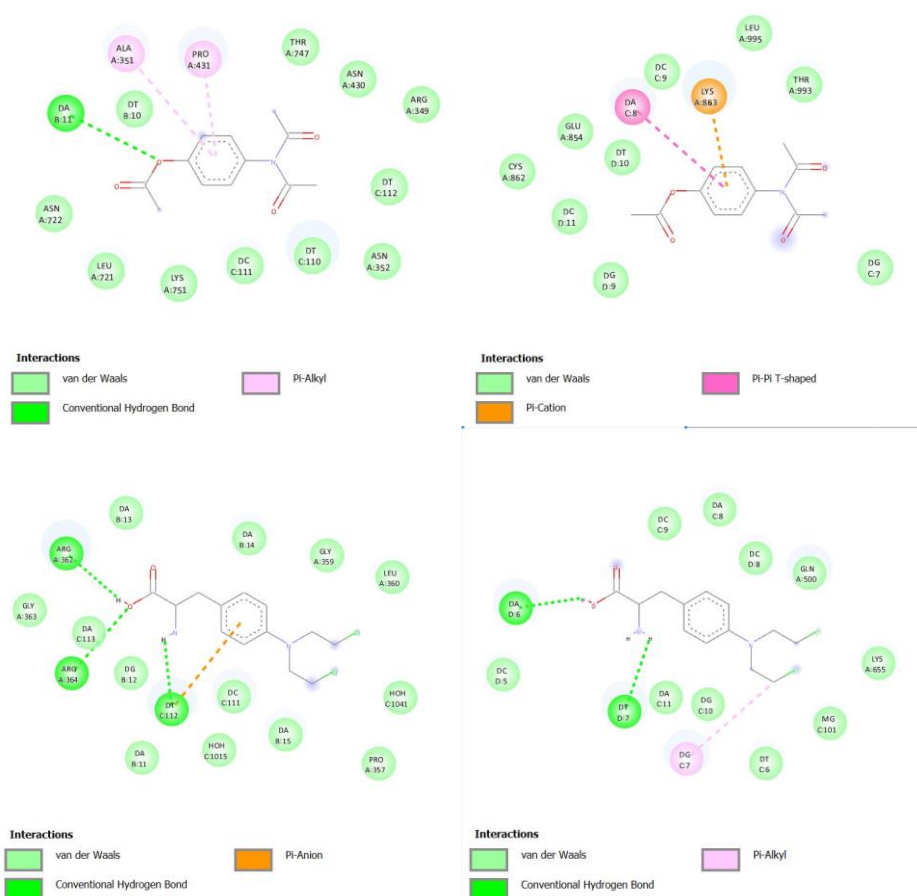


Figure 9.

Three-dimensional (3D) and two-dimension (2D) a residual interactions network of the best selective compounds with the active site of topoisomerase I and II.

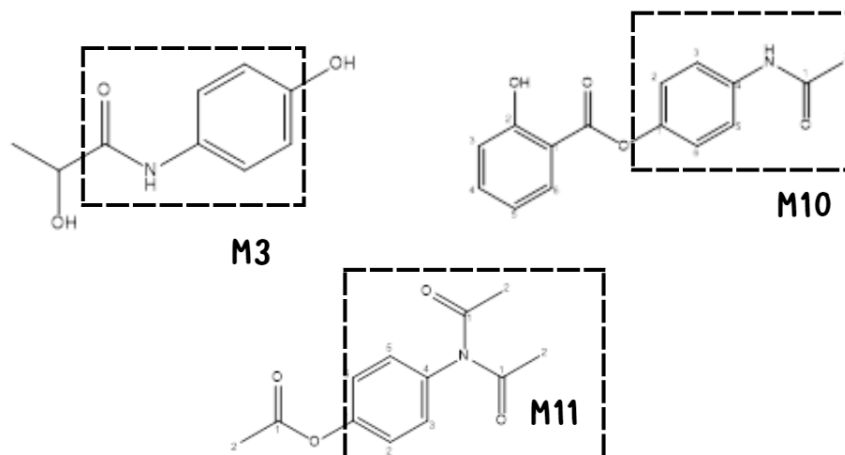
According to the data, it has been determined that M3, M10 and M11 showed the vina score more than Melphalan as positive control in topoisomerase I and II. **Figure 9** and **Table 4** show the corresponding residual amino acid and DNA interaction of the isolated compounds and standard drugs melphalan against Human Topoisomerase I and II on silico experiment. Their compounds are likely to exhibit excellent ADMET properties (**Figure 9**).

Previous studies have primarily focused on classical topoisomerase inhibitors such as camptothecin in the treatment of breast cancer (Tesauro et al., 2019). However, no studies to date have explored the use of acetanilide derivatives for dual inhibition of topoisomerase I and II. Our research not only introduces a new class of topoisomerase inhibitors but also demonstrates their potential efficacy in overcoming resistance associated with single-enzyme inhibition.

Conclusion:

Investigating the chemical constituents of the series of new compounds and an unexplored design led to the successful use of topoisomerase I and II of breast cancer cells in silico. 2-hydroxy-*N*-(4-hydroxyphenyl) propanamide (M10) exhibited superior inhibition of both topoisomerases compared to the positive controls (Melphalan). These in silico analyses suggest substantial potential for pharmacological activity in vivo. This research project

explores the intriguing pharmacological properties of newly synthesized compounds, presenting a promising avenue for breakthroughs in cancer research.



References:

1. Chen C, Lü L.M, Lin P.H, Yao Q. J Cell Mol Med. 2010;14(4): 840-860.
2. Thai A.A, Solomon B.J, Sequist L.V, Gainor J.F, Heist, R.S. Lung cancer, Lancet. 2021;398:535-554.
3. Foo J, Michor F. J. Theor Biol. 2014;355:10-20.
4. Krátký M, Vinšová J. Curr. Pharm. Des. 2011;17:3494-505.
5. Gonec T, Kos J, Zadrazilova I, Pesko M, Govender R, Keltosova S, Chambel B, Pereira D, Kollar P, Imramovsky A, Mahony J.O., Coffey A, Cizek A, Kralova K, Jampilek J. Molecules. 2013;18:9397-9419.
6. Gonec T, Zadrazilova I, Nevin E, Kaueroval T, Pesko M, Kos J, Oravec M, Kollar P, 4, Coffey A, Mahony J.O., Cizek A, Kralova K, Jampilek J. 2015;20:9767-9787.
7. Gonec T, Kos J, Zadrazilova I, Pesko M, Govender R, Keltosova S, Chambel B, Pereira D, Kollar P, Imramovsky A, Mahony J.O, Coffey A, Cizek A, Kralova K, Jampilek J. Molecules. 2017;22:1709.
8. Kos J, Kapustikova I, Clements C, Gray A.I, Jampilek J. Monatshefte für Chemie - Chem. Mon. 2018;149:887-892.
9. Tesauo C, Simonsen A. K, Andersen M. B, Petersen K. W, Kristoffersen E. L, Algreen L, Hansen N. Y, Andersen A. B, Jakobsen A. K, Stougaard M, Gromov P, Knudsen B. R, Gromova I. BMC Cancer. 2019;19.



DEVELOPMENT OF NATURAL INDICATOR FILM BASED ON GELATIN INCORPORATED WITH ORCHID EXTRACT

Sarocho Lapate, Siriyakorn Pijit, Sutinee Girdthep, Jitnapa Sirirak*

Department of Chemistry, Faculty of Science, Silpakorn University Nakhon Pathom 73000, Thailand

*e-mail: sirirak_j@silpakorn.edu

Abstract:

In this work, the incorporation of orchid extract into gelatin and lactic acid film (GLBO) was prepared using solvent-casting method and used as acid-base indicator film. The mechanical and physicochemical characterization with sensitivity analysis in various pH conditions of the film were studied. The performance of GLBO indicator film was also evaluated by monitoring its response to ammonia and hydrochloric vapor. The results showed that the GLBO film was sensitive to pH, which was indicated by its color change from reddish pink to yellow as pH increased. Moreover, there were clear color changes: reddish pink to green and reddish pink to orange of GLBO indicator film with respect to the vapor of ammonia and hydrochloric, respectively. These results indicated that GLBO film could be used as a biodegradable acid-base indicator film.

Introduction:

Orchid flower *Dendrobium Sonia* 'Earsakul' (**Figure 1**) contains various anthocyanin compounds.¹ These compounds enable orchid extract to function as an acid-base indicator.² In neutral conditions, anthocyanin displays a purple color. When it turns acidic, it appears red, and in a basic, it turns green. Biodegradable films have become popular nowadays because of environmental and pollution problems.³ These films are made from materials that can naturally break down, making them eco-friendly and sustainable.⁴ In this work, we prepared indicator film using biodegradable materials including gelatin, lactic acid and orchid extract.

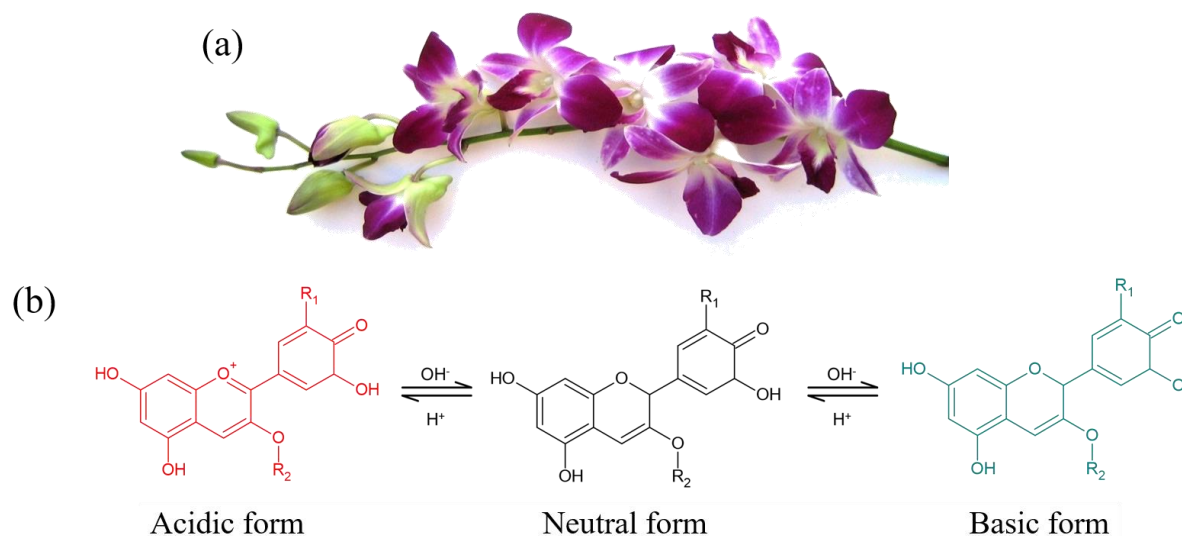


Figure 1. Orchid flower *Dendrobium Sonia* 'Earsakul' (a) and the chemical structures of anthocyanins at different pH (b).

Methodology:

Orchid extract was prepared using the method described in Chaneam's publication in 2018.² Fresh *Dendrobium* Sonia "Earsakul" orchids were dried for 2-3 days using a solar drying facility until fully dried. Only the purple petal parts of dried orchids were then cut and used for color extraction. The dried purple petal and the distilled water with the ratio 1:20 was heated at 60°C for 15 minutes, followed by filtration through cheesecloth and 11-micron filter paper in a pressure filtration apparatus to obtain 100% concentrated *Dendrobium* orchid extract. Gelatin (28% w/v) was dissolved in 100 ml orchid extract at 50°C. 2% w/v of lactic acid and 2% w/v of boric acid were then added to the solution and stirred for 20 minutes. After that the solution was sonicated with an ultrasonic cleaner for 60 minutes to remove air bubbles. The bubble-free solutions (3.5 mL) were poured onto a polytetrafluorethylene (PTFE) coated dishes (3.5 cm diameter), and then the film-forming solutions were left in the vacuum oven at 50 °C for 24 h to obtain dried hard indicator films. The films were stored in a desiccator at room temperature before use. Film characterization including surface color, thickness and mechanical properties were then performed. The surface color was represented in the CIELAB, or CIE L* a* b*, system. L* values is represented the color's lightness from 0 (black) to 100 (white). The a* value is represented red/green intensity, where positive a* and negative a* indicate red and green, respectively. The b* value is represented yellow/blue intensity, where positive b* and negative b* indicate yellow and blue, respectively. Moreover, the sensitivity of film in different pH conditions and the sensitivity of film to ammonia vapor/hydrochloric vapor were investigated.

Results and Discussion:

Appearance and surface color of films

The appearance of the indicator films made from: gelatin-lactic acid-boric acid (GLB) and gelatin-lactic acid-boric acid-orchid extract (GLBO) was displayed in **Figure 2**. Both GLB and GLBO film were transparent and glossy. The color of GLB was pale yellow, while the addition of orchid extract (GLBO) gave a reddish pink color film. The surface color analysis using a colorimeter was shown in **Table 1**. GLB film showed a high b* value according to its yellowish color, while GLBO film showed a high a* value corresponding to its reddish pink color.

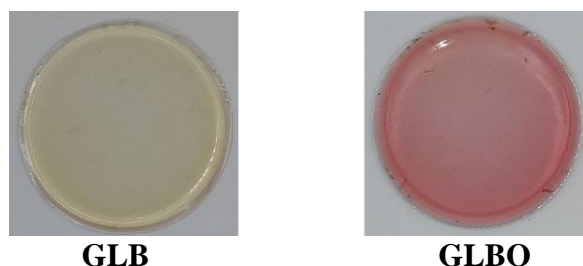


Figure 2. The indicator films made from: gelatin-lactic acid-boric acid (GLB) and gelatin-lactic acid-boric acid-orchid extract (GLBO).

Table 1. The surface color of indicator films.

| Film | L* | a* | b* |
|------|------------|------------|------------|
| GLB | 92.55±0.44 | -3.61±0.29 | 17.77±0.44 |
| GLBO | 76.49±1.04 | 10.01±0.56 | 8.79±0.21 |



Sensitivity of indicator film in different pH conditions

As can be seen in **Figure 3**, the results of the sensitivity of the GLBO indicator film that had been dipped in pH 1-14 buffer for 3 minutes showed that the indicator film could change color from red to yellow upon the pH conditions. This color variation upon the pH conditions was also similar to those observed in recently reported acid-base indicator film using anthocyanin as indicator shown in **Table 2**.

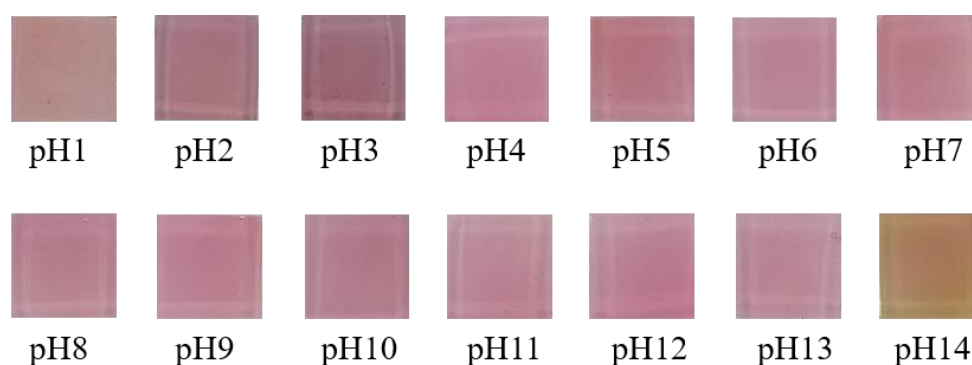


Figure 3. The color of GLBO indicator film in different pH conditions.

Table 2. Recently reported acid-base indicator film using anthocyanin as indicator.

| Source of anthocyanin | Polymer basis | Color variation pH buffer range | References |
|--|--|---------------------------------|------------------------------------|
| Black rice | Pectin/chitosan | pH 1-13, red to blue | Fei et al. (2023) ⁵ |
| Red cabbage | Pectin/sodium alginate/cellulose nanocrystals | pH 2-12, red to greenish-yellow | Wang et al. (2023) ⁶ |
| Butterfly pea flower | Sugarcane wax/agar | pH 2-12, red to green | Jiyong et al. (2022) ⁷ |
| Roselle | Polyvinyl alcohol (PVA)/hydroxypropyl methylcellulose (HPMC) | pH 3-13, red to green | Hu et al. (2023) ⁸ |
| Red Dragon Fruit Peel | Cassava Starch/Chitosan | pH 1-13, red to yellow | Anugrah et al. (2022) ⁹ |
| Blueberry | Pectin/sodium alginate/xanthan gum | pH 2-12, red to green | Cui et al. (2023) ¹⁰ |
| Orchid flower <i>Dendrobium</i> Sonia 'Earsakul' | Gelatin | pH 1-14, red to yellow | This work |

Thickness and mechanical properties of films

Table 3 demonstrated that the thickness and strength at break of GLBO were slightly higher than those of GLB. Moreover, compared to GLB, although GLBO had lower Young's modulus, its % elongation at break was much higher than the others due to the addition of orchid extract.

Table 3. Thickness and mechanical properties of indicator films.

| Film | Thickness (mm) | Strength at break (MPa) | % Elongation at break | Young's modulus (MPa) |
|------|----------------|-------------------------|-----------------------|-----------------------|
| GLB | 0.54±0.05 | 0.70±0.13 | 47.60±7.61 | 0.57±0.15 |
| GLBO | 0.58±0.04 | 0.77±0.20 | 65.81±9.15 | 0.49±0.04 |

Sensitivity of indicator film to ammonia vapor and hydrochloric vapor

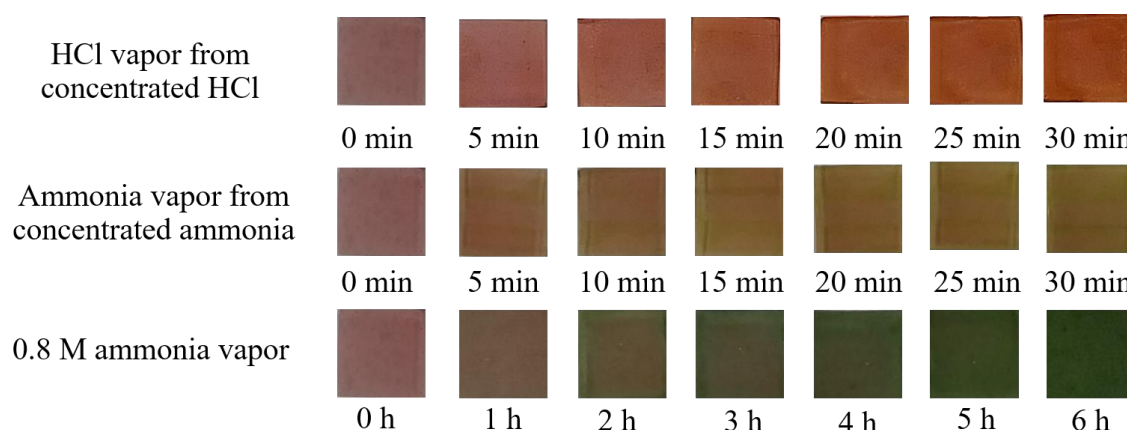


Figure 4. The color of GLBO indicator film responses to 0.8 M ammonia vapor, ammonia vapor from concentrated ammonia and hydrochloric vapor from concentrated hydrochloric.

Sensitivity of GLBO indicator film to ammonia vapor and hydrochloric vapor was investigated and the results were shown in **Figure 4**. It can be seen that the color of GLBO film was changed from reddish pink to orange within 15 minutes after contacted with vapor of 37% hydrochloric. GLBO film also changed the color to pale green after contacted with vapor of ammonia at least 15 minutes. Moreover, for the lower concentration of ammonia vapor at 0.8 M, the color change of GLBO film from reddish pink to green was occurred at the edge of the film within 2 hours of contact time and the GLBO film became green color by 6 hours. These clear color changes of GLBO film responding to ammonia or hydrochloric vapor indicated that GLBO film could be used at acid-base indicator film.

Conclusions:

The natural indicator film (GLBO) was prepared by combining orchid extract with gelatin and lactic acid. GLBO film had reddish pink color with the L^* , a^* and b^* values of 76.49 ± 1.04 , 10.01 ± 0.56 and 8.79 ± 0.21 , respectively. GLBO indicator film was changed the color from reddish pink to yellow according to the pH conditions, after it had been dipped in pH 1-14 buffer. Moreover, the noticeable changes of GLBO color from reddish pink to



orange responding to 37% HCl vapor occurred within 15 minutes. The clear color change from reddish pink to green was also observed after the film was contacted with ammonia vapor. These results suggested that GLBO film had the potential to be applied as a biodegradable acid-base indicator film.

Acknowledgements:

This research was financially supported Faculty of Science, Silpakorn University (Grant Number SRIF-JRG-2567-10).

References:

1. Tongkhan S, Thookpan K, Kumjorn S, Hobunthad S, Hobanthad T. TSTJ. 2024; 32(1): 1–11.
2. Sukaram T, Sirisakwisut P, Sirirak J, Nacapricha D, Chaneam S. Int. J. Environ. Anal. Chem. 2018; 98(10): 907–920.
3. Dirpan A, Andi FA, Muspirah. Polymers 2023; 15(13): 2781
4. Moshood T D, Nawanir G, Mahmud F, Mohamad F, Ahmad M H, AbdulGhani A. CRGSC 2022; 5: 100273.
5. Zeng F, Ye Y, Liu J, Fei P. Food Chem. X., 2023; 17: 100531.
6. Lei Y, Yao Q, Jin Z, Wang Y C. Food Chem. 2023; 404: 134528.
7. Hashim S B, Tahir H E, Liu L, Zhang J, Zhai X, Mahdi A A, Awad F N, Hassan M M, Xiaobo Z, Jiyong S. Food Chem. 2022; 373: 131514.
8. Huang J, Hu Z, Li G, Chin Y, Pei Z, Yao Q, Li D, Hu Y. Food Res. Int. 2023; 173: 113416.
9. Pramitasari R, Gunawicahya L N, Anugrah D S B. Polymers 2022; 14.19: 4142.
10. Li Y, Hu Z, Huo R, Cui Z. Heliyon. 2023; 9(3):e14421.



KINETICS AND ISOTHERM OF CRYSTAL VIOLET ADSORPTION USING ACTIVATED CARBON FROM COFFEE GROUNDS

Sirikorn Khaophong,¹ Ranoo Seemai,¹ Phongnarin Aonchart,¹ Preedaporn Kanjanasamranwong,² and Panita Kongsune^{1,3,*}

¹Department of Chemistry, Faculty of Science and Digital Innovation, Thaksin University, Phatthalung 93210, Thailand

²Department of Mathematic and statistic, Faculty of Science and Digital Innovation, Thaksin University, Phatthalung 93210, Thailand

³Innovative Material Chemistry for Environment Center, Department of Chemistry, Faculty of Science and Digital Innovation, Thaksin University, Phatthalung 93210, Thailand

*e-mail: dpanita@tsu.ac.th

Abstract:

Water pollution by organic dyes poses a critical environmental threat due to their persistence, toxicity, and detrimental impacts on aquatic ecosystems and human health. This study investigates the adsorption capacity of activated carbon synthesized from coffee grounds (CGAC) for the removal of crystal violet (CV) from aqueous solutions. The CGAC was prepared by pyrolyzing coffee grounds at 600 °C for 4 hours, followed by chemical activation with KOH. The structural and chemical properties of CGAC were characterized using scanning electron microscopy (SEM), energy dispersive X-ray spectroscopy (EDS), Fourier transform infrared (FTIR) spectroscopy, and pH at the point of zero charge (pHpzc) techniques. The study found that the maximum CV removal efficiency of 91.41% was achieved under optimal conditions: an initial CV concentration of 300 mg·L⁻¹, an adsorbent dose of 0.5 g, a contact time of 120 minutes, at 30 °C and 240 rpm. The adsorption kinetics followed a pseudo-second order model, while the adsorption isotherm conformed to the Freundlich model, suggesting that CV adsorption onto CGAC occurs as multilayer adsorption on a heterogeneous surface.

Introduction:

Crystal violet (CV), also known as gentian violet, is a synthetic dye belonging to the class of triarylmethane dyes. It is commonly used in various applications due to its intense violet color and strong staining properties. In the fields of microbiology and histology, crystal violet is widely employed as a staining agent, particularly in the Gram staining procedure, which differentiates between Gram-positive and Gram-negative bacteria. Aside from its laboratory uses, crystal violet is also a hazardous pollutant in wastewater from textile, printing, and other industries, due to its toxicity and resistance to biodegradation. As a result, there has been significant interest in developing efficient methods to remove crystal violet from contaminated water. The lack of proper knowledge in selecting appropriate technology and the high costs of treatment often make it difficult for small-scale industries to afford wastewater treatment. If untreated, this wastewater can lead to contamination of natural water sources. Even a dye concentration of 1 mg/L can cause unpleasant visual effects, affect light penetration in water, and have environmental impacts.¹

Currently, wastewater treatment technologies in the dyeing industry include biological, chemical, and physical processes, each with its own limitations. For example, biological treatment requires microbes, and chemical precipitation may be inefficient for low-concentration wastewaters. One method for treating dye wastewater is adsorption using

materials with high surface areas, which is effective for both inorganic and hard-to-degrade organic substances.² Adsorption is favored due to its low cost, short treatment time, and ability to operate at ambient temperature and pressure.³

Activated carbon is a product derived from natural or organic materials that contain carbon and hydrogen as major components. Through activation, a black product with a porous structure and high surface area is obtained, which has excellent adsorption properties.⁴ Activated carbon can be produced from any carbon-containing material, such as coal or biomass such as coconut shells, palm shells, and wood. Recently, new, low-cost, and easily available materials, such as agricultural wastes, have been explored for activated carbon production, including bagasse⁵, rice straw⁶, peanut shells⁷, tea residues⁸, and coffee grounds⁹. Among these, coffee grounds have a high carbon content, making them suitable for activated carbon production, which is especially attractive for use as an adsorbent.

In this study, activated carbon was prepared from coffee grounds and activated with potassium hydroxide (KOH) to adsorb CV dye. The effects of the kinetics and isotherms parameters of the of CV solution on adsorption were studied for practical applications in dye removal from wastewater.

Methodology:

Preparation of CGAC

Moisture was removed from coffee grounds by drying them at 105 °C for 24 hours. Dried coffee grounds were mixed with 85% w/w KOH and water in a 1:1 ratio by weight. The mixture was stirred well and allowed to soak at room temperature for 24 hours. The mixture was then placed into crucible and carbonized at 600 °C for 4 hours. It was washed with distilled water, and the surface was adjusted to pH 7 with HNO₃. Subsequently, it was dried at 105 °C for 24 hours. The resulting product was coffee ground activated carbon (CGAC).

Characterization of CGAC

The approximation properties CGAC were analyzed. The FT-IR spectra of CGAC was recorded in a range of 4000 - 400 cm⁻¹ (G8044AA, Agilent Technologies). The SEM in conjunction with EDS was applied for surface morphology and elemental analysis CGAC (Oxford, Merlin compact).

Surface acidity/basicity

The surface acidity was estimated by mixing 0.25 g of each adsorbent with 25 mL of 0.05 M NaOH solution in a conical flask for 48 hours at room temperature. After the mixtures separated, the filtrates were titrated with 0.05 M HCl. The surface basicity was obtained by a similar procedure, while 25 mL of 0.05 M HCl solution was contacted with 0.25 g of adsorbents and the titration solution was 0.05 M NaOH.

Batch adsorption experiment

The adsorption capacity of CGAC was tested for the removal of crystal violet (CV) from an aqueous solution. The effects of kinetic, isotherm, and thermodynamic parameters on CV adsorption were studied. A 0.5 g sample of CGAC was soaked in 150 mL of CV solution, with concentrations ranging from 100 to 400 mg·L⁻¹, for 15 to 180 minutes at temperatures between 30 and 50°C, with agitation at 240 rpm. The initial and final concentrations of CV were analyzed using a UV-Visible spectrophotometer at 590 nm.

The removal percentages (% removal) was calculated using Equation [1]

$$\% \text{ Removal} = \left(\frac{C_0 - C_e}{C_0} \right) \times 100 \quad [1]$$

Where C_0 and C_e are the initial and equilibrium concentrations ($\text{mg} \cdot \text{L}^{-1}$) of adsorbate solution.

The adsorption capacity at equilibrium (q_e) in $\text{mg} \cdot \text{g}^{-1}$ unit was calculated as equation [2].

$$q_e = \left(\frac{C_0 - C_e}{W} \right) \times V \quad [2]$$

Where W , and V are mass of adsorbents (g) and volume of the solution (L), respectively.

Results and Discussion:

SEM images were used to characterize the morphology of CGAC (**Figure 1a**). The results indicate that the surface of CGAC exhibit increased porous structures, channels, or voids. Element analysis of CGAC using EDS is presented in **Figure 1b**. The EDS data suggests that CGAC has a higher carbon content, leading to increased graphitization and the removal of volatile compounds.

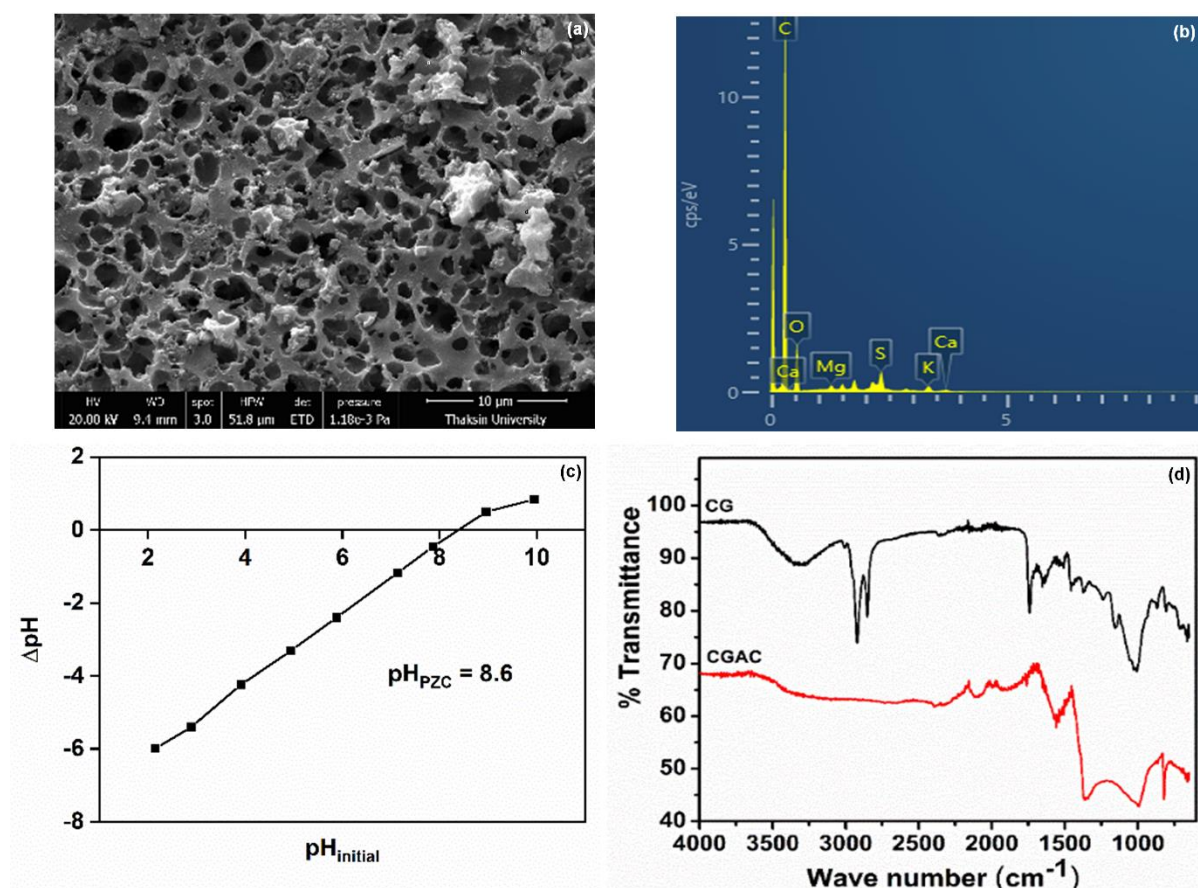


Figure 1.

(a) SEM image of CGAC adsorbent (b) EDS spectrum of CGAC adsorbent (c) pH_{PZC} of CGAC adsorbent and (d) The FTIR spectrum of CG and CGAC adsorbents.

In this study, we measured the pH of CGAC to determine whether the activated carbon was acidic or basic in nature. Additionally, measuring the pH_{PZC} allowed us to understand whether the activated carbon contained positive, negative, or neutral charges. The pH_{PZC} values are plotted and observed in **Figure 1c**. The pH of the PZC for CGAC is 8.6, respectively. This indicates that when the pH_{PZC} is exceeded, the solution becomes negatively charged, promoting the absorption of cationic species. This effect may be attributed to the activation and carbonization procedure, which eliminates volatile components and significantly dries the material.¹⁰ It has been observed that an activated carbon content of 1–20% is suitable for effective pollution adsorption. For the adsorbents used in this study (CGAC), the adsorption process is favored at $\text{pH} \leq \text{pH}_{\text{PZC}}$, which is 8.6.

To verify changes in the surface functional groups before and after carbonization on the surface of CGAC, the FT-IR spectra of coffee grounds (CG) and CGAC were investigated. Figure 1d reveals that the spectra of the activated carbon and coffee grounds exhibit distinct differences. This is evident from the absorption bands in the range of 2850–2950 cm^{-1} , which correspond to asymmetric and symmetric C–H stretching. The 1700–1750 cm^{-1} range corresponds to C=O esters in hemicellulose, and 1030 cm^{-1} corresponds to C–OH. The main absorption peaks for CGAC are observed at 1620, 1250, 1030, and 600–700 cm^{-1} , corresponding to unsaturated compounds C=C, asymmetric C–O–C stretching, C–OH stretching, and C–H bending, respectively.¹¹ The activation with potassium hydroxide contributes to the removal of residual volatile matter, facilitating the release of volatiles, leading to the decomposition of the structure, which is released in the form of volatile compounds or possibly a reaction between the activator and the carbon structure during carbonization. This results in the insertion of the activator into the carbon structure, increasing the porosity.

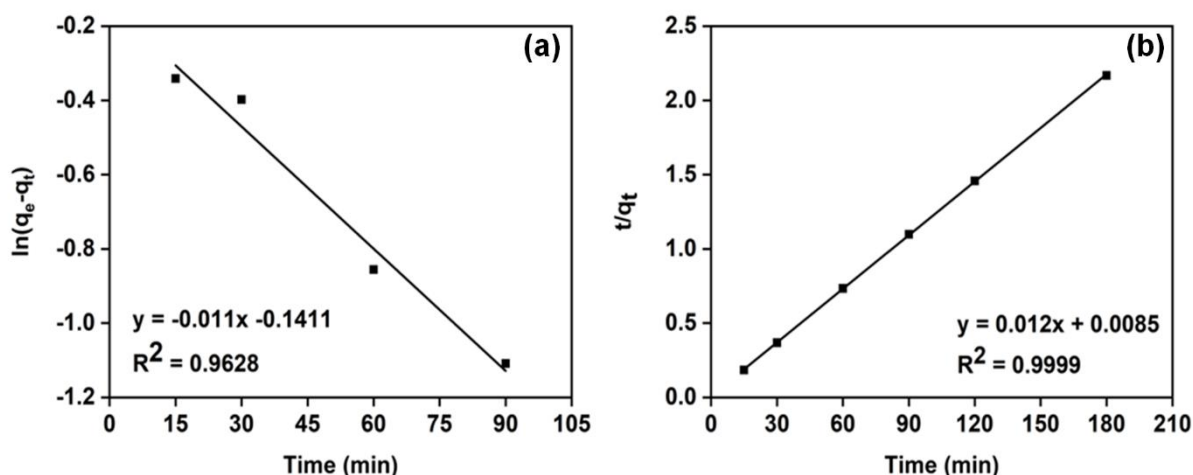
Oxygen and nitrogen atoms are important factors that affect the surface properties of activated carbon. Oxygen-containing functional groups, such as hydroxyl, and nitrogen-containing functional groups, such as amine, are commonly found on the surface. Higher oxygen content makes the surface more acidic, while higher nitrogen content makes it more basic. Acidic and basic surface functionalities are determined by Boehm titration¹² and summarized in **Table 1**. The total surface area of CGAC was more basic than acidic due to their higher nitrogen content. This indicates that the surface of the activated carbon is highly basic.

Table 1.
Acidic and basic values of CGAC adsorbent.

| Adsorbent | Acidic site (mol/g) | Basic site (mol/g) |
|-----------|---------------------|--------------------|
| CGAC | 0.61 | 1.77 |

Kinetics model on CV adsorption

Results from the study on the adsorption kinetics of CV dye using activated carbon from coffee grounds, based on the pseudo-first-order and pseudo-second-order reaction models, as shown in **Figure 2(a-b)** and **Table 2**, revealed that the pseudo-second-order model provided a better fit than the pseudo-first-order model. This is because the R^2 value was closer to 1. Additionally, when comparing the adsorption capacity at equilibrium (q_e), it was found that the pseudo-second-order model's calculated equilibrium adsorption capacity ($q_{e,\text{cal}}$) was more consistent with the experimental equilibrium adsorption capacity ($q_{e,\text{exp}}$) than that of the pseudo-first-order model, as shown in **Table 2**. This indicates that the adsorption of CV dye using activated carbon from coffee grounds is a chemisorption process.

**Figure 2.**

Kinetics plots of (a) pseudo-first-order and (b) pseudo-second-order on CV adsorption capacity by CGAC adsorbents.

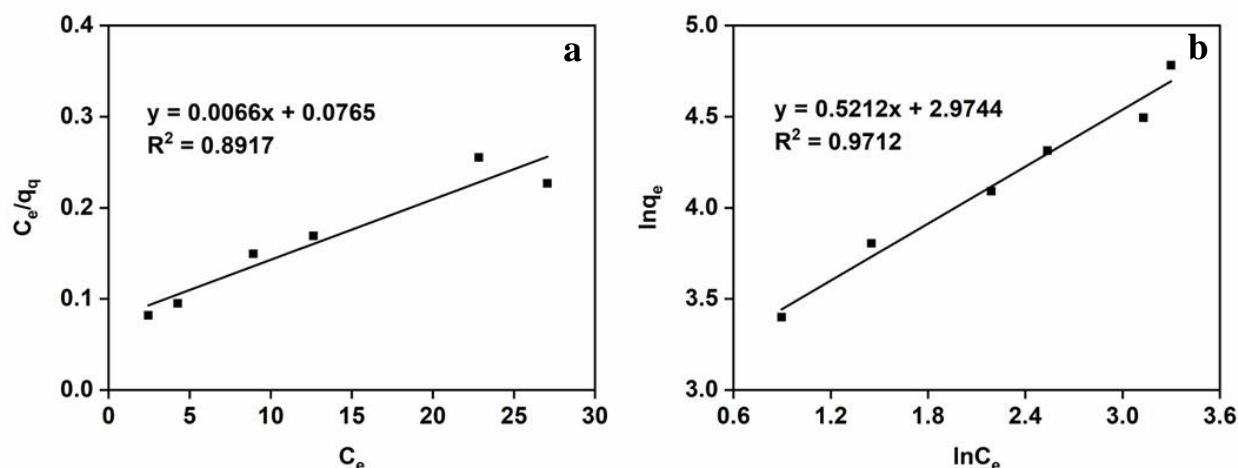
Table 2.

Parameters of the kinetic pseudo-first-order, pseudo-second-order of CGAC adsorbents on CV adsorption.

| Model/Equation | Parameters | | | |
|---|--|--|-----------------------|--------|
| | $q_{\text{exp}} (\text{mg} \cdot \text{g}^{-1})$ | $q_{\text{cal}} (\text{mg} \cdot \text{g}^{-1})$ | $K (\text{min}^{-1})$ | R^2 |
| Pseudo-first order ³ $\ln(q_e - q_t) = \ln q_e - k_1 t$ | 82.27 | 0.7226 | 0.0253 | 0.9628 |
| Pseudo-second order ⁴ $\frac{1}{q_t} = \frac{1}{k_2 q_e^2} + \frac{t}{q_e}$ | | 83.33 | 0.0169 | 0.9999 |

Isotherm model on CV adsorption

Adsorption isotherms describe the specific relationship between the adsorption capacity and the concentration of the remaining adsorbate at a constant temperature. The two most commonly used models are the Freundlich and Langmuir isotherms. The Langmuir isotherm assumes monolayer sorption ¹³, while the Freundlich isotherm accounts for heterogeneous surface energies and multilayer adsorption. ¹⁴ The adsorption isotherms of CV dye using activated carbon from coffee grounds, when using the Langmuir and Freundlich adsorption isotherms, linear graphs were obtained as shown in **Figures 3(a-b)**, respectively. Parameters of the Langmuir and Freundlich isotherms were shown in Table 3. It was found that the adsorption isotherm corresponded more closely to the Freundlich isotherm than the Langmuir isotherm, as the correlation coefficient (R^2) of the Freundlich isotherm was 0.9712, which is closest to 1. This indicates that the adsorption of CV dye involves multilayer adsorption on the heterogeneous surface of activated carbon from coffee grounds, with a K_F value of 0.256 and a $1/n$ value of 1.9186, as shown in **Table 3**. Considering the $1/n$ value, which is greater than 1, it can be explained that the adsorbent surface has a large amount available for adsorption.

**Figure 3.**

Isotherm plots of (a) Langmuir and (b), Freundlich models on on CV adsorption capacity by CGAC adsorbents.

Table 3.

Parameters of the Langmuir and Freundlich isotherms for CGAC adsorbents on CV adsorption.

| Model/Equation | Parameters | |
|---|-------------------------|--------|
| Langmuir ⁵ | $K_L(L \cdot mg^{-1})$ | 0.0863 |
| $\frac{C_e}{q_e} = \frac{1}{q_m K_L} + \frac{C_e}{q_m}$ | $q_m (mg \cdot g^{-1})$ | 151.52 |
| | R^2 | 0.8917 |
| Freundlich ⁶ | $K_F (L \cdot mg^{-1})$ | 0.2560 |
| $\ln q_e = \ln K_F + \frac{1}{n} \ln C_e$ | n | 1.9186 |
| | R^2 | 0.9712 |

Conclusion:

The activated carbon from coffee grounds, prepared by activating the coffee grounds with KOH at a 1:1 weight ratio for 24 hours and carbonized at 600°C for 4 hours, exhibited a highly porous surface. The surface of the activated carbon is highly basic, with a pH at the point of zero charge of 8.6, indicating that the surface carries a negative charge. The maximum adsorption capacity was found to be 82.27 mg/g (91.41%). Additionally, the adsorption process was a pseudo-second-order reaction models, and the adsorption behavior corresponded to the Freundlich isotherm, indicating multilayer adsorption due to the heterogeneous nature of the adsorbent surface.

Acknowledgements:

This work was supported by National Higher Education, Science, Research and Innovation Policy Council, Thaksin University (Fundamental Research Fund; TSU-66A105000013) Fiscal Year 2024. The authors would like to thank the Department of Chemistry, Faculty of Science and Digital Innovation, Thaksin University, for providing research facilities.

References:

1. Lee J.W, Choi S.P, Thiruvengkatachari R, Shim W.G, Moon H. Dyes Pigm. 2006;69(3):196–203.
2. Anukulprasert J, Soonsorn C, Weerayutsill P, Khuanmar K. FEAT J. 2017;3(2):115–23.
3. Mahaninia MH, Rahimian P, Kaghazchi T, Chin. J. Chem. Eng. 2015;23(1):50–6.
4. Onsaikaew K, Panya P. JST. 2021;16(3):105–19.
5. Hanh N.T, Nghiem D.G, Tinh N.T, Dat N.M, Bao L.M, Buu T.T, et al. Biomass & Bioenergy. 2023;174:106823.
6. Bao Z, Lotfy V.F, Zhou X, Fu S, Basta A.H. Ind Crops Prod. 2024;212:118298.
7. Kushwaha R, Singh R.S, Mohan D. C Bioresour. Technol. 2023;375:128831.
8. El-Sayed M.Y, Alsohaimi I.H, Alrashidi A.N, Aldawsari A.M, Alshahrani A.A, Hassan H M A. Diam. Relat. Mater. 2023;136:109945.
9. Campbell R, Xiao B, Mangwandi C. J. Environ. Manage. 2024;366:121682.
10. Rattanaphan S, Rungrotmongkol T, Kongsune P. Renew Energy. 2020;145:622–31.
11. Naushad M, Alqadami A.A, Al Othman Z A, Alsohaimi I H, Algamdi M S, Aldawsari A M. J Mol Liq. 2019;293:111442.
12. Schönherr J, Buchheim J R, Scholz P, Adelhelm P. Carbon. 2018;4(2):22.
13. Langmuir I. J Am Chem Soc. 1918;40:1361-403.
14. Freundlich H M F. Over the Adsorption in Solution. J Phy Chem. 1906;57:385–470.



MOLECULAR DYNAMICS ANALYSIS OF CORE PROTEIN ALLOSTERIC MODULATORS: INSIGHTS INTO HBCAG AND HBEAG INTERACTIONS FOR HEPATITIS B INHIBITION

Wigrom Yogboworn, Pornthep Sompornpisut*

Center of Excellence in Computational Chemistry, Department of Chemistry, Faculty of Science, Chulalongkorn University, Bangkok, 10330, Thailand

*e-mail: pornthep.s@chula.ac.th

Abstract:

Hepatitis B, caused by the hepatitis B virus (HBV), primarily affects the liver, and can lead to severe complications, including drug resistance and chronic infection. Numerous studies have linked these conditions to the presence of hepatitis B core antigen (HBcAg) and hepatitis B e antigen (HBeAg). HBeAg, in particular, is known to the innate immune response, resulting in diminished immunity and delayed disease diagnosis and treatment. Despite this, the molecular structure, and interactions between inhibitors and HBeAg remain poorly understood, posing a significant challenge to the development of effective treatments. This work aims to elucidate the molecular interactions between the core protein allosteric modulator (HAP_R01) and HBeAg through molecular dynamic simulations. By analyzing the simulation results, we have identified key molecular properties and interactions within the protein-ligand system that contribute to HBeAg inhibition. These findings provide valuable insight into the molecular mechanism of HBeAg inhibition and could guide the development of new therapeutic strategies for hepatitis B.

Introduction:

Hepatitis B is a serious global liver infection caused by the hepatitis B virus (HBV). Each year, HBV is responsible for over 4 million acute infections and approximately 600,000 deaths worldwide, with more than 200 million suffering from chronic HBV infection. Hepatitis B manifests in two phases: the acute phase lasting less than six months, and the chronic phase, where infection persists beyond six months, often resulting in a lifelong condition.¹ Chronic hepatitis B significantly increases the risk of liver failure, liver cancer, and cirrhosis. The virus spreads through contact with infected blood, semen, or other bodily fluids, and transmission can occur through sexual contact, sharing needles, or from mother to child during birth. Common symptoms include fatigue, loss of appetite, abdominal pain, nausea, and jaundice. Vaccination remains the most effective means of preventing hepatitis B.

Hepatitis B virus particles, known as Dane particles, are spherical and feature an outer envelope composed of glycoproteins and hepatitis B surface antigen (HBsAg), which is embedded within the lipid bilayer that surrounds the icosahedral nucleocapsid. The nucleocapsid, or virus capsid, contains the hepatitis B core antigen (HBcAg), a phosphoprotein that encases the viral genome. This genome is characterized by covalently closed circular DNA (cccDNA) and includes endogenous DNA polymerase necessary for replication. The HBV precore protein and HBeAg are critical viral tolerogens, playing a significant role in modulating the host's innate and adaptive immune responses. Notably, HBcAg and HBeAg share a high degree of sequence similarity, differing primarily in the presence of 10 amino acids and the absence of 34 amino acids at their respective amino- and carboxy-termini.

Acute hepatitis B infection is typically a short-term phase that may resolve on its own without the need for medical intervention. However, doctors often recommend rest, proper nutrition, and close monitoring as the patients' immune systems combat the virus. In severe cases, antiviral medications may be necessary to prevent serious complications. For those with chronic hepatitis B infection, lifelong treatment is often required to reduce the risk of liver disease and to prevent the transmission of the virus to others. Several antiviral medications, including entecavir, tenofovir, lamivudine, adefovir, and telbivudine, are available to slow the progression of liver damage, and these drugs are typically administered orally on a continuous basis. Interferon alfa-2b (Intron A) has been used as an alternative to long-term antiviral, though it is associated with side effects such as nausea, vomiting, and depression. Given these limitations, there is a pressing need for new, more effective approaches to HBV treatment that can offer a more robust cure for the virus.

The relationship between HBcAg and HBeAg was investigated by Michael and co-workers². It showed that both proteins share structural similarity due to their derivative from the same protein codon, with the exception of the N-terminal peptide and the absence of an RNA-binding arginine-rich domain in HBeAg (**Figure 1A**). Given these similarities, they explored the ability of HBcAg to aggregate and form the viral capsid of HBV. Their study revealed that HBcAg forms a dimer through the interaction of C61 residues from each monomer unit, creating a disulfide bridge. In contrast, HBeAg forms a disulfide bridge between C61 and C (-7) (a residue in the propeptide), which prevents the aggregation of HBeAg dimers and, consequently, its participation in viral capsid assembly. However, if conditions were created to disrupt or prevent the disulfide bridge interaction between C61 and C (-7), it could increase the likelihood of HBeAg dimer aggregation, similar to HBcAg, potentially capsid assembly.

Recently, Zhou and co-workers investigated core protein allosteric modulators (CpAM), including heteroaryldihydropyrimidine (HAP, **Figure 1B**) and sulfamoylbenzamide (SBA), as inhibitors of HBV replication. Due to the critical role of HBcAg in viral replication, it has been targeted for antiviral therapy.³ Their study found that HAP_R01 and SBA_R01 are effective in inhibiting encapsidated HBV DNA. Furthermore, HAP_R01 was observed to reduce the level of core protein and viral capsid. Complementary research by Yan and co-workers demonstrated that HAP specifically inhibits HBeAg and HBV DNA replication.⁴

In this study, we employed molecular dynamics (MD) simulations to explore the structures, dynamics, and interactions of HBV proteins with ligands. The analysis focused on the structural properties, inter- and intramolecular interactions of protein-ligand systems, and water molecules in the binding site. Water molecules can mediate protein-ligand interactions by forming hydrogen bonds between polar or charged residues and inhibitors⁵, emphasizing their role in enhancing or disrupting inhibitor binding. Our aim is to deepen the understanding of the structural relationships between core protein allosteric modulator (HAP_R01) and hepatitis B antigens, which may lead to the discovery of new potential treatments for hepatitis B.

Methodology:

System setup

Models of hepatitis B antigens and the core protein allosteric modulator (HAP_R01) were constructed for different antigen types (HBcAg and HBeAg) based on the 3D crystallographic structures with PDB codes 5WRE and 3V6Z (**Figure 1C and 1D**)². Missing hydrogen atoms were added to all structure models to ensure completeness. A control system model was established, consisting of hepatitis B core protein (HBcAg), ligand (HAP_R01:7TL), and crystal water mo

lecules from PDB:5WRE. The carboxyl groups of the ligand were modified to reflect ionization, given that its pKa is 3-4 at pH 7. This control system was then adapted by replacing the hepatitis B e antigen structure from PDB:3V6Z while retaining the same coordinates. Each model system was solvated with TIP3P water molecules⁶ in a simulation box containing 0.1 M NaCl. The setup of these systems was carried out using TCL scripts in VMD 1.9.3.

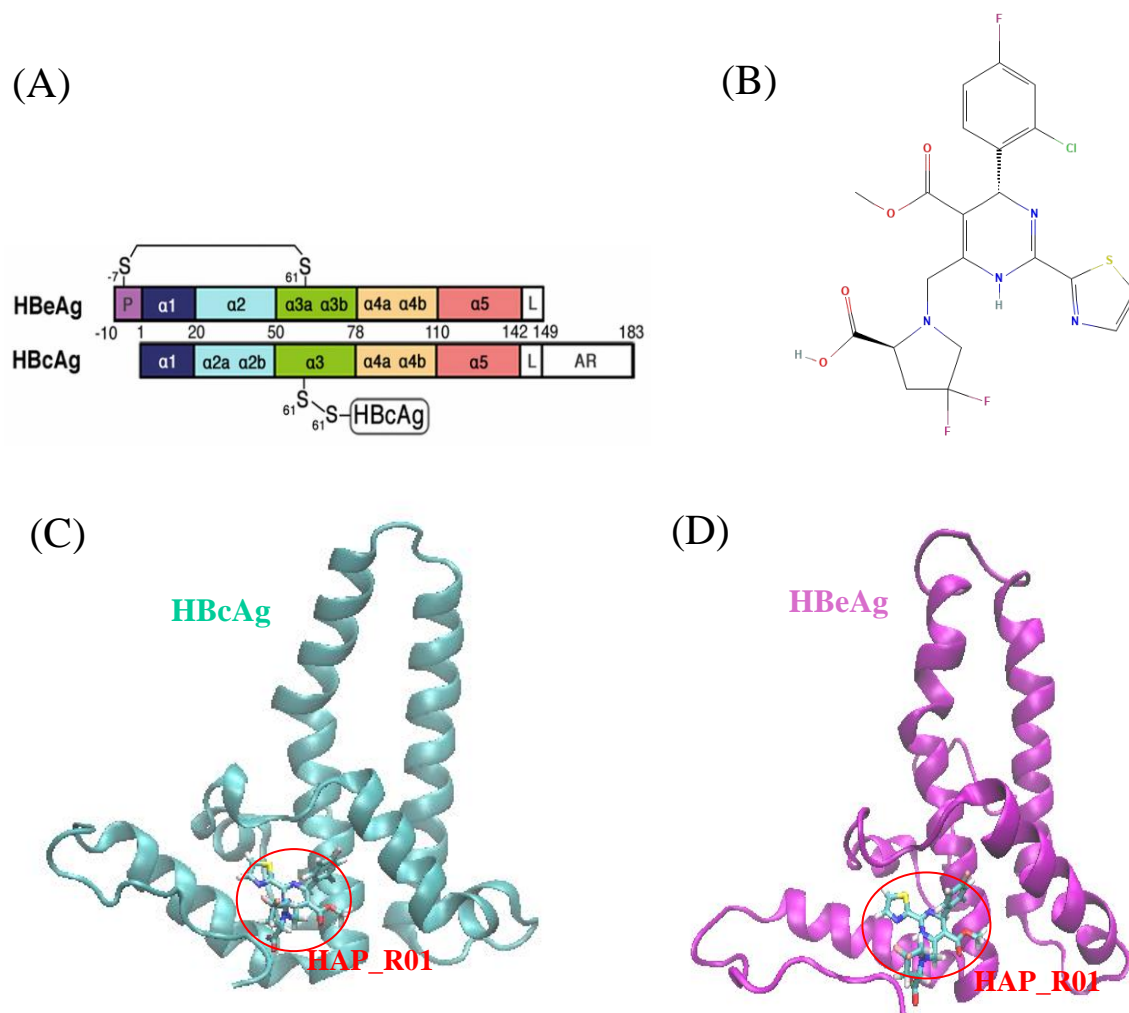


Figure 1.

(A) a schematic representation comparing the structural domains of the hepatitis B e antigen (HBsAg) and hepatitis B core antigen (HBcAg). The diagram highlights the similarities and differences in their amino acid sequences and structural elements.² (B) A chemical structure diagram of heteroaryldihydropyrimidine (HAP_R01). (C) and (D) structure models of HBcAg-HAP_R01 and HBsAg-HAP_R01 complexes with the PDB code: 5WRE and 3V6Z².

MD simulations

MD simulations were carried out using NAMD software⁷ with CHARMM36 force field parameters⁸. Ligand topology and parameter files were generated using CHARMM-GUI. The simulations were performed in an NPT ensemble with periodic boundary conditions. All covalent bonds to hydrogen atoms were constrained using the LINCS algorithm⁹ and water geometry was kept rigid using the SETTLE method¹⁰. A distance cutoff of 12 Å was employed for electrostatic and van der Waals interactions. Electrostatic interactions were calculated with particle mesh Ewald summation method¹¹. The temperature

of all systems was maintained at 300 K using a Langevin thermostat with a damping coefficient of 1 ps^{-1} . The pressure was held constant at 1 atm using the Nose–Hoover Langevin piston method¹². Energy minimization was performed to remove any unfavorable atomic contacts, with the protein and ligand initially fixed in their positions while water and counterion were allowed to equilibrate for approximately 1 ns. Subsequently, the systems were equilibrated through 1 ns MD simulations with position restraints on protein-ligand complexes. All MD simulations were carried out with a time step of 2 fs, and each system was simulated for 100ns with three independent replications.

Trajectory analysis

All trajectory analyses were performed using TCL scripts in VMD. MD trajectories were extracted from the production phases during the last 20 ns of the simulations to ensure that the system had reached thermodynamic equilibrium, and this period provided stable data with minimal deviation for structural analysis.

The root-mean-square deviation (RMSD) as a function of simulation time were computed to assess the flexibility of the protein-ligand complex. RMSDs were computed relative to the initial structure, focusing on the heavy atoms of both the protein and ligand.

Results and Discussion

Structure and flexibilities of protein-ligand systems

The RMSD as a function of time for protein-ligand complex systems indicates that both the protein and ligand structures remain relatively stable throughout the simulations (**Figure 2**). In the HBcAg system, the HBcAg structure and its associated ligand exhibit high stability with minimal fluctuation. Similarly, in the HBeAg system, the HBeAg structure and its ligand also show high stability with a narrow range of fluctuation. There is a slight rise in RMSD around 30 ns, but it quickly returns to its equilibrium value, indicating no significant or lasting increase in RMSD.

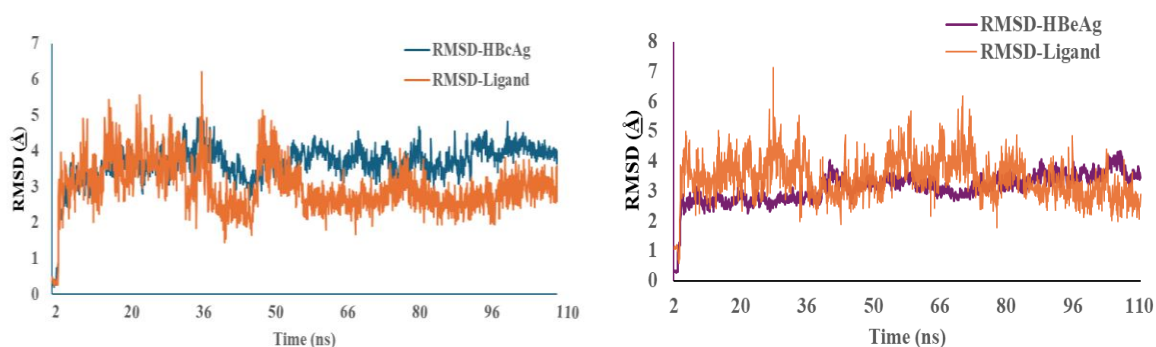


Figure 2.

The RMSD of the protein backbone for HBcAg (left, cyan) and HBeAg (right, purple) with the ligand (HAP_R01) shown in orange, plotted as a function of time for the analyzed protein-ligand complexes.

Protein-ligand contacts and H-bond

An analysis of hydrogen bonding (H-bond) focused on the interactions between the protein and ligand. The geometric criteria used to determine an H-bond included a donor-acceptor distance of less than 3.5 Å and a donor-hydrogen-acceptor angle within $180^\circ \pm 60^\circ$. Interactions with a donor-acceptor distance of more than 3.5 Å were considered no H-bond. The percentage occupancy of each H-bond was computed over all frames of the last 20 ns of the simulation. The interactions between residues are shown in **Table 1** and **Table 2**. Four significant interactions were identified between the protein and ligand, involving the amino

acids Thr43, Trp112, Leu40, and Ser151 surrounding the ligand. Weak H-bond interactions in the HBeAg and HBcAg systems are illustrated in **Figure 3** and **Figure 4**.

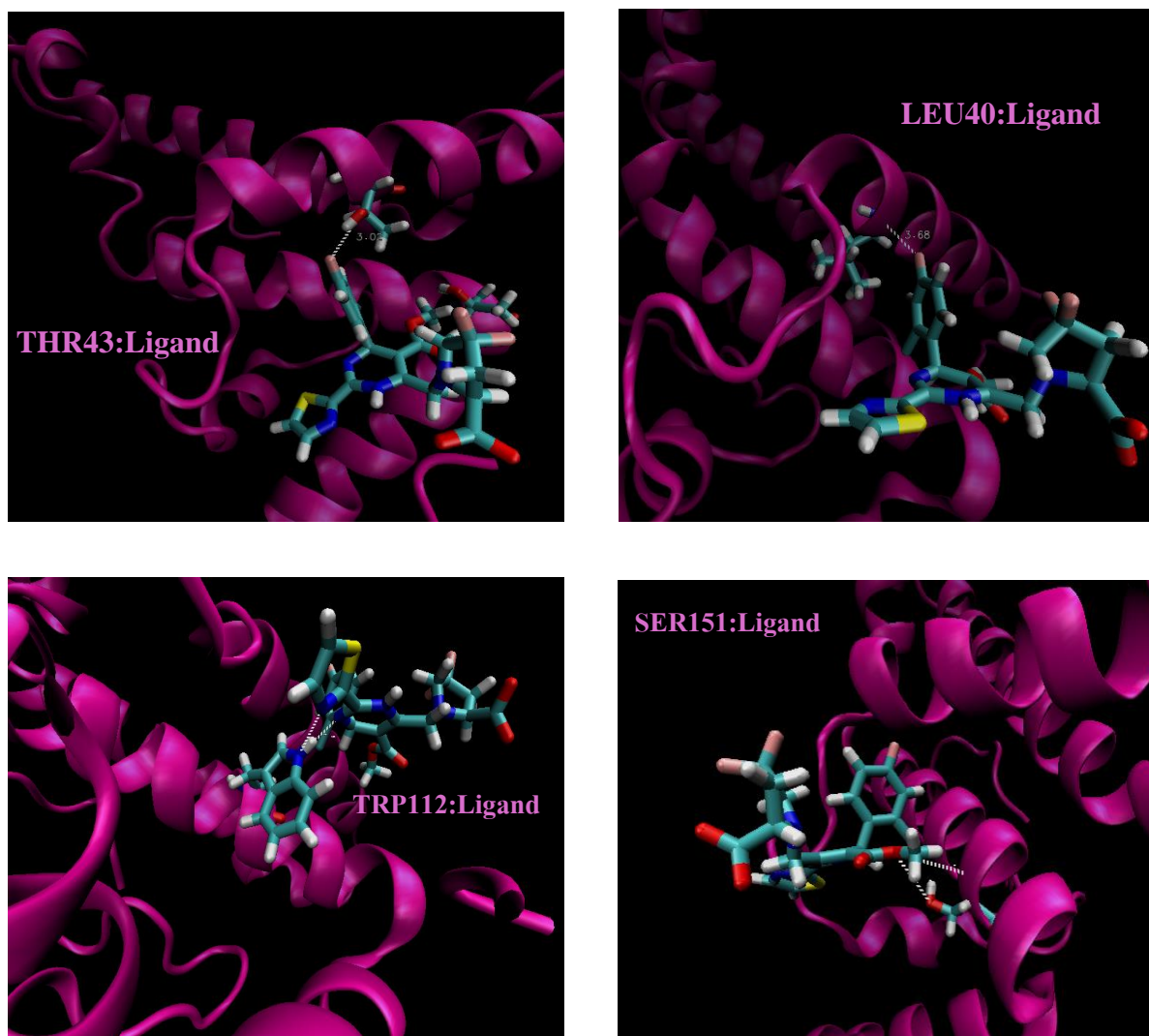
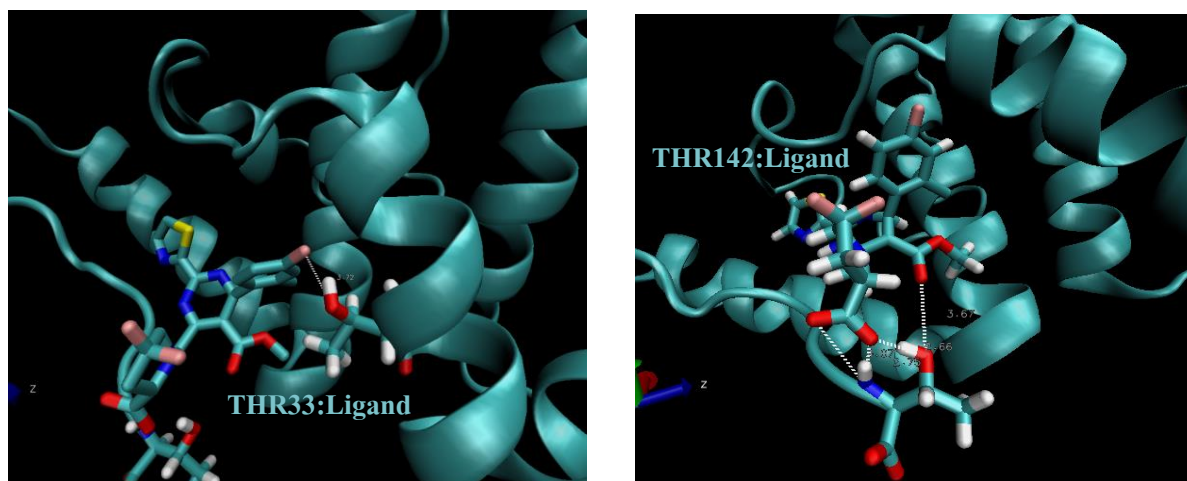
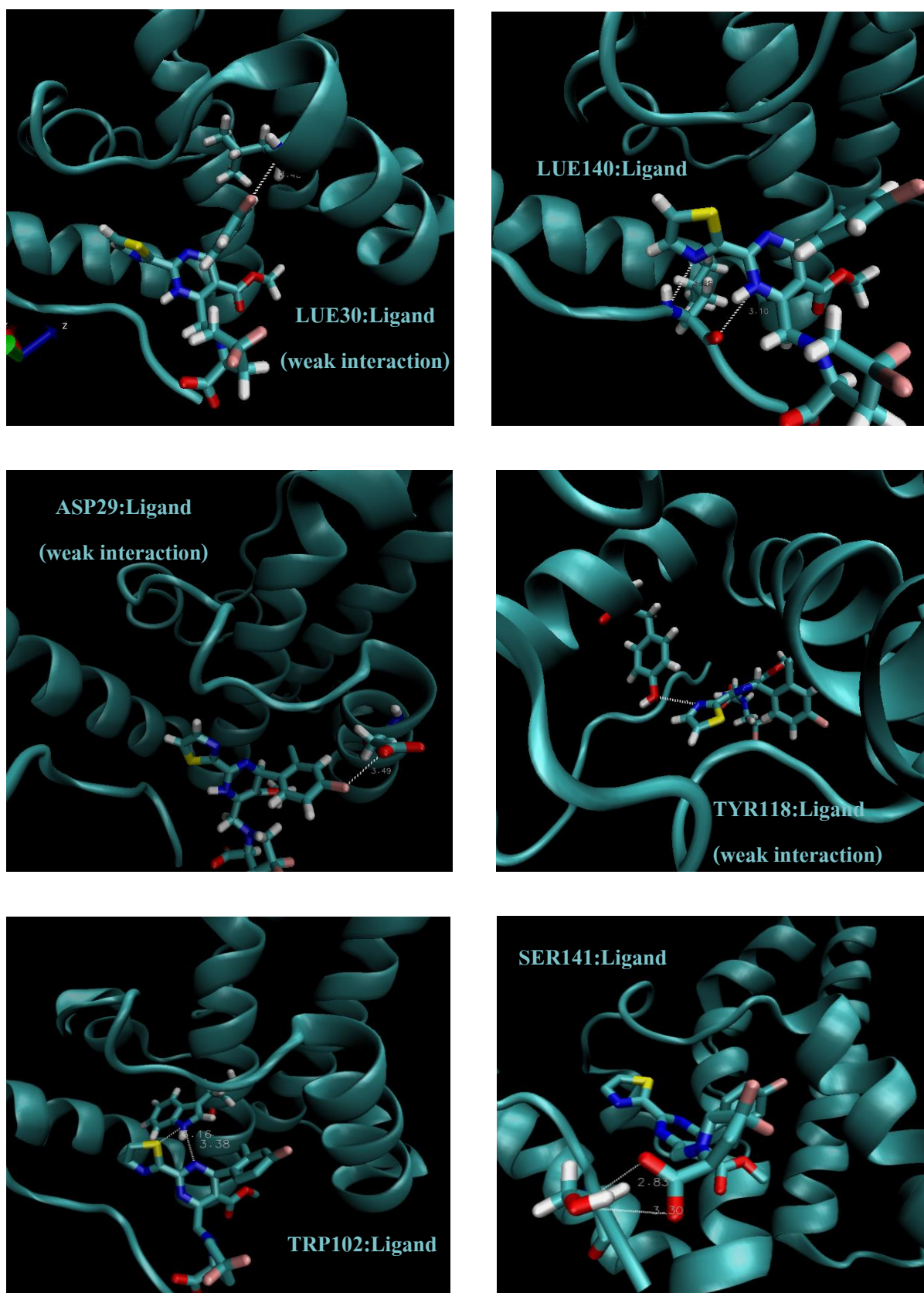


Figure 3.

Proposed interactions between HBeAg and HAP_R01, highlighting the high percentage occupancy of H-bond involving Thr43, Leu40, Trp112 and Ser 151 with the ligand.



**Figure 4.**

Proposed interactions between HBcAg and HAP_R01, highlighting the high percentage occupancy of H-bond involving Thr33, Thr142, Leu30, Leu140, Asp29, Tyr118, Trp102 and Ser 141 with ligand.

Table 1.

Hydrogen bond interactions between donor and acceptor residues with corresponding distances of HBeAg system.

| Donor residue/atom | Acceptor atom (HAP_R01) | Distance(Å) |
|--------------------|----------------------------|-------------------|
| Thr43/O-H | F | 3.25 |
| Leu40/N-H | F | 3.97 (not H-bond) |
| Trp112/N-H | S | 3.60 (not H-bond) |
| N-H | N | 3.38 |
| N-H | N | 3.36 |
| Ser151/O-H | O | 4.24 (not H-bond) |
| N-H | O | 4.22 (not H-bond) |

Table 2.

Hydrogen bond interactions between donor and acceptor residues with corresponding distances of HBcAg system.

| Donor residue/atom | Acceptor atom (HAP_R01) | Distance(Å) |
|--------------------|----------------------------|-------------------|
| Thr33/O-H | F | 3.43 |
| Thr142/N-H | O | 2.88 |
| N-H | O | 3.93(not H-bond) |
| O-H | O | 2.88 |
| O-H | O | 4.09 (not H-bond) |
| Donor residue/atom | Acceptor atom (HAP_R01) | Distance(Å) |
| Leu30/N-H | F | 4.15 (not H-bond) |
| Leu140/N-H | N | 3.45 |
| N-H | O | 3.18 |
| Tyr118/O-H | N | 4.21(not H-bond) |
| Trp102/N-H | S | 3.67(not H-bond) |
| N-H | N | 3.64(not H-bond) |
| N-H | N | 3.12 |
| Ser141/O-H | O | 2.73 |
| | O | 3.37 |

Protein-ligand systems and the presence of water molecules

An analysis of hydrogen bonding (H-bond) involving water molecules was conducted to examine the interactions between the protein and ligand. The percentage occupancy of each H-bond was calculated over all frames from the last 20 ns of the simulation. We

observed the presence of water molecules around the ligand and certain specific amino acids. Three key interactions were identified between the protein, ligand, and water molecules, involving the amino acids Leu140, Ser141, and Thr33 surrounding the ligand. We propose that the network of water molecules surrounding and interacting with the protein or ligand may stabilize or destabilize these interactions. The presence of water molecules in the HBcAg-inhibitor system is illustrated in **Figure 5**.

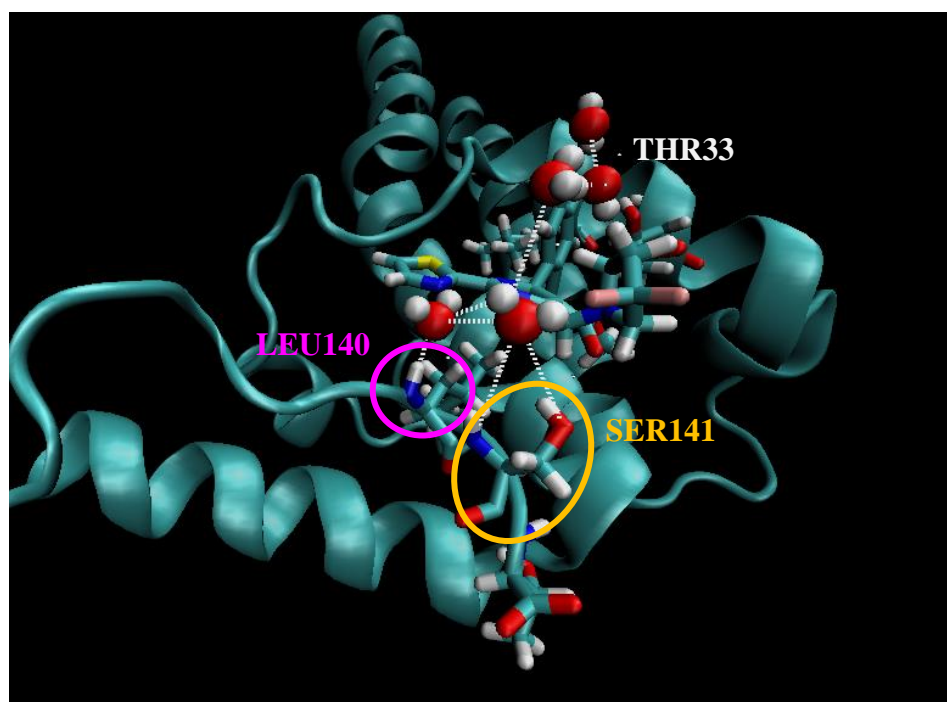


Figure 5.

Proposed interactions of water molecules between HBcAg and HAP_R01, highlighting the high percentage occupancy of H-bond involving Leu140, Ser 141 and Thr33 and with ligand.

Conclusion:

In this study, we investigated the core protein allosteric modulator (HAP_R01) and the proteins HBcAg and HBeAg using molecular dynamics (MD) simulations. Our results demonstrated that both protein-ligand complexes remained stable throughout the simulations, with no significant differences in interaction preference between the HBcAg and HBeAg systems. Consistent interaction between the ligand and several amino acids, including Ser141, Ser151, Thr33, Thr43, Thr142, Trp102, Trp112, Leu30 and Leu140 were observed in both systems. Notably, the Asp29 and Tyr118 -ligand interactions were specific to the HBcAg system. We identified Thr33, Thr43, Trp102, Trp112, Ser141 and Ser151 as a particularly strong binding site for the ligand, due to its structural functional group and the flexibility of both the protein and ligand, which may facilitate the formation of multiple hydrogen bonds (up to two) at this site. These strong interactions, observed in both systems, suggest that targeting these sites could enhance the efficacy of inhibitors against the hepatitis B virus. Moreover, Thr142 may play a significant role in binding with ligands, due to the formation of multiple hydrogen bonds (up to three) at this site in HBcAg system. Moreover, we observed that the presence of water molecules around the ligand stabilizes hydrogen bonds, as indicated by the distances between the protein and ligand. Water molecules surrounding specific amino acids, including Thr43, Leu140, and Ser141, assist in stabilizing the ligand's binding with hepatitis B antigens. We hope these findings provide valuable insights for optimizing and developing therapeutic treatments for hepatitis B.

Acknowledgements:

The authors would like to thank Chulalongkorn University for their support, as well as the Development and Promotion of Science and Technology (DPST) scholarship for providing financial assistance towards the completion of this work.

References:

1. Shepard C.W, Hepatitis B. *Epidemiologic Reviews*. 2006;28(1):112-125.
2. DiMattia M.A; Watts N.R, Stahl S.J, Grimes J.M, Steven A.C, Stuart D. I, Wingfield P.T. *Structure* (London, England: 1993). 2013;21(1):133-142.
3. Zhou Z, Hu T, Zhou X, Wildum S, García-Alcalde F, Xu Z, Wu D, Mao Y, Tian X, Zhou Y, Shen F, Zhang Z, Tang G, Nájera I, Yang G, Shen H.C, Young J.A, Qin N. *Scientific Reports*. 2017;7(1).
4. Yan Z, Wu D, Hu H, Zeng J, Yu X, Xu Z, Zhou Z, Zhou X, Yang G, Young J.A.T, Gao L. *Hepatology* (Baltimore, Md.). 2019;70(1):11-24.
5. Ishchenko A.Y, Iukhnevich A, Medvedev M.G. *Chemical Communications*. 2019;55(96): 14438-14441.
6. Jorgensen W.L, Chandrasekhar J, Madura J.D, Impey R.W, Klein M.L.J. *Chem. Phys.* 1983;79(2):926-935.
7. Phillips J.C, Braun R, Wang W, Gumbart J, Tajkhorshid E, Villa E, Chipot C, Skeel R. D., Kalé L, Schulten K. *J. Comput. Chem.* 2005;26(16):1781-1802.
8. Guvench O, Mallajosyula S.S, Raman E.P, Hatcher E, Vanommeslaeghe K, Foster T.J, Jamison F.W, MacKerell A.D. *J. Chem. Theory Comput.* 2011;7(10):3162-3180.
9. Hess B, Bekker H, Berendsen H.J, Fraaije J.G.E.M. *J. Comput. Chem.* 1997;18(12):1463-1472.
10. Miyamoto S, Kollman P.A. *J. Comput. Chem.* 1992;13(8):952-962.
11. Essmann U, Perera L, Berkowitz M.L, Darden T, Lee H, Pedersen L.G.J. *Chem. Phys.* 1995;103(19):8577-8593.
12. Martyna G. J, Tobias D.J., Klein M.L. *J. Chem. Phys.* 1994;101(5):4177-4189.

D-MATHEMATICS / STATISTICS / COMPUTER SCIENCE / DATA SCIENCE / AI



A GENDER EQUALITY ANALYSIS OF THE PARIS 2024 OLYMPIC GAMES

Kittimasak Naijit,* Chaichana Kulworatit

Department of Computer Science, School of Science,
King Mongkut's Institute of Technology Ladkrabang, Bangkok, Thailand
*kittimasak.na@kmitl.ac.th, chaichana.kul@kmitl.ac.th

Abstract:

This study provides an in-depth analysis of gender equality at the Paris 2024 Olympic Games, focusing on participation rates, performance outcomes, resource allocation, and the impact of gender equality policies. The research reveals that female athletes constituted 49% of participants and won 47% of the total medals, demonstrating significant progress toward gender parity. However, notable disparities persist, particularly in traditionally male-dominated sports like weightlifting, boxing, and wrestling, where female participation remains lower. Additionally, resource allocation continues to favor male athletes in some sports, affecting access to quality training and financial support. The study underscores the importance of ongoing efforts to address these gaps, highlighting the positive impact of IOC gender policies, such as the inclusion of mixed-gender events, on promoting inclusivity. The findings suggest that while substantial progress has been made, further measures are necessary to achieve true gender equality across all Olympic disciplines, particularly in sports with historical and cultural biases. This research contributes valuable insights for policymakers and sports organizations aiming to advance gender equity in global sports events.

Introduction:

The Olympic Games represent the pinnacle of international sports, bringing together athletes from diverse backgrounds and cultures to compete at the highest level. Since their modern inception in 1896, the Olympic Games have evolved in many ways, but one of the most significant developments has been the increasing focus on gender equality. Historically, women were largely excluded from the Games, but over time, the International Olympic Committee (IOC) and other governing bodies have implemented various measures to ensure greater gender parity in both participation and opportunities. The Paris 2024 Olympic Games stand as a landmark event in the ongoing journey toward gender equality, with policies and initiatives aiming to further close the gap between male and female athletes. This research focuses on analyzing gender equality at the Paris 2024 Olympic Games by examining various critical factors. It seeks to evaluate whether equal opportunities are being provided to athletes of both genders, particularly in terms of participation rates, access to resources, and performance outcomes. Additionally, the study explores the impact of international and national policies designed to promote gender equality in sports and assesses the extent to which these efforts have translated into tangible outcomes for female athletes.

This study examines gender equality at the Paris 2024 Olympic Games, recognizing that true equality extends beyond participation numbers to include societal attitudes, economic disparities, and cultural perceptions. The Games provide a global stage to analyze these factors, with athletes from diverse nations and backgrounds. By comparing Paris 2024 with previous Olympics, this research offers insights into the progress made and the remaining challenges in achieving gender equality in sports. The findings will contribute to ongoing discussions and provide valuable data for policymakers and sports organizations,

highlighting areas for improvement and successful strategies that can be applied to future events. Ultimately, the study aims to ensure that the core values of the Olympic Games – excellence, friendship, and respect – are upheld for all athletes, regardless of gender.

Methodology:

This study utilized a mixed-method approach to analyze gender equality at the Paris 2024 Olympic Games. Quantitative data was collected from official Olympic reports, athlete participation records, and medal distributions. This data was used to examine key factors such as gender representation in athlete participation and performance outcomes. The research also included a qualitative component, which involved interviews with athletes, coaches, and officials to gain insights into their experiences with gender-related policies and resource allocation. The analysis was divided into four areas:

1. **Participation and Representation:** Data on male and female athlete participation across 46 sports was collected and analyzed to assess gender balance in both traditional and emerging sports.

2. **Medal Distribution:** The study examined the distribution of medals across genders and sports to identify performance trends and disparities.

3. **Resource Allocation:** Financial support, access to training facilities, and coaching representation were analyzed to evaluate gender-based differences in resource allocation.

Comparative analysis with previous Olympic Games was employed to track progress and identify persistent challenges in achieving gender equality. The study also considered the impact of international policies, such as the International Olympic Committee's gender equity initiatives, on the results observed in the Paris 2024 Games.

Results and Discussion:

The results of this study demonstrate that the Paris 2024 Olympic Games have made significant strides toward gender equality in various aspects, from participation and performance to policy impact. However, certain challenges persist, particularly in specific sports and areas such as resource allocation. The findings highlight the importance of continued efforts to promote gender equality across all Olympic disciplines and support the development of policies that address existing disparities. By focusing on these areas, future Olympic Games can build on the progress made in Paris 2024 and work toward achieving true gender parity in global sports.

1. **Participation and Representation:**

- **Equal Representation in Participation:** The Paris 2024 Olympic Games achieved near gender parity, with female athletes making up 49% of participants, reflecting the IOC's efforts to promote equality through policy initiatives.

- **Sport-Specific Variation:** While overall participation was balanced, disparities persisted in certain sports. Male-dominated sports like boxing and wrestling had fewer female competitors, while artistic swimming and gymnastics remained predominantly female. However, newer sports like skateboarding and 3x3 basketball showed more balanced gender participation, highlighting progress in promoting diversity across non-traditional sports.

2. **Medal Distribution and Performance:**

- **Gender Balance in Medals:** A comparative analysis of medal distribution revealed that both male and female athletes achieved similar success rates, with women winning approximately 47% of the total medals. Certain sports, such as athletics and swimming, showed strong performances from both genders, with no significant differences in the number of medals won.

- **Sport-Specific Disparities:** In weightlifting and shooting, men still won more medals, while women dominated artistic gymnastics and swimming. Despite progress in



gender equality, some sports still show performance gaps due to historical factors, resource access, or societal gender perceptions.

3. Resource Allocation and Support:

- Resource Disparities: Despite progress, financial support and access to quality training facilities remain unequal. Female athletes in sports like cycling and boxing receive less funding and sponsorship compared to males, while sports like tennis and athletics show more equitable distribution.

- Coaching Representation: Female athletes remain underrepresented in coaching, especially in team sports like football and basketball. However, individual sports like gymnastics and swimming have seen a rise in female coaches.

4. Athlete and Coach Perspectives:

- Positive Perceptions of Gender Equality: Athletes and coaches acknowledged progress toward gender equality at Paris 2024, with female athletes feeling more supported and respected, and gaining improved access to resources and opportunities.

- Challenges in Male-Dominated Sports: In sports like boxing and wrestling, gender stereotypes persist, with female athletes feeling the need to work harder to gain recognition compared to their male counterparts.

5. Policy Impact on Gender Equality:

- Success of IOC Gender Policies: IOC policies, including gender-balanced teams and mixed-gender events, positively impacted gender equality at the Games, fostering a more inclusive competition and ensuring equal representation in delegations.

- Areas for Improvement: Despite progress, challenges remain in enforcing equal opportunities across all sports and countries, particularly where cultural norms hinder female athletes' participation.

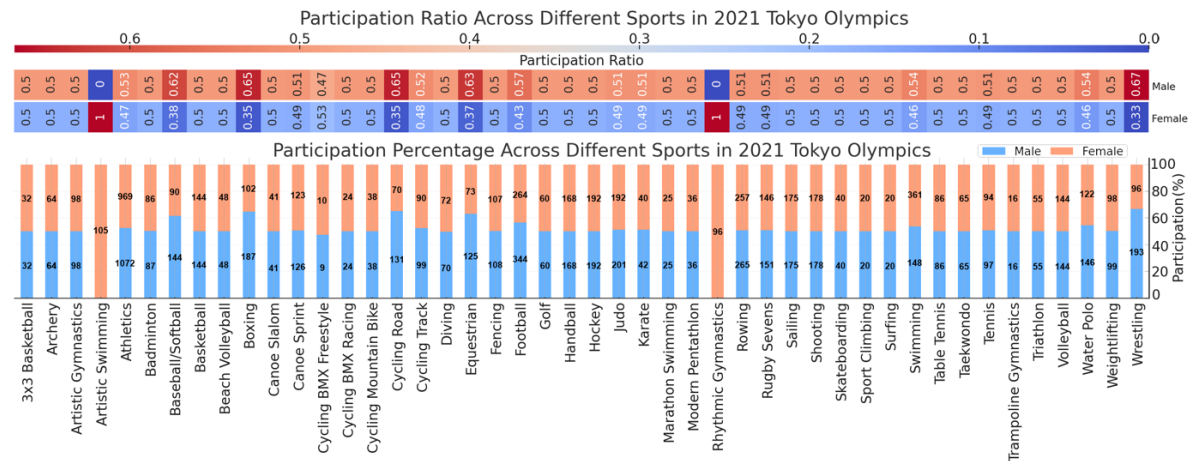


Figure 1.
Gender Participation at the Tokyo 2021 Olympic Games

The Tokyo 2021 Olympic Games made significant strides in gender equality, achieving nearly 49% female participation and introducing several mixed-gender events to promote balance. However, some sports still had more events for men, and challenges in resource allocation. In contrast, the Paris 2024 Olympics aim for 50% female participation, with a strong push for full gender parity by expanding mixed-gender events and ensuring equal representation across all sports. Additionally, Paris 2024 focuses on addressing structural barriers, including improved funding, access to training, building on the progress made in Tokyo and moving closer to true gender equality in the Olympics.

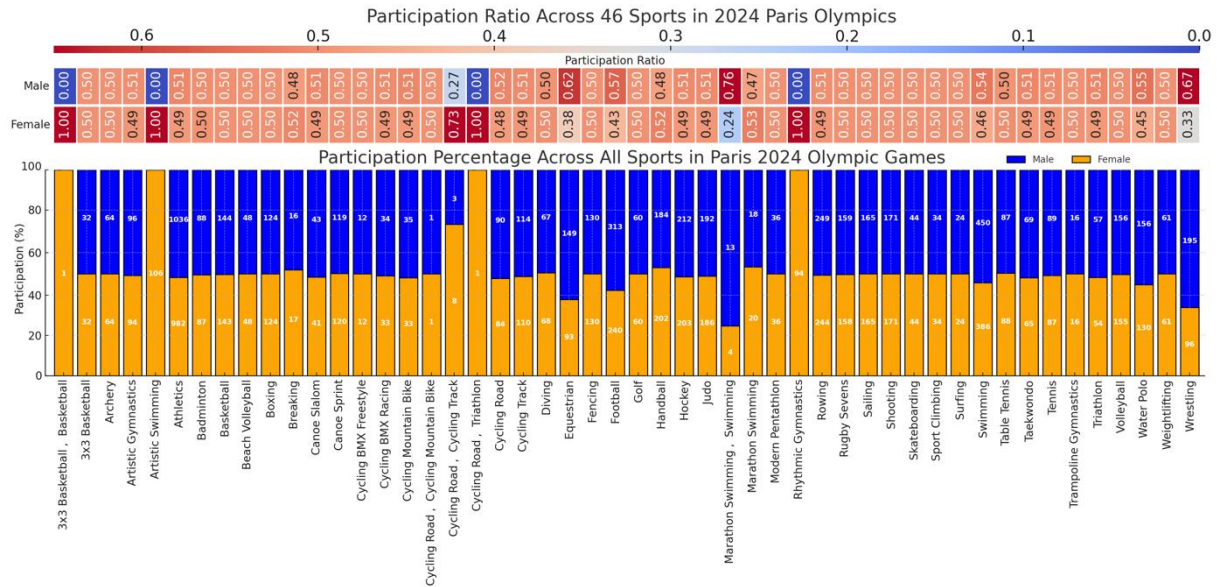


Figure 2.
Gender Participation at the Paris 2024 Olympic Games

Figure 2 presents the percentage of male and female athletes participating in 46 sports, offering key insights into the gender balance across various Olympic disciplines. Here are some significant observations:

1. **Gender Imbalance in Strength-Based Sports:** Strength-based sports like Weightlifting, Boxing, and Wrestling exhibit a higher percentage of male athletes compared to female athletes. This reflects traditional trends where male athletes dominate sports that emphasize physical strength, which may be influenced by societal expectations, historical biases, and the nature of physical training required for these sports.

2. **Gender Balance in Skill-Based Sports:** Several skill-based sports, such as Badminton, Table Tennis, and Archery, show a more balanced distribution of male and female participants. These sports may attract more balanced participation due to factors such as gender-neutral skill sets, equal opportunities in training, and promotion across both genders.

3. **Female Dominated Sports:** Sports like Rhythmic Gymnastics, Artistic Swimming, and Equestrian have a significantly higher percentage of female athletes, sometimes nearing 100%. This pattern aligns with historical trends where these sports have been associated with female participation due to artistic elements, cultural traditions, and limited male entry points.

4. **Gender Equality in Certain Sports:** Sports such as Swimming, Athletics, and Shooting show a more equal gender distribution. These sports have likely benefited from gender equality initiatives over the years, with increased opportunities for women to compete at the highest levels. The more even distribution in these sports may reflect concerted efforts by sporting organizations to promote inclusivity and gender equity.

The percentage distribution of gender participation highlights ongoing disparities in male-dominated and female-dominated sports, while also revealing areas where gender balance has been achieved. The continued push for equality in participation, especially in strength-based sports, remains crucial for future Olympic games. Efforts to encourage female participation in traditionally male-dominated sports and promote male involvement in female-dominated sports could help achieve a more balanced representation across all disciplines.

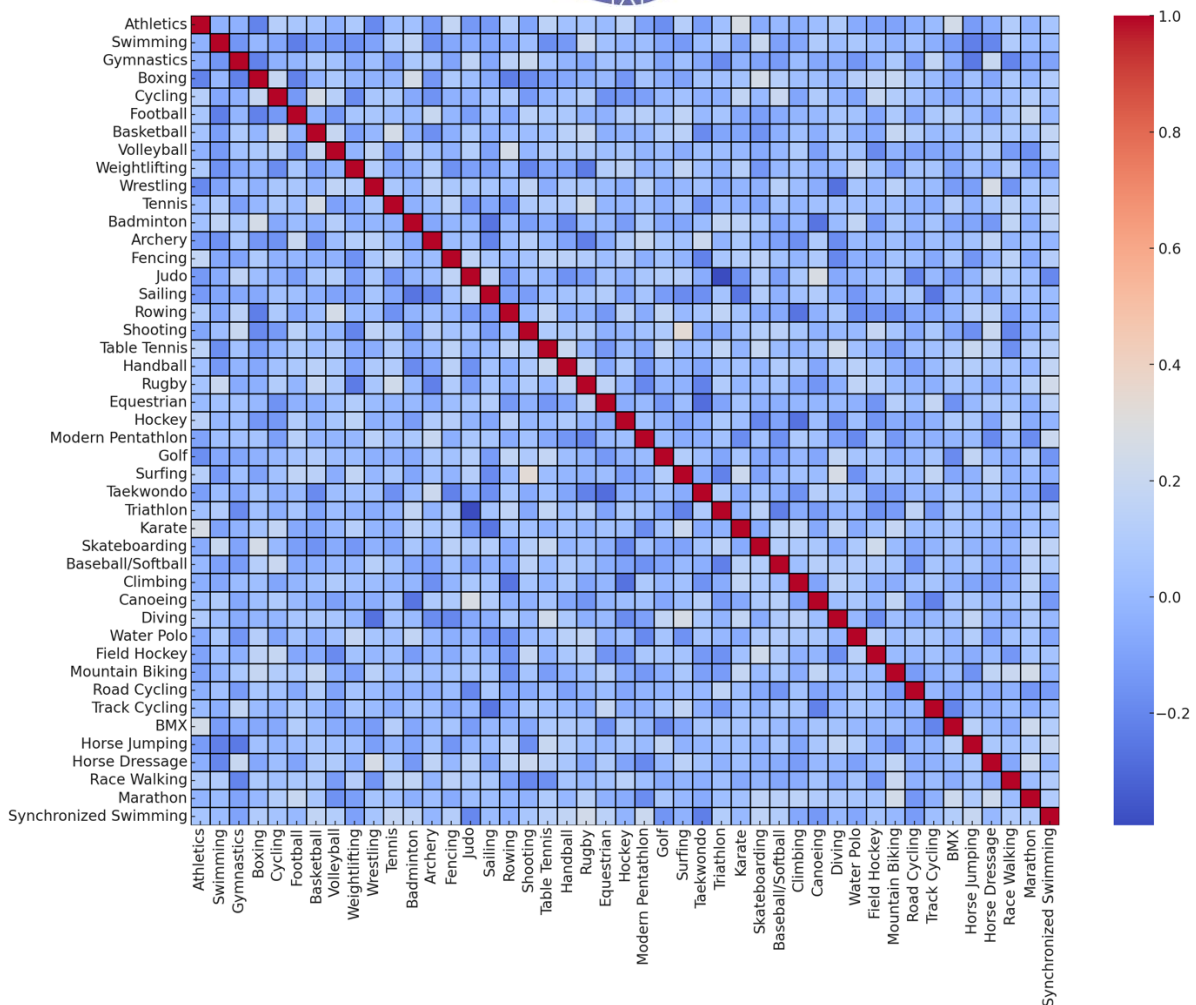


Figure 3.
Relationship between Sports in the Correlation Matrix

The Correlation Matrix that illustrates the relationships between 46 Olympic sports offers insight into how these relationships may be influenced by gender dynamics. Here's an analysis of the potential connections between sports and gender:

1. Gender Segregation in Sports Participation: Certain sports have traditionally seen gender segregation, often driven by cultural and social norms. For example, sports that emphasize strength, such as wrestling and weightlifting, tend to have more male participants, while sports like gymnastics and swimming often have a higher proportion of female athletes. Analyzing the correlations between these sports can reveal patterns related to gender:

- **Positive Correlation:** Sports with similar characteristics, such as athletics and wrestling (male-dominated) or gymnastics and volleyball (female-dominated), tend to show a high positive correlation. This indicates that athletes who participate in one sport are likely to participate or perform well in related sports that appeal to the same gender group.

- **Negative Correlation:** A negative correlation may be seen between sports with contrasting characteristics. For example, fencing and gymnastics (more technical, often female-dominated) may have a negative correlation with sports like wrestling and weightlifting (strength-based, often male-dominated). This indicates that athletes who excel in one type of sport may not typically participate in the other, further reflecting gender-based preferences in sports.

2. Correlation of Sports Popular in One Gender: Some sports may exhibit a strong positive correlation because they are predominantly popular among one gender:

- Strength-based sports like wrestling, weightlifting, and cycling may have strong positive correlations due to a larger male participation rate.
- Skill-based or artistic sports like gymnastics, martial arts (Taekwondo, Karate), and swimming may have stronger correlations among female participants who are more prevalent in these sports.

3. Impact of Gender Equity Policies in Sports: The push for gender equality in Olympic sports, including the introduction of more mixed-gender events and policies that promote equal opportunities for women, has positively impacted gender balance in sports like tennis and badminton. These sports may show more balanced correlations between genders, reflecting a trend towards greater gender equity.

4. Emerging Trends in New Sports: Newer sports like skateboarding and climbing, which have recently been added to the Olympic program, show less clear patterns of gender dominance. These sports have attracted a more balanced mix of male and female participants, helping reduce traditional gender divides. As a result, they may show moderate correlations with both strength-based and skill-based sports, reflecting their appeal to a more diverse group of athletes.

The relationships between different sports, as shown in the Correlation Matrix, provide insight into the gender dynamics of the Olympics. The matrix reveals that certain sports still exhibit significant gender segregation based on traditional cultural and skill-based preferences, while others, particularly newer sports and those benefiting from gender equity policies, are showing more balance. The ongoing efforts to promote gender equality in the Olympics continue to influence participation trends and may help close the gap in future events.

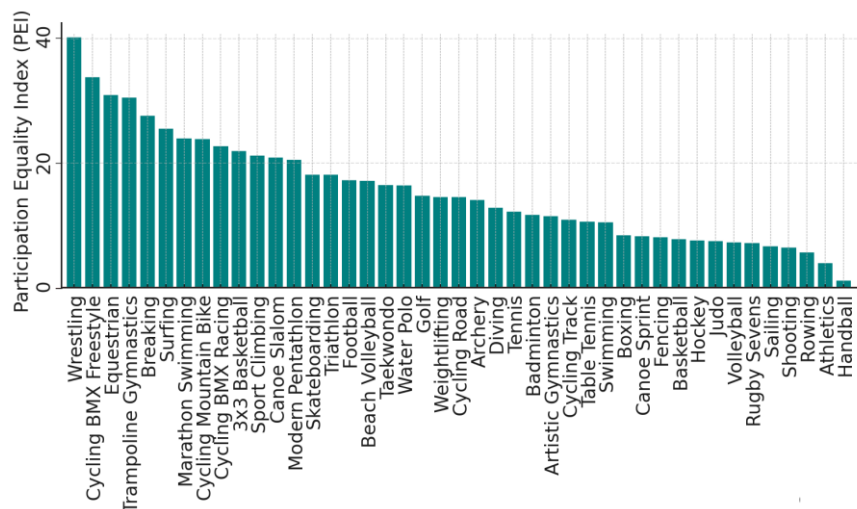


Figure 4.
Participation Equality Index (PEI) Across All Sports

Figure 4 above displays the Participation Equality Index (PEI), comparing the difference between the percentage of male and female athletes across different sports. The key points include:

- Low PEI Values indicate sports where male and female athlete participation is relatively balanced, suggesting better gender equality.
- High PEI Values highlight sports with significant disparities in participation, where either male or female athletes dominate, indicating areas that may need efforts to achieve a more balanced participation.



The Participation Equality Index (PEI) measures gender balance in sports participation. It is calculated by taking the absolute difference between the percentage of male and female athletes in a sport.

1. Calculate Male and Female Percentages

$$\text{Male Percentage} = (\text{Number of Male Athletes} / \text{Total Athletes}) \times 100$$

$$\text{Female Percentage} = (\text{Number of Female Athletes} / \text{Total Athletes}) \times 100$$

2. Calculate the PEI

$$\text{PEI} = |\text{Male Percentage} - \text{Female Percentage}|$$

The Participation Equality Index (PEI) graph illustrates the gender balance in athlete participation across various sports. Here's a detailed discussion of the results.

1. High PEI Values: Sports like Cycling BMX Freestyle, Wrestling, and Equestrian are on the left side of the graph, indicating high PEI values. This suggests a significant gender disparity in participation, with one gender (likely male) having a much higher representation than the other. These sports might require targeted initiatives to encourage more balanced participation, such as increasing visibility and opportunities for the underrepresented gender.

2. Moderate PEI Values: Sports such as Trampoline Gymnastics, Breaking, and Surfing have moderate PEI values. This indicates that while there is some gender imbalance, it is less pronounced than in the sports with higher PEI values. These sports show progress toward gender equality, but there is still room for improvement to achieve a more balanced representation.

3. Low PEI Values: On the right side of the graph, sports like Handball, Athletics, and Rowing have low PEI values. This suggests that these sports have achieved a relatively balanced participation between male and female athletes. These sports can be considered as examples of good practices in promoting gender equality, where efforts to balance participation appear to have been successful.

Figure 4 shows a general trend where some sports have made significant strides toward gender equality (low PEI), while others still exhibit substantial disparities (high PEI). The diversity in PEI values across sports highlights that while some sports are closer to achieving gender parity, others may need more focused efforts to reduce gender disparities.

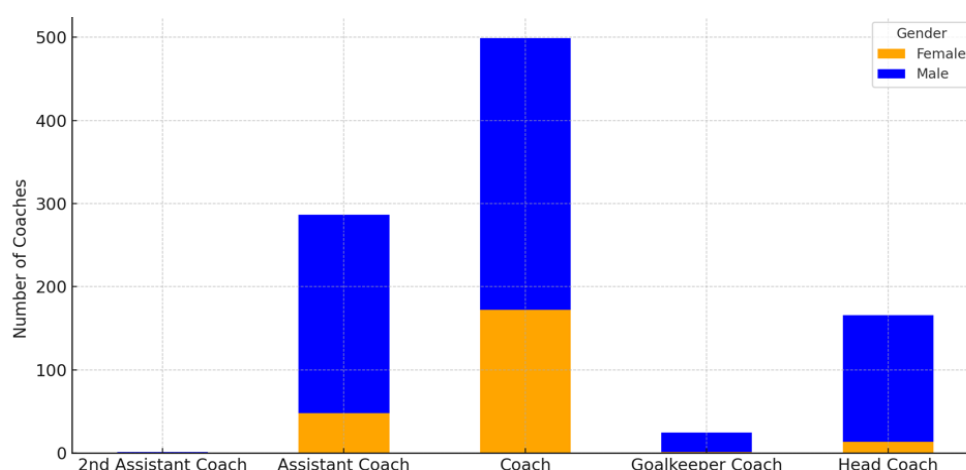


Figure 5.

Gender and Function Distribution Among Coaches in the Olympic Games

Figure 5 showing the distribution of coaches by gender and role (Head Coach and Coach) in the Olympic Games, several key points can be observed and discussed:

1. Gender Imbalance Among Coaches:

- Male Coaches: The graph clearly indicates that male coaches significantly outnumber female coaches across both roles (Head Coach and Coach). This imbalance is especially pronounced in the Coach role, where there are considerably more male coaches.

- Female Coaches: Despite increasing support for gender equality in sports, female coaches remain underrepresented, particularly in the Head Coach role. This could suggest limitations in opportunities for women to hold leadership positions within sports teams.

2. Role Distribution:

- Coach Role: This role has a higher number of both male and female coaches, as sports teams typically require multiple coaches to handle various aspects of training and athlete management. The larger number of coaches in this role reflects the structure of sports teams, where many coaches assist in different capacities.

- Head Coach Role: The Head Coach position has fewer coaches overall, as each team typically has only one person in this role. The graph reveals that male coaches dominate this role, suggesting a gender disparity in opportunities for women to lead sports teams.

3. Impact of This Imbalance:

- Barriers to Advancement for Female Coaches: The gender imbalance, particularly in the Head Coach role, highlights potential barriers that female coaches may face in advancing their careers. These barriers may include fewer opportunities for leadership roles or lingering societal perceptions that men are better suited to lead sports teams.

- Progress Toward Gender Equality: While the number of female coaches remains lower, the presence of women in the Coach role suggests progress in breaking down gender barriers. Their involvement in sports teams could be an important step toward achieving more leadership opportunities, such as the Head Coach role, in the future.

Recommendations for Improvement

1. Support for Female Coaches: More support and opportunities should be provided for female coaches to access higher-level roles, such as Head Coach, particularly in popular sports. This could involve mentorship programs, targeted leadership training, and initiatives to increase visibility and recognition of female coaches.

2. Policies to Promote Gender Equality: Clear policies aimed at promoting gender equality should be implemented, including funding for training programs and scholarships that help develop female coaches and equip them for leadership roles in sports.

This analysis highlights a significant gender imbalance among Olympic coaches, particularly in key leadership roles such as Head Coach. Although there is some progress with women entering the coaching ranks, gender inequality remains an issue that requires ongoing attention and efforts from stakeholders in the sports industry. Addressing these disparities will help pave the way for more equitable representation of women in coaching and leadership roles in sports.

While the Correlation Matrix primarily focuses on the relationships between different sports in which Thai athletes participated, it also provides an indirect lens through which we can discuss the broader topic of gender dynamics in sports participation and performance. Here are some key insights that could be tied back to gender-related factors:

1. Gender-Specific Sports Participation: Many sports traditionally show a divide between male and female participation due to societal norms, physical demands, and historical development within the sport. For example, Weightlifting and Boxing have historically been male-dominated sports due to their emphasis on strength and combat, whereas sports like Gymnastics and Swimming often have higher female representation, particularly at the elite level. The low correlations between these sports might suggest that male and female athletes are often segregated by the types of sports they compete in, further reflecting gender norms and biases in sports selection and participation.



2. Specialization in Gender-Dominated Sports: Specialized training in gender-dominated sports (e.g., Weightlifting for men and Gymnastics for women) can lead to distinct skill sets that do not necessarily translate well across other sports. This could explain the low or negative correlations in the matrix. For instance, athletes who excel in Taekwondo or Boxing (often male-dominated sports) may not perform as well in sports like Sailing or Golf, which have a more balanced or even female-dominated participation rate in some regions. This reinforces the notion that athletes are likely to stick to sports that align with societal gender expectations, rather than explore cross-discipline opportunities.

3. Gender and Mixed Sports Correlations: Some sports, such as Badminton and Shooting, have more balanced gender representation, with both male and female athletes competing at high levels. The slightly higher correlations between these sports and others might indicate that athletes in gender-diverse sports are more versatile or exposed to a broader range of skills. For instance, the correlation between Badminton and Swimming could reflect this versatility. In contrast, sports that are heavily skewed towards one gender may show lower correlations with other sports because the training is highly specialized and tied to gender expectations within those disciplines.

4. Gender Imbalances and Opportunity: The fact that certain sports like Boxing and Weightlifting have low correlations with other sports may also point to the limited opportunities for female athletes in these areas. Despite increasing participation from women, the structural challenges and societal biases that restrict women's access to these sports likely influence the low correlations observed. Shooting, which has shown a higher positive correlation with other sports, is often a sport where gender differences are minimized due to the focus on precision and skill rather than physical strength. This can indicate that sports with a more balanced gender representation or less reliance on physical gender differences might foster more cross-disciplinary versatility among athletes.

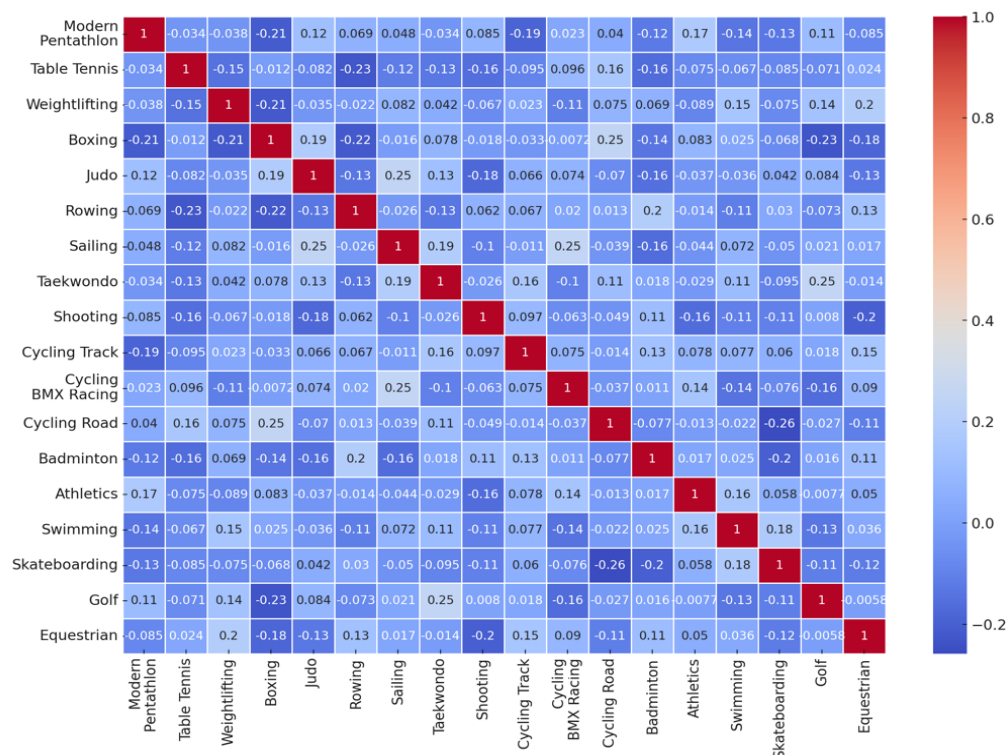


Figure 6.
Gender Dynamics Based on the Correlation Matrix for Thai Athletes

While the Correlation Matrix is not directly reflective of gender per se, the patterns of correlation (or lack thereof) between certain sports can be linked to traditional gender roles and the specialization of male and female athletes in particular disciplines. Sports with more balanced gender representation may foster a wider range of transferable skills, while those dominated by one gender tend to show lower correlations with other sports, reflecting the effects of gender norms and biases in sports participation and specialization. Understanding these dynamics can inform future efforts to promote greater gender equality in sports and encourage cross-disciplinary development for athletes of all genders.

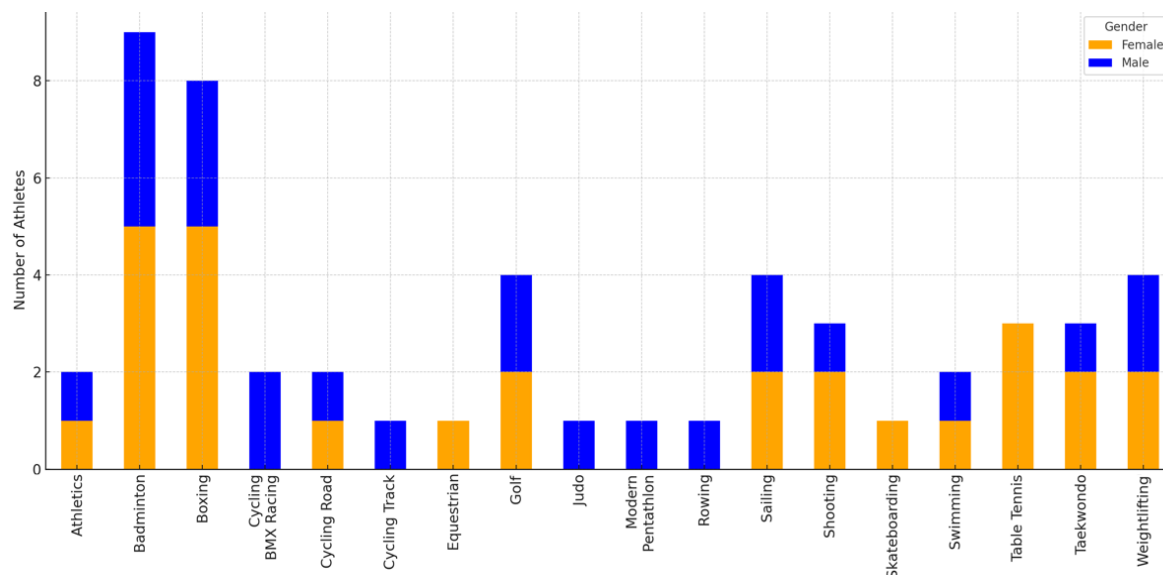


Figure 7.

Participation of Thai Athletes in the Olympic Games by Gender and Sports

Figure 7 illustrates the participation of Thai athletes in the Olympic Games, separated by gender and sport, the following analysis can be made:

1. **Participation by Male and Female Athletes:** Male Athletes dominate participation across various sports and are more numerous in sports like Boxing, Weightlifting, Football, and Shooting. This reflects a higher participation rate in strength-based and endurance sports traditionally dominated by men. Female Athletes have significant participation in sports such as Weightlifting, Badminton, and Boxing, showcasing their importance in skill-based sports and individual competitions that require agility and specialized abilities.

2. **Gender Balance in Sports:** Sports such as Badminton and Weightlifting display a near balance between male and female athletes, highlighting progress in gender equality within these disciplines. Female athletes are showing strong performances and are equally represented compared to their male counterparts in these sports. On the other hand, some sports still exhibit gender imbalance. For example, Football, Shooting, and Boxing have a significantly higher number of male participants, indicating that women may face more barriers or fewer opportunities to compete in these traditionally male-dominated sports.

3. **Sports with Strong Female Representation:** Weightlifting and Badminton are sports where female Thai athletes excel and contribute significantly. Female athletes in Weightlifting, in particular, have gained international recognition and brought home numerous accolades, which explains the notable participation of women in this sport.

This analysis highlights the differing opportunities for male and female athletes in the Olympic Games, with some sports showing significant gender disparities. While progress is being made in sports such as Weightlifting and Badminton, others like Football and Boxing still need greater support to promote gender equality.

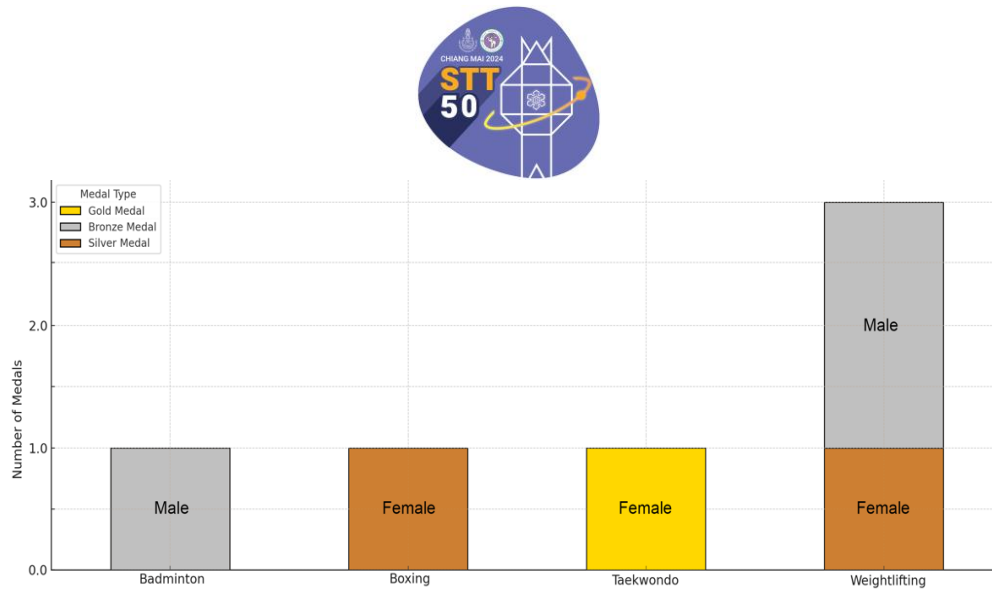


Figure 8.

Medal Distribution for Thai Athletes by Sports and Gender in the Olympic Games

Figure 8 provides a detailed view of the medal distribution for Thai athletes in the Olympic Games. Here's a breakdown of the insights:

1. Sport-Specific Success

- **Weightlifting:** This sport shows the most significant success for Thailand, with both male and female athletes earning medals. Male athletes have won both bronze and silver medals. Female athletes have also contributed significantly, particularly with bronze medals. This showcases Thailand's strong performance in weightlifting across both genders.

- **Badminton:** This sport shows male dominance, with male athletes securing bronze medals. Badminton is known to be one of Thailand's standout sports, especially in international competitions.

- **Boxing:** Female athletes are the primary contributors here, winning silver medals. Thailand has a strong tradition in boxing, and the inclusion of female medalists highlights the growing prominence of women in the sport.

- **Taekwondo:** Similar to boxing, female athletes have achieved success, winning gold medals. This reflects the rise of women in combat sports in Thailand and their ability to reach the highest levels of success.

2. Gender and Medal Distribution

- **Male Athletes:** Have won medals in weightlifting and badminton. The medals are more distributed across the medal spectrum (bronze and silver).

- **Female Athletes:** Have won medals across three sports in weightlifting, boxing, and taekwondo. Female athletes have earned a significant number of gold and silver medals, particularly in combat sports (boxing and taekwondo), indicating their strong performance in these areas.

3. Concentration of Medals

The medals for Thailand are concentrated in a small number of sports, with the largest haul coming from weightlifting and combat sports (boxing and taekwondo). This suggests that Thailand's focus and strengths lie in these sports, and they have successfully cultivated both male and female athletes who excel in these disciplines.

Thailand's strong performance in a limited number of sports, particularly weightlifting and combat sports, with contributions from both male and female athletes. While the number of sports represented is relatively small, the success in these areas reflects targeted excellence and investment in these disciplines. Additionally, the graph emphasizes the rising prominence of female athletes in traditionally male-dominated sports such as boxing and taekwondo.

Conclusion:

The analysis of gender equality at the Paris 2024 Olympic Games reveals significant progress in achieving balance between male and female athletes across multiple dimensions, including participation, performance outcomes, resource allocation, and policy implementation. The Participation Equality Index (PEI) indicates that several sports, particularly handball and athletics, have successfully achieved gender balance, with nearly equal participation rates between genders. However, the study also identifies persistent disparities in sports like wrestling, BMX freestyle, and equestrian, where female participation remains significantly lower, reflecting ongoing gender inequality in certain disciplines.

Additionally, the research highlights that resource allocation—such as financial support, access to training facilities—continues to favor male athletes in some sports, which impacts the opportunities and competitiveness of female athletes. The analysis of IOC policies shows that initiatives promoting mixed-gender events, increasing female quotas, and encouraging equal representation have played a crucial role in supporting gender equality systematically. However, the study falls short of offering actionable solutions to address the cultural and structural barriers that limit female participation in certain sports.

For Thai athletes, these developments bring both challenges and opportunities. Thai female athletes, excelling in sports like taekwondo, weightlifting and boxing, could gain from the increased focus on gender equality. However, existing disparities in participation and resources highlight the need for ongoing support and policies to ensure they can compete equally with male counterparts, especially in male-dominated sports.

While the Paris 2024 Olympic Games demonstrate marked progress in gender equality, this research underscores the need for continued efforts to ensure that all sports can achieve true gender balance. Future policies should focus on increasing opportunities, visibility, and support for female athletes, particularly in sports where they are currently underrepresented. Moreover, there should be a systematic development and refinement of policies aimed at addressing cultural and structural issues to achieve comprehensive gender equality. These findings provide critical insights for policymakers, sports organizations, and stakeholders committed to advancing gender equity in global sports.

Acknowledgements:

All computational resources were supported by Department of Computer Science, School of Science, King Mongkut's Institute of Technology Ladkrabang, Bangkok, Thailand.

References:

1. Buchy M., Shakya S., *Energy for Sustainable Development*, 2023;76:1-9.
2. Carla D., Dina A., Pedro M. *Journal of Hospitality, Leisure, Sport & Tourism Education*, 2023;32:1-23.
3. Emma E., Gabriella E., Mary L., *Clinics in Sports Medicine*, 2024;43:221-232.
4. Johanna A., Toni S., *Sport Management Review*, 2023;16:498-513.
5. Jun Myung S., *Pacific-Basin Finance Journal*, 2022;75.
6. Khanduja V., *Journal of ISAKOS*, 2024;3:251-252.
7. Michael D., Ram Haddas, Edward M., Shaun Nelms, Katherine Rizzzone, *Clinics in Sports Medicine*, 2024;43:271-277.
8. Shelley J., *Teaching and Teacher Education*. 2022;111:1-13.
9. Smith J., McNair G., Bushnell A., Saldana L., Kathryn E., *Mental Health and Physical Activity*, 2023;25.
10. Spagnolo M., Capodanno D., *American Heart Journal*, 2024;272:113-115.
11. Wendy J., Gregore I., Tracy L. *The Lancet*, 2016;388:1249-1348.



ADAPTIVE KALMAN FILTER FOR IMPROVED LANE TRACKING

Chadaporn Keatmanee^{1,*}, Anusart Chamornmano¹, Banlang Sinprasert¹, Apirak Jirayusakul¹, Supatra Sahaphong¹, Matthew N. Dailey², Somchok Sakjirapong², Aayush B. Rana², Mongkol Ekpanyapong³

¹Department of Computer Science, Faculty of Science, Ramkhamkaeng University, Thailand

²Department of Information and Communication Technology, Asian Institute of Technology (AIT), Pathum Thani, Thailand

³Department of Industrial Systems Engineering, Asian Institute of Technology (AIT), Pathum Thani, Thailand

*e-mail: chadaphone@ru.ac.th

Abstract:

Several intelligent transportation system applications depend on obtaining accurate estimates of the vehicle's trajectory for the lane the vehicle is driving in. However, lane marking detections are usually noisy, requiring robust estimation methods and filtering. We propose a method for tracking lane boundaries in real time using an adaptive extended Kalman filter to smooth noisy lane boundary measurements while the vehicle is in motion. We develop a precise model of lane boundary geometry and vehicle dynamics allowing for curved lanes and turns. Extensive simulation and real-world experiments demonstrate the efficiency of the method. The lane tracker reduces noise in lateral distance observations by more than 50% and tangent angle observations by more than 70%. A new adaptive covariance method outperforms the standard EKF by 10% in lateral distance and 5% in tangent angle. The system as a whole provides excellent real-time performance and lane tracing accuracy at low cost.



Analytical solutions of some conformable fractional differential equations

Araya Hamkarnhak,¹ Kanit Mukdasai^{2,*}

^{1,2}Department of Mathematics, Faculty of Science, Khon Kaen University, Khon Kaen 40002, Thailand

*e-mail: Kanit@kku.ac.th

Abstract

We present the solutions of some conformable fractional differential equations by model transformations, conformable fractional derivative and integral. Moreover, we study the solutions of some modified conformable fractional equations. Finally, numerical examples are given to demonstrate the effectiveness of the proposed method.

Introduction

Fractional calculus has resurfaced and gained momentum due to its potential in engineering systems, multidisciplinary fields, biology, medicine, and applied sciences. Its wide range of applications includes areas like linear anomalous diffusion equations and their characteristics [5], modeling biological phenomena, respiratory tissue, and drug diffusion [7]. At the same time, fractional calculus has found its way to sensors, analog, and digital filters [10]. Solving differential equations plays a major role in Engineering, Physics, Biology, and other fields like economics and medicine, see [1, 2, 3]. The fractional calculus [9, 13, 14] is a fractional order derivative by defining a new definition of fractional derivative [8] from that differs from the limit derivative definition. Many years ago, many mathematicians paid attention to fractional derivatives, and many different forms of fractional derivatives have been defined, but the most popular is the fractional derivative as the follows: The Riemann-Liouville fractional derivative and the Caputo fractional derivative [8] given by

- i) Riemann-Liouville Definition: If n is a positive integer and $\alpha \in [n-1, n)$, the α^{th} derivative of f is given by

$${}^{RL}\mathcal{D}_a^\alpha f(t) = \frac{1}{\Gamma(n-\alpha)} \frac{d^n}{dt^n} \int_a^t \frac{f(x)}{(t-x)^{\alpha-n+1}} dx,$$

where Γ is gamma function.

- ii) Caputo Definition: If n is a positive integer and $\alpha \in [n-1, n)$, the α^{th} derivative of f is given by

$${}^C\mathcal{D}_a^\alpha f(t) = \frac{1}{\Gamma(n-\alpha)} \int_a^t \frac{f^{(n)}(x)}{(t-x)^{\alpha-n+1}} dx,$$

where Γ is gamma function.

Currently, all efforts are directed toward ensuring that fractional derivative definitions conform to the typical characteristics of the standard derivative. The only universally shared property among all fractional derivative definitions is linearity. However, each definition comes with its own set of limitations or drawbacks:

- (i) The Riemann-Liouville derivative does not satisfy ${}^{RL}\mathcal{D}^\alpha(c) = 0$ (${}^C\mathcal{D}^\alpha(c) = 0$ for the Caputo derivative), if α is not a natural number.



(ii) All fractional derivatives do not satisfy the known product rule

$$\mathcal{D}^\alpha(fg)(t) = f(t)\mathcal{D}^\alpha g(t) + g(t)\mathcal{D}^\alpha f(t).$$

(iii) All fractional derivatives do not satisfy the known quotient rule

$$\mathcal{D}^\alpha(f/g)(t) = \frac{g(t)\mathcal{D}^\alpha f(t) - f(t)\mathcal{D}^\alpha g(t)}{g^2(t)}.$$

(iv) All fractional derivatives do not satisfy the chain rule

$$\mathcal{D}^\alpha(f \circ g)(t) = f^\alpha(g(t))g^\alpha(t).$$

(v) All fractional derivatives do not satisfy $\mathcal{D}^\alpha \mathcal{D}^\beta(f) = \mathcal{D}^{\alpha+\beta}(f)$ in general.

Therefore, the definition of conformable fractional derivatives [8] was created to solve the above problem. Moreover, this definition makes the above problems consistent with various derivative rules. The definition is as follows:

$$\mathcal{T}^\alpha f(t) = \lim_{\varepsilon \rightarrow 0} \frac{f(t + \varepsilon(t - t_0)^{1-\alpha}) - f(t)}{\varepsilon}, \text{ for all } t > t_0 \text{ and } \alpha \in (0, 1].$$

For the above reasons, we are interested in adopting a conformable fractional derivative definition. Because it has similar properties to the usual derivative definition and is the definition that has received the most attention. For this proposal, we have presented a method for finding solutions of fractional differential equations and obtained through numerical, graphical.

Preliminaries

In this section, we introduce some basic definitions and theorems of the conformable fractional differential of order $0 < \alpha \leq 1$.

Definition 1. [8] Let $\alpha \in (0, 1]$, The conformable fractional derivative of function $f: [t_0, \infty) \rightarrow \mathbb{R}$ is given by

$$\mathcal{T}^\alpha f(t) = \lim_{\varepsilon \rightarrow 0} \frac{f(t + \varepsilon(t - t_0)^{1-\alpha}) - f(t)}{\varepsilon}, \quad t > t_0.$$

If f is α -differentiable in some (t_0, a) , $a > t_0$, and $\lim_{t \rightarrow t_0^+} \mathcal{T}^\alpha f(t)$ exists, then define $\mathcal{T}^\alpha f(t_0) = \lim_{t \rightarrow t_0^+} \mathcal{T}^\alpha f(t)$.

Definition 2. [4] The left-sided sequential modified conformable fractional derivative of order $\alpha \in (0, 1]$ of a function $f: [t_0, \infty) \rightarrow \mathbb{R}$ is given by

$$\mathcal{T}_{t_0}^{2\alpha} f(t) = \lim_{\varepsilon \rightarrow 0} \frac{f^{(\alpha)}(t + \varepsilon(t - t_0)^{1-\alpha}) - f^{(\alpha)}(t)}{\varepsilon}, \quad t > t_0.$$

Definition 3. [11] Let $\alpha \in (0, 1]$, The conformable fractional integral of function $f: [t_0, \infty) \rightarrow \mathbb{R}$ is continuous such that $\mathcal{J}^\alpha(f(t))$ exists. Then

$$\mathcal{J}^\alpha f(t) = \int_{t_0}^t (x - t_0)^{\alpha-1} f(x) dx, \quad t > t_0.$$



Definition 4. [4] The left-sided sequential modified conformable fractional integral of order $\alpha \in (0, 1]$ of a function $f(t) \in C_\mu, \mu \geq -\alpha, t > t_0$ is given by

$$\mathcal{J}_{t_0}^{2\alpha} f(t) = \frac{1}{\alpha} \int_{t_0}^t \frac{((t-t_0)^\alpha - (x-t_0)^\alpha) f(x)}{(x-t_0)^{1-\alpha}} dx.$$

Lemma 1. [11] Let $\alpha \in (0, 1]$ and $f : [t_0, \infty) \rightarrow \mathbb{R}$ be a continuous function such that $\mathcal{J}^\alpha(f(t))$ exists, then

$$\mathcal{T}^\alpha[\mathcal{J}^\alpha f(t)] = f(t),$$

and

$$\mathcal{J}^\alpha[\mathcal{T}^\alpha f(t)] = f(t) - f(t_0).$$

Remark 1. [6] Typical Maclaurine series, which you should know

$$\begin{aligned} e^t &= 1 + t + \frac{t^2}{2} + \frac{t^3}{3!} + \cdots = \sum_{n=0}^{\infty} \frac{t^n}{n!}; \quad t \in \mathbb{R}, \\ \cosh(t) &= 1 + \frac{t^2}{2} + \frac{t^4}{4!} + \cdots = \sum_{n=0}^{\infty} \frac{t^{2n}}{(2n)!}; \quad t \in \mathbb{R}, \\ \sinh(t) &= t + \frac{t^3}{3!} + \frac{t^5}{5!} + \cdots = \sum_{n=0}^{\infty} \frac{t^{2n+1}}{(2n+1)!}; \quad t \in \mathbb{R}. \end{aligned}$$

Lemma 2. [12] Let $t_0 \in \mathbb{R}$ and $f_n(t) : [t_0, \infty) \rightarrow \mathbb{R}$ be a continuous and nonnegative function such that $\sum_{n=0}^{\infty} f_n(t) < \infty, \forall n \in \mathbb{N} \cup \{0\}$. Then

$$\mathcal{J}^\alpha \left(\sum_{n=0}^{\infty} f_n(t) \right) = \sum_{n=0}^{\infty} (\mathcal{J}^\alpha f_n(t)).$$

Results and Discussion

Theorem 1. Let $x(t)$ be a continuous function for $t \in [t_0, \infty)$, $t_0 \in \mathbb{R}$. For $\alpha \in (0, 1]$, $A, x_0 \in \mathbb{R}$ and $n \in \mathbb{N}$, a solution of a conformable fractional ordinary differential equation

$$\mathcal{T}^\alpha x(t) = A(t-t_0)^n, \quad x(t_0) = x_0, \quad t \geq t_0, \quad (1)$$

is given by

$$x(t) - x_0 = \frac{A(t-t_0)^{\alpha+n}}{\alpha+n}. \quad (2)$$

Proof. Let $x(t)$ be a continuous function for $t \in [t_0, \infty)$ and $x(t)$ be a solution of (1). Consider

$$\mathcal{T}^\alpha x(t) = A(t-t_0)^n, \quad x(t_0) = x_0, \quad t \geq t_0.$$

By Definition 3 and Lemma 1, we obtain

$$\begin{aligned} \mathcal{J}^\alpha \mathcal{T}^\alpha x(t) &= \mathcal{J}^\alpha A(t-t_0)^n \\ x(t) - x(t_0) &= A \int_{t_0}^t (s-t_0)^{\alpha-1} (s-t_0)^n ds \\ &= A \int_{t_0}^t (s-t_0)^{\alpha-1+n} ds \\ &= \frac{A(t-t_0)^{\alpha+n}}{\alpha+n}. \end{aligned}$$

Therefore, a solution of (1) is $x(t) - x_0 = \frac{A(t-t_0)^{\alpha+n}}{\alpha+n}$. □



We plot solutions of (1). We compare the different values of α

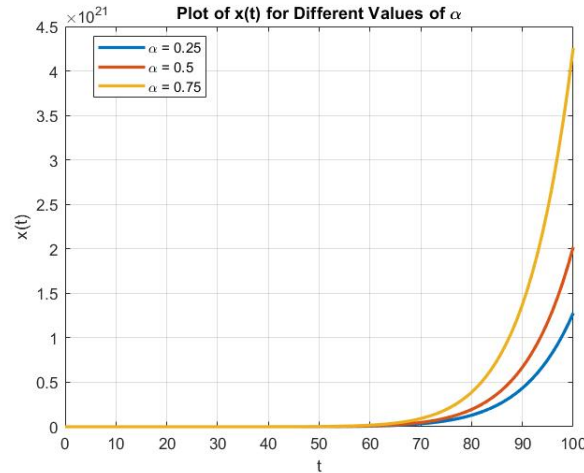


Figure 1: Solution of (1) $A = 1$, $x(0) = 0$, $n = 1$ with $\alpha = 0.25$ (blue), $\alpha = 0.5$ (red) and $\alpha = 0.75$ (yellow).

Theorem 2. Let $x(t)$ be a continuous function for $t \in [t_0, \infty)$, $t_0 \in \mathbb{R}$. For $\alpha \in (0, 1]$, $A, x_0 \in \mathbb{R}$ and $n \in \mathbb{N}$, a solution of a conformable fractional ordinary differential equation

$$\mathcal{J}^\alpha x(t) = Ae^{t-t_0}, \quad x(t_0) = x_0, \quad t \geq t_0, \quad (3)$$

is given by

$$x(t) - x_0 = \sum_{n=0}^{\infty} \frac{A(t-t_0)^{\alpha+n}}{n!(\alpha+n)}. \quad (4)$$

Proof. Let $x(t)$ be a continuous function for $t \in [t_0, \infty)$ and $x(t)$ be a solution of (3). Consider

$$\mathcal{J}^\alpha x(t) = Ae^{(t-t_0)}, \quad x(t_0) = x_0, \quad t \geq t_0.$$

By Definition 3, Lemma 1, Remark 1 and Lemma 2, we obtain

$$\begin{aligned} \mathcal{J}^\alpha \mathcal{J}^\alpha x(t) &= \mathcal{J}^\alpha Ae^{(t-t_0)} \\ x(t) - x(t_0) &= \mathcal{J}^\alpha A \sum_{n=0}^{\infty} \frac{(t-t_0)^n}{n!} \\ &= \mathcal{J}^\alpha A \left(1 + (t-t_0) + \frac{(t-t_0)^2}{2} + \frac{(t-t_0)^3}{6} + \dots \right) \\ &= \mathcal{J}^\alpha A(1) + \mathcal{J}^\alpha A(t-t_0) + \mathcal{J}^\alpha \frac{A(t-t_0)^2}{2} + \mathcal{J}^\alpha \frac{A(t-t_0)^3}{6} + \dots \\ &= A \int_{t_0}^t (s-t_0)^{\alpha-1} (1) ds + A \int_{t_0}^t (s-t_0)^{\alpha-1} (s-t_0) ds \\ &\quad + \frac{A}{2} \int_{t_0}^t (s-t_0)^{\alpha-1} (s-t_0)^2 ds + \dots \\ &= \frac{A(t-t_0)^\alpha}{\alpha} + \frac{A(t-t_0)^{\alpha+1}}{\alpha+1} + \frac{A(t-t_0)^{\alpha+2}}{2(\alpha+2)} + \frac{A(t-t_0)^{\alpha+3}}{6(\alpha+3)} + \dots \end{aligned}$$

Therefore, a solution of (3) is $x(t) - x_0 = \sum_{n=0}^{\infty} \frac{A(t-t_0)^{\alpha+n}}{n!(\alpha+n)}$. □



We plot solutions of (3). We compare the different values of α

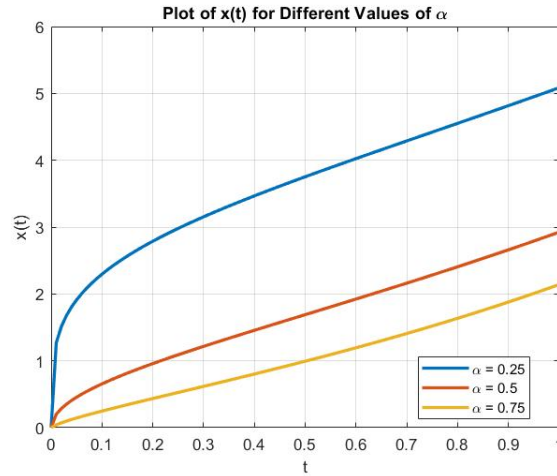


Figure 2: Solution of (3) $A = 1$, $x(0) = 0$, $n = 1$ with $\alpha = 0.25$ (blue), $\alpha = 0.5$ (red) and $\alpha = 0.75$ (yellow).

Theorem 3. Let $x(t)$ be a continuous function for $t \in [t_0, \infty)$, $t_0 \in \mathbb{R}$. For $\alpha \in (0, 1]$, $A, x_0 \in \mathbb{R}$ and $n \in \mathbb{N}$, a solution of a conformable fractional ordinary differential equation

$$\mathcal{I}^\alpha x(t) = A \sinh(t - t_0), \quad x(t_0) = x_0, \quad t \geq t_0, \quad (5)$$

is given by

$$x(t) - x_0 = \sum_{n=0}^{\infty} \frac{A(t - t_0)^{\alpha+2n+1}}{(2n+1)!(\alpha+2n+1)}. \quad (6)$$

Proof. Let $x(t)$ be a continuous function for $t \in [t_0, \infty)$ and $x(t)$ be a solution of (5). Consider

$$\mathcal{I}^\alpha x(t) = A \sinh(t - t_0), \quad x(t_0) = x_0, \quad t \geq t_0.$$

By Definition 3, Lemma 1, Remark 1 and Lemma 2, we obtain

$$\begin{aligned} \mathcal{I}^\alpha \mathcal{I}^\alpha x(t) &= \mathcal{I}^\alpha A \sinh(t - t_0) \\ x(t) - x(t_0) &= \mathcal{I}^\alpha A \sum_{n=0}^{\infty} \frac{(t - t_0)^{2n+1}}{(2n+1)!} \\ &= \mathcal{I}^\alpha A \left((t - t_0) + \frac{(t - t_0)^3}{6} + \frac{(t - t_0)^5}{120} + \dots \right) \\ &= \mathcal{I}^\alpha A(t - t_0) + \mathcal{I}^\alpha \frac{A(t - t_0)^3}{6} + \mathcal{I}^\alpha \frac{A(t - t_0)^5}{120} + \dots \\ &= A \int_{t_0}^t (s - t_0)^{\alpha-1} (s - t_0) ds + \frac{A}{6} \int_{t_0}^t (s - t_0)^{\alpha-1} (s - t_0)^3 ds \\ &\quad + \frac{A}{120} \int_{t_0}^t (s - t_0)^{\alpha-1} (s - t_0)^5 ds + \dots \\ &= \frac{A(t - t_0)^{\alpha+1}}{(\alpha+1)} + \frac{A(t - t_0)^{\alpha+3}}{6(\alpha+3)} + \frac{A(t - t_0)^{\alpha+5}}{120(\alpha+5)} + \dots \end{aligned}$$

Therefore, a solution of (5) is $x(t) - x_0 = \sum_{n=0}^{\infty} \frac{A(t - t_0)^{\alpha+2n+1}}{(2n+1)!(\alpha+2n+1)}$. □



We plot solutions of (5). We compare the different values of α

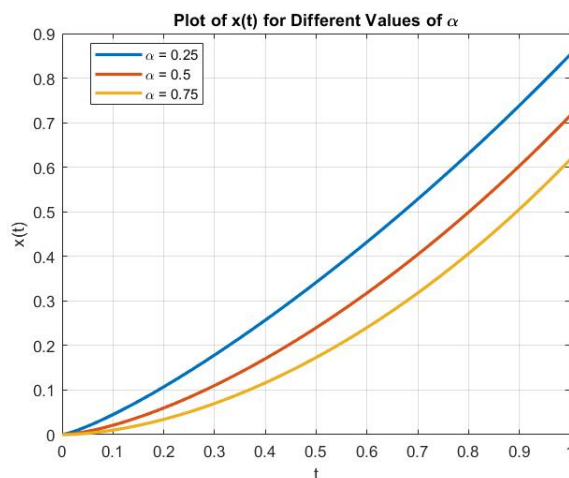


Figure 3: Solution of (5) $A = 1$, $x(0) = 0$, $n = 1$ with $\alpha = 0.25$ (blue), $\alpha = 0.5$ (red) and $\alpha = 0.75$ (yellow).

Theorem 4. Let $x(t)$ be a continuous function for $t \in [t_0, \infty)$, $t_0 \in \mathbb{R}$. For $\alpha \in (0, 1]$, $A, x_0 \in \mathbb{R}$ and $n \in \mathbb{N}$, a solution of a conformable fractional ordinary differential equation

$$\mathcal{I}^\alpha x(t) = A \cosh(t - t_0), \quad x(t_0) = x_0, \quad t \geq t_0, \quad (7)$$

is given by

$$x(t) - x_0 = \sum_{n=0}^{\infty} \frac{A(t-t_0)^{\alpha+2n}}{(2n)!(\alpha+2n)}. \quad (8)$$

Proof. Let $x(t)$ be a continuous function for $t \in [t_0, \infty)$ and $x(t)$ be a solution of (7). Consider

$$\mathcal{I}^\alpha x(t) = A \cosh(t - t_0), \quad x(t_0) = x_0, \quad t \geq t_0.$$

By Definition 3, Lemma 1, Remark 1 and Lemma 2, we obtain

$$\begin{aligned} \mathcal{I}^\alpha \mathcal{I}^\alpha x(t) &= I^\alpha A \cosh(t - t_0) \\ x(t) - x(t_0) &= \mathcal{I}^\alpha A \sum_{n=0}^{\infty} \frac{(t-t_0)^{2n}}{(2n)!} \\ &= \mathcal{I}^\alpha A \left(1 + \frac{(t-t_0)^2}{2} + \frac{(t-t_0)^4}{24} + \dots \right) \\ &= \mathcal{I}^\alpha A(1) + \mathcal{I}^\alpha A \frac{(t-t_0)^2}{2} + \mathcal{I}^\alpha A \frac{(t-t_0)^4}{24} + \dots \\ &= A \int_{t_0}^t (s-t_0)^{\alpha-1} ds + \frac{A}{2} \int_{t_0}^t (s-t_0)^{\alpha-1} (s-t_0)^2 ds \\ &\quad + \frac{A}{24} \int_{t_0}^t (s-t_0)^{\alpha-1} (s-t_0)^4 ds + \dots \\ &= \frac{A(t-t_0)^\alpha}{(\alpha)} + \frac{A(t-t_0)^{\alpha+2}}{2(\alpha+2)} + \frac{A(t-t_0)^{\alpha+4}}{24(\alpha+4)} + \dots \end{aligned}$$

Therefore, a solution of (7) is $x(t) - x_0 = \sum_{n=0}^{\infty} \frac{A(t-t_0)^{\alpha+2n}}{(2n)!(\alpha+2n)}$. □



We plot solutions of (7). We compare the different values of α

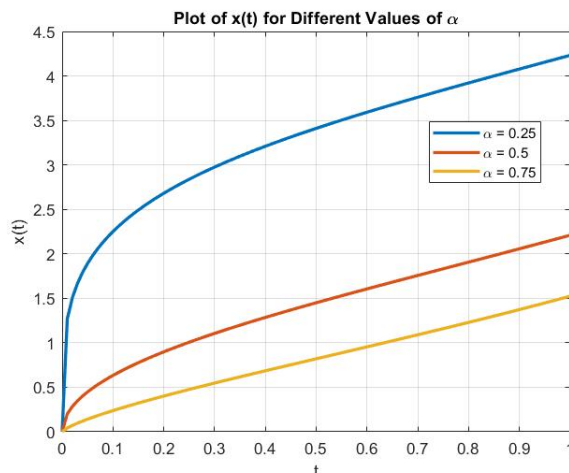


Figure 4: Solution of (7) $A = 1$, $x(0) = 0$, $n = 1$ with $\alpha = 0.25$ (blue), $\alpha = 0.5$ (red) and $\alpha = 0.75$ (yellow).

Theorem 5. Let $x(t)$ be a continuous function for $t \in [t_0, \infty)$, $t_0 \in \mathbb{R}$. For $\alpha \in (0, 1]$, $A, x_0 \in \mathbb{R}$ and $n \in \mathbb{N}$, a solution of a modified conformable fractional ordinary differential equation

$$\mathcal{J}_{t_0}^{2\alpha} x(t) = A(t - t_0)^n, \quad x(t_0) = x_0, \quad t \geq t_0, \quad (9)$$

is given by

$$x(t) - x_0 = \frac{A(t - t_0)^{2\alpha+n}}{(\alpha + n)(2\alpha + n)}. \quad (10)$$

Proof. Let $x(t)$ be a continuous function for $t \in [t_0, \infty)$ and $x(t)$ be a solution of (9). Consider

$$\mathcal{J}_{t_0}^{2\alpha} x(t) = A(t - t_0)^n, \quad x(t_0) = x_0, \quad t \geq t_0.$$

By Definition 4 and Lemma 1, we obtain

$$\begin{aligned} \mathcal{J}_{t_0}^{2\alpha} \mathcal{J}_{t_0}^{2\alpha} x(t) &= \mathcal{J}_{t_0}^{2\alpha} A(t - t_0)^n \\ x(t) - x(t_0) &= \frac{A}{\alpha} \int_{t_0}^t \frac{((t - t_0)^\alpha - (s - t_0)^\alpha)(s - t_0)^n}{(s - t_0)^{1-\alpha}} ds \\ &= \frac{A}{\alpha} \int_{t_0}^t ((t - t_0)^\alpha - (s - t_0)^\alpha)(s - t_0)^{n-1+\alpha} ds \\ &= \frac{A}{\alpha} \int_{t_0}^t (t - t_0)^\alpha (s - t_0)^{n-1+\alpha} ds - \frac{A}{\alpha} \int_{t_0}^t (s - t_0)^{n-1+2\alpha} ds \\ &= \frac{A(t - t_0)^{2\alpha+n}}{\alpha(n + \alpha)} - \frac{A(t - t_0)^{2\alpha+n}}{\alpha(n + 2\alpha)} \\ &= \frac{A(t - t_0)^{2\alpha+n}}{(\alpha + n)(2\alpha + n)}. \end{aligned}$$

Therefore, a solution of (9) is $x(t) - x_0 = \frac{A(t - t_0)^{2\alpha+n}}{(\alpha + n)(2\alpha + n)}$. □



We plot solutions of (9). We compare the different values of α

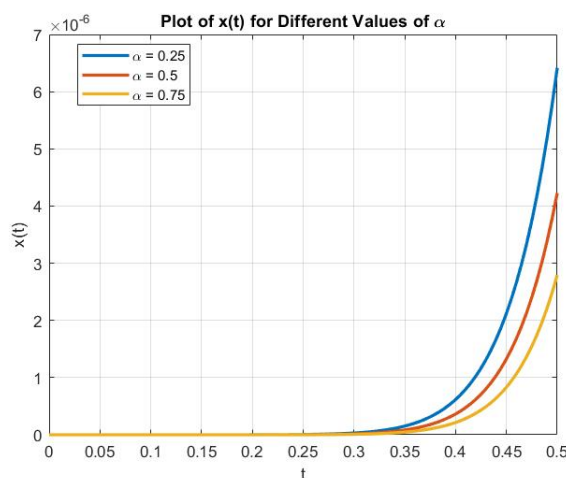


Figure 5: Solution of (9) $A = 1$, $x(0) = 0$, $n = 1$ with $\alpha = 0.25$ (blue), $\alpha = 0.5$ (red) and $\alpha = 0.75$ (yellow).

Theorem 6. Let $x(t)$ be a continuous function for $t \in [t_0, \infty)$, $t_0 \in \mathbb{R}$. For $\alpha \in (0, 1]$, $A, x_0 \in \mathbb{R}$ and $n \in \mathbb{N}$, a solution of a modified conformable fractional ordinary differential equation

$$\mathcal{J}_{t_0}^{2\alpha} x(t) = Ae^{t-t_0}, \quad x(t_0) = x_0, \quad t \geq t_0, \quad (11)$$

is given by

$$x(t) - x_0 = \sum_{n=0}^{\infty} \frac{A(t-t_0)^{2\alpha+n}}{n!(\alpha+n)(2\alpha+n)}. \quad (12)$$

Proof. Let $x(t)$ be a continuous function for $t \in [t_0, \infty)$ and $x(t)$ be a solution of (11). Consider

$$\begin{aligned} \mathcal{J}_{t_0}^{2\alpha} x(t) &= Ae^{(t-t_0)}, \\ x(t_0) &= x_0, \quad t \geq t_0. \end{aligned}$$

By Definition 4, Lemma 1, Remark 1 and Lemma 2, we obtain

$$\begin{aligned} \mathcal{J}_{t_0}^{2\alpha} \mathcal{J}_{t_0}^{2\alpha} x(t) &= \mathcal{J}_{t_0}^{2\alpha} Ae^{(t-t_0)} \\ x(t) - x(t_0) &= \mathcal{J}_{t_0}^{2\alpha} A \sum_{n=0}^{\infty} \frac{(t-t_0)^n}{n!} \\ &= \mathcal{J}_{t_0}^{2\alpha} A \left(1 + (t-t_0) + \frac{(t-t_0)^2}{2} + \frac{(t-t_0)^3}{6} + \dots \right) \\ &= \mathcal{J}_{t_0}^{2\alpha} A(1) + \mathcal{J}_{t_0}^{2\alpha} A(t-t_0) + \mathcal{J}_{t_0}^{2\alpha} \frac{A(t-t_0)^2}{2} + \mathcal{J}_{t_0}^{2\alpha} \frac{A(t-t_0)^3}{6} + \dots \\ &= \frac{A}{\alpha} \int_{t_0}^t \frac{(t-t_0)^\alpha - (s-t_0)^\alpha}{(s-t_0)^{1-\alpha}} ds + \frac{A}{\alpha} \int_{t_0}^t \frac{((t-t_0)^\alpha - (s-t_0)^\alpha)(s-t_0)}{(s-t_0)^{1-\alpha}} ds \\ &\quad + \frac{A}{2\alpha} \int_{t_0}^t \frac{((t-t_0)^\alpha - (s-t_0)^\alpha)(s-t_0)^2}{(s-t_0)^{1-\alpha}} ds \\ &\quad + \frac{A}{6\alpha} \int_{t_0}^t \frac{((t-t_0)^\alpha - (s-t_0)^\alpha)(s-t_0)^3}{(s-t_0)^{1-\alpha}} ds + \dots \\ &= \sum_{n=0}^{\infty} \frac{A(t-t_0)^{2\alpha+n}}{n!(\alpha+n)(2\alpha+n)}. \end{aligned}$$



Therefore, a solution of (11) is $x(t) - x_0 = \sum_{n=0}^{\infty} \frac{A(t-t_0)^{2\alpha+n}}{n!(\alpha+n)(2\alpha+n)}$. □

We plot solutions of (11). We compare the different values of α

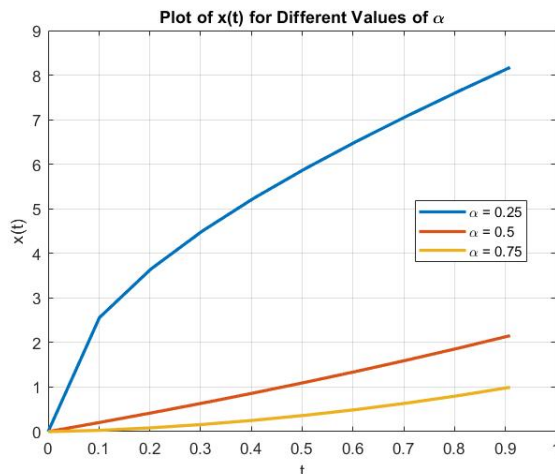


Figure 6: Solution of (11) $A = 1$, $x(0) = 0$, $n = 1$ with $\alpha = 0.25$ (blue), $\alpha = 0.5$ (red) and $\alpha = 0.75$ (yellow).

Theorem 7. Let $x(t)$ be a continuous function for $t \in [t_0, \infty)$, $t_0 \in \mathbb{R}$. For $\alpha \in (0, 1]$, $A, x_0 \in \mathbb{R}$ and $n \in \mathbb{N}$, a solution of a modified conformable fractional ordinary differential equation

$$\mathcal{J}_{t_0}^{2\alpha} x(t) = A \sinh(t - t_0), \quad x(t_0) = x_0, \quad t \geq t_0, \quad (13)$$

is given by

$$x(t) - x_0 = \sum_{n=0}^{\infty} \frac{A(t-t_0)^{2\alpha+2n+1}}{(2n+1)!(\alpha+2n+1)(2\alpha+2n+1)}. \quad (14)$$

Proof. Let $x(t)$ be a continuous function for $t \in [t_0, \infty)$ and $x(t)$ be a solution of (13). Consider

$$\mathcal{J}_{t_0}^{2\alpha} x(t) = A \sinh(t - t_0), \quad x(t_0) = x_0, \quad t \geq t_0.$$

By Definition 4, Lemma 1, Remark 1 and Lemma 2, we obtain

$$\begin{aligned} \mathcal{J}_{t_0}^{2\alpha} \mathcal{J}_{t_0}^{2\alpha} x(t) &= \mathcal{J}_{t_0}^{2\alpha} A \sinh(t - t_0) \\ x(t) - x(t_0) &= \mathcal{J}_{t_0}^{2\alpha} A \sum_{n=0}^{\infty} \frac{(t-t_0)^{2n+1}}{(2n+1)!} \\ &= \mathcal{J}_{t_0}^{2\alpha} A \left((t-t_0) + \frac{(t-t_0)^3}{6} + \frac{(t-t_0)^5}{120} + \dots \right) \\ &= \mathcal{J}_{t_0}^{2\alpha} A(t-t_0) + \mathcal{J}_{t_0}^{2\alpha} \frac{A(t-t_0)^3}{6} + \mathcal{J}_{t_0}^{2\alpha} \frac{A(t-t_0)^5}{120} + \dots \\ &= \frac{A}{\alpha} \int_{t_0}^t \frac{((t-t_0)^\alpha - (s-t_0)^\alpha)(s-t_0)}{(s-t_0)^{1-\alpha}} ds + \frac{A}{6\alpha} \int_{t_0}^t \frac{((t-t_0)^\alpha - (s-t_0)^\alpha)(s-t_0)^3}{(s-t_0)^{1-\alpha}} ds \\ &\quad + \frac{A}{120\alpha} \int_{t_0}^t \frac{((t-t_0)^\alpha - (s-t_0)^\alpha)(s-t_0)^5}{(s-t_0)^{1-\alpha}} ds + \dots \\ &= \sum_{n=0}^{\infty} \frac{A(t-t_0)^{2\alpha+2n+1}}{(2n+1)!(\alpha+2n+1)(2\alpha+2n+1)}. \end{aligned}$$



Therefore, a solution of (13) is $x(t) - x_0 = \sum_{n=0}^{\infty} \frac{A(t-t_0)^{2\alpha+2n+1}}{(2n+1)!(\alpha+2n+1)(2\alpha+2n+1)}$. □

We plot solutions of (13). We compare the different values of α

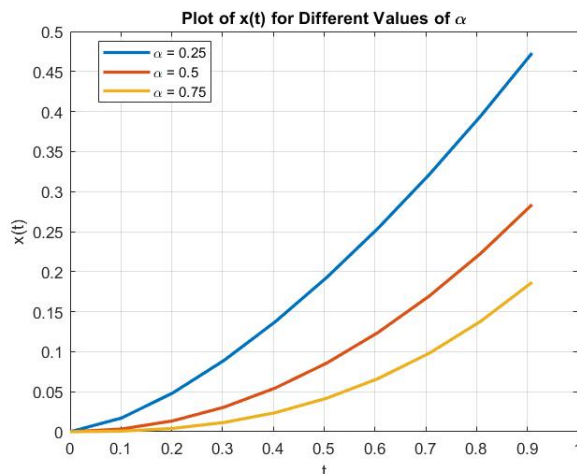


Figure 7: Solution of (13) $A = 1$, $x(0) = 0$, $n = 1$ with $\alpha = 0.25$ (blue), $\alpha = 0.5$ (red) and $\alpha = 0.75$ (yellow).

Theorem 8. Let $x(t)$ be a continuous function for $t \in [t_0, \infty)$, $t_0 \in \mathbb{R}$. For $\alpha \in (0, 1]$, $A, x_0 \in \mathbb{R}$ and $n \in \mathbb{N}$, a solution of a modified conformable fractional ordinary differential equation

$$\mathcal{J}_{t_0}^{2\alpha} x(t) = A \cosh(t - t_0), \quad x(t_0) = x_0, \quad t \geq t_0, \quad (15)$$

is given by

$$x(t) - x_0 = \sum_{n=0}^{\infty} \frac{A(t-t_0)^{2\alpha+2n}}{(2n)!(\alpha+2n)(2\alpha+2n)}. \quad (16)$$

Proof. Let $x(t)$ be a continuous function for $t \in [t_0, \infty)$ and $x(t)$ be a solution of (15). Consider

$$\mathcal{J}_{t_0}^{2\alpha} x(t) = A \cosh(t - t_0), \quad x(t_0) = x_0, \quad t \geq t_0.$$

By Definition 4, Lemma 1, Remark 1 and Lemma 2, we obtain

$$\begin{aligned} \mathcal{J}_{t_0}^{2\alpha} \mathcal{J}_{t_0}^{2\alpha} x(t) &= \mathcal{J}_{t_0}^{2\alpha} A \cosh(t - t_0) \\ x(t) - x(t_0) &= \mathcal{J}_{t_0}^{2\alpha} A \sum_{n=0}^{\infty} \frac{(t-t_0)^{2n}}{(2n)!} \\ &= \mathcal{J}_{t_0}^{2\alpha} A \left(1 + \frac{(t-t_0)^2}{2} + \frac{(t-t_0)^4}{24} + \dots \right) \\ &= \mathcal{J}_{t_0}^{2\alpha} A(1) + \mathcal{J}_{t_0}^{2\alpha} \frac{A(t-t_0)^2}{2} + \mathcal{J}_{t_0}^{2\alpha} \frac{A(t-t_0)^4}{24} + \dots \\ &= \frac{A}{\alpha} \int_{t_0}^t \frac{(t-t_0)^\alpha - (s-t_0)^\alpha}{(s-t_0)^{1-\alpha}} ds + \frac{A}{2\alpha} \int_{t_0}^t \frac{((t-t_0)^\alpha - (s-t_0)^\alpha)(s-t_0)^2}{(s-t_0)^{1-\alpha}} ds \\ &\quad + \frac{A}{24\alpha} \int_{t_0}^t \frac{((t-t_0)^\alpha - (s-t_0)^\alpha)(s-t_0)^4}{(s-t_0)^{1-\alpha}} ds + \dots \\ &= \sum_{n=0}^{\infty} \frac{A(t-t_0)^{2\alpha+2n}}{(2n)!(\alpha+2n)(2\alpha+2n)}. \end{aligned}$$



Therefore, a solution of (15) is $x(t) - x_0 = \sum_{n=0}^{\infty} \frac{A(t-t_0)^{2\alpha+2n}}{(2n)!(\alpha+2n)(2\alpha+2n)}$. □

We plot solutions of (15). We compare the different values of α

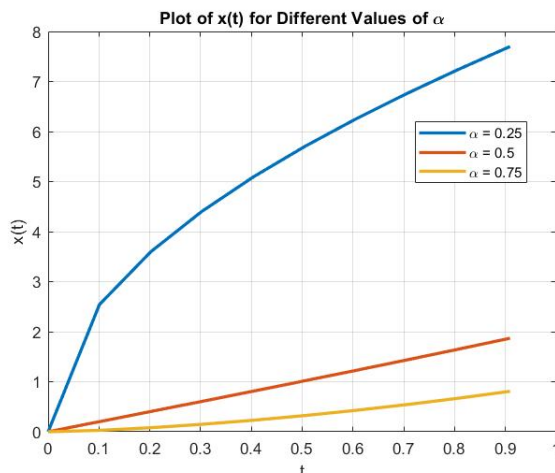


Figure 8: Solution of (1) $A = 1$, $x(0) = 0$, $n = 1$ with $\alpha = 0.25$ (blue), $\alpha = 0.5$ (red) and $\alpha = 0.75$ (yellow).

Conclusion

We study the solutions of some conformable fractional differential equations using model transformations, conformable fractional derivatives, and integrals. Moreover, we study the solutions of some modified conformable fractional equations. We present numerical examples that correspond to the derived theory.

Acknowledgements

This work is supported by the Development and Promotion of Science and Technology Talents Project (DPST) and National Research Council of Thailand (NRCT) and Khon Kaen University (Mid-Career Research Grant NRCT5-RSA63003-07).

References

- [1] AlAhmad R, Al-Jararha M. Italian J. Pure Appl. Math. 2021;45:673–688.
- [2] AlAhmad R, Al-Jararha M, AlMefleh H. Jordan J. Math. Stat. 2015;11:155–167.
- [3] Al-Ahmad S, Anakira N, Mamat M, Suliman I. M, AlAhmad R. TWMS J. Appl. Eng. Math. (Accepted). 1
- [4] El-Ajou A. Alexandria Engineering Journal. 2020;59.4:2239-2249.
- [5] Gazizov R. K, Lukashchuk S. Y. Mathematics. 2021;9:11 pages.
- [6] Herman R. University of north carolina wilmington. 2023.



- [7] Ionescu C, Lopes A, Copot D, Machado J. A. T, Bates J. H. T. Commun. Nonlinear Sci. Numer. Simul. 2017;51:141–159.
- [8] Khalil R, Al Horani M, Yousef A, Sababheh M. Journal of computational and applied mathematics, 2014;264: 65–70.
- [9] Kilbas A. A, Srivastava H. M, Trujillo J. J. 2006;204:.
- [10] Muresan I, Birs I. R, Dulf E. H, Copot D, Miclea L. Sensors. 2021;21:.
- [11] Musraini M, Efendi R, Lily E, Hidayah P. Pure and Applied Mathematics Journal. 2019;8.5:83.
- [12] Nantapat P, Kanit M. Annual Pure and Applied Mathematics Conference. 2024;:159-171.
- [13] Podlubny I. 1998;:.
- [14] Samko S. G. Theory and applications. 1993;:.



APPLICATION FOR PILL AND CAPSULE MEDICINE IDENTIFICATION BY PHYSICAL IDENTITIES

Orraya Suwanno, Rasryne Hirankalyakorn,* Attaporn Wangpoonsarp, Ruchdee Binmad
Faculty of management sciences, Prince of Songkla university, Thailand
*e-mail: rasryne.h@psu.ac.th

Abstract:

The Development of tablet and capsule pills physical identification searching system or drug identification system is a development of pills database management system the helps solving problem for the pharmacists of Drug Information Center of Songklanagarind Hospital in Identification of the drugs. The original problems are when the pharmacists receive diverse types of medicines from their patients with without drug name packaging, therefore, lack the information of the medicines. Although the pharmacists can use their experiences to identify the medicines, the processes usually take a long time and yet the result may not be accurate. Therefore, the researcher has developed the Drug Identification System which is a web application used to identify the unknown drugs using their physical appearances, including types, shapes, colors, marks, sizes, tracteries, and letters on the medicines. This application helps finding the information in short time, yields benefits for pharmacists and their patients in treatments. From the results of the study, trying to identify the sample of 100 types of drugs, the completeness of searching (Recall) is 1, the accuracy from searching (Precision) is 0.71, and the quality of the overall searching (F-Measure) is 0.83. And from the evaluating using the Lean Management theory, the result shows that the whole original processes of identifying drugs and reduced to only 4 steps. Originally, the time consumed in the operation for both inpatient and outpatient cases are 24 hours 32 minutes 44 seconds, and 2 hours 32 minutes 44 seconds, respectively. With the help from the application, the time for both cases are reduced to only 22 minutes and 8 seconds, which are 85.51% and 98.50% more efficient, for inpatient cases and outpatient cases, respectively. From overall results, the study proves that the Drug Identification System can identify the medicines using their physical appearances, and therefore, reduce the time consumed in searching the medicines information significantly.

Introduction:

In Thailand, from statistical data from the Drug Control Division Registration of drug formulas from 1983-2012, a total of 29,424 drug formulas were registered. Drugs can be divided into 3 types according to their physical characteristics as follows:

1. Solid dosage forms such as tablets, capsules, powders
2. Semi-solid dosage forms such as ointments, creams
3. Liquid dosage forms such as liquid medicine

Although these three forms of medicine, there will be prevalence in both production and consumption. But it was found that most of the drugs registered in the drug formula are in solid form. It can be seen that the most commonly used forms of medicine both in medical facilities and in general pharmacies are tablets and capsules. This is due to maintaining good

physical and chemical conditions. It is also convenient to consume. In addition, letters or symbols representing the manufacturer or type of medicine can be printed on the tablets.

From this variety of tablet and capsule forms, this causes pharmacists to encounter various problems in remembering the characteristics of pills. Therefore, it is not possible to indicate important drug information in the beginning. This is a problem in classifying these pills which must analysis from the Pharmacy Information Center. Pharmacy Department, Songklanagarind Hospital which is a center providing information about medicines by pharmacists. In order to obtain accurate drug information for further distribution to patients.

The Pharmacy Information Center also encountered problems in analyzing the identity of drugs for doctors. Patients have to wait a very long time to enter the treatment process, for example

1. Difficulty in analyzing patient treatment. In cases where the patient has used other types of medicine before being admitted to the hospital There is no drug labeling.
2. Many drugs are very similar. This causes difficulty in preliminary classification.
3. It is a new drug in drug registration or has little use. So, pharmacists are not familiar with the tablets.
4. Tablet packaging lost. This makes it impossible to read important information that details the drug in the first place.

To solve such problems in the drug information center, it takes a pharmacist's expertise and memory to be able to receive drug information quickly and correctly. In the case where the pharmacist does not know the information from the medicine, it will enter the process of analyzing or confirming the identity of the pills.

Begin by asking for additional information about medicines from the patient, the patient's relatives, or the doctor and nurse about the details of the medicine, such as the source of the medicine. The patient's symptoms are matched with the patient identification number so that the pharmacist can check the patient's medical history.

If the patient or the doctor has the medicine tablets included, the pharmacist will be able to search for those elements as well, such as the packaging that has the details of the pills on it, etc. But in case of the medicine has only pills, the pharmacist can only find out the physical identity of the pill.

By the way, find out the identity of this pill. This will require the ability of the pharmacist in terms of experience and analysis of the possibility of symptoms along with the physical characteristics of the tablets.

Therefore, the results can be used as preliminary information. That can be used to search from additional trusted sources. Sometimes the Pharmacy Information Center is unable to provide answers for patients and doctors managing their own conditions. You can only keep a sample of the medicine you received. to continue searching for answers. Causing the deterioration of the tablets until causing that stored drug information to disappear Due to the problems that occurred, pharmacists were unable to respond as well as they should. Figure 1. shows an example of the working process of the Pharmacy Information Center. To receive information

The research aims to solve the problems in storing drug data and methods for searching for drugs based on physical characteristics by creating a tool that is a drug database management system using Web Service technology to help store information in a useful drug database. Including the process of searching for drug information using methods to identify the physical characteristics of tablets such as tablet type, shape, size, color, and print on the tablet [1].

By specifying such characteristics, user will be able to search for drug information results. The tool is called "Drug Identification System"



Researchers hope the system will help improve patient health safety from drug use and solve problems for the Pharmacy Information Center, Pharmacy Department, Songklanagarind Hospital regarding the difficulty in classifying the most effective drugs mentioned above.

Methodology:

In this research, the researchers defined the tablet and capsule retrieval system which refers to a tool used for physical identification. That can be seen from the external appearance of the pill, such as the pill type, shape, color, size, notch, letters, and various symbols on the pill. From the method of classifying the specific characteristics of pills, it will be possible to retrieve drug information in the database system.

System Development Life Cycle

This research method based on the System Development Life Cycle (SDLC) theory [3] to develop a drug identification system. By specifying the physical identity as shown in Table 1.

Table 1. System Development Life Cycle

| SDLC Model | Activities |
|---|---|
| 1. Analysis process | <ul style="list-style-type: none"> - Identify the problems from users and analyze the feasibility of the system. - Study the physical information of drug and analyze tablets by characterizing tablets and capsules. - Find out how to identify pills. |
| | <ul style="list-style-type: none"> - Study the theory or methods of searching for information by identifying pills. - Study and analyze appropriate technology for system development. |
| 2. Design process | <ul style="list-style-type: none"> - Define the scope of research and use of the developed system. - Design a database of tablets and capsules. - Design user interface. - Design the structure of the system. |
| 3. Developing process | <ul style="list-style-type: none"> - Develop a systematic database of tablets and capsules (Database) - Develop data processing system (Server) - Develop user interface (Client) |
| 4. Testing and evaluating process | <ul style="list-style-type: none"> - System testing with users. - Test accuracy pill and capsule information retrieval by physical identification and analyze the reduction of steps in the work process. - Evaluate the system according to the research objectives. - Summary of evaluation results from users. |
| 5. Presentation and delivery process | <ul style="list-style-type: none"> - Report the system performance. - Deliver the system. |

Theory of pharmaceutical data analysis to classify the physical characteristics of tablets and capsules.

The researchers studied methods for characterizing the physical characteristics of tablets and capsules from the journal MIMS which very well known in the pharmaceutical industry in collecting medicines information that available in the world.

The MIMS journal and search system uses a pharmacology search methodology by trade name or some physical characteristics of the drug, such as color, type of drug, shape, and size. However, MIMS data retrieval methods are still not responsive to queries of the pharmacy information center because some physical characteristics are still missing. As a result, sometimes results are not received from searches.

The researcher therefore combined the physical classification theory from MIMS and the physical classification theory of the Pharmacy Information Center. All drug data were collected and analyzed to further classify physical characteristics. Including the physical classification theory of the tablet and capsule identification database system in Thailand by the Faculty of Pharmacy, Ubon Ratchathani University.

Technological theories used in developing Drug Identification systems.

The researcher analyzed the feasibility of appropriate tools and theories for development according to the research scope. Technological theories to develop research tools as follows.

1. Web Application Technology

A web application is an application program that can be accessed with a web browser through a computer network such as the Internet or an intranet. The main benefit of web applications is that they can be accessed from anywhere. Therefore, there is no restriction on the source of use. Web applications can be updated and maintained without distribution and install the software on the user's machine [4].

In this research, web application technology will be used to manage the drug information management system and search for information on tablets and capsules. It mainly identifies the physical identity of the pharmacist at the drug information center.

2. Web Service Technology

A Web Service is a service offered by an electronic device to another electronic device, communicating with each other via the Internet. Different software systems often need to exchange data with each other, and a Web service is a method of communication that allows two software systems to exchange this data over the Internet. The software system that requests data is called a service requester, whereas the software system that would process the request and provide the data is called a service provider. Different software may use different programming languages, and hence there is a need for a method of data exchange that doesn't depend upon a particular programming language. Most types of software can, however, interpret XML tags. Thus, Web services can use XML files for data exchange [5]. In practice, a web service commonly provides an object-oriented web-based interface to a database server, utilized for example by another web server, or by a mobile app, that provides a user interface to the end-user.

3. MySQL

MySQL, the most popular Open Source SQL (Structured Query Language) database management system, is developed, distributed, and supported by Oracle Corporation. MySQL is a database management system. To add, access, and process data stored in a computer database, we need a database management system such as MySQL Server. Since computers are very good at handling large amounts of data, database management systems play a central



role in computing, as standalone utilities, or as parts of other applications. MySQL software is Open Source which means that it is possible for anyone to use and modify the software. Anybody can download the MySQL software from the Internet and use it without paying anything. MySQL Server was originally developed to handle large databases much faster than existing solutions and has been successfully used in highly demanding production environments for several years. Although under constant development, MySQL Server today offers a rich and useful set of functions. Its connectivity, speed, and security make MySQL Server highly suited for accessing databases on the Internet.

4. Software Architecture

Drug Identification system is a system developed in client-server architecture which divides development into 2 parts; web application and server. Web application is the part used to manage data or import drug information and is used for pills and capsules physical identification. Servers are used to process data by receive commands from client users via web applications. Servers is used to connect to the system's database to read and record data, it searches for tablet and capsule information received from users. They are all linked or communicated online and follow Web Service standards, which makes the system work more efficiently [2]. As shown in Figure 1.

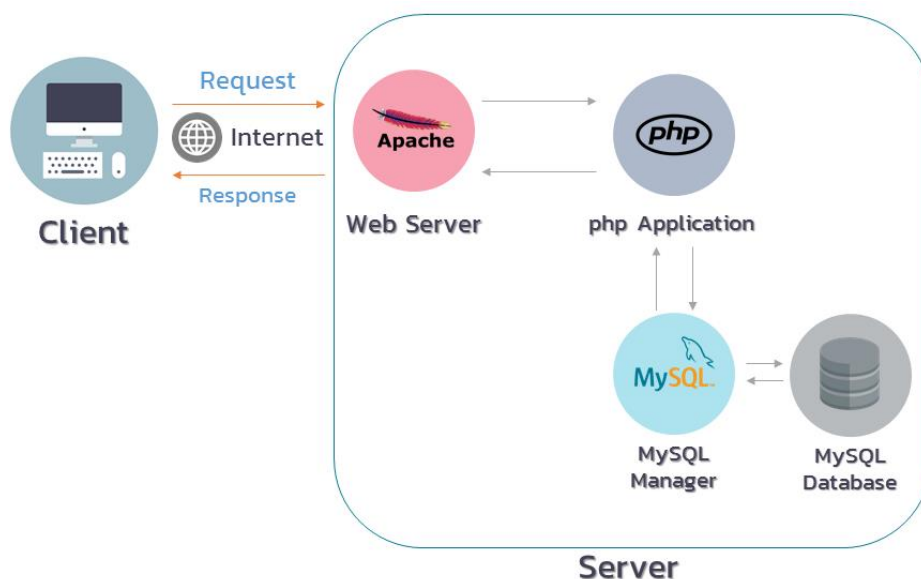


Figure 1. Drug Identification system Architecture

Results and Discussion:

The result of Drug Identification System can be evaluating the retrieval effectiveness of the physical identification tablet and capsule retrieval system. The researcher evaluated the results in terms of completeness, accuracy and precision. The researcher collected samples of 100 pills into the Drug Identification System database. In the evaluation, the results from data extraction will be displayed as the results of 3 groups of variables as shown in Table2.

1. Retrieved and Relevant Data is a group of drug data that the system can identify and is accurate drug data.

2. Retrieved and Irrelevant is a group of drug information that the system can identify but incorrect drug information.
3. Not Retrieved and Relevant is A group of valid drug information but the system cannot identify it.

Table 2. Shows the evaluation results of Drug Identification System.

| Variables for measuring results | Displayed results | Description |
|---------------------------------------|-------------------|--|
| 1. Retrieved and Relevant Data | 100 items | From a sample of 100 pills, the system can identify all 100 pills and provide accurate results. |
| 2. Retrieved and Irrelevant | 2 items | The reason that two incorrect entries were found was due to the search algorithm. System fonts will be stored as text and use search conditions in the form %Like%, some drug lists have the same identifying letters in some parts were displayed together. The design of the search conditions is to manage discrepancies in identifying patterns that contain letters, such as: Pharmaceutical company symbol displayed in letters. |
| 3. Not Retrieved and Relevant | 0 items | Data item not found. |

We calculate the values that show completeness and accuracy and to measure the quality of the overall data search results as in Table 3.

Table 3. Pre-Lean results.

| Variables | Value | Remarks |
|--|-----------------------------|---|
| Recall (Completeness value) | $= 100/(100+0)$ $= 1$ | Measured by the ratio between the amount of correctly retrieved information with the total amount of valid data of the system |
| Precision (Accuracy value) | $= 100/(100+2)$ $= 0.98$ | Measured by the ratio between the amount of correctly retrieved information with the total amount of information |



| | | |
|--|---------------------------------------|---------------------------------|
| | | retrieved |
| F-Measure | $= (2 * 1 * 0.98 / (1 + 0.98)) * 100$ | Average of precision and recall |
| (Overall quality of search results) | $= 99\%$ | |

Efficiency evaluation results for improving work with Lean Management

We evaluate results to improve working with Lean Management by comparing the different time between the current system without Drug Identification System (Pre-Lean) with the new system with Drug Identification System (Post Lean) based on Lean Management theory. Table 4 shows the Pre-Lean results.

Table 4. Pre-Lean results.

| Work system | Values | Results |
|-----------------|--|--------------------------------------|
| Pre-Lean | The sum of the value duration. | = 505 minutes (8 hours 25 minutes) |
| | The sum of the total duration of the work steps. | = 525 minutes (8 hours 45 minutes) |
| | Efficiency percentage | $= (505/525) \times 100$ = 96.20% |

Drug Identification System was launched in the Pharmacy Information Center, Songklanagarind Hospital, to test work processes and reduce work time (Post Lean). The working process has been modified and the efficiency evaluation results as shown in Table 5.

Table 5. Post Lean results.

| Work system | Values | Results |
|------------------|--|----------------------------------|
| Post Lean | The sum of the value duration. | = 90 minutes (1 hour 30 minutes) |
| | The sum of the total duration of the work steps. | = 90 minutes (1 hour 30 minutes) |
| | Efficiency percentage | $= (90/90) \times 100$ = 100% |

Table 6. shows the comparison of efficiency values between Pre-Lean and Post Lean. From the Pre-Lean process, it took a total of 8 hours and 45 minutes to complete the operation. With Drug Identification system, total process time is 1 hour 30 minutes. Post Lean is reduced 7 hours 15 minutes, the process of searching for tablet and capsule information has been made simpler and faster.

Table 6. comparison of efficiency values between Pre-Lean and Post Lean

| Evaluation | Pre-Lean | Post Lean | Different |
|-------------------------|--------------------|--------------------|---------------------|
| Time | 8 hours 25 minutes | 1 hours 30 minutes | -7 hours 15 minutes |
| Efficiency (percentage) | 96.20% | 100% | +3.80% |

Conclusion:

Drug Identification System is a development of pills database management system the helps solving problem for the pharmacists of Drug Information Center of Songklanagarind Hospital in Identification of the drugs. From 29,424 drug formulas which were registered in Drug Control Division Registration, this system helps finding the information in short time. The results of study prove that the Drug Identification can identify the medicines using their physical appearances, and therefore, reduce the time consumed in searching the medicines information significantly.

References:

1. Alamgir A. Therapeutic Use of Medicinal Plants and Their Extracts. 2017;1:187–193.
2. Galster M, Weyns D. Journal of Systems and Software. 2023;202:1-22
3. Nayan B. R. ACM SIGSOFT Software Engineering Notes. 2010;35:8-13.
4. Pratiksha D, Shivani S, Monali S, Sumangala B, Dhiraj D. IJRASET. 2022;10:359-366
5. Jalal S, Yadav D, Negi C. IJCA. 2019; 41: 51-62.



Applying Machine Learning Techniques for Snake Species Identification

Sathit Prasomphan^{1*}, Pissinee Chunsanit¹, Chatchawun Nat Taktanachote¹

Department of Computer and Information Science,
King Mongkut's University of Technology North Bangkok, Bangkok, 10800 THAILAND
*e-mail: sathit.p@sci.kmutnb.ac.th

Abstract:

The identification of snake species is crucial for ecological studies, safety measures, and biodiversity conservation. This research explores the application of machine learning techniques, specifically YOLOv8, to automate snake species identification using images. The dataset, sourced from the Queen Saovabha Memorial Institute, includes 1,150 images of 23 snake species, which were augmented to 2,764 images to enhance model performance. YOLOv8, a prominent one-stage object detection model known for its efficiency and accuracy, was employed due to its improvements in accuracy and speed over previous versions and its capability to train on a single GPU. The proposed system utilizes a two-model approach: the first model detects bounding boxes around potential snakes, while the second model classifies the species within these boxes. Images are pre-processed through auto-orientation and resizing to 416x416 pixels to ensure consistency. The data is split into training (70%), validation (20%), and testing (10%) sets. Ultralytics HUB facilitates the training and validation processes using a YAML configuration file to manage parameters. The model structure includes a backbone for feature extraction, a neck for connecting components, and a head for bounding box and class prediction. This approach aims to improve accuracy in snake species identification and provide a scalable solution for ecological and safety applications.

Introduction:

Most Thai people fear a creature called a "snake" because they do not know which species of snake they encounter and whether it is venomous. In the past, when the internet was not easily accessible, information about snakes was scarce, and accurate information was not readily available to the public. This led to misunderstandings about different snake species, or the inability to distinguish between venomous and non-venomous snakes. As a result, some people, upon encountering a snake in their living area, chose to kill it to avoid the potential danger of venom. This research was developed to help address the issue of identifying snake species, allowing people to easily check the species of a snake from a picture and access detailed information. The snake data used focuses on Thai snake species commonly found near human habitats. The developers created a system that works on a web application and Line, allowing users to search for information through the web application by using images, snake names, or snake characteristics, as well as through a chatbot. The model was developed using YOLOv8. Test results showed that the model's prediction accuracy for snake species is between 83.92%, making this application useful for real-world daily use.

Related Theory:

A. Machine Learning

Machine Learning (ML) [1][5] is the use of mathematics and computer science to teach computers to learn and make judgments without having to follow strict rules. Machine learning can read and interpret the information offered by humans so that they can make the judgments that human desire. There are numerous versions, including the following tasks.

First, predict new types of data that machine learning has never seen before, what is the value, and what category does it belong to. Second, group data by using information in the same group that has similar qualities. Third, separate particular types of data from the rest of the data, such as speech from voice and environment. Fourth, learning from the original interests to introduce new pieces of information that humans are predicted to be interested. The advantages of machine learning are numerous. Anyone or any organization that wants to employ machine learning in their job.

Machine learning can be divided into two categories. The first category is supervised learning which provide a class label in the dataset. For instance, regression that can find numerical responses, such as nutritional information for child, what the expected height of this child is. Classification that come up with a categorical answer, such as a prophecy for the Thoracic X-ray image, whether or not the patient has lung cancer (the answer is yes/no, hence the name is binary). The second category is unsupervised learning which the fact that no one knows the correct answer. For example, clustering which build communication strategies with diverse categories of customers, group information, such as donor information, into three groups. Other non-clustering difficulties, such as detecting part data, are addressed in section. Other example of unsupervised learning are anomaly detection, recommendation system that provides material that users are likely to be interested.

B. Related work.

In [2], this paper evaluates the effectiveness of five advanced machine-learning techniques—decision tree J48, nearest neighbors, k-nearest neighbors (k-NN), backpropagation neural network, and naive Bayes—in solving the problem of snake species identification based on images. Traditionally, identifying snake species is done manually by observing traits like head shape, body pattern, color, and eye shape. The study focuses on 22 snake species found in Malaysia, compiling their images into a database named the Snakes of Perlis Corpus. The researchers propose an intelligent method for automatically identifying snake species from images, which is useful for content retrieval systems. Their experiments reveal that the backpropagation neural network and nearest neighbor techniques are particularly accurate, achieving over 87% accuracy when using the CEDD descriptor in this classification task.

In [3], this study highlights the importance of automated snake image identification, particularly for snakebite management. It compares various state-of-the-art machine learning methods, both holistic and neural network-based, for classifying snake species. The research was conducted on six snake species in Lar National Park, Tehran, Iran. Key findings include Holistic methods like k-nearest neighbors (k-NN), support vector machine (SVM), and logistic regression (LR) combined with dimension reduction techniques like principal component analysis (PCA) and linear discriminant analysis (LDA) were tested. The use of PCA did not significantly improve accuracy (remaining below 50%), but using LDA improved accuracy, especially with SVM, achieving 84%. Convolutional neural networks (CNN), specifically MobileNetV2, outperformed holistic methods, reaching an accuracy of 93.16%. The study also revealed that deep activation layers in CNN are crucial for identifying snake species based on color patterns and shape. The results suggest that MobileNetV2 is a powerful algorithm for snake image classification, and it could be used on mobile devices, paving the way for developing mobile applications for snake identification.

In [4] the study tested four convolutional neural network (CNN) models—VGG16, ResNet50, MobileNetV2, and DenseNet121—across various experiments with different numbers of classes. The results showed that VGG16, DenseNet121, and MobileNetV2 achieved the highest accuracies, with VGG16 performing the best, achieving 97.09% accuracy when classifying 45 different snake species.



Methodology:

In this section, procedures and methods of developing application was described as follows.



Figure 1. System architecture overview.

Figure 1 provides an overview of the system architecture. The system architecture details are as follows. The administrator has the capability to add, delete, and edit data directly from the mobile application. User can use the mobile application while exploring snake species, gaining access to detailed snake information. The database operations consist of various activities. Administrative actions, such as adding, deleting, or editing snake information, are logged and stored in the database. The data related to these actions are transmitted to the server, enabling seamless information exchange within the system. Figure 2 illustrates the system's use case diagram, interactions and the roles involved.

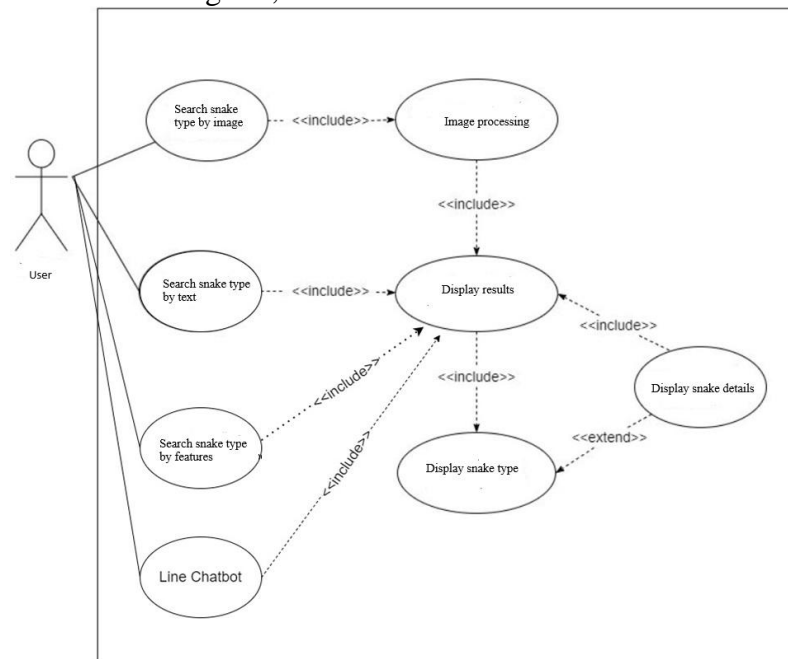






Figure 2. Use case diagram.

In this research, a dataset to train the YOLOv8 network is utilized for identifying snake species. The dataset is sourced from the Queen Saovabha Memorial Institute's snake






farm. YOLO, which stands for "You Only Look Once," is a prominent object detection model within the one-stage detectors category, contrasting with two-stage detectors. YOLO employs a sliding window strategy combined with classification to process and classify each window in an image. YOLOv8 has shown improvements over YOLOv7 in both accuracy (average precision) and speed (FPS), with its notable strength being the capability to train efficiently on a single GPU. The snake species detection process involves two models. In the first model, user-uploaded images are processed to identify bounding boxes around detected objects, each with an associated probability score. These outputs are passed to the second model, which determines the specific type of snake. The system accommodates images of various sizes and resolutions by automatically resizing them to 416x416 pixels according to YOLO format. The integrated algorithm performs object detection to identify the snake and then classifies its species, presenting the results to the user.

The following are details of the proposed algorithms. First, a preprocessing is performed. This step adjusts the orientation of images to align with predefined conditions or rules, ensuring accurate and consistent data for analysis. Next, images are resized to 224x224 pixels to standardize input for training. The dataset consists of 1,150 images, which are augmented to 2,764 images, representing 23 snake species. Table 1 shows example of snake using in the experiment. The images are divided into 2,421 train set images, 232 validation set images, and 111 test set images. After that Ultralytics HUB is used for training, testing, and validating images, utilizing a YAML file to specify dataset locations and training parameters such as the number of epochs, batch size, and learning rate. To setup parameters, Ultralytics HUB enables users to configure various YOLOv8 model parameters through the YAML file, including the number of classes, anchor box sizes, and model features. The model structure composed of backbone, which extracts key features from the images, neck that connects the backbone to the head, and head which responsible for predicting bounding boxes and object classes.

Table 1: Example of snake to use in the experiment.

| Image | Name | Train | Valid | Test |
|---|--------------------|-------|-------|------|
|  | Reticulated python | 102 | 10 | 5 |
|  | Burmese python | 78 | 7 | 4 |
|  | sunbeam snake | 93 | 9 | 4 |
|  | Javan wart snake | 111 | 10 | 5 |



| | | | | |
|--|--------------------------|-----|----|---|
|  | Rainbow mud snake | 81 | 8 | 4 |
|  | Copperhead racer | 117 | 10 | 5 |
|  | Oriental rat snake | 93 | 9 | 5 |
|  | Indochinese rat snake | 78 | 7 | 4 |
|  | Small-banded kukri snake | 102 | 10 | 5 |

Results and Discussion:

This section focuses on presenting the outcomes of the mobile application, highlighting its functionality within the predefined scope of the project. Specifically, it delves into the Home Page of the application, which serves as the main menu. The application's home page is presented in Figure 3. Example of searching snake by properties is shown in Figure 4. Line Chabot is shown in Figure 5.

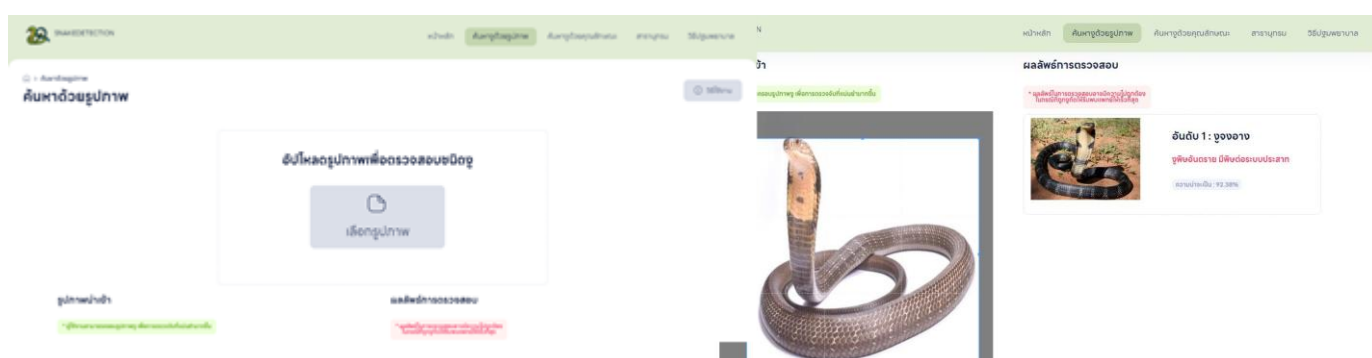


Figure 3. Show application's Home Page.

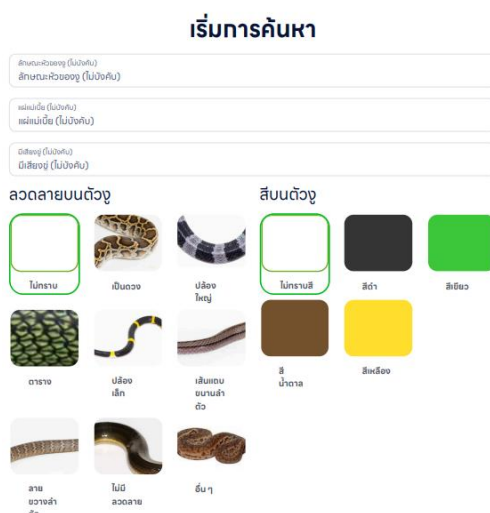


Figure 4. Searching snake by properties.

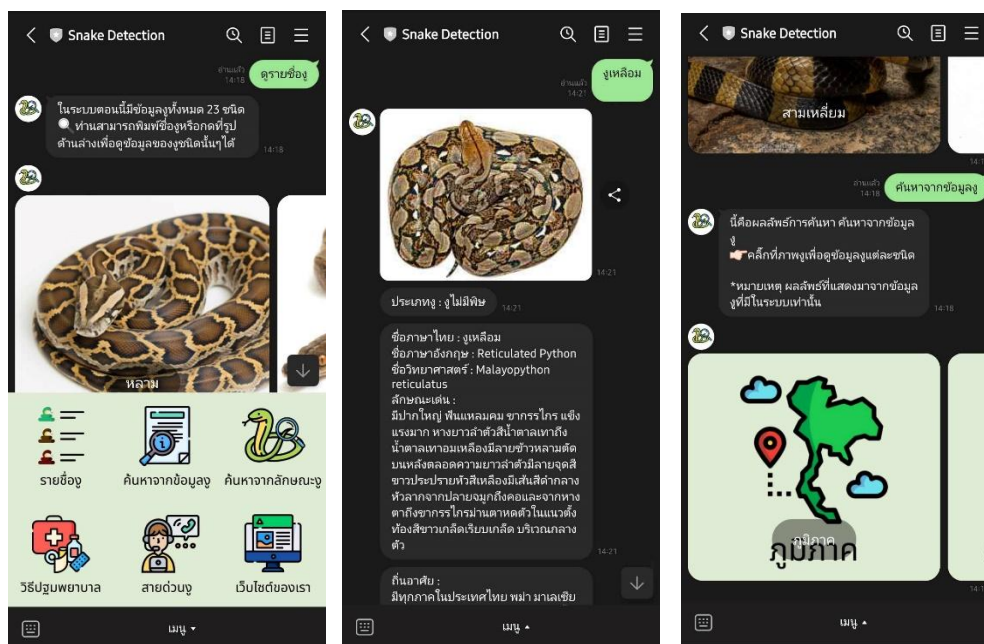


Figure 5. Line Chabot.

Performance Indexed

The confusion matrix is a potent technique for assessing the performance of classification results. It provides a detailed representation of predicted and actual classes, aiding in the visualization of classification errors. The matrix is structured such that each row corresponds to the predicted class, and each column represents the original class. The evaluation metrics derived from the confusion matrix include precision, recall, F1 score, and accuracy, calculated using the following equations::

$$Precision = \frac{TP}{TP+FP} \quad (1)$$



where TP is the true positive value and FN is the false negative value. Recall is the value that measures the number of correct predicting answers for each class and is divided by the total number of that class which is the ground truth.

$$F1 - Score = 2 \frac{Precision \times Recall}{Precision + Recall} \quad (3)$$

where Precision is the precision value calculated from (1) and Recall is the recall value calculated from (2).


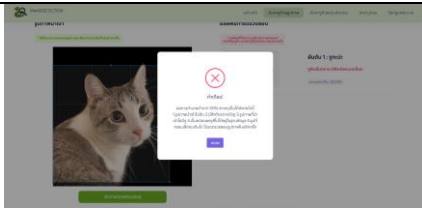

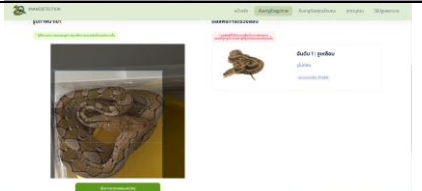
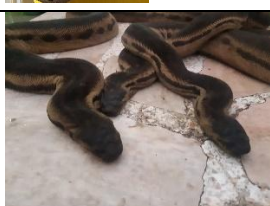
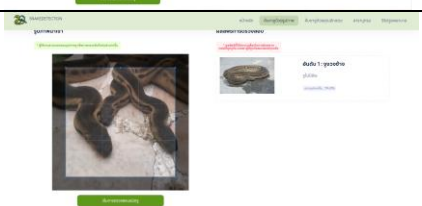
$$Accuracy = \frac{TP + TN}{N} \quad (4)$$

where TP is the true positive value, TN is the true negative value, and N is total number of images.

The classification results obtained by applying the proposed algorithms to detect the snake image were used to demonstrate the experimental findings. Consequently, the classification accuracy ensures the efficiency of our image classification algorithms. **Table. 1** illustrates the categorization accuracy. The experimental results indicate that adopting a convolutional neural network for training to detect a snake species in image can be successfully. The proposed algorithms can be utilized to classify the type of snake with an accuracy rate of 87.92 percent.

Web Application for detecting species of snakes with Machine Learning can use images to find information about snakes nearby and can search for information about snakes by the data uses 10 images to measure performance. The criteria used to measure data accuracy is an average data accuracy of 91% to 99%.

Table 2: Comparison of average accuracy of classification with proposed classification technique.

| No | Image | Result | Accuracy | Classification result |
|----|---|--|----------|-----------------------|
| 1 |  |  | 30.33% | false |
| 2 |  |  | 91.62% | true |
| 3 |  |  | 79.61% | true |


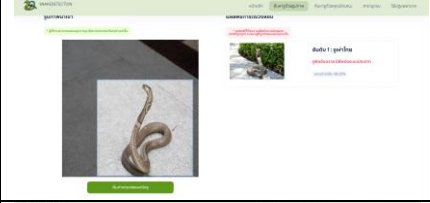

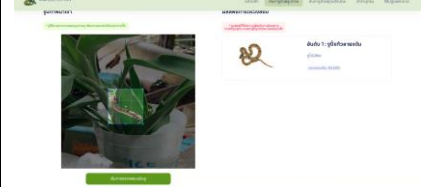

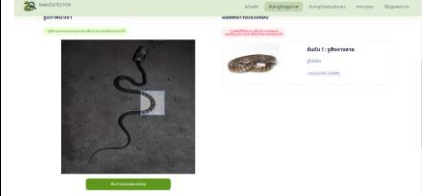

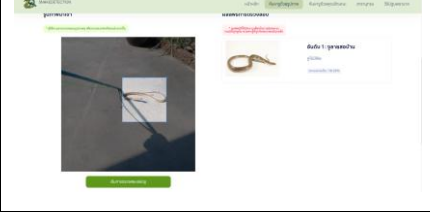






| | | | | |
|----|---|--|--------|------|
| 4 |  |  | 86.32% | true |
| 5 |  |  | 84.65% | true |
| 6 |  |  | 62.49% | true |
| 7 |  |  | 78.32% | true |
| 8 |  |  | 56.57% | true |
| 9 |  |  | 96.58% | true |
| 10 |  |  | 68.24% | true |

Table 3: Comparison of average precision of classification between traditional deep learning and proposed classification technique

| Classification technique | Precision |
|--------------------------------|---------------|
| AlexNet | 85.18% |
| YOLO | 82.67% |
| CNN | 84.85% |
| <i>proposed classification</i> | 83.92% |



Conclusion:

In conclusion, this section provides a comprehensive overview of the operational outcomes of the application of applying machine-learning techniques for snake species identification. The model was developed using YOLOv8. Test results showed that the model's prediction accuracy for snake species is 83.92%, making this application useful for real-world daily use.

References:

1. Prasomphan, S., Niyomrat, P., Tainsakukdej, B., Kuarkamphun, T., Deejungwiphat, N. (2022). Khon Gesture Detection with Deep Learning Algorithms. In: Nagar, A.K., Jat, D.S., Marín-Raventós, G., Mishra, D.K. (eds) Intelligent Sustainable Systems. Lecture Notes in Networks and Systems, vol 333. Springer, Singapore. https://doi.org/10.1007/978-981-16-6309-3_24.
2. Amir, A., Zahri, N.A.H., Yaakob, N., Ahmad, R.B. (2017). Image Classification for Snake Species Using Machine Learning Techniques. In: Phon-Amnuaisuk, S., Au, T.W., Omar, S. (eds) Computational Intelligence in Information Systems. CIIS 2016. Advances in Intelligent Systems and Computing, vol 532. Springer, Cham. https://doi.org/10.1007/978-3-319-48517-1_5.
3. Rajabizadeh, M., Rezghi, M. A comparative study on image-based snake identification using machine learning. Sci Rep 11, 19142 (2021). <https://doi.org/10.1038/s41598-021-96031-1>.
4. Ahmed, K., Gad, M.A. & Aboutabl, A.E. Snake species classification using deep learning techniques. Multimed Tools Appl 83, 35117–35158 (2024).
5. Deng L and Yu D, "Deep learning: methods and applications foundations and trends," Signal Processing, 2014;7(3-4): 197–387.



CARIES DETECTION IN PRIMARY TEETH USING A DEEP LEARNING-BASED CONVOLUTIONAL NEURAL NETWORK

Ploypailin Komtui,¹ Wannakamon Panyarak,² Wattanapong Suttapak,³ Kittichai Wantanajittikul,⁴ Onnida Wattanarat^{1,*}

¹Department of Orthodontics and Pediatric Dentistry, Faculty of Dentistry, Chiang Mai University, Chiang Mai 50200, Thailand

²Department of Oral Biology and Diagnostic Sciences, Faculty of Dentistry, Chiang Mai University, Chiang Mai 50200, Thailand

³School of Information and Communication Technology, University of Phayao, Phayao 56000, Thailand

⁴Department of Radiological Technology, Faculty of Associated Medical Technology, Chiang Mai University, Chiang Mai 50200, Thailand

*e-mail: onnida.wattanarat@cmu.ac.th

Abstract:

The diversity of dentists and the severity of carious lesions contribute to the variability in the efficacy in caries detection. For effective caries management, the integration of artificial intelligence (AI) has emerged as a promising strategy. You Only Look Once version 8 (YOLOv8) was used to evaluate the efficacy of detecting dental caries in bitewing radiographs of primary teeth according to the International Caries Classification and Management System (ICCMS™). It was trained and validated by inputting 100 annotated bitewing radiographs under intersection over union (IoU) threshold 50 and 75. According to the 3-class classification of caries severity (initial stage: class RA, moderate stage: class RB, and extensive stage: class RC), the highest average precision was in class RC (0.67) while the lowest was in class RA (0.29). In the 6-class classification, YOLOv8 achieved precision, recall, F1-score, mAP50 and mAP75 at 0.51, 0.38, 0.40, 0.38, and 0.17, respectively. The highest average precision was in class RC6 (0.68) while the lowest was in class RA1 (0.11). This validation results of YOLOv8 demonstrated promising efficacy in the detection and classification of moderate to advanced caries lesions on bitewing radiographs in primary teeth, but its performance in detecting initial caries lesions remains limited.

Keywords: Artificial intelligence, Bitewing radiographs, Deep learning, Dental caries, Objects detection, Primary teeth

Introduction:

Dentists commonly rely on intraoral radiographs for dental caries detection. Bitewing radiography stands out as an effective technique for identifying proximal caries in enamel and dentin. The sensitivity of bitewing radiography for detecting proximal cavitated carious lesions was approximately 0.64 (range: 0.59–0.70).¹ When non-cavitated or initial carious lesions were included, the sensitivity significantly decreased to 0.24 (range: 0.21–0.26), emphasizing the need to explore more sensitive detection methods.¹ Several essential factors contribute to the variability in the efficacy in caries detection, including the diversity of dentists and the severity of carious lesions. Numerous studies have substantiated that the superior accuracy in caries detection was provided from experienced dentists.²⁻⁵ This variance in performance leads to the inconsistency observed in making decision for caries diagnosis and treatment planning. To decrease this inherent inconsistency, the integration of artificial intelligence (AI) for caries diagnosing has emerged as a promising strategy.

The use of AI is increasing in the field of dentistry, especially for caries detection and diagnosing.^{6,7,9-11} Deep learning-based convolutional neural network is subtype of AI which autonomously recognize and learn patterns in extensive datasets without human aid.⁸ Previous studies covered not only the application of AI in dental radiographs, but also extended to three-dimensional dental imaging and intra-oral photography. Deep learning has demonstrated a range of efficacy in caries detection, achieving accuracy rates between 68% to 99%, and sensitivity rates between 25% to 99.8%.⁹ You only look once (YOLO) is one of the most outstanding deep learning models for object detection tasks due to its high performance. This model exhibited the fastest operating time compared to other object detection algorithms. Moreover, the updated version of YOLO demonstrated enhanced small object detection capabilities, potentially making it suitable for detecting proximal initial lesions. Recent study in 2023 by Panyarak et al. found that YOLOv7 yielded better efficacy in caries detection in permanent teeth than YOLOv3.¹⁰ YOLOv8, which was established by Ultralytic in January 2023, this iteration displayed a wide range of abilities within the domain of vision AI tasks. These tasks include detection, segmentation, pose estimation, tracking, and classification. Nonetheless, there are no studies involving YOLOv8 for caries detection on bitewing radiographs in primary teeth. To fill these gaps, our study was designed to evaluate the efficacy of YOLOv8 for detecting caries in primary teeth on bitewing radiographs.

Methodology:

Dataset selection and preparation

A total of 100 bitewing radiographs of primary teeth without patient's information from 2017 to 2022 were randomly collected from PACs system of the pediatric dental clinic, faculty of dentistry, Chiang Mai University. The protocol of this study was approved by the Human Experimentation Committee of the faculty of dentistry, Chiang Mai University. The YOLO model, which demonstrated good performance in the previous studies concerning caries detection on bitewing radiographs in permanent teeth, was used in this study.^{6,10,11} Bitewing radiographs of primary teeth with at least the crowns of one dental arch being detectable were included in this study. Low quality radiographs were excluded from this study including low quality of contrast, blurred images, and excessive distortion. Permanent teeth, overlapping of proximal surfaces of more than half of the enamel, and abnormalities of enamel and dentin, such as amelogenesis imperfecta, dentinogenesis imperfecta, and dentin dysplasia, were also excluded from this study. All bitewing radiographs were annotated by two experts who are an oral radiologist and a pediatric dentist with 7-18 years of experience. The experts proceeded to precisely identify by drawing a rectangular bounding box to enclose each carious lesion on primary teeth (an example is shown in Figure 1.) and labeled the depth of lesion into six levels according to the International Caries Classification and Management System (ICCMSTM). The detection performance was assessed regarding two classifications as follows:

- 6 classes:

1. RA1: radiolucency in the outer 1/2 of the enamel
2. RA2: radiolucency in the inner 1/2 of the enamel
3. RA3: radiolucency limited to the outer 1/3 of dentin
4. RB4: radiolucency reaching the middle 1/3 of dentin
5. RC5: radiolucency reaching the inner 1/3 of dentin
6. RC6: radiolucency into the pulp

- 3 classes:

1. RA: initial stage (RA1, RA2 and RA3)
2. RB: moderate stage (RB4)



3. RC: extensive stage (RC5 and RC6)

After the drawing and labeling were complete, all bitewing radiographs were exported into eXtensible Markup Language (XML) image files and used as dataset for testing YOLOv8 performance.



Figure 1.

An example of annotation using the Labelling program. The numbers represent the level of carious lesion. The number 2, 3, and 5 indicate RA2 (radiolucency in the inner 1/2 of the enamel), RA3 (radiolucency limited to the outer 1/3 of dentin), and RC5 (radiolucency reaching the inner 1/3 of dentin), respectively.

Model training and validation

The training process for YOLOv8 was conducted using 100 labeled bitewing radiographs with input of 1,280x1,280-pixel image. After the training process, the performance of the model was validated using 4-fold validation which served as a crucial step in assessing the model's robustness and accuracy.

Performance evaluation

Terms that are used in the field of object detection algorithm including: “Ground truth boxes” are defined as hand-labeled boxes by experts that contain caries lesion in the picture. “Predicted boxes” are labeled boxes by the model which were predicted to contain caries lesion. “Intersection over union (IoU)” is the area overlap ratio between the ground truth box and the predicted box. Maximum of the IoU ratio is 1, which signifies a high degree of confidence in the extent of overlap between a ground truth box and a predicted box, effectively reaching 100%.⁶ In this study, performance metric at IoU configured to the threshold at 50% (IoU₅₀) and 75% (IoU₇₅) were investigated. “True Positive (TP)” was considered as a correct detection when $\text{IoU} \geq \text{threshold}$. On the other hand, “False Positive (FP)” was considered as an incorrect detection when $\text{IoU} < \text{threshold}$. “False Negative (FN)” was indicated as an undetected ground-truth bounding box. However, the concept of “True Negative (TN)” is not applicable in object detection tasks because there are many possible bounding boxes that should not be detected within an image. The appropriate evaluation metrics for the object detection task commonly include precision, recall, F1-score, average precision, and mean average precision.¹¹

Precision or Positive Predictive Value (PPV) is a proportion of correct positive predictions from total positive predictions. The formula for calculation is:

$$\text{Precision} = \frac{\text{True Positives}}{\text{True Positives} + \text{False Positives}}$$

Recall or Sensitivity refers to the ability of the model to correctly detect lesions from total lesions. This value is calculated as:

$$\text{Sensitivity} = \frac{\text{True Positives}}{\text{True Positives} + \text{False Negatives}}$$

F1-score represents a balanced combination of precision and recall, resulting in a metric that falls within the range of 0 to 1, with a score of 1 indicating the highest level of accuracy. The computed formula is:

$$\text{F1-score} = 2 \times \frac{\text{Precision} \times \text{Recall}}{\text{Precision} + \text{Recall}}$$

Average precision (AP) represents the area under the Precision-Recall (PR) curve after interpolation. The AP range is calculated individually for each class. Modified AP calculation reported by Panyarak et al. is as follow:⁶

$$\text{AP} = \sum_{r \in \{0,0.1,0.2,\dots,1\}} \text{Pinterp}(r)$$

According to this formula, $\text{Pinterp}(r)$ is the highest precision value at each recall level from interpolated PR curve, r represents recall and $p(\hat{r})$ represents precision at recall level \hat{r} . This value can be calculated as:

$$\text{Pinterp}(r) = \max_{\hat{r} \geq r} p(\hat{r})$$

Mean average precision (mAP) is the average of AP values from all classes divided by sum of the numbers in each object category (N). The formula is as follow:⁶

$$\text{mAP} = \frac{\sum_{i=1}^N \text{AP}_i}{N}$$

From this formula, AP_i is interpolated AP of object category.

Results and Discussion:

The major findings from this study indicated that YOLOv8 yielded a promising efficacy in caries detection on bitewing radiographs in primary teeth. The YOLO model was selected for caries detection in this study due to its excellent performance and status as the fastest object detection model in previous tests.^{6,10-11} This model is one of deep learning algorithms which can do single-step detection, location detection, and object classification at the same time. Nowadays, YOLO is increasingly being used in dentistry, notably for proximal caries identification, and it performs effectively.^{6,9,11} However, there is currently a lack of research on the bitewing of primary teeth, and its performance in early caries detection and diagnosis remains inconclusive.

Prevalence of diseases or lesions impacts the precision value of tests. As the prevalence increases, the precision also increases. Therefore, when the population exhibits a high prevalence of caries, precision tends to increase while recall remains unaffected. Consequently, it is essential to comprehensively consider caries prevalence of the population in this study which is presented in Table 1. Examples of bitewing radiographs showing YOLOv8 caries predictions classified into three classes and six classes according to the ICCMSTM scoring system are presented in Figure 2. A good object detector should detect all ground-truth objects (FN=0, high recall) while identifying only relevant items (FP=0, high precision).¹² As a result, the F-1 score of a good object detection model, which shows the harmony between precision and recall, should be high. The YOLOv8's performance on caries detection from validation results (k0-4) at IoU₅₀ and IoU₇₅ was summarized in Table 2.

**Table 1.**

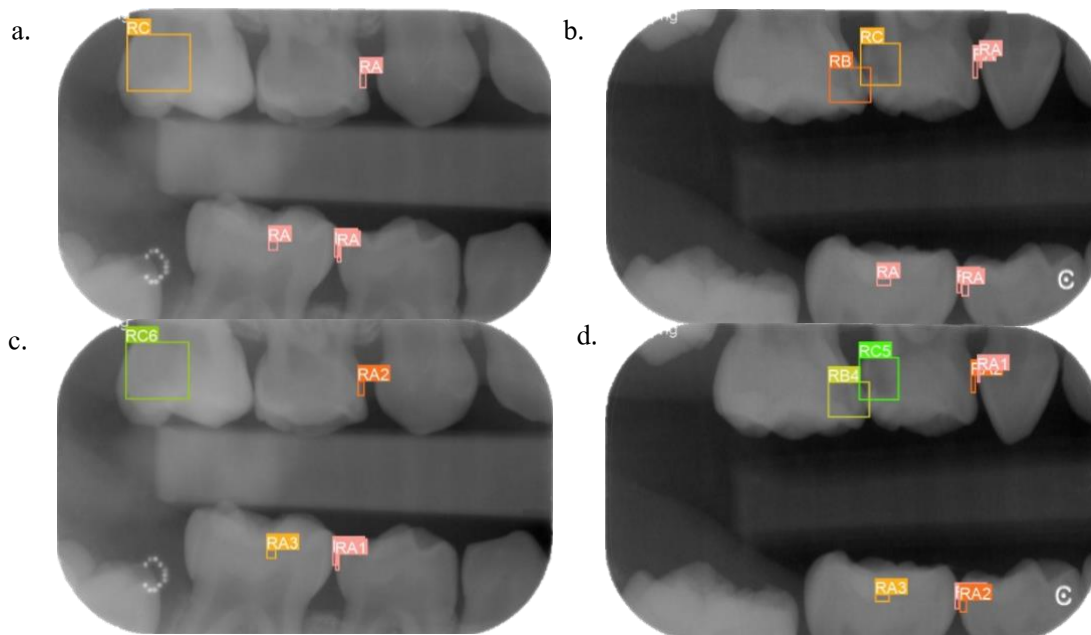
The number of caries lesions classified according to the International Caries Classification and Management System (ICCMS™) into three and six classes was used for the training and validation datasets.

| ICCMS™ Classification | Number of lesions for training and validation |
|------------------------|---|
| 3-class classification | |
| RA ^a | 261 |
| RB ^b | 57 |
| RC ^c | 90 |
| 6-class classification | |
| RA1 | 42 |
| RA2 | 99 |
| RA3 | 120 |
| RB4 | 57 |
| RC5 | 41 |
| RC6 | 49 |

^aInitial stage (including RA1, RA2 and RA3)

^bModerate stage (including RB4)

^cExtensive stage (including RC5 and RC6)

**Figure 2.**

Examples of bitewing radiographs showing caries predictions

classified into three classes (a, b) and six classes (c, d).

Table 2.

The performance of YOLOv8 on caries detection from the validation process.

| Classification | Precision | Recall | F1-score | AP _{IoU50} | AP _{IoU75} | mAP _{IoU50} | mAP _{IoU75} |
|-----------------------------|-----------|--------|----------|---------------------|---------------------|----------------------|----------------------|
| 3-class ICCMS TM | | | | | | | |
| RA ^a | 0.47 | 0.26 | 0.33 | 0.29 | 0.05 | | |
| RB ^b | 0.57 | 0.30 | 0.37 | 0.38 | 0.17 | | |
| RC ^c | 0.67 | 0.65 | 0.64 | 0.67 | 0.16 | | |
| All classes | 0.57 | 0.41 | 0.45 | | | 0.45 | 0.13 |
| 6-class ICCMS TM | | | | | | | |
| RA1 | 0.28 | 0.08 | 0.12 | 0.11 | 0.01 | | |
| RA2 | 0.39 | 0.38 | 0.36 | 0.25 | 0.05 | | |
| RA3 | 0.59 | 0.36 | 0.40 | 0.37 | 0.09 | | |
| RB4 | 0.61 | 0.20 | 0.29 | 0.30 | 0.12 | | |
| RC5 | 0.54 | 0.58 | 0.56 | 0.55 | 0.42 | | |
| RC6 | 0.67 | 0.69 | 0.65 | 0.68 | 0.34 | | |
| All classes | 0.51 | 0.38 | 0.40 | | | 0.38 | 0.17 |

AP, average precision; *IoU50*, intersection over union configured to the threshold at 50%; *IoU75*, intersection over union configured to the threshold at 75%; *mAP*, mean average precision; *ICCMSTM*, the International Caries Classification and Management System

^aInitial stage (including RA1, RA2 and RA3)

^bModerate stage (including RB4)

^cExtensive stage (including RC5 and RC6)

In the performance of YOLOv8 for 6-class detection and classification, the precision for class RA1 was quite low at 0.28. In addition, the recall was very low at 0.08, resulting in a low F1-score. This outcome was consistent with the precision observed in the 3-class detection and classification for class RA (initial stage). The YOLOv8 model may generate a high number of false negatives or fail to detect lesions because initial lesions are difficult to distinguish, and the amount of film used for training may have been insufficient.

Average precision is a suitable evaluation metric for multiclass comparisons as it measures the agreement between the testing dataset and the ground truth dataset.¹³ In this study, YOLOv8 demonstrated lower average precision in detecting initial caries, with a value of 0.29 for RA, compared to 0.67 for RC (extensive caries). These findings are consistent with those reported by Panyarak et al. for YOLOv3, which showed average precision values of 0.57 for RA and 0.67 for RC at *IoU*₅₀.⁶ Additionally, their investigation of YOLOv7 performance revealed that the average precision for RA1 from the validation test was lower than that for RC6, with values of 0.34 and 0.64, respectively.¹⁰ Although the performance of YOLOv8 in detecting initial caries was inferior to that of YOLOv3 and YOLOv7, it demonstrated comparable capabilities in detecting deeper-stage caries. This discrepancy may be attributed to several factors, including the limited number of training datasets, the



difficulty in distinguishing initial lesions from sound tooth structures, and distinctions of anatomy and mineral content between primary and permanent teeth. These results suggest that increasing the size of the training datasets could enhance the performance of YOLOv8 in diagnosing caries in primary teeth.

The mAP results indicate that YOLOv8 performed better in 3-class than in 6-class detection and classification. This finding is consistent with other research on YOLO's performance in caries detection, which has shown that classification complexity affects performance.⁶ The less complex the classification, the more effective YOLO tends to be. Our study revealed that mAP at IoU₇₅ is lower than at IoU₅₀ in both classifications, this result aligns with Panyarak et al.'s investigations of YOLOv3 and YOLOv7.^{6,10} However, increasing the IoU threshold means that the predicted box is closer to the ground truth box, indicating greater accuracy for the dentist. A more precise box corresponds to a more accurate model. Therefore, enhancing model performance at higher IoU thresholds is recommended to improve its effectiveness.

Research conducted by Bayraktar and Ayan in 2022 revealed that YOLOv3 achieved a PPV of 86.58%, exceeding the performance of YOLOv8 in our study.¹¹ This disparity could be attributed to the differing tasks assigned to YOLO, which may influence the outcomes. While their study focused only on caries detection without classifying caries depth, our research utilized the ICCMSTM for caries classification which is much more difficult. In the same year, an evaluation of YOLOv3 for caries detection using the ICCMSTM reported a higher mAP than our study (0.41 versus 0.38).⁶ This discrepancy may be attributed to differences in the training dataset sizes between the studies; while they used 2,575 bitewing films to train YOLOv3, we used only 100 bitewing films for YOLOv8.⁶ In 2024, Ayhan et al. evaluated the performance of YOLOv7 and found that the recall, precision, and F1-score values for caries detection were 0.83, 0.87, and 0.82, respectively.¹⁴ YOLOv7 outperformed our results, where YOLOv8 achieved recall, precision, and F1-score values of 0.38, 0.51, and 0.40, respectively. This superior performance may be associated with the larger training dataset for YOLOv7 (1,170 bitewing films) and the relatively uncomplicated task assigned to the model (annotating tooth numbers and decay together without identifying the caries level).¹⁴ These findings are consistent with another study that assessed the mAP of YOLOv7 at IoU₅₀ after training with 2,400 bitewing films,¹⁰ revealing that YOLOv7 outperformed YOLOv8 in our study with an mAP of 0.56 versus 0.83. These studies emphasize the critical roles that the complexity of caries classification and the quantity of training data play in determining the performance of YOLO models.

The quality and quantity of training data are essential for the successful performance of deep learning models, particularly in detecting caries in primary teeth. This task is challenging due to the complex anatomy and low mineral content of the tooth structure, which makes it difficult to differentiate between caries and healthy tooth tissue. A limitation of this study is the small size of the training dataset. Therefore, using larger and more diverse datasets could enhance the efficacy of model. In addition, modifying the training method to determine the optimal threshold for caries detection may further increase the accuracy of models. For a better deep learning process, the algorithm's training procedure may involve learning dental anatomy prior to testing on the task of caries detection. However, these approaches have drawbacks because they need time-consuming annotation to accurately label a large number of caries lesions.¹⁰

Conclusion:

The validation results of YOLOv8 demonstrated promising efficacy in the detection and classification of moderate to advanced caries lesions on bitewing radiographs in primary teeth. However, its performance in detecting initial caries lesions remains limited. Enhancing the dataset size and refining the algorithm's training approach could improve YOLOv8's efficacy in detecting and classifying carious lesions at all stages.

Acknowledgements:

We gratefully acknowledge Department of Pediatric Dentistry Department of Chiangmai, Faculty of Dentistry, Chiang Mai University for my research development.

References:

1. Schwendicke F, Tzschoppe M, Paris S. J Dent. 2015;43:924-933.
2. Hegde S, Gao J, Vasa R, Cox S. Dentomaxillofac Radiol. 2023;52:20220279.
3. Diniz MB, Rodrigues JA, Neuhaus KW, Cordeiro RCL, Lussi A. Clin Oral Investig. 2010;14:515-523.
4. Wenzel A, Haiter-Neto F, Gotfredsen E. Caries Res. 2007;41:170-176.
5. Geibel M-A, Carstens S, Braisch U, Rahman A, Herz M, Jablonski-Momeni A. Clin Oral Invest. 2017;21:2761-2770.
6. Panyarak W, Suttapak W, Wantanajittikul K, Charuakkra A, Prapayasatok S. Clin Oral Investig. 2023;27:1731-1742.
7. Chen YW, Stanley K, Att W. Quintessence Int. 2020;51:248-57.
8. Chartrand G, Cheng PM, Vorontsov E, Drozdal M, Turcotte S, Pal CJ, Kadoury S, Tang A. Radiographics. 2017;37:2113-2131.
9. Mohammad-Rahimi H, Motamedian SR, Rohban MH, Krois J, Uribe SE, Mahmoudinia E, Rokhshad R, Nadimi M, Schwendicke F. J Dent. 2022;122:104115.
10. Panyarak W, Wantanajittikul K, Charuakkra A, Prapayasatok S, Suttapak W. J Digit Imaging. 2023;36:2635-2647.
11. Bayraktar Y, Ayan E. Clin Oral Investig. 2022;26:623-632.
12. Padilla R, Netto SL, da Silva EAB. IWSSIP. 2020:237-242.
13. Davis J, Goadrich M. ICML. 2006:233-240.
14. Ayhan B, Ayan E, Bayraktar Y. Clinical Oral Investigations. 2024;28:178.



New delay-dependent uniform stability analysis for the conformable fractional system with delay and nonlinear perturbations

Sastra Boonyachan,¹ Kanit Mukdasai^{2,*}

^{1,2}Department of Mathematics, Faculty of Science, Khon Kaen University, Khon Kaen 40002, Thailand

*e-mail: Kanit@kku.ac.th

Abstract

This work explores the application of the Lyapunov-Razumikhin theorem to the analysis of conformable fractional system with delay and nonlinear perturbations. Specifically, it focuses on elucidating the concepts of Razumikhin-type uniform stability for this system. New delay-dependent uniform stability criterion is derived as a linear matrix inequality (LMI) for the system by using a common Lyapunov functional and some inequalities. Moreover, an application of our theorem is presented via a numerical example.

Introduction

Fractional differential systems have been widely investigated due to their applications in science and engineering, including solving nonlinear equations, associative memory, data analysis, optimization, and intelligent control [3, 2, 5, 4, 9, 8, 1, 10]. The advantages of fractional-order calculus are that it can increase the flexibility of a system with infinite memory and genetic characteristics. There have been studies and developments in the theoretic aspects such as asymptotic behavior, periodicity, controllability, etc. This paper aims to construct Razumikhin type uniform stability and a theorem for the conformable fractional system with delay. Moreover, a numerical example is given to show that our theorem can be applied uncomplicated.

In [11], R. Khalil et al. introduced the concept of the conformable fractional derivative. Over the recent years, numerous scholars have explored various definitions and properties associated with conformable fractional derivatives, distinct from the Caputo, Grunwald-Letnikov, and Riemann-Liouville fractional derivatives. It is worth noting that these alternative definitions have garnered attention due to their departure from conventional norms, as they do not adhere to the established rules governing fractional derivatives,

$$\begin{aligned} T_{t_0}^\alpha \mu(t)v(t) &= \mu(t)T_{t_0}^\alpha v(t) + v(t)T_{t_0}^\alpha \mu(t), \\ T_{t_0}^\alpha \frac{\mu(t)}{v(t)} &= \frac{v(t)T_{t_0}^\alpha \mu(t) - \mu(t)T_{t_0}^\alpha v(t)}{v(t)^2}, \end{aligned}$$

where

$$T_{t_0}^\alpha = \lim_{\zeta \rightarrow 0} \frac{\mu(t + \zeta(t - t_0)^{1-\alpha}) - \mu(t)}{\zeta},$$

for all $t > t_0$ and $\alpha \in (0, 1]$.

This proposal aims to develop a Razumikhin-type framework for establishing a uniform stability theorem tailored to conformable fractional system incorporating delay and nonlinear perturbations. Furthermore, we present a practical numerical example to illustrate the straightforward applicability of our theorem in real-world scenarios.

Methodology:

In this section, we approach some preliminary definitions and necessary lemmas.

Definition 1. [7] For a function $\mu : [t_0, \infty) \rightarrow \mathbb{R}$, the conformable fractional derivative of μ of order α is defined by

$$T_{t_0}^\alpha \mu(t) = \lim_{\varsigma \rightarrow 0} \frac{\mu(t + \varsigma(t - t_0)^{1-\alpha}) - \mu(t)}{\varsigma}, \quad (1)$$

for all $t > t_0$ and $\alpha \in (0, 1]$. This is the first definition.

If the conformable fractional derivative of $\mu(t)$ of order α exists on (t_0, ∞) , then the function $\mu(t)$ is said to be α -differentiable on the interval (t_0, ∞) .

Definition 2. [7] Given the function $\mu : [t_0, \infty) \rightarrow \mathbb{R}$, the conformable fractional integral starting from t_0 of μ of order α , where $0 < \alpha \leq 1$ is defined by

$$I_{t_0}^\alpha \mu(t) = \int_{t_0}^t (s - t_0)^{\alpha-1} \mu(s) ds. \quad (2)$$

Lemma 1. [7] Given $\alpha \in (0, 1)$ and a continuous function $\mu : [t_0, \infty) \rightarrow \mathbb{R}$, we have

$$T_{t_0}^\alpha (I_{t_0}^\alpha \mu(t)) = \mu(t), \quad (3)$$

for all $t > t_0$.

Lemma 2. [7] Given a α -differentiable function $\mu : [t_0, \infty) \rightarrow \mathbb{R}$ with $\alpha \in (0, 1]$, we have

$$I_{t_0}^\alpha (T_{t_0}^\alpha \mu(t)) = \mu(t) - \mu(t_0), \quad (4)$$

for all $t > t_0$.

Lemma 3. [7] Given a symmetric positive definite matrix P and a α -differentiable function $\mu : [t_0, \infty) \rightarrow \mathbb{R}$ with $\alpha \in (0, 1]$. Then $T_{t_0}^\alpha \mu^T(t) P \mu(t)$ exists on $[t_0, \infty)$ and

$$T_{t_0}^\alpha \mu^T(t) P \mu(t) = 2\mu^T(t) P T_{t_0}^\alpha \mu(t), \quad (5)$$

for all $t > t_0$.

Consider the conformable fractional system with delay and nonlinear perturbation,

$$T_{t_0}^\alpha \mu(t) = g(t, \mu(t-h)), \quad t \geq t_0, \quad (6)$$

where $0 < \alpha \leq 1$, $\mu(t) \in \mathbb{R}^n$ is the state vector, and $g : \mathbb{R} \times C([-h, 0], \mathbb{R}^n) \rightarrow \mathbb{R}^n$. For each solution $\mu(t)$ of (6), we assume the initial condition

$$\mu(t_0 + s) = \sigma(s), \quad s \in [-h, 0], \quad (7)$$

where $\sigma \in C([-h, 0], \mathbb{R}^n)$.

Lemma 4. [6] Suppose that $k_1, k_2, k_3 : \mathbb{R}^+ \rightarrow \mathbb{R}^+$ are continuous non decreasing functions, $k_1(s)$ and $k_2(s)$ are positive for $s > 0$, $k_1(0) = k_2(0) = 0$, and k_2 is strictly increasing. If there exists a differentiable functional $V : \mathbb{R} \times \mathbb{R}^n \rightarrow \mathbb{R}^+$ such that

$$k_1(\|\mu\|) \leq v(t, \mu) \leq k_2(\|\mu\|), \quad (8)$$

for $t \in \mathbb{R}$, $\mu \in \mathbb{R}^n$, and for any given $t_0 \in \mathbb{R}$ the conformable fractional derivative of V along the solution $\mu(t)$ of conformable system (6) satisfies.

$$T_{t_0}^\alpha V(t, \mu(t)) \leq -k_3(\|\mu(t)\|), \quad (9)$$

whenever $V(t + \theta, \mu(t + \theta)) \leq V(t, \mu(t))$, for all $\theta \in [-h, 0]$, then conformable system (6) is uniformly stable.



Consider the conformable fractional linear system with delay and nonlinear perturbation

$$T_{t_0}^\alpha x(t) = Ax(t) + Bx(t-h) + f(t, x(t)) + g(t, x(t-h)), \quad t \geq t_0, \quad (10)$$

where $0 < \alpha \leq 1$, $x(t) \in \mathbb{R}^n$ is state vector, A, B are known real constant matrices and h is a positive real constant. For each solution $x(t)$ of (10), we assume the initial condition

$$x(t) = \phi(t), t \in [-h, 0].$$

where $\phi \in C([-h, 0]; \mathbb{R}^n)$. The uncertainties $f(\bullet)$, $g(\bullet)$ represent the nonlinear parameter perturbation with respect to the state $x(t)$ and $x(t-h)$ are bounded in magnitude of the form

$$f^T(t, x(t))f(t, x(t)) \leq \varepsilon^2 x^T(t)x(t), \quad (11)$$

$$g^T(t, x(t-h))g(t, x(t-h)) \leq \delta^2 x^T(t-h)x(t-h), \quad (12)$$

where ε and δ are given constant.

Results and Discussion:

Theorem 1. Given the positive scalars $\alpha, \varepsilon, \delta$ and h , system (10) is uniformly stable if there exist a symmetric positive definite matrix K and the positive scalars β_1 and β_2 such that the following symmetric linear matrix inequality hold:

$$\begin{bmatrix} J & KB & K & \\ * & \beta_2 \delta^2 I - h\alpha K & 0 & 0 \\ * & * & -\beta_1 I & 0 \\ * & * & * & -\beta_2 I \end{bmatrix} < 0, \quad (13)$$

where $J = KA + A^T K + \beta_1 \varepsilon^2 I + h\alpha K$.

Proof. Let K be a symmetric positive definite matrix. Consider the Lyapunov-Razumikhin functional of the form

$$V(t) = x^T(t)Kx(t).$$

Taking the conformable fractional derivative of $V(t)$ along the trajectory of system (10), we have

$$\begin{aligned} T_{t_0}^\alpha V(t) &= x^T(t)KT_{t_0}^\alpha x(t), \\ &= 2x^T(t)K[Ax(t) + Bx(t-h) + f(t, x(t)) \\ &\quad + g(t, x(t-h))]. \end{aligned} \quad (14)$$

Form (11)-(12), we obtain

$$0 \leq \beta_1 \varepsilon^2 x^T(t)x(t) - \beta_1 f^T(t, x(t))f(t, x(t)), \quad (15)$$

$$0 \leq \beta_2 \delta^2 x^T(t-h)x(t-h) - \beta_2 g^T(t, x(t-h))g(t, x(t-h)), \quad (16)$$

for $\beta_1, \beta_2 > 0$. Form $V(t+\theta, x(t+\theta)) \leq V(t, x(t))$, for all $\theta \in [-h, 0]$, we obtain

$$0 \leq h\alpha x^T(t)Kx(t) - h\alpha x^T(t-h)Kx(t-h), \quad (17)$$

for $\alpha, h > 0$. According to (14)-(17), it is straightforward to see that

$$T_{t_0}^\alpha V(t) \leq \xi^T(t) \begin{bmatrix} J & KB & K & K \\ * & \beta_2 \delta^2 I - h\alpha K & 0 & 0 \\ * & * & -\beta_1 I & 0 \\ * & * & * & -\beta_2 I \end{bmatrix} \xi(t), \quad (18)$$

$$J = KA + A^T K + \beta_1 \varepsilon^2 I + h\alpha K,$$

where $\xi(t) = \text{col}\{x^T(t), x^T(t-h), f^T(t, x(t)), g^T(t, x(t-h))\}$.

If condition (13) holds, then system (10) is uniformly stable. \square

Numerical Example:

In this section, a numerical example is given in order to present the effectiveness of our main result by showing the maximum upper bound of the parameter δ .

Example 1. Consider the conformable fractional linear system with delay

$$T_{t_0}^\alpha x(t) = Ax(t) + Bx(t-h) + f(t, x(t)) + g(t, x(t-h)). \quad (19)$$

Solving LMI (13) with $A = \begin{bmatrix} -2 & 0 \\ 0 & -0.9 \end{bmatrix}$, $B = \begin{bmatrix} -0.1 & 0 \\ -0.1 & -0.1 \end{bmatrix}$, $h = 0.3$, $\alpha = 0.8$, and $\varepsilon = 0.1$, we obtain the parameters $\beta_1 = 46.7206$, $\beta_2 = 12.1075$, and $K = \begin{bmatrix} 19.7711 & 1.0874 \\ 1.0874 & 10.4502 \end{bmatrix}$, which guarantee uniform stability of system (19) when $\delta = 0.22$.

The permissible upper bounds δ for various h, α and $\varepsilon = 0.1$ are show δ in Table 1.

Table 1: The least upper bounds of δ for different h and α when $\varepsilon = 0.1$.

| Theorem 1 | $h = 0.2$ | $h = 0.4$ | $h = 0.6$ |
|----------------|-----------|-----------|-----------|
| $\alpha = 0.6$ | 0.0931 | 0.4105 | 0.4746 |
| $\alpha = 0.8$ | 0.2627 | 0.4636 | 0.4764 |
| $\alpha = 1.0$ | 0.3556 | 0.4793 | 0.4799 |

From system (19), we let $A = \begin{bmatrix} -2 & 0 \\ 0 & -0.9 \end{bmatrix}$, $B = \begin{bmatrix} -0.1 & 0 \\ -0.1 & -0.1 \end{bmatrix}$, $h = 0.5$, $\alpha = 0.95$, $f(x_i(t)) = 0.1(|x_i(t) + 1| - |x_i(t) - 1|)$, $g(x_i(t-h)) = 0.1(|x_i(t-h) + 1| - |x_i(t-h) - 1|)$, $i = 1, 2$, and $\phi(t) = [2 \quad -4]^T$, $\forall t \in [-0.5, 0]$. Figure 1. shoes the trajectories of solution $x(t)$ of example 1

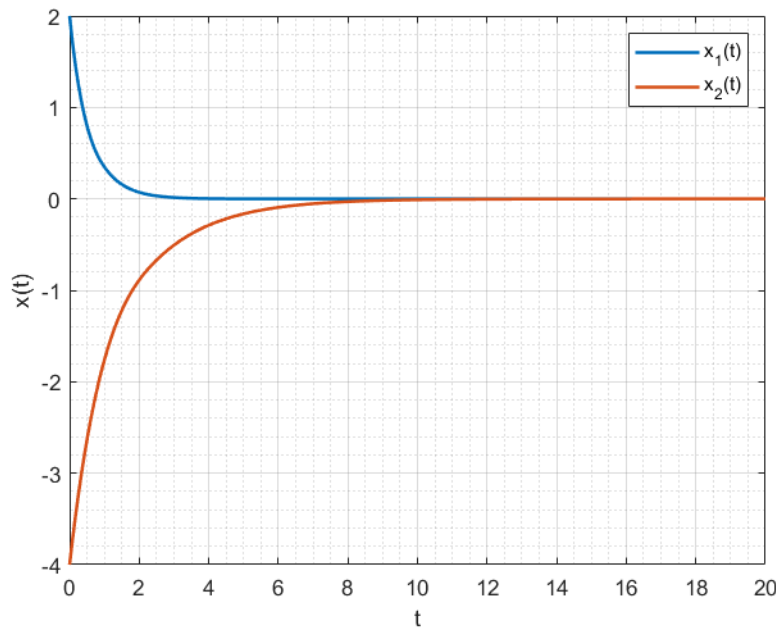


Figure 1: The trajectories of solution $x(t)$ of example 1.



Conclusion

In this work, the authors introduce a novel approach to investigate the uniform stability of a conformable fractional linear system with a delay and nonlinear perturbation. We employ the Lyapunov-Razumikhin theorem along with specific inequalities and a Lyapunov-Razumikhin functional in their analysis. The proposed method yields a new delay-dependent uniform stability criterion for a considered system. To support their findings, the authors provide a numerical example illustrating the advantages and practicality of their approach.

Acknowledgements

This work is supported by the Development and Promotion of Science and Technology Talents Project (DPST) and National Research Council of Thailand (NRCT) and Khon Kaen University (Mid-Career Research Grant NRCT5-RSA63003-07).

References

- [1] Chu, X., Xu, L., & Hu, H. (2020). Exponential quasi-synchronization of conformable fractional-order complex dynamical networks. *Chaos, Solitons & Fractals*, 140, 110268.
- [2] Cochocki, A., & Unbehauen, R. (1993). *Neural networks for optimization and signal processing*. John Wiley & Sons, Inc.
- [3] He, D., & Xu, L. (2020). Exponential stability of impulsive fractional switched systems with time delays. *IEEE Transactions on Circuits and Systems II: Express Briefs*, 68(6), 1972-1976.
- [4] Hsieh, W. W., & Tang, B. (1998). Applying neural network models to prediction and data analysis in meteorology and oceanography. *Bulletin of the American Meteorological Society*, 79(9), 1855-1870.
- [5] Hsu, C. F., & Chang, C. W. (2016). Intelligent dynamic sliding-mode neural control using recurrent perturbation fuzzy neural networks. *Neurocomputing*, 173, 734-743.
- [6] Kaewbanjak, N., Chartbupapan, W., Nonlaopon, K., & Mukdasai, K. (2021). The Lyapunov-Razumikhin theorem for the conformable fractional system with delay. *AIMS Math*, 7, (4795-4802).
- [7] Musraini M, Rustam Efendi, Endang Lily, & Ponco Hidayah. (2019). classical properties on conformable fractional calculus. *Pure Appl. Math. J.*, 8(83-87)
- [8] Pershin, Y. V., & Di Ventra, M. (2010). Experimental demonstration of associative memory with memristive neural networks. *Neural networks*, 23(7), 881-886.
- [9] Xu, L., Liu, W., Hu, H., & Zhou, W. (2019). Exponential ultimate boundedness of fractional-order differential systems via periodically intermittent control. *Nonlinear Dynamics*, 96, 1665-1675.
- [10] Xia, Y., & Feng, G. (2007). A new neural network for solving nonlinear projection equations. *Neural Networks*, 20(5), 577-589.
- [11] Khalil, R., Alhorani, M., Yousef dan, A., & Sababheh, M. (2014). A definition of fractional derivative, *J. Comput. Appl. Math.*, 264, 65-70.



NUMERICAL SOLUTION OF THE ABSOLUTE VALUE EQUATIONS USING TWO STEP ITERATIVE METHOD

Asma Yafad,* Nifatamah Makaje, Aniruth Phon-On

Department of Mathematics and Computer Science, Faculty of Science and Technology,
Prince of Songkla University, Pattani Campus, 94000, Thailand

*e-mail: Asmawal098@gmail.com

Abstract:

In this paper, we propose and analyze a novel technique for solving absolute value equations. This method employs a two-step approach, utilizing a generalized Newton technique as the predictor and a modified fixed-point method as the corrector. Convergence results are obtained under mild assumptions. We demonstrate the convergence of the proposed method and provide numerical experiments to illustrate the method's efficiency and high accuracy.

Introduction:

Consider the system of absolute value equation (AVE) represented by:

$$Ax - |x| - b = 0 \quad (1)$$

where $A \in \mathbb{R}^{n \times n}$, $b \in \mathbb{R}^n$, and $|x|$ denotes the vector of absolute values of each component of x . A more general version of this system (GAVE) is:

$$Ax - Q|x| - b = 0 \quad (2)$$

where $Q \in \mathbb{R}^{n \times n}$, this generalized form was initial introduced by Rohn¹ in 2004 and has since been extensively studied by various researchers. The importance of the absolute value equation (1) lies in its ability to reduce complex problems, such as linear programs, quadratic programs, bimatrix games and many other applications to a linear complementarity problem (LCP²). Mangasarian and Meyer³ (2006) illustrated that the general NP-hard LCP, introduced by Cottle and Dantzig² in 1968 and others, includes many mathematical programming problems, among which AVE are more straightforward. Furthermore, Mangasarian^{3,4} demonstrated the equivalence between AVE (1) and LCP, spurring significant interest in the study of AVE.

In recent years, numerous numerical techniques have been developed to address absolute value equations (AVE). Haghani⁵ proposed and analyzed the convergence properties of the generalized Traub's approach. Prokopyev⁶ examined the unique solvability of AVEs and their connection with linear complementarity problems (LCPs). Li⁷ employed the Accelerated Over-Relaxation (AOR) method for solving AVEs. Abdallah et al⁸ solved AVEs using complementarity functions. Fakharzadeh and Sham⁹ introduced a mixed-type splitting technique for solving AVEs, while Ali et al.¹⁰ developed a fixed-point iteration method. Ke and Ma¹¹ suggested an SOR-like method, and Feng and Liu¹² proposed a two-step iterative method along with an improved generalized Newton method. Additionally, the matrix multisplitting method for solving AVEs was discussed by Dehghan and Shirilord¹³. Khan et al.¹⁵ established two-step technique with the generalized Newton technique as predictor step and corrector step is the Simpson's method, along with several other approaches [16-24]. These advancements underscore the significant interest and progress in developing efficient methods for solving absolute value equations.

In this paper, we introduce a new two-step iterative method for solving AVE (1). This method is inspired by the Newton technique proposed by Khan et al¹⁵ and the fixed-point

iteration method introduced by Mann²⁰. Therefore, we refer to this new approach as the Newton Technique Fixed-Point Iteration (NTFPI) method. Our method utilizes the well-established Newton method as a predictor step, followed by a modified fixed-point method as a corrector step. This novel iterative technique is both straightforward and exhibits rapid convergence to the solution of AVE (1). Comparative analysis with existing methods demonstrates the advantages of the proposed NTFPI method. Furthermore, we present several numerical examples to illustrate its effectiveness.

Methodology:

Preliminary

Let us consider the following:

$$f(x) = Ax - |x| - b. \quad (3)$$

The generalized Jacobian of f at x is given by

$$f'(x) = \partial f(x) = A - H(x),$$

where $H(x) = \text{diag}(\text{sign}(x)) = \partial|x|$ is a diagonal matrix and $H(x)x = |x|$.

To solve the AVE (1), we can apply the Newton technique (NT) introduced by Khan et al.¹⁵ which is expressed as:

$$\begin{aligned} t^{(k)} &= x^{(k)} - (A - H(x^{(k)}))^{-1}b, \\ x^{(k+1)} &= x^{(k)} - 6 \left(f'(x^{(k)}) + 4f' \left(\frac{x^{(k)} + t^{(k)}}{2} \right) + f'(t^{(k)}) \right)^{-1} f(x^{(k)}), \quad k = 0, 1, 2, \dots \end{aligned} \quad (4)$$

Another approach is the modified fixed-point iteration (MFPI) method proposed by Yu, D., Chen, C., & Han, D²³. This method begins by reformulating the AVE (1) as a two-by-two block nonlinear equation

$$\begin{aligned} Ax - Qy &= b \\ Qy - |x| &= 0 \end{aligned} \quad (5)$$

where $Q \in \mathbb{R}^{n \times n}$ is invertible. If $Q = I$, then (5) is equivalent to AVE (1). When A and Q is nonsingular, the MFPI iteration formula is

$$\begin{aligned} x^{(k+1)} &= A^{-1}(Qy^{(k)} + b), \\ y^{(k+1)} &= (1 - \tau)y^{(k)} + \tau Q^{-1}|x^{(k+1)}|, \end{aligned} \quad (6)$$

where $\tau > 0$ is a parameter. Note that the inverse of Q is involved at each step of the MFPI method, which increases the computational cost of each iteration, especially if Q is dense or ill-conditioned. One strategy for choosing Q is let it be a diagonal matrix, particularly a scalar matrix. For instance, in numerical example provided by Yu et al.²³, Q is set to be $Q = (1/q)I$ with $q = q_l + 100 > 0$ and I is the identity matrix order n .

It has been demonstrated that both sequences $\{x^{(k)}\}$ generated by Equations (4) and (6) converge to the exact solution of AVE (1) when $0 < \|A^{-1}\| < 1$.



Propose method

In 1953 Mann²⁰ presented a fixed point iteration for solving nonlinear equation in real space \mathbb{R} , which inspired the development of our method. We extend this idea to the corrector step. The iterative method is defined as follows:

$$\begin{aligned} y^{(k)} &= x^{(k)} - (A - H(x^{(k)}))^{-1} f(x^{(k)}) \\ x^{(k+1)} &= (1 - \beta_k) y^{(k)} + \beta_k (A^{-1} |y^{(k)}| + A^{-1}(b)) \quad , \quad k = 0, 1, 2, \dots \end{aligned} \quad (7)$$

where the iteration parameter β_k lies in the interval $(0, 1)$.

Note that in iterative formula (7), the proposed method uses the NT technique by Khan et al.¹⁵ as the predictor step, while the fixed-point technique is utilized as the corrector step. The following algorithm outlines the proposed technique:

Algorithm for NTFPI technique

Step 1: Choose an initial vector $x^{(0)} \in \mathbb{R}^n$, $k = 0$ and set β_k within the interval $(0, 1)$.

Step 2: Compute $y^{(k)} = x^{(k)} - (A - H(x^{(k)}))^{-1} f(x^{(k)})$.

Step 3: Using $y^{(k)}$, compute $x^{(k+1)} = (1 - \beta_k) y^{(k)} + \beta_k (A^{-1} |y^{(k)}| + A^{-1}(b))$.

Step 4: If the stopping criterion $RES = \frac{\|Ax^{(k)} - |x^{(k)}| - b\|}{\|b\|} < \varepsilon$ is met, then terminated

otherwise update $k = k + 1$ and return to step 2.

Numerical examples

To demonstrate the effectiveness of the proposed method, we present three numerical examples. All experiments were conducted using SCILAB. In the comparisons, NT, MFPI and NTFPI represent the Newton technique (4), the modified fixed-point iteration method (6) and our proposed method, respectively. Let IT, RES and T denote the iteration steps, the residual error and the CPU time in seconds, respectively. The residual error is defined as:

$$RES = \frac{\|Ax - |x| - b\|}{\|b\|}.$$

In all tests, the initial vector was set to zero and the process was terminated if the current iteration met the convergence criteria $RES \leq 10^{-6}$ or if the maximum number of iteration $\max_k = 1000$ was exceeded.

Example 1 ([15]): Consider a matrix A whose singular values are all greater than 1. We generate a random instance of such a matrix as follows:

$$A = R^T R + nI_n$$

where $R = rand(n, n)$ is a random matrix with dimension n by n and $b = (A - I_n)x^*$ with $x^* = (1, 1, 1, \dots, 1)^T \in \mathbb{R}^n$. Set the parameters as shown in Table 1. We note that the exact solution is $(1, 1, 1, \dots, 1)^T \in \mathbb{R}^n$. The numerical results are shown in Table 3.

Table 1. Parameters for solving the AVE given in Example 1

| Parameters | n | | | |
|----------------------------|---------------------|---------------------|---------------------|---------------------|
| | 40 | 60 | 80 | 100 |
| q_l | 0.025 | 0.017 | 0.013 | 0.01 |
| τ | 1.12 | 1.12 | 1.12 | 1.12 |
| β_k at iteration k | $\frac{1}{(1+k)^9}$ | $\frac{1}{(1+k)^9}$ | $\frac{1}{(1+k)^9}$ | $\frac{1}{(1+k)^9}$ |

Example 2 ([23]): Consider the AVE (1) with the matrix A given by

$$A = \hat{A} + \mu I_{m^2} \quad (\mu \geq 0) \quad \text{with} \quad \hat{A} = \text{Tridiag}(-I_m, S_m, -I_m) \in \mathbb{R}^{m^2 \times m^2}$$

$$S_m = \text{tridiag}(-1, 4, -1) \in \mathbb{R}^{m \times m}, \text{ and } b = (1, 1, 1, \dots, 1)^T \in \mathbb{R}^{m^2},$$

where $I_m \in \mathbb{R}^{m \times m}$ is the identity matrix, and set the parameters as shown in Table 2. The numerical results are illustrated in Table 4.

Table 2. Parameters for solving the AVE given in Example 2

| μ | Parameters | m | | | |
|-------|----------------------------|---------------------|---------------------|---------------------|---------------------|
| | | 40 | 60 | 80 | 100 |
| 2.4 | q_l | 0.2574 | 0.2578 | 0.2580 | 0.2581 |
| | τ | 1.24 | 1.24 | 1.25 | 1.25 |
| | β_k at iteration k | $\frac{1}{(1+k)^9}$ | $\frac{1}{(1+k)^9}$ | $\frac{1}{(1+k)^9}$ | $\frac{1}{(1+k)^9}$ |
| 4 | q_l | 0.1258 | 0.1259 | 0.1259 | 0.1260 |
| | τ | 1.13 | 1.13 | 1.13 | 1.13 |
| | β_k at iteration k | $\frac{1}{(1+k)^9}$ | $\frac{1}{(1+k)^9}$ | $\frac{1}{(1+k)^9}$ | $\frac{1}{(1+k)^9}$ |

It is important to note that NT and MFPI methods converge to the unique solution of the AVE (1) when $\|A^{-1}\| < 1$, which is a sufficient condition for the AVE (1) to have a unique solution (see Proposition 1.1²³). However, the MFPI method still converges for some examples with $\|A^{-1}\| \geq 1$. This observation motivated us to experiment with our proposed method with the same example illustrated by Yu et al.²³.

Example 3 ([23]): Consider the matrix A given by

$$A = \begin{pmatrix} 1 & 3 \\ -0.01 & 1 \end{pmatrix},$$

And assume the following parameters $Q = I$, $b = Ax^* - |x^*|$ with

$$x^* = (1, -1)^T, \quad \beta_k = \frac{1}{(1+k)^9}, \quad \tau = 0.9 \quad \text{and} \quad x^{(0)} = y^{(0)} = (0, 0)^T.$$

Under these conditions, the numerical results are illustrated in Table 5.



Table 3. The comparison of NT, MFPI and NTFPI in Example 1

| n | NT | | | MFPI | | | NTFPI | | |
|-----|----|-----------|----------|------|-----------|-----------|-------|-----------|-----------|
| | IT | RES | T | IT | RES | T | IT | RES | T |
| 40 | 2 | 6.590D-16 | 0.001061 | 6 | 0.0000002 | 0.0005491 | 2 | 4.711D-16 | 0.0006308 |
| 60 | 2 | 1.297D-15 | 0.001224 | 6 | 0.0000002 | 0.0007883 | 2 | 1.236D-15 | 0.0013531 |
| 80 | 2 | 2.538D-15 | 0.002804 | 6 | 0.0000002 | 0.0021498 | 2 | 9.970D-16 | 0.0014559 |
| 100 | 2 | 3.683D-15 | 0.005781 | 6 | 0.0000002 | 0.0033967 | 2 | 1.808D-15 | 0.0018003 |

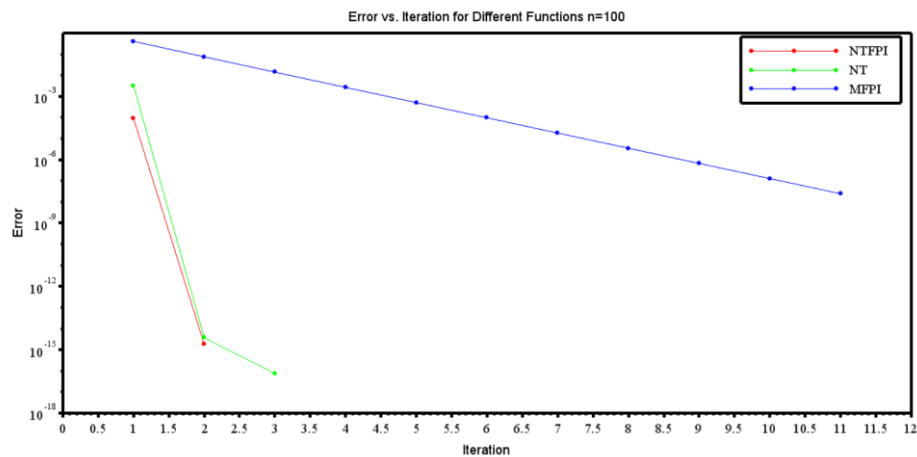


Figure 1. Comparison residual error of NTFPI with NT and MFPI for Example 1

Table 4. The comparison of NT, MFPI and NTFPI in Example 2

| μ | Method | | 40 | 60 | 80 | 100 |
|-------|--------|-----|-----------|-----------|-----------|-----------|
| 2.4 | NT | IT | 2 | 2 | 2 | 2 |
| | | RES | 4.391D-16 | 4.678D-16 | 1.446D-15 | 1.506D-15 |
| | | T | 0.881144 | 17.435459 | 82.162508 | 295.71435 |
| | MFPI | IT | 9 | 9 | 9 | 9 |
| | | RES | 0.0000007 | 0.0000006 | 0.0000005 | 0.0000005 |
| | | T | 0.09375 | 0.1875 | 1.078125 | 14.90625 |
| | NTFPI | IT | 2 | 2 | 2 | 2 |
| | | RES | 4.073D-16 | 4.341D-16 | 5.746D-16 | 5.504D-16 |
| | | T | 0.3756533 | 8.7747658 | 40.160259 | 138.16518 |
| 4 | NT | IT | 2 | 2 | 2 | 2 |
| | | RES | 2.320D-16 | 2.412D-16 | 3.862D-16 | 4.259D-16 |
| | | T | 0.921875 | 17.640625 | 137.32812 | 604.39062 |
| | MFPI | IT | 6 | 6 | 6 | 6 |
| | | RES | 0.0000003 | 0.0000002 | 0.0000002 | 0.0000002 |
| | | T | 0.046875 | 0.28125 | 0.796875 | 6.71875 |
| | NTFPI | IT | 2 | 2 | 2 | 2 |
| | | RES | 2.318D-16 | 2.392D-16 | 2.414D-16 | 2.467D-16 |
| | | T | 0.328125 | 7.984375 | 88.109375 | 480.3125 |

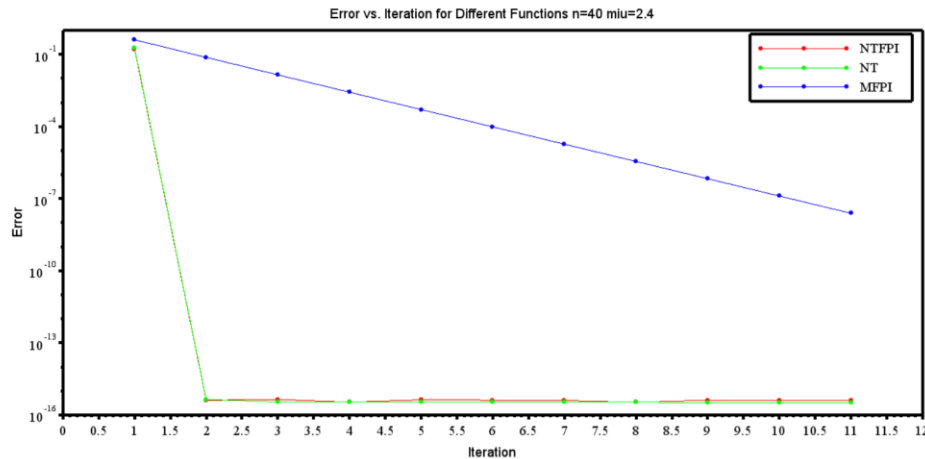


Figure 2. Comparison residual error of NTFPI with NT and MFPI for Example 2

Table 5. The comparison of NT, MFPI and NTFPI in Example 3

| n | NT | | | MFPI | | | NTFPI | | |
|-----|----|-----|-----------|------|-----------|--------|-------|-----|-----------|
| | IT | RES | T | IT | RES | T | IT | RES | T |
| 2 | 2 | 0 | 0.0002996 | 1015 | 9.982D-09 | 0.0137 | 2 | 0 | 0.0003793 |

From Tables 3 and 4, it is evident that all tested methods can efficiently compute the solution of AVE (1). However, the NTFPI method outperforms the MFPI method in both computing time and the number of iterations, although it shows only slight differences when compared to the NT method. Additionally, as shown in Table 5, the MFPI method requires 1015 iteration steps to converge, while both the NT and NTFPI methods converge within just 2 iterations based on the stopping criterion $\|Ax^{(k)} - |x^{(k)}| - b\| \leq 10^{-8}$.

To compare the speed of convergence, we present the convergence curves for the three algorithms to solve Examples 1 and 2, as shown in Figure 1. and Figure 2. The curves indicate that the convergence rates of the NTFPI and NT methods are quite similar. However, the NTFPI method converges slightly faster than the NT method and achieves higher precision in residual error with slightly less computational time. Furthermore, the number of functional evaluations required at each step of NTFPI method is lower than that of NT method.

Overall, these findings suggest that the proposed NTFPI method can rapidly compute the solution of the AVE (1) under certain conditions, making it highly effective for solving large-scale problems. Moreover, the NTFPI method still converges for some cases where $\|A^{-1}\| \geq 1$, indicating its robustness. We conclude that the proposed NTFPI method is both feasible and effective for solving AVEs. Nevertheless, it is important to note that the theoretical conditions necessary to guarantee the convergence of the NTFPI method, particularly when $\|A^{-1}\| \geq 1$, require further investigation.

Conclusion:

In this paper, we propose a new iterative method for solving the AVE (1). The effectiveness of the proposed method is demonstrated numerically through three examples. Our results show that the NTFPI method converges more quickly than the MFPI method when comparing the number of iterations. Although the number of iterations required for the NTFPI method is the same as for the NT method, the NTFPI method performs fewer functional



evaluations per iteration compared to the NT method. Future research will focus on a theoretical analysis to establish the convergence of this new method. Additionally, the method may be extended to solve the generalized GAVE (2).

References:

1. Rohn J. A theorem of the alternatives for the equation $Ax + B|x| = b$. *Linear Multilinear Algebra*. 2004;52(6):421–426.
2. Cottle RW, Dantzig G. Complementary pivot theory of mathematical programming. *Linear Algebra Appl*. 1968;1(1):103–125.
3. Mangasarian, O.L.: Absolute value programming. *Comput. Optim. Appl*. 1968;36, 43–53.
4. Mangasarian O.L. Absolute value equation solution via concave minimization. *Optim Lett*. 2007;1(1):3–8.
5. Haghani FK. On generalized Traub's method for absolute value equations. *J Optim Theory Appl*. 2015;166(2):619–625.
6. O.A. Prokopyev, On equivalent reformulations for absolute value equations, *Comput. Optim. Appl*. 2009; 44:363–372.
7. C.-X. Li, A preconditioned AOR iterative method for the absolute value equations, *Int. J. Comput. Methods*. 2017;4 (2):1750016.
8. L. Abdallah, M. Haddou, T. Migot, Solving absolute value equation using complementarity and smoothing functions, *J. Comput. Appl. Math*. 2018; 327:196–207.
9. A.J. Fakharzadeh, N.N. Shams, An Efficient Algorithm for Solving Absolute Value Equations, *J. Math. Extension*. 2021;15: 1–23.
10. R. Ali, A. Ali, M.M. Alam, A. Mohamed, Numerical Solution of the Absolute Value Equations Using Two Matrix Splitting Fixed Point Iteration Methods, *J. Func. Spac*. 2022, <https://doi.org/10.1155/2022/7934796>.
11. F. Ke Yi, C.F. Ma, SOR-like iteration method for solving absolute value equations, *Appl. Math. Comput*. 2017; 311:195-202.
12. Feng, J., & Liu, S. 2019. A new two-step iterative method for solving absolute value equations. *J. Inequal. Appl*. 2019:1-8.
13. Dehghan, M., & Shirilord, A. Matrix multisplitting Picard-iterative method for solving generalized absolute value matrix equation. *Appl Numer Math*. 2020;158: 425-438.
14. Iqbal, J., Iqbal, A., & Arif, M. Levenberg–Marquardt method for solving systems of absolute value equations. *J. Comput. Appl. Math*. 2015;282: 134-138.
15. Khan, A., Iqbal, J., Akgül, A., Ali, R., Du, Y., Hussain, A., Nisar, K.S., Vijayakumar, V. A Newton-type technique for solving absolute value equations. *Alex.Eng. J.*. 2023; 64:291-296
16. Ke, Y. The new iteration algorithm for absolute value equation. *Appl. Math. Lett*. 2020; 99:105990.
17. O. L. Mangasarian, R. R. Meyer, Absolute value equation, *Linear Algebra Appl.*, 2006;419:359–367. 1, 2.2
18. Hu S-L, Huang Z-H, Zhang Q. A generalized Newton method for absolute value equations associated with second order cones. *J Comput Appl Math*. 2011;235(5):1490–1501.
19. Feng, J., & Liu, S. An improved generalized Newton method for absolute value equations. *SpringerPlus*. 2016;5: 1-10.
20. Mann, WR: Mean value methods in iteration. *Proc. Am. Math. Soc*. 1953;4: 506-510.
21. Ali, Rashid, Kejia Pan, and Asad Ali. "Two new iteration methods with optimal parameters for solving absolute value equations." *Int. J. Appl. Comput. Math*. 2022;8.3: 123.

22. Yu, D., Chen, C., & Han, D. A modified fixed point iteration method for solving the system of absolute value equations. *Optimization*. 2022;71(3): 449-461.
23. Ali, R., & Pan, K. Two new fixed point iterative schemes for absolute value equations. *Jpn. J. Ind. Appl. Math.* 2023;40(1): 303-314.
24. Ali, R., Zhang, Z., & Awwad, F. A. The study of new fixed-point iteration schemes for solving absolute value equations. *Heliyon*, 2024;10(14).



ODD GRACEFUL LABELING OF VERTEX DUPLICATION IN PATH GRAPHS

Nawarat Jitaksorn,¹ Chantawan Noisri,² Siwaporn Saewan^{3,*}

¹Students, Department of Mathematics and Statistics, Faculty of Science and Digital Innovation, Thaksin University, Phatthalung, 93210, Thailand

² Dr., Department of Mathematics and Statistics, Faculty of Science and Digital Innovation, Thaksin University, Phatthalung, 93210, Thailand

³ Assoc. Prof. Dr., Department of Mathematics and Statistics, Faculty of Science and Digital Innovation, Thaksin University, Phatthalung, 93210, Thailand

*e-mail: siwaporn@tsu.ac.th

Abstract:

Let G be a simple connected graph. An odd graceful labeling of a graph is an assignment of distinct odd integers to the vertices of a graph such that, when edges are labeled by the absolute difference between the labels of their endpoints, the resulting edge labels are distinct consecutive odd integers. In this paper, we explore some results on the odd graceful labeling of the new graph obtained by the duplication a vertex of a path graph by a new vertex.

Introduction:

Let G be a simple graph with a vertex set $V(G)$ and edge set $E(G)$. Let $q = |E(G)|$ be the number of the edges of G . The **endpoints** of an edge is a set of two vertices connects to each edge. The vertices are in the endpoint of each edge are called **incident** with the edge. The vertices which are incident with a common edge are **adjacent**. A **simple graph** G is a graph with each edge in $E(G)$ connects two distinct vertices in $V(G)$. The **Neighbourhood** of a vertex v in a graph G is the set of all vertices which are adjacent to v . The set of the neighbourhood of a vertex v is denoted by $N(v)$. For more detail, the reader can see in, Gross and Yellen³. A labeling of a graph G is a function f such that carries a set of graph elements into the set of integers. Gnanajothi² introduced a labeling called an odd graceful graph. A graph G with q edges to be odd graceful if there is an injection f from $V(G)$ to $\{0, 1, 2, \dots, 2q-1\}$ such that, when each edge xy is assigned the label $|f(x) - f(y)|$.

Definition 1 A function f is called an **odd graceful labeling** of a simple graph G with $|E(G)| = q$ edges if $f : V(G) \rightarrow \{0, 1, 2, \dots, 2q-1\}$ is injective and the induced function $f^* : E(G) \rightarrow \{1, 3, 5, \dots, 2q-1\}$ defined by

$$f^*(uv) = |f(u) - f(v)|$$

is bijective. A graph which has an odd graceful labeling is called an odd graceful graph.

Seoud and Abdel-Aal⁴ determine all connected odd graceful graphs of order at most 6. In addition, they proved that if G is odd graceful, then $G \cup K_{m,n}$ for all $m, n \geq 1$, splitting of complete bipartite graph, Cartesian product of paths, symmetric product for paths with null graph, conjunction of paths and conjunction of paths with stars are odd graceful. Abdel-Aal¹ proved that the m -shadow graphs for paths, complete bipartite graphs and symmetric product between paths and null graphs are odd graceful. Vaidya and Shah⁶ proved that the splitting graph and the shadow graph of bistar $B_{n,n}$ admit odd graceful labeling.

Definition 2 The duplication of a vertex v of a graph G produces a new graph by adding a new vertex v' such that

$$N(v) = N(v')$$

where $N(v)$ denotes the set of neighborhoods of a vertex v .

The duplication of a vertex v_1 of a path P_3 by a new vertex v'_1 shown in Figure 1.



Figure 1.

In this paper, we prove some results on the odd graceful labeling of the new graph obtained by the duplication a vertex of a path graph P_n by a new vertex.

Methodology:

1. Conduct a comprehensive study on odd graceful labeling.
2. Investigate various graph operations.
3. Determine the odd graceful labeling for the new graph created by duplicating a vertex in the path graph P_n with a new vertex. The duplication of a vertex v_1 of a path P_n by a new vertex v'_1 shown in Figure 2 and the duplication of a vertex v_2 of a path P_n by a new vertex v'_2 shown in Figure 3.

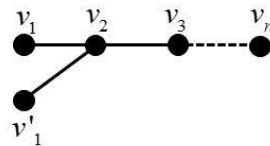


Figure 2.

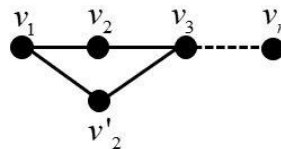


Figure 3.

4. Formulate new theorems related to odd graceful labeling.

Results and Discussion:

Theorem 1. Let P_n be a path with $V(P_n) = \{v_1, v_2, v_3, \dots, v_n\}$. The graph obtained by duplicating a vertex v_1 in a path P_n is an odd graceful graph.

Proof. Let P_n be a path with n vertex and let v_i where $1 \leq i \leq n$ be the successive vertices of the P_n such that v_i is adjacent to v_{i+1} . Let G be the graph obtained by duplicating a vertex v_1 of P_n by a vertex v'_1 . Hence $|E(G)| = q = n$, $V(G) = \{v_1, v_2, v_3, \dots, v_n\} \cup \{v'_1\}$ and $|V(G)| = n + 1$.

We define the vertex labeling $f : V(G) \rightarrow \{0, 1, 2, \dots, 2n - 1\}$ as follows.

$$f(v'_1) = 1.$$

If n is even

$$f(v_i) = i - 2, \quad i = 2, 4, 6, 8, \dots, n.$$



$$\{f(v_i) \mid i = 2, 4, 6, \dots, n\} = \{0, 2, 4, \dots, n-2\}.$$

$$f(v_i) = 2n - i, \quad i = 1, 3, 5, 7, \dots, n-1.$$

$$\{f(v_i) \mid i = 1, 3, 5, 7, \dots, n-1\} = \{2n-1, 2n-3, 2n-5, \dots, 2n-(n-1) = n+1\}.$$

If n is odd

$$f(v_i) = i - 2, \quad i = 2, 4, 6, 8, \dots, n-1.$$

$$\{f(v_i) \mid i = 2, 4, 6, \dots, n-1\} = \{0, 2, 4, \dots, n-3\}.$$

$$f(v_i) = 2n - i, \quad i = 1, 3, 5, 7, \dots, n.$$

$$\{f(v_i) \mid i = 1, 3, 5, 7, \dots, n\} = \{2n-1, 2n-3, 2n-5, \dots, 2n-n = n\}.$$

Clearly f is an injective.

From the vertex labeling f . Next, we consider the induced edge labeling function $f^*: E(G) \rightarrow \{1, 3, 5, \dots, 2q-1 = 2n-1\}$ such that $f^*(uv) = |f(u) - f(v)|$ as follows.

$$f^*(v_1'v_2) = 1.$$

$$f^*(v_1v_2) = 2n-1.$$

$$f^*(v_iv_{i+1}) = 2n-2i-1, \quad i = 2, 3, 4, \dots, n-1.$$

$$\{f^*(v_iv_{i+1}) \mid i = 2, 3, 4, \dots, n-1\} = \{2n-3, 2n-5, 2n-7, \dots, 3\}.$$

Thus

$$\begin{aligned} \{f^*(E(G))\} &= \{f^*(v_1'v_2)\} \cup \{f^*(v_1v_2)\} \cup \{f^*(v_iv_{i+1}) \mid i = 2, 3, 4, \dots, n-1\} \\ &= \{1, 3, 5, \dots, 2n-3, 2n-1\}. \end{aligned}$$

It is obvious that f^* is a bijective. Then G is the odd graceful graph. \square

Figure 4 show the odd graceful graph G with the odd graceful labeling in Theorem 1 when $n = 3, 5, 7$.

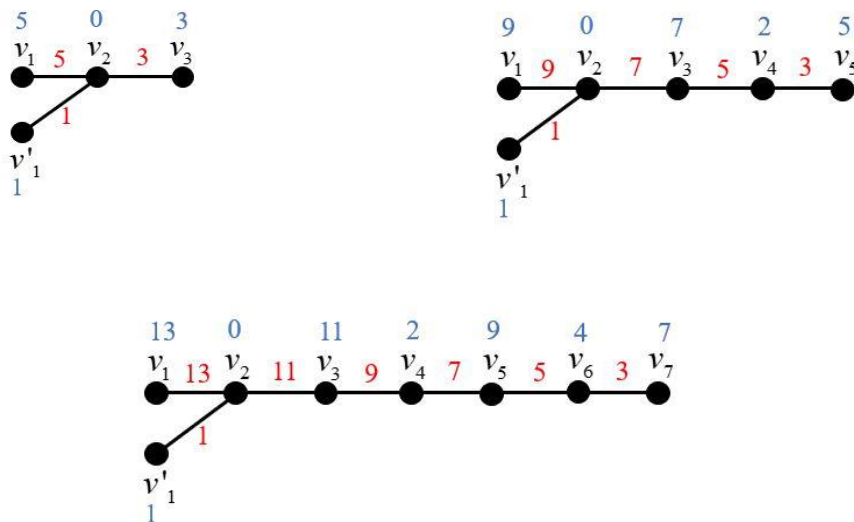


Figure 4.

The odd graceful graph G when $n = 4, 6, 8$ show in Figure 5.

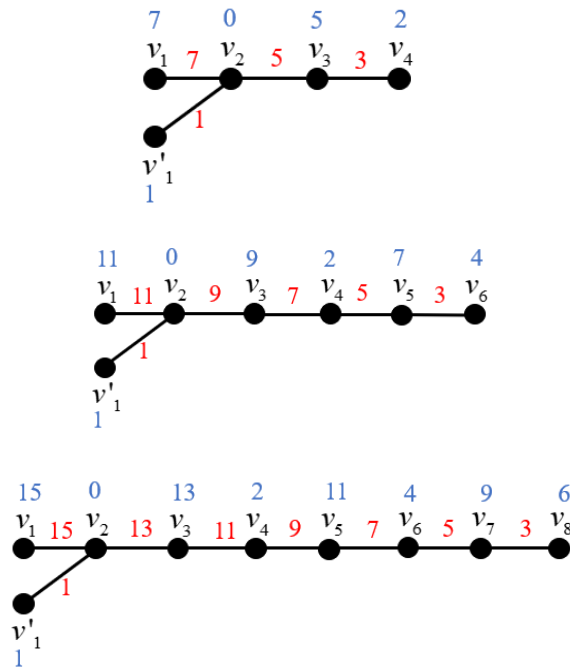


Figure 5.

Theorem 2. Let P_n be a path with $V(P_n) = \{v_1, v_2, v_3, \dots, v_n\}$. The graph obtained by duplicating a vertex v_2 in a path P_n is an odd graceful graph.

Proof. Let P_n be a path with n vertex and let v_i where $1 \leq i \leq n$ be the successive vertices of the P_n such that v_i is adjacent to v_{i+1} . Let G be the graph obtained by duplicating a vertex v_2 of P_n by a vertex v'_2 . Hence $|E(G)| = q = n+1$, $V(G) = \{v_1, v_2, v_3, \dots, v_n\} \cup \{v'_2\}$ and $|V(G)| = n+1$.

We define the vertex labeling $f : V(G) \rightarrow \{0, 1, 2, \dots, 2(n+1)-1\}$ as follows.

$$f(v'_2) = 3.$$

If n is even

$$f(v_i) = 2(n+1) - i + 1, \quad i = 2, 4, 6, \dots, n.$$

$$\{f(v_i) | i = 2, 4, 6, \dots, n\} = \{2(n+1) - 1, 2(n+1) - 3, 2(n+1) - 5, \dots, n+3\}.$$

$$f(v_i) = i - 1, \quad i = 1, 3, 5, 7, \dots, n-1.$$

$$\{f(v_i) | i = 1, 3, 5, 7, \dots, n-1\} = \{0, 2, 4, \dots, n-2\}.$$

If n is odd

$$f(v_i) = 2(n+1) - i + 1, \quad i = 2, 4, 6, \dots, n-1.$$

$$\{f(v_i) | i = 2, 4, 6, \dots, n-1\} = \{2(n+1) - 1, 2(n+1) - 3, 2(n+1) - 5, \dots, n+4\}.$$

$$f(v_i) = i - 1, \quad i = 1, 3, 5, 7, \dots, n.$$

$$\{f(v_i) | i = 1, 3, 5, 7, \dots, n-1\} = \{0, 2, 4, \dots, n-1\}.$$

Clearly f is an injective.

From the vertex labeling f . Next, we consider the induced edge labeling function $f^* : E(G) \rightarrow \{1, 3, 5, \dots, 2q-1 = 2(n+1)-1\}$ such that $f^*(uv) = |f(u) - f(v)|$ as follows.

$$f^*(v_1 v'_2) = 3.$$



$$f^*(v_3v'_2) = 1.$$

$$f^*(v_iv_{i+1}) = 2(n+1) - 2i + 1, \quad i = 1, 2, 3, 4, \dots, n-1$$

$$\{f^*(v_iv_{i+1}) \mid i = 1, 2, 3, 4, \dots, n-1\} = \{2(n+1) - 1, 2(n+1) - 3, 2(n+1) - 5, \dots, 5\}.$$

Thus

$$\begin{aligned} \{f^*(E(G))\} &= \{f^*(v_1v'_2)\} \cup \{f^*(v_3v'_2)\} \cup \{f^*(v_iv_{i+1}) \mid i = 1, 2, 3, 4, \dots, n-1\} \\ &= \{1, 3, 5, \dots, 2(n+1) - 3, 2(n+1) - 1\}. \end{aligned}$$

It is obvious that f^* is a bijective. Then G is the odd graceful graph. \square

Figure 6 show the odd graceful graph G with the odd graceful labeling in Theorem 2 when $n = 3, 5, 7$. The odd graceful graph G when $n = 4, 6, 8$ show in Figure 7.

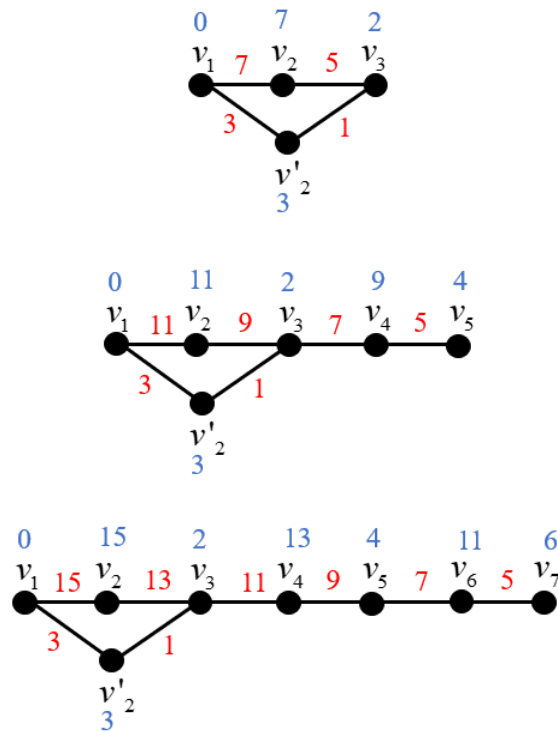
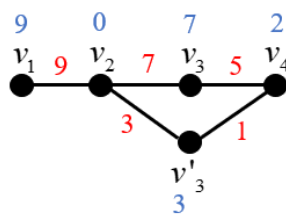


Figure 6.



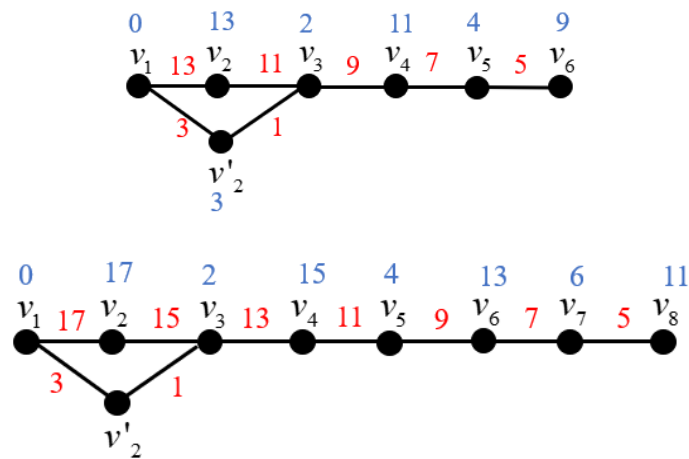


Figure 7.

Conclusion:

Motivated by the recent work of an odd graceful labeling, we proved the new theorem of odd graceful labeling of the graph G obtained by duplication a vertex of a path graph P_n by a new vertex.

References:

1. Abdel-Aal, M. E. GRAPH-HOC. 2013. Vol. 5, No. 2.
2. Gnanajothi, R.B. Topics in graph theory, Ph.D. thesis, Madurai Kamaraj University, India.
3. Gross, J.L. and Yellen J. Graph theory and Its Applications. Chapman & Hall/CRC Taylor & Francis Group. 2006.
4. Seoud, M.A. and Abdel-Aal M.E. Ars Combin. 2013. Vol. 108, pp.161-185.
5. Vaidya, S.K. and Shah, N.H. International Journal of Mathematics and Soft Computing. 2013, Vol.3, No.1, 61-68.



OPTIMIZING THE PARAMETERS OF PROFIT-RELATIVE VIGOR INDEX STRATEGY FOR INVESTMENT IN GOLD MARKET

Worarat Srisurat, Weenakorn Ieosanurak, Watcharin Klongdee*.

Department of Mathematics, Faculty of Science, Khon Kaen University, Khon Kaen 40002, Thailand

*e-mail: kwatch@kku.ac.th

Abstract

This research investigates the profitability of gold trading strategies using both the traditional Relative Vigor Index (Classical RVI formula) and a newly improved version (Adjusted RVI formula). We utilized daily gold price data from January 1, 2021, to December 31, 2023, and subsequently tested the performance of these strategies on data from January 1, 2024, to June 30, 2024. For the Classical RVI formula, we determined the optimal value of N denotes the days used in the RVI, which was found to be 16. Conversely, for the Adjusted RVI formula, we identified the top 5 optimal sets of parameters. The parameters considered include N , the number of lookback days used in the simple moving average formula; T , the number of lookback days used in the Denominator (DT) and Numerator (NT) formulas; the Signal Line (SL); and w , the weight factor. Our experimental results indicate that the Adjusted RVI formula, which has optimized the best parameters including $N = 4$, $T = 49$, and $w = 0.91$, performs significantly better than the Classical RVI formula in terms of profitability, achieving an increase of 96.66%. Specifically, the Adjusted RVI formula consistently generated higher returns throughout the testing period, validating its effectiveness in producing reliable and profitable trading signals in the gold market. These findings underscore the potential benefits of using the Adjusted RVI formula over the Classical RVI formula, particularly for traders and investors looking to enhance their strategies in the dynamic gold market.

Key words: Relative Vigor Index, Classical RVI formula, adjusted RVI formula, Gold price, trading strategy, Optimal Parameters, Technical Analysis.

Introduction

As reported by the World Gold Council, the global gold market has become a subject of heightened interest, and the price of gold is considerably above its historical norm. Gold stands out as an exceptional asset, exhibiting features of both a commodity and a form of money [9]. It functions as a reservoir of riches, a standard of worth, and a channel for trade. Also, Ciner [2] said that gold is a highly marketable investment. Gold prices can serve as an indicator of the health of the economy. In times of crisis and elevated risk aversion, many investors turn to gold, the ultimate haven, to protect their capital.

Technical Analysis [7] refers to the study and analysis of price movements in financial markets using charts and various indicators. Examples of commonly used tools in technical analysis include moving averages, the relative strength index (RSI), the moving average convergence divergence (MACD), and the relative vigor index (RVI). Benefits of technical analysis include: predicting future price trends: It helps forecast potential future movements of asset prices, providing valuable information for making investment decisions. Identifying entry and exit points: It aids in determining optimal points for buying and selling to enhance profit opportunities. Understanding market conditions: It offers insights into market conditions and investor behavior, which can be used to develop appropriate investment strategies. This approach is based on the belief that historical data



and price patterns reflect future price movements.

In various research studies, technical analysis tools such as RSI and MACD are commonly used to analyze price movements and make investment decisions. However, RVI has not been studied in depth.

Examples of studies that primarily focus on RSI and MACD include: Nithya et al. (2014) [8] analyzed three stocks from the banking sector using MACD and RSI. they used a descriptive method to study the price trend of three stocks using MACD and RSI charting techniques of technical analysis. They also suggest that the investment is based on the risk appetite of the investor. Jensen and Benington (1999) [5] researched technical analysis and found that past data is not a reliable indicator of future price movements. Their study primarily used RSI and MACD. Allen and Karjalainen (2011) [1] established that technical trading rules do not result in above-average returns compared to a buy-and-hold strategy, considering transaction expenses. Their research also included the use of RSI and MACD. Hardiyanti W. and Darnius O. (2021) [4] compared the analytical results for gold futures from August 1, 2018, to July 31, 2019. They found that the total profit for the year using the MACD signal indicator was 532.39 points per lot, while the total annual profit using the RVI signal indicator was 1304.84 points per lot. This indicates that the RVI is a highly effective tool in the gold market.

Despite the popularity of RSI and MACD, RVI which measures the strength of price movements, has not been extensively studied in most research. Investigating RVI may provide additional insights and enhance understanding of this technical indicator's role in financial market analysis.

Studying RVI can help fill gaps in knowledge about technical indicators and diversify the methods used for analyzing price movements. Research on RVI might reveal whether this indicator provides more valuable information in specific markets or under certain conditions. Additionally, examining RVI could lead to the development of more effective and reliable analytical tools for investors.

Therefore, studying the RVI is both important and intriguing for expanding our understanding and enhancing technical analysis tools in financial markets.

The study examines the profitability of gold trading strategies utilizing the RVI. We analyzed gold price data from January 1, 2021, to December 31, 2023. After defining the trading strategy, we identified the optimal parameters for the RVI strategy in the gold exchange rate. Additionally, we revised the RVI formula to make it more general by determining the appropriate parameters for the modified formula to maximize profits in the gold market.

Methodology

In this section, we will discuss the data used in the research and the scope of the indicators employed as guidelines for developing the RVI strategy. This encompasses the buyer-seller index indicators, the scope of parameters used in the RVI strategy, and the software employed in strategy development.

Data used in the research

The data used in the study and strategy development consists of daily gold price data from January 1, 2021, to December 31, 2023 (the data shown in Figure 1). Test the parameters from January 1 to June 30, 2024 (the data shown in Figure 2). The research aims to analyze the return rates (profits and losses) to make informed decisions regarding selling and maximize overall investment gains.

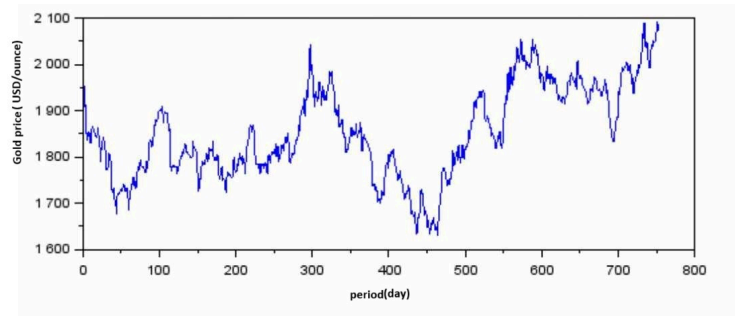


Figure 1: Daily gold prices for training from January 1, 2021, to December 31, 2023.

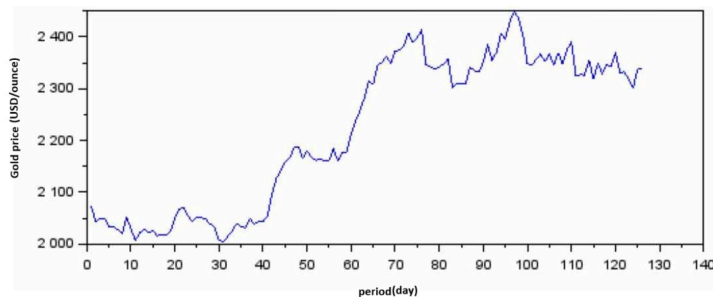


Figure 2: Daily gold prices for testing from January 1 to June 30, 2024.

Indicator

For the research, the leading indicators studied and used as a guideline for developing a new strategy include the buyer-seller index indicators. The scope of the RVI values is set from -1 to 1, as it represents the possible range of RVI and provides analyzable values.

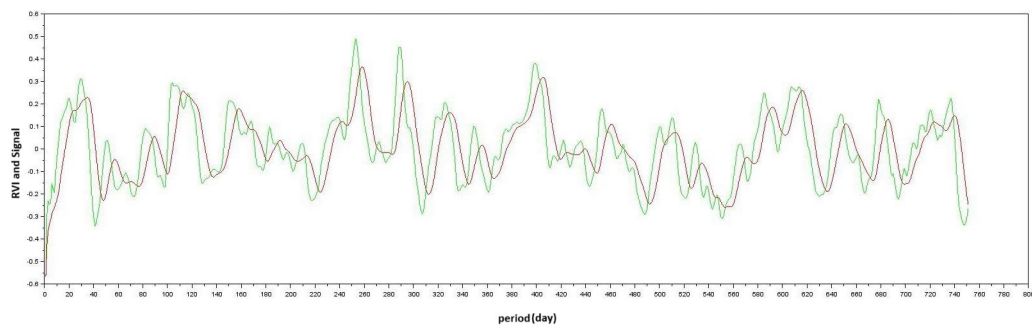


Figure 3: The classical RVI values of the gold prices from January 1, 2019, to December 31, 2019.

Figure 3 shows an example of $RVI(i, N = 2)$; the experiment's outcome that we have shown produces the most significant profit in the modified formula. The signal line, often known as the red line, also represents the weighted moving average of the RVI value.

The RVI is a technical indicator used in financial markets to assess the strength of price movements. Developed by John Ehlers [3] in 1995, the RVI measures the relative vigor of a price trend by comparing the current closing price to the previous closing price. Specifically, it gauges



the strength of the market trend and evaluates the likelihood of either a continuation or reversal of that trend.

The classical RVI formula

$$\text{NUMERATOR}_i = \frac{a + (2 \times b) + (2 \times c) + d}{6}, \quad (1)$$

$$\text{DENOMINATOR}_i = \frac{e + (2 \times f) + (2 \times g) + h}{6}, \quad (2)$$

$$\text{RVI}(i, N) = \frac{\sum_{j=i}^{i-N+1} \text{NUMERATOR}_j}{\sum_{j=i}^{i-N+1} \text{DENOMINATOR}_j}, \quad (3)$$

$$\text{Signal Line}_i = \frac{\text{RVI}(i, N) + 2 \times \text{RVI}(i-1, N) + 2 \times \text{RVI}(i-2, N) + \text{RVI}(i-3, N)}{6}, \quad (4)$$

N is the number of lookback days used in the NUMERATOR and DENOMINATOR,

where a = Close price – Open price at time i , b = Close price – Open price One Bar Prior to a at time $i-1$, c = Close price – Open price One Bar Prior to b at time $i-2$, d = Close price – Open price One Bar Prior to c at time $i-3$, e = High price – Low price of Bar a at time i , f = High price – Low price of Bar b at time $i-1$, g = High price – Low price of Bar c at time $i-2$, h = High price – Low price of Bar d at time $i-3$.



Figure 4: $\text{RVI}(i, N = 10)$ chart of gold price daily (XAU/USD) at time 24 Feb 2022 to 31 Oct 2022.

Figure 4 shows daily gold prices at the top of Figure 4 and the $N = 10$ day backward looking Relative Vigor Index (RVI) at the bottom of Figure 4. In the bottom panel, the RVI signal (green line) represents the RVI, and the red line represents the signal line (red line). When these two lines cross, it indicates a trading signal (buy or sell signals) shown in Buy and Sell signals section.

Buy and Sell signals

The occurrence of a buy or sell signal must meet all conditions as follows;



Buy signal

This section will discuss the Buying strategies in the gold market from our research.

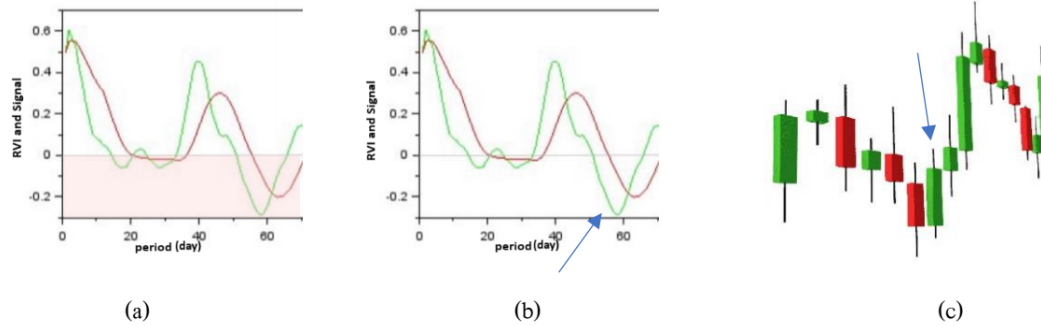


Figure 5: Rule - The process of entering a buy order.

Figure 5 the X-axis represents the period of days, and the Y-axis represents the values of the RVI and Signal.

Consider the following conditions for opening a buy order:

1. The RVI value (green line) must be below 0, as shown in Figure 5(a).
2. The RVI value (green line) must cross above the Signal line (red line) and form an upward angle, as shown in Figure 5(b).
3. A closing price must be higher than the opening price at the time corresponding to conditions 1 and 2, as indicated by the green candlestick with an arrow in Figure 5(c) (Bullish candlestick pattern).

Sell signal

This section will discuss the selling strategies in the gold market from our research.

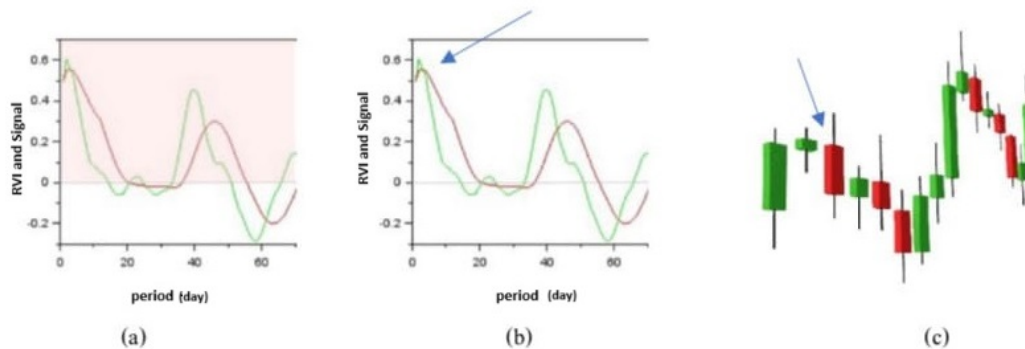


Figure 6: Rule - The process of entering a sell order.



Figure 6 the X-axis represents the period, and the Y-axis represents the values of the RVI and Signal.

Consider the following conditions for opening a sell order:

1. The RVI value (green line) must be above 0, as shown in Figure 6(a).
2. The RVI value (green line) must cross below the Signal line (red line) and form a downward angle, as shown in Figure 6(b).
3. A closing price must be lower than the opening price at the time corresponding to conditions 1 and 2, as indicated by the red candlestick with an arrow in Figure 6(c) (Bearish candlestick pattern).

Parameter scope

We use sufficient initial capital for trading one ounce of gold and for subsequent trades, ensuring that we only consider trading one ounce per order. The classical RVI formula has one parameter, so we optimized the parameter N to find its optimal value. In the same way, the adjusted RVI formula has three parameters, so we optimize three parameters: N , T , and w . Each parameter has specific constraints, which are defined as follows:

1. N denotes the days used in the RVI, such that $N = 3, 4, 5, \dots, 100$.
2. T denotes the number of data used in NUMERATOR (NT), DENOMINATOR (DT), and Signal Line (SL), such that $T = 1, 2, \dots, 100$.
3. The weight factor of the adjusted RVI formula, w ranges between 0 and 1.

Adjusted RVI formula

We will present the adjusted RVI formula. We aimed to make it more general, and thus, we revised the formula as follows: Let O_n, C_n, H_n , and L_n be the open, closed, highest, and lowest prices, respectively, of time period n . Let $p_n = C_n - O_n$ and $q_n = H_n - L_n$, we have

$$NT(i) = \frac{w}{2}p_i + \frac{1-w}{T} \sum_{k=1}^{i-T} p_{i-k} + \frac{w}{2}p_{i-T-1}, \quad (5)$$

and

$$DT(i) = \frac{w}{2}q_i + \frac{1-w}{T} \sum_{k=1}^{i-T} q_{i-k} + \frac{w}{2}q_{i-T-1}. \quad (6)$$

The relative vigor index of period N is defined by

$$RVI(i, N) = \frac{NT(i) + NT(i-1) + NT(i-2) + \dots + NT(i-N+1)}{DT(i) + DT(i-1) + DT(i-2) + \dots + DT(i-N+1)}, \quad (7)$$

and the signal line of period i is given by

$$SL(i) = \frac{w}{2}RVI(i, N) + \frac{1-w}{T} \sum_{k=1}^{i-T} RVI(i-k, N) + \frac{w}{2}RVI(i-T-1, N), \quad (8)$$

where the weight factor is $w \in (0, 1)$, $T = 1, 2, \dots, 100$, $N = 3, 4, 5, \dots, 100$, i is number of data.

Note: If $w = \frac{1}{3}$, and $T = 2$, the adjusted RVI formula will revert to the classical RVI formula.



Optimizing parameter algorithm

1. **Benchmark Creation:** Begin by establishing a benchmark using the classical RVI formula to determine the optimal value of N for the gold price data under evaluation. The optimal N is defined as the one that yields the highest profit.
2. **Parameter Setup:** This study employs the Scilab program and utilizes daily gold price data spanning from January 1, 2021, to December 31, 2023, to develop the RVI strategy. The parameter ranges are defined as follows: N varies from 3 to 100 ($N = 3, 4, 5, \dots, 100$), Prior T ranges from 1 to 100 ($T = 1, 2, 3, \dots, 100$), and the parameter w ranges from 0.00 to 0.99 in increments of 0.01.
3. **Experimental Design:** Develop and execute a program to identify the optimal parameters for the adjusted RVI formula. The program should search for and display the top 5 sets of parameters that yield the highest profits. Create a function to maximize profit, where the inputs are N , T , and w . The function should return the profit from the investment using these specific values. The top five parameter sets will be determined by comparing the profits across all possible parameter combinations within the specified ranges.
4. **Validation:** After identifying the top 5 sets of optimal parameters, test these parameters on gold price data from January 1 to June 30, 2024. The goal is to confirm that the adjusted RVI formula produces higher profits compared to the classical RVI formula, as hypothesized.

Results and Discussion

We use the strategy described in Section for trading gold, where k represents the occurrence of an order, T_k denotes the days on which the k th signal occurred, Price_{T_k} is the price of gold on the date T_k , and the order refers to either a buy or sell action. Finally, The profit from the k -th trade is given by:

$$\text{Profit}_k = \text{Price}_{T_k} - \text{Price}_{T_{k-1}},$$

where:

Price_{T_k} is the price of gold at the time of closing the order,

$\text{Price}_{T_{k-1}}$ is the price of gold at the time of opening the order.

Results of classical RVI formula

From the parameter optimization algorithm based on the classical RVI formula, as Equation (1)-(4), the best result for parameter N is 16. Additionally, we show investment result base on classical with $N = 16$. as shown in Table 1. According to Table 1, the first signal occurred on the day $T_1 = 54$ (March 22, 2021), when the gold price was 1738.10 USD/ounce, and we opened a buy order for one troy ounce. The subsequent signal was a sell signal on day $T_2 = 80$ (April 28, 2021), in which the gold price was 1773.90 USD/ounce. We closed the buy order and got a profit of $1773.90 - 1738.10 = 35.80$ USD. After that, we opened a sell order (short sale) for one troy ounce of gold. Subsequently, on the day $T_3 = 128$ (July 7, 2021), in which the gold price was 1802.10 USD/ounce. The next signal we received a buy signal, and the sell order was closed and took a profit of $1773.90 - 1802.10 = -28.20$ USD. Similarly, when the $T_{36} = 737$ (December 6, 2023) at the price of 2047.90 USD/ounce, the sell signal was triggered, and the existing buy order was closed, resulting in a profit of 63.2 USD. Upon encountering the final signal at $T_{37} = 752$ (December 28, 2023) the price



of 2083.90 USD/ounce, the sell order was closed, yielding a profit of $2047.90 - 2083.50 = -35.6$ USD. Trading according to this strategy resulted in a total profit of 853.4 USD.

Table 1: Buy and sell signals of the classical RVI formula, where $N=16$.

| k | T_k | $Price_{T_k}$ | Order | | Profits |
|-----|-------|---------------|-------|-------|---------|
| | | | Open | Close | |
| 1 | 54 | 1738.10 | Buy | | 0 |
| 2 | 80 | 1773.90 | | Buy | 35.80 |
| | | | Sell | | |
| 3 | 128 | 1802.10 | | Sell | -28.20 |
| | | | Buy | | |
| 4 | 137 | 1811.40 | | Buy | 9.30 |
| | | | Sell | | |
| 5 | 155 | 1778.20 | | Sell | 33.20 |
| | | | Buy | | |
| 6 | 172 | 1793.50 | | Buy | 15.30 |
| | | | Sell | | |
| 7 | 189 | 1758.40 | | Sell | 35.10 |
| | | | Buy | | |
| 8 | 201 | 1770.50 | | Buy | 12.10 |
| | | | Sell | | |
| 9 | 242 | 1798.20 | | Sell | -27.70 |
| | | | Buy | | |
| 10 | 255 | 1825.10 | | Buy | 26.90 |
| | | | Sell | | |
| 11 | 275 | 1804.10 | | Sell | 21 |
| | | | Buy | | |
| 12 | 292 | 1943.80 | | Buy | 139.75 |
| | | | Sell | | |
| 13 | 310 | 1954.20 | | Sell | -10.40 |
| | | | Buy | | |
| 14 | 327 | 1955.60 | | Buy | 1.40 |
| | | | Sell | | |
| 15 | 347 | 1815.90 | | Sell | 139.70 |
| | | | Buy | | |
| 16 | 365 | 1813.50 | | Buy | -2.40 |
| | | | Sell | | |
| 17 | 392 | 1719.10 | | Sell | 94.40 |
| | | | Buy | | |
| 18 | 409 | 1776.70 | | Buy | 57.60 |
| | | | Sell | | |
| 19 | 425 | 1728.60 | | Sell | 48.10 |
| | | | Buy | | |

| k | T_k | $Price_{T_k}$ | Order | | Profits |
|--------------|-------|---------------|-------|-------|---------|
| | | | Open | Close | |
| 20 | 455 | 1656.30 | | Buy | -72.30 |
| | | | Sell | | |
| 21 | 463 | 1650.00 | | Sell | 6.30 |
| | | | Buy | | |
| 22 | 483 | 1815.20 | | Buy | 165.20 |
| | | | Sell | | |
| 23 | 490 | 1792.30 | | Sell | 22.90 |
| | | | Buy | | |
| 24 | 495 | 1797.70 | | Buy | 5.40 |
| | | | Sell | | |
| 25 | 543 | 1845.40 | | Sell | -47.70 |
| | | | Buy | | |
| 26 | 559 | 1995.90 | | Buy | 150.50 |
| | | | Sell | | |
| 27 | 587 | 2037.00 | | Sell | -41.10 |
| | | | Buy | | |
| 28 | 621 | 1923.70 | | Buy | -113.30 |
| | | | Sell | | |
| 29 | 628 | 1929.50 | | Sell | -5.80 |
| | | | Buy | | |
| 30 | 646 | 1999.90 | | Buy | 70.40 |
| | | | Sell | | |
| 31 | 655 | 1947.10 | | Sell | 52.80 |
| | | | Buy | | |
| 32 | 674 | 1942.50 | | Buy | -4.60 |
| | | | Sell | | |
| 33 | 701 | 1934.30 | | Sell | 8.20 |
| | | | Buy | | |
| 34 | 717 | 1973.50 | | Buy | 39.20 |
| | | | Sell | | |
| 35 | 725 | 1984.70 | | Sell | -11.20 |
| | | | Buy | | |
| 36 | 737 | 2047.90 | | Buy | 63.20 |
| | | | Sell | | |
| 37 | 752 | 2083.50 | | Sell | -35.60 |
| | | | | | |
| Total Profit | | | | | 853.40 |

Figure 7 shows the daily close price data and the Classical RVI of XAU/USD using the Classical RVI strategy with optimal parameter $N = 16$. The blue line in the daily close price data chart represents the daily close price data of XAU/USD. In the RVI chart, the green line represents the RVI of XAU/USD, and the red line is the Signal line. The following graph displays the buy and sell signals as shown in Table 1. By RVI indicator with the strategy in Section , we found the first buy order signal at $T_1 = 54$ (March 22, 2021). When time passes, using the RVI indicator with the strategy described in Section , we encounter the second signal on day 80, at $T_2 = 80$ (April 28, 2021). An open sell order signal prompts us to close the buy order. After that, signals continued to appear until we encountered the final signal on day 752. We closed the sell order at $T_{37} = 752$ (December 28, 2023).

Note: Figure 7 shows that the black dots indicate the opening of a buy order, while the pink dots represent the opening of a sell order.



Figure 7: The gold price chart and the crossing between the RVI value (green line) and the signal line (red line) with optimal parameter $N=16$.

Results of adjusted RVI formula

From the experimental results, the top 5 optimal sets of parameters for the gold market during the period from January 1, 2021, to December 31, 2023, were identified. The most suitable parameters for the adjusted RVI formula, ranked from highest to lowest, are as follows:

Table 2: The top 5 optimal sets of parameters in adjusted RVI formula.

| N | T | w | Total Profit |
|-----|-----|------|--------------|
| 4 | 49 | 0.91 | 1677.20 |
| 4 | 49 | 0.89 | 1673.80 |
| 4 | 49 | 0.90 | 1673.80 |
| 4 | 49 | 0.87 | 1640.20 |
| 4 | 49 | 0.88 | 1640.20 |

From the parameter optimization algorithm based on the adjusted RVI formula, the best result for the parameter is shown in Table 2. The experimental results show that the buy and sell signals generated by all 5 sets of parameters are identical.

We will present the buy and sell signals obtained from optimizing the best parameters, which are $N = 4$, $T = 49$, and $w = 0.91$. The details of the signals are as follows:

Form Table 3, the first signal occurred on the day $T_1 = 57$ (March 25, 2021), when the gold price was 1725.50 USD/ounce, and we opened a buy order for one troy ounce. The subsequent signal was a sell signal on day $T_2 = 110$ (June 10, 2021), in which the gold price was 1896.40 USD/ounce. We closed the buy order and got a profit of $1896.40 - 1725.50 = 171.30$ USD. After that, we opened



a sell order (short sale) for one troy ounce of gold. Subsequently, on the day $T_3 = 117$ (June 21, 2021), in which the gold price was 1782.90 USD/ounce. The next signal we received a buy signal, and the sell order was closed and took a profit of $1896.40 - 1782.90 = 113.50$ USD. Similarly, when the $T_{34} = 713$ (November 1, 2023) at the price of 1987.50 USD/ounce, the Buy signal was triggered, and the existing Sell order was closed, resulting in a profit of 155.70 USD. Upon encountering the final signal $T_{35} = 722$ (November 14, 2023) at the price of 1966.50 USD/ounce, the buy order was closed, yielding a profit of $1987.50 - 1966.50 = 21.00$ USD. Trading according to this strategy resulted in a total profit of 1677.20 USD.

Table 3: Buy and sell signals of the adjusted RVI formula with $N = 4$, $T = 49$, and $w = 0.91$.

| k | T_k | $Price_{T_k}$ | Order | | Profits |
|-----|-------|---------------|-------|-------|---------|
| | | | Open | Close | |
| 1 | 57 | 1725.50 | Buy | | 0 |
| 2 | 110 | 1896.40 | | Buy | 171.30 |
| 3 | 117 | 1782.90 | Sell | | 113.50 |
| 4 | 123 | 1763.60 | Buy | | -19.30 |
| 5 | 140 | 1881.80 | | Sell | -38.20 |
| 6 | 141 | 1799.20 | Buy | | -2.60 |
| 7 | 164 | 1795.20 | | Sell | 2.00 |
| 8 | 168 | 1816.00 | Buy | | 20.80 |
| 9 | 188 | 1757.00 | | Sell | 59.00 |
| 10 | 251 | 1814.1 | Buy | | 57.10 |
| 11 | 260 | 1827.30 | | Sell | -13.20 |
| 12 | 263 | 1812.40 | Buy | | -14.90 |
| 13 | 275 | 1804.10 | | Sell | 8.30 |
| 14 | 299 | 2000.40 | Buy | | 196.30 |
| 15 | 307 | 1921.50 | | Sell | 78.90 |
| 16 | 311 | 1939.80 | Buy | | 18.30 |
| 17 | 319 | 1937.80 | | Sell | 2.00 |
| 18 | 358 | 1850.20 | Buy | | -87.60 |
| | | | | Sell | |

| k | T_k | $Price_{T_k}$ | Order | | Profits |
|--------------|-------|---------------|-------|-------|---------|
| | | | Open | Close | |
| 19 | 366 | 1819.60 | | Buy | 30.60 |
| 20 | 370 | 1838.40 | Sell | | 18.80 |
| 21 | 390 | 1713.40 | Buy | | 125.00 |
| 22 | 445 | 1709.30 | | Sell | -4.10 |
| 23 | 455 | 1656.30 | Buy | | 53.00 |
| 24 | 520 | 1930.00 | | Sell | 273.70 |
| 25 | 530 | 1878.50 | Buy | | 51.50 |
| 26 | 559 | 1995.90 | | Sell | 117.40 |
| 27 | 583 | 1999.00 | Buy | | -3.10 |
| 28 | 592 | 2037.10 | | Sell | 38.10 |
| 29 | 622 | 1929.30 | Buy | | 107.50 |
| 30 | 639 | 1980.80 | | Sell | 51.20 |
| 31 | 643 | 1963.70 | Buy | | 17.10 |
| 32 | 679 | 1932.80 | | Sell | -30.90 |
| 33 | 694 | 1831.80 | Buy | | 101.00 |
| 34 | 713 | 1987.50 | | Sell | 155.70 |
| 35 | 722 | 1966.50 | Buy | | 21.00 |
| | | | | Buy | |
| Total Profit | | | | | 1677.2 |

Figure 8 shows the daily close price data and the adjusted RVI of XAU/USD using the adjusted RVI strategy with the parameter in Table 2. The blue line in the daily close price data chart represents the daily close price data of XAU/USD. In the RVI chart, the green line represents the RVI of XAU/USD, and the red line is the Signal line. The following graph displays the buy and sell signals as shown in Table 3. By RVI indicator with the strategy in section , we found the first buy order signal at $T_1 = 57$ (March 25, 2021). When time passes, using the RVI indicator with



the strategy described in Section , we encounter the second signal on day 110, at $T_2 = 110$ (June 10, 2021). An open sell order signal prompts us to close the buy order. After that, signals continued to appear until we encountered the final signal on day 722. We closed the buy order at $T_{35} = 722$ (November 14, 2023).

Note: Figure 8 shows that the black dots indicate the opening of a buy order, while the pink dots represent the opening of a sell order

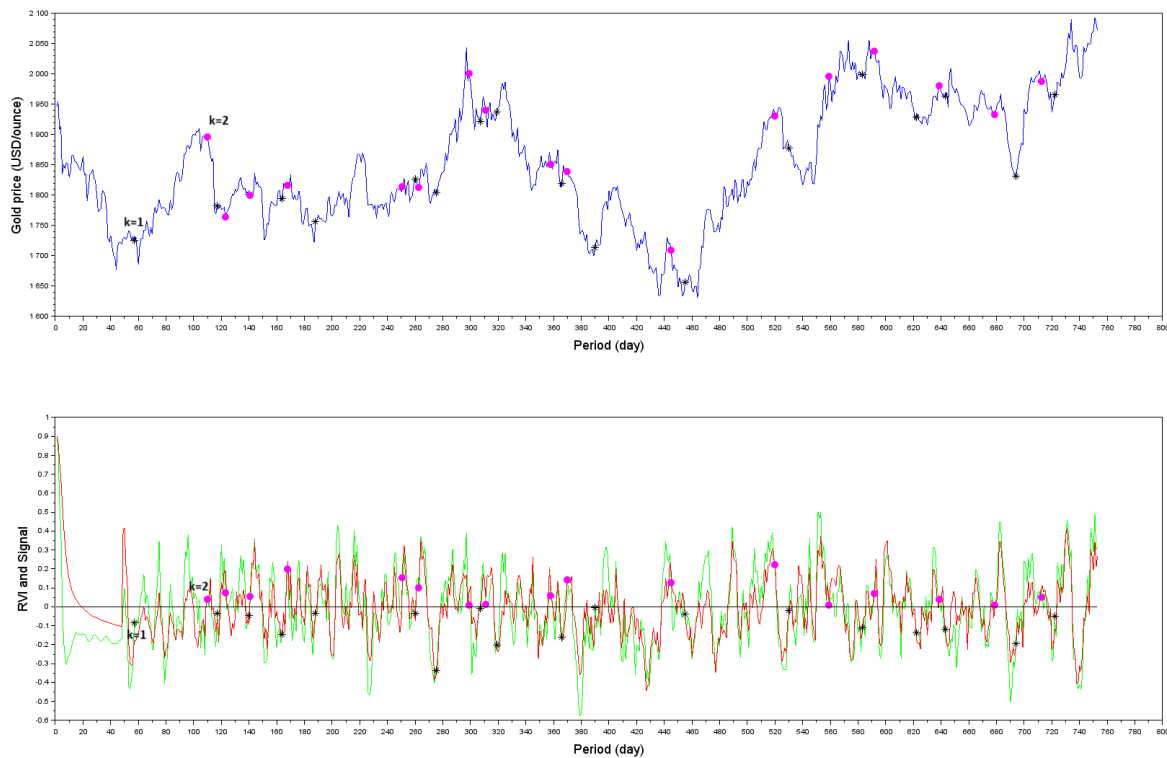


Figure 8: The price chart (top) and the crossing between the RVI value (green line) and the signal line (red line) with the best parameters of the adjusted RVI formula (bottom).

Method for Testing Parameters

Classical RVI formula

Form Table 4, for validation purposes, we tested the classical RVI formula with parameters $N = 16$ against the gold price from January 1 to June 30, 2024, it was found that there were a total of 4 trading signals. The first signal occurred on $T_1 = 58$ (March 25, 2024) with a sell order. Upon encountering the second signal on $T_2 = 94$ (May 15, 2024) at a price of 2405.80 USD/ounce, the sell order was closed and a buy order was opened. This resulted in a profit of $2176.40 - 2405.80 = -229.40$ USD, a common occurrence when following signals that do not yield profits. The third signal resulted in a profit of $2345.40 - 2405.80 = -60.40$ USD. The final signal resulted in an additional profit of $2345.40 - 2349.10 = -3.70$ USD, bringing the total profit to -293.50 USD.

Table 4: Buy and sell signals of the classical RVI formula, where $N=16$.

| k | T_k | $Price_{T_k}$ | Order | | Profits |
|--------------|-------|---------------|-------|-------|---------|
| | | | Open | Close | |
| 1 | 58 | 2176.40 | Sell | | 0 |
| 2 | 94 | 2405.80 | | Sell | -229.40 |
| | | | Buy | | |
| 3 | 101 | 2345.40 | | Buy | -60.40 |
| | | | Sell | | |
| 4 | 116 | 2349.10 | | Sell | -3.70 |
| | | | | | |
| Total Profit | | | | | -293.50 |

Adjusted RVI formula

From Table 5, for validation purposes, we tested the adjusted RVI formula with the best parameters from the 5 sets against in table 2 of the gold price from January 1 to June 30, 2024, it was found that there were a total of 3 trading signals. The first signal occurred on $T_1 = 50$ (March 13, 2024) with a buy order. Upon encountering the second signal on $T_2 = 117$ (June 17, 2024) at a price of 2329.00 USD/ounce, the buy order was closed and a sell order was opened. This resulted in a profit of $2329.00 - 2180.80 = 148.20$ USD. The final signal resulted in an additional profit of $2329.00 - 2336.60 = -7.60$ USD, resulting in a total profit of 140.60 USD.

Table 5: Buy and sell signals of the adjusted RVI formula with $N = 4$, $T = 49$, and $w = 0.91$.

| k | T_k | $Price_{T_k}$ | Order | | Profits |
|--------------|-------|---------------|-------|-------|---------|
| | | | Open | Close | |
| 1 | 50 | 2180.80 | Buy | | 0 |
| 2 | 117 | 2329.00 | | Buy | 148.20 |
| | | | Sell | | |
| 3 | 125 | 2336.60 | | Sell | -7.60 |
| | | | | | |
| Total Profit | | | | | 140.60 |

Conclusion

This research investigates trading strategies in the gold market using the relative vigor index (RVI) strategy, both in its traditional form and an enhanced version with fixed returns. The training data spans from January 1, 2021, to December 31, 2023, with testing data from January 1 to June 30, 2024. In the initial phase, we examined the profitability of a trading strategy employing the Classical RVI formula in the gold market. From the experimental results, it was found that the highest profit, with an optimal parameter $N = 16$, was 853.40 USD. We used a maximum investment of 2,083.5 USD/ounce for each trading transaction, with a profit calculated as

$$\text{Percentage Profit} = \left(\frac{853.40}{2083.5} \right) \times 100 \approx 40.95\%.$$

Thus, the profit represents approximately 40.95% of the investment.

In the next part, we studied the potential for achieving maximum profits in the gold market using the adjusted RVI formula, which we newly enhanced. We identified the top 5 sets of parameters that yielded identical trading signals and profits, as shown in Table 2. Across these 5 parameter sets, we found that only the values of w denote 0.91, 0.89, 0.90, 0.87, and 0.88 differed slightly, while $N = 4$ and $T = 49$ remained consistent. The experiments revealed that the adjusted formula



led to profits as high as 1677.20 USD. We used a maximum investment of 1966.5 USD/ounce for each trading transaction, with a profit calculated as

$$\text{Percentage Profit} = \left(\frac{1677.20}{1966.50} \right) \times 100 \approx 85.29\%.$$

Thus, the profit represents approximately 85.29% of the investment.

When comparing the maximum profit from the classical RVI formula with the adjusted RVI formula, it was found that the profit increased to

$$\frac{1677.20 - 853.40}{853.40} \times 100 \approx 96.66\%,$$

which demonstrates an increase in profit of approximately 96.66% from using the adjusted RVI formula compared to the classical RVI formula.

Finally, we applied the best-performing parameters to test on new data, specifically the gold price from January 1 to June 30, 2024. As hypothesized, the adjusted RVI formula generated higher profits compared to the classical RVI formula. The highest profit obtained from the classical RVI formula was -293.50 USD, whereas the adjusted RVI formula yielded a maximum profit of 140.60 USD, confirming our hypothesis that the adjusted RVI formula outperforms the classical RVI formula in generating profits.

Acknowledgements

I would like to express my gratitude to the reviewers from the STT50 conference for their valuable advice and guidance in preparing this document. Additionally, I would like to thank the support from the Development and Promotion of Science and Technology Talents Project

References

- [1] Allen F, Karjalainen R. Using genetic algorithms to find technical trading rules. *J Financ Econ.* 1999;51(2):245–271.
- [2] Ciner C. On the long-run relationship between gold and silver: A note. *Global Finance J.* 2011;12(3):299–303.
- [3] Ehlers J. The Relative Vigor Index (RVI): A new indicator for trend analysis. *J Tech Anal.* 1995;20(4):55–63.
- [4] Hardiyanti W, Darnius O. Risk value analysis of gold futures trading investment using fundamental analysis, technical analysis, and value at risk. *J Res Math Trends Technol (JoRMTT).* 2021;3(1):8–19.
- [5] Jensen MC, Benington GA. Random walk and technical theories: Some additional evidence. *J Finance.* 1970;25(3):469–482.
- [6] Kwon KY, Kish RJ. Technical trading strategies and return predictability: NYSE. *Appl Financ Econ.* 2002;12(9):639–653.
- [7] Murphy JJ. *Technical analysis of the futures markets: A comprehensive guide to trading methods and applications.* New York Institute of Finance. 1986.



- [8] Nithya J, Tamizhchelvan G. Effectiveness of technical analysis in banking sector of equity market. IOSR J Bus Manag (IOSR-JBM). 2014;16(7):20–28.
- [9] Smith J, Johnson R. Gold price forecasting and its impact on global investments. Journal of Economic Analysis. 2023;45(3):210–225.
- [10] Zhang J, Chung H, Lo WL. Clustering-based adaptive crossover and mutation probabilities for genetic algorithms. IEEE Trans Evol Comput. 2007;11(3):326–335.



PREDICTING CHRONIC INSOMNIA USING LSTM TECHNIQUE OF MACHINE LEARNING

Panunya Sungkaew, Thunyarut Jirineethumakul, Rateya Bhuthontharaj, Siriporn

Sakboonyarat*, Boonnatee Sakboonyarat

Department of Mathematics and Computing Science, Mahidol Wittayanusorn School,
Nakhon Pathom, Thailand

*e-mail: siriporn.sak@mwit.ac.th

Abstract:

Insomnia, a prevalent sleep disorder worsened by modern lifestyles, causes severe sleep deprivation and health risks. Chronic insomnia, distinguished by persistent sleeplessness, significantly impacts health and well-being more than acute forms. To address this, we propose a machine learning-based self-monitoring solution using actigraphy data. With the use of this method, it should be possible to find a new solution to diagnose chronic insomnia efficiently and reduce reliance on costly and time-consuming lab-based sleep tests. We utilized actigraphy data from 45 insomnia patients and 41 healthy controls, focusing on RGB light collected from an interactive environment. Initially, we grouped the data into smaller segments and represented each group with statistical values. Preprocessing involved filtering out zero values using thresholds of 20, 40, and 60 percent. Subsequently, we applied the Fast Fourier Transform (FFT) to the filtered data. Finally, we employed the Long Short-Term Memory (LSTM) technique to build and train our models. Evaluating accuracy, specificity, sensitivity, and AUC score revealed that the tool can potentially be enhanced in order to use RGB light data collected from actigraphy to predict chronic insomnia as a new solution for insomnia point-of-care diagnosis.

Introduction:

Insomnia is a prevalent sleep disorder characterized by difficulties in initiating and maintaining sleep or experiencing non-restorative sleep. These sleep disturbances lead to significant daytime impairments, negatively impacting overall health, well-being, and productivity. Chronic insomnia, distinguished by persistent sleep problems for at least three months, poses a greater public health risk compared to acute forms. It can exacerbate existing medical conditions, increase the risk for depression and anxiety, and negatively affect cognitive function and daily performance. According to the research "Insomnia: Definition, Prevalence, Etiology, and Consequences" among every 10 people, a person is affected by chronic insomnia, highlighting its widespread prevalence and the urgent need for effective interventions.¹

Deep learning, a part of machine learning, has seen numerous applications in the medical field. It has the ability to model complex patterns and relationships within large datasets using neural networks with multiple layers to automatically extract features and learn representations leading to a superior performance in tasks such as medical images, X-rays, MRIs, and CT scans analysis. Also used for predictive analytics, for instance, recurrent neural networks (RNNs) and Long Short-Term Memory (LSTM) networks are employed to predict disease outbreaks, patient deterioration, and readmission rates. These models analyze patient records and time-series data to predict future health events. The rise of deep learning over the past decade is attributed to advances in computational power, its efficiency and versatility making it a powerful tool in both academic research and industry applications.^{2,3,4,5}



Fast Fourier Transform (FFT) is a technique that is considered one of the most important numerical algorithms of the 20th Century by the IEEE magazine Computing in Science & Engineering⁶. It is commonly used to enhance the model's training. It is a mathematical way to transform time-domain data into frequency domain. This process is essential for feature extraction in time-series analysis, enabling the identification of periodic patterns and trends that are not readily apparent in the time domain. In deep learning models, FFT is used to preprocess time-series data, enhancing the model's ability to capture relevant features for improved prediction accuracy.⁷

From the prior research of Angelova M. et al. The authors had done research on using Random forest and Support Vector Machine techniques of machine learning to predict acute insomnia along with the use of k-fold cross validation and threshold filtering resulting in the accuracy of 84% and 73% respectively. This shows a promising result for further research. However, the use of machine learning alone is a manual process of feature extraction. Meanwhile, deep learning techniques are more flexible and it does not require manual pattern finding, on the other hand, the machine finds patterns itself. Researchers find deep learning an interesting technique to be used with such predictions.

The combination between FFT and LSTM techniques has been studied from the research in the field of energy science for real-time power quality disturbances recognition. The research gives a promising result⁹, ensuring that the combination of FFT and LSTM model can be used for real-life application. However, there is no evidence of the use of such a combination for the prediction of insomnia. Thus, this research focuses on the study of FFT and LSTM techniques for chronic insomnia

This project aims to develop a novel machine learning-based solution for diagnosing chronic insomnia using actigraphy data by using LSTM networks and FFT, we aim to create a self-monitoring tool that can efficiently and accurately identify chronic insomnia, reducing the need for costly and time-consuming lab-based sleep tests. This approach has the potential to provide timely and accessible diagnostics, ultimately improving the quality of life for individuals suffering from chronic insomnia.



Methodology:

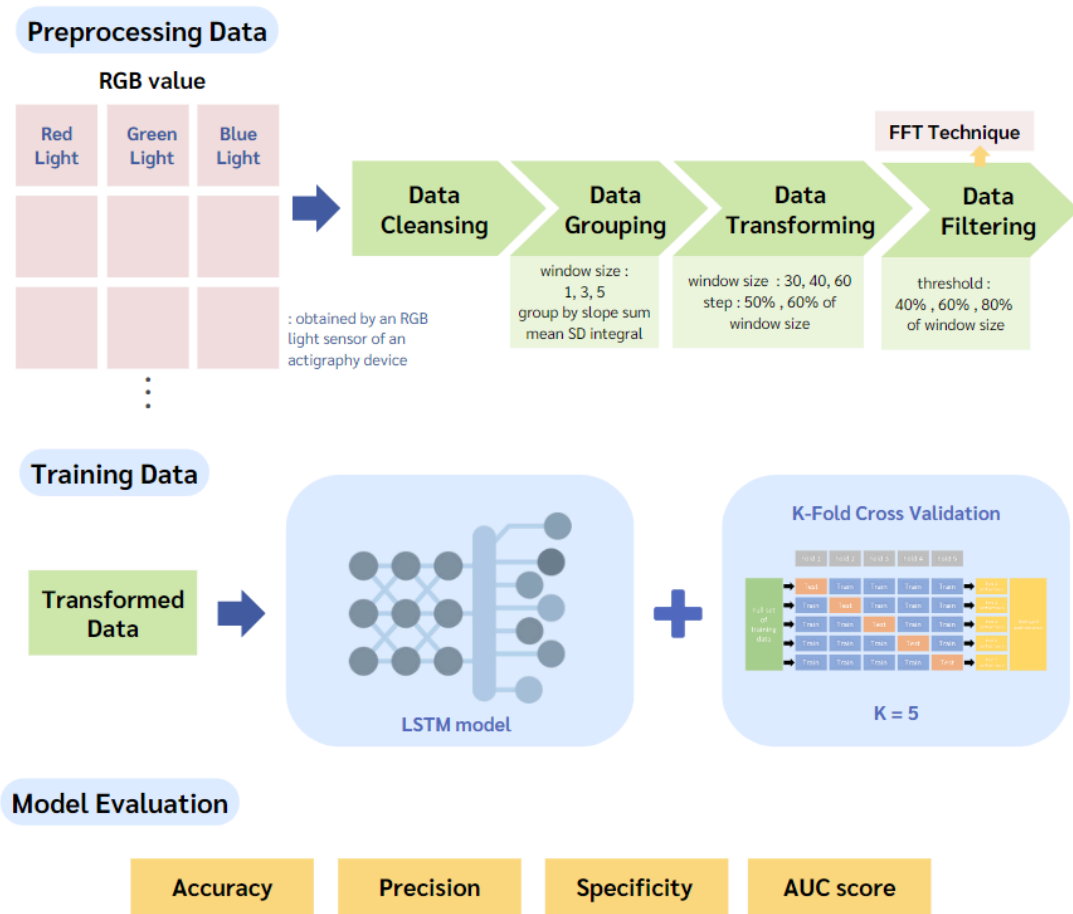


Figure 1.
Workflow Overview

Material

Hardware:

Three laptops:

1. Lenovo Ideapad 3 with Intel Core i5
2. Acer Swift 3 with AMD Ryzen 5 5000 series
3. Acer Swift 3 with Intel Core i5

Software:

Python 3.9.17

Data Preprocessing

We conducted a thorough review of relevant research and sourced public datasets. Our research utilizes actigraphy time series data from a publicly accessible data source, which has been used in previous research, as referenced in publication¹⁰ (supplementary material). The original data collection received approval from the University of Glasgow Ethics Committee.⁸



These datasets are derived from wrist-worn actigraphy devices and consist of time series data collected every minute. The dataset includes 86 subjects, comprising 45 individuals with a condition and 41 without.

For data cleansing, we extracted three factors from the RGB light sensor of the actigraphy devices: red light, green light, and blue light. We selected data from 08:00 to 22:00, the designated period during which the subject is required to remain in bed. Unnecessary data outside this time range was removed. Missing data was filled using statistical means to ensure the completeness of the dataset, and outliers were filtered out to enhance accuracy and consistency for analysis.

Post-cleaning, the data for each subject was consolidated and categorized into two groups: those with the condition and those without.

Due to the insufficient coherence of the data trends, as identified by scatter matrix analysis, it was necessary to group the data by calculating representative statistical measures for each segment. These measures include the mean, sum, slope, area under the curve, and standard deviation (SD). This approach was chosen to capture essential characteristics of the data that may be obscured in raw form, allowing for more meaningful analysis and pattern recognition. By summarizing the data with these statistical measures, we can better understand and interpret the underlying trends and variations. The data were grouped into 3 sizes: 1, 3, and 5.

To prepare the data for transformation using the fast Fourier transform (FFT) technique, additional window sizes of 30, 40, and 60 were established. These window sizes were chosen to balance between capturing sufficient data detail and computational efficiency, as they allow the FFT to analyze various frequency components effectively. Overlapping segments were created with overlapping percentages of 50% and 60%. This overlapping approach enhances the resolution of the frequency domain representation, providing a more continuous and accurate analysis of the data.

Given that some bins contained a high number of zero values, a threshold was applied to eliminate such segments. This approach was adopted to ensure that the analysis focused on segments with meaningful data and avoided potential biases introduced by bins with predominantly zero values. Thresholds were set at 40%, 60%, and 80% of the data within each window. The filtered data was then subjected to the fast Fourier transform for further analysis.

Model Training

After conducting comprehensive data preprocessing, we developed a Long Short-Term Memory (LSTM) model to predict the presence or absence of a medical condition in patients using RGB data structured as time series. The model was trained using Python and TensorFlow. The model architecture consists of an input layer followed by two key layers. The first layer is a hidden layer, which employs the ReLU (Rectified Linear Unit) activation function to introduce non-linearity and enable the model to learn complex patterns. This hidden layer is followed by an output layer with a single neuron that uses the sigmoid activation function, suitable for binary classification tasks. The Adam optimizer was selected due to its capacity to adaptively adjust the learning rate during training, thereby enhancing the efficiency and speed of the training process. Moreover, Adam is proficient in managing gradient fluctuations that may arise during training. For the loss function, binary cross entropy was employed, as it is well-suited for binary classification tasks and facilitates the model's ability to discern between the two classes effectively. The evaluation metric used was accuracy. Setting the number of epochs to 7 is a conservative choice, providing a baseline for



training without risking overfitting, especially useful for smaller datasets where extensive training might lead to overfitting. The batch size of 16 is relatively small, which can facilitate more frequent updates and potentially better generalization, particularly when dealing with limited data. Smaller batch sizes help with convergence and can be advantageous when computational resources are constrained. Furthermore, we implemented k-fold cross-validation to fully utilize the dataset for both training and testing the model. By partitioning the data into k subsets, we performed k iterations of training and evaluation, each time using a different subset as the validation set. This technique mitigates partitioning bias and provides a more robust assessment of the model's generalizability and performance.

Model Testing

In model evaluation, we often use metrics such as Accuracy, Sensitivity, Specificity, and AUC (Area Under the Curve) to assess the performance of various models. Each metric has its significance and application. Let TN, TP, FN, FP represent the number of true negatives, true positives, false negatives, and false positives, respectively. Accuracy is calculated using equation (1), which indicates the overall correctness of the model's predictions. Sensitivity is calculated using equation (2), which measures the model's ability to correctly identify true positives. Specificity is calculated using equation (3), which evaluates the model's ability to correctly identify true negatives. The area under curve (AUC) represents the area under the ROC (Receiver Operating Characteristic) curve. It indicates the model's ability to distinguish between positive and negative classes, with values ranging from 0 to 1. An AUC close to 1 signifies a model with excellent discriminatory ability.

$$Accuracy = \frac{TP + TN}{TP + TN + FP + FN} \quad (1)$$

$$Precision = \frac{TP}{TP + FP} \quad (2)$$

$$Specificity = \frac{TN}{TN + FN} \quad (3)$$

Results and Discussion:

As a result of the model training, incorporating variations in grouping size, grouping method, threshold, window size, and window step, it yielded 198 sets of analyses. The models are evaluated based on 4 metrics including accuracy, sensitivity, specificity, and the area under curve (AUC) along with their corresponding standard deviations. Of these, 18 sets were selected for further analysis as they exhibited all evaluated scores exceeding a minimum of 0.6.

Table 1.
The evaluated scores of 18 sets of analyses selected

| Method | Accuracy | Sensitivity | Specificity | AUC Score |
|------------------|-------------|-------------|-------------|-------------|
| 5-slope-60-60-60 | 0.68 ± 0.03 | 0.73 ± 0.05 | 0.62 ± 0.06 | 0.74 ± 0.03 |
| 5-slope-80-60-50 | 0.71 ± 0.03 | 0.73 ± 0.04 | 0.67 ± 0.15 | 0.77 ± 0.05 |
| 3-slope-60-30-50 | 0.67 ± 0.02 | 0.70 ± 0.05 | 0.62 ± 0.13 | 0.78 ± 0.02 |



| | | | | |
|---------------------|-------------|-------------|-------------|-------------|
| 5-slope-80-30-50 | 0.66 ± 0.02 | 0.70 ± 0.06 | 0.61 ± 0.05 | 0.74 ± 0.02 |
| 3-integral-60-30-50 | 0.67 ± 0.02 | 0.70 ± 0.08 | 0.62 ± 0.07 | 0.78 ± 0.02 |
| 5-slope-40-40-50 | 0.67 ± 0.02 | 0.69 ± 0.05 | 0.65 ± 0.08 | 0.75 ± 0.02 |
| 3-mean-60-60-60 | 0.67 ± 0.03 | 0.69 ± 0.04 | 0.63 ± 0.08 | 0.71 ± 0.03 |
| 1-none-40-40-60 | 0.65 ± 0.02 | 0.68 ± 0.03 | 0.63 ± 0.05 | 0.70 ± 0.02 |
| 3-sum-60-40-60 | 0.66 ± 0.04 | 0.68 ± 0.05 | 0.64 ± 0.08 | 0.78 ± 0.03 |
| 1-none-40-40-50 | 0.65 ± 0.01 | 0.67 ± 0.05 | 0.64 ± 0.04 | 0.72 ± 0.01 |
| 3-mean-60-40-50 | 0.64 ± 0.02 | 0.67 ± 0.09 | 0.62 ± 0.15 | 0.77 ± 0.03 |
| 5-slope-40-30-60 | 0.67 ± 0.03 | 0.66 ± 0.08 | 0.68 ± 0.06 | 0.79 ± 0.03 |
| 1-none-80-30-60 | 0.71 ± 0.02 | 0.66 ± 0.09 | 0.75 ± 0.05 | 0.78 ± 0.01 |
| 1-none-40-30-60 | 0.68 ± 0.01 | 0.65 ± 0.06 | 0.71 ± 0.04 | 0.76 ± 0.02 |
| 5-integral-40-30-60 | 0.66 ± 0.03 | 0.65 ± 0.09 | 0.68 ± 0.06 | 0.77 ± 0.03 |
| 1-none-40-30-50 | 0.68 ± 0.01 | 0.61 ± 0.09 | 0.73 ± 0.04 | 0.77 ± 0.02 |
| 1-none-40-40-60 | 0.71 ± 0.01 | 0.60 ± 0.12 | 0.77 ± 0.06 | 0.79 ± 0.02 |
| 1-none-40-40-50 | 0.72 ± 0.02 | 0.60 ± 0.12 | 0.77 ± 0.06 | 0.75 ± 0.03 |

Table 1. displays the evaluated scores—accuracy, sensitivity, specificity, and area under the curve (AUC)—along with their standard deviations (SD), expressed as mean ± SD, for the 18 analysis sets that exceeded the minimum of 0.6. Each analysis set is denoted in the format GS-GM-T-WS-WSt, where GS is grouping size, GM is grouping method, T is threshold (%), WS is window size, and WSt is window step (%).

It is appropriate to assert that sensitivity holds the highest significance, as it ensures that patients with chronic insomnia are accurately diagnosed. This metric along with other scores exceeding 0.6 emphasize its critical importance. Therefore, the most significant method is with grouping size of 5 grouped by slope, threshold of 60%, window size of 60 and window step of 60% which results in accuracy, sensitivity, specificity, and AUC being 0.68, 0.73, 0.62, and 0.74 respectively.

From the experiment with all 198 methods using a combination of LSTM and FFT technique, up to 18 methods can be enhanced to get a better result. As it can be seen that the result of 7 of the selected methods are ungrouped, it can be discussed that it is a result of a limited size of data.

In light of the research findings, It is significant that the limited data size is the main impact of the resulting evaluation score. After preprocessing and using threshold to filter windows, the filtered data reduces vastly from its raw data. The utilization of a grouping method, which demonstrated promising evaluation scores during the model's initial training and testing phases, would likely benefit from this increased data diversity. This strategy has the potential to improve the model's overall performance, thereby advancing its capability as a novel solution for point-of-care diagnosis of chronic insomnia. Moreover, the Long-Short Term Memory technique of machine learning is specifically used for time series data. However, the data after fast fourier transformation turned the data into the form of frequency which can be more suitable with other RNN models. Lastly, the dataset provides two significant features; RGB and activity, which is the number of movements in a time epoch of 1 minute.

The model's efficacy could be significantly enhanced by employing a larger dataset, which would ensure sufficient variation for robust analysis. The use of other type RNN



models may also make a significant increase on the overall evaluation score and the use of additional features provided by the dataset is another way to enhance the efficacy.

Conclusion:

From using RGB light data collected from actigraphy to explore a variety of methods including variations in grouping size, grouping method, threshold, window size, and window step and using LSTM and FFT technique to deal with data to predict chronic insomnia. The evaluation through 4 metrics including accuracy, sensitivity, specificity, and the area under curve (AUC) having 18 methods exceeding the minimum of 0.6 for all scores shows that the tool can potentially be enhanced to be a new solution for point-of-care diagnosis.

Considering the limitation from the limited data size of this research, further study can focus more on the expansion of data size to enlarge the training and testing sets of the model, and the adjustment of the model technique to other RNN. Lastly, the use of an additional feature can be beneficial and the grouping method can potentially be used along to increase the overall evaluation score.

Acknowledgements:

This project is part of the Science Project course at Mahidol Wittayanusorn School. The project team applied foundational knowledge from classroom learning, supplemented by additional research, to complete this project.

We extend our sincere gratitude to our project advisors, Ms. Siriporn Sakboonyarat and Mr. Boonnatee Sakboonyarat, for their valuable guidance, advice, and assistance in successfully completing this project.

We also thank the staff of Mahidol Wittayanusorn School for organizing the Science Project course and providing necessary equipment and facilities, which have afforded students the opportunity to explore their interests and undertake this project.

Finally, we express our heartfelt thanks to our parents and all others involved for their advice and encouragement throughout the course of this project.

The project team hopes that this work will be beneficial to those interested in the study of chronic insomnia and apologize for any errors that may be found and appreciate your understanding.

References:

1. Morin, C. M., & Jarrin, D. C. JCSM. 2007;3:S7-S10
2. LeCun Y, Bengio Y, Hinton G. Nature. 2015;521:436-444.
3. Schmidhuber J. Neural Netw. 2015;61:85-117.
4. Hochreiter S, Schmidhuber J. Neural Comput. 1997;9:1735-1780.
5. Greff K, Srivastava RK, Koutník J, Steunebrink BR, Schmidhuber J. IEEE Trans Neural Netw Learn Syst. 2017;28:2222-2232.
6. Dongarra J. & Sullivan F. Guest Editors Introduction to the top 10 algorithms. IEEE Computing in Science & Engineering. 2000;2;22-23.
7. Herff, C., & Krusinski, D. J. Fundamentals of Clinical Data Science. 2019:85-99
8. Angelova, M., Karmakar, C., Zhu, Y., Drummond, S. P. A., & Ellis, J. Automated Method for Detecting Acute Insomnia Using Multi-Night Actigraphy Data. IEEE Access. 2020;8:74413-74422.



9. Cen A., Kim D. O., A fused CNN-LSTM model using FFT with application to real-time power quality disturbances recognition. *Energy Science & Engineering*. 2023;11;2267-2280.
10. Angelova, Maia et al. [Dataset]. Dryad. 2021. <https://doi.org/10.5061/dryad.b8gtht7bh>
11. Celik, O., & Altunaydin, S. S. *JETOL*. 2018;1:26-40.
12. Lichstein, K. L., Durrense, H. H., Taylor, D., Bush, A. J., & Riedel, B. W. *BRT*. 2003;41:427-445.
13. Michael S. Gashler and Stephen C. Ashmore. *Neurocomputing*. 2016;188:3-11.
14. Yuyang You, Xuyang Zhong, Guozheng Liu, Zhihong Yang. *Artificial Intelligence in Medicine*. 2022;127:102279



PRICING OPTION ON COMMODITY UNDER SCHWARTZ MODEL BY USING FINITE DIFFERENCE METHOD

Peerawit Kalaphakdee, Khamron Mekchay*

Department of Mathematics and Computer Science, Faculty of Science, Chulalongkorn University, Bangkok 10330 Thailand

* e-mail: Khamron.m@chula.ac.th

Abstract:

This work aims for finding prices of options with underlying assets considered as commodities, where the price of commodity is assumed to follow a mean-reverting Ornstein-Uhlenbeck (OU) process, namely, the Schwartz one-factor model. The prices of both European and American options are obtained by employing the finite different methods (FDMs) for solving parabolic partial differential equations (PDEs) generated from Feynman-Kac theorem. In this work we constructed three FDMs to solve PDEs, namely FTCS, BTCS, and CN methods. The accuracy of FDMs are validated and confirmed by numerical examples for European options by compared with analytical results from Black-Scholes type (BS-type) formula and with Monte-Carlo (MC) simulations based on Euler-Maruyama method. The results for American options are obtained accordingly, and compared the behavior with results in literature.

Introduction:

An option, which is one type of derivative securities, is a very popularly tool of financial assets because it has high flexibility. It is a contract which gives an option holder a right to exercise or not exercise with no obligation to sell or buy underlying assets with the agree price at or before the end of the contract. This financial instrument, which is used to various underlying assets such as stock, commodity products, currencies, has many benefits in financial markets, i.e., it can be used for dealing with hedging, risk management, speculation, etc. Recently, there are many volumes of investment involving commodities in financial market, including other financial products related to commodities such as options, futures, etc. In Thailand, the futures, options and other derivatives on commodities are traded on TFEX (Thailand Futures

Exchange). Research on pricing of these financial products involving commodities are now in focus of many researchers.

Commodities are one type of investment products or assets that can be used as raw materials in productions of other goods or services. Commodities are naturally occurring goods or materials that are collected and processed for usages, which can be grouped into those from agriculture, and from mining. The prices of commodities usually behave according to the dynamic or markets, which will move toward the long-run mean, known as the mean-reversion property of commodity price. The dynamic of the commodity price process that can present this property was first described by the mean reverting Ornstein-Uhlenbeck (OU) process. Later, in 1997 Schwartz [1] proposed mean-reverting processes for commodities known as Schwartz's models, including one-factor, two-factor, and three-factor models depending on the number of processes in the model. The price process of commodity is essential for valuation of the prices of other financial products with underlying assets are commodities.

The first model of option on commodity was proposed in 1976 by Black [2], where the commodity prices was developed based on stocks appeared in 1973 by Black-Scholes [3] and Mertons [4]. There were also other results that developed tools for option pricing. For example, the CRR model proposed by Cox, Ross, and Rubinstein [5] in 1979, calculated the closed-form expression of fair premium for valuation of the European options on stock. Hull-White method proposed by Hull and White [6] in 1990, estimated the fair premium of European and American options on bonds.

Recently, in 2022 Nonsoong [7] studied the option prices on commodities based on Schwartz one-factor model with time-dependent parameters and obtained formulas for European and American options. In [7], the formulas for options prices were obtained from solutions of partial differential equations (PDEs) using analytical techniques such as Fourier transform and characteristic method. He also obtained Black-Scholes type (BS-type) formula for European options. However, the formula for American options in [7] relies on the knowledge of the optimal exercise curve, which is assumed to be given. In general, it requires additional techniques to get this optimal exercise curve for American option on commodity, therefore, in practise, it is not easy to find American option prices based on [7].

In this work, we want to obtain results in parallel with the work of Nonsoong [7] by finding prices of options on commodities governed by Schwartz one-factor model. In contrast to [7], this work emphasize on applying numerical methods for finding option prices. The concepts for finding American option prices is developed based on that from trinomial tree methods for option pricing introduced by Hull and White [6, 8] without using the knowledge of



the optimal exercise curve, which is another point different from [7]. The FDMs for parabolic PDEs such as forward in time central in space (FTCS), backward in time central in space (BTCS), and Crank-Nicolson (CN) schemes will be employed for finding option prices.

Methodology:

Commodity price

Commodities, such as agricultural or natural products, are considered as important products in economics whose prices often behave differently from other financial assets, such as stocks, derivatives, etc. The prices of commodities usually has one important behavior called the mean-reverting property, where the prices adjust according to the markets and move toward the long-run mean. Thus, the mathematical model with stochastic process for commodity price should have this property.

In this work, we use a well known Schwartz one-factor model to represent the commodity price process, which has the form of stochastic difference equation (SDE) [1]

where S_t is the price of commodity at time t , $\kappa > 0$ is the speed of adjustment of the price, θ is

$$dS_t = \kappa(\theta - \ln S_t)S_t dt + \sigma S_t dW_t, \quad (1)$$

for underlying assets of options, which is important for determining the option prices.

Option pricing

The option prices (or premium) depend according on the prices of underlying assets, which, in this work, is assumed to follow the process (1). The probability properties of the process S_t described by (1) is required in order to obtain options prices. The valuations for European and American options for put and call can be described as follows.

European option

European option is a contract that the writer gives the holder the right, but no obligation, to sell (called 'put option') or buy (called 'call option') underlying asset at a certain price (called 'strike price') at the expiration date. One can find the option price by evaluate the present value

of the expected pay-off at the expiration date. Namely, the price of option starting at time t before the expiration time T , $t < T$, with initial underlying asset price S , strike price K and risk-free interest rate r can be obtained from

$$v(t, S; \phi) = e^{-r(T-t)} \mathbb{E} [(\phi K - \phi S_T)^+ | S_t = S], \quad (2)$$

where $\mathbb{E}[\dots | \dots]$ is the conditional expectation with $\phi = 1$ for put option, $\phi = -1$ for call option, and $(\phi K - \phi S_T)^+ = \max\{\phi K - \phi S_T, 0\}$ is the pay-off at the expiration time T .

In literature, there are several methods for finding European option prices depending on the ways of finding the conditional expectation, which, therefore, depend on the process of S_t .

Black-Scholes type formula (BS-type)

For close form formula of European option with underlying asset following the process (1), Nonsoong [7] derived the formula based on the idea of Black-Scholes formula for options on stocks, and referred to this as BS-type formula. The formula is given as follows:

$$v(S, t; \phi) = \phi K e^{-r(T-t)} N[\phi d_1] - \phi e^{-r(T-t)+m(T)+\frac{g(T)}{2}} N[\phi d_2], \quad (3)$$

where

$$m(T) = (\ln S_t) e^{-\kappa(T-t)} + \frac{\sigma^2}{2\kappa} (e^{-\kappa(T-t)} - 1) + \theta (1 - e^{-\kappa(T-t)}),$$

$$g(T) = \frac{\sigma^2}{2\kappa} (1 - e^{-2\kappa(T-t)}), \quad d_1 = \frac{\ln K - m(T)}{\sqrt{g(T)}}, \quad d_2 = d_1 - \sqrt{g(T)},$$

and $N[\cdot]$ is the cumulative distribution function of the standard normal distribution with $\phi = 1$ for put option, $\phi = -1$ for call option.

American option

American option is a contract similar to European option, however, for American type, the holders can exercise at any time before the expiration (called 'early exercise') depending on the price of underlying asset S_t and the strike price K . Thus, the price American option must be higher than that of European. The valuation of the option prices still depends on the price process of underlying asset S_t , the strike price K , and the starting price of S_t , however, it more difficult due to the early exercise condition. Therefore, the option prices also depend on the

optimal time to exercise the option to have the maximum pay-off, namely,

$$V(t, S; \phi) = \sup_{\tau \leq T} \mathbb{E} \left[e^{-r(\tau-t)} (\phi K - \phi S_\tau)^+ | S_t = S \right], \quad (4)$$

where we can consider τ as the exercised time with $\phi = 1$ for put option, $\phi = -1$ for call option.

Finite difference method (FDM)

This section described the numerical methods for finding European and American option prices described previously. In this work, we apply the concepts of FDMs for solving PDEs representing the option prices. We first introduce the Feynman-Kac theorem, which transforms the problem of finding conditional expectations of the underlying asset price process S_t governed by (1) into the problem of finding the solutions of PDEs.

Feynman-Kac theorem and PDE

According to the Feynman-Kac theorem, the conditional expectations that appear in (2) and (4) can be obtained by solving PDEs with suitable conditions. For underlying asset with price process (1), the European option prices $v(t, S)$ for $(t, S) \in [0, T] \times [0, \infty]$ is obtained by solving parabolic PDE (backward heat equation):

$$\frac{\partial v}{\partial t} + \kappa (\alpha - \ln S) S \frac{\partial v}{\partial S} + \frac{1}{2} \sigma^2 S^2 \frac{\partial^2 v}{\partial S^2} = rv, \quad (5)$$

with terminal condition is $v(T, S) = (\phi K - \phi S)^+$ and $\phi = 1$ for put option, $\phi = -1$ for call option.

In order to solve PDE (5) numerically using FDMs, we change variable $\tau = T - t \in [0, T]$, and obtain forward heat equation:

$$-\frac{\partial u}{\partial \tau} + \kappa (\alpha - \ln S) S \frac{\partial u}{\partial S} + \frac{1}{2} \sigma^2 S^2 \frac{\partial^2 u}{\partial S^2} = ru \quad (6)$$

when initial condition is $u(0, S) = (\phi K - \phi S)^+$ with $\phi = 1$ for put option, $\phi = -1$ for call option.

Domain and discretization

To implement FDMs for solving PDE (6), we first discretize a subdomain $[0, T] \times [0, S_{\max}]$ of $[0, T] \times [0, \infty]$ by using time step Δt as $\Delta t = T/n$ and price step ΔS as $\Delta S = (S_{\max})/m$, where S_{\max} is the upper bound of considered prices, and n, m are the numbers of equal sub-intervals for the time and price intervals, respectively.

The discretization produces grid points (or 'node') (τ_i, S_j) , where $\tau_i = i\Delta t$ and $S_j = j\Delta S$ for $i = 0, 1, \dots, n$ and $j = 0, 1, \dots, m$, respectively. The PDE (6) evaluated at interior grid point (τ_i, S_j) gives

$$-\frac{\partial u}{\partial \tau}(\tau_i, S_j) + \kappa(\theta - \ln S_j)S_j \frac{\partial u}{\partial S}(\tau_i, S_j) + \frac{1}{2}\sigma^2 S_j^2 \frac{\partial^2 u}{\partial S^2}(\tau_i, S_j) = ru(\tau_i, S_j) \quad (7)$$

for $i = 1, 2, \dots, n-1$ and $j = 1, 2, \dots, m-1$. For convenience in writing, we will use $u_{i,j} := u(\tau_i, S_j)$ for the following parts. Note that, the PDE (6) is the heat equation, in literature there are three standard schemes of FDMs [9] that we can use for solving this problem: (i) the forward in time central in space (FTCS) scheme, (ii) the backward in time central in space (BTCS) scheme, and (iii) Crank-Nicolson (CN) scheme. We apply these three schemes of FDM for this PDE as follows.

Forward in time central in space (FTCS)

This FTCS scheme is considered as an explicit FDM because the time derivative is approximated by forward difference, namely, the values in the next time step is obtained directly from the current time step. Since the space derivatives are approximated by central differences, this FTCS scheme has truncation error of order $O(\Delta\tau + \Delta^2 S)$. The approximations of derivatives of PDE (7) are the followings:

$$\begin{aligned} \frac{\partial u}{\partial \tau}(\tau_i, S_j) &\approx \frac{u(\tau_{i+1}, S_j) - u(\tau_i, S_j)}{\Delta\tau}, \\ \frac{\partial u}{\partial S}(\tau_i, S_j) &\approx \frac{u(\tau_i, S_{j+1}) - u(\tau_i, S_{j-1})}{2\Delta S}, \\ \frac{\partial^2 u}{\partial S^2}(\tau_i, S_j) &\approx \frac{u(\tau_i, S_{j+1}) - 2u(\tau_i, S_j) + u(\tau_i, S_{j-1}))}{\Delta S^2}. \end{aligned}$$

We can write PDE (7) using value at interior node (τ_{i+1}, S_j) for $ru(\tau_{i+1}, S_j)$ on the right hand side, we get a linear system $\vec{u}_{i+1} = A\vec{u}_i + \vec{b}_i$:

$$\begin{bmatrix} u_{i+1,1} \\ u_{i+1,2} \\ \vdots \\ u_{i+1,m-2} \\ u_{i+1,m-1} \end{bmatrix} = \begin{pmatrix} a_{11} & a_{12} & 0 & \cdots & 0 \\ a_{21} & a_{22} & a_{23} & \ddots & \vdots \\ 0 & a_{23} & a_{33} & \ddots & 0 \\ \vdots & \ddots & \ddots & \ddots & a_{m-2,m-1} \\ 0 & \cdots & 0 & a_{m-1,m-2} & a_{m-1,m-1} \end{pmatrix} \begin{bmatrix} u_{i,1} \\ u_{i,2} \\ \vdots \\ u_{i,m-2} \\ u_{i,m-1} \end{bmatrix} + \begin{bmatrix} a_{1,0}u_{i,0} \\ 0 \\ \vdots \\ 0 \\ a_{m-1,m}u_{i,m} \end{bmatrix}$$

where \vec{u}_i denotes the values of interior nodes at time τ_i , \vec{b}_i is the vector of the boundary values, A is the matrix of coefficients a_{jk} ,

$$\begin{aligned} a_{j,j} &= \frac{1}{(1+r\Delta\tau)} (1 - \sigma^2 j^2 \Delta\tau), \\ a_{j,j+1} &= \frac{1}{(1+r\Delta\tau)} \left(\frac{1}{2} \kappa (\theta - \ln(j\Delta S)) j \Delta\tau + \frac{1}{2} \sigma^2 j^2 \Delta\tau \right), \\ a_{j,j-1} &= \frac{1}{(1+r\Delta\tau)} \left(-\frac{1}{2} \kappa (\theta - \ln(j\Delta S)) j \Delta\tau + \frac{1}{2} \sigma^2 j^2 \Delta\tau \right), \end{aligned}$$

with the initial condition $\vec{u}_0 := (u_{0,1}, u_{0,2}, \dots, u_{0,m-1})^T$. This explicit FTCS scheme is computed iteratively from the initial \vec{u}_0 to the final \vec{u}_n when $\tau = T$.

Backward in time central in space (BTCS)

This BTCS scheme is considered as an implicit FDM because the time derivative in PDE (7) is approximated by backward scheme, thus, the values in the current time step are related and cannot be obtained explicitly from the previous values. The BTCS scheme also has truncation error of order $O(\Delta\tau + \Delta^2 S)$ with the approximation of time derivative

$$\frac{\partial u}{\partial \tau}(\tau_i, S_j) \approx \frac{u(\tau_i, S_j) - u(\tau_{i-1}, S_j)}{\Delta\tau},$$

and using central differences for the space derivatives similar to that in FTCS. By rename the index from i to $i + 1$, we can write the scheme as a linear system $A\vec{u}_{i+1} = \vec{u}_i - \vec{b}_{i+1}$:

$$\begin{pmatrix} a_{11} & a_{12} & 0 & \cdots & 0 \\ a_{21} & a_{22} & a_{23} & \ddots & \vdots \\ 0 & a_{23} & a_{33} & \ddots & 0 \\ \vdots & \ddots & \ddots & \ddots & a_{m-2,m-1} \\ 0 & \cdots & 0 & a_{m-1,m-2} & a_{m-1,m-1} \end{pmatrix} \begin{bmatrix} u_{i+1,1} \\ u_{i+1,2} \\ \vdots \\ u_{i+1,m-2} \\ u_{i+1,m-1} \end{bmatrix} = \begin{bmatrix} u_{i,1} \\ u_{i,2} \\ \vdots \\ u_{i,m-2} \\ u_{i,m-1} \end{bmatrix} - \begin{pmatrix} a_{10}u_{i+1,0} \\ 0 \\ \vdots \\ 0 \\ a_{m-1,m}u_{i+1,m} \end{pmatrix}$$

where \vec{b}_{i+1} is the vector of the boundary values at τ_{i+1} , A is the matrix of coefficients a_{jk} ,

$$\begin{aligned} a_{j,j} &= 1 + \sigma^2 j^2 \Delta\tau + r \Delta\tau, \\ a_{j,j+1} &= -\frac{1}{2} \kappa (\theta - \ln(j \Delta S)) j \Delta\tau - \frac{1}{2} \sigma^2 j^2 \Delta\tau, \\ a_{j,j-1} &= \frac{1}{2} \kappa (\theta - \ln(j \Delta S)) j \Delta\tau - \frac{1}{2} \sigma^2 j^2 \Delta\tau, \end{aligned}$$

with initial condition $\vec{u}_0 := (u_{0,1}, u_{0,2}, \dots, u_{0,m-1})^T$. The implicit scheme BTCS can be solved iteratively using $\vec{u}_{i+1} = A^{-1}(\vec{u}_i - \vec{b}_{i+1})$, starting from the initial \vec{u}_0 to the final \vec{u}_n when $\tau = T$.

Crank–Nicolson (CN)

This CN scheme is the average of FTCS and BTCS schemes, thus is an implicit FDM having truncation error of order $O(\Delta^2\tau + \Delta^2S)$. The CN scheme can be written in the form of linear system $A\vec{u}_{i+1} + \vec{p}_{i+1} = B\vec{u}_i + \vec{q}_i$:

$$\begin{aligned}
 & \begin{pmatrix} a_{11} & a_{12} & 0 & \cdots & 0 \\ a_{21} & a_{22} & a_{23} & \ddots & \vdots \\ 0 & a_{23} & a_{33} & \ddots & 0 \\ \vdots & \ddots & \ddots & \ddots & a_{m-2,m-1} \\ 0 & \cdots & 0 & a_{m-1,m-2} & a_{m-1,m-1} \end{pmatrix} \begin{bmatrix} u_{i+1,1} \\ u_{i+1,2} \\ \vdots \\ u_{i+1,m-2} \\ u_{i+1,m-1} \end{bmatrix} + \begin{bmatrix} a_{10}u_{i+1,0} \\ 0 \\ \vdots \\ 0 \\ a_{m-1,m}u_{i+1,m} \end{bmatrix} \\
 &= \begin{pmatrix} b_{11} & b_{12} & 0 & \cdots & 0 \\ b_{21} & b_{22} & b_{23} & \ddots & \vdots \\ 0 & b_{23} & b_{33} & \ddots & 0 \\ \vdots & \ddots & \ddots & \ddots & a_{m-2,m-1} \\ 0 & \cdots & 0 & b_{m-1,m-2} & b_{m-1,m-1} \end{pmatrix} \begin{bmatrix} u_{i,1} \\ u_{i,2} \\ \vdots \\ u_{i,m-2} \\ u_{i,m-1} \end{bmatrix} + \begin{bmatrix} b_{10}u_{i,0} \\ 0 \\ \vdots \\ 0 \\ b_{m-1,m}u_{i,m} \end{bmatrix}
 \end{aligned}$$

where \vec{p}_{i+1} and \vec{q}_i are the vectors for the boundary values at τ_{i+1} and τ_i , respectively, A and B are the matrices of coefficients a_{jk} , b_{jk} , respectively,

$$\begin{aligned}
 a_{j,j} &= -1 - \frac{1}{2}\sigma^2 j^2 \Delta\tau - \frac{1}{2}r\Delta\tau, \\
 a_{j,j+1} &= \frac{1}{4}\kappa(\theta - \ln(j\Delta S))j\Delta\tau + \frac{1}{4}\sigma^2 j^2 \Delta\tau, \\
 a_{j,j-1} &= -\frac{1}{4}\kappa(\theta - \ln(j\Delta S))j\Delta\tau + \frac{1}{4}\sigma^2 j^2 \Delta\tau, \\
 b_{j,j} &= -1 + \frac{1}{2}\sigma^2 j^2 \Delta\tau + \frac{1}{2}r\Delta\tau, \\
 b_{j,j+1} &= -\frac{1}{4}\kappa(\theta - \ln(j\Delta S))j\Delta\tau - \frac{1}{4}\sigma^2 j^2 \Delta\tau, \\
 b_{j,j-1} &= \frac{1}{4}\kappa(\theta - \ln(j\Delta S))j\Delta\tau - \frac{1}{4}\sigma^2 j^2 \Delta\tau,
 \end{aligned}$$

and with the initial condition $\vec{u}_0 := (u_{0,1}, u_{0,2}, \dots, u_{0,m-1})^T$. The CN scheme can be computed iteratively using $\vec{u}_{i+1} = A^{-1}(B\vec{u}_i + \vec{q}_i - \vec{p}_{i+1})$, starting from the initial \vec{u}_0 to the final \vec{u}_n when $\tau = T$.

FDMs for American option

According to results of Nonsoong [7], the analytical formula of American option prices on commodity requires the knowledge of the optimal early exercise curves, which is not accessible easily in practise. In this work, we adapt the concept of trinomial tree for American option introduced by Hull and White [6]. From the concept of trinomial tree, the price of American

option at time t is the maximum value between the pay-off if the exercise occurs at time t and the discounted value of the expected pay-off of the next time step $t + \Delta t$ when it is not exercised, namely

$$V(t, S) = \max\{(\phi K - \phi S)^+, e^{-r\Delta t} \mathbb{E}[(\phi K - \phi S_{t+\Delta t})^+ | S_t = S]\}.$$

where $\phi = 1$ for put and $\phi = -1$ for call. Based on this concept, the computation for the option price at time t can be computed backward from the exercised date T , where the pay-off is known as $(\phi K - \phi S)^+$.

For FDMs, we can compute American option prices $V(t, S)$ by estimating the discounted pay-off from the next time step $e^{-r\Delta t} \mathbb{E}[(\phi K - \phi S_{t+\Delta t})^+ | S_t = S]$ by solving PDE (5) or (6). To obtain all values at (t, S) , we solve the PDE backward from the final time T to the current time t by updating the values for each time step, starting from the final time T .

Note that for PDE (6), at the final time T we have $\tau = 0 = \tau_0$, and we know the condition \vec{u}_0 . The algorithm for finding option prices are given as follow.

Algorithm for FDMs for American option

Given initial vector \vec{u}_0

for $i = 0, 1, 2, \dots, n - 1$ **do**

Solve **if** method = FTCS

$$\tilde{u}_{i+1} = A\tilde{u}_i + \vec{b}_i$$

else if method = BTCS

$$\tilde{u}_{i+1} = A^{-1}(\tilde{u}_i - \vec{b}_{i+1})$$

else if method = CN

$$\tilde{u}_{i+1} = A^{-1}(B\tilde{u}_i - \vec{p}_{i+1} + \vec{q}_i)$$

end if

Update $\vec{u}_{i+1} = \max\{\tilde{u}_{i+1}, (\phi \vec{K} - \phi \vec{S})^+\}$

end for where: $\vec{S} = (S_1, S_2, \dots, S_{m-1})^T$ and $\vec{K} = (K, K, \dots, K)^T$, when $\phi = 1$ for put option and $\phi = -1$ for call option.

Boundary condition (BC)

Since the FDMs are implemented on bounded sub-domain of the PDE, the suitable boundary conditions are required for the methods. The BCs for European and American option are

described as follows.

BCs of European option

Put option: When the underlying asset price $S = 0$, the put option must be exercised, and the present value $e^{-r\tau}K$. However, if the underlying asset price is S_{\max} , one should not exercise the put option, thus the value is 0. Thus, the BCs for put option are:

$$p(\tau, 0) = e^{-r\tau}K, \quad p(\tau, S_{\max}) = 0. \quad (8)$$

Call option: When the underlying asset price $S = 0$, one should not exercise the call option, thus the value is 0. However, when the underlying asset price is S_{\max} , one should exercise that call option with the value is the price of option at (τ, S_{\max}) . Thus, the BCs for call option are:

$$c(\tau, 0) = 0, \quad c(\tau, S_{\max}) = e^{-r\tau} \mathbb{E} [(S_T - K)^+ | S_{T-\tau} = S_{\max}]. \quad (9)$$

For implementation, the BC $c(\tau, S_{\max})$ is taken from the analytical formula, the BS-type formula presented in [7].

BCs of American option

Put option: Similar to European option, one should exercise put option immediately when the price of underlying asset is 0 with pay-off K , and should not exercise when the price is very high, $S_{\max} > K$, thus the option value is 0. The BCs for put option are:

$$P(\tau, 0) = K, \quad P(\tau, S_{\max}) = 0. \quad (10)$$

Call option: Similar to European call option, when the price of underlying asset is 0, one should not exercise the call option, thus the value of option is 0. When the price of underlying asset is high S_{\max} , one should exercise the call option immediately with the pay-off $S_{\max} - K$. Therefore, the BCs for call option are:

$$C(\tau, 0) = 0, \quad C(\tau, S_{\max}) = S_{\max} - K. \quad (11)$$

Monte Carlo simulation

Monte Carlo simulation relies on statistical property of a random process. This section provides details on the estimation of European option prices based on simulations of sample paths for prices of the underlying governed by the process (1). The simulations of sample paths of process (1) are given by the Euler-Maruyama method as follows.

Euler-Maruyama (EM) method

For S_t following the process (1), the EM method generate a sample path $\{S_{t_i}(\omega_k; S)\}$ with $S_0 = S$ according to the formula:

$$S_{t_{i+1}} = S_{t_i} + \kappa(\theta - \ln S_{t_i})S_{t_i}\Delta t + \sigma S_{t_i}\mathcal{N}(0, 1)\sqrt{\Delta t}, \quad (12)$$

where $t_i := i\Delta t$, $i = 0, 1, 2, \dots, n$, $\Delta t = T/n$, and $\mathcal{N}(0, 1)$ is the standard normal distribution with mean 0 and variance 1, and for $k = 1, 2, \dots, M$ when M is the number of sample paths.

The European option price is computed based on the conditional expectation, and we can estimate this value using the MC simulation. For example, the expected pay-off starting at $t = 0$ with price S is estimated from

$$\mathbb{E}[(\phi K - \phi S_T)^+ | S_0 = S] = \frac{1}{M} \sum_{k=1}^M (\phi K - \phi S_T(\omega_k; S))^+,$$

where the expected value of S_T given $S_0 = S$ is estimated from the average of the final values $S_T(\omega_k; S)$ from M sample paths generated from $S_0 = S$. In this case, the prices of European option is the present value of the expected pay-off

$$v(0, S) = e^{-rT} \frac{1}{M} \sum_{k=1}^M (\phi K - \phi S_T(\omega_k; S))^+. \quad (13)$$

The other values of $v(t, S)$ can be obtained similarly by setting the initial $S_t = S$ and generate sample paths to get the final value $S_T(\omega_k)$.

Early exercise premium (EEP)

When comparing between the American and European options, we know that the prices of American options are always higher than that from European, because the American options

can be exercised anytime. The extra price paid for American options is known as the ‘early exercise price’ (EEP), defined as

$$W(t, S; \phi) = V(t, S; \phi) - v(t, S; \phi),$$

where $V(t, S)$ and $v(t, S)$ are the prices of American and European options, respectively. In literature, Nonsoong [7] obtained analytical formula for American options on commodity based on the derivation of $W(t, S)$ as a solution of PDE, however, the result relies on the assumption that the optimal exercise curve is known. In this work, we want to show that we can obtain this EEP numerically using FDMs, where the results are illustrated in the next section.

Numerical Experiments and Results:

To validate the accuracy of the three FDMs described in the previous section for finding option prices, we perform numerical experiments and compare the results with those obtained from MC simulations and from BS-type formula for European option prices.

The numerical examples will be implemented on Schwartz one-factor model when considering commodities with mean-reverting property as underlying assets. We set parameters for the process (1) as follows: the speed of adjustment of the price $\kappa = 0.1$, the long-run mean of the log price $\theta = 2$, and the volatility of the price $\sigma = 0.25$. In order to obtain option prices, we assume that the options have the expiry date $T = 1$, the strike price $K = 25$, and the risk-free interest rate $r = 0.05$ for both put and call. The derivation of option prices for this underlying process are given as follows.

European option price

The European option prices for both put and call will be obtained by the three FDMs (FTCS, BTCS, and CN), and then compare with those results from BS-type formula and MC simulations.

FDMs

For three FDMs (FTCS, BTCS, and CN) described in the previous sections, we set the following parameters: the time step $\Delta t = 6.25 \times 10^{-4}$, the price step $\Delta S = 0.625$, so that the domain $(t, S) \in [0, 1] \times [S_{\min}, S_{\max}]$ is discretized by using $(n, m) = (1600, 160)$, when using $S_{\min} = 0$ and $S_{\max} = 100$.

The results from the three FDMs of European option prices for put and call $v(0, S)$, when the options start at $t = 0$ with initial underlying asset price S , are shown in Fig 1. The examples, Fig 2. shows 3D plots based on FTCS scheme for option prices $v(t, S)$ that start at time $t \in [0, 1]$ with initial underlying asset price S (Fig 2.a for put prices, and Fig 2.b for call prices).

BS-type formula

According to the BS-type formula (3) given previously, when applying the formula for the selected parameters, we have the followings.

$$m(1) = (\ln S_t)e^{-0.1(1-t)} + 0.03125(e^{-0.1(1-t)} - 1) + 2(1 - e^{-0.1(1-t)}),$$

$$g(1) = 0.03125(1 - e^{-0.2(1-t)}), \quad d_1 = \frac{\ln 25 - m(1)}{\sqrt{g(1)}}, \quad d_2 = d_1 - \sqrt{g(1)}.$$

Since the BS-type formula provides analytical results for European option prices, thus, the results from BS-type formula is considered as exact solutions and will be used for checking the accuracy for the FDMs. The plots of put and call option prices $v(0, S)$ from BS-type formula is shown in Fig 1.

Monte-Carlo simulation

To confirm the accuracy for the FDMs, in addition to BS-type formula, we perform MC simulations to obtain European option prices by setting time step $\Delta t = 6.25 \times 10^{-4}$ for EM method and using 10, 000 sample paths, namely, for EM method (12):

$$S_{t+\Delta t} = S_t + 0.1(2 - \ln S_t)S_t 6.25 \times 10^{-4} + 0.25S_t \mathcal{N}(0, 1)\sqrt{6.25 \times 10^{-4}},$$

The European put and call option prices $v(0, S)$ from MC simulations are also shown in Fig 1. for comparisons.

Comparison for European option prices

The results from three FDMs are compared with analytical solutions generated from BS-type formula and statistical results from MC simulations as shown in Fig 1. The plots of these

results from all methods are well matched in Fig 1., which confirm and validate the accuracy of the three FDMs proposed in this work for European option prices.

In order to understand in detail on the accuracy of these methods, we also compare the absolute errors by using BS-type formula as the analytical solution. The absolute errors for put and call option prices $v(0, S)$ from three FDMs (FTCS, BTCS and CN) and from MC simulations are shown in Table 1. We see that the results from the three FDMs are quite similar in terms of absolute error with small values (< 0.15), which implies that these three FDMs are quite accurate and their results are not so different. When comparing FDMs with MC simulations, results from MC seems to give a little smaller errors, however, in computation MC simulations take a long time to get more accurate values when compared to FDMs (data about time used are not shown).

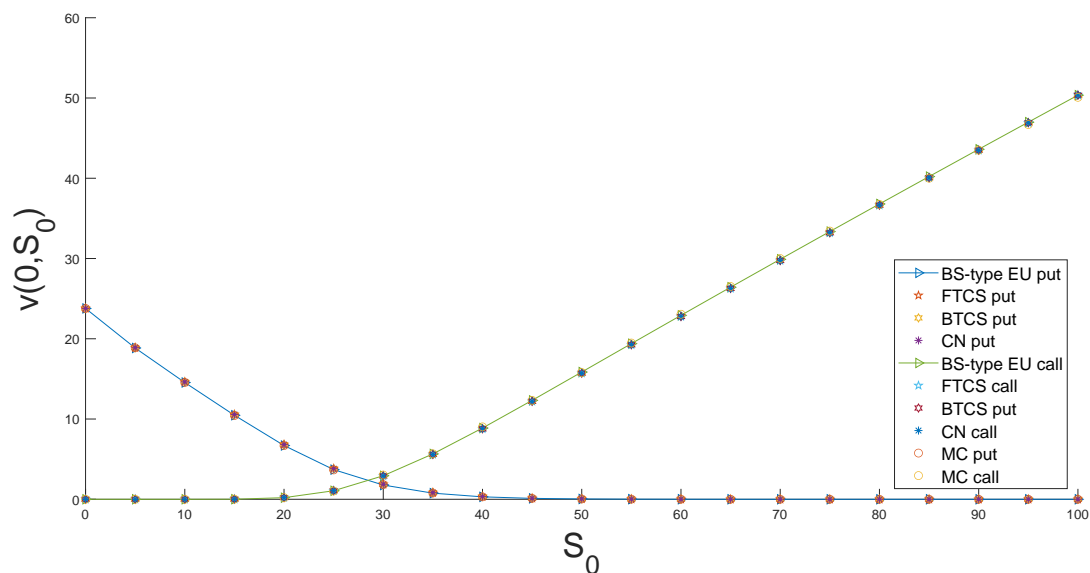


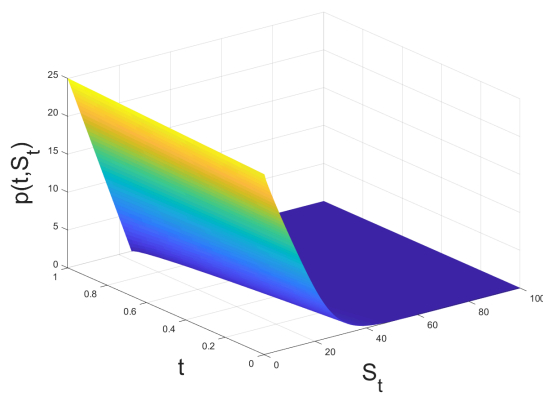
Figure 1.

European option prices $v(0, S)$ from BS-type, FTCS, BTCS, CN and MC with $K = 25$, $T = 1$, and $r = 0.05$ starting at $t = 0$ with initial underlying asset price S .

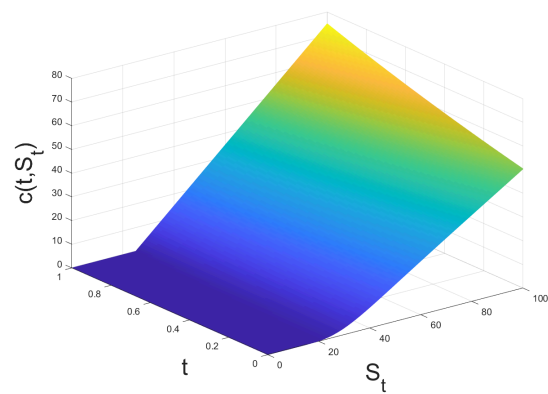
Table 1.

Absolute errors of results from FDMs and MC when compared with BS-type result for European option prices $v(0, S)$.

| Spot | Put options | | | | Call options | | | |
|------|-------------|--------|--------|--------|--------------|--------|--------|--------|
| | FTCS | BTCS | CN | MC | FTCS | BTCS | CN | MC |
| 5 | 0.0402 | 0.0402 | 0.0402 | 0.0210 | 0.0000 | 0.0000 | 0.0000 | 0.0000 |
| 10 | 0.0742 | 0.0741 | 0.0741 | 0.0058 | 0.0000 | 0.0000 | 0.0000 | 0.0000 |
| 15 | 0.0954 | 0.0953 | 0.0954 | 0.0369 | 0.0020 | 0.0020 | 0.0020 | 0.0061 |
| 20 | 0.1166 | 0.1162 | 0.1165 | 0.0096 | 0.0099 | 0.0097 | 0.0098 | 0.0047 |
| 25 | 0.1229 | 0.1223 | 0.1226 | 0.0377 | 0.0060 | 0.0057 | 0.0059 | 0.0332 |
| 30 | 0.1008 | 0.1006 | 0.1008 | 0.0520 | 0.0243 | 0.0239 | 0.0241 | 0.0899 |
| 35 | 0.0660 | 0.0665 | 0.0663 | 0.0171 | 0.0659 | 0.0647 | 0.0654 | 0.0109 |
| 40 | 0.0365 | 0.0373 | 0.0369 | 0.0013 | 0.1013 | 0.0996 | 0.1005 | 0.1449 |
| 45 | 0.0180 | 0.0187 | 0.0184 | 0.0020 | 0.1250 | 0.1231 | 0.1241 | 0.0038 |
| 50 | 0.0082 | 0.0087 | 0.0084 | 0.0038 | 0.1394 | 0.1375 | 0.1385 | 0.0662 |



(a) Put option



(b) Call option

Figure 2.

3D plots European option prices $v(0, S)$ from FTCS scheme with $K = 25$, $T = 1$ and $r = 0.05$.

In the following Fig 3., we plot the put and call option prices $v(0, S; K)$ (Fig 3.a and Fig 3.b, respectively) when the strike price K varies from 19, 21, ..., 31. The behavior of prices for options agree with that studied in literature, namely, the put prices increase when strike prices K increase, and the call prices decrease when strike prices K increase.

American option prices

The settings for FDMs for finding American options prices are the same as that for European options, in terms of discretization of the domain and schemes (FTCS, BTCS, and CN) and that for the option contracts. Note that, there will be no analytical results and MC simulations

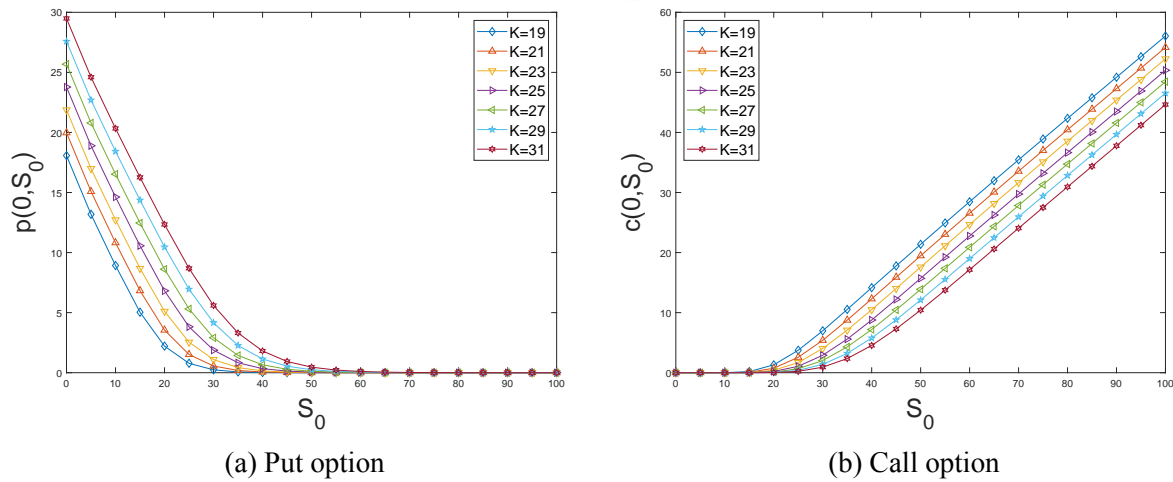


Figure 3.

European option prices $v(0, S)$ with $K = 19, 21, 23, 25, 27, 29, 31$, $T = 1$ and $r = 0.05$.

for comparison to validate our results. However, the behavior of the results from FDMs will be given and compare with that in literature.

The plots of Figs 4. and 5. show the American option put and call prices, respectively. We can see that the results from these three FDMs are almost the same for both put and call prices. We can observe that the prices from FDMs converge to the pay-off $(S - K)^+$ for call prices when S is high and to pay-off $(K - S)^+$ for put prices when S is low, which is corresponding to the early exercises of the option, namely, one should exercise option when the starting underlying price is too high for call, and when the starting underlying price is too low for put. These results confirm that the prices generated from FDMs are accurate in this sense.

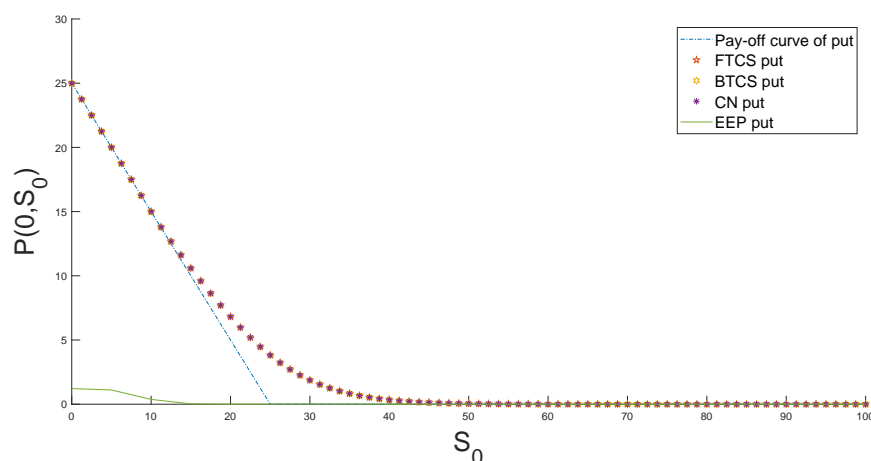


Figure 4.

American put option prices $P(0, S)$ with $K = 25$, $T = 1$, and $r = 0.05$ starting at $t = 0$ and Early exercise premium (EEP) for put.

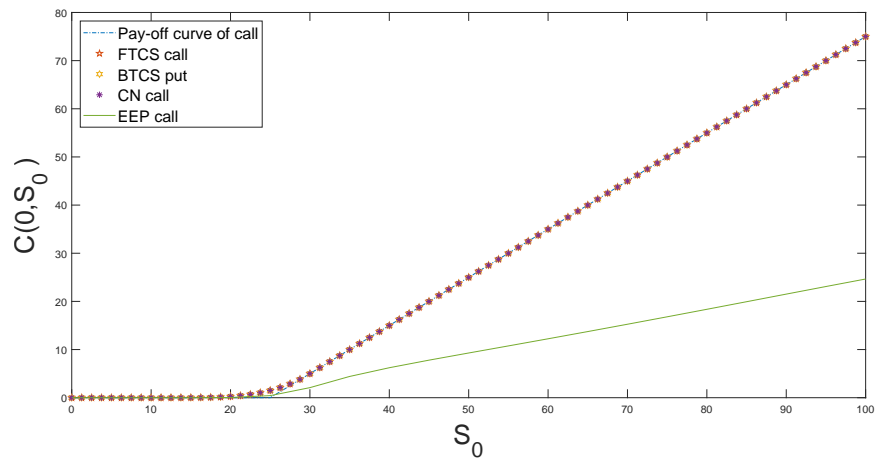


Figure 5.

American call option prices $C(0, S)$ with $K = 25$, $T = 1$, and $r = 0.05$ starting at $t = 0$ and Early exercise premium (EEP) for call.

We also plot the early exercise premium (EEP) for both put and call options in Figs 4. and 5. respectively. These plots represent the differences between the American and European option prices, which can tell us about the values of option corresponding to the early exercises. Note that the EEP is non-negative, which shows that the American options prices is always higher than that of European option prices, due to the fact that the holder of American options can exercise the option at anytime before the expiration date.

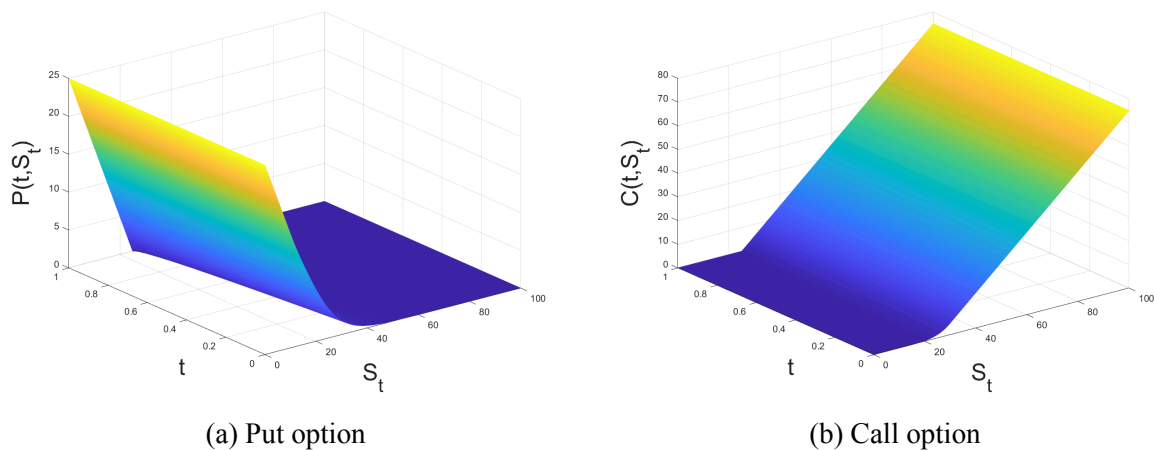


Figure 6.

American option prices $V(0, S)$ with $K = 19, 21, 23, 25, 27, 29, 31$, $T = 1$ and $r = 0.05$.

Fig 6. shows 3D plots of American option prices $V(t, S)$ from FTCS scheme for both put and call, for the price when it starts at t with initial underlying asset price S .

Conclusion:

In this work we employed the finite different methods (FDMs) for finding option prices by solving parabolic partial differential equations (PDEs) generated from Feynman-Kac theorem for the prices of options. The underlying assets for options are considered as commodities driven by Schwartz one-factor model, which represent a mean-reverting process for commodity prices. Three finite different schemes (FTCS, BTCS, and CN) were adjusted to solve PDEs for European and American options, for both put and call. The accuracy of all three FDMs were validated and confirmed via numerical examples for European options by comparing with analytical results from BS-type formula and with Monte-Carlo simulations generated using Euler-Maruyame method. The results for American options were also obtained accordingly, where behavior of option prices agree with results in literature. The results investigated in this work will be useful in practise due to the accuracy and efficiency of the methods, when dealing with options under Schwartz one-factor model, which can also modified for other underlying price processes such as CIR [10] or time-dependent parameter OU processes.

Acknowledgements:

We thank the AMCS Program, Department of Mathematics and Computer Science, Faculty of Science, Chulalongkorn University for partially financial support.

References:

- [1] Schwartz ES. The stochastic behavior of commodity prices: implications for valuation and hedging. *J Financ.* 1997;52:923–973.
- [2] Black F. The pricing of commodity contracts. *J Financ Econ.* 1976;3:167–179.
- [3] Black F, Scholes M. The pricing of options and corporate liabilities contracts. *J Politic Econ.* 1973;81:637–654.
- [4] Merton RC. An intertemporal capital asset pricing model. *Econometrica.* 1973;41:867–887.
- [5] Cox JC, Ross SA, Rubinstein M. Option pricing: A simplified approach. *J Financ Econ.* 1979;7:229–263.
- [6] Hull J, White A. Valuing derivative securities using the explicit finite difference method. *J Financ Econ.* 1990;25:87–100.
- [7] Nonsoong P. Valuation of american commodity options. Dissertation, Chulalongkorn University, Bangkok, Thailand, 2022.
- [8] Hull J. Options, Futures and Other Derivatives, 9th Edn. Pearson Education Inc, Prentice Hall, New Jersey, 2013.
- [9] Burden LR, Faires DJ. Numerical Analysis, 9th Edn. Brooks/Cole, Cengage Learning, Boston, 2010.

- [10] Cox JC, Ingersoll JE, Ross SA. A theory of the term structure of interest rates. *Econometrica*. 1985;53:385-407.



QNN Trainer : A Tool to Support Quantum Neural Network Training and Model Development

Jakrkapong Sritantanont, Pavarit Chamchanta, Thanawat Kongrak*, Chinnapong Angsuchotmetee

Division of Computational Science, Faculty of Science, Prince of Songkla University
e-mail: 6510210119@email.psu.ac.th

Abstract:

Quantum computing marks a significant advancement in computational paradigms, yet its applications are limited by the availability of qubits and the high costs of quantum hardware. In machine learning, a Quantum Neural Network (QNN) are gaining attention for their potential to enhance processing speeds and performance. However, their implementation remains unintuitive for many data scientists. This study presents the QNN Trainer, a tool designed to enable data scientists to easily experiment with a QNN. Tested with CSV files from publicly available datasets, our results demonstrate that a QNN can be effectively integrated with existing data, revealing insights into their speed and effectiveness. This work aims to enhance accessibility and experimentation in the intersection of quantum computing and machine learning.

Introduction:

Quantum Neural Network (QNN) [1], [2] represent a novel intersection of quantum computing and machine learning. QNN work by modeling a quantum circuit equivalent of traditional neural networks, allowing basic training and weight adjustment to be performed on a quantum computer. QNN has been explored in various studies, demonstrating their potential for improved speed and efficiency in learning tasks. However, despite the availability of libraries for developing QNN, many data scientists find these tools challenging to use due to their complexity and the steep learning curve associated with quantum programming [3].

When developing a quantum program for quantum machine learning, several libraries can be used. One well-known option is Qiskit by IBM [4], which offers a simulator for running on a local machine and an interface to submit jobs to an actual quantum machine on IBM's network. Another prominent library is PennyLane.ai [5], specifically designed for developing quantum machine learning models such as QNN. Despite the availability of these libraries, the learning curve for new data scientists working on QNNs remains steep due to the time and effort required to implement them.

To address these challenges, we propose the QNN Trainer, an intuitive graphical user interface (GUI) designed specifically for data scientists who may not have extensive backgrounds in quantum computing. The QNN Trainer simplifies the process of developing and experimenting with QNN by allowing users to easily load CSV files, select quantum backends, and submit jobs for execution without requiring deep technical knowledge of quantum mechanics. This streamlined approach not only enhances accessibility but also encourages broader experimentation with QNN, facilitating the integration of quantum computing into mainstream data science practices.

Related Technologies and Studies:

Related technologies and studies that are described in this section are (1) Quantum Neural Network, and (2) Quantum Computing Libraries. They are described as follows.

A. Quantum Neural Network

Quantum Neural Network (QNN) [6] is a quantum program that is designed to combine concepts of a traditional Artificial Neural Network (ANN) [7] with quantum programming to develop an equal representation of ANN in a quantum circuit form such that, a train / test mechanism as done in ANN can be carried out in a quantum computer machine. A simple quantum version of ANN is represented in Figure 1.

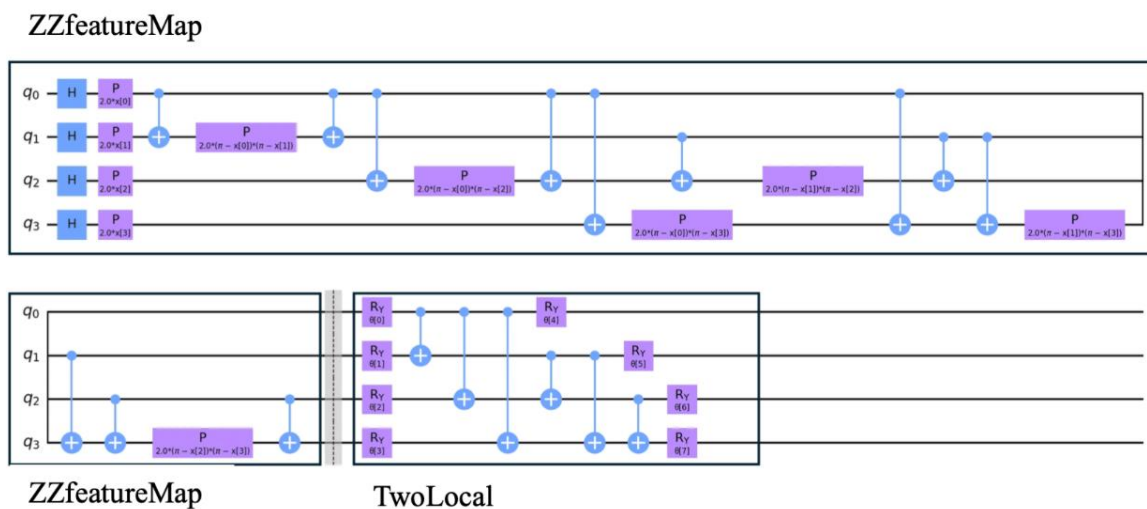


Figure 1: A QNN circuit using ZZFeatureMap and TwoLocal¹

Figure 1 depicts a simple quantum version of a traditional artificial neural networks. The network involves two main part which are (1) ZZFeatureMap [8] and (2) TwoLocal [9]. It should be noted that the figure consists of two main circuit rows. The second row is actually a continuation of the first row, but they are written in two separate rows to ensure the diagram fits on the page. The figure shows a circuit with 4 input qubits, with ZZFeatureMap and TwoLocal connected to each other. The details of ZZFeatureMap and TwoLocal are as follows.

- ZZFeatureMap

ZZFeatureMap is the first part of QNN which involve converting numerical data from dataset into a format capable to be used in quantum computer. This is done by using a controlled-Z gate which can be used to rotate Qubit in a specific angle such that, their rotation angle can represent a numerical value of the data to be represented. This process is done to ensure that we can have enough feature spaces to train the model while using a smaller number of qubits [8]. The data can be later sent to TwoLocal layer, which is the next part of QNN.

¹ <https://medium.com/swlh/qa2-explaining-variational-quantum-classifiers-b584c3bd7849>



- TwoLocal

TwoLocal, so called a Variational Ansatz circuit [9], is used in QNN to replicate an activation function and training process of a traditional ANN. Ansatz circuit involves rotating a single qubit and entangling two entangling qubits gate such that their values can be later adjusted by adjusting the rotation, which later makes related entangling qubits value to change, in the same way that ANN can use just training weight during learning process. TwoLocal uses a process so called Variational Quantum Eigen (VQE) [10] solver to carry the same process. The number of parameters that can be tuned or adjusted can be increased by increasing number of TwoLocal layers, referring as increasing number of *repetitions*.

A combination of ZZFeatureMap and TwoLocal helps to represent a quantum version of ANN in quantum computer that can be used for training any data that can be used in a traditional feedforward ANN.

B. Quantum Programming Library

A quantum programming library is a type of software that assists researchers and developers in creating, testing, and executing quantum algorithms on quantum computers. These libraries simplify the process of building quantum circuits and performing quantum operations without requiring in-depth knowledge of the underlying hardware. By providing user-friendly tools and clear documentation, quantum programming libraries enable users to explore the capabilities of quantum computing for various applications, including machine learning, optimization, and cryptography.

- Qiskit [4]

Qiskit is one of the most widely used quantum programming libraries, developed by IBM. It offers a comprehensive set of tools for constructing and managing quantum circuits, simulating quantum systems, and executing algorithms on IBM's quantum hardware. Qiskit is organized into several components, including Terra (for circuit construction), Aer (for simulation), and Ignis (for error mitigation). This modular design allows users to create complex quantum applications while utilizing extensive tutorials and guides. Qiskit also supports the integration of classical and quantum computing, making it a suitable choice for hybrid algorithms that leverage both types of computing.

- Cirq [11]

Cirq is another prominent quantum programming library, developed by Google. It is specifically designed for creating, simulating, and running quantum circuits on Google's quantum processors. Cirq emphasizes flexibility and usability, allowing users to define custom quantum gates and operations. This library is particularly well-suited for research and experimentation with quantum algorithms, as it provides tools for building and optimizing quantum circuits. Cirq integrates seamlessly with Google's quantum hardware, enabling users to test their algorithms on actual quantum devices. Its focus on performance and ease of use makes it a valuable resource for researchers in the field of quantum computing.

- PennyLane [5]

PennyLane is a quantum programming library that focuses on the integration of quantum computing with machine learning. Developed by Xanadu, PennyLane allows users to create quantum circuits that can be optimized using gradient-based methods. This capability is particularly useful for applications in quantum machine learning. The library supports various quantum devices and simulators, enabling users to execute their algorithms on different platforms. PennyLane's approach to combining quantum computing with machine learning techniques provides new opportunities for research and application, making it a significant tool for those investigating the intersection of these two fields.

There are also other library or framework such as Amazon Braket which allows us to experiment on quantum computing through a web service API Gateway [12]. Though the availability of Quantum Programming library is widely available. Developing them is still required a steep learning curved which make it difficult for a data scientist to develop a QNN model.

Methodology:

In this study, we propose a software named QNN Trainer. As the name suggests, this software is a program that allows any data scientist to develop a QNN model easily. The technology stack used for developing our QNN Trainer, currently QNN Trainer v0.1.0, is as follows.

- | | |
|--------------------------------------|------------------|
| - Based programming language : | Python 3.10 |
| - Graphical User Interface Library : | Pyside 6 |
| - Quantum Programming Library : | PennyLane 0.37.0 |
| - Training Library Backend : | Tensorflow 2.15 |
| - Physical Quantum Backend Library: | Qiskit 0.11.0 |

The main GUI of QNN Trainer is depicted in Figure 2 as follows.

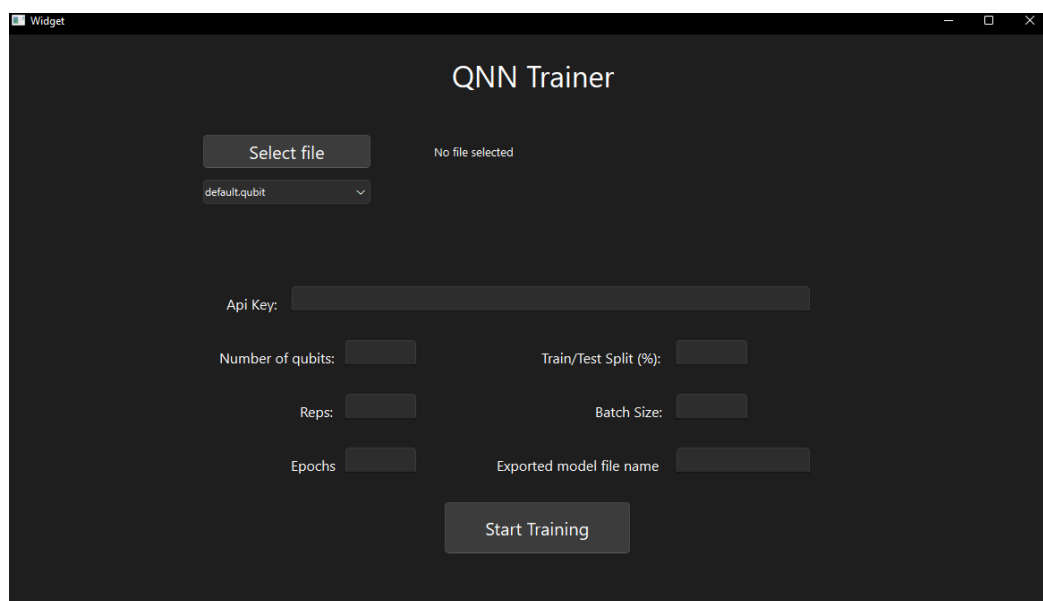


Figure 2: QNN Trainer Main GUI



The main GUI of QNN Trainer allows users to upload CSV data into the program. In this version, only a simple UTF-8-based CSV file, where each line contains solely numerical data and the final data column contains a classified class, is supported. The program still does not include a built-in data cleaning tool. Data scientists will need to prepare and clean their data beforehand before using QNN Trainer.

After the data file is selected, users can choose a quantum machine to run the program on. The implementation is based on the PennyLane library. Thus, in this version, we support quantum machines as listed in the current PennyLane-supported library. The supported quantum machines are detailed in Table 1 as follows.

Table 1: Supported quantum machine backend in QNN Trainer v0.1.0

| Quantum Machine | Description |
|-----------------|--|
| default.qubit | PennyLane quantum circuits simulator |
| lightning.qubit | High performance quantum circuits simulator which supports noise modeling |
| qiskit.aer | IBM Qiskit quantum simulator which support both ideal case simulation and noisy quantum simulation |
| qiskit.ibmq | A physical quantum machine on IBM Q cloud |

After selecting a quantum machine backend, QNN Trainer supports a PCA-based feature selection technique. This feature arises from the necessity of having one qubit per feature, which can be costly. Therefore, it is essential to optimize the number of features sent to the QNN training process. Users can simply select the number of features to be used via the GUI, and the program will automatically (1) select the required features, (2) create a ZZFeatureMap layer with a number of qubits corresponding to the selected features, (3) construct a TwoLocal layer with specific number of repetitions and connect it to the ZZFeatureMap, and (4) initiate the training process using PennyLane with the Keras library as the backend. A screenshot of the training process is shown in Figure 3 below.

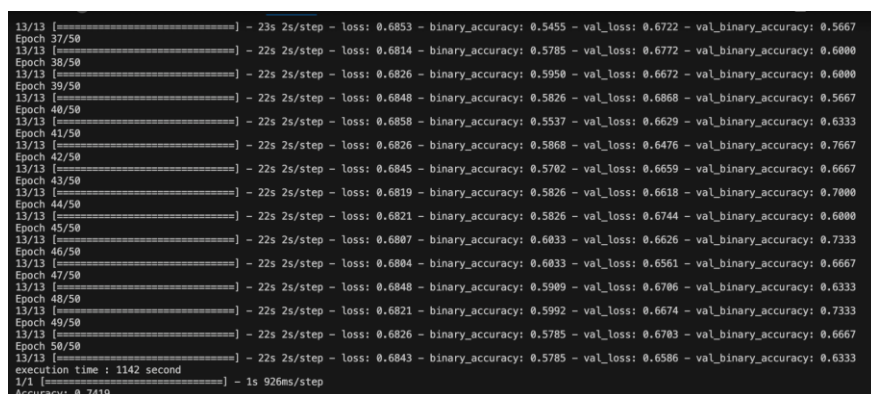


Figure 3: Screenshot of the training process of QNN Trainer

It can be seen from Figure 3 that the training process of QNN Trainer relies on Keras Layer backend of PennyLane library. This means that the training process is relied on Keras

library which makes screenshot as in Figure 3 similar to a traditional ANN training using Keras. The sourcecode of QNN Trainer is available online on Github on <https://github.com/meen2161/QNN-Trainer>

Validation Results and Discussion

To validate our QNN Trainer, we have tested our program using several benchmarking datasets. The selected datasets used to validate our program are (1) PIMA Indian Diabetes², (2) Heart Attack Analysis & Prediction³, and (3) COVID Patient⁴. It is important to note that model accuracy or loss is not the primary objective of this validation process, as this study focuses on developing a QNN training tool. Therefore, we conducted a thorough test on all supported qubit machine backends and evaluated the running time of each quantum simulator backend for 50 epochs. The time taken for training each dataset for 50 epochs on each backend is presented in Table 3.

Table 3: Running time of training each selected dataset for 100 epochs on each quantum backend

| Dataset | Running time on Quantum Simulator Backend (seconds) | | |
|---------------|---|-----------------|------------|
| | default.qubit | lightning.qubit | qiskit.aer |
| PIMA | 60 | 127 | 3,001 |
| COVID Patient | 271 | 564 | 12,390 |
| Heart Disease | 26 | 51 | 1,126 |

The table presents the running times of the QNN Trainer on three different quantum simulator backends—default.qubit, lightning.qubit, and qiskit.aer—across three distinct datasets: PIMA Indian Diabetes, COVID Patient, and Heart Disease. The results indicate that the default.qubit backend generally exhibits the shortest running times, with PIMA taking 60 seconds, COVID Patient taking 271 seconds, and Heart Disease taking only 26 seconds. In contrast, the lightning.qubit backend shows longer running times, with PIMA at 127 seconds, COVID Patient at 564 seconds, and Heart Disease at 51 seconds. The qiskit.aer backend demonstrates the longest running times across all datasets, with PIMA taking 3,001 seconds, COVID Patient taking 12,390 seconds, and Heart Disease taking 1,126 seconds. These results highlight significant variations in performance among the different quantum simulator backends, suggesting that the choice of backend can greatly influence the time required to run QNN training process.

It is important to note that in this experiment, a shorter running time does not necessarily indicate better performance due to the differences in the nature of each simulator. In this case, default.qubit may run faster than the other simulators because it does not account for quantum noise simulation, which may occur on a physical machine. Lightning.qubit incorporates quantum noise simulation, resulting in longer running times. Qiskit.aer offers both ideal and noisy simulations, which may require longer running times but can provide a more accurate

² <https://www.kaggle.com/datasets/uciml/pima-indians-diabetes-database>

³ <https://www.kaggle.com/datasets/rashikrahmanpritom/heart-attack-analysis-prediction-dataset>

⁴ <https://www.kaggle.com/datasets/meimzri/covid19-dataset/code>



qubit simulation than the others. Researchers should carefully plan when designing their QNN networks on simulator to test their networks on.

Conclusions and Future Work

In this study, we introduce QNN Trainer, currently at version 0.1.0. QNN Trainer is designed to help users develop their own Quantum Neural Network (QNN) models utilizing the ZZFeatureMap and TwoLocal circuit. This software allows data scientists to upload a CSV file and initiate the QNN training process without needing to manually program the QNN model.

As the current version is hard-coded with a specific QNN-based structure, our future work will focus on two main areas: (1) expanding the range of available models to include options such as the Quantum Support Vector Machine (QSVM) or alternative QNN variants that do not rely on the ZZFeatureMap and Ansatz, like the EstimatorQNN, and (2) further investigating the parameters of the ZZFeatureMap and Ansatz, including the impact of Ansatz repetitions on accuracy and the effects of using different observation operators (e.g., transitioning from Hermitian to Pauli operators).

Acknowledgements:

The authors would like to acknowledge helps and supports from Division of Computation Science, Faculty of Science, Prince of Songkla University for providing all machines, equipments and related cloud infrastructure for conducting experiments.

References:

- [1] M. Schuld, I. Sinayskiy, and F. Petruccione, “An introduction to quantum machine learning,” *Contemp Phys*, vol. 56, no. 2, pp. 172–185, Apr. 2015, doi: 10.1080/00107514.2014.964942.
- [2] Z. A. Jia, B. Yi, R. Zhai, Y. C. Wu, G. C. Guo, and G. P. Guo, “Quantum Neural Network States: A Brief Review of Methods and Applications,” *Adv Quantum Technol*, vol. 2, no. 7–8, p. 1800077, Aug. 2019, doi: 10.1002/QUTE.201800077.
- [3] M. Cerezo, G. Verdon, H. Y. Huang, L. Cincio, and P. J. Coles, “Challenges and opportunities in quantum machine learning,” *Nature Computational Science* 2022 2:9, vol. 2, no. 9, pp. 567–576, Sep. 2022, doi: 10.1038/s43588-022-00311-3.
- [4] R. Wille, R. Van Meter, and Y. Naveh, “IBM’s Qiskit Tool Chain: Working with and Developing for Real Quantum Computers,” *Proceedings of the 2019 Design, Automation and Test in Europe Conference and Exhibition, DATE 2019*, pp. 1234–1240, May 2019, doi: 10.23919/DATE.2019.8715261.

- [5] V. Bergholm *et al.*, “PennyLane: Automatic differentiation of hybrid quantum-classical computations,” Nov. 2018, Accessed: Aug. 31, 2024. [Online]. Available: <https://arxiv.org/abs/1811.04968v4>
- [6] Z. A. Jia, B. Yi, R. Zhai, Y. C. Wu, G. C. Guo, and G. P. Guo, “Quantum Neural Network States: A Brief Review of Methods and Applications,” *Adv Quantum Technol*, vol. 2, no. 7–8, p. 1800077, Aug. 2019, doi: 10.1002/QUTE.201800077.
- [7] C. M. Bishop, “Neural networks and their applications,” *Review of Scientific Instruments*, vol. 65, no. 6, pp. 1803–1832, Jun. 1994, doi: 10.1063/1.1144830.
- [8] V. Havlíček *et al.*, “Supervised learning with quantum-enhanced feature spaces,” *Nature* 2019 567:7747, vol. 567, no. 7747, pp. 209–212, Mar. 2019, doi: 10.1038/s41586-019-0980-2.
- [9] M. Cerezo *et al.*, “Variational quantum algorithms,” *Nature Reviews Physics* 2021 3:9, vol. 3, no. 9, pp. 625–644, Aug. 2021, doi: 10.1038/s42254-021-00348-9.
- [10] M. Cerezo, K. Sharma, A. Arrasmith, and P. J. Coles, “Variational quantum state eigensolver,” *npj Quantum Information* 2022 8:1, vol. 8, no. 1, pp. 1–11, Sep. 2022, doi: 10.1038/s41534-022-00611-6.
- [11] A. Tyagi, “Cirq: A Python Framework for Creating, Editing, and Invoking Quantum Circuits DESIGN DOCUMENT Team 8 Name Role Victory Omole Project Client”, Accessed: Aug. 31, 2024. [Online]. Available: <https://sdmay20-08.sd.ece.iastate.edu>
- [12] J. Garcia-Alonso, J. Rojo, D. Valencia, E. Moguel, J. Berrocal, and J. M. Murillo, “Quantum Software as a Service Through a Quantum API Gateway,” *IEEE Internet Comput*, vol. 26, no. 1, pp. 34–41, 2022, doi: 10.1109/MIC.2021.3132688.



Solution Sets of Some Two-Term Quadratic Equations involving Floor Functions

Wasawat Kitcharoensubdee,¹ Ratinan Boonklurb,^{1,*} Atiratch Laoharenoo²

¹Department of Mathematics and Computer Science, Faculty of Science, Chulalongkorn University, Bangkok, Thailand

²Department of Mathematics and Computer Science, Kamnoetvidya Science Academy, Rayong, Thailand

*e-mail: ratinan.b@chula.ac.th

Abstract:

In this paper, we provide solution sets of two-term quadratic equations with some unknowns are replaced by the floor function of an unknown, namely $\lfloor x \rfloor^2 - c = 0$, $\lfloor x^2 \rfloor - c = 0$, $x\lfloor x \rfloor - c = 0$, $\lfloor x \rfloor^2 + b\lfloor x \rfloor = 0$, $x\lfloor x \rfloor + bx = 0$, $x\lfloor x \rfloor + b\lfloor x \rfloor = 0$, $\lfloor x \rfloor^2 + bx = 0$ and $x^2 + b\lfloor x \rfloor = 0$.

Introduction:

For a real number x , the floor function of x , denoted by $\lfloor x \rfloor$, is the greatest integer less than or equal to x . We have basic properties about the floor function which we often use in this article as follows:

- 1) $\lfloor x \rfloor = m$ if and only if $m \leq x < m + 1$.
- 2) $\lfloor x \rfloor \leq x \leq \lfloor x \rfloor + 1$ for every $x \in \mathbb{R}$.
- 3) for every $x \in \mathbb{R}$ for every $n \in \mathbb{Z}$ $x \geq n$ if and only if $\lfloor x \rfloor \geq n$.
- 4) for every $x \in \mathbb{R}$ for every $n \in \mathbb{Z}$ $x < n$ if and only if $\lfloor x \rfloor < n$.

The floor function is usually introduced in Calculus where the limit and continuity are considered, see [1] In addition, it is also useful in several branches of mathematics or business where we need to use the greatest integer value of that real number instead of its own value. In mathematics competitions, we also encounter equations involving floor functions. It is very interesting that if the equation involving the floor function is given, then whether we can find the complete solution set for it or not. Of course, one can try by considering polynomial equations with some unknowns are replaced by $\lfloor x \rfloor$. For linear equation, $a\lfloor x \rfloor + b = 0$, it is very easy to find the complete solution set depending on the parameters a and b . Thus, in this article, we would like to explore some quadratic equations involving floor functions in the unknown. Matsko [2] analyzed behaviors of solutions of 7 quadratics equations involving floor functions namely,

- | | |
|--|--|
| E1) $\lfloor x \rfloor^2 + b\lfloor x \rfloor - c = 0$ | E2) $\lfloor x \rfloor^2 + bx - c = 0$ |
| E3) $x\lfloor x \rfloor + bx - c = 0$ | E4) $\lfloor x^2 \rfloor + bx - c = 0$ |
| E5) $x\lfloor x \rfloor + b\lfloor x \rfloor - c = 0$ | E6) $x^2 + b\lfloor x \rfloor - c = 0$ |
| E7) $\lfloor x^2 \rfloor + b\lfloor x \rfloor - c = 0$ | |

However, the complete solutions for these 7 equations depending on the parameters b and c are not provided. This article presents the complete solutions for some of these equations for the cases $b = 0$ or $c = 0$.

Methodology:

Case $b = 0$

First, let us consider the case where $b = 0$. E1) – E7) becomes only 3 forms which are

$$\lfloor x \rfloor^2 - c = 0, \lfloor x^2 \rfloor - c = 0 \text{ and } x\lfloor x \rfloor - c = 0.$$

Theorem 1 provides the complete solution set for the first 2 equations above.

Theorem 1 (i) $[x]^2 - c = 0$ has a solution if and only if c is a square integer. In the case that it has a solution, the solution set is $[-\sqrt{c}, -\sqrt{c} + 1) \cup [\sqrt{c}, \sqrt{c} + 1)$.

(ii) $[x^2] - c = 0$ has a solution if and only if $c \in \mathbb{N} \cup \{0\}$. In the case that it has a solution, the solution set is $(-\sqrt{c+1}, -\sqrt{c}] \cup [\sqrt{c}, \sqrt{c+1})$.

Proof (i) Let a be a solution of $[x]^2 - c = 0$. Then, $[a]^2 = c$. Thus, c is a square integer. Next, let c be a square integer. There is an integer n such that $c = n^2 = [n]^2$. Thus, $[x]^2 - c = 0$ has a solution. In the case that $[x]^2 - c = 0$ has a solution, let $a \in \{x \mid [x]^2 - c = 0\}$. Then, $[a]^2 = c$. Since c is a square integer, $[a] = -\sqrt{c}$ or $[a] = \sqrt{c}$. By the property of floor function, we have $a \in [-\sqrt{c}, -\sqrt{c} + 1) \cup [\sqrt{c}, \sqrt{c} + 1)$ if and only if $[a] = -\sqrt{c}$ or $[a] = \sqrt{c}$.

(ii) Let a be a solution of $[x^2] - c = 0$. Then, $[a^2] = c$. Thus, c is a nonnegative integer. Next, let c be a nonnegative integer. Then, choose $x = \sqrt{c} \in \mathbb{R}$, we have $[x^2] - c = [c] - c = c - c = 0$. In the case that $[x^2] - c = 0$ has a solution, let $a \in \{x \mid [x^2] - c = 0\}$. Then, $[a^2] = c$. By the property of floor function, $a^2 \in [c, c + 1)$. Since c is a nonnegative integer and $a^2 \in [c, c + 1)$ if and only if $a \in (-\sqrt{c+1}, -\sqrt{c}] \cup [\sqrt{c}, \sqrt{c+1})$, the proof is complete. \square

For the last equation $x[x] - c = 0$. If $c = 0$, by the fact that $[x] = 0$ if and only if $x \in [0, 1)$, it is easy to see that the solution set is $[0, 1)$. Thus, for the case $c \neq 0$, we give the solution set of this equation in Theorem 2.

Theorem 2 Let $c \neq 0$ and S be a solution set of $x[x] - c = 0$.

- (i) If there is an $n \in \mathbb{N}$ such that $c \in (n^2, n(n+1))$, then $S = \{\frac{c}{n}\}$.
- (ii) If there is an $n \in \mathbb{N}$ such that $c \in ((n-1)n, n^2)$, then $S = \{-\frac{c}{n}\}$.
- (iii) If there is an $n \in \mathbb{N}$ such that $c = n^2$, then $S = \{n, -n\}$.
- (iv) If $c < 0$ or there is an $n \in \mathbb{N}$ such that $c = n(n+1)$, $S = \emptyset$.

Proof (i) Assume that there is an $n \in \mathbb{N}$ such that $c \in (n^2, n(n+1))$.

Let $a = \frac{c}{n}$. Then, $a \in (n, n+1)$ and $[a] = n$. Thus, $a[a] - c = (\frac{c}{n})n - c = 0$, i.e., $a \in S$.

Next, suppose that $a \neq \frac{c}{n}$.

Case $a < 0$. There exists a positive integer m such that $-m \leq a < -m + 1$, i.e., $[a] = -m$. Thus, $m(m-1) < a[a] \leq m^2$.

If $m \leq n$, then $a[a] \leq m^2 \leq n^2 < c$. Thus, $a[a] - c < 0$.

If $m > n$, then $m \geq n+1$ and we have $a[a] > m(m-1) \geq (n+1)n > c$.

Thus, $a[a] - c > 0$.

Case $0 \leq a < 1$. Then, $a[a] - c = -c \neq 0$.

Case $1 \leq a < \frac{c}{n}$. Then, $1 \leq [a] \leq \left\lfloor \frac{c}{n} \right\rfloor = n$. Thus, $a[a] - c < (\frac{c}{n})n - c = 0$.

Case $a > \frac{c}{n}$. Then, $[a] \geq \left\lfloor \frac{c}{n} \right\rfloor = n$. Thus, $a[a] - c > (\frac{c}{n})n - c = 0$.

These 4 cases imply that $a \notin S$.

(ii) Assume that there is an $n \in \mathbb{N}$ such that $c \in ((n-1)n, n^2)$. Let $a = -\frac{c}{n}$.

Then, $a \in (-n, -n+1)$ and $[a] = -n$. Thus, $a[a] - c = (-\frac{c}{n})(-n) - c = 0$, i.e., $a \in S$.

Next, suppose that $a \neq -\frac{c}{n}$.

Case $a \geq 1$. There exists a positive integer m such that $m \leq a < m+1$, i.e., $[a] = m$. Thus, $m^2 < a[a] \leq m(m+1)$.

If $m < n$, then $m \leq n-1$ and we have $a[a] \leq m(m+1) \leq (n-1)n < c$.

Thus, $a[a] - c < 0$.



If $m \geq n$, then $a[a] > m^2 \geq n^2 > c$. Thus, $a[a] - c > 0$.

Case $0 \leq a < 1$. Then, $a[a] - c = -c \neq 0$.

Case $-\frac{c}{n} < a < 0$. Then, $-n = \left\lfloor -\frac{c}{n} \right\rfloor \leq [a] < 0$.

Thus, $a[a] - c < \left(-\frac{c}{n}\right)(-n) - c = 0$.

Case $a < -\frac{c}{n}$. Then, $[a] \leq \left\lfloor -\frac{c}{n} \right\rfloor = -n$. Thus, $a[a] - c > \left(-\frac{c}{n}\right)(-n) - c = 0$

These 4 cases imply that $a \notin S$.

(iii) Assume that there is an $n \in \mathbb{N}$ such that $c = n^2$. Let $a \in \{-n, n\}$.

Then, $a[a] - c = (\pm n)(\pm n) - c = n^2 - n^2 = 0$. Next, suppose that $a \notin \{-n, n\}$.

Case $a < -n$. Then, $[a] < -n$ and $a[a] - c > -n(-n) - n^2 = 0$.

Case $-n < a < 0$. Then, $-n \leq [a] \leq -1$ and $a[a] - c < -n(-n) - n^2 = 0$.

Case $0 \leq a < n$. Then, $0 \leq [a] < n$ and $a[a] - c < n^2 - n^2 = 0$.

Case $a > n$. Then, $[a] \geq n$ and $a[a] - c > n^2 - n^2 = 0$.

These 4 cases imply that $a \notin S$.

(iv) Assume that $c < 0$ or there is an $n \in \mathbb{N}$ such that $c = n(n+1)$.

Case $c < 0$. Let $x \in S$. Then, $x[x] - c \geq 0 - c > 0$.

Case there is an $n \in \mathbb{N}$ such that $c = n(n+1)$. Let $x \in S$. Thus, $x[x] = n(n+1)$.

If $x > 0$, then $[x] \leq x < [x] + 1$. Thus,

$$[x]^2 \leq x[x] (= n(n+1)) < ([x] + 1)[x] < ([x] + 1)^2.$$

$$\text{That is } [x] \leq \sqrt{n(n+1)} < [x] + 1 \text{ and } \left\lfloor \sqrt{n(n+1)} \right\rfloor = [x].$$

$$\text{However, } n^2 < n(n+1) < (n+1)^2, \text{ i.e., } n < \sqrt{n(n+1)} < n+1.$$

$$\text{We have that } [x] = \left\lfloor \sqrt{n(n+1)} \right\rfloor = n \text{ and } n(n+1) = x[x] = xn.$$

$$\text{Thus, } x = n+1 \text{ and } [x] = n+1 \text{ which contradicts with } [x] = n.$$

If $x < 0$, then $[x] \leq x < [x] + 1$. Thus,

$$[x]^2 \geq x[x] (= n(n+1)) > [x]([x] + 1) > ([x] + 1)^2.$$

$$\text{That is } ([x] + 1) > -\sqrt{n(n+1)} \geq [x] \text{ and } \left\lfloor -\sqrt{n(n+1)} \right\rfloor = [x].$$

$$\text{However, } -(n+1) < -\sqrt{n(n+1)} < -n. \text{ We have that}$$

$$[x] = \left\lfloor -\sqrt{n(n+1)} \right\rfloor = -(n+1) \text{ and}$$

$$n(n+1) = x[x] = -x(n+1). \text{ Thus, } x = -n \text{ and } [x] = -n \text{ which contradicts with } [x] = -(n+1). \quad \square$$

Case $c = 0$

First, we consider some easier equations where there are common factors among 2 terms in the equations which are E1, E3 and E5.

Theorem 3 Let S be a solution set of $[x]^2 + b[x] = 0$.

(i) If $b \in \mathbb{Z}$, then $S = [0, 1) \cup [-b, -b+1)$. (ii) If $b \notin \mathbb{Z}$, then $S = [0, 1)$.

Proof (i) Assume that $b \in \mathbb{Z}$. Let $a \in S = [0, 1) \cup [-b, -b+1)$. Then, $[a] = 0$ or $[a] = -b$. if and only if $[a]^2 + b[a] = [a]([a] + b) = 0$

(ii) Assume that $b \notin \mathbb{Z}$.

Let $a \in [0, 1)$. Then, $[a] = 0$ and $[a]^2 + b[a] = [a]([a] + b) = 0$.

Next, suppose that $a \notin [0, 1)$. Then, $[a] \neq 0$. Since $b \notin \mathbb{Z}$, $[a] + b \neq 0$.

Thus, $[a]^2 + b[a] = [a]([a] + b) \neq 0$. \square

Theorem 4 Let S be a solution set of $x[x] + bx = 0$.

(i) If $b \in \mathbb{Z}$, then $S = \{0\} \cup [-b, -b+1)$. (ii) If $b \notin \mathbb{Z}$, then $S = \{0\}$.

Proof (i) Assume that $b \in \mathbb{Z}$. Let $a \in S = \{0\} \cup [-b, -b+1)$. Then, $a = 0$ or $[a] = -b$.

if and only if $a[a] + ab = a([a] + b) = 0$

(ii) Assume that $b \notin \mathbb{Z}$. Let $a = 0$. Then, $a[a] + ab = a([a] + b) = 0$. Next, suppose that $a \neq 0$. Since $b \notin \mathbb{Z}$, $[a] + b \neq 0$. Thus, $a[a] + ab = a([a] + b) \neq 0$. \square

Theorem 5 Let S be a solution set of $x[x] + b[x] = 0$.

(i) If $b \in (-1, 0]$, then $S = [0, 1)$

(ii) If $b \in (-\infty, -1] \cup (0, \infty)$, then $S = [0, 1) \cup \{-b\}$.

Proof (i) Assume that $b \in (-1, 0]$. Let $a \in S = [0, 1)$.

Then, $[a] = 0$. Thus, $a[a] + b[a] = [a](a + b) = 0$. Next, suppose that $a \notin [0, 1)$.

Case $a < 0$. Then, $[a] < 0$ and $a + b < 0$. Thus, $a[a] + b[a] = [a](a + b) > 0$.

Case $a \geq 1$. Then, $[a] \geq 1$ and $a + b > 0$. Thus, $a[a] + b[a] = [a](a + b) > 0$.

These 2 cases imply that $a \notin S$.

(ii) Assume that $b \in (-\infty, -1] \cup (0, \infty)$. Let $a \in S = [0, 1) \cup \{-b\}$.

Then, $[a] = 0$ or $a = -b$ if and only if $a[a] + b[a] = [a](a + b) = 0$. \square

Next, we consider equations E2 and E6 which cannot be factorized and the unknown does not involve $[x^2]$.

Theorem 6 Let S be a solution set of $[x]^2 + bx = 0$.

(i) If there is an $n \in \mathbb{N}$ such that $b \in \left[-n, -\frac{n^2}{n+1}\right)$, then $S = \left\{0, -\frac{n^2}{b}\right\}$.

(ii) If there is an $n \in \mathbb{N}$ such that $b \in \left[-\frac{n^2}{n+1}, -(n-1)\right)$, then $S = \{0\}$.

(iii) If there is an $n \in \mathbb{N}$ such that $b \in \left[\frac{(n+2)^2}{n+1}, n+4\right)$, then $S = \left\{0, -\frac{1}{b}, -\frac{(n+3)^2}{b}\right\}$.

(iv) If there is an $n \in \mathbb{N}$ such that $b \in \left[n+2, \frac{(n+1)^2}{n}\right)$,

then $S = \left\{0, -\frac{1}{b}, -\frac{(n+1)^2}{b}, -\frac{(n+2)^2}{b}\right\}$.

(v) If $b = 0$, then $S = [0, 1)$.

(vi) If $b \in (0, 1)$, then $S = \{0\}$.

(vii) If $b \in [1, 2)$, then $S = \left\{-\frac{1}{b}, 0\right\}$.

(viii) If $b \in [2, 3)$, then $S = \left\{-\frac{4}{b}, -\frac{1}{b}, 0\right\}$.

Proof (i) Assume that there is an $n \in \mathbb{N}$ such that $b \in \left[-n, -\frac{n^2}{n+1}\right)$. We have that $n \leq -\frac{n^2}{b} < n+1$. Let $x \in \left\{0, -\frac{n^2}{b}\right\}$.

If $x = 0$, then $[x]^2 + bx = 0$.

If $x = -\frac{n^2}{b}$, then $\left[-\frac{n^2}{b}\right] = n$. Thus, $[x]^2 + bx = \left[-\frac{n^2}{b}\right]^2 + b\left(-\frac{n^2}{b}\right) = n^2 - n^2 = 0$.

Next, suppose that $x \notin \left\{0, -\frac{n^2}{b}\right\}$.

Case $x < 0$. Then, $x^2 + b[x] > 0$.

Case $0 < x < n$. Then, $[x] \leq n-1$.

Hence, $[x]^2 + bx < (n-1)^2 + n\left(-\frac{n^2}{n+1}\right) = \frac{-n^2-n+1}{n+1} = -n + \frac{1}{n+1} < 0$.

Case $n \leq x < -\frac{n^2}{b}$. Then, $[x] = n$. We have that $[x]^2 + bx > n^2 - n^2 = 0$.

Case $-\frac{n^2}{b} < x < n+1$. Then, $[x] = n$. We have that $[x]^2 + bx < n^2 - n^2 = 0$.

Case $x \geq n+1$. Then, $[x] \geq n+1$.

We have $[x]^2 + bx \geq (n+1)^2 - n(n+1) = n+1 > 0$.

These 5 cases imply that $x \notin S$.



(ii) Assume that there is an $n \in \mathbb{N}$ such that $b \in \left[-\frac{n^2}{n+1}, -(n-1)\right)$. If $x = 0$, then $[x]^2 + bx = 0$. Let $x \neq 0$.

Case $x < 0$. Then, $[x]^2 + bx > 0$.

Case $0 < x < n$. Then, $0 \leq [x] \leq n-1$.

We have that $[x]^2 + bx < (n-1)^2 - (n-1)n < 0$.

Case $x \geq n$. Then, $[x]^2 + bx > n^2 + \left(-\frac{n}{n+1}\right)n^2 = \frac{n^2}{n+1} > 0$.

These 3 cases imply that $x \notin S$.

(iii) Assume that there is an $n \in \mathbb{N}$ such that $b \in \left[\frac{(n+2)^2}{n+1}, n+4\right)$.

We have $-1 \leq -\frac{n+1}{(n+2)^2} \leq -\frac{1}{b} < -\frac{1}{n+4} < 0$

and $-(n+3) \leq -\frac{(n+1)(n+3)^2}{(n+2)^2} \leq -\frac{(n+3)^2}{b} < -\frac{(n+3)^2}{n+4} < -(n+2)$.

If $x = 0$ or $x = -\frac{1}{b}$ or $x = -\frac{(n+3)^2}{b}$, then $[x] = 0$ or $[x] = -1$ or $[x] = -(n+3)$, respectively. Thus, $[x]^2 + bx = 0$ or $[x]^2 + bx = (-1)^2 + b\left(-\frac{1}{b}\right) = 0$ or

$[x]^2 + bx = (-(n+3))^2 + b\left(-\frac{(n+3)^2}{b}\right) = 0$, respectively.

Now, suppose that $x \notin \left\{0, -\frac{1}{b}, -\frac{(n+3)^2}{b}\right\}$.

Case $x > 0$. Then, $[x]^2 + bx > 0$

Case $-\frac{1}{b} < x < 0$. Then, $[x] = -1$. We have that $[x]^2 + bx > 1 - 1 = 0$.

Case $-(n+2) \leq x < -\frac{1}{b}$. Then, we consider the followings

If $-1 \leq x < -\frac{1}{b}$, then $[x] = -1$. Thus, $[x]^2 + bx < 1 + (-1) = 0$.

If $-(n+2) \leq x < -1$, then there is a positive integer $1 \leq k \leq n+1$ such that $-k-1 \leq x < -k$, that is, $[x] = -k-1$. Note that

$$[x]^2 + bx < (k+1)^2 + b(-k) = k^2 + (2-b)k + 1 \leq k^2 + \left(\frac{-n^2-2n-2}{n+1}\right)k + 1$$

, where the last inequality follows from the fact that $b \geq \frac{(n+2)^2}{n+1}$.

It is easy to see that if $t \in [2, \infty)$, then $f(t) := t^2 + \left(\frac{-n^2-2n-2}{n+1}\right)t + 1$

is an increasing function. If $k \geq 2$, then $f(k) < f(n+1)$. In addition.

$$f(1) = 1 - n - \frac{1}{n+1} < 0 = (n+1)^2 + -n^2 - 2n - 2 + 1 =$$

$$f(n+1)$$

Thus, for $1 \leq k \leq n+1$, we have $[x]^2 + bx < f(k) \leq f(n+1) = 0$.

Case $-\frac{(n+3)^2}{b} < x < -(n+2)$. Then, $[x] = -(n+3)$.

We have that $[x]^2 + bx > (n+3)^2 - (n+3)^2 = 0$.

Case $-(n+3) \leq x < -\frac{(n+3)^2}{b}$. Then, $[x] = -(n+3)$.

We have that $[x]^2 + bx < (n+3)^2 - (n+3)^2 = 0$.

Case $x < -(n+3)$. Then, there is a positive integer $k \geq n+3$ such that

$-k-1 \leq x < -k$, that is, $[x] = -k-1$. Note that

$$[x]^2 + bx > (k+1)^2 + b(-k-1) = k^2 + (2-b)k + (1-b) > k^2 + (-n-2)k + (-n-3)$$

, where the last inequality follows from the fact that $b < n+4$.

It is easy to see that if $t \in [n+3, \infty)$, then

$f(t) := t^2 + (-n-2)t + (-n-3)$ is an increasing function on $[n+3, \infty)$.

Thus, for $k \geq n+3$, we have

$$[x]^2 + bx > f(k) \geq f(n+3) = (n+3)^2 + (-n-2)(n+3) + (-n-3) = 0$$

These 6 cases imply that $x \notin S$.

(iv) Assume that there is an $n \in \mathbb{N}$ such that $b \in \left[n+2, \frac{(n+1)^2}{n}\right)$. We have $-1 \leq -\frac{1}{n+2} \leq -\frac{1}{b} < -\frac{n}{(n+1)^2} < 0$, $-(n+1) \leq -\frac{(n+1)^2}{n+2} \leq -\frac{(n+1)^2}{b} < -n$ and $-(n+2) \leq -\frac{(n+2)^2}{b} < -\frac{n(n+2)^2}{(n+1)^2} < -(n+1)$. If $x = 0$ or $x = -\frac{1}{b}$ or $x = -\frac{(n+1)^2}{b}$ or $x = -\frac{(n+2)^2}{b}$, then $[x] = 0$ or $[x] = -1$ or $[x] = -(n+1)$ or $[x] = -(n+2)$, respectively.

Thus, $[x]^2 + bx = 0$ or $[x]^2 + bx = (-1)^2 + b\left(-\frac{1}{b}\right) = 0$ or

$$[x]^2 + bx = (-(n+1))^2 + b\left(-\frac{(n+1)^2}{b}\right) = 0$$

$$\text{or } [x]^2 + bx = (-(n+2))^2 + b\left(-\frac{(n+2)^2}{b}\right) = 0 \text{ respectively.}$$

Now, suppose that $x \notin \left\{0, -\frac{1}{b}, -\frac{(n+1)^2}{b}, -\frac{(n+2)^2}{b}\right\}$

Case $x > 0$. Then, $[x]^2 + bx > 0$.

Case $-\frac{1}{b} < x < 0$. Then, $[x] = -1$. We have that $[x]^2 + bx > 1 - 1 = 0$.

Case $-n \leq x < -\frac{1}{b}$. Then, we consider the followings

If $-1 \leq x < -\frac{1}{b}$, $[x] = -1$. We have that $[x]^2 + bx < 1 - 1 = 0$.

If $-n \leq x < -1$, where $n \geq 2$, then there is a positive integer $1 \leq k \leq n-1$

such that $-k-1 \leq x < -k$, that is, $[x] = -k-1$. Note that

$$[x]^2 + bx < (k+1)^2 + b(-k) = k^2 + (2-b)k + 1 \leq k^2 - nk + 1,$$

where the last inequality follows from the fact that $b \geq n+2$. If

$n = 2$, then $k = 1$ and $k^2 - nk + 1 = 0$, done. Let $n \geq 3$ and

$f(t) := t^2 - nt + 1$. It is easy to see that if $t \in \left[1, \frac{n}{2}\right)$, then $f(t)$ is a

decreasing function. While, if $t \in \left[\frac{n}{2}, n-1\right]$, then $f(t)$ is an

increasing function. Notice that $f(1) = f(n-1) = 2 - n \leq 0$. We

can conclude that $[x]^2 + bx < f(k) \leq f(n-1) \leq 0$.

Case $-\frac{(n+1)^2}{b} < x < -n$. Then, $[x] = -(n+1)$.

$$\text{We have that } [x]^2 + bx > (n+1)^2 - (n+1)^2 = 0.$$

Case $-(n+1) \leq x < -\frac{(n+1)^2}{b}$. Then, $[x] = -(n+1)$.

$$\text{We have that } [x]^2 + bx < (n+1)^2 - (n+1)^2 = 0.$$

Case $-\frac{(n+2)^2}{b} < x < -(n+1)$. Then, $[x] = -(n+2)$.

$$\text{We have that } [x]^2 + bx > (n+2)^2 - (n+2)^2 = 0.$$

Case $-(n+2) \leq x < -\frac{(n+2)^2}{b}$. Then, $[x] = -(n+2)$.

$$\text{We have that } [x]^2 + bx < (n+2)^2 - (n+2)^2 = 0.$$

Case $x < -(n+2)$, then there is a positive integer $k \geq n+2$ such that $-k-1 \leq x < -k$, that is, $[x] = -k-1$.

Note that



$$\lfloor x \rfloor^2 + bx > (k+1)^2 + b(-k-1) = k^2 + (2-b)k + (1-b) > k^2 + \left(\frac{-n^2-1}{n}\right)k + \left(\frac{-n^2-n-1}{n}\right)$$

, where the last inequality follows from the fact that $b < \frac{(n+1)^2}{n}$. It is easy to see that if $t \in [n+2, \infty)$, then $f(t) := t^2 + \left(\frac{-n^2-1}{n}\right)t + \left(\frac{-n^2-n-1}{n}\right)$ is an increasing function.

Thus, for $k \geq n+2$, we have

$$\lfloor x \rfloor^2 + bx > f(k) \geq f(n+2) = (n+2)^2 + \left(\frac{-n^2-1}{n}\right)(n+2) + \left(\frac{-n^2-n-1}{n}\right) = \frac{n^2+2n-3}{n} \geq 0.$$

These 8 cases imply that $x \notin S$.

(v) It is done since $\lfloor x \rfloor = 0$ if and only if $x \in [0, 1)$.

(vi) Let $b \in (0, 1)$. If $x = 0$, then $\lfloor x \rfloor^2 + bx = 0$. Let $x \neq 0$.

Case $x > 0$. Then, $\lfloor x \rfloor^2 + bx > 0$.

Case $x < 0$. Then, $\lfloor x \rfloor \leq -1$. We have that $\lfloor x \rfloor^2 = (-\lfloor x \rfloor)^2 \geq -\lfloor x \rfloor \geq -x > -bx$.

Thus, $\lfloor x \rfloor^2 + bx > 0$.

These 2 cases imply that $x \notin S$.

(vii) Let $b \in [1, 2)$. We have $-1 \leq -\frac{1}{b} < -\frac{1}{2}$. Let $x \in S = \left\{-\frac{1}{b}, 0\right\}$. If $x = -\frac{1}{b}$, then $\left\lfloor -\frac{1}{b} \right\rfloor = -1$. If $x = 0$, then $\lfloor x \rfloor^2 + bx = 0$. Thus, $\lfloor x \rfloor^2 + bx = (-1)^2 + b\left(-\frac{1}{b}\right) = 0$.

Now, suppose that $x \notin S$.

Case $x > 0$. Then, $\lfloor x \rfloor^2 + bx > 0$.

Case $-\frac{1}{b} < x < 0$. Then, $\lfloor x \rfloor = -1$. Thus, $\lfloor x \rfloor^2 + bx > 1 + (-1) = 0$.

Case $-1 \leq x < -\frac{1}{b}$. Then, $\lfloor x \rfloor = -1$. Thus, $\lfloor x \rfloor^2 + bx < 1 + (-1) = 0$.

Case $x < -1$. Then, $\lfloor x \rfloor < -1$. We have that $\lfloor x \rfloor^2 = (-\lfloor x \rfloor)^2 > -\lfloor x \rfloor \geq -x > -bx$.

Thus, $\lfloor x \rfloor^2 + bx > 0$.

These 4 cases imply that $x \notin S$.

(viii) Let $b \in [2, 3)$. We have $-\frac{1}{2} \leq -\frac{1}{b} < -\frac{1}{3}$ and $-2 \leq -\frac{4}{b} < -\frac{4}{3}$. Let $x \in \left\{-\frac{4}{b}, -\frac{1}{b}, 0\right\}$. If $x = -\frac{4}{b}$, then $\left\lfloor -\frac{4}{b} \right\rfloor = -2$. Thus, $\lfloor x \rfloor^2 + bx = (-2)^2 + b\left(-\frac{4}{b}\right) = 0$. If $x = -\frac{1}{b}$, then $\left\lfloor -\frac{1}{b} \right\rfloor = -1$. Thus, $\lfloor x \rfloor^2 + bx = (-1)^2 + b\left(-\frac{1}{b}\right) = 0$. Finally, If $x = 0$, then $\lfloor x \rfloor^2 + bx = 0$.

Next, suppose that $x \notin \left\{0, -\frac{1}{b}, -\frac{4}{b}\right\}$.

Case $x > 0$. Then, $\lfloor x \rfloor^2 + bx > 0$.

Case $-\frac{1}{b} < x < 0$. Then, $\lfloor x \rfloor = -1$. Thus, $\lfloor x \rfloor^2 + bx > 1 + (-1) = 0$.

Case $-1 \leq x < -\frac{1}{b}$. Then, $\lfloor x \rfloor = -1$. Thus, $\lfloor x \rfloor^2 + bx < 1 + (-1) = 0$.

Case $-\frac{4}{b} < x < -1$. Then, $\lfloor x \rfloor = -2$. Thus, $\lfloor x \rfloor^2 + bx > 4 + (-4) = 0$.

Case $-2 \leq x < -\frac{4}{b}$. Then, $\lfloor x \rfloor = -2$. Thus, $\lfloor x \rfloor^2 + bx < 4 + (-4) = 0$.

Case $x < -2$. Then, $\lfloor x \rfloor < -2$.

We have that $\lfloor x \rfloor^2 = (-\lfloor x \rfloor)^2 > -2\lfloor x \rfloor \geq -2x \geq -bx$. Thus, $\lfloor x \rfloor^2 + bx > 0$.

These 6 cases imply that $x \notin S$. □

Theorem 7 Let S be a solution set of $x^2 + b\lfloor x \rfloor = 0$.

(i) If there is an $n \in \mathbb{N}$ such that $b \in \left(n-1, \frac{n^2}{n+1}\right]$, then $S = \{-\sqrt{bn}, 0\}$.

- (ii) If there is an $n \in \mathbb{N}$ such that $b \in \left(\frac{n^2}{n+1}, n\right]$, then $S = \{-\sqrt{b(n+1)}, -\sqrt{bn}, 0\}$.
- (iii) If $b \in (-1, 0]$, then $S = \{0\}$.
- (iv) If $b \in (-2, -1]$, then $S = \{0, \sqrt{|b|}\}$.
- (v) If $b \in (-3, -2]$, then $S = \{0, \sqrt{|b|}, \sqrt{2|b|}\}$.
- (vi) If there is an $n \in \mathbb{N}$ such that $b \in \left(-(n+4), -\frac{(n+2)^2}{n+1}\right]$, then $S = \{0, \sqrt{(n+2)|b|}, \sqrt{(n+3)|b|}\}$.
- (vii) If there is an $n \in \mathbb{N}$ such that $b \in \left(-\frac{(n+1)^2}{n}, -(n+2)\right]$, then $S = \{0, \sqrt{n|b|}, \sqrt{(n+1)|b|}, \sqrt{(n+2)|b|}\}$.

Proof (i) Assume that there is an $n \in \mathbb{N}$ such that $b \in \left(n-1, \frac{n^2}{n+1}\right]$. We have that $-n < -\frac{n\sqrt{n}}{\sqrt{n+1}} \leq -\sqrt{bn} < -\sqrt{n(n-1)} < -(n-1)$. Then, $\lfloor -\sqrt{bn} \rfloor = -n$. If $x = -\sqrt{bn}$, then $x^2 + b[x] = (-\sqrt{bn})^2 + b[-\sqrt{bn}] = bn + (-bn) = 0$. If $x = 0$, then $x^2 + b[x] = 0$. Next, suppose that $x \notin \{-\sqrt{bn}, 0\}$.

Case $x > 0$. $x^2 + b[x] > 0$.

Case $-\sqrt{bn} < x < 0$. Then, $\lfloor x \rfloor \geq -n$. Thus, $x^2 < bn = (-b)(-n) \leq -b[x]$. Hence, $x^2 + b[x] < 0$.

Case $x < -\sqrt{bn}$. Then, $\lfloor x \rfloor \leq -n$. Thus, $x^2 > bn = (-b)(-n) \geq -b[x]$. Hence, $x^2 + b[x] > 0$.

These 3 cases imply that $x \notin S$.

(ii) Assume that there is an $n \in \mathbb{N}$ such that $b \in \left(\frac{n^2}{n+1}, n\right]$. We have that

$$-(n+1) \leq -\sqrt{n(n+1)} \leq -\sqrt{b(n+1)} \leq -n \leq -\sqrt{bn} < -\frac{n\sqrt{n}}{\sqrt{n+1}} < -(n-1).$$

Then, $\lfloor -\sqrt{bn} \rfloor = -n$ and $\lfloor -\sqrt{b(n+1)} \rfloor = -(n+1)$. If $x = -\sqrt{b(n+1)}$, then $(-\sqrt{b(n+1)})^2 + b[-\sqrt{b(n+1)}] = b(n+1) + (-b(n+1)) = 0$. If $x = -\sqrt{bn}$, then $(-\sqrt{bn})^2 + b[-\sqrt{bn}] = bn + (-bn) = 0$. If $x = 0$, then $x^2 + b[x] = 0$. Next, suppose that $x \notin \{-\sqrt{b(n+1)}, -\sqrt{bn}, 0\}$.

Case $x > 0$. Then, $x^2 + b[x] > 0$.

Case $-\sqrt{bn} < x < 0$. Then, $\lfloor x \rfloor \geq -n$. Thus $x^2 < bn = (-b)(-n) \leq -b[x]$. Hence, $x^2 + b[x] < 0$.

Case $-\sqrt{b(n+1)} < x < -\sqrt{bn}$. Then,

If $-n \leq x < -\sqrt{bn}$, then $\lfloor x \rfloor = -n$. Thus, $x^2 > bn = (-b)(-n) = -b[x]$.

Hence, $x^2 + b[x] > 0$.

If $-\sqrt{b(n+1)} < x < -n$, then $\lfloor x \rfloor = -(n+1)$. Thus, $x^2 < b(n+1) = -b(-(n+1)) = -b[x]$. Hence, $x^2 + b[x] < 0$.

Case $x < -\sqrt{b(n+1)}$. Then, $\lfloor x \rfloor \leq -(n+1)$.

Thus, $x^2 > b(n+1) = (-b)(-(n+1)) \geq -b[x]$. Hence, $x^2 + b[x] > 0$.

These 4 cases imply that $x \notin S$.

(iii) Let $b \in (-1, 0]$. If $x = 0$, then $x^2 + b[x] = 0$. Let $x \neq 0$.

Case $x < 0$. Then, $x^2 + b[x] > 0$.

Case $x > 0$. Then,

If $x \in (0, 1)$, then $\lfloor x \rfloor = 0$. Thus, $x^2 + b[x] = x^2 > 0$.

If $x \in [1, \infty)$, then $x^2 \geq x \geq \lfloor x \rfloor > -b[x]$. Thus, $x^2 + b[x] > 0$.



These 2 cases imply that $x \notin S$.

(iv) Let $b \in (-2, -1]$. If $x = 0$, then $x^2 + b[x] = 0$. If $x = \sqrt{|b|}$, then $[x] = \lfloor \sqrt{|b|} \rfloor = 1$ and we have $x^2 + b[x] = -b + b = 0$. Next, suppose that $x \notin \{0, \sqrt{|b|}\}$.

Case $x < 0$. Then, $x^2 + b[x] > 0$.

Case $x > 0$.

If $x \in (0, 1)$, then $[x] = 0$. Thus, $x^2 + b[x] = x^2 > 0$.

If $x \in [1, \sqrt{|b|})$, then $x^2 + b[x] < -b + b(1) = 0$.

If $x > \sqrt{|b|}$, then $x^2 + b[x] > -b + b(1) = 0$.

These 2 cases imply that $x \notin S$.

(v) Let $b \in (-3, -2]$.

If $x = 0$, then $x^2 + b[x] = 0$. If $x = \sqrt{|b|}$, then $[x] = \lfloor \sqrt{|b|} \rfloor = 1$ and we have $x^2 + b[x] = -b + b = 0$. If $x = \sqrt{2|b|}$, then $[x] = \lfloor \sqrt{2|b|} \rfloor = 2$ and we have $x^2 + b[x] = -2b + 2b = 0$. Next, suppose that $x \notin \{0, \sqrt{|b|}, \sqrt{2|b|}\}$.

Case $x < 0$. Then, $x^2 + b[x] > 0$.

Case $x > 0$.

If $x \in (0, 1)$, then $[x] = 0$. Thus, $x^2 + b[x] = x^2 > 0$.

If $x \in [1, \sqrt{|b|})$, then $x^2 + b[x] < -b + b(1) = 0$.

If $x \in (\sqrt{|b|}, 2)$, then $x^2 + b[x] > -b + b(1) = 0$.

If $x \in [2, \sqrt{2|b|})$, then $x^2 + b[x] < -2b + b(2) = 0$.

Note that for $b = -2$, $[2, \sqrt{2|b|}) = \emptyset$.

If $x > \sqrt{2|b|}$, then $x^2 + b[x] > -2b + b(2) = 0$.

These 2 cases imply that $x \notin S$.

(vi) Assume that there is an $n \in \mathbb{N}$ such that $b \in \left(- (n+4), -\frac{(n+2)^2}{n+1}\right]$.

We have that $n+2 < \frac{(n+2)\sqrt{n+2}}{\sqrt{n+1}} \leq \sqrt{(n+2)|b|} < \sqrt{(n+2)(n+4)} < n+3$ and

$n+3 < \frac{(n+2)\sqrt{n+3}}{\sqrt{n+1}} \leq \sqrt{(n+3)|b|} < \sqrt{(n+3)(n+5)} < n+4$.

Then, $\lfloor \sqrt{(n+2)|b|} \rfloor = n+2$ and $\lfloor \sqrt{(n+3)|b|} \rfloor = n+3$.

Let $x \in S = \{0, \sqrt{(n+2)|b|}, \sqrt{(n+3)|b|}\}$. If $x = 0$, then $x^2 + b[x] = 0$.

If $x = \sqrt{(n+2)|b|}$, then $x^2 + b[x] = (n+2)(-b) + b(n+2) = 0$.

If $x = \sqrt{(n+3)|b|}$, then $x^2 + b[x] = (n+3)(-b) + b(n+3) = 0$. Next, suppose that $x \notin \{0, \sqrt{(n+2)|b|}, \sqrt{(n+3)|b|}\}$.

Case $x < 0$. Then, $x^2 + b[x] > 0$.

Case $x \in (0, 1)$. Then, $[x] = 0$. Thus, $x^2 + b[x] = x^2 > 0$.

Case $1 \leq x < \sqrt{(n+2)|b|}$. Then, we consider the followings

If $1 \leq x < n+2$, then there is a positive integer $1 \leq k \leq n+1$ such that $k \leq x < k+1$, that is, $[x] = k$.

Note that

$$x^2 + b[x] < (k+1)^2 + bk = k^2 + (2+b)k + 1 \leq k^2 + \left(\frac{-n^2-2n-2}{n+1}\right)k + 1,$$

where the last inequality follows from the fact that $b \leq -\frac{(n+2)^2}{n+1}$.

Let $f(t) := t^2 + \left(\frac{-n^2-2n-2}{n+1}\right)t + 1$. It is easy to see that if $t \in [3, \infty)$, then $f(t) := t^2 + \left(\frac{-n^2-2n-2}{n+1}\right)t + 1$ is an increasing function.

If $k \geq 3$, then $f(k) < f(n+1)$.

In addition,

$$f(1) = 1 - n - \frac{1}{n+1} < 0 = (n+1)^2 + -n^2 - 2n - 2 + 1 = f(n+1)$$

and $f(2) = \frac{-2n^2+n+1}{n+1} \leq 0 = f(n+1)$. Thus, for $1 \leq k \leq n+1$, we have $[x]^2 + bx < f(k) \leq f(n+1) = 0$.

If $n+2 \leq x < \sqrt{(n+2)|b|}$, then $[x] = n+2$.

$$\text{Thus, } x^2 + b[x] < (n+2)(-b) + b(n+2) = 0$$

Case $\sqrt{(n+2)|b|} < x < n+3$. Then, $[x] = n+2$.

We have that $x^2 > (n+2)(-b) = -b[x]$. Hence, $x^2 + b[x] > 0$.

Case $n+3 \leq x < \sqrt{(n+3)|b|}$. Then, $[x] = n+3$.

Thus, $x^2 < (n+3)(-b) = (-b)[x]$. Hence, $x^2 + b[x] < 0$.

Case $x > \sqrt{(n+3)|b|}$. Then, $[x] \geq n+3$.

Thus, $x^2 > (n+3)(-b) = b(-(n+3)) \geq b(-[x]) = -b[x]$. Hence, $x^2 + b[x] > 0$.

These 6 cases imply that $x \notin S$.

(vii) Assume that there is an $n \in \mathbb{N}$ such that $b \in \left(-\frac{(n+1)^2}{n}, -(n+2)\right]$

We have that $n < \sqrt{n(n+2)} \leq \sqrt{n|b|} < n+1$,

$n+1 < \sqrt{(n+1)(n+2)} \leq \sqrt{(n+1)|b|} < \frac{(n+1)\sqrt{n+1}}{\sqrt{n}} < n+2$, and

$n+2 \leq \sqrt{(n+2)|b|} < \frac{(n+1)\sqrt{n+2}}{\sqrt{n}} < n+3$. Then, $\lfloor \sqrt{n|b|} \rfloor = n$, $\lfloor \sqrt{(n+1)|b|} \rfloor = n+1$ and $\lfloor \sqrt{(n+2)|b|} \rfloor = n+2$. Let $x \in S = \{0, \sqrt{n|b|}, \sqrt{(n+1)|b|}, \sqrt{(n+2)|b|}\}$.

If $x = 0$, then $x^2 + b[x] = 0$. If $x = \sqrt{n|b|}$, then $x^2 + b[x] = n(-b) + b(n) = 0$.

If $x = \sqrt{(n+1)|b|}$, then $x^2 + b[x] = (n+1)(-b) + b(n+1) = 0$.

If $x = \sqrt{(n+2)|b|}$, then $x^2 + b[x] = (n+2)(-b) + b(n+2) = 0$.

Next, suppose that $x \notin \{0, \sqrt{n|b|}, \sqrt{(n+1)|b|}, \sqrt{(n+2)|b|}\}$.

Case $x < 0$. Then, $x^2 + b[x] > 0$.

Case $x \in (0, 1)$. Then, $[x] = 0$. Thus, $x^2 + b[x] = x^2 > 0$.

Case $1 \leq x < \sqrt{n|b|}$. Then, we consider the followings

If $1 \leq x < n$, where $n \geq 2$, then there is a positive integer $1 \leq k \leq n-1$

such that $k \leq x < k+1$, that is, $[x] = k$. Note that

$$x^2 + b[x] < (k+1)^2 + bk = k^2 + (2+b)k + 1 \leq k^2 - nk + 1,$$

where the last inequality follows from the fact that $b \leq -(n+2)$.

If $n = 2$, then $k = 1$ and $k^2 - nk + 1 = 0$, done. Let $n \geq 3$ and

$f(t) := t^2 - nt + 1$. It is easy to see that if $t \in \left[1, \frac{n}{2}\right]$, then $f(t)$ is a decreasing function. While, if $t \in \left[\frac{n}{2}, n-1\right]$, then $f(t)$ is an increasing function. Notice that $f(1) = f(n-1) = 2 - n \leq 0$.

We can conclude that $[x]^2 + bx < f(k) \leq f(n-1) \leq 0$.

If $n \leq x < \sqrt{n|b|}$, then $[x] = n$. Thus, $x^2 + b[x] < n(-b) + b(n) = 0$.

Case $\sqrt{n|b|} < x < n+1$. Then $[x] = n$.



Thus, $x^2 > n(-b) = -b[x]$. Hence, $x^2 + b[x] > 0$.

Case $n + 1 \leq x < \sqrt{(n + 1)|b|}$. Then $[x] = n + 1$.

Thus, $x^2 < (n + 1)(-b) = -b[x]$. Hence, $x^2 + b[x] < 0$.

Case $\sqrt{(n + 1)|b|} < x < n + 2$. Then $[x] = n + 1$.

Thus, $x^2 > (n + 1)(-b) = -b[x]$. Hence, $x^2 + b[x] > 0$.

Case $n + 2 \leq x < \sqrt{(n + 2)|b|}$. Then $[x] = n + 2$.

Thus, $x^2 < (n + 2)(-b) = -b[x]$. Hence, $x^2 + b[x] < 0$.

Case $x > \sqrt{(n + 2)|b|}$. Then $[x] = n + 2$.

Thus, $x^2 > (n + 2)(-b) = b(-(n + 2)) \geq b(-[x]) = -b[x]$. Hence, $x^2 + b[x] > 0$.

These 8 cases imply that $x \notin S$. \square

Results:

It is shown that the existence of solutions to E1 – E7 in the case that $b = 0$ depends on the property of c . This is because the range of the floor function can only be integers.

| Equation | Condition | Solution set |
|-----------------|-------------------------------|--|
| $[x]^2 - c = 0$ | $c = n^2$ | $[-\sqrt{c}, -\sqrt{c} + 1) \cup [\sqrt{c}, \sqrt{c} + 1)$ |
| $[x^2] - c = 0$ | $c \in \mathbb{N} \cup \{0\}$ | $(-\sqrt{c} + 1, -\sqrt{c}] \cup [\sqrt{c}, \sqrt{c} + 1)$ |
| $x[x] - c = 0$ | $c \in (n^2, n(n + 1))$ | $\{\frac{c}{n}\}$ |
| | $c \in ((n - 1)n, n^2)$ | $\{-\frac{c}{n}\}$ |
| | $c = n^2$ | $\{n, -n\}$ |
| | $c < 0$ | \emptyset |

Table 1 solution sets of E1 – E7 in the case that $b = 0$

On the other hand, for $c = 0$, we have that 0 is always one of our solutions for E1 – E7. Conditions on b determine whether the solution includes other real numbers rather than 0 or not. However, for this case, we can extract the solution sets only for E1, E2, E3, E5 and E6.

| Equation | Condition | Solution set |
|--------------------|---|---|
| $[x]^2 + b[x] = 0$ | $b \in \mathbb{Z}$ | $[0, 1) \cup [-b, -b + 1)$ |
| | $b \notin \mathbb{Z}$ | $[0, 1)$ |
| $x[x] + bx = 0$ | $b \in \mathbb{Z}$ | $\{0\} \cup [-b, -b + 1)$ |
| | $b \notin \mathbb{Z}$ | $\{0\}$ |
| $x[x] + b[x] = 0$ | $b \in (-1, 0]$ | $[0, 1)$ |
| | $b \in (-\infty, -1] \cup (0, \infty)$ | $b \in (-\infty, -1] \cup (0, \infty)$ |
| $[x]^2 + bx = 0$ | $b \in [-n, -\frac{n^2}{n+1})$ | $\{0, -\frac{n^2}{b}\}$ |
| | $b \in [-\frac{n^2}{n+1}, -(n-1))$ or $b \in (0, 1)$ | $\{0\}$ |
| | $b \in [\frac{(n+2)^2}{n+1}, n+4)$ | $\{0, -\frac{1}{b}, -\frac{(n+3)^2}{b}\}$ |
| | $b \in [n+2, \frac{(n+1)^2}{n})$ | $\{0, -\frac{1}{b}, -\frac{(n+1)^2}{b}, -\frac{(n+2)^2}{b}\}$ |
| | $b = 0$ | $[0, 1)$ |
| | $b \in [1, 2)$ | $\{-\frac{1}{b}, 0\}$ |
| | $b \in [2, 3)$ | $\{-\frac{4}{b}, -\frac{1}{b}, 0\}$ |

| | | |
|------------------|---|--|
| $x^2 + b[x] = 0$ | $b \in \left(n - 1, \frac{n^2}{n+1}\right]$ | $\{-\sqrt{bn}, 0\}$ |
| | $b \in \left(\frac{n^2}{n+1}, n\right]$ | $\{-\sqrt{b(n+1)}, -\sqrt{bn}, 0\}$ |
| | $b \in (-1, 0]$ | $\{0\}$ |
| | $b \in (-2, -1]$ | $\{0, \sqrt{ b }\}$ |
| | $b \in (-3, -2]$ | $\{0, \sqrt{ b }, \sqrt{2 b }\}$ |
| | $b \in \left(-\frac{(n+4)^2}{n+1}, -\frac{(n+2)^2}{n+1}\right]$ | $\{0, \sqrt{(n+2) b }, \sqrt{(n+3) b }\}$ |
| | $b \in \left(-\frac{(n+1)^2}{n}, -(n+2)\right]$ | $\{0, \sqrt{n b }, \sqrt{(n+1) b }, \sqrt{(n+2) b }\}$ |

Table 2 solution sets of E1, E2, E3, E5 and E6 in the case that $c = 0$

From the results, one may realize that some solution sets may be finite while some are infinite. In addition, for the finite case, there may be more than 2 solutions compared to the solution of a regular quadratic equation.

Conclusion and Discussion:

It can be seen that exploring the set of solutions for equations E4 and E7 in the case that $c = 0$ is difficult due to the term $[x^2]$. Of course, some mathematical programming packages, like Mathematica, will be useful to collect data and notice the relation between each parameter b and the solutions. Thus, our future work is trying to find all solutions to equations E4 and E7 in this case. We also try to cooperate parameters b and c together in each equation which will be more complicated.

Acknowledgements:

I would like to express my sincere thanks to my thesis advisor, Dr. Ratinan Boonklurb and Dr. Atiratch Laoharenoo, for supporting me and giving more ideas for this research and I would like to extend my sincere thanks to the scholarship for Graduate Students, Graduate School, Chulalongkorn University for financial support during 2020-2022.

References:

1. J. Stewart. Calculus: Early Transcendentals (7th Edition). 2012, 105.
2. Vincent J. Matsko. Quadratics and the Floor Function, Mathematics Magazine. 2020;93:2, 104-112.



THE CENTER COLORING OF CORONA PRODUCT OF CYCLES AND PATHS

Kanokwan Saeoueng,¹ Orasa Nunkaw,² Siwaporn Saewan^{3,*}

¹Students, Department of Mathematics and Statistics, Faculty of Science and Digital Innovation, Thaksin University, Phatthalung, 93210, Thailand

²Dr., Department of Mathematics and Statistics, Faculty of Science and Digital Innovation, Thaksin University, Phatthalung, 93210, Thailand

³Assoc. Prof. Dr., Department of Mathematics and Statistics, Faculty of Science and Digital Innovation, Thaksin University, Phatthalung, 93210, Thailand

*e-mail: si_wa_pon@hotmail.com

Abstract:

Center coloring is a type of the vertex coloring of the simple connected graph G . The center coloring of the graph G is an assignment of colors to each vertex v of G , such that different vertex distance from the center are assigned different colors. The center coloring number of the graph G , denote $C_c(G)$, is the minimum number of colors required for the center coloring of G . In this paper we consider on the center coloring number of the new graph obtained by the corona product of the path P_n and the cycle C_m .

Introduction:

Let G be the simple graph with a nonempty vertex set $V(G)$ and an edge set $E(G)$. The elements of $V(G)$ are called vertices and the elements of $E(G)$ are called edges. The **endpoints** of an edge $e = uv$ is the set of two vertices u and v connects to each edge $e = uv$. The vertices u and v are in the endpoint of each edge e are called **incident** with the edge e . The vertices which are incident with a common edge are **adjacent**. A **path** $v_0 - v_k$ in a graph G is an alternating sequence

$$v_0 e_1 v_1 e_2 \dots e_k v_k,$$

of vertices and edges in G such that $e_i = v_{i-1}v_i$ and the vertices in a sequence are distinct. The graph G is **connected** if for every pair of a vertex u and a vertex v , there is a path from a vertex u to a vertex v . The **length** of the path in the graph G is the number of edge-steps in the path. The **distance** $d(u, v)$ from a vertex u to a vertex v in the graph G is the length of the shortest $u - v$ path. The **eccentricity** of a vertex v in the graph G , denote by $e(v)$, is the distance from v to a vertex farthest from v . That is

$$e(v) = \max_{u \in V(G)} \{d(u, v)\}.$$

The graph G with the eccentricity of every vertices shown in Figure 1.

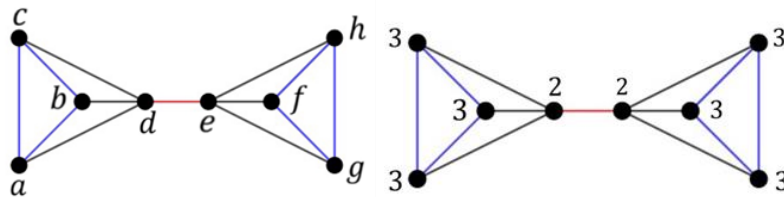


Figure 1.



The **radius** of the graph G , denoted $rad(G)$, is the minimum of the vertex eccentricities. That is $rad(G) = \min_{v \in V(G)} \{e(v)\}$.

A **central vertex** v of the graph G is a vertex with minimum eccentricity. Thus, $e(v) = rad(G)$. in Figure 1, d and e are central vertex of graph G , shown in Figure 2.

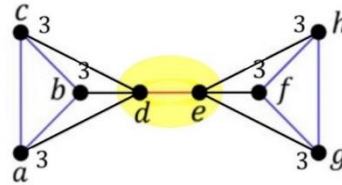


Figure 2.

The **center** of the graph G is the subgraph induced by the set of central vertices of G . The graph is **self-centered** if every vertex is in the center. For more detail in basic concept of graph theory, the reader can see in Gross and Yellen¹ and Bondy and Murty². The **center coloring** of the graph G was introduced by Yorgancioglu et al.³. The center coloring of the connected graph G is an assignment of colors to each vertex of G , such that different distance vertices from the center are assigned different colors. The **center coloring number** of a connected graph G , denote $C_c(G)$, is the minimum number of colors required for the center coloring of G . In 2018 Yorgancioglu et al.⁴ was shown the relation between the center coloring and the other colorings of the connected graph. Yorgancioglu and Dündar⁵ studied the behavior of the center coloring of the new graphs obtained by some graph operations.

Let G and H be the simple connected graph. The **Corona Product** graph $G \circ H$ is defined as the graph obtained from the graph G and the graph H by taking one copy of G and $|V(G)|$ copies of H and then joining by an edge such that each vertex of the i^{th} vertex of G to every vertex in the i^{th} copy of H . The corona product graph $P_2 \circ C_3$ and $C_3 \circ P_2$ shown in Figure 3 respectively.

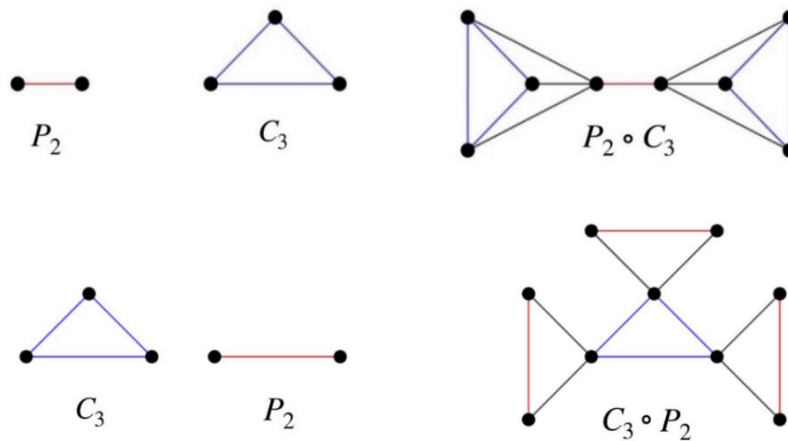


Figure 3.

In this paper, we consider the center coloring of the corona product graph $P_n \circ C_m$ and $C_m \circ P_n$ and we get center coloring number of the new graph $C_c(P_n \circ C_m)$ and $C_c(C_m \circ P_n)$.

Methodology:

Studying on the corona product of the graph $P_n \circ C_m$ is formed by taking one copy of P_n and $|V(P_n)|$ copy of C_m and then connecting the i^{th} vertex of the path P_n to every vertex in the i^{th} copy of the cycle C_m . Finding the center coloring number of the new graph $P_n \circ C_m$. The center coloring number of $P_1 \circ C_m$ where $m = 3, 4, 5$ shown in Figure 4. The center coloring number of $P_3 \circ C_m$ where $m = 3, 4$ shown in Figure 5. The center coloring number of $P_5 \circ C_m$ where $m = 3, 4$ shown in Figure 6. The center coloring number of $P_7 \circ C_m$ where $m = 3, 4$ shown in Figure 7.

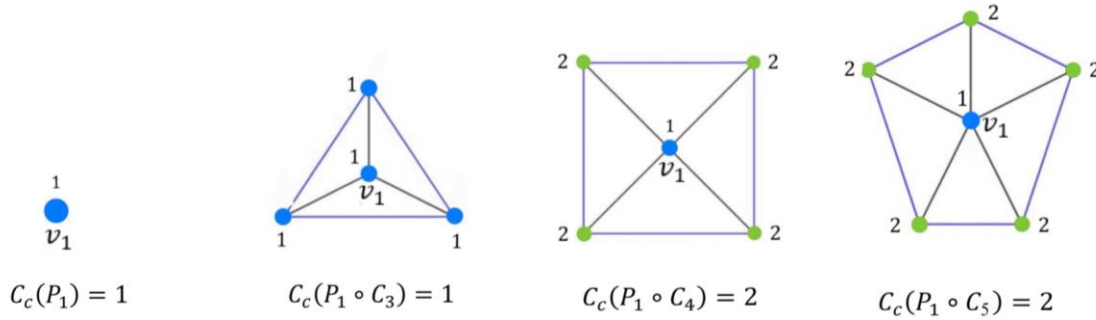


Figure 4.

In Figure 4, the path P_1 has the vertex v_1 as the central vertex. Therefore, $C_c(P_1) = 1$. For the graph $P_1 \circ C_3$ has all vertices as central vertices. Since the eccentricity of all vertices is 1, Since the eccentricity of central vertices (a maximum distance between the center of the graph and any other vertices of the graph) is 0 Therefore, $C_c(P_1 \circ C_3) = 1$. For the graphs $P_1 \circ C_4$ and $P_1 \circ C_5$ also have v_1 as the central vertex. Since the eccentricity of central vertices is 1 Therefore, $C_c(P_1 \circ C_4) = C_c(P_1 \circ C_5) = 2$, is determined by the following colorings: Color 1 for the central vertex, and Color 2 for the vertices at a distance of 1 from the central vertex.

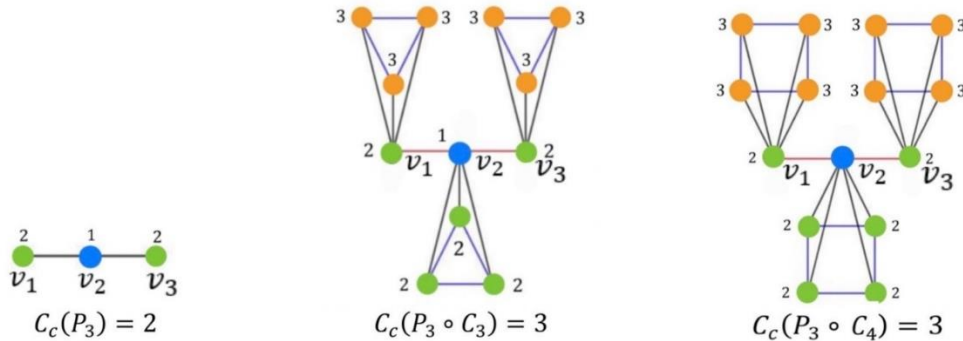


Figure 5.

In Figure 5, the path P_3 has the vertex v_2 as the central vertex. Since the eccentricity of central vertices is 1 Therefore, $C_c(P_3) = 2$. For the graphs $P_3 \circ C_3$ and $P_3 \circ C_4$ also have v_2 as the central

vertex. Since the eccentricity of central vertices is 2 Therefore, $C_c(P_3 \circ C_3) = C_c(P_3 \circ C_4) = 3$, is determined by the following colorings: Color 1 for the central vertex, Color 2 for the vertices at a distance of 1 from the central vertex, and Color 3 for the vertices at a distance of 2 from the central vertex.

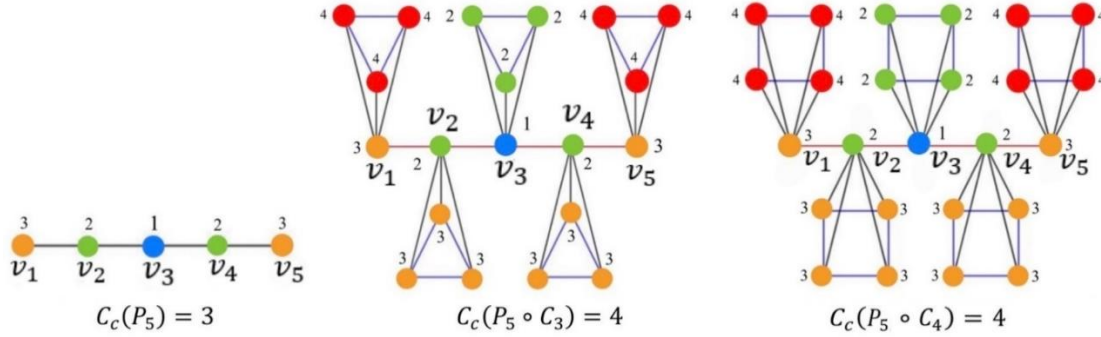


Figure 6.

In Figure 6, the path P_5 has the vertex v_3 as the central vertex. Since the eccentricity of central vertices is 2 Therefore, $C_c(P_5) = 3$. For the graphs $P_5 \circ C_3$ and $P_5 \circ C_4$ also have v_3 as the central vertex. Since the eccentricity of central vertices is 3 Therefore, $C_c(P_5 \circ C_3) = C_c(P_5 \circ C_4) = 4$, is determined by the following colorings: Color 1 for the central vertex, Color 2 for the vertices at a distance of 1 from the central vertex, Color 3 for the vertices at a distance of 2 from the central vertex, and Color 4 for the vertices at a distance of 3 from the central vertex.

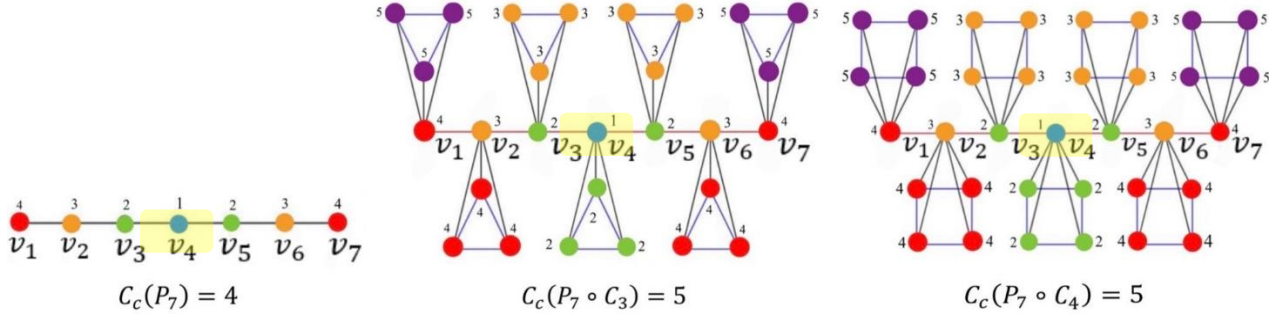


Figure 7.

In Figure 7, the path P_7 has the vertex v_4 as the central vertex. Since the eccentricity of central vertices is 3 Therefore, $C_c(P_7) = 4$. For the graphs $P_7 \circ C_3$ and $P_7 \circ C_4$ also have v_4 as the central vertex. Since the eccentricity of central vertices is 4 Therefore, $C_c(P_7 \circ C_3) = C_c(P_7 \circ C_4) = 5$, is determined by the following colorings: Color 1 for the central vertex, Color 2 for the vertices at a distance of 1 from the central vertex, Color 3 for the vertices at a distance of 2 from the central vertex, Color 4 for the vertices at a distance of 3 from the central vertex, and Color 5 for the vertices at a distance of 4 from the central vertex.

The center coloring number of $P_2 \circ C_m$ where $m = 3, 4$ shown in Figure 8. The center coloring number of $P_4 \circ C_m$ where $m = 3, 4$ shown in Figure 9.

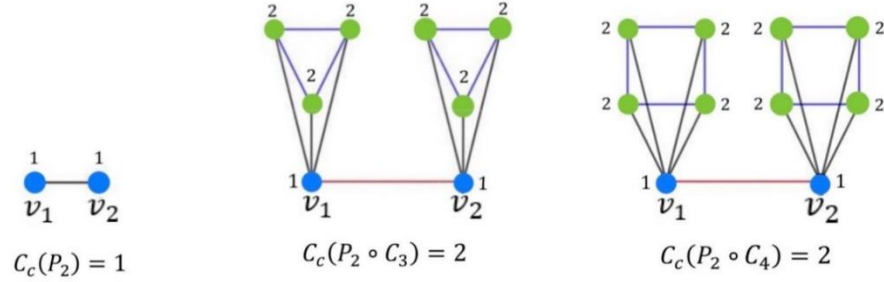


Figure 8.

In Figure 8, the path P_2 has vertices v_1 and v_2 as central vertices. Therefore, $C_c(P_2) = 1$. For the graphs $P_2 \circ C_3$ and $P_2 \circ C_4$ also has v_1 and v_2 as central vertices. Since the eccentricity of the central vertices is 1 Therefore, $C_c(P_2 \circ C_3) = C_c(P_2 \circ C_4) = 2$, is determined by the following colorings: Color 1 for the central vertex, and Color 2 for the vertices at a distance of 1 from the central vertex.

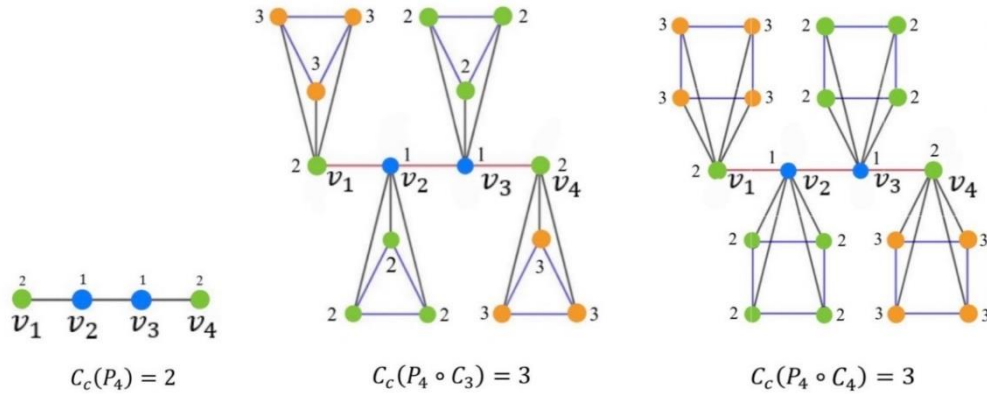


Figure 9.

In Figure 9, the path P_4 has vertices v_2 and v_3 as central vertices. Since the eccentricity of central vertices is 1 Therefore, $C_c(P_4) = 2$. For the graphs $P_4 \circ C_3$ and $P_4 \circ C_4$ also has v_2 and v_3 as central vertices. Since the eccentricity of the central vertices is 2 Therefore, $C_c(P_4 \circ C_3) = C_c(P_4 \circ C_4) = 3$, is determined by the following colorings: Color 1 for the central vertex, Color 2 for the vertices at a distance of 1 from the central vertex, and Color 3 for the vertices at a distance of 2 from the central vertex.



The corona product of the graph $C_m \circ P_n$ is formed by taking one copy of C_m and $|V(C_m)|$ copy of P_n and then connecting the i^{th} vertex of the cycle C_m to every vertex in the i^{th} copy of the path P_n . Finding the center coloring number of the new graph $C_m \circ P_n$. The center coloring number of $C_3 \circ P_3$, $C_4 \circ P_3$ and $C_5 \circ P_3$ shown in Figure 10.

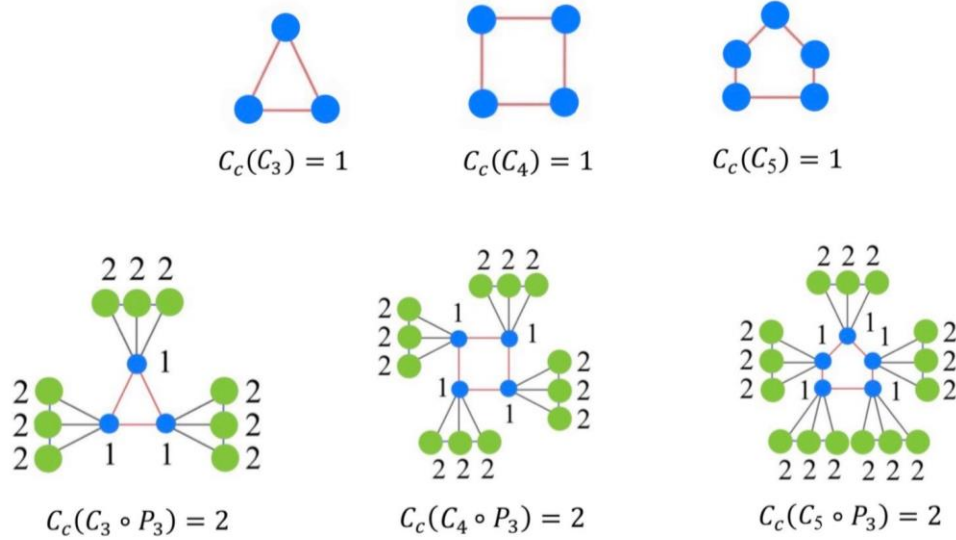


Figure 10.

In Figure 10, the cycle C_m for $m = 3, 4, 5$ has all vertices as central vertices, since the eccentricity of all vertices is 1, and the eccentricity of central vertices is 0. Therefore, $C_c(C_m) = 1$. For these graphs. For the graph $C_m \circ P_n$ the graph C_m is always central. Since the eccentricity of the central vertices is 1 Therefore, $C_c(C_n \circ P_m) = 2$. is determined by the following colorings: Color 1 for the central vertices, and Color 2 for the vertices at a distance of 1 from the central vertex.

Establishing the new theorem of the center coloring number.

Results and Discussion:

Theorem 1. Let P_n be the path with n vertices and C_m be the cycle with m vertices. The center coloring number of the corona product graph $P_n \circ C_m$ is

$$C_c(P_n \circ C_m) = \left\lceil \frac{n}{2} \right\rceil + 1.$$

Proof. Let P_n be the path with n vertices and C_m be the cycle with m vertices. Let $v_1, v_2, v_3, \dots, v_n$ be the successive vertices of P_n and $u_1^i, u_2^i, u_3^i, \dots, u_m^i$ be the successive vertices of the i^{th} copy of C_m . Let $P_n \circ C_m$ be the corona product graph with $n + mn$ vertices.

If n is odd, except when $n = 1$, then the center of the path P_n is a single vertex $v_{\frac{n+1}{2}}$ and $e(v_{\frac{n+1}{2}}) = \frac{n-1}{2}$. So



$$d\left(v_{\frac{n+1}{2}}, v_1\right) = d\left(v_{\frac{n+1}{2}}, v_n\right) = \frac{n-1}{2},$$

where v_1 and v_n are vertices in P_n . The distance $d\left(v_{\frac{n+1}{2}}, v_1\right)$ and $d\left(v_{\frac{n+1}{2}}, v_n\right)$ are the maximum distance from the center to any vertices in a path P_n .

Hence, $\frac{n-1}{2}$ colors are needed for $n-1$ vertices: $v_1, v_2, v_3, \dots, v_{\frac{n+1}{2}-1}, v_{\frac{n+1}{2}+1}, \dots, v_n$ and one color is needed for central vertex $v_{\frac{n+1}{2}}$. Then

$$C_c(P_n) = \frac{n-1}{2} + 1 = \left\lceil \frac{n}{2} \right\rceil.$$

Consider the corona product graph $P_n \circ C_m$. We have the center vertex of the corona product graph $P_n \circ C_m$ is a single vertex $v_{\frac{n+1}{2}}$. So

$$d\left(v_{\frac{n+1}{2}}, v_1\right) = d\left(v_{\frac{n+1}{2}}, v_n\right) = \frac{n-1}{2},$$

where v_1 and v_n are vertices in $P_n \circ C_m$. For the vertices $u_1^1, u_2^1, u_3^1, \dots, u_m^1$ adjacent to v_1 and the vertices $u_1^n, u_2^n, u_3^n, \dots, u_m^n$ are adjacent to v_n . We have

$$d\left(v_{\frac{n+1}{2}}, u_1^1\right) = d\left(v_{\frac{n+1}{2}}, u_2^1\right) = \dots = d\left(v_{\frac{n+1}{2}}, u_m^1\right) = \frac{n-1}{2} + 1 = \left\lceil \frac{n}{2} \right\rceil,$$

and

$$d\left(v_{\frac{n+1}{2}}, u_1^n\right) = d\left(v_{\frac{n+1}{2}}, u_2^n\right) = \dots = d\left(v_{\frac{n+1}{2}}, u_m^n\right) = \frac{n-1}{2} + 1 = \left\lceil \frac{n}{2} \right\rceil.$$

The distance $d\left(v_{\frac{n+1}{2}}, u_j^1\right)$, $j = 1, 2, 3, \dots, m$ and $d\left(v_{\frac{n+1}{2}}, u_j^n\right)$, $j = 1, 2, 3, \dots, m$ are the maximum distance from the center to any vertices in the corona product graph $P_n \circ C_m$.

Hence, $\frac{n-1}{2} + 1$ colors are needed for $n + mn - 1$ vertices and one color are needed for central vertex $v_{\frac{n+1}{2}}$. Then

$$C_c(P_n \circ C_m) = \frac{n-1}{2} + 1 + 1 = \left\lceil \frac{n}{2} \right\rceil + 1.$$

If n is even, then the center of the path P_n are two vertices $v_{\frac{n}{2}}$ and $v_{\frac{n}{2}+1}$. Since $e(v_{\frac{n}{2}}) = e(v_{\frac{n}{2}+1}) = \frac{n}{2}$. So

$$d\left(v_{\frac{n}{2}}, v_1\right) = d\left(v_{\frac{n}{2}+1}, v_n\right) = \frac{n}{2} - 1,$$

where v_1 and v_n are vertices in P_n . The distance $d\left(v_{\frac{n}{2}}, v_1\right)$ and $d\left(v_{\frac{n}{2}+1}, v_n\right)$ are the maximum distance from the center to any vertices in a path P_n .

Hence, $\frac{n}{2} - 1$ colors are needed for $n-2$ vertices: $v_1, v_2, v_3, \dots, v_{\frac{n}{2}-1}, v_{\frac{n}{2}+2}, \dots, v_n$ and one color is needed for the central vertices $v_{\frac{n}{2}}$ and $v_{\frac{n}{2}+1}$. Then

$$C_c(P_n) = \frac{n}{2} - 1 + 1 = \frac{n}{2} = \left\lceil \frac{n}{2} \right\rceil.$$

Consider the corona product graph $P_n \circ C_m$. We have the center of the corona product graph $P_n \circ C_m$ are two vertices $v_{\frac{n}{2}}$ and $v_{\frac{n}{2}+1}$. So



$$d\left(v_{\frac{n}{2}}, v_1\right) = d\left(v_{\frac{n}{2}+1}, v_n\right) = \frac{n}{2} - 1,$$

where v_1 and v_n are vertices in $P_n \circ C_m$. For the vertices $u_1^1, u_2^1, u_3^1, \dots, u_m^1$ adjacent to v_1 and the vertices $u_1^n, u_2^n, u_3^n, \dots, u_m^n$ are adjacent to v_n . We have

$$d\left(v_{\frac{n}{2}}, u_1^1\right) = d\left(v_{\frac{n}{2}}, u_2^1\right) = \dots = d\left(v_{\frac{n}{2}}, u_m^1\right) = \frac{n}{2} - 1 + 1 = \frac{n}{2},$$

and

$$d\left(v_{\frac{n}{2}+1}, u_1^n\right) = d\left(v_{\frac{n}{2}+1}, u_2^n\right) = \dots = d\left(v_{\frac{n}{2}+1}, u_m^n\right) = \frac{n}{2} - 1 + 1 = \frac{n}{2}.$$

From the maximum distance from the center to any vertices.

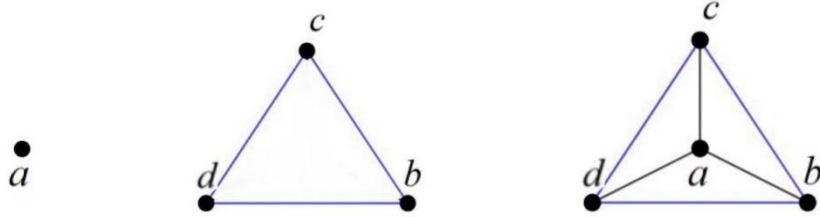
Hence $\frac{n}{2}$ colors are needed for $n + mn - 2$ vertices and one color are needed for the central vertices $v_{\frac{n}{2}}$ and $v_{\frac{n}{2}+1}$. Then

$$C_c(P_n \circ C_m) = \frac{n}{2} + 1 = \left\lfloor \frac{n}{2} \right\rfloor + 1.$$

□

Remark The center coloring number of the corona product graph $P_1 \circ C_3$ is

$$C_c(P_1 \circ C_3) = 1.$$



From remark the path P_1 has the vertex v_1 as the central vertex. Therefore, $C_c(P_1) = 1$. For the graph $P_1 \circ C_3$ have vertex 4 vertices, all vertices as central vertices. Since the eccentricity of all vertices is 1, Since the eccentricity of central vertices (a maximum distance between the center of the graph and any other vertices of the graph) is 0 Therefore, $C_c(P_1 \circ C_3) = 1$.

Theorem 2. Let C_m be the path with m vertices and P_n be the cycle with n vertices. The center coloring number of the corona product graph $C_m \circ P_n$ is $C_c(C_m \circ P_n) = 2$.

Proof. The cycle C_m has all vertices as central vertices, since the eccentricity of all vertices is 1, and the eccentricity of central vertices is 0. Therefore, $C_c(C_m) = 1$. For the graph $C_m \circ P_n$ the graph C_m is always central. Since the eccentricity of the central vertices (a maximum distance between the center of the graph and any other vertices of the graph) is 1 Therefore, $C_c(C_n \circ P_m) = 2$. is determined by the following colorings: Color 1 for the central vertices, and Color 2 for the vertices at a distance of 1 from the central vertex. □

**Conclusion:**

In this paper, we determine the center coloring number for the graph $P_n \circ C_m$, which is formed by $P_n \circ C_m$ is the corona product of the path P_n and n copy of the cycles C_m as well as for the graph $C_m \circ P_n$ created by the corona product of the cycle C_m and m copy of the paths P_n .

References:

1. Gross, J. L. and Yellen, J. Chapman & Hall/CRC Taylor & Francis Group. 2006.
2. Bondy, J.A. and Murty, U.S.R. Elsevier Science Publishing Co., Inc. 1979.
3. Yorgancioglu, Z., Dundar, P. and Berberler, M. E. Journal of Discrete Mathematical Sciences, 2015; 18: 531-540.
4. Yorgancioglu, Z. O., Dünder, P. and Gursoy, M. U. NESciences, 2018; 3(1):28-37.
5. Yorgancioglu, Z.O. and Dünder, P. Open Access Library Journal, 2021; 8: e7318.

E-ENERGY / ENVIRONMENTAL & EARTH SCIENCE / MATERIALS SCIENCE /
CHEMICAL TECHNOLOGY



ADSORPTION OF CHROMIUM BY ACID-MODIFIED DRAGON FRUIT PEEL

Kwanchanok Thongnak, Anawat Pinisakul*

Department of Chemistry, Faculty of Science, King Mongkut's University of Technology Thonburi, Thailand

*e-mail: anawat.pin@kmutt.ac.th

Abstract:

The research studied to use acid-modified dragon fruit peel (*Selenicereus undatus*) for adsorption of chromium (III), chromium (VI) and chromium (III) mixed with chromium (VI) in synthetic wastewater. The experimental conditions were studied consisting of contact times, pH values and adsorbent dosages. Adsorption isotherms were evaluated. Moreover, the laboratory wastewater was treated by this adsorbent. Adsorption column was setup to treat the laboratory wastewater. From experimental results, the suitable contact times were 120 minutes for all types of chromium. Percent of chromium adsorption was increased when increasing adsorbent dosage. The suitable pH values for chromium (III), chromium (VI) and chromium (III) mixed with chromium (VI) adsorption were 3, 2 and 3, respectively. Adsorption of chromium (III), chromium (VI) and chromium (III) mixed with chromium (VI) were explained by Freundlich isotherm. When using acid-modified dragon fruit peel dosage of 30 g/L, 35.40% of chromium in laboratory wastewater was adsorbed. Acid-modified dragon fruit peel was more suitable for adsorption column than dragon fruit peel without modification.

Introduction:

Heavy metals are used in many purposes such as lead in battery production, chromium in textile industries and steel production and mercury in pesticides and fungicides. Moreover, some heavy metals are used in environmental analysis such as manganese in biochemical oxygen demand, chromium in chemical oxygen demand and copper in Total Kjeldahl Nitrogen. After finished experiment, wastewater was separated to treat but there were some chemicals were contaminated to water in laboratory room and having adverse effects to environment and human health.

Chromium is the one of heavy metals used in environmental laboratory. When chromium contaminated in water, there were chromium (III) and chromium (VI). The standard effluent from factory of Thailand regulated the concentration of chromium (III) to be not more than 0.75 mg/L and concentration of chromium (VI) to be not more than 0.25 mg/L [1]. Toxicity of chromium (VI) was higher than chromium (III). Chromium (VI) was absorbed to body better than chromium (III) in ingestion or respiration. The toxic symptoms of chromium were squeamish, vomit, stomachache, kidney failure, chronic wound to cancer [2]. Chromium can be removed from the wastewater by several process such as chemical precipitation, electrochemical precipitation, ion exchange and adsorption [3].

Adsorption is the process that adsorbate to be removed by accumulating on the surface of adsorbent. Activated carbon is normally used to remove the pollutants. Due to high cost of activated carbon, the biological adsorbents such as fruit peels were the alternative materials because of low cost and easy to find. There were cellulose, tannin, lignin and pectin in the fruit peels which contained functional group of hydroxyl, amino and carboxylic that can adsorb heavy metals. Mallampati et al. [4] used fruit peel to adsorb heavy metals in water

using 3 types of fruit, avocado, Hami melon and dragon fruit. Peels were washed and dried. The peels can adsorb cation well such as Pb^{2+} and Ni^{2+} , while heavy metal in anion form such as $\text{Cr}_2\text{O}_7^{2-}$ can not be adsorbed because the surface of peel contained functional group of $-\text{OH}$ and $-\text{COOH}$. Marta Lopez-Garcia et al. [5] studied the adsorption of chromium (VI) by acid-modified banana peel. Some part of chromium (VI) was reduced to chromium (III) and to be adsorbed fitting with Langmuir isotherm. Wang et al. [6] used pectin to adsorb heavy metals. Pectin had functional group to adsorb heavy metals. If pH was less than 4, less amount of heavy metal cation was adsorbed because of protonation of pectin. Some heavy metals can be precipitated. When pectin was modified by addition functional group $-\text{SO}_3$, $-\text{CONH}_2$ and $-\text{SH}$ to increase capability of heavy metal cation adsorption. Mahmoud et al. [7] synthesized hydrogel pectin from mandarin orange peel for chromium (VI) and lead (II) adsorption in water. When increase pH, decrease adsorption of chromium (VI) but increase lead (II) adsorption. Langmuir isotherm can be used to explain.

This work used dragon fruit peel to be biological adsorbent to remove chromium. Dragon fruit was the one of popular fruit to be consumed in Thailand. Dragon fruit peel contained pectin which had heavy metal adsorption capability [6], but higher content of pectin may not be suitable to prepare adsorbent in column. Acid-modified dragon fruit peel was used to study. The objectives of this work were to study the characteristics of acid-modified dragon fruit peel adsorbent, to study the efficiency of chromium (III), chromium (VI) and chromium (III) mixed with chromium (VI) adsorption, to evaluate the adsorption isotherm of chromium and to study the adsorption of chromium in laboratory wastewater in batch and column.

Methodology:

Preparation of dragon fruit peel adsorbent and acid-modified dragon fruit peel adsorbent. For dragon fruit peel adsorbent, dragon fruit peel was washed by deionized water, then, dried at 60°C in oven until stable weight. Grind and select size of 150-250 micrometer. For acid-modified dragon fruit peel adsorbent, added 0.2 M HCl to grinded dragon fruit peel adsorbent at ratio of gram of adsorbent to mL of solution of 1:100 for 4 hr [5], washed by deionized water until neutral pH, filtration and dried at 60°C , then, grind and select size of 150-250 micrometer. Dragon fruit peel adsorbent and acid-modified dragon fruit peel adsorbent were analyzed functional group by FT-IR, surface morphology and percent of element by SEM-EDS, pH values (1 g adsorbent to 100 mL water) and pH at point of zero charge (pH_{pzc}).

Synthetic 10 mg/L Cr(III) wastewater was prepared from 1000 mg/L standard chromium (III) solution. Synthetic 1000 mg/L Cr(VI) wastewater was prepared from $\text{K}_2\text{Cr}_2\text{O}_7$ and synthetic 10 mg/L Cr(VI) wastewater was prepared from synthetic 1000 mg/L Cr(VI) wastewater. Synthetic 10 mg/L Cr(III) mixed with 10 mg/L Cr(VI) wastewater was prepared from 1000 mg/L Cr(III) and Cr(VI) solution.

Determination of suitable time for chromium adsorption. 20 g/L of acid-modified dragon fruit peel adsorbent were added to 100 mL of synthetic 10 mg/L Cr(III) wastewater, synthetic 10 mg/L Cr(VI) wastewater and synthetic 10 mg/L Cr(III) mixed with 10 mg/L Cr(VI) wastewater at pH of 2.4 and temperature of 30°C . Shake at 120 rpm for 1, 3, 5, 10, 15, 30, 45, 60, 90, 120, 150 and 180 minutes, then, filtered the mixtures and analyzed Cr by atomic absorption spectrophotometer. The experiment was duplicate. The amount of chromium adsorbed per weight of adsorbent (q_e) and percent of chromium adsorption were calculated by equations 1 and 2.



$$q_e = \frac{(C_0 - C_e)V}{W} \quad (1)$$

$$\text{Percent of chromium adsorption} = \left(\frac{C_0 - C_e}{C_0} \right) \times 100 \quad (2)$$

When,

q_e = Amount of chromium adsorbed per weight of adsorbent (mg/g) at equilibrium

C_0 = Initial chromium concentration (mg/L)

C_e = Equilibrium chromium concentration (mg/L)

V = Volume of wastewater (L)

W = Weight of adsorbent (g)

Determination of suitable pH value for chromium adsorption. 20 g/L of acid-modified dragon fruit peel adsorbent were added to 100 mL of synthetic 10 mg/L Cr(III) wastewater, synthetic 10 mg/L Cr(VI) wastewater and synthetic 10 mg/L Cr(III) mixed with 10 mg/L Cr(VI) wastewater at temperature of 30 °C with shaking time of 120 minutes. The initial pH values were adjusted in the range of 2-8, then, filtered the mixtures and analyzed Cr by atomic absorption spectrophotometer. The experiment was duplicate.

Study of the effect of amount of adsorbent for chromium adsorption. Acid-modified dragon fruit peel adsorbent dosage of 0.5, 1, 2, 5, 10 and 20 g/L were added to 100 mL of synthetic 10 mg/L Cr(III) wastewater, synthetic 10 mg/L Cr(VI) wastewater and synthetic 10 mg/L Cr(III) mixed with 10 mg/L Cr(VI) wastewater at pH of 3, 2 and 3, respectively, and temperature of 30 °C with shaking time of 120 minutes, then, filtered the mixtures and analyzed Cr by atomic absorption spectrophotometer. The experiment was duplicate. Adsorption isotherms (Langmuir and Freundlich model, equations 3 and 4) were calculated.

Langmuir model (linear form)

$$\frac{1}{q_e} = \frac{1}{Q_m K_L} \cdot \frac{1}{C_e} + \frac{1}{Q_m} \quad (3)$$

When,

Q_m = Maximum capacity (mg/g)

K_L = Langmuir constant (L/mg)

C_e = Equilibrium concentration (mg/L)

Freundlich model (linear form)

$$\log q_e = \frac{1}{n} \log C_e + \log K_F \quad (4)$$

When,

n = Freundlich exponent (dimensionless)

K_F = Freundlich constant ($\text{mg}^{1-1/n} \text{L}^{1/n} \text{g}^{-1}$)

Chromium adsorption efficiencies from laboratory wastewater. Laboratory wastewater from environmental laboratory in Department of Chemistry, Faculty of Science, KMUTT. Acid-modified dragon fruit peel adsorbent was used at dosages of 1, 5, 10, 20 and 30 g/L to 100 mL of wastewater at pH of 3, and temperature of 30 °C with shaking time of 120 minutes at 120 rpm, then, filtered the mixtures and analyzed Cr by atomic absorption spectrophotometer.

The experiment was duplicate. Used adsorbents were kept for analysis by SEM-EDS and X-ray Fluorescence (XRF), including adsorption isotherm.

Chromium removal by adsorption column. Dragon fruit peel adsorbent and acid-modified dragon fruit peel adsorbent of 2.5 g were used filled into two 50 mL-syringes to be adsorption columns. Laboratory wastewater pH of 2.0 and 3.0 were fed to dragon fruit peel column and acid-modified dragon fruit peel column with flow rate of 5 drop per minute or 0.25 mL/minute by infusion set with column height of 11 cm. The water samples were collected at time of 5, 10, 15, 20, 25, 30, 45, 60, 90, 120, 150, 180, 210, 240 and 270 minutes, then, filtered the mixtures and analyzed Cr by atomic absorption spectrophotometer. The experiment was duplicate. The Thomas constant (k_{Th}) and adsorption capacity (q_0) were determined from Thomas model [8] as shown in equation (5), by plotting $\ln \frac{C_0}{C_t}$ versus t to give the value of k_{Th} and q_0 .

$$\ln \frac{C_0}{C_t} - 1 = \frac{k_{th} q_0 m}{Q} - k_{th} C_0 t \quad (5)$$

where,

C_t = Chromium concentration at time t , (min)

k_{th} = Thomas constant (mL/(min.mg))

q_0 = adsorption capacity (mg/g)

m = mass of adsorbent (g)

Q = Volumetric flow rate (mL/min)

The 50% of the breakthrough time can be determined from Yoon-Nelson model as shown in equation (6) [9].

$$\ln \frac{C_t}{C_0 - C_t} = k_{YN} t - \tau k_{YN} \quad (6)$$

where,

k_{YN} = Rate constant (mn⁻¹)

τ = Time required for 50 % adsorbate breakthrough (min)

Results and Discussion:

Preparation of adsorbent. Some characteristics of acid-modified dragon fruit peel adsorbent and dragon fruit peel adsorbent was shown in Table 1.

Table 1. Some characteristics of dragon fruit peel adsorbent and acid-modified dragon fruit peel adsorbent

| Characteristic | Dragon fruit peel adsorbent | Acid-modified dragon fruit peel adsorbent |
|-------------------|-----------------------------|---|
| Color | Pink | Brown |
| pH | 4.68 | 3.20 |
| pH _{pzc} | 4.25 | 2.25 |

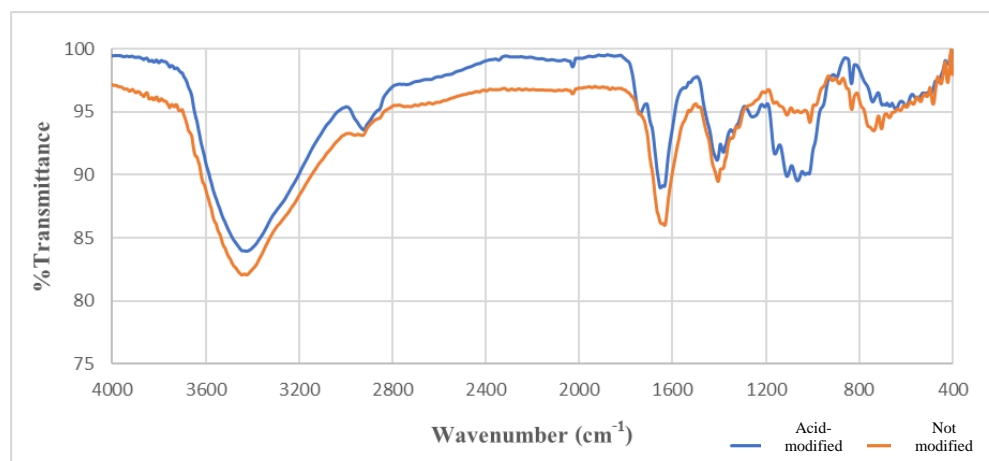
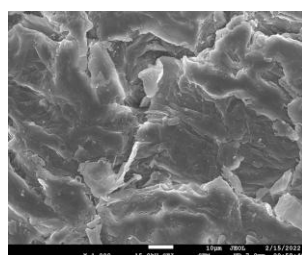


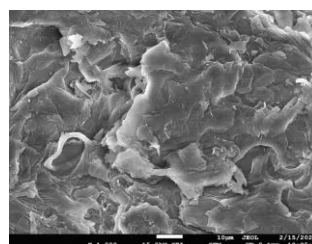
Figure 1. FT-IR spectrum of dragon fruit peel adsorbent and acid-modified dragon fruit peel adsorbent

From Figure 1, wavenumber in FT-IR of dragon fruit peel adsorbent of 3444.32 cm^{-1} was functional group of O-H and N-H stretching [10], 2920.25 cm^{-1} to be C-H stretching of methyl ester in galacturonic acid with correspond to pectin in dragon fruit [11], 1633.09 cm^{-1} and 1403.51 cm^{-1} to be COO^- stretching with correspond to pectin [10]. Wavenumber in FT-IR of acid-modified dragon fruit peel adsorbent of 3424.60 cm^{-1} was functional group of O-H and N-H stretching [10], 2923.15 cm^{-1} to be C-H stretching of methyl ester in galacturonic acid with correspond to pectin in dragon fruit [11], 1740.51 cm^{-1} and 1650.36 cm^{-1} to be C=O and COO^- stretching with correspond to pectin [12].

From Figure 2, SEM-EDS analysis, the surface of dragon fruit peel adsorbent and acid-modified dragon fruit peel adsorbent was rough and containing pores. The elemental compositions of dragon fruit peel adsorbent were carbon, oxygen and potassium of 50.36%, 43.83% and 5.81% by weight, while carbon and oxygen of 49.78% and 50.22% by weight, respectively. Less potassium content in acid-modified dragon fruit peel adsorbent may be from washing step.



(a)



(b)

Figure 2. Surface morphological analysis by SEM. (a) dragon fruit peel adsorbent and (b) acid-modified dragon fruit peel adsorbent at 1000x

Determination of suitable time for chromium adsorption.

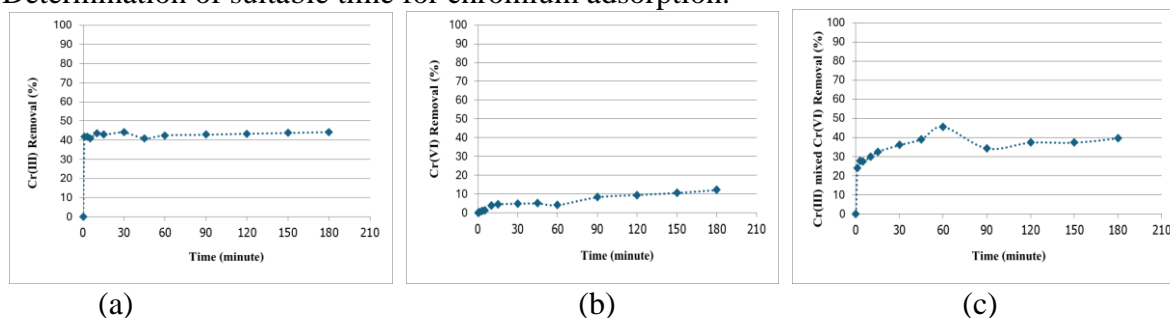


Figure 3. Chromium adsorption efficiencies at various times from synthetic wastewater of (a) Cr(III), (b) Cr(VI) and (c) Cr(III) mixed with Cr(VI)

From Figure 3, approximately of more than 40% of Cr(III) was rapidly adsorbed by acid-modified dragon fruit peel adsorbent within 1 minutes (Figure 3 (a)). The equilibrium time of stable Cr(III) adsorption was found at 120 minutes. For Cr(VI) adsorption, 10% of Cr(VI) was adsorbed steadily at equilibrium time of 120 minutes (Figure 3 (b)) while 38% of Cr(III) mixed with Cr(VI) was adsorbed steadily at equilibrium time of 120 minutes (Figure 3 (c)). Thus, the equilibrium times of Cr adsorption were 120 minutes. Cr(III) may be adsorbed by carboxyl group (-COOH) and hydroxy group (-OH) while Cr(VI) may be adsorbed by amino group (-NH) [13]. The Cr adsorption efficiencies by acid-modified dragon fruit peel adsorbent were less than those of dragon fruit peel adsorbent because of washing of pectin in acid-modified dragon fruit peel adsorbent [14].

Determination of suitable pH value for chromium adsorption.

From Figure 4(a), the highest Cr(III) removal was found at pH of 3 with removal efficiencies of 75% but the precipitation of Cr(III) began at pH of 6. The pH of 3 was selected for next experiment. For Cr(VI) adsorption in Figure 4(b), the maximum Cr(VI) removal was found at pH of 2 with removal efficiencies of 40%. The pH of 2 was selected for next experiment. For Cr(III) mixed with Cr(VI) wastewater, the highest content of Cr was adsorbed at pH of 3 with 49% chromium removal. The pH of 3 was selected for next experiment.

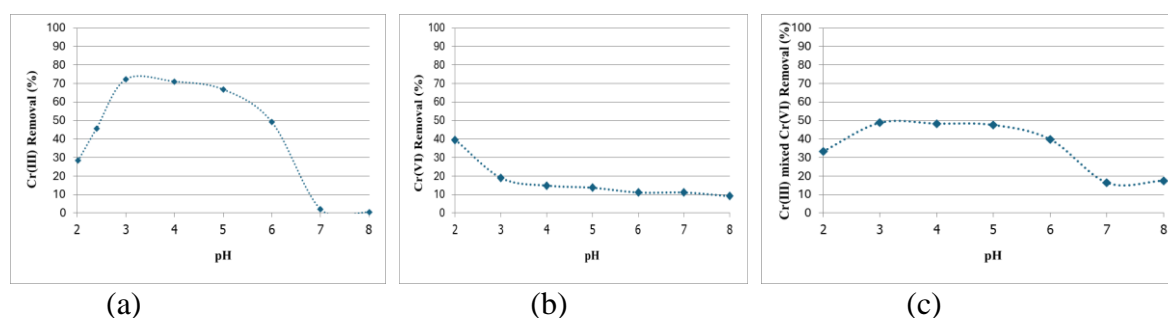


Figure 4. Chromium adsorption efficiencies at various pH values from synthetic wastewater of (a) Cr(III), (b) Cr(VI) and (c) Cr(III) mixed with Cr(VI)



Study of the effect of amount of adsorbent for chromium adsorption.

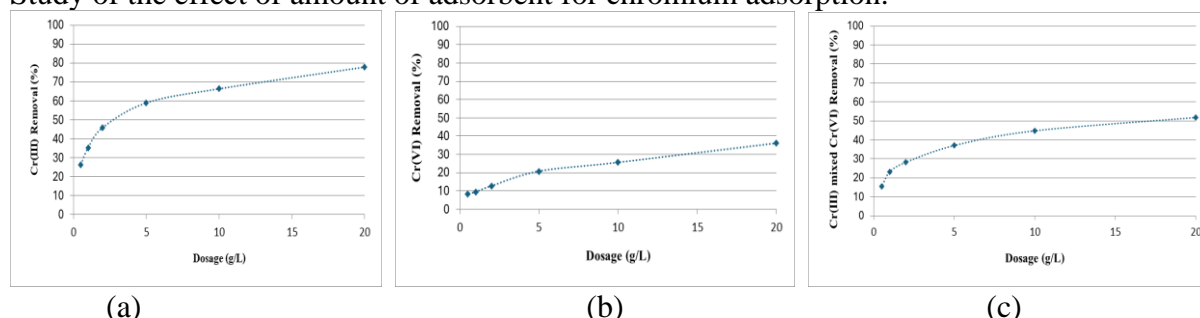


Figure 5. Chromium adsorption efficiencies at various adsorbent amount from synthetic wastewater of (a) Cr(III), (b) Cr(VI) and (c) Cr(III) mixed with Cr(VI)

From Figure 5, it was found that when increased adsorbent dosage, the chromium removal efficiencies were increased, the maximum of 78%, 36% and 52% for Cr(III), Cr(VI) and Cr(III) mixed with Cr(VI), respectively, because of higher surface area of adsorbent.

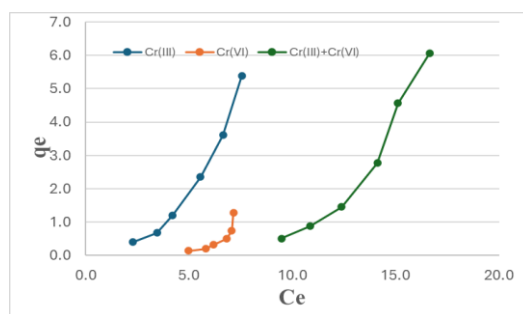


Figure 6. Plot graph between C_e and q_e of Cr(III), Cr(VI) and Cr(III) mixed with Cr(VI) adsorption by acid-modified dragon fruit peel adsorbent

From Figure 6, it was found that the adsorption pattern of Cr(III), Cr(VI) and Cr(III) mixed with Cr(VI) adsorption by acid-modified dragon fruit peel adsorbent cannot be fitted with Langmuir isotherm because of no stable at the end of graphs. The adsorption isotherm graph of for Cr(III), Cr(VI) and Cr(III) mixed with Cr(VI) were shown in Figure 7. From Table 2, the adsorption of Cr(III), Cr(VI) and Cr(III) mixed with Cr(VI) by acid-modified dragon fruit peel adsorbent cannot be explained by Langmuir isotherm because of negative values of Langmuir constants. Thus, the adsorption of Cr(III), Cr(VI) and Cr(III) mixed with Cr(VI) by acid-modified dragon fruit peel adsorbent should be explained by Freundlich model with high R^2 values.

Table 2. Constant values from isotherms of synthetic wastewater experiments

| Synthetic Wastewater | Langmuir | | | Freundlich | | |
|---------------------------|---------------------------------|---------------------------------|-------|--|-------|-------|
| | Q_m (mg g^{-1}) | K_L (L mg^{-1}) | R^2 | K_F ($\text{mg g}^{-1})(\text{mg L}^{-1})^{1/n}$ | n | R^2 |
| Cr(III) | -1.091 | -0.117 | 0.991 | 0.053 | 0.450 | 0.981 |
| Cr(VI) | -0.0762 | -0.129 | 0.979 | 1.524×10^{-5} | 0.181 | 0.886 |
| Cr(III) mixed with Cr(VI) | -0.421 | -0.0602 | 0.961 | 1.841×10^{-5} | 0.221 | 0.992 |

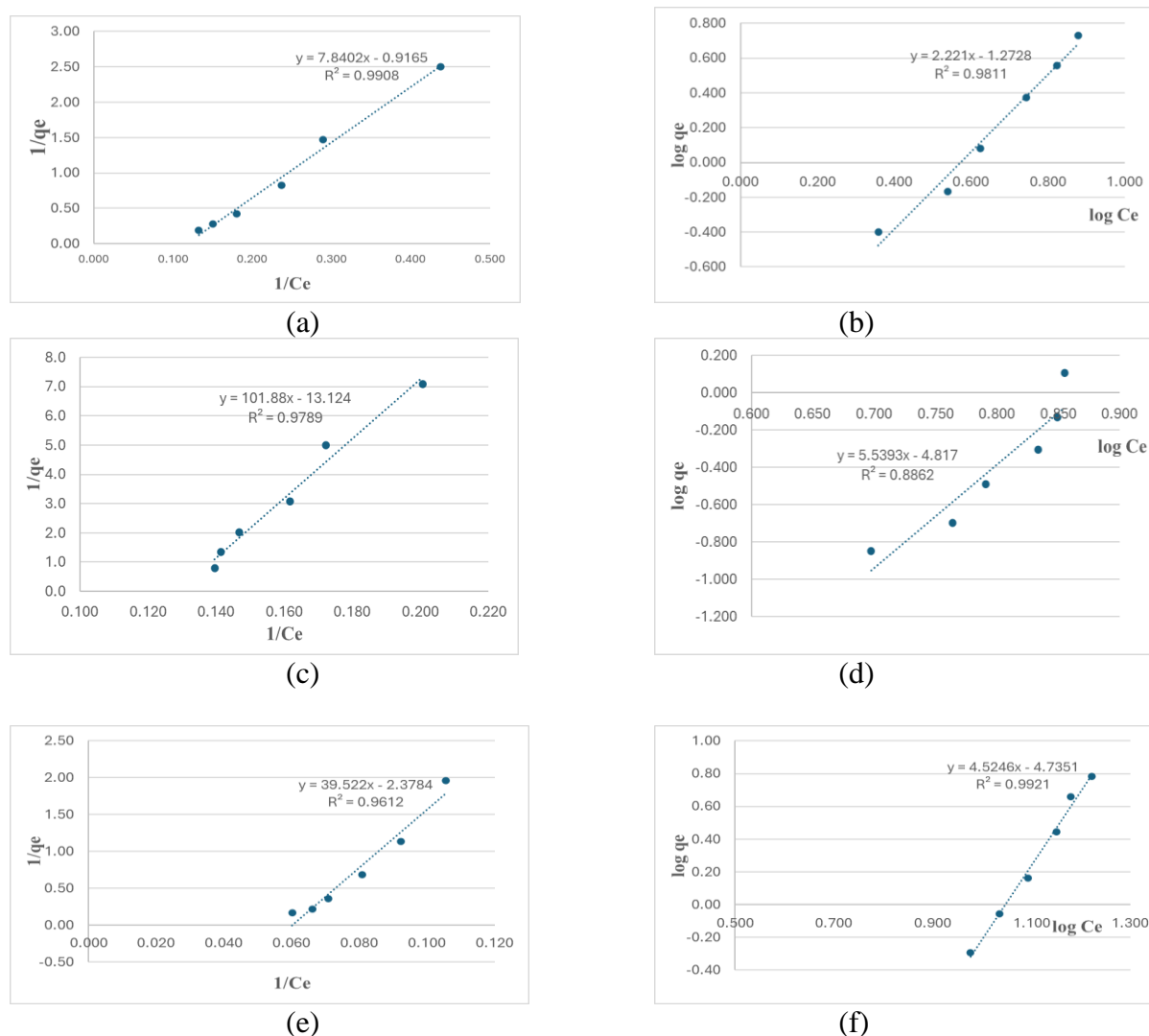


Figure 7. Isotherm graph of chromium adsorption by acid-modified dragon fruit peel adsorbent

- (a) Langmuir model for Cr(III), (b) Freundlich model for Cr(III)
 (c) Langmuir model for Cr(VI), (d) Freundlich model for Cr(VI)
 (e) Langmuir model for Cr(III) mixed with Cr(VI) (f) Freundlich model for Cr(III) mixed with Cr(VI)

Chromium adsorption efficiencies from laboratory wastewater.

From Figure 8, when acid-modified dragon fruit peel adsorbent dosages were increased, the chromium removal efficiencies were increased. The chromium from laboratory wastewater were removed 35.40%, when using adsorbent dose of 30 g/L. From Figure 9, it was found that the adsorption pattern of chromium adsorption by acid-modified dragon fruit peel adsorbent from laboratory wastewater cannot be fitted with Langmuir isotherm because of no stable at the end of graphs. From Figure 10, the constant from Langmuir and Freundlich models were shown in Table 3. Due to the negative values of Langmuir constants, Langmuir model was not suitable to explain the adsorption of chromium from laboratory wastewater by acid-modified dragon fruit peel adsorbent. The Freundlich model should be used to explain with high R^2 .

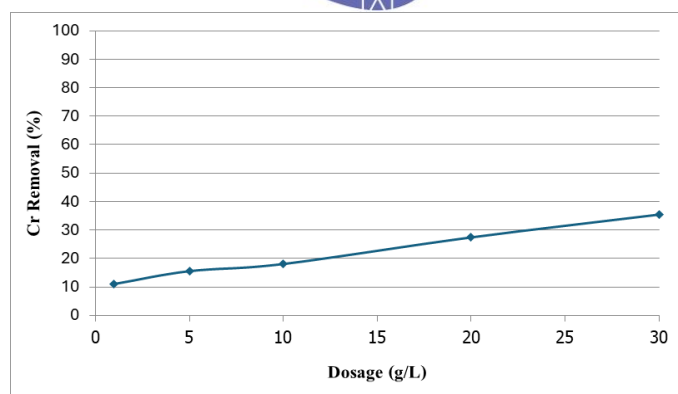


Figure 8. Chromium adsorption efficiencies at various adsorbent amount from laboratory wastewater

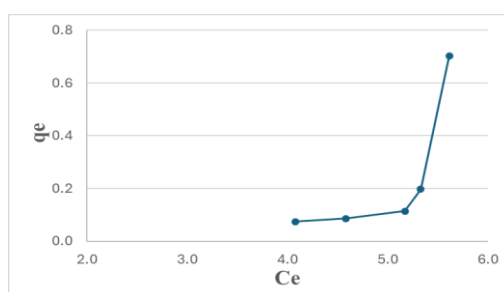


Figure 9. Plot graph between C_e and q_e of chromium adsorption by acid-modified dragon fruit peel adsorbent from laboratory wastewater

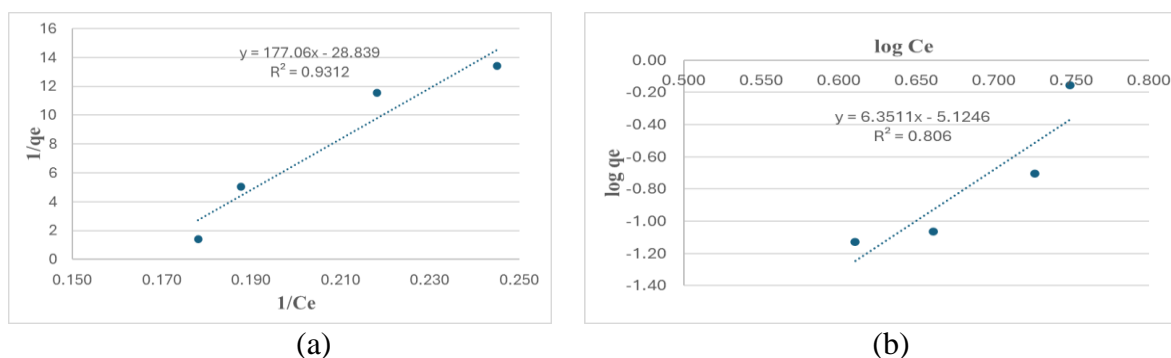


Figure 10. Isotherm graphs of (a) Langmuir Model and (b) Freundlich Model for Cr adsorption from laboratory wastewater

Table 3. Constant values from isotherms of laboratory wastewater experiments

| Synthetic Wastewater | Langmuir | | | Freundlich | | |
|-----------------------|---------------------------------|---------------------------------|-------|--|-------|-------|
| | Q_m (mg g^{-1}) | K_L (L mg^{-1}) | R^2 | K_F ($\text{mg g}^{-1})(\text{mg L}^{-1})^{1/n}$ | n | R^2 |
| Laboratory Wastewater | -0.0347 | -0.163 | 0.931 | 7.499×10^{-6} | 0.157 | 0.806 |

After adsorption, the surface of acid-modified dragon fruit peel adsorbent was rough as shown in Figure 11. From XRF analysis, 1.04% of Cr content was found. It was proof that chromium was adsorbed.

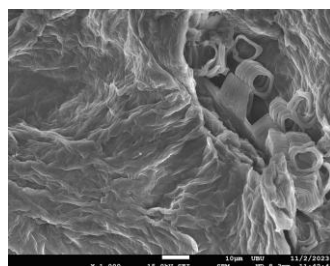


Figure 11. Surface morphological analysis by SEM of acid-modified dragon fruit peel adsorbent after adsorption.

Chromium removal by adsorption column.

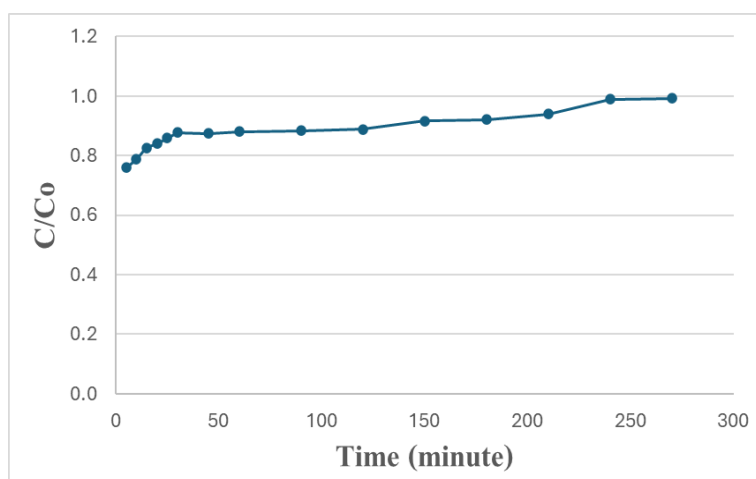


Figure 12. Fraction of chromium (C/C_0) and time when using adsorption column filled by acid-modified dragon fruit peel adsorbent.

From Figure 12, when using acid-modified dragon fruit peel adsorbent, chromium was adsorbed within first 5 minutes. The average chromium adsorption efficiencies were 26% and gradually decreased until no adsorption within 240 minutes. The dragon fruit peel adsorbent cannot setup to be adsorption column because of clogging from adsorbent containing higher content of pectin. The acid-modified dragon fruit peel adsorbent contained less pectin because of the washing step after modification by acid to remove pectin from dragon fruit peel. Thus, the suitable adsorbent to be used in column was the acid-modified dragon fruit. From Figure 13, the Thomas constant (k_{th}) and adsorption capacity (q_0) were 0.00016 mL/(min.mg) and 511 mg/g, respectively. Due to Thomas model is based on the Langmuir model. The constants from Thomas model may not be suitable for explanation. When Yoon-Nelson model (Figure 14) was used, the rate constant (k_{YN}) of 0.0113 mn^{-1} and time required for 50 % adsorbate breakthrough (τ) of 113 minutes were found.

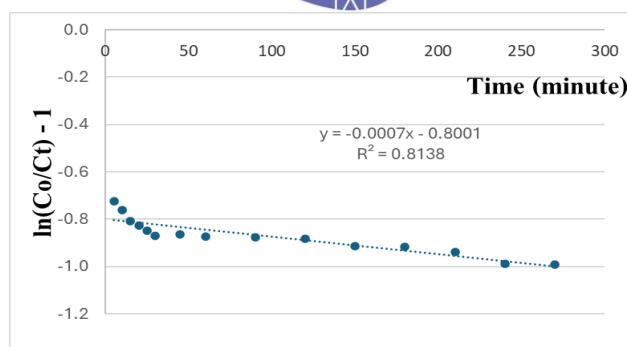


Figure 13. Plot of Thomas Model

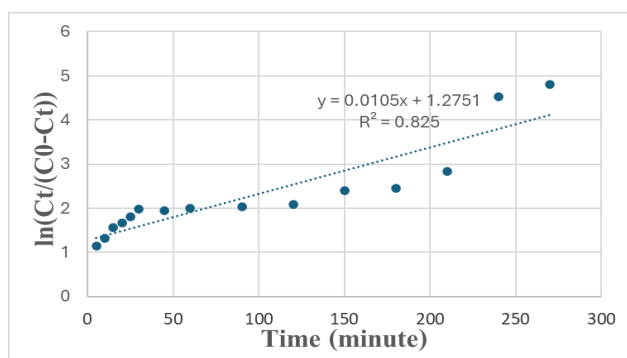


Figure 12. Plot of Yoon-Nelson model

Conclusion:

Chromium can be adsorbed by acid-modified dragon fruit peel. The suitable pH values for chromium (III), chromium (VI) and chromium (III) mixed with chromium (VI) adsorption were 3, 2 and 3, respectively. Adsorption of chromium (III), chromium (VI) and chromium (III) mixed with chromium (VI) can be explained by Freundlich isotherm. The acid-modified dragon fruit peel of 30 g/L can remove 35.40% of chromium in laboratory wastewater. To setup adsorption column, the acid-modified dragon fruit peel was more suitable than dragon fruit peel without acid-modification.

Acknowledgements:

This work was supported by Department of Chemistry, Faculty of Science, King Mongkut's University of Technology Thonburi. The author would like to thank Ms. Thunchanok Thongsamer and Mrs. Ponwarin Wilams for isotherm and column data analysis.

References:

1. Notification of Ministry of Industry. Royal Gazette, 134, Special Section 153 D. 2017;2.
2. Jirachat Srisan. Journal of Department of Science Service. 2017;189:10-12. (in Thai)
3. Ashraf, A., Bibi, I., Niazi, N.K., Ok, Y.S., Murtaza, G., Shahid, M., Kunhikrishnan, A., Li, D. and Mahmood, T. International Journal of Phytoremediation. 2017;19,7:605-613.
4. Mallampati, R., Xuanjun, L., Adin, A. and Valiyaveetil, S. ACS Sustainable Chemistry & Engineering. 2015;3:1117-1124.
5. López-García, M., Lodeiro, P., Herrero, R., Barriada, J.L., Rey-Castro, C., David, C. and Sastre de Vicente, M.E. Bioresource Technology. 2013;139:181-189.

6. Wang, R., Liang, R., Dai, T., Chen, J., Shuai, X. and Liu, C. Trends in Food Science & Technology. 2019;91:319–329.
7. Mahmoud, M.E. and Mohamed, A.K. International Journal of Biological Macromolecules. 2020; 164:920–931.
8. Chen, S., Yue, Q., Gao, B., Li, Q., Xu, X., & Fu, K. Bioresource Technology. 2012;113: 114-120.
9. Yoon, Y.H. and Nelson, J.H. American Industrial Hygiene Association Journal. 1984;45:509-516.
10. Puccini, M., Licursi, D., Stefanelli, E., Vitolo, S., Raspolli Galletti, A.M. and Heeres, H.J. Chemical Engineering Transaction. 2016;50:223-228.
11. Rahmati, S., Abdullah, A., Momeny, E. and Kang, O. L. International Food Research Journal 2015. ;22,1:233-239.
12. Koziol, A., Sroda-Pomianek, K., Gorniak, A., Wikiera, A., Cyprych, K. and Malik, M. Multidisciplinary Digital Publishing Institute. 2022;12,546:pp.1-13.
13. Zaid, R.M., Zularisam, A.W. Mimi Sakinah, A.M. Australian Journal of Basic and Applied Sciences. 2016;10,17:69-74.
14. Thongnak, K., Pinisakul, A. CRU - National Conference in Science and Technology: NCST 6th. 2023;C-1.



AMINE-SURFACE-MODIFIED MgO AS AN ADSORBENT FOR CO₂ REMOVAL FROM BIOGAS

Preecha Kasikamphaiboon*, Uraiwan Khunjan

Department of Science, Faculty of Science and Technology, Prince of Songkla University, Pattani Campus, Pattani, 94000, Thailand

*e-mail: preecha.kas@psu.ac.th

Abstract:

Biogas, a renewable and sustainable energy source, primarily consists of methane (CH₄) and carbon dioxide (CO₂). The energy content of biogas is directly proportional to the CH₄ concentration and, therefore, can be increased by removing CO₂ in the upgrading process. This work presents the surface modification of MgO with amine and its application for CO₂ adsorption from biogas. MgO was synthesized and then surface-modified with monoethanolamine (MEA) to obtain final products containing 0, 10, 20 and 30% MEA by weight. Adsorption of CO₂ was performed using simulated biogas containing 40% CO₂ and 60% N₂. Surface area and pore diameter of the synthesized adsorbents decrease with increasing MEA loading. The results show that MgO modified with MEA effectively remove CO₂ from the gas streams. The optimal MEA loading for MgO surface modification is 20 wt%, giving a maximum CO₂ adsorption capacity of 2.67 mmol/g.

Introduction:

Biogas is clean energy produced from the fermentation of wastes such as animal manure, industrial wastewater and agricultural waste to cause the decomposition of organic substances in anaerobic conditions by a variety of bacteria. The main components of biogas are 60-70% methane (CH₄), a combustible gas that can be used as an alternative energy source, and 30-40% carbon dioxide (CO₂). In addition, biogas also contains small amounts of other gases such as hydrogen (H₂), nitrogen (N₂) and hydrogen sulfide (H₂S)^{1,2}. Therefore, the heat of combustion of biogas depends on the proportion of methane. Thailand is currently producing more biogas, which both households and industries can use to replace and reduce the import of fossil fuels, the price of which is constantly rising. However, the use of biogas is still limited since it contains less CH₄ than natural gas. The heating value from biogas combustion is therefore not high enough to be used as fuel in vehicles. Reducing the amount of CO₂ in biogas can increase its methane content. In many countries, progress has been made to allow biogas to be used in place of natural gas in vehicles and other types of engines. Removing CO₂ from biogas can be done in several ways. One highly effective method is adsorption with solids, including activated carbon³, zeolites⁴, and mesoporous materials⁵. Magnesium oxide (MgO) is a mesoporous material with medium-sized pores and a relatively large surface area, and it has a high capacity to adsorb various substances. However, the use of MgO for CO₂ removal is limited due to its low adsorption capacity. Increasing the selectivity of MgO to be specific to CO₂ can be achieved by modifying its surface with other chemicals that have weak alkaline properties, such as amines^{6,7}.

In this study, mesoporous MgO was synthesized and surface-modified with monoethanolamine (MEA). The surface-modified MgO with different MEA loadings was used for CO₂ adsorption in simulated biogas. The CO₂ adsorption was carried out in a fixed bed adsorption column. Cyclic adsorption/desorption of CO₂ was also performed to evaluate regenerability and stability of the prepared adsorbents.

Methodology:

1. Synthesis of mesoporous MgO

The synthesis of magnesium oxide particles was performed using the sol-gel method⁸ previously reported with some modification by dissolving $\text{Mg}(\text{NO}_3)_2 \cdot 6\text{H}_2\text{O}$ and oxalic acid $((\text{COOH})_2 \cdot 2\text{H}_2\text{O})$ with the molar ratio of 1:1 separately in ethanol. The two solutions were then mixed using magnetic stirring to form a thick white gel, and the solution was stirred for 12 hours. The resulting solution was dried at 100 °C for 24 h. Finally, the dried solid was crushed and sieved through 270 mesh and then calcined at 600 °C for 2 hours to obtain magnesium oxide (MgO) particles. Equation (1) and (2) express the chemical reactions that occur during the sol-gel and calcination steps, respectively⁸.



2. Surface modification of MgO with amine

Monoethanolamine (MEA) was used to modify the surface of MgO by using the wet impregnation method described in the literature⁹ with some modification. To prepare amine-surface-modified MgO containing 10, 20 and 30% MEA by weight, the desired amount of MEA was dissolved in 50 ml of methanol under stirring for 15 min. Then 10 g of MgO was added to the MEA-methanol solution, and the resulting slurry was stirred for 30 min. The slurry was then dried at 100°C for 3 hours to obtain MgO adsorbents impregnated with MEA. The prepared MgO adsorbents were designated as 10%MEA-MgO, 20%MEA-MgO, and 30%MEA-MgO, representing 10, 20, and 30% MEA by weight in the adsorbents, respectively.

3. Characterization of the prepared adsorbents

The adsorbents' crystal structures were studied using powder X-ray diffraction (PXRD) on a Philips X'Pert MPD diffractometer using Cu-K α radiation. The N₂ adsorption-desorption isotherms were determined at -196 °C using a Micromeritics ASAP2060 volumetric analyzer. The isotherms were used to calculate the adsorbents' surface area, pore volume, and average pore diameter using the Brunauer-Emmett-Teller (BET) and Barrett-Joyner-Halenda (BJH) methods.

4. CO₂ adsorption study

CO₂ adsorption and desorption were investigated in a stainless-steel adsorption column of 160 mm in length and 25 mm in inner diameter with an experimental setup as shown in Figure 1. In this study, simulated biogas was used as feed gas stream. The simulated biogas was produced by mixing CO₂ (99.99% purity) and N₂ (99.99% purity) from gas cylinders at the desired flow rates to obtain a 40% CO₂ and 60% N₂ concentration, which is a typical concentration of CO₂ found in biogas¹⁰. To perform adsorption/desorption tests, 15 g of adsorbent was packed into the adsorption column and heated to 100 °C in a N₂ stream at 50 mL/min for 60 min. After the adsorption column was cooled to the adsorption temperature (30 °C), the adsorption tests began by feeding simulated biogas into the adsorption column at 50 mL/min. After the adsorption process was completed, the adsorbed CO₂ was desorbed by heating the adsorbent to 150 °C in a N₂ gas stream for 60 min. Six adsorption-desorption cycles were done on the same sample to determine the adsorbent's regenerability. A gas chromatograph equipped a TCD detector was used to measure the CO₂ contents in the feed and treated gas streams. The breakthrough curve data from the CO₂ adsorption tests were used to calculate the adsorbents' equilibrium capacity using Equation (3)¹¹:



$$q = \frac{QC_0}{22.4m} \int \left(1 - \frac{C_t}{C_0}\right) dt \quad (3)$$

where q is the equilibrium CO_2 adsorption capacity (mmol/g), C_0 and C_t are the inlet and outlet CO_2 concentrations (volume fraction), respectively, t is the adsorption time (min), Q is the feed volumetric flow rate (ml/min) at standard temperature and pressure (STP), and m is the adsorbent mass (g).

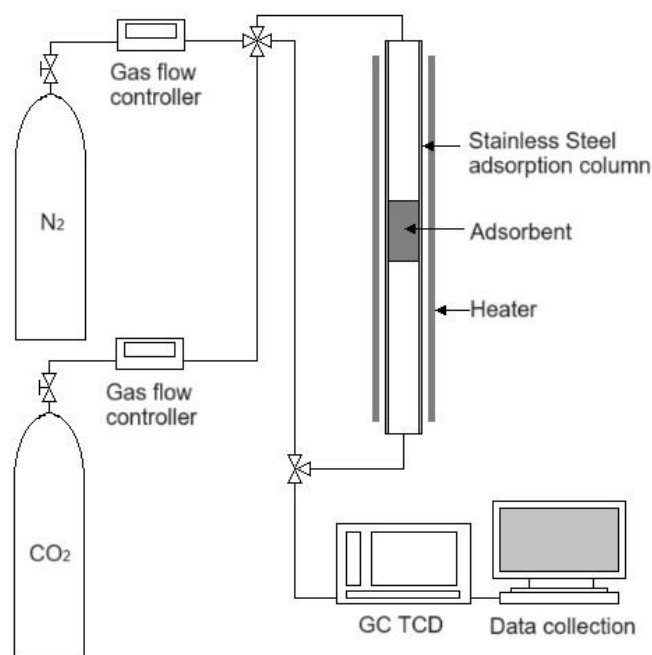


Figure 1. Experimental setup for CO_2 adsorption/desorption.

Results and Discussion:

1. Characterization of MgO and MEA-MgO

The XRD patterns of MgO at different MEA loadings are shown in Figure 2. The unmodified MgO has well-defined diffraction peaks at 36.9° , 42.9° , 62.3° , 74.7° and 78.6° . These are MgO characteristic peaks that are in accordance with previous research¹²⁻¹⁴, confirming a high degree of purity and crystallinity of the prepared MgO samples. The diffraction patterns of MgO and MgO with different MEA loadings are nearly identical, suggesting that the MgO structure is preserved after MEA loading. However, as MEA loadings increase, MgO diffraction intensity falls. According to the previous study¹⁵, diffraction intensities are proportional to the degree of pore filling. As a result, loading amine into the support's pore channels may cause intensity loss¹⁶, as observed in MCM-41 loaded with polyethylenimine (PEI)⁹.

The N_2 adsorption-desorption isotherms of MgO with different MEA loadings are shown in Figure 3. All samples exhibit type IV isotherms with hysteresis loops, according to the International Union of Pure and Applied Chemistry (IUPAC) classification¹⁷. The isotherm's hysteresis loop results from capillary condensation in mesopores. The N_2 adsorption decreases as MEA loading increases. When the MEA loading reaches 30 wt%, the mesopores of MgO are almost fully filled with MEA molecules, limiting N_2 entry into the pores and causing 30%-MEA- MgO to become non-porous¹⁸.

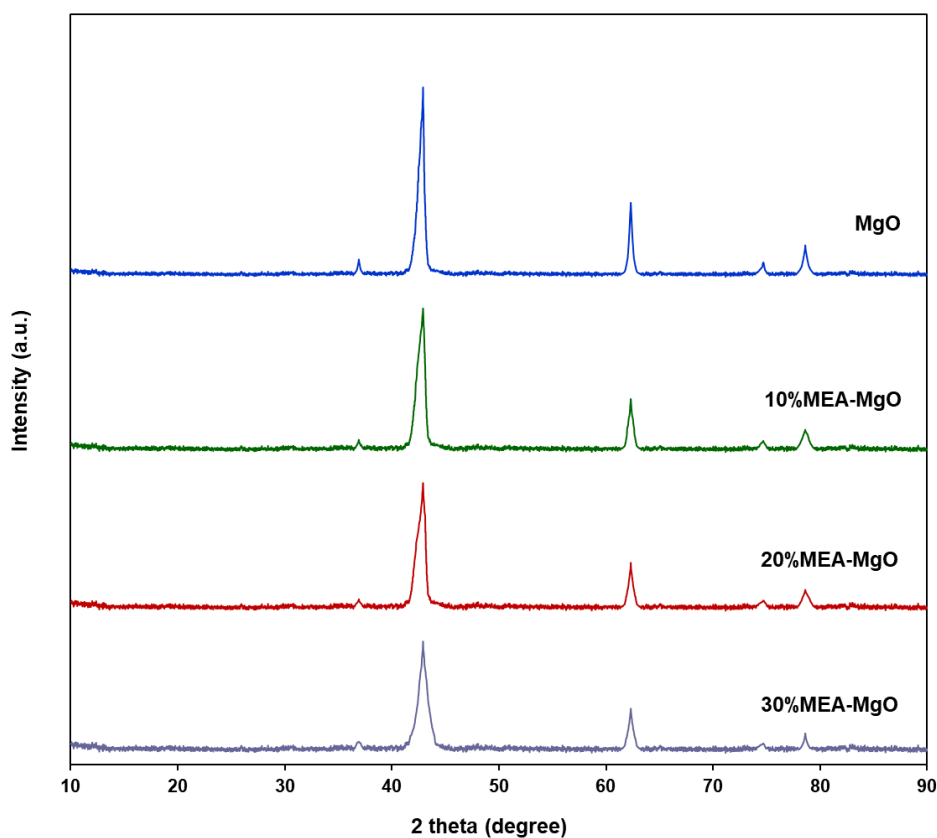


Figure 2. XRD patterns of MgO and MEA-MgO.

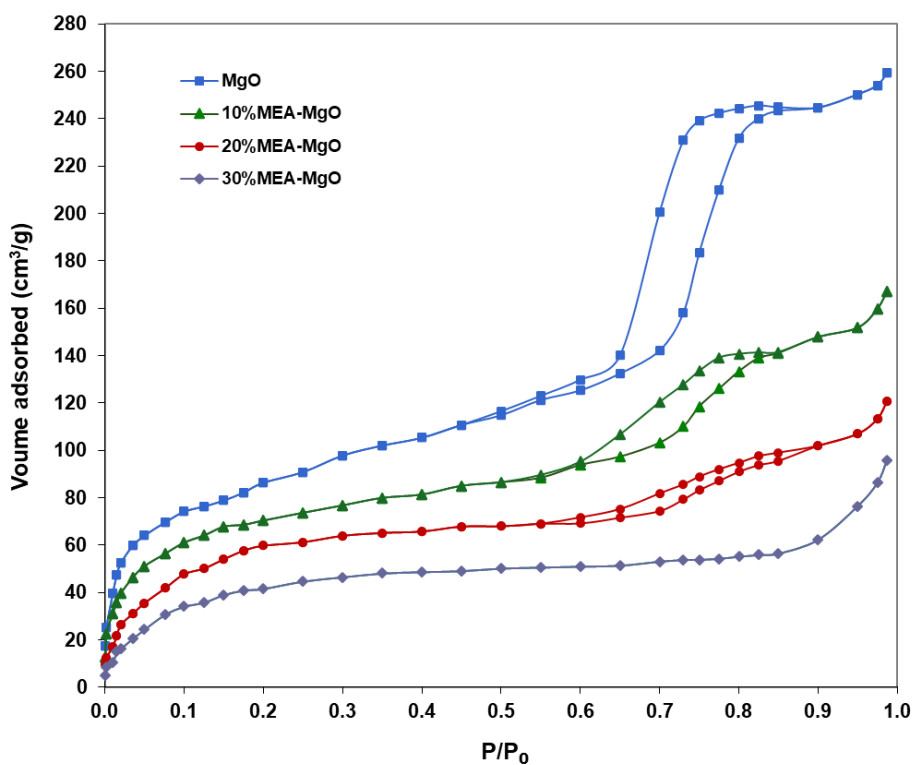


Figure 3. N₂ dsorption-desorption isotherms of MgO and MEA-MgO.



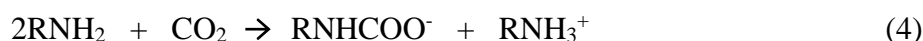
Table 1 shows surface area, pore volume, and average pore diameter of MgO and MEA-MgO calculated from the N₂ adsorption-desorption isotherms using the BET and BJH methods. The pore size of MgO decreases from 6.8 to 3.9 nm after loading 10% MEA, confirming that MEA is loaded into the MgO pore channels. As MEA loading increases, the pore size drops further. When the MEA loading reaches 30 wt%, the pore size drops to 1.3 nm, suggesting that the pores are nearly filled with MEA. The samples' surface area and pore volume show the same patterns as their pore size. Loading MEA onto MgO significantly lowers surface area and pore volume, as clearly seen for 30% MEA-MgO. This is because the high MEA content plugs the pores and covers the adsorbent's surface^{19,20}.

Table 1. Surface area, pore volume and average pore diameter of MgO and MEA-MgO.

| Adsorbent | BET surface area (m ² /g) | pore volume (cm ³ /g) | pore diameter (nm) |
|-------------|---|-------------------------------------|-----------------------|
| MgO | 196 | 0.75 | 6.8 |
| 10% MEA-MgO | 112 | 0.49 | 3.9 |
| 20% MEA-MgO | 47 | 0.33 | 2.7 |
| 30% MEA-MgO | 18 | 0.16 | 1.3 |

2. CO₂ adsorption

Figure 4 and Table 2 show the breakthrough curves and the adsorption capacities from the CO₂ adsorption study using MgO with different MEA loading, respectively. As shown in Figure 4, The unmodified MgO adsorbs CO₂ to saturation in about 17 minutes, yielding a low adsorption capacity of 0.74 mmol/g. An increase in amine loading within a reasonable range enhances the breakthrough time and adsorption capacity of the adsorbents, which is consistent with the previous findings^{21,22}. The unmodified MgO has a certain capacity to adsorb CO₂, and the adsorption mechanism mainly involves physical forces. When the MgO surface is modified with MEA, the adsorption mechanism changes. MEA attached to the surface of MgO adsorbs CO₂ with a reaction as shown in Equation (4)²³, which is chemical adsorption and more specific than physical adsorption. As a result, MgO modified with MEA has a higher capacity to adsorb CO₂. As MEA loading increases, more amine active sites for CO₂ adsorption are available. The maximum breakthrough time and adsorption capacity of 38 min and 2.67 mmol/g, respectively, are obtained when the MEA loading reaches 20%. However, further increasing MEA loading to 30% drops the breakthrough time and the adsorption capacity to 32 min and 2.23 mmol/g, respectively. Too high loadings may cause MEA molecules to cluster in the pore or cover the adsorbent's surface, preventing CO₂ passage to the active sites in the pores^{22,24}. Therefore, the optimal MEA loading for MgO surface modification is 20 wt%.



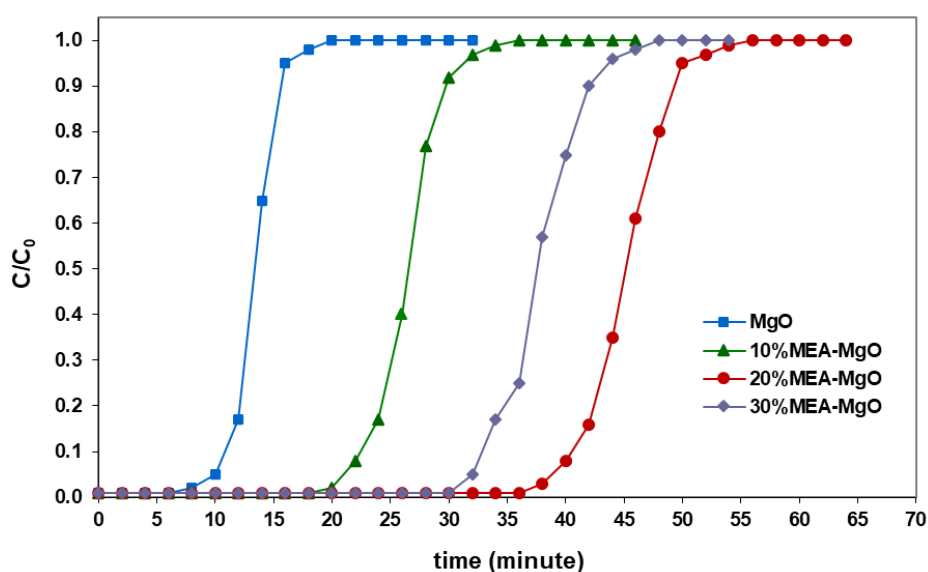


Figure 4. Breakthrough curves of MgO and MEA-MgO.

Table 2. CO₂ adsorption capacities of MgO and MEA-MgO.

| Adsorbent | Adsorption capacity (mmol CO ₂ /g) |
|-------------|--|
| MgO | 0.74 |
| 10% MEA-MgO | 1.61 |
| 20% MEA-MgO | 2.67 |
| 30% MEA-MgO | 2.23 |

To investigate adsorbent stability and regenerability, unmodified MgO and 20% MEA-MgO were used. The cyclic CO₂ adsorption capacity of unmodified MgO and 20% MEA-MgO was assessed by running six CO₂ adsorption-desorption cycles using simulated biogas as feed gas. Figure 5 shows that the adsorption capacity of the unmodified MgO drops very slightly from the first to the sixth cycle of reuse, indicating that the regeneration was almost complete. This is probably due to the physical adsorption mechanism, which involves a weak bonding force between MgO and CO₂. As a result, during regeneration, CO₂ virtually fully detaches from the MgO pores. Compared to the unmodified MgO, a greater decrease in adsorption capacity of 20% MEA-MgO from the first to the sixth cycle is observed. This can be explained that the adsorption of CO₂ on MEA-MgO is mainly chemical adsorption that has a relatively strong bonding force, causing incomplete regeneration. However, the loss of adsorption capacity of 20% MEA-MgO between the first and sixth cycle is only 8.61%, which is lower than that of some amine-based adsorbents reported in the previous study^{21,25}. These results indicate that 20% MEA-MgO has a stable CO₂ adsorption capacity and strong regenerability, both of which are desirable features for practical use as CO₂ adsorbents.

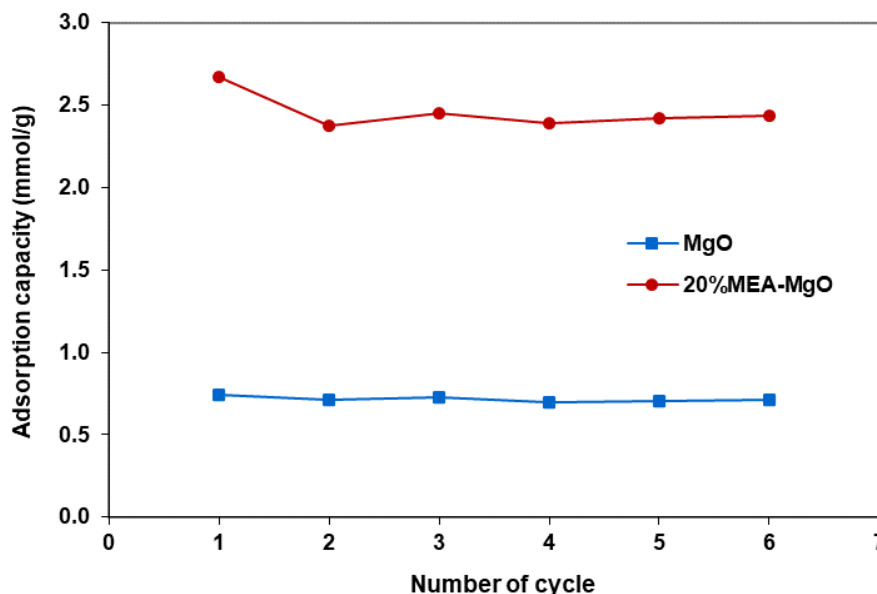


Figure 5. Cyclic CO₂ adsorption capacities of MgO and 20%MEA-MgO.

Conclusion:

MgO was synthesized and modified with MEA to obtain adsorbents containing 10, 20 and 30%MEA. The CO₂ adsorption capacity of the prepared adsorbents with different MEA loadings is significantly higher than that of the unmodified MgO. Increasing MEA loading from 0 to 20% enhances CO₂ adsorption capacity. However, a further increase in MEA loading to 30% causes the adsorption capacity to drop. A maximum CO₂ adsorption capacity of 2.67 mmol/g is obtained at 20% MEA loading (20%MEA-MgO). The regenerability and stability of 20%MEA-MgO was tested by performing six cycles of adsorption and desorption. The CO₂ adsorption capacity decreases slightly in the second to sixth cycle, indicating that 20%MEA-MgO is a highly regenerable and stable material for use as a CO₂ adsorbent.

References:

1. Lombardi L, Carnevale E. Energy. 2013;62:88-94.
2. Rasi S, Veijanen A, Rintala J. Energy. 2007;32:1375-1380.
3. Xu C, Ruan C, Li Y, Lindh J, Stromne M. Adv. Sustain. Syst. 2017;2:1700147.
4. Wang Y, Du T, Song Y, Che S, Fang X, Zhou L. Solid State Sci. 2017;73:27-35.
5. Ma B, Lin R, He H, Wu Q, Chen S. Compos. Part B Eng. 2020;185:107782.
6. Das D, Meikap, BC. Indian Chem. Eng. 2020;63:425-447.
7. Gibson JAA, Gromov AV, Brandani S, Campbell EEB. Microporous Mesoporous Mater. 2015;208: 129-139.
8. Kumar A, Kumar J. J.Phys. and Chem. Solids. 2008;69:2764-2772.
9. Xu X, Song C, Andrésen JM, Miller BG, Scaroni AW. Microporous Mesoporous Mater. 2003;62:29-45.
10. Appels L, Baeyens J, Degreè J, Dewil R. Prog. Energy Combust. Sci. 2008;34:755-781.
11. Chang H, Wu ZX. Ind. Eng. Chem. Res. 2009;48:4466-4473.
12. Ding YD, Song G, Zhu X, Chen R, Liao Q. RSC Adv. 2015;5:30929-30935.
13. Han KK, Zhou Y, Lin WG, Zhu JH. Microporous Mesoporous Mater. 2013;169:112-119.
14. Zhou W, Upreti S, Whittingham MS. Electrochem. Commun. 2011;13:1102-1104.

15. Wang X, Guo Q, Zhao J, Chen L. *Int. J. Greenh. Gas Con.* 2015;37:90-98.
16. Xu X, Song C, Andresen JM, Miller BG, Scaroni AW. *Energy Fuels*. 2002;16:1463-1469.
17. Sing KSW, Everett DH, Haul RAW, Moscou L, Pierotti RA, Rouquerol J, Siemieniewska T. *Pure Appl. Chem.* 1985;57:603-619.
18. Ahmed S, Ramli A, Yusup S. *Int. J. Greenh. Gas Con.* 2016;51:230-238.
19. Ye Q, Jiang J, Wang C, Liu Y, Pan H, Shi Y. *Energy Fuels* 2012;26:2497-2504.
20. Wang X, Ma X, Song C, Locke DR, Siefert S, Winans RE, Möllmer J, Lange M, Möller A, Gläser R. *Microporous Mesoporous Mater.* 2013;169:103-111.
21. Irani M, Gasem KAM, Dutcher B, Fan M. *Fuel*. 2016;183:601-608.
22. Yao M, Dong Y, Hu X, Feng X, Jia A, Xie G, Hu G, Lu J, Luo M, Fan M. *Energy Fuels*. 2013;27:7673-7680.
23. Chatti R, Bansawal AK, Thote JA, Kumar V, Jadhav P, Lokhande SK, Biniwale RB, Labhsetwar NK, Rayalu SS. *Microporous Mesoporous Mater.* 2009;121:84-89.
24. Jiao J, Cao J, Xia Y, Zhao L. *Chem. Eng. J.* 2016;306:9-16.
25. Guo L, Yang J, Hu G, Hu X, DaCosta H, Fan M. *Nano Energy* 2016;25:1-8.



AN EARTHQUAKE PRECUSORY SIGN FROM GROUNDWATER LEVEL FLUCTUATION OF A DISTRICT IN CHIANG MAI PROVINCE, THAILAND

Sorawat Siangpipop^{1,*}, Siriporn Chaisri², Niti Mankhemthong¹, Pisanu Wongpornchai¹

¹Department of Geological Sciences, Faculty of Science, Chiang Mai University, 239 Huay Kaew Road, Suthep Sub District, Mueang District, Chiang Mai, Thailand 50200

²Department of Physics and Materials Science, Faculty of Science, Chiangmai University, 239 Huay Kaew Road, Suthep Sub District, Mueang District, Chiang Mai, Thailand 50200

* e-mail: sorawat_s@cmu.ac.th

Abstract:

The amount of seismic activity in Chiang Mai Province, Thailand, from 2013 to 2017, including a notable earthquake of 4.0 magnitude, raised concerns in the study area. The phenomenon coincided with groundwater recharge activities, prompting an investigation into the potential correlation between groundwater levels and seismic events. This study examined the relationship between the groundwater level change rate (or groundwater level fluctuations) and earthquake occurrence rates (or earthquake rates) by utilizing the local earthquake catalog from the Thai Meteorological Department (TMD) and the groundwater level data from the Department of Groundwater Resources (DGR). The analysis revealed a noticeable correlation between fluctuations in groundwater levels and earthquake activity with a time lag. The observed time lag suggests the gradual transmission of pore-fluid pressure into seismogenic zones. These findings highlight the role of groundwater recharge in triggering earthquakes and might carry an implication for earthquake prediction and hazard assessment. Further research into this correlation could enhance our understanding of seismic precursors and lead to more effective strategies for mitigating seismic risks in the future.

Introduction:

Chiang Mai Province in Northern Thailand encompasses the western slopes of the Thanon Thong Chai Range, with elevations rising towards Thailand's highest peak, Doi Inthanon. The province is characterized by earthquakes originating from mapped faults by Department of Mineral Resources (DMR)¹, which extends approximately 35 km^{1, 2}. In 2017, the area experienced a notable earthquake with a magnitude of 4.0ML, accompanied by a series of seismic events in preceding years and subsequent aftershocks. Although these earthquakes were of moderate magnitude, the region had not seen significant seismic since the 5.1ML event in 2006^{1, 3}. Predictions suggest the potential for a future earthquake in the region, possibly reaching a magnitude of 5.5ML¹, emphasizing the need to understand the underlying causes of this seismic activity for effective hazard assessment.

Seismic activity primarily driven by tectonic movements, leading to stress accumulation in the Earth's crust and subsequent release through faulting. However, previous studies have highlighted additional factors, such as water table fluctuations and anthropogenic inductions, which can impact seismicity by altering the cycle of stress accumulation and release⁴⁻⁶. The equilibrium of crustal fault is delicate, where even minor changes can trigger seismic events following Coulomb frictional law. The presence of fluids along faults can chemically or mechanically influence fault strength and promote failure⁷⁻⁹. This is particularly relevant in the seismogenic zone of brittle crust, where fluids can circulate through fractures or fault zones¹⁰. Despite the relatively small stress changes induced by annual-scale water load

variations (less than a few kPa), these fluctuations have been suggested to moderate ongoing seismicity in various tectonically active regions (e.g., California)¹¹. Studies by Johnson and Fu¹², as well as Rigo and Souriau¹³, have highlighted the role of water loads in driving periodic seismicity patterns and modulating earthquakes in California and Pyrenees, respectively. This underscores the complex relationship between crustal stress, water loads, and seismic activity. Additionally, groundwater variations have been observed to respond to crustal deformation processes well before the occurrence of significant earthquake, as observed in Tono, Japan^{14, 15}, suggesting that such hydrological changes could serve as potential early indicators of seismic events.

This study aims to integrate the local earthquake catalog provided by the Thai Meteorological Department (TMD)³ and the groundwater level data from the Department of Groundwater Resources (DGR)¹⁶ spanning 2010 to 2021. **Figure 1** illustrates the distribution of earthquake events, categorized into 85 micro earthquakes (< 3.0ML), 5 minor earthquakes (3.0-3.9ML), and one light earthquake (4.0-4.9ML). Additionally, data from three DGR wells at varying depths (shallow to deep) within the same site were utilized. Both datasets used in this study are available online and easily accessible, though they are still in the process of being further developed. The seismic catalog employed in this study does not differentiate between mainshocks and aftershocks, recording all earthquakes using the local magnitude scale (ML) with TMD seismic instruments. Due to data collection limitations, the analysis was constrained to one-year intervals, as shown in **Figure 2**. The primary object is to investigate the potential influence of groundwater level fluctuations on earthquake rates in an area of Chiang Mai Province, Thailand. Key aspects of this analysis include assessing the correlation coefficient and identifying potential time shifts between these data in time series.

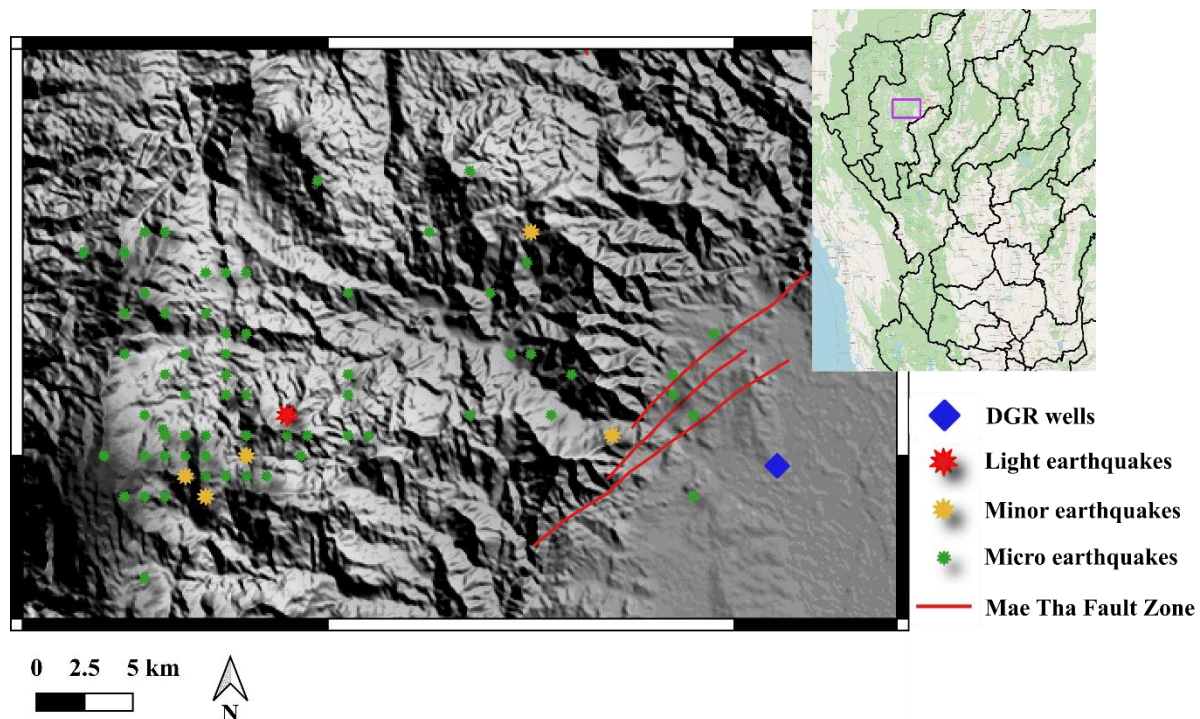


Figure 1.

A district in Chiang Mai Province in purple square, showing the locations of groundwater wells and recorded earthquakes from 2010-2021. The red star marks a light earthquake with a magnitude of 4.0 ML that occurred in 2017.

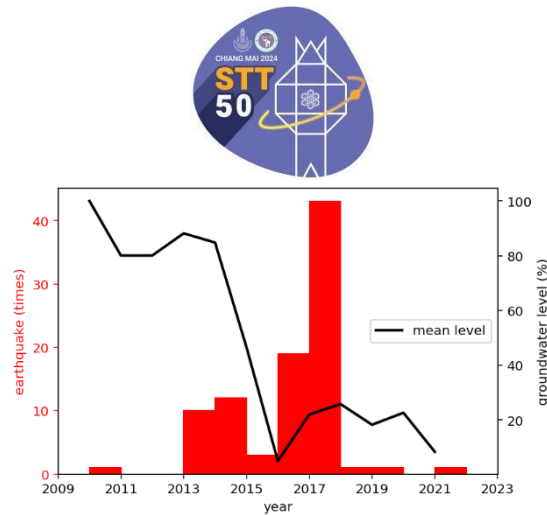


Figure 2.

The annual earthquake occurrences (represented by red bars) are shown alongside the average groundwater levels (depicted by the solid black line as a percentage)

Methodology:

Since the groundwater levels were measured at various depths, we then normalized them as percentages relative to the maximum value, with the highest-level set to 100%, as depicted in **Figure 2**. Subsequently, the mean percentages were used for further analysis. We next calculated the derivative of both average groundwater level and yearly earthquake occurrences to obtain earthquake rates (or earthquake occurrence rates) and groundwater level fluctuations (or the groundwater level change rates), respectively. Next, we examined both graphs to identify any potential time shifts between them. Once a time shift was detected, it was applied to the groundwater fluctuation data. Additionally, we analyzed the variation in earthquake rates across different depths and magnitudes.

Results and Discussion:

The initial result is plotted in **Figure 3** (left). This plot suggests a weak correlation between earthquake rates and groundwater level fluctuations, as indicated by a correlation coefficient of $R = 0.00$. However, a more in-depth analysis revealed a one-year time lag between the two, as illustrated in **Figure 3** (right). Shifting the groundwater level fluctuations by one year noticeably improved the correlation, resulting in a correlation coefficient of -0.71 . This indicates a noticeable inverse relationship between earthquake rates and groundwater level fluctuations when considering a one-year time lag within the annual timeframe.

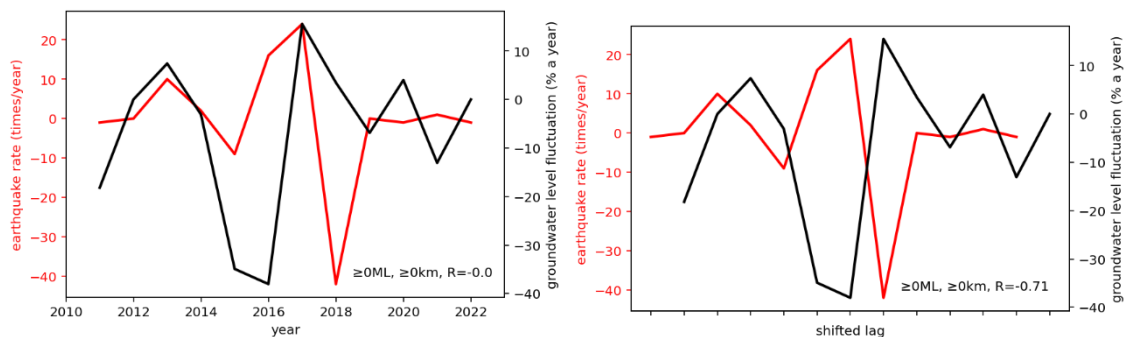


Figure 3.

The plots compare earthquake rates (red line) to groundwater level change rates or groundwater level fluctuation (black line) both without (left) and with (right) a one-year time shift applied to the groundwater level fluctuation.

Further analysis examined the relationship between varying depths and magnitudes of earthquake events and their impact on shifted groundwater level fluctuations and earthquake rates. Beginning with earthquake events at a minimum depth at 0 km and extending to at least 4 km in 1 km increments (**Figure 4**), it is noteworthy that all depths exhibited modest correlation coefficients (R values) ranging from -0.66 to -0.69 . The analysis also varied earthquake magnitudes, starting from a minimum of 0 ML and extending to at least 3 ML, as depicted in **Figure 5**. Notably, the correlations between groundwater level fluctuations and earthquake rates decreased significantly with increasing magnitude. Specifically, the correlation coefficient dropped from $R = -0.72$ for earthquakes of at least 1 ML to $R = -0.48$ for those of at least 3 ML. This decline could be attributed to the reduced frequency of earthquakes occurring at higher magnitudes.

Two principal mechanisms have been proposed to explain how hydrological factors can influence earthquake occurrence: change in pore-fluid pressure at seismogenic volumes and direct stress effect on fault planes. The former mechanism involves delayed changes in seismicity activity due to hydrological variations, influenced by earthquake depth and hydraulic diffusivity. Conversely, direct loading effects exhibit minimal or no time lag between hydrological changes and earthquake rates^{7, 11, 12, 17}.

The state of effective stress within the medium undergoes continuous changes as the pore-fluid pressure evolves in space and time⁶. This study suggests that variations in pore-fluid pressure may relate to earthquake initiation during 2013-2017, with a roughly one-year delay for hydraulic diffusion to affect the seismogenic volume or earthquake hypocenter due to considered timeframe. While other earthquake catalogs may not show the exact same patterns, our findings simply suggest a possible association between local earthquake accumulation and groundwater levels.

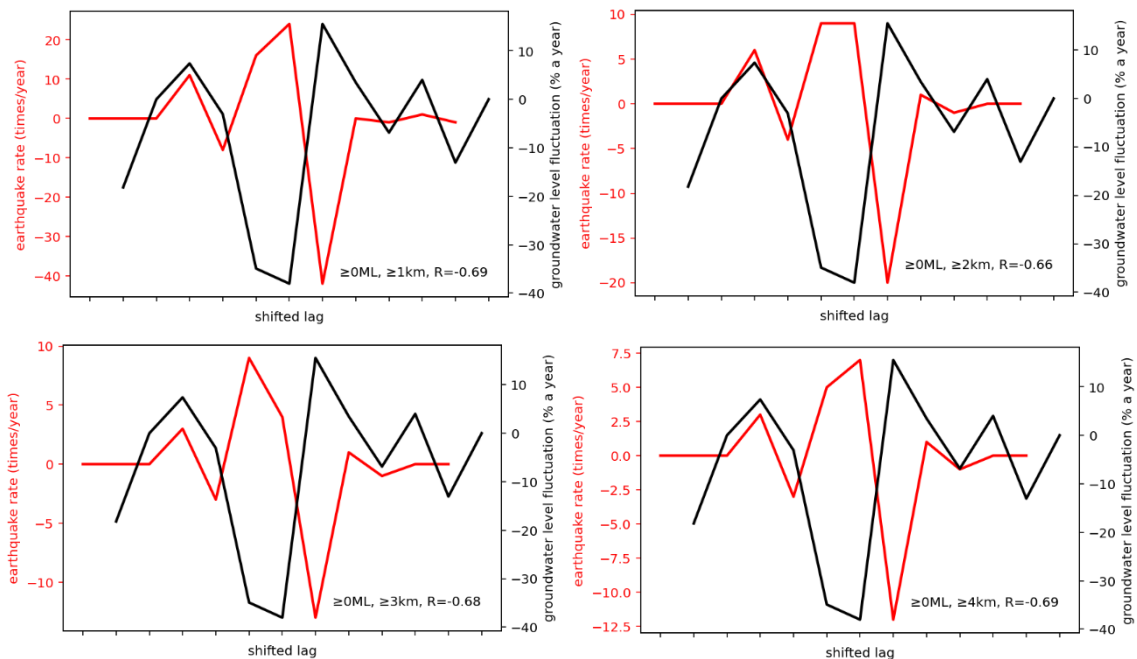


Figure 4.

The plots show the variations of earthquake rates (red line) with groundwater level fluctuations (black line) for earthquakes occurring at depths between at least 1 km to at least 4 km with a one-year time shift applied to the groundwater level fluctuation.

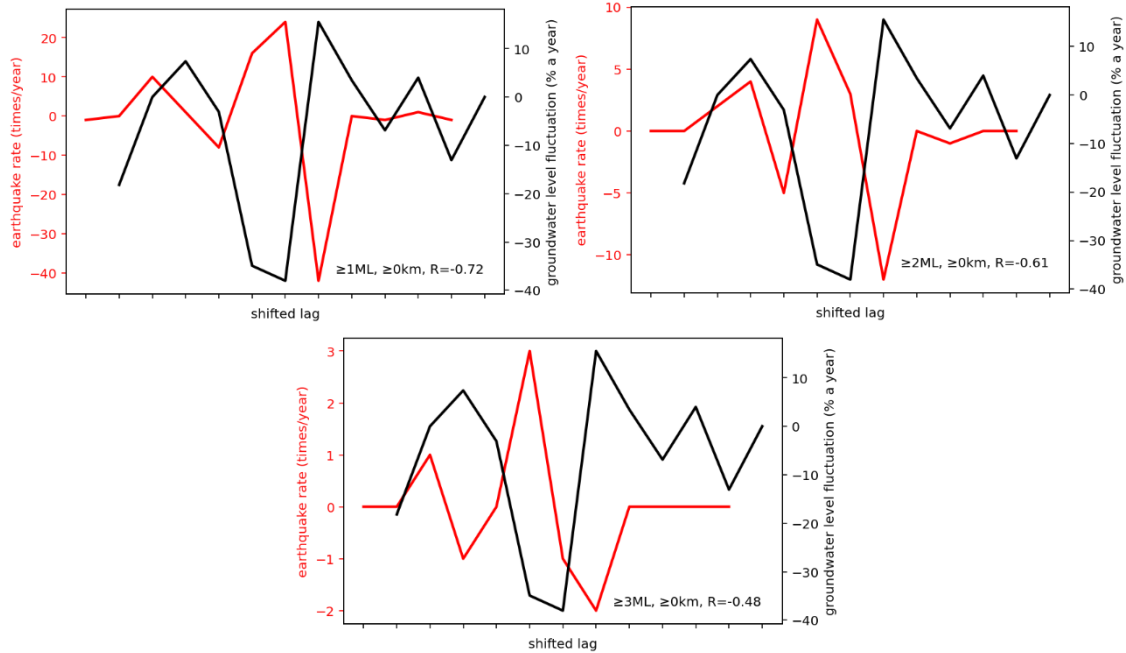


Figure 5.

The plots show the variations of earthquake rates (red line) with groundwater level fluctuations (black line) for earthquakes ranging in magnitude from 1 to 3 ML with a one-year time shift applied to the groundwater level fluctuation.

Since the groundwater level fluctuations shows the noticeable relationship with the earthquake rates, we propose that groundwater data could be used in conjunction with other factors such as *b* value, geochemical anomaly, and strain energy - known as seismicity precursors^{7, 13, 18-21} - for improving earthquake prediction and hazard assessment in the study area. These factors collectively reflect crustal stress levels.

Additions factors should be explored further:

- 1) Earthquake cycle and stress accumulation: earthquakes are related to stress build-up along faults lines often as a result of previous seismic. The observed accumulation may have occurred within an ongoing earthquake cycle^{20, 22, 23}.
- 2) Synchronization and previous earthquakes: earthquakes can synchronize through advances or delays²⁴. Therefore, the observed stress accumulation could have been influenced by earthquakes occurring elsewhere.
- 3) Correlation with Earth's rotation: seismic activity may show modest correlation with Earth's rotation²³. Astronomical processes have also been suggested to contribute to gradually stressing the Earth's crust, as faults require only minor stress changes to trigger earthquakes^{22, 25}.

Future research directions in seismicity rely on direct measurements of stress, deformation, and pore-fluid pressure in the near earthquakes zone. A borehole observatory located near fault zones would be crucial for such studies. Although constraining all physical parameters before an earthquake is challenging, near-field observations of the rupture tip zone would offer valuable insights into underlying physical processes¹⁷. Detecting tectonic stress directly is challenging, making it difficult to provide evidence for increased stress^{20, 23}. Additionally, mineral zonation is understood to result from repeated arrival of fluids, with each arrival leaving an imprint in vein¹⁰. Therefore, understanding the controls on earthquakes timing is fundamental for comprehending the earthquake's precursory nature and determining

time-dependent earthquake hazard. Notably, the time-lag shifting might vary when more detailed time-series data is incorporated in future work.

Conclusion:

Groundwater level fluctuations, in the study area of Chiang Mai Province, appear to correlate with earthquake rates, while the other considered factors seem to have equal to lesser correlation. However, this conclusion is preliminary and specific to the studied district. Further, in-depth research is needed to strengthen these findings, and extending the study to other areas is essential for drawing conclusions on a regional scale. We are acknowledging that both catalogs are incomplete and developing, our study prioritizes implementing online-available data for convenient use as seismic precursors. This work also aims to promote instrument maintenance and improvement for cooperative use across various research fields.

Considering societal concerns, it is important to note that hydrologically derived stress variations are minor compared to long-term tectonic stresses, particularly in regions unaffected by major climate change or large-scale aquifer depletion¹¹.

Acknowledgements:

I would like to extend my sincere appreciation and gratitude to the National Science and Technology Development Agency (NSTDA), Thailand, for the financial support, which made this research possible. Their funding has greatly contributed to the progress and success of this study. I also express my gratitude to the Thai Meteorological Department (TMD) and the Department of Groundwater Resources (DGR) for providing the catalog data used in this research.

References:

1. DMR, Department of Mineral Resources. 2017 [cited 2024 19 April] (in Thai).
2. DMR, Department of Mineral Resources. 2023 [cited 2024 17 January] (in Thai).
3. TMD, Thai Meteorological Department. 2023 [cited 2024 03 April] (in Thai).
4. Bragato, PL. *Frontiers in Earth Science*, 2021. **9**: p. 790412.
5. Hornbach, MJ, et al. 2015. **6**(1): p. 1-11.
6. Zhai, G, et al. *Proceedings of the National Academy of Sciences*. 2019. **116**(33): p. 16228-16233.
7. D'Agostino, N, et al. *Geophysical Research Letters*, 2018. **45**(22): p. 12,253-12,262.
8. Hauksson, E and M-A Meier. *Pure and Applied Geophysics*, 2019. **176**(3): p. 1061-1081.
9. Sibson, RH. *Nature*, 1974. **249**(5457): p. 542-544.
10. Fabbri, O, H Raimbourg, and H Leclère. *Comptes Rendus. Géoscience*, 2024. **356**(S2): p. 423-466.
11. Craig, TJ, K Chanard, and E Calais. *Nature communications*, 2017. **8**(1): p. 2143.
12. Johnson, CW, Y Fu, and R Bürgmann. *Science*, 2017. **356**(6343): p. 1161-1164.
13. Rigo, A, A Souriau, and M Sylvander. *Journal of Seismology*, 2018. **22**: p. 337-352.
14. King, CY, et al. *Journal of Geophysical Research: Solid Earth*, 1999. **104**(B6): p. 13073-13082.
15. King, CY, et al. *Geophysical Journal International*, 2000. **143**(2): p. 469-477.
16. DGR, Department of Groundwater Resources. 2023 (in Thai).
17. Savage, HM, et al. *Scientific Drilling*, 2017. **23**: p. 57-63.
18. De Luca, G, G Di Carlo, and M Tallini. *Scientific reports*, 2018. **8**(1): p. 15982.
19. El-Isa, ZH and DW Eaton. *Tectonophysics*, 2014. **615**: p. 1-11.
20. Li, Y and X Chen. *Pure and Applied Geophysics*, 2021: p. 1-17.
21. Sreejith, K, et al. *Scientific reports*, 2018. **8**(1): p. 16697.
22. Bendick, R and R Bilham. *Geophysical Research Letters*, 2017. **44**(16): p. 8320-8327.



23. Chen, X, Y Li, and L Chen. Geomatics, Natural Hazards and Risk, 2022. **13**(1): p. 2151-2165.
24. Scholz, CH. Bulletin of the Seismological Society of America, 2010. **100**(3): p. 901-909.
25. Scafetta, N and A Mazzarella. Natural Hazards, 2015. **76**(3): p. 1807-1829.



AN EXPERIMENT ON THE MECHANICAL PROPERTIES OF THE CIRCULAR HOLE ROCK UNDER ANISOTROPY CONDITIONS

Wimon Sukplum* and Kanmanee Soonsin

Department of Geotechnology, Faculty of Technology, Khon Kaen University, Thailand

*e-mail: wimosu@kku.ac.th

Abstract:

Discontinuities such as bedding planes in sedimentary rocks or laminations in metamorphic rocks can affect the stability of rocks. Furthermore, the evolution of strength and failure around a hole in compressed rocks is the most critical factor affecting rock properties during geotechnical engineering work. This research evaluated the effects of different hole diameters and loading directions on specimens using the Phra Wihan sandstone Formation of the Khorat Group. The rock samples were prepared in a prismatic shape of 100 x 50 x 50 mm from different orientations, including intact rocks and rocks with 12 mm and 20 mm diameter holes. Three specimens were prepared parallel to the loading direction, while the others were inclined. The uniaxial compressive strength test, the failure evolution of the specimens, and the effects of anisotropic stress on crack networks were analyzed. The results show that compressive strength decreases with hole diameter, where the inclined plane is slightly higher than the parallel plane. Furthermore, the failure of evolution in the specimens can be divided into three types: tensile crack, shear crack, and tensile to shear crack.

Introduction:

The mechanical properties of circular holes in rocks exhibit variations based on the direction of anisotropy. Numerous studies suggest that the shape of a hole significantly affects the strength of rock, with circular holes having the least impact, while triangular holes exert the greatest influence¹. Furthermore, the orientation of isotropic planes influences the displacement behavior of tunnels, with the greatest displacement occurring perpendicular to the isotropic planes when subjected to hydrostatic stress². Moreover, experiments on rock samples with varying hole positions and diameters demonstrate significant changes in stress-strain behavior, peak strength, failure patterns, and energy conversion, highlighting the critical role of hole orientation in influencing mechanical properties and failure modes³. The risk of geological hazards, such as roof collapse, rock spalling, and rock bursts, in underground engineering increases significantly when static and dynamic stress concentrations are combined⁴⁻⁵.

Additionally, many underground projects must contend with geological structures, such as faults and folds, characterized by well-developed bedding, which are generally less stable.⁶⁻⁷ Rocks with varying bedding angles exhibit different mechanical properties and failure modes when subjected to both dynamic and static stresses⁸⁻¹⁰. These findings collectively underscore the significant influence of anisotropy orientation on the mechanical behavior of rocks containing circular holes, particularly in terms of strength, deformation, and failure modes. This research investigates the effects of discontinuities and the presence of holes in rocks, with a particular emphasis on the Phra Wihan sandstone Formation of the Khorat Group. Discontinuities, such as bedding planes and holes, significantly affect rock stability and behavior during activities like blasting excavation. The experiment involved rock samples shaped orthogonally, with varying hole sizes and loading orientations. The tests

included uniaxial compressive tests on both intact rocks and those with holes, analyzing failure patterns, crack propagation, and the effects of anisotropic stress, as well as calculating elastic modulus and Poisson's ratio. This study offers valuable insights into how discontinuities and hole dimensions influence rock behavior, which is essential for geotechnical engineering applications.

Experimental procedures:

The specimen preparation and experimental procedures

The tests conducted in this study utilized the Phra Wihan Sandstone Formation, which is part of the non-marine deposits of the Khorat Plateau, collectively known as the Khorat Group¹¹. The formation is predominantly thick-bedded to massive white sandstones, with occasional thin beds of reddish-brown to gray claystone (**Figure 1**). Block samples were collected from an outcrop in Khon Kaen Province, Northeast Thailand. These blocks were then sliced to obtain prismatic specimens with average dimensions of 50 mm in thickness, 50 mm in width, and 100 mm in height (see **Figure 2**). Two types of specimens were prepared: one group with bedding planes parallel to the loading direction and another with bedding planes inclined to the loading direction. Holes with diameters of 12 mm and 20 mm were drilled into the center of the specimens using a diamond hole saw. The loading surfaces of all specimens were polished in accordance with the standards set by the International Society for Rock Mechanics (ISRM)¹². Six specimens with bedding planes parallel to the loading direction were prepared for uniaxial compression tests, while additional specimens were prepared for both uniaxial and ultrasonic wave velocity measurements. These included two intact rock samples, two with 12 mm diameter holes, and two with 20 mm diameter holes (see **Figure 3**). Specimens with bedding planes inclined to the loading direction were prepared in a similar manner. Thus, six specimens were required for each bedding plane angle, resulting in a total of 12 specimens.



Figure 1.

The block samples of the Phra Wihan Sandstone Formation.

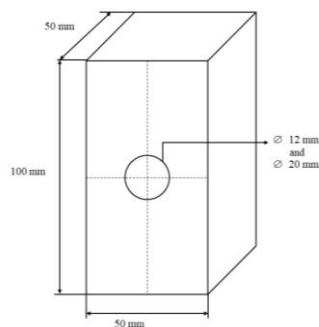


Figure 2.

The typical dimensions of the specimens for laboratory tests.

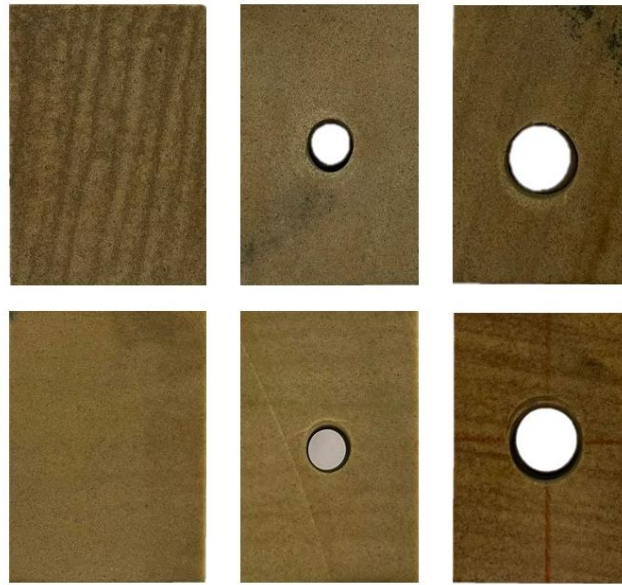


Figure 3.

Two types of specimens: (top) bedding planes inclined to the loading direction and (bottom) parallel to the loading direction.

Physical properties

The physical properties of nine representative specimens, selected from all block samples, were determined. Two properties, density and porosity, were evaluated for these specimens. These properties were conducted by the water replacement method following the testing standard of ISRM¹², and their values are tabulated in **Table 1**.

Table 1.

An average physical property of the representative specimens.

| Sample No. | Dry density (g/cc) | Porosity (%) |
|----------------|--------------------|--------------|
| PW-1 | 2.10 | 6.77 |
| PW-2 | 2.21 | 6.42 |
| PW-3 | 2.24 | 5.44 |
| PW-4 | 2.16 | 4.00 |
| PW-5 | 2.20 | 3.25 |
| PW-6 | 2.42 | 6.49 |
| PW-7 | 2.21 | 4.03 |
| PW-8 | 2.26 | 2.99 |
| PW-9 | 2.26 | 5.37 |
| Average | 2.23 | 4.97 |

Experimental setup

All specimens were tested under dry conditions and assessed for unconfined compressive strength (UCS). The testing procedure for UCS adhered to the standards set by ASTM¹³. Two electrical strain gauges were attached to the surfaces of the specimens, as illustrated in **Figure 4**, to measure axial and lateral strains. Consequently, the static elastic modulus (E_s) and Poisson's ratio (ν_s) were calculated based on the relationship between the stress-strain curves.



Figure 4.

The specimens with the electrical strain gauge (left) axial strain and (right) lateral strain.

The first group of specimens was tested under static load conditions to measure the maximum stresses. After that, the second group of specimens was tested under increased static load conditions at initial, 50%, and 75% stress states, calculated from the first group of tests. Meanwhile, the ultrasonic wave velocities of the P-wave and S-wave were measured. Consequently, the dynamic elastic modulus (E_d) and Poisson's ratio (ν_d) were calculated using the following equations:

$$E_d = \rho V_s^2 \frac{(V_p^2 - 4V_s^2)}{V_p^2 - V_s^2} \quad (1)$$

$$\nu_d = \frac{V_p^2 - 2V_s^2}{2(V_p^2 - V_s^2)} \quad (2)$$

Where V_p and V_s represent the compression (P-wave) and shear (S-wave) velocities, respectively, and ρ is the density of the specimen.

Test results and discussion:

Table 2 presents the static unconfined compressive strength of six specimens under two different bedding direction conditions. The data indicates that compressive strength decreases with an increase in hole diameter. Moreover, specimens with bedding planes inclined to the loading direction exhibit slightly higher compressive strength than those with bedding planes parallel to the loading direction. According to Deere and Miller's engineering classification of rocks, the strength of the specimens can be categorized into various levels based on strength and modulus ratio. The intact specimens are classified as having medium strength, while those with holes are classified as having high strength.

Failure characteristics of the specimen were divided into two types, as depicted in **Figure 5**. The diagram illustrates two types of failure modes associated with different crack inclinations: (1) tensile crack (T) and (2) shear crack (S). The inclination of the fracture significantly influences the failure mode of the specimens. With respect to bedding plane inclination, shear cracks (S) predominantly occur around the hole, while tensile cracks (T) primarily manifest outside the pre-existing crack. When the bedding is parallel to the loading direction, tensile cracks (T) appear symmetrically on both the upper and lower sides of the



hole, indicating that tensile stress concentration occurs at the hole. Additionally, tensile (T) and shear (S) cracks are observed at the tangents of the pre-existing crack in relation to the hole and the original crack.

The ultrasonic wave velocities, dynamic elastic modulus (E_d), Poisson's ratio (ν_d), the static elastic modulus (E_s), and Poisson's ratio (ν_s) at different stress states are tabulated in **Table 3-4**. The results indicate that both P-wave and S-wave velocities increase with rising stress levels and then slightly decrease when the stress reaches 75%, as shown in **Figure 6**. The wave velocities in specimens with inclined bedding planes are higher than those in other orientations. Furthermore, the dynamic elastic modulus (E_d) and static elastic modulus (E_s) exhibit a similar trend to the wave velocities. For specimens DY-02, DY-04, and DY-05, all parameters decrease at 75% of the stress state due to the onset of cracking.

Table 2.
Summary of static loading test.

| Type of specimens | Conditions | No. | Density | UCS | Elastic Modulus (E_s) | Poisson's ratio (ν_s) |
|-------------------|------------|-------|-------------------|-------|---------------------------|-----------------------------|
| | | | g/cm ³ | MPa | GPa | |
| Parallel | Intact | ST-01 | 2.21 | 66.50 | 20.22 | 0.32 |
| | Hole 12 mm | ST-02 | 2.14 | 51.81 | 26.07 | 0.44 |
| | Hole 20 mm | ST-03 | 2.05 | 29.77 | 31.85 | 0.66 |
| Inclined | Intact | ST-04 | 2.21 | 86.09 | 22.09 | 0.26 |
| | Hole 12 mm | ST-05 | 2.13 | 62.01 | 33.40 | 0.32 |
| | Hole 20 mm | ST-06 | 2.13 | 31.69 | 21.73 | 0.24 |

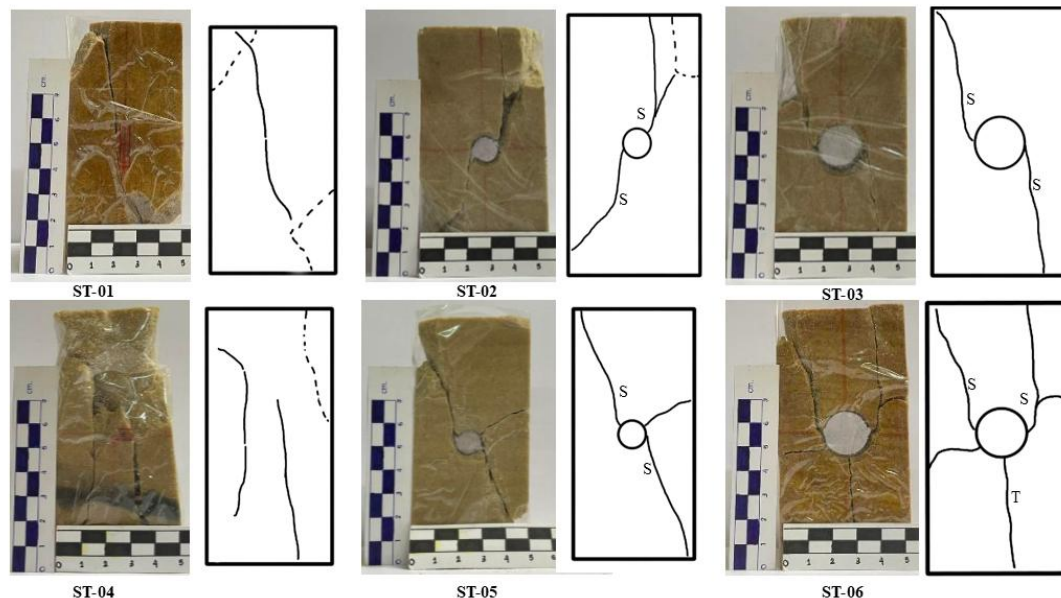


Figure 5.
Failure characteristic of specimens under static loading test.

Table 3.
Summary of ultrasonic wave velocities and dynamic elastic modulus in stress state conditions.

| Type of specimens | Conditions | No. | Stress state | P-wave | S-wave | Elastic Modulus (Ed) | Poisson's ratio (vd) |
|-------------------|------------|-------|--------------|--------|--------|----------------------|----------------------|
| | | | | m/s | m/s | GPa | |
| Parallel | Intact | DY-01 | Initial | 2468 | 1526 | 12.25 | 0.19 |
| | | | 50% | 2691 | 1869 | 15.97 | 0.03 |
| | | | 75% | 2740 | 1870 | 16.45 | 0.06 |
| | Hole 12 mm | DY-02 | Initial | 2381 | 1495 | 11.03 | 0.17 |
| | | | 50% | 2787 | 1816 | 15.67 | 0.13 |
| | | | 75% | 2509 | 1746 | 13.20 | 0.03 |
| | Hole 20 mm | DY-03 | Initial | 2457 | 1515 | 12.05 | 0.19 |
| | | | 50% | 2637 | 1736 | 14.82 | 0.12 |
| | | | 75% | 2673 | 1771 | 15.30 | 0.11 |
| Inclined | Intact | DY-04 | Initial | 2222 | 1131 | 7.59 | 0.33 |
| | | | 50% | 2671 | 1887 | 15.98 | 0.00 |
| | | | 75% | 2530 | 1489 | 12.26 | 0.24 |
| | Hole 12 mm | DY-05 | Initial | 2346 | 1574 | 13.58 | 0.09 |
| | | | 50% | 2705 | 1857 | 18.27 | 0.05 |
| | | | 75% | 2542 | 1690 | 15.84 | 0.10 |
| | Hole 20 mm | DY-06 | Initial | 2519 | 1764 | 13.31 | 0.02 |
| | | | 50% | 2537 | 1776 | 13.50 | 0.02 |
| | | | 75% | 2642 | 1762 | 14.33 | 0.10 |

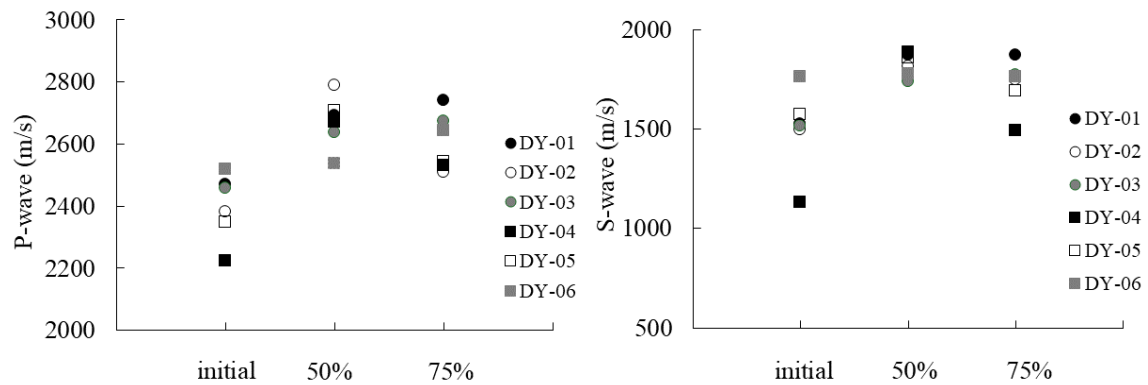


Figure 6.
P-wave (left) and S-wave (right) velocities at different stress conditions

**Table 4.**

Summary of static elastic modulus and Poisson's ratio under different stress levels.

| Type of specimens | Conditions | No. | Stress state | Elastic Modulus (Es) | Poisson's ratio (vs) |
|-------------------|------------|-------|--------------|----------------------|----------------------|
| | | | | GPa | |
| Parallel | Intact | DY-01 | Initial | 9.10 | 0.13 |
| | | | 50% | 21.06 | 0.87 |
| | | | 75% | 21.53 | 1.38 |
| | Hole 12 mm | DY-02 | Initial | 9.57 | 0.09 |
| | | | 50% | 23.97 | 0.52 |
| | | | 75% | 19.13 | 0.89 |
| | Hole 20 mm | DY-03 | Initial | 11.63 | 0.05 |
| | | | 50% | 21.47 | 0.11 |
| | | | 75% | 51.43 | 0.97 |
| Inclined | Intact | DY-04 | Initial | 19.10 | 0.10 |
| | | | 50% | 23.46 | 0.36 |
| | | | 75% | 47.86 | 0.53 |
| | Hole 12 mm | DY-05 | Initial | 21.04 | 0.18 |
| | | | 50% | 25.62 | 0.45 |
| | | | 75% | 42.66 | 0.79 |
| | Hole 20 mm | DY-06 | Initial | 27.90 | 0.03 |
| | | | 50% | 78.75 | 0.14 |
| | | | 75% | 55.41 | 0.28 |

The study reveals a significant effect of hole diameter on the static elastic modulus (Es) and Poisson's ratio (vs), with both properties increasing as the hole diameter enlarges. Moreover, the Es values for the two types of specimens, those aligned parallel to the loading direction and those inclined to it, are notably higher than the dynamic elastic modulus (Ed) by factors of approximately 2.65 and 1.53, respectively (**Figure 7**). The failure characteristics of the specimens under varying stress conditions were identified when the stress level increased to 75%, particularly in those with holes. In specimens with parallel bedding planes, tensile cracks (T) and shear cracks (S) primarily initiated outside the hole and extended outward. In contrast, specimens with inclined bedding planes exhibited a sequence of crack types: tensile-to-shear cracks (TS), shear cracks (S), and tensile cracks (T). Shear cracks (S) predominantly formed around the hole, while tensile-to-shear cracks (TS) mainly appeared outside the pre-existing crack. Additionally, tensile cracks (T) occurred symmetrically on both the upper and lower sides of the hole, indicating a concentration of tensile stress at that location. The study also identified a significant effect of hole diameter on failure characteristics, with larger holes exhibiting more pronounced pre-existing cracks compared to smaller ones. Furthermore, pre-existing cracks around the hole were more prevalent in specimens with inclined planes than in those with parallel planes (**Figure 8**).

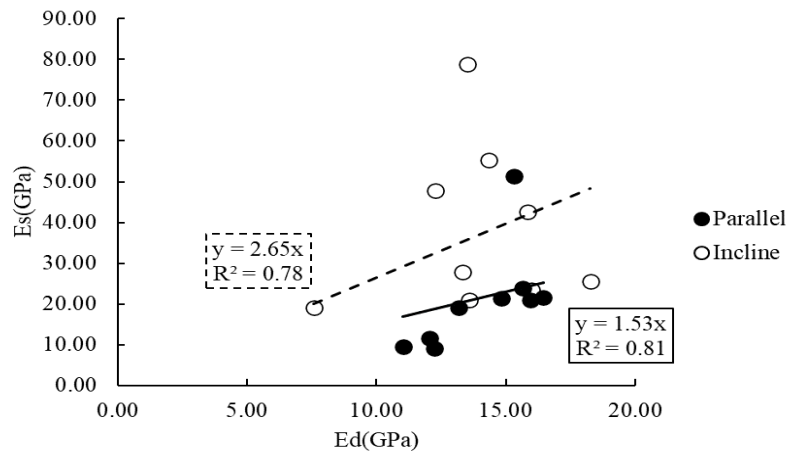


Figure 7.

Relationship between static elastic modulus (E_s) and Dynamic elastic modulus (E_d)

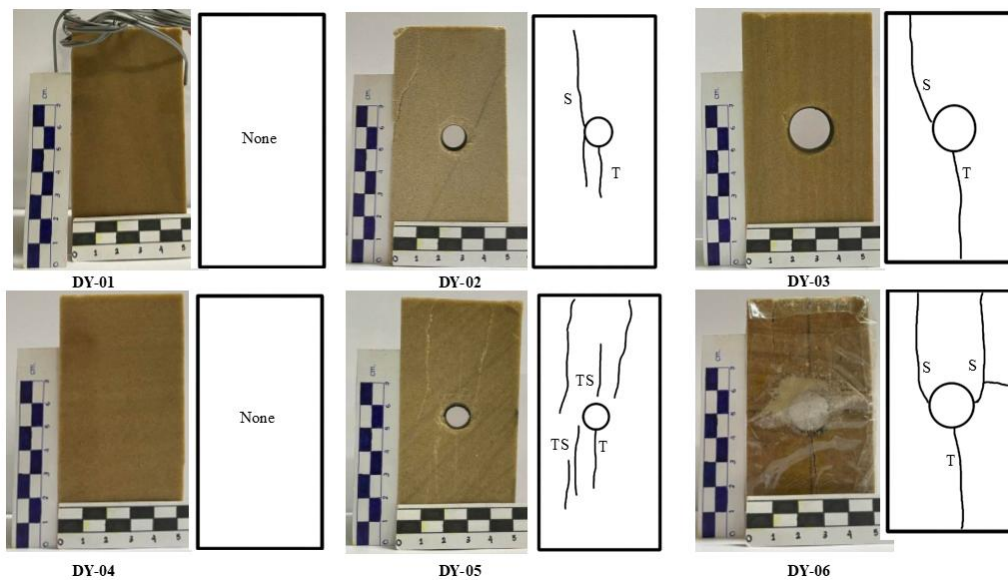


Figure 8.

Failure characteristic of specimens at 75% of stress levels.

Conclusions:

The study concludes that hole diameter and bedding plane orientation significantly influence the mechanical properties and failure characteristics of specimens. Specifically, an increase in hole diameter results in decreased compressive strength, though specimens with bedding planes inclined to the loading direction exhibit slightly higher compressive strength compared to those with parallel bedding planes. The study also identifies distinct failure modes, with tensile cracks occurring symmetrically around the hole in specimens with parallel bedding planes, while a combination of tensile and shear cracks appears in those with inclined bedding planes. Additionally, both dynamic and static elastic moduli, as well as Poisson's ratios, increase with hole diameter, with static moduli being notably higher than dynamic ones. Finally, the presence and distribution of pre-existing cracks are more prominent in specimens with larger holes and inclined bedding planes.



Acknowledgements:

The authors extend their sincere gratitude to the Department of Geotechnology, Faculty of Technology, Khon Kaen University, for providing the necessary support and facilities for this study in the Geomechanics Laboratory.

References:

1. Zhaofeng C, Yonghui S. *Geotech Geol Eng.* 2021;39: 3437–3447.
2. Maazallahi V, Majdi A. *Arab J Geosci.* 2020; 13: 547.
3. Xiao F, Li R, Xing L. *Adv. Civ. Eng.* 2021;6: 1-14.
4. Jiang Q, Feng X-t, Chen J, Huang K, Jiang Y-l. *Eng Geol.* 2013;152(1):38–47.
5. Hu L, Ma K, Liang X, Tang C, Wang Z, Yan L. *Tunn Undergr Space Technol.* 2018;81:602–618.
6. Jeon S, Kim J, Seo Y, Hong C. *Int J Rock Mech Min Sci.* 2004;41(3):486.
7. Hao YH, Azzam R. *Tunn Undergr Space Technol.* 2005;20(1): 49–61.
8. Jia P, Tang CA. *Tunn Undergr Space Technol.* 2008;23(5):500–507.
9. Yang X, Kulatilake PHSW, Jing H, Yang S. *Tunn Undergr Space Technol.* 2015;50:129–142.
10. Zhang Z, Chen F, Li N, Swoboda G, Liu N. *Tunn Undergr Space Technol.* 2017;61: 1–11.
11. Booth J, Sattayarak N. *The geology of Thailand.* 2011; 185-222.
12. Brown E.T. *ISRM suggested methods.* 1981; 113-116.
13. ASTM D7012-14. *ASTM International;* 2014.



EFFECT OF COBALT ADDITION ON MICROSTRUCTURE AND MECHANICAL PROPERTY OF SINTERED MULTIPHASE STEELS

Nipon Chumchery^{1*}, Bhanu Vetayanugul², Thanyaporn Yotkaew², Monnapas Morakotjinda², Nattaya Tosangthum², Ruangdaj Tongsri², Viseth Putsaccada³

¹Functional Materials for Novel Engineering Applications Research Team, Engineering Design and Computation Research Group.

²Particulate Materials Processing Technology Research Team, Material Processing and Manufacturing Automation Research Group.

^{1, 2}MTEC, National Science and Technology Development Agency, Paholyothin Road, Khlong Nueng, Klong Luang, Pathum Thani, 12120, Thailand.

³Department of Mechanical Engineering, School of Engineering, King Mongkut's Institute of Technology Ladkrabang, Bangkok, 10520, Thailand.

*e-mail: niponc@mtec.or.th

Abstract:

Sintered steels are widely applied in several industrial fields. However, they are limited to some applications due to their porous nature, leading to poor ductility. In this work, the approach to enhance ductility, indicated by high total elongation, was conducted to improve sintered steel matrix. Two reference sintered steels were produced from two different metal powders, such as pre-alloyed Fe-4.0Ni-0.5Mo-0.2Mn (ATOMET4801) and diffusion-alloyed Fe-4.0Ni-1.5Mo-2.0Cu (DistaloyHP1) powders. The base powders were mixed with 4.0 wt.% silicon carbide and different cobalt powder contents (0.0-3.0 wt. % with 0.5 increments). Both sintered steels showed common microstructural features consisting of a black particle enveloped with multiphase matrix consisting of bainitic ferrite laths, retained austenite blocks and films, and martensite blocks. Both sintered steels showed promising tensile strength and elongation. With cobalt modification, strength and elongation values increased with increasing cobalt content in both sintered steel types. Strength-ductility synergy was achieved in both cobalt-added sintered steel systems. Cobalt was more effective when added to sintered Fe-4.0Ni-0.5Mo-0.2Mn composite.

Introduction:

One benefit of the powder metallurgy process is its ability to combine sintering and heat treatment into one step known as sinter hardening. Microstructures of sintered carbon steels can be tailored to achieve different mechanical characteristics through alloy design and controlled cooling rates¹. After sintering, if the cooling rate is slow, carbon steels commonly exhibit the formation of ferrite and carbide precipitation structures. Alloying elements can alter the phase transformation scenarios in sintered steels. So far as we know, all alloying elements, except cobalt (Co) and aluminum (Al), slow down the kinetics of pearlite transformation². The advantage is that it is possible to produce lower-transformation product structures that create a wide variety of high strength and hardness under slow cooling.

Ridley et al.³ found that the manganese (Mn), is partitioned between the ferrite and the cementite during the pearlite transformation, which significantly retards the pearlite transformation rate and slows down the bainitic transformation kinetics. Ochiai et al.⁴ claimed that Chromium (Cr) and Molybdenum (Mo) increase the eutectoid temperature, promoting the high strength of pearlite by refining the inter-lamellar spacing. Silicon (Si) is a ferrite stabilizer

that inhibits carbide precipitation⁵. Nickel (Ni) plays a role in lowering the pearlite start (Ps) and the bainite start (Bs) temperatures and can also move both pearlite and bainite transformation curves to the right-hand side of the continuous cooling transformation (CCT) diagram^{6,7}. Copper (Cu) addition in a hot rolled ferrite-based lightweight steel resulted in a higher volume fraction of retained austenite due to bainitic transformation delay has been reported by Wang et al.⁸

Many previous studies investigated the combined effect of alloying elements on the microstructure of sintered composites. SiC, a source of Si and C, was added to pre-alloy powders, such as Fe-Mo⁹⁻¹¹, Fe-Cr-Mo¹, Fe-Mo-Mn¹², and Fe-Mo-Mn-Ni¹³. The sintered composite exhibited a microstructure with graphite-bearing particles embedded in the metal matrix when the SiC content was approximately 4 wt.%. The matrix structure of the sintered composites strongly depends on the pre-alloyed base powder composition. In the Fe-Mo-Mn/SiC system, the microstructure closely resembled that of an austempered ductile iron; that is, it consists of black particles consisting of SiC residue graphite shell, embedded in the multiphase matrix consisting of ferrite, pearlite, and ausferrite¹⁴. Ruangchai et al.¹⁵ proved that the increase in Mo content in sintered Fe-Mo-Si-C composites resulted in a lower fraction of black particles but a higher fraction of matrix. According to the previous work¹³, as the amount of Ni increased, so did the proportion of ausferrite structure in the matrix of the sintered Fe-Ni-Si-C composite. Therefore, increased nickel content led to higher strength and ductility. Despite the high tensile strength, the elongation values were still quite low. The trade-off between strength and ductility is a well-known dilemma. Gao et al.¹⁶ reported that the dual-phase lamellar microstructure is a possible approach for overcoming the strength-ductility trade-off in materials.

Based on the previous works, it was stated that cobalt (Co) can accelerate bainitic transformation⁵, varied cobalt (Co) and fixed 4 wt.% SiC were added to pre-alloyed Fe-4.0Ni-0.5Mo-0.2Mn (ATOMET4801) and diffusion-alloyed Fe-4.0Ni-1.5Mo-2.0Cu (DistaloyHP1) powders under the idea that faster bainitic transformation would enhance bainitic ferrite plates, resulting in a high proportion of ausferrite having a dual-phase lamellar structure. The expectation is to improve elongation without compromising the strength of the sintered composite.

Methodology:

The two base metal powders employed in this work were Fe-4.0Ni-0.5Mo-0.2Mn powder (ATOMET4801 from Rio Tinto of Canada) produced by the atomization technique and Fe-1.5Mo-2.0Cu-4.0Ni (Distaloy HP1 of Hoganas of Sweden) produced by diffusion bonding. Fixed 4.0 wt.% SiC and varied Co contents of 0.0, 0.5, 1.0, 1.5, 2.0, 2.5, and 3.0 wt.% were added to the pre-alloyed powder. The powder mixture was mixed with 1 wt.% zinc stearate as a lubricant before compacting into tensile test bars with a green density of 6.5 g/cm³. Then the powder compacts were sintered at 1280 °C for 45 minutes in a vacuum furnace (Schmetz of Germany) at a pressure of 1.28×10^{-5} MPa. After sintering, the specimens were slowly cooled with 0.1 °C/s.

To prepare specimens for optical microscopy (OM) and scanning electron microscopy (SEM), the following actions were taken, cutting, mounting, grinding (180 to 1200 grit silicon carbide papers), polishing (6, 3, and 1 µm diamond suspension), and etching with 2 % nital in ethanol for 10 seconds. Specimens were hot mounted in phenolic resin at around 180 °C using a mounting press. Two-stage tint etching (color metallography) was applied to separate bainite, martensite, and ferrite regions. The polished surface was pre-etched with 4% picral for 1-2 min. before being etched with 10 g of Na₂S₂O₅ in 100 ml of distilled water.



Phase identification was carried out by using the X-ray diffraction (XRD) technique. The polished specimens were employed for XRD characterization. XRD was performed by using a Rigaku TTRAX III X-ray diffractometer with copper source (wavelength of 1.54 Å) and conditions including step size of 0.2°, time 0.5 s/step, and angle of 30-100°.

Results and Discussion:

Microstructure of sintered composite without Co addition

The sintered Fe-4.0Ni-0.5Mo-0.2Mn with 4.0 wt.%SiC added composite (R1) showed microstructural features consisting of black particles enveloped with ausferrite and martensite islands (Figure 1(a)). The SEM image of the matrix area is shown in Figure 1(b). Two-stage tinting indicated that the ferrite grain surrounding a black particle and bainitic ferrite (BF) plate tinted blue, and the martensite island tinted brown (Figures 1(c) and 1(d)). According to De et al.¹⁷, the two-stage tint method revealed martensite as brown, bainite as dark blue, and ferrite as white. Proeutectoid carbide was seen along prior austenite grain boundaries (Figure 1(c)).

The sintered Fe-1.5Mo-2.0Cu-4.0Ni with 4.0 wt.% SiC added composite (R2) had the same general microstructural characteristic as the previous one, with black particles embedded in the metal matrix (Figure 2(a)). The matrix of this sintered composite consists of acicular plates of BF confirmed by blue color tinting and blocks of martensite confirmed by brown color tinting (Figures 2(c) and 2(d)). BF and blocks of martensite in the matrix area were clearly seen in the SEM image Figure 2(b).

Ni was observed to increase the production of acicular ferrite and hinder the presence of granular bainite¹⁸. The copper addition of ≥ 2.0 wt% could change the microstructure of the Fe-Mo-Si-C sintered composite from pearlite to ausferrite completely¹¹. Regarding the nominal composition of both sintered composites, all elements act as austenite stabilizers and suppress eutectoid transformation. The combined effect of these alloying elements shows austenite stabilization sufficient for acicular ferrite and martensite formation at low temperatures under the cooling rate of 0.1°C/s.

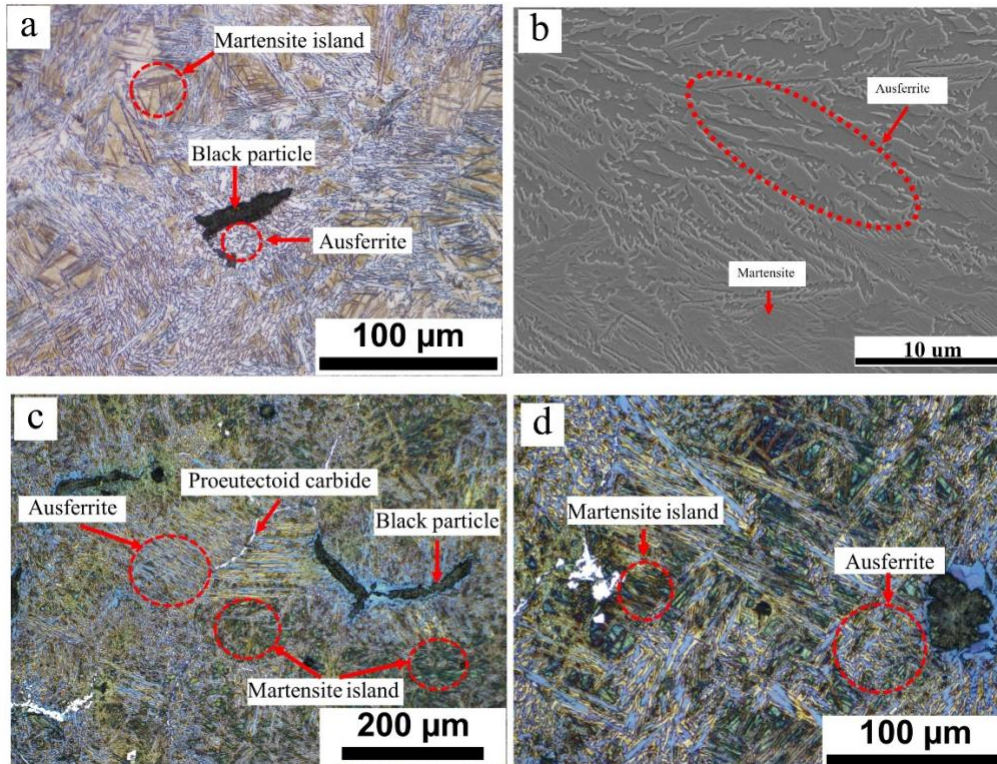


Figure 1. Microstructure of sintered Fe-4.0Ni-0.5Mo-0.2Mn-4.0SiC composite; (a) OM, etched with 2 % Nital, (b) SEM, etched with 2 % Nital, (c) and (d) OM, two-stage tinted.

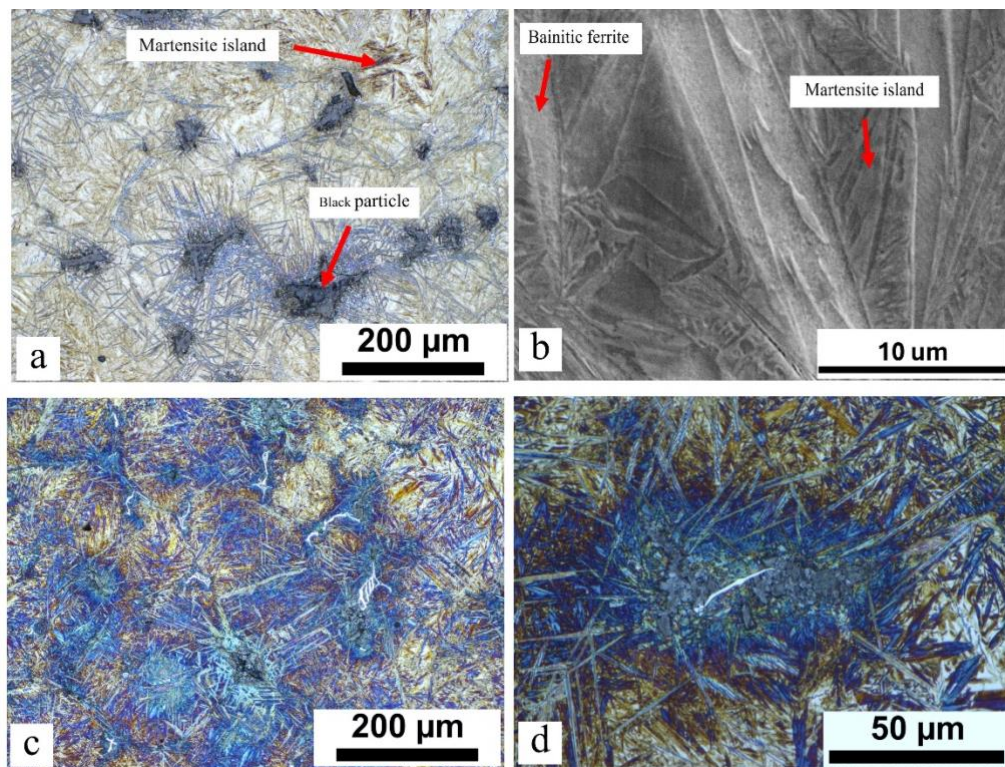
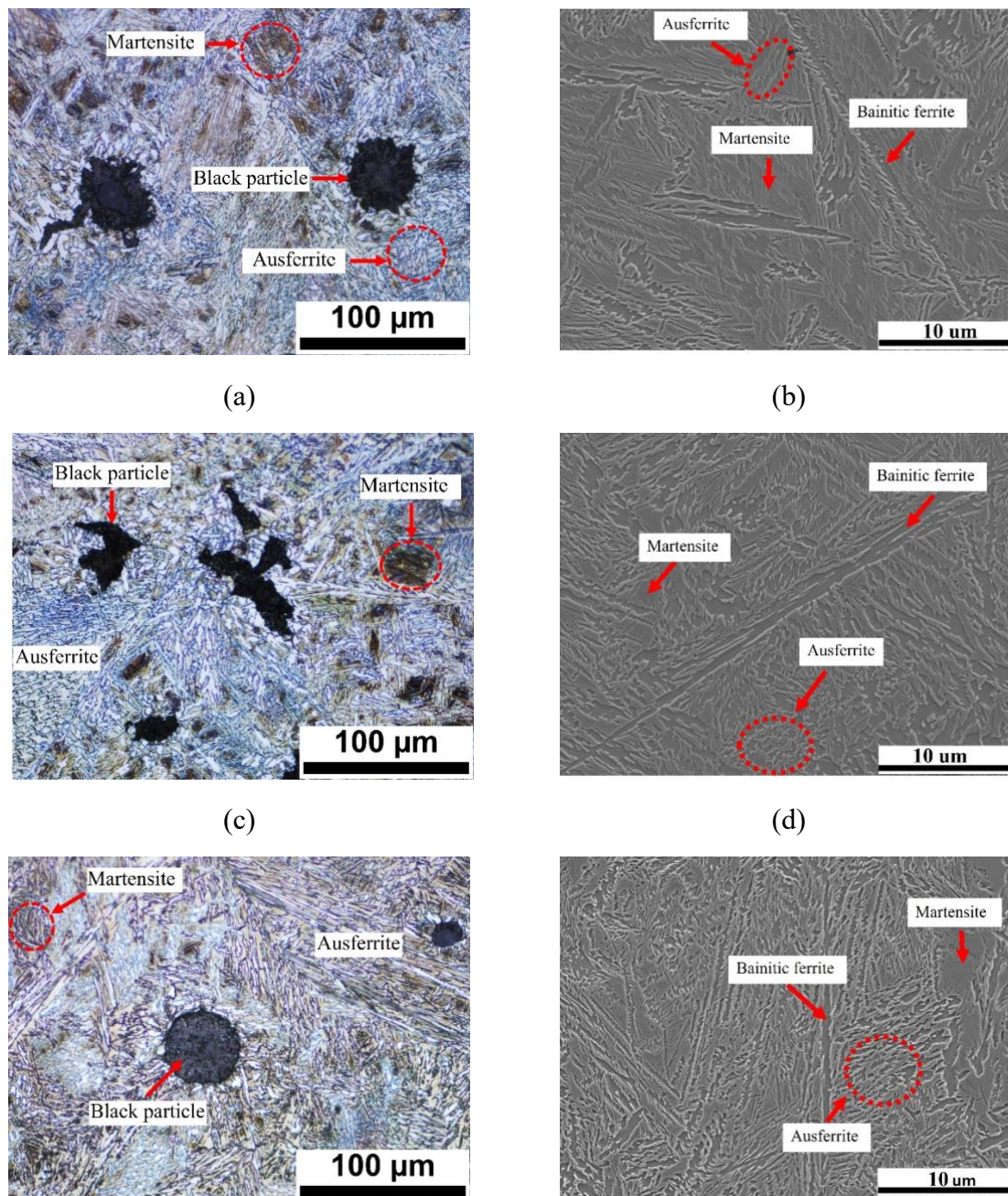




Figure 2. Microstructure of sintered Fe-4.0Ni-1.5Mo-2.0Cu-4.0SiC composite; (a) OM, etched with 2 % Nital, (b) SEM, etched with 2 % Nital, (c and d) OM, two-stage tinted

Microstructure of sintered composite with Co addition

The matrix microstructure of the sintered Co-bearing R1 composites gradually changed as shown in Figure 3. It can be seen in the increase in BF plates (associated with the increase in ausferrite) and refining of martensite islands as the amount of Co added increased. The sintered composites with ≥ 2.0 wt.% Co addition exhibited little martensite islands. It may be implied that cobalt affects both the shape and ratio of BF/martensite islands. The result is consistent with previous research reporting that Co can promote BF transformation¹⁹.



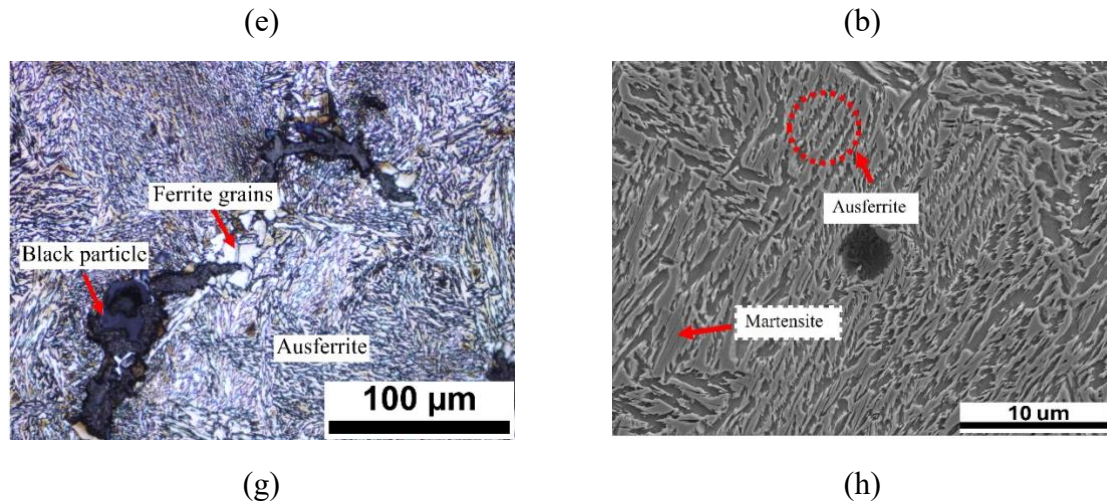
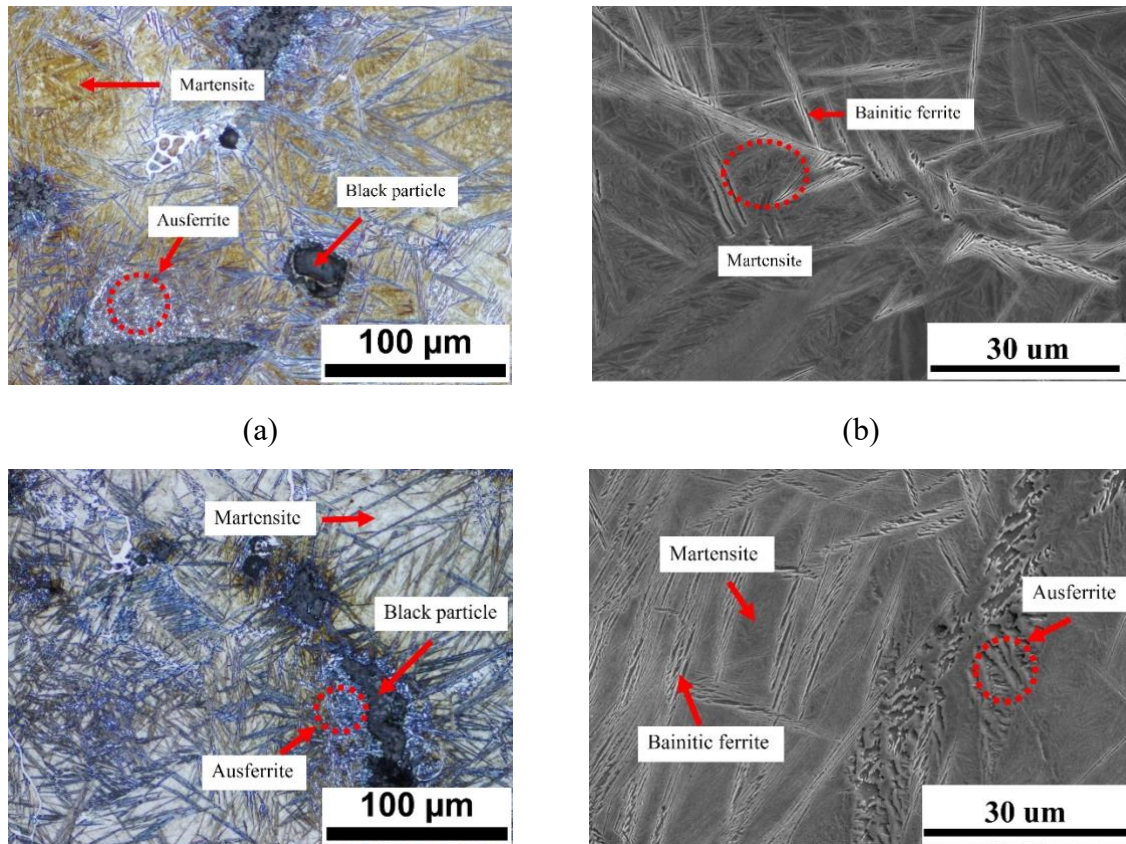


Figure 3. Microstructure of sintered Fe-4.0Ni-0.5Mo-0.2Mn-4.0SiC composites with Co addition of (a) 0.5 wt.%; OM (b) 0.5 wt.%; SEM (c) 1.0 wt.%; OM, (d) 1.0 wt.%; SEM, (e) 2.0 wt.%; OM (f) 2.0 wt.%; SEM, (g) 3.0 wt.%; OM (h) 3.0 wt.%; SEM,

The matrix microstructure of the sintered Co-bearing R2 composite (Figure 4) indicated that the refinement of both the acicular BF plate and martensite block increased with the Co concentration increase. However, martensite blocks were easily found in all sintered composites. This is attributed to the presence of 2.0 wt.% Cu in the base powder. The lamellar dual-phase structure was clearly seen in the sintered alloy with 3.0 wt.% Co addition. (Figure 4 (h)).



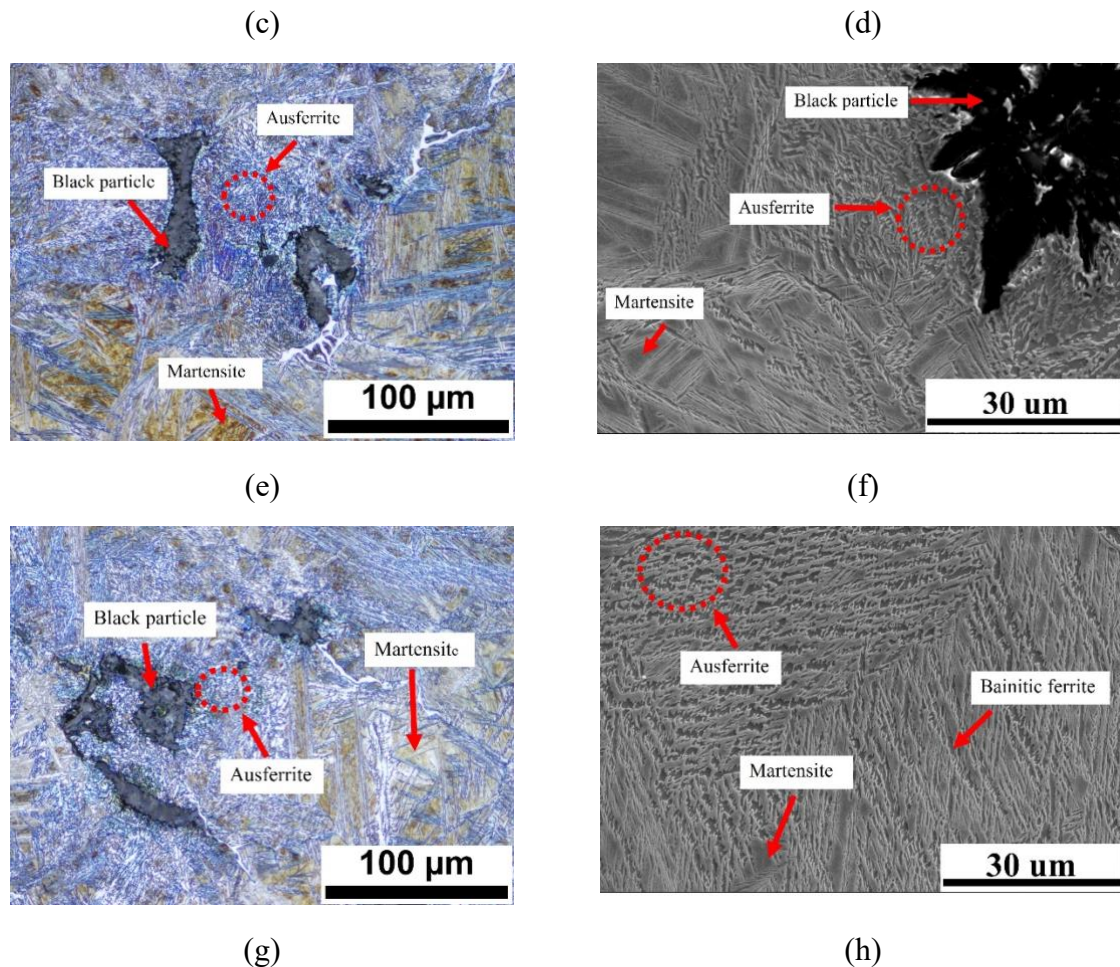


Figure 4. Microstructure of sintered Fe-4.0Ni-0.5Mo-0.2Mn-4.0SiC composites with Co addition of (a) 0.5 wt.%; OM (b) 0.5 wt.%; SEM (c) 1.0 wt.%; OM, (d) 1.0 wt.%; SEM, (e) 2.0 wt.%; OM (f) 2.0 wt.%; SEM, (g) 3.0 wt.%; OM (h) 3.0 wt.%; SEM,

Phase characterization

The XRD patterns of the sintered R1 and R2 with various cobalt added composites are shown in Figures 5(a) and 5(b), respectively. It can be seen that all compositions of sintered composite in this work showed peaks corresponding to two different crystal structures. The first is the body-centered cubic (bcc) crystal structure belonging to BF and martensite. The second is a face-centered cubic (fcc) crystal structure belonging to the austenite phase. The results showed a higher intensity of the face-centered cubic (fcc) crystal structure in the sintered R1 composite compared to R2. It is possible that the sintered R1 composite may contain higher amounts of austenite.

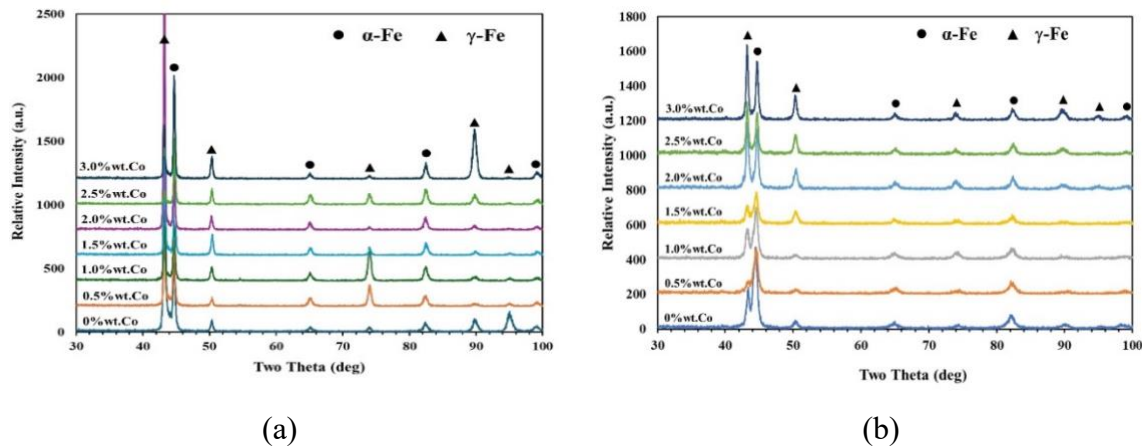


Figure 5. XRD pattern of the sintered composites (a) Fe-4.0Ni-0.5Mo-0.2Mn-4.0SiC (b) Fe-4.0Ni-0.5Mo-0.2Mn-4.0SiC with varying cobalt content.

Mechanical property

Figure 6 (a) depicts a plot of stress-strain curves for sintered R1 composites that vary Co content. All compositions of sintered R1 composites exhibited ultimate tensile strengths (UTS) of more than 800 MPa. The values of elongation were observed to increase with increasing Co content.

Figure 6 (b) depicts a plot of stress-strain curves for sintered R2 composites that vary Co content. The UTS strength of sintered steel increased slightly with increasing Co content up to 1 wt.%. Exceeding 1 wt.% Co added, UTS showed a relatively constant value of approximately 1200 MPa. The elongation value slightly increased with increasing Co content.

Sintered R1 composites containing 3% Co by weight can produce elongation values as high as 7%, which is remarkable for sintered composites. Tensile strength and ductility improve with increased Co content, showing an avoidance of the strength-ductility trade-off dilemma. Linking mechanical characteristics with microstructure, it was discovered that the microstructure of BF and thin MA plates in sintered composites enhances both tensile strength and ductility. This is consistent with the previous work¹⁶, which reported that the dual-phase lamellar microstructure showed the strength-ductility trade-off better than the equiaxed structure. Although strength-ductility synergy was obtained in both R1 and R2 sintered steels, cobalt proved more effective when added to sintered R1 steels.

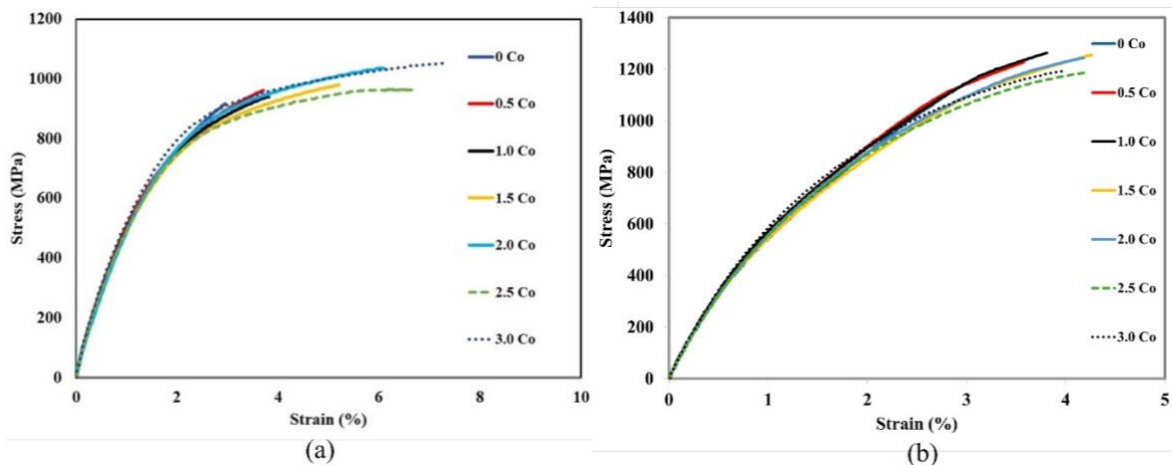




Figure 6. Stress-strain curves of sintered composites as a function of Co content.

Conclusion:

This work investigated the influence of Co addition on BF transformation acceleration of two base powders, pre-alloyed Fe-4.0Ni-0.5Mo-0.2Mn (ATOMET4801) and diffusion-alloyed Fe-4.0Ni-1.5Mo-2.0Cu (DistaloyHP1). Both sintered composites showed common microstructural features consisting of a black particle enveloped with a multiphase matrix consisting of bainitic ferrite laths, retained austenite blocks and films, and martensite blocks. Both sintered steels showed promising tensile strength and elongation. With cobalt modification, strength and elongation values increased with increasing cobalt content in both sintered steels. Strength-ductility synergy was achieved in both cobalt added sintered steel systems. Cobalt was more effective when added to the sintered Fe-4.0Ni-0.5Mo-0.2Mn composite.

Acknowledgements:

This work is financially supported via the project ‘Design and manufacturing of replacement parts for railway applications (P1951261)’ under NSTDA, Pathum Thani, Thailand. Technical supports are obtained from National Metal and Materials Technology Center (MTEC), Pathum Thani,

References:

1. Srijumpun W, Wiengmoon A, Morakotjinda M, Krataitong R, Yotkaew T, Tosangthum N and Tongsri R. *Mater. Des.* 2015; 88: 693-701.
2. Caballero FG, Bhadeshia HKDH, *Curr. Opin. Solid State Mater. Sci.* 2004; 8: 251-257.
3. Ridley N. *Metall. Trans. A.* 1984; 15: 1019.
4. Ochiai I, Nishida S, and Tashiro H. *Wire J. Int.* 1993; 26: 50-61
5. Caballero FG, Santofimia MJ, Capdevila C, Andrés CG and García-Mateo C. *ISI Int.* 2002; 46: 1479
6. Tian J, Xu G, Jiang Z, Hu H and Zhou M. *Met. Mater. Int.* 2018; 24: 1202-1212
7. Kong J and Xie C. *Mater. Des.* 2006; 27: 1169-1173
8. Wang J, Wang Z, Wang X, Yang Q, Jin X and Wang L. *Scr. Mater.* 2017; 129: 25-29
9. Ruangchai K, Wiengmoon A, Krataitong R, Yotkaew T, Tosangthum N and Tongsri R. *J. Phys. Conf. Ser.* 2018; 1144: 012147
10. Morakotjinda M, Kongmun P, Wanalerkngam A, Tosangthum N, Yotkaew T, Kijamnajsuk S, Tongsri R. *Silicon* 2023; 15:7995–8008
11. Morakotjinda M, Yotkaew T, Vetayanugul B, Wanalerkngam A, Tongsri R. *Mater. Chem. Phys.* 2023; 296: 127226
12. Wanalerkngam A, Boonmee S, Krataitong R, Morakotjinda M, Pongsak W, Tosangthum N, Tongsri R. *IOP Conf. Ser. Mater. Sci. Eng.* 2021; 1137: 012029
13. Kaewkam T, Kansuwan P, Ohtake N, Wila P, Krataithong R, Tosangthum N, Yotkaew T, Tongsri R. *IOP Conf. Ser. Mater. Sci. Eng.* 2021; 1137: 012035
14. Nithimethakul T, Karin P, Ohtake N, Wila P, Yodkaew T, Vetayanugul B, Morakotjinda M, Tongsri R. *IOP Conf. Ser. Mater. Sci. Eng.* 2021; 1137: 012028.
15. Ruangchai K, Wiengmoon A, Morakotjinda M, Tosangthum N, Tongsri R. *J. Phys. Conf. Ser.* 2018; 1144: 012099
16. Gao YF, Zhang W, Shi PJ, Ren WL, Zhong YB. *Mater. Today Adv.* 2020; 8: 100103
17. De AK, Speer JG, Matlock DK, *Adv. Mater. Proc.* 2023; 16: 27-30

18. Lee SG, Lee DH, Sohn SS, Kim WG, Um KK, Kim KS, Lee S, Mater. Sci. Eng. A. 2017; 697: 55-65.
19. Garcia-Mateo C, Caballero F, Bhadeshia HKDH. ISIJ Int. 2003; 43:1238-1243.



ELECTROSPUN CELLULOSE ACETATE FIBERS CONTAINING CHALCONE CRUDE EXTRACT

Chidchanok Meechaisue,^{1,*} Jariya Romsaiyud²

¹Materials Technology Department, Faculty of Science, Ramkhamhaeng University, Bangkapi, Bangkok

²Department of Chemistry and Center of Excellence for Innovation in Chemistry (PERCH-CIC), Faculty of Science, Ramkhamhaeng University, Bangkok, 10240, Thailand.

*e-mail: chidchanok.m@ru.ac.th

Abstract:

Chalcone is a natural compound found in various plants such as licorice, angelica and some citrus fruits. Its structure, a type of flavonoid, is key to its biological activities which include antioxidant, anti-inflammatory, antimicrobial and anticancer properties. The application of chalcone, a natural compound, for these biological activities through controlled release from nanofiber mats *via* the electrospinning technique is of interest. In this research, yellowish crude chalcone was prepared and recrystallized using an ethanolic solution. Various amounts of the chalcone crude extract, specifically 5, 10, 15, and 20 wt.%, were incorporated into a neat cellulose acetate (CA) solution (17% w/v in a 2:1 v/v mixture of acetone and dimethylacetamide) to fabricate ultra-fine fiber mats using the electrospinning technique, under a fixed electric field of 20 kV at a distance of 15 cm. The effects of chalcone crude extract content on the morphological appearance and diameter of the as-spun fibers were investigated using a scanning electron microscope (SEM). The morphological appearance of the obtained fibers was not significantly influenced by this incorporation; the fibers remained smooth, and the average diameters of the chalcone-loaded CA fibers ranged from 393 ± 71 and 482 ± 100 nm. The diameter of the fibers increased with increasing chalcone concentration.

Introduction:

Chalcone, a natural compound found in various plants, is a type of flavonoid that has garnered significant attention due to its potential therapeutic properties.¹ Extracted from sources like licorice, angelica, and some citrus fruits,²⁻⁴ chalcone is characterized by its distinct chemical structure, which includes two aromatic rings connected by a three-carbon α,β -unsaturated carbonyl system.⁵ This structure is key to its biological activities, which include antioxidant, anti-inflammatory, antimicrobial, and anticancer effects.⁶ Research has shown that chalcone extract can inhibit the growth of certain cancer cells, reduce oxidative stress, and modulate immune responses, making it a promising candidate for drug development.⁷ Its natural origin and diverse biological activities have sparked interest in its application in pharmaceuticals, nutraceuticals, and even cosmetics, where it could serve as a natural additive with multiple health benefits.⁸

Electrospinning is an advanced fabrication technique that has garnered interest for its ability to produce nanofibers from polymer solutions.⁹ The electrospinning process involves the formation of a charged jet of polymer solution that stretches and solidifies into nanofibers as it is drawn from a syringe through a needle under high voltage. This method not only enables the creation of fibers with unique physical properties but also serves as an effective platform for integrating various natural products with antibacterial properties.¹⁰ By harnessing the benefits of natural extracts, researchers can develop innovative materials that enhance antibacterial activity, making them suitable for a variety of applications including wound dressings, filters, and coatings.¹¹ Natural products such as plant extracts, essential oils, and

other bioactive compounds have been traditionally used in medicine for their therapeutic benefits including antimicrobial effects.¹²

The novel electrospinning technique that incorporates chalcone extract represents a cutting-edge approach in the development of advanced nanomaterials for biomedical and pharmaceutical applications. This technique is particularly advantageous for creating materials with high surface area, porosity, and the ability to encapsulate bioactive compounds like chalcone. When chalcone extract is included in the electrospinning process, the resulting nanofibers can serve as a delivery system that offers controlled release, protection of the bioactive compound, and targeted therapeutic effects.¹³ The process typically involves dissolving chalcone extract in a suitable polymer solution, which is then electrospun into nanofibers. The polymer matrix can be selected based on its biocompatibility, degradation rate, and ability to interact with chalcone to optimize its release and bioactivity. This technique has significant potential in drug delivery systems, wound healing, and tissue engineering. For instance, chalcone-loaded nanofibers can be used as wound dressings that not only protect the wound but also deliver the anti-inflammatory and antimicrobial properties of chalcone directly to the site.¹⁴ Additionally, in cancer treatment, these nanofibers could be designed to release chalcone in a controlled manner, enhancing its anticancer effects while minimizing side effects.

In this research, the integration of chalcone extract into electrospun fibers represents a promising area of research and development, offering innovative solutions for a variety of medical and pharmaceutical challenges. This approach has the potential to combine the physical properties of the nanofibers-such as increased surface area, porosity, and mechanical strength-with the therapeutic benefits of the chalcone, creating a new class of materials that harness the natural healing properties. The incorporation of such extracts in electrospun fibers represents a forward-thinking strategy for developing advanced biomedical applications while utilizing sustainable and natural resources. Further studies could elucidate the optimal conditions for incorporating the extract and evaluating its efficacy in various applications.

Methodology:

Materials

Cellulose acetate (CA; white powder; $M_w \approx 30,000$ Da; acetyl content = 39.8 wt.%; degree of acetyl substitution = 2.4) was purchased from Sigma-Aldrich (USA). Ethyl alcohol, acetone and dimethyl acetamide from Labscan Asia (Thailand) were of analytical reagent grade and used without further purification.

Preparation of Chalcone crude extract

Chalcones, also known as 1,3-diaryl-2-propen-1-ones, are a class of polyphenolic compounds that fall under the flavonoid family. These compounds serve as precursors to both flavonoids and isoflavonoids, playing a crucial role in their biosynthesis. Structurally, chalcones are characterized by an open-chain configuration, where two aromatic rings (designated as A and B rings) are connected via a three-carbon α,β -unsaturated carbonyl system. Chalcone consists of two isomers, trans and cis, with the trans structure being more stable than the cis structure as shown in **Figure 1**.

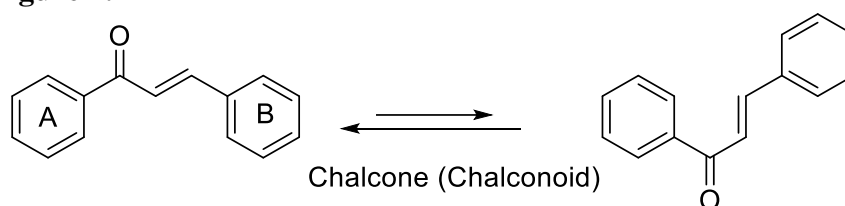


Figure 1.
General structure of Chalcone (Chalconoid).



Licorice root, typically *Glycyrrhiza* spp., were washed, cleaned dried and grinded into a fine powder to increase the surface area for extraction. The powdered root was then subjected to solvent extraction using 95% ethanol. The licorice powder was thoroughly mixed with the solvent and left to macerate for several hours to overnight at room temperature. After the maceration process, the mixture is filtered to remove solid particles, leaving behind a liquid extract rich in chalcones. This extract is then concentrated using a rotary evaporator, which removes the solvent under reduced pressure and low temperature, yielding a more concentrated chalcone extract (Buchi Labortechnik AG, Flawil, Switzerland, at the temperature of 45 °C, pressure of 350 mbar and the speed of 60 rpm).

HPLC-MS analysis was performed to confirm the presence and structure of chalcones in the crude extract using a C18 reverse-phase column. The mobile phase consisting of solvent A (0.1% formic acid in water) and solvent B (acetonitrile) was set to a gradient elution program. Mass spectrometric detection was performed in the positive. The retention time for chalcone was observed to be approximately 9 minutes. The chromatogram showed a prominent peak corresponding to chalcone, confirming its presence in the extract.

This analytical data supports the structural integrity of the active chalcone compounds, validating the extraction method and confirming the active ingredients.

Preparation of electrospun Chalcone crude extract-loaded Cellulose acetate fibers

Cellulose acetate (CA) powder was dissolved in 2:1 v/v acetone/dimethyl acetamide (DMAC) to prepare the CA solution at a fixed concentration of 17% w/v. Chalcone-containing CA solutions were prepared by dissolving the CA powder and chalcone crude extract in various amounts, i.e. 5, 10, 15, and 20 wt.% based on the weight of CA powder in the acetone/DMAC mixture.

The as-prepared solutions were then electrospun under a fixed electric field of 20 kV/15 cm by connecting the emitting electrode of positive polarity from a Gamma High-Voltage Research ES30P high voltage DC power supply to the solutions in a 10-ml syringe. The gauge-20 stainless steel needle used as the nozzle, and the grounding electrode to a rotating drum, used as the fiber-collecting device. The solutions were controlled feeding rate by a syringe pump (NE1000 Quality In Sensing (QIS) Company Limited, Netherlands). The electrospun fibers were continuously collected for 12 h., resulting in the fiber mats of 15±5 mm in thickness.

Characterization of electrospun Chalcone crude extract-loaded CA fibers

The effects of chalcone crude extract content on the electrospinnability of chalcone crude extract-loaded CA spinning solutions and the morphological appearance of its as-spun fibers were investigated by a JEOL JSM-IT500HR scanning electron microscope (SEM). Each specimen was coated with a thin layer of gold using JEOL JFC-1100E sputtering device in a vacuum for SEM observation. Diameter of electrospun fibers were measured from SEM images, with the average values being calculated from at least 50 measurements.

Results and Discussion:

Electrospinnability of Chalcone crude extract-loaded CA fibers

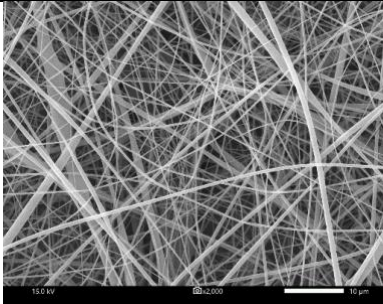
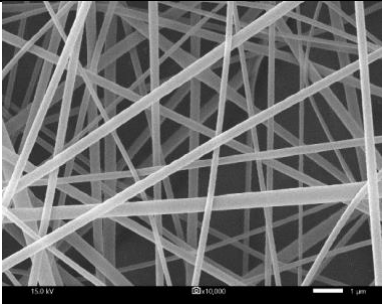
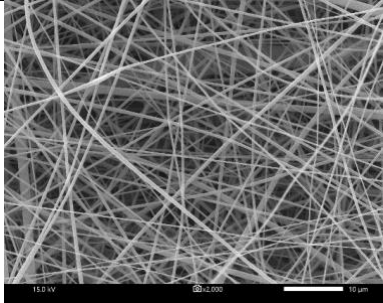
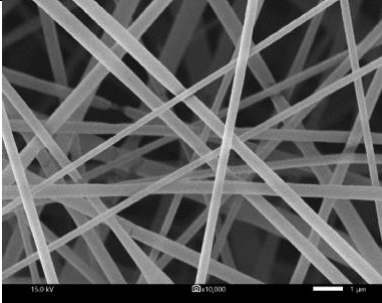
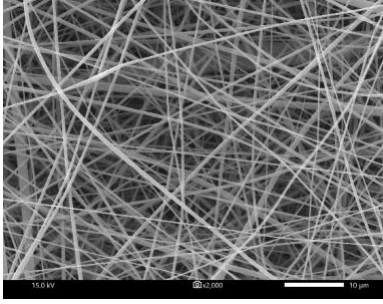
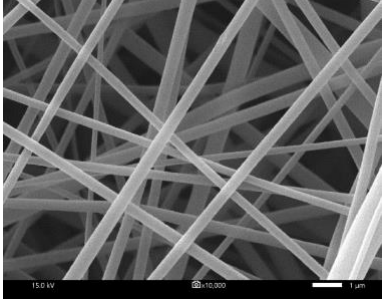
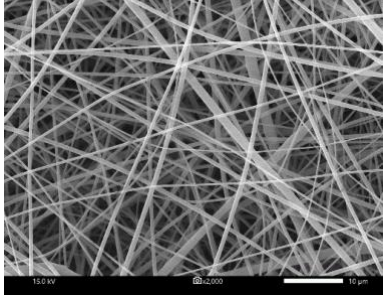
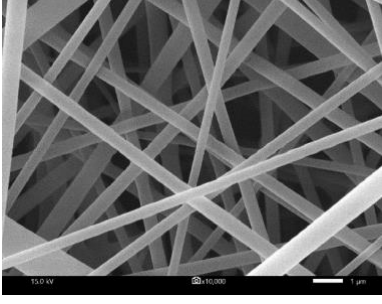
The yellowish chalcone, extract from Licorice root, in various concentration (i.e. 5, 10, 15, and 20% w/v) mixed with the solutions of neat CA 17% w/v in 2:1 v/v acetone/DMAC and CA solution. All as-prepared solutions show well mixing with clear yellow color. These solutions were electrospun at a fixed electric field of 20 kV/15 cm. The cross-sectionally round fibers were obtained from all as-prepared solutions and no presence of crude extract chalcone aggregation was observed on the surface of the fibers, described that the as-loaded crude extract chalcone was perfectly incorporated well within the fibers. The color appearance of chalcone

crude extract-loaded CA fiber mats was white, even though the clear yellow color of as-loaded chalcone crude extract.

Morphological appearance of Chalcone crude extract-loaded CA fibers

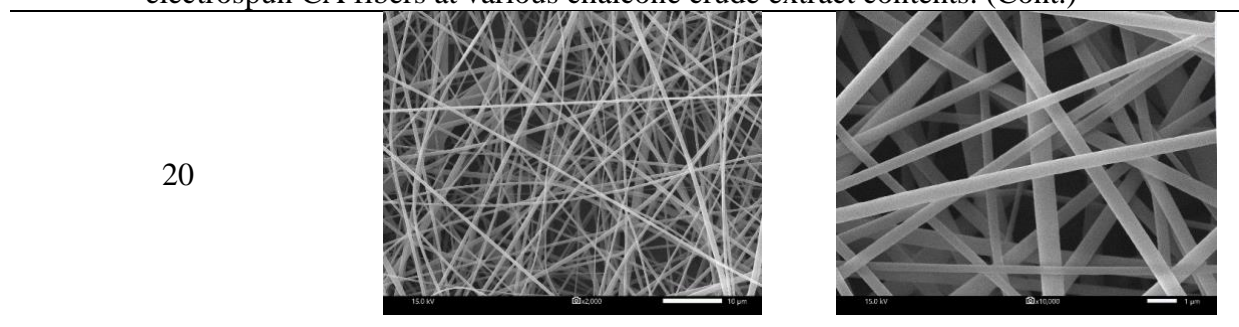
Selected SEM images of the as-spun neat CA fibers and chalcone crude extract-loaded CA fibers in various concentrations (i.e. 5, 10, 15, and 20% w/v) are shown in **Table 1**. The ultra-fine fibers from each chalcone crude extract-loaded CA solutions have a smooth surface, the largest fiber size of 20% wt. chalcone crude extract was observed. Fiber diameters of neat and chalcone crude extract-loaded CA fibers are shown in **Table 2**.

Table 1.
Selected scanning electron micrographs of neat and chalcone crude extract-loaded electrospun CA fibers at various chalcone crude extract contents.

| Chalcone crude extract content (wt. %) | Chalcone crude extract-loaded electrospun CA fibers | |
|--|---|---|
| | SEM image with x2000 | SEM image with x10000 |
| 0 |  |  |
| 5 |  |  |
| 10 |  |  |
| 15 |  |  |

**Table 1.**

Selected scanning electron micrographs of neat and chalcone crude extract-loaded electrospun CA fibers at various chalcone crude extract contents. (Cont.)

**Table 2.**

Fiber diameters of the chalcone crude extract-loaded electrospun CA fibers.

| Chalcone content (wt. %) | Fiber diameters (nm) |
|-----------------------------|-------------------------|
| 0 | 361 ± 74 |
| 5 | 393 ± 71 |
| 10 | 401 ± 80 |
| 15 | 443 ± 95 |
| 20 | 482 ± 100 |

The diameter of the neat CA fibers were 361±74 nm, while those of the chalcone crude extract-loaded CA fibers ranged between 393±71 and 482±100 nm. These chalcone crude extract-loaded electrospun fibers were larger than those neat CA, it was also shown that the chalcone crude extract present in the electrospun fibers. This result agreed with the report of loading drug i.e. NAP, IND, IBU, and SUL in the electrospun CA fibers which the average fiber diameter of neat CA was 231 nm while drug loaded-CA was in the range of 263-297 nm and did not affect their morphology.¹⁵ Research also showed the incorporation of active compound of curcumin in the electrospun CA fibers, and the average fiber diameter of neat CA was 301 nm while curcumin loaded-CA in various amount were in the range of 314-340 nm.¹⁶

In Table 2, the results clearly indicate that the ultra-fine fiber diameter increased by increasing the chalcone crude extract concentrations, described by more amount of chalcone crude extract incorporation in the solution then resulted more content in the electrospun fiber. The optimum chalcone crude extract with the concentration of 20 wt.% in CA solution, fabricated the electrospun fiber with average diameter of 482±100 nm.

Conclusion:

In the present contribution, yellowish chalcone crude were prepared from Licorice root, and recrystallized using an ethanolic solution. These chalcone crude extract were added to the neat cellulose acetate (CA) solution (17% w/v in 2:1 v/v acetone/ dimethylacetamide) in various amount of 5, 10, 15, and 20 wt.% based on the weight of CA powder. The as-prepared solutions of neat CA and chalcone crude extract-loaded CA were then fabricated into ultra-fine fibers via electrospinning at a fixed electric field of 20 kV/15 cm. The effects of chalcone crude extract contents on the morphological appearance and diameter of the electrospun fibers were investigated by a scanning electron microscope (SEM). The morphological appearance of electrospun fibers from each solution was observed with smooth fibers, no presence of crude

extracted aggregation on the fiber surface. The fiber size of chalcone crude extract-loaded CA was larger than the neat CA. The average diameters the chalcone crude extract-loaded CA fibers ranged between 393 ± 71 and 482 ± 100 nm. The electrospun fiber diameter increased by increasing the chalcone crude extract concentration. These as-prepared electrospun fiber mats were further studied for biological activities.

Acknowledgements:

The authors acknowledge the support from Faculty of Science, Ramkhamhaeng University.

References:

1. Mobinikhaledi MK, Jamalifar H. Medicinal Chemistry Research. 2012; 2: 1811-1816.
2. Safaei-Ghomi J, Bamoniri AH, Soltanian-Telkabadi M. Chemistry of Heterocyclic Compounds. 2006; 42: 892-897.
3. Wijayanti WL, Swasono TR, Wonkoo L, Jumina J. MDPI molecules. 2021; 2-10.
4. Smulovich KS, Orlova NA, Shakirov EV, Shelkovnikov VV. Russian chemical Bulletin, International Edition. 2010; 59: 1408-1413.
5. Hiba AJ, Lutfun N, Mohammad AJ, Sharon AM, Kenneth JR, Satyajit DS. Biomolecules. 2021; 11: 1203-1239.
6. Rudrapal M, Khan J, Dukhyil AAB, Alarousy RMII, Attah EI, Sharma T, Khairnar SJ, Bendale AR. Molecules. 2021; 26: 7177-7197.
7. Bahare S, Cristina Q, Imane C, Nasreddine EO, Abdelaali B, Javad SR, Abdelhakim B, Muhammad A, Mehwish I, Anca OD, Constantin C, Gerardo LG, Abhijit D, Miquel M, Daniela C, Víctor L, Francisco L. Frontiers in Pharmacology. 2021; 11: <https://doi.org/10.3389/fphar.2020.592654>.
8. Gayathri R, Deepu B, Baladhandapani A, Prasanna R, Nanjan P, Kondapa NB, Eun JO, Ho YC, Prakash G, Byeong-Cheol A. Pharmaceuticals. 2022; 15: 1250-1284.
9. Balu AVM, Sivakamavalli J, Masanari K. Journal of Composites Science. 2024; 8: 32-50.
10. Abdulhamid AA, Irfan F. Polymers. 2023; 15: 65-108.
11. Yuqing L, Yongping L, Hualei Z, Baolin G. Asian Journal of Pharmaceutical Sciences. 2022; 17: 353-384.
12. Natalia V, Elisavet S, Chrysoula (Chrysa) V, Zacharias T, Georgios R, Christina T, Eugenia B. Antibiotics. 2022; 11: 1014-1036.
13. Jiajia X, Tong W, Yunqian D, Younan X. Chemical Reviews. 2019; 119: 5289-5415.
14. Chunlin Z, Wen Z, Chunquan S, Wannian Z, Chengguo X, Zhenyuan M. Chemical Reviews. 2017; 117: 7762-7810.
15. Tungprapa S, Jangchud I, Suphapol P. Polymer. 2007; 48: 5030-5041.
16. Suwantong O, Ruktanonchai U, Suphapol P. Polymer. 2008; 49: 4239-4247.



EXPERIMENTAL HEAT TREATING OF GREEN TO YELLOW APATITE FROM MADAGASCAR

Buntita Yimyoo, Kanyarat Kwansirikul,* Phisit Limtrakun

Department of Geological Sciences, Faculty of Science, Chiang Mai University, Chiang Mai, Thailand 50200

*e-mail: kanyarat.k@cmu.ac.th

Abstract:

Apatite is a phosphate mineral. Gem-quality green to blue apatite crystals are desirable in the gem and jewelry trade, although their hardness is quite low. In this study, thirty natural rough green to yellow apatite samples from Madagascar were experimentally heat treated under oxidizing and reducing conditions to observe the change of their colors and characterized gemological properties using gemological standard methods, and some advanced techniques. Specific gravities and refractive indices of the samples are in the same range as those from other localities across the world. They were inert under short-wave and long-wave UV radiation before heat treatment whereas they showed weak to moderate orange fluorescence under short-wave radiation after heat treatment. Fractures and healed fractures were found in every sample, and hollow or filled tube inclusions were observed in most samples when viewed under a microscope. The samples were heated six times at a maximum temperature of 300, 400, 500, 600, 700, and 800°C at each condition, with a soaking time of 1 hour at each maximum temperature. The result of the heating experiments revealed that the temperatures between 600°C to 700°C could change the green hue of the samples to a more blue color but the yellow hue of the samples tended to be faded and turned colorless with a decrease in transparency. The fracture inclusions were more developed after heat treatment. Chemical composition analysis using micro-EDXRF revealed the major and important trace elements related to color-causing were calcium, phosphorus, manganese, iron, cesium, and neodymium. The UV-Visible-NIR absorption spectra of the samples exhibited a broad absorption between 600-700 nm related to the color center of Ce^{3+} - SiO^{3-} and SO^{3-} and the peaks approximately at 580, 750, and 803 nm due to Nd^{3+} . After heating the green apatite samples at the temperature between 600°C to 700°C, the intensity of the absorption band between 600-700 nm increased, corresponding to the change of the green to more blue color.

Introduction:

Apatite is a phosphate mineral with a general chemical formula $\text{Ca}_5(\text{PO}_4)_3(\text{F}, \text{Cl}, \text{OH})$. It can occur as a common accessory mineral widely distributed in several geologic environments including magmatic, sedimentary, metamorphic, and hydrothermal systems.¹ Apatite is enriched with trace elements and halogen elements, such as iron, manganese, rare earth elements (REE), fluorine, and chlorine.¹ Apatite can be divided into three groups depending on hydroxyl, chlorine, and fluorine contents. They include hydroxylapatite, chlorapatite, and fluorapatite.² However, fluorapatite is the most common of the three groups used for gemstones and generally referred to simply as apatite within the gem trade whereas hydroxylapatite is much less common and chlorapatite is very rare.^{1,2,3} The formation of apatite can provide important information on the geological history of magma evolution and processes that have affected rocks and minerals.¹

Fluorapatite with chemical formula $\text{X}_5(\text{Z}\text{O}_4)_3\text{Y}$ is hexagonal with space group $\text{P6}_3/\text{m}$ and two formula units per unit cell.³ According to its chemical formula $\text{X}_5(\text{Z}\text{O}_4)_3\text{Y}$, X is an ion represented by Ca^{2+} , which can be isomorphically replaced by Mg, Fe, Mn, Sr^{2+} , and

REE³⁺. Z is an ion represented by P⁵⁺ and also Si, S, C, V, etc., whereas Y is an additional anion. Ca²⁺ occupies two kinds of positions in the apatite lattice, represented by Ca1 (coordination 9 with 9 oxygen ions) and Ca2 (coordination 7 with 6 oxygen ions and an additional anion).³ Apatite structures can tolerate relatively large structural distortions and allow different substitutions.³ Deposits of apatite have been found in many countries across the world. Gem-quality apatite crystals are discovered in many places, including Brazil, Myanmar, Mexico, and Madagascar.¹ Although apatite has a hardness of 5 on the Mohs scale, making it too soft to be used as a gemstone for jewelry, the wide range of colors in nature of apatite is still attractive. Transparent stones with desirable colors, such as neon blue, can be faceted into gemstones and are still sought-after in the gem trade. Gem-quality apatite crystals are transparent to translucent. Most apatites are commonly green to blue but can also be colorless, yellow, pink, brown or violet. The blue and green apatites are commercialized in the gem trade.¹ It is well known that natural apatites can contain impurities of transition metals such as Mn, Fe, Ti, and Cr as well as the REEs of Ce, Pr, Sm, Nd, Er, Tm, and Ho. Because of the wide range of impurities, there is much doubt about the origin of the color.^{1,3,4,5} The intense blue apatites seen in the gem and jewelry trade today most typically result from the heat treatment of a natural stone. Neon blue to green apatites are often confused with the color of Paraíba tourmaline, which has higher prices. Moreover, mineral collectors prized them not only for their interesting colors but also for their beautiful fluorescence. This leads to the increasing usage of apatites for jewelry nowadays.

As mentioned above, the neon blue to green color apatite is similar to that of Paraíba tourmaline. This kind of apatite is imitated or sold as the Paraíba tourmaline to deceive the customers. However, apatite has a hardness of only 5, whereas tourmaline has a hardness of 7 to 7.5. Aside from a destructive scratch test to determine the hardness, distinguishing faceted apatite from tourmaline can sometimes prove challenging. Moreover, the greenish blue apatite in the gem trade often comes from the heat treatment of green apatite. The main purposes of this experiment are to investigate the change of colors of green and yellow apatite samples when heating at different temperatures and find out the optimum temperature to change the green and yellow apatites to blue or greenish blue ones. This experimenting heating study also extends to determining the gemological properties of the apatite samples before and after heat treatment.

Methodology:

Thirty samples of natural rough apatites from Madagascar ranging from 1.11 to 6.94 ct. were studied. The samples were polished at least on one side of each crystal for comparison of the color change before and after heat treatment. The apatite samples were divided into six groups depending on the apparent color, including dark green, light green, bluish green, greenish yellow, brownish yellow, and yellowish brown groups. All samples were transparent to translucent. The samples were heated under oxidizing and reducing conditions to compare the change of colors in different conditions and analyzed for the gemological properties, chemical compositions, and spectroscopic features. The analytical gemological techniques included specific gravity, refractive index, fluorescence, and internal features using standard gemological instruments. Twelve samples from the six groups were selected for chemical composition analysis by Bruker M4 TORNADO micro X-ray fluorescence spectrometer (energy dispersive system). The obtained chemical data were measured from single crystal samples. Ultraviolet-visible-near infrared (UV-Vis-NIR) absorption spectra for all thirty samples were recorded throughout 300-1000 nm before and after heat treatment using a Hitachi U4001 spectrophotometer with a slit width of 2 mm and a scan speed of 300 nm/min. The Ultraviolet-Visible-Near infrared absorption spectra can give information related to electron transitions of trace elements or other structural defects. Heat-treating experiments



were carried out six times with a SANTE electric furnace, under oxidizing and reducing conditions at 300°C, 400°C, 500°C, 600°C, 700°C and 800°C soaked for 1 hour at each temperature. The heating rate is 3°C per minute and the samples were slowly cooled down to room temperature before being removed from the furnace. The heat-treating experiments and gemological analyses were done at the Department of Geological Sciences, Faculty of Science, Chiang Mai University, Chiang Mai, Thailand. The chemical composition analysis was carried out at the Gems and Geological Items Analysis Section, Department of Mineral Resources, Bangkok.

Results and Discussion:

The colors of thirty natural rough apatites from Madagascar ranged from light green to yellowish brown, and they were transparent to translucent (Figure 1). The studied samples were classified into two categories: green hue and yellow hue. The two categories were also subdivided into six groups depending on their initial color appearance viewed under a daylight fluorescence lamp. They consisted of light green, dark green, bluish green, greenish yellow, brownish yellow, and yellowish brown groups. The specific gravity of all samples ranged from 3.17 to 3.22. The refractive indices for n_e were 1.638 to 1.643 and n_o were 1.633 to 1.640 with birefringence between 0.003 and 0.007. Those values were consistent with natural apatites from other localities worldwide. The samples were inert under short-wave and long-wave ultraviolet radiation before heat treatment. For internal features observed under a gemological microscope, hollow or filled tubes and fractures or healed fractures were found in every sample. Some samples showed pyrrhotite crystals, calcite crystals, two-phase inclusion, fluid inclusion, and orange to brown stains along fractures.

The twelve samples were selected from the six groups for chemical analysis. The chemical data of the samples from the six groups revealed a major weight percentage oxide of P_2O_5 and CaO . Minor and trace elements detected were Mg, Si, S, Cr, Mn, Fe, Cl, and REEs, including Sr, Y, La, Ce, Nd, Sm, Tb, Dy, Yb, Lu, and Pb. The concentrations of the major elements and the trace elements, which were probably related to the colors, were shown in Table 1. The obtained chemical compositions corresponded to the general chemical formula of apatite; $X_5(ZO_4)_3Y$. X was an ion represented by Ca^{2+} , which can be isomorphically replaced by Mg, Fe, Mn, Sr^{2+} , and REE^{3+} .¹ Z was an ion represented by P^{5+} and also Si, S, etc., whereas Y is an additional anion.¹

The 30 apatite samples were heated under oxidizing and reducing conditions at 300°C, 400°C, 500°C, 600°C, 700°C, and 800°C at each condition with a soaking time of 1 hour at each maximum temperature. The changes in the samples' colors were compared before and after heat treatment (Tables 2 and 3). The heating experiment of the samples in both conditions showed a similar trend of color changes. The initial colors of all samples started to change after heating at 400°C to 500°C. Most samples in the green hue groups, after heating at 600°C, showed the fading of green hue intensity and showed more blue color, whereas the samples in the yellow hue groups tended to be colorless. After heating at 700°C, the colors of most samples in the green hue groups turned more blue with variations of blue color intensities. The colors of most samples in the yellow hue groups turned nearly colorless. After heating at 800°C, all samples lost their colors and appeared more colorless or white. Heating the samples with a green hue under oxidizing exhibited a slightly better change of colors when compared to heating those samples under reducing conditions. They showed brighter blue. The appropriate heating temperature to change green apatite to blue apatite is suggested at 600°C to 700°C. After heat treatment, nearly most samples were fluorescent under short-wave ultraviolet radiation. They fluoresced weakly to moderate orange. There

was no significant change in the specific gravity and refractive indices. The fractures, healed fractures, and tubes in the heated stones were more developed. The orange-to-brown stained fractures turned darker to dark brown or black (Figure 2).

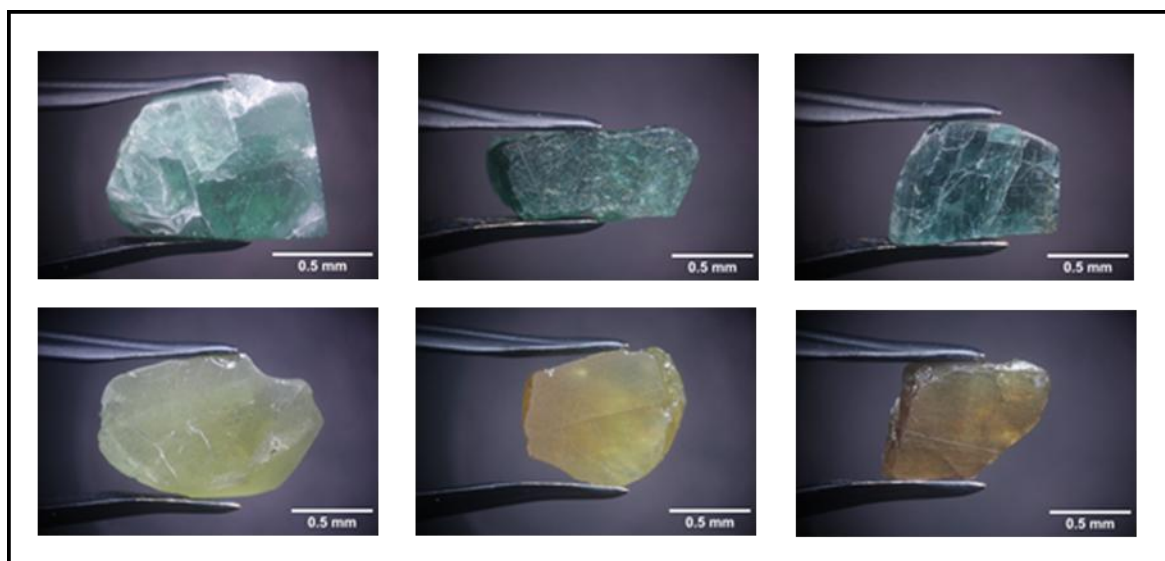


Figure 1.

A set of representative samples in six groups including light green, dark green, bluish green (left to right, respectively, in the upper row), greenish yellow, brownish yellow, and yellowish brown (left to right, respectively, in the lower row).

Table 1.

Chemical compositions of some elements in weight percent oxides of the selected apatite samples from Madagascar determined by micro-XRF.

| Chemical composition (wt.%) | Light Green | Dark Green | Bluish Green | Greenish Yellow | Brownish Yellow | Yellowish Brown |
|--------------------------------|-------------|-------------|--------------|-----------------|-----------------|-----------------|
| P ₂ O ₅ | 47.66-49.19 | 47.66-47.68 | 49.19-49.94 | 47.90-51.81 | 47.77-48.97 | 48.77-49.19 |
| CaO | 47.56-47.73 | 47.56-47.73 | 47.17-47.31 | 45.58-46.62 | 45.15-46.26 | 45.93-46.25 |
| MnO | 0.01-0.03 | 0.01-0.03 | 0.03-0.04 | 0.01-0.02 | 0.01-0.03 | 0.03-0.05 |
| Fe ₂ O ₃ | 0.01-0.02 | 0.01-0.02 | 0.01-0.02 | 0.03-0.75 | 0.02-0.43 | 0.03-0.04 |
| Ce ₂ O ₃ | 0.20-0.25 | 0.20-0.25 | 0.21-0.23 | 0.86-0.87 | 0.52-0.63 | 0.78-0.83 |
| Nd ₂ O ₃ | 0.05-0.08 | 0.04-0.08 | 0.11-0.12 | 0.43-0.45 | 0.28-0.29 | 0.42-0.57 |

The UV-Vis-NIR absorption spectra of the unheated apatite samples with a green hue showed significantly a broad absorption band between 600-700 nm related to the color center Ce³⁺-SiO³⁻ radical and SO³⁻, whereas those apatite samples with a yellow hue showed absorption bands mainly at 580, 750, and 803 nm due to Nd³⁺.⁶ After heating under both conditions, the absorption band of the color center Ce³⁺-SiO³⁻ radical and SO³⁻ still appeared. However, when the temperature reached 700°C, the intensity of that band was increased in most samples with the green hue corresponding to the appearance of a brighter blue color. When the samples turned colorless or white after heating at 800°C, the absorption band of the color center Ce³⁺-SiO³⁻ radical and SO³⁻ disappeared (Figure 3). The samples with a yellow



hue showed absorption bands mainly at 580, 750, and 803 nm, but the absorption band of the color center $\text{Ce}^{3+}\text{-SiO}^{3-}$ radical and SO^{3-} did not appear. After heat treatment, the absorption bands of Nd^{3+} still appeared. The fading of the yellow color hardly affected the intensity of those bands (Figure 4).

Table 2.
Representative of color changing of natural apatite samples from Madagascar before and after heat treatment at different temperatures under oxidizing conditions.

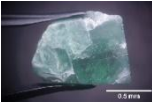
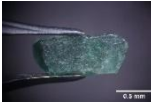
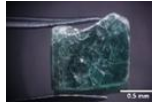
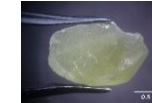
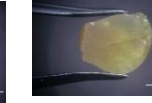







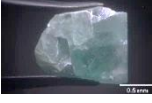



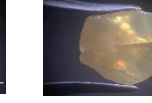
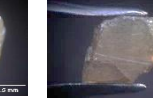




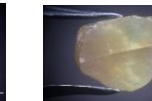
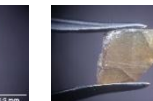





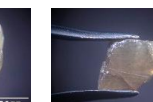













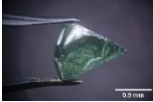

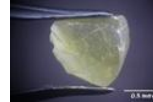
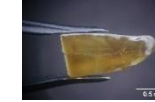

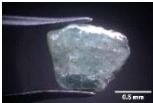
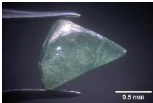
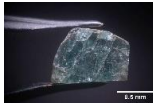
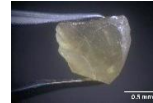

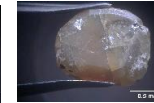
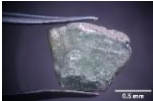
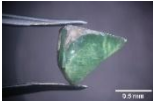
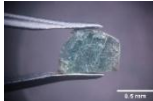


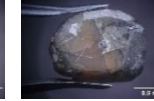
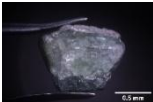

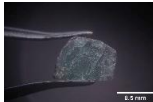

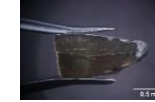




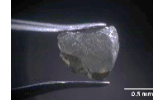
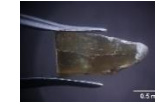
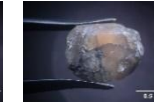





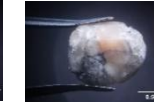


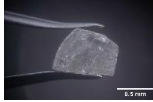

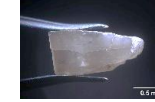

| Group | Light Green | Dark Green | Bluish Green | Greenish Yellow | Brownish Yellow | Yellowish Brown |
|----------|---|---|---|--|---|---|
| Unheated |  |  |  |  |  |  |
| 300°C |  |  |  |  |  |  |
| 400°C |  |  |  |  |  |  |
| 500°C |  |  |  |  |  |  |
| 600°C |  |  |  |  |  |  |
| 700°C |  |  |  |  |  |  |
| 800°C |  |  |  |  |  |  |

Table 2.
Representative of color changing of natural apatite samples from Madagascar before and after heat treatment at different temperatures under reducing conditions.

| Group | Light Green | Dark Green | Bluish Green | Greenish Yellow | Brownish Yellow | Yellowish Brown |
|----------|---|---|---|--|---|---|
| Unheated |  |  |  |  |  |  |
| 300°C |  |  |  |  |  |  |
| 400°C |  |  |  |  |  |  |
| 500°C |  |  |  |  |  |  |
| 600°C |  |  |  |  |  |  |
| 700°C |  |  |  |  |  |  |
| 800°C |  |  |  |  |  |  |

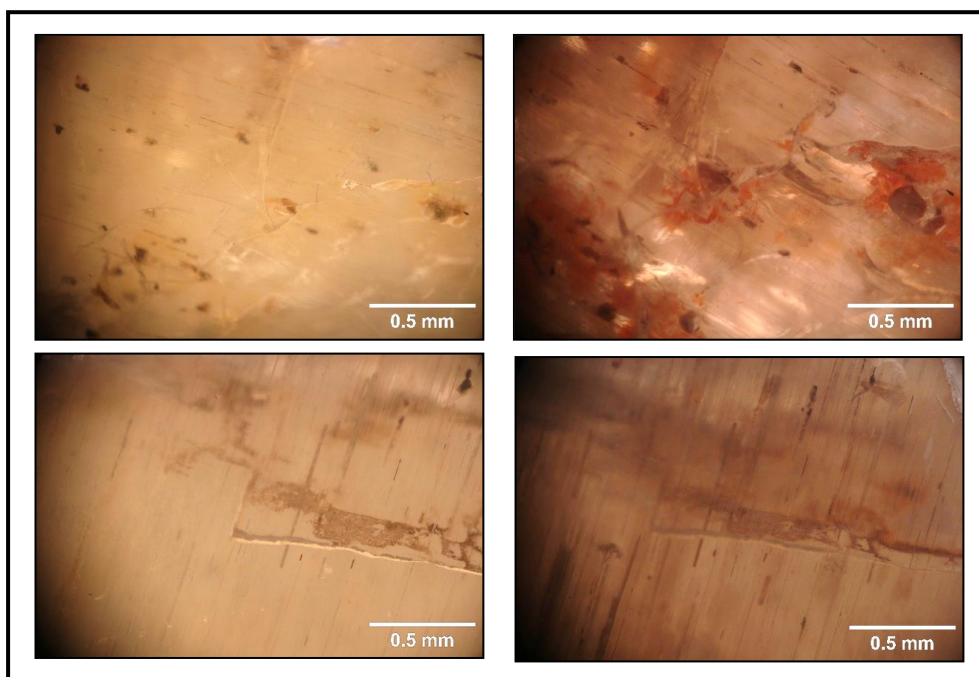


Figure 2. Comparisons of the fractures and healed fractures (the upper row), and tubes (the lower row) in the representative apatite samples before (left column) and after heat treatment (right column).

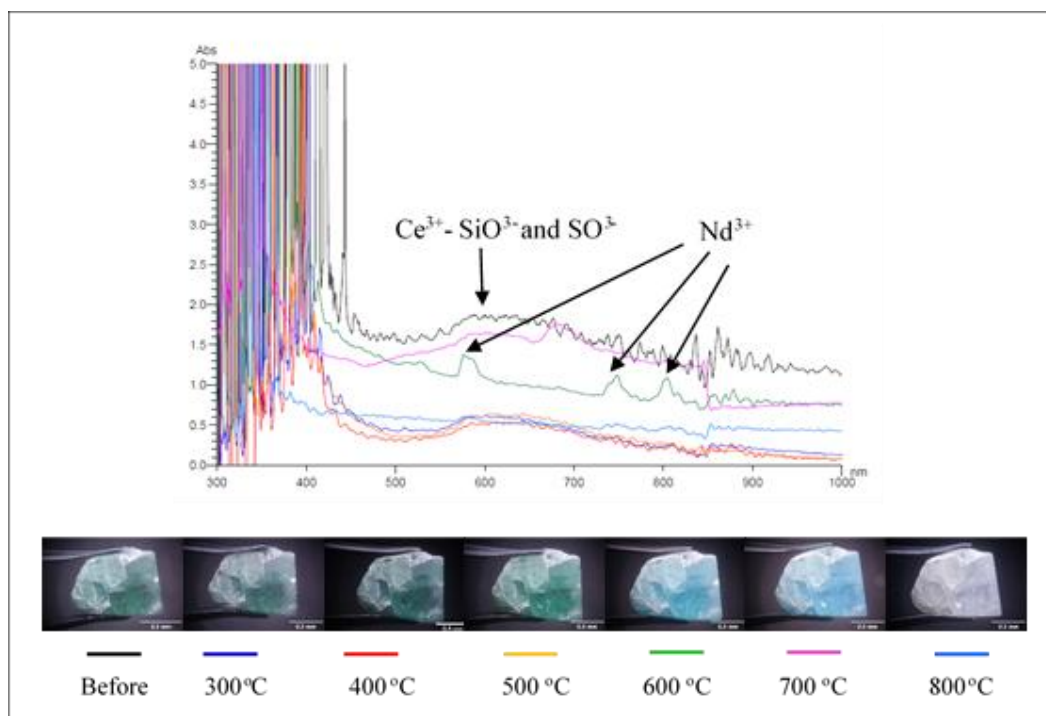


Figure 3. The UV-Vis-NIR absorption spectra of the green apatite samples from Madagascar before and after heat treatment under oxidizing conditions at different temperatures.

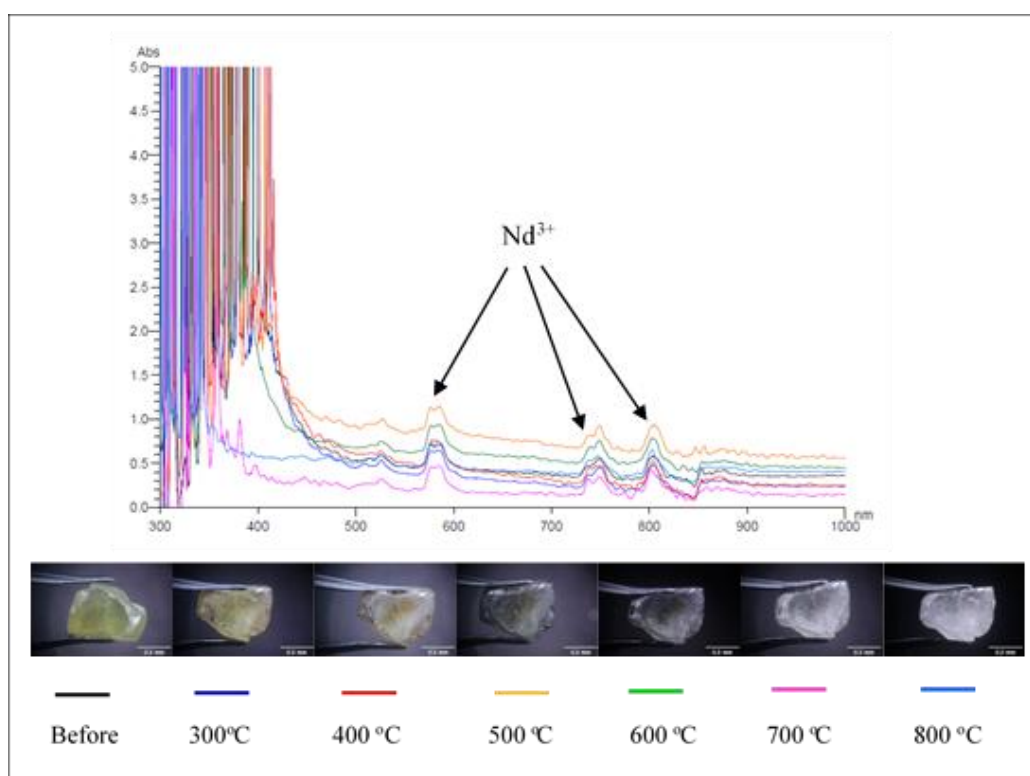


Figure 4. The UV-Vis-NIR absorption spectra of the yellow apatite samples from Madagascar before and after heat treatment under reducing conditions at different temperatures.

Conclusion:

The gemological properties of the studied apatite samples from Madagascar indicated that they were consistent with natural apatite from other localities worldwide. Chemical compositions showed calcium and phosphorus as major elements. The important trace elements relating to the cause of color included manganese, iron, cesium, and neodymium. This heating experiment showed that the temperature has a great effect on apatite colors. The heat treatment of apatite under oxidizing and reducing conditions exhibited a similar result with a slight color saturation difference. The green to bluish green apatite samples could change to a more blue color after heating between 600°C and 700°C whereas those ranges of temperatures could change the yellow to brown apatite samples to nearly colorless or white stones. After heating at 800°C, the apatite samples tended to lose their initial colors. Both green and yellow apatite samples became nearly colorless or white stones. The transparency of all samples after heat treatment decreased. The samples showed more developed fracture inclusions. The UV-Vis-NIR absorption spectra of all samples indicated that the cause of the colors of the green to blue apatites was related to the presence of a photochromatic center of cesium in the crystal structure.

Acknowledgements:

The authors would like to thank the 50th Geological Anniversary Chiang Mai University and Faculty of Science, Chiang Mai University for providing financial support for this research. Thanks are extended to Mr. Siwakon Chimnakphant, staffs at the Department of Geological Sciences, Faculty of Science, Chiang Mai University, and staffs at the Gems and Geological



Items Analysis Section, Department of Mineral Resources, Bangkok for providing the facilities.

References:

1. Zhang ZY, Xu B, Yuan PY, Wang ZX. Crystals. 2022;12(8):1067.
2. Silva GPS, Nunes MCS, Ulsen C, Künzel R, Yoshimura EM, Trindade NM. J. Lumin. 2021;231:117802.
3. Yuan P, Xu B, Wang ZX, Liu D. Crystals. 2022;12(4):461.
4. Hughes JM, Ertl A, Bernhardt HJ, Rossman GR, Rakovan J. Am Miner. 2004;89:629-632.
5. Ribeiro HB, Guedes KJ, Pinheiro MVB, Greulich-Weber S, Krambrock K. Phys. Stat. Sol. (c). 2005;2(1):720-723.
6. Chindudsadeegul P, Jamkratoke M. Spectrochim Acta A Mol Biomol Spectrosc. 2018;204:276-280.



GEOLOGICAL CHARACTERISTICS OF THE KAENG KHUT KHU RAPID AT CHIANG KHAN, LOEI PROVINCE: GEOHERITAGE SIGNIFICANCE IN THE GREATER MEKONG RIVER BASIN

Vimoltip Singtuen^{1,*}, Burapha Phajuy², Prawit Bumroongroch¹, Punya Charusiri^{3,4}

¹Department of Geotechnology, Faculty of Technology, Khon Kaen University, Khon Kaen, Thailand

²Department of Geological Sciences, Faculty of Science, Chiang Mai University, Chiang Mai, Thailand

³Department of Mineral Resources, Bangkok, Thailand

⁴MESA RU, Department of Geology, Faculty of Science, Chulalongkorn University, Bangkok, Thailand

*e-mail: vimoltipst@gmail.com, vimosi@kku.ac.th

Abstract:

The Kaeng Khut Khu Rapid, located in Chiang Khan, Loei Province, is a prominent geological feature within the Mekong River, marking a significant geoheritage site at the border between Thailand and Laos PDR. This study classifies the rocks at this rapid through field observations and petrographic analysis. Field investigations reveal that the rapid has been influenced by at least four lineament directions: NE-SW, NW-SE, NEE-SWW, and NWW-SEE. Petrographic analysis identifies the rocks as altered coarse-ash tuff and shallow intrusive igneous rocks. The tuff is characterized by a pyroclastic texture with poorly sorted, subangular pyroclasts, containing crystal fragments of quartz and altered feldspars, as well as silicified rock fragments ranging from 0.05 to 0.2 mm. Secondary minerals, including epidote, clay minerals, and silica replacement, are also present. The shallow intrusive rocks, with their fine-grained texture, are primarily composed of felsic minerals and can be classified as granodiorite and granite. These pyroclastic and intrusive rocks are believed to have originated from volcanic activity during the Permian to Triassic periods and have undergone silicification due to silica-rich solutions following recent tectonic movements, which has rendered them resistant to water erosion. Surrounded by the waters of the Mekong River, this geoheritage site is best visited between February and May when the river's low levels reveal the rapid and offer clear views of the landscape encompassing both Thailand and Laos PDR. As a result, the Kaeng Khut Khu Rapid stands out as one of Thailand's most important geoheritage sites, combining natural beauty with cultural significance and serving as a key tourist attraction.

Introduction:

Geotourism has emerged as a highly popular form of alternative tourism in the 20th century, aimed at raising public awareness of geological heritage [1-5]. Many geologists define geotourism as a subset of nature-based tourism that primarily focuses on geological aspects [6]. Geotourism typically occurs in geologically significant areas or geosites, which are characterized by a diversity of geological features such as rocks, minerals, fossils, landforms, landscapes, soils, and other georesources [7]. Geological heritage or geoheritage refers to geologically important areas that provide scientific insights into Earth's processes, possess aesthetic value, and can be linked to local lifestyles, culture, and history, while also offering the potential for local economic development. These heritage sites can be categorized into seven types: type minerals, type rocks, fossils, hot springs, landforms,

structural geology, and type stratigraphy. This concept offers numerous benefits to local and national communities, including economic, geological, natural, historical, cultural, and social advantages.

Currently, Thailand is advancing geotourism knowledge across multiple dimensions nationwide, focusing on developing geologically unique and prominent tourist sites, such as sandstone landforms, limestone landforms, hot springs, and waterfalls. These efforts aim to elevate these areas to the status of geological heritage, geoparks, and geoconservation sites, promoting sustainable tourism in the future [8-10]. To date, over 830 geological sites have been surveyed and listed by the Department of Mineral Resources across the country. Applying geological knowledge to explain the characteristics and history of these sites not only disseminates academic knowledge but also fosters a conservation mindset, preserving these geological sites as valuable heritage of Thailand.

Kaeng Khut Khu, located in the middle of the Mekong River in Chiang Khan Subdistrict, Chiang Khan District, Loei Province, as shown in Figure 1, reveals exposed rocks visible during the low-water season (February to May). This site is a major tourist attraction in Loei Province. However, the rocks at this site have not been systematically classified on the geological map of Loei Province; they are known only as granodiorite and diorite intrusive igneous rocks. Additionally, no detailed research has been conducted on the rocks at this site. Therefore, this project aims to study the lithology and petrology of the rocks at Kaeng Khut Khu in the Mekong River to clarify the origin and specific names of the exposed rocks and to support its designation as a new geological heritage site in Thailand. This study will also facilitate the integration of geological data between Thailand and the Lao People's Democratic Republic.

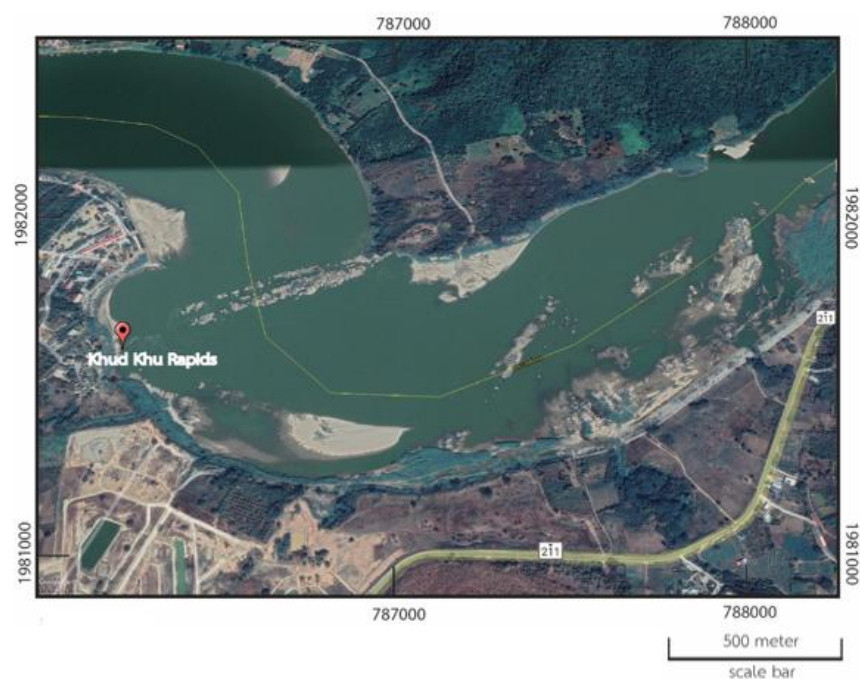


Figure 1. The satellite image shows the location of Kaeng Khut Khu Rapids at Chiang Khan, Loei Province (modified from Google Earth Pro, 2024)

Methodology:

The materials and equipment used in this study include relevant research reports, field instruments (such as a geological compass, hammer, camera, measuring tape, and diluted hydrochloric acid), topographic maps, geological maps, and a polarizing light microscope. Additionally, photographs related to the study area will be utilized for detailed analysis and



discussion in this research. The methodology is divided into field surveys (including location identification, rock description, geological structure measurement, photography, and rock sampling) and the examination of thin rock sections, 0.03 millimeters thick, under a polarizing light microscope to classify rock types and their constituent minerals. For structural geological analysis, fracture orientation data collected from the field will be analyzed using the GeoRose software to determine the primary structural orientation. Satellite imagery will also be analyzed using Google Earth, along with topographic and geological maps, to explain the formation of Kaeng Khut Khu. The field data for this study was collected in early May 2024, coinciding with the end of the dry season.

Results and Discussion:

The Chiang Khan area in Loei Province is predominantly covered by sedimentary rocks dating back to the Paleozoic Era. In the eastern part of the area, sedimentary rocks from the Middle Carboniferous period, approximately 300 to 350 million years ago, are present. These rocks consist of interbedded shale, sandstone, and limestone (indicated by the gray symbol on the map). These sedimentary rocks have undergone metamorphism into hornfels, quartzite, and marble. The contact metamorphic rocks can be found in areas adjacent to granodiorite. The igneous rocks observed in the study area are primarily granodiorite and granite (indicated by the pink symbol on the map), which intruded during the Late Permian to Early Triassic periods, around 250 million years ago. These rocks are associated with the formation of mineral deposits in the region, including iron ore, barite, and gold, as shown in Figure 2. Additionally, along the Mekong River's banks, there is an accumulation of recent fluvial sediments, such as gravel, sand, and soil.

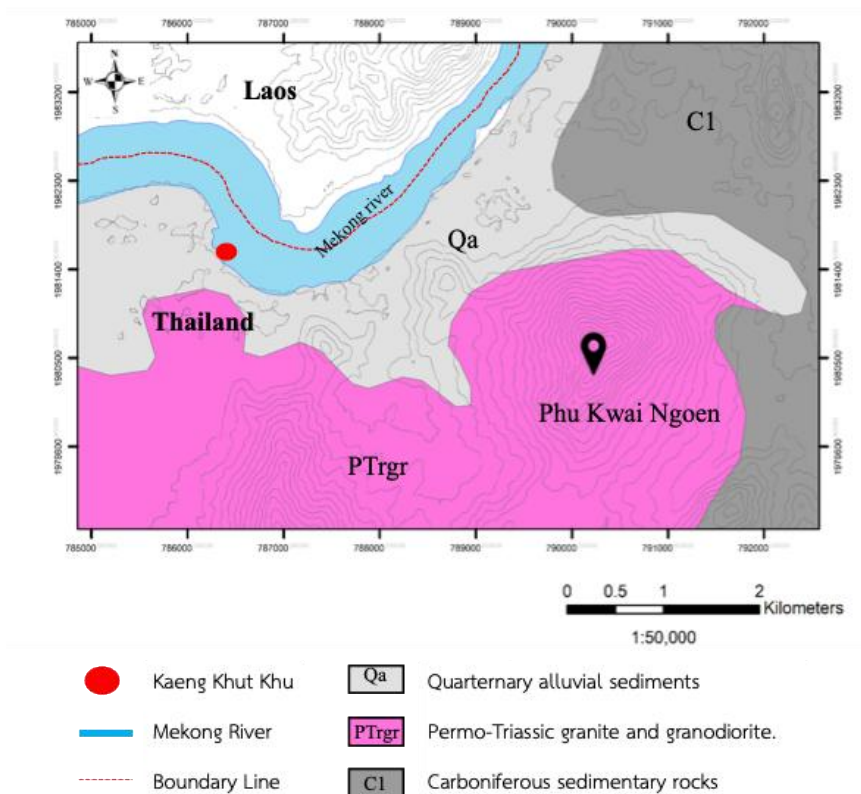


Figure 2. Geologic map of the northern part of Loei Province (Geological data from DMR, 2007).

Kaeng Khut Khu is an outcrop that spans the Mekong River in an almost north-south direction, located at a bend in the river, as indicated by the red point on the geological map (Figure 2). The outcrop consists of intrusive igneous rocks (diorite and granodiorite), which have intruded into the surrounding sedimentary and tuffaceous rocks. The igneous rocks are more resistant to river erosion compared to the surrounding sedimentary rocks, resulting in a prominent ridge of igneous rock that forms the outcrop in the middle of the Mekong River.

Field surveys revealed that the Kaeng Khut Khu outcrop has numerous joints or fracture planes, as shown in Figure 3. The outcrop is clearly exposed and relatively accessible, especially when the water level in the Mekong River recedes. The exposed rock is approximately 3.5 meters wide and 1 meter high, with at least two intersecting fracture planes visible (Figure 3). The rock samples collected from the field exhibit a fine-grained texture, with fresh surfaces displaying gray, pink, and white colors, while weathered surfaces show dark brown and light green hues. The constituent minerals of the rock cannot be identified with the naked eye. The samples show a moderate degree of weathering and contain numerous quartz veins.



Figure 3. The outcrop at Kaeng Khut Khu, located in Chiang Khan Subdistrict, Chiang Khan District, Loei Province, at coordinates 47Q 786317E 1981617N (the geologist in the image is 175 cm tall).

Based on the orientation of the joints measured in the field using a compass, the GeoRose software analysis identified at least four fault orientations: northeast-southwest (NE-SW), northwest-southeast (NW-SE), nearly east-west (NEE-SWW), and nearly west-east (NWW-SEE), as illustrated in Figure 4.

The fracture patterns observed in the rock formations at Kaeng Khut Khu align with the major linear structures, including the principal faults trending northeast-southwest (NE-SW) and nearly east-northeast-west-southwest (NEE-SWW), as well as the minor faults trending northwest-southeast (NW-SE). The Mekong River may have flowed along these geological linear structures, which could include fractures or faults oriented nearly west-northwest-east-southeast (NWW-SEE) and northeast-southwest (NE-SW). The Kaeng Khut Khu area is characterized by a sudden change in the river's flow direction.

A lithological study of ten rock samples from the study area, examined under a polarized light microscope, identified three rock types: (1) coarse ash tuff interlayered with fine ash tuff, (2) fine-grained granodiorite, and (3) fine-grained granite or aplite, as illustrated in Figure 5.

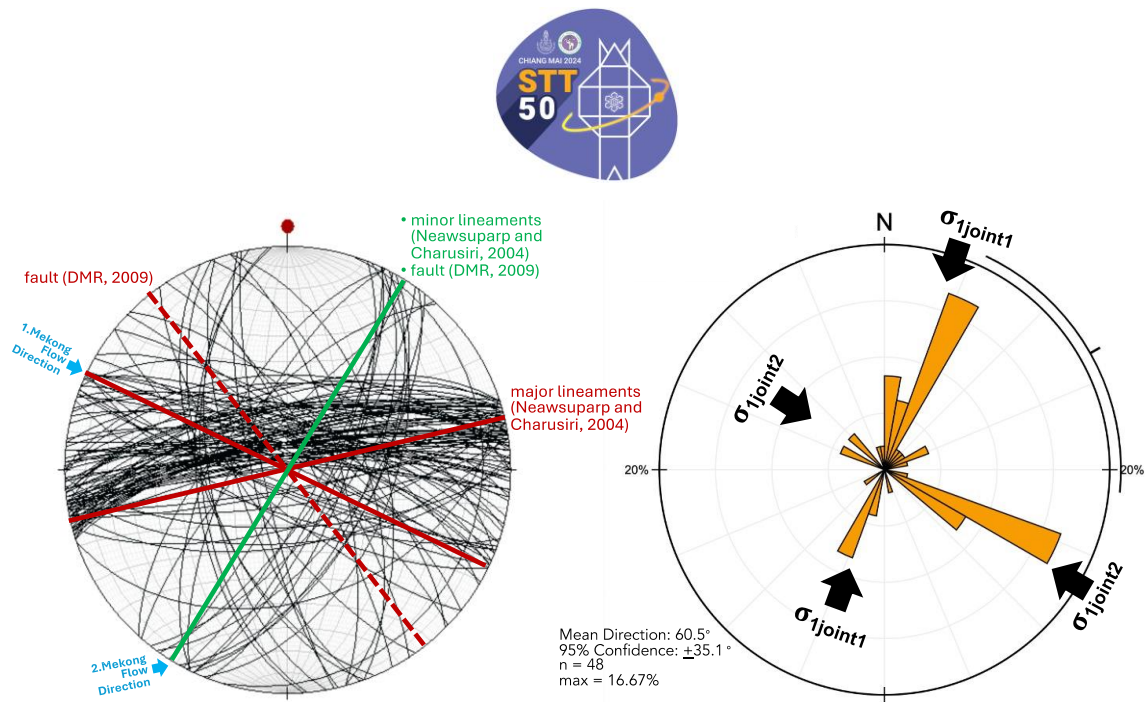


Figure 4. The diagram illustrates the two-dimensional orientation of fractures in comparison to both minor and major faults, as well as the direction of the Mekong River.

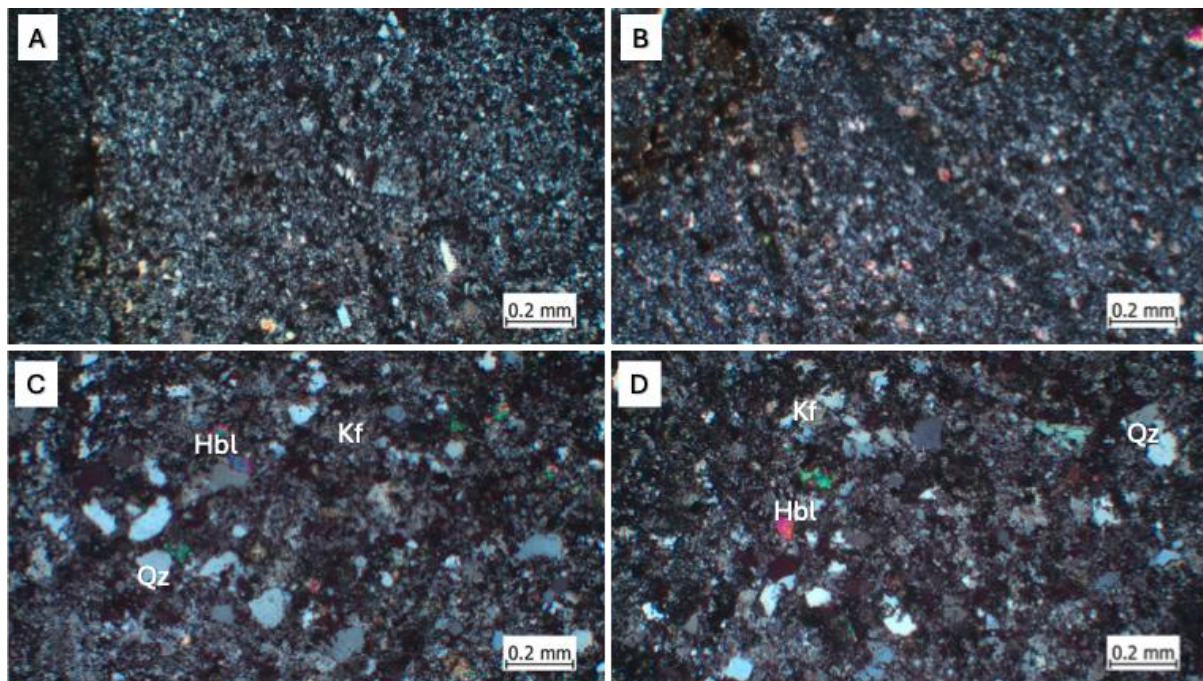


Figure 5. Photomicrographs of thin sections from rock samples at Kaeng Khut Khu under polarized light microscopy: (A) and (B) coarse ash tuff interlayered with fine ash tuff, (C) fine-grained granodiorite, and (D) fine-grained granite. Qz: quartz, Kf: k-feldspars, and Hbl: hornblende.

The coarse ash tuff, interlayered with fine ash tuff, exhibits a pyroclastic texture with poorly sorted volcanic clasts ranging in size from 0.05 to 0.2 millimeters. These clasts consist of quartz, altered feldspars, and rock fragments replaced by silica. Some parts of the tuff show the parallel alignment of volcanic sediments, while secondary minerals include epidote, clay minerals, and silica replacements in the groundmass.

The granodiorite displays a fine-grained, holocrystalline texture with equigranular crystals. The mineral composition includes quartz, alkaline feldspars, plagioclase, hornblende, and opaque minerals. Based on its texture and mineralogy, this rock is classified as microgranodiorite. In contrast, the fine-grained granite exhibits a similar fine-grained, holocrystalline, equigranular texture but differs in having a higher quartz content and very little plagioclase. This fine-grained granite is also referred to as microgranite or aplite, and the texture indicates that both rock types formed from shallow intrusions that crystallized into fine-grained textures.

Kaeng Khut Khu is a significant natural tourist attraction in Loei Province, with historical and cultural ties to the livelihoods of fishermen and the waterways of both Thailand and Laos. Additionally, Kaeng Khut Khu contributes to the biodiversity of the Mekong River Basin by providing habitat for aquatic species and slowing water flow during floods. This area has become one of the key tourist destinations in northeastern Thailand and is well-suited for preservation to foster learning about both natural and cultural heritage. Collaborative efforts among relevant organizations could enhance the site's educational, tourism, and conservation value in partnership with the local community. These initiatives could include revitalizing tourism development plans, promoting community-led boat tours, improving Chiang Khan's tourism maps to include Kaeng Khut Khu, refining academic information signage, and supporting educational camps for students, researchers, and the general public to promote geological heritage.

Kaeng Khut Khu is a prominent medium-sized geological formation in the middle of the Mekong River, distinguished by its rock formations, geological structures, geomorphology (river rapid), and landscape. It was formed from volcanic eruptions during the Permian to Triassic periods, approximately 250 million years ago. The erupted volcanic sediments accumulated as tuff, which later intruded by magma, forming igneous intrusions. Subsequently, the area underwent silica replacement due to tectonic activity, resulting in a durable rock resistant to erosion. Kaeng Khut Khu's formation is closely linked to geological processes such as volcanic eruptions, sedimentation, tectonic movements, and silica replacement. Moreover, the site is integral to the Mekong River's diverse ecosystem, as well as the cultural and lifestyle practices of communities along the riverbanks. These characteristics make Kaeng Khut Khu an ideal candidate for recognition as a geological heritage site in Thailand, supporting the conservation of natural resources.

Conclusion:

Kaeng Khut Khu is a large rapid obstructed flow of the Mekong River, which serves as the border between Thailand and Laos. Geological surveys have identified at least four linear geological structures within the rock formation, which may represent faults or fractures resulting from tectonic activity. Petrographic studies using polarized light microscopy have revealed that Kaeng Khut Khu consists of (coarse ash interbedded with fine ash) tuffaceous rocks interlayered with shallow intrusive rocks, specifically granodiorite and granite (aplite). These rocks were formed from volcanic eruptions during the Permian to Triassic periods, approximately 250 million years ago. The volcanic sediments accumulated and solidified into tuff, which was later intruded by magma. Subsequently, the area underwent silica replacement or silicification due to tectonic activity, leading to the formation of fractures and faults in the Quaternary period. The silicification has resulted in a hardened structure that is resistant to erosion. Kaeng Khut Khu is classified as a medium-sized geomorphological feature, distinguished by its significant geological structures, geomorphology, and landscape. The site is also deeply connected to the cultural heritage, lifestyle, and natural environment of the region, making it a prime candidate for recognition as a geological heritage site in Thailand.



Acknowledgements:

Financial backing for this research was partially provided by the Science Promotion Fund Research and Innovation (NRCT Fund) of Thailand through grants aimed at enhancing the research potential of new-generation lecturers (grant number 191808 and contract number N42A670855). The authors would like to acknowledge the Department of Geotechnology, Faculty of Technology, Khon Kaen University as well as the Department of Geological Sciences, Faculty of Science, Chiang Mai University, for their support in conducting the laboratory studies. Special thanks are extended to Miss Juthatip Khonman, Mr. Napat Joosakoon, and Miss Sainamphueng Wohankla for their assistance in field observations and sample collection.

References:

1. Ruban DA, Zorina SO, Conrad CP. *Palaeogeogr. Palaeoclimatol. Palaeoecol.* 2010;295:226-235.
2. Henriques MH, Pena dos Reis R, Brilha J, Mota T. *Geoheritage.* 2011;3:117-128.
3. Prosser, C.D. *Proc. Geol. Assoc.* 2013;124:568–580.
4. Ruban DA. *Tour. Manag. Perspect.* 2015;15:1-15.
5. Brilha J. *Geoheritage.* 2016;8:119-134.
6. Gray M. *Environ. Conserv.* 2011;38: 271 – 274. 10.1017/S0376892911000117.
7. Gray M. *Proc. Geol. Assoc.* 2008;119:287-298. 10.1016/S0016-7878(08)80307-0.
8. Singtuen V, Won-in K. *Geo. J. Tourism. Geosites.* 2018;22(2):548–560. 10.30892/gtg.22223-310.
9. Singtuen V, Gałka E, Phajuy B, Won-in K. *Geoheritage.* 2019;11:1955–1972. 10.1007/s12371-019-00410-0.
10. Singtuen V, Phajuy B. *Quaest. Geogr.* 2020;39(3):57–68. 10.2478/quageo-2020-0023.



GEOLOGICAL FEATURES INFLUENCING THE DISTRIBUTION OF METALLURGICAL SLAGS IN BAN WANG HAT, SUKHOThai PROVINCE: IMPLICATIONS FOR A SIGNIFICANT IRON ORE DEPOSIT

Vimoltip Singtuen,^{1,*} Burapha Phajuy²

¹Department of Geotechnology, Faculty of Technology, Khon Kaen University, Khon Kaen, Thailand

²Department of Geological Sciences, Faculty of Science, Chiang Mai University, Chiang Mai, Thailand

*e-mail: vimoltipst@gmail.com, vimosi@kku.ac.th

Abstract:

Ban Wang Hat, located in northern Sukhothai Province, is a significant site of prehistoric iron smelting, dating back to the Sukhothai Kingdom during the 13th to 14th centuries. Despite the abundant presence of metallurgical slags and ancient kilns, some of their intended uses remain undocumented. This study employs a comprehensive approach, integrating field investigations, sample characterizations, portable X-ray fluorescence (pXRF) geochemical analyses, and geological interpretations to classify the mineral deposits in the area. Field observations reveal three notable occurrences of metallurgical slags associated with Permian tuffaceous sandstone and Permo-Triassic volcanic rocks containing quartz and metal veins. Macroscopic examination of the slags highlights metallic characteristics, with sections exhibiting vitreous and resinous luster, along with high density and slight magnetic properties. Geochemical analysis identifies volcanic rocks such as rhyolite, dacite, andesite, basaltic andesite, and basalt, characterized by porphyritic and pyroclastic textures. The slags show elevated levels of FeO, MgO, MnO, TiO₂, Bi, Sn, Zn, and Cu, indicating a potential link to metallurgical smelting of hydrothermal ore deposits, consistent with the area's lithological and geological features.

Introduction:

Iron has been crucial to the economic and political development of the lower or southern Northeast region of Thailand since the Iron Age (5th century BCE to early 6th century CE). Its impact spans agriculture, civil engineering, and warfare. The predominant method of ancient iron production in Thailand involved direct or bloomery smelting, in contrast to the indirect or blast furnace smelting process, which produces liquid cast iron. The bloomery process encompasses two primary reactions: the reduction of iron oxides to metallic iron and the separation of impurities from the iron ore into a liquid slag, resulting in the formation of a bloom [1]. This intermediary product consists of metallic iron with varying carbon contents, generally in the form of malleable (soft) iron, and accompanying slag [1]. Subsequent refinement through smithing is required to consolidate the iron into a billet and remove excess slag.

Smelting generates substantial amounts of slag, residues, and technical ceramics as by-products, distinguishing it from primary smithing and object forging. This by-product generation is a distinctive marker of iron production sites in Thailand and other regions. The widespread occurrence of iron slag deposits, often found in heaps or mounds across the Thai landscape, underscores the deep connection between iron production and local communities. Despite extensive historical documentation and identification of iron production sites in Thailand, our understanding of iron smelting technology is limited to a few

archaeometallurgically investigated sites, including Ban Di Lung, Ban Krabueng Nok, Ban Dong Phlong [2], Ban Khao Din Tai, and Ban Sai Tho 7, all dating to the late prehistoric period.

The potential for later iron production exists; however, the lack of systematic dating complicates the reconstruction of historical iron smelting practices. Moreover, the evolution of technologies and production organization over time remains poorly understood based on current evidence. Studies outside Thailand provide limited insights into historical smelting practices. Notable examples include 8th–9th century CE iron smelting in Saphim, Northwest Lao PDR [3–4], and iron production during the Angkorian Khmer period [5–7] through to the post-Angkorian Khmer period in Cambodia [8–12]. In Cambodia, the distribution of 18–22 slag deposits/sites, particularly around Preah Khan of Kompong Svay east of Angkor, demonstrates the continuity of iron smelting activities from the mid-13th to the early 17th centuries, with potential pre-13th century production [8–12]. This highlights the potential for dating slag deposits within specific locales to different historical periods.

In the northwestern region of Sukhothai Historic Town, Thailand, ancient metallurgical slags are found near Mae Ramphan Upstream or Mae Ramphan Reservoir, approximately 40 kilometers from Sukhothai Historical Park (Figure 1). Despite their proximity to iron ore deposits, including the Permian Kiu Lom Formation of the Ngao Group (tuffaceous sandstone, tuffaceous shale, and tuff) and Permo-Triassic volcanic rocks (rhyolite, andesite, tuff, and agglomerate) associated with faults (NW-SE direction), there is a hypothesis regarding the absence of metallurgical materials near these sites. This research aims to explore and categorize the geochemical characteristics of slags and igneous rocks to contribute to understanding the historical implications associated with the geological features and resources of the region.

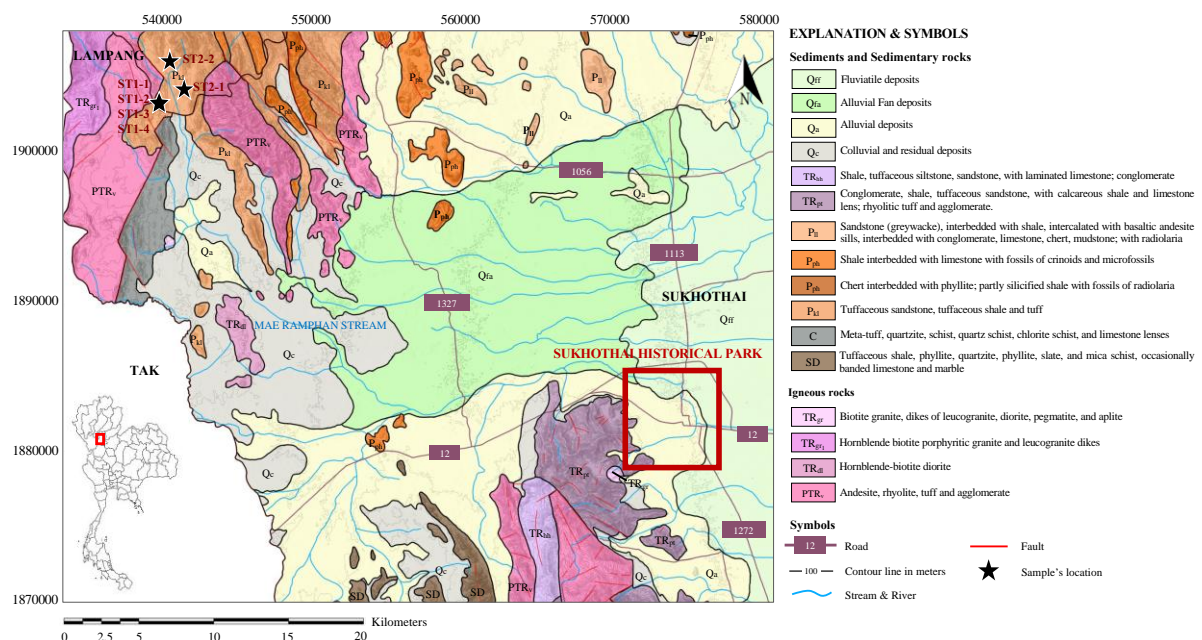


Figure 1. Geological map of the western part of Sukhothai Province and study locations in Ban Wang Hat (Geological data adapted from DMR [1]).

Methodology:

The methodology employed in this study encompasses bibliometric analysis, field observation, macroscopic examination, and geochemical analysis, with a focus on major and trace elements. Field surveys and data collection involved acquiring detailed information on



slags and associated rocks, including attributes such as color, texture, mineral composition, and degree of weathering. Approximately 5-6 representative samples of slags and rocks were collected from each study site, located both south and north of the Mae Ramphan Reservoir. Geochemical analysis of these samples was conducted using a Portable X-ray Fluorescence (XRF) analyzer (Olympus Vanta model) at the Department of Geotechnology, Faculty of Technology, Khon Kaen University. This analysis aimed to determine the types and concentrations of major and trace elements present in the rocks, facilitating the classification of their geochemical traits and the assignment of specific rock nomenclature. XRF analysis was performed on the unblemished and unweathered surfaces of the samples, although it is important to note that this instrument cannot measure elements with low atomic numbers, typically those below twelve. The insights gained from the macroscopic examination and geochemical analysis will be used to identify rocks associated with the distribution of slags, ultimately contributing to the understanding of the underlying ore deposits in the area.

Results and Discussion:

Field observations were conducted in the Mae Ramphan Upstream area, covering both the southern (47Q 540104E 1903365N) and northern (47Q 540448E 1906304N) regions of the Mae Ramphan Reservoir. In the southern area, a creek has exposed metallurgical slags, as shown in Figure 2A. Over 50 pieces of metallurgical slag, ranging in size from a few centimeters to over 20 centimeters, were observed. These slags exhibited various characteristics including dullness, glassiness, vitreousness, metallic luster, and some displayed vesicular textures and notably high density (Figure 2B). The nearby hill features volcanic rocks such as rhyolite porphyry and andesite porphyry (Figure 2C), as well as tuff associated with a stockwork of quartz and metal veins. In the northern part of the reservoir, metallurgical slags were less abundant but shared similar characteristics to those found in the southern region (Figure 2D). These slags are located along the slope of the rhyolite mountain, as depicted in Figure 2E.

Measurements were taken from 30 slag and rock samples collected from the northern part of Ban Wang Hat Village, Sukhothai Province, as illustrated in Figure 3. All samples were obtained from areas adjacent to the Mae Ramphan Reservoir. The analysis was conducted using a portable X-ray fluorescence (XRF) analyzer, selected for its non-destructive and in-situ measurement capabilities.

Macroscopic examination of the metallurgical slag samples revealed distinct features. Some samples displayed dark gray to black coloration reminiscent of metal, while others had brown and light gray surfaces marked by pores and irregular black and white particles (Figures 3A-3G). Additionally, surface color variations ranged from white to pale yellow, with vitreous and resinous lusters. Certain samples exhibited a ribbon-like texture, indicative of melting and flow under heat. Notably, many of the slags exhibited high density and slight magnetism.

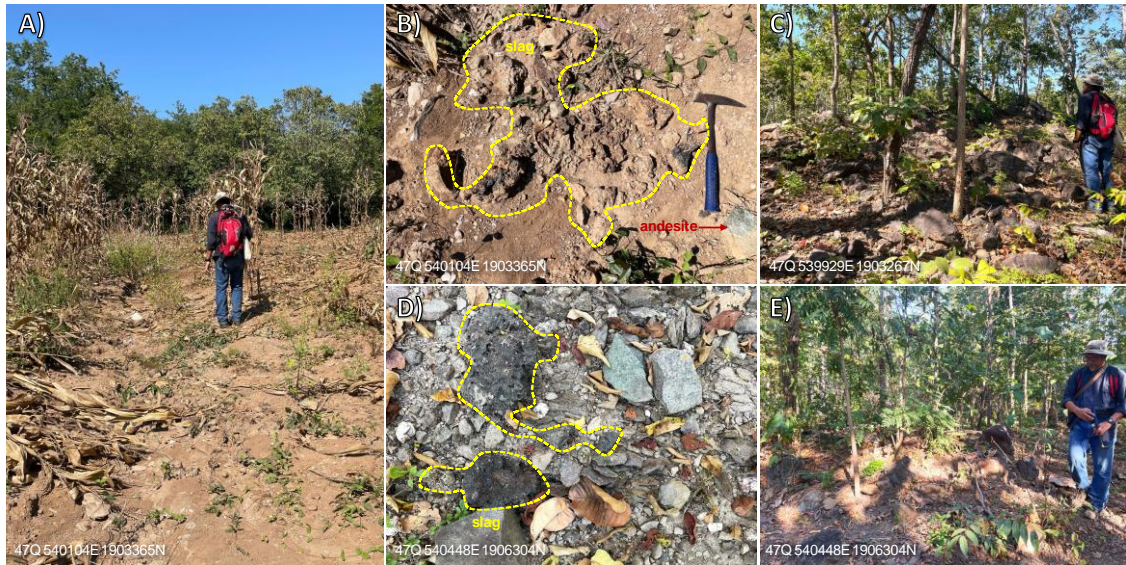


Figure 2. Field investigation and sample distribution. (A) Distribution of slags in a small stream located at coordinates 47Q 540104E 1903365N. (B) Metallurgical slags and glass-like materials observed in situ. (C) Outcrop of diorite porphyry in the southern area. (D) Presence of metallurgical slags alongside volcanic rocks. (E) Outcrop of rhyolitic tuff in the northern area.

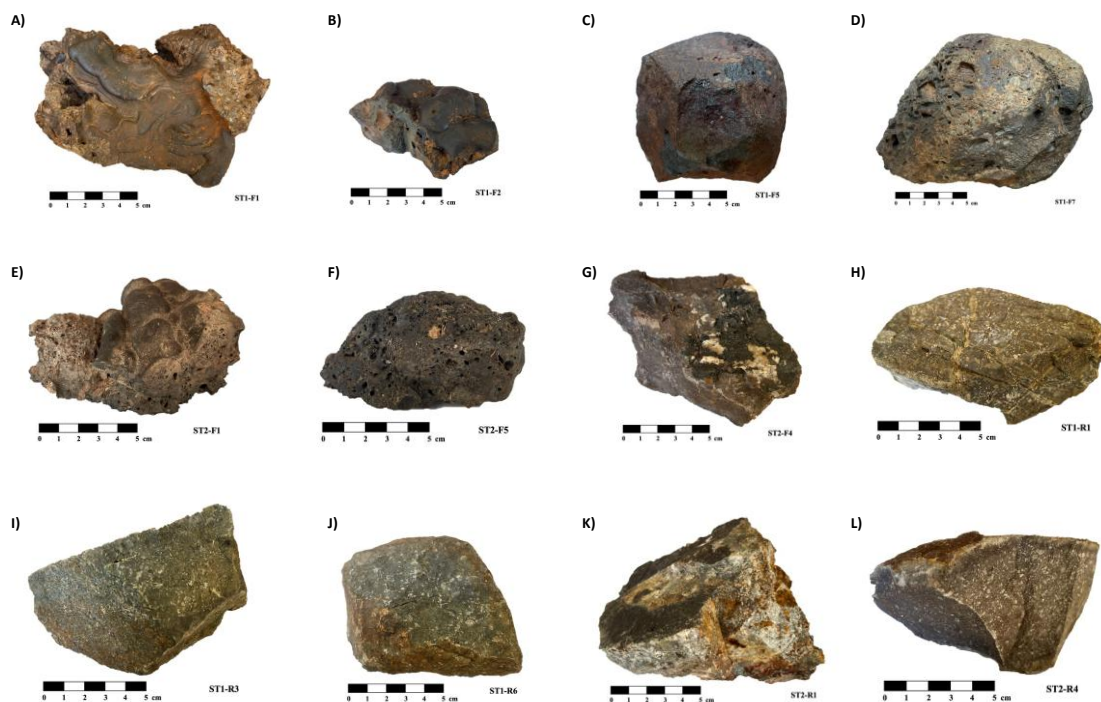


Figure 3. Macroscopic Analysis of Metallurgical Slags and Rock Samples. (A-D) Slags and flux materials collected from the southern part of the Mae Ramphan Reservoir. (E-G) Slags and flux materials from the northern part of the Mae Ramphan Reservoir. (H) Rhyolite porphyry featuring quartz and metal veins. (I) Andesite porphyry associated with quartz and metal veins. (J) Andesite porphyry rich in plagioclase. (K) Quartz stockwork containing metal. (L) Rhyolite porphyry.



In the southern part of the reservoir, volcanic rocks exhibited a porphyritic texture, including both rhyolite and andesite, with numerous quartz replacements observed in fractures and veins (Figures 3H-3J). Certain cavities within these rocks were found to be infilled with dark-colored metal minerals, which displayed metallic lusters and slight magnetism, particularly within quartz stockwork zones (Figures 3I, 3K). In contrast, the northern region of the reservoir is characterized by the presence of andesite and rhyolite porphyry (Figure 3L).

The geochemical analysis classified the volcanic rocks into various categories based on the SiO_2 vs. K_2O diagram of Ewart (1982). The classifications include high-K rhyolite, low-K rhyolite, dacite, low-K dacite, andesite, low-K andesite, basaltic andesite, low-K basaltic andesite, absarokite (basaltic-trachyandesite), and low-K basalt (Figure 4). These volcanic rocks are derived from different magma suites, encompassing alkaline, high-K calc-alkaline, and low-K series.

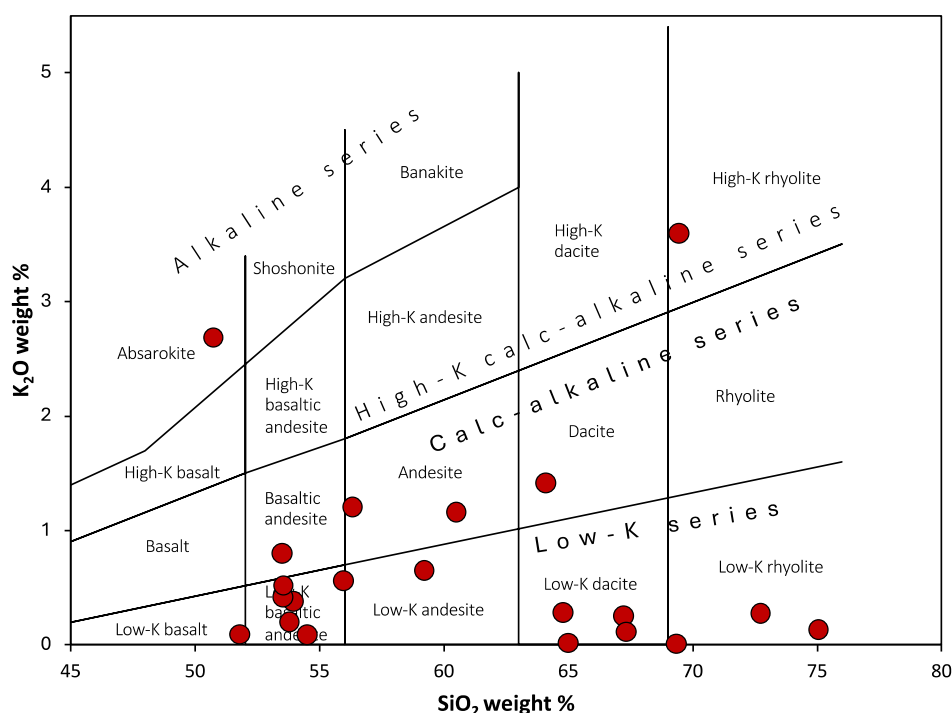


Figure 4. Classification diagram of volcanic rocks by using SiO_2 and K_2O for rock name and magma series (diagram modified from [Ewart, 1982].

The volcanic rocks present in the studied area are part of the Chiang Khong-Lampang-Tak volcanic belt, which is characterized by a diverse array of volcanic rock types erupted over various geological periods from the Permian to the Jurassic [13]. These rocks originate from multiple magma sources [13]. However, the accumulation of metallic ores in the region is likely a post-volcanic event. After the deposition of volcanic rocks, tectonic movements led to the formation of faults, creating voids where hydrothermal solutions rich in silica and metals could accumulate. The physicochemical conditions of these hydrothermal fluids, which became trapped, are investigated through the study of fluid inclusions found in quartz veins. The cavities within the quartz are coated with black and/or dark brown iron

oxides/hydroxides, likely consisting of goethite (black), limonite (yellow-brown), as well as magnetite and hematite (black with magnetism).

The analyzed slag exhibits significant geochemical features, particularly in its primary oxide composition, which predominantly consists of metal oxides. Analysis based on a diagram comparing primary oxide compounds reveals high concentrations of iron oxide (FeO) in the metal slag, with smaller amounts of magnesium oxide (MgO), titanium oxide (TiO₂), and manganese oxide (MnO), as illustrated in Figure 5. Additionally, notable trace metals detected in the slag include bismuth (Bi), zinc (Zn), and copper (Cu). Some samples also show substantial levels of antimony (Sb), tin (Sn), lead (Pb), and arsenic (As). These findings indicate that historical metal smelting activities may have contributed to the presence of trace metal elements in the slag, providing insights into the smelting processes employed.

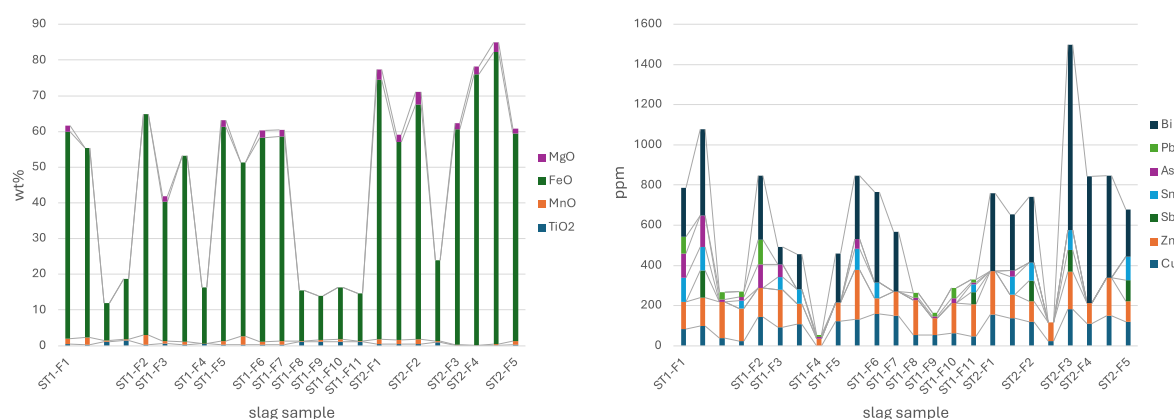


Figure 5. The volume comparison diagrams illustrate the concentrations of metal oxides (left) and metal elements (right) in metallurgical slags, as analyzed using a portable X-ray fluorescence (XRF) analyzer.

Ancient iron smelting, a practice of significant historical importance, was crucial for the production of tools, weaponry, and construction materials. This complex steel smelting procedure demanded considerable technical expertise and was intrinsically linked to iron mining operations. Geological knowledge was employed to locate iron ore deposits in mountainous regions, which facilitated the extraction of solid iron ore. Historical records reveal that ancient civilizations sought out metallic resources conducive to smelting at high temperatures to extract iron, resulting in the production of steel. The by-product of this process, known as iron slag, was often regarded as waste.

The origins of metal smelting are frequently attributed to ancient Egyptian civilizations, with the Hittites recognized as early adopters of iron smelting around 3,500 years ago, particularly for tool and weapon production. Steel smelting required high temperatures, typically exceeding 1,550 degrees Celsius. Despite the technological constraints of antiquity, the smelting process predominantly involved the reduction of iron ore oxides, culminating in the formation of solid slag.

Conclusion:

Ban Wang Hat in Sukhothai Province, a site rich in artifacts and remnants of ancient metal smelting activities, offers significant insights into historical metallurgical practices. Archaeological evidence suggests continuous human habitation from prehistoric times through the era when Sukhothai served as the capital, approximately during the 13th to 14th centuries. This study has identified metal slag deposits in the upstream region of Huai Mae Ramphan Creek, characterized by a range of colors including black, brown, and gray, and exhibiting metallic, glassy, and matte textures. Some samples demonstrate notably high



specific gravity and weak magnetic properties. Chemical analysis of these slags reveals substantial concentrations of iron oxide (FeO) and notable quantities of bismuth (Bi), zinc (Zn), and copper (Cu). These findings, in line with the principle that ore production typically occurs near the source of mineral deposits, suggest the presence of metal ore sources near the headwaters of Huai Mae Ramphan Creek. Geochemical investigations further indicate that the area's volcanic rocks exhibit porphyritic and pyroclastic textures and comprise a diverse range of compositions, including rhyolite, dacite, andesite, basaltic andesite, and basalt. These rocks, formed from both alkaline and calc-alkaline magma suites, were subsequently altered by hydrothermal solutions—metal-bearing fluids—that filled geological voids created by differential faulting and precipitated silica and iron deposits.

Acknowledgements:

This project is funded by National Research Council of Thailand (NRCT), specifically under the Humanities and Social Sciences Subject Group (reference number 4731651), which supported investigations into significant geological resources and provided evidence pertinent to the hypothesis regarding the construction of the Sukhothai Kingdom. The authors also wish to acknowledge the Department of Geotechnology, Faculty of Technology, Khon Kaen University, for their assistance with laboratory studies.

References:

1. Juleff G. *Nature*. 1996;379:60–63.
2. Nitta E. *Bull. Indo-Pacific Prehistory Assoc.* 1997;16:153–160.
3. Evrard O, Pryce TO, Sprenger G, Chiemsisouraj C. *J Southeast Asian Stud.* 2016;47(1):109–140.
4. Pryce O, Chiemsisouraj C, Zeitoun V, Forestier H. *Hist Metall.* 2011;45:81–89.
5. Leroy S, Hendrickson M, Delqu'e-Kolic E, Vega E, Dillmann P. *PLoS One*. 2015; 10:0141052.
6. Leroy S, Hendrickson M, Bauvais S, Vega E, Blanchet T, Disser A, Delque-Kolic E. *Archaeol Anthropol Sci.* 2018;10(8):2137–2157.
7. Hendrickson M, Leroy S, Castillo C, Hua Q, Vega E, Phon K. *Antiquity*. 2019;93(372):1586–1606.
8. Pryce TO, Hendrickson M, Phon K, Chan S, Charlton MF, Leroy S, Dillmann P, Hua Q. *J Archaeol Sci.* 2014;47:142–163.
9. Hendrickson M, Hua Q, Pryce O. *Radiocarbon*. 2013;55:31–47.
10. Hendrickson M, Leroy S, Hua Q, Phon K, Vuthy V. *Asian Perspect.* 2017;56:55–91.
11. Hendrickson M, Pryce O, Sonnemann T, Phon K, Hua Q, Chan S. *Preah Khan of Kompong Svay*. 2018;42:32.
12. Uchida E, Murasugi M, Kuroda A, Lu Y. *Heritage*. 2019;2(2):1724–1738.
13. Phajuy B, Singtuen V. *Science Asia*. 2019;45(4):350–360.



GREEN SYNTHESIS OF TITANIUM DIOXIDE USING *Brassica oleracea* LEAF EXTRACT FOR PHOTOCATALYTIC DEGRADATION OF RHODAMINE B DYE

Akkarapong Jaidej and Nuttaya Pongstabodee*

Department of Chemical Technology, Faculty of Science, Chulalongkorn University, Bangkok, Thailand.

*email:sangobtip.p@chula.ac.th

Abstract:

Water is a vital natural resource essential for all life, supporting irrigation, navigation, and consumption. However, water pollution, particularly from hazardous dyes, poses a significant threat to aquatic ecosystems and human health. Proper treatment of dye-contaminated wastewater is crucial before its release into natural water bodies, as even minute concentrations (0.005 mg/L) can visibly alter water color and impact aquatic life. This research explores photocatalytic degradation of Rhodamine B dye in synthetic wastewater using titanium dioxide (TiO_2), with a focus on enhancing its performance in the visible light spectrum through copper addition. The study compares chemical and green synthesis methods for TiO_2 preparation, emphasizing environmentally friendly approaches. Plant extracts are being used as a reducing agent to achieve environmentally friendly and pollution-free synthesis. From the patterns of X-ray diffraction (XRD), chemically synthesized TiO_2 exhibited anatase-type structure (JCPDS 00-021-1272) while green-synthesized TiO_2 showed both anatase and brookite-type structures (JCPDS 00-029-1360). For the photocatalytic performance, it was found that green-synthesized TiO_2 achieved 100% Rhodamine B degradation under UV light, outperforming chemical synthesis. After loading 0.5% wt Cu on green-synthesized TiO_2 , it demonstrated 100% degradation and 97% efficiency under visible light within 120 minutes. This research contributes to the development of efficient, environmentally friendly photocatalysts for dye removal from wastewater, addressing critical water pollution challenges.

Introduction:

In today's economy, industries are striving to enhance production efficiency and add value to their products through technology and color decoration. This is particularly evident in the textile, printing, paper, and incense industries, which are experiencing significant expansion and continually improving their production processes to increase productivity. Rhodamine B ($\text{C}_{28}\text{H}_{31}\text{ClN}_2\text{O}_3$) is one of popular basic dyes used in these industries. However, it is a carcinogen and can cause skin problems, respiratory inflammation, hemolysis, and liver and kidney degeneration.¹ These harmful effects have led to an investigation in removing dye contaminants from wastewater using various methods such as photocatalysis, adsorption, centrifugation, and filtration. Photocatalysis involves catalyzing reactions through the combined action of light and a catalyst, replacing traditional heat activation with light activation. In this process, electron-hole pairs are generated on the semiconductor by light with energy greater than or equal to the band gap of the semiconductor.² Titanium dioxide photocatalysis is an effective method for decomposing dyes without producing toxic substances for the environment.¹ It is corrosion-resistant and retains its effectiveness upon reuse. However, its 3.2 eV band gap limits its use to UV light, which constitutes less than 5% of the solar spectrum. Additionally, electron-hole recombination during photocatalysis reduces its activity.³ Therefore, metal loading onto titanium dioxide can reduce the band gap energy, lowering the energy required for photocatalysis.⁴ Various methods for synthesizing titanium dioxide include co-precipitation, electrolysis, photochemical, and sol-gel

techniques.⁵ These methods often require synthetic reducing agents, which are usually strong and toxic. Therefore, plant extracts are preferable for achieving an environmentally friendly and pollution-free synthesis.^{6,7} Plant-based reducing agents offer greener alternatives.⁸ This research aims to use extracts from *Brassica oleracea* leaves to synthesize copper-loaded titanium dioxide for degrading Rhodamine B dye in synthetic wastewater under light irradiation.

Methodology:

Materials

Titanium tetra isopropoxide (TTIP, $C_{12}H_{28}O_4Ti$, 97%), Ethanol (C_2H_5OH , 96%), Rhodamine B ($C_{28}H_{31}ClN_2O_3$), Copper (II) nitrate trihydrate ($Cu(NO_3)_2 \cdot 3H_2O$) and deionized water. *Brassica oleracea* leaves were collected from the local market. All chemicals and reagents used are of analytic grade and were used without further purification.

Synthesis of titanium dioxide

Soft-template method was selected to synthesize titanium dioxide. Firstly, 3.64 grams of cetyl trimethyl ammoniumbromide was dissolved in a mixture of 100 mL deionized water and 25 mL ethanol. After stirring the sample for 30 minutes, 14.35 mL of titanium isopropoxide was added drop by drop while stirring continuously for 24 hours. The suspension was washed with ethanol and dried in an oven at 80 °C. Finally, the powders were calcined at 450 °C for 2 hours.

Synthesis of green titanium dioxide

Firstly, *brassica oleracea* leaves were washed thoroughly with water, then cut into small pieces and dry them at 50°C. Next, 50 grams of the dried leaves were boiled in 100 mL of deionized water at 50 °C for 1 hour. The mixture was filtered to obtain the *brassica oleracea* leaf extract. 5 mL of the leaf extract and 5 mL of titanium isopropoxide was added to 25 mL of deionized water. The mixture was stirred using a magnetic stirrer for 3 hours at 70°C. After that, the mixture was cooled down to room temperature. The white residue was then separated using filter paper and calcined at 400 °C for 3 hours.

Synthesis of green copper-titanium dioxide

Copper nitrate trihydrate was dissolved in 25 mL of deionized water to obtain the solution with a desired concentration. 3 mL of the leaf extract and 5 mL of titanium isopropoxide was then added to the aqueous solution. The mixture was stirred using a magnetic stirrer for 3 hours at 70°C. After that, the mixture was cooled down to room temperature. The residue was then separated using filter paper and calcined at 400 °C for 3 hours.

Characterization

The titanium dioxide samples were characterized by X-Ray Diffraction (XRD). The crystallinity of the samples was analyzed using X-ray diffraction (Bruker AXS Model D8) with Cu-K α radiation at 2 θ range of 10°-80°.

Photocatalytic degradation of Rhodamine B dye

15 ml of rhodamine B dye solution with different concentrations was taken in a stoppered conical flask. 75 mg of titanium dioxide samples was added to the flask. Furthermore, the mixture was kept in a dark chamber for 1 hour to attain the adsorption-desorption equilibrium. The photodegradation of Rhodamine B dye under UV-visible irradiation was recorded at 30-minute intervals from 0 to 120 minutes. The collected samples



were filtered through Whattman filter paper and the filtrate was analyzed using UV-spectrophotometer at 554 nm.

Results and Discussion:

X-Ray Diffraction

The X-ray diffraction technique analyzed the crystalline phase and average crystalline size of green and chemical titanium dioxide, as shown in Figure 1.

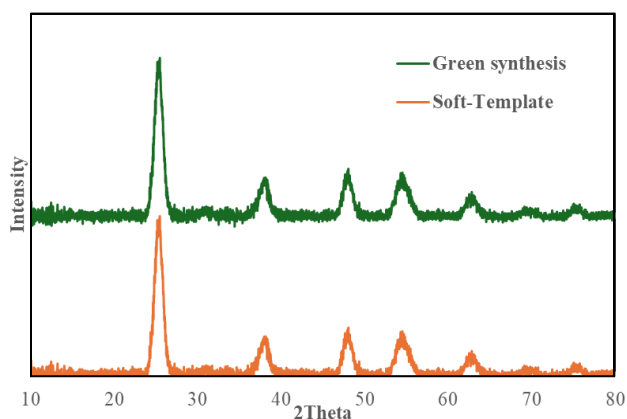


Figure 1. XRD pattern of TiO₂ synthesis via green and soft-template method

From the pattern of TiO₂ synthesis via soft-template method, the diffraction peaks at 2θ of 25.30°, 37.00°, 48.0°, 55.1°, 62.7°, and 75.05° correspond to the Bragg reflection planes of (101), (004), (200), (211), (204), and (215) (JCPDS card no. 00-021-1272), respectively. The observed peak at 2θ of 25.30° represents the high crystalline nature of TiO₂. From the pattern of green TiO₂, the diffraction peaks at 2θ of 25.3°, 25.7°, 30.8°, and 38.0° represent to the Bragg reflection planes of (120), (111), (121), and (040) (JCPDS card no. 00-029-1360). These angles indicate the presence of the brookite phase, which is found in smaller amounts compared to the anatase phase.⁹ The average crystalline size of TiO₂ was calculated from the XRD pattern using the Debye Scherer formula. The average particle sizes for the soft-template and green synthesis methods were found to be 15.17 nm and 7.71 nm, respectively. The advantage of catalysts with a mixed anatase-brookite phase is that they can achieve charge separation, which helps reduce electron-hole recombination. This results in favorable energy alignment at the heterojunction between anatase and brookite, where electrons can move from the conduction band (CB) of brookite to the CB of anatase, while holes can move from the valence band (VB) of anatase to the VB of brookite. This charge separation effectively reduces recombination¹⁰, enhancing the photocatalytic activity of the material.

From Figure 2, The XRD patterns of green titanium dioxide synthesized using different amounts of leaf extract (1, 5, 15, and 30 milliliters) show the positions of the characteristic peaks of anatase and brookite phases. The average particle sizes of green titanium dioxide synthesized with these varying extract amounts are 8.64, 8.04, 7.59, and 7.95 nm, respectively. As the extract amount increases, the particle size decreases, indicating the extract acts as a stabilizing agent, counteracting electrostatic forces and reducing particle agglomeration.¹¹ A smaller particle size leads to a larger surface area, enhancing the catalyst's active surface area for catalytic reactions and light interaction. From Table 1, it is observed that the proportion of the anatase phase increases with the amount of extract used. This suggests that leaf extract can inhibit the phase transition from anatase to brookite by acting as a capping agent.

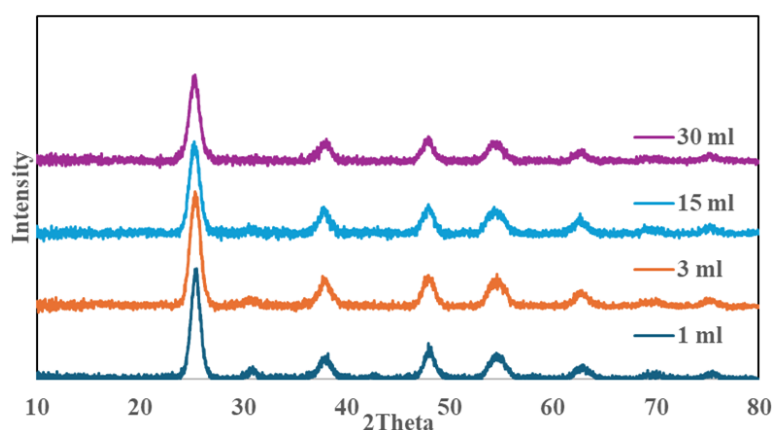


Figure 2. XRD pattern of green TiO₂ with various amounts of the extract

Table 1. Properties of green TiO₂ photocatalyst with various amounts of the extract

| Volume of extract (mL) | Anatase | Brookite | Crystalline size (nm) (101) |
|---------------------------|---------|----------|--------------------------------|
| 1 | 83.22 | 16.78 | 8.64 |
| 3 | 66.87 | 33.13 | 8.04 |
| 15 | 77.46 | 22.54 | 7.59 |
| 30 | 75.00 | 25.00 | 7.95 |

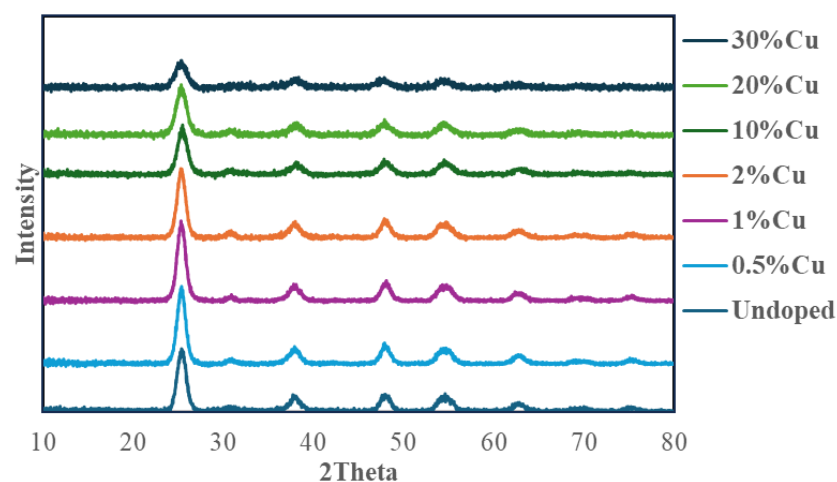


Figure 3. XRD pattern of green TiO₂ with varying Cu contents

XRD patterns for titanium dioxide with varying Cu content (0-30 wt%), as shown in Figure 3, express the characteristic peaks of anatase and brookite phases. No characteristic peaks corresponding to the Cu phase were detected. The intensity of the titanium dioxide peaks decreased with increasing Cu concentration, likely due to disruptions in the crystal structure caused by the insertion of Cu particles into the titanium dioxide lattice.⁷ Given the similar ionic radii of Cu⁺ (0.072 nm) and Ti⁴⁺ (0.062 nm), the Cu dopant can be incorporated into the titanium lattice.¹² The Cu particles may be well dispersed within the titanium dioxide matrix. Titanium dioxide has a tetragonal structure ($a=b \neq c$). From Table 2, that lattice parameters "a" and "b" slightly increase with Cu doping, while lattice parameter "c" slightly decreases compared to undoped titanium dioxide. This indicates that Cu is incorporated into the TiO₂ lattice, with values closely matching the standard database for anatase ($a = 3.785 \text{ \AA}$,



$b = 3.785 \text{ \AA}$, and $c = 9.514 \text{ \AA}$).¹³ The crystallite sizes of titanium dioxide for Cu doping concentrations of 0.5, 1, 2, 10, 20, and 30 wt% are 8.51, 8.32, 7.69, 7.60, 6.86, and 6.79 nm, respectively. It is evident that the crystallite size decreases as the Cu dopant concentration increases.

Table 2. Properties of green Cu-TiO₂ photocatalysts

| Catalyst | Anatase | Brookite | a,b (Å) | c (Å) | Crystalline size (nm) (101) |
|------------------------|---------|----------|---------|--------|--------------------------------|
| 0Cu-TiO ₂ | 66.87 | 33.13 | 3.8007 | 9.4990 | 8.04 |
| 0.5Cu-TiO ₂ | 89.69 | 10.31 | 3.7900 | 9.4915 | 8.51 |
| 1Cu-TiO ₂ | 84.85 | 15.15 | 3.7913 | 9.5017 | 8.32 |
| 2Cu-TiO ₂ | 80.00 | 20.00 | 3.7965 | 9.4933 | 7.69 |
| 10Cu-TiO ₂ | 88.89 | 11.11 | 3.7635 | 9.4519 | 7.60 |
| 20Cu-TiO ₂ | 82.76 | 17.24 | 3.7929 | 9.4886 | 6.86 |
| 30Cu-TiO ₂ | 84.85 | 15.15 | 3.8048 | 9.4883 | 6.79 |

Photocatalytic degradation Rhodamine B dye

Figure 4 demonstrates the photocatalytic activity of green and chemical titanium dioxide. Higher percentage degradation of 100% was achieved when using green TiO₂, compared to the soft template method. The mixed anatase-brookite phase enhances photocatalytic activity by facilitating charge separation and preventing electron-hole recombination. Particle size also plays a critical role, with green synthesis yielding smaller particles (7.71 nm) compared to the soft template method (15.17 nm), thus providing a larger surface area for catalytic reactions.⁷

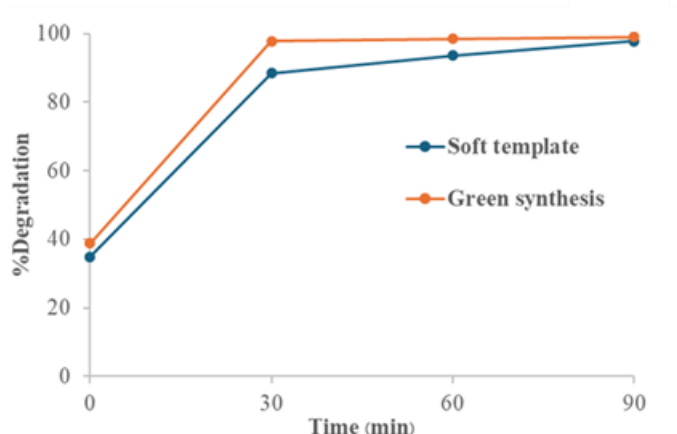


Figure 4. Degradation of Rhodamine B dye using green and chemical TiO₂ photocatalyst at initial dye concentration 10 mg/L, under ultraviolet light irradiation.

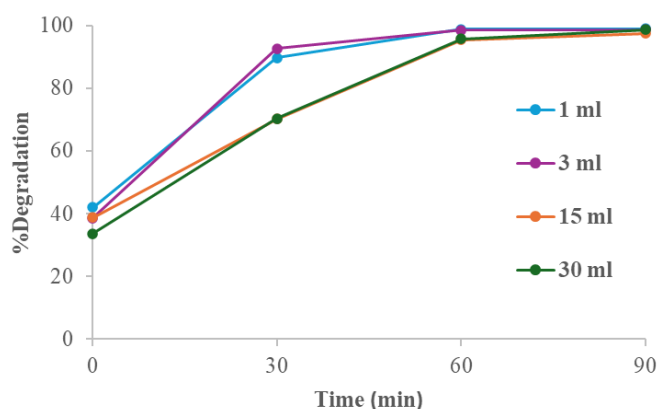


Figure 5. Degradation of Rhodamine B dye using green TiO₂ photocatalyst with various amount of the extract at initial dye concentration 10 mg/L, under ultraviolet light irradiation.

Figure 5 shows that green titanium dioxide synthesized with 1 and 3 mL of the extract achieved nearly 100% color removal within 90 minutes. Higher extract amounts (15-30 mL) resulted in lower efficiency, likely due to a higher proportion of brookite phase, which enhances the reduction reaction sites for O₂, forming highly reactive OH• species.¹⁴ Given the solar spectrum contains less than 5% UV light, the addition of Cu to titanium dioxide reduces the energy required for activation, enabling effective visible light photocatalysis. Under visible light irradiation, Rhodamine B undergoes N-deethylation, forming Rhodamine 110 (Rh-110), which can be tracked by the hypsochromic shift in peak absorption. This transformation helps neutralize the excess negative charge on green TiO₂ by adsorbed oxygen molecules, forming superoxide radicals.

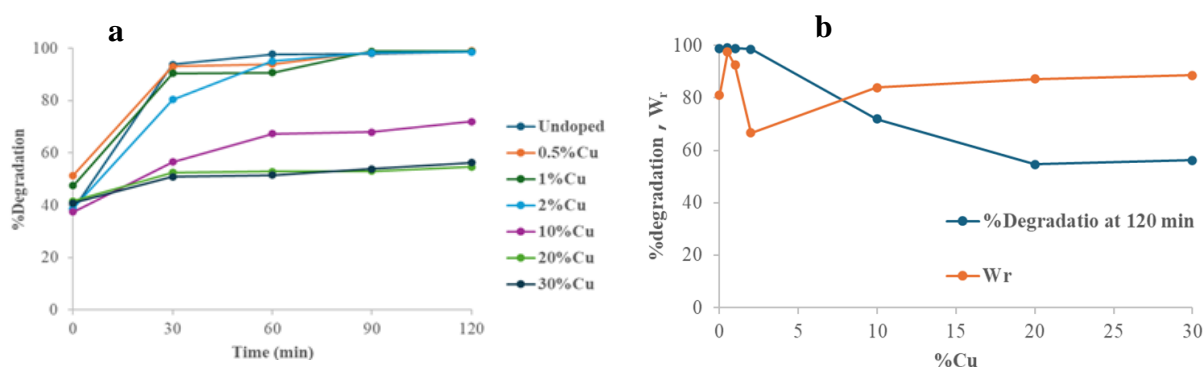


Figure 6. (a) Degradation and (b) Removal efficiency (W_r) of Rhodamine B dye using green Cu-TiO₂ photocatalyst at initial dye concentration 10 mg/L, under visible light irradiation.

To determine the photocatalytic activity under visible irradiation, two simultaneous processes occur. As exposure to visible light continues, the initial absorbance peak at 554 nm decreases, indicating the degradation of Rhodamine B. Concurrently, a hypsochromic shift is observed, with a new peak appearing at 498 nm, corresponding to Rhodamine 110 (Rh-110). This shift is a result of the N-deethylation process, where ethyl groups are removed from the aminodiethyl groups of Rhodamine B. Ethyl groups act as auxochromes, influencing the absorption maximum; their removal causes the observed hypsochromic shift. The formation of Rh-110 and the subsequent neutralization of excess negative charge on green TiO₂ by adsorbed oxygen molecules lead to the generation of superoxide radicals (O₂•⁻). This process modifies the production of reactive oxygen species (ROS), favoring the formation of superoxide radicals over hydroxyl radicals (OH•). To evaluate the conversion efficiency (W_c) of Rhodamine B to Rh-110, the following equation is used:



$$W_c = (n_a/n_t) \times 100$$

where n_a is the actual number of moles of the transformed substance, and n_t is the theoretical number of moles. This formula allows for the quantification of the conversion efficiency, reflecting the effectiveness of the photocatalytic process. The conversion efficiency also enables the calculation of removal efficiency (W_r). Removal efficiency describes the photocatalytic degradation of RhB molecules, resulting from the destruction of chromophores.

$$W_r = 100 - W_c$$

Conversion efficiency and removal efficiency should be analyzed together, rather than in isolation, when evaluating photocatalytic performance. Figure 6 demonstrates that at copper concentrations of 0.5%, 1%, 2%, 10%, 20%, and 30% by weight, the percentage degradation of Rhodamine B correlates directly with both conversion efficiency (W_c) and removal efficiency (W_r), as detailed in Table 3. Conversion efficiency (W_c) reflects the amount of Rhodamine 110 (Rh-110) remaining after the reaction, while removal efficiency (W_r) accounts for the overall removal of both Rhodamine B and Rh-110, indicating a clear solution.¹⁵ The results indicate that a 0.5% copper concentration achieves the highest degradation and removal efficiencies, at 100% and 97%, respectively. This suggests that 0.5% Cu is the optimal concentration for photocatalytic applications under visible light irradiation. Higher copper concentrations lead to cluster formation, which increases electron-hole recombination and consequently reduces photocatalytic activity.

Table 3. Rhodamine B degradation using green Cu-TiO₂ photocatalyst with various amounts of copper loading at initial dye concentration 10 mg/L, under visible light irradiation.

| %Cu | %degradation | W_c (%) | W_r (%) |
|-----|--------------|-----------|-----------|
| 0.5 | 100 | 3 | 97 |
| 1 | 100 | 8 | 92 |
| 2 | 100 | 33 | 67 |
| 10 | 72 | 16 | 84 |
| 20 | 53 | 13 | 87 |
| 30 | 54 | 11 | 89 |

Among the various copper loadings tested, 0.5% Cu demonstrated the highest efficiency in degrading Rhodamine B dye. This concentration was therefore selected to investigate the effect of varying initial dye concentrations. Figure 7 illustrates the results for dye concentrations ranging from 6 to 60 mg/L. At the initial stages, an increase in RhB concentration led to a higher number of dye molecules adsorbed on the catalyst surface, which resulted in a notable reduction in the number of available active sites. Additionally, the penetration of light energy to the catalyst was hindered by the presence of dye molecules.¹⁶ Despite this, over a period of 120 minutes, some dye degradation occurred as dye molecules gradually decomposed. As indicated in Table 4, the removal efficiency (W_r) was highest at a concentration of 10 mg/L, achieving a value of 97%, which signifies optimal performance for achieving a clear solution.

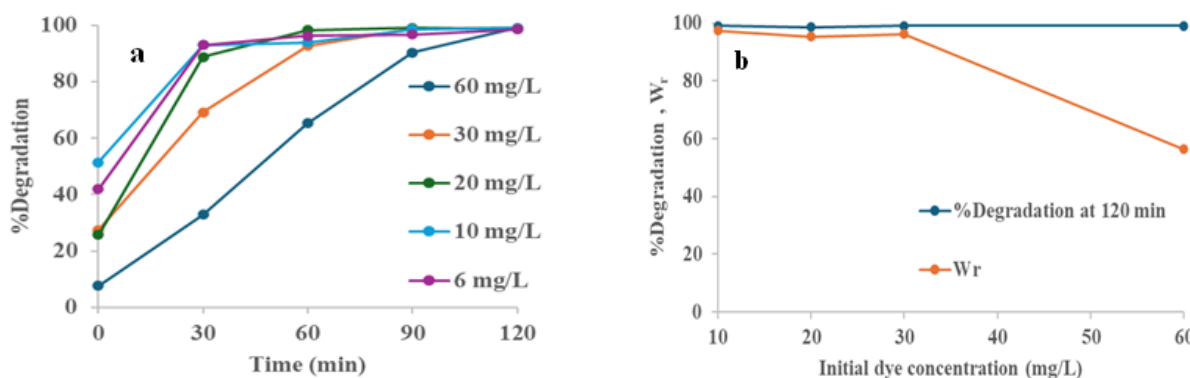


Figure 7. (a) Degradation and (b) Removal efficiency (W_r) of Rhodamine B dye using green 0.5% Cu-TiO₂ photocatalyst at different initial dye concentrations under visible light irradiation.

Table 4. Rhodamine B degradation using green 0.5% Cu-TiO₂ photocatalyst at different initial dye concentrations under visible light irradiation

| Initial dye concentration | %degradation | W_c (%) | W_r (%) |
|---------------------------|--------------|-----------|-----------|
| 6 | 100 | 7 | 93 |
| 10 | 100 | 3 | 97 |
| 20 | 100 | 5 | 95 |
| 30 | 100 | 4 | 96 |
| 60 | 100 | 44 | 56 |

Conclusion:

The synthesis of green titanium dioxide using environmentally friendly methods proves both practical and sustainable. The soft-template method yielded titanium dioxide with solely the anatase phase, while the use of *Brassica oleracea* leaf extract as a reducing agent produced a mixed anatase-brookite phase. This mixed phase is advantageous as it forms heterojunctions that facilitate charge separation and mitigate electron-hole recombination. Titanium dioxide synthesized via the soft-template and green methods had particle sizes of 15.17 nm and 7.71 nm, respectively. The smaller particle size from green synthesis provides a larger surface area, enhancing light exposure. To improve photocatalytic activity under visible light, copper was incorporated into the titanium dioxide. The mixed anatase-brookite phase was retained, and no distinct Cu peaks were detected, suggesting effective dispersion and integration of Cu within the titanium dioxide lattice. For Rhodamine B degradation, the green titanium dioxide achieved a degradation rate of 100%, compared to 98% with the soft-template method, under UV light within 90 minutes. The optimal Cu concentration for Rhodamine B degradation was 0.5% wt, resulting in 100% degradation and a removal efficiency (W_r) of 97% under visible light irradiation within 120 minutes. Increasing the initial dye concentration initially slowed degradation due to reduced light penetration caused by dye molecules obstructing the catalyst. However, with extended irradiation time, degradation increased. The most effective dye concentration was found to be 10 mg/L, with a degradation rate of 100% and a removal efficiency of 97% under visible light within 120 minutes.



References:

1. Ahuj T, Brighu U, Saxena K. J Water Process Eng, 2023;53:103759.
2. Hampel B, Pap Z, Sapi A, Szamosvolgyi A, Baia L, Hernadi K. Catalyst, 2020;10:85.
3. Rahman Md, Rahman Md, Alum N. Curr. Res. Green Sustainable Chem., 2023;7:100383.
4. Ying Pei L, Ying Chin L. Key Eng Mater, 2019;797:87-91.
5. Pushpamalini T, Keerthana M, Sangavi R, Nagaraj A, Kamaraj P. Mater Today, 2021;40:S180-S184.
6. Al-Buriah A, Al-Gheethi A, Kumar P, Radin M, Yusof H, Alshalif A, Khalifa N. Chemosphere, 2022;287:132162.
7. Reddam H, Elmail R, Lloria S, Monrós Tomás G, Reddam Z, Coloma-Pascual F. Bol. Soc. Esp. Ceram. Vidrio, 2020;59:38-148.
8. Ze See X, Sieng Yeo W, Saptorio A. Chem. Eng. Res. Des., 2024;206:108-109.
9. Niteen S, Sudhir S, Govind G, Sunit B. ChemistrySelect, 2021;6:8861-8867.
10. Chalastara K, Guo F, Elouatik S, Demopoulos G. catalyst, 2020;10:2-18.
11. Sukidpaneenid S, Soison P, Jarussophon S, Weerapreechachai S, Huajaipet P, Chawengkijwanich C. Adv Powder Technol, 2024;35:104552.
12. Kayani Z, Ashfaq M, Riaz S, Naseem S. Opt. Mater., 2022;132:12809.
13. Hossain S, Ahmed S. Results Mater., 2023;20:100492.
14. Guang Li J, Ishigaki T, Sun X. J. Phys. Chem. C. 2007;111:4969-4976.
15. Spilarewicz-Stanek K, Jakimińska A, Kisielewska A, Batory D, Piwoński I. mater., 2020;13:3-21.
16. A. Kahtani. J Biomater Nanobiotechnol, 2017;8:66-82.



HYDROGEN PRODUCTION FROM CO₂ GASIFICATION OF BIOCHAR USING CaCO₃ INCORPORATED WITH CATALYTIC WATER-GAS SHIFT REACTION

Bannarat Jaroendee,¹ Nipitpon Panarmasar,² Prapan Kuchonthara^{2,3,*}

¹Department of Petrochemistry and Polymer Science, Faculty of Science, Chulalongkorn University, Bangkok, Thailand

²Department of Chemical Technology, Faculty of Science, Chulalongkorn University, Bangkok, Thailand

³Center of Excellence in Catalysis for Bioenergy and Renewable Chemicals, Bangkok, Thailand

*e-mail: prapan.k@chula.ac.th

Abstract:

Alternative renewable energy consumption has been interesting in reducing CO₂ emissions that are causing the global warming problem. Biochar, one of the quality carbon sources, offers potential sustainable hydrogen production. The most widely used method to produce hydrogen is steam reforming. However, the amounts of CO₂ are still emitted during the process. The CO₂ sorption-enhanced water-gas shift (SEWGS) reaction is a technology that combines CO₂ adsorption with hydrogen production. The calcium looping process involves two main chemical reactions, CaO carbonation with CO₂ and catalytic WGS. In order to produce rich hydrogen, syngas from CO₂ gasification of biochar incorporated with catalytic WGS was investigated. This study aimed to study hydrogen production via CO₂ gasification of biochar conjugated with catalytic-enhanced WGS. In gasification, calcium carbonate (CaCO₃) was used as an in-situ CO₂ source while A bimetallic Ni-Cu/γ-Al₂O₃ and a precursor for the catalyst in the SEWGS reaction. The catalyst was employed in conjunction with CaO which could be derived from the calcination of CaCO₃. Results reveal that utilizing CaCO₃ significantly increases syngas production at 900°C. In the subsequent SEWGS reaction at 700°C, the combined effect of CO₂ adsorption by CaO and the catalytic activity of Ni-Cu/γ-Al₂O₃ results in a higher yield and concentration of hydrogen. The structural and catalytic properties of the materials were characterized using X-ray diffractometry (XRD) and temperature-programmed reduction (TPR).

Introduction:

Energy plays an important role in technological, industrial, and economic around the world. The major energy resource is fossil energy. The amount of carbon dioxide emission from fossil fuels has risen adding to threatening the environment and having a massive impact on global warming. The demand for energy consumption has constantly increased consequence fossil fuel has reduced due to economic and industrial growth. Reaching net zero emissions has interest worldwide. To address this issue, renewable energy has become increasingly important and has been the subject of research for decades. One of the most interesting forms of renewable energy is hydrogen, due to its clean and non-toxic properties. It can be produced from biomass through thermochemical processes.¹⁻³ Biochar known as carbon long-term storage that is produced from biomass pyrolysis can be a good feedstock to achieve fuel energy. It found that gasification of biochar produces less tar and a high reaction rate due to high porosity.^{4, 5} The gasification process is efficient and has the potential to minimize negative environmental impacts.⁶ Using CO₂ as a gasifying agent in biochar gasification, mainly produces CO through Boudouard reaction.⁷ It can be represented by equation (2). Subsequently, a standard reaction known as the water-gas shift reaction (WGS) involves reacting carbon monoxide with steam in the presence of a catalyst to produce carbon dioxide

and additional hydrogen.⁸ This process can be represented by equation (3). However, carbon dioxide is still involved in the hydrogen production process either as a reactant or as a product. The calcium oxide-based sorbent is used in the carbon dioxide capture process to enhance hydrogen yield. Research into the use of in-situ CaO derived from CaCO₃ in calcium looping is also of significant interest because CaO and CaCO₃ are abundant, environmentally friendly, and cost-effective.⁹ Moreover, CaO can act as a catalyst in biomass gasification and pyrolysis and as an adsorbent to enrich hydrogen in gas production.¹⁰⁻¹³



CaCO₃ is not only used as a carbon dioxide capture but also as a carbon dioxide resource.¹⁴ It can generate carbon dioxide as a syngas for the gasification of biochar that can be expressed by calcination as shown in equation (1). The gas product mainly contains CO because of the utilization of CO₂ gasification of biochar. Since the WGS plays a major role in hydrogen production, using a proper catalyst can enhance hydrogen productivity. The Ni-based catalyst is one of the catalysts that has been widely used in steam reforming of hydrocarbons due to their high catalytic activity. The bimetallic Ni-Cu is the most interesting catalyst that has been studied due to its selectivity to WGS instead of another reaction which is methanation. Thus using bimetallic Ni-Cu gains selectivity and catalytic activity improvement compared to mono-metallic catalysts.^{15, 16} However, several factors contribute to hydrogen production such as biomass type, temperature, amount of feedstock ratio including catalyst.¹⁷⁻²³

Therefore, to achieve a decrease in carbon dioxide emissions released into the atmosphere. This work aimed to study hydrogen production from biochar by utilization of CO₂ released from CaCO₃. A two-stage fixed-based reactor was employed to investigate the combination of two systems between CO₂ gasification and CaO-based sorption-enhanced water-gas shift reaction. The effect of CaCO₃, CaO, and the bimetallic catalyst were examined with the purpose of the high yield of hydrogen.

Methodology:

2.1. Material Synthesis

In this study, 5 wt% of bimetallic Ni-Cu on a γ -Al₂O₃ support was used as a WGS catalyst. The Ni-Cu/ γ -Al₂O₃ catalyst was synthesized by the wet impregnation method. Ni(NO₃)₂·6H₂O (KemAus, Australia, pure 99%) and Cu(NO₃)₂·3H₂O (Qrec, New Zealand, pure 99.5%) were used as a precursor. A solution containing these precursors was dissolved in 20 mL of deionized water, followed by the addition of 10 g of Al₂O₃. The solution was stirred at 90 °C for 3 h. After that, the catalyst was dried at 110 °C for 24 h and calcined at 500 °C for 3 h. Biochar derived from bamboo was used as a biomass feedstock, with particle diameters ranging from 250 to 425 μm . Industrial high-purity calcium carbonate (CaCO₃) (KemAus, Australia, Analytical reagent) was used as a CO₂ resource. Calcium oxide (CaO) is used as CO₂ adsorption, which is purchased from KemAus, Australia.

2.2. Material Characterization

Biochar was characterized based on their compositions through the proximate analysis and Ultimate analysis, which are shown in Table 1. The Ni-Cu/ γ -Al₂O₃ bimetallic catalysts were examined for their crystallinity by the X-ray diffraction (XRD) technique; Bruker, model D8 advance with CuK α radiation $\lambda = 1.5406 \text{ \AA}$ and an X-ray power of 40 kV and 40 mA. over a range of $2\theta = 5^\circ$ to 80° . The catalyst was also characterized using temperature-programmed reduction (TPR).



2.3. Equipment configuration

The experiments were conducted using a two-stage fixed-bed reactor system, designed for biochar gasification at 900 °C followed by a WGS at 700 °C. A schematic diagram of the reactor setup is shown in **Figure 1**. The system comprises of two separate stages, with the initial stage dedicated to biochar gasification, and the subsequent stage focusing on the WGS, involving the utilization of CaO alongside a bimetallic Ni-Cu/ γ -Al₂O₃ catalyst. At first, quartz wool was placed in both the first and second stages of the reactor to prevent the samples from falling. In the second stage, a mixture of 1 g of 5 wt% Ni-5 wt% Cu/ γ -Al₂O₃ catalyst and 0.56 g of calcium oxide was introduced. For the first stage, A mixture of 0.12 g of biochar and 1 g of CaCO₃ was placed into a silicone tube, positioned at the top of the upper section of the reactor to regulate the feeding. Prior to starting the experiment, the reactors were purged with nitrogen (N₂) at a flow rate of 100 mL/min for 30 minutes to remove any residual air. Nitrogen is not considered in gas concentration calculation. After purging, both electric furnaces were heated up to their target temperatures. Once the desired temperatures were achieved, the N₂ flow rate was reduced to 40 mL/min, and steam/N₂ was introduced at the same flow rate. Herein, water was pumped into the system at a rate of 0.1 mL/min. The biochar and CaCO₃ mixture contained in the silicone tube was then dropped into the first stage. The released volatiles subsequently passed through the second stage. After that, the condensable volatiles produced were trapped in an ice-cooled flask and water vapor was adsorbed by silica gel. The remaining gas products were collected in gas bags at 5-minute intervals for a total duration of 30 minutes.

Table 1. Proximate and ultimate analysis of bamboo char

| | Proximate analysis (wt%) | | | | Ultimate analysis (wt%) | | | |
|-------------|--------------------------|----------------|----------------|-----------------|-------------------------|------|-------|------|
| | M ^a | V ^a | A ^a | FC ^a | C | H | O | N |
| Bamboo char | 6.97 | 21.54 | 1.41 | 70.08 | 75.17 | 2.84 | 21.33 | 0.66 |

^aFor proximate analysis, M, V, A and FC stand for moisture, volatiles, ash and fixed carbon, respectively.

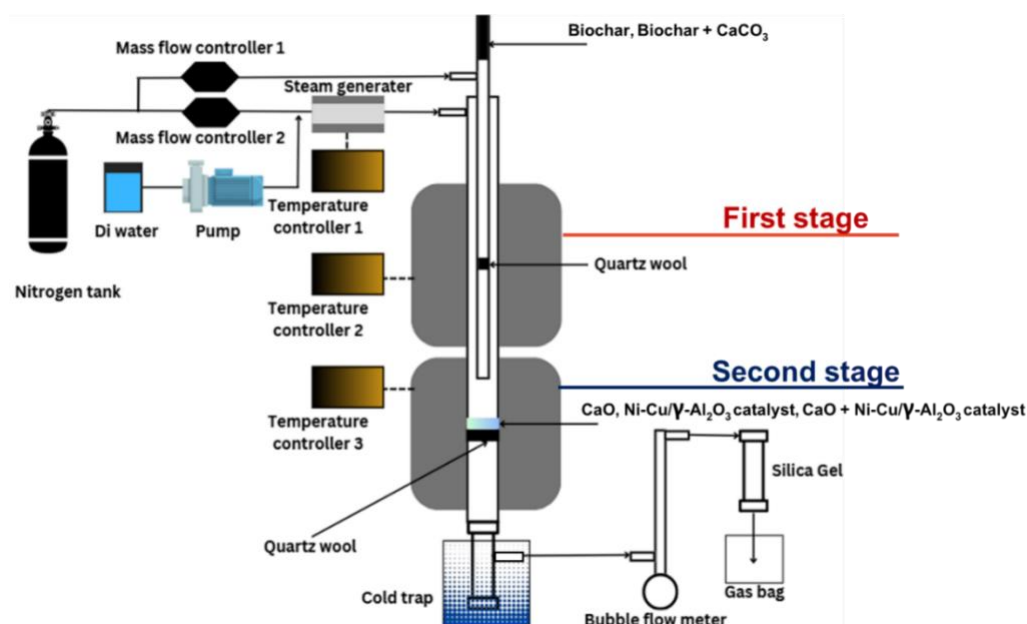


Figure 1. Schematic diagram of Equipment configuration setup.

3.1. Proximate and ultimate analyses

Table 1 indicates that bamboo was rich in fixed carbon content (70.08 wt%). The bamboo had a low amount of moisture, volatile, and ash content components (6.97, 1.41, and 21.54 wt%). Ultimate analysis reveals the elemental content such as carbon, hydrogen oxygen, and nitrogen. The analysis investigates the purity of total carbon and the results show the high fixed carbon and high carbon content which is a suitable property for the gasification process.²⁴

3.2. XRD Characterization

The XRD patterns of the Al₂O₃-supported Ni-Cu/ γ -Al₂O₃ catalyst, shown in **Figure 2**, exhibit broad diffraction peaks at 36.99°, 45.75°, and 67.18°, characteristic of γ -Al₂O₃. Notably, no distinct peaks corresponding to crystalline NiO or CuO phases are observed. This suggests that the Ni and Cu species may be highly dispersed, either as small crystalline domains below the detection limit of XRD or as amorphous oxide phases that interact with γ -Al₂O₃ support.²⁵

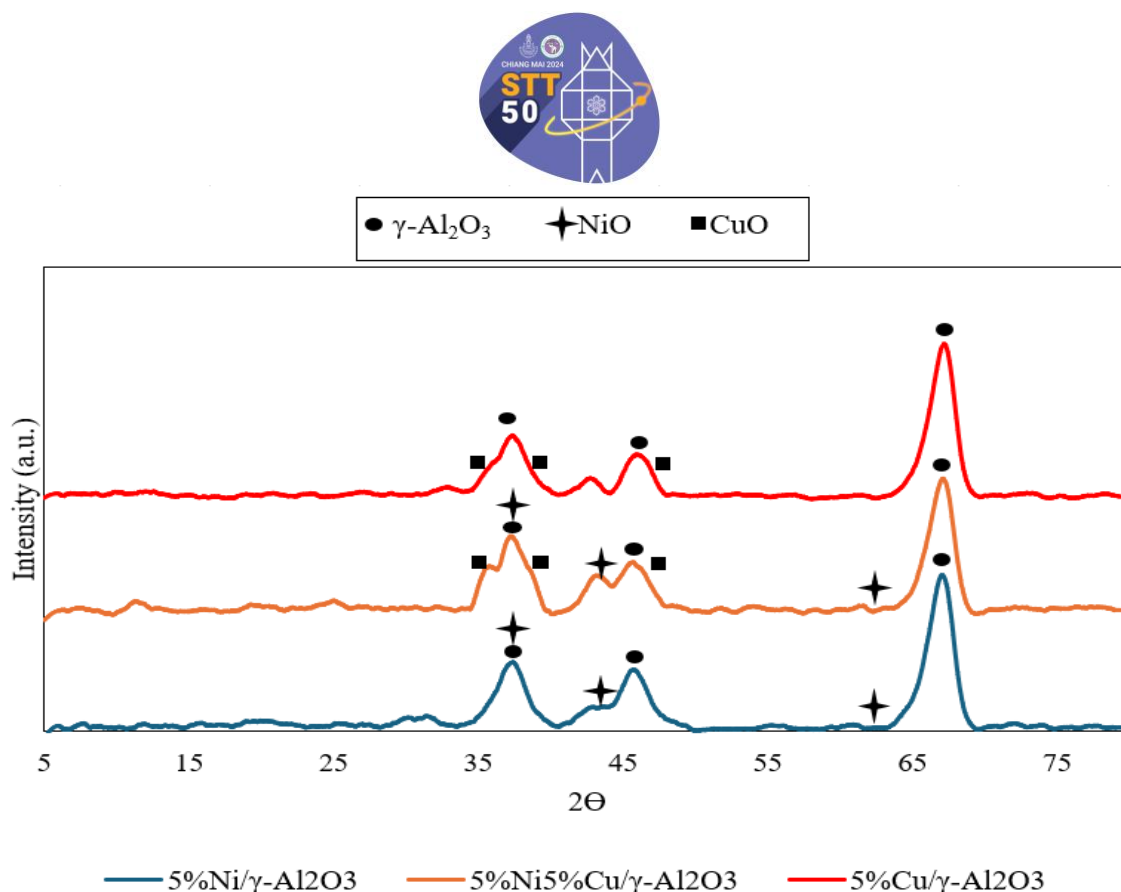


Figure 2. XRD patterns of catalysts.

3.3 Hydrogen-Temperature-Programmed Reduction (H_2 -TPR)

The H_2 -TPR 5%Ni5%Cu/ γ - Al_2O_3 was subsequently tested for clarification. The reducibility of the catalysts was evaluated using H_2 -TPR, with the results displayed in **Figure 3**. The 5 wt% Ni/ γ - Al_2O_3 catalyst exhibited characteristic reduction peaks over a broad temperature range of 500–800 °C. This broad range indicates a well-dispersed NiO phase with a small crystalline size, which promotes strong interactions between NiO and the Al_2O_3 support. These interactions promote the formation of $NiAl_2O_4$ and the entering of NiO into the pore structure, leading to a high reduction temperature of 733 °C, attributed to the reduction of bulk NiO.²⁶ The H_2 -TPR profile of the 5 wt% Cu/ γ - Al_2O_3 catalyst displayed a distinct reduction peak at 253 °C, corresponding to the reduction of CuO to Cu^0 .²⁷ For the bimetallic Ni-Cu/ γ - Al_2O_3 catalyst, reduction peaks for both NiO and CuO were observed. The peak at 252 °C was attributed to the reduction of CuO, while the peak in the range of 550–580 °C was associated with the reduction of NiO. The presence of Cu lowers the reduction temperature of NiO, as Cu facilitates the reduction of NiO and improves the dispersion of Ni species.^{28, 29} The H_2 -TPR results confirm that both NiO and CuO are present in the prepared Ni-Cu/ γ - Al_2O_3 catalyst.

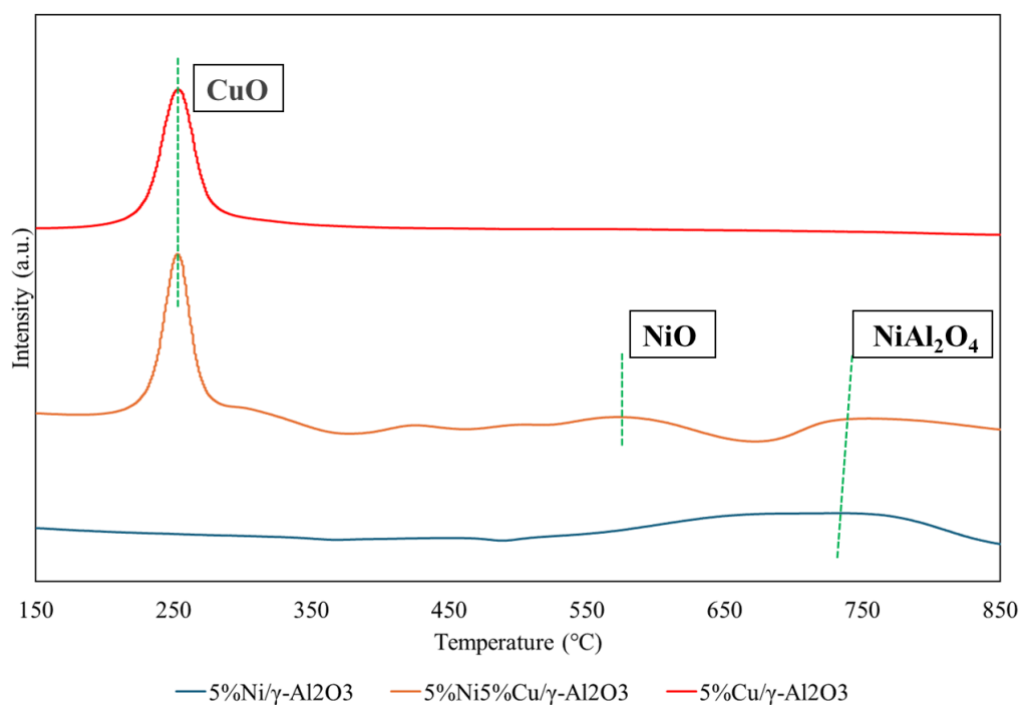


Figure 3. H₂-TPR spectra of catalysts.

3.4 Scanning electron microscopy (SEM) micrographs and energy-dispersive X-ray spectroscopy (EDS)

To determine the morphology of the added Ni-Cu/ γ -Al₂O₃, scanning electron microscopy (SEM) micrographs and energy-dispersive X-ray spectroscopy (EDS) analysis were obtained, as shown in **Figure 4a-e**. The SEM images of Ni-Cu/ γ -Al₂O₃ were indistinguishable from those of Al₂O₃. The EDS maps of Ni, Cu, O, and Al were more informative and showed uniform distributions of Ni and Cu over the entire surface. The weight percentages of elements and the EDS spectrum are shown in **Figure 4f**.

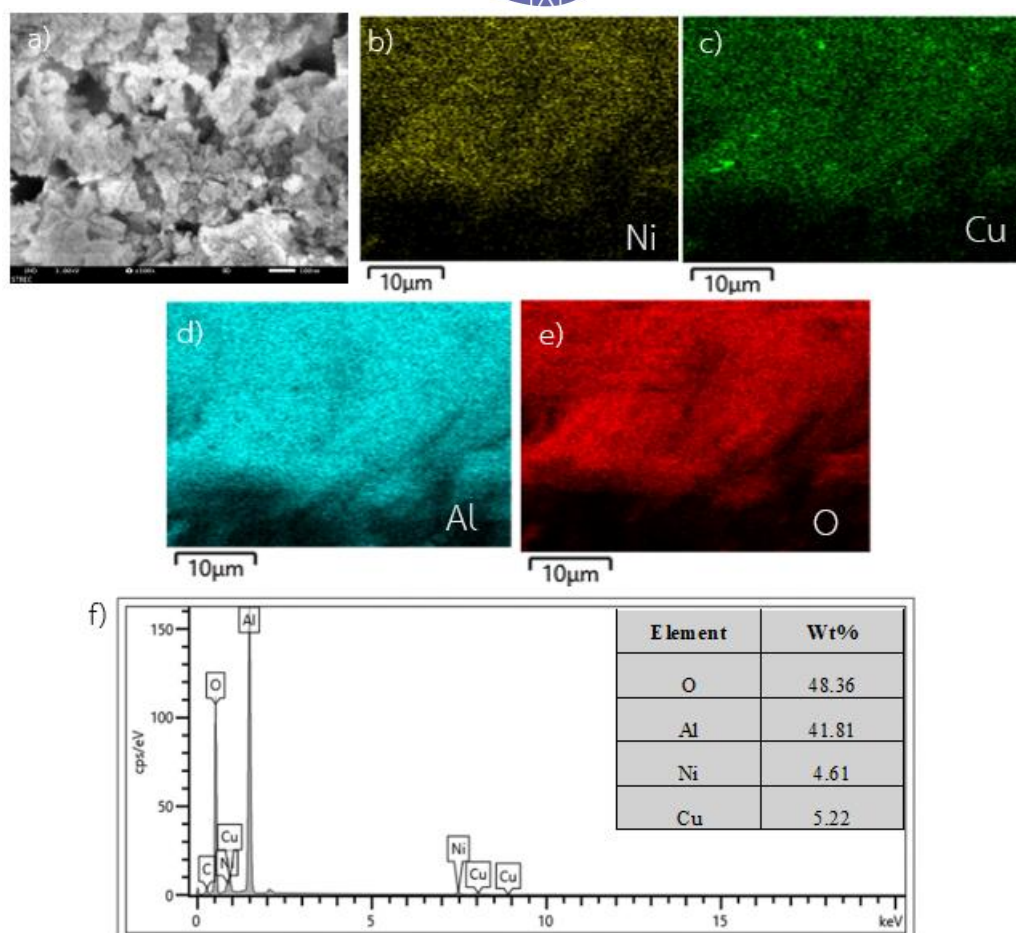


Figure 4. (a) SEM image of the 5%Ni5%Cu/γ-Al₂O₃ sample; (b–d) are EDS maps of Ni, Cu, Al and O, taken from the region indicated by the (a) and (f) are EDS spectrum, also showing the weight percentages on the table.

3.5. Gasification of biochar

Gas composition was analyzed using Gas Chromatography (GC) regarding standard gases. Hydrogen (H₂), nitrogen (N₂), carbon monoxide (CO), and carbon dioxide (CO₂) were detected, while methane (CH₄) was not observed in any of the experiments conducted after the biochar gasification at 900 °C. **Figure 5** shows the comparison of syngas composition resulting from CO₂ gasification using different feedstocks. The BBC-CaCO₃ sample, which utilized CaCO₃, produced 6.46 mmol/g of H₂, 56.88 mmol/g of CO, and 41.20 mmol/g of CO₂. In contrast, the BBC-CO₂ sample, which used direct CO₂, yielded 5.89 mmol/g of H₂, 27.01 mmol/g of CO, and 21.94 mmol/g of CO₂. These results suggest the calcination generated CO₂, promoting the Boudouard reaction, which contributes to higher CO yield.

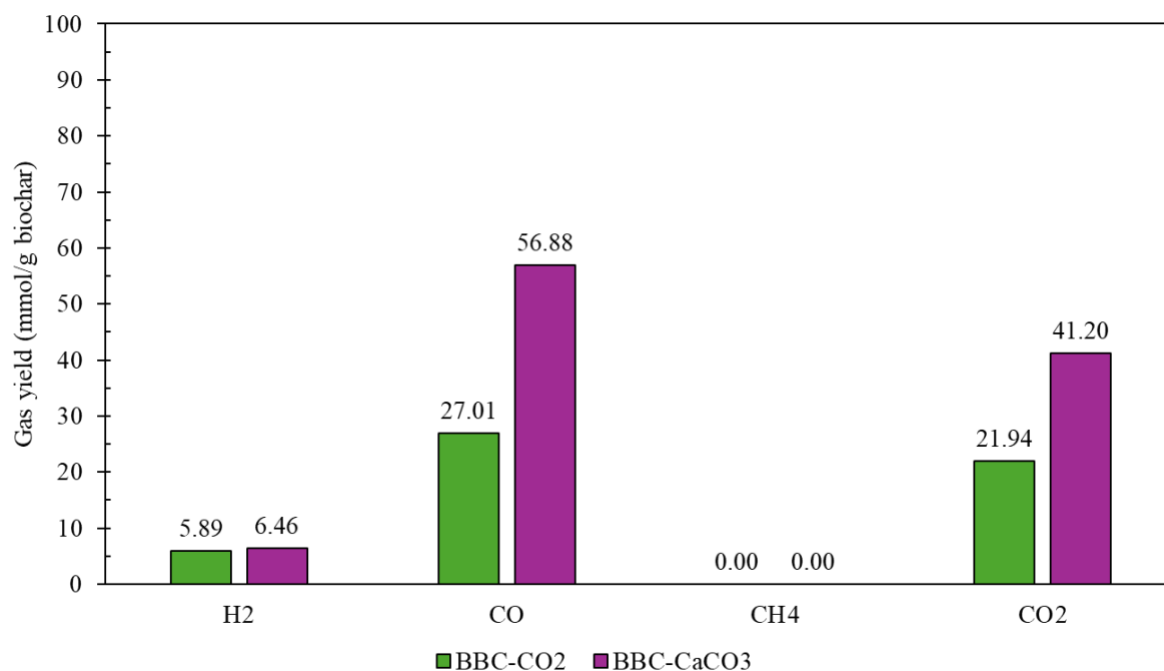


Figure 5. The comparison of syngas composition between using CO₂ and CaCO₃ for CO₂ gasification

Figure 6 illustrates the syngas composition resulting from gasification with CaCO₃ in the absence of steam. The abbreviation BBC-Al₂O₃ refers to the experiment using bamboo biochar in the first stage (the gasification zone) and inert Al₂O₃ in the second stage (catalytic WGS). The BBCCaCO₃-Al₂O₃ condition involves using CaCO₃ with bamboo biochar in the first stage, while the second stage still contains Al₂O₃. Under the BBCCaCO₃-Al₂O₃ condition, a significant increase in CO yield is observed, rising from 2.61 to 56.88 mmol/g of biochar. Simultaneously, CO₂ concentration also increases to 44.38 mmol/g. This confirms the role of CaCO₃ as a potential CO₂ source, promoting CO₂ gasification of biochar at the desired temperature. Furthermore, the BBCCaCO₃-CaO/Al₂O₃ condition, where bamboo biochar and CaCO₃ are mixed in the first stage and CaO/Al₂O₃ is used in the second stage, demonstrates a substantial reduction in CO₂ concentration (from 44.38 to 23.65 mmol/g) compared to BBCCaCO₃-Al₂O₃. This reduction indicates the effective CO₂ capture by the CaO sorbent in the second stage.³⁰

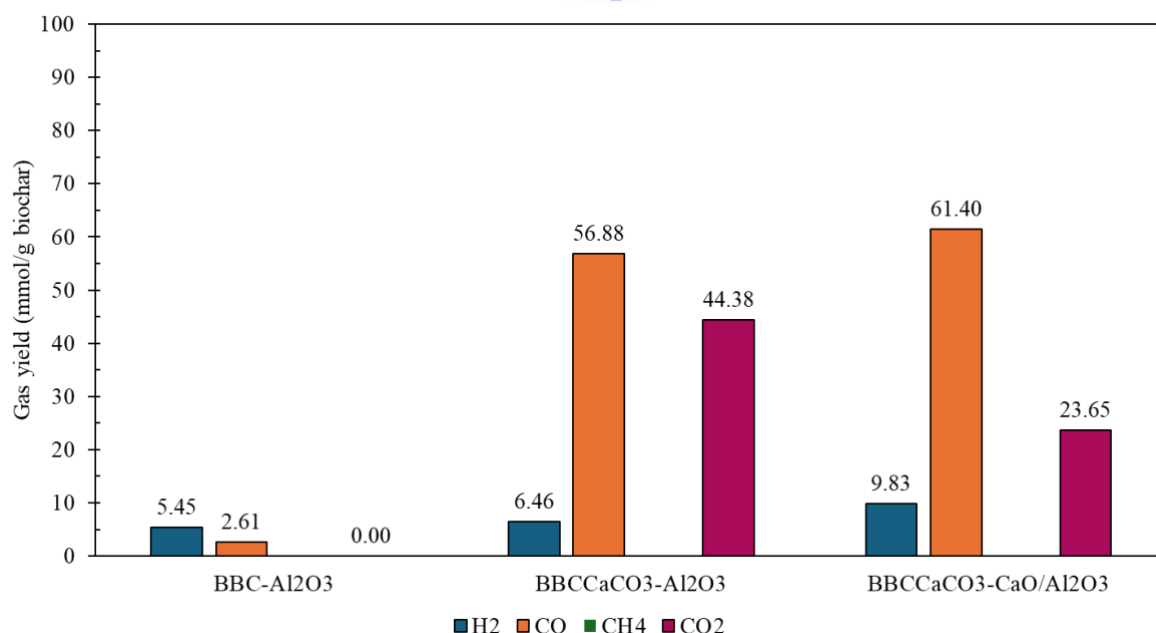


Figure 6. Syngas composition with no steam treatment.

3.6. Catalytic WGS

Figure 7 illustrates the impact of steam addition (-S) in the second stage on the gas composition. In the BBCCaCO₃-Al₂O₃-S condition (bamboo biochar and CaCO₃ in the first stage, Al₂O₃ with steam in the second stage), CO production increased significantly from 1.31 to 57.93 mmol/g, while CO₂ production reached 48.32 mmol/g, primarily due to enhanced CO₂ gasification. In contrast, the BBCCaCO₃-CaO/Al₂O₃-S condition, with CaO added to the second stage, showed a slight decrease in both CO (44.52 mmol/g) and CO₂ (36.19 mmol/g) due to the CO₂ adsorption capacity of CaO. Subsequently, the WGS was promoted, resulting in increased hydrogen production. Compared to BBCCaCO₃-Al₂O₃-S without CaO, introducing the bimetallic Ni-Cu/ γ -Al₂O₃ catalyst in the second stage decreased CO from 57.93 to 31.48 mmol/g, while it increased H₂ from 6.14 to 19.66 mmol/g, and CO₂ from 48.32 to 56.25 mmol/g. This indicates that the catalyst enhances CO consumption, driving both H₂ and CO₂ production through the WGS reaction. Finally, the BBCCaCO₃-CaONiCu/Al₂O₃-S condition, combining CaO and the catalyst, resulted in the highest H₂ yield (a further increase of 5.56 mmol/g compared to BBCCaCO₃-NiCu/Al₂O₃-S), while CO decreased by 12.29 mmol/g. CO₂ production also decreased by 12.97 mmol/g due to carbonation by CaO. These results demonstrate the effectiveness of combining CaO and the Ni-Cu/ γ -Al₂O₃ catalyst in maximizing hydrogen production.

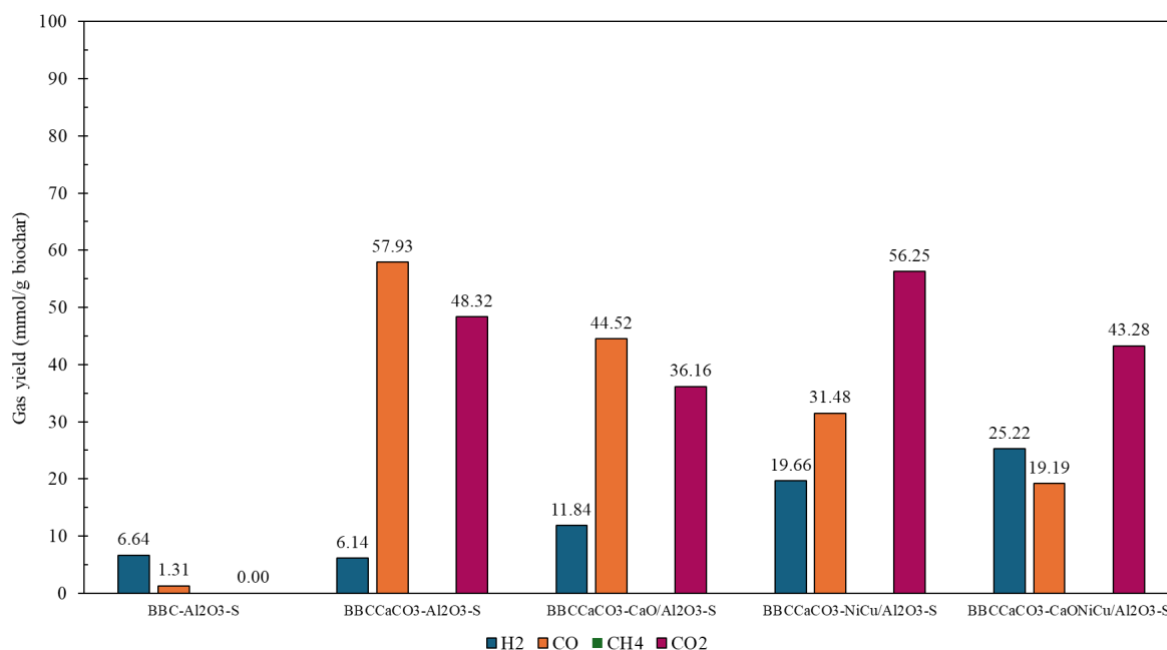


Figure 7. Syngas composition with steam treatment.

Conclusion:

This study experimentally investigates hydrogen-rich production via CO₂ gasification of biochar in a two-stage fixed-bed reactor system. The process utilizes CaCO₃ as an in-situ CO₂ source, coupled with a bimetallic 5%Ni5%Cu/ γ -Al₂O₃ catalyst and CaO as a sorbent. The addition of CaO derived from CaCO₃ calcination, was found to significantly enhance hydrogen production due to CO₂ sorption. The bimetallic catalyst further promotes hydrogen generation by driving the water-gas shift reaction. When both CaO and the catalyst are used together, the highest hydrogen yield is achieved, demonstrating the benefits of their combined use. These findings offer valuable insights for the development of advanced hydrogen production processes within a CO₂ looping framework, with potential for reducing CO₂ emissions through the utilization of biochar.

Acknowledgements:

This research was supported by Chulalongkorn University. Synthesis and characterization instruments were supported by Department of Chemical Technology, Faculty of Science, Chulalongkorn University.

References:

1. Pareek A, Dom R, Gupta J, Chandran J, Adepu V, Borse PH. Mater. Sci. Energy Technol. 2020;3:319-27.
2. Nnabuiife SG, Oko E, Kuang B, Bello A, Onwualu AP, Oyagha S, Whidborne J. Sustainable Chemistry for Climate Action. 2023;2:100024.
3. Midilli A, Ay M, Dincer I, Rosen MA. Renewable Sustainable Energy Rev. 2005;9:255-71.
4. Abdullah H, Wu H. Energy Fuels. 2009;23:4174-81.
5. Tomczyk A, Sokołowska Z, Boguta P. Rev. Environ. Sci. Bio/Technol. 2020;19:191-215.
6. Farzad S, Mandegari M, Görgens J. Biofuel Res. J. 2016;3:483-95.
7. Duman G, Uddin MA, Yanik J. Fuel Process. Technol. 2014;118:75-81.
8. Chen W-H, Chen C-Y. Appl. Energy. 2020;258:114078.



9. Pecharaumporn P, Wongsakulphasatch S, Glinrun T, Maneedaeng A, Hassan Z, Assabumrungrat S. *Int. J. Hydrogen Energy*. 2019;44:20663-77.
10. Islam M. *Fuel*. 2020;267:
11. Ortiz C, Valverde JM, Chacartegui R, Perez-Maqueda LA, Giménez P. *Renewable Sustainable Energy Rev*. 2019;113:109252.
12. Acharya B, Dutta A, Basu P. *Int. J. Hydrogen Energy*. 2010;35:1582-9.
13. Zhang L, Zhang B, Yang Z, Yan Y. *RSC Advances*. 2014;4:39145-55.
14. Wang K, Chen J, Wang T, Hong J, Zhao P, Anthony E. *Chem. Eng. J*. 2023;472:144857.
15. Kawi S, Ashok J, Wai MH. *ChemCatChem*. 2018;10:
16. Gkanas E, Khzouz M. *Fuel*. 2018;232:
17. Syarif T, Sulisty H, Sediawan W, Budhijanto B. *Jurnal Bahan Alam Terbarukan*. 2018;6:198-204.
18. Gómez-Vásquez RD, Castiblanco EA, Zapata Benabith Z, Bula Silvera AJ, Camargo-Trillos DA. *Biomass Bioenergy*. 2021;153:106207.
19. Zhang G, Suo XL, Sheng JG, Tan X. *IOP Conference Series. Earth and Environmental Science*. 2021;701:
20. Selvarajoo A. *IOP Conference Series: Earth and Environmental Science*. 2020;489:012033.
21. Perander M, DeMartini N, Brink A, Kramb J, Karlström O, Hemming J, Moilanen A, Kontinen J, Hupa M. *Fuel*. 2015;150:464-72.
22. Hwang K-R, Lee C-B, Park J-S. *J. Power Sources*. 2011;196:1349-52.
23. Chimpae S, Wongsakulphasatch S, Vivanpatarakij S, Glinrun T, Wiwatwongwana F, Assabumrungrat S. *IOP Conf. Ser.: Mater. Sci. Eng*. 2020;736:022006.
24. You S, Ok YS, Chen SS, Tsang DCW, Kwon EE, Lee J, Wang C-H. *Bioresour. Technol*. 2017;246:242-53.
25. Zhu T, Song H, Li F, Chen Y. *Catalysts*. 2020;10:274.
26. Chen S, Zhou G, Xie H, Jiao Z, Zhang X. *Appl. Catal., A*. 2019;569:35-44.
27. Mao Q, Gao Z, Liu X, Guo Y, Wang Y, Ma D. *Catal. Sci. Technol*. 2024;14:3448-58.
28. Nataj SMM, Alavi SM, Mazloom G. *J. Energy Chem*. 2018;27:1475-88.
29. Wu Y, Gui W, Liu X, Zhang L, Wang S, Wang Z, Zhang C. *Catal. Lett*. 2020;150:2427-36.
30. Sun S, Lv Z, Qiao Y, Qin C, Xu S, Chunfei W. *Carbon Capture Sci. Technol*. 2021;1:100001.



HYDROGEOCHEMICAL CHARACTERIZATION AND SALINITY PROCESSES IN GROUNDWATER OF KHOK SI SUBDISTRICT, KHON KAEN PROVINCE, THAILAND

Sutthipong Taweelarp*, Arisara Khotmanee, Potpreecha Pondthai, Porramin Jamnongpen
Department of Geotechnology, Faculty of Technology, Khon Kaen University, Thailand
*e-mail: sutthita@kku.ac.th

Abstract:

This study investigates the hydrogeochemical characteristics and salinity processes of groundwater in the Khok Si Subdistrict area, located in Mueang Khon Kaen District, Khon Kaen Province. Ten groundwater samples were systematically collected and analyzed for major ions to determine the hydrogeochemical facies and to understand the mechanisms influencing groundwater composition. The analysis identified two primary facies: Sodium-Chloride, which predominates in the southern part of the study area, and Calcium-Bicarbonate, which is mainly present in the northern discharge zones. Multivariate statistical methods, including Hierarchical Cluster Analysis and Principal Component Analysis, were employed to identify patterns and correlations among ion concentrations. The results indicate that groundwater salinity is primarily controlled by the dissolution of soluble salts and the weathering of silicate minerals. Geochemical diagrams, including the Gibbs and Gaillardet plots, were used to assess the impact of various geochemical processes, revealing that water-rock interactions and evaporation significantly affect groundwater chemistry. This comprehensive analysis provides valuable insights into the hydrogeochemical processes in the region, highlighting the importance of continuous groundwater quality monitoring and informing sustainable water resource management strategies.

Introduction:

Groundwater is a vital resource in many regions, particularly in northeastern Thailand, where surface water supplies may be limited and irrigation infrastructure is insufficient. In Khon Kaen Province, which is located in northeastern Thailand, groundwater is extensively used for both consumption and agricultural purposes. However, the province faces significant challenges due to increasing groundwater salinity.^{1,2} This rising salinity is attributed to a combination of anthropogenic activities, such as over-pumping and land use changes, as well as natural processes related to the underlying geology.³ The Maha Sarakham Formation, which underlies extensive areas of Khon Kaen Province, consists of clastic sedimentary rocks and evaporites.⁴ As groundwater flows through these geological formations, soluble salts from the evaporites dissolve, resulting in elevated salinity levels in the groundwater.

Khok Si Subdistrict, located within Khon Kaen Province, faces a significant challenge due to high groundwater demand and increasing groundwater salinization. To effectively manage and protect this important resource, it is essential to understand the hydrogeochemical processes driving salinization. This study aims to evaluate the hydrogeochemical characteristics of groundwater in Khok Si Subdistrict, identify the primary factors contributing to salinization, and assess the potential impacts on groundwater quality and availability. Multivariate statistical methods, including Hierarchical Cluster Analysis and Principal Component Analysis, are utilized to identify and assess the mechanisms behind these processes. The goal is to gain a comprehensive understanding of groundwater's hydrogeochemical characteristics through both graphical and multivariate statistical approaches. This deeper insight into hydrogeochemical processes and groundwater evolution

will support effective management and sustainable utilization of groundwater resources while addressing future salinization concerns.

Methodology:

Study Area

This study focuses on the Khok Si Subdistrict area within Mueang Khon Kaen District, Khon Kaen Province, which covers approximately 36 square kilometers. The region encompasses both residential and agricultural zones. The study area (**Figure 1**) is situated within the Khon Kaen Basin, at the western edge of the Khorat Plateau. The near-surface materials consist of unconsolidated Quaternary alluvial sediments, with thicknesses ranging from a few meters to over 5 meters. These sediments are composed of a mixture of loess, fine-grained materials, and gravel.⁵

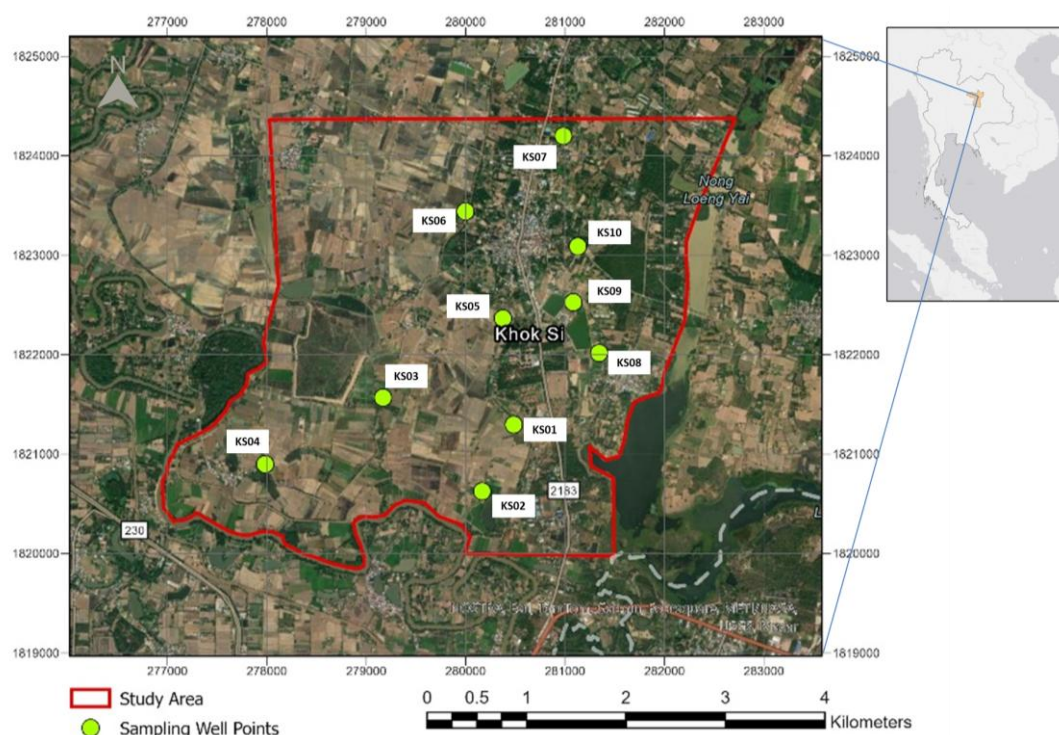


Figure 1 The location of the study area and the distribution of sampling points

Groundwater Collection and Hydrogeochemical Analysis

In February 2024, ten groundwater samples were collected from the locations shown in **Figure 1**. These samples were obtained from domestic wells, all of which were less than forty meters deep. The samples were stored in high-density polyethylene plastic containers, with preserved under acidified conditions and under non-acidified conditions. Well locations and surface elevations were determined using RTK GNSS modules. Field measurements included the depth to the water table, pH, electrical conductivity (EC), and temperature.

Groundwater samples from the study area were analyzed at the Geochemical Laboratory of the Department of Geotechnology, Faculty of Technology, Khon Kaen University, following standard methods for water and wastewater examination. Major anion, including chloride (Cl^-), carbonate (CO_3^{2-}), and bicarbonate (HCO_3^-), were determined through titration, while nitrate (NO_3^-) was measured using the cadmium reduction method, sulfate (SO_4^{2-}) was analyzed using the turbidimetric method, and fluoride (F^-) was measured using SPADNS Method. For major cations, including calcium (Ca^{2+}), magnesium (Mg^{2+}),



potassium (K^+), and sodium (Na^+), flame atomic absorption spectrometry was employed. The accuracy of the chemical analyses was verified using the ion balance equation, with ion balance errors for the samples found to be within the acceptable range of $\pm 5\%$.

To gain a comprehensive understanding of the hydrogeochemical processes in the study area, a combination of analytical methods was employed. The analysis began with the use of Piper diagrams⁶ to determine the hydrogeochemical facies of the groundwater samples, providing a visual representation of their geochemical characteristics. Subsequently, multivariate statistical methods, including Hierarchical Cluster Analysis (HCA), were applied to group samples with similar characteristics, which facilitated the identification of hydrogeochemical relationships and the definition of chemical endmembers from various origins. Additionally, Principal Component Analysis (PCA) was utilized to reduce the complexity of the groundwater chemistry data, emphasizing the key factors influencing hydrogeochemical processes. Together, these methods provided a detailed and coherent understanding of the hydrogeochemical dynamics within the study area, allowing for more informed interpretation of the groundwater chemistry.

Results and Discussion:

Hydrogeological and Hydrogeochemical Characteristics

Fieldwork data indicate that hydraulic heads in the study area range from 122.48 to 133.64 meters above mean sea level, as shown in the contour map in **Figure 2**. The groundwater flow direction primarily follows the topographic gradient, moving from north to south.

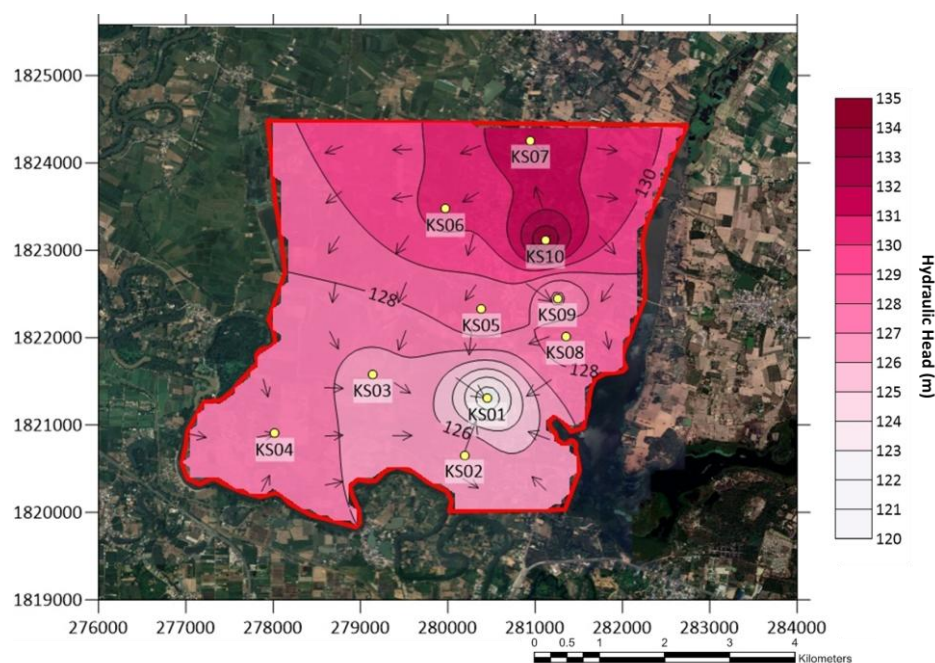


Figure 3 Groundwater contour map and groundwater flow directions of the study area

The results and statistical summary of field measurements and laboratory chemical analyses of groundwater samples, including maximum, minimum, mean, and standard deviation values, are presented in **Table 1**. Groundwater samples from the study area show a wide range of salinity indicators, reflecting significant variations in mineral content. EC ranges from 799 to 20,740 $\mu S/cm$, highlighting the diversity in salinity levels, from fresh to saline groundwater. TDS display a similar range, from 198.67 mg/L to 6,545.33 mg/L,

further emphasizing the variability in dissolved substances. Cl^- concentrations range from 7.26 mg/L to 2,570.5 mg/L, and Na^+ concentrations vary from 14.3 mg/L to 1,608.25 mg/L, both contributing significantly to the overall salinity. K^+ concentrations, though less variable, range from 0.96 mg/L to 12.11 mg/L, having a relatively minor effect on salinity.

Table 1 Results and statistical information of physical and chemical parameters in groundwater samples.

| Sample | EC ($\mu\text{S}/\text{cm}$) | pH | Temp. ($^{\circ}\text{C}$) | Concentration (mg/L) | | | | | | | | | |
|--------|-----------------------------------|------|---------------------------------|----------------------|---------------|--------------|------------------|------------------|-----------------|--------------------|---------------|--------------|------------------|
| | | | | TDS | Na^+ | K^+ | Ca^{2+} | Mg^{2+} | NO_3^- | SO_4^{2-} | Cl^- | F^- | HCO_3^- |
| KS01 | 5,063 | 6.49 | 28.71 | 1,329.33 | 313.70 | 1.56 | 70.94 | 46.30 | 4.97 | 25.64 | 526.36 | 0.65 | 301.77 |
| KS02 | 6,878 | 6.39 | 28.47 | 1,865.33 | 451.30 | 9.31 | 102.20 | 39.30 | 0.00 | 25.18 | 866.68 | 0.61 | 218.86 |
| KS03 | 3,745 | 7.03 | 28.28 | 778.67 | 255.40 | 0.96 | 66.53 | 6.20 | 3.69 | 9.33 | 358.47 | 0.00 | 98.76 |
| KS04 | 20,740 | 5.89 | 28.94 | 6,545.33 | 1,608.25 | 4.45 | 362.32 | 45.80 | 0.00 | 16.13 | 2570.50 | 0.00 | 76.81 |
| KS05 | 7,880 | 6.76 | 29.26 | 2,220.00 | 689.40 | 12.11 | 8.42 | 10.90 | 3.85 | 35.79 | 939.28 | 0.00 | 302.38 |
| KS06 | 3,437 | 6.78 | 29.82 | 921.33 | 209.60 | 6.19 | 98.80 | 13.40 | 125.35 | 19.27 | 276.25 | 0.00 | 160.94 |
| KS07 | 799 | 5.98 | 29.10 | 198.67 | 14.30 | 3.53 | 25.91 | 5.42 | 0.00 | 0.58 | 7.26 | 0.22 | 98.15 |
| KS08 | 1,725 | 6.52 | 29.45 | 489.33 | 20.22 | 1.82 | 89.37 | 18.00 | 26.12 | 16.16 | 36.30 | 0.33 | 189.60 |
| KS09 | 1,988 | 6.98 | 29.27 | 492.00 | 94.35 | 4.17 | 45.09 | 15.53 | 0.00 | 0.86 | 121.61 | 0.20 | 188.99 |
| KS10 | 1,878 | 6.52 | 29.13 | 421.33 | 63.70 | 4.07 | 49.20 | 8.34 | 30.62 | 2.70 | 43.56 | 0.00 | 187.77 |
| Mean | 5,413.30 | 6.53 | 29.04 | 1,526.13 | 372.02 | 4.82 | 91.88 | 20.92 | 19.46 | 15.17 | 574.63 | 0.20 | 182.40 |
| Min | 799 | 5.89 | 28.28 | 198.67 | 14.30 | 0.96 | 8.42 | 5.42 | 0.00 | 0.58 | 7.26 | 0.00 | 76.81 |
| Max | 20,740 | 7.03 | 29.82 | 6,545.33 | 1,608.25 | 12.11 | 362.32 | 46.30 | 125.35 | 35.79 | 2570.50 | 0.65 | 302.38 |
| S.D. | 5,559.46 | 0.36 | 0.44 | 1,785.48 | 458.54 | 3.35 | 94.72 | 15.53 | 36.88 | 11.23 | 737.48 | 0.24 | 74.70 |

The analysis of hardness components reveals significant variations in Ca^{2+} and Mg^{2+} concentrations. Ca^{2+} concentrations range from 6.2 mg/L to 362.32 mg/L, while Mg^{2+} concentrations vary from 5.42 mg/L to 46.3 mg/L. These variations contribute to the overall hardness of the groundwater, which can impact water quality and its suitability for various uses. Higher concentrations of these elements indicate increased water hardness, an important factor in determining the suitability of the groundwater for domestic and agricultural purposes.

Regarding anion concentrations, HCO_3^- concentrations range from 98.15 mg/L to 301.77 mg/L, affecting the alkalinity and buffering capacity of the groundwater. Sulfate concentrations vary from 0 to 125.35 mg/L, which can impact overall water quality. NO_3^- concentrations, ranging from non-detectable to varying amounts, may influence water quality, particularly in areas with agricultural influence. F^- concentrations range from 0.2 mg/L to 0.65 mg/L, affecting water hardness and health-related properties. Temperature measurements show minimal variation, ranging from 28.28 $^{\circ}\text{C}$ to 29.82 $^{\circ}\text{C}$, and pH values range from 5.89 to 7.03, indicating that the groundwater is generally neutral to slightly acidic.

The correlation matrix (**Table 2**) provides insights into the relationships between various groundwater parameters within the study area. EC shows a very strong positive correlation with TDS and chloride Cl^- , indicating that these factors are major contributors to the overall salinity of the groundwater. Na^+ also exhibits a strong positive correlation with both EC and TDS, reinforcing its role as a key driver of groundwater salinity.

Ca^{2+} and Mg^{2+} display a moderate correlation with EC and TDS, suggesting that while these cations contribute to the mineral content and hardness of the water, their impact on overall salinity is less pronounced compared to Na^+ and Cl^- .

NO_3^- shows weak correlations with most other parameters, implying that nitrate contamination in groundwater may originate from sources distinct from those affecting mineral content. K^+ also exhibits low correlations with most other parameters, indicating a relatively minor role in influencing groundwater chemistry.

The overall conclusion from the correlation analysis is that groundwater salinity in the study area is primarily influenced by Na^+ and Cl^- , with EC and TDS serving as reliable



indicators of salinity levels. In contrast, NO_3^- levels are likely influenced by different processes, potentially related to agricultural activities or other sources of contamination. This analysis enhances the understanding of the dominant geochemical processes in the study area and can inform water resource management strategies.

Table 2 Correlation analysis matrix of physical and chemical parameters in groundwater samples.

| | EC | TDS | Na^+ | K^+ | Ca^{2+} | Mg^{2+} | NO_3^- | SO_4^{2-} | Cl^- | F^- | HCO_3^- |
|--------------------|--------|--------|---------------|--------------|------------------|------------------|-----------------|--------------------|---------------|--------------|------------------|
| EC | 1 | | | | | | | | | | |
| TDS | 0.9982 | 1 | | | | | | | | | |
| Na^+ | 0.9965 | 0.9948 | 1 | | | | | | | | |
| K^+ | 0.5443 | 0.5311 | 0.5655 | 1 | | | | | | | |
| Ca^{2+} | 0.9324 | 0.9402 | 0.9073 | 0.3498 | 1 | | | | | | |
| Mg^{2+} | 0.7466 | 0.7373 | 0.7088 | 0.3311 | 0.7400 | 1 | | | | | |
| NO_3^- | 0.3191 | 0.3303 | 0.3099 | 0.4125 | 0.4335 | 0.1645 | 1 | | | | |
| SO_4^{2-} | 0.5967 | 0.5728 | 0.6041 | 0.7370 | 0.4200 | 0.6143 | 0.3856 | 1 | | | |
| Cl^- | 0.9978 | 0.9962 | 0.9971 | 0.5531 | 0.9202 | 0.7458 | 0.3000 | 0.6000 | 1 | | |
| F^- | 0.2496 | 0.2449 | 0.2127 | 0.2581 | 0.2760 | 0.6960 | 0.1600 | 0.4820 | 0.2627 | 1 | |
| HCO_3^- | 0.2196 | 0.1948 | 0.2122 | 0.6123 | 0.0684 | 0.4418 | 0.2508 | 0.7459 | 0.2050 | 0.5709 | 1 |

Hydrogeochemical Facies

A Piper diagram⁶ is a graphical tool used to visualize the chemical composition of groundwater samples, facilitating the identification of hydrogeochemical facies within the study area. The diagram in **Figure 3** reveals two main hydrogeochemical facies. The predominant type is the Sodium-Chloride facies, represented by seven out of ten samples. The remaining three samples fall into the Calcium-Bicarbonate facies, located in the northern part of the study area. This northern zone, characterized by a high hydraulic head, is identified as a discharge zone, suggesting that groundwater movement in this area may influence its chemical composition. This classification of hydrogeochemical facies offers valuable insights into the spatial distribution of groundwater types and elucidates the geochemical processes affecting water quality across the study area.

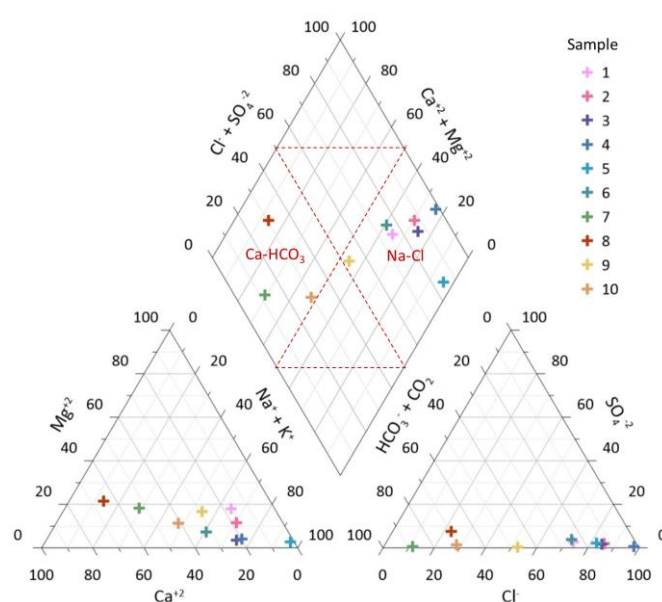


Figure 3 Piper trilinear diagram representing the hydrochemical facies

Multivariate Statistical Analysis

HCA is a multivariate statistical technique used to categorize groundwater samples by grouping them into clusters based on their hydrochemical characteristics. The process begins by assessing the samples to identify patterns of similarity and then groups those with comparable hydrochemical properties into clearly defined groups.⁷ The results are presented in **Figure 4** as a dendrogram, which illustrates the geochemical relationships between samples and the underlying processes. Shorter distances between clusters indicate higher similarity, while longer distances suggest greater differences.⁸ The analysis reveals two distinct clusters of groundwater samples. The first cluster is characterized by high salinity, with elevated concentrations of ions such as Na^+ , Cl^- , and Ca^{2+} . The second cluster represents low salinity, with lower overall ion concentrations, potentially indicating areas with fresher groundwater that may have recently recharged or are less affected by salinization.

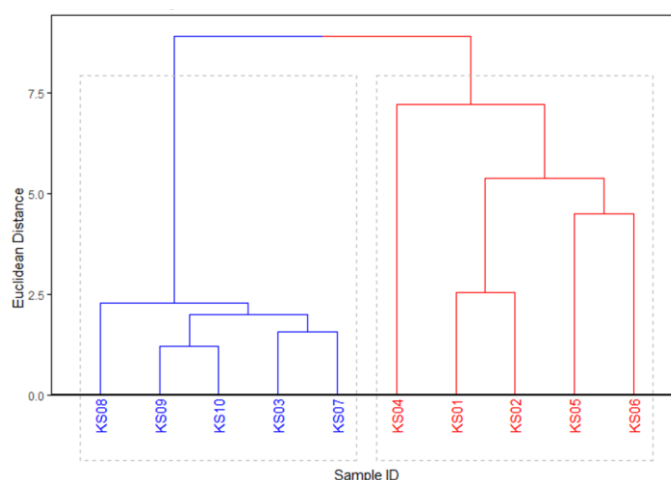


Figure 4 Dendrogram from HCA showing the two identified cluster

PCA was conducted to analyze ion concentrations across nine variables, with the aim of reducing the data to key components that capture the variance among intercorrelated variables. Based on the Kaiser criterion, which retains only components with eigenvalues greater than one to limit the influence of less significant variables⁹, three principal components were identified. These components, detailed in **Table 3** and illustrated by the PCA loading scores in **Figure 5**, explain 84.44% of the total variance. This indicates that they are effective in identifying the primary sources of variation in hydrochemistry.

Table 3 Principal component loadings and explained variance for three components.

| Variable | PC1 | PC2 | PC3 |
|--------------------|-------|-------|-------|
| Na^+ | 0.50 | 0.13 | 0.13 |
| K^+ | 0.15 | -0.32 | 0.53 |
| Ca^{2+} | 0.44 | 0.31 | -0.07 |
| Mg^{2+} | 0.42 | -0.17 | -0.36 |
| NO_3^- | -0.13 | 0.06 | 0.42 |
| SO_4^{2-} | 0.27 | -0.45 | 0.26 |
| Cl^- | 0.51 | 0.12 | 0.08 |
| F^- | 0.04 | -0.41 | -0.56 |
| HCO_3^- | -0.01 | -0.60 | 0.05 |
| Eigenvalue | 3.59 | 2.41 | 1.59 |
| Variance % | 39.93 | 26.81 | 17.70 |
| Cumulative % | 39.93 | 66.74 | 84.44 |

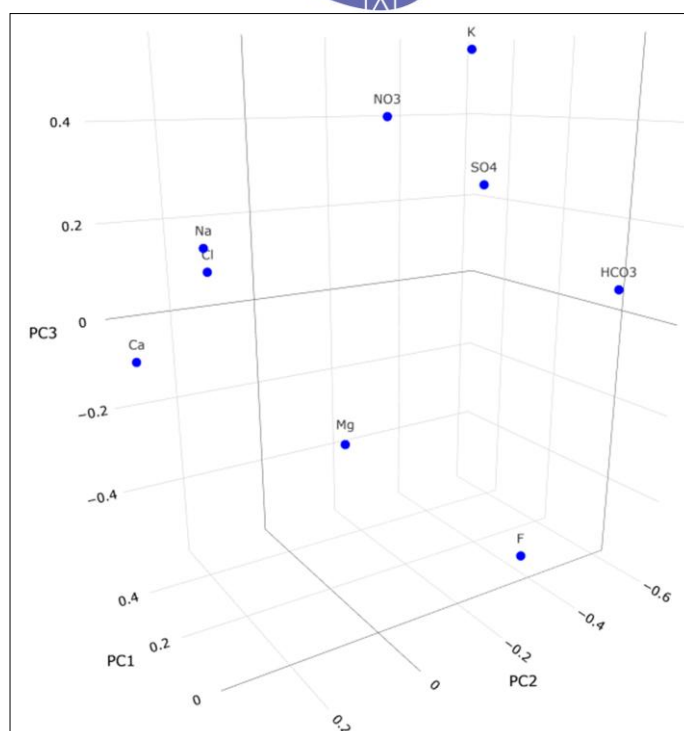


Figure 5 Plot of PCA loading scores for dataset of groundwater samples

PC1 is primarily associated with salinity and mineral content, driven by high concentrations of Na^+ and Cl^- , indicating that groundwater samples with elevated salinity are represented by PC1. PC2, in contrast, is linked to higher concentrations of Ca^{2+} and HCO_3^- , suggesting that it reflects water hardness. PC3 is associated with factors related to the presence of K^+ and NO_3^- which can be influenced by fertilizers used in agricultural activities and may also serve as potential indicators of contamination.

Hydrogeological Process

The Gibbs diagram¹⁰ is a widely used tool for identifying the influence of three major geochemical processes: precipitation, rock weathering, and evaporation-crystallization. As shown in **Figure 6**, the positioning of groundwater samples indicates that the majority of the groundwater in the study area is primarily influenced by water-rock interactions. However, sample KS04 is an exception; it plots within the evaporation dominance zone, suggesting that this particular sample is significantly affected by evaporation processes.

To verify and characterize the water-rock interaction processes in the groundwater, a Gaillardet diagram¹¹ was employed. This diagram categorizes groundwater interaction processes into three types: evaporite dissolution, silicate weathering, and carbonate dissolution. As shown in **Figure 7**, the majority of samples are located near the silicate weathering zone, suggesting that the dissolution of clay minerals along the flow path is a predominant process. However, groundwater samples from areas with high salinity are situated in the halite dissolution zone, which confirms the presence of rock salt from the Maha Sarakham Formation underlying this region. This analysis emphasizes the diverse geochemical processes that influence groundwater composition in the study area.

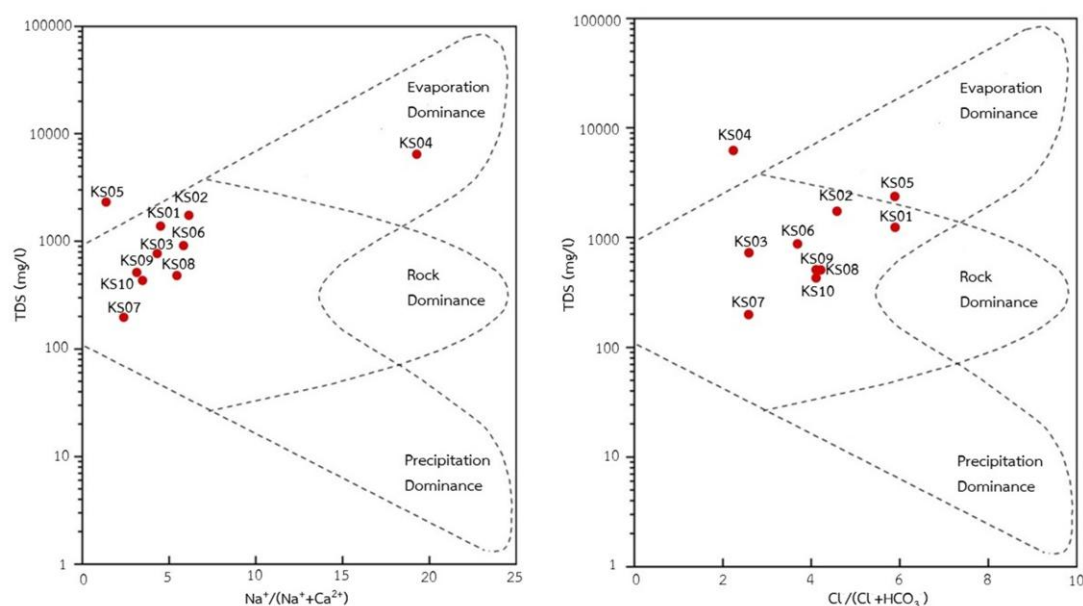


Figure 6. Gibb diagram showing the mechanism controlling groundwater chemistry

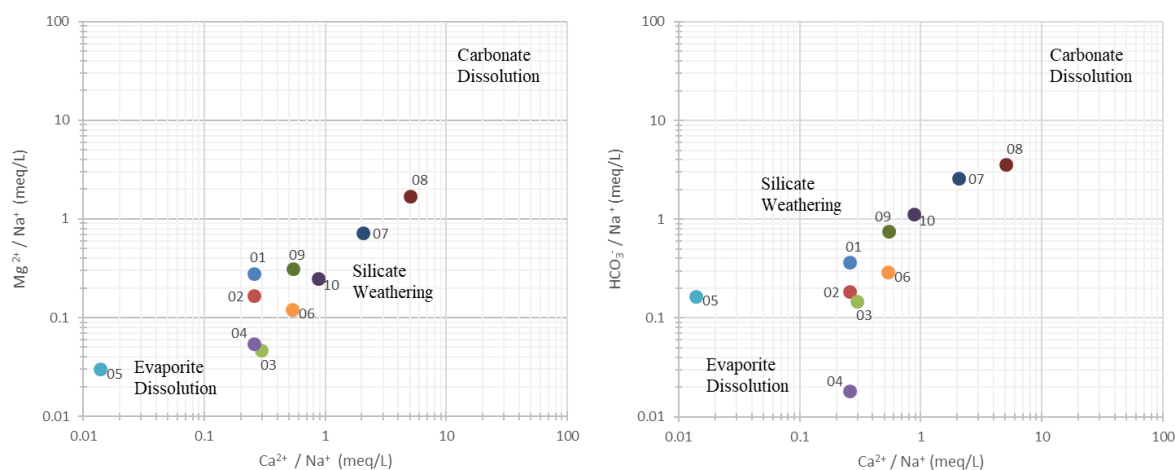


Figure 7. Gaillardet diagram for groundwater samples

Conclusion:

This study has provided essential insights into the hydrogeochemical processes influencing groundwater quality in the Khok Si Subdistrict, with a particular emphasis on salinity. The hydrogeochemical analysis, supported by multivariate statistical methods and geochemical diagrams, has revealed that groundwater in this area is predominantly characterized by Sodium-Chloride and Calcium-Bicarbonate facies. Most groundwater samples are classified under the Sodium-Chloride facies, which predominates in the southern parts of the study area. In contrast, the Calcium-Bicarbonate facies are more common in the northern regions, where a higher hydraulic head indicates a discharge zone.

The Gibbs and Gaillardet diagrams further emphasize the significant role of water-rock interaction processes, notably silicate weathering, in shaping groundwater chemistry. The analysis also identified zones of high salinity, particularly in areas where the Maha Sarakham Formation is present, suggesting that halite dissolution is a key factor contributing to elevated salinity levels.



This comprehensive evaluation of groundwater chemistry not only clarifies the complex interactions between natural processes, such as rock weathering and evaporite dissolution but also emphasizes the importance of ongoing monitoring of salinity distribution in groundwater. This monitoring is essential for ensuring the sustainable use of groundwater resources in the region. Effective groundwater management will be crucial for addressing the challenges posed by high salinity and for meeting the water needs of both residential and agricultural sectors in northeastern Thailand.

Acknowledgements:

The authors would like to thank the Department of Geotechnology, Faculty of Technology, Khon Kaen University, for their support in providing access to laboratories and facilities.

References:

1. Arjwech R, Everett ME, Wanakao P, Songklanakarin J. *Sci. Technol.* 2019;41(5):974-983
2. Dissataporn C, Yacouba K, Mihara M, Yasutomi R. *J Jpn Soc Soil Phys.* 2002;89:35-42
3. Li C, Gao X, Li S, Bundschuh J. *Environ Sci Pollut Res*, 2020;27:41157-41174
4. Utha-Aroon C. *J SE Asian Earth Sci.* 1993; 8:193-206
5. Nettasana T, Craig J, Tolson B. *Hydrogeol J.* 2012; 20:1355-1374.
6. Piper AM. *Trans. Am. Geophys. Union.* 1944;25(6):914-928
7. Güler C, Thyne GD, McCray JE, Turner AK. *Hydrogeol J.* 2002;10(4):455-474.
8. Selmane T, Dougha M, Hasbaia M, Ferhati A, Redjem A. *Acta Geochim.* 2022;41(5):893-909.
9. Cloutier V, Lefebvre R, Therrien R, Savard MM. *J Hydrol.* 2008;353:294-313.
10. Gibbs RJ. *Science.* 1970;170:1088-1090
11. Gaillardet J, Dupre B, Louvat P, Allegre CJ. *Chem Geol.* 1999;159:3-30



MODELS FOR ESTIMATING MONTHLY AVERAGE DAILY GLOBAL SOLAR RADIATION FROM AIR TEMPERATURE: CASE STUDY SONGKHLA PROVINCE THAILAND

Marina Mani,^{1*} Suwit Khongpakdee,¹ Jakkree Boonlakhorn¹

¹Department of Physical Science, Faculty of Science and Digital Innovation, Thaksin University, Songkhla Campus, Songkhla 90000, Thailand

*e-mail: sumsiyha@gmail.com

Abstract:

This study aimed to develop a model for estimating the monthly average daily of global solar radiation from the atmospheric temperature (maximum, minimum, and average daily air temperature) of Songkhla province, Thailand. The development of the model started with the collection of global solar radiation and atmospheric temperature data from Songkhla province meteorological station over ten years (2009-2018). Then, it was taken to find the Ångström-Prescott model was $\overline{H} / \overline{H}_o = -0.0145 + 0.0573 \Delta T$. The model was validated by using atmospheric temperature data from two years (2019-2021) to predict solar radiation and compared with data from the Songkhla province meteorological station. The statistical analysis results from the coefficient of determination (R^2), relative error (% \mathcal{E}), root mean square difference (RMSE), and mean bias error (MBE) equal to 0.8444 - 0.8865, 4.98%, 0.8596 - 1.5669 and -1.1251 - 0.0448 respectively.

Introduction:

Thailand is located in the tropical southeast of Asia, between latitude 5.37 °N and 20.27 °N, and between longitude 97.22 °E and 105.37 °E, which is close to the equator, so it receives a lot of solar radiation during April and May. As for Songkhla Province, which is the research area in the southern part of Thailand, it is located on the east coast of the lower southern region, with an average elevation of 4 meters above sea level. It receives an average annual solar radiation of 5.28 - 5.56 kWh/(m² day). [1] For Songkhla Province, the total solar radiation intensity, air temperature, relative humidity, and daily cloud cover data from the Meteorological Department of Thailand were used because the Songkhla Meteorological Station in the Eastern Southern Region does not have data to measure the global solar radiation intensity.

The data of global solar radiation measurements are due to the cost and maintenance; as a result, the frequently used models are based on empirical methods of the development of empirical equations to estimate global solar radiation from weather stations [2]. These methods use historical weather data of the location under study [3]. The empirical models are classified into three categories: cloud models [4,5], sunshine duration models [6-8], and temperature models [9,10]. The simplest parameter to use in modeling the total radiation intensity on a horizontal surface is the air temperature and commonly available parameters such as maximum, minimum, and average temperature. Model of base air temperature can be used in a wide range of global solar radiation. The results are important for contributing to models that estimate global solar radiation on horizontal surfaces using meteorological data.

In this study, the purpose is to build a monthly average daily global solar radiation term forecasting model based on meteorological data for the Songkhla Province of global solar radiation. These data include global solar radiation and air temperature. The new empirical model correlates the monthly average daily global solar radiation (\overline{H}) with the theoretical monthly average daily extraterrestrial solar radiation on a horizontal surface (\overline{H}_o),

via the monthly average daily maximum, minimum, and average air temperature. The coefficients in these equations of empirical models were the predicted global solar radiation values, calculated from ten correlations that were compared with measured values from meteorological data. The statistical parameters used in the work, are the coefficient of determination (R^2), relative error ($\% \mathcal{E}$), root mean square difference (RMSE), and mean bias error (MBE). Finally, measured values are compared to calculations from models using statistical parameters for consideration.

Methodology:

This work presents to build and evaluate different models of global solar radiation. Prepare data on the monthly average daily of global solar radiation and temperature (maximum, minimum, and average daily air temperature) of Songkhla province obtained from measurements from the Meteorological Department of Thailand, which are used for the development of models. Data of measurements from meteorological between ten years (2009-2018) and the model was validated by using atmospheric temperature data from two years (2019-2021).

Input Parameter

For this case, monthly average daily of global solar radiation data (\overline{H}) are used [6], monthly average daily mean air temperature (T), maximum air temperature (T_{\max}), minimum air temperature (T_{\min}), and the difference between maximum and minimum temperature (ΔT). They refer to a whole year. These values are shown in table 1.

Table 1
Parameter for input to the global solar models.

| Month | \overline{H} (MJ/m ² day) | T_{\max} (°C) | T_{\min} (°C) | ΔT (°C) | T (°C) |
|-----------|---|--------------------|--------------------|--------------------|-------------|
| January | 16.27 | 30.1 | 22.7 | 7.4 | 3.7 |
| February | 20.39 | 31.8 | 22.3 | 9.5 | 4.7 |
| March | 21.20 | 33.5 | 22.9 | 10.6 | 5.3 |
| April | 20.18 | 33.8 | 23.9 | 9.9 | 4.9 |
| May | 18.78 | 33.7 | 24.6 | 9.1 | 4.5 |
| June | 17.63 | 33.4 | 24.2 | 9.2 | 4.6 |
| July | 17.55 | 33.1 | 24.0 | 9.1 | 4.5 |
| August | 18.03 | 33.6 | 24.0 | 9.6 | 4.8 |
| September | 16.70 | 32.6 | 24.0 | 8.6 | 4.3 |
| October | 15.54 | 31.8 | 23.9 | 7.9 | 3.9 |
| November | 13.75 | 30.7 | 23.3 | 7.4 | 3.7 |
| December | 12.88 | 29.9 | 23.0 | 6.9 | 3.4 |

The monthly average daily extraterrestrial solar radiation on a horizontal surface (H_o), for the latitude of the location degrees (ϕ) can be calculated by using the equation [6].

$$\overline{H_o} = \frac{24}{\pi} \cdot I_{sc} \cdot r \cdot \left[\cos(\phi) \cdot \cos(\delta) \cdot \sin(\omega_s) + \frac{\pi}{180} \cdot \omega_s \cdot \sin(\phi) \cdot \sin(\delta) \right] \quad (1)$$



Where I_{sc} is the solar constant ($118.108 \text{ MJ/m}^2\text{day}^{-1}$) [6, 11]. The eccentricity correction factor of the Earth's orbit computed equation [6] and n_{day} is the day number of the year (starting 1 January).

$$r = 1 + 0.033 \cdot \cos\left(\frac{360 n_{day}}{365}\right) \quad (2)$$

The solar declination angle (δ) in degrees is given as equation [6].

$$\delta = 123.45 \cdot \sin\left(\frac{284 + n_{day}}{365}\right) \quad (3)$$

The sunset hour angle (ω_s) in degree, for the zenith angle to $\theta_s = 90^\circ$ as equation [6].

$$\omega_s = \cos^{-1}\left[\frac{-\sin\phi \cdot \sin\delta}{\cos\phi \cdot \cos\delta}\right] \quad (4)$$

Models

The type of model was first introduced by Angström-Prescott [5,6] presented their method as based on monthly average daily extraterrestrial solar radiation on a horizontal surface [6] (H_o). Several empirical have been on the common availability of daily maximum, minimum, and average air temperature. Some researchers have found that regression coefficients in linear models are location-dependent, i.e. they depend on latitude, climate conditions, etc [12].

These models were chosen as representative of the existing models that utilize air temperature data. The models were validated by ten models for measurement of the monthly average daily of global solar radiation and estimate the monthly average daily of global solar radiation.

Model 1. A linear model can be written in a general form as [5]:

$$\overline{H} = H_o [a + b \Delta T] \quad (5)$$

Model 2. Exponential model, this model is used by several researchers [13].

$$\overline{H} = H_o [a \cdot \exp(b \cdot T)] \quad (6)$$

Model 3. The logarithmic 1 model can be written as:

$$\overline{H} = H_o [a + b \cdot \ln(T)] \quad (7)$$

Model 4. The logarithmic 2 model can be written as:

$$\overline{H} = H_o [a + b \cdot \ln(\Delta T)] \quad (8)$$

Model 5. The power 1 model is exploited by Allen [14] and Lewis [15] as:

$$\bar{H} = H_o \left[a \cdot T^b \right] \quad (9)$$

Model 6. The power 2 model can be written as:

$$\bar{H} = H_o \left[a \cdot (\Delta T)^b \right] \quad (10)$$

Model 7. The quadratic model can be written as:

$$\bar{H} = H_o \left[a + bT + cT^2 \right] \quad (11)$$

Model 8. The cubic 1 model can be written as:

$$\bar{H} = H_o \left[a + b\Delta T + cT^2 + dT^3 \right] \quad (12)$$

Model 9. The cubic 2 model can be written as:

$$\bar{H} = H_o \left[a + b\Delta T + \Delta T^2 + d(\Delta T)^3 \right] \quad (13)$$

Model 10. The cubic 3 model can be written as:

$$\bar{H} = H_o \left[a + bT + c(\Delta T)^2 + dT^3 \right] \quad (14)$$

Comparison Method

The models of the monthly average daily of global solar radiation were evaluated based on the following statistical test; the coefficient of determination (R^2), relative error (% \mathcal{E}), root mean square difference (RMSE) and mean bias error (MBE) [16].

The parameter R^2 represents measure (\bar{H}_m) to determine how certain a predicted (\bar{H}_p) values of \bar{H} for the i-th month. A value of R^2 is defined as:

$$R^2 = 1 - \frac{\sum_{i=1}^n (\bar{H}_p - \bar{H}_m)^2}{\sum_{i=1}^n (\bar{H}_m - \bar{H})^2} \quad (15)$$

The \mathcal{E} is represents the difference between the measure and the predicted values of \bar{H} , as a percent of the measurement value, and is defined as:

$$\mathcal{E} = \left(\frac{\bar{H}_m - \bar{H}_p}{\bar{H}_m} \right) \cdot 100\% \quad (16)$$

The RMSE provides the short-term performance of the models and is a measure of the variation in the predicted values of all the measured data. A low value of RMSE is desirable and defined as:



$$RMSE = \sqrt{\sum_{i=1}^n \frac{(\bar{H}_p - \bar{H}_m)^2}{n}} \quad (17)$$

The MBE is an indicator for the average deviation of the predicted values from measured data. A low MBE value is desirable. A positive value gives the average overestimation of predicted values. The MBE is defined as:

$$MBE = \frac{1}{n} \cdot \sum_{i=1}^n (\bar{H}_p - \bar{H}_m) \quad (18)$$

Results and Discussion:

In Table 2, using the equation of the Angstrom-Prescott model (equation 5), the monthly average daily extraterrestrial solar radiation on a horizontal surface (\bar{H}_o), the ratios of (\bar{H} / \bar{H}_o), and the average difference between maximum and minimum temperature ($\overline{\Delta T}$) are shown.

Table 2
Calculated values of model parameters.

| Month | \bar{H}_o (MJ/m ² day) | \bar{H} / \bar{H}_o (-) | $\overline{\Delta T}$ (°C) |
|-----------|--|------------------------------|-------------------------------|
| January | 35.94 | 0.41 | 7.4 |
| February | 37.21 | 0.50 | 9.5 |
| March | 37.64 | 0.51 | 10.6 |
| April | 36.50 | 0.50 | 9.9 |
| May | 34.51 | 0.49 | 9.1 |
| June | 33.27 | 0.48 | 9.2 |
| July | 33.63 | 0.47 | 9.1 |
| August | 35.33 | 0.46 | 9.6 |
| September | 36.93 | 0.41 | 8.6 |
| October | 37.21 | 0.38 | 7.9 |
| November | 36.25 | 0.34 | 7.4 |
| December | 35.45 | 0.33 | 6.9 |

The regression coefficient of linear for the Angstrom-Prescott model then taken to find was $\bar{H} / \bar{H}_o = -0.0145 + 0.0573 \Delta T$, the coefficients a and b equal -0.0145 and 0.0573 respectively. The correlation between the calculated ratios of (\bar{H} / \bar{H}_o) and $\overline{\Delta T}$ is shown in Figure 1.

To evaluate its performance, the values of the monthly average daily of global solar radiation were evaluated from equation (5). Then, the comparison obtained from global solar radiation measured at meteorological and results are shown in Figure 2, it was observed that the values relative error (% \mathcal{E}), root mean square difference (RMSE), and mean bias error (MBE) equal 4.98, 0.23 and 3.15 respectively. These results indicated the values of the monthly average daily global solar radiation estimate agree well with those obtained from measurement.

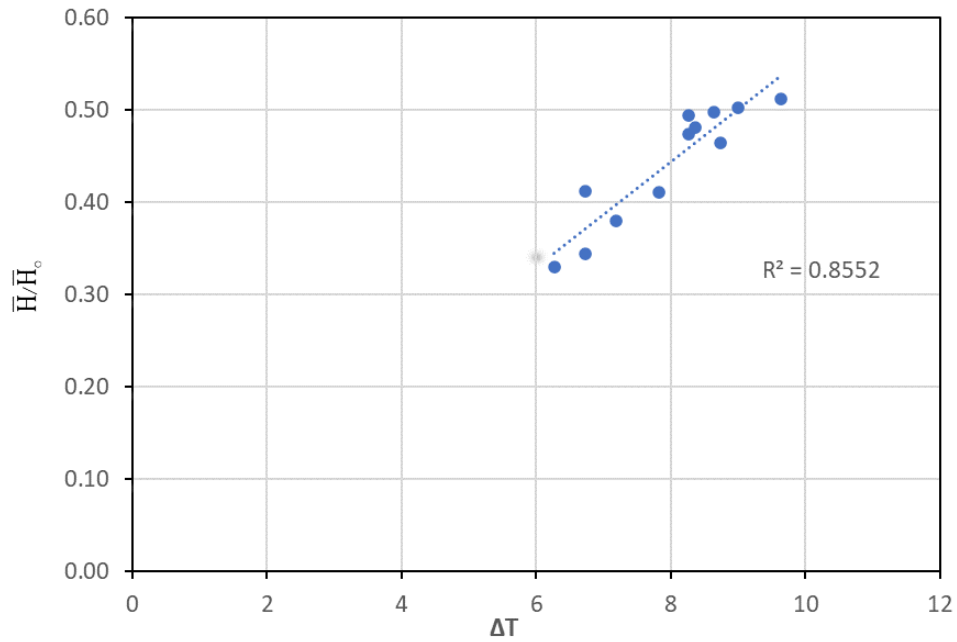


Figure 1.

Correlation between the ratio of monthly average daily global to monthly average daily extraterrestrial radiation (\bar{H} / \bar{H}_0) and the average difference between max average daily global radiation from maximum and minimum temperature (ΔT).

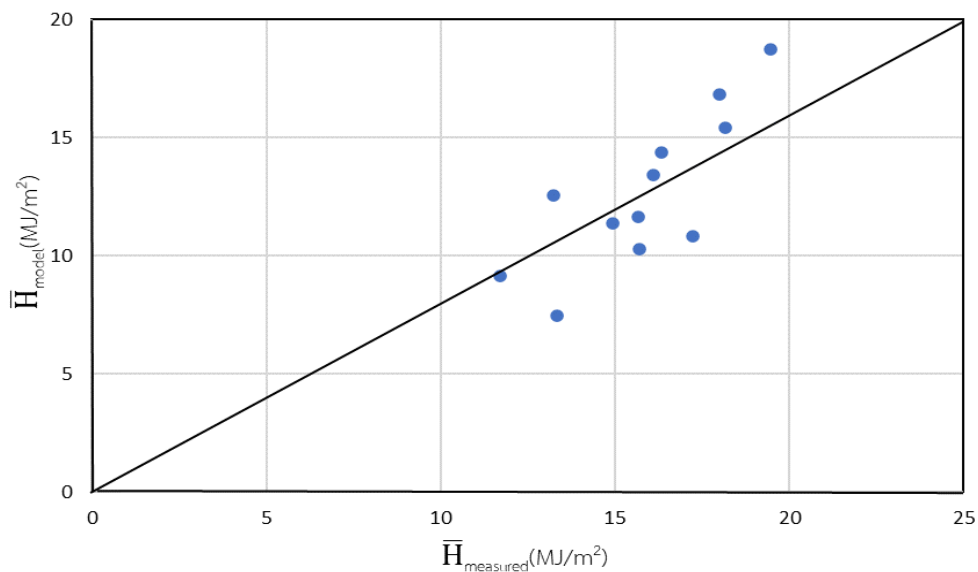


Figure 2.

Comparison between monthly average daily global radiation from prediction and average daily global radiation from measurement.

The section of the most appropriate values of monthly average daily of global solar radiation models, based on the correlation values, between \bar{H} from measured in two years (2019-2021) and \bar{H} from models numbers. The coefficient for each considerate of the global solar radiation model with the results is shown in Table 3.



In Table 4, statistical test values obtained from the exploitation of statistical test methods for the ten considered models are shown

The minimum value of MBE is -0.0096 for the linear model, while RMSE is 0.8502 is the minimum of the quadratic model and R^2 is 0.8813 for the maximum quadratic model.

The measure values (\bar{H}_m) and the predicted values (\bar{H}_p) for each solar global radiation model are shown in Figure 3.

The mathematical models for the analysis results of the most suitable model using statistical values and from Figure 3, it was found that model seven, which is a quadratic equation, is the most appropriate in terms of the relationship.

Table 3
Considered models and coefficients (a, b, c, and d) for Songkhla province, Thailand.

| Model number | Model type | Coefficients |
|--------------|---------------|--|
| 1 | Linear | a = -0.0163 b = 0.0573 |
| 2 | Exponential | a = 0.1627 b = 0.2474 |
| 3 | Logarithmic 1 | a = -0.2383 b = 0.4929 |
| 4 | Logarithmic 2 | a = -0.5800 b = 0.4929 |
| 5 | Power 1 | a = 0.1071 b = 1.0221 |
| 6 | Power 2 | a = 0.0527 b = 1.0221 |
| 7 | Quadratic | a = -0.6736 b = 0.4237 c = -0.0358 |
| 8 | Cubic 1 | a = -0.0468 b = -0.0026 c = -0.0622 d = -0.0075 |
| 9 | Cubic 2 | a = 2.0923 b = -0.7483 c = 0.1009 d = -0.0041 |
| 10 | Cubic 3 | a = -0.3873 b = 0.4237 c = -0.0327 d = -0.0358 |

Table 4
Obtained statistical test values in Songkhla province, Thailand.

| Model number | Model type | MBE (MJ/m ² day) | RMSE (MJ/m ² day) | R ² (-) |
|--------------|---------------|--------------------------------|---------------------------------|-----------------------|
| 1 | Linear | -0.0096 | 0.9201 | 0.8557 |
| 2 | Exponential | 0.0039 | 0.9906 | 0.8444 |
| 3 | Logarithmic 1 | -0.0125 | 0.8838 | 0.8673 |
| 4 | Logarithmic 2 | -0.0108 | 0.8837 | 0.8673 |
| 5 | Power 1 | 0.0228 | 0.9209 | 0.8579 |
| 6 | Power 2 | 0.0347 | 0.9211 | 0.8579 |
| 7 | Quadratic | 0.0288 | 0.8602 | 0.8813 |
| 8 | Cubic 1 | 0.0251 | 0.8596 | 0.8834 |
| 9 | Cubic 2 | -1.1251 | 1.4670 | 0.8865 |
| 10 | Cubic 3 | 0.0448 | 1.5669 | 0.8813 |

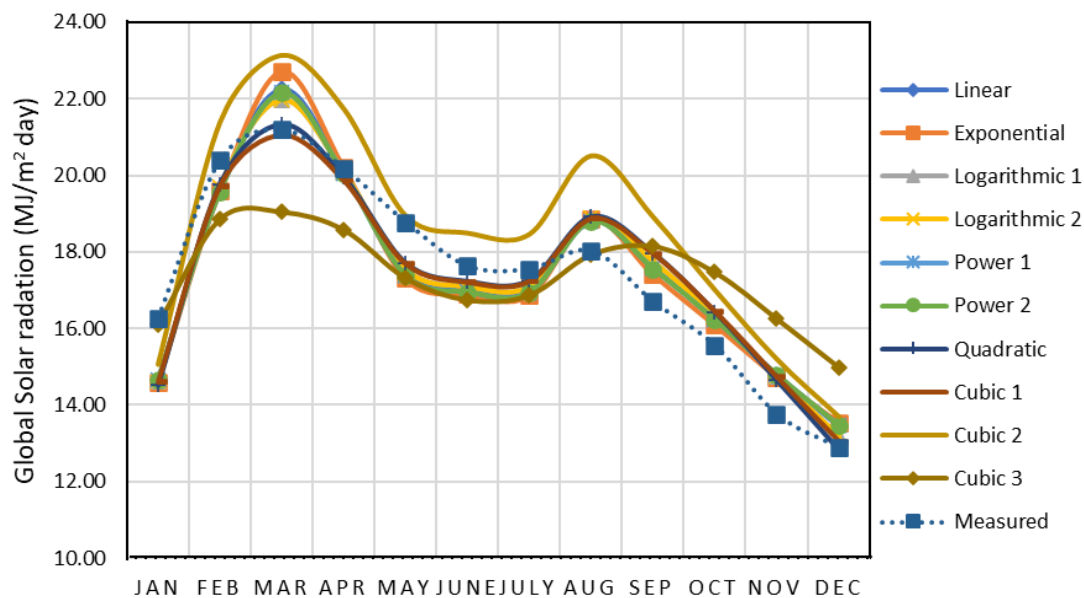


Figure 3.

Measured and predicted values of the \bar{H} value for each solar radiation model.

Conclusion:

This paper studies values of the monthly average daily of global solar radiation of ten empirical models and evaluates to measure values of \bar{H} for the Songkhla province, Thailand. Evaluated using daily air temperature data for estimating daily global solar radiation. These models have the advantage of using meteorological data that are commonly available, and the tested models used were to adequately estimate daily global solar radiation from daily air temperature.

By analyzing various air temperature variables, propose an equation in the form of:

$$\bar{H} = \bar{H}_o(-0.6736 + 0.4237T - 0.0358T^2) \quad (19)$$



Model 7 is the quadratic model of maximum value for the coefficient of determinations $R_{\max}^2 = 0.8813$, the temperature-based models can be used for estimating global solar radiation in the Songkhla province, Thailand was in good agreement.

Acknowledgements:

We would like to thank the Department of Physical Science, Faculty of Science and Digital Innovation, Thaksin University, Songkhla Campus, Songkhla, Thailand.

References:

1. Janjai S, Tosing K. A new model for calculating global radiation from cloud cover data for Thailand. Proceeding of The First Regional Conference on Energy Technology Towards a clean Environment. JGSEE. 1-2 December 2000. Chiang Mai, Thailand.
2. Bulut H, Buyukalaca O. Simple model for the generation of daily global solar radiation in Turkey. Appl Energy. 2007;84:477-91.
3. Yang K, Koike T, Ye BS. Improving estimation of hourly, daily, and monthly solar radiation by importing global data sets. Agric Forest Meteorol. 2006;137(1):43-55.
4. Supit I, Van Kappel RR. A simple method to estimate global radiation. Sol Energy. 1998;63:147-60.
5. Angström A. Solar and terrestrial radiation. Quart J Roy Met Soc. 1924;50:121-5.
6. Duffie JA, Beckman WA. Solar engineering of thermal process. New York: Wiley; 1991.
7. Kirtikara K, Siriprayuk T, Namprakai P. The use of regression equation for estimating solar radiation from meteorological data. Proceeding of The Third Conference on Renewable Energy and Application KMITT. 4-6 November 1981. Bangkok, Thailand.
8. Klein SA. Calculating of monthly average insolation on tilted surface. Solar Energy. 1977;19(4):325-329.
9. Benson RB, Paris MV, Sherry JE, Justus CG. Estimation of daily and monthly direct, diffuse and global solar radiation from sunshine duration measurements. Solar Energy. 1984;32(4):523-535.
10. Tiris M, Tiris C, True IE. Correlation of monthly-average daily global, diffuse and beam radiations with hours of bright sunshine in Gebze, Turkey. Energy Conversion and Management. 1996;37(9):1417-1421.
11. Thekaekara, MP. Solar radiation measurement: Techniques and instrumentation. Solar Energy. 1976;18(4):309-325.
12. Rietveld, MR. A new method for estimating the regression coefficients in the formula relating solar radiation to sunshine. Agricultural Meteorology. 1978;19(2&3):243-252.
13. Brislow, KL, Campbell, GS. On the relationship between incoming solar radiation and daily maximum and minimum temperature. Agricultural and Forest Meteorology. 1984;31(2):159-166.
14. Allen, RG. Self-calibrating method for estimating solar radiation from air temperature. Journal of Hydrologic Engineering; 1997;2(2): 56-57.
15. Lewis G. Estimates of irradiance over Zimbabwe. Solar Energy. 1983;31(6):609-612.
16. Iqbal, M. An introduction to solar radiation. 1983; New York. Academic Press.

NEW DISCOVERY OF VERTEBRATE FOSSILS AT PHUWAT SITE, NONG BUA LAMPHU PROVINCE, THAILAND

Aut Sriwisan,¹ Sita Manitkoon,² Prapasiri Warapeang,² Kasidit Eiamlaor,³ Pongkhun Funong,¹ Sirawit Jaisabai,³ Warot Thuvadarakul,⁴ Jakkrapat Weluwanarak,⁵ Chatcharin Somboon,⁶ Veerathep Somdee,⁷ Patchanop Boonsai,⁸ Nuttapong Ketmount,⁹ Yupa Thasod^{1,*}

¹ Department of Geological Sciences, Faculty of Science, Chiang Mai University, 239 Huay Kaw Road, Suthep Subdistrict, Chiang Mai 50200, Thailand

² Palaeontological Research and Education Centre, Mahasarakham University, Kamriang, Maha Sarakham 44150, Thailand; Vertebrate Palaeontology and Evolution Research Unit, Excellence Center in Basin Studies and Applied Paleontology, Mahasarakham University, Khamriang, Maha Sarakham 44150, Thailand

³ Department of Geology, Faculty of Science, Chulalongkorn University, Bangkok 10330, Thailand

⁴ Department of Biology, Faculty of Science, Chulalongkorn University, Bangkok 10330, Thailand

⁵ Independent Researcher, Unit 10/ 10-12 Park Avenue, Burwood, New South Wales 2134, Australia

⁶ Independent Researcher, 139 Moo 5 Ban Ton Sub-district, Phra Yuen District, Khon Kaen 40320 Thailand

⁷ Independent Researcher, 54/2 Moo 7, Huasai subdistrict, Bangkhla District, Chachoengsao 24110, Thailand

⁸ Independent Researcher, Nuanchan 26, 9/58, Jirathip village, Bangkok 10230, Thailand

⁹ Department of Biology, Faculty of Science Pibulsongkram Rajabhat, Phitsanulok 65000, Thailand

*e-mail: yupa.t@cmu.ac.th

Abstract:

This research reports a new finding of vertebrate fossils from the Sao Khua Formation at the Phu Wat site in Nong Bua Lamphu Province. They include some isolated theropod teeth of Carnosauria and Spinosaurid, phalange and fibula of theropod dinosaurs, a pedal claw of a dromaeosaurid, and a tibia to cf. Baryonychinae. Other fossils are sauropod dinosaurs, Actinopterygian fish, Hybodontid sharks, Testudines, and Crocodyliformes. These fossils indicate the paleoecology of land and lake. The finding of dromaeosaurid and cf. Baryonychinae indicates they were first found in Thailand and Southeast Asia.

Introduction:

The Phu Wat site, a unique location for paleontological research, is situated at N 16° 56' 28.6296" and E 102° 26' 43.7352" in Khok Muang Subdistrict, of Non Sang District, Nong Bua Lamphu Province, northwest Khon Kaen Province in northeastern Thailand (Figure 1). The fossil was unearthed in the rocks of the Sao Khua Formation, which consists of red clays, sandstones, and conglomerates. These sediments were deposited in a floodplain with large, meandering, bedload-rich channels and freshwater lakes, indicating a stable, humid, subtropical climate regime¹. Gymnosperm palynology suggests a warm, predominantly seasonally dry subtropical climate². Fossils were collected from weathered conglomeratic rock at the base of a hill.

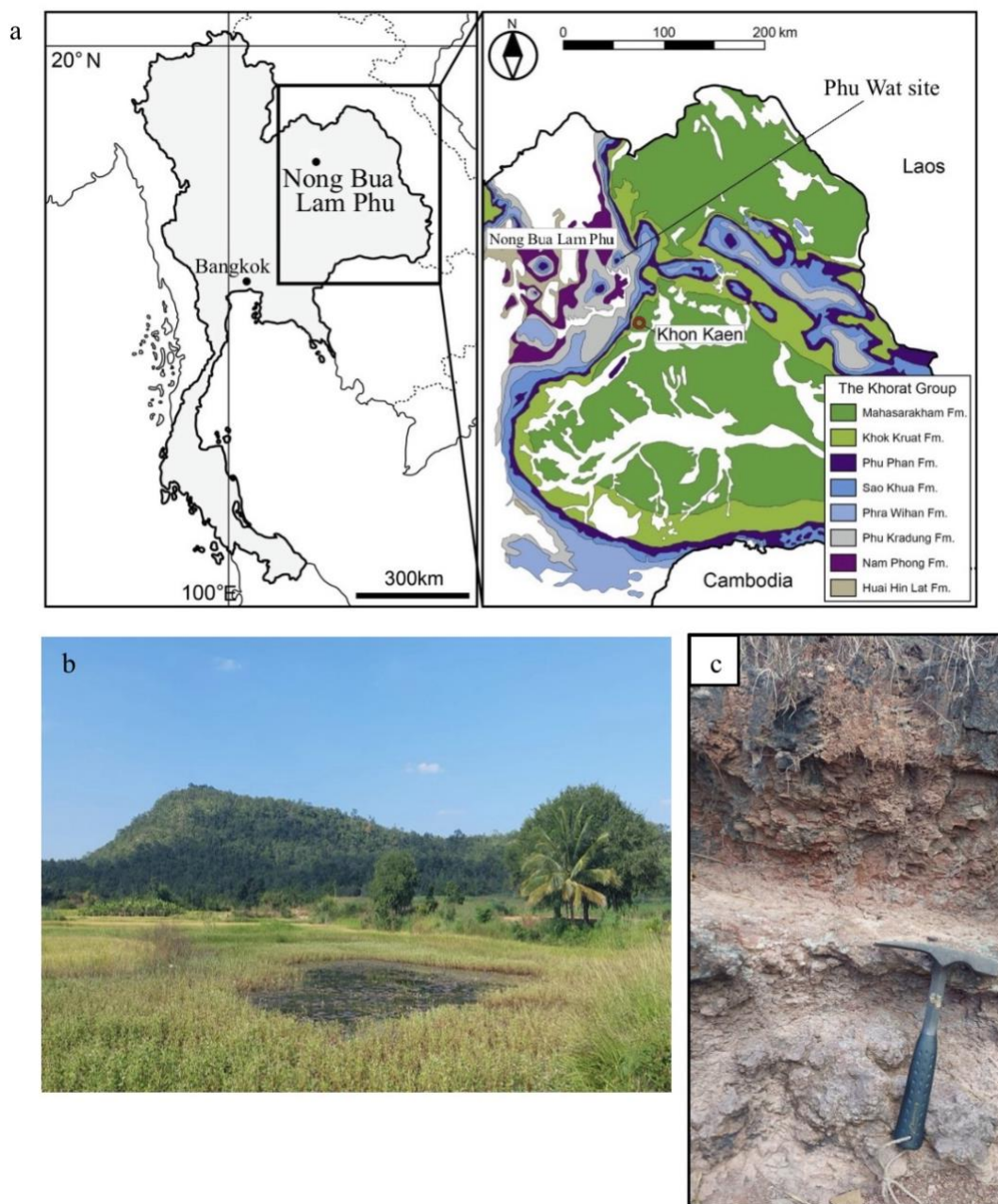


Figure 1.

Study area. (a) Map of the Phu Wat site, Nong Bua Lamphu Province showing location and geological maps (modified from³), (b) cuesta geomorphology of the Phu Chan, a small hill at the Phu Wat site (looking NW), (c) lithologic characters at the Phu Wat site composed of brown to reddish brown calcareous siltstone to conglomerate.

The age of the Sao Khua Formation is primarily determined through relative dating using lithostratigraphy and biostratigraphy, suggesting an upper Jurassic age^{4,5}. However, palynological assemblages indicate that the succession from the Phu Kradung to the Sao Khua Formations was deposited during the Berriasian or later². Additionally, non-marine bivalves point to a Barremian age⁶. Radiometric dating of detrital zircons reveals that the middle to upper parts of the Sao Khua Formation were deposited between 133.8 (± 1.8) to 132.4 (± 2) million years ago, corresponding to the late Valanginian to early Hauterivian¹. The Sao Khua



Formation, deposited in an alluvial floodplain, is rich in vertebrate fossils discovered at numerous sites in northeastern Thailand, including Khon Kaen, Kalasin, Nong Bua Lamphu, Sakon Nakhon, and Mukdahan. The diverse fossil assemblage includes Chondrichthyan fishes (freshwater Hybodont sharks), Actinopterygian fishes, turtles, crocodilians, pterosaurs, and dinosaurs⁷. Theropod dinosaurs from the Sao Khua Formation include a possible Compsognathid⁸, teeth of the Spinosaurid *Siamosaurus suteethorni*⁹, the basal Coelurosaur *Siamotyrannus isanensis*¹⁰, the Ornithomimosaur *Kinnareemimus khonkaenensis*¹¹, a partial skull of a Carcharodontosaurid¹², and two Megaraptorans, *Vayuraptor nongbualamphuensis* and *Phuwiangvenator yaemniyomi*¹³. Sauropod dinosaurs include *Phuwiangosaurus sirindhornae*¹⁴, a Diplodocoidea "Taxon C," and a possible Brachiosaurid "Taxon B"¹⁵. An early Ornithurine bird humerus fragment has also been found in this formation¹⁶. Other notable fossils include a tooth from an Ornithocheiridae pterosaur¹⁷. In the present paper, we discuss new specimens of vertebrate fossils from the Phu Wat site housed in the Palaeontological Research and Education Centre (PRC) collected several years ago¹⁸. These specimens enhance our understanding of the fossil assemblage of the Sao Khua Formation and reconstruct its paleoecology.

Methodology:

Vertebrate fossils were (1) identified as the main vertebrate groups, (2) measured and described the appearance features and their characteristics, and (3) compared the features and characters with literature and classification. Theropod teeth morphology is described after Averianov and Skutschas (2009)¹⁹ and Hendrickx et al. (2015)²⁰. Dromaeosaurid claw is described after Senter (2007)²¹ and Brilhante et al. (2022)²².

Results and Discussion:

The Phu Wat site reveals a high diversity of predatory dinosaurs including Carnosauria, Baryonychinae, and Dromaeosauridae. Each of these theropod groups exhibits different niche adaptations. In contrast, a remaining herbivore dinosaur consists of a Brachiosauridae-like sauropod.

Systematic Paleontology

INFRAORDER CARNOSAURIA von Huene, 1920

PWA1-26 is a tooth that retains serrations on both margins and is lenticular in the crown top view. It shows arcuate enamel wrinkles extending across the labial and lingual edges. This specimen exhibits a ziphodont tooth shape (Figure 2). Based on their shape—compressed in distal view, pointed and serrated edges (denticles) on both sides of the margin these teeth can be classified as Carnosauria²⁰. Carnosauria fossils have previously been reported from the Sao Khua Formation^{9,12}.

SUPERFAMILY MEGALOSAUROIDEA Fitzinger, 1843

FAMILY SPINOSAURIDAE Stromer, 1915

PWA1-1 is an isolated, fragmentary tooth measuring approximately 53.59 mm in posterior carina length. This specimen preserves a part of the crown and root but lacks the upper part of the crown. The lingual and labial sides exhibit a coarse ridge, and the serrated

carina is highly reduced (Figure 3). It is classified as a spinosaurid tooth due to its characteristic conical shape, smooth enamel, and numerous fine ridges with a non-existent serrated carina. The ridge pattern of the Phu Wat spinosaurid is a smooth enamel surface on the crown with more than 20 fine ridges on each side. This pattern bears a stronger resemblance to the Khok Kruat spinosaurid morphotype (PM2016-1-003) than to the *Siamosaurus* morphotype (PM2016-1-006), with a wrinkled enamel surface on the crown with 16 coarse ridges on each side²³.

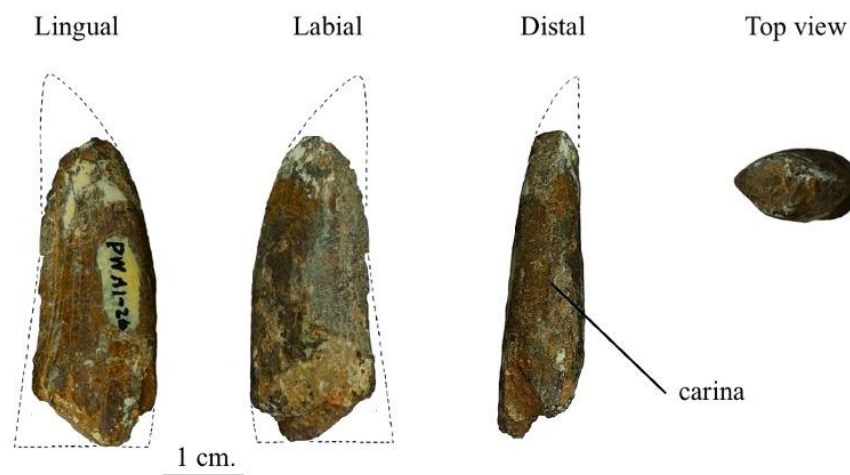


Figure 2.

Carnosauria tooth from the Phu Wat site (PWA1-26) and the character of Carnosaur tooth represent by the sample PWA1-26 showing the serration on both sides of lingual and labial views, and carinae in distal view, with lenticular shape in the top view.

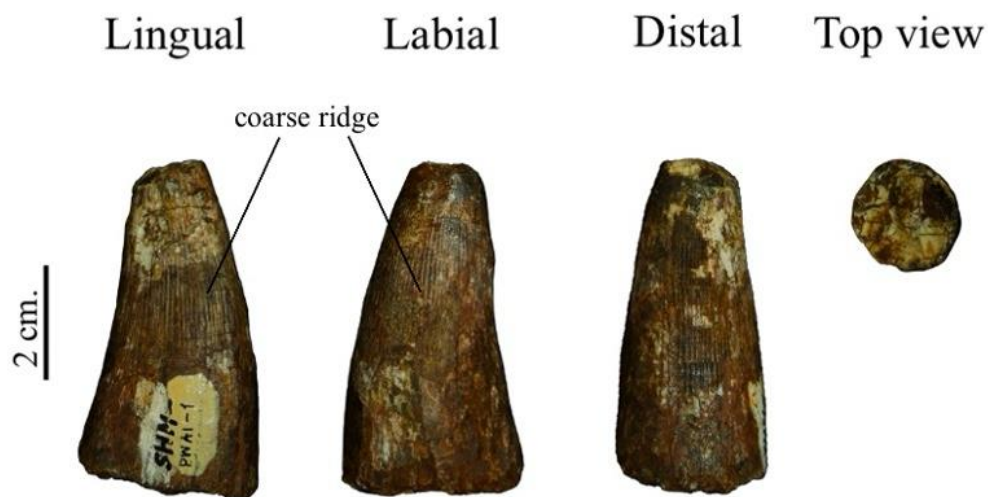


Figure 3.

Spinosaurid tooth (PWA1-1) presents a coarse ridge in the lingual and labial views, with no serrated carina.



SUPERFAMILY MEGALOSAUROIDEA Fitzinger, 1843

FAMILY SPINOSAURIDAE Stromer, 1915

cf. Baryonychinae

PWA1-3 is a fragmentary right tibia, with the proximal end measuring 90.42 mm in proximodistal length. Most of the shaft is broken, and the proximal surface is eroded. The anteroposterior length of the proximal end is 75.2 mm, and its maximum width is 40 mm, suggesting it may belong to a medium-sized theropod. The specimen is poorly preserved, with no fibula crest visible. However, a ridge on the lateral side of the tibia appears to originate laterodistally from the cnemial crest, indicating that the fibula crest is offset from the cnemial crest. The cnemial crest projects anteriorly and is slightly higher than the medial and lateral condyles. In the proximal view, the cnemial crest is round and slightly curved, and the proximal articular surface is longer anteroposteriorly compared to its width. The *incisura tibialis* is located on the lateral side of the cnemial crest, showing slight concavity without an accessory ridge, distinguishing it from Allosauroid theropods^{24,25}. The lateral condyle is poorly developed and very round in proximal view, while the medial condyle points dorsally and is notably taller than the lateral condyle (Figure 4). Based on the offset characteristic of the fibula crest relative to the cnemial crest, PWA1-3 can be assigned to a tetanuran theropod^{26,27}. The absence of a pronounced notch between the proximal articular condyles indicates that it is not an allosauroid^{25,28} by weakly developed *incisura tibialis* contrasts allosauroids^{25,29} and coelurosaurs^{30,31,32}. The ratio between the anteroposterior and mediolateral length of the proximal end of PWA1-3 is 1:1.85, somewhat similar to *Allosaurus*³³. Still, it differs from the extreme elongation seen in *Suchomimus*²⁹. The tibia also tapers towards the distal end of the cnemial crest, making the proximal outline resemble those of *Suchomimus* and *Camarillasaurus*³⁴. Based on these similarities, we tentatively assign PWA1-3 to Spinosauridae, possibly Baryonychinae.

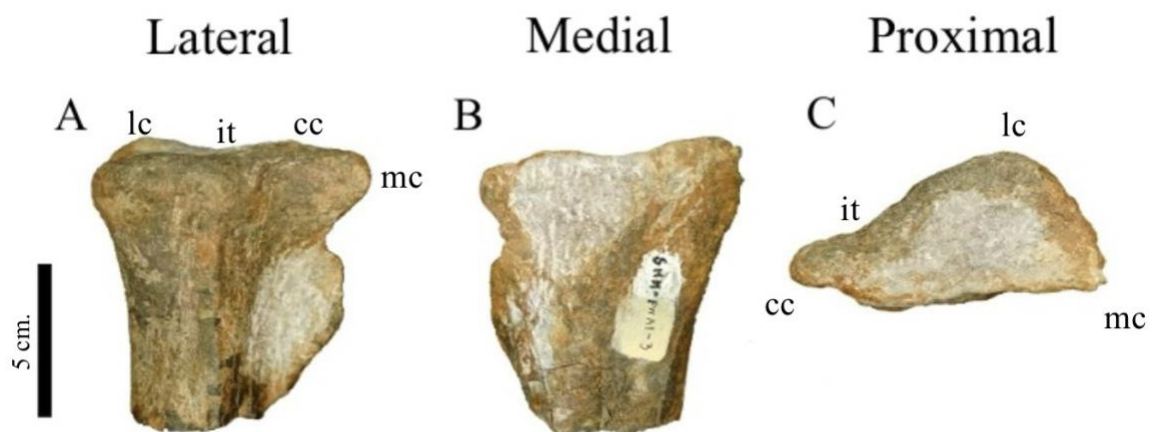


Figure 4.

cf. Baryonychinae right tibia (PWA1-3) in (A) lateral, (B) medial, and (C) proximal views; It shows the characteristic of Neotheropods by presented lateral condyle (lc): cnemial crest (cc), medial condyle (mc) and *incisura tibialis* (it) at the proximal part of the tibia.

INFRAORDER COELUROSAURIA von Huene, 1920

DIVISION MANIRAPTORA Gauthier, 1986

FAMILY DROMAEOSAURIDAE Matthew and Brown, 1922

PWA1-512 is the proximal half of an ungual phalanx from a small theropod, measuring approximately 7.58 mm. The dorsopalmar width is 5.10 mm, and the mediolateral width is 2.55 mm. The specimen retains most of its proximal region, with a markedly curved medial cotyle. A flexor tubercle is visible, and the overall shape is sharply curved (Figure 5). This specimen can be identified as the second pedal digit of a dromaeosaurid based on the following characteristics: a narrow and tall proximal portion in cross-section, a strongly concave ventral margin in lateral and medial views, a convex dorsal margin, absence of a proximodorsal lip and dorsal margin arches, and a well-developed flexor tubercle with an enlarged notch. A blood groove is present on both the lateral and medial surfaces. A distal break reveals a distinctive cross-sectional configuration, with the base of the dorsal margin edge forming a low arch that creates a rouleaux triangle-like shape above a sulcus. In contrast, the ventral margin edge expands to the palmar region. The medial margin is rounder than the lateral, with an extensive ventral margin. Additional features, such as a round dorsopalmar profile, a sharp keel on the ventral palmar region medially displaced, and nearly symmetrical blood grooves (with the left blood groove slightly lower than the right) further support its classification as a non-eudromaeosaurid²². These morphological characteristics have not been previously reported in any species from the Sao Khua Formation, marking the first record of Dromaeosauridae from Thailand. Based on the Phu Wat dromaeosaurid pedal claw size, it could be small, similar to the *Microraptor*. They probably represented an arboreal habitat.

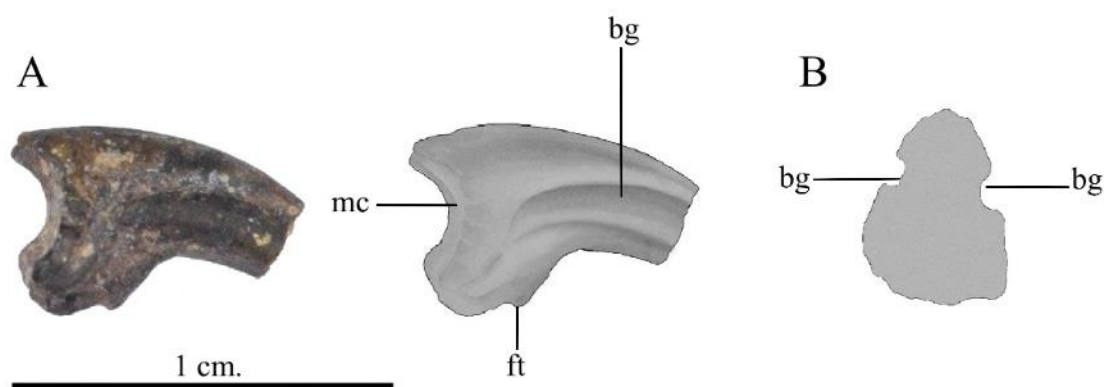


Figure 5.

Characteristics of the Dromaeosaurid pedal claw (PWA1-512), displaying the morphology of the claw in medial view (A) and cross-section of distal surface (B). Key structures include the medial cotyle (mc), blood groove (bg), and flexor tubercles (ft).

ORDER SAURISCHIA Seeley, 1888

SUBORDER THEROPODA Marsh, 1881

PWA1-8 is identified as an isolated phalanx measuring 36.08 mm in length. This phalanx is elongated and slender, with a weakly developed collateral ligament pit on its lateral surface. It has a slightly asymmetrical appearance in the ventral view, featuring a discernible ventral heel and a well-developed distal articular surface (Figure 7A). The overall shape resembles phalanx I of digit III of *Vespersaurus*, with its distal articulation being lateromedially compressed. The distal end has well-developed extensor and collateral pits and is ventrally depressed between the condyles³⁵. However, the distal end of PWA1-8 is more extended than *Vespersaurus*'s. Another specimen PWA1-4 is identified as an isolated fibula approximately 87.5 mm in length. Its medial surface features a distinct medial fossa and ridge, indicative of interosseous membrane attachment (Figure 7B). Notably, the morphology of this medial fossa differs from that observed in derived coelurosaurs and the broadly shallow surfaces characteristic of spinosaurids, instead resembling the condition seen in *Ceratosaurus* and *Majungasaurus*³⁶. Additionally, the lateral surface bears a scar indicative of *muscular iliofibularis* attachment, while the posterior surface features a prominent ridge. Thus, PWA1-8 and PWA1-4 can be interpreted roughly as they probably belong to theropod dinosaurs.

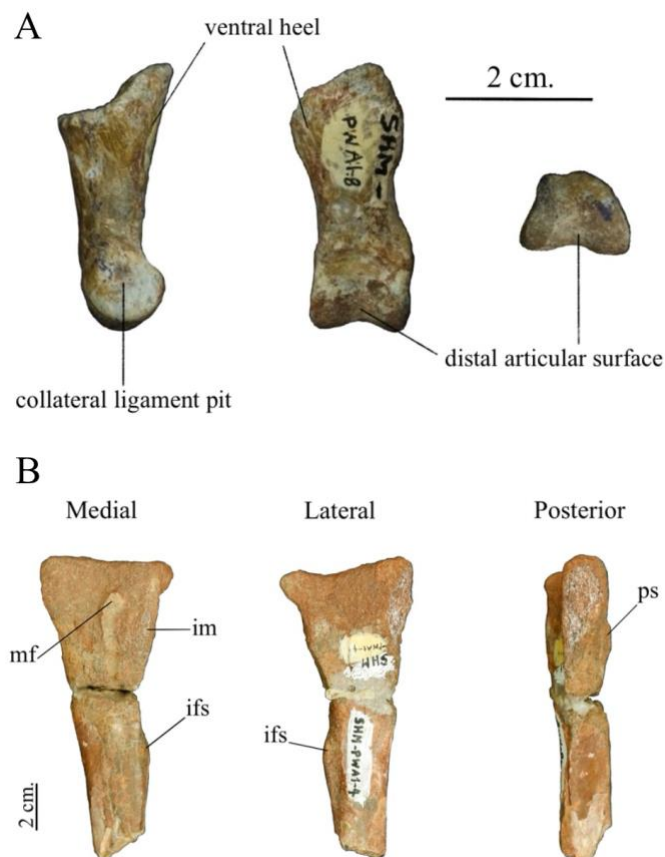


Figure 7.

Theropod bones (A) Isolated phalanx (PWA1-8) and (B) fibula (PWA1-4) containing some morphology that is a scar for *muscular iliofibularis* (ifs), ridge for the attachment of interosseus membrane (im), medial fossa (mf) and posterior surface (ps).

SUBORDER SAUROPODA Marsh, 1878

PWB-724 is identified as right metatarsal-IV (Figure 8). It is 223 mm in length. The proximal part has a wide, smooth, L-shaped surface, similar to the *Camarasaurus*³⁷, and the distal part is slightly twisted. The proximal surface has an embayed ventromedial edge. The shallow and concave articular facet for metacarpal III occupies about half of the shaft. The distal articular surface is a trapezoidal shape with little rugosity and is much smaller than the proximal end. The distal condyles are beveled about 16 degrees medially. This specimen is identified as the right metatarsal-IV of a sauropod based on comparison with *Venenosaurus*³⁸, *Sonorasaurus*^{39,40}, *Camarasaurus*³⁷, KUV 142200⁴¹, *Apatosaurus*⁴², *Tornieria* (“*Barosaurus*”) *africanus*⁴³, and *Galeamopus*⁴⁴. PWB-724 is more gracile than *Apatosaurus*'s but the shape outline is comparable to *Venenosaurus*'s. The characteristic of the distal articular surface that beveled medially, making the medial side of the bone shorter than the lateral one, has been identified as a synapomorphy for Brachiosauridae^{45,46}. However, the beveled articular surface of PWB-724 is not as strong as seen in *Sonorasaurus* and is more similar to a smaller Brachiosauridae, *Venenosaurus*.

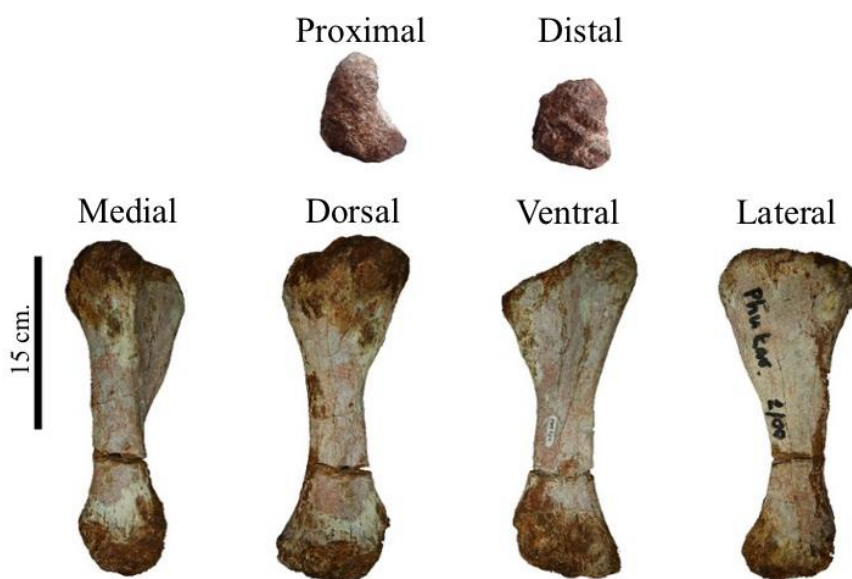


Figure 8.

The metatarsal of a sauropod (PWB-724) is in several views.

Excluding dinosaur fossils, the Phu Wat site reveals a high diversity of faunal fossils including Actinopterygian, Hybodontid, Testudines, and Crocodyliformes (Figure 9). The fossil assemblage indicates a freshwater environment.

Actinopterygians Isolated fragmentary actinopterygian fossils consisting of teeth and scales (Figure 9A, 9E). The teeth specimens are characterized by a hemispherical (peg-like) shape and a smooth surface, which signifies a relation to a group of Pycnodontiform fishes⁴⁷. The fish scales display a rhomboidal (diamond-shaped) ganoid scale pattern. The lack of pegs on the dorsal and ventral margins signifies an affinity with Ginglymodi^{48,49}.

Heteroptychodus sp. Numerous isolated Hybodontid teeth were collected (Figure 9B). The preserved parts of the teeth include the crown, and most specimens exhibit a parallelogram-



shaped outline, asymmetric and almost flat, with parallel ridges running along the surface (top view). The crown is low and densely packed with strong ornamentation. The largest tooth measures 17.45 mm in length. These specimens are resembling to *Heteroptychodus* teeth. **Crocodyliform** PWA1-116 is an isolated poorly preserved tooth that measures 20.29 mm in length, however, it presents serrated carinae on the lateral side, with shallow grooves and slightly slanting ventrally toward the crown's central region (Figure 9C), resembling crocodilian affinities.

Testudines PWA1-756 is a poorly preserved fragmented shell plate, measured approximately 17.29 mm in length, displaying a strong vermiculated ridges ornamentation pattern combined with deep pits (Figure 9D) which possibly signify affinities with Trionychoidea⁵⁰.

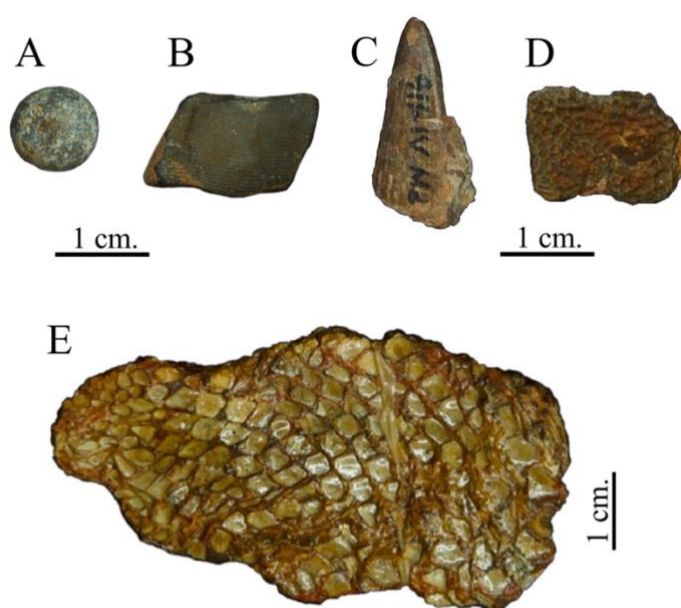


Figure 9.

Other vertebrate fossils from the Phu Wat site include A) hemispherical tooth of Actinopterygian, B) tooth of *Heteroptychodus* sp., C) Crocodyliform tooth, D) Testudines shell plate, and E) Actinopterygian scales.

Paleodiet and Paleoecology interpretation

The theropod dinosaur may have various diets; Carnosauria possesses blade-like teeth for hunting large prey like sauropod dinosaurs. The co-occurrence of Carnosauria and sauropods is observed throughout dinosaur evolutionary history. In contrast, Spinosauridae, specifically Baryonychinae, exhibit conical teeth resembling those of crocodiles and pterosaurs, suggesting a diet primarily focused on piscivores. However, evidence from related taxa in other countries, such as Baryonyx from England, indicates a more varied diet, including fish scales and juvenile Iguanodon bones. Additionally, Spinosauridae teeth on the cervical vertebrae of ornithocheirid pterosaurs from the Santana Formation further support the dietary diversity within this group. Small-sized Dromaeosauridae, bird-like dinosaurs, suggest an ability to fly or glide and a generalist diet that includes fish, birds, and small mammals. The

presence of Dromaeosauridae at the Phu Wat site signifies the existence of this dinosaur group in Southeast Asia. This discovery enriches our knowledge of dinosaur diversity and suggests that small theropod dinosaurs occupied specific ecological niches during this epoch—the finding of cf. Baryonychinae at the Phu Wat site indicated the diversity of Spinosauridae in the Sao Khua Formation; not only *Siamosaurus* in the Spinosaurinae subfamily but also Baryonychinae coexisted in the same formation. A Brachiosauridae-like sauropod material correlates with the discovery of this group from the same formation, suggesting the existence of giant sauropods in this area. However, the absence of small herbivorous dinosaurs, as found in other sites of the Sao Khua Formation may be attributed to poor preservation based on the highly fragmentary nature of the recovered fossils rather than resource competition in the ecological niche. The discovery of crocodyliform material in this study is a very limited number; only a few teeth represent it, but they do not present a scute (a bony external plate) or other commonly found material parts. This differs from other sites in the Sao Khua Formation. The Testunides fossils found at the Phu Wat site include at least two types: Adocidae *Isanemys srisuki* from a previous report and in this study which possibly a member in a group of Trionychoidea, signify a high diversity in turtles. The diversity of Actinopterygii fish found here is similar to that of the Phu Phan Thong site. Meanwhile, previous reports from the Phu Wat on Chondrichthyes fossils included records of two species *Heteroptychodus steinmanni* and *Hybodus* spp. This study also found many *Heteroptychodus* teeth. The reconstruction of the paleoecology of the Cretaceous Phu Wat site is shown in Figure 10.

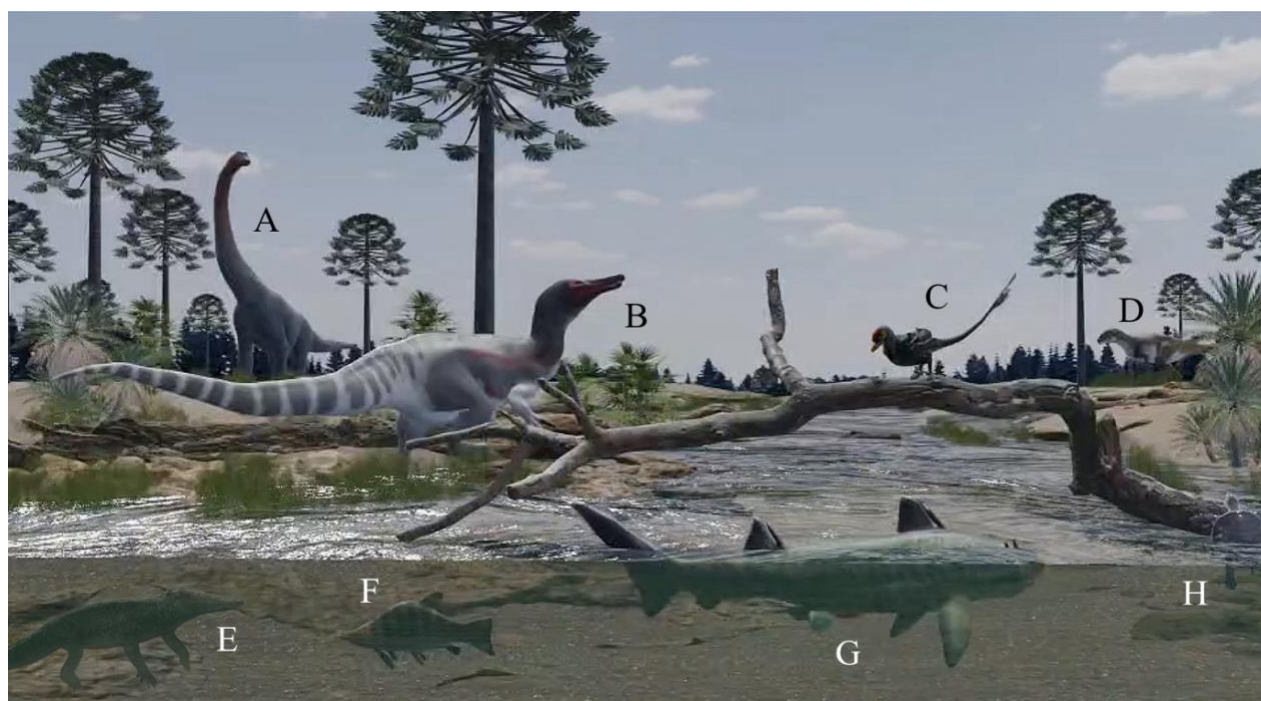


Figure 10.

The Cretaceous Paleoecology reconstruction of the Phu Wat site (A) Sauropod (B) Baryonychinae (C) Dromaeosauridae (D) Carnosauria (E) Crocodyliform (F) Actinopterygians (G) *Heteroptychodus* sp. (H) Testudines (illustrated by Chatcharin Somboon, this work).

Conclusion:

The vertebrate fossils discovered from the Phu Wat site, Nong Bua Lamphu Province help us understand the complexity of this ancient ecology and emphasize the richness of vertebrate fauna in the Sao Khua Formation. This research is significant due to several fundamental



discoveries, including the first records of the pedal claw of Dromaeosauridae and tibia of cf. Baryonychinae in Thailand and Southeast Asia. Additionally, the sauropod material and the teeth of Carnosauria and Spinosaurid findings not only enhance our understanding of the distribution of these taxa but also underscore the importance of the Phu Wat site as a crucial fossil assemblage in Thailand.

Acknowledgements:

We thank Chiang Mai University, Graduate School, CMU, and the Department of Geological Sciences, Faculty of Science, CMU, for their academic and laboratory support. We thank the Cretaceous Research and anonymous reviewers for their constructive comments on an early version of the manuscript. Special thanks are also given to PRC staff for allowing access to their collections and support. We gratefully thank all the friends who contributed to this work. The authors also acknowledge anonymous reviewers' critical comments and suggestions, significantly improving the manuscript.

References:

1. Tucker RT, Hyland EG, Gates TA, Ryan King M, Roberts EM, Foley EK, Berndt D, Hanta R, Khansubha S, Aswasereelert W, Zanno LE. *Palaeogeogr. Palaeoclimatol. Palaeoecol.* 2022;601.
2. Racey A, Goodall JGS. In Buffetaut E, Cuny G, Le Loeuff J, Suteethorn V. (Eds), *Geol. Soc. Spec. Publ.* 2009;315:69–84.
3. Kozu S, Sardud A, Saesaengseerung D, Pothichaiya C, Agematsu S, Sashida K. *Geosci. Front.* 2017;8.
4. Department of Mineral Resources, Bangkok, Thailand. 1992;1–129.
5. Sattayarak N, Srigulawong S. *TGJ Special Issue.* 2008;1:1–40.
6. Tumpeesawan S, Sato Y, Nakhpadungrat S. *TNH.* 2010;10:93106.
7. Buffetaut E, Suteethorn V. *Bull. N.M. Mus. Nat. Hist. Sci.* 1998;14:205-210.
8. Buffetaut E, Ingavat R. *C. R. Acad. Sci.* 1984;298:915-918.
9. Buffetaut E, Ingavat R. *Rev. Paléobiol.* 1986;5:217-220.
10. Samathi A, Butler RJ, Chanthasit P. *ISAD2015.* 2015;30.
11. Buffetaut E, Suteethorn V, Tong H. In Buffetaut E, Cuny G, Le Loeuff J, Suteethorn V. (Eds), *Geol. Soc. Spec. Publ.* 2009;315:1229-243.
12. Buffetaut E, Suteethorn V. In Royo-Torres R, Gascó F, Alcalá L. (Eds) 10th Annual Meeting of the European Association of Vertebrate Palaeontologists, Teruel (Spain). 2012;20:1-290.
13. Samathi A, Chanthasit P, Sander P. *Acta Palaeontol. Pol.* 2019;64.
14. Martin V, Buffetaut E, Suteethorn V. *C. R. Acad. Sci.* 1994;319:1085-1092.
15. Suteethorn S, Le Loeuff J. In the 10th Conference of EAVP. 2012;249-251.
16. Buffetaut E, Dyke G, Suteethorn V, Tong H. *C. R. Palevol.* 2005;4:681-686.
17. Buffetaut E, Suteethorn V, Cuny G, Khansubha S, Tong H, Le Loeuff J, Cavin L. The 1st International Conference on Palaeontology of Southeast Asia, Mahasarakham University Journal. 2003;23:69-82.
18. Srisuk P. *Bulletin of the Srisuk's House Museum. Series A (Paleontology).* 2000;2:1-22.
19. Averianov AO, Skutschas PP. *Proceedings ZIN RAS.* 2009;4:363–378.
20. Hendrickx C, Mateus O, Araújo R. J. *Vertebr. Paleontol.* 2015;15:5–61.
21. Senter P. *Bull. Gunma Mus. Natu. Hist.* 2007;11:1–6.

22. Brilhante N, França TCD, Castro F., Costa L, Currie P, Azevedo S, Delcourt RA. *Hist Biol* 2022;34:2195-2204.
23. Wongko K, Buffetaut E, Khamha S, Lauprasert K. *TNH*. 2019;19:8–20.
24. Hutt S. MPhil thesis. University of Portsmouth. 1999.
25. Naish D. *Proceedings Proc Geol Assoc*. 2003;114:319-326.
26. Rauhut OWM. *Special Papers in Palaeontology*. 2003;69:1-213.
27. Rauhut OWM. *Geol. Mag.* 2005;142:97–107.
28. Currie PJ, Zhao X. *Can. J. Earth Sci.* 1994;30: 2037–2081.
29. Sereno PC, Dutheil DB, Iarochene M, Larsson HCE, Lyon GH, Magwene PM, Sidor CA, Varricchio, DJ, Wilson JA. *Science*. 1996;272:986–991.
30. Azuma Y, Currie PU. *Can. J. Earth Sci.* 2000;37:1735–1753. Carrano M. J. *Vertebr. Paleontol.* 2007;27:163-179.
31. Harris JD. *Bull. N.M. Mus. Nat. Hist. Sci.* 1998;13:1–75.
32. Holtz TR. *Gaia*. 2000;15:5–61.
33. Gilmore CW. *Bull. U.S. Natl. Mus.* 1920;110:1–154.
34. Samathi, A, Sander P, Chanthasit P. *Hist. Biol.* 2021;33:1-15.
35. Langer MC, Martins NDO, Manzig PC, Ferreira GD, Marsola JDA, Fortes E, Lima R, Santana LCF, Vidal LDS, Lorençato RDS. *Sci. Rep.* 2019;9:9379.
36. Carrano M. J. *Vertebr. Paleontol.* 2007;27:163-179.
37. Tschopp ED, Oliver W, Thomas F, Winand B. *Palaeontol. Electron.* 2015;18244A:1–65.
38. Tidwell V, Carpenter K, Meyer S. In Tanke, Darren H., Carpenter, Kenneth (eds.). *Mesozoic Vertebrate Life. Life of the past*. Bloomington & Indianapolis: IU Press. 2001;139–165.
39. Ratkevich R. *JANAS*. 1998;31:71–82.
40. D'Emic MD, Foreman BZ, Jud NA. *J. Paleontol.* 2016;90:102–132.
41. Maltese A, Tschopp E, Holwerda F, Burnham D. *PeerJ*. 2018;6:e5250.
42. Upchurch P, Tomida Y, Barrett P. *Nat. Sci. Mus. Monogr.* 2004;26:1-118.
43. Janensch W. *Palaeontogr. Supplement*. 1961;7:177–235.
44. Tschopp ED, Mateus, O. *PeerJ*. 2007;5:e3179.
45. D'Emic MD. *Zool. J. Linn. Soc.* 2012;166:624–671.
46. Mannion PD, Upchurch P, Barnes R, Mateus O. *Zool. J. Linn. Soc.* 2013;168:98–206.
47. Detlev T, Kevin S, Sebastian S. *Hist. Biol.* 2021;33:868–879.
48. Tong H, Buffetaut E, Suteethorn V, Suteethorn S, Cuny G, Cavin L, Deesri U, Martin JE, Wongko K, Naksri W, Claude J. *Ann. Paléontol* 2019;105:223-237.
49. Cavin L, Deesri U, Suteethorn V. *Geol. Soc. Spec. Publ., London*. 2009;315:125-139.
50. Manitkoon S, Deesri U, Lauprasert K, Warapeang P, Nonsrirach T, Nilpanapan A, Wongko K, Chanthasit P. *Foss. Rec.* 2022;25:83-98.



Phase Transition and Mechanical Properties of Calcined Flue Gas Desulfurization (FGD) Waste as a Potential Substitute for Natural Calcium Sulfate Subhydrate

Teeratada Yanwattana,^{1,2} Nattakan Soykeabkaew,^{1,2} Sitthi Duangphet,^{1,2} Somwan Chumphongphan,^{1,2} Uraiwan Intatha,^{1,2} Nattaya Tawichai^{1,2,*}

¹School of Science, Mae Fah Luang University, 333 MI, Muang, Chiangrai, 57100, Thailand

²Center of Innovative and Materials for Sustainability (iMatS), Mae Fah Luang University, Thailand

(*Corresponding author's e-mail: nattaya.taw@mfu.ac.th)

Abstract

In response to increasing environmental concerns, researchers have explored the potential of using Flue Gas Desulfurization (FGD) waste as a replacement for natural calcium sulfate sub-hydrate. This study focused on the calcination of FGD waste from the Mae Moh Power Plant in Thailand under different conditions. The calcination experiments were conducted at a constant temperature of 150°C and varying pressures (110, 160 and 190 kPa), with the duration of calcination ranging from 0 to 40 minutes. The optimal calcination time was found to be 23 minutes, resulting in a crystallization water content of 6.2%. Chemical analysis using X-ray fluorescence (XRF) confirmed a phase transition from calcium sulfate dihydrate to calcium sulfate hemihydrate. X-ray diffraction (XRD) patterns further supported this transformation. Rietveld refinement was used to analyze the proportions of alpha- and beta-phases in the resulting calcium sulfate hemihydrate. Scanning electron microscopy (SEM) revealed a semi-rod-like particle morphology with a size distribution of 50 to 90 microns. The sample under pressure 110 kPa displayed significant flexural and compressive strengths (4.31 MPa and 6.69 MPa, respectively), indicating its potential as a raw material for construction and casting applications. The results of this study demonstrate the feasibility of utilizing FGD waste as a viable alternative to natural calcium sulfate sub-hydrate. The optimized calcination conditions and the promising mechanical properties of the resulting product highlight its potential applications in various industries.

Keywords: FGD gypsum, calcination, calcium sulfate dihydrate, alpha-HH

Introduction

In Thailand, coal was chosen as the primary fuel for power plants to generate electricity due to its lower cost and price than other fuel types such as oil and gas. However, coal combustion produces a significant amount of carbon monoxide (CO) and sulfur dioxide (SO₂) gasses, in turn, affects the emission of greenhouse gases and is expected to lead to changes in the climate. Flue gas desulfurization (FGD) systems are utilized in coal power plants to capture SO₂ from flue gas before it is released into the atmosphere. The by-product of this process is calcium sulfate dihydrate (CaSO₄·2H₂O), also known as flue gas desulfurization gypsum (FGD gypsum) or synthetic gypsum. FGD gypsum can dehydrate to be calcium sulfate hemihydrate (CaSO₄·0.5H₂O) in two forms: alpha-calcium sulfate hemihydrate (alpha-HH) and beta-calcium sulfate hemihydrate (beta-HH) [1]. The current research focuses on producing α-Calcium Sulfate Hemihydrate from FGD gypsum. However, the existing processes are complex, time-consuming, and expensive. Therefore, it is important to explore the potential of producing α-Hemihydrate under vapor pressure without using crystal modifiers. This involves examining the influence of vapor pressure in the calcination process on alpha-hemihydrate formation and studying the properties of FGD gypsum from different sources.

The data obtained from this research has the potential to drive increased utilization of FGD gypsum. It could be more widely used than natural gypsum due to its lower cost, while also helping to conserve landfill space and preserve natural gypsum, which is a limited resource.

Materials and methods

Preparation of raw materials

The FGD gypsum used in this study was obtained from the Mae Moh power plant in Lampang Province, Thailand. Initially, the FGD gypsum was pulverized using a mortar and pestle to ensure that the particles were uniformly fine. The water was then filtered at 250 micrometers using a sieve shaker to eliminate primary impurities such as gravel, rock, sand, or coal. After this, the FGD gypsum will undergo grinding and filtration before being characterized and utilized as a raw material in the calcination process.

Transformation from FGD gypsum to calcium sulfate hemihydrate

In order to determine the precise duration for calcining FGD gypsum to attain Hemihydrate (6.2% CW), an experimental calcination involving 500 g at 150°C was conducted. The sample was manually stirred or shaken every minute. Subsamples were then extracted and subjected to %CW analysis using a moisture analyzer at 10-minute intervals. Subsequently, the resulting data was graphed to ascertain the correlation between %CW and calcination duration. The primary objective is to identify the calcination duration required to achieve Hemihydrate (6.2% CW).

Characterizations

The chemical composition of the purified FGD gypsum and alpha-HH prepared with different CuCl_2 contents was determined using X-ray fluorescence spectroscopy (XRF, M4 TORNADO, BRUKER, Germany). The phase formation of the materials was identified using X-ray diffraction spectrometry (XRD, X'Pert PRO MPD, PANalytical B.V., Holland). The quantitative alpha-HH phase was also determined through Rietveld refinement using X'pert HighScore software. The morphologies of FGD gypsum and alpha-HH were observed using scanning electron microscopy (SEM, MIRA 4, TESCAN, Czech Republic), and the particle size distribution powder was analyzed using Powder-spectral-sensify (PSD, HARIBA). The setting time and expansion on setting were tested according to ASTM C472-99 and ASTM C59/M-00, respectively. The obtained solids were formed into rectangular bars measuring 25 cm x 2.5 cm x 2.5 cm. The flexural strength in the 3-point bending mode was tested in accordance with ASTM C1161. Water absorption was calculated according to eq. (1), where M1 = mass after soaking (g), and M2 = mass after drying (g).

Results and discussion

The experiment analyzed the optimization of calcination time for 500 grams of FGD gypsum at a temperature of 150°C. The results indicated that calcination under 160 and 190 kPa pressure required less time compared to calcination under dry and wet atmospheric pressure conditions (Table 1). Specifically, the calcination of FGD gypsum to hemihydrate (6.2% CW) under 160 and 190 KPa pressure conditions took 23 minutes, whereas it took 24 minutes under dry and wet atmospheric pressure conditions (Table 1). Gypsum with a natural purity ranging from 95% to 100% exhibits a crystalline water content (%CW) between 19.8% and 20.9%. FGD gypsum ($\text{CaSO}_4 \cdot 2\text{H}_2\text{O}$) closely approximates the %CW of natural gypsum (refer to Table 1), indicating its classification as high-purity gypsum. The %CW of Calcium Sulfate Sub-Hydrate ($\text{CaSO}_4 \cdot n\text{H}_2\text{O}$) resulting from calcination under varying conditions was maintained within the 6.0% to 6.2% range (refer to Table 1), aligning with the %CW of Calcium Sulfate Hemihydrate ($\text{CaSO}_4 \cdot 0.5\text{H}_2\text{O}$) derived from calculations. Commercial Calcium Sulfate Sub-Hydrate ($\text{CaSO}_4 \cdot n\text{H}_2\text{O}$) exhibits a %CW exceeding 6.2%, suggesting the presence of more than 0.5 water molecules within its crystals (refer to Table 1).

Table 1. Crystal of water of FGD gypsum at each calcination time.

| Time (min) | % Crystal of water | | |
|---------------|--------------------|------------------|------------------|
| | 101 kPa | 160 kPa | 190 kPa |
| 0 | 20.19 \pm 0.03 | 20.19 \pm 0.03 | 20.19 \pm 0.03 |
| 10 | 12.05 \pm 0.02 | 11.82 \pm 0.05 | 11.34 \pm 0.07 |
| 20 | 7.64 \pm 0.10 | 7.59 \pm 0.01 | 7.52 \pm 0.04 |
| 30 | 4.46 \pm 0.06 | 3.39 \pm 0.11 | 3.45 \pm 0.01 |
| 40 | 1.19 \pm 0.02 | 1.03 \pm 0.06 | 0.81 \pm 0.02 |

Through the calcination process of 100% FGD gypsum under dry atmospheric pressure, a subhydrate yield of approximately 81.92% is produced (Table 2). This closely aligns with the anticipated value of 78.16%, representing the residual weight resulting from the transformation of Dihydrate ($\text{CaSO}_4 \cdot 2\text{H}_2\text{O}$) to Hemihydrate ($\text{CaSO}_4 \cdot 0.5\text{H}_2\text{O}$) during calcination. Calcination under wet atmospheric pressure, including conditions of 160 and 190KPa, yields a reduced subhydrate amount (Table 2). This reduction is attributed to the interaction between hemihydrate and the present vapor or steam during the calcination process, which leads to a rehydration process, forming dihydrate on the inner surface of the kettle.

Table 2. Data from the calcination of FGD Gypsum under each condition.

| | 101 kPa | 160 KPa | 190 KPa | Commercial Plaster |
|-------------------------|-----------------|-----------------|-----------------|-----------------------|
| Crystal of Water (%) | 6.12 \pm 0.15 | 6.18 \pm 0.17 | 6.04 \pm 0.19 | 6.38 \pm 0.01 |



| | | | | |
|------------------|-------------|-------------|-------------|---|
| Yield (%) | 71.55 ±0.94 | 71.21 ±1.01 | 70.02 ±1.28 | - |
|------------------|-------------|-------------|-------------|---|

Initially, it is noted that FGD gypsum exhibits an approximately 0.53% higher calcium content in comparison to commercial subhydrate, while containing around 1.63% less sulfur. Moreover, both FGD gypsum and all subhydrates resulting from the calcination of FGD gypsum demonstrate impurity levels approximately 2-3 times higher than commercial subhydrate, as indicated in Table 3. Subsequent analysis revealed that following the calcination of FGD gypsum, the calcium content decreases by a minimum of 1.4%, while the sulfur content experiences an increase of at least 1.5%. It is essential to note that the impurities present in FGD gypsum do not consist of environmentally concerning elements, as delineated in Table 3.

Table 3. Chemical composition of FGD Gypsum, Subhydrate obtained

| Element | FGD Gypsum | Dry Atmospheric | Wet Atmospheric | 160 KPa | 190 KPa | Commercial grade |
|------------------|------------|-----------------|-----------------|-------------|---------|------------------|
| CaO | 55.05 | 53.62 | 53.59 | 53.56 | 53.60 | 54.52 |
| SO ₂ | 43.27 | 44.78 | 44.82 | 44.94 | 44.83 | 44.90 |
| SiO ₂ | 0.49 | 0.50 | 0.49 | 0.43 | 0.47 | 0.17 |
| AlO ₂ | 0.49 | 0.42 | 0.43 | 0.41 | 0.41 | 0.17 |
| Mg ₂ | 0.43 | 0.41 | 0.43 | 0.43 | 0.44 | 0.16 |
| IO ₂ | 0.28 | 0.27 | 0.26 | 0.25 | 0.26 | 0.09 |

The diffraction peak patterns of subhydrate derived from FGD gypsum calcination exhibit noteworthy similarity, thereby necessitating precise differentiation. These patterns can be categorized into two distinct groups. The initial group displays a singular peak at 20–21 degrees, denoting subhydrate resulting from calcination under conditions of both dry atmospheric pressure and wet atmospheric pressure. Conversely, the second group manifests a dual peak at 20–21 degrees, signifying subhydrate obtained from calcination under the conditions of 160 and 190 KPa, as well as the commercial subhydrate (refer to Figure 1). The two subhydrate groups exhibit distinct peak patterns. The peak pattern of the first group closely resembles the subhydrate containing 0.5 molecules of water, also known as hemihydrate, while the peak pattern of the second group closely resembles the subhydrate containing 0.6 molecules of water. It is notable that the FGD subhydrate, obtained through calcination under all conditions, lacks a double peak at 25 degrees (Figure 1). Consequently, all FGD subhydrates are categorized as alpha-type, also referred to as Alpha-Subhydrate. In contrast, the commercial subhydrate displays a double peak at 25 degrees (Figure 1), resulting in its classification as Beta-Subhydrate.

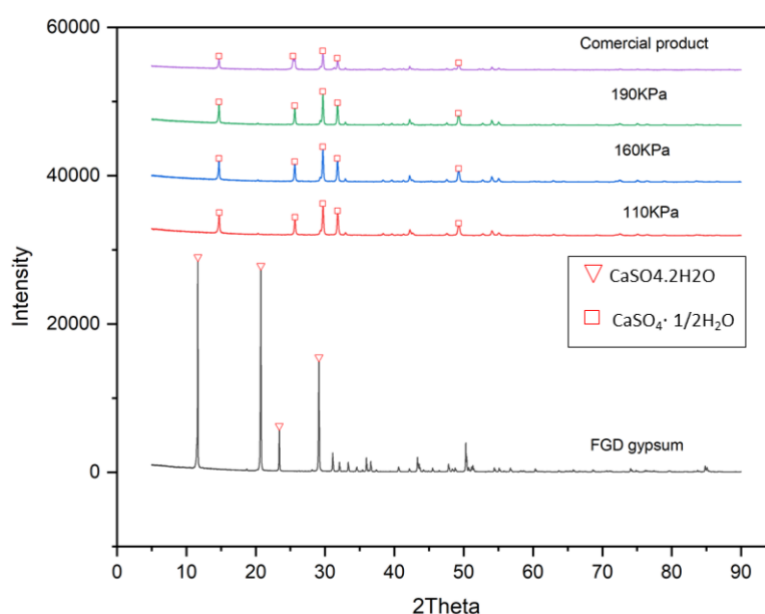


Figure 1. XRD patterns of samples.

FGD gypsum initially exhibits a monoclinic crystalline structure, with some monoclinic particles interconnected in an orthorhombic arrangement. Notably, rod-like particles similar to those depicted in Figure 2 (a) have been identified. Subsequently, sub-hydrates obtained from both dry atmospheric-pressure and wet atmospheric-pressure calcination, including commercially available sub-hydrates, demonstrate a trigonal crystalline structure, with some trigonal particles interconnected in a hexagonal configuration. Additionally, similar rod-like particles have been observed in the sub-hydrates depicted in Figure 2 (b), (c), and (f). Moreover, sub-hydrates obtained from calcination at both 160 KPa and 190 KPa pressures exhibit a monoclinic crystalline structure, with interconnected monoclinic particles displayed in an orthorhombic arrangement. Furthermore, particles exhibiting a triclinic crystalline structure have been observed (Figure 2: (d)-(e)). An additional noteworthy observation pertains to the closed calcination processes, specifically the wet atmospheric-pressure calcination, as well as the calcination at 160 KPa and 190 KPa pressures, wherein sub-hydrate particles obtained demonstrate indeterminate interconnections, resulting in crystal imperfections. It is evident that certain sub-hydrate particles are formed by the bonding of smaller sub-hydrate particles to each other (Figure 2: (b), (c), (d)).

FGD gypsum, upon calcination, exhibits a particle size of 76.79 μm , which is further reduced during the process. Dry atmospheric-pressure calcination yields the smallest particle-size subhydrate, while wet atmospheric-pressure calcination at 160 KPa and 190 KPa pressures results in larger particles. Upon calcination, FGD gypsum undergoes vapor contact in the kettle, leading to an indefinite directional bonding of subhydrate particles and consequently larger subhydrate particle sizes. In comparison, commercial subhydrate derived from natural gypsum displays significantly smaller particle sizes than FGD subhydrate, with similar size distribution characteristics.

In the study, subhydrate properties were evaluated under various calcination conditions and compared with commercial and FGD subhydrates. Notably, the water requirement ratio of subhydrate from Dry Atmospheric-pressure calcination is higher than subhydrates from Wet Atmospheric-pressure, 160 KPa, and 190 KPa calcination, suggesting an inverse relationship with particle size and crystal water content. The dispersion of slip water is better in subhydrates from closed conditions and commercial subhydrate. Additionally, the Dry Atmospheric pressure subhydrate exhibits a faster setting time than subhydrates from other conditions, while the commercial subhydrate has a longer setting time. Density remains consistent across FGD subhydrate samples, but it's higher in those molded with commercial subhydrate. Water absorption is similar for FGD subhydrate samples under various conditions but lower in commercial subhydrate samples due to their higher density, indicating reduced porosity. These findings provide valuable insights into subhydrate properties in different calcination scenarios.

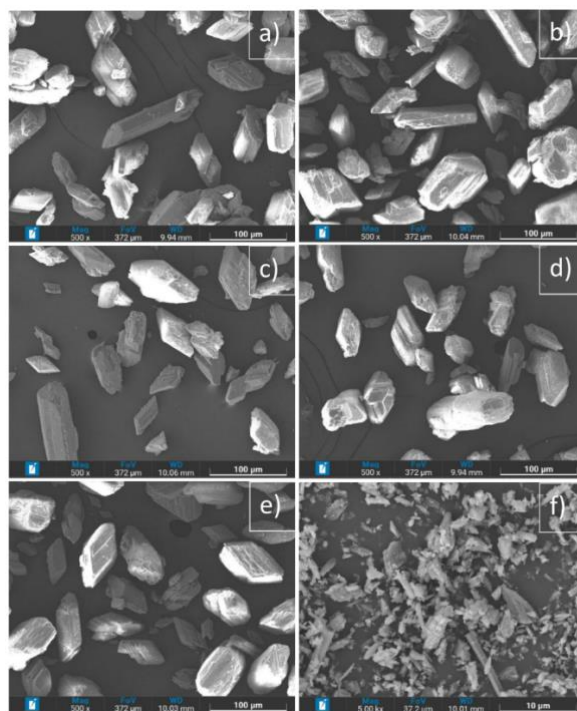


Figure 2. SEM image of (a) FGD Gypsum; (b) Subhydrate obtained from the Dry Atmospheric-pressure calcination; (c) Subhydrate obtained from the Wet Atmospheric-pressure calcination; (d) Subhydrate obtained



from the calcination at 160 KPa of pressure; (e) Subhydrate obtained from the calcination at 190 KPa of pressure; (f) Commercial Subhydrate.

In the conducted study, we conducted an evaluation of the properties of subhydrates under various calcination conditions and conducted a comparative analysis with commercial and FGD subhydrates. An observation of note is that the water requirement ratio of subhydrate derived from Dry Atmospheric-pressure calcination surpasses that of subhydrates from Wet Atmospheric-pressure, 160 KPa, and 190 KPa calcination. This suggests an inverse correlation with particle size and crystal water content. It was also established that the dispersion of slip water is superior in subhydrates from closed conditions and commercial subhydrate. Furthermore, the subhydrate from Dry Atmospheric pressure manifests a swifter setting time compared to subhydrates from alternative conditions, while the commercial subhydrate exhibits a longer setting time. Despite density remaining consistent across FGD subhydrate samples, it is higher in those fashioned with commercial subhydrate. Although water absorption levels are akin for FGD subhydrate samples under varied conditions, they are lower in commercial subhydrate samples due to their escalated density, indicative of reduced porosity. These findings bestow valuable insights into subhydrate properties across diverse calcination scenarios.

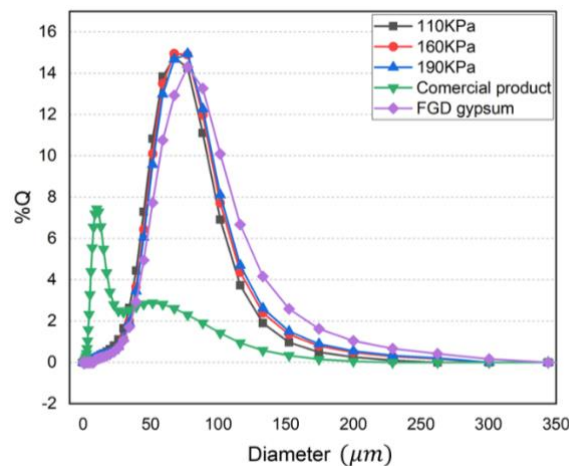


Figure 3. Particle size distribution.

The FGD subhydrate is derived from dry atmospheric-pressure calcination. The experimental sample, when molded, exhibits the highest specific flexural strength, surpassing subhydrates obtained from calcination at 160 kPa of pressure, wet atmospheric-pressure calcination, commercial subhydrate, and calcination at 190 kPa of pressure. The reduced specific flexural strength of subhydrates obtained from wet atmospheric-pressure calcination, calcination at 160 kPa of pressure, and calcination at 190 kPa of pressure is attributed to vapor presence during calcination. This vapor induces chaotic bonding among subhydrate particles and introduces crystal imperfections, detrimentally impacting particle orientation when formed into experimental samples or products, consequently diminishing mechanical properties (refer to Table 3).

Table 4. Results from the Rehydration of each Suhydrate to Dihydrate.

| Element | 110 KPa | 160 KPa | 190 KPa | Commercial grade |
|------------------------------|--------------|--------------|--------------|---------------------|
| Water requirement ratio | 0.559 ±0.011 | 0.541 ±0.018 | 0.532 ±0.015 | 0.667 ±0.013 |
| Dispersion of slip (cm) | 16 ±1.23 | 17 ±0.94 | 16 ±1.70 | 20 ±0.56 |
| Initial Setting time (min) | 6 ±0.15 | 6 ±0.26 | 5.30 ±0.42 | 8 ±0.33 |
| Final Setting time (min) | 15 ±0.21 | 14.30 ±0.15 | 15.00 ±0.10 | 21 ±0.08 |
| Density (g/cm ³) | 1.08 ±0.056 | 1.10 ±0.067 | 1.10 ±0.036 | 1.02 ±0.051 |
| Water absorption (%) | 29.28 ±0.66 | 29.44 ±0.25 | 28.94 ±0.80 | 37.47 ±0.16 |

Of note, calcination at 190 kPa of pressure, representing the highest-pressure level resulting from the sum of atmospheric pressure at 100 kPa and vapor pressure at 90 kPa, causes an increased amount of vapor to be

retained in the kettle during calcination compared to other conditions. Elevated vapor quantity augments the bonding rate of the subhydrate and exacerbates crystal imperfection.

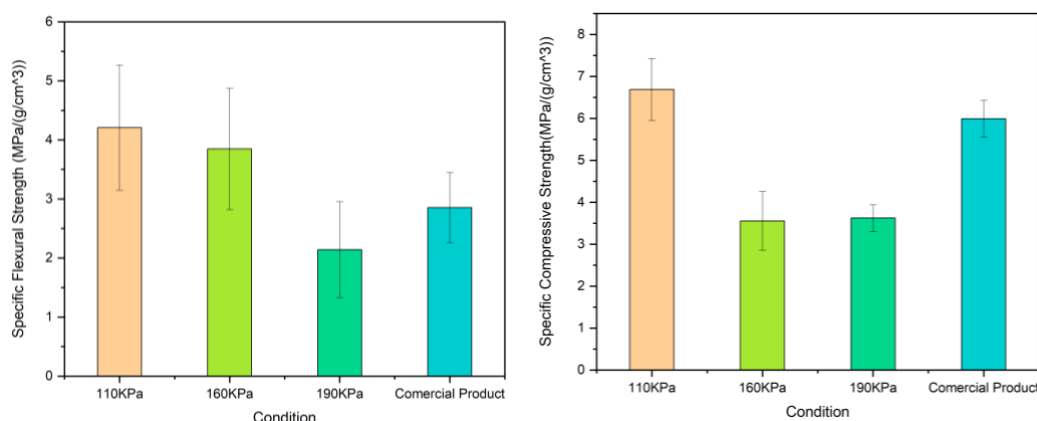


Figure 4. Specific flexural strength and compressive strength of the samples in various conditions.

Conclusions

The optimization of the calcination process for FGD gypsum to hemihydrate at 160 and 190 kPa pressures resulted in an efficient duration of 23 minutes, slightly faster than the 24 minutes required under dry and wet atmospheric pressure conditions. Throughout the calcination process, the crystallization water content (%CW) was consistently maintained between 6.0% and 6.2%, aligning with the characteristics of high-purity calcium sulfate hemihydrate. The initial purity of FGD gypsum closely resembled that of natural gypsum, with a calcium content 0.53% higher and a sulfur content 1.63% lower than commercial subhydrate. Post-calcination, the calcium content decreased by a minimum of 1.4%, while the sulfur content increased by at least 1.5%. XRD patterns delineated the subhydrates into two distinct groups based on their calcination conditions, showcasing different peak patterns for subhydrates calcined under atmospheric pressure compared to higher pressure (160 and 190 kPa). FGD subhydrates were categorized as alpha-type (alpha-subhydrate), whereas commercial subhydrate was classified as beta-subhydrate. SEM imaging unveiled variations in crystalline structures: dry and wet atmospheric-pressure calcination resulted in trigonal structures, while high-pressure calcination (160 and 190 kPa) yielded monoclinic structures with some triclinic particles. FGD subhydrate particles exhibited greater size compared to commercial subhydrate particles, with dry atmospheric-pressure calcination producing the smallest particles among FGD subhydrates. Subhydrates from dry atmospheric-pressure calcination showcased the highest specific flexural strength, surpassing those from high-pressure and wet atmospheric-pressure calcination due to fewer vapor-induced bonding imperfections. Commercial subhydrate manifested longer setting times and higher density, resulting in reduced water absorption and porosity compared to FGD subhydrates. This study underscores the potential of FGD gypsum as a viable raw material for construction and casting applications, offering mechanical properties comparable to or surpassing those of commercial subhydrates. The diverse calcination conditions enable the customization of subhydrate properties, positioning FGD gypsum as a flexible and sustainable alternative to natural gypsum.

Acknowledgments

This research project was supported by Mae Fah Luang University (Fundamental Fund: fiscal year 2023 by Thailand Science Research and Innovation (TSRI), and National Science Research and Innovation Fund (NSRF)).

References

- [1] K. Luo, C Li, L Xiang and P Ning. Influence of temperature and solution composition on the formation of calcium sulfates. *Particuology* 2010; **8**(3), 240.
- [2] Nadeesha H. Koralegedaraa , Patricio X. Pintob , Dionysios D. Dionysiouc , Souhail R. Al-Abed. Recent advances in flue gas desulfurization gypsum processes and applications.
- [3] M. T. M. Carvalho, M. I. G. Leles and R. M. C. Tubino. TG AND DSC STUDIES ON PLASTER RESIDUES AS RECYCLED MATERIAL.
- [4] C. Leiva, C. García Arenas, L.F. Vilches, J. Vale, A. Gimenez, J.C. Ballesteros, C. Fernández-Pereira. Use of FGD gypsum in fire resistant panels.
- [5] Fu, L., Xia, W., Mellgren, T., Moge, M. and Engqvist, H. (2017) Preparation of High Percentage α Calcium Sulfate Hemihydrate via a Hydrothermal Method. *Journal of Biomaterials and Nanobiotechnology*, 8, 36-49.



- [6] Ying Li¹, Peng-xuan Duan, Yuan-chao Miao and Qing Li. Preparation of α High-strength Gypsum from FGD Gypsum by Autoclaved Semi-dry Process.



PHYSICAL AND CHEMICAL PROPERTIES OF POTASSIUM SOAP LUBRICANTS SYNTHESIZED FROM VEGETABLE OILS OR OLEIC ACID FOR APPLICATION ON CONVEYOR BELT SYSTEMS

Thitiphan Chimsook^{1,*}

¹Faculty of Science, Program of Chemistry, Program of Applied Chemistry, Maejo University, Chiang Mai, Thailand 50290

*e-mail: thitiphan.cs@gmail.com

Abstract:

Lubricants reduce friction by creating a protective barrier between surfaces in contact. This research focused on developing potassium soap-based lubricants for applications such as chains and conveyor belts. Potassium oleate was produced through the saponification of oleic acid with aqueous potassium hydroxide (20-40% w/v). To explore alternative formulations, vegetable oils (olive and palm olein oil) or their mixtures with oleic acid were reacted with potassium hydroxide (20-40% w/v). The physical and chemical properties of the resulting lubricants, including pH, flash foam, foam drainage, and the time taken for a steel object to slide down inclined planes at 20°, 30°, and 45°, were assessed and compared to commercial lubricant soaps (liquid and gel samples). The results showed that the optimized condition for lubricant soap synthesized from oleic acid and a 20% w/v aqueous solution of potassium hydroxide (KOH) had the following properties: pH 10.12, flash foam 50.0 mL, foam drainage at 5 minutes 50.0 mL, and a sliding time on a 30° inclined plane of 23 seconds, comparable to commercial lubricant soaps (pH 10.10-11.92). Additionally, lubricants synthesized from olive and palm olein oils, or their mixtures with oleic acid, using a 40% w/v KOH solution were effective. The optimized conditions for soaps from each oil alone were pH 12.15 and 12.16, flash foam 50.0 and 47.0 mL, foam drainage at 5 minutes 46.0 and 43.0 mL, and sliding times of 29 and 32 seconds, respectively. For mixtures of olive oil or palm olein with oleic acid (1:1 v/v) using a 20% w/v KOH solution, the optimized conditions were: pH 10.14 and 10.16, flash foam 50.0 and 48.0 mL, foam drainage at 5 minutes 48.0 and 47.0 mL, and sliding times of 26 and 25 seconds, respectively. Therefore, vegetable oils containing oleic acid can be synthesized as effective soap lubricants, either alone or mixed with pure oleic acid, using an appropriate aqueous KOH solution.

Introduction:

Soap lubricants have found a significant role in various industrial applications. They are primarily composed of metal salts of fatty acids, offering unique properties that make them suitable for specific conditions. There are types of soap lubricants for examples metal soap greases, stearate soap lubricants and linseed soap lubricants. For, metal soap greases are commonly used in industrial settings. They are produced by reacting metallic soaps (like lithium, calcium, or sodium stearate) with mineral oil. They offer good water resistance, shear stability, and load-carrying capacity. Soap lubricants are used in many industrial applications such as metal working, conveyor systems, textile industry, and paper industry. The advantages of soap lubricants are biodegradability, cost-effective, and good emulsifying properties. For conveyor systems, soap-based lubricants can be used on conveyor belts to reduce friction, prevent wear, and improve product handling. Many soap-based lubricants are environmentally friendly and biodegradable. They can be more economical compared to synthetic lubricants in certain applications. Moreover, soaps can form stable emulsions, which is beneficial in some industrial processes. While soap lubricants offer several

advantages, it's essential to select the right type and formulation based on specific industrial requirements. Factors like load, speed, temperature, and the nature of the materials involved should be carefully.¹

Vegetable oils are a potential renewable source of fatty acids for producing lubricating soaps. Bio-based lubricants, including vegetable oil-based lubricants, have been identified as environmentally friendly alternatives to mineral-based lubricants, offering superior lubricant properties, renewability, and biodegradability. Oleic acid, a common fatty acid found in many vegetable oils, is particularly interesting due to its properties. Using vegetable oils, particularly olive oil or palm olein oil to synthesize soap lubricants for conveyor belts is a promising area of research and development. It aligns with the growing demand for environmentally friendly and sustainable solutions. Potassium soap-based lubricants, also known as bio-lubricants, are bio-lubricants derived from vegetable oils. They are renewable and offer reduced environmental impact compared to synthetic lubricants which are based on petroleum, a non-renewable resource, and contribute to environmental pollution.²⁻⁴ Potassium soap is synthesized from triglyceride oil with potassium hydroxide through a saponification reaction. It is a yellowish-white solid, with a melting point of 200-204 °C, and is soluble in water, methanol, and ethanol. The synthesized potassium soap has been shown to possess antibacterial activity against *Staphylococcus aureus* and *Escherichia coli*, indicating its potential as an antibacterial agent.⁵ Moreover, silver nanoparticles incorporated into potassium oleate soap have been used to enhance the antimicrobial properties of natural rubber latex foam, demonstrating the potential for potassium oleate in lubricant applications.⁶ Potassium oleate is a potassium salt of oleic acid, a fatty acid commonly found in vegetable oils. It is a surfactant, meaning it reduces surface tension between substances. Potassium oleate is commonly used in soap production due to its surfactant properties and antibacterial activity. It is synthesized from vegetable oils such as olive oil, palm olein oil and others through a saponification reaction with potassium hydroxide, resulting in a yellowish-white solid that is soluble in water, methanol, and ethanol. Due to its fatty acid composition, palm olein-based potassium soaps tend to have good detergency and emulsifying properties. They might exhibit slightly higher foaming tendencies compared to olive oil-based soaps. For olive oil-based potassium soaps, they are often prized for their skin-friendly properties. They tend to produce softer and more emollient lubricants.

This study focuses on synthesizing potassium soap lubricants derived from oleic acid-rich vegetable oils for application in conveyor belt systems. Olive oil and palm olein oil were employed as feedstocks. The synthesized soaps underwent evaluation for chemical and physical properties, including appearance, pH, foam volume, and stability. Comparative analysis with a commercial potassium oleate-based lubricant was conducted. The ultimate goal is to develop a sustainable, performance lubricant for conveyor belt systems by optimizing soap properties through variations in vegetable oil type, oleic acid and potassium hydroxide concentration. The results of this study have practical implications for the application of industrial soap lubricants in conveyor belt systems and other material handling operations.

Methodology:

2.1 Materials

Potassium hydroxide (KOH) and oleic acid, the primary components for soap lubricant formulation, were acquired from Sigma-Aldrich. Distilled water was produced in-house. Olive oil, and palm olein oil were commercially obtained from local sources in Chiang Mai. All chemicals and solvents were of analytical grade and used without additional purification.



2.2 Methods

2.2.1 Fatty acid analysis

Olive oil and palm olein oil were synthesized into fatty acid methyl esters (FAMES) through esterification, employing a modified Roslan et al. method [๑๖๑๑]. FAMES were prepared by a two-step process involving transesterification with methanolic NaOH followed by esterification with boron trifluoride in methanol. The resulting FAMES were extracted using n-heptane and purified through liquid-liquid extraction. The purified FAMES were analyzed using GC-MS equipped with an Agilent 6890N gas chromatograph and an Agilent 5973 mass selective detector. Compound identification was based on mass spectral matching against the NIST17 library.⁷⁻⁸

2.2.2 Preparation of potassium soap-based lubricants.

Potassium soap-based lubricants were synthesized through saponification reactions. Firstly, synthesis of potassium oleate using pure oleic acid reacted with 20%, 30%, or 40% (w/v) potassium hydroxide solutions. Oleic acid was heated to 80 °C before being added to a potassium hydroxide solution (20%, 30%, or 40% w/v). The resulting mixture was stirred vigorously at high speed for one hour, then cooled to room temperature. The soap was subsequently separated and washed with distilled water. Secondly, potassium soaps were synthesized by reacting olive oil or palm olein oil with 20%, 30%, or 40% (w/v) potassium hydroxide solutions. Olive oil or palm olein oil was heated to 80 °C and then added to a potassium hydroxide solution (20%, 30%, or 40% w/v). The mixture was stirred vigorously for one hour before being cooled to room temperature. The resulting soap was separated and washed with distilled water. Thirdly, potassium soaps were synthesized by reacting a 1:1 (v/v) mixture of olive oil or palm olein oil and pure oleic acid with 20%, 30%, or 40% (w/v) potassium hydroxide solutions. The mixture was heated to 80 °C, stirred vigorously for one hour, cooled to room temperature, and the resulting soap was separated and washed with distilled water. All synthesized soaps were evaluated based on yield, texture, color, pH, flash foam (foam volume; mL), and foam drainage (foam stability; mL). Flash foam means immediate foam volume after shaking or initial foam volume. Meanwhile, foam drainage is foam volume after standing for 5 minutes or foam stability after 5 minutes. Additionally, their lubricating efficiency was assessed by measuring the time taken for a steel object to slide down inclined planes of 20°, 30° and 45° coated with the respective soap.⁹

Results and Discussion:

Soap is a salt of fatty acids used in cleaning and lubrication products. The process of soap making is called saponification, which is the hydrolysis of esters (triglycerides, such as vegetable oils or animal fats) with a strong base like sodium hydroxide or potassium hydroxide. This reaction produces the corresponding sodium or potassium salt of the fatty acid and an alcohol (glycerol). This research aims to synthesize potassium salts of fatty acids from vegetable oils rich in oleic acid and potassium hydroxide for application as lubricants in conveyor belt systems. Two types of vegetable oils were used: olive oil, palm olein oil. The synthesized soaps will be tested for their chemical and physical properties, such as appearance, pH, flash foam after shaking at 5, 10, 15 mins, and foam drainage. The results will be compared to commercial lubricants containing potassium oleate. Three experimental methods were employed including 1) synthesis of potassium oleate: pure oleic acid was reacted with 20%, 30%, or 40% (w/v) KOH solution 2) synthesis of potassium soaps from vegetable oils: Each of the two vegetable oils (olive oil, palm olein oil) was reacted with 20%, 30%, or 40% (w/v) KOH solution 3) synthesis of potassium soaps from a mixture of vegetable oil and oleic acid: A 1:1 (v/v): mixture of each vegetable oil and pure oleic acid

was reacted with 20%, 30%, or 40% (w/v) KOH solution, respectively. The lubricating efficiency of each sample were evaluated by measuring the time required for a steel object to slide down a model coated with the lubricant on inclined surfaces of 20°, 30°, and 45°. The properties of the synthesized soaps will be compared to a commercial lubricant containing potassium oleate. This research aims to develop a sustainable and potentially more effective lubricant for conveyor belt systems using vegetable oil-based soaps. By varying the type of vegetable oils and the concentration of potassium hydroxide, the results performed the optimization of the synthesized soaps and their properties.

3.1 Fatty acid compositions

The fatty acid profiles of olive oil, and palm olein oil are presented in Table 1. Olive oil exhibited higher oleic acid contents than palm olein oil. Oleic acid was the primary source of monounsaturated fatty acids (MUFAs) in two types of oils. Notably, palm olein oil contained high palmitic acid as saturated fatty acids (SFAs). Lauric and myristic acids were found in palm olein oil. The fatty acid compositions obtained in this study align with previous reports.¹⁰⁻¹¹

Table 1.
Fatty acid compositions of olive oil, and palm olein oil.

| Fatty acids | Fatty acids content (% , Mean \pm SD) | |
|---------------------------------|---|------------------|
| | Olive oil | Palm olein oil |
| C12:0 (Lauric) | ND ^a | 0.21 \pm 0.08 |
| C14:0 (Myristic) | ND ^a | 0.69 \pm 0.10 |
| C16:0 (Palmitic) | 11.92 \pm 1.01 | 37.21 \pm 0.13 |
| C18:0 (Stearic) | 3.12 \pm 0.15 | 4.32 \pm 0.05 |
| C20:0 (Arachidic) | 0.31 \pm 0.02 | 0.19 \pm 0.09 |
| C22:0 (Behenic) | 0.10 \pm 0.14 | 0.12 \pm 0.09 |
| C16:1 (Palmitoleic) | 0.87 \pm 0.04 | 0.29 \pm 0.11 |
| C18:1 (Oleic) | 79.08 \pm 0.11 | 47.32 \pm 0.02 |
| C18:2n-6 (Linoleic) | 7.41 \pm 0.08 | 10.97 \pm 0.13 |
| C18:3n-3 (α -Linolenic) | 0.71 \pm 0.12 | 0.18 \pm 0.10 |
| C20:1 (Eicosenic) | 0.21 \pm 0.15 | 0.13 \pm 0.06 |

^aND = not detected.

3.2 Physical and chemical properties of potassium soap-based lubricants.

The synthesis of lubricant soaps containing potassium oleate using 20%, 30%, or 40% (w/v) potassium hydroxide solutions and pure oleic acid as starting materials showed that the soap made with a 20% (w/v) potassium hydroxide solution exhibited properties most similar to commercial lubricants (liquid and gel samples). These properties included texture, color, pH, flash foam (foam volume after shaking), foam drainage at 5, 10, and 15 minutes (foam stability), and faster sliding distances on 20°, 30°, and 45° inclined angles. All synthesized lubricants were colorless gels with a pH range of 10.12-12.17. Among the 20-40% KOH (w/v) solutions, higher concentrations of KOH resulted in decreased flash foam and foam drainage, and longer sliding times on inclined planes. The optimized lubricant soap made from oleic acid and a 20% w/v aqueous potassium hydroxide (KOH) solution had a pH of 10.12, flash foam of 50.0 mL, foam drainage at 5 minutes of 50.0 mL, and sliding times on 20°, 30°, and 45° inclined planes of 42, 23, and 21 seconds, respectively, comparable to commercial lubricant soaps (pH 10.10-11.92). The foam drainage results were presented in Figure 1.

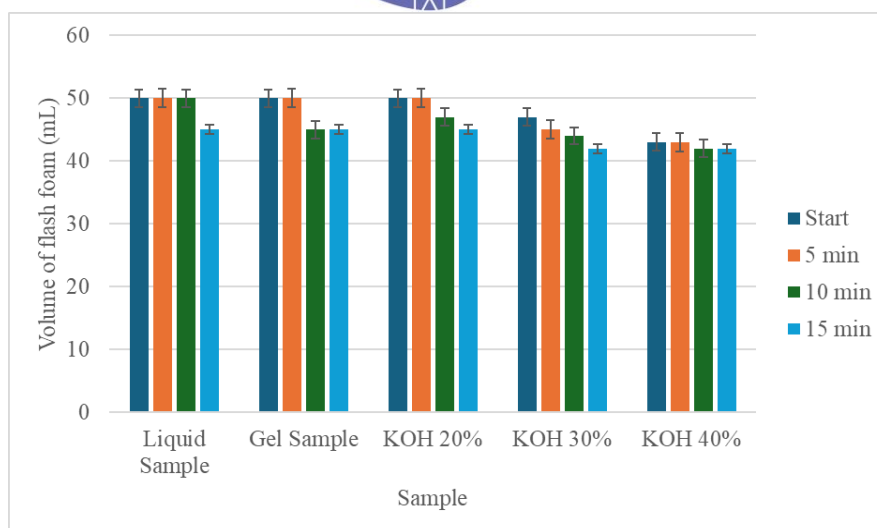


Figure 1.

The foam drainage of KOH (20, 30, 40% w/v) and oleic acid compared to two commercial soap lubricants in liquid and gel samples.

Secondly, the synthesis of lubricant soaps containing potassium oleate using 20%, 30%, and 40% (w/v) KOH was conducted with olive oil and palm olein oil. All synthesized olive oil-based and palm olein oil-based lubricants were pale yellow gels with a pH range of 12.08-12.12. Higher concentrations of KOH (20-40% w/v) resulted in increased flash foam and foam drainage, as well as shorter sliding times on inclined planes. The optimized lubricant soap made from olive oil and a 40% w/v KOH solution had a pH of 12.08, flash foam of 50.0 mL, foam drainage at 5 minutes of 46.0 mL, and sliding times of 41, 29, and 24 seconds on 20°, 30°, and 45° inclined planes, respectively. Moreover, the optimized lubricant soap made from palm olein oil and a 40% w/v KOH solution had a pH of 12.10, flash foam of 47.0 mL, foam drainage at 5 minutes of 43.0 mL, and sliding times of 44, 32, and 28 seconds on 20°, 30°, and 45° inclined planes, respectively. Results revealed that both olive oil and palm olein oil-based soaps with 20-40% (w/v) KOH exhibited flash foam comparable to commercial samples. However, the foam drainage of both synthesized soaps was lower than that of the commercial samples. Olive oil-based soap demonstrated a higher flash volume than palm olein oil-based soap, aligning with the theoretical understanding of the higher oleic acid content in olive oil. Furthermore, in the sliding times on 20°, 30°, and 45° inclined planes, the olive oil-based soap, due to its higher flash foam and foam drainage, exhibited shorter times compared to the palm olein oil-based soap across 20°, 30°, and 45° incline angles. The foam drainage results for palm olein oil-based and olive oil-based soaps were shown in Figures 2 and 3.

The viscosity of synthesized soap lubricants was 30-70 cP at 25°C.¹² The viscosity of soap lubricants can vary widely depending on their composition and the specific formulation used. For soap-based lubricants like those synthesized in your study, viscosity is typically influenced by factors such as the concentration of potassium hydroxide (KOH), the type and ratio of oils used (pure oleic acid, olive oil, palm olein oil), and any additives or impurities present. In general, pure oleic acid-based soaps tend to have higher viscosity due to their long-chain fatty acids. Vegetable oil-based soaps (such as those from olive oil or palm olein oil) can have varying viscosities depending on the specific fatty acid profile of the oil. Higher KOH concentrations typically result in lower viscosity because the increased soap

concentration can break down the oil more effectively, reducing overall thickness. Moreover, mixtures of oils with oleic acid may achieve a balanced viscosity, offering good lubrication properties while maintaining a manageable consistency.

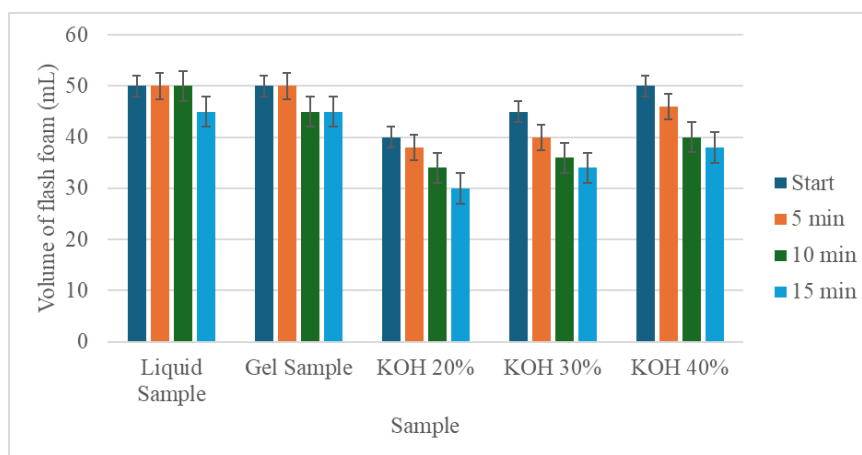


Figure 2.

The foam drainage of KOH (20, 30, 40% w/v) and olive oil compared to two commercial soap lubricants in liquid and gel samples.

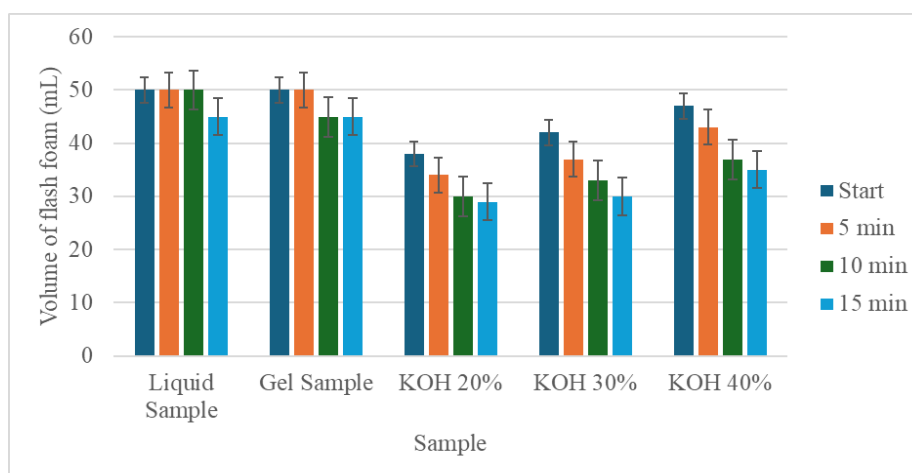


Figure 3.

The foam drainage of KOH (20, 30, 40% w/v) and palm olein oil compared to two commercial soap lubricants in liquid and gel samples.

Thirdly, a study was conducted to synthesize lubricating soaps using potassium oleate as a primary component by mixing pure oleic acid with vegetable oils (containing oleic acid) and KOH. The starting materials included 20%, 30%, or 40% (w/v) KOH and a 1:1 (v/v) mixture of vegetable oils (olive oil or palm olein oil) with pure oleic acid. All synthesized vegetable oil-pure oleic acid-based lubricants were pale yellow gels with a pH range of 10.14-10.16. Higher concentrations of KOH (20-40% w/v) resulted in decreased flash foam and foam drainage, as well as longer sliding times on inclined planes. The optimized lubricant soap made from a 1:1 v/v mixture of olive oil and oleic acid with a 20% w/v KOH solution had a pH of 10.14, flash foam of 50.0 mL, foam drainage at 5 minutes of 48.0 mL, and sliding times of 42, 26, and 23 seconds on 20°, 30°, and 45° inclined planes, respectively. Similarly, the optimized lubricant soap made from a 1:1 v/v mixture of palm olein oil and



oleic acid with a 20% w/v KOH solution had a pH of 10.16, flash foam of 48.0 mL, foam drainage at 5 minutes of 47.0 mL, and sliding times of 43, 25, and 22 seconds on 20°, 30°, and 45° inclined planes, respectively. Results revealed that all synthesized vegetable oil-pure oleic acid-based lubricants with 20-40% (w/v) KOH exhibited flash foam comparable to commercial samples. However, the foam drainage of both synthesized soaps was lower than that of the commercial samples. The olive oil: oleic acid (1:1 v/v) based soap demonstrated a higher flash volume than the palm olein oil: oleic acid (1:1 v/v) based soap, consistent with the higher oleic acid content in olive oil. Additionally, pure oleic acid usage resulted in increased flash foam, foam drainage, and shorter sliding times on inclined planes when using low concentration of KOH at 20%. For the sliding times on 20°, 30°, and 45° inclined planes, the synthesized olive oil-based soap, due to its higher flash foam and foam drainage, exhibited shorter times compared to the synthesized palm olein oil-based soap. The foam drainage results are shown in Figures 4 and 5.

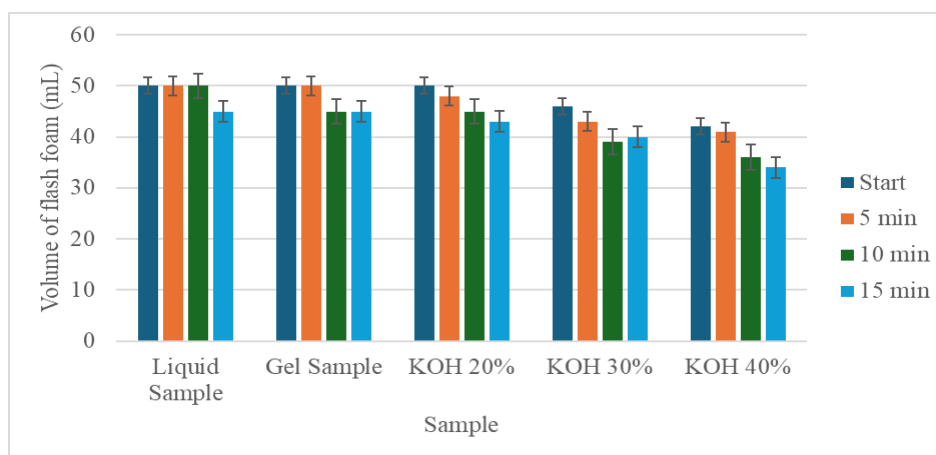


Figure 4.

The foam drainage of KOH (20, 30, 40% w/v) and olive oil-pure oleic acid (1:1 v/v) compared to two commercial soap lubricants in liquid and gel samples.

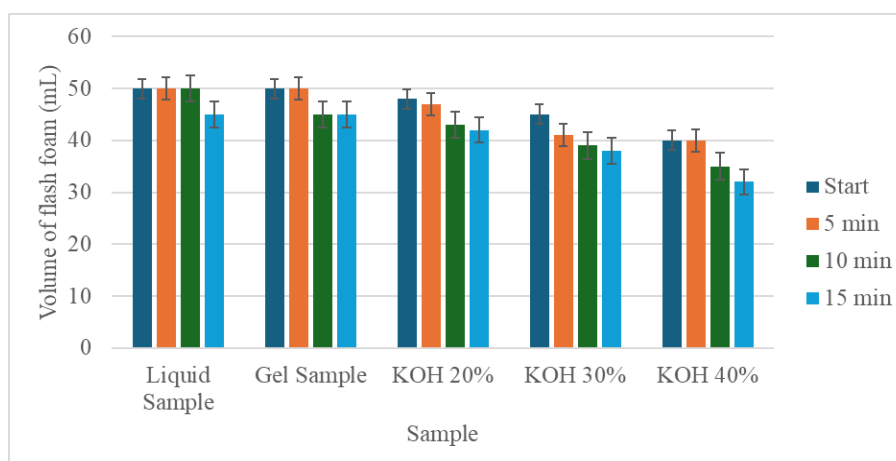


Figure 5.

The foam drainage of KOH (20, 30, 40% w/v) and palm olein oil-pure oleic acid (1:1 v/v) compared to two commercial soap lubricants in liquid and gel samples.

There are many factors affecting lubricant properties such as fatty acid composition, KOH concentration, water content, and additives. The type and ratio of fatty acids influence the lubricant's viscosity, foaming, emulsifying, and detergency properties. The amount of KOH used affects the soap formation and the final product's pH. Water content involves the lubricant's consistency and stability. In addition, the choice and concentration of additives significantly impact the lubricant's performance. Oleic acid significantly affects the quality of soap lubricants due to its chemical properties and how it interacts with other components in the formulation. Oleic acid, being a long-chain fatty acid, provides excellent lubricating properties. It forms a slippery film on surfaces, reducing friction and wear, which is essential for applications like chains, conveyor belts, and bearings. The ability of oleic acid to form a stable, protective film enhances the durability and effectiveness of the lubricant. Oleic acid contributes to the foam stability of the soap lubricant. A balanced foam profile is important for certain applications where foam can act as a cushion or barrier. Higher concentrations of oleic acid can lead to increased initial foam (flash foam) and stable foam over time (foam drainage). This characteristic is useful in applications where foam helps in reducing direct contact between surfaces. Moreover, oleic acid helps in maintaining an optimal pH level for the soap lubricant, usually in the range of 9-12. This is crucial for ensuring the lubricant's stability and compatibility with various materials. Therefore, the addition of oleic acid can enhance the chemical stability of the soap lubricant, preventing degradation and extending its shelf life. Using oleic acid, particularly from vegetable oil sources, can be cost-effective. Blending oleic acid with other oils like palm olein can reduce reliance on more expensive commercial chemical lubricants and oleic acid sourced from renewable vegetable oils supports sustainability, making the lubricant more environmentally friendly.¹³

The quantity of potassium hydroxide (KOH) significantly affects the properties of soap lubricants. Higher KOH concentrations usually decrease the amount of flash foam (initial foam volume after shaking) because the soap becomes more soluble and disperses more easily in water. High KOH concentrations can lead to faster foam drainage (foam stability over time), meaning the foam breaks down quicker. Lower KOH concentrations may result in more stable foam that lasts longer. The quantity of KOH directly impacts the pH level of the soap lubricant. Higher KOH concentrations increase the pH, making the soap more alkaline. A highly alkaline soap might be more effective in certain cleaning or lubricating applications but could also be harsher on materials. The amount of KOH affects the soap's lubrication properties. Higher concentrations can lead to reduced sliding efficiency due to the lower viscosity and quicker foam breakdown, resulting in less effective lubrication. In this study, lubricants synthesized with different KOH concentrations showed varying properties. The 20% KOH performed lubricants with a balanced pH, adequate flash foam, and good foam stability. These lubricants demonstrated optimal sliding times on inclined planes, similar to commercial lubricants. Meanwhile, 30-40% KOH resulted in decreased flash foam and quicker foam drainage, with longer sliding times, indicating reduced lubrication efficiency. Therefore, the quantity of KOH is a critical factor in determining the quality and performance of soap lubricants. By adjusting the KOH concentration, you can fine-tune the saponification process, viscosity, foam properties, pH level, and overall lubrication efficiency to meet specific application requirements.

Conclusion:

The study demonstrated that the choice of vegetable oil and the concentration of potassium hydroxide significantly impacted the properties of the synthesized lubricating soaps. While synthesized potassium oleate provided better lubrication properties than soaps synthesized from vegetable oils (palm olein/olive oil), the addition of pure oleic acid mixed with vegetable oils improved the properties of the soaps and offered a more favorable foam



profile, which could be beneficial in certain applications. Based on this research, blended palm olein-oleic acid is proposed as a cost-effective alternative for industrial conveyor belt lubricants, reducing reliance on commercial chemical lubricants.

Acknowledgements:

This research was funded by the Faculty of Science, Maejo University. The author expresses sincere gratitude to the Faculty for its financial support and to the Programs of Chemistry and Applied Chemistry for their instrumental assistance and support.

References:

1. Syahir AZ, Zulkifli NWM, Masjuki HH, Harith MH. *J Clean Prod.* 2017;168: 997-1016.
2. Sinaga MS, Tambun R, Ardhiyani M, Ardhiyani FDP. *ARN J Eng Appl Sci.* 2023;18(13):1500-1507.
3. Pathak V, Gupta D, Kumar N. *SAE Tech Pap.* 2014;01:1477.
4. Uppar R, Dinesha P, Kumar S. *Environ Dev Sustain.* 2024;26(2):1-27.
5. Arellano H, Nardello-Rataj V, Szunerits S, Boukherroub R, Fameau A-L. *Adv Colloid Interface Sci.* 2023;318: 102952.
6. Rathnayake I, Ismail H, Azahari B, Rajapakse S. *Polym-Plast Technol.* 2013;52(9):885-891.
7. Roslan NA, Ramli NAS, Zolkarnain N, Ishak SA, Ghazali RM. *J Anal Sci.* 2023;27(4):702–715.
8. Toishimanov M, Nurgaliyeva M, Serikbayeva A, Suleimenova Z, Myrzabek K, Shokan A, Myrzabayeva N. *Appl Sci.* 2023;13:7910.
9. Pečar D, Goršek A. *Acta Chim Slov.* 2015;62(1):237-241.
10. Kemény Z, Recseg K, Hénon G, Kövári K, Zwobada F. *J Am Oil Chem' Soc.* 2001;78:973-979.
11. Ayyildiz1 HF, Topkafa M, Kara H, Hussain Sherazi1 ST. *Int J Food Prop.* 2015;18:2064-2076.
12. Kurniawati Y, Paramita V. *J Voc Appl Res.* 2022;4(1):7-12.
13. Naveen Prasad BS, Sivamani S. *Int J Res Eng.Sci.* 2021;9(7):29-34.



PREPARATION OF PATTANI CLAY CERAMSITE CONTAINING FLY ASH FROM BIOMASS POWER PLANT AND PORE-FORMING REAGENTS

Susana Binmamu¹, Arifah Neerahing¹, Netnapid Ongsuwan², Kierdparinya Loonjang³, Paowarit Yuso³, Saowapa Chotisuwan^{3,*}

¹Faculty of Education, Prince of Songkla University, Pattani Campus

²Department of Food Science and Nutrition, Faculty of Science and Technology, Prince of Songkla University, Pattani Campus

³Department of Science, Faculty of Science and Technology, Prince of Songkla University, Pattani Campus

*e-mail: saowapa.c@psu.ac.th

Abstract:

Lightweight ceramic aggregates or ceramsite can be used in gardening, construction backfilling, sewage treatment, and refractory materials. This study examined process of ceramsite preparation by combining Pattani clay, fly ash from a biomass power plant, and pore-forming reagents. To make ceramsite pellets, different ratios of raw materials were used, 55, 60, 65, 70 and 75 percent of clay; 35, 30, 25, 20, and 15 percent fly ash; and 10 percent pore-forming reagents (5 types), such as cockle shell, tapioca starch, rice husks, sawdust, and iron(III) oxide chemical waste. The pellets were, then, fired at 1,000 °C in a muffle furnace using a step firing process. A stereomicroscope, apparent density, water absorption, and shrinkage were used to describe the physical and morphological properties of ceramsite. The surface functional group was characterized by a Fourier transform infrared spectrometer (FTIR). The results of the study found that the optimum raw material ratio based on low apparent density, suitable shrinkage, and water absorption for creating ceramsite was 70% clay, 20% fly ash, and 10% pore-forming reagent (sawdust). It has an apparent density of 1.89 g/cm³, 30.45% water absorption, and 4.73% shrinkage. For its application as a gardening material, good ceramsite should possess low density, high porosity, and high water absorption.

Introduction:

Ceramic aggregates such as heavyweight, lightweight, or ceramsite can be applied as adsorbents or for water retention. Ceramsite is a porous substance that has a bulk density of less than 1.20 g/m³ or an apparent density of less than 2.00 g/cm³.¹ The material has great porosity, a significant specific surface area, low apparent and bulk density, as well as minimal toxicity. Typically, it has a circular shape with a diameter ranging from 5 to 20 mm. Its chemical composition includes SiO₂, Al₂O₃, Fe₂O₃, MgO, Na₂O, and K₂O.² The majority of ceramite serve as absorbents for wastewater, filter materials, aerated bricks, and concrete. Ceramsite can be produced by subjecting clay, shale, and fly ash to a temperature range of 950–1300 °C. The diagram by Riley shows that the ideal composition range for preparing ceramsite is 53–79% SiO₂, 10–25% Al₂O₃, and 13–26% fluxing agent like feldspar.³ Feldspar is preferred because it contains high amounts of K₂O and Na₂O, which can decrease the flux content in the raw material, lower the calcination temperature, and widen the temperature range for producing ceramsite.⁴ Fly ash is a substantial byproduct from electric power plants utilizing biomass; it comprises numerous inorganic substances, predominantly silica, calcium oxide, and other metal oxides,⁵ making it suitable as a fluxing agent for ceramsite.⁶ In order to achieve consistent porosity in the ceramsite and guarantee enough porosity, it is necessary to introduce porous reagents, which are capable of generating gas. Pore-forming reagents, or porous reagents, used to produce ceramsite are biomass from industrial sources such as

sugarcane bagasse, rice husks, and sawdust. This biomass contains organic matter that can be burned out to form pores in ceramsite after firing at high temperatures.

The aim of this work was to prepare and characterize low-cost ceramsite containing Pattani clay, fly ash, and various pore-forming reagents.

Methodology:

Materials

Pattani clay was collected from local pottery in Mueng Pattani, and wood fly ash was achieved from the Pattani green biomass power plant. Cockle shell from Pattani fresh market, commercial tapioca starch, rice husks, sawdust, and waste chemicals from the chemistry laboratory; expired iron (III) oxide), were used as pore-forming reagents in this work. All materials were dried at 105 °C for 2 hours, ground into fine powder, and sieved through a 250-µm sieve before mixing.

Preparation of ceramsite

Green ceramsite samples were prepared by dry mixing 55-75% Pattani clay, 15-35% fly ash, and 10% pore-forming reagents (as shown in Table 1). The dried mixture was mixed with deionized water to obtain 30% moisture (dry basis). The spherical forming was performed with a pellet molding machine to form 8-10 mm-diameter spherical pellets. They were dried at 105 °C for 2 hours to obtain green ceramsite, then fired at 1000 °C with various steps of firing to obtain ceramsite.

Table 1. Materials composition of ceramsite

| Raw materials | I | II | III | IV | V |
|----------------------|----|----|-----|----|----|
| Pattani clay | 55 | 60 | 65 | 70 | 75 |
| Fly ash | 35 | 30 | 25 | 20 | 15 |
| Pore-forming reagent | 10 | 10 | 10 | 10 | 10 |

Characterization of ceramsite

Morphology, surface functional groups, and crystallinity of synthesized ceramsite were characterized by various techniques such as stereomicroscope (Stemi 2000-C, Zeiss, Germany), Fourier transform infrared spectrophotometer (FT-IR) (Tensor 27, Bruker, Germany), and X-ray diffraction spectrophotometer (XRD Empyrean, Panalytical, Netherlands) with an X-ray tube. Cu tube, X-ray generator: 40 kV and 30 mA, wavelength: 0.154 nm (Cu K_α), Scan range (2θ): 5-80°, step size (2θ): 0.026°, time/step: 70.125 sec.

The physical property such as firing shrinkage, apparent density, water absorption of synthesized ceramsite were also measured as follow.

$$\text{Firing shrinkage (\%)} = \frac{D_i - D_f}{D_i} \times 100$$

Where D_i and D_f are initial and final diameter (mm) of ceramsite before and after firing process, respectively.

$$\text{Apparent density (g/cm}^3\text{)} = \frac{m}{V}$$

Where m and V are mass (g) and volume (cm³) of ceramsite, respectively. The volume of ceramsite was determined by subtracting the volume of water in the cylinder before and after the immersion of a precisely weighed ceramsite sample in that cylinder.



$$\text{Water absorption (\%)} = \frac{m_2 - m_1}{m_1} \times 100$$

Where m_1 and m_2 are dried and saturated weight (g) of ceramsite before and after 1 h water absorption test, respectively.

Results and Discussion:

Different ratios of Pattani clay and pore-forming agents, which contain various amounts of organic matter that can be burned off, were expected to give ceramsite with low density, high porosity, and high water absorption. Additionally, differences in morphology such as color, crystallinity, chemical, or physical interaction between these inorganic mixtures were investigated.

Morphology of ceramsite

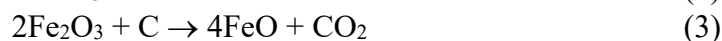
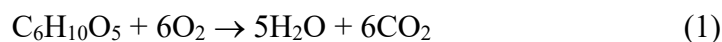
Morphology of ceramsite samples containing 55-75% Pattani clay, 15-35% fly ash, and 10% pore-forming reagents were characterized by stereomicroscope as shown in Figure 1. The ceramsite samples show a nearly spherical shape with a diameter around 7.79 ± 0.35 mm.



Figure 1. Green and fired ceramsite (a) Pattani clay, ceramsite containing 70 % Pattani clay, 20 % fly ash and 10% (b) cockle shell; (c) tapioca starch; (d) rice husks; (e) sawdust; and (f) iron(III) oxide, after calcined at 1,000°C.

Color of green ceramsite samples were dark representing organic matter in Pattani clay except for cockle shell formula showing off white due to white color of CaCO_3 in cockle shell. After firing at 1,000 °C, the color of all samples was pale to deep brown representing Iron (III) oxide in Pattani clay, from pure Pattani clay to Iron (III) oxide formula, respectively. The main chemical composition of Pattani clay composes of SiO_2 (47-58%), Al_2O_3 (24-27%) Fe_2O_3 (2-3%), and TiO_2 (1%) after firing at 900 °C showing good property based on high amount of SiO_2 , Al_2O_3 , and Fe_2O_3 which can be used as raw material for

making pottery.⁷ In this work, all mixture formula showed good toughness during forming spherical pellets due to the property of the main raw material; Pattani clay. During firing, the calcination and reduction reaction occurred such as the following reactions.⁸ Equation (1) shows a combustion reaction of organic matter in rice husk, equation (2) represents the calcination reaction of CaCO_3 in cockle shell, and equation (3) exhibits reduction of Fe_2O_3 by carbon left in the clay mixture during the firing process.



Pores are formed after these gases leave the ceramsite, giving porous materials, as shown in Figure 2, which represents the cross-sectional morphology of the ceramsite, which contains 20% fly ash and 10% pore-forming reagents in this work. Ceramsite containing 20% fly ash shows the best properties compared to other fly ash compositions. All five pore-forming reagents, such as cockle shell, tapioca starch, rice husks, sawdust, and iron (III) oxide, can form ceramsite with small pores and still not sinter or melt at this firing condition. This property will be suitable for applications as a water or organic pollutant absorbent.

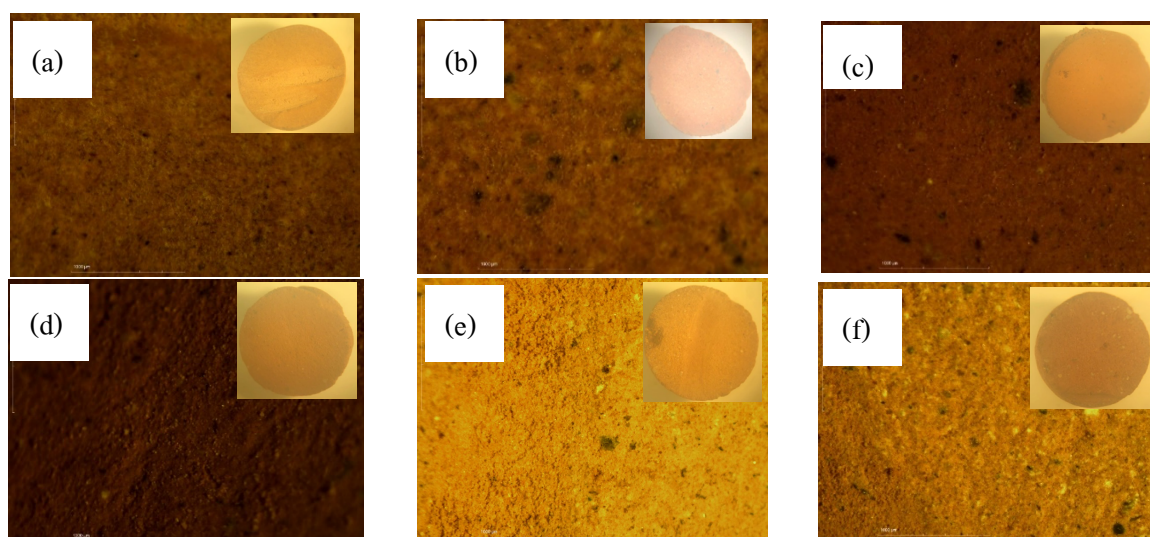


Figure 2. Cross section images (1.6X) of ceramsite (a) Pattani clay (PA), ceramsite containing 70 % Pattani clay, 20 % fly ash (FA) and 10% of (b) cockle shell; (c) tapioca starch; (d) rice husks; (e) sawdust; and (f) iron(III) oxide, after firing at 1,000°C.

Surface functional groups of ceramsite characterized by FT-IR

The surface interaction of Pattani clay with fly ash, and pore-forming reagents after firing process was characterized by FT-IR, as shown in Figure 2. The weak absorption intensity of surface hydroxyl groups ($-\text{OH}$) was still observed at wavenumber $3600\text{--}3700\text{ cm}^{-1}$, representing the humidity environment.⁹ The main FT-IR band around 1000 cm^{-1} represents Si-O-Si and Si-O-Al tetrahedrons of geopolymer.^{9,10} The C-H band at 800 cm^{-1} represents organic matters in Pattani clay that disappear after firing at 1000°C . The Al-O and Fe-O bands also appear at 679 and 532 cm^{-1} , respectively. The shift of Si-O-Si from a higher wavenumber in bare Pattani clay ceramsite to a lower wavenumber in other ceramsite can be explained by forming a rich aluminum phase where the Si^{4+} was partially replaced by Al^{3+} , resulting in a change in the Si-O bond.⁹

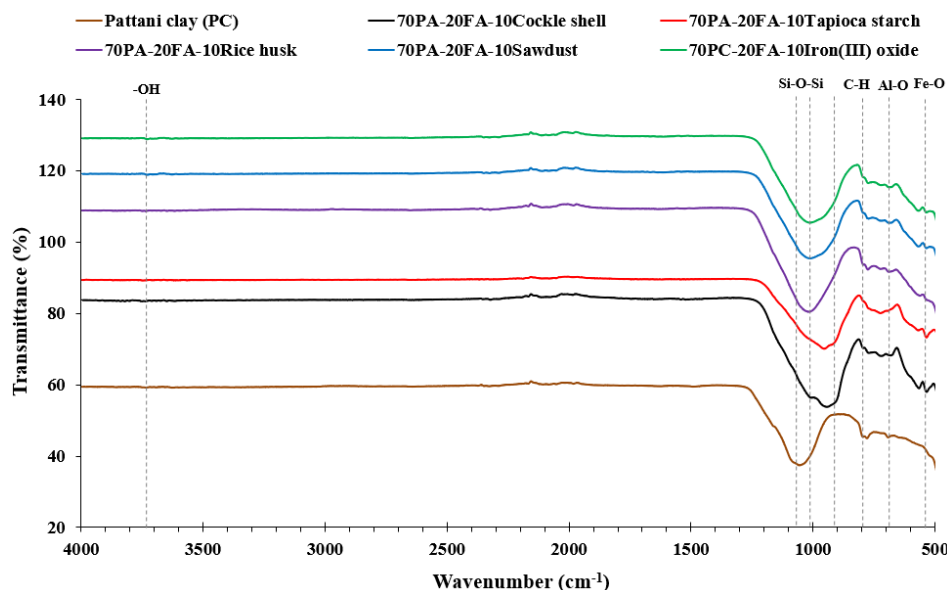


Figure 3. FT-IR spectra of Pattani clay, ceramsite containing 70 % Pattani clay, 20 % fly ash and 10% cockle shell; tapioca starch; rice husks; sawdust; iron(III) oxide, after firing at 1,000°C.

Crystallinity of ceramsite

The crystallinity of the synthesized ceramsite containing 70% Pattani clay, 20% fly ash, and 10% cockle shell, sawdust, and rice husks after being fired at 1,000 °C was characterized by XRD compared with bare Pattani clay and bare fly ash, as shown in Figure 4.

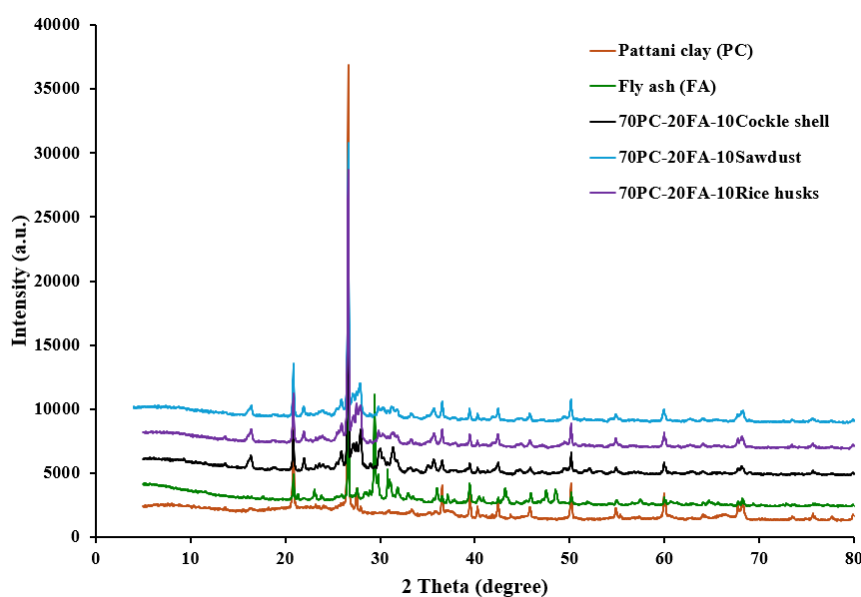


Figure 4. XRD patterns of (a) bare Pattani clay, (b) bare fly ash, compared with ceramsite containing 70% Pattani clay, 20 % fly ash and 10% of (c) cockle shell, (d) sawdust, and (e) rice husks, after firing at 1,000°C.

XRD analysis indicates that the predominant inorganic phase of Pattani clay consists of quartz (SiO_2), seen at 2θ values of around 20.9° , 26.8° , 37.1° , 39.6° , and 50.2° .⁹ The primary constituents of fly ash, including quartz (SiO_2), were seen at 2θ values of approximately 20.9° , 26.8° , 37.1° , 39.6° , and 50.2° . XRD data at 2θ approximately 29.4° reveals the presence of calcite (CaCO_3),¹¹ which is produced by the chemical adsorption of carbon dioxide gases onto the CaO in fly ash. The XRD pattern of the fly ash utilized in this study resembles that of rubber wood ash (RWA), with CaO and SiO_2 as the primary constituents.⁵ Upon firing at 1000°C , the primary composition remains in the quartz (SiO_2) phase, with new XRD diffractions at 2θ approximately 16.5° , 22.1° , 25.8° , 27.9° , 29.6° , and 30.4° , suggesting the formation of new phases, potentially including kaolinite ($\text{Al}_2\text{Si}_2\text{O}_5(\text{OH})_4$), mullite ($3\text{Al}_2\text{O}_3 \cdot 2\text{SiO}_2$), microcline (KAlSi_3O_8), oligoclase ($(\text{Ca}, \text{Na})(\text{Al}, \text{Si})_4\text{O}_8$), and nepheline ($\text{Na}_3\text{K}(\text{Al}_4\text{Si}_4\text{O}_{16})$).¹¹ These stages can enhance the mechanical strength of ceramsite after firing process.

Physical property of ceramsite

The firing shrinkage percentage of ceramic aggregate samples is shown in Figure 5. The firing shrinkage percentages of all samples are not too high, 3–8%. It was shown that increasing the amount of fly ash (decreasing Pattani clay) from 15 to 35% increases firing shrinkage, especially for formulas containing tapioca starch and sawdust. Fly ash can act as a fluxing agent to reduce the sintering temperature of clay and form dense materials. The firing shrinkage trend of ceramic aggregate samples containing 20% fly ash, 10% sawdust, and tapioca starch is quite similar due to their main composition of hydrocarbon matter, which were burned off completely during firing process. The firing shrinkage data indicates that ceramsite containing 15–20% fly ash and 10% all-pore-forming agent except rice husks and iron(III) oxide will be the suitable formula.

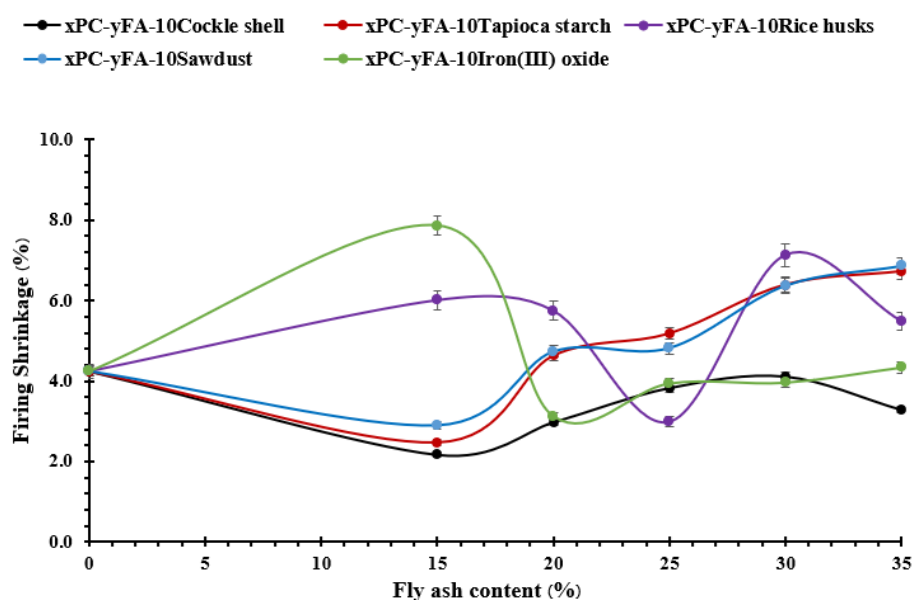


Figure 5. Firing shrinkage of ceramsite containing x% (55–75) Pattani clay, y% (15–35) fly ash and 10% of (a) cockle shell, (b) tapioca starch, (d) rice husks, (e) sawdust, and (f) iron(III) oxide, after firing at $1,000^\circ\text{C}$.

Ceramic aggregate samples were tested for apparent density, as shown in Figure 6, which indicates that some samples are higher than 2.00 g/cm^3 and higher than other ceramsite



samples containing only fly ash and pulverized coal prepared by multilayer coating ($1.02\text{--}1.49\text{ g/cm}^3$).¹² The apparent density of all samples except 10% iron (III) oxide was lower than that of bare Pattani clay aggregate (2.25 g/cm^3). The synthesized ceramic aggregates containing 10% iron (III) oxide may be defined as heavyweight ceramic aggregates, as other work contains red mud, activated charcoal, and barium sulfate, which show apparent density ($2.1\text{--}4.1\text{ g/cm}^3$) after firing at $1000\text{--}1350\text{ }^\circ\text{C}$.¹² Higher amount of organic matters and small particle size of pore-forming agent such as tapioca starch, was expected to show lowest apparent density. Additionally, the more fly ash amount, the lower apparent density was expected. However, the apparent density of ceramic aggregates containing 15–30% fly ash is not much different except at 15% fly ash containing sawdust, which is lower than others.

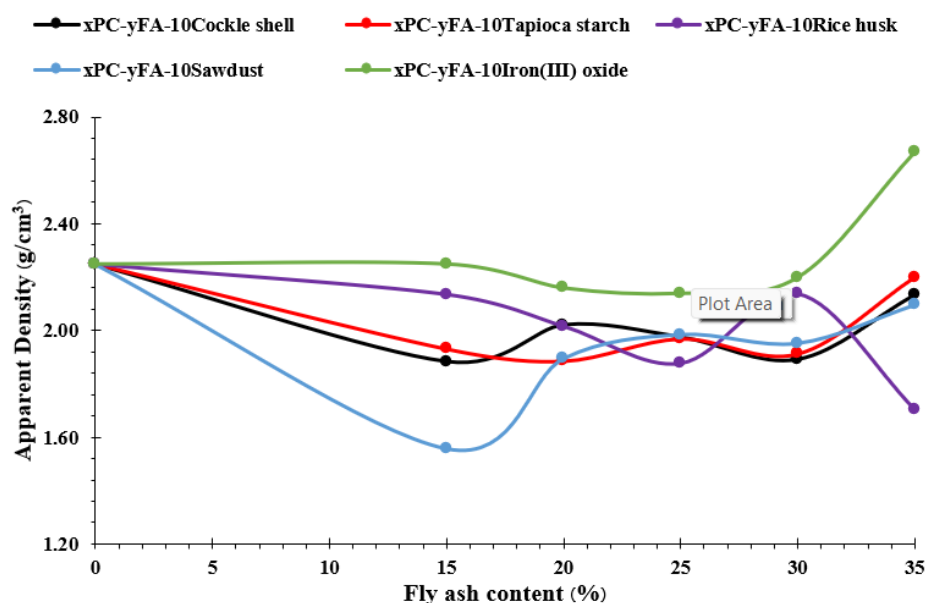


Figure 6. Apparent density of ceramsite containing x% (55–75) Pattani clay, y% (15–35) fly ash and 10% of (a) cockle shell, (b) tapioca starch, (d) rice husks, (e) sawdust, and (f) iron(III) oxide, after firing at $1,000^\circ\text{C}$.

Water absorption of synthesized ceramsite was observed as shown in Figure 7, indicating good water absorption ($19.1\text{--}32.5\%$) for ceramsite occurred for 15–20% fly ash and all pore-forming reagents except iron (III) oxide (12.6%).

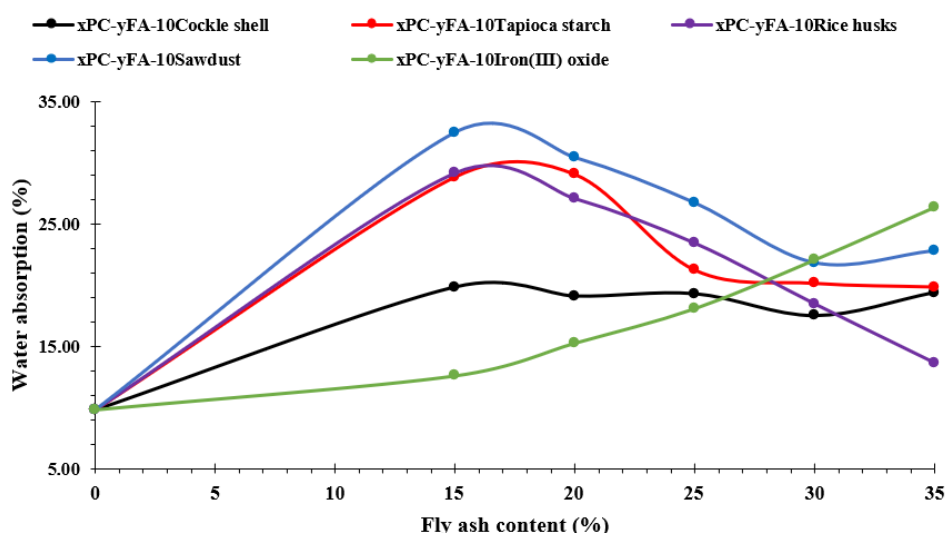


Figure 7. Water absorption of ceramsite containing x% (55-75) Pattani clay, y% (15-35) fly ash and 10% of (a) cockle shell, (b) tapioca starch, (d) rice husks, (e) sawdust, and (f) iron(III) oxide, after firing at 1,000°C.

Ceramsite containing 10% sawdust shows higher water absorption at 15–25% fly ash than others. The water absorption percentages of samples in this work are in the same range as fly ash ceramsite containing 10% coal (as a pore-forming reagent) (10–30% water absorption), and higher than other ceramsite.¹³ From the data above, ceramsite containing 70% Pattani clay, 20% fly ash, and 10% sawdust with an apparent density of 1.89 g/cm³, 30.45% water absorption, and 4.73% shrinkage, will be suitable for applications as water or wastewater absorbents and will be studied further for water retention and filter materials.

Conclusion:

Ceramsite containing 55-75% Pattani clay, 15-35% fly ash from the Pattani green biomass power plant, and 10% pore-forming reagents such as cockle shell, tapioca starch, rice husks, sawdust, and expired chemical iron (III) oxide, can be successfully prepared and characterized. The suitable ceramsite was 70% Pattani clay, 20% fly ash, and 10% sawdust, with an apparent density of 1.89 g/cm³, 30.45% water absorption, and 4.73% shrinkage.

Acknowledgements:

We are grateful to the central instrument center of the Faculty of Science and Technology at Prince of Songkla University, Pattani campus, for granting us access to the FT-IR and the Office of Scientific Instrument and Testing, PSU, for the XRD.

References:

1. Pei J, Pan X, Qi Y, Yu, H, Tu, G. *Constr. Build. Mater.* 2022, 346, 128410.
2. He H, Zhao P, Yue Q, Gao B, Yue D, Li Q. *Renew. Energy.* 2015, 76:45–52.
3. Tsai CC, Wang KS, Chiou IJ. 2006. *J. Hazard Mater.* 2006, 134 (1–3):87–93.
4. Li P, Luo S-H, Zhang L, Wang Q, Huang X, Zhang Y, Liu X, Liang J, Duan, X. *Sep. Purif. Technol.* 2021, 276, 119380.
5. Raketh M, Jariyaboon R, Kongjan P, Trably E, Reungsang A, Sripitak B, Chotisuwan S. *Biochem. Eng. J.* 2021, 173, 108084.
6. Luo, B, Li, P, Li, Y, Ji, J, He, D, Tian, Q, Chen, Y. *Green Process. Synth.* 2021, 10(1), 157–168.



7. Bordeepong S, Pansuke P, Sukolrat A. UTK Res J. 2019, 13: 1-13. (In Thai).
8. Wang C, Huang C, Xu H, Yuan N, Liu X, Bai L, He X, Liu R. J. Environ. Manage. 2022, 308, 114611.
9. Silvestro L, Scolaro TP, Ruviano AS, Lima GTS, Gleize PJP, Pelisser F. Constr. Build. Mater. 2023, 370, 130641.
10. Nguyen KD, Thu TT, Tran ATH, Le OTK, Sagadevan S, Kaus NHM. ACS Omega. 2023, 8(44): 41258-41272.
11. Kwek SY, Awang H, Cheah CB, Mohamad HJ. Build. Eng. 2022, 49, 104039.
12. Zheng W, Li Y, Zhu Y, Wang F, Zhao D, Yang Y, Li H. ACS Appl. Mater. Interfaces. 2023, 15:42753–42763.
13. Raghubanshi AS, Mudgal M, Kumar A, Chouhan RK, Srivastava AK. Constr. Build. Mater. 2021, 313, 125376.



RECOVERY OF ALUMINIUM FROM LAMINATED PLASTIC USING SINGLE SCREW PYROLYZER

Thanakorn Iowasri,¹ Prasert Reubroycharoen^{2,*}

¹Program of Petrochemistry and Polymer Science, Faculty of Science, Chulalongkorn University, Bangkok, Thailand, 10330

²Department of Chemical Technology, Faculty of Science, Chulalongkorn University, Bangkok, Thailand, 10330

*e-mail: prasert.r@chula.ac.th

Abstract:

Aluminium laminated plastic is commonly used in packaging for food, beverages, and medicines. However, due to its multilayer composition, it is considered unrecyclable using conventional methods and can contribute to environmental pollution. This study investigates the pyrolysis of aluminium laminated plastic using a single screw pyrolyzer, aiming to evaluate the effects of operating temperature on the yield of solid and aluminium, and to identify the optimal conditions for achieving the highest aluminium purity. The study focuses solely on varying the operating temperature. Experimental results demonstrate that while the pyrolysis process allows for the recycling of aluminium laminated plastic, some carbon residue remains on the solid product, indicating the need for additional cleaning methods to remove impurities. The results show that an operating temperature of 475°C is optimal for achieving the highest aluminium purity of 89.31% and a substantial aluminium yield of approximately 32%.

Introduction:

Aluminium laminated plastic plays a crucial role in modern industry as a primary component of packaging due to its inertness, lightness, toughness, and strength.¹ Effective packaging must protect contents from moisture, light, and air. Aluminium laminated plastic typically consists of multiple material layers, including paperboard, plastic, pigment, adhesive agents, and aluminium foil, combined through mechanical and thermal processes.² This type of packaging is widely used for food, beverages, medicine, and household chemicals. Conventional methods of eliminating excess plastic waste, such as incineration or landfill, have direct adverse effects on the environment and ecosystem. Conventional methods of eliminating excess plastic waste, such as incineration or landfill, have direct adverse effects on the environment and ecosystem.³ Although various organic or green methods have been developed for recycling aluminium laminated plastic, these methods often fail to achieve high aluminium purity. Some processes require additional steps to enhance purity and treat used chemicals, further complicating recycling efforts. Moreover, scaling up these processes can be prohibitively expensive.^{4,5,6}

Recently, pyrolysis has emerged as an alternative process to mitigate the environmental impact of plastic waste and has garnered significant attention from scientists and researchers. Pyrolysis is a thermochemical decomposition process that breaks down organic materials, particularly polymers, plastics, and multilayer plastics, at high temperatures in the absence of oxygen or in an inert gas atmosphere. This process can produce various petroleum products and fuels, such as gas, distillate, and char, with the proportions dependent on the operating temperature, which is a crucial factor.^{7,8} For aluminium laminated plastic waste, pyrolysis can effectively separate aluminium layers from the plastic. During this process, the plastic layers

are pyrolyzed and converted into oil and gas, while the aluminium can be recovered and reused. Current laboratory-scale studies on pyrolysis have demonstrated promising conditions for plastic pyrolysis and aluminium recycling; however, these methods have not yet been successfully scaled up to industrial level.^{3,7,8} Additional parameters need to be considered, and maintaining the optimal operating temperature remains a critical factor. The objective of this study is to identify the optimal operating conditions, particularly the temperature, to achieve the highest purity of aluminium product and to efficiently scale up the process to an industrial level, considering physical, chemical, and economic aspects.

Methodology:

A. Materials

Aluminium laminated plastic waste was sourced from various types of packaging, including food, snack, and beverage containers. Only aluminium laminated plastic waste was used and mixed. Before being fed into the pyrolyzer, the waste was prepared by reducing its size to 10-15 cm and removing moisture, small-particle trash, and other contaminants, such as wires or different types of plastic waste (Figure 1). A single screw pyrolyzer was established at Chak Daeng Temple in Samut Prakan, Thailand (Figure 2). Liquefied petroleum gas (LPG) with a weight of 48 kg, used as fuel, was procured from PTT Public Company Limited, Thailand.



Figure 1. Aluminium laminated plastic waste



Figure 2. Compound of the single screw pyrolyzer; conveyor (left) and reactor (right)



B. Study of operating temperature

5 kg of aluminium laminated plastic waste was fed into the single screw pyrolyzer, operating at a rotational speed of 14 rpm for the screw feeder and 8 rpm for the screw reactor. Initially, the operating temperature was set and maintained at 425°C. The waste was pyrolyzed in the reactor for 90-120 minutes, during which the first solid product was generated. After an additional 60 minutes, the process was completed, and the final solid product was obtained. For subsequent experiments, the operating temperature was increased to 450°C and 475°C, respectively.

C. Analysis of materials

The weight of all feed waste and solid products was recorded to calculate the percentage of product yield. Both feed waste and solid products were calcined in a furnace at 600°C for 1 hour to determine the net aluminium yield. Energy Dispersive X-ray (EDX) analysis was performed to assess the elemental composition of both feed waste and solid products, and to determine the aluminium purity after calcination.

Results and Discussion:

A. Study of raw material

Feed waste was analyzed by EDX to assess the elemental composition as shown in Table 1 below.

Table 1. Characterization of feed waste by EDX

| Composition | Amount (%) ^a |
|---------------------|-------------------------|
| Organic matter | 54.77 |
| Al content | 43.23 |
| Humidity and others | 2.00 |

^aThe results from the source of raw materials

To determine the product yield, 1 g of feed waste was calcined at 600°C for 1 hour in a furnace. After calcination, the weight of the solid residue was 0.21 g, which represents the net weight of aluminium content. The aluminium yield was calculated to be 21%. The weight loss observed corresponds to the carbon residue that was completely decomposed from the aluminium laminated plastic waste.

B. Physical property of solid product

The obtained aluminium products are shown (Figure 3). The black stains adhering to each aluminium product are due to the formation of hydrocarbon substances during the pyrolysis process, such as char or wax, which were not fully pyrolyzed. This carbon residue contributes to the observed solid product yield. The solid product from operations at 475°C appeared notably cleaner, exhibiting greater silveriness compared to those from lower temperatures. This observation indicates a reduction in carbon residue with increasing operating temperature. Consequently, a further cleaning process is necessary to remove any remaining carbon residue or impurities post-pyrolysis. Improved cleaning could enhance the purity of the aluminium and potentially improve its mechanical properties for subsequent applications.



Figure 3. Physical property of solid product after pyrolysis process through single screw reactor in each operating temperature; 425, 450 and 475°C, respectively

C. Effect of temperature in solid product

During pyrolysis, the plastic layer decomposes, separating from the aluminium layer and generating hydrocarbon substances, including oil and gas. However, due to limitations in reactor design, the yields of these hydrocarbon substances could not be accurately measured. Consequently, only the solid product, which consists of aluminium and carbon residue, was recorded. The yield of the solid product and aluminium at each temperature is reported in Table 2.

Table 2. Study of temperature impacting on product yield and Al yield

| Operating temperature (°C) | Product yield (%) ^a | Al yield (%) ^b |
|----------------------------|--------------------------------|---------------------------|
| 425 | 92.00 | 23.71 |
| 450 | 90.00 | 32.11 |
| 475 | 86.00 | 31.81 |

^aThe weight of total solid product

^bThe weight of aluminium after calcination

^{a,b}The results from experiment without repetition

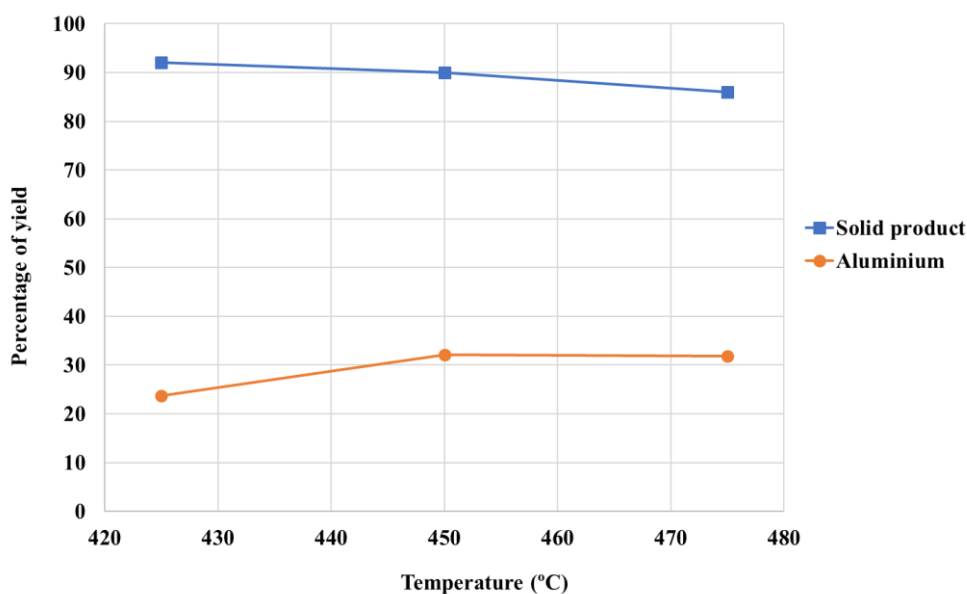


Figure 4. The relation between operating temperature to yield of product



The results indicate that the yield of solid product decreases with increasing temperature, although the aluminium yield tends to be slightly higher (Figure 4). Higher temperatures promote the decomposition of plastic or carbon content more effectively than lower temperatures, resulting in a lighter weight of the solid product. This finding is consistent with investigations by Korkmarz et al. (2009), Undri et al. (2014), and Miskolczi et al. (2024).^{9,10,11} However, it is important to note that the weight of the solid product in this study may also include carbon residue, not just aluminium. Typically, plastic decomposes into pyrolytic substances in several phases depending on the operating temperature. At temperatures below 400°C, the plastic decomposes into wax and char. At medium temperatures (between 400-600°C), the process produces oil composed mainly of naphtha, kerosene, and gasoline. Temperatures exceeding 600°C yield gas products and light hydrocarbons.⁷ In this study, the temperature parameter could not be varied beyond 480°C due to limitations of the single screw reactor, as higher temperatures could adversely affect the reactor's material properties.

Table 3. Chemical composition of solid product from pyrolysis in each experiment

| Operating temperature (°C) | Chemical composition (%) ^a | | | | | |
|----------------------------|---------------------------------------|--------|-------|-------|-------|--------------|
| | Al | Ca | Fe | Ti | Cr | Other metals |
| 425 | 83.173 | 9.944 | 6.449 | 0.253 | 0.041 | 0.140 |
| 450 | 85.860 | 10.143 | 3.170 | 0.396 | 0.045 | 0.386 |
| 475 | 89.311 | 5.673 | 4.663 | 0.179 | 0.051 | 0.123 |

^aThe analysis by EDX

Comparison to the results of characterization of feed waste in Table 1., it demonstrates that pyrolysis process can well operate and provide higher purity of aluminium. As Table 3. shown, the highest aluminium purity of 89.31% was achieved at an operating temperature of 475°C. This indicates that pyrolysis of aluminium laminated plastic waste at higher temperatures is effective in providing purer aluminium and ensuring more complete pyrolysis. At this temperature, the aluminium yield was approximately 32%, which is comparable to the yield observed at 450°C. These results confirm that higher operating temperatures are advantageous for achieving better purity in pyrolysis, assuming there are no limitations imposed by the reactor.

Conclusion:

This research investigated the pyrolysis of aluminium laminated plastic at various temperatures (425°C, 450°C, and 475°C) using a single screw pyrolyzer to evaluate the effects of operating temperature on solid product yield, aluminium yield, and aluminium purity. The results indicate that the aluminium obtained from each experiment was still contaminated with carbon residue due to incomplete pyrolysis. However, the contamination decreased with increasing temperature. The findings show that the solid product yield decreased as the temperature increased, while the aluminium yield remained relatively stable or slightly improved. At an operating temperature of 475°C, the process achieved the highest aluminium purity of 89.31% and a high aluminium yield of approximately 32%. Despite these results, further mechanical cleaning methods are necessary to remove residual carbon. Additionally, without limitations imposed by the reactor design, higher temperatures could potentially enable more complete pyrolysis and produce even purer aluminium products.

Acknowledgements:

This study obtained assistance from Chak Daeng Temple, Samut Prakan, Thailand. Analysis and some experiment method were supported by Department of Chemical Technology, Faculty of Science, Chulalongkorn University.

References:

1. Riedewald F, Wilson E. *Waste Manag.* 2022;138:172–179.
2. Bolzon G, Cornaggia G, Mahdieh S, Andrea G, Alberto M. *Beverages.* 2015;1:183–193.
3. Mohammad NS, Halim HR. *Fuel Process Technol.* 2009;90:545–552.
4. Kulkarni AK, Daneshvarhosseini S, Yoshida H. *J. Supercrit. Fluids.* 2011;55:992–997.
5. Olafsson G, Jägerstad M, Öste R, Wesslén B. *J. Food Sci.* 1993;5:215–219.
6. Nieminen J, Anugwom I, Kallioinen M, Mänttari M. *Waste Manag.* 2020;107:20–27.
7. Chairul I, Rinny J, Iryanti FN. *Reaktor.* 2018;18(1):38–44.
8. Czajczyńska D, Nannou T, Anguilano L, Krzyżyńska R, Ghazal H, Spencer N, Jouhara H. *Energy Procedia.* 2017;123:387–394.
9. Korkmaz A, Yanik J, Brebu M, Vasile C. *Waste Manag.* 2009;29:2836–2841
10. Undri A, Rosi L, Frediani M, Frediani P. *J. Fuels.* 2014;133:7–16
11. Miskolczi N, Gao NB, Quan C. *JAAP.* 2024;180:106520



SYNTHESIS OF Mg-MODIFIED MESOPOROUS SILICA ADSORBENT VIA SOFT TEMPLATE FOR SELECTIVE ADSORPTION OF CONGO RED DYE CONTAMINATED IN WASTEWATER

Chanya Thawonsuk and Nuttaya Pongstabodee*

Department of Chemical Technology, Faculty of Science, Chulalongkorn University, Bangkok, Thailand

*email: sangobtip.p@chula.ac.th

Abstract:

The extensive use of organic dyes in pharmaceutical, food, textile, and paint industries has raised significant environmental and health concerns, with some natural and synthetic dyes showing carcinogenic potential. Adsorption has emerged as a crucial strategy for organic dye removal. This research investigates the adsorption of anionic dyes using Mg-modified mesoporous silica adsorbents. Soft template method was carried out for mesoporous silica preparation. To enhance adsorption capacity, magnesium was then suggested to load on the mesoporous silica. Congo red (CR) dye as an anionic dye was selected to study. The effects of magnesium loading, initial dye concentration, and operating time on the percentage of dye removal were investigated. Moreover, the characterization of sorbents was determined by means of N₂-physisorption, X-ray diffraction analysis, Fourier transform infrared spectroscopy (FTIR), and the point of zero charge (pH_{pzc}). The experiment results elucidated that 30%wt of magnesium loading demonstrated a high dye removal efficiency within 15 minutes of operating time. This research contributes to the development of efficient adsorbents for anionic dye removal, addressing critical environmental challenges associated with industrial dye usage. The study provides insights into the optimization of Mg-modified mesoporous silica adsorbents and their performance in treating anionic dye-contaminated water.

Introduction:

The fast fashion industry's rapid production cycles, driven by consumer demand for the latest trends, have led to significant environmental impacts. Notably, the textile industry contributes to approximately 20% of water pollution, primarily due to dye residues from manufacturing processes. These dyes pose serious threats to human health and the environment, including carcinogenic and mutagenic effects.¹ Of particular concern are azo dyes, known for their phototoxicity and carcinogenic properties.^{2,3} Adsorption has been used as a preferred treatment method due to its high performance with less cost.⁴ This research addresses the critical need for effective dye removal from textile wastewater through the development of advanced adsorbent materials. Even though magnesium oxide nanoparticles express their effective dye adsorption, they challenge in separation due to their small size. Mesoporous silica possesses a large specific surface area and have customizable structure for enhanced adsorption.^{5,6} This research then addresses to investigate in synthesis and characterization of Mg-modified mesoporous silica adsorbents for improved dye adsorption in wastewater treatment. This research contributes to the development of more effective and sustainable wastewater treatment solutions for the textile industry, addressing the environmental challenges posed by fast fashion and rapid production cycles. The study aims to provide insights into the synthesis and performance of novel adsorbent materials, potentially leading to improved water treatment technologies and reduced environmental impact of textile manufacturing processes.

Methodology:

Synthesis of mesoporous silica⁷

Mesoporous silica (MS) was synthesized using a soft-template method. 1.3 g of cetyltrimethylammonium bromide (CTAB) was dissolved in 133 mL of deionized water. 14 mL of ethanol and 6.5 mL of ammonium hydroxide (NH₄OH) were added to the previous solution. The solution was homogenized through stirring. After that, 4.15 mL of tetraethyl orthosilicate (TEOS) was added to the precursor solution and stirred at room temperature for 2 h. Then the suspension was washed with deionized water until natural pH was achieved. The suspension was dried in an oven at 100 °C. Finally, the dried powders were calcined at 550 °C for 3 h and designated as calcined mesoporous silica (MS_{cal}).

Synthesis of Mg/MS⁸

1.3 g of cetyltrimethylammonium bromide (CTAB) was dissolved in 133 mL of deionized water. 0.5 g of MS_{cal} was dispersed into the CTAB solution and ultrasonicated for 30 min. After that, 17 mL of magnesium nitrate (Mg(NO₃)₂) solution with a concentration of 0.9 mol L⁻¹ was added to the precursor solution. After stirring for 1 h., 1.3 mL of NH₄OH was then added and stirred for 4 h at 50 °C. Further, the suspension was washed with deionized water until natural pH was obtained. The suspension was dried in an oven at 100 °C and labeled as 30Mg/MS.

Characterization of adsorbent

The crystallinity of the adsorbent was analyzed using X-ray diffraction (Bruker AXS Model D8) with Cu-K α radiation at 2 θ range of 10°-80°. The specific surface area was determined via nitrogen physisorption (Micrometrics). The surface functional group was evaluated by means of Fourier Transform Infrared Spectroscopy (Thermo Scientific, Nicolet) in the range of 4000-400 cm⁻¹ under atmospheric conditions. The point of zero charge (pH_{pzc}) was determined by the salt addition method. 0.2 g of adsorbent was dispersed in 40 mL of 0.1 M NaNO₃ solution. After that adjust the pH of the solution to desired pH value by 0.1 M HNO₃ and 0.1 M NaOH. The final pH of the solution was measured after shaking the solution overnight.

Adsorption performance

This experimental setup allows for the determination of crucial information about the adsorbent's capacity. The wide range of initial concentrations (100-700 mg L⁻¹) enables comprehensive dye removal, while the fixed contact time of 5 h ensures the system approaches equilibrium. Firstly, 0.1 g of adsorbent were dispersed in 100 mL of CR solution with different concentrations. The pH of the sample was constant at 7. The use of UV-vis spectrophotometry provides accurate quantification of residual dye concentrations after shaking the sample for 5 h at room temperature. Dye removal percentage was calculated as:

$$\% \text{ Removal} = [(C_0 - C_t) / C_0] \times 100$$

where C₀ and C_t are initial dye concentration (mg L⁻¹) and dye concentration at time t (mg L⁻¹), respectively.

Results and Discussion:

Characterization

This synthesis method employs CTAB as a structure-directing agent and TEOS as the silica source. The soft-template approach allows for controlled pore formation and structure development. The calcination step removes the organic template, creating the final mesoporous structure.



XRD analysis provides crucial information about the crystalline structure and phase composition of the synthesized materials. XRD patterns of MS_{cal} and 30Mg/MS were shown in **Figure 1**. It could be seen that the pattern of MS_{cal} exhibited the main peak of the (101) plane of silica was noticed at 23° . From the pattern of 30Mg/MS adsorbent, it can be elucidated the phase of $MgO_3 \cdot SiO_2 \cdot H_2O$. The two amorphous peaks at 2Θ of 35° and 60° might associate with the formation of magnesium silicate hydrate (MSH).^{9,10} The formation of the Mg-loaded sample indicates the successful incorporation of Mg into the silica matrix, potentially altering the material's surface properties and adsorption characteristics. The presence of amorphous peaks suggests a degree of structural disorder, which may contribute to the material's porosity and surface area. These structural features are likely to play a significant role in the adsorbent's performance for dye removal applications.

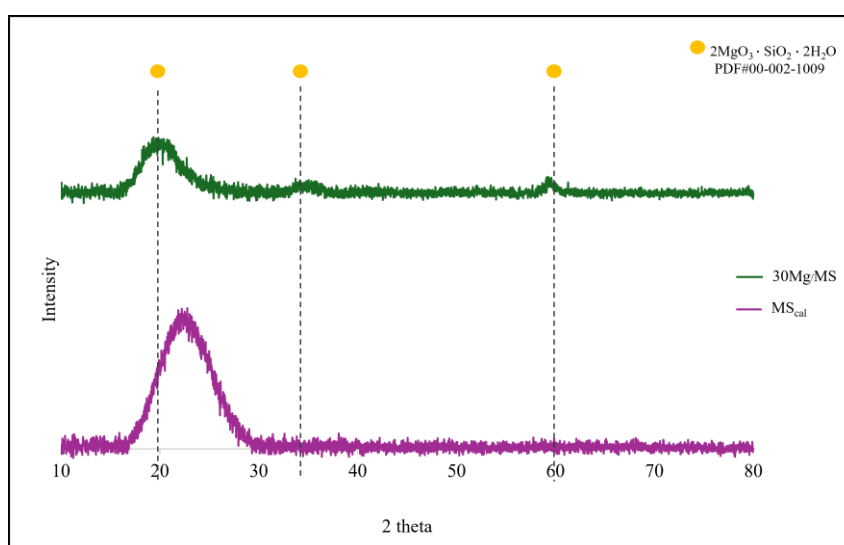


Figure 1. XRD pattern of MS_{cal} and 30Mg/MS

The textural properties of MS_{cal} and 30Mg/MS were evaluated using N_2 -physorption. The BET surface area and pore volume are shown in **Table 1**. A decrease in BET surface area was observed for 30Mg/MS compared to MS_{cal} . Mg loading resulted in partial coverage of the MS_{cal} surface. The pore volume of 30Mg/MS remained comparable to that of MS_{cal} . Mg loading did not significantly occlude or fill the pores of MS_{cal} . These observations suggest that the Mg loading process primarily affects the external surface of the mesoporous silica, rather than infiltrating the pore structure. Since the molecular size of Congo red could reach up to 2 nm, the mesoporous structure of MS_{cal} plays a limited role in adsorption process. Consequently, the removal performance might depend on the surface chemistry of the external surface of adsorbent. However, the mesoporous structure could contribute to the dispersion of CTAB and Mg.

Table 1. Textural properties of adsorbents

| Adsorbent | S_{BET}^a ($m^2 g^{-1}$) | Pore volume ($cm^3 g^{-1}$) | Pore size (nm) |
|------------|---------------------------------|----------------------------------|-------------------|
| MS_{cal} | 197.31 | 0.154 | 2.86 |
| 30Mg/MS | 60.58 | 0.195 | 11.01 |

^aBET surface area

The morphologies of MS_{cal} and 30Mg/MS were analyzed using SEM, as presented in **Figure 2**. The MS_{cal} exhibits a uniform rod-like shape, which can be attributed to the use of the NH_4OH catalyst. This catalyst facilitates the formation of elongated CTAB micelles, resulting in the rod-shaped morphology of the sorbent. In contrast, 30Mg/MS exhibits a flower-like structure attribute to the deposition of Mg. This morphological change leads to a decrease in the surface area of 30Mg/MS compared to MS_{cal} , as Mg forms predominantly on the external surface of MS_{cal} . However, the formation of flower-like structure increase the pore size, enhancing the overall porosity of the sorbent.

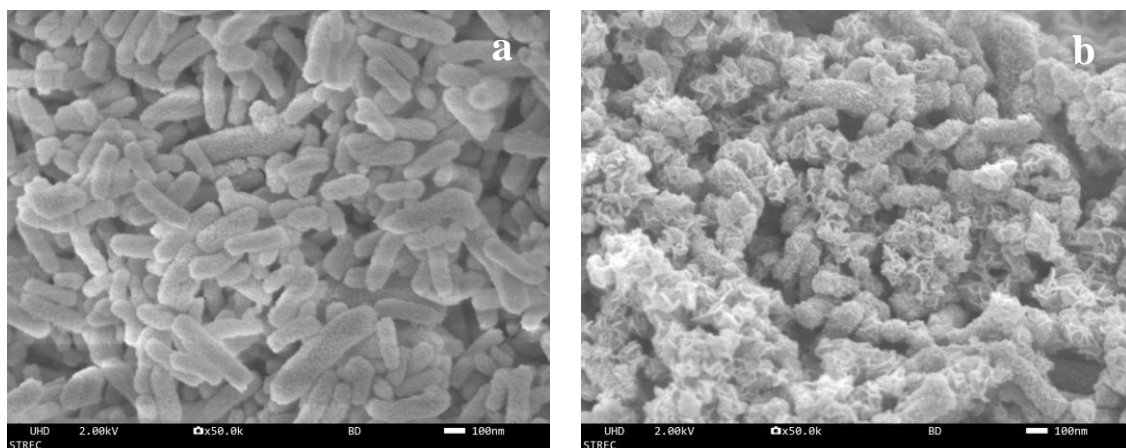


Figure 2. SEM images of MS_{cal} [a] and 30Mg/MS [b]

This FTIR analysis provides crucial information about the surface chemistry of the synthesized materials. FTIR spectroscopy was employed to investigate the surface functional groups of MS_{cal} and 30Mg/MS, as shown in **Figure 3**. The bands at 2920 and 2850 cm^{-1} can be attributed to the C–H vibration of CTAB. The band at 1480 cm^{-1} ascribed to the C–H bending of CTAB. These bands were observed only in the spectra of 30Mg/MS. They disappeared in the spectra of MS_{cal} due to surfactant removal during calcination. Silica framework vibrations was noticed at 1230 and 1070 cm^{-1} which represent to Si–O–Si asymmetric stretching, at 790 cm^{-1} and 463 cm^{-1} which correspond to Si–O stretching and Si–O bending, respectively. The peaks of Si–O–Mg vibration and Mg–O stretching, which are the characteristic peaks of MSH, were observed at 1028 and 462 cm^{-1} , respectively. Shifts in existing silica bands were observed after Mg loading, indicating Mg incorporation into MS_{cal} . The observed changes in the spectra upon Mg loading confirm the successful modification of the mesoporous silica surface. Moreover, the bands at 1626 and 3800 to 3000 cm^{-1} indicate the presence of H–O–H bending and O–H bending. These related to surface-adsorbed water in both materials.^{6,11,12}

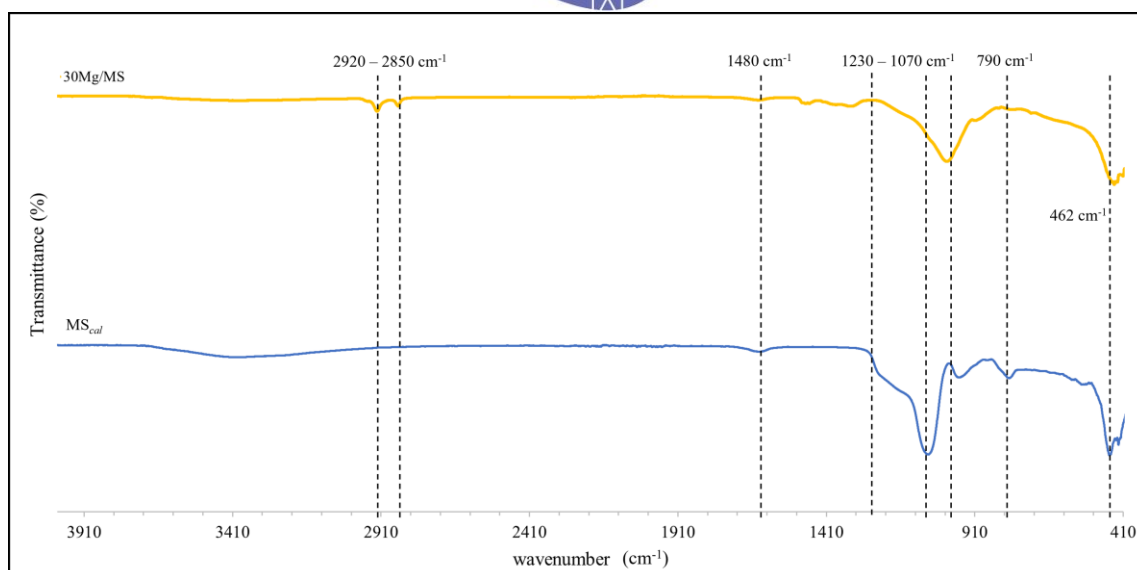


Figure 3. FTIR analysis of MS_{cal} and 30Mg/MS

The point of zero charge (pH_{pzc}) was determined to understand the adsorption mechanism. As shown in **Figure 4**, the pH_{pzc} values of Mg/MS and CR were found to be 9.8 and 11, respectively. When the pH is greater than the pH_{pzc} , the surface of the adsorbent exhibits a positive charge. Conversely, when the pH is less than the pH_{pzc} , the surface of the adsorbent is negatively charged. By adjusting the pH of the CR solution to 7, the functional groups on the surface of the adsorbent (Si–O–Mg, Si–O–H) became positively charged. The CR, which contains sulfonate groups ($R-SO_3^-$), is in a protonated form at this pH, allowing for electrostatic interaction between the sulfonate groups in CR and the protonated functional groups on the surface of the adsorbent (Si–O–Mg, Si–O–H). showed a protonated form that can provide electrostatic interaction between sulfonate group ($R-SO_3^-$) in CR and protonated functional group on the surface of adsorbent (Si–O–Mg, Si–O–H).

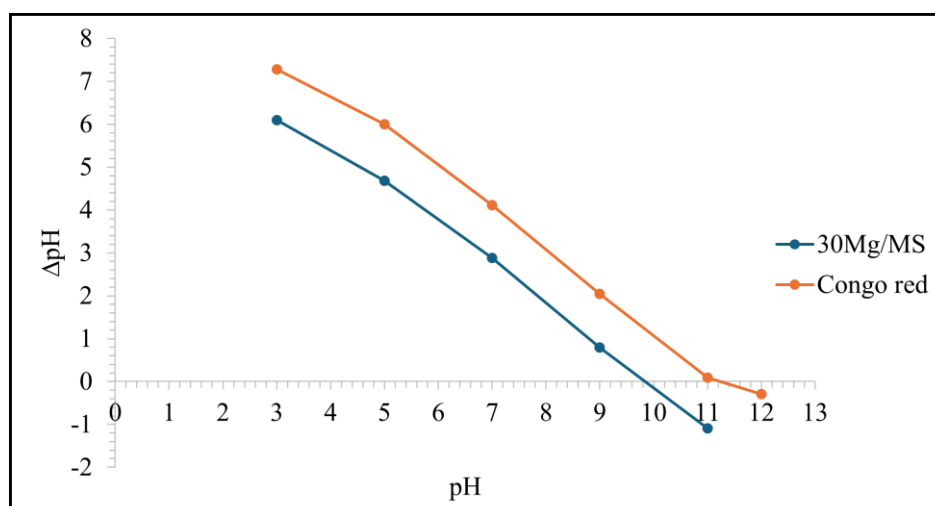


Figure 4. The point of zero charge of adsorbent and congo red

The experimental results demonstrated the adsorption of CR on 30Mg/MS at different initial concentrations ($100-700 \text{ mg L}^{-1}$). The adsorption capacity was increased from 100 to 591 mg g^{-1} as the CR concentration increased from 100 to 700 mg L^{-1} , with over 99% of CR

being removed (**Figure 5**). This increase in adsorption capacity can be attributed to higher concentration gradient at elevated CR concentrations, which promotes the transfer of dye molecules to the adsorbent surface. At pH 7, the functional group of the dye exhibited a negative charge due to the sulfonate group (R-SO_3^-), while the surface of the adsorbent was protonated, showing Si-O-H and Si-O-Mg groups. The adsorbent also contained a surfactant (CTA^+) that can exhibit a positive charge, enabling electrostatic interaction between the adsorbent and the dye. Furthermore, the Congo red dye contains amine and azo groups ($-\text{NH}_3$, $\text{N}=\text{N}$), which can form hydrogen bonds with the Si-O-H groups on the adsorbent surface.⁵ The incorporation of Mg onto MS_{cal} improved the adsorption performance through hydrogen bonding and electrostatic interactions. As shown in **Figure 6**, 30Mg/MS achieved 100% removal of Congo red dye within 15 minutes of operation, compared to MS_{cal} .

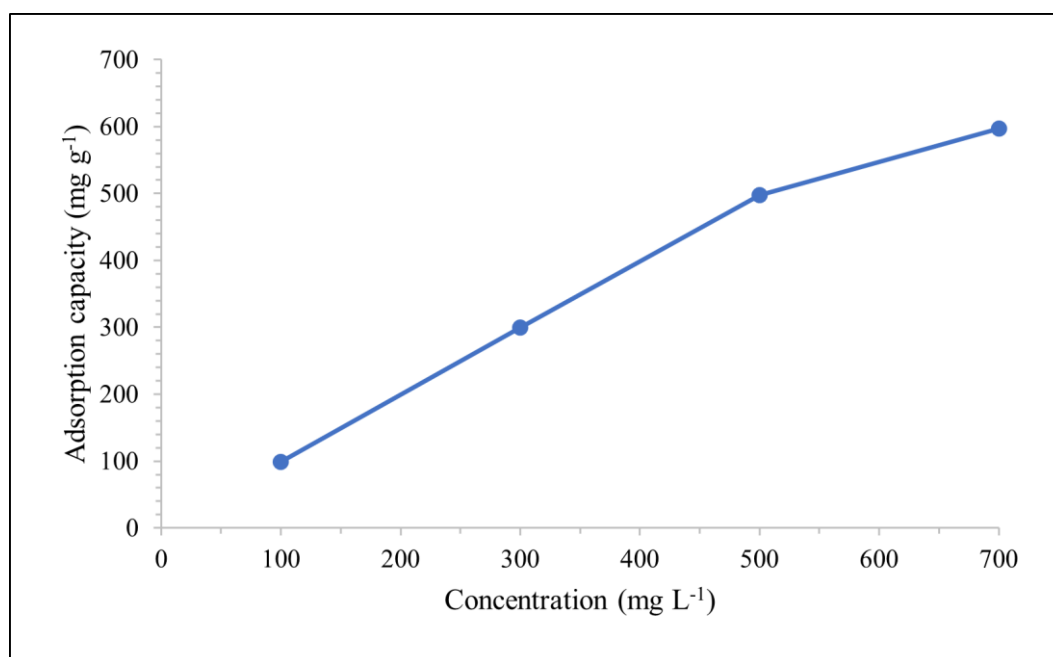


Figure 5. Adsorption capacity of 30Mg/MS when varying initial Congo red concentrations from 100 mg L^{-1} to 700 mg L^{-1} . Conditions: adsorbent dosage = 0.1 g , $\text{pH} = 7$ and time 0-5 h

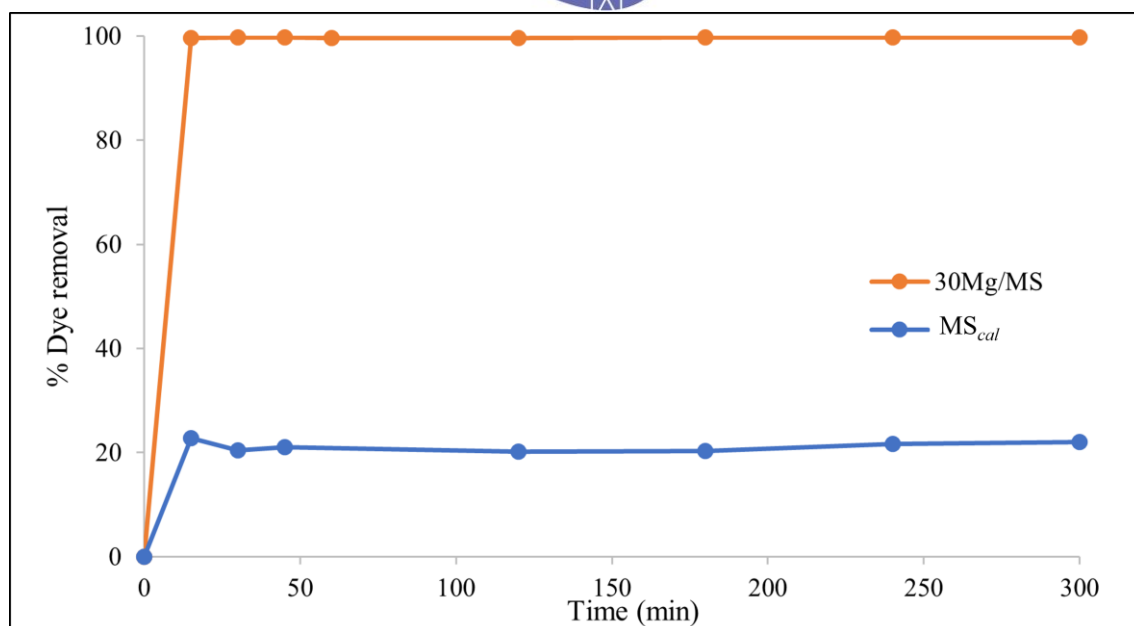


Figure 6. Percentage of dye removal when using MS_{cal} and 30Mg/MS.

Conditions: Initial dye concentration = 500 mg L⁻¹, adsorbent 0.1 g, pH = 7 and time 0-5 h

Conclusion:

This study investigates the removal of Congo red dye using MS_{cal} and 30Mg/MS as an adsorbent. MS_{cal} was synthesized using the soft template method, and the incorporation of Mg into MS_{cal} enhanced its adsorption capacity. The 30Mg/MS demonstrated a 100% removal efficiency and an adsorption capacity of 591 mg g⁻¹ for Congo red at an initial concentration of 700 mg L⁻¹ and pH 7. Analysis of the adsorption mechanism, through the point of zero charge studies, indicates that electrostatic interactions and hydrogen bonding play significant roles in the adsorption process between 30Mg/MS and the dye molecules.

Acknowledgement:

This work was supported by the Department of Chemical Technology, Faculty of Science, Chulalongkorn University.

References:

1. Liu Qian. Earth and Environmental Science. 2020;514
2. Bruno Lellis, Cintia Zani Favaro-Polonio, Joao Alencar Pamphile, Julio Cesar Polonio. Biotechnology Research and Innovation. 2019;3;275-290
3. Usman Mariam Onize, Aturagaba Godwin. Water Science & Technology. 2022;6-7
4. Zhang Ying, Bai Lizhen, Zhou Wenfeng, Lu Runhua, Gao Haiziang, Zhang Sanbing. Journal of Molecular Liquids. 2016;219;89
5. Guo Ting, Bulin Chaoke. Journal of Physics and Chemistry of Solids. 2021;158;1-2
6. Pei Yanyan, Jiang Zhuwu, Yuan Liangjie. Colloids and Surfaces A. 2019;581;2-4
7. Vazquez Naiara, Gonzalez Zoilo, Ferrari Bengona, Castro Yolanda. Boletín De La Sociedad Española De Cerámica y Vidrio. 2017;56;140
8. Pei Yanyan, Wang Man, Xu Zuefeng, Yuan. Journal of Colloid and Interface Science. 2015;453;195-196
9. Zhang Tingting, Zou Jing, Wang Baomin, Wu Zhenlin, Jia Yuan, Cheeseman Christopher. Materials. 2018;18;4

10. Douillard Jean Marc, Salles Fabrice. Phenomenology of Water Adsorption at Clay Surfaces. 2004;123
11. Nagpal Mudita, Kakkar Rita. Research on Chemical intermediates. 2020;46;2507
12. Hachemaoui Mohammed, Boukoussa, Chaibim Wahiba, Sassi Mohamed, Hamacha Rachida. Materials Chemistry and Physics. 2020;581;123704



THE EVALUATING ECONOMIC, MEDICAL AND ENVIRONMENTAL BENEFITS OF Malabar spinach EXTRACTS

Suphakchayaporn Tajai, Waewdaw Rupean*

Bunyawat Witthayalai School, Lampang, 52000, Thailand

*e-mail: Aeywaewdaw@gmail.com

Abstract:

Malabar spinach (*Basella Alba* L. and *Basella rubra* L.) is a fast-growing perennial vine which is wildy cultivated as a cool-season vegetable. (Ajay et al. 2021) Malabar spinach or pak plang is to be found in every part of Thailand, particularly in marshes and humid areas of northern Thailand. This paper investigates the multifaceted benefits of Malabar spinach (*Basella Alba*), focusing on its economic, medicinal and environmental value. The study explores how Malabar spinach can be utilized in skincare products and evaluates its potential role in reducing global warming through improved watershed management. The findings reveal that Malabar spinach is rich in antioxidants, vitamins, and minerals, making it beneficial for skincare. Additionally, its use in watershed management could help mitigate soil erosion and reduce water runoff, contributing to environmental sustainability.

Keywords: Malabar spinach, skincare products, value and beneficial, antioxidants, watershed management, reducing global warming

Introduction:

Thailand is one of the wealthiest and most developed countries in Southeast Asia. Field crops which have been planted in mountains areas for more than 50 years. Today the primary economic activity is agriculture of growing corn requires planting and ploughing fields, and making and spreading fertilizer, all activities that burn fossil fuels and emit nitrous oxide, another powerful pollutants and many farmers still burn their crop waste, which has resulted in the deforestation of large areas and the destruction of habitats, biodiversity and watersheds.¹ An evaluation was conducted on the potential benefits of Malabar spinach in watershed management. This included assessing its role in reducing soil erosion and improving water retention in hilly and watershed areas. Malabar spinach protects soil on the hill, a versatile plant native to upper northern Thailand. This report examines the potential of Malabar spinach extracts in skincare products and their role in environmental management, particularly in addressing issues related to flooding and global warming;

Ban Pong Community has been fire-free for the last 10 years. Just a five-minute walk into the forest is the first of the hand-built small check dams. Molded by cement and soil that are packed together to form its walls, these dams reduce post-fire erosion, aid in revegetation, and create fire breaks to reduce future risks. They also retain water to keep the village supplied year-round. The community has made substantial progress to protect their lifeline from deforestation and degradation from forest fires.²

Malabar spinach has nutritional value and traditional medicinal uses. Malabar spinach leaves contain nutritional value; a good source of vitamin A and C, calcium, potassium and iron, with many other vitamins and minerals in lower quantities. It has over 3 times more vitamin

¹ <https://www.bangkokpost.com/>

² <https://iucn.org/story/202406/community-tackles-forest-fires-sustainable-forestry-northern-thailand>

C than spinach, and over 1.5 times more vitamin A than kale. Shoots have many medicinal properties, and are febrifuge, diuretic and laxative, whereas roots are used to treat diarrhea. Leaf poultice is applied to treat boils and sores. The purple fruit juice is used to treat eye infections, and as a food colorant and dye.³ However, the fresh leaves and stems of both *Basella* species are rich in protein, vitamin A, vitamin C, Ca, Fe, Mg, P, K, Na, Zn, Cu, Mn and Se and also having essential amino acids and flavones. (Ajeet et al. 2018) Furthermore, the development of value-added products from *Basella rubra* could significantly boost its market value. By emphasizing its extensive medicinal and nutritional properties, this review calls for increased scientific inquiry and commercialization efforts to fully exploit the benefits of *Basella rubra*. (Singh et al. 2024) Pharmacological review reveals the pharmacological activity and its therapeutic value of plant. The popularity of the plant was highly enhanced by ideological belief in the herb as a cure for multiple diseases. The detailed pharmacological activities of plant are thus given: (Shankul, 2013)

Methodology:

Preparation of Extract: Fresh Malabar spinach leaves were air-dried to preserve their bioactive compounds. The dried leaves were then processed using a rotary evaporator to concentrate the active ingredients and obtain a potent extract.

Chemical Analysis: The Malabar spinach extract was analyzed using Fourier Transform Infrared Spectroscopy (FT-IR) to identify key chemical components and confirm the presence of antioxidants. Specific compounds, such as flavonoids and phenolic acids, were quantified to evaluate their antioxidant potential.

Product Development and Testing: A skincare serum and facial mask were formulated with the Malabar spinach extract. The products were tested on a sample group of 40 participants. A questionnaire was used to assess user satisfaction and product efficacy, with data analyzed by taking the frequency in the category divide the frequency by the total number of results and multiply by 100.

Expected results Malabar spinach could be a fit for farmers marketing to customers seeking locally grown food crops including herbs which as mountain producers to market their high quality mountain products especially on watershed area such as coffee, cocoa, honey. Demand of many customers leading to potential environmental benefits.

Results and Discussion:

Results: Nutritional and Medicinal Value: The analysis confirmed that Malabar spinach extract is rich in antioxidants, including flavonoids and phenolic acids. It also contains significant amounts of vitamins A, B, and C, as well as minerals like iron and calcium. Malabar spinach contains 98.7 mg. /100g vitamin C, 5% protein, 1.5% Fiber, 0.7% fat, 250.0 mg. /100g Ca, 4.0 mg. (Maisuthisakul et al. 2008) Common chemical compounds that possess antioxidant activity have been characterized as vitamin C or vitamin E Thai herb extracts. Some herbs can be considered as good sources as natural antioxidants and hyperglycemia inhibitors (Krittalak et al. 2018).

Product Efficacy: Survey results indicated that 80% of participants reported positive effects from using the Malabar spinach serum and facial mask, citing improvements in skin

³ <http://docs-do-not-link.udc.edu/causes/Fact-Sheet-Malabar-spinach-Basella-alba-is-a-Nutritious-and-Ornamental-Plant.pdf>



hydration and texture. The remaining 20% were neutral regarding the product's effects to use 0%.

The web-based version of the Questionnaire:⁴

Table 1.

| Questionnaire | Sample group | Percentage |
|-----------------------------|--------------|------------|
| 1.It was good to use | 40 | 80 |
| 2.It was neutral to use | 40 | 20 |
| 3.It was side effect to use | 40 | 0 |

Discussion: The study demonstrates that Malabar spinach extract is not only valuable for skincare due to its antioxidant and nutrient content but also has potential environmental benefits. By improving watershed management through increased cultivation of Malabar spinach, it is possible to address some aspects of global warming, such as soil erosion and water runoff. (Filipe, et al. 2023) Malabar spinach plant (rain water harvesting) is the most effective strategy for increasing soil moisture in water-shortage zones since soil moisture conservation (recharging shallow aquifers) is the key to good productivity. Standardizing rain water harvesting (RWH) practices are urgently needed to boost water production for rain-fed, self-sufficient household water demands as well as agricultural for higher yield and productivity.⁵

Conclusion:

Malabar spinach offers considerable economic, medicinal and environmental benefits. Its use in skincare products is supported by its rich antioxidant profile, while its application in environmental management could help mitigate issues related to flooding and global warming. Future research should focus on optimizing cultivation practices and expanding the scope of environmental impact assessments to develop and spread Malabar spinach plant technologies that are more efficient and economical as alternatives, as well as to design and create alternative policy instruments and social institutions that support the adoption of Malabar spinach plant practices, there is a need to offer training and extension services. (P. Saco, et al. 2012)

Reference:

1. Ajay Chaurasiya, Rajesh Kumar Pal, Pradeep Kumar Verma, Avineet Katiyar, Razauddin and Narendra Kumar. An updated review on Malabar spinach (*Basella alba* and *Basella rubra*) and their importance. *J Pharmacogn Phytochem.* 2021;10(2):1201-1207.
2. Ajeet Singh, Pradeep K. Dubey, Rajan Chaurasiya, Nitin Mathur, Gangesh Kumar, Sujeet Bharati & P. C. Abhilash. Indian spinach: an underutilized perennial leafy vegetable for nutritional security in developing world; 2018; 3(1): 195–205.

⁴ https://aiforthai.in.th/service_sa.php

⁵ <https://www.rainyfilters.com/about-us/blogs/how-rainwater-harvesting-reduces-soil-erosion>

3. Cornell University. 2006. "Explore Cornell: Home gardening flower growing guides." Cornell University Home Gardening.
4. Dan Sun, Weixin Zhang, Yongbiao Lin, Zhanfeng Liu, Weijun Shen, Lixia Zhou, Xingquan Rao, Suping Liu, Xi-an Cai, Dan He, Shenglei Fu. Soil erosion and water retention varies with plantation type and age. 2018; 422: 1-10.
5. Filipe Milosz, Richard M. Franken, Laura Zapatero, Mohamed Abdulla, Stanislaw Hindu, Simone Cavetto Emir, Marco Pittarello, Paul Newell Price, René L.M. Schils, Pete Smith, Tom Vanwalleghe. The role of grassland for erosion and flood mitigation in Europe: A meta-analysis how more. 2023; 108443: 348.
6. Krittalak Pasakawee, Somdet Srichairatanakool, Thunnop Laokuldilok and Niramon Utama-ang. Antioxidant Activity and Starch-digesting Enzyme Inhibition of Selected Thai Herb Extracts. 2018; 45(1): 263-276.
7. Kumar S, Prasad AK, Iyer SV, Vaidya SK. Systematic pharmacognostical, phytochemical and pharmacological review on an ethnomedicinal plant, *Basella alba* L. Journal of Pharmacognosy and Phytotherapy. 2013; 5(4):53-58.
8. Maisuthisakul P, Pasuk S, Ritthiruangdej P. Relationship between antioxidant properties and chemical composition of some Thai plants. J Food Compost Anal 2008; 21: 229-240.
9. Moore, D. S., Notz, W. I, & Flinger, M. A. (2013). The basic practice of statistics (6th ed.). New York, NY: W. H. Freeman and Company.
10. P. M. Saco, corresponding author 1 K. R. McDonough, 1 J. F. Rodriguez, 1 J. Rivera-Zayas, 2 and S. G. Sandi. The role of soils in the regulation of hazards and extreme events. 2021; 376(1834): 20200178.
11. S. Sravan Kumar, P. Manoj, and P. Giridhar corresponding author. Fourier Transform infrared spectroscopy (FTIR) analysis, chlorophyll content and antioxidant properties of native and defatted foliage of green leafy vegetables. 2015; 52(12): 8131–8139.
12. Singh, Abhishek and Mal, Dipika and Swain, Aparna Rani and Mohapatra, Ankus. Exploring the Nutritional and Medicinal Potential of Indian Spinach (*Casella rubra* L.): A Comprehensive Review. 2024; 27: 437-446.



Footnotes:

1. BANGKOK POST EPAPER; <https://www.bangkokpost.com/>
2. IUCN Conservation Centre. Community efforts to protect the Ngao Model Forest, tucked away in the hills on a winding 250-kilometer drive from Thailand's second largest city of Chiang Mai, have been underway for the last 60 years. <https://iucn.org/story/202406/community-tackles-forest-fires-sustainable-forestry-northern-thailand>
3. Mamatha Hanumappa. Malabar spinach (Basella Alba) is a Nutritious and Ornamental Plant September 2019, <http://docs-do-not-link.udc.edu/causes/Fact-Sheet-Malabar-spinach-Basella-alba-is-a-Nutritious-and-Ornamental-Plant.pdf>
4. AI for Thai Service, Sentiment Analysis., https://aiforthai.in.th/service_sa.php
5. Rain water harvesting; malabar spinach is the key to address some aspects of global warming., <https://www.rainyfilters.com/about-us/blogs/how-rainwater-harvesting-reduces-soil-erosion>



Toughness Enhancement of Polylactic Acid filled with Ultrafine Fully Vulcanized Natural Rubber Powder Grafted with Methyl Methacrylate Monomer

Panyawutthi Rimdusit, Krittapas Charoensuk, Ibrahim Lawan, Sarawut Rimdusit*

Center of Excellence in Polymeric Materials for Medical Practice Devices, Department of Chemical Engineering, Faculty of Engineering, Chulalongkorn University, Bangkok 10330, Thailand

*e-mail: Sarawut.r@chula.ac.th

Abstract:

The utilization of ultrafine fully vulcanized powder natural rubber (UFPNR) as a biobased toughening agent for polylactic acid (PLA) was successfully investigated. The bio-based filler was produced by grafting methyl methacrylate (MMA) monomer onto deproteinized natural rubber and vulcanized through electron beam irradiation and subsequent solid powder production via spray drying process to obtain MMA-grafted UFPNR. Interestingly, low particle aggregation and agglomeration of the UFPNR were obtained as confirmed by the micrographs obtained using scanning electron microscopy (SEM). PLA composites were prepared with varying PLA/UFPNR weight ratios (100/0, 95/5, 90/10, and 85/15) using hot pressing. Additionally, the obtained composites were characterized for flexural, thermal, and viscoelastic properties. Flexural tests revealed outstanding toughening performance with 5-15 wt% UFPNR fillers in the PLA composites. Notably, the PLA composite with 5wt% UFPNR exhibited the highest flexural toughness, achieving a 4.5 times improvement from 2,501 kJ/m³ to 11,280 kJ/m³. For the thermal properties, an increase of about 14 °C in the thermal degradation temperature at 5% weight loss (T_{d5}) was achieved with the 85/15 wt/wt composite. Additionally, the UFPNR-toughened PLA composites showed no adverse effects on the glass transition temperature (T_g), as the T_g s of the composites were comparable to that of neat PLA. Overall, these results indicated the high potential of the UFPNR in the toughness and thermal stability enhancement of PLA.

Introduction:

Natural rubber (NR) is one of the abundant agricultural products found in Thailand and other parts of Southeast Asia. It has a chemical structure of *cis*-1,4-polyisoprene and originates from the Brazilian Para rubber tree (sp. *Hevea brasiliensis*). The outstanding properties of NR are good heat dispersion, elasticity, resilience, abrasion resistance, and flexibility at cold temperatures which has been applied to many industrial applications such as gloves, tires, and automotive parts. Nevertheless, there are some undesirable properties such as hydrophobicity, heat sensitivity, and low tensile strength. There are many chemical modification techniques for improving NR properties, for example, halogenation¹, hydrogenation², epoxidation³, and graft copolymerization^{4,5}. Among these techniques, graft copolymerization is a feasible and efficient technique for rubber modification. The procedure commenced by grafting different vinyl monomer onto natural rubber to modify the NR properties, for example, styrene (St) for improving thermal stability⁶, methyl methacrylate (MMA) for thermal and damping enhancement⁴, and poly(N-vinyl caprolactam) for thermo-

responsive property⁷. Additionally, adding vinyl monomer onto NR form a core-shell structure as the rigidity of the shell from monomer covers the rubber core and improved the compatibility with polymer matrix^{8,9}.

Ultra-fine full vulcanized powdered rubber (UFPR) is a crosslinked rubber induced by irradiation and is produced powder by spray drying, the size of rubber particles are approximately 100 nm. Its advantages are not only improved the toughness but also enhanced thermal property of polymer matrix^{10,11}. Recently, many research focused on NR modification instead of using synthetic rubber, for example, Lin et al¹² conducted a research on reduce the aggregation of NR by using a coagent, ditrimethylol propane tetraacrylate (DTMPTA). Their results showed an enhancement in the vulcanization efficiency which was confirmed by the low swelling property and the high crosslinking density. Furthermore, the particles size can be reduced to as small as $3.6 \pm 1.1 \mu\text{m}$ compared to unirradiated NR with the sizes of $2\text{--}10 \mu\text{m}$ ¹³ approximately. Rimdusit et al¹⁴ studied on the vulcanization of graft-copolymerization onto NR using St monomer to reduce the tackiness and improve solvent resistance and thermal property. Their results showed less particles agglomeration because of high crosslinking network formation which was confirmed by the decreased swelling ratios. The size of particles were obtained at $5.95 \pm 3.03 \mu\text{m}$ with irradiation dose of 300 kGy. According to research, irradiation induced crosslinking on NR is an efficient method for modifying the intrinsic nature of NR, large particles size and stickiness. In contrast, the particles size tends to increase with the addition of monomer by graft-copolymerization.

Conventional plastic, such as polyethylene terephthalate, polyvinyl chloride, polystyrene, causes long degradation time, high energy decomposition, and high carbon emissions which damages both environment and living organisms¹⁵. These plastics are the outcome of many applications such as food containers, piping, styrofoam in which Asian countries were accounted for 60% of total plastic pollution of global marine¹⁶. To address such problems, biodegradable polymers are selected as an alternative strategy to replace petroleum-based materials and one of outstanding materials in term of processibility and mechanical properties was polylactic acid (PLA). PLA, derived from biomass sources such as sugar, corn, beet, makes it a useful application that is related to biocompatibility and biodegradability. It is a thermoplastic polyester that is applied in packaging, medical devices, and automotive parts^{8,17}. However, the brittleness posed a significant challenge for utilizing in applications which led to many research involving on improve this disadvantage such as blending with other polymer¹⁸, blending with elastomer¹⁷, and reinforcement¹⁹. Among these techniques, blending elastomer is a direct approach and simple technique for improving toughness. Graft-copolymerization using vinyl monomer onto DPNR to improve and functionalize the surface property to enhance interfacial interaction of targeted polymer and was further subsequently produce UFPR to improve dispersion in polymer matrix, especially MMA monomer that compatible with PLA²⁰.

This research focuses on enhancing the toughness of PLA by incorporating ultrafine fully vulcanized powdered natural rubber (UFPNR) as filler. Furthermore, the effects of UFPNR content on the mechanical and thermal properties of PLA were evaluated, the recorded results suggests that the utilization of the UFPNR as filler in PLA goes beyond significant improvement in toughness and retain the intrinsic thermal properties of the composites.

Methodology:

Preparation of Deproteinized natural rubber grafted with polymethyl methacrylate (DPNR-g-PMMA)

The preparation methods of NR-g-PMMA was performed according to literature as reported by Nguyen *et al.*⁴ and Kochthongrasamee *et al.*⁵ Methyl methacrylate monomer was



extracted with 10 wt% NaOH solution and washed with de-ionized water until neutral, and dried with $\text{MgSO}_4 \cdot 7\text{H}_2\text{O}$ to remove inhibitor. Graft-copolymerization conducted in a 500 cm³ (1000 mL) glass reactor and equipped with a mechanical stirrer above water bath. Deproteinized natural rubber latex (DPNR, 60% dry rubber content (DRC)) was diluted to 30% DRC with deionized water (DI water) and 0.8 wt% sodium dodecyl sulfate solution (emulsifier) and stirred for 5 min. After that, feeding N₂ gas into DPNR latex and stirring at 400 rpm for 1 hour to remove the dissolved oxygen while set temperature at 50 °C. Tetraethylene pentaamine (TEPA) and tert-butyl hydroperoxide (TBHPO) (redox initiator, with 1:1 mol ratio) were added at 0.5 phr (parts per hundreds of dry rubbers) to initiate grafting reaction and followed by adding MMA monomer. The reaction was kept for 6 hours to obtain deproteinized natural rubber grafted with methyl methacrylate (DPNR-g-PMMA). Graft copolymerization recipe showed in **Table1**.

| Ingredients | ^a SDS (wt%) | ^b TEPA:TBHPO (1:1 mole ratio, phr) | ^c MMA (phr) |
|---------------|------------------------|--|------------------------|
| DPNR-g-PMMA5 | 0.8 | 0.5 | 5 |
| DPNR-g-PMMA10 | | | 10 |
| DPNR-g-PMMA15 | | | 15 |
| DPNR-g-PMMA20 | | | 20 |

^a Sodium dodecyl sulfate

^b Tetraethylene pentaamine: Tert-butyl hydroperoxide

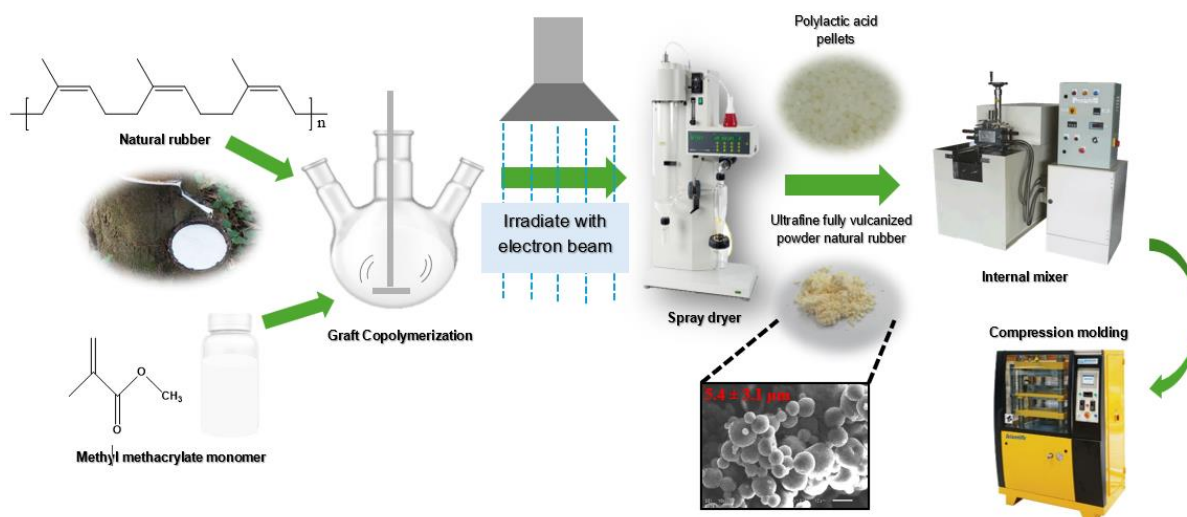
^c Methyl methacrylate monomer

E-beam irradiation onto NR-g-PMMA and spray drying

The DPNR-g-PMMA latex was diluted to 20% DRC and added ditrimethylol propane tetraacrylate (DTMPTA) at 3 phr. The latex was stirred for 10 min and carried with Tupperware as container before subjecting to crosslink via e-beam irradiation. E-beam irradiation condition is 10 MeV of electron energy, beam power of 50 kW with irradiation dose at 300 kGy. The crosslinked latex was sprayed by the spray dryer to produce ultrafine fully powder natural rubber grafted polymethyl methacrylate (UFPNR-g-PMMA) with the following condition: inlet temperature 150 °C, 7 mL/min feed flow rate, and 500 L/h air flow rate.

Preparation of PLA/UFPNR composites

Polylactic acid (PLA) granules and the synthesized UFPNR-g-PMMA were dried in oven 80 °C for 24 hours to eliminate the moisture before using. The dried PLA was blended with various UFPNR contents (0, 5, 10, and 15 wt%) by using an internal mixer at 50 rpm, 180 °C for 5 min until homogeneous mixture²¹. The respective homogenous formulations were poured into molds to produce the PLA/UFPNR composites (100/0, 95/5, 90/10, and 85/15) by hot press molding at 190 °C, 60 bar for 1 min, followed by cooldown at room temperature in atmospheric pressure.



Scheme 1. Diagram of UFPNR production and fabrication of PLA/UFPNR composite.

Characterization of the PLA/UFPNR composites

Flexural test was carried out under three-point bending mode using INSTRON 5567 universal testing machine (1 kN load cell, Norwood, USA). The PLA/UFPNR composites were prepared according to ASTM D790 standard²². The specimen dimensions were 90 mm x 12.7 mm x 3.00 mm with a span to depth ratio of 16 at room temperature (23 °C).

Thermogravimetric analysis (TGA) was performed using a thermogravimetric analyzer (model TGA1 Module Mettler-Toledo, Thailand). The tests were conducted by heating from 30 to 600 °C with heating rate of 20 °C/min under N₂ atmosphere (feeding rate 50 cm³/min).

Viscoelastic property, i.e. the glass transition temperature (T_g) of PLA/UFPNR composite were determined using dynamic mechanical analysis (DMA) (model DMA1, Mettler Toledo, Switzerland) at 1 Hz and 3 °C/min using a dual cantilever mode. The dimensions of the test specimen were 20.4 mm x 10 mm x 2 mm. The testing temperature was in the range of 30 to 100 °C⁸.

Results and Discussion:

A. Morphology of UFPNR-g-PMMA

The obtained UFPNR morphology after irradiation induced crosslinking with e-beam irradiation are shown in Figure 2. As can be seen in Figure 2a, UFPNR-g-PMMA has a yellowish color with a fine particle and showed less aggregation. Furthermore, the histogram measured from 100 particles size showed an average particle size of $4.86 \pm 2.73 \mu\text{m}$. In Figure 2b, the morphological structure of UFPNR-g-PMMA was recorded by SEM. In general, NR has a high molecular weight with high variation in particle size distribution that resulting in the stickiness and uniqueness of this material. However, the large particles size could be reduced by grafting monomer to form the shell layer onto NR and was further vulcanized by irradiation⁴.

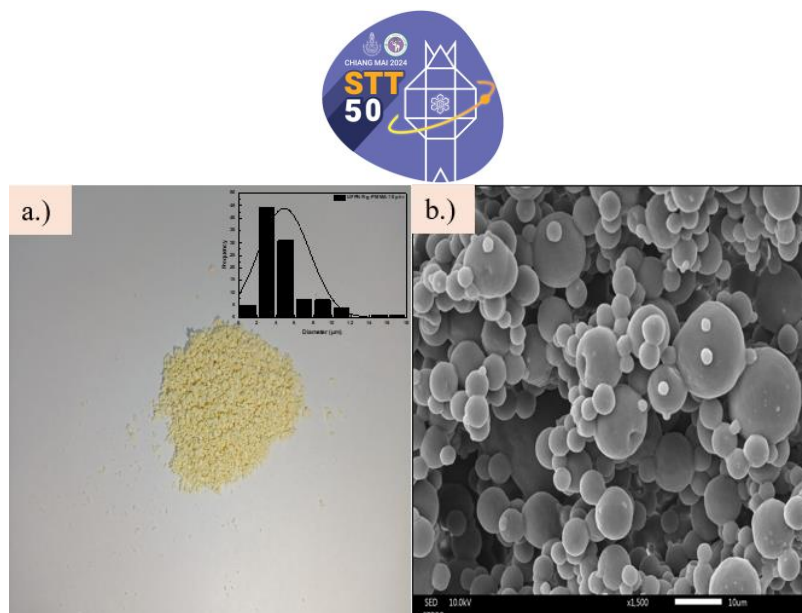


Figure 1. UFPNR particles produced from crosslinked rubber a.) Physical appearance and the particles size distribution b.) Scanning electron micrograph of UFPNR (DPNR-g-PMMA).

B. Flexural properties of the PLA/UFPNR composites

The detail of flexural stress-strain curve of PLA/UFPNR composites (100/0, 95/5, 90/10, and 85/15 wt/wt) is depicted in Figure 2 (a), while the numerical data is presented in Table 1. It was observed that neat PLA exhibits brittle behavior, with a flexural strength of approximately 102 MPa, a flexural modulus of 3.3 GPa, and a flexural strain of about 4.1%. In contrast, incorporating UFPNR into the PLA matrix increased flexural strain while decreasing both flexural strength and modulus because the presence of stress concentrator-UFPNRs helped reduce stress concentration points within the polymer matrix, inducing ductility in the PLA composite. This led to a significant enhancement in flexural toughness, increasing from 2,501 kJ/m³ in neat PLA to around 11,280 kJ/m³ with the addition of only 5 wt% UFPNR. Furthermore, Figure 2(b-e) confirms the ductile behavior of the composites, as evidenced by the whitening zone observed on the surface of the specimens at the bending point¹⁷. However, the flexural toughness of the composites decreased to 10,104 kJ/m³ and 8,659 kJ/m³ with an increase in UFPNR content to 10 and 15 wt%, respectively. This decline is attributed to the excessive UFPNR content, which exceeded the optimal balance point for the flexural properties.

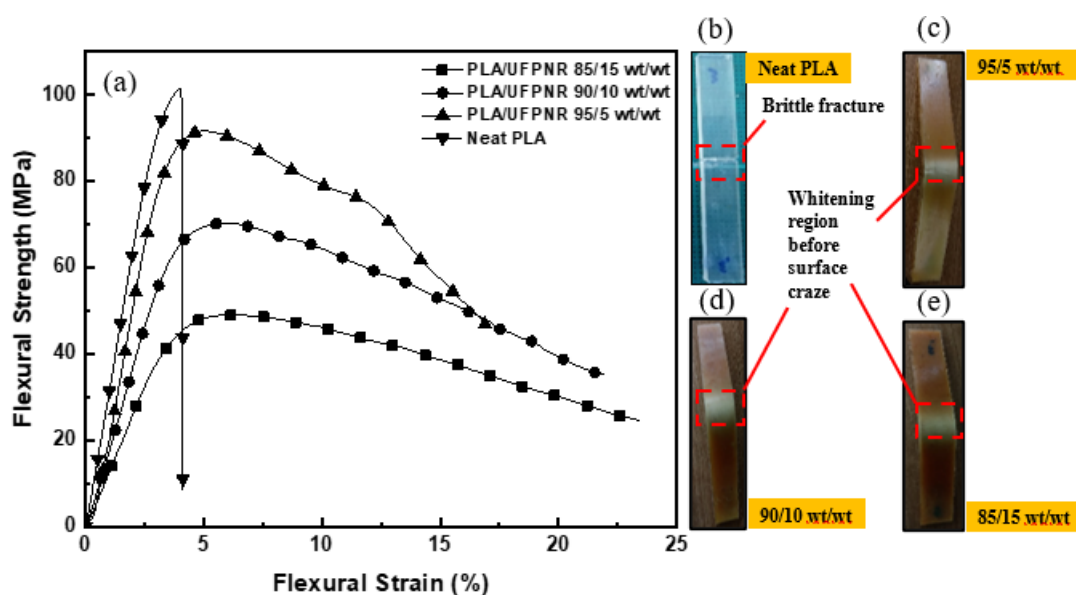


Figure 2. Flexural stress-strain curve of (a) PLA/ UFPNR at various rubber content and photograph of PLA/UFPNR at ratio of (b) 100/0, (c) 95/5, (d) 90/10, and (e) 85/15 wt/wt.

Table 1. Mechanical properties of PLA and PLA/UFPNR at different composition.

| Formula (wt/wt) ^a | Flexural Strength (MPa) ^b | Flexural Strain (%) | Flexural Modulus (GPa) ^b | Toughness (kJ/m ³) ^c |
|------------------------------|--------------------------------------|---------------------|-------------------------------------|---|
| Neat PLA (100/0) | 102±3 | 4.1±1.0 | 3.3±0.2 | 2501±652 |
| PLA/UFPNR (95/5) | 92±0 | 16.1±2.0 | 3.2±0 | 11280±1522 |
| PLA/UFPNR (90/10) | 65±6 | 20.9±1.7 | 1.8±0.1 | 10104±1673 |
| PLA/UFPNR (85/15) | 49±2 | 23.5±1.9 | 1.3±0.2 | 8659±1261 |

^a Weight per Weight ratio

^b Gigapascal

^c Kilojoules per cubic meter (calculate from the area under the stress-strain area)

C. Thermal stability of the PLA/UFPNR composite

In this work, thermal stability of the PLA/UFPNR composites in term of degradation temperature at 5% wt loss (T_{d5}) was examined. The detail of TGA curve of PLA/UFPNR at different composition (100/0, 95/5, 90/10, and 85/15 wt/wt) and UFPNR is shown in Figure 3, while the numerical data is presented in Table 2. The TGA thermograms showed T_{d5} values of 343 °C for UFPNR and 312 °C for neat PLA. Addition of UFPNR into PLA enhanced the thermal stability of the PLA/UFPNR composites, with T_{d5} increasing to 314, 324, and 326 °C with the addition of 5, 10, 15wt% UFPNR, respectively. This improvement followed the rule of mixtures. Generally, a conventional PLA/elastomer blend exhibit reduced thermal stability due to the low thermal stability of elastomer materials^{23,24}. However, in this work demonstrated enhanced T_{d5} of PLA composites, attributed to their inherent two-phase system^{25,26}.

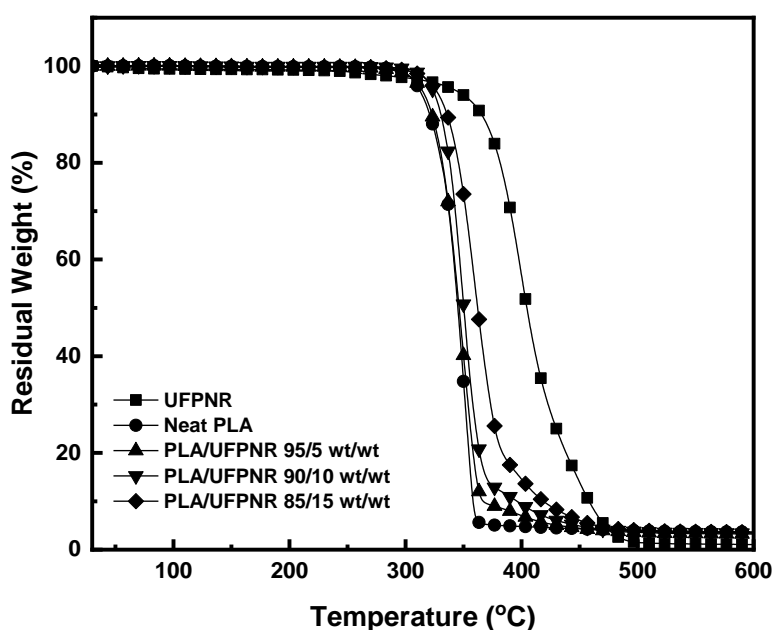


Figure 3. Thermal degradation of UFPNR, PLA, and PLA/UFPNR.

Table 2.

TGA thermogram of UFPNR, PLA, and PLA/UFPNR.

| Formula (wt/wt) ^a | Degradation Temperature at 5 wt% loss (T _{d5} , °C) | Residue Weight at 600 °C (%) |
|------------------------------|--|------------------------------|
| UFPNR | 343 | 1.0 |
| Neat PLA | 312 | 3.6 |
| (100/0) | | |
| PLA/UFPNR | 314 | 3.2 |
| (95/5) | | |
| PLA/UFPNR | 324 | 3.4 |
| (90/10) | | |
| PLA/UFPNR | 326 | 3.6 |
| (85/15) | | |

^a Weight per weight ratio

D. Viscoelastic property of the PLA/UFPNR composites

PLA/UFPNR composites were evaluated their viscoelastic properties by dynamic mechanical analyzer. Storage modulus is the ability of material to store energy elastically which is used to determine the stiffness of material at varying temperatures. As depicted in Figure 4 (a), neat PLA shows the highest storage modulus value and decreases as the UFPNR content increases. These results are associated to low modulus values of the UFPNR. As incorporating high content of UFPNR, the storage modulus decreased slightly at 5wt%. In contrast, a significant decrease in storage modulus was presented after addition more than 15wt% of PLA/UFPNR composite²⁷. This behavior could be accounted to rubber-toughening

system in which the rubber parts dominate over the polymer matrix, hence reduce the thermos-mechanical properties beyond 15 wt% of UFPNR.

Tan δ is generally used to measure the glass transition temperature (T_g) of materials and is determined by the fraction between loss modulus and storage modulus or damping²⁸. The values of PLA at varying UFPNR content are shown in Table 3. According to Figure 4 (b), all ratio of PLA/UFPNR composite showed the T_g in a range of 65-67 °C indicating no interaction between PLA and UFPNR. These results confirmed that incorporating of UFPNR into PLA doesn't negatively affect the T_g of PLA composite.

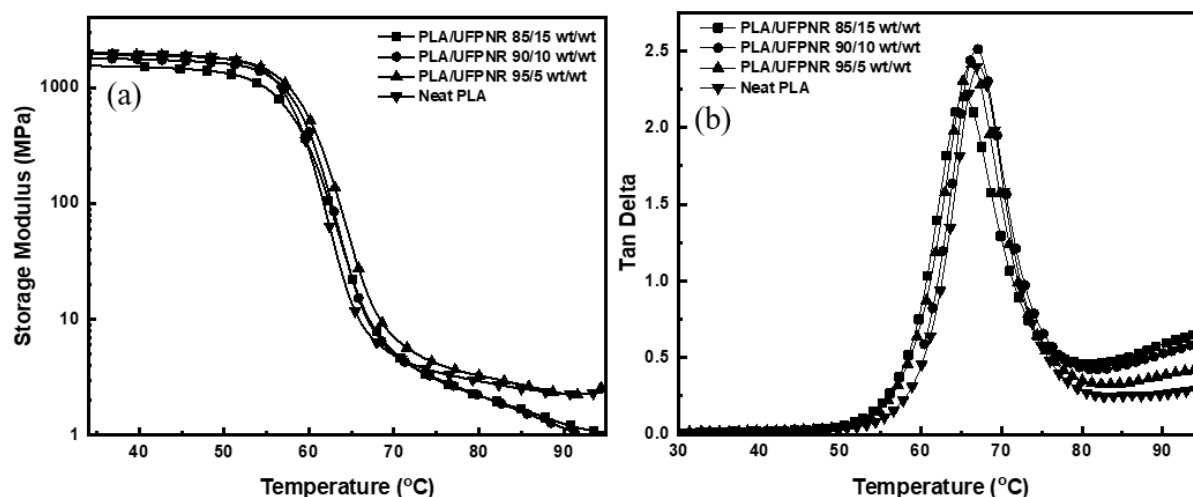


Figure 4. Storage modulus (a) and Tan δ (b) of PLA and PLA/UFPNR composites.

Table 3.

TGA thermogram of UFPNR, PLA, and PLA/UFPNR.

| Formula (wt/wt) ^a | Storage Modulus (MPa) | T_g (°C) |
|------------------------------|-----------------------|------------|
| Neat PLA (100/0) | 2005 | 67 |
| PLA/UFPNR (95/5) | 1959 | 66 |
| PLA/UFPNR (90/10) | 1792 | 67 |
| PLA/UFPNR (85/15) | 1551 | 65 |

^a Weight per weight ratio

Conclusion:

The ultrafine fully vulcanized powder natural rubber (UFPNR-g-PMMA) was successfully prepared and achieved. According to the flexural results, flexural toughness was continuously increased with incorporating UFPNR only at 5-15 wt%, representing the good toughening efficiency at low filler loading. Moreover, findings reveal that the utilization of the UFPNR as a filler in the composite has significantly toughened the PLA. Flexural toughness of neat PLA was increased from 2501 ± 652 kJ/m³ to 11280 ± 1522 kJ/m³ with the addition of only adding 5 wt% of UFPNR-g-PMMA (ca. 4.5-fold improvement). Also, improvement in the thermal stability of the composites have been achieved, T_{d5} of PLA/UFPNR composites from 312 °C of that neat PLA to 326 °C, while the addition doesn't negatively affect the T_g of PLA. These results demonstrate the potential of using the UFPNR-g-PMMA as a toughening filler in rigid polymers.



Acknowledgements:

Thailand Institute of Nuclear Technology (Public Organization) for supporting the electron beam radiation. National Research Council of Thailand (NRCT) and Chulalongkorn University (N42A660910) and Thailand Science Research and Innovation Fund Chulalongkorn University (No. 6641/2556).

References:

1. Choothong N, Kosugi K, Yamamoto Y, Kawahara S. *React Func Polym.* 2017; 113: 6-12.
2. Kongparakul S, Ng F, Rempel G. *APPL CATAL A-GEN.* 2011; 405.
3. Ahmad H S, Ismail H, Rashid A A. *Proce Chem.* 2016; 19: 359-365.
4. Nguyen T N, Duy H N, Anh D T, Thi T N, Nguyen T H, Van N N, Quang T T, Huy T N, Thi T T. *Int Jour of Polym Sci.* 2020;2020:9037827–9037838.
5. Kochthongrasamee T, Prasassarakich P, Kiatkamjornwong S. *Jour of App Polym Sci.* 2006; 101: 2587-2601.
6. Tran A D, Nhan N, Thuong N, Nghia P, Yamamoto Y, Kosugi K, Kawahara S, Thuy T. *Jour Braz Chem Soc.* 2017; 28: 669-675.
7. Phetrong S, Sansuk C, Tangboriboonrat P, Paoprasert P. *Macro Research;* 2017, 25: 799-805.
8. Zhao Q, Ding Y, Yang N, Ning N, Fu Q. *Polym Testing.* 2013; 32: 299-305.
9. Zhou C, Lin H, Ming C, Wu G. *Polym Eng & Sci.* 2012; 52.
10. Wang X, Qi G, Zhang X, Gao J, Li B, Song Z, Qiao J. *Sci China Chem.* 2012; 55: 713-717.
11. Wang Q, Zhang X, Liu S, Gui H, Lai J, Lin Y, Gao J, Huang F, Song Z, Tan B, Qiao J. *Polym.* 2005; 46: 10614-10617.
12. Lin Y, Amornkitbamrung L, Mora P, Jubsilp C, Hemvichian K, Soottitantawat A, Ekgasit S, Rimdusit S. *Polymers.* 2021; 13: 289.
13. Taewattana R, Jubsilp C, Suwanmala P, Rimdusit S. *Rad Phy Chem.* 2018; 145: 184-192.
14. Rimdusit N, Jubsilp C, Mora P, Hemvichian K, Thuy T, Karagiannidis P, Rimdusit S. *Polymers.* 2021; 13: 3447.
15. Blettler M C M, Wantzen K M. *Water Air & Soil Pollution.* 2019; 230.
16. Dauvergne P. *Global Env Change.* 2018; 51: 22-31.
17. Bitinis N, Verdejo R, Cassagnau P, Lopez-Manchado M A. *Mat Chem Phy.* 2011; 129: 823-831.
18. Jiang L, Wolcott M P, Zhang J. *Biomacro.* 2006; 7: 199-207.
19. Yusoff R B, Takagi H, Nakagaito A N. *Ind Crops Pros.* 2016; 94: 562-573.
20. Zhang G, Zhang J, Wang S, Shen D. *Jour Polym Sci Part B: Polym Phy.* 2003; 41: 23-30.
21. Li Z, Song S, Zhao X, Lv X, Sun S. *Mats.* 2017; 10: 957.
22. ASTM Standard D790, Standard Test Methods for Flexural Properties of Unreinforced and Reinforced Plastics and Electrical Insulating Materials. <https://www.ansi.org>. (accessed 2/24, 2024).
23. Sun M, Huang S, Yu M, Han K. *Polymers.* 2021; 13: 1953
24. Han D H, Choi M C, Jeong J H, Choi K M, Kim H S. *Comp Interfaces.* 2016; 23: 771-780.
25. Ding R, Duan Y, Sun Y, Yuan Q, Tien T T, Zuniga M G, Oh E, Nam J D, Suhr J. *Ind Crops Prod.* 2023; 194.
26. Cosme J G L, Silva V M, Nunes R R C, Picciani P H S. *Mat Sci App.* 2016; 7: 210-219.
27. Fekete I, Ronkay F, Lendvai L. *Polymer Testing.* 2021; 99.
28. Gupta M K, Singh R. *Materialstoday: Proceedings.* 2018; 5: 6109-6114.

F-FOOD SCIENCE AND TECHNOLOGY/AGRICULTURAL SCIENCE



2 IN 1 INNOVATIVE APPARATUS FOR CHEMICAL DETECTION IN AGRICULTURAL AND ENVIRONMENTAL APPLICATIONS

Chanya Jirapawasut, Chanoknon Kongkanta*, Matthew Hema, Kiattipoom Rodpun, Chakrit Samarnrak

Mahidol Wittayanusorn School, Phutthamonthon, Nakhon Pathom, Thailand

*e-mail: chanoknon.kon_g32@mwit.ac.th

Abstract:

Water and soil are the main factors affecting agriculture, contributing to worldwide economic development. According to the latest data, the world's significant economic crops, such as rice, will decrease production by 35-40%. This decline is attributed to factors such as poor-quality water and soil. In addition, ineffective agricultural management, for example, the leaching of fertilizers into water sources, has led to excessive nitrate and phosphate levels in water bodies, resulting in eutrophication phenomena. The project development team is inspired to innovate an automatic 2-in-1 detection prototype using nitrate (NO_3^-) and phosphate (PO_4^{3-}) as test samples. This innovation is intended for agricultural and environmental applications, integrating colorimetric analysis and light absorption. The team utilizes the Griess reaction for nitrate and the molybdenum blue reaction for phosphate for the colorimetric analysis. The maximum absorbance wavelengths (λ_{max}) were determined to be 390.6 nm and 830.8 nm, respectively. Calibration curves provide R-square values exceeding 0.99 for both reactions. In the prototype, blue (460 nm) and red (620 nm) LEDs are selected to measure light absorbance for nitrate and phosphate analysis using an RGB measure the light absorbance for nitrate and phosphate analysis. Compared to standard spectrophotometer, this is more affordable and convenient than conventional test kits. This facilitates the development of cultivation techniques, including fertilizing with an appropriate quantity of N and P.

Keywords: *Colorimetric Analysis; Nitrate; Phosphate; Substances Assessment Model; Colorimetric Analysis.*

Introduction:

Water and soil are natural resources consisting of inorganic and organic matter. In soil, plant nutrients are positive ions (cations) and negative ions (anions). Nutrients are crucial for plant growth and agricultural productivity. These nutrients are classified based on the quantity's plants need: macronutrients, which are required in large amounts, and micronutrients, which are needed in smaller amounts. For instance, macronutrients include potassium ions (K^+), calcium ions (Ca^{2+}), magnesium ions (Mg^{2+}), nitrate (NO_3^-), and phosphate (PO_4^{3-}).

Due to their essential roles in plant nutrition, Nitrate (NO_3^-) and phosphate (PO_4^{3-}) are widely used to indicate the soil and water quality using the colorimetric method. Nitrate is a key component in the synthesis of proteins, which are crucial for metabolism and vegetative growth. Phosphate is integral to energy transfer in plants and is also a component of nucleic acids. A deficiency of these minerals in the soil can adversely affect plant growth and crop yields (Silva, J. A., & Uchida, R. S., 2000). Nevertheless, the excessive presence of these ions in the water bodies can lead to eutrophication, a phenomenon where nutrients cause the rapid growth of algae. This algal bloom depletes oxygen levels (dead zone), harms aquatic life, and changes biodiversity (Chislock et al., 2013).

The conventional laboratory tests and testing kits are expensive, inconvenient, time-consuming, and produce low-accuracy results. In colorimetric reactions, the intensity of the produced colors varies based on the concentration of the ions present. The light absorbance value will be utilized to determine the concentration. The Griess Reagent is employed to detect nitrite (NO_2^-) by converting nitrate (NO_3^-) into nitrite (NO_2^-) via reduction, which produces a yellow-colored compound. The molybdenum blue (MB) reaction is incorporated to detect phosphate (PO_4^{3-}), which produces a blue-colored compound. This research focuses on the development of AgriSense, an apparatus designed to automatically detect nitrate (NO_3^-) and phosphate (PO_4^{3-}) concentrations in soil and water.

Methodology:

Nitrate Colorimetric Analysis:

A reagent mixture was prepared containing 0.05 M Potassium Nitrate (KNO_3), saturated Sulfanilic acid ($\text{C}_6\text{H}_7\text{NO}_3\text{S}$), 6 M Hydrochloric acid (HCl), and Zinc powder. Additionally, a reagent of 0.1 M Naphthalene (C_{10}H_8) in Cyclohexane (C_6H_{12}) was prepared. The prepared reagents were then mixed with Potassium Nitrate (KNO_3) solutions of varying concentrations, resulting in a yellow-colored solution. The solution was subsequently transferred to a cuvette for absorbance measurements using a SpectroVis® Plus spectrophotometer, within the wavelength range of 350 nm to 900 nm, to determine the maximum absorbance wavelength (λ_{max}).

Phosphate Colorimetric Analysis:

A reagent mixture was prepared containing 14 mM Sodium Molybdate (Na_2MoO_4) and 0.5 M Sulfuric Acid (H_2SO_4). Additionally, a reagent of 54 mM Dehydroascorbic Acid ($\text{C}_6\text{H}_8\text{O}_6$) was prepared. These reagents were then mixed with Sodium Orthophosphate (Na_3PO_4) solutions of varying concentrations, resulting in a blue-colored product. The solution was subsequently transferred to a cuvette for absorbance measurement using a SpectroVis® Plus spectrophotometer in the wavelength range of 350 nm to 900 nm to determine the maximum absorbance wavelength (λ_{max}).

Pump Calibration:

The peristalsis pump in the AgriSense was calibrated to determine the flow rate, measured in mL/s, which is crucial for pump operation timing via a relay module connected to an ESP32 board. A circuit consisting of a peristalsis pump, a battery, and a switch was assembled. The time required for the pump to fill volumetric flasks of different volume (10, 20, 50, and 100 mL) was recorded. From this data, the flow rate was calculated and used to optimize the subsequent coding process for accurate liquid dispensing.

Prototype Development:

The AgriSense was designed using Onshape, incorporating a variety of materials and components. These include a 4 cm thick acrylic sheet, a 4 cm thick plywood piece, and PLA material for 3D-printed components. The system is equipped with several key components: a 28BYJ-48 stepper motor with a ULN2003 driver module, a TCS3200 RGB sensor module, a 10 mm RGB LED, a 49E hall sensor, a 12 mm neodymium magnet, a 2x16 LCD display, and four peristaltic pumps connected to 3 mm internal diameter tubing. Four chemical containers were integrated to support the apparatus's chemical reactions.

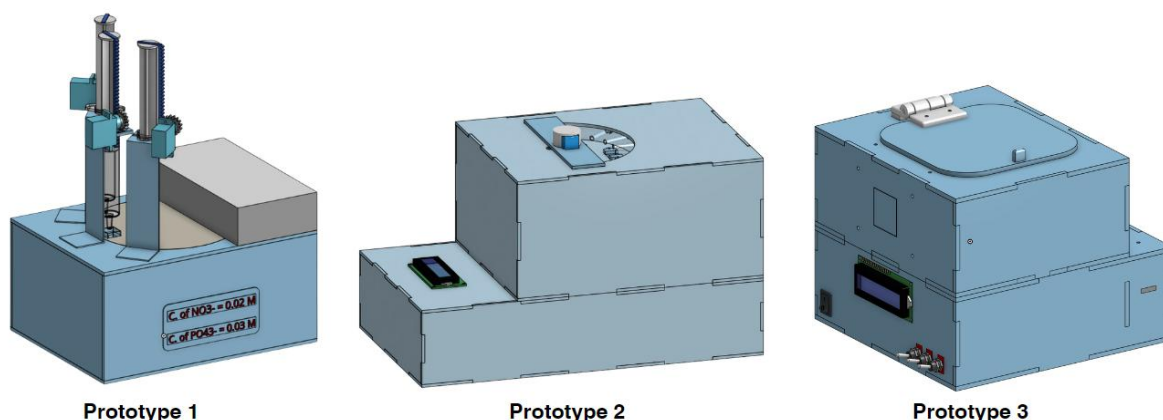


Figure 1.

The Prototypes development

Calibration Curve Evaluation:

Different concentrations of nitrate and phosphate samples are prepared for testing in the AgriSense apparatus. The according reagent is then added to the sample with a reaction wait time of 2 minutes. The sample is then inserted into the innovation to evaluate the RGB value. The transmittance was calculated and later converted to absorbance using Equation (1) and Equation (2). By plotting the absorbance value at the maximum absorbance wavelength (λ_{\max}) versus RGB LED peak wavelength (λ_{LED}), the linear correlation is then verified. The wavelength λ_{LED} is, therefore, suitable to be used instead of λ_{\max} . The range of peak wavelength in RGB LED and RGB sensor are examined in datasheets to match each other, ensuring the highest absorbance evaluation sensitivity. Next, different concentrations of samples of nitrate and phosphate are evaluated respectively. After recording the data, the calibration curve is constructed by plotting linear graphs with concentration on the x-axis and absorbance value on the y-axis.

$$\text{Transmittance} = \frac{\text{RGB}_{\text{final}} - \text{RGB}_{\text{initial}}}{\text{RGB}_{\text{initial}}} \quad (1)$$

$$\text{Absorbance} = -\log_{10}(\text{Transmittance}) \quad (2)$$

Innovation Procedure:

Upon initiation in Fig 3A, the stepper motor rotates to align to the 0-degree disc position utilizing a maximum magnetic flux measurement in Fig 3B, configuring the system for the introduction of a sample. The user prepares a 1 mL sample of the substance to be evaluated in a cuvette. The user then inserts a sample cuvette into a cuvette disc shown in Fig 3C. Next, the user is required to press the number pad to select the according cuvette position. The disc then rotates to align the inserted cuvette to the 0-degree disc position. Consequently, the user selects the mode of ions to be tested via the number pad. The cuvette disc then rotates to add reagents for either nitrate or phosphate detection in Fig 3E and 3F. For nitrate detection, a 460 nm blue RGB LED is utilized to measure the RGB value of the sample. For phosphate detection, a 620 nm red RGB LED is utilized to measure the RGB value of the sample. By inputting the absorbance value into the equation from the previous calibration curve, the concentration of the sample is calculated and shown on the LCD screen in Fig 3G and 3H.

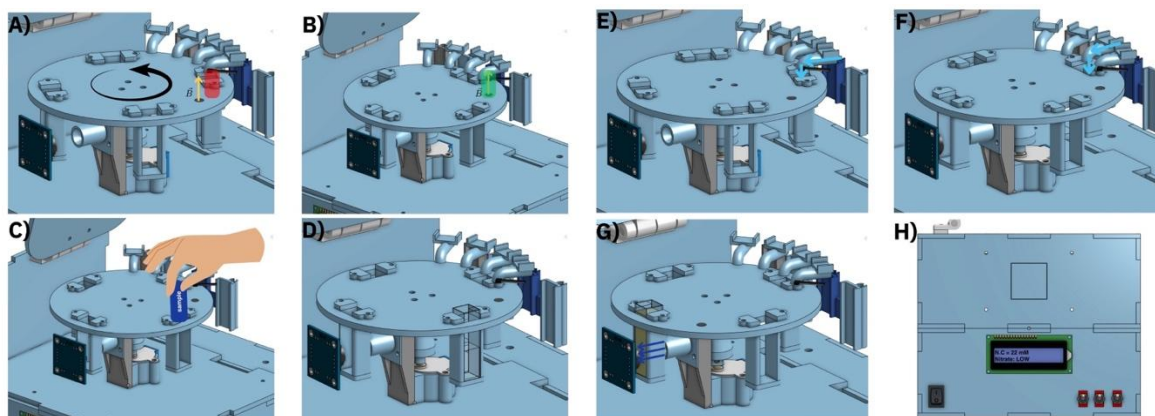


Figure 3.
The process of Innovation

Accuracy Test:

The coefficient of determination, or R-squared, is used to validate the linearity of the Absorbance-Concentration and λ_{\max} - λ_{LED} relationship. The absorbance values at λ_{LED} from the standard spectrophotometer and the innovation are recorded upon testing the innovation. Root Mean Squared and Average Percentage Error are then performed on the data.

Results and Discussion:

Nitrate Colorimetric Analysis:

Seven different concentrations of Potassium Nitrate, 8, 16, 40, 80, 120, 160, and 200 μM , were tested following the typical nitrate component in soil. The R-squared value of the absorbance value measured at 390.6 nm is 0.995 in Fig 4b. At the maximum absorbance wavelength (λ_{\max}), this precision ensures the reproducibility of the reaction.

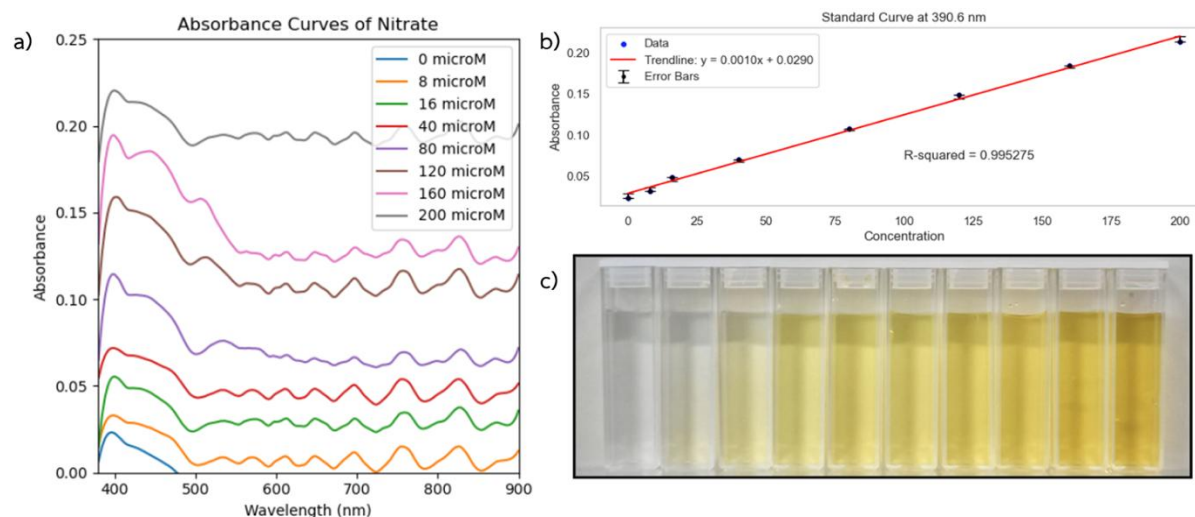


Figure 4.
Nitrate analysis result: a) Absorbance curve b) Standard curve
c) Solution in different concentrations

Phosphate Colorimetric Analysis:

Seven different concentrations of Sodium Orthophosphate, 2.625, 5.25, 10.5, 21, 42, 63 and 84 mM, were evaluated according to the typical phosphate component in soil. The R-squared



value of the absorbance value measured at 830.6 nm is 0.993 in Fig 5b. At the maximum absorbance wavelength(λ_{\max}), this precision ensures the reproducibility of the reaction.

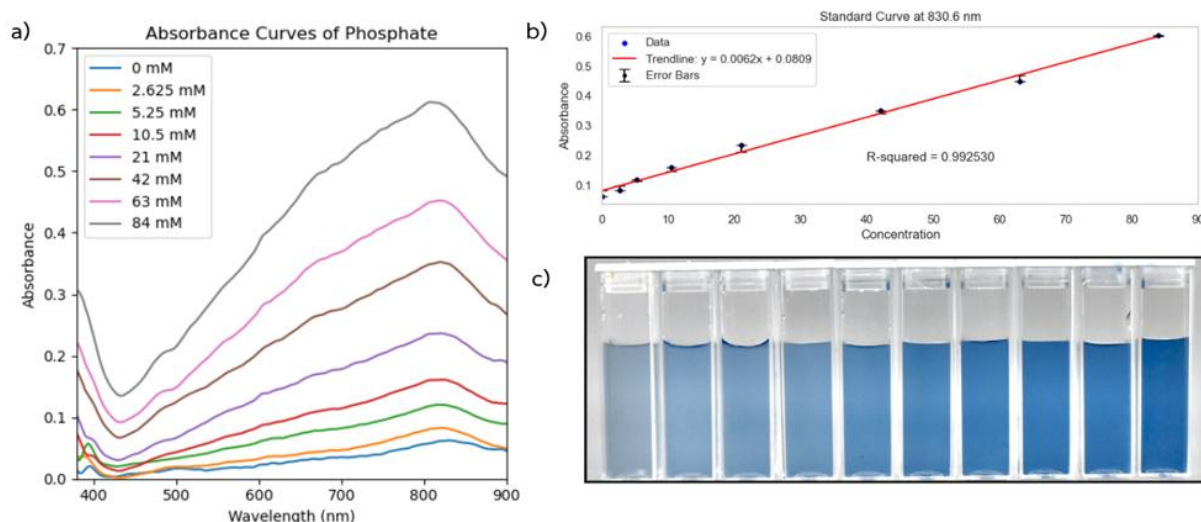


Figure 5.

Phosphate analysis result: a) Absorbance curve b) Standard curve
c) Solution in different concentrations

Pump Calibration:

We conducted a calibration of the peristaltic pump used in the innovation device to determine standard values for controlling the pump's flow using Arduino. The experiment involved filling water into volumetric flasks and measuring the time taken to fill the water up to the flask's marked line. Four different flask volumes were used: 10, 25, 50, and 100 mL, with each volume measurement repeated three times to obtain average times. The results were plotted on a graph illustrating the relationship between time (seconds) and the volume of the volumetric flasks (mL), yielding a standard flow rate of 1.688 mL/s derived from the graph's slope. The R-square value of 1.000 indicates the high accuracy of the pump used for dispensing substances in the innovation device.

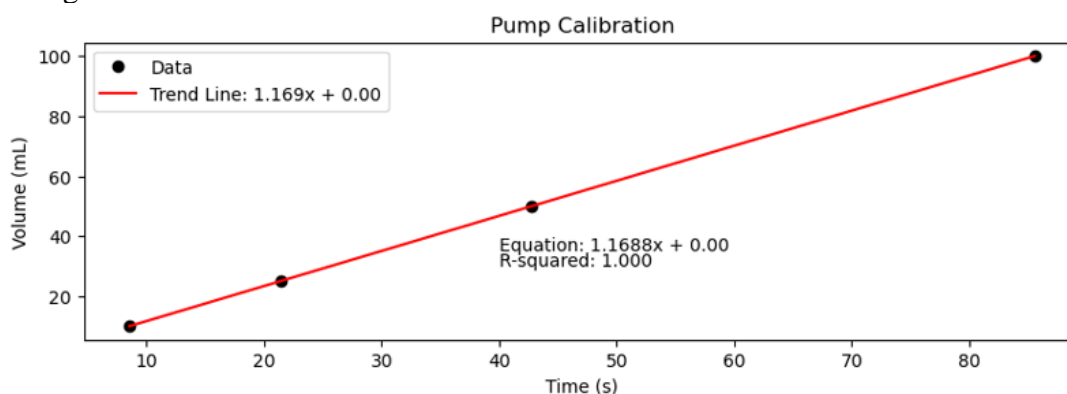


Figure 6.

Graph of water pump calibration

The study of absorbance values at the wavelengths of LED light: From the study of the relationship between absorbance data at the maximum absorption wavelength (λ_{\max}) and the

wavelength used in the innovation, it was found that for nitrate: 390 nm vs. 460 nm and phosphate: 830 nm vs. 660 nm, the data exhibited a linear relationship with R-squared values as high as 0.9994 and 0.9980, respectively. This indicates a strong correlation, suggesting that wavelengths other than the maximum absorption wavelength can be effectively used to determine concentrations.

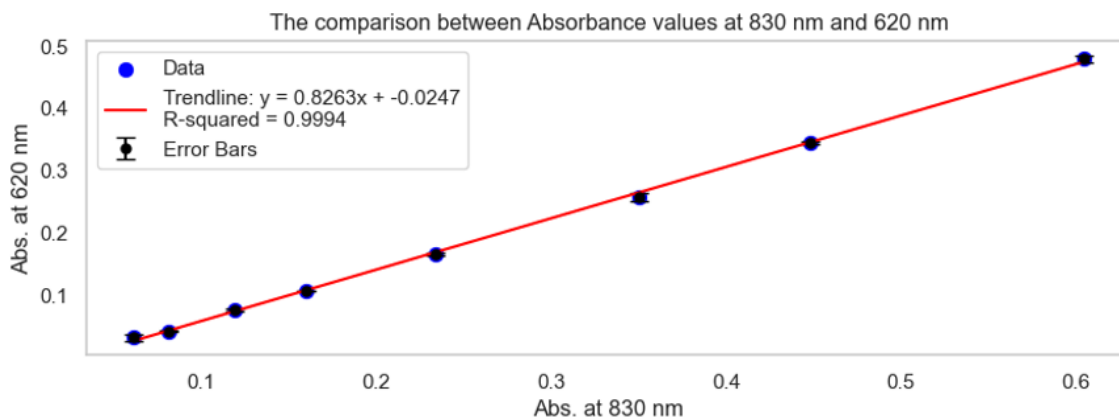


Figure 7.

Graph showing the relationship of absorbance values at the wavelength range of 830 nm compared to 620 nm (using a red LED light)

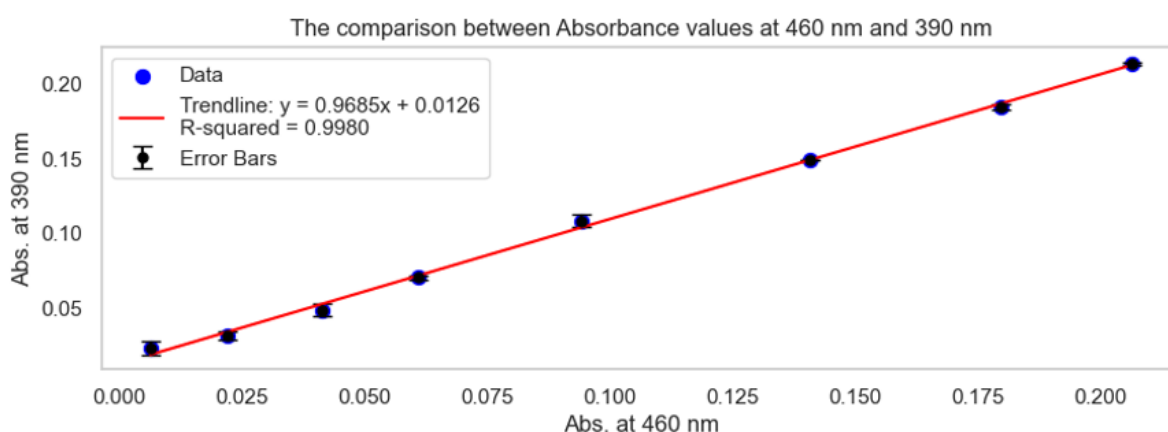


Figure 8.

Graph showing the relationship of absorbance values at the wavelength range of 390 nm compared to 460 nm (using a blue LED light)

Prototype Accuracy:

Our device was compared for measuring light absorbance at two different wavelengths based on the reactions used to determine concentration 460 nm for nitrate reactions and 620 nm for phosphate reactions—it was found that the team's device had a percentage error ranging from 3% to 7%. This indicates that the innovation in this project has an average efficiency of 95% when compared to a spectrophotometer.

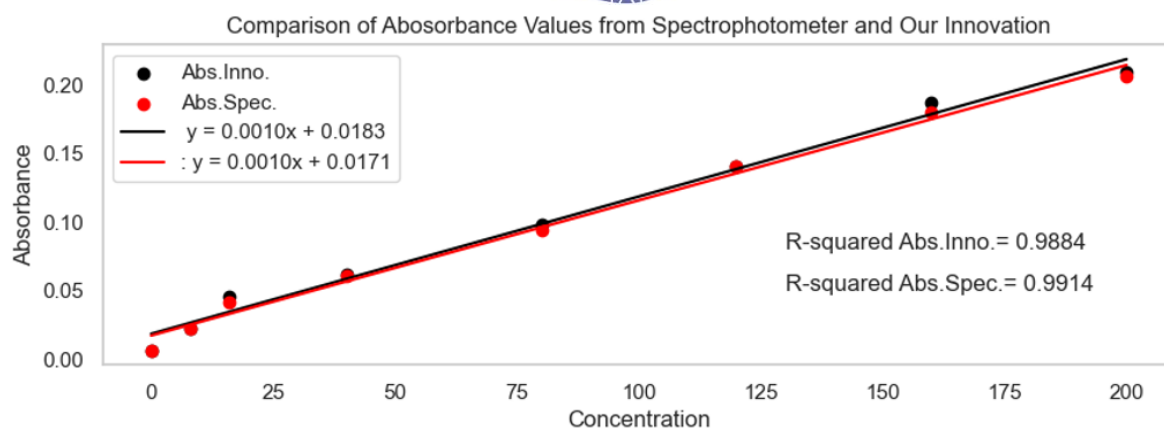


Figure 9.

Graph comparing absorbance values at 460 nm measured by a spectrophotometer and by the innovation device.

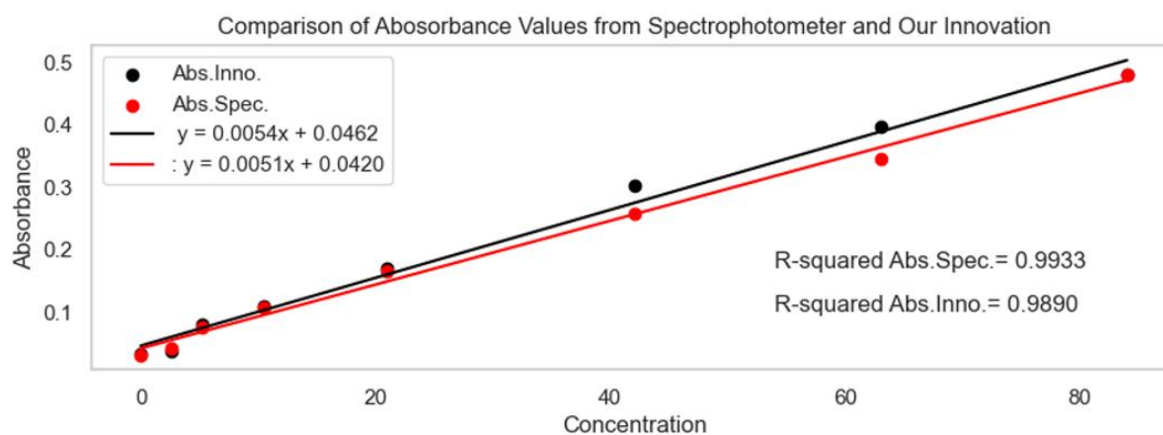


Figure 10.

Graph comparing absorbance values at 620 nm measured by a spectrophotometer and by the innovation device.



Figure 11.
Final Prototype

Conclusion:

The development and testing of the innovation presented in this study demonstrates a significant advancement in cost-effective and efficient methods for colorimetric analysis of nitrate (NO_3^-) and phosphate (PO_4^{3-}) ions. By utilizing RGB sensors in conjunction with an ESP32 controller, this innovative device successfully measures absorbance at specific wavelengths, allowing for the precise determination of ion concentrations. The choice of wavelengths—390 nm for nitrate and 830 nm for phosphate—corresponds to the optimal absorption peaks identified through rigorous experimentation using traditional spectrophotometry.

The data reveals a strong linear correlation between absorbance and concentration at these wavelengths, with R-square values of 0.9952 and 0.9925 for nitrate and phosphate, respectively. This high degree of correlation confirms the accuracy and reliability of the innovation in analyzing these critical ions.

To accommodate the limitations of the RGB sensor, which operates at non-peak wavelengths (460 nm for blue and 620 nm for red LEDs), further analysis was conducted to evaluate the relationship between absorbance and concentration at these alternative wavelengths. Remarkably, the results showed that the linear correlation remained strong, with R-square values above 0.99 for both ions, thus validating the feasibility of using these alternative wavelengths for accurate concentration measurements.

The innovation's peristaltic pump, crucial for the precise delivery of reagents, was also rigorously tested. The pump exhibited exceptional accuracy with an R-square value of 1.00 and a flow rate of 1.688 mL/s, ensuring the reliability of reagent addition during analysis.

In comparison with a spectrophotometer, the innovation achieved an overall accuracy of approximately 95%, with a 3% error in nitrate measurement and a 7% error in phosphate measurement. These findings highlight the innovation's effectiveness as a viable alternative to more expensive spectrophotometric equipment, offering comparable performance at a fraction of the cost.

In conclusion, the prototype innovation developed in this project represents a significant step forward in the field of colorimetric analysis, providing a practical, low-cost solution for the accurate detection and quantification of nitrate and phosphate ions. The successful application of this device underscores its potential for broader use in environmental monitoring and agricultural applications, where maintaining nutrient balance is essential for ecosystem health and productivity. Future work will focus on further refinement and expansion of the device's capabilities to include additional analytes and improve user accessibility.

Acknowledgement:

This project was made possible through the generous support and assistance of many individuals and organizations. It would not have reached its completion without the contributions of everyone involved. I would like to express my sincere gratitude at this moment. Special thanks go to Dr. Kiattipoom Rodpun, a chemistry teacher, and Mr. Chakrit Samarnrak, a physics teacher at Mahidol Wittayanusorn School, who acted as project advisors. Their guidance, insightful ideas, and continuous support in solving problems were invaluable to the project's success. The project team is deeply grateful for their help.

References:

1. Chislock, M. F., Doster, E., Zitomer, R. A. & Wilson, A. E. (2013) Eutrophication: Causes, Consequences, and Controls in Aquatic Ecosystems. *Nature Education Knowledge* 4(4):10



2. Hu X, Shi J, Shi Y, Zou X, Tahir HE, Holmes M, Xu Y. A dual-mode sensor for colorimetric and fluorescent detection of nitrite in hams based on carbon dots-neutral red system. *Meat Science*. 2019; 147: 127-134. doi:10.1016/j.meatsci.2018.09.006.
3. Li D, Ma Y, Duan H, Deng W, Li D. Griess reaction-based paper strip for colorimetric/fluorescent/SERS triple sensing of nitrite. *Biosensors and Bioelectronics*. 2018; 99: 389-398. doi:10.1016/j.bios.2017.08.008.
4. Mengel DB. Fundamentals of Soil Cation Exchange Capacity (CEC). Purdue University Cooperative Extension Service. Retrieved June 16, 2023.
5. Nagul EA, McKelvie ID, Worsfold P, Kolev SD. The molybdenum blue reaction for the determination of orthophosphate revisited: Opening the black box. *Analytica Chimica Acta*. 2015; 890: 60-82. doi:10.1016/j.aca.2015.07.030.
6. Nam J, Jung IB, Kim B, Lee SM, Kim SE, Lee KN, Shin DS. Colorimetric hydrogel biosensor for rapid detection of nitrite ions. *Sensors and Actuators B: Chemical*. 2018; 270: 112-118.
7. Uchida, R. (2000) Essential Nutrients for Plant Growth: Nutrient Functions and Deficiency Symptoms. In: Silva, J.A. and Uchida, R., Eds., *Plant Nutrient Management in Hawaii's Soils, Approaches for Tropical and Subtropical Agriculture*, College of Tropical Agriculture and Human Resources, University of Hawaii at Manoa, Honolulu, 31-55.
8. Soil Science Society of America book series. *Methods of Soil Analysis*. 1986. doi:10.2136/sssabookser5.1.2ed.



Effect of fermented soybean powder on metabolic changes in high fat diet-treated rats

Thanat Panyafong and Teera Chewonarin*

Department of Biochemistry, Faculty of Medicine, Chiang Mai University, Chiang Mai 50200, Thailand

*e-mail: teera.c.@cmu.ac.th

Abstract:

This study aimed to investigate the effects of fermented soybean powder (FSB) on rats fed a high-fat diet (HFD). During the first 4 weeks, HFD-fed rats exhibited a significant increase in fasting blood glucose levels compared to normal rats ($P<0.05$). FSB was administered at doses of 100 and 1,000 mg/kg body weight for the subsequent 4 weeks. HFD-fed rats showed a significant increase in final body weight compared to normal rats ($P<0.05$). In contrast, serum triglyceride levels in HFD-fed rats were significantly lower than in normal rats ($P<0.05$). Although FSB administration slightly increased serum triglyceride levels compared to HFD-only rats, the difference was not statistically significant. Additionally, total cholesterol levels in HFD-fed rats treated with FSB were significantly lower than those in HFD-only rats ($P<0.05$). Interestingly, HFD-fed rats exhibited a significant increase in LDL-cholesterol compared to normal rats ($P<0.05$), while FSB administration significantly reduced LDL-cholesterol levels in HFD-fed rats ($P<0.05$). HFD-fed rats also showed a significant increase in serum ALT levels compared to normal rats ($P<0.05$); however, FSB administration did not significantly increase serum ALT or AST levels. Therefore, FSB treatment may alleviate serum lipid levels in HFD-fed rats without inducing hepatotoxicity. In conclusion, fermented soybean powder demonstrated a cholesterol-lowering effect in rats fed a high-fat diet.

Introduction:

Nowadays, the dietary risk factors are a particular concern that cause non-communicable diseases remain the most cause of premature morbidity and mortality¹. High fat diet (HFD) increases the risk of several non-communicable diseases (NCDs) such as hypertension, diabetes type 2, dyslipidemia and cancer^{2,3}. High fat accumulation in adipose tissue resulted in insulin resistance leading to stable hyperglycemia overtime^{4,5,6,7}. Moreover, high blood sugar level is a key factor that causes dyslipidemia because of insulin resistance. In addition, dyslipidemia can lead to a change liver metabolism and can damage the liver⁸. The body weight control or use functional food might improve serum lipid level in high fat diet condition. The production and consumption of fermented soybean are widespread in asia⁹. Several fermented soybean products such as natto, cheonggukjang and tempeh could decrease lipid accumulation and showed hypoglycemic activity in rats fed with high fat diet^{10,11}. It exhibits the ability to reduce total cholesterol and LDL-cholesterol^{12,13}. Moreover, it decreases the levels of LDL-cholesterol in high-fat-diet-induced obese rat¹⁴. In this study, fermented soybean, Thai Lanna food was used for testing our hypothesis. Therefore, the effect of fermented soybean powder on lipid accumulation, blood sugar level, lipid profile change in rats received high fat diet (HFD) was investigated.

Methodology:

Preparation of fermented soybean powder (FSB) Soybean from Thanya Farm Company limited; Thailand was purchased. Dried soybean was soaked and boiled. The cooled down soybean was then naturally fermented for 3 days according to Thua-nao production. The 50 °C dried-fermented soybean was finely grinded, and then suspended in distilled water at concentration 25 mg/ml and 250 mg/ml for feeding to rat experiment at concentration 100 mg/kg.bw and 1,000 mg/kg.bw, respectively.

Animal experiment protocol Eight-week-old male Wistar rats with 250-300 g were obtained from the Nomura Siam international company limited, Thailand. The protocol of animal experiment was approved by animal ethics committee; Faculty of Medicine, Chiang Mai University. Total 40 rats, 10 of them were randomly selected for normal control group with standard laboratory chow throughout the experiment. To produce high fat diet (HFD) induced obese rats, other 30 rats were fed with high fat diet containing 50% calories from fat. After 4 weeks, rats were divided to 2 conditions rats' model. Normal rats in group 1, were received normal diet and distilled water, whereas HFD rats in group 2-4 were received high fat diet and orally fed distilled water (group 2), 100 mg/kg.bw FSB (group 3) and 1,000 mg/kg.bw FSB (group 4), respectively for 4 weeks. The bodyweight and fasting blood glucose level were recorded weekly using digital balance and glucometer (Easy G, OPTIMA, Taiwan). On week 9, all rats were fasted, measured for final bodyweight and then sacrificed. After sacrifice, blood samples were collected for measurement of serum lipid and liver function test.

Measurement of serum lipid and liver function All serum samples from rats were subjected to measure for triglyceride, total cholesterol, low-density lipoprotein (LDL)-cholesterol, aspartate transaminase (AST) and alanine transaminase (ALT) at central laboratory of Maharaj Nakorn Chiang Mai Hospital, Faculty of medicine, Chiang Mai University.

Statistical analysis: All calculations were done using Microsoft Excel version 2013 and presented as mean \pm standard deviation (SD). Statistical significance in all data were determined by one-way ANOVA followed by Turkey's multiple, while student's *t*-test was used to compare the difference between two experimental groups using GraphPad Prism software version 9. $P < 0.05$ was considered statistically significant.

Results and Discussion:

Effect of FSB on body weight and blood glucose level in HFD rats

The effect of FSB on final bodyweight and fasting blood glucose level is presented in Figure 1. The results showed that final bodyweight was significantly higher in HFD control group (533.33 ± 35.62 g) than in normal control group (492.78 ± 25 g). On the other hand, HFD treated rats with FSB group showed similar final bodyweight to HFD control group ($P > 0.05$). Fasting blood glucose was significantly higher in HFD control group than in the normal control group ($P < 0.05$) while in the HFD treated with FSB group (group 3 and 4) showed slightly higher than HFD control group in week 5-7 ($P > 0.05$), whereas HFD treatment with FSB at 100 mg/kg.bw group (124.56 ± 5.96 mg/dl) was significantly higher than HFD control group only on week 8 ($P < 0.05$). Therefore, the treatment of FSB might affect the food and calories consumption in HFD-treated rats. Several research have indicated that rats received high fat diet develop overweight conditions and elevated fasting blood glucose level within 4 weeks^{15,16}. In this study, HFD rats showed that initiation phase of obesity and insulin resistance, however, a longer duration may be necessary to induce more pronounced obesity and insulin resistance, which we plan to investigate further. High-fat diet consumption can lead



to an increase in fasting blood glucose in HFD-treated rats. Unfortunately, the administration of FSB in HFD rats resulted in a slight increase in fasting blood sugar during weeks 7 and 8. This suggests that FSB may impair glucose utilization. The mechanism behind this effect should be further investigated and repeated in future studies.

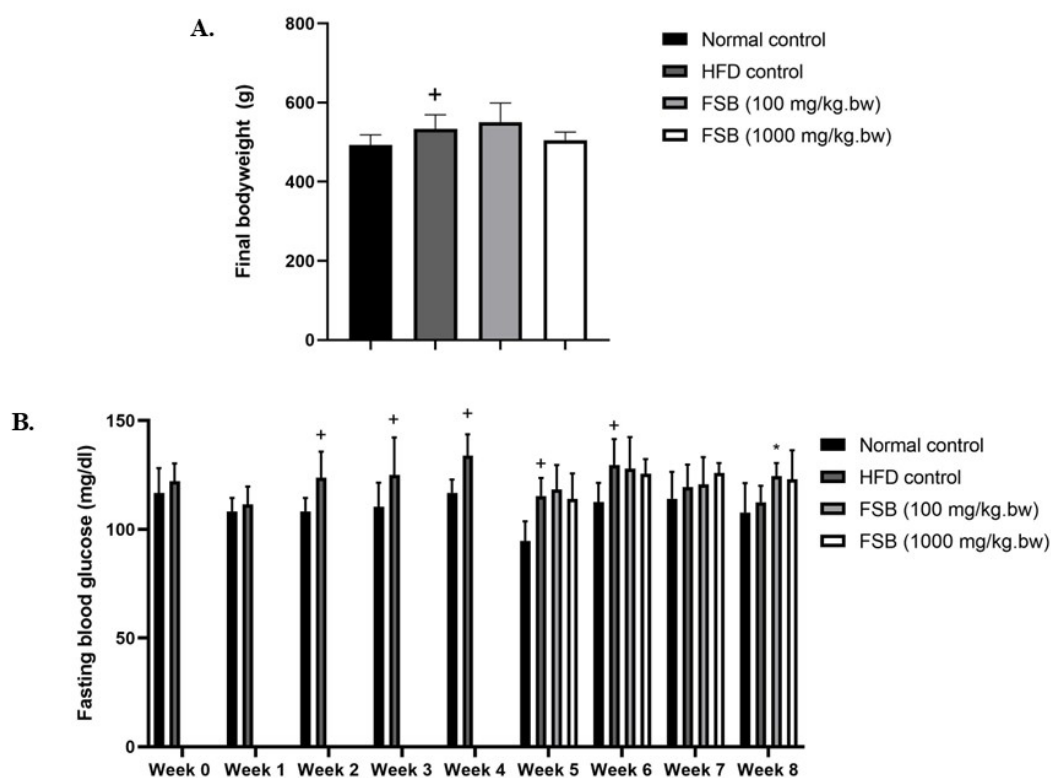


Figure 1. Effect of FSB on (A) final bodyweight (g) and (B) fasting blood glucose level (mg/dl) in HFD rats and HFD rats treated with FSB at the concentration 100 mg/kg.bw and 1,000 mg/kg.bw. Results were presented as mean \pm standard deviation ($n = 9$ each group). $+P < 0.05$ compared normal control group; $*P < 0.05$ compared HFD control group.

Effect of FSB on serum lipid in HFD rats

The serum level of triglyceride was significantly lower in HFD group (70.78 ± 22.99 mg/dl) compared to normal diet group (163 ± 34.31 mg/dl). In this experiment, the HFD control group showed slightly increased serum level of triglycerides compared to normal control group in previous study¹⁷. We identified that the elevated serum level of triglycerides observed in the in the normal control group may be attributed to a measurement error. In comparison to our previous study¹⁷ and other reports, where the normal control group exhibited serum triglyceride levels within the range of 50-70 mg/dl, these levels were slightly lower than those observed in the HFD control group. By the way, administration of FSB at concentration 100 mg/kg.bw and 1,000 mg/kg.bw did not alter the serum level of triglyceride compared to HFD control group ($P > 0.05$). HFD treated with FSB did not show a significant difference in serum triglycerides level compared to HFD control rat, indicating FSB no effect on improving serum triglycerides levels in HFD control rat. The serum level of total cholesterol in HFD control group was similar to normal control group ($P > 0.05$). The administration of FSB at concentration 100 mg/kg.bw and 1,000 mg/kg.bw could significantly decrease serum level of total cholesterol level to 66.56 ± 14.71 mg/dl and 50.56 ± 6.93 mg/dl, respectively compared to HFD control group. Beside of total cholesterol, LDL-cholesterol was significantly increased in HFD control group up to

10.67 ± 2.12 mg/dl compared to the normal control group (6 ± 2.24 mg/dl). Administration of FSB at concentration 100 mg/kg.bw and 1,000 mg/kg.bw could significantly decrease serum level of LDL-cholesterol to 7.44 ± 2.88 mg/dl and 4.89 ± 1.76 mg/dl, respectively compared to HFD control group as shown in Figure 2. Therefore, the treatment of FBS could decrease serum level of total cholesterol and LDL-cholesterol in HFD-treated rats. The research of Jia Y-j et. al. indicated that rats received high fat diet were significantly higher serum level of LDL-cholesterol while serum level of total cholesterol was not difference¹⁸. Park S et. al. showed that fermented soybean reduced total cholesterol and LDL-cholesterol in HFD rats¹⁹. This study has demonstrated that the treatment with high fat diet can increase the present of LDL-cholesterol in rat serum. Although FBS did not alter the blood glucose and triglyceride level in high fat diet treated rats, FSB administration can decrease serum level of total cholesterol and LDL-cholesterol in these rats.

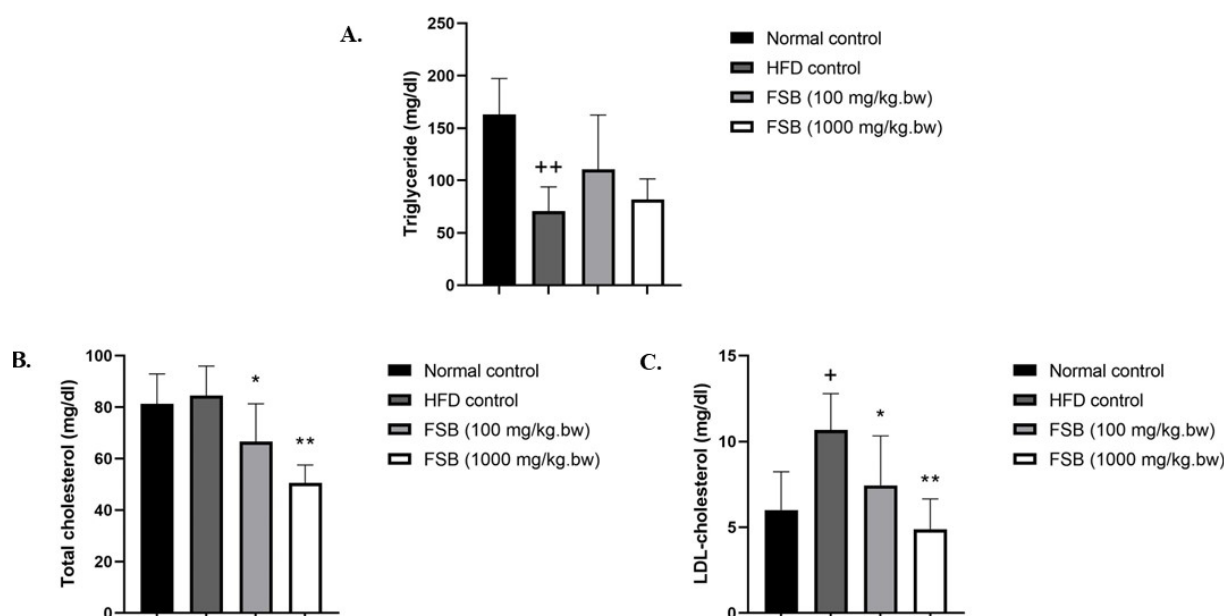


Figure 2. Effect of FSB on serum level of (A) triglyceride (mg/dl), (B) total cholesterol (mg/dl) and (C) LDL-cholesterol (mg/dl) in HFD rats and HFD rats treated with FSB at the concentration 100 mg/kg.bw and 1,000 mg/kg.bw. Results were presented as mean ± standard deviation (n = 9 each group). +*P* < 0.05 compared normal control group; ++*P* < 0.0001 compared normal control group; **P* < 0.05 compared HFD control group; ***P* < 0.0001 compared HFD control group.

Effect of FSB on liver damage in HFD rats

Serum level of AST in HFD control group was similar to normal control group, as well as HFD treated rats was similar to FSB group (*P* > 0.05). On the other hand, Serum level of ALT was significantly increased in HFD control group to 56.78 ± 30.99 U/L compared to the normal control group (31.33 ± 14.42 U/L). Administration of FSB at concentration 1,000 mg/kg.bw did not alter serum level of ALT (*P* > 0.05) as shown in Figure 3. The results indicated that HFD-fed rats was significantly increase serum level of AST and ALT, that increased when liver damage occurs²⁰. In this study, the HFD control group showed slightly increase in serum level of AST and ALT, though they remained within the normal range, and the FSB did not affect these enzyme level in the serum. Therefore, administration of FSB in HFD rats did not exhibit any signs of liver damage.

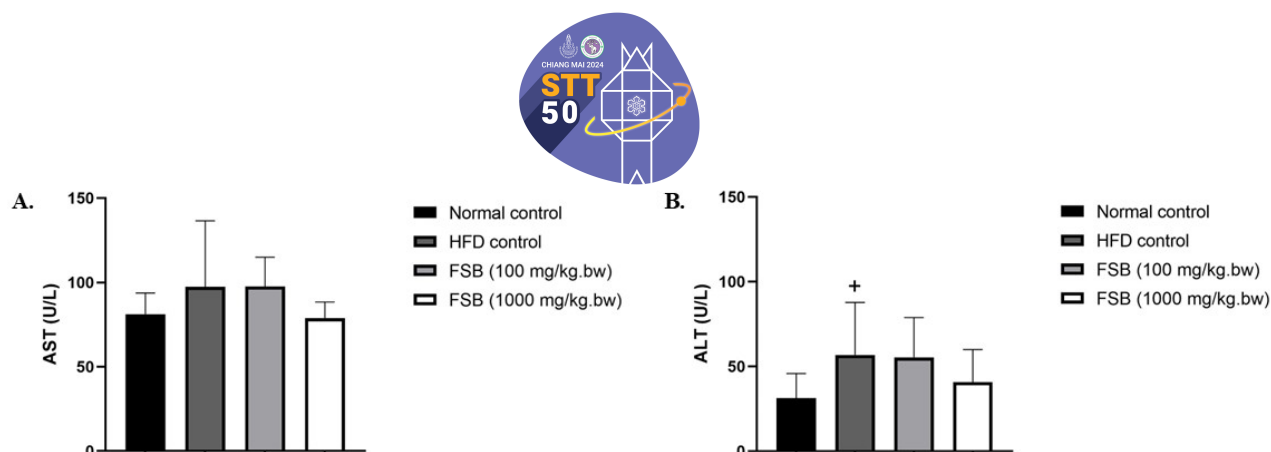


Figure 3. Effect of FSB on serum level of (A) AST (U/L) and (B) ALT (U/L) in HFD rats and HFD rats treated with FSB at the concentration 100 mg/kg.bw and 1,000 mg/kg.bw.

Results were presented as mean \pm standard deviation (n = 9 each group).

+ $P < 0.05$ compared normal control group.

Conclusion:

Fermented soybean powder has no ability to improve triglyceride levels but could slightly increase the bodyweight and fasting blood sugar in high-fat diet-treated rats. However, it can reduce total cholesterol and LDL cholesterol in rats consuming high-fat diet. Therefore, fermented soybean powder may influence only cholesterol clearance in rats receiving a high-fat diet.

Acknowledgements:

This writing of this article was supported by the Fundamental Fund 66; FF 66 Chiang Mai University, Thailand.

References:

1. Thapsuwan S, Phulkerd S, Chamrathirong A, Gray RS, Jindaratnaporn N, Loyfah N, et al. *BMJ Nutrition, Prevention & Health*. 2024;7:78-87.
2. Ma D, Sakai H, Wakabayashi C, Kwon J-S, Lee Y, Liu S, et al. *Journal of Epidemiology*. 2017;27:568-73.
3. Peng W, Chen S, Chen X, Ma Y, Wang T, Sun X, et al. *The Lancet Regional Health: Western Pacific*. 2023;43:1-19.
4. He M-Q, Wang J, Wang Y, Sui J, Zhang M, Ding X, et al. *Chronic Diseases and Translational Medicine*. 2020;6:198-207.
5. Ji T, Fang B, Wu F, Liu Y, Cheng L, Li Y, et al. *Nutrients*. 2023;15:1-15.
6. Kuipers EN, Held NM, In het Panhuis W, Modder M, Ruppert PMM, Kersten S, et al. *American journal of physiology Endocrinology and metabolism*. 2019;317:820-830.
7. Lackey DE, Lazaro R, Li P, Johnson A, Hernandez-Carretero A, Weber N, et al. *American journal of physiology Endocrinology and metabolism*. 2016;311:989-97.
8. Kathak RR, Sumon AH, Molla NH, Hasan M, Miah R, Tuba HR, et al. *Scientific Reports*. 2022;12:1-8.
9. do Prado FG, Pagnoncelli MGB, de Melo Pereira GV, Karp SG, Soccol CR. *Microorganisms*. 2022;10:1-24.
10. Kwak CS, Park SC, Song KY. *Journal of medicinal food*. 2012;15:1-9.
11. Huang C-H, Chen C, Shieh C-C, Chang S-H, Tsai GJ. *Metabolites*. 2022;12:1-12.
12. Arumugam S, Dioletis E, Paiva R, Fields MR, Weiss TR, Secor ER, et al. *Journal of medicinal food*. 2019;560-563.
13. Jung S, Haddad EH, Kaur A, Sirirat R, Kim A, Oda K, et al. *Nutrients*. 2021;13:1-16.
14. Kim N-H, Kim HM, An H-J, Um J-Y, Moon PD, Kim S-j, et al. *BioFactors*. 2008;33.

15. Srinivasan K, Viswanad B, Asrat L, Kaul CL, Ramarao P. Pharmacological research. 2005;52 4:313-20.
16. Srinivasan K, Ps P, Kaul CL, Ramarao P. Methods and findings in experimental and clinical pharmacology. 2004;26 5:327-33.
17. Sakuludomkan W, Yeewa R, Subhawa S, Khanaree C, Bonness AI, Chewonarin T. Journal of Nutrition and Metabolism. 2021;2021.
18. Jia Y-j, Liu J, Guo Y-L, Xu R-x, Sun J-W, Li JJ. Journal of Geriatric Cardiology:JGC. 2013;10:361-8.
19. Park S, Lee J-J, Shin H-W, Jung S, Ha J-H. International Journal of Environmental Research and Public Health. 2021;18:1-19.
20. Lasker S, Rahman MM, Parvez F, Zamila M, Miah P, Nahar K, et al. Scientific Reports. 2019;9:1-15.



ENHANCEMENT OF HEALTH BENEFIT OF OKARA THROUGH MIX-CULTURE FERMENTATIONS FOR DEVELOPMENT INTO FUNCTIONAL FOOD PRODUCT

Supakarn Sukviset¹, Niracha Udompornvirat², Tharida Khaenkhokkruad², Wiramsri Sripochanart^{2,*}

¹Department of Food Science, School of Food Industry, King Mongkut's Institute of Technology Ladkrabang, Bangkok, Thailand

²Division of Fermentation Technology in Food Industry, School of Food Industry, King Mongkut's Institute of Technology Ladkrabang, Bangkok, Thailand

*E-mail: Wiramsri.sr@kmitl.ac.th

Abstract:

Microorganisms play a significant role in promoting enzyme production, especially in the food industry. This research investigated by sequential fermentation of okara using *Rhizopus oligosporus* fungi and *Bacillus subtilis* bacteria for 72 h to enhance the functional properties of okara, with the potential to be developed as a functional food. The study aimed to evaluate the activity of the produced protease enzyme, the degree of protein hydrolysis, and the antioxidant activity of fermented okara to enhance the functional food properties in rice sprinkling powder product. The results showed that the protease activity and the degree of protein hydrolysis increased with fermentation time. Additionally, okara fermented with *R. oligosporus* and *B. subtilis* had an antioxidant activity (IC₅₀) value of 178.83 mg/mL, as determined by the 2,2-Diphenyl-1-picrylhydrazyl (DPPH radical scavenging assay), which was higher than the control okara that was not fermented. When the fermented okara was processed into rice sprinkling powder product by using a tray dryer at 70 °C for 18 h, the antioxidant activity (IC₅₀) value was found to be 6.78 mg/mL, indicating a significant increase compared to the fermented okara that was not processed into rice sprinkling powder.

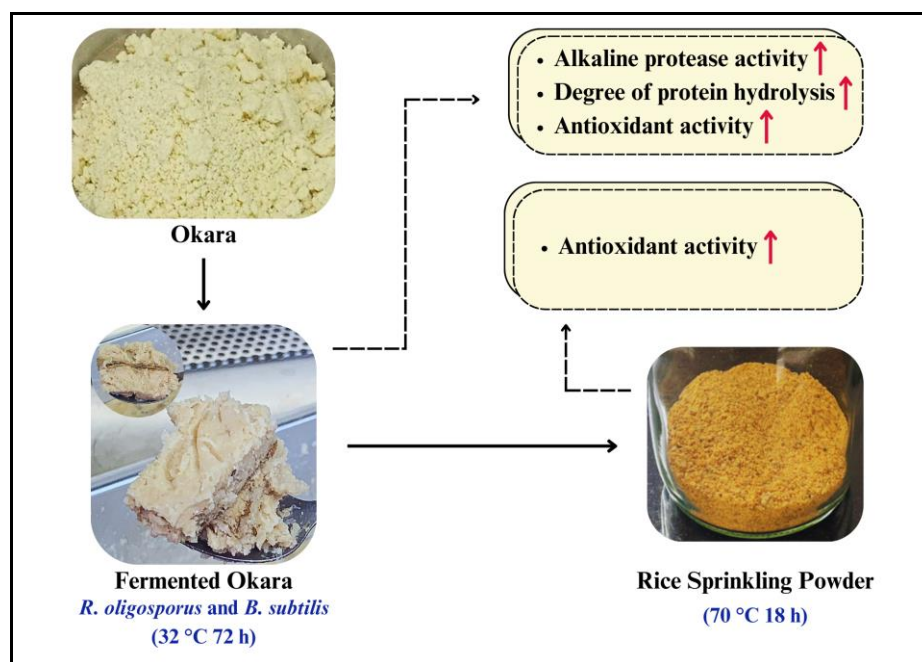


Figure 1.

An overview of the complete procedure.

Introduction:

Okara, is a by-product of soy milk and tofu processing, with approximately 4 million tons produced worldwide each year.¹ This makes it a highly produced by-product that is often underutilized, as okara's utilization is minimal. Most of it is used as animal feed or discarded as waste, as it is a perishable raw material with a short shelf life. Due to the increasing consumption of soybeans, huge quantities of okara are produced worldwide each year.² Therefore, it is of great interest to devise techniques to add value to okara. Dried okara contains approximately 50% dietary fiber and 20% protein, along with a large number of isoflavones, saponins, minerals, and other nutrients.³ Fermentation is an important process that can further enhance the functional properties of okara. The enzymes and protein degradation produced during the fermentation process promote okara's numerous biological activities, such as its enhanced antioxidant properties.⁴ Okara is thus a highly beneficial health ingredient.

The improvement of okara properties includes chemical, enzymatic, fermentation, and physical methods.⁵ Among these methods, the fermentation process using *Rhizopus oligosporus*, an aerobic fungus, is particularly effective. This fungus produces a wide range of extracellular enzymes, including carbohydrases, proteases, lipases, and phosphatases.⁶ *R. oligosporus* is commonly used in the preparation of tempeh, a traditional Indonesian soybean product, and is also used for okara fermentation.^{2,4} Fermented okara has been reported to have higher antioxidant capacity since the fungal enzymes can hydrolyze the dietary fiber of okara and potentially release fermentable sugars for bacterial growth. The spores of the probiotic bacteria *Bacillus* are stable, survive well during processing and storage, and thus have been used in various functional foods.⁷ The extracellular enzymes, such as carbohydrases, proteases, lipases, and phosphatases, secreted by these bacteria accelerate the degradation of lignocellulosic structures and other antinutrients found in okara.⁸ Therefore, the biotransformation of okara by *Bacillus* spp. has great potential to enhance its digestibility, improve its texture quality, and reduce the unpleasant taste of okara. Fermentation decomposes large complex molecules in okara into small molecules, amino acids, and short-chain fatty acids. In addition, antioxidant levels have been found to increase after fermentation.⁹

In this research, okara was fermented using the fungus *Rhizopus oligosporus* and the bacterium *Bacillus subtilis* to study the activity of the produced protease enzyme, the degree of protein hydrolysis, and the antioxidant properties to enhance the functional properties of okara.

Methodology:

Material

Okara, kindly obtained from Lactasoy Co., Ltd., was stored in a freezer at -20 °C. *Rhizopus oligosporus* TISTR3138 and *Bacillus subtilis* TISTR001 were purchased from the Thailand Institute of Scientific and Technological Research (TISTR). Casein, carbonate-bicarbonate buffer (Carlo Erba, Italy), and trichloroacetic acid (PanReac, Spain) were used for the alkaline protease activity assay. *o*-Phthaldialdehyde (OPA) (Sigma, United States), sodium tetraborate (Carlo Erba, Italy), sodium dodecyl sulfate (Carlo Erba, Italy), and β -mercaptoethanol (Sigma, United States) were used for the degree of protein hydrolysis assay. Additionally, 2,2-Diphenyl-1-picrylhydrazyl (DPPH) (SRL, India) was used for the antioxidant activity assay.

Microorganism and inoculum preparation

Bacillus subtilis TISTR001 starter culture was prepared according to the steps of Li¹², with modifications. The starter culture was increased in number by incubating in Trypticase



Soy Broth (TSB) for 48 h at 37 °C. Then, the culture was transferred onto Trypticase Soy Agar (TSA) and incubated for 48 h at 37 °C. The bacterial growth was observed, and the culture purity was checked under a microscope. Afterward, the culture was kept on a TSA slant until white mucus developed. It was then stored in a refrigerator at 5-10 °C to be used as a starter culture (stock culture). The starter culture was prepared by using the slant agar culture to make a bacterial suspension. One tube of bacteria was used, to which 2 mL of sterile distilled water was added and shaken to obtain a bacterial suspension for cultivation on okara.

The okara fermentation and rice sprinkling powder baking processes

Study of okara fermentation was modified from the method of Gunawan-Puteri¹³. Weigh 1 kg of okara and sterilize it by steaming at 121 °C for 30 minutes. Let the okara cool to room temperature, then add *R. oligosporus* TISTR3138 at a concentration of 3 Log CFU/g okara and incubate for 24 h. Subsequently, introduce *B. subtilis* TISTR001 at a concentration of 7 Log CFU/g okara, mix well, then pack 100 g of okara in a 12 × 17 cm perforated plastic bag, and incubate at 35 ± 2 °C for 72 h. Collect samples for analysis every 24 h and store them at -20 °C for further analysis.

For rice sprinkling powder baking process was modified from the method of Siripongvutikorn and Rajchasom^{31,32}. Weigh 100 g of fermented okara, place it in a baking tray to a thickness of approximately 1-1.5 mm, and cover with a thin white cloth. Dry it using a tray dryer (Progress, Thailand) at 70 °C for 18 h until the moisture content was lower than 10%. Then, grind it into a fine powder and store it in a desiccator to prevent moisture.

Alkaline protease activity

Extraction of fermented okara was modified from the method of Verardo¹⁴ by preparing the sample with distilled water in a 1:1 ratio. The mixture was then placed in a shaker and centrifuged at 9000 rpm at 4 °C for 15 min. The supernatant was analyzed for alkaline protease activity.

The analysis of alkaline protease activity was modified from the method of Kim¹⁵. To perform the analysis, 0.1 mL of the crude extract supernatant was incubated with 0.9 mL of 0.5% (w/v) casein solution in 0.1 M carbonate-bicarbonate buffer (pH 9.5) at 45 °C for 20 min. The reaction was immediately stopped by immersing the mixture in a cold water bath and adding 2 mL of 10% (w/v) trichloroacetic acid solution. The mixture was then filtered using filter paper No. 1. The absorbance of the clear filtrate was measured at a wavelength of 280 nm. The enzyme activity was calculated using the absorbance values and a standard curve of tyrosine solution at concentrations ranging from 0 to 140 µg/mL, according to equation (1). One unit of alkaline protease enzyme activity is defined as the amount of enzyme that causes an increase in absorbance at 280 nm by 0.01 per minute under these conditions.

$$\text{Alkaline protease activity (Unit)} = \frac{\text{OD}_{280} \times \text{Total volume (mL)} \times \text{Dilution}}{\text{Slope} \times \text{Sample volume (mL)} \times \text{Incubation time}} \quad (1)$$

Degree of protein hydrolysis (%DH)

The Degree of protein hydrolysis analysis was adapted from Ma.¹⁶ First, 1 g of okara was extracted with 10 mL of deionized distilled water (Milli-Q water). The mixture was then centrifuged at 9000 rpm for 5 min and sonicated for 5 min. The supernatant was extracted

using an orbital shaker for 1 h, then boiled in boiling water for 15 min and filtered using No. 1 filter paper. The supernatant was stored at -20 °C for further analysis.

The Degree of protein hydrolysis was determined using the *o*-Phthaldialdehyde (OPA) method according to Nielsen.¹⁷ Freshly prepare the OPA reagent as follows: mix 25 mL of 100 mM sodium tetraborate buffer (pH 9.3), 2.5 mL of 20% (w/v) sodium dodecyl sulfate, 40 mg of OPA dissolved in 1 mL of methanol, and 100 µL of β-mercaptoethanol, then adjust the final volume to 50 mL.

Prepare the serine standard solution by dissolving 0.05 g of serine in 500 mL of deionized water. In test tubes, add 150 µL of the sample solution, serine standard solution, and a blank. Add 1.5 mL of the OPA reagent to each tube and mix by shaking for 5 seconds. Allow the mixture to stand for 2 min before measuring the absorbance at 340 nm.

The Degree of protein hydrolysis was calculated according to equations (2)-(4), where V represents the total volume of the prepared sample (L), X denotes the sample weight (g), and P is the percentage of protein in the sample (percent by weight). For calculations, let β represent the specificity of soy protein (0.342) and α represent the specificity of soy protein (0.97), where h denotes the number of peptide bonds degraded and h_{tot} denotes the total number of peptide bonds per equivalent protein (with a soy protein specificity of 7.8).

$$\text{Serine} - \text{NH}_2 = \left[\frac{\text{OD}_{\text{sample}} - \text{OD}_{\text{blank}}}{\text{OD}_{\text{standard}} - \text{OD}_{\text{blank}}} \right] \times 0.9516 \frac{\text{meqv}}{\text{L}} \times V \times \frac{100}{X \times P} \quad (2)$$

$$h = \frac{\text{Serine} - \text{NH}_2 - \beta}{\alpha} \quad (3)$$

$$DH = \frac{h}{h_{\text{tot}}} \times 100\% \quad (4)$$

Antioxidant activity assay

The DPPH radical scavenging method (2,2-Diphenyl-1-picrylhydrazyl), as modified from Yamasaki and Chatatikun^{18,19}, assesses the ability of a test substance to scavenge DPPH free radicals using the hydrogen atom technique. DPPH solution appears purple in ethanol, and it turns yellow when reacted with a substance exhibiting antioxidant activity. The test was conducted by adding 60 µL of either a Trolox standard solution or a prepared sample solution from the extract (at concentrations ranging from 0 to 1,000 mg/mL) into a 96-well plate. Then, 140 µL of a 0.16 mM methanolic DPPH radical solution was added, mixed well, and the plate was left in the dark for 30 minutes. The absorbance was measured using a Multimode Microplate Reader (PerkinElmer, United Kingdom) at a wavelength of 517 nm. The percentage of scavenging activity was calculated according to equation (5). IC₅₀ represents the concentration of the extract required to achieve a 50% reduction in scavenging activity.

$$\% \text{ Scavenging activity} = 100 \times \left[\frac{\text{Abs}_{\text{control}} - \text{Abs}_{\text{sample}}}{\text{Abs}_{\text{control}}} \right] \quad (5)$$

Statistical analysis

In this study, each experiment was carried out in triplicate. The study's data were reported as mean ± standard deviation. Statistical analysis was performed on all data using SPSS Statistics 27.0 software (SPSS Inc., Chicago, IL) and One-way analysis of variance



(ANOVA). Duncan's post-hoc test (significance level $p < 0.05$) was utilized to evaluate the differences between the groups.

Results and Discussion:

The okara fermentation process was studied by first fermenting with *Rhizopus oligosporus* for 24 h, followed by *Bacillus subtilis* for 72 h. The fermentation was conducted at 32 °C, with samples taken for analysis every 24 h. In this experiment, two sets of samples were analyzed: 1) a control sample set, which consisted of fermented okara without microorganisms (UFO), and 2) a sample set fermented by *Rhizopus oligosporus* and *Bacillus subtilis* (FMO). The alkaline protease activity, degree of protein hydrolysis, and antioxidant activity were analyzed. Additionally, the fermented okara was dried to produce rice sprinkling powder (RSP), which was then analyzed for antioxidant activity and compared with the fermented okara (FMO).

Fermented okara and Rice sprinkling powder products

Fermented okara fermented with *R. oligosporus* for 24 h, following this, fermentation was continued with *B. subtilis* for 72 h. This fermentation reduced the unpleasant odor of okara, resulting in a distinctive aroma similar to that of natto and cheese.¹¹ This change is likely due to the fermentation process, where microorganisms convert insoluble dietary fiber into soluble dietary fiber. The sample fermented with *B. subtilis* also showed higher amounts of maltose, hemicellulose sugars, branched-chain aromatic amino acids, and hydrophobic amino acids.¹¹ Additionally, okara processed with *B. subtilis* contained higher levels of acetoin, carboxylic acids, pyrazines, and branched-chain fatty acids.¹¹ Consequently, the okara developed a unique smell and improved nutritional value, making it suitable for processing into food products, such as rice sprinkling powder, as illustrated in Figure 2.

Important chemical characteristics of this processed rice sprinkling powder include a water activity (A_w) of 0.5382 ± 0.002 and a percent moisture content of 6.25 ± 0.042 .



Figure 2.

(a) Fermented okara and (b) Rice sprinkling powder product.

Alkaline protease enzyme activity

The study of alkaline protease activity in fermented okara, as shown in Figure 3, compared the enzyme activity of the control set that was not fermented with microorganisms (UFO) and the sample fermented with microorganisms (FMO). The results indicated that the enzyme activity increased continuously from 4.28 U/g at the start to 26.92 U/g at 72 h. In comparison with the UFO control set, which did not contain added microorganisms and was fermented with natural microorganisms of unknown species, the enzyme activity in FMO was significantly higher ($p < 0.05$), reflecting the efficiency of the introduced microorganisms.

Additionally, the increased protease activity positively affected the protein degradation rate, leading to a higher production of small peptides. The fermentation process uniquely promotes the degradation of soy protein into amino acids, peptides, and ammonia, enhancing the functional properties and performance of okara. This process likely also contributed to the increased antioxidant activity.²⁰

The study of Rashad screened different strains of microorganisms grown in okara medium after 48 h of growth for the production of extracellular protease using *Bacillus subtilis* NRRL B-94. The protease activity was 26.5 U/g,³⁰ which was consistent with this study which okara was fermented using *R. oligosporus* and *B. subtilis* for 72 h and had a protease activity of 26.92 U/g. Furthermore, in the study of Wang in which soybean meal was fermented using *Bacillus velezensis*, the protease activity increased to a maximum at 38 h at 286 U/mL.²⁰ When compared with the results of this study in which *R. oligosporus* and *B. subtilis* were fermented for 72 h, the protease activity was higher at 897 U/mL, indicating that this experiment can significantly increase the efficiency of alkaline protease enzyme activity.

It is well-documented that proteases can efficiently hydrolyze proteins into biopeptides, which possess excellent antioxidant, anti-inflammatory, and antimicrobial properties, as well as functional benefits. Meitauza, a traditional fermented food made from okara, is widely consumed by Chinese people due to its delicious taste and high biopeptide content, serving as a functional health food. The microorganisms used in Meitauza production produce protease enzymes, suggesting that the nutritional quality and antioxidant activity of okara can be significantly enhanced through fermentation.²¹ Solid-state fermentation (SSF) is a key method for enzyme production. Okara has been successfully utilized as an excellent substrate for SSF to improve its nutritional composition and antioxidant activity.⁹

In the fermentation process, additional carbon sources, such as sucrose and starch, are utilized for energy conversion during SSF, leading to the synthesis of amino acids and the production of proteins.²² Thus, SSF is effective in promoting microbial production of proteases. Due to the high levels of protease production, SSF fermentation by microorganisms efficiently hydrolyzes legume proteins into easily absorbable peptides and small amino acids. Consequently, the nutritional composition of the final product can be significantly improved.^{9,21}

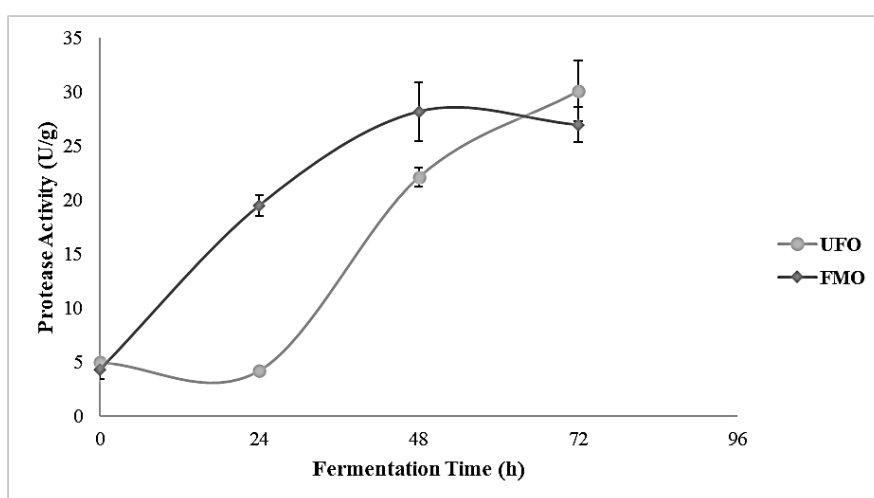


Figure 3.

Alkaline protease activity in fermented okara of UFO, control, and FMO, using microorganisms.

Degree of protein hydrolysis (%DH)



The study of the degree of protein hydrolysis in fermented okara, as shown in Table 1, compares the control (UFO) with samples fermented using FMO microorganisms. It was observed that the degree of protein hydrolysis generally increased with the fermentation period. After 72 h of fermentation, the degree of protein hydrolysis reached 44.43%, which was comparable to the control that did not include microorganisms. The higher degree of protein hydrolysis indicates that the fermentation process, facilitated by microorganisms, effectively hydrolyzes large, complex protein molecules into smaller amino acid molecules. This observation aligns with the increase in alkaline protease enzyme activity over the fermentation period, which produces smaller peptides that are easier to digest. Furthermore, the resulting amino acids contribute to a higher concentration of biological peptides or bioactive substances. These bioactive substances, formed through protease-catalyzed hydrolysis²³, also enhance antioxidant properties.²⁴ These characteristics are highly advantageous for functional foods.

Table 1. Degree of protein hydrolysis obtained for the fermented okara with FMO microorganisms and control UFO.

| Fermentation Time (h) | Degree of protein hydrolysis (%DH) | |
|-----------------------|------------------------------------|----------------------------|
| | UFO | FMO |
| 0 | ND | ND |
| 24 | ND | 12.29 ± 9.09 ^{bc} |
| 48 | 19.75 ± 14.19 ^b | 40.38 ± 8.21 ^a |
| 72 | 42.60 ± 15.15 ^a | 44.43 ± 0.10 ^a |

Results presented in means ± standard deviation (SD) (n = 3) and means with different letters for the same column are significantly different ($p < 0.05$). ND = Non detected

Antioxidant activity

The study of antioxidant property in okara fermented for 72 h is presented in Table 2. The comparison was made between the UFO control sample, the FMO fermented sample, and the rice sprinkling powder sample. The results were expressed as the concentration required for the sample to exhibit 50% antioxidant activity (IC₅₀). A lower IC₅₀ value indicates higher antioxidant activity, meaning that the sample with a lower concentration required to achieve 50% antioxidant activity demonstrates greater antioxidant potential.

The results of the antioxidant activity experiment for okara, including the UFO control, okara fermented with FMO microorganisms for 72 h, and rice sprinkling powder, are presented in Table 2. The rice sprinkling powder exhibited the highest antioxidant activity, followed by okara fermented with FMO microorganisms, with the UFO control (okara without microorganisms) showing the lowest antioxidant activity. These differences were statistically significant ($p < 0.05$). The antioxidant activity of fermented okara was positively correlated with the number of peptides present.²⁸ Additionally, the presence of phenolic compounds and amino acids such as lysine, glycine, valine, and histidine—known for their antioxidant properties—might contribute to the increased antioxidant activity^{26,27} observed in the fermented okara. The enhanced antioxidant activity may also be attributed to intracellular antioxidant peptides from the microorganisms and their hydrogen-donating ability. Thus, the

high antioxidant activity and increased levels of small peptides suggest that fermented okara has significant potential for developing healthy foods.²⁸

The samples fermented with FMO microorganisms differed from the UFO control, which was fermented with natural, unknown microorganisms. This suggests that FMO exhibits higher antioxidant activity compared to UFO because the fermentation process using starter cultures increases the number of small peptides, which are bioactive compounds that enhance antioxidant properties.²⁸ Additionally, the drying process significantly improved antioxidant properties compared to the samples fermented with FMO microorganisms. This improvement may be attributed to increased antioxidant properties due to the oxidation of polyphenols, the increase in reducing sugars, and the production of α - and β -glucosidase enzymes during fermentation. These enzymes degrade and release phenolic compounds from the cell wall into free forms known as aglycone isoflavones. Consequently, there is a significant increase in antioxidant capacity because the heat used in drying breaks down the cell wall of the okara, releasing more phenolic compounds into free forms.²⁹ For the above reasons, the rice sprinkling powder has a significantly higher antioxidant activity than the sample fermented with FMO microorganisms. ($p < 0.05$)

Table 2. IC₅₀ of fermented okara and rice sprinkling powder in DPPH radical scavenging activities.

| Sample | IC ₅₀ of DPPH radical scavenging activity (mg/mL) |
|------------------------------|--|
| Trolox | 0.02 ± 0.003 ^c |
| UFO: 72 h | Unable to detect |
| FMO: 72 h | 178.83 ± 0.003 ^a |
| RSP (Rice Sprinkling Powder) | 6.78 ± 0.006 ^b |

IC₅₀ values are given as means ± standard deviation (SD) (n = 3) and means with different letters for the same column are significantly different ($p < 0.05$).

Conclusion:

In summary, sequential fermentation of okara using *Rhizopus oligosporus* TISTR3138 and *Bacillus subtilis* TISTR001 for 72 h can significantly improve the functional properties of okara, which achieved peak alkaline protease activity and significant protein hydrolysis. Moreover, the antioxidant activity as assessed by the DPPH radical scavenging assay showed higher free radical scavenging ability after fermentation than unfermented okara. When processed into rice sprinkling powder, the free radical scavenging ability was significantly increased ($p < 0.05$), indicating superior antioxidant properties. These findings highlight the potential for the development of fermented okara by sequential fermentation with microorganisms. Which can enhance antioxidant capacity and increase the production of bioactive peptides. This is considered to be an enhancement and support for fermented okara and its processed form as valuable ingredients with the potential to be used as functional food applications.

Acknowledgements:

This research was partly supported by financial support from the Special Problems Grant, encompassing tools and the study area, School of Food Industry, King Mongkut's Institute of Technology Ladkrabang, Thailand.

References:



1. Vong W, Hua X, Liu S. *LWT*. 2018;90:316–322.
2. O'Toole D. J. *Agric. Food Chem.* 1999;47(2):363–371.
3. Jankowiak L, Trifunovic O, Boom R, Van der Goot A. *J. Food Eng.* 2014;124:166–172.
4. Zhu Y, Fan J, Cheng Y, Li L. *Food Control*. 2008;19(7):654–661.
5. Kang F, Yang W, Lu F, Li Y, Ma H, Li B. *Food Ind Sci Technol*. 2016;37(2):374–378.
6. Varzakas T. *Process Biochem.* 1998;33(7):741–747.
7. Elshagabee F, Rokana N, Gulhane R, Sharma C, Panwar H. *Front. microbiol.* 2017;8.
8. Su Y, Liu C, Fang H, Zhang D. *Microb. Cell Fact.* 2020;19:173.
9. Gupta S, Lee J, Chen W. *J. Agric. Food Chem.* 2018;66.
10. Li B, Yang W, Nie Y, Kang F, Goff H, Cui S. *Food Hydrocoll.* 2019.
11. Keong L, Toh M, Lu Y, Liu S. *Food Biosci.* 2023;55:103056.
12. Li L, Jin J, Hu H, Deveau I, Foley S, Chen H. *J. ind. microbiol. biotechnol.* 2022;49.
13. Puteri M, Hassanein T, Prabawati E, Wijaya C, Mutukumira A. *Procedia Chem.* 2015;14:263–269.
14. Verardo V, Serea C, Segal R, Caboni M. *J. Cereal Sci.* 2011;54(2):211–217.
15. Kim S, Lee D, Cheigh C, Choe E, Lee S, Hong Y, Choi H, Pyun Y. *J. ind. microbiol. biotechnol.* 2006;33(6):436–444.
16. Ma C, Liu W, Kwok K, Kwok F. *Food Res. Int.* 1997;29(8):799–805.
17. Nielsen P, Petersen D, Dambrmann C. *J. Food Sci.* 2001;66.
18. Yamasaki K, Hashimoto A, Kokusenya Y, Miyamoto T, Sato T. *Chem. Pharm. Bull.* 1994;428:1663–5.
19. Chatatikun M, Chiabchalard A. *J. Chem. Pharm. Res.* 2013;5:97–102.
20. Wang C, Qiu X, Hou R, Liu J, Li L, Mao X. *Innov. Food Sci. Emerg. Technol.* 2023;85:103311.
21. Zheng L, Yu X, Wei C, Qiu L, Yu C, Xing Q, Fan Y, Deng Z. *LWT*. 2019;108990.
22. Zhao G, Ding L, Pan Z, Kong D, Hadiatullah H, Fan Z. *Food Chem.* 2019;271:606–613.
23. Sbroggio M, Montilha M, Figueiredo V, Georgetti S, Kurozawa L. *Food Sci. Technol. (Campinas)*. 2016;36.
24. Sitanggang A, Sinaga W, Wie F, Fernando F, Krusong W. *Food Sci. Technol.* 2019;40.
25. Colla L, Reinehr C, Manfredini P, Cavanhi V, Costa J. *Sustain. food technol.* 2023;1.
26. Strazzullo G, De Giulio A, Tommonaro G, La Pastina C, Poli A, Nicolaus B, De Prisco R, Saturnino C. *Int. J. Food Prop.* 2007;10(2):321–329.
27. Wade A, Tucker H. *J. Nutr. Biochem.* 1998;9:308–315.
28. Zhu Y, Cheng Y, Wang L, Fan J, Li L. *Int. J. Food Prop.* 2008;11(3):519–529.
29. Madrau M, Piscopo A, Sanguinetti A, Del Caro A, Poiana M, Romeo F, Piga A. *Eur. Food Res. Technol.* 2009;228:441–448.
30. Rashad M, Sitohy M, Sharobeem S, Mahmoud A, Nooman M, Al-Kashef A. *AFS.* 2010;32(2):100.
31. Siripongvutikorn S, Banphot P, Rampoei N, Thantrirat J. *Ital. J. Food Sci.* 2023;35(4):88–101.
32. Rajchasom S, Seelum N, Takonkeaw S. *RMUTP sci. J.* 2020;14:2.



ENHANCEMENT OF OCTENYL SUCCINYLATION OF CASSAVA STARCH VIA DRY HEATING TREATMENT

Nialmas Samuela,¹ Wascharin Udchumpisai,¹ Yuree Wandee^{1,*}

¹School of Bioresources and Technology, King Mongkut's University of Technology Thonburi (Bang Khun Thian Campus), Bang Khun Thian, Bangkok 10150, Thailand

* e-mail: yuree.wan@kmutt.ac.th

Abstract:

Cassava starch was esterified with octenyl succinic acid (OSA) using dry heat treatment (DHT) at 150°C for different times (1, 2, and 3 h). The degree of substitution (DS), FTIR, reducing sugar, pasting properties, and emulsifying capacity were evaluated. Dry-heat treated octenyl succinylated (DHT-OS) starch had higher DS and RE than octenyl succinylated (OS) starch. As heating time increased, the DS and reducing sugar content increased. OSA-modified starches revealed two new peaks at 1719 and 1573 cm⁻¹, confirming the formation of ester carbonyl groups of OSA. The pasting viscosity and pasting temperature of the DHT-OS starches were lower than those of the unheated OS starch. In addition, all DHT-OS starches have a strong capacity to bind with oil, effectively stabilizing the emulsion with minimal separation of water and cream phases even after 30 days. According to their functional properties, DHT-OS starches could be used as emulsifying agents in food products.

Introduction:

Starch is a crucial ingredient in the food and non-food industry. However, native starch is often modified to produce desirable functional properties. The substitution of starch with octenyl succinic anhydride (OSA) is permitted for use in food products, with a maximum OSA level of 3% based on dry starch weight. Esterified starch with OSA is an ingredient that has both hydrophilic (glucose part of starch) and hydrophobic (octenyl part), allowing it to function effectively as an emulsifying agent, stabilizing oil-water mixtures by interacting with both phases ^[1, 2]. Typically, OSA-modified starch has a high viscosity compared to its native form, which limits the amount that can be used in food ^[3].

Dry heat treatment (DHT) is a physical modification that affects the structure of both crystalline and amorphous regions within starch granules while retaining starch granules intact. These alterations to structures result in changes in their physicochemical properties. DHT conditions include the use of low moisture levels (<10%) for a certain time (1–4 h) at the temperature of 110°C–150°C ^[4, 5]. DHT has been reported to induce the esterification of organic acid groups (e.g. citric acid), which hydrolyze molecules inside the starch chain and enhance solubility and emulsion capacity^[6, 7]. Dry heating in the presence of OSA can influence both the size of the starch chains and the degree of substitution by reaction pH, as the substitution favors alkaline pH whereas thermal degradation favors acidic pH ^[8].

Cassava is one of the most important economic in Thailand. There has been extended research on cassava starch with OSA, exploring its potential in various applications due to its improved functional properties. However, few studies have reported on cassava starch through DHT combined with OSA esterification. Thus, this study investigates the effect of dry heat treatment on the efficiency of octenyl succinylation of cassava starch and its physiochemical properties.

Methodology:

Materials

Cassava starch was purchased from local market, Bangkok, Thailand. Octenyl succinic anhydride (OSA) was purchased from Sigma Aldrich. All other chemicals used in this study were analytical grade.

Preparation of OSA-modified cassava starch

Cassava starch (100 g, dry weight basis) was suspended in 50 mL of 2% of sodium carbonate solution with stirring for 30 min at $30 \pm 2^\circ\text{C}$. OSA (3.0% of the weight of the starch) was added, and the dispersion was continuously stirred for 30 min. After that, the slurry was placed on an aluminum tray and dried in a hot air oven (MEM-1 UF30 model, Memmert, Germany) at 60°C until the moisture content was less than 10%, ground, and sifted through a 200 μm -sieve. Subsequently, the starch sample was heated at 150°C in a hot air oven for 1, 2, and 3 h. After cooling to room temperature, the pH was adjusted to 7, twice washed with 80% ethanol, and dried for 18 h at 40°C . The OSA-modified cassava starches were ground and kept in plastic bags until analysis.

Determination of degree of substitution (DS)

The DS of OSA-modified starch was measured slightly modified Jiranuntakul and Pancha-aroon^[9] with modification. The starch sample (1 g, dwb) was mixed with 25 mL of 2.5 N HCl-isopropyl alcohol for 30 min with a magnetic stirrer. Subsequently, 100 mL of 90% isopropyl alcohol was added and stirred for 10 min. The suspension was filtrated through a glass filter No. 4, and the residue was washed with distilled water until no chloride ions were detected by 0.1 N AgNO_3 solution, followed by washing with 90% isopropyl alcohol. The residue was re-suspended in 300 mL of distilled water and then boiled for 20 min. The solution was titrated with 0.1 N NaOH 0.1N using phenolphthalein as an indicator. The DS was calculated with the following equation:

$$DS = \frac{0.162 \times (A \times M)}{1 - ((0.21 \times \frac{A \times M}{W}))} \times 100$$

where A is the titration volume of the NaOH solution (mL), M is the molarity of the NaOH solution (N), and W is the dry weight (g) of the starch sample. The value 0.162 is the molecular weight of the glucosyl unit (g/mol) and 0.210 is the molar mass of the octenyl succinate group (g/mol). The reaction efficiency (RE) was calculated as follows:

$$RE = \frac{\text{Measured DS}}{\text{Theoretical DS}} \times 100$$

The theoretical DS was calculated by assuming that all of the added OSA reacted with the starch to form the ester derivative.

Analysis of reducing sugar

Reducing sugar content of native and modified starches was measured using the methods established by Somogyi^[10] and Nelson^[11].

Fourier Transform Infrared Spectroscopy (FTIR) Analysis

The functional groups of the starch samples were analyzed on solid samples using a Spectrum Two FTIR spectrometer (PerkinElmer, USA) equipped with Universal Attenuated Total Reflectance (UATR; Single Reflection Diamond) and Spectrum 10™ software. The



spectra were recorded with a resolution of 4 cm^{-1} from $550\text{--}4000\text{ cm}^{-1}$, with a background spectrum recorded before each analysis. Spectra preprocessing consisted of a baseline correction and normalized the maximum peak intensity.

Pasting properties

Pasting properties of native and OSA-modified cassava starches were performed by a Rapid Visco Analyzer (RVA, 4500 model Perten Instruments). The starch was mixed with water in the RVA canister at a concentration of 8% (w/w; dwb) and loaded into RVA. The slurry was homogenized using a paddle-type stirrer. A programmed heating and cooling cycle was set for 13 min, wherein it was first held at 50°C for 1 min, heated to 95°C at an increasing rate of $12^{\circ}\text{C}/\text{min}$, maintained at 95°C for 2.5 min, and then cooled to 50°C at the same rate and held at 50°C for 2 min.

Emulsion stability

Each starch sample (0.6 g, dwb) in 18 mL of distilled water was heated in a boiling water bath for 20 min with vigorous vortexing at 10 min intervals and then cooled to room temperature. After that, 2 mL of palm oil dyed with oil red O was added and the mixture was homogenized using an ultrasonic homogenizer (UP200S; Hielscher Ultrasonics, Teltow, Germany) at 100% amplitude and full cycle for 2 min. Emulsion stability was demonstrated by phase separation of oil and water phase observed before and after storage for 1 month.

$$\text{Emulsification capacity}(\%) = \frac{\text{volume of cream layer}}{\text{total volume of emulsion}} \times 100$$

Statistical analysis

The experimental data were analyzed using SPSS software version 21 (SPSS Institute Inc., Chicago, IL, USA). Analysis of variance (ANOVA) was performed with Duncan's new multiple-range tests at a significance level of 0.05. All analyses were performed in at least triplicate.

Results and Discussion:

Degree of substitute and reaction efficiency

The degree of substitution (DS) and reaction efficiency (RE) of modified cassava starches are presented in **Table 1**. The DS and RE of the octenyl succinylated (OS) starch were 0.0107, and 45.50, respectively. In this study, the pH used for modification was quite high at, pH 10 resulting in OS starch with lower DS and RE than those of previous studies Jiranuntakul and Pucha-arnon^[9], where cassava starch was modified with 3% OSA at pH 8, achieving DE and RE of 0.0154 and 66.49, respectively. Liu and Li^[12] demonstrated that the optimum pH for octenyl succinylation was reported to be 8.0–8.4. However, the dry-heating treatment could enhance the substitution reaction. After OS starch was subjected to dry heating at 150°C for 1–3 h, the DS and RE were significantly increased as the heating time increased, from 0.0160 to 0.0173 and 67.96 to 75.30%, respectively. During DHT, heat can increase the mobilities of starch molecules and OSA and activate their functional groups, promoting the formation of ester bonds between the starch hydroxyl group and the OSA. Similarly, Kim and Sandhu^[13] found that the DS of waxy rice starch increased when the heating temperature was increased.

Reducing sugar

As shown in **Table 1**, the reducing sugar content of native cassava starch was 1.34 mg/g. Reducing sugar content typically presents in very low amounts in cassava starch. However, the amount of reducing sugar in native cassava starch in this study may have resulted from incomplete starch or partial hydrolysis during extraction and processing. The reducing sugar was increased to 1.88 mg/g after esterification with OSA. This increase might be due to a slight loss of crystallinity^[12], damage to the inner crystal^[8, 14] or destroyed hydrogen bonding of starch molecules^[13] during esterification with OSA. The amount of reducing sugar increased as a result of the DHT. As the heating time increased, the reducing sugar content of DHT-OS starches significantly increased to 2.57–3.48 mg/g, respectively. According to Li and Zhang^[15], heat could separate glycosidic linkages and disrupt hydrogen bonds probably due to a partial thermal degradation of amylose and amylopectin molecular and crystalline structures^[16].

Table 1

Degree of substitute, reaction efficiency, and reducing sugar of modified cassava starch

| Sample | Degree of substitute | Reaction efficiency (%) | Reducing sugar (mg/g) | Emulsion capacity (%) |
|----------|-------------------------------|----------------------------|--------------------------|--------------------------|
| Native | - | - | 1.34 ± 0.07 ^e | - |
| OS | 0.0107 ± 0.0009 ^c | 45.50 ± 2.90 ^c | 1.88 ± 0.08 ^d | 12.5 ± 0.01 ^c |
| DHT1h-OS | 0.0160 ± 0.0012 ^b | 67.96 ± 3.65 ^b | 2.57 ± 0.16 ^c | 37.5 ± 0.01 ^b |
| DHT2h-OS | 0.0167 ± 0.0012 ^{ab} | 71.63 ± 3.65 ^{ab} | 3.05 ± 0.12 ^b | 75.0 ± 0.01 ^a |
| DHT3h-OS | 0.0173 ± 0.0012 ^a | 75.30 ± 3.70 ^a | 3.48 ± 0.02 ^a | 75.0 ± 0.01 ^a |

Mean ± S.D with the different letters in the column are significantly different ($p \leq 0.05$).

Functional group OSA starch

Esterification of starch with OSA involves substituting the hydroxyl groups of starch molecules for carbonyl groups of OSA. The insertion of carbonyl groups into starch molecule structure can be confirmed through FT-IR spectroscopy. The FT-IR spectra of native, OS, and DHT-OS starches are shown in **Figure 1**.

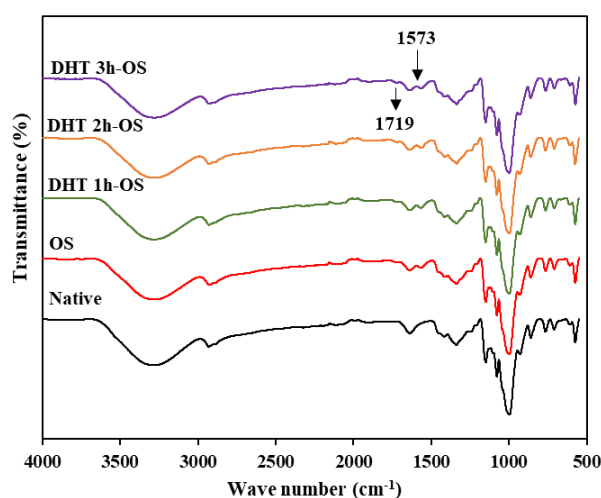


Figure 1.

FT-IR of native and OSA-modified cassava starches.



Compared to native cassava starch, the spectra of OSA-modified starch showed two new peaks at 1719 and 1573 cm^{-1} . The new peaks located at 1719 cm^{-1} corresponded to the IR stretching vibration of C=O of ester carbonyl groups, whereas the peak at 1573 cm^{-1} revealed the asymmetric stretching vibration of carboxylate (RCOO^-)^[7, 8, 17]. These results indicate the formation of ester carbonyl groups of OSA has occurred.

Pasting properties

The RVA pasting profiles of native and OSA-modified cassava starches are shown in **Figure 2.**, and the corresponding data are summarized in **Table 2.** Peak viscosity, breakdown, final viscosity, and setback of native cassava starch were 261.3, 72.7, 210.4, and 77.0 RVU, respectively, and its pasting temperature was 72.7°C. OS cassava starch had a significantly higher paste viscosity (304.6 RVU) and final viscosity (241.5 RVU) with a lower setback (46.1 RVU) as compared to native cassava starch. These data indicated that the substituting hydroxyl groups in starch molecules with carbonyl groups of OSA disturbed the ordered structure of starch granules, allowing them to swell more than native starch^[18]. However, after OS starch was heated for 1 h, the peak viscosity decreased, while the setback increased due to the degradation of the starch molecule during heating (**Table 1**). Although the starch molecule became smaller with increased heating time, this did not affect peak viscosity, which might be attributed to the high DS. However, the smaller molecule affected the rearrangement during cooling, as evidenced by the significantly decreased setback. The decrease in setback indicates a lower tendency toward the retrogradation in DHT-OS starches, which is related to their gel formation.

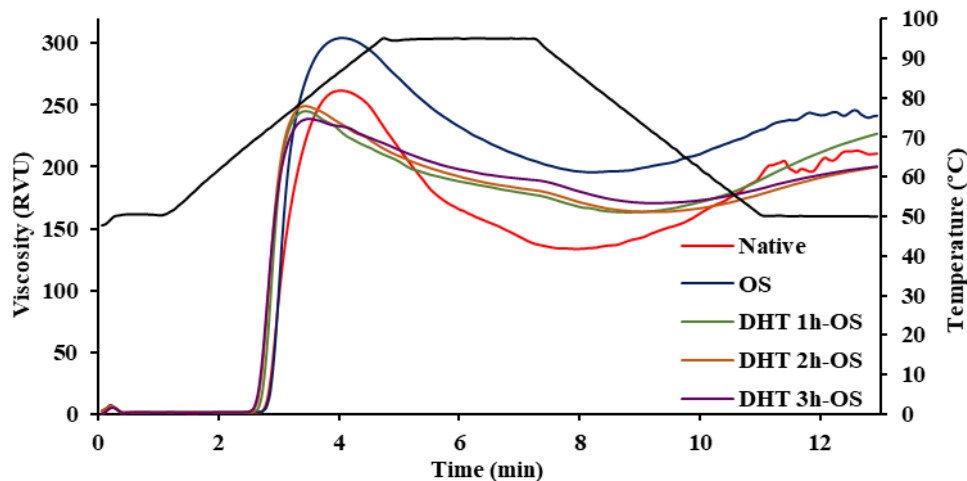


Figure2.
Pasting profiles of native and OSA-modified cassava starches.

Table 2.

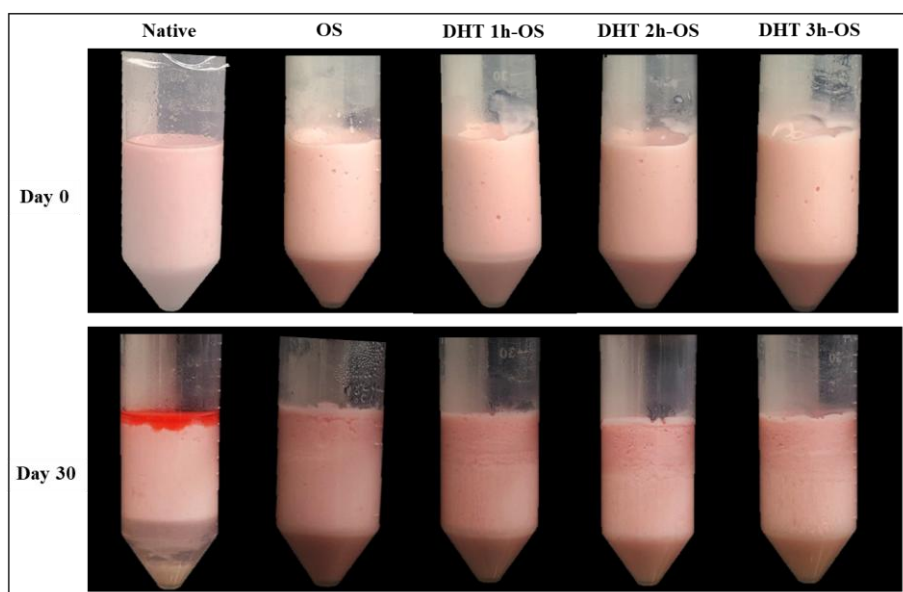
The RVA parameters of native and OSA-modified cassava starches

| Sample | Peak viscosity (RVU) | Break down (RVU) | Final Visco (RVU) | Setback (RVU) | Pasting Temp. (°C) |
|----------|---------------------------|--------------------------|---------------------------|--------------------------|-------------------------|
| Native | 261.3 ± 0.1 ^b | 72.7 ± 0.1 ^a | 210.4 ± 0.1 ^b | 77.0 ± 0.1 ^a | 72.6 ± 0.1 ^a |
| OS | 304.6 ± 9.8 ^a | 73.3 ± 0.4 ^a | 241.5 ± 11.5 ^a | 46.1 ± 12.2 ^c | 72.7 ± 0.8 ^a |
| DHT1h-OS | 245.4 ± 27.6 ^b | 71.6 ± 0.4 ^b | 227.2 ± 1.6 ^{ab} | 63.8 ± 3.8 ^b | 71.1 ± 0.1 ^b |
| DHT2h-OS | 249.1 ± 11.3 ^b | 71.1 ± 0.1 ^{bc} | 199.7 ± 11.5 ^c | 36.3 ± 0.9 ^{cd} | 70.6 ± 0.5 ^b |
| DHT3h-OS | 246.8 ± 12.1 ^b | 70.8 ± 0.5 ^c | 200.3 ± 17.6 ^c | 29.7 ± 3.3 ^d | 70.3 ± 0.1 ^b |

Mean ± S.D with the different letters in the column are significantly different ($p \leq 0.05$).

Emulsion capacity and stability

Starch modified with OSA resulted in molecules with both hydrophilic and hydrophobic properties, giving it an amphiphilic character and enhancing its interfacial properties. **Figure 3.** illustrates photographs of oil-in-water emulsions stabilized by native and OSA-modified cassava starches immediately after homogenization and after storage for 30 days.

**Figure 3.**

Emulsion stabilized with native and OS cassava starches after storage at $30 \pm 2^\circ\text{C}$ for 0 and 30 days.

Native cassava starch in its gelatinized form was characterized as emulsifying, indicating creaming after homogenization. Starch molecules in native starch are hydrophilic, so the swollen starch granules likely physically impede the coalescence of oil droplets, thus stabilizing the emulsion after homogenization. Kasprzak and Macnaughtan ^[19] reported that native cassava starch in its gelatinized form at a concentration of 4% was emulsifying but did not form stable emulsions during storage. This study found that not all parts of native starch can bind to oil, leading to complete separation of the oil phase (cleared red color) after storing at room temperature for 1 day. The layer of the oil phase increased after prolonged



storage for 30 days, with the water and creamy layers distinctly separating. Native starch is classified as a non-chemical emulsifier, which may be less effective and stable than chemically modified starch/flour or other emulsifiers.

On the other hand, all OSA-modified starches were effective in stabilizing the emulsion. After 30 days of storage, OSA-modified starches were able to bind strongly to the oil in emulsions, resulting in no oil separation. While the water and cream layers began to separate, it was not yet clearly defined. However, we attempted to measure the emulsion index (EI) as shown in **Table 1**. The EI of OS starch was 12.5%. The EI values were all significantly increased with the increase of DS values. However, there were no significant differences in EI values between the DHT2h-OS and DHT3h-OS starches, which both had an EI value of 75.0%.

Conclusion:

The dry-heat treatment (DHT) was a simple method and effectively improved the modification of cassava starch by esterification with OSA. Heating enhanced the reaction efficiency, and the higher reducing sugar content suggested the formation of small molecules as compared to unheated OS starch. The emulsification capability of OS starch was significantly increased after dry-heating. Based on the findings, we plan to continue investigating the effect of DHT-OS starch on starch gel characteristics and emulsion rheology, as well as its potential use in high-fat food products.

Acknowledgements:

This research project is supported by King Mongkut's University of Technology Thonburi (KMUTT), Thailand Science Research and Innovation (TSRI), and National Science, Research and Innovation Fund (NSRF) Fiscal Year 2025 Grant number XXXXX.

References:

1. Choi, H.-D., Hong, J.S., Pyo, S.m., Ko, E., Shin, H.-Y., and Kim, J.-Y., *Carbohydr Polym*, 2020. 239: p. 116241.
2. Xiao, J., Li, Y., and Huang, Q., *Trends Food Sci Technol*, 2016. 55: p. 48–60.
3. Xiao, X., Yussof, N.S., Mat Lazim, A., and Utra, U., *J. Food Sci.*, 2020. 4: p. 753–763.
4. Chandanasree, D., Gul, K., and Riar, C.S., *Food Hydrocoll*, 2016. 52: p. 175–182.
5. Oh, I.K., Bae, I.Y., and Lee, H.G., *Int J Biol Macromol*, 2018. 108: p. 568–575.
6. Lim, X.X., Zulkurnain, M., Yussof, N.S., and Utra, U., *E-Polym*, 2023. 23(1): p. 20228090.
7. Wu, X., Zhang, J., Yan, X., Wu, X., Zhang, Q., and Luan, M., *J. Food Meas. Charact.*, 2024. 18(3): p. 2076–2085.
8. Han, J.-A., Chung, H.-J., and Lim, S.-T., *Food Hydrocoll*, 2019. 89: p. 563–569.
9. Jiranuntakul, W., Pancha-arnon, S., and Uttapap, D., *Starch - Stärke*, 2014. 66(11-12): p. 1071–1078.
10. Somogyi, M., *J. Biol. Chem*, 1937. 117(2): p. 771–776.
11. Nelson, N., *J. Biol Chem*, 1944. 153(2): p. 375–380.
12. Liu, W., Li, Y., Goff, H.D., Nsor-Atindana, J., and Zhong, F., *Food Hydrocoll*, 2018. 84: p. 210–218.
13. Kim, H.-N., Sandhu, K.S., Lee, J.H., Lim, H.S., and Lim, S.-T., *Food Chem.*, 2010. 119(3): p. 1189–1194.

14. He, G.-Q., Song, X.-Y., Ruan, H., and Chen, F., *J. Agric. Food Chem*, 2006. 54(7): p. 2775–2779.
15. Li, Y., Zhang, H., Shoemaker, C.F., Xu, Z., Zhu, S., and Zhong, F., *Carbohydr Polym*, 2013. 92(2): p. 1647–1652.
16. Lei, N., Chai, S., Xu, M., Ji, J., Mao, H., Yan, S., . . . Sun, B., *Int J Biol Macromol*, 2020. 147: p. 109–116.
17. Wang, W., Liu, C., Zhang, H., Zhu, X., Wang, L., Zhang, N., and Yu, D., *Food Res Int.*, 2022. 161: p. 111845.
18. Zhang, J., Ran, C., Jiang, X., and Dou, J., *LWT*, 2021. 152: p. 112320.
19. Kasprzak, M.M., Macnaughtan, W., Harding, S., Wilde, P., and Wolf, B., *Food Hydrocoll*, 2018. 81: p. 409–418.



IMPACT OF WATER AND GLUCOSE DURING STEAM-HEAT MOISTURE TREATMENT ON PHYSICOCHEMICAL PROPERTIES OF CASSAVA FLOUR

Walaiwan Panyapoo¹, Wascharin Udchumpisai¹ and Yuree Wandee^{1,*}

¹School of Bioresources and Technology, King Mongkut's University of Technology Thonburi (Bang Khun Thian Campus), Bangkok 10150, Thailand

*e-mail: yuree.wan@kmutt.ac.th

Abstract:

Cassava flour was modified by steam-heat moisture treatment (S-HMT) to improve its properties. It was impregnated with distilled water or glucose (5% based on 100g flour) with various moisture contents (20%, 25%, and 30%) and heated for 30 min in a steamer. After S-HMT using a high moisture level, some starch granules exhibited a large hole, with some granules clustering due to partial gelatinization. S-HMT with both water (S-HMT_w) and glucose addition (S-HMT_G) significantly influenced the pasting properties of the flour, leading to a reduction in peak viscosity and breakdown and an increase in pasting temperature and setback. These effects were particularly pronounced with the addition of glucose. The solubility and water absorption capability of S-HMT_G were higher than those of S-HMT_w, whereas oil absorption did not differ. On the other hand, in their gelatinized form, the S-HMT_G flours have more stabilized emulsions than S-HMT_w and native flour.

Introduction:

Cassava is one of Thailand's most significant economic crops, with well-developed applications in both food and non-food industries. Cassava is a major food staple that contains no gluten, making cassava flour an ideal alternative to wheat, particularly for the formulation of gluten-free products [1]. One of the most prevalent applications of cassava flour as a replacement for wheat flour is in baked products [2-4]. However, bakery products made from cassava flour still have an unfavorable appearance and crumb texture, particularly in terms of softness and springiness due to the absence of gluten in cassava. This limitation restricts its utilization in the food industry [5, 6]. Modification of cassava flour might further enhance its functionality in gluten-free products. Hydrothermal modification has been reported to improve the physicochemical properties of gluten-free starches/flours, enhancing their potential for use in bakery products [7].

Heat-moisture treatment (HMT), one of the important physical treatments, uses simple, inexpensive, ecologically safe processes without by-products of chemical reagents. HMT of starches/flours involves treating starch granules at low moisture levels (<35% moisture w/w) at temperatures (84–120 °C) that are above the glass transition temperature (*T_g*) but below the gelatinization temperature for a certain period (15 min–16 h). A variety of dry-heat sources (e.g., convection oven and microwave) [8, 9] and wet-heat sources (e.g., autoclave, steamer) [10], have been utilized in HMT. A recent study comprehensively examined the impact of steam-heat-moisture treatment conditions on the structural and functional properties of cassava flour and starch [7, 10]. Duda, Ma [7] reported that cassava flour complexation with sodium stearoyl lactylate, achieved through S-HMT, resulted in distinct bread properties.

Sugars are commonly used in starch-based foods to optimize processing operations and enhance food quality by influencing the gelatinization and retrogradation of starch [11, 12]. Juansang, Puttanlek [13] studied the effects of sugar alcohol (e.g., erythritol, xylitol, sorbitol) as plasticizers in HMT on the physicochemical properties of canna starch. The results showed that these plasticizers could significantly enhance the HMT of canna starch, as indicated by a

considerable change in pasting profiles compared to water. Glucose is used extensively in the food industry for various applications. As a small plasticizer, it may participate in the interactions between starch granules, potentially affecting the formation of intercalated structures and altering the properties of starch. Lee, Zhang ^[14] studied the combined effect of dry heating and glucose addition on starch properties. The results showed that the addition of glucose during dry heating induced a synergistic effect on the pasting viscosity.

However, few studies have reported the effect of glucose on the physicochemical properties of cassava flour particularly when combined with HMT. Thus, this study investigates the effect of steam-heat moisture treatment with glucose compared to distilled water at various moisture contents on the physicochemical properties of cassava flour. This study will provide new insights into the application of cassava flour in gluten-free starchy products.

Methodology:

Materials

Cassava flour was commercially purchased in local supermarkets. The food-grade glucose was purchased from Krungthepchemi Company Limited, Other chemicals used in this study were analytical grade.

Preparation of steam-heat moisture treatment (S-HMT) cassava flour

The moisture content of cassava flour was adjusted to 20%, 25%, and 30% by adding the appropriate amounts of distilled water, or distilled water containing glucose 5% (based on dry starch) into the containers and mixing well. Samples were transferred to open aluminum containers, heated for 30 min in a steamer, and then dried in a hot air oven at 40 °C for 18 h. The modified flours were ground and passed through a 200 µm sieve.

Morphology

The morphology of native and modified cassava flours was examined using a scanning electron microscope (SEM, Phenom ProX, Thermo Fisher Scientific Inc., USA). Samples were prepared by sprinkling the flour onto double-sided adhesive tape attached to a circular specimen stub and then coated with gold. The samples were observed at an accelerating voltage of 5 kV with magnifications of 1,000x

Determination of degree of gelatinization (DG)

DG of native and modified flours was analyzed according to the method described by Birch and Priestley ^[15], with some modifications. Briefly, a 20 mg (dwb) sample was dispersed in 10 mL of 0.15M KOH solution, gently agitated for 5 min, and then centrifuged (Z326K, Hermle, Germany) at 2,880×g for 10 min. One mL of the supernatant was mixed with 9 mL of 0.017 M HCl and 0.1 ml of 2.5% iodine reagent was then added. After mixing, the absorbance was measured at 620 nm using a spectrophotometer. The DG was calculated using a standard curve that plotted the DG against absorbance.

The DG standard was prepared by heating the CF suspension (50% w/w) in an autoclave at 121 °C for 1 h and drying it at 50 °C for 18 h in a hot air oven. The dried flour was ground and passed through a 200 µm sieve to obtain the fully gelatinized CF. The DG was assessed by mixing the fully gelatinized CF with raw CF in various ratios (0, 20, 40, 60, 80, and 100%).

Determination of glucose content

Sample (0.5 g, dwb) were mixed with 10 mL of 80% ethanol in a 15-mL centrifuge tube and mixed using a vortex mixer. The mixture was sonicated (Elma E180H, Germany) at 80 °C for 30 min, followed by centrifuging at 3136×g for 10 min. The liberated glucose in the supernatant was determined using a glucose oxidase/peroxidase assay kit.



Pasting properties

The pasting properties of samples were determined using a Rapid Visco Analyzer (RVA; 4500; Perten Instruments). The starch was mixed with water in the RVA canister at a concentration of 8% w/w (dry weight basis; dwb) and loaded into RVA. The slurry was homogenized using a paddle-type stirrer. A programmed heating and cooling cycle was set for 13 min, wherein it was first held at 50 °C for 1 min, then heated to 95 °C with an increasing rate of 12 °C/min, maintained at 95 °C for 2.5 min, and then cooled to 50 °C at the same rate and held at 50 °C for 2 min.

Solubility and water/oil absorption capabilities

The solubility and water/oil absorption capabilities were determined using a modified method from Rodboontheng, Uttapap^[16] and Mathobo, Onipe^[17]. The sample (1 g, dwb) was mixed with 9 mL of distilled water or olive oil in a 15-mL centrifuge tube and kept at 30 °C for 30 min. The mixture was centrifuged at 25 °C and 3136×g for 10 min. The supernatant was carefully drawn off until no excess liquid remained on the surface of the sediment. The sediment was weighed to determine water/oil absorption capability. The solubility in water was measured by drying the supernatant to constant weight in a hot air oven at 105 °C and then weighed. The solubility and water/oil absorption capabilities were calculated as follows:

$$\text{Solubility (\%)} = \frac{\text{Weight of the wet mass sediment}}{\text{Weight of sample (g dry basis)}} \times 100$$

$$\text{WAC (g/g)} = \frac{\text{Volume of absorbed water}}{\text{weight of sample (g dry basis)}}$$

$$\text{OAC (g/g)} = \frac{\text{Volume of absorbed oil}}{\text{weight of sample (g dry basis)}}$$

Emulsification stability

Each flour sample (0.6 g, dwb) in 18 mL of distilled water was heated in a boiling water bath for 20 min with vigorous vortexing at 10 min intervals and then cooled to room temperature. After that, 2 mL of olive oil dyed with oil red O was added and the mixture was homogenized using an ultrasonic homogenizer (UP200S; Hielscher Ultrasonics, Teltow, Germany) at 100% amplitude and full cycle for 2 min. Emulsion stability was demonstrated by phase separation of oil and water phase observed before and after storage for 15 days.

Statistical analysis

All analyses were carried out in duplicate. The experimental data were analyzed using analysis of variance (ANOVA) and expressed as mean values ± standard deviations. A Duncan test was conducted to examine significant differences among experimental mean values ($P \leq 0.05$).

Results and Discussion:

Effect of moisture content and glucose addition on the degree of gelatinization

The free glucose in native cassava flour was 0.1%, and the glucose content did not change after HMT using water as a plasticizer (HMT_W) (**Table 1**). The moisture content did not affect the amount of glucose, while partial gelatinization of HMT_W occurred at a high moisture level (30%) with a degree of gelatinization (DG) value of 7.7%.

A notable amount of free glucose (3.5–3.8%) was obtained after adding 5% glucose before HMT (HMT_G), indicating that some of the glucose may have penetrated the granules and interacted with starch molecules. The moisture content did not affect the amount of glucose that interacts with the starch molecules. The DG values of HMT_G were significantly higher than those of HMT_W at the same moisture level. Moreover, the DG value of HMT_G significantly increased as the moisture level increased. This might be because glucose can attract water molecules, and when this solute is absorbed on the surface, it causes the starch surface to swell and gelatinize.

Table 1.

Glucose content, degree of gelatinization, solubility, and water/oil absorption capabilities of native and HMT cassava flours

| Sample | Glucose content (%) | DG (%) | Solubility (%) | WAC (g/g) | OAC (g/g) | Emulsification stability (%) |
|---------------------|------------------------|-------------------------|------------------------|-------------------------|------------------------|------------------------------|
| CF | 0.1 ± 0.1 ^c | 0.4 ± 0.1 ^c | 0.4 ± 0.1 ^b | 2.8 ± 0.3 ^d | 2.4 ± 0.2 ^a | 65.0 ± 2.5 ^b |
| 20-HMT _W | 0.1 ± 0.1 ^c | 0.5 ± 0.2 ^c | 0.6 ± 0.2 ^b | 2.8 ± 0.2 ^d | 2.4 ± 0.2 ^a | 66.7 ± 1.4 ^b |
| 25-HMT _W | 0.1 ± 0.1 ^c | 0.5 ± 0.1 ^c | 0.7 ± 0.2 ^b | 3.4 ± 0.2 ^{bc} | 2.4 ± 0.1 ^a | 66.7 ± 2.9 ^b |
| 30-HMT _W | 0.1 ± 0.1 ^c | 7.7 ± 0.3 ^b | 0.9 ± 0.2 ^b | 4.2 ± 0.4 ^a | 2.4 ± 0.2 ^a | 85.0 ± 4.3 ^a |
| 20-HMT _G | 3.5 ± 0.1 ^b | 0.7 ± 0.5 ^c | 4.2 ± 0.4 ^a | 3.0 ± 0.3 ^{cd} | 2.3 ± 0.2 ^a | 85.0 ± 2.5 ^a |
| 25-HMT _G | 3.5 ± 0.1 ^b | 5.4 ± 0.8 ^b | 4.0 ± 0.2 ^a | 3.7 ± 0.6 ^b | 2.5 ± 0.2 ^a | 87.5 ± 0.1 ^a |
| 30-HMT _G | 3.8 ± 0.1 ^a | 16.9 ± 0.6 ^a | 4.0 ± 0.3 ^a | 4.5 ± 0.7 ^a | 2.4 ± 0.2 ^a | 87.5 ± 0.1 ^a |

All values are means of triplicates ± standard deviation. Different letters in the same column indicate a statistically significant difference ($p \leq 0.05$).

Granule morphology

The morphologies of native and HMT cassava flours under SEM are illustrated in **Figure 1**. Most starch granules in cassava flour have round or truncated shapes with some collapsed granules observed as well. Granule morphologies of all flours after S-HMT with water at different moisture levels (20-HMT_W, 25-HMT_W, and 30-HMT_W) were still similar to those of the native flour in which some granules were melted and granule fragments with a rough surface could be observed at high moisture content. Additionally, the large holes in the middle of the granule were noticed with increased moisture content. The modification of HMT using glucose as a plasticizer with 20% moisture content (20-HMT_G) did not change the morphology of the starch granules. However, at higher moisture levels (25-HMT_G and 30-HMT_G), agglomerations and pores/holes were observed in the granules. This result is caused by the high gelatinization of surface granules (**Table 1**). The formation of fissures, holes, and cavities on the starch granules could result from partial starch gelatinization caused by high moisture content and the glucose presence in S-HMT. Several studies have reported that after



HMT, more holes, cavities, and channels were observed on the surface of starch granules [18-20].

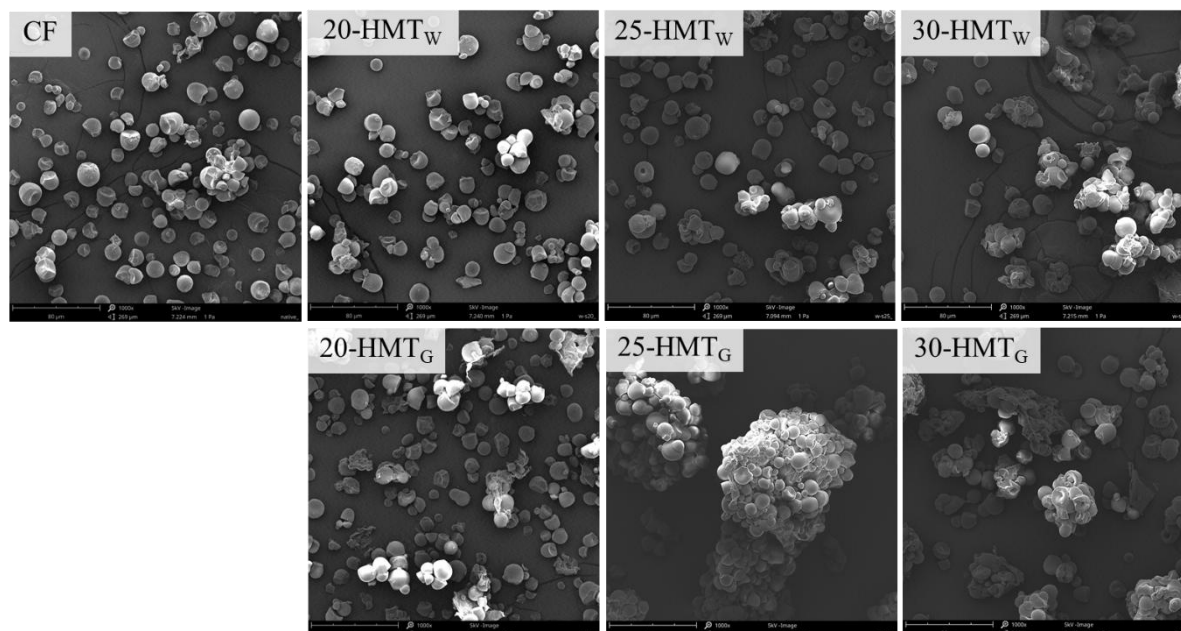


Figure 1.

Granule morphology native and HMT cassava flours (1,000x, bar as 80 μ m).

Pasting Properties

The pasting profiles of native and HMT cassava flours are shown in **Figure 2**, and their corresponding pasting parameters are summarized in **Table 2**. The S-HMT significantly altered the pasting properties of cassava flour. HMT plasticized with water and glucose had similar pasting profiles. All S-HMT flours had higher pasting temperatures (79.0–84.0 $^{\circ}$ C) compared to the native cassava flour (72.4 $^{\circ}$ C), and this trend continued as the moisture content increased. The peak viscosity and breakdown were gradually decreased, whereas the final viscosity and setback increased for all S-HMT flours. The results indicated that there had been improvement in the thermostability, shear stability, and retrogradation.

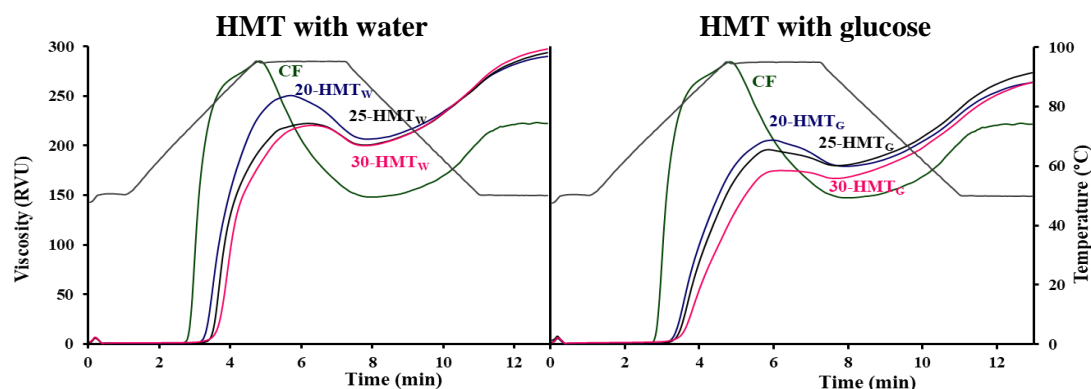


Figure 2.

Pasting profiles of native and HMT cassava flours.

The S-HMT plasticized with glucose appears to have a greater effect on the pasting properties than those with water. At the same moisture level, S-HMT_G flours had higher pasting temperatures, lower peak viscosity, breakdown, and final viscosity, and a comparable setback value compared to S-HMT_W flours. The results, as shown in **Table 1**, indicate that some glucose may be able to penetrate the starch granules and perhaps form hydrogen bonds with starch molecules. This interaction stabilizes starch structures and makes them more resistant to gelatinization. Shittu and Raji, 1982^[21] reported that sugar penetrated the starch granules and formed crosslinks between the starch chains in the amorphous region. This restricted chain mobility and granules swelling, resulting in increased gelatinization temperature.

Table 2.
RVA parameter of native and HMT cassava flours.

| Sample | Pasting Temp. (°C) | Peak Viscosity (RVU) | Final Viscosity (RVU) | Breakdown (RVU) | Setback (RVU) |
|---------------------|-------------------------|--------------------------|---------------------------|--------------------------|-------------------------|
| CF | 72.4 ± 0.6 ^f | 286.8 ± 3.7 ^a | 222.5 ± 2.4 ^c | 138.8 ± 6.4 ^a | 74.5 ± 0.3 ^c |
| 20-HMT _W | 79.0 ± 0.4 ^e | 251.1 ± 2.5 ^b | 289.7 ± 2.6 ^a | 44.8 ± 4.4 ^b | 83.4 ± 1.2 ^b |
| 25-HMT _W | 81.2 ± 0.4 ^c | 222.7 ± 5.7 ^c | 293.7 ± 4.3 ^a | 22.2 ± 4.2 ^{cd} | 93.3 ± 1.5 ^a |
| 30-HMT _W | 83.2 ± 0.1 ^b | 220.9 ± 3.2 ^c | 297.9 ± 5.6 ^a | 20.7 ± 1.0 ^d | 97.6 ± 2.8 ^a |
| 20-HMT _G | 80.4 ± 0.5 ^d | 206.8 ± 2.2 ^d | 264.6 ± 9.2 ^b | 27.0 ± 3.6 ^c | 84.7 ± 4.1 ^b |
| 25-HMT _G | 81.5 ± 0.1 ^c | 196.7 ± 2.6 ^e | 274.2 ± 1.6 ^b | 16.4 ± 4.0 ^d | 93.8 ± 1.7 ^a |
| 30-HMT _G | 84.0 ± 0.9 ^a | 176.0 ± 4.8 ^f | 264.5 ± 10.6 ^b | 8.4 ± 2.3 ^e | 96.9 ± 5.3 ^a |

All values are means of triplicates ± standard deviation. Different letters in the same column indicate a statistically significant difference ($p \leq 0.05$).

Solubility

As shown in Table 1, the solubility of all HMT_W flours (0.6–0.9%) in water at 30 °C was comparable to that of the native flour (0.4%). On the other hand, all HMT_G flours exhibited the highest solubility in water (4.0–4.2%). Even though a higher moisture content can range the DG of HMT_G, it has no influence on the solubility at ambient temperature.

Water and oil binding capacities

The capability of native and HMT flour to hold water or oil (both adsorption and absorption) is presented in **Table 1**. The water binding capacity of HMT_W and HMT_G flours (2.8 and 3.3 g/g, respectively) at the moisture level of 20% did not differ significantly from that of the native flour (2.8 g/g). however, increasing the moisture level to 25% and 30% resulted in significantly higher water binding capacity in both S-HMT plasticized with water and glucose. The water binding capacity was related to the degree of gelatinization of S-HMT flours. However, the modification of cassava flour by S-HMT did not increase the hydrophobicity, as the oil-holding capacity was not significantly different from that of the native flour.

Emulsification capacity and stability

Figure 3 shows the photographs of oil-in-water emulsion capacities of native and S-HMT cassava flours immediately after homogenization and after storage for 15 days. Both native and S-HMT flours in their gelatinized form were characterized as emulsifying, indicating creaming after homogenization. Cassava flour contains starch, protein, and fiber, which contribute to its emulsifying capabilities. It is classified as a non-chemical emulsifier, which may be less effective and stable than chemically modified starch/flour or other emulsifiers. Kasprzak et al,



2018 ^[22] reported that gelatinized native cassava starch at a concentration of 4% was emulsifying but did not form stable emulsions during storage.

Starch molecules in both native and S-HMT flours are hydrophilic, so the swollen starch granules likely physically impede the coalescence of oil droplets, thus stabilizing the emulsion ^[23]. After 15 days of storage, native flour could not bind strongly to oil, resulting in the complete separation of the oil phase (transparent red color), with the water and creamy layers separated. The emulsion stability of native flour was 65.0% (**Table 1**). The emulsion of all S-HMT flours plasticized with water and glucose shows a pale red color on the top layer compared to native flour. Among S-HMT plasticized with water, 30-HMT_w has significantly greater emulsion stability (85.0%) than native flour. The emulsion stability of all S-HMT plasticized with glucose exhibited significantly better emulsion stability (85.0–87.5%) than that of native flour.

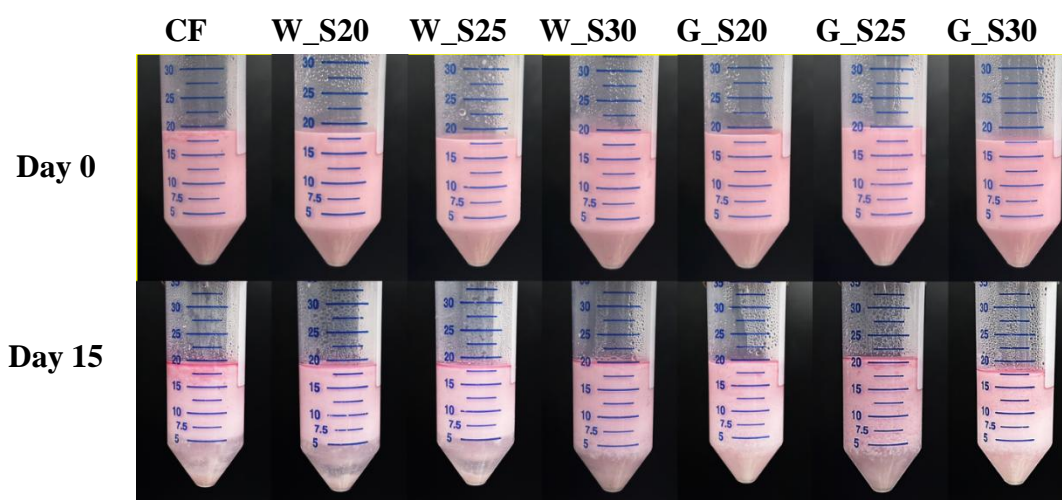


Figure 3.

Emulsification capacity of native and HMT cassava flours stored for 15 days.

Conclusion:

Cassava flour modified by S-HMT has a comprehensive alteration in its physicochemical properties, which are influenced by moisture content and plasticizer type. The S-HMT with the highest moisture content (30%) was extensively gelatinized, causing starch granules to stick together and present a hole on their surface. The use of glucose as a plasticizer in the HMT process induced a more significant change in pasting characteristics including higher pasting temperature, lower peak viscosity and breakdown, as well as higher solubility, and emulsion stability that of water. Based on the findings, S-HMT cassava flour plasticized with glucose has potential applications in various food applications, including gluten-free flour products.

Acknowledgements:

This research project is supported by King Mongkut's University of Technology Thonburi (KMUTT), Thailand Science Research and Innovation (TSRI), and National Science, Research and Innovation Fund (NSRF) Fiscal year 2025 Grant number XXXXXX.

References:

1. Zhu, F., *Composition, structure, physicochemical properties, and modifications of cassava starch*. Carbohydrate Polymers, 2015. **122**: p. 456-480.
2. Lu, H., et al., *Study on quality characteristics of cassava flour and cassava flour short biscuits*. 2020. **8**(1): p. 521-533.
3. Pérez Sira, E., et al., *Cassava flour as an alternative to produce gluten-free baked goods and pastas*. 2017. p. 87-104.
4. Sangpueak, R., et al., *Flour on Gluten-Free Muffins from Different Edible Cassava Varieties in Thailand*. 2022. **11**(24): p. 4053.
5. Jensen, S., et al., *Addition of cassava flours in bread-making: Sensory and textural evaluation*. LWT - Food Science and Technology, 2015. **60**(1): p. 292-299.
6. Morgan, N.K. and M. Choct, *Cassava: Nutrient composition and nutritive value in poultry diets*. Animal Nutrition, 2016. **2**(4): p. 253-261.
7. Dudu, O.E., et al., *Bread-making potential of heat-moisture treated cassava flour-additive complexes*. LWT, 2020. **130**: p. 109477.
8. Deka, D. and N. Sit, *Dual modification of taro starch by microwave and other heat moisture treatments*. Int J Biol Macromol, 2016. **92**: p. 416-422.
9. Watcharatewinkul, Y., et al., *Pasting properties of a heat-moisture treated canna starch in relation to its structural characteristics*. Carbohydrate Polymers, 2009. **75**(3): p. 505-511.
10. Dudu, O.E., et al., *Impact of steam-heat-moisture treatment on structural and functional properties of cassava flour and starch*. International Journal of Biological Macromolecules, 2019. **126**: p. 1056-1064.
11. Gonera, A. and P. Cornillon, *Gelatinization of Starch/Gum/Sugar Systems Studied by using DSC, NMR, and CSLM*. Starch - Stärke, 2002. **54**(11): p. 508-516.
12. Rumpold formerly: Bauer, B.A. and D. Knorr, *Effect of Salts and Sugars on Pressure-induced Gelatinisation of Wheat, Tapioca, and Potato Starches*. Starch - Stärke, 2005. **57**(8): p. 370-377.
13. Juansang, J., et al., *Pasting properties of heat-moisture treated canna starches using different plasticizers during treatment*. Carbohydrate Polymers, 2015. **122**: p. 152-159.
14. Lee, S.-J., et al., *Effect of combination of dry heating and glucose addition on pasting and gelling behavior of starches*. International Journal of Biological Macromolecules, 2021. **183**: p. 1302-1308.
15. Birch, G.G. and R.J. Priestley, *Degree of Gelatinisation of Cooked Rice*. Starch - Stärke, 1973. **25**(3): p. 98-100.
16. Rodboontheng, W., et al., *Simple thermal and freezing treatments to improve absorption capacity and alter digestibility of canna starch granules*. International Journal of Biological Macromolecules, 2022. **194**: p. 861-869.
17. Mathobo, V.M., et al., *Optimisation of the techno-functional and thermal properties of heat moisture treated Bambara groundnut starch using response surface methodology*. Scientific Reports, 2023. **13**(1): p. 2261.
18. Kawabata, A., et al., *Microscopic Observation and X-Ray Diffractometry of Heat/Moisture-Treated Starch Granules*. Starch - Stärke, 1994. **46**(12): p. 463-469.
19. Xiao, Y., et al., *Differences in physicochemical properties and in vitro digestibility between tartary buckwheat flour and starch modified by heat-moisture treatment*. LWT, 2017. **86**: p. 285-292.
20. Suriya, M., C.K. Reddy, and S. Haripriya, *Functional and thermal behaviors of heat-moisture treated elephant foot yam starch*. International Journal of Biological Macromolecules, 2019. **137**: p. 783-789.



21. Shittu, T.A., A.O. Raji, and L.O. Sanni, *Bread from composite cassava-wheat flour: I. Effect of baking time and temperature on some physical properties of bread loaf*. Food Research International, 2007. **40**(2): p. 280-290.
22. Kasprzak, M.M., et al., *Stabilisation of oil-in-water emulsions with non-chemical modified gelatinised starch*. Food Hydrocolloids, 2018. **81**: p. 409-418.
23. Xiao Xian, L., et al., *Modified tuber starches as potential stabilizer for food-grade Pickering emulsions*. Food Research, 2020. **4**: p. 753-763.



SCREENING OF COMPARISON ON FLOWER HONEY PRODUCTS BY USING SDS-PAGE ANALYSIS COMBINED WITH LC-MS

Ekawit Threenet,¹ Phitsamai Taprakhon,² Achara Kleawkla,^{3,*} Winai Wiriyaalongkorn,⁴ Siriwat Boochaisri,⁵ Watcharin Jantawan,⁶

^{1, 2, 3} Division of Chemistry, Faculty of Science, Maejo University, Chiang Mai, 50290, Thailand

⁴ Faculty of Agricultural Production, Maejo University, Chiang Mai, 50290, Thailand

⁵ Division of Biology, School of Sciences, University of Phayao, Phayao 56000, Thailand

⁶ The Office of Agricultural Research and Extension, Maejo University, Chiang Mai, 50290, Thailand

*e-mail: achara_kleawkla@yahoo.co.uk

Abstract:

The objective of this research is to use the pattern of protein in flower honey to study the initial characteristics that are the identity in terms of quantity and expression of proteins in honey from flowers and different sources, resulting in an increase in the value of the product. Characteristic analysis of honey was investigated from 7 products in San Sai market of Chiang Mai province, including Sun Forest brand honey, Doi Kham honey, Suan Chitralada honey and Busara Kham Honey obtained from longan flowers, Good Bee honey obtained from sunflowers, Doi Tung honey obtained from macadamia flowers and unspecified wild honey obtained from mixed forests. The result appeared that the Sunforest brand honey was in the extra white range but others were in the white range on comparing with the USDA color standard designation. The pH analysis 3.5-5.3, conductivity 183.53-742.97 $\mu\text{S}/\text{cm}$, moisture 5.10-7.43%, reducing sugar content 2.63-4.27 mg/ml and sweetness 73.5-80.0 %Brix of honey from all products were found to be in the standard regulation. When analyzing the expression of proteins from all 7 types of honey samples with appropriate condition of sodium dodecyl sulfate polyacrylamide gel electrophoresis (SDS-PAGE) to analyze the type of protein with liquid chromatography - mass spectrometry (LC-MS) techniques, it showed that all 18 protein bands sent for analysis could be identified 14 protein bands and found two important proteins. The first protein was a FAD-binding PCMH-type domain-containing protein (60.0 kDa), detected in protein bands across both longan flower honey and other flower honeys. This suggests the protein could serve as a general marker for flower-derived honeys. However, specific protein bands of this protein at 106.7 and 20.4 kDa were found only in Doi Kham longan honey, indicating they may act as a geographical indicator for this regional honey. The second protein was pectin esterase (62.1 kDa), detected in protein bands at 57.5 and 33.9 kDa exclusively in longan flower honey samples. This implies the presence of pectin esterase at these molecular weights could be a reliable marker for identifying honey from longan flowers. These findings demonstrated the potential of protein profiling for honey authentication and traceability. The identified markers may be of help to distinguish longan honey and determine its geographical origin, contributing to more robust honey quality control in the future.

Introduction:

Current research on honey involves studying the amount of protein in honey obtained from various types of flowers. In honey, protein comes from flower pollen and each type of pollen has a different amount of protein, so it is possible to identify the type of protein in honey that

comes from which flower. Di Girolamo *et al.*¹ studied and analyzed the protein concentration in honey from 5 types of flowers, namely, chestnut, acacia, sunflower, eucalyptus and orange flowers, using sodium dodecyl sulfate polyacrylamide gel electrophoresis (SDS-PAGE) technique to study the protein bands and identify the proteins by mass spectrometry with a linear ion trap mass spectrometer type LTQ-XL, which can identify almost all protein components in honey, called royal jelly proteins 1–5, which are proteins obtained from the bees themselves, not from the flowers of plants. However, Azevedo *et al.*² showed proteome comparison for discrimination between honeydew and floral honeys from botanical species *Mimosa scabrella* Benthham by principal component analysis. It found that the proteome profile showed 160 protein spots in honeydew honey and 84 spots in the floral honey. Borutinskaitė *et al.*³ also found that identified proteins (Bna, polygalacturonase, non-specific lipid-transfer protein, GAPDH and others) were present in pollen and blossom honey from rape seed *Brassica napus* L. for the nutritional value of plant pollen -enriched honey. Zhang *et al.*⁴ demonstrated novel proteins on one type of *Ziziphus jujuba*-derived protein and two type of *Apis mellifera*-derived proteins as marker for floral origin of jujube (*Ziziphus jujuba* Mill.) honey. Lewkowski *et al.*⁵ assessed the impact of different food sources (sugar solutions with different additives) on honey proteome composition. Muresan *et al.*⁶ studied the honey origin by melissopalynology and protein pattern analysis of SDS-PAGE to determine the origin and type of flowers on Apiaceae, Boraginaceae, Brassicaceae, Compositae and Fabaceae (*Trifolium* sp.) used by bees for honey production. The SDS-PAGE showed that honeys of different flower origins shared protein bands between 45 and 85 kDa. From past research, characteristic study of protein expression has been used to study honey in many countries. However, for Thailand, there is no research in this field. Therefore, for this research, it is necessary to use the pattern of protein in flower honey to study the initial characteristics that are the identity in terms of quantity and expression of proteins in honey from flowers and different sources, resulting in an increase in the value of the product.

Methodology:

1. Sample collection

The research collected 7 types of honey products sold in Thailand, with product samples received on September 23, 2022, consisting of 4 types of longan flower honey: Sunforest honey (S1), Doi Kham honey(S2), Suan Chitlada honey(S3), and Busarakham Honey (S4), while Goodbee honey was obtained from sunflowers (S5), Doi Tung honey was obtained from macadamia flowers (S6), and unspecified honey was wild honey from mixed deciduous forests in Buriram Province (S7). All samples were stored in amber bottles at a low temperature around 4°C prior to analyzes.

2. Physicochemical analyzes^{7, 8, 9, 10}

2.1. Color value (CV)

The color value of honey was determined on united states department of agriculture (USDA color standard designation) using a UV-visible spectrophotometer (UV-VIS spectrophotometer) Genesys 20 model at a wavelength of 635 nm.

2.2 pH value (potential of hydrogen ion)

The pH value of honey products was determined in 10% w/v solution of honey products was prepared in DI water (deionized water) and then tested for acidity or alkalinity using a pH meter.

2.3 Electrical conductivity (EC)

The electrical conductivity of honey products was analyzed in 20% w/v solution (DI water) of honey products. The electrical conductivity of the honey products was tested using a conductivity meter model 712 conductometer.

2.4 Moisture content (MC)



Moisture content analysis of honey products was determined on a moisture content analysis to determine the weight remaining after evaporation of water and volatile matter from the product under a specified temperature.

2.5 Reducing sugar content (RSC)

Analysis of reducing sugar content according was investigated on 1 ml of honey product in a test tube and adding 1.0 ml of 3, 5-dinitrosalicylic acid (DNS) solution, shaking to mix, heating for 10 min and cooling rapidly by immersing in ice for 3-5 min. After that, add 10 ml of DI water (deionized water) and mix well. After that, the absorbance was measured using a UV-VIS spectrophotometer, model Genesys 20, at a wavelength of 540 nm.

2.6 Sweetness (%Brix)

Sweetness analysis was studied by using refractometer.

3. Protein extraction

The protein extraction method was according to the method of Ramon *et al.*¹¹ these honey samples were weighed 25.00 g of honey product, added 2.50 ml of 1.5 M acetate buffer solution and 1.50 ml of 0.5 M sodium chloride to dissolve the honey sample. They were adjusted the volume with distilled water in a 50.00 ml volumetric flask, pipeted 6.00 ml of the solution, added 0.15% deoxycholate 0.10 ml to precipitate the protein and incubated at room temperature for 10 min. After that, precipitants were added 0.10 ml of 72% trichloroacetic acid and centrifuged the solution at 6,000 rpm for 15 min. The precipitants were collected and dissolved with DI water (deionized water) and store at -20°C.

4. One-dimensional gel electrophoresis

Each of the extraction procedures was used for quantitative analysis by modified Lowry's method¹² and was used for qualitative analysis by SDS-PAGE. Each of the protein extractions was mixed with a sample buffer containing 0.0625 M Tris HCl, pH 6.8, 10% SDS, 10% glycerol, 0.1% 2-mercaptoethanol and 0.01% bromophenol blue. Concisely, the final concentration of each protein extract was adjusted to 100 µg per sample, boiled for 5 min and stored at -70°C until electrophoresis was performed. In SDS-polyacrylamide denaturing gels, stacking gels (4 %) and separating gel (12.5 %) were applied for separating different range of protein extraction. Electrode buffer solution contained 0.025 M Tris, 0.192 M glycine, 0.1% SDS at pH 8.3. The 100 µg sample/well was applied to gels in each different experiment. Broad range (Bio-Rad CL161-0318, USA) of molecular weight marker was carried out on a vertical slab gel electrophoresis apparatus (AE-6530 mPAGE, Atto Corporation, Tokyo, Japan). Constant current (20 mA/gel) was applied to the electrophoresis gel. After electrophoresis, gels were stained with 0.25% Coomassie brilliant blue R250 in 90 ml of methanol: acetic acid: water (5.7: 1: 7.5). In Coomassie brilliant blue R-250 staining, gels were fixed in a solution of 50% methanol and 10% acetic acid for 1 h, stained for 15 min in a conventional Coomassie brilliant blue R-250 solution, and developed in de-staining solution (25% methanol and 7% acetic acid) for overnight prior to scanning.

5. Gel Analysis¹³

Gels were scanned on the image scanner (Gel Doc XR System, Bio-Rad, USA), gel documentation system consisting of a high sensitivity multichrome camera according to the manufacturer's specifications. Differential protein bands between physiological disorder syndromes and normal longan fruit were excised for next step on mass spectrometry identification.

6. Mass Spectrometry and Protein Identification¹³

Selected protein bands based on increase or decrease of protein expression of different samples were manually excised from only preparative gels in Coomassie brilliant blue R-250 staining using sterile lancet. These gel bands were examined by using protein analysis and peptide mass profiling using liquid chromatography tandem mass spectrometry (LC-MS/MS) at the faculty of medical technology, of Mahidol university, Thailand. Mass spectrometry data were automatically registered, analyzed, and searched by using National Center for Biotechnology Information public protein databases (NCBI databases). MASCOT search engine (Matrix Science Ltd., London, UK) was used for peptide mapping. Data identifications were registered when search results of protein score greater than 52 were significant ($p < 0.05$).

Results and Discussion:

The result of physicochemical property (Table 1) demonstrated that the Sunforest brand honey (S2) was in the extra white range but others were in the white range on comparing with the USDA color standard designation. The pH analysis 3.5-5.3, conductivity 183.53-742.97 $\mu\text{S}/\text{cm}$, moisture 5.10-7.43%, reducing sugar content 2.63-4.27 mg/ml and sweetness 73.5-80.0 %Brix of honey from all products were found to be in the standard regulation.

Table 1. Physical and chemical values of honey products (Mean \pm SD)

| Sample | Color | pH | % Brix | MC (%) | EC ($\mu\text{S}/\text{cm}$) | RSC (mg/ml) |
|--------|--|-----|-------------------|--------|----------------------------------|-------------------|
| S1 | White ^c (0.256 \pm 0.001) | 5.3 | 77.00 \pm 00.00 | 3.85% | 183.533 \pm 0.153 ^a | 2.737 \pm 0.222 |
| S2 | Extra White ^a (0.181 \pm 0.001) | 5.0 | 76.50 \pm 00.00 | 3.85% | 203.200 \pm 0.361 ^b | 2.633 \pm 0.310 |
| S3 | White ^d (0.271 \pm 0.001) | 5.2 | 78.00 \pm 00.00 | 3.85% | 224.700 \pm 7.189 ^c | 3.840 \pm 0.300 |
| S4 | White ^f (0.313 \pm 0.001) | 4.6 | 78.00 \pm 00.00 | 2.70% | 325.467 \pm 0.153 ^d | 2.700 \pm 0.278 |
| S5 | White ^e (0.307 \pm 0.002) | 4.3 | 80.00 \pm 00.00 | 4.00% | 375.267 \pm 0.153 ^e | 4.033 \pm 1.218 |
| S6 | White ^g (0.199 \pm 0.001) | 4.1 | 78.50 \pm 00.00 | 2.90% | 434.600 \pm 0.265 ^f | 3.163 \pm 0.622 |
| S7 | White ^b (0.266 \pm 0.001) | 3.5 | 73.50 \pm 00.00 | 2.02% | 742.967 \pm 0.451 ^g | 3.287 \pm 1.565 |

^{a,b,c,d,f,g} Significant at $p = 0.005$

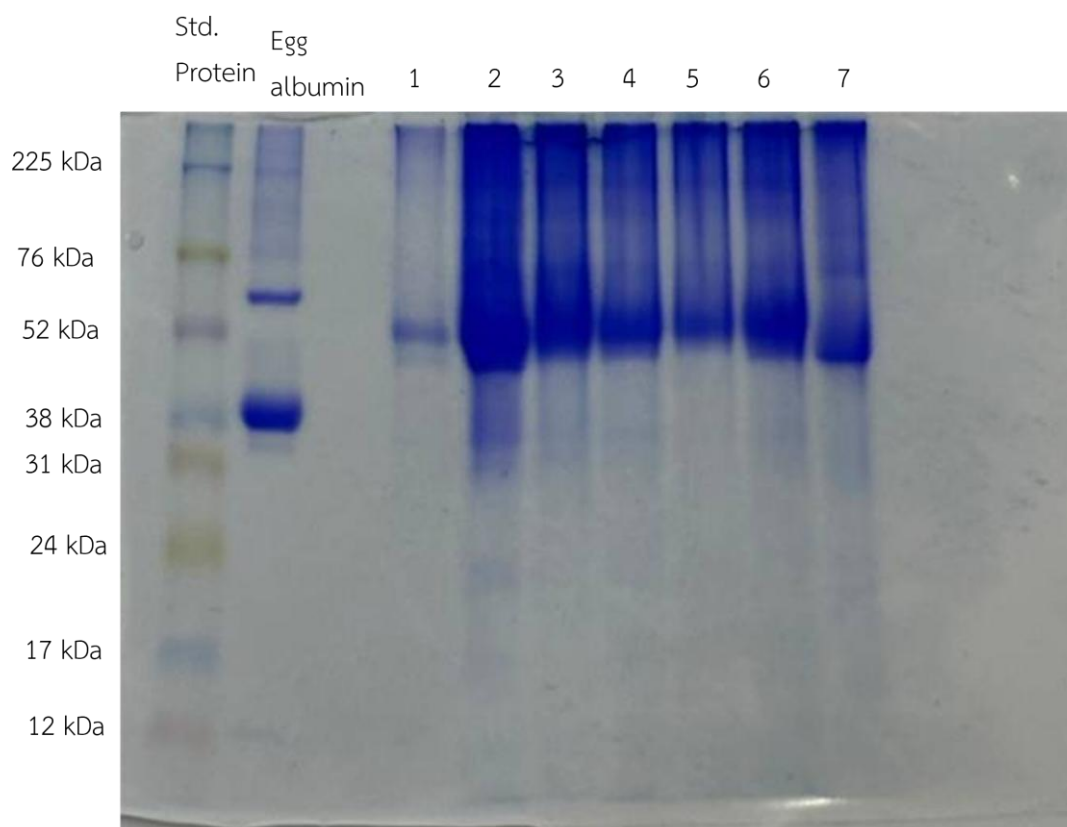
Note: MC = moisture content, EC = electrical conductivity, RSC = Reducing sugar content

The results SDS-PAGE with LC -MS (Fig.1) showed that out of 18 protein bands, 14 protein bands were identified, with three major proteins. The first one was FAD-binding PCMH-type



domain-containing protein (60.0 kDa), which was expressed in the gel at 6 positions: 191.8 (H1 and H2), 117.5 (H3), 106.7 (H4 and H5), 87.1 (H6 and H7), 67.6 (H8 and H10), and 20.4 (H14) kDa, respectively. It was noted that the positions 191.8, 117.5, 87.1, and 67.6 were proteins found in both longan and other flower honeys, which may mean that this protein may act as a general indicator for flowers. However, this protein at positions 106.7 and 20.4 kDa was found only in Doi Kham longan honey, which may be used as a protein band as a geographical indicator. For the second protein, pectin esterase (62.1 kDa), it was expressed in the gel at 2 positions, 57.5 (H9) and 33.9 (H13) kDa, respectively. Only longan honey, but honey from other flowers, did not express this protein. Therefore, pectin esterase at this position can be a protein band indicating the type of longan honey. For the third protein, DCD domain-containing protein (67.8 KDa) found at position 33.9 (H16) KDa is a protein found only in wild honey that cannot identify the type of flower. Therefore, it cannot be a band indicating the geographical location. This protein also had a low score (score = 36), which was lower than ion scores = 42 (estimated at $p = 0.05$). Therefore, this protein is unclear in the interpretation.

A



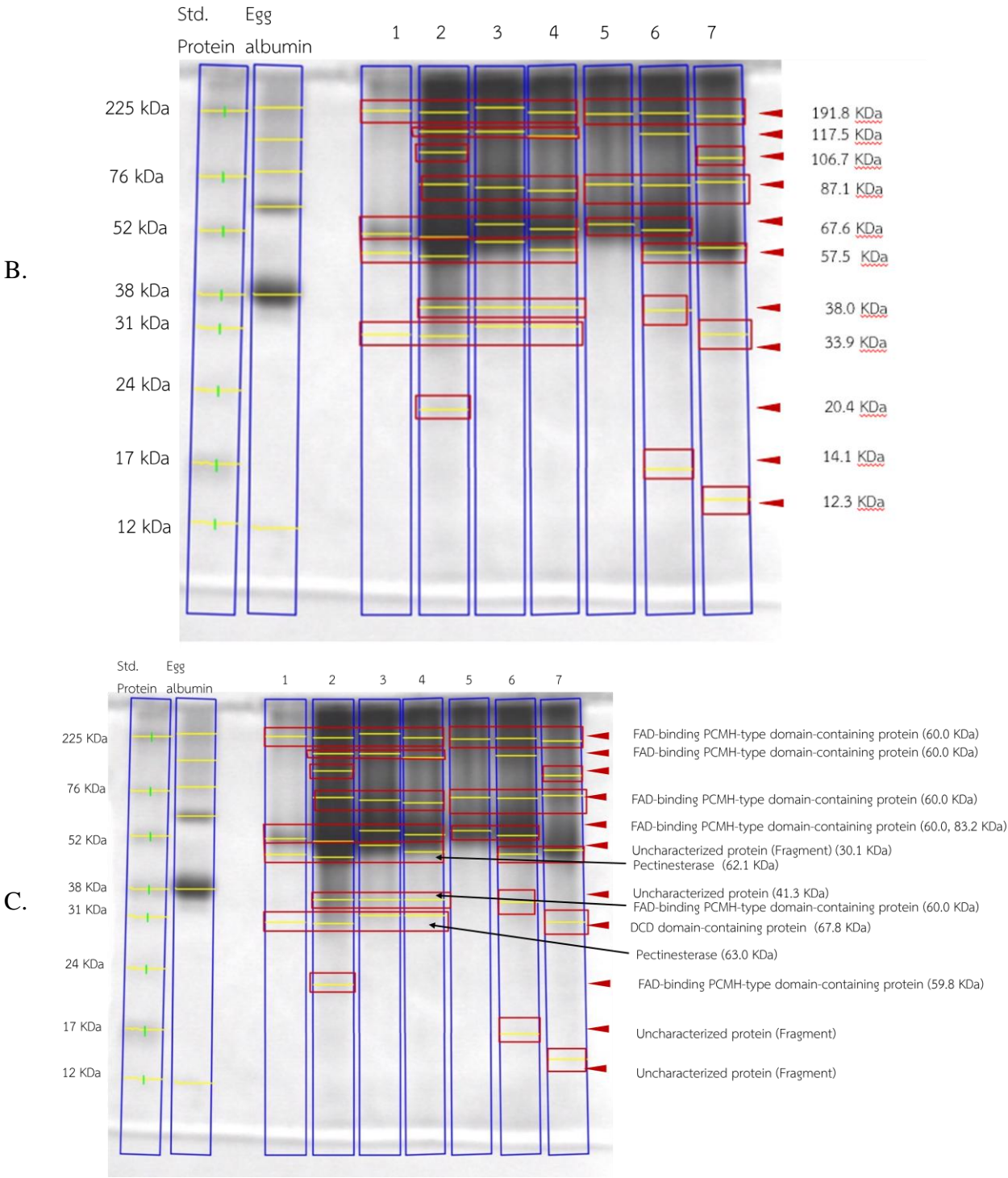


Fig. 1. The expression of protein in honey products (1-7) on gel of SDS-PAGE by Coomassive staining (A), SDS-PAGE by Coomassive staining in gel documentary (B) and SDS- PAGE by Coomassive staining in gel documentary with LC-MS (C) on 15% gel at 100 μ g/well gel. Notices; Line Std. = Standard protein marker, Line Egg = Egg albumin.

Conclusion:

This study concluded that some fractions of FAD-binding PCMH-type domain-containing protein (60.0 kDa) may act as a general protein marker for flower honey and as a



geographical indicator in longan honey and some fractions of pectin esterase (62.1 kDa) could be a protein bands indicating the type of honey from longan flowers. However, this research is just a basic experiment to find protein marker of flowers and geographic sources of longan honey that require further advanced studies in the future.

Acknowledgements: This study was supported by the Thailand Science Research and Innovation (TSRI), National Science Research and Innovation Fund (NSRF) and Fundamental Fund (FF) in 2024. We also thank Mrs. Pimporn Manochai for her kind help in facility at Division of Chemistry, Faculty of Science, Maejo University, Chiang Mai.

References:

1. Di Girolamo F, D'Amato A, Righetti PG. *J Proteomics*. 2012;75(12):3688-3693.
2. Azevedo MS, Valentim-Neto PA, Seraglio SKT, da Luz, CFP, Arisi ACM, Costa ACO. *J Sci Food Agric*. 2017;97(13):4515-4519.
3. Borutinskaitė V, Treigytė G, Matuzevičius D, Zaikova I, Čeksterytė V, Navakauskas D, Navakauskienė R. *J Apic Sci*. 2017;61(1):73-92.
4. Zhang Y, Wang Y, Zhao H, Zhang G, Peng D, Cao W. *J Agric Food Chem*. 2019;67(44):12255-12263.
5. Lewkowski, O., Mureşan, C. I., Dobritsch, D., Fuszard, M., & Erler, S. (2019). *Insects*, 10(9), 282.
6. Muresan, C.I.; Cornea-Cipcigan, M.; Suharoschi, R.; Erler, S.; Mărgăoan, R. *Lwt*, 2022, 154, 112883.
7. Bogdanov S, Martin P, Lullmann C. *Apidologie*. 1997;Extra Issue:1-59.
8. El Sohaim SA, Masry SHD, Shehata MG. *Ann Agric Sci*. 2015;60(2):279-287.
9. Ratiu IA, Al-Suod H, Bukowska, M, Ligor, M, Buszewski B. *Molecules*. 2019;25(1):34.
10. Idris YMA, Mariod AA, Hamad SI. *Int. J. Food Prop*. 2011;14(2):450-458.
11. Ramón-Sierra, JM, Ruiz-Ruiz JC, de la Luz Ortiz-Vázquez E. *Food Chem*, 2015;183:43-48.
12. Kashyap ML, Hynd BA, Robinson K. *J. lipid res*. 1980;21(4):491-495.
13. Khoontawad J, Laothong U, Roytrakul S, Pinlaor P, Mulvenna J, Wongkham C, Pinlaor S. 2012; *PLoS ONE*: e45460.



TEA PRODUCTION FROM YOUNG LEAF OF SAN PA TONG RICE VARIETY AND EVALUATION OF THE PHYTOCHEMICAL CONSTITUENTS AND ANTIOXIDATION ACTIVITIES

Anakhaorn Srisaipet,* Sirintip Patairat

Department of Chemistry, Faculty of Science, Maejo University, Chiangmai 50290, Thailand

*e-mail: anakhaorn@hotmail.com

Abstract:

This study investigated the production process of young leaf tea from San Pa Tong variety rice leaves, analyzed the phytochemical constituents of the tea produced, and evaluated its antioxidation activities. The soft green color with good smell is obtained from the 9-day-old leaves of the San Pa Tong rice variety. The tea is processed by drying the fresh young leaves at 80°C for 60 minutes. The phytochemical constituents and antioxidation activities of San Pa Tong young leaves tea were enhanced through extraction with hot water. The young leaf tea extract revealed the presence of reducing sugar, saponin, flavonoids, and terpenoids. The antioxidant properties and reducing power of the young leaf tea were identified via hot water-based extraction. The results showed that the total phenolic content was 28.4 mg GAE/g sample, the antioxidant capacity was 3.81 mg/g for the DPPH assay, and the FRAP value was 267 μ mol/g sample. For all, the young leaves of San Pa Tong rice variety can be utilized for the production of a novel herbal drink with high potential for phytochemical and antioxidant compounds, contributing to a healthy food product.

Introduction:

Phytochemicals are active ingredients exclusively found in plants. These compounds encompass phenolics, tocopherols, sterol derivatives, and others [1]. Phenolic compounds exhibit antioxidant activity by inhibiting the formation of reactive oxygen species, thereby promoting human health.

Tea is one of the most widely consumed beverages in the world. It is well-known that regular tea consumption offers numerous health benefits, including antioxidant, anti-inflammatory, antimicrobial, and anti-carcinogenic effects. Phytochemical constituents found in tea leaves collectively account for up to 30% of their dry weight [2-5]. Green tea, oolong tea, and black tea, the three primary tea categories, are predominantly derived from the young green shoots of the tea plant [6]. The young green shoots of the plant contain abundant phytochemicals such as phenolics, terpenes, flavonoids, and anthocyanins, which are acknowledged as bioactive compounds.

Rice (*Oryza sativa* L.) is a vital food crop in Asia and serves as the staple crop of Thailand, facing challenges from both biotic and abiotic factors that limit its production. In particular, the San Pa Tong Rice Variety stands out for its exceptional aromatic scent and uniquely soft texture, exclusive to Thailand's northern regions in Chiangmai Province. This study aims to focus on the production processes of young leaf tea from San Pa Tong variety rice leaves and to investigate the phytochemical constituents and antioxidative activities of the resulting tea product, aiming to evaluate its potential health-enhancing properties.

Methodology:

1. Plant materials

Seeds of the San Pa Tong rice variety, bought at an organic market in Sansai, Chiangmai, Thailand, were soaked in water overnight. They were placed in trays (40×25×10 cm) filled with coconut dust, kept at room temperature under natural daylight, and watered daily. On the 9th day, the leaves were collected, washed in distilled water, and air-dried at room temperature. Afterward, they were cut into 2 cm long segments. These samples, representing young leaves of the San Pa Tong rice, were used as materials for studying tea production processes.

2. Exploring Tea Production Methods

Trim the young leaves of San Pa Tong rice and bake them in a hot air oven at 80°C for 30, 45, and 60 minutes. Afterwards, analyze the tea product from the young leaves for its physical properties through qualitative observation by the observer.

3. Phytochemical Extraction Process

The tea leaf products are ground using a blender and mortar. Subsequently, the ground tea leaves are extracted for 15 minutes using various solvents: hot water (80°C), 70% ethanol, 0.1% TCA, sodium acetate buffer pH 5, and potassium phosphate buffer pH 7.4. These extracts are stirred for 30 minutes, then centrifuged at 15,000 rpm for 15 minutes at 4°C, and the supernatant is collected for subsequent analysis (first extraction). The residue remaining from the first extraction is then extracted with acetone under stirring for 30 minutes at room temperature (except for the residue from ethanol extraction). This mixture is centrifuged at 15,000 rpm for 15 minutes at 4°C, and the supernatant is collected for subsequent analysis (second extraction), improved from Calzuola I. et al. [7]. The samples are then analyzed for phytochemical constituents.

4. Phytochemical constituents

4.1 Testing for Reducing Sugars

Mixed 2 ml of the analyte sample with 5 ml of Benedict's reagent and heated it in a boiling water bath for 5 minutes. Observe for the formation of a brick-red precipitate indicating the presence of Reducing Sugars [8].

4.2 Test for Saponins

Take 2 milliliters of the extract and boil it in a water bath for 5 minutes. Afterward, shake vigorously to generate foam, then let it stand for 10 minutes. Observing the formation of thick, persistent foam suggests the presence of saponins [9].

4.3 Test for Flavonoids

Take 2 milliliters of the extract and boil it in a water bath until the volume reduces to 1 milliliter. Then, add 2-3 drops of sodium hydroxide solution. The solution will turn clear yellow. Afterward, add 2-3 drops of hydrochloric acid; it will turn colorless, demonstrating the presence of flavonoids [10].

4.4 Test for Anthraquinone

Add 10 milliliters of benzene to 2 milliliters of the extract and shake thoroughly to mix. Then, filter the mixture and add 5 milliliters of a 10% ammonia solution to the filtered solution, shaking well to mix. Observe for the formation of a red or purple layer in the ammonia phase (lower layer); this indicates the presence of alkaloids [9].

4.5 Test for Tanin

Add 5 milliliters of water to 2 milliliters of the extract. Then, add 2-3 drops of 10% ferric chloride and shake well to mix. If a dark green or deep blue color is observed, tannin is present [9].



4.6 Test for terpenoids

Add 2 milliliters of chloroform to 5 milliliters of the extract, then slowly add 3 milliliters of sulfuric acid to allow for layer separation. Afterwards, observe for a red-brown color between the layers of the solution, indicating the presence of terpenoids [9].

5. Antioxidation properties

5.1 The total phenolic content (Folin – Ciocalteu assay)

The total phenolic content (TPC) was determined using the modified Folin-Ciocalteu photometric method [11]. The reaction mixture was prepared by combining 0.5 mL of the sample (1000 ppm) with 1 mL of 10% Folin-Ciocalteu reagent, followed by the addition of 1 mL of 7% Na_2CO_3 solution. The solution was adjusted to a final volume of 5 mL with distilled water. The absorbance was measured at 765 nm after 2 hours of incubation in the dark at room temperature, using a blank as a reference. Gallic acid was used as the standard. The total phenolic content was expressed as milligrams of Gallic acid equivalents (GAE) per gram of crude extract.

5.2 Ferric Reducing Antioxidant Power assay (FRAP)

The total antioxidant potential of a sample was assessed using a modified assay for Fe^{3+} to Fe^{2+} reduction. 0.1 mL of the sample was added to a test tube containing 3 mL of FRAP reagent, followed by the addition of 0.3 mL of deionized water. The absorbance was measured at 595 nm after incubating for 10 minutes. A standard curve was constructed using various concentrations of Gallic acid [12]. The results were reported as micromoles of Gallic acid equivalents (GAE) per gram of sample.

5.3 Free radical scavenging activity (DPPH assay)

The radical scavenging activity of the tea was measured to assess antioxidant activity using the DPPH method [11]. In brief, 0.2 mL of the sample solution (100–1000 ppm) in methanol was added to 3 mL of a 0.3 mM DPPH solution. The mixtures were set aside in a dark area for 2 hours, and the absorbance was measured at 517 nm, using an equal amount of DPPH and methanol as a blank. Reference standard compound being used was ascorbic acid.

The percent DPPH scavenging effect was calculated by using following equation:

$$\text{DPPH scavenging effect (\%)} = A_0 - A_1 / A_0 \times 100$$

Where A_0 was the absorbance of control reaction and A_1 was the absorbance in presence of test or standard sample.

Results and Discussion:

Tea production processes

Trim the young leaves of San Pa Tong rice and bake them in a hot air oven at 80°C for 30, 45, and 60 minutes. The physical properties of the tea product are shown in Table 1.

Table 1

The physical properties of the tea product from young leaves of San Pa Tong rice

| Temperature | Time (min) | Physical |
|-------------|------------|--|
| 80°C | 30 | Appears moist Greenish-yellow color Smells of green odor |
| | 45 | Appears moist Greenish-yellow color Smells of green odor |
| | 60 | Light green color Aroma |

In the study of tea production from young leaves of San Pa Tong glutinous rice, the leaves were baked at 80°C for varying durations: 30 and 45 minutes. Data were collected through direct observation of physical characteristics to establish baseline information and to detect real-time changes. The tea leaves obtained had a greenish-yellow color and emitted a green odor characteristic of rice leaves, which aligns with the findings reported by Sakulnarmrat K. et al. in 2018 [13]. Tea baked for 60 minutes exhibited a light green color and an aroma suitable for consumption. Additionally, it was observed that when the tea baked for 30 and 45 minutes was stored at room temperature, its color changed to yellow. This change may be attributed to the remaining moisture in the tea, which affects the alteration of various components in the leaves. Therefore, it can be concluded that using 9-day-old rice leaves baked at 80°C for 60 minutes is an appropriate process for tea production. The tea can then be studied for its phytochemical composition, including the analysis of total phenolic compounds and the evaluation of antioxidant activity.

Phytochemical constituents

The ground tea leaves were extracted for 15 minutes using various solvents: hot water (80°C), 70% ethanol, 0.1% TCA, sodium acetate buffer pH 5, and potassium phosphate buffer pH 7.4. The extracts were analyzed for phytochemical constituents, and the results are shown in Table 2.

The extraction of tea from young leaves of the San Pa Tong rice variety using different solvents revealed that each solvent extracted phytochemicals differently, depending on the solvent's properties. The study found that hot water (80°C, 15 minutes) was the most effective solvent for extracting a wide range of phytochemicals. Therefore, in subsequent experiments, hot water will be used to extract compounds from the young leaves of the San Pa Tong rice variety for further analysis of the total phenolic content.

**Table 2.**

The phytochemical constituents of the tea product from young leaves of San Pa Tong rice

| Solvent | Phytochemical | |
|-----------------------------------|--|--|
| | 1 st Extraction | 2 nd Extraction |
| Hot water (80°C) | Reducing sugar Terpenoids Saponins Flavonoids | Reducing sugar Terpenoids Saponins Flavonoids |
| 70% Ethanol | Reducing sugar Terpenoids Flavonoids | Not determined |
| 0.1% TCA | Reducing sugar Saponins Flavonoids | Terpenoids |
| Sodium acetate buffer pH 5 | Flavonoids | Terpenoids |
| Potassium phosphate buffer pH 7.4 | Reducing sugar Flavonoids | Terpenoids |

Antioxidation properties

The young leaves of the San Pa Tong rice variety were dried at 80°C for 60 minutes and then extracted with hot water to produce the tea and study their antioxidant capacity using various techniques. The total phenolic content (TPC) was determined using the modified Folin-Ciocalteu photometric method. The radical scavenging activity of the tea was measured to evaluate its antioxidant activity using the DPPH method. The total antioxidant potential was assessed using a modified assay for Fe³⁺ to Fe²⁺ reduction, with the results presented in Table 3.

Table 3.

Antioxidant potential of tea

| Type of tea | Antioxidation properties | | |
|--------------------------------------|--------------------------|----------------|-------------------------------|
| | TPC (mg GAE/g sample) | DPPH (mg/g) | FRAP value (μmol/g sample) |
| Young leaf San Pa Tong rice tea | 28.4±0.3 | 3.81 | 267.0±10.0 |
| Khao Dok Mali 105 leaf rice tea [13] | 36.6±1.6 | 4.67 | 215.3±13.1 |
| Homnil leaf rice tea [13] | 16.4±1.1 | 4.52 | 441.9±13.1 |
| Green tea [13] | 32.8±1.6 | 3.57 | 685.5±21.7 |

The antioxidant potential of rice leaf tea extracts was evaluated using three parameters: TPC, DPPH, and FRAP values. The TPC values measured in young leaf San Pa Tong rice tea were similar to those in Khao Dok Mali 105 leaf rice tea and green tea, and higher than those in Homnil leaf rice tea. The DPPH radical scavenging activities were

closely associated with green tea, although they were lower than those of Khao Dok Mali 105 leaf rice tea and Homnil leaf rice tea. In contrast, the superior FRAP values in young leaf San Pa Tong rice tea were similar to those of Khao Dok Mali 105 leaf rice tea, but they were lower than those in Homnil leaf rice tea [13]. Notably, among the total antioxidation activity accessions of young leaf San Pa Tong rice tea, significantly positive correlations were observed among the three parameters.

Conclusion:

In summary, young leaves of the San Pa Tong rice variety can be utilized for the production of a novel herbal drink. They are good sources of phytochemicals and exhibit high antioxidant potential. This study indicates that young leaves of the San Pa Tong rice variety present interesting properties for a healthy drink product.

Acknowledgements:

The authors wish to thank the National Research Council of Thailand University for financial supports.

References:

1. Sumczynski D, Kotásková E, Družbíkova H, Mlček J. Food Chemistry. 2016;211:339–346.
2. Drynan J.W, Clifford M.N, Obuchowicz J, Kuhnert N. Natural Product Reports. 2010.;27(3):417–762.
3. Lucci P, Saurina J, Núñez, O. TrAC Trends in Analytical Chemistry. 2017;88:1–24.
4. Da Silva Pinto M, Food Research International. 2013;53(2):558–567.
5. Liu Z, Bruins M.E, Ni, L, Vincken J. P. Journal of Agricultural and Food Chemistry. 2018;66: 8469–8477.
6. Zandi P, Gordon M.H. Food Chemistry. 2018;64(3):285–288.
7. Calzuola I, Marsili V, Gianfranceschi G. G. Journal of Agricultural and Food Chemistry. 2004;52:5201–5206.
8. Official method of analysis of AOAC international. 17th Edition. AOAC International, Maryland, USA.
9. Harborne J.B. Phytochemical methods: A guide to Modern Technique of Plant Analysis. Chapman and Hall Ltd., London. 1973;40–150.
10. Bao J, Cai Y, Sun M, Wang G, Corke H. Journal of Agricultural and Food Chemistry. 2005;53:2324–2332.
11. Shao Y, Xu F, Sun X, Bao J. Beta T. Journal of Cereal Science. 2014;59:211–218.
12. Sakulnarmrat K, Konczak I. Food Chemistry. 2012;134:1011–1019.
13. Sakulnarmrat K, Dalar A, Bengu A.S, Konczak I. Integrative Food, Nutrition and Metabolism. 2018;5(6):1–11.

SP2-BIOMATERIALS AND MEDICAL DEVICES



A CYTOPROTECTIVE EFFECTS OF NANOPARTICLES DELIVERY OF RECOMBINANT HUMAN SECRETORY LEUCOCYTE PROTEASE INHIBITORS ON BACTERIAL LIPOPOLYSACCHARIDE INDUCE CELL INJURY

Chayapol Jawannatoom^{1,2}, Wannapat Chouyratchakarn^{1,2}, Sarawut Kumphune^{1,2*}

¹Biomedical Engineering Institute, Chiang Mai University, Chiang Mai 50200, Thailand

²Biomedical Engineering and Innovation Research Center, Chiang Mai University, Mueang Chiang Mai District, Chiang Mai, 50200 Thailand

*e-mail: sarawut.kumphune@cmu.ac.th

Abstract:

Bacterial sepsis is a life-threatening illness caused after the immune system becomes excessively stimulated in response to an infection. This leads to an overproduction of inflammatory cytokines, which causes dysfunction and damage in several organ systems. Lipopolysaccharides (LPS) are molecules found on the surface membranes of pathogenic bacteria. LPS can induce the production of inflammatory cytokines, which leads to cellular damage and cell death. The management in a sepsis patient involves prioritizing the treatment of the infection, providing support for vital organs, and regulating the inflammatory response. The secretory leukocyte protease inhibitor (SLPI) exhibits numerous physiological activities, especially the regulation of inflammation, and possessing anti-bacterial properties. However, SLPI has a short half-life in blood circulation; the carrier for SLPI is still needed. One of the well-known carriers for protein delivery is lipid nanoparticles (LNPs). In this study, we hypothesized that LNPs delivery of recombinant human SLPI (rhSLPI) could protect LPS-induced cellular injury. The cytotoxicity of LPS was evaluated using the human embryonic kidney (HEK293T) cell lines as a mimic in vitro sepsis model. The results showed that 100 µg/mL of LPS increased lactate dehydrogenase (LDH) activity level, indicating cellular injury, and significantly reduced cellular viability as measured by the MTT assay. rhSLPI was loaded into the LNPs, which were fabricated by the thin film hydration method. The physical characterization of SLPI-loaded LNPs showed a size of 108.00 ± 0.32 nm and a zeta potential of -58.65 ± 1.54 mV. Pre-treatment of SLPI-loaded LNPs, at concentrations of 1, 10, and 100 µg/mL, on HEK293T cells prior to exposure to 100 µg/mL of LPS could significantly increase cell viability when compared to the LPS treated group. In conclusion, the SLPI-LNPs have the potential to provide cellular protection in the bacterial LPS mimic bacterial sepsis could be a potential novel therapeutic agent against systemic sepsis.

Introduction:

Sepsis is an emergency condition characterized by a systemic immune response to an infection that results in organ dysfunction and death.¹ Globally, sepsis affects more than 30 million individuals per year, with mortality rates of approximately 41 percent in Europe and 28.3 percent in the United States.^{2, 3} Microorganism infection, particularly bacteria in blood circulation, causes sepsis. A prospective nationwide cohort study of consecutive adult patients with sepsis showed that the most common pathogen was *Escherichia coli* (21.5%), followed by *Klebsiella pneumoniae* (9.0%).⁴ In response, the innate immune system, including neutrophils, macrophages, monocytes, and natural killer cells of the host cells, is stimulated to produce proinflammatory cytokines, to eliminate the microorganism.⁵ The innate immune cells bind to pathogen-associated molecular patterns (PAMPs), such as bacterial endotoxins, or damage-associated molecular patterns (DAMPs), which are the intracellular molecules secreted by damaged cells. These pathogenic factors bind to specific

monocyte and macrophage receptors, including C-type leptin receptors, NOD-like receptors, and toll-like receptors (TLRs). Signal transduction pathway activation releases proinflammatory cytokines, such as TNF- α , IL-1 β , and IL-6. The increasing production of inflammatory cytokines produces a 'cytokine storm' in host. This event affects many cells and organs, resulting in cellular damage and leading to organ dysfunction.⁶

On the surface membranes of the pathogenic bacteria, there are the molecules called lipopolysaccharide (LPS), including endotoxin, which can be released and accumulate in bloodstream.⁷ In circulation, LPS will be recognized by Toll-like receptor-4 (TLR-4) located on the immune cell surface, which can enhance the production of proinflammatory cytokines. Moreover, LPS can increase protease-activated receptor-2 (PAR-2) expression, which activates the inflammation,⁸ and LPS can induce protease activity such as caspase-3, which could activate cellular apoptosis.⁹ Therefore, using Gram-negative bacteria's lipopolysaccharide (LPS) can represent the model of an in vitro study that mimic the pathophysiology of bacterial sepsis.

There are various studies aimed at treating the sepsis conditions; however, the specific therapy remains unclear.¹⁰ The antibiotic drugs are widely used for eliminating the microorganism infection in circulation. During suspected or confirmed cases of sepsis, the broad-spectrum antibiotic drugs are initiated for the treatment of sepsis.¹¹ However, the use of broad-spectrum antibiotics poses the risk of developing multidrug-resistant (MDR) organisms, necessitating higher doses or changes in antibiotic therapy for septic patients.¹¹ This can lead to adverse effects for the patient. Anti-inflammatory drugs for sepsis are still undergoing investigation, with the focus on regulating the overproduction of proinflammatory cytokines.¹²

Secretory leukocyte protease inhibitor (SLPI) provides an anti-inflammatory effect by attenuating nuclear factor kappa B (NF- κ B) transcription,¹³ resulting the transcription of pro-inflammatory genes.¹⁴ In addition, SLPI also showed anti-apoptotic activity, and its antiprotease activity also contributes to cell differentiation and viability.^{15, 16} Moreover, an in vitro study demonstrated the antimicrobial activity of SLPI against gram-positive and gram-negative microorganisms.¹⁷ SLPI is one of the candidates for use in sepsis management, due to its anti-inflammatory and antimicrobial activity. However, the use of SLPI in therapeutics has limitations. The circulation's protease enzyme can break down the SLPI in the bloodstream, resulting in a short half-life. As a result, the SLPI delivery system is still required for stability and to extend its half-life.

This study aimed to investigate the cytoprotective effects of SLPI in the bacterial LPS mimic bacterial sepsis by fabricating the lipid nanoparticles (LNPs) by thin film hydration method to deliver the recombinant human SLPI (rhSLPI) (**Figure 1a**). Pre-treatment of the HEK293T cell line with SLPI-loaded LNPs, after that, the LPS was treated to perform in vitro sepsis conditions and measure the cell viability (**Figure 1b**).

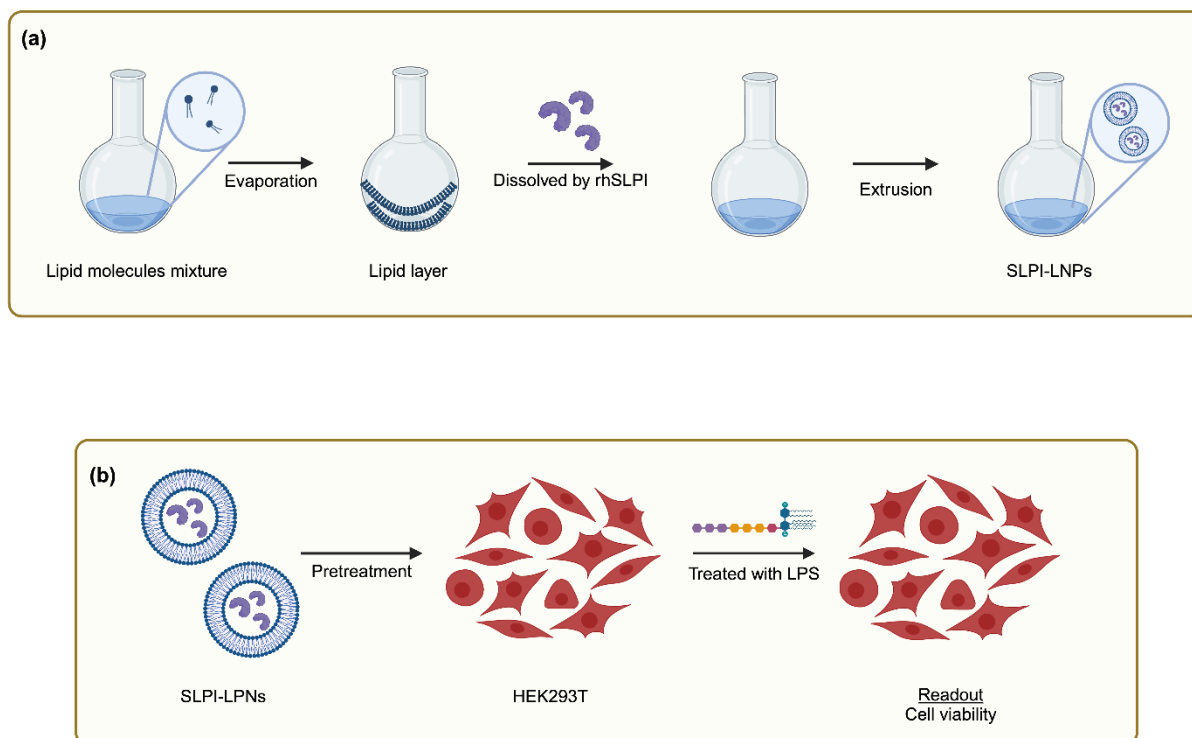


Figure 1.

Schematic diagram. (a) Lipid nanoparticles fabrication, (b) Pretreatment of SLPI-LNPs in sepsis conditions

Methodology:

Reagent and chemical

Dulbecco's modified Eagle's medium (DMEM), fetal bovine serum (FBS) and trypsin-EDTA were purchase from Gibco (Gibco BRL; Life Technologies Inc. New York, USA). Lipopolysaccharide O55:B5 was purchase from Sigma-Aldrich (USA).

Cell culture and sub-culture

The human embryonic kidney cell line (HEK293T) was purchased from American Type Cell Culture (ATCC-CRL3216) and cultured in Dulbecco's Modified Eagle Medium (DMEM) supplemented with 10% (v/v) heat-inactivated Fetal Bovine Serum (FBS), penicillin, and streptomycin. The cells were maintained under conditions of 37 °C under 5% carbon dioxide (CO₂) and 95% air throughout the experiment. When the cells density exceeds 70 - 80% confluence, the cells were sub-cultured.

SLPI-LNPs fabrication

The protocol for liposome nanoparticle preparation was performed by following the previous report¹⁸ by the conventional thin film hydration method. The lipid molecules mixture ratio was 7:3 of DOPS: Cholesterol, in chloroform: methanol. Then the mixture was removed by a rotary evaporator until a dry thin film lipid was formed on the flask. Rehydrating was performed by dissolving the lipid film with sterile distilled water for blank-LNPs and the recombinant human SLPI (rhSLPI) in sterile distilled water for SLPI-LNPs. The lipid nanoparticles were reduced in size by extrusion with a mini extruder. The blank-

LNPs and SLPI-mRNA were characterized for their physical properties and used in the next experiments.

Characterization of lipid nanoparticles

The nanoparticles were measured size, polydispersity index (PDI), and zeta potential by Zetasizer Pro (Malvern Panalytical, UK). The PDI is measured to evaluate the distribution of the particles molecular weight. The larger the PDI, the higher the molecular weight distribution.¹⁹ The zeta potential is a measurement of the electrical charge around the surface of nanoparticles, which exhibit the stability of nanoparticles.

Determination of cellular injury and viability of LPS

LPS was diluted by 1% fetal bovine serum in Dulbecco's modified Eagle's medium (DMEM) the final concentration of LPS was 100 µg/mL. The HEK293T cells were seeded to 96-well plate at a concentration of 100,000 cells/mL for 200 µL/well, which were divided into two groups including control group and LPS treated group. In LPS treated group, cells were treated with 100 µg/mL of LPS dissolve in culture medium for 24 hours. After that, the cell viability and cell injury in the treated condition were determined by MTT assay and released LDH activity assay, respectively.

Pre-treatment of SLPI-LNPs

The HEK293T cells were seeded to 96-well plate at a concentration of 100,000 cells/mL for 200 µL/well, which were divided into three groups, including control, treated blank-LNPs and treated SLPI-LNPs. The HEK293T cells were treated 1, 10, 100 µg/mL of blank-LNPs or SLPI-LNPs for 2 hours. After that, 100 µg/mL of LPS was added to the cells in both groups and incubated for further 24 hours. At the end of treatment protocol, cell viability was determined by MTT cell viability assay.

MTT cell viability assay

The culture medium was replaced with 0.5 mg/mL MTT reagent and incubated for 2 hours at a temperature of 37 °C. Afterwards, the MTT reagent was removed, and dimethyl sulfoxide (DMSO) was added to dissolve the formazan crystal. The optical density (OD) was assessed using a spectrophotometer at a wavelength of λ 570 nm.

LDH cell injury measurement

The released LDH activity was quantified from the collected sample by Pierce Lactate Dehydrogenase (LDH) Cytotoxicity Assay Kit. The collected medium was mixed with the reaction mixture in a 1:1 ratio, resulting in a total volume of 100 µL and incubated at room temperature for 30 minutes. Subsequently, 50 µL of stop solution was added. The absorbance was measured at a wavelength of λ 490 nm and λ 680 nm.

Statistical analysis

All experiments performed in triplicate. Data reported as mean \pm standard error. The unpaired t-test was calculated to determine the significance of all group data. The p value <0.05 was considered as significant.

Results and Discussion:

Characteristic of lipid nanoparticles

The results of LNP characterization revealed that the sizes of blank LNPs and SLPI LNPs were 107.70 ± 0.42 nm and 108.00 ± 0.32 nm, respectively (**Figure 2a**). The PDI of



blank-LNPs and SLPI-LNPs were 0.071 ± 0.010 and 0.083 ± 0.003 , respectively (**Figure 2b**). The zeta potential of blank-LNPs and SLPI-LNPs were -65.64 ± 3.34 mV and -58.65 ± 1.54 mV, respectively (**Figure 2c**). The particles size of SLPI-LNPs were greater than blank-LNPs significantly and the zeta potential of SLPI-LNPs were significantly lower than blank-LNPs. PDI in both group of nanoparticles showed nonsignificant different. The greater the zeta potential, the greater charge on the particle surfaces, which results in stronger repulsive forces between the particles that prevents the aggregation and enhance the particle stability.²⁰ The zeta potential of blank-LNPs and SLPI-LNPs are more than ± 30 mV which provide the stability of lipid particles and indicate the monodisperse of LPNs.²¹ The negative charge of particle surface can also pass through cell barrier, however, a more negative charge on particle surfaces indicates lower cell permeability comparing with the positive charge.²² Therefore, further engineering of the LNP surfaces to synthesize a more positive charge is necessary to enhance the particles' ability to permeate the cell membrane effectively. Nevertheless, further experimentation is required to examine the shape of the nanoparticles, such as by the utilization of a transmission electron microscope (TEM). Moreover, the percentage of drug encapsulation and release profile needs to be determined.

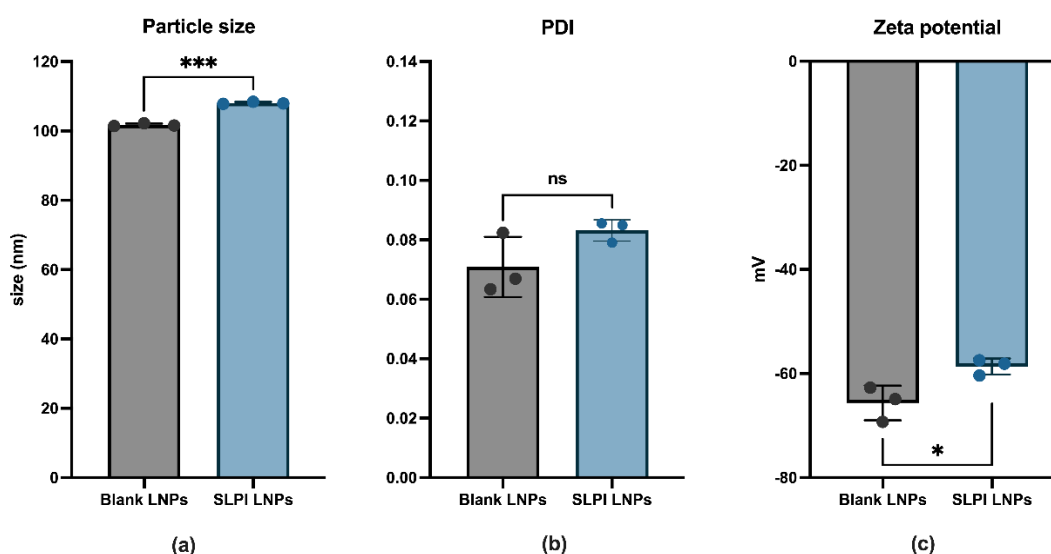


Figure 2.

Characteristic of lipid nanoparticles. (a) particles size, (b) polydispersity index (PDI), (c) zeta potential. * $p < 0.05$, ** $p < 0.01$, *** $p < 0.001$.

LPS treatment induce cellular toxicity in HEK293T cells

Following the administration of LPS, the LDH levels in the collected medium were measured. The fold change in LDH activity release for the control group was 0.075 ± 0.004 , while for the LPS group was 0.106 ± 0.013 . The LDH level released in LPS-treated cells showed a considerable increase compared to the control group, as shown in **Figure 3a**. The elevation in LDH level in the medium suggests that there has been disruption to the cell membranes, resulting in cellular apoptosis, necrosis, or other types of cellular injury.²³

The MTT cell viability assay showed that the percent cell viability of LPS treated group was 67.10 ± 1.91 percent, which significantly lower than that of control group (**Figure 3b**), indicated that the LPS treatment cause cell death. This finding has a favorable relationship with the findings of the observed increase in LDH-release. Thus, an in vitro

treatment using bacterial LPS could serve as a model to replicate the cellular pathophysiology observed in response to bacterial sepsis.

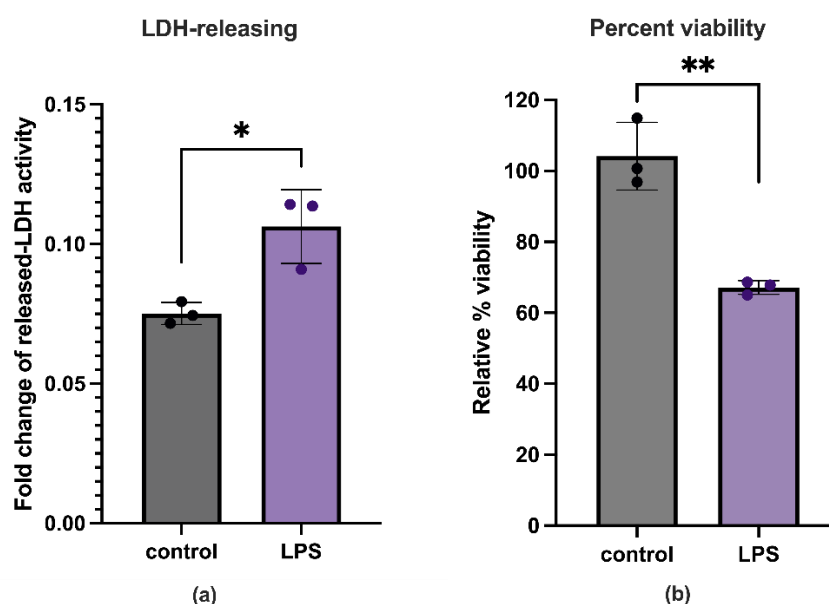


Figure 3.

Cytotoxicity of lipopolysaccharide. (a) Cell injury by LDH assay, (b) cell viability by MTT assay. * $p < 0.05$, ** $p < 0.01$, *** $p < 0.001$.

Pretreatment of SLPI-loaded lipid nanoparticles showed cytoprotective effect in LPS-induced cellular toxicity

The percentage of cell viability in blank-LNPs treated group (1, 10 and 100 $\mu\text{g/mL}$) followed by LPS exposure showed a significant reduction in cell viability at all concentration when compared to the control group $59.30 \pm 2.58\%$, $54.72 \pm 1.90\%$, and $58.88 \pm 0.54\%$, respectively. Pre-exposure to SLPI-LNPs at concentrations of 1, 10, and 100 $\mu\text{g/mL}$ before being exposed to LPS resulted in significantly increased cell viability of $97.75 \pm 5.77\%$, $92.44 \pm 6.52\%$, and $78.15 \pm 6.03\%$, respectively (**Figure 4**). The findings indicate that the percentage of viable cells considerably increased when they were pretreated with SLPI-LNPs, as compared to blank-LNPs, at each concentration prior to being exposed to LPS. Although, the MTT assay can be interfered by LNPs due to their lipid droplets,²⁴ this study analyzed the relative percentage of cell viability comparing between blank-LNPs and SLPI-LNPs, in the similar concentration used in the study. Therefore, the interference could be normalized by using blank-LPNs and might not affect the interpretation of the result. This suggests that SLPI-LNPs have a protective effect against cellular toxicity generated by LPS. Thus, SLPI-LNPs have the potential to offer a new and effective therapeutic impact for systemic sepsis.

Nevertheless, although the MTT assay showed a declining tendency with increased concentrations of LNPs, further experiments are required to explore the harmful effects of blank-LNPs and SLPI-LNPs. Furthermore, it is necessary to evaluate the cytoprotective properties of SLPI-LNPS both before and after treatment in order to simulate the therapeutic application for sepsis patients and counteract LPS-induced cellular damage.

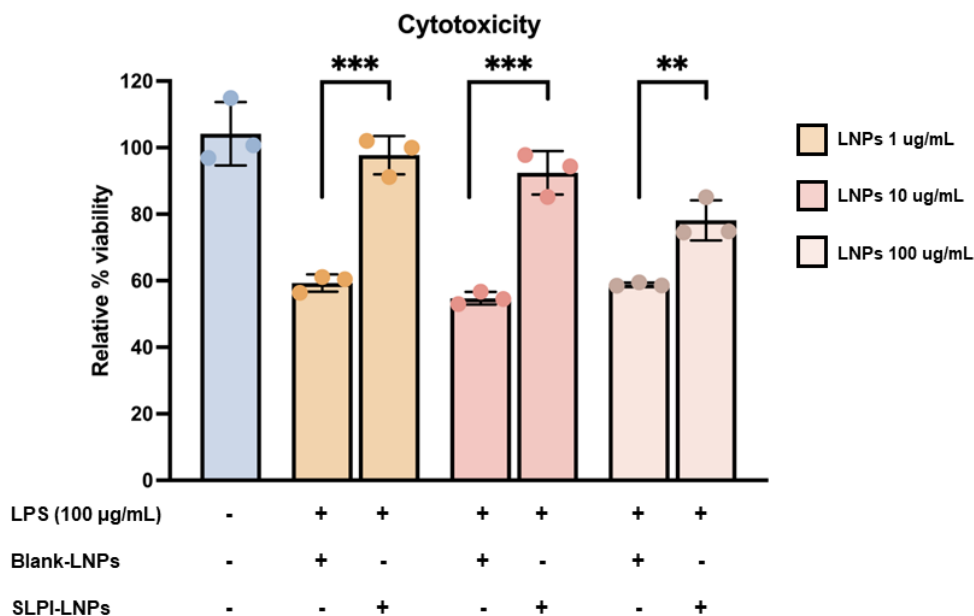


Figure 4.

Cytoprotective effect of SLPI in LPS-induced cellular toxicity.

* $p < 0.05$, ** $p < 0.01$, *** $p < 0.001$.

Conclusion:

In conclusion, the SLPI-LNPs have cytoprotective benefits against cellular damage generated by bacterial LPS. The cytoprotective properties in different organs should be investigated and the nanoparticles should also be designed to improve the specificity towards particular organs. Furthermore, further investigation is required to determine whether SLPI-LNPs might be utilized for their anti-inflammatory properties in conjunction with their anti-bacterial activity in sepsis situations.

Acknowledgements:

The present study was supported by Chiang Mai University for SK, the TA/RA scholarship from Multidisciplinary and Interdisciplinary School, Chiang Mai University. We would like to acknowledge Biomedical Engineering Institute (BMEI), Chiang Mai University for academic activity support to attend STT50.

References:

1. Kaukonen KM, Bailey M, Suzuki S, Pilcher D, Bellomo R. *Jama*. 2014;311(13):1308-16.
2. Gyawali B, Ramakrishna K, Dhamoon AS. *SAGE Open Med*. 2019;7:2050312119835043.
3. Levy MM, Artigas A, Phillips GS, Rhodes A, Beale R, Osborn T, et al. *Lancet Infect Dis*. 2012;12(12):919-24.
4. Umemura Y, Ogura H, Takuma K, Fujishima S, Abe T, Kushimoto S, et al. *Int J Infect Dis*. 2021;103:343-51.
5. Vincent JL, Moreno R, Takala J, Willatts S, De Mendonça A, Bruining H, et al. *Intensive Care Med*. 1996;22(7):707-10.
6. Chousterman BG, Swirski FK, Weber GF. *Semin Immunopathol*. 2017;39(5):517-28.
7. Solov'eva T, Davydova V, Krasikova I, Yermak I. *Marine drugs*. 2013;11:2216-29.

8. Chao H-H, Chen P-Y, Hao W-R, Chiang W-P, Cheng T-H, Loh S-H, et al. *Journal of Biomedical Science*. 2017;24(1):85.
9. Karahashi H, Amano F. *J Leukoc Biol*. 1999;66(4):689-96.
10. Evans T. *Clin Med (Lond)*. 2018;18(2):146-9.
11. Martínez ML, Plata-Menchaca EP, Ruiz-Rodríguez JC, Ferrer R. *J Thorac Dis*. 2020;12(3):1007-21.
12. Freeman BD, Natanson C. *Expert Opin Investig Drugs*. 2000;9(7):1651-63.
13. Lentsch AB, Jordan JA, Czermak BJ, Diehl KM, Younkin EM, Sarma V, Ward PA. *Am J Pathol*. 1999;154(1):239-47.
14. Taggart CC, Greene CM, McElvaney NG, O'Neill S. *J Biol Chem*. 2002;277(37):33648-53.
15. Klimenkova O, Ellerbeck W, Klimiankou M, Ünalán M, Kandabarau S, Gigina A, et al. *Blood*. 2014;123(8):1239-49.
16. Subramaniam D, Hollander C, Westin U, Erjefält J, Stevens T, Janciauskiene S. *Respirology*. 2011;16(2):300-7.
17. Hiemstra PS, Maassen RJ, Stolk J, Heinzl-Wieland R, Steffens GJ, Dijkman JH. *Infect Immun*. 1996;64(11):4520-4.
18. Gibbons AM, McElvaney NG, Taggart CC, Cryan SA. *J Microencapsul*. 2009;26(6):513-22.
19. Shrivastava A. *Introduction to Plastics Engineering*: William Andrew Publishing; 2018. p. 17-48.
20. Jarzynska K, Gajewicz-Skretna A, Ciura K, Puzyn T. *Computational and Structural Biotechnology Journal*. 2024;25:3-8.
21. Németh Z, Csóka I, Semnani Jazani R, Sipos B, Haspel H, Kozma G, Kónya Z, Dobó DG. *Pharmaceutics*. 2022; 14(9):1798.
22. Ross AM, Cahalane RM, Walsh DR, Grabrucker AM, Marcar L, Mulvihill JJE. *Pharmaceutics*. 2023;15(1).
23. Kumar P, Nagarajan A, Uchil PD. *Cold Spring Harb Protoc*. 2018;2018(6).
24. Angius F, Floris A. *Toxicol In Vitro*. 2015;29(2):314-9.



CARDIAC CELL MEMBRANE-COATED MESOPOROUS SILICA NANOPARTICLES FOR DELIVERY TO CARDIAC TARGETS

Fapraphan Pikwong^{1,2}, Jiraporn Kamsarn^{1,2}, Phornsawat Baipaywad^{1,2}, Hansoo Park³, Sarawut Kumphune^{1,2*}

¹Biomedical Engineering Institute, Chiang Mai University, Chiang Mai 50200, Thailand

²Biomedical Engineering and Innovation Research Center, Chiang Mai University, Mueang Chiang Mai District, Chiang Mai, 50200 Thailand

³School of Integrative Engineering, Chung-Ang University, Seoul, 06974, Republic of Korea.

*e-mail: sarawut.kumphune@cmu.ac.th

Abstract:

Ischemic heart disease (IHD) is a major cause of death worldwide, with almost 9 million fatalities in 2019. Using nanoparticles to deliver therapeutic molecules is beneficial for myocardial ischemia/reperfusion (I/R) injury. However, nanoparticles have significant limits when applied to effectively target cells and organs. Cell membranes are employed for covering synthetic nanoparticles to improve their targeting abilities, enhance their stability, and reduce their toxicity. Cell membranes from several cell types, such as red blood cells (RBC), immune cells (WBC), platelets, cancer cells, and stem cells, have been reported to enhance selective delivery. However, using cardiac cell membranes for coating nanoparticles has not been reported before. In this study, cardiac cell membrane (cCM) was extracted from human ventricular myocytes (AC16) and coated on mesoporous silica nanoparticles (MSN) to form a novel cardiac cell membrane-coated mesoporous silica nanoparticle (cCMCMSN). The cCMCMSN were characterized for size, zeta potential, protein coating, and morphology. The result showed that MSN, cCM, and cCMCMSN have a size of 94.33 nm, 117.30 nm, and 109.50 nm, respectively, and zeta potentials of -33.40 ± 0.05 mV, -33.56 ± 0.47 mV, and -32.57 ± 0.46 mV, respectively. Transmission electron microscopic examination showed a thin layer of cell membrane surrounding MSN, suggesting the successful coating process, which was confirmed by the appearance of protein on cCMCMSN. In conclusion, this is the first study to show cardiac cell membranes could be coated with nanoparticles. These nanoparticles will be used for drug delivery, especially for the treatment of cardiovascular diseases.

Keywords: ischemic heart disease, cardiac cell membrane-coated nanoparticles, mesoporous silica nanoparticles, targeted drug delivery, nanoparticles

Introduction:

Cardiovascular disease (CVD) is a leading cause of death worldwide, with ischemic heart disease (IHD) representing the most prevalent cause.¹ In addition, IHD causes myocardial infarction (MI), a serious condition marked by necrosis in ischemia (I) of the cardiac muscle caused by insufficient circulation through the coronary arteries.² Currently, treatments such as cardiac bypass surgery are employed to restore the supply of blood, a process called reperfusion, which leads to cell death known as reperfusion injury.³ Both injuries are called “ischemia/reperfusion (I/R) injuries,” which are a significant research challenge to finding a cure for heart attack.

Nanomaterials have demonstrated significant potential for challenges associated with off-target side effects, long-term toxicity, and limited diagnostic or therapeutic efficacy.⁴ Nanoparticles are able to improve the stability, bioavailability, and efficacy of encapsulation to control drug release and drug delivery into cells or tissues.⁵ However, nanoparticles

present limitations in terms of uncontrolled immune responses and specific targets when applied to administration.⁶ Therefore, the application of surface modification of nanoparticles has the potential to enhance the specificity of specific targets.⁷

Cell membrane-coated nanoparticles (CMCNPs) are an innovative kind of biomimetic nanoparticles combining cellular membranes with engineered nanoparticles to efficiently deliver therapeutic drugs.⁸ The application of a natural cell membrane for covering nanoparticles provides enhanced stability, decreased immune system response, and a prolonged circulation half-life. Furthermore, it provides a variety of cell-like biological functions due to the presence of functioning membrane proteins.⁹ Previous studies have demonstrated that CMCNPs have been applied in cardiovascular disease (CVD), including red blood cells (RBCs) to improve compatibility within the bloodstream,¹⁰ immune cells (WBCs) for targeted delivery of nanoparticles to inflammatory sites,¹¹⁻¹³ platelets for the treatment of atherosclerosis,¹⁴ cancer cells to prolong the half-life of nanoparticles,¹⁵ and stem cells to reduce ischemia/reperfusion (I/R) injury.¹⁶ However, the use of cardiac cell membrane-coated nanoparticles has never been demonstrated.

This study aimed to fabricate cardiac cell membrane-coated mesoporous silica nanoparticles (cCMCMSN) **Figure 1.** and investigate their physical characteristics for drug loading purposes.

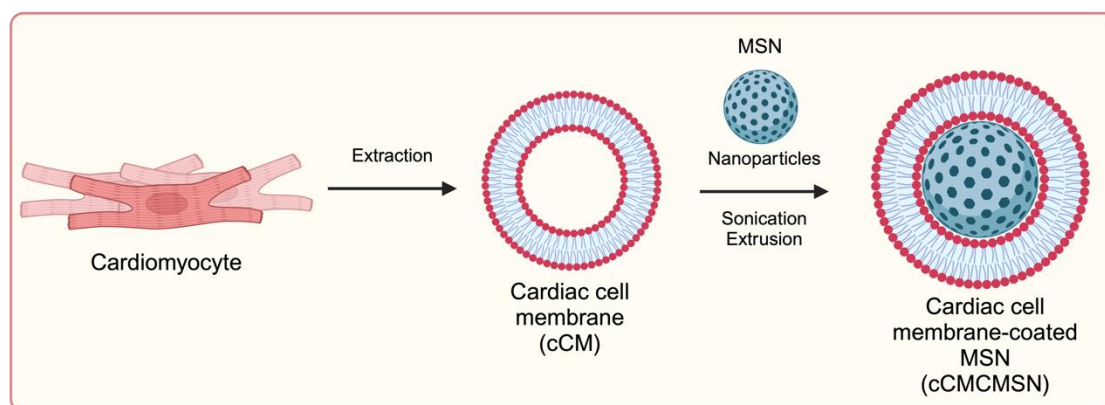


Figure 1.

Schematic diagram of cardiac cell membrane-coated mesoporous nanoparticles

Methodology:

Chemical and reagent

Tetraethyl orthosilicate (TEOS, 98.0%), cetyltrimethylammonium ammonium bromide (CTAB), Tris-HCl, magnesium sulfate, and ethanol were purchased from Sigma-Aldrich (Milwaukee, Wis., USA). We purchased Sodium hydroxide and hydrochloric acid from RCI Labscan Limited (Thailand). Dulbecco's Modified Eagle Medium (DMEM), Fetal bovine serum (FBS), penicillin, streptomycin, and trypsin-EDTA were purchased from Gibco (Gibco BRL; Life Technologies Inc., New York, USA).

Cell and cell culture

Human Cardiomyocyte Cell Line (AC16) was purchased from American Type Cell Culture (ATCC-CRL3568). Cells were cultured in DMEM supplemented with 10% (v/v) of fetal bovine serum (FBS) and 5000 units/mL of penicillin/streptomycin. Cells were kept at 37°C in a humidified atmosphere of 95% air and 5% carbon dioxide.



Synthesis of mesoporous silica nanoparticles (MSN)

The MSN was synthesized by a modified Stober method.¹⁷ Briefly CTAB was incubated with DI water and ethanol at 50 °C for 20 min with stirring at 750 rpm. Then, TEOS and sodium hydroxide were added to the solution and incubated at 50 °C for 2 h. After that, the solution was incubated at room temperature. After incubation, the solution was centrifuged at 5200 ×g for 10 min and then extracted with HCl and ethanol twice. The nanoparticles were washed three times with ethanol, water, and ethanol and dried under freeze-dry.

Extraction and preparation of c-CMMSN

The extraction protocol was followed by Jang Y, et al.¹⁸ The AC16 cell line was cultured in a T-175 flask and harvested by trypsin-EDTA. The cells were resuspended in 10 mL of TM buffer that contains 50 mM Tris-HCL, pH 7.4, 10 mM magnesium sulfate, and 1 tablet of DETA-free protease inhibitor. The cells were homogenized by the probe homogenizer at 6000 rpm for 5 min and sonicated by the probe sonicator at 150 W for 5 min. Then, the solution was centrifuged at 100,000 ×g at 4 °C for 1 h. The supernatant was discarded, and the pellet was collected. The cell membrane was determined by the Bradford assay. For coating, MSN was incubated with the cell membrane in a mass ratio of 2:1. The solution was sonicated by the probe sonicator at 150 W plus 2 sec for 5 min, centrifuged at 10,000 ×g for 10 min at 4 °C, and extruded through 200 nm of polycarbonate membrane.

Physical characteristics of nanoparticles

The nanoparticles were measured for size, polydispersity index (PDI), and zeta potential by Zetasizer (Malvern, England). The morphology of nanoparticles was evaluated by transmission electron microscopy (TEM) JEM 2010. The sample was fixed with 2% glutaraldehyde for 30 min and stained with phosphotungstic acid (PTA) for 15 s.

Determination of cell membrane proteins by sodium dodecyl sulfate-polyacrylamide gel electrophoresis (SDS-PAGE)

The samples were mixed with SDS sample buffer and boiled at 95 °C for 5 min. The protein was separated by using 10% polyacrylamide gel at 120 v. The protein was stained with Coomassie Brilliant Blue R250, followed by appropriate destaining.

Encapsulation of nanoparticles

Encapsulation was performed by incubating 10 mg of MSN with 0.04 mM of rhodamine B. The solution was incubated for 24 h. After incubation, cCM was added to the solution, then sonicated and extruded through 200 nm of polycarbonate membrane. The nanoparticles were washed twice with DI. Washing solutions were measured for rhodamine B concentration at 554 nm.

Statistical analysis

All data were evaluated by mean ± standard deviation (SD). The Tukey-Kramer test was calculated to determine the significance of all group data. A p-value of less than 0.05 was considered statistically significant.

Results and Discussion:

Physical characteristics

The result showed that the size of MSN, cCM, and cCMCMSN was 94.33 ± 19.22 nm, 117.30 ± 17.41 nm, and 109.50 ± 18.99 nm, respectively **Figure 2a**. The PDI of MSN, cCM, and cCMCMSN are 0.34 ± 0.03 , 0.68 ± 0.02 , and 0.48 ± 0.05 , respectively **Figure 2c**. The zeta potential of nanoparticles was -33.40 ± 0.05 mV, -33.56 ± 0.47 mV, and -32.57 ± 0.46 mV, respectively **Figure 2b**. The zeta potential of cCM and cCMCMSN was significantly lower than MSN. The PDI of nanoparticles was 0.33 ± 0.03 , 0.86 ± 0.02 , and 0.48 ± 0.05 , respectively. The PDI was significantly different from each other.

This study is the first study of synthesized cardiac cell membrane-coated mesoporous silica nanoparticles for delivery to a specifically targeted heart. In this study, we extracted the cell membrane by the probe homogenizer and enhanced the existence of fragments by the probe sonicator. Following ultracentrifugation, the cell membrane was exposed to sonication to produce vesicles. Subsequently, MSN was exposed to the cell membrane and received sonication to coat the particles with the cell membrane. We ensured the coating of MSN with a cell membrane by extruding through a polycarbonate membrane.

The physical characteristics represented by the dimensions of cCMCMSN are larger than MSN because it consists of the cCM coating, which is a thin cell membrane surrounding the MSN. The size of the cCM is less than 200 nm because it was extruded through a 200 nm polycarbonate membrane **Figure 2a**. The PDI is used to determine the quantity of variety in a size distribution of particles.¹⁹ In this study, the PDI of particles was between 0.1 to 0.7 which represented monodispersed particles **Figure 2b**. Zeta potential was used to quantify the electric charge present on the surface of the nanoparticle. The zeta potential of cCM was similar to MSN, resulting, in the charge of cCMCMSN was not different from MSN **Figure 2c**. The stability of particles is determined by the zeta potential value at a surface potential, typically more than ± 35 mV, which prevents coagulation by electrostatic repulsion.²⁰ MSN, cCM, and cCMCMSN can cause high PDI due to the particles having a negative charge higher than -35 mV, which leads to their aggregation.

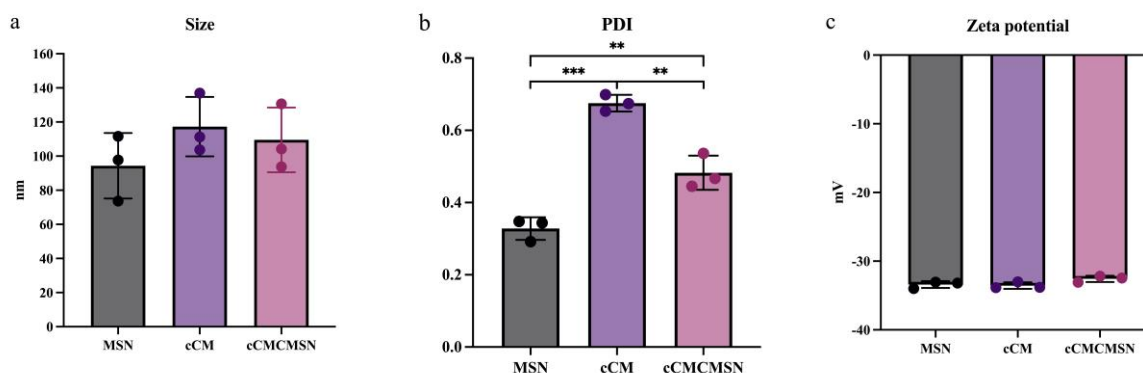


Figure 2.

Physical characteristics of nanoparticles. a) size, b) PDI, and c) zeta potential. * $p < 0.05$, ** $p < 0.01$, *** $p < 0.001$.

Morphology of nanoparticles

The TEM was used to identify and determine the morphology of nanoparticles **Figure 3**. The result showed that MSN was a spherical shape with porous particles **Figure 3a**, cCM presents the double layer of the membrane which was a round shape, and hollow particles **Figure 3b**, and cCMCMSN showed a spherical shape, a thick edge of particles, and a smooth surface **Figure 3c**. The result represented MSN and cCMCMSN have similar diameters.

The morphology of particles presented by TEM. MSN were initially sphere particles with porous which were extracted by CTAB²¹ **Figure 3a**. The cCM was a round shape and



double layers of membrane, which were extracted from cardiac cells **Figure 3b**. The surface of MSN was changed to a thin layer when covered with the cell membrane surrounding **Figure 3c**.

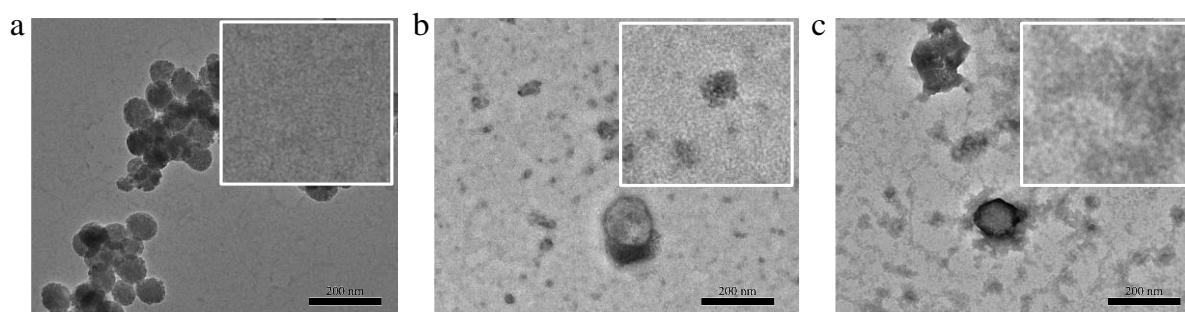


Figure 3.

Images of TEM. a) MSN, b) cCM, and c) cCMCMSN. Scale bar, 200 nm.

Determination of cell membrane protein on cCMCMSN

The SDS-PAGE was used to separate protein from coated nanoparticles. The result showed that cell lysis, cCM, and cCMCMSN presented bands of proteins. The bands of protein presence on cCMCMSN were similar to the protein presented from the isolated cardiac cell membrane (cCM). However, there were no proteins present in MSN **Figure 4**.

The membrane protein ingredients of MSN, cCM, and cCMCMSN were demonstrated by SDS-PAGE **Figure 4**. The cell lysis (AC19 cells) was separated to be the whole proteins for evaluation with other nanoparticles. cCM, extracted AC16 cells, had protein ingredients similar to cell lysis. However, some bands disappeared due to centrifugation for isolating membrane fragments from other cell components, such as mitochondria.⁵ The MSN had no protein bands suggesting they were not coated with cell membrane. cCMCMSN presented a similar protein band pattern as cCM, indicating that MSN was coated with cCM.

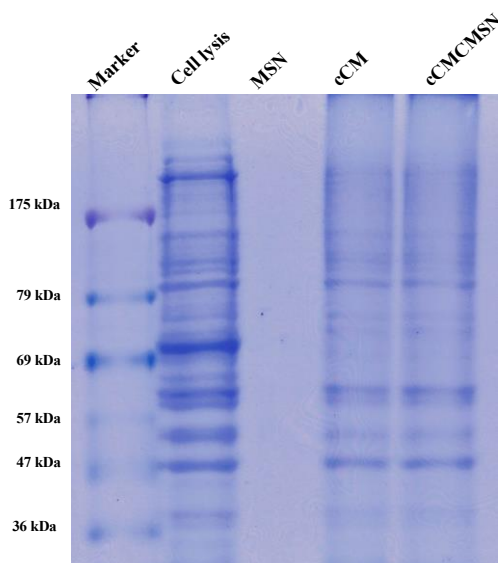


Figure 4.

Proteins are separated by SDS-PAGE containing protein marker, cell lysis, cCM, MSN, and cCMCMSN. Stained with Coomassie Brilliant Blue.

Encapsulation efficiency

The result showed encapsulation of MSN and cCMCMSN is $94.15 \pm 1.60\%$, and $94.53 \pm 0.81\%$, respectively.

In this study, we successfully encapsulated rhodamine B into nanoparticles. MSN can encapsulate rhodamine B almost 95 % of mass rhodamine B. In addition, cCM-coated MSN showed a percentage of encapsulation efficiency similar to MSN.

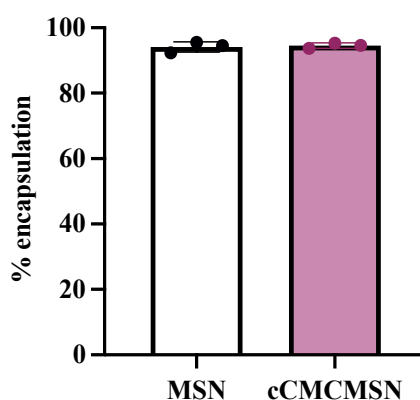


Figure 5.

Encapsulation of MSN and cCMCMSN

There are various limitations in this current study. The nanoparticles synthesized in this study have not been evaluated for drug release, cytotoxicity, and especially for selectivity targeting cardiac cells. Therefore, further determination of this study will focus on evaluating drug release, cytotoxicity, and specificity to cardiac cells. This has the potential to provide additional knowledge into the process of cell membrane coating and drug delivery.

The previous work indicated that secretory leukocyte protease inhibitor (SLPI) exhibits a cardioprotective effect against myocardial ischemia/reperfusion (I/R) injury.²²⁻²⁴ The previous study showed that gelatin-coated silica nanoparticles (GSNPs) utilized for encapsulating SLPI can decrease cell death during simulated ischemia/reperfusion (I/R) conditions.²⁵ The further study, we will utilize the cCMCMSN technique for delivering SLPI specifically to the heart, to reduce cellular damage caused by ischemia/reperfusion (I/R). We will perform a study outside of a living organism on a heart that has been separated from the body, or we will use an animal model where we tie off the left anterior descending (LAD) coronary artery. The purpose of this study is to evaluate how successful cCMCMSN is in delivering SLPI specifically to the heart, to lower the extent of tissue damage caused by a heart attack and improve the overall function of the heart.

Conclusion:

In conclusion, this is the first study of cardiac cell membrane-coated mesoporous silica nanoparticles for cardiac delivery. We could extract and isolate the cardiac cell membrane by using homogenization, and sonication and coat it by sonication and extrusion. The cCMCMSN has the potential to be used for the delivery of drugs.

Acknowledgements:

The present study was supported by Chiang Mai University for SK, CMU Presidential Scholarship 2023 from Multidisciplinary and Interdisciplinary School, Chiang Mai University for FP. We would like to acknowledge Biomedical Engineering Institute (BMEI),



Chiang Mai University for travel grant to attend STT50. This project was funded by National Research Council of Thailand (NRCT): High-Potential Research Team Grant Program Contract no. N42A650870.

References:

1. Khan MA, Hashim MJ, Mustafa H, Baniyas MY, Al Suwaidi S, AlKatheeri R, et al. *Cureus*. 2020;12:e9349.
2. Gunata M, Parlakpınar H. *Cell Biochem Funct*. 2021;39:190-217.
3. Maxwell SR, Lip GY. *Int J Cardiol*. 1997;58:95-117.
4. Patra JK, Das G, Fraceto LF, Campos EVR, Rodriguez-Torres MdP, Acosta-Torres LS, et al. *Journal of Nanobiotechnology*. 2018;16:71.
5. Fernández-Borbolla A, García-Hevia L, Fanarraga ML. *Int J Mol Sci*. 2024;25.
6. Kiaie SH, Majidi Zolbanin N, Ahmadi A, Bagherifar R, Valizadeh H, Kashanchi F, et al. *J Nanobiotechnology*. 2022;20:276.
7. Hu C-MJ, Zhang L, Aryal S, Cheung C, Fang RH, Zhang L. *Proceedings of the National Academy of Sciences*. 2011;108:10980-5.
8. Luk BT, Zhang L. *J Control Release*. 2015;220:600-7.
9. Zhu C, Ma J, Ji Z, Shen J, Wang Q. *Molecules*. 2021;26.
10. Xia Q, Zhang Y, Li Z, Hou X, Feng N. *Acta Pharmaceutica Sinica B*. 2019;9:675-89.
11. Chu D, Dong X, Shi X, Zhang C, Wang Z. *Adv Mater*. 2018;30:e1706245.
12. Peng R, Ji H, Jin L, Lin S, Huang Y, Xu K, et al. *J Immunol Res*. 2020;2020:8131754.
13. Thamphiwatana S, Angsantikul P, Escajadillo T, Zhang Q, Olson J, Luk BT, et al. *Proc Natl Acad Sci U S A*. 2017;114:11488-93.
14. Wang S, Duan Y, Zhang Q, Komarla A, Gong H, Gao W, et al. *Small Struct*. 2020;1.
15. Fang RH, Hu C-MJ, Luk BT, Gao W, Copp JA, Tai Y, et al. *Nano Letters*. 2014;14:2181-8.
16. Wang M, Xin Y, Cao H, Li W, Hua Y, Webster TJ, et al. *Biomaterials Science*. 2021;9:1088-103.
17. Rahmani S, Durand J-O, Charnay C, Lichon L, Férid M, Garcia M, et al. *Solid State Sciences*. 2017;68:25-31.
18. Jang Y, Cho YS, Kim A, Zhou X, Kim Y, Wan Z, et al. *ACS Appl Mater Interfaces*. 2024;16:17129-44.
19. Danaei M, Dehghankhold M, Ataei S, Hasanzadeh Davarani F, Javanmard R, Dokhani A, et al. *Pharmaceutics*. 2018;10.
20. Vaisman L, Marom G, Wagner HD. *Advanced Functional Materials*. 2006;16:357-63.
21. Kankala RK, Han YH, Xia HY, Wang SB, Chen AZ. *J Nanobiotechnology*. 2022;20:126.
22. Nernpermpisooth N, Prompant E, Kumphune S. *Exp Ther Med*. 2017;14:5793-800.
23. Mongkolpathumrat P, Kijawornrat A, Suwan E, Unajak S, Panya A, Pusadee T, et al. Anti-Protease Activity Deficient Secretory Leukocyte Protease Inhibitor (SLPI) Exerts Cardioprotective Effect against Myocardial Ischaemia/Reperfusion. *Biomedicines* [Internet]. 2022; 10(5).
24. Kongpol K, RY, Nitirut Nernpermpisooth, SK. Recombinant human secretory leukocyte protease inhibitor ameliorated vessel preservation in experimentally isolated rat arteries: Issue: 9; 2020. 107-14 p.
25. Pikwong F, Phutiyothin C, Chouyatchakarn W, Baipaywad P, Mongkolpathumrat P, Kumphune S. *Heliyon*. 2023;9:e20150.



IMMOBILIZATION OF RECOMBINANT HUMAN SECRETORY LEUKOCYTE PROTEASE INHIBITOR (RHSLPI), BY PLASMATIZATION ON TITANIUM SURFACE, ENHANCED OSTEOBLAST CELL ADHESION

Wannapat Chouyatchakarn^{1,2}, Norrapon Vichiansan³, Phornsawat Baipaywad^{1,2}, Chayarop Supanchart^{2,4}, Nithi Atthi⁵, Suruk Udomsom^{1,2}, Sarawut Kumphune^{1,2*}

¹Biomedical Engineering Institute, Chiang Mai University, Chiang Mai 50200, Thailand

²Biomedical Engineering and Innovation Research Center, Chiang Mai University, Mueang Chiang Mai District, Chiang Mai, 50200 Thailand

³Center of integrated Engineering, Faculty of Engineering, Chiang Mai University, Chiang Mai 50200, Thailand

⁴Department of Oral and Maxillofacial Surgery, Faculty of Dentistry, Chiang Mai University, Chiang Mai 50200, Thailand

⁵Thai Microelectronics Center (TMEC), National Science and Technology Development Agency (NSTDA), 111 Thailand Science Park, Phahonyothin Road, Khlong Nueng, Khlong Luang, Pathum Thani, 12120, Thailand

*e-mail: sarawut.kumphune@cmu.ac.th

Abstract:

Osseointegration is a crucial process in which bone cell ingrowth into a metal medical or dental implant. Titanium (Ti) surface modification was used to improve the osseointegration and success rate of implantation. Surface modification by plasmatisation or protein coating has been shown to improve osteoblasts adhesion. Our recent study showed that coating Ti surface with recombinant human secretory leukocyte protease inhibitor (rhSLPI) enhanced osteoblast adhesion, proliferation, and differentiation. However, plasmatisation of Ti surface enhancing rhSLPI coating and efficiency for osteoblast adhesion has never been studied. In this study, we hypothesized that a plasma-treated titanium coating with rhSLPI could enhance physical properties of Ti and osteoblast adhesion. Firstly, The Ti was treated with Argon plasma under the pressure of 1.1×10^{-1} Tor at 2 W for 2 min and then coated with 10 $\mu\text{g/mL}$ recombinant human SLPI (rhSLPI) for 24 h. The physical characteristics were investigated, including surface morphology, hydrophilicity, and roughness. Moreover, human fetal osteoblast 1.19 (hFOB 1.19) was used to evaluate cell adhesion. The results indicated that rhSLPI-coated PTi had higher surface hydrophilicity and roughness compared to rhSLPI-coated Ti by using sessile drop method and non-contact roughness measurement method, respectively. The ELISA confirmed that rhSLPI was coated on PTi. Finally, the scanning electron microscope (SEM) revealed that the rhSLPI-coated PTi could provide higher cell adhesion and cell spreading on the surface. In conclusion, rhSLPI coating on plasmatised Ti could be a novel strategy for immobilizing rhSLPI that enhances osseointegration and successful of implantation.

Introduction:

For decades, titanium and its alloy have been widely used for dental and orthopedic implantation to replace missing or lost teeth or bones [1]. The outstanding properties of titanium and its alloy are biocompatibility, high strength, resistance to corrosion, and low allergenicity [2]. Moreover, the key success for dental and orthopedic implantation is osseointegration, which is the phenomenon of connection between living bone tissue and the

surface of implant materials [3]. However, the successful rate of implantation reduce in elderly patients and those with bone disorders and other comorbidities [4]. Furthermore, the effectiveness of bone implantation also depends on physical properties of the Ti including the roughness, morphology, chemistry, hydrophilicity, and hydrocarbon impurity of the Ti surface [5, 6]. Therefore, modification of Ti surface could be an alternative strategy to improve osseointegration [7].

Plasma is the fourth stage of matter, which is the ionized gas [3]. The plasma contains various active molecules, including free electrons, free radicals (hydroxyl radicals; OH^\cdot), and energetic photons (UV), etc. [3, 8]. The plasmas have been used to treat material surfaces for hydrocarbon decontamination, increase surface energy, wettability, sterilization, etc. [9, 10]. Moreover, the non-thermal plasma has been used to treat the Ti surface to enhance osteoblast cell adhesion, proliferation, and mineralization [11, 12]. In addition, the pure Ti discs were treated with Argon-based non-thermal plasma to improve the rat's periodontal ligament fibroblast-like cells spreading [13]. Hence, plasma-enhanced chemical vapor deposition (PEVCD), which is non-thermal plasma in vacuum conditions was used in this current study to treat Ti surface. Previous study showed that plasma treatment to modify the Ti surface could enhance osteoblast adhesion [14]. Moreover, plasmatization on the surface also enhances biomolecules immobilization on Ti surface [14].

The SLPI is an 11.7 kDa serine protein that was secreted from mucosal tissues [15]. Moreover, SLPI has interesting pharmacological properties, such as being able to reduce cell death from apoptosis, reduce inflammation, and increase antioxidants, antibacterial, fungi, and viruses infection, and improve wound healing, bone cell proliferation, and differentiation [15-17]. In the previous study, rhSLPI coating on titanium in phosphate-buffered saline (PBS) was found to be non-toxic to human bone cells, and significantly enhanced human bone cell adhesion [18]. It is suggested that SLPI could also be a candidate for a coating agent due to it could provide other benefits, such as reducing inflammation [19], promoting osteoblast cell differentiation and mineralization [20], increasing wound healing [15], and reducing infection [21]. Nevertheless, the application of a simple coat of rhSLPI on Ti may exhibit limited durability, especially under *in vivo* conditions, hence impacting the practicality of using rhSLPI coating on Ti implants in clinical settings. The objective of this work is to create a more effective method for coating recombinant human SLPI onto plasma-treated Ti in order to improve the adherence of human osteoblast cells.

Methodology:

The surface modification of Ti was separated into 2 major steps, which is plasma treatment and rhSLPI immobilization (Figure 1).

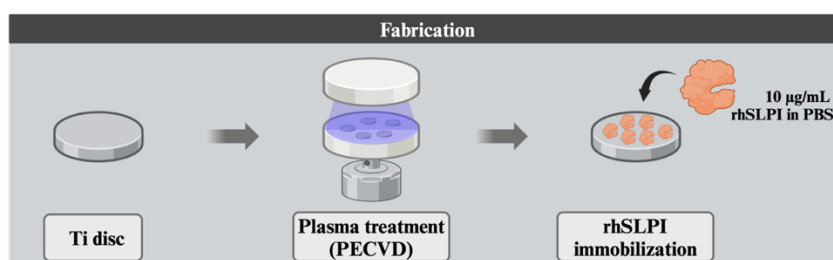


Figure 1. A schematic diagram of experimental design. The study includes the fabrication step where the Ti was treated with plasma and then coated with rhSLPI.

Material and chemical reagents



The grade 4 titanium discs (Ti) were cut into 5.5 mm in diameter and 0.5 mm in thickness and 12 mm in diameter and 0.5 in thickness for 96 well plate and 24 well plate, respectively. The Ti was washed in acetone, ethanol, and ultrapure water (10 min in each step) in an ultrasonic bath. Then the Ti was autoclaved and placed in a hot air oven until dried.

Recombinant human secretory leukocyte peptidase inhibitor (rhSLPI) was purchased from Sino Biology Inc. (Beijing, China), and Dulbecco's modified Eagle's medium (DMEM): Ham's F-12 media, foetal bovine serum (FBS), and trypsin-EDTA were purchased from Gibco BRL; Life Technologies Inc. (New York, USA).

Cell type and cell culture

The hFOB 1.19 cell was purchased from American Type Cell Culture (ATCC CRL-11372TM). Cells were cultured with a 1:1 mixture of Ham's F12 Medium and Dulbecco's Modified Eagle's Medium, with 2.5 mM L-glutamine (without phenol red), supplemented with 10% (v/v) foetal bovine serum (FBS), a one percent of 5,000 units/ml of penicillin, and 5000 µg/ml of streptomycin (Gibco®). For culture conditions, the hFOB 1.19 cells were cultured at 37°C with 5% carbon dioxide (CO₂) and 95% air.

Surface modification

The samples were randomly divided into four groups: the conventional titanium discs with/without rhSLPI as a control (Ti ± rhSLPI) and plasma-treated titanium discs with/without rhSLPI as an experimental group (PTi ± rhSLPI). The plasma-enhanced chemical vapor deposition system (PECVD) was used for Ti surface treatment. The Ti discs were treated with Argon plasma under the pressure of 1.1×10^{-1} Tor at 2 W for 2 min for both sides of the surface.

rhSLPI coating

The Ti or PTi were placed into the well plate. Then 10 µg/mL of rhSLPI was diluted in PBS which is the optimal concentration that could enhance cell adhesion from the previous study [18] and added to well at 100 µL/well. The well plate was sealed with parafilm and incubated at 4°C for 24 h.

Surface characterization

The Ti surface characterization was divided into 3 experiments, including surface morphology, surface hydrophilicity, and roughness. The surface morphology was observed by field emission scanning electron microscope (FE-SEM, JSM-IT800; JEOL, Tokyo Japan).

The Ti surface was analyzed hydrophilicity by using the sessile drop method, which is 5 µL of deionized water was dropped on the Ti surface and captured photo of the water droplet. Then, the photos were analyzed the contact angle of a water droplet on the surface of Ti.

Finally, the roughness of the Ti surface was determined by using the non-contact roughness measurement method of a 3D measuring laser microscope (OLS5100 LEXT; Olympus®, Tokyo Japan) at 20x magnification. The data was calculated into average roughness (Ra) and compared to control groups.

Determination of rhSLPI adsorption on titanium surface

The adsorption of rhSLPI on the Ti surface was determined by using a single-wash sandwich enzyme-linked immunosorbent assay (ELISA) kit (Abcam, Cambridge UK). After the coating assay, the Ti was washed with PBS for 5 min thrice on an orbital shaker and air

dried at room temperature. Then the Ti was transferred into a new 96-well plate and incubated with the anti-rhSLPI antibody coated with HRP for 1 h on an orbital shaker at room temperature. After incubation, the solution was discarded and washed thrice with 350 μL /well washing buffer. The TMB working solution was added and incubated at room temperature for 10 min. Finally, the stop-working solution was added and determined by a microplate spectrophotometer (O.D. 450 nm).

Adhesion assay

The adhesion assay was used to determine the adhered cells by using the FE-SEM for cellular morphology. Firstly, cells were seeded to 96 well plate at the concentration of 2.5×10^5 cells/mL and incubated for 20 min at 37°C with 5% CO₂ and 95% air. Then the culture media was removed, and the adhered cells were fixed on the Ti surface with 2.5% (v/v) glutaraldehyde and incubated at room temperature for 30 min. Then, the Ti was replaced with a new 96-well plate and dried in a hot air oven overnight. The number of adhered cells were showed as a preliminary quantitative data by count the adhered cells per unit area under SEM. The morphology of adhered cells was observed under FE-SEM.

Statistical analysis

Statistical analysis was analyzed using commercially available software (GraphPad Prism version 10, San Diego, CA, USA). All data are expressed as mean \pm SD. All comparisons were assessed for significance using an unpaired t-test or ANOVA, followed by, when appropriate, the Turkey-Kramer test. A p-value less than 0.05 was considered statistically significant.

Results and Discussion:

Physical characteristics

The morphology of the Ti and PTi surfaces was observed by scanning electron microscope (Figure 2A). The surface of both uncoated Ti and PTi showed scratch lines without a particular appearance on the surface. In contrast, the surface of both rhSLPI-coated Ti and PTi showed a mucus-like appearance coated on the surface. The rhSLPI-coated Ti showed a significantly reduced contact angle compared to uncoated (22.34° \pm 3.386° vs. 13.36° \pm 4.735°, $p < 0.05$), while rhSLPI-coated PTi was not significantly different to uncoated PTi. However, rhSLPI-coated PTi more greatly reduced the angle than rhSLPI-coated Ti (1.297° \pm 2.246° vs. 13.360° \pm 4.735°, $p < 0.05$, respectively) (Figure 2B). For surface roughness, the rhSLPI-coated Ti showed significantly greater in average surface roughness (Ra) when compared with rhSLPI-coated PTi (0.346 \pm 0.014 μm vs. 0.421 \pm 0.045 μm , $p < 0.05$, respectively) (Figure 2C).

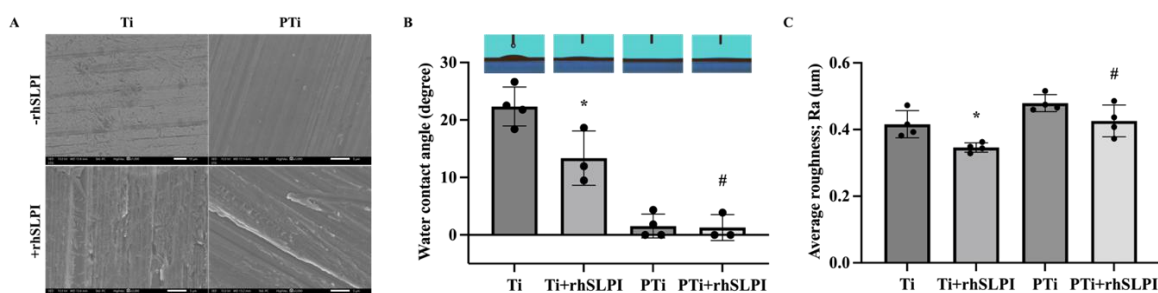


Figure 2. The physical characteristics of modified Ti surface. Scanning electron microscope (SEM) showed the surface morphology of Ti surfaces (A), including uncoated Ti, rhSLPI-coated Ti, uncoated PTi, and rhSLPI-coated PTi. The hydrophilicity of the Ti surface was



measured by the water contact angle method (B). The surface roughness was determined by using the non-contact roughness measurement method (C).

The presence of rhSLPI on surfaces was confirmed by using an enzyme-linked immunosorbent assay (ELISA). The result showed that rhSLPI protein on Ti + rhSLPI and PTi + rhSLPI (0.332 ± 0.059 and 0.312 ± 0.064 , $p < 0.05$, respectively) was significantly higher than control of each group. Nevertheless, there is no statistical difference between PTi + rhSLPI and Ti + rhSLPI (Figure 3).

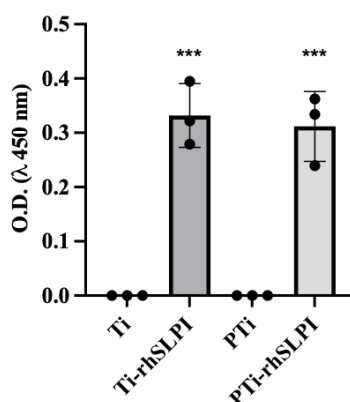


Figure 3. The adsorption of rhSLPI on Ti surface. After protein coating, the Ti was measured protein by using ELISA.

The current study, the grade 4 titanium disc, which is a high purity titanium, was used since its properties include biocompatibility, high corrosion resistance, and suitability for dental implants and screws [2]. However, grade 4 Ti still faces a drawback compared to grade 5 Ti, also known as Ti-6Al-4V, which is widely used in dental implantation due to its higher strength [22]. However, in this study, the grade 4 Ti is used as a model for studying metal implant coatings, and further studies will be conducted on medical grade Ti and other implant materials.

The physical characteristics were observed by surface morphology, hydrophilicity, and roughness. The morphology of both rhSLPI uncoated Ti and PTi have scratch lines, which occurred from the cutting process. While rhSLPI-coated Ti and PTi have a mucus-like appearance on the surface, which might be the rhSLPI protein coating on the surface (Figure 2A). Determination of SLPI level by ELISA confirmed the presence of rhSLPI on the Ti and PTi surface, suggesting that rhSLPI was coated on both of Ti and PTi (Figure 3). Furthermore, coating Ti with rhSLPI increased its hydrophilicity, which is consistent with previous study [18]. The hydrophilicity greatly increased after the surface was treated with plasma and coated with rhSLPI (Figure 2B). Although rhSLPI-coated PTi had less roughness than uncoated PTi, the difference was not statistically significant, while rhSLPI-coated Ti had significantly less roughness than uncoated Ti (Figure 2C). the decreasing of surface roughness after rhSLPI coating that might be due to the protein layer filling and covering the grooves of both Ti and PTi surface.

Human osteoblast cell adhesion and spreading on modified Ti

hFOB 1.19 cells were seeded on Ti and PTi that were coated with rhSLPI and incubated for 20 min. After incubation, the morphology of adhered cells on the surface was

observed under SEM (Figure 4). The results showed that adhered cells on control uncoated was less cell number attached on the surface (15 cells/observe field) (Figure 4A) with small round morphology (Figure 4C). However, rhSLPI coated Ti showed greater number of adherent cells on surface (20 cells/observe field) (Figure 4B) and cells exhibited grater cytoplasmic expansion compared to uncoated Ti (Figure 4D). The cells on PTi without rhSLPI showed the number of cells attached to the PTi surface similar to rhSLPI coated Ti (Figure 4E) (28 cells/observe field). In contrast, the morphology of cells showed that had more spreading and extension compared to Ti \pm rhSLPI, but cells were round in shape (Figure 4F). Additionally, rhSLPI coated PTi showed more spreading, extension, and expansion of cells cytoplasm, resulting the shape of cells was flatten compared to Ti \pm rhSLPI and PTi – rhSLPI (Figure 4H).

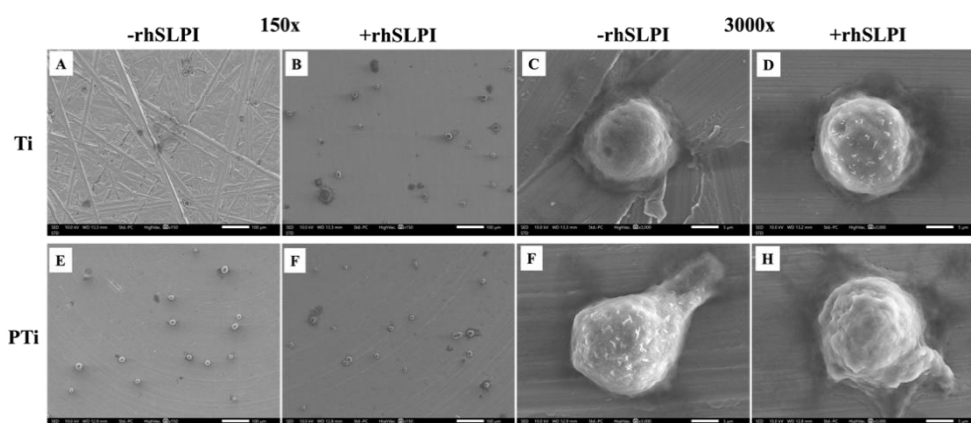


Figure 4. The morphology of adhered cells on Ti surface. The SEM images showed the morphology of hFOB 1.19 cells on Ti \pm rhSLPI and PTi \pm rhSLPI.

After the Ti surface was modified, human foetal osteoblast cells were used to observe the efficacy of modified Ti to enhance cell adhesion. The results showed that rhSLPI-coated PTi enhanced cell adhesion and spread higher than the control group. Moreover, the combination of plasma treatment and rhSLPI coating revealed that had higher cell adhesion, spreading, and extension compared to rhSLPI-coated Ti and uncoated PTi (Figure 4H). The previous studies showed that plasma-treated Ti could improve early cell adhesion on the Ti surface since the Ti surface after plasma treatment exhibited higher surface energy, wettability, and hydrocarbon decontamination [9, 10]. The increase in surface energy improves surface wettability or hydrophilicity, allowing more protein adsorption, particularly adhesion-associated proteins, on the material surface, resulting in more cells adhering to the surface [23]. Moreover, the *in vitro* study revealed that the hydrocarbon layer on the Ti surface could reduce cell attachment and suppress cell spreading [24]. After modification, rhSLPI was used to improve the efficacy of Ti to enhance osteoblast cell adhesion. The previous studies revealed that rhSLPI-encapsulated liposome nanoparticles could enhance human osteoblast cell adhesion, proliferation, and differentiation [25]. Additionally, the rhSLPI was used to coat Ti with a simple coat technique, increasing human osteoblast cell adhesion, spreading, proliferation, and differentiation through focal adhesion kinase (FAK) and extracellular-signal-regulated kinase (ERK) signaling pathway [18, 26]. In addition to enhancing osteoblast cell activities, SLPI also has anti-inflammation, and anti-microorganism, increasing cell survival, and proliferation, and improving wound healing [15-17]. Thus, the combination of plasma treatment and rhSLPI coating on Ti might be used as a novel surface modification technique for metal implant material in real clinical usage in dental and orthopedic implantation



However, the present study also had some limitations. Firstly, the cytotoxicity of modified Ti has not been demonstrated. Nevertheless, previous studies showed that rhSLPI, Ti, rhSLPI coated Ti and PTi are nontoxic [3, 18]. In this study, the evaluation of cell adhesion provided only preliminary quantitative and qualitative results that lacked the accurate quantitative result. Moreover, several issues must be considered for further investigation such as stability, protein release, cytotoxicity, cell proliferation, and cell differentiation. Finally, the present study revealed *in vitro* effects that lacked the data for clinical impact. For future study, the *in vivo* study should be performed, particularly in animal experiments to reveal the real effect of rhSLPI-coated PTi.

Conclusion:

The conclusion of this current study, this is the first study to develop Ti surface modification technique by using a combination of plasma treatment and rhSLPI that could enhance human osteoblast cell adhesion.

Acknowledgements:

The present study was supported by CMU Presidential Scholarship 2023 from Multidisciplinary and Interdisciplinary School, Chiang Mai University for WC. We would like to acknowledge Biomedical Engineering Institute (BMEI), Chiang Mai University for travel grant to attend STT50. We would like to thank the Agriculture and Bio Plasma Technology Center (ABplas), Science and Technology Park (STeP), Chiang Mai University for providing laboratory facilities.

References:

1. Hossain N, Islam MA, Shakib Ahmed MM, Chowdhury MA, Mobarak MH, Rahman MM, Helal Hossain MD. Advances and significances of titanium dental implant applications. Results in Chemistry. 2024;7:101394.
2. Ahn T-K, Lee DH, Kim T-s, Jang Gc, Choi S, Oh JB, et al. Modification of Titanium Implant and Titanium Dioxide for Bone Tissue Engineering. In: Chun HJ, Park K, Kim C-H, Khang G, editors. Novel Biomaterials for Regenerative Medicine. Singapore: Springer Singapore; 2018. p. 355-68.
3. Yan M, Hartjen P, Gosau M, Vollkommer T, Grust ALC, Fuest S, et al. Effects of a Novel Cold Atmospheric Plasma Treatment of Titanium on the Proliferation and Adhesion Behavior of Fibroblasts. International Journal of Molecular Sciences. 2022;23(1):420.
4. Qiao K, Xu L, Tang J, Wang Q, Lim KS, Hooper G, et al. The advances in nanomedicine for bone and cartilage repair. Journal of Nanobiotechnology. 2022;20(1):141.
5. Borges AMG, Benetoli LO, Licínio MA, Zoldan VC, Santos-Silva MC, Assreuy J, et al. Polymer films with surfaces unmodified and modified by non-thermal plasma as new substrates for cell adhesion. Materials Science and Engineering: C. 2013;33(3):1315-24.

6. Lee H, Jeon HJ, Jung A, Kim J, Kim JY, Lee SH, et al. Improvement of osseointegration efficacy of titanium implant through plasma surface treatment. *Biomedical Engineering Letters*. 2022;12(4):421-32.
7. Yeo I-SL. Modifications of Dental Implant Surfaces at the Micro- and Nano-Level for Enhanced Osseointegration. *Materials*. 2020;13(1):89.
8. Robert E, Darny T, Dozias S, Iseni S, Pouvesle JM. New insights on the propagation of pulsed atmospheric plasma streams: From single jet to multi jet arrays. *Physics of Plasmas*. 2015;22(12):122007.
9. Swart KM, Keller JC, Wightman JP, Draughn RA, Stanford CM, Michaels CM. Short-term plasma-cleaning treatments enhance in vitro osteoblast attachment to titanium. *J Oral Implantol*. 1992;18(2):130-7.
10. Canullo L, Genova T, Tallarico M, Gautier G, Mussano F, Botticelli D. Plasma of Argon Affects the Earliest Biological Response of Different Implant Surfaces: An In Vitro Comparative Study. *Journal of Dental Research*. 2016;95(5):566-73.
11. Canullo L, Genova T, Gross Trujillo E, Pradies G, Petrillo S, Muzzi M, et al. Fibroblast Interaction with Different Abutment Surfaces: In Vitro Study. *International Journal of Molecular Sciences*. 2020;21(6):1919.
12. Duske K, Koban I, Kindel E, Schröder K, Nebe B, Holtfreter B, et al. Atmospheric plasma enhances wettability and cell spreading on dental implant metals. *J Clin Periodontol*. 2012;39(4):400-7.
13. Michaels CM, Keller JC, Stanford CM. In vitro periodontal ligament fibroblast attachment to plasma-cleaned titanium surfaces. *J Oral Implantol*. 1991;17(2):132-9.
14. Wieland F, Bruch R, Bergmann M, Partel S, Urban GA, Dincer C. Enhanced Protein Immobilization on Polymers-A Plasma Surface Activation Study. *Polymers (Basel)*. 2020;12(1).
15. Nugteren S, Samsom JN. Secretory Leukocyte Protease Inhibitor (SLPI) in mucosal tissues: Protects against inflammation, but promotes cancer. *Cytokine Growth Factor Rev*. 2021;59:22-35.
16. Majchrzak-Gorecka M, Majewski P, Grygier B, Murzyn K, Cichy J. Secretory leukocyte protease inhibitor (SLPI), a multifunctional protein in the host defense response. *Cytokine Growth Factor Rev*. 2016;28:79-93.
17. McNeely TB, Dealy M, Dripps DJ, Orenstein JM, Eisenberg SP, Wahl SM. Secretory leukocyte protease inhibitor: a human saliva protein exhibiting anti-human immunodeficiency virus 1 activity in vitro. *J Clin Invest*. 1995;96(1):456-64.



18. Leelasukseree R, Chouyratchakarn W, Phutiyothin C, Pikwong F, Srisopar O, Baipaywad P, et al. Recombinant human secretory leukocyte protease inhibitor (rhSLPI) coated titanium enhanced human osteoblast adhesion and differentiation. *Scientific Reports*. 2023;13(1):23013.
19. Menckeberg CL, Hol J, Simons-Oosterhuis Y, Raatgeep HC, de Ruiter LF, Lindenberg-Kortleve DJ, et al. Human buccal epithelium acquires microbial hyporesponsiveness at birth, a role for secretory leukocyte protease inhibitor. *Gut*. 2015;64(6):884.
20. Choi BD, Lee SY, Jeong SJ, Lim DS, Cha HJ, Chung WG, Jeong MJ. Secretory leukocyte protease inhibitor promotes differentiation and mineralization of MC3T3-E1 preosteoblasts on a titanium surface. *Mol Med Rep*. 2016;14(2):1241-6.
21. Fernie-King BA, Seilly DJ, Davies A, Lachmann PJ. Streptococcal inhibitor of complement inhibits two additional components of the mucosal innate immune system: secretory leukocyte proteinase inhibitor and lysozyme. *Infect Immun*. 2002;70(9):4908-16.
22. Elias CN, Lima JHC, Valiev R, Meyers MA. Biomedical applications of titanium and its alloys. *JOM*. 2008;60(3):46-9.
23. Pistilli R, Genova T, Canullo L, Faga MG, Terlizzi ME, Gribaudo G, Mussano F. Effect of Bioactivation on Traditional Surfaces and Zirconium Nitride: Adhesion and Proliferation of Preosteoblastic Cells and Bacteria. *Int J Oral Maxillofac Implants*. 2018;33(6):1247-54.
24. Hayashi R, Ueno T, Migita S, Tsutsumi Y, Doi H, Ogawa T, et al. Hydrocarbon Deposition Attenuates Osteoblast Activity on Titanium. *Journal of dental research*. 2014;93.
25. Chouyratchakarn W, Phutiyothin C, Pikwong F, Chaiwarit T, Baipaywad P, Kumphune S. Development of liposome nanoparticles for delivering recombinant human secretory leukocyte protease inhibitor (rhSLPI) for enhancing osteoblast proliferation, adhesion, and differentiation: The Graduate School, Chiang Mai University Chiang Mai; 2023.
26. Jeong SJ, Wang G, Choi BD, Hwang YH, Kim BH, Ko YM, Jeong MJ. Secretory Leukocyte Protease Inhibitor (SLPI) Increases Focal Adhesion in MC3T3 Osteoblast on Titanium Surface. *J Nanosci Nanotechnol*. 2015;15(1):200-4.

SP7-CEMENT AND CONCRETE: SCIENCE, TECHNOLOGY AND APPLICATIONS
TOWARDS GREEN AND SUSTAINABLE FUTURE



Effect of Plasma Activated Water on Early-Age Hydration Reaction and Strength Activity Index of Fly-Ash Cement Paste

Kittiphat Kochchamong, Pitiwat Wattanachai*, Sattaya Chaiwithee, Thaloengsak Keereemasthong

Department of Civil Engineering, Faculty of Engineering, Chiang Mai University, 50200, Thailand

*e-mail: Pitiwat@step.cmu.ac.th

Abstract:

This study explores the impact of Plasma-Activated Water (PAW) on the early-stage properties of cementitious mixtures incorporating varying levels of fly ash (FA) replacement. Plasma technology, which utilizes a plasma jet process with argon and 2% oxygen, offers a cleaner energy approach by generating reactive species that enhance chemical reactions. Cement pastes were prepared with a water-to-cement ratio of 0.289, with FA replacement at 0%, 10%, 20%, and 30%. The PAW used in this experiment was produced through this innovative plasma process. The findings demonstrate that PAW reduces the hydrated temperature, which correlates with a drop in the strength activity index (SAI) for PAW samples. Despite this, PAW-treated samples exhibited increased strength with higher FA replacement, in contrast to normal water samples, which showed a decrease in strength as FA replacement increased. SEM analysis confirmed that PAW samples developed a denser microstructure with more additional C-S-H formation from FA particles compared to normal samples. These samples exhibited an upward trend in strength with increasing fly ash replacement, indicating potential long-term improvements when using PAW. These findings suggest that PAW has the potential to enhance the performance of cementitious mixtures by improving pozzolanic reactivity while offering environmental benefits.

Introduction:

Concrete is a fundamental construction material used worldwide, and improving its environmental impact is essential. Efforts to make concrete more sustainable include substituting Ordinary Portland Cement (OPC) with supplementary cementitious materials (SCMs) such as fly ash, ground granulated blast furnace slag (GGBFS), and silica fume. Fly ash, a major by-product from coal-fired power plants like the Mae Moh power plant, is particularly valuable. Recognizing its benefits, the construction industry uses fly ash to enhance concrete properties, including workability, durability, and long-term strength [1]. Its pozzolanic properties help generate additional calcium silicate hydrate (C-S-H), boosting concrete performance.

However, SCMs often exhibit lower initial reactivity compared to OPC, which can impact early-age strength development. The binding mechanisms and rate of strength gain of SCMs can also differ from OPC. To achieve similar performance, particularly in early strength and workability, Plasma-Activated Water (PAW) presents a promising solution. Plasma-activated water (PAW) has primarily been researched in biological fields, particularly in food and agriculture [2], but its application in materials work, especially in construction materials is still unexplored.



This study examined the effects of PAW on the early properties of cementitious mixtures with varying levels of fly ash (FA) replacement. It included temperature measurement to explore hydration reactions, strength activity index (SAI) tests to evaluate PAW's effectiveness with different fly ash levels, and morphological comparisons to confirm PAW's impact.

Methodology:

1. Materials

The cement used in the test was Type I Ordinary Portland cement with an average particle size of 9.08 μm . Fly Ash was obtained from the Mae Moh power plant in Lampang province, Thailand, with an average particle size of 12.46 μm . Both cumulative particle sizes are shown in Figure 1.

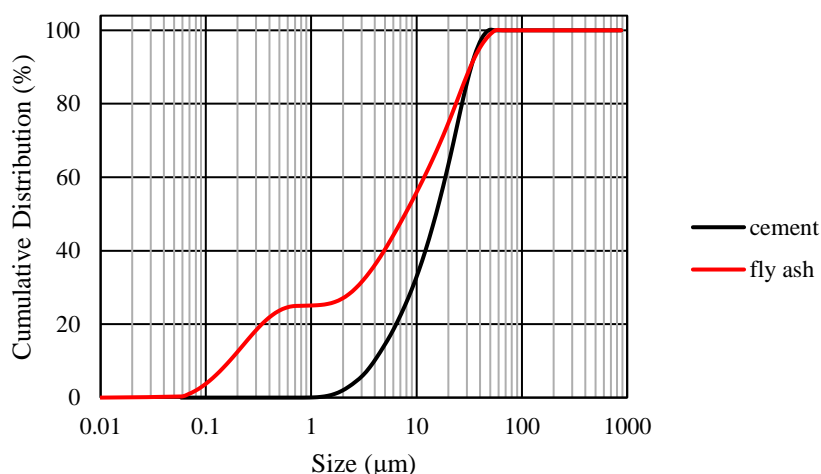


Figure 1 Cumulative particle size distribution of cement and fly ash

2. Preparation of Plasma-activated water (PAW)

Plasma-activated water (PAW) was produced using a specialized plasma jet system at the Agriculture and Bio Plasma Technology Laboratory (ABPlas), Science and Technology Park, Chiang Mai University. The process involved generating plasma radicals with argon gas (Ar) and an AC power supply (230 V/30W) applied to 1 liter of tap water. The system operated for 1 hour, with Ar gas flowing at 4 liters/min. The evaluation of the PAW's pH level and H_2O_2 content is shown in Table 1. It is shown that the water after the plasma process has a pH value of about 9.1 higher than normal water, which is 7.82, and a concentration of about 11 ppm higher than normal water.

Table 1 Properties of normal water and plasma-activated water (PAW)

| Sample | Temperature ($^{\circ}\text{C}$) | pH | H_2O_2 (ppm) |
|------------------------------|------------------------------------|------|------------------------------|
| Normal Water | 29.6 | 7.82 | 0 |
| Plasma Activated Water (PAW) | 33.0 | 9.1 | 11 |



Sawangrat, C [3] studied the effectiveness of pinhole plasma jet-activated water against degrading pesticides and decontaminating microorganisms in chili. The results showed that PAW can be used as a sanitizer in food production due to the reactive oxygen species (ROS), such as H_2O_2 , hydroxyl radicals, and ozone, which are generated during the plasma process. These ROS exhibit strong oxidative properties that can break down chemical bonds in pesticides and microbial cell membranes, effectively neutralizing contaminants.

3. Mix Proportion

The samples were prepared by mixing cement with normal water and plasma-activated water (PAW) at a w/c ratio of 0.289 with 0, 10, 20, and 30% fly ash replacement as shown in Table 2. The prepared cement pastes were cast in cube steel mold according to ASTM C109 [4].

Table 2 Mix proportion of samples

| Sample code | Mix proportion (%wt) | | | |
|-------------|----------------------|---------|--------------|------|
| | Cement | Fly ash | Normal water | PAW |
| nOPC | 100 | - | 28.9 | - |
| nFA10 | 90 | 10 | 28.9 | - |
| nFA20 | 80 | 20 | 28.9 | - |
| nFA30 | 70 | 30 | 28.9 | - |
| pFA10 | 90 | 10 | - | 28.9 |
| pFA20 | 80 | 20 | - | 28.9 |
| pFA30 | 70 | 30 | - | 28.9 |

4. Temperature measurement

The hydration temperature measurement using 62-L0071, CONTROLS calorimeter and UCAM-60B, KYOWA data logger. The cement paste samples were prepared using a w/c ratio of 0.289. The temperature of the hydrated cement paste is measured in this experiment as a function of time (min) using a temperature sensor thermocouple.

5. Strength Activity Index

The compressive strength test on the cement paste cube 50 x 50 x 50 mm. was prepared with a compression test machine according to the ASTM C109 [4] after 3 and 7 days of moisture curing. After that, the specimens were soaked with acetone to stop further reaction and stabilize the samples. Each specimen was immersed for 24 hours in a container and placed in individual Ziplock bags to prevent moisture absorption.

6. Scanning Electron Microscope (SEM)

Scanning Electron Microscope (SEM) is used to analyse fractured cement pastes microstructure at the Department of Packaging Technology, Faculty of Agro-Industry, Chiang Mai University. Samples were coated with gold (Au) for 60 seconds with JEOL Smart Coater. Then the sample was imported into the JEOL-IT200 SEM.

Results and Discussion:

Temperature Measurement

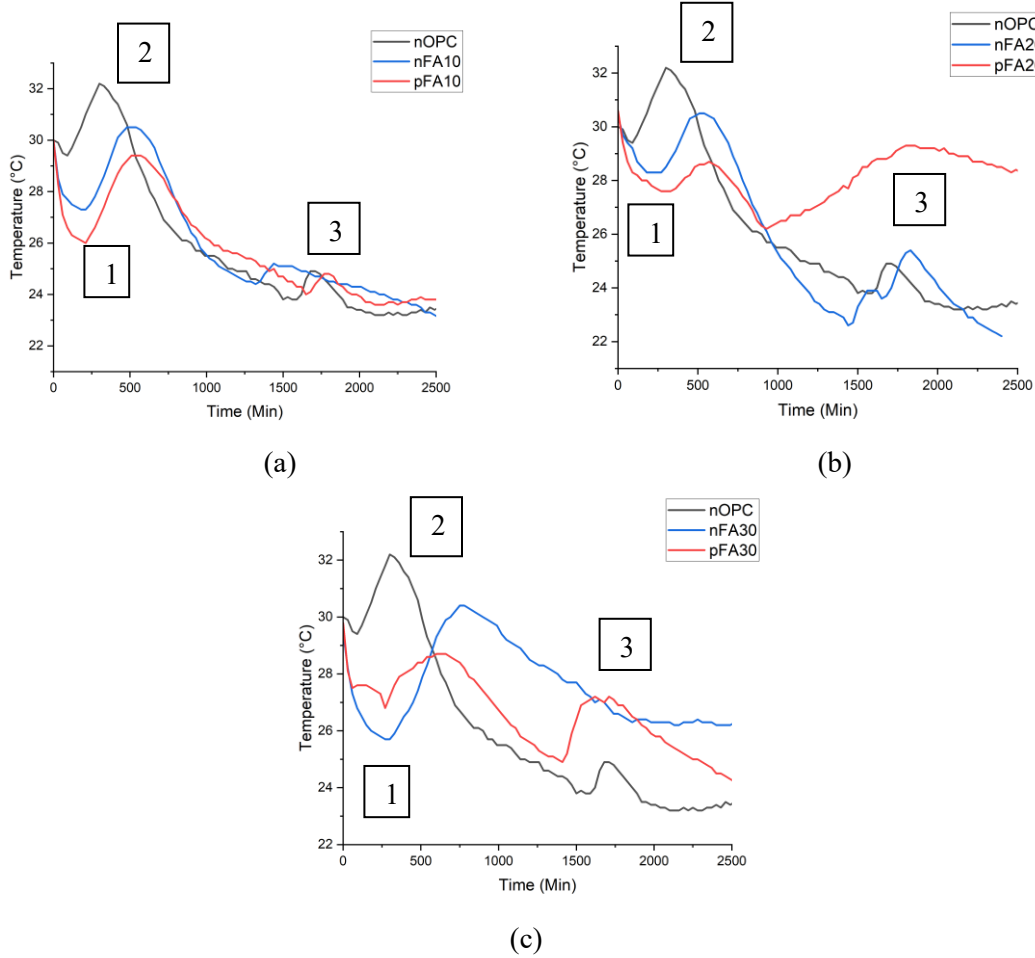


Figure 2 Hydration Heat results of (a) FA10 (b) FA20 (c) FA30

The results show that plasma-activated water (PAW) impacts the hydration temperature in three distinct phases, as illustrated in Figure 2. In the initial phase, nOPC shows a smaller temperature drop compared to nFA and pFA, likely due to the absence of hydration compounds in the fly ash samples. Interestingly, pFA experiences a larger temperature drop than nFA, suggesting a greater reduction in reactive compounds, such as OPC, and lower Ca^{2+} dissolution [5]. In the second phase, characterized by the hydration temperature peak and the growth of hydrated products (C-S-H and CH) [6], pFA shows a lower peak compared to nFA, indicating that PAW treatment more significantly affects pFA's reactivity. In the third phase, pFA displays a higher peak of additional hydrated products, such as ettringite (AFt) and aluminat ferrite monosulfate (AFm) [7], compared to nFA and nOPC. Mandal, R [8] studied the effect of electrolyzed water on cement hydration, showing that the increased presence of OH^- ions (higher pH) in electrolyte water (EW) accelerates the early hydration of C_3S by enhancing dissolution, nucleation, and crystal growth processes. The presence of H_2O_2 in PAW likely provides excess water, accelerating the reaction of ettringite with the remaining C_3A to form AFm. This suggests that PAW enhances the formation of these compounds more effectively in pFA.



Strength Activity Index (SAI)

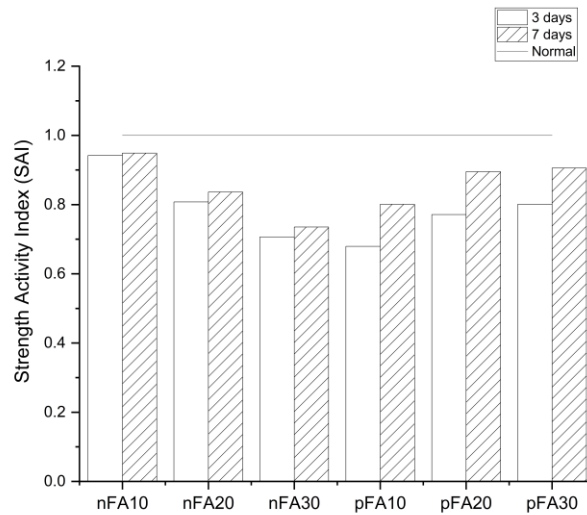


Figure 3 Strength activity index (SAI) of cement paste samples

Table 3 Compressive Strength (MPa) and Strength Activity Index (SAI) results

| Sample | Compressive Strength (MPa) | | Strength Activity Index (SAI) | |
|--------|----------------------------|--------|-------------------------------|--------|
| | 3 Days | 7 Days | 3 Days | 7 Days |
| nOPC | 58.612 | 63.311 | - | - |
| nFA10 | 55.208 | 60.082 | 0.942 | 0.949 |
| nFA20 | 47.338 | 52.953 | 0.808 | 0.836 |
| nFA30 | 41.424 | 46.558 | 0.707 | 0.735 |
| pFA10 | 39.829 | 50.711 | 0.680 | 0.801 |
| pFA20 | 45.217 | 56.680 | 0.771 | 0.895 |
| pFA30 | 46.967 | 57.353 | 0.801 | 0.906 |

The results shown in Figure 3 and Table 3 indicate a decrease in strength activity index for all fly ash replacement mixtures. The decrease in strength with higher fly ash content is anticipated due to the reduced production of hydration products from cement, though strength improves with longer curing times. Conversely, in PAW mixtures, the 3 days PAW samples show lower SAI than normal water mixtures, attributable to the hydrated temperature effects. The higher H_2O_2 content in PAW leads to more additional products (AFt, AFm) instead of C-S-H, resulting in lower initial strength. However, after 7 days, PAW mixtures accelerate pozzolanic reactivity, leading to increased strength with higher fly ash replacement. Compared to the normal OPC using 0.5 ppm hydrogen-rich water [9], The results showed that the compressive strength of 7 days is 31.65 MPa compared to normal water which is 17.73 MPa. It is also confirmed that there is an increase in the strength while using only 0.5 ppm of hydrogen-rich water. These findings suggest that PAW can enhance the strength of fly ash replacement mixtures more effectively than normal water mixtures.



Scanning Electron Microscope (SEM)

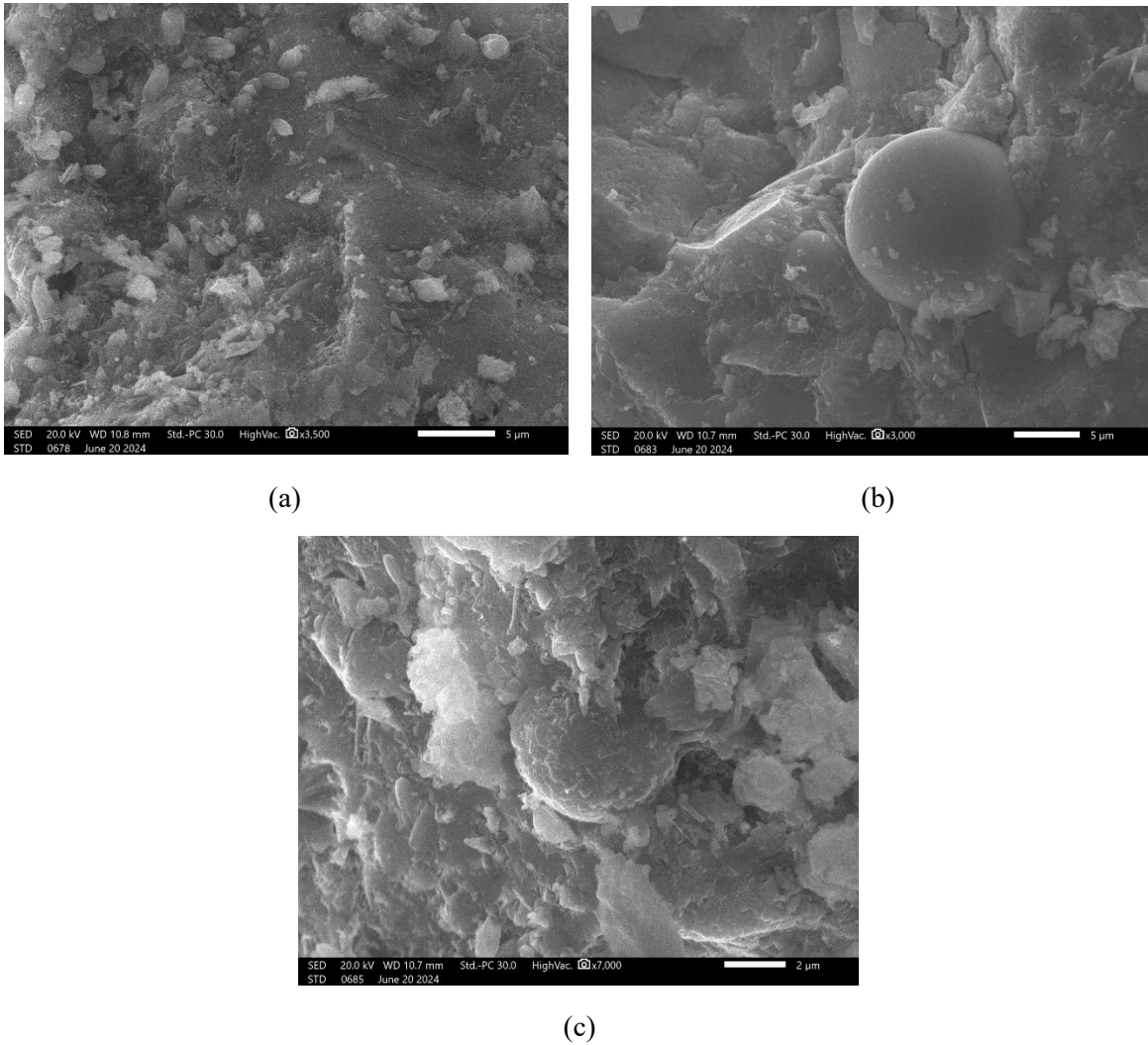


Figure 4 SEM results of (a) nOPC (b) nFA30 (c) pFA30 at 7 days

The SEM analysis reveals the morphology of nOPC, nFA30, and pFA30 samples at 7 days. In the nOPC sample, a typical spread of C-S-H is observed. However, in the nFA30 sample, cracks are visible around the fly ash particles, indicating that the fly ash in the normal water has not yet fully reacted to form additional C-S-H, leaving the particles loose [10]. In contrast, the pFA30 sample shows that the fly ash particles have already generated the pozzolanic reaction, resulting in a denser microstructure [11]. This suggests that PAW accelerates pozzolanic activity, enhancing the reactivity of fly ash, and leading to higher compressive strength compared to normal water.



Conclusion:

Based on the research presented in this paper, the following conclusions can be drawn:

1. PAW influences the hydration reaction across three distinct phases, notably reducing the temperature drop in the initial phase and lowering the peak in the second phase compared to normal water mixtures. This behavior indicates that PAW affects the reactivity of fly ash more significantly, particularly enhancing the formation of additional hydrated products such as ettringite and aluminite ferrite monosulfate in the third phase.
2. The strength activity index (SAI) of fly ash replacement mixtures decreases initially, which is consistent with the hydrated temperature findings. PAW mixtures exhibit lower initial strength at 3 days, due to the higher H_2O_2 content in PAW leading to the formation of additional products instead of C-S-H. However, by 7 days, PAW significantly accelerates pozzolanic reactivity, increasing strength, particularly at higher fly ash replacement levels. This suggests that PAW has the potential to enhance the long-term strength of fly ash mixtures more effectively than normal water.
3. SEM analysis shows that PAW-treated samples have a denser microstructure, with fly ash particles fully engaged in the pozzolanic reaction, unlike in normal water mixtures where fly ash remains loosely bound, indicative of accelerated pozzolanic activity and higher compressive strength.

Overall, the study concludes that PAW has the potential to improve the performance of cementitious mixtures with fly ash, particularly by enhancing pozzolanic reactivity and increasing potential in long-term strength which is a future work focusing on investigating the long-term strength and reactivity for up to 90 days of curing ages.

References:

- [1] Bui PT, Ogawa Y, Kawai K. Long-term pozzolanic reaction of fly ash in hardened cement-based paste internally activated by natural injection of saturated $Ca(OH)_2$ solution. *Materials and Structures*. 2018;51(6).
- [2] Sawangrat C, Leksakul K, Bonyawan D, Anantana T, Jomjunyong S. Decontamination of pesticide residues on tangerine fruit using non-thermal plasma technology. *IOP Conference Series: Earth and Environmental Science*. 2019;347(1):012048.
- [3] Sawangrat C, Phimolsiripol Y, Leksakul K, Thanapornpoonpong S-n, Sojithamporn P, Lavilla M, et al. Application of Pinhole Plasma Jet Activated Water against *Escherichia coli*, *Colletotrichum gloeosporioides*, and Decontamination of Pesticide Residues on Chili (*Capsicum annuum* L.). *Foods*. 2022;11(18).
- [4] ASTM. ASTM C109 / C109M-20a. In Standard Test Method for Compressive Strength of Hydraulic Cement Mortars (Using 2-in. or [50-mm] Cube Specimens). West Conshohocken, PA: ASTM International. (2020).
- [5] Chakraborty S, Jo BW, Sikandar MA. Hydration Mechanism of the Hydrogen-Rich Water Based Cement Paste. *The Journal of Physical Chemistry C*. 2016;120(15):8198-209.



- [6] Hewlett, P. C. Lea's chemistry of cement and concrete, 4th ed.; Hewlett, P. C., Ed.; Elsevier Butterworth Heinemann: Oxford, U.K., 2006.
- [7] Bullard, J. W.; Jennings, H. M.; Livingston, R. A.; Nonat, A.; Scherer, G. W.; Schweitzer, J. S.; Scrivener, K. L.; Thomas, J. J. Mechanisms of cement hydration. *Cem. Concr. Res.* 2011, 41, 1208– 1223.
- [8] Mandal R, Panda SK, Chakraborty S. Effect of electrolyzed water (EW) in accelerating the cement setting and hydration as demonstrated by the analytical techniques. *Construction and Building Materials.* 2021;311.
- [9] Jo BW, Chakraborty S, Sikandar MA, Lee YS. Prediction of the Failure Stress of Hydrogen-rich Water Based Cement Mortar Using the Weibull Distribution Model. *KSCE Journal of Civil Engineering.* 2018;22(5):1827-39.
- [10] Ying J, Xi X. Microstructure and Chloride Diffusion Properties of Hardened Fly Ash Cement Paste with Three-dimensional Graphene. *International Journal of Concrete Structures and Materials.* 2022;16.
- [11] B. Uzbaş, A. Aydin, Analysis of Fly Ash Concrete with Scanning Electron Microscopy and X-Ray Diffraction, *Advances in Science and Technology Research Journal* 13 (2019) 100-110

SP9-GENERATIVE AI: AN EMERGING AI TECHNOLOGY



AUTOMATIC SEGMENTATION OF CARIES EXTENSIONS IN BITEWING RADIOGRAPH USING *YOLOv8* WITH DENTAL CROSS-SECTIONS AS GROUND TRUTH

Napat Supasiripenpong,¹ Watcharaphong Ariyakriangkai,^{2*} Wattanapong Suttapak,³ Wannakamon Panyarak,⁴ Kittichai Wantanajittikul,⁵ Sumana Jittadecharaks⁶

^{1,2}Department of Restorative Dentistry and Periodontology, Faculty of dentistry Chiangmai University, Chiang Mai University, Chiang Mai, Thailand

³Division of Computer Engineering, School of Information Communication and Technology, University of Phayao

⁴Division of Oral and Maxillofacial Radiology, Department of Oral Biology and Diagnostic Sciences, Faculty of Dentistry, Chiang Mai University,

⁵Department of Radiologic Technology, Faculty of Associated Medical Sciences, Chiang Mai University

⁶Department of Restorative Dentistry and Periodontology, Faculty of dentistry Chiangmai University, Chiang Mai University

*e-mail: watcharaphong.a@cmu.ac.th

Abstract

This study was to evaluate the effectiveness of machine learning using You Only Look Once version 8 (YOLOv8), to appropriately detect and segment carious lesions in bitewing radiographs compared to cross-sectioned teeth as ground truth. One hundred bitewing radiographs obtained from 502 cross-sectioned extracted human teeth were annotated in pixel-based segmentation by three experienced dentists. The data were divided into 4 groups (class 0 ; sound teeth, RA1-3 ; initial caries, RB4 ; moderate caries, and RC5-6 ; extensive caries) according to the stage of carious lesions according to ICCMSTM. We tested YOLOv8's performance for carious segmentation and overall segmentation including the ICCMSTM carious stages, enamel, dentin, pulp and NCCL. Evaluation metrics were precision, recall, F1-score, and mAP0.5. YOLOv8 revealed the highest precision for RA1 segmentation at 100% while RC6 segmentation showed the highest recall at 80.0%, F1-score at 65.6% and mAP0.5 at 71.2%. For the overall segmentation, YOLOv8 could segment dentin with the highest precision, similarly to segment RA1 (100%), recall at 98.8%, F1-score at 99.4%, and mAP0.5 at 99.5%. RA2 demonstrated 0% in precision, recall, and F1-score. In Conclusion YOLOv8 was effective in detection and segmentation the stages of carious lesions in bitewing radiographs at an acceptable level.

Keywords: Bitewings Radiographs, Deep Learning, Dental caries

Introduction

Currently, the concept of managing carious lesions has changed from extension for prevention to conservative treatment. This is a minimally invasive treatment⁽¹⁾ as stated by a new paradigm of lesion management under the principles of international caries management (International Caries Classification and Management System: ICCMSTM). The focus is on preventing dental caries and controlling the progression of the disease. The criteria for classifying the stages of dental caries are detection the lesion, followed by diagnosing and evaluating the extent of the caries⁽²⁾ as accurate detection and classification of carious lesions are essential for effective treatment.

Areas with substantial biofilm accumulation and poor saliva penetration are particularly prone to dental caries, such as proximal area⁽³⁾. The location is not clearly visible clinically. In this case, the use of bitewing radiograph aid offers more clarity in diagnostic^(4,5). However, the efficacy of this approach still depends on the dentist's experience in detecting and classifying the stages of the lesion.⁽⁶⁾

To reduce the errors, artificial intelligence (AI) has been used in dentistry. AI acts as a tool that mimics the human brain, possessing capabilities to solve problems and develop autonomously through learning. A key element in AI is machine learning, which facilitates self-learning. Deep learning, analogous to the neural network, necessitates the input of Big data to function effectively⁽⁷⁾. Today, deep learning models are widely used, leading to the development of various neural network types based on the data volume involved. An example of this is the convolutional neural network (CNN), which is particularly suited for unstructured data types such as images⁽⁸⁾. In dentistry, CNNs are utilized to detect carious lesions in adjacent surfaces from bitewing radiographs⁽⁹⁾. Recent studies focusing on permanent teeth indicate that deep learning with CNNs demonstrates higher accuracy in identifying carious lesions in bitewing radiographs compared to traditional detection by dentists⁽¹⁰⁾. The CNN of interest, You Only Look Once (YOLO) version 8 (YOLOv8), was released in January 2023 by Ultralytics, the same company that developed YOLOv5. This version has been enhanced to improve prediction speed and object detection performance. Currently, there are still only a few studies investigating the effectiveness of version 8, particularly in the field of dentistry⁽¹¹⁾.

However, although many studies have been explored its use in dentistry, its actual use is not widespread due to many limitations^(12, 13), as such, the development of deep learning models applied in dentistry continues to be a topic of significant interest. Therefore, this study was undertaken to evaluate the effectiveness of deep learning using CNNs, state-of-the-art of YOLOv8, to appropriately detect and segment carious lesions in bitewing radiographs compared to cross-section teeth.

Materials and methods

1.Data collection

This study design was approved Institutional Review Board of the Faculty of Dentistry, Chiang Mai University, Thailand. (approval no.2023/4).

A total of 264 human permanent premolars and 238 human permanent molars with and without carious lesions were stored in 0.1% thymol solution (0.1% thymol solution, Caelo, Hilden, Germany)⁽¹⁴⁾. These teeth were extracted either due to orthodontic treatment, extensive carious lesions, or other reasons upon the patients' consents. One observer primarily selected the eligible teeth by visual-tactile examination and divided teeth into four groups according to the stage of carious lesions according to the ICCMSTM including : Group 1 sound teeth or teeth without any pathology; Group 2 initial caries or teeth with carious lesions from outer 1/2 of enamel to outer 1/3 of dentin; Group 3 moderate caries or teeth with carious lesions reaching the middle 1/3 of dentin; and Group 4 extensive caries or teeth with carious lesions from the inner 1/3 of dentin to pulp. Teeth were unrestored or retained root, and teeth with crown restorations were excluded.

All teeth were randomly arranged into 100 patterns and subjected to be radiographs with bitewing technique using size 2 intraoral digital photostimulable phosphor storage plate (PSP plate: CarestreamTM 7600, Rochester, New York, USA). Each pattern consists of 8 teeth (4 upper and 4 lower teeth) mimicking ideal bitewing positioning. Each radiograph was arranged to

include all 4 the stages of carious lesions. The arranged teeth were placed in a flat surface and a PSP plate was mounted with an extension cone paralleling film holder (XCP; Kerr Corporation, Brea, CA, USA), with the long axes perpendicular to the central beam of radiation and positioned at a fixed distance of 55 mm. A 14.5 mm thick acrylic resin was placed between the radiation source and the teeth to simulate soft tissues^(15, 16).

All radiographs were acquired using an intraoral x-ray unit (Heliodont Plus™, Dentsply Sirona Corp., USA, 70 kV, 7 mA, exposure time 0.16 s) and scanned with a film scanner (Carestream CS 7600 Scanner, Carestream™, Rochester, NY, USA).

After taking radiographs, each tooth was embedded in a self-cured clear acrylic resin block and sectioned using a cutting machine (IsoMet™, BUEHLER, Illinois, USA) to create cross-sectional slices in the proximal-proximal direction. If carious lesions were present, the segment with the deepest and most prominent lesions was selected. The example of sectioned teeth are shown in Figure 1.



Figure 1.
Sectioned second premolar and second molar.

2. Ground truth preparation, annotation and model training

All 100 dental bitewing radiographs showing visible tooth structure, including crown, 3/4 of root, and restoration, were annotated in pixel-based segmentation⁽¹⁷⁾ by three dentists, including an oral and maxillofacial radiologist with 8 year's experience, and a specialist in restorative dentistry in 10 year's experience, and a general dentist with 5 year's experience using *Labelme software* (*Labelme 2015*, <https://github.com/CSAILVision/LabelMeAnnotationTool>)⁽¹⁸⁾. The imported radiographic images are in the Joint Photographic Experts Group (.JPEG) format, maintaining a resolution of 1280 × 1280 pixels. We labelled 11 categories of data: enamel, dentin, pulp, restorations, non-carious cervical lesion (NCCL) and 4 groups of carious lesions. To determine the carious data, a visual comparison of the cross-sectioned teeth was used. Labeling and calibration followed instructions from a handbook, which explained the radiographic interpretation according to the ICCMS™ scoring system including 0, RA, RB, RC. All labelled 11 categories are described in Table 1. During the annotation process, all of radiographs were displayed on radiographic workstation. The display ratio of the images was 1:1. The viewing took place in a room with dimmed lights. Annotations were based on the consensus of at least two out of three reviewers. From 100 radiographs, 75 radiographs were used for training and 25 radiographs were split for validation processes. Data augmentation techniques were applied randomly, including 0 to 10% image

translation, 0 to 10% image scaling (both up and down), and up to 50% horizontal flipping. We utilized 4-fold cross-validation to evaluate the performance of YOLOv8 model.

Table 1.
Definition, label, characteristics, and number of counted data.

| Definition | Label | Characteristics | Number of data |
|--------------------------------------|-------------|---|----------------|
| 0 Sound teeth | enamel | Enamel | 894 |
| | dentin | Dentin | 799 |
| | pulp | Pulp | 791 |
| | restoration | Restoration | 95 |
| | NCCL | Non-carious Cervical Lesions | 68 |
| RA Initial caries | RA 1 | Expressed caries in outer 1/2 of enamel | 51 |
| | RA 2 | Expressed caries in inner 1/2 of enamel to enamel – dentin junction | 110 |
| | RA 3 | Expressed caries in outer 1/3 of dentin | 198 |
| RB Moderate caries | RB 4 | Expressed caries in middle 1/3 of dentin | 93 |
| RC Extensive caries | RC 5 | Expressed caries in inner 1/3 of dentin | 60 |
| | RC 6 | Expressed caries into pulp | 92 |

We performed two experiments to test the model's categorization performance; Experiment 1, carious segmentation including NCCL; Experiment 2, overall segmentation. All radiographs were set to a resolution of 1280×1280 pixels, with an Intersection over Union (IoU) threshold of 0.5 and a confidence threshold of 0.001 for evaluating the performance of YOLOv8.

3. Performance Evaluation

The metric to evaluate performance of YOLOv8 model is a real-time object detection and image segmentation algorithms using precision, recall, F1-score, IoU and mAP.

Precision is defined as the ratio of correctly predicted positive observations to the total predicted positives wherein it is essential to tell what proportion of the identified positives are actually correct⁽¹⁹⁾.

$$\text{Precision} = \frac{\text{true positive}}{\text{true positive} + \text{false positive}}$$

Recall is measuring how well the model captures all the actual positives⁽²⁰⁾.

$$\text{Recall} = \frac{\text{true positive}}{\text{true positive} + \text{false negative}}$$

F1-score is a value used to show accuracy which uses the harmonic mean of precision and recall or specificity in binary classification statistical analysis. This value will be in the range of 0-1, with a high value indicating high efficiency⁽²¹⁾.

$$\begin{aligned} \text{F1-score} &= \frac{2 \times \text{precision} \times \text{recall}}{\text{precision} + \text{recall}} \\ &= \frac{\text{true positives}}{\text{true positives} + \frac{1}{2} (\text{false positives} + \text{false negatives})} \end{aligned}$$

Performance of the object detector is calculated as the average of average precisions (AP) across various intersection over union (IoU) thresholds and different classes. For each class, the AP was determined by integrating the area under the precision-recall (PR) curve. For instance, with an IoU threshold set at 0.5, a predicted bounding box must overlap the ground truth bounding box by at least 50% to be considered a true positive. The mean average precision (mAP) of 0.5 is calculated as follows

$$\text{mAP}_{0.5} = \frac{1}{C} \sum_{c=1}^n \text{AP}_{0.5}$$

The model performance parameters using IoU50 and a confidence threshold of 0.01 is based on a previous study by Wannakamon et al. in 2023, presenting results on caries detection using YOLOv3 vs. YOLOv7. Therefore, we are considering the idea of assessing YOLOv8 on caries segmentation according to its promising performance in dental radiographic images⁽²²⁾.

Results

The results from the model's performance evaluation across all three experiments are presented in Table 2 and Figure 2.

Table 2.
YOLOv8 segmentation performance including precision, recall and F1 score

| | Metric | Precision | | Recall | | F1-score | |
|----------------|--------------------|-----------|---------|--------|---------|----------|---------|
| | Class | Caries | Overall | Caries | Overall | Caries | Overall |
| Group 1 | enamel | | 0.943 | | 0.870 | | 0.905 |
| | dentin | | 1.000 | | 0.988 | | 0.994 |
| | pulp | | 0.980 | | 0.980 | | 0.980 |
| | restoration | | 0.780 | | 0.680 | | 0.730 |
| | NCCL | 0.343 | 0.547 | 0.467 | 0.474 | 0.395 | 0.508 |
| Group 2 | RA1 | 1.000 | 1.000 | 0.000 | 0.000 | 0.000 | 0.000 |
| | RA2 | 0.313 | 0.000 | 0.038 | 0.000 | 0.067 | 0.000 |
| | RA3 | 0.381 | 0.436 | 0.194 | 0.120 | 0.258 | 0.188 |
| Group 3 | RB4 | 0.511 | 0.547 | 0.250 | 0.789 | 0.336 | 0.646 |
| Group 4 | RC5 | 0.293 | 0.547 | 0.571 | 0.765 | 0.388 | 0.637 |
| | RC6 | 0.556 | 0.628 | 0.800 | 0.571 | 0.656 | 0.598 |

For carious segmentation precision, RA1 had the highest score at 100%, while the lowest score was shown in RC5 at 29.3%. RC6 had the highest recall at 80.0% and an F1-score of 65.6%,

while RA1 had a recall and F1-score of 0. Overall segmentation showed the highest precision in dentin segmentation (100%), similarly, RA1.YOLOv8 also performed best in dentin segmentation with the highest recall at 98.8%, and F1-score with dentin at 99.4%. However, the performance was lowest when segmenting RA1 and RA2 with 0% of recall and F1-score.

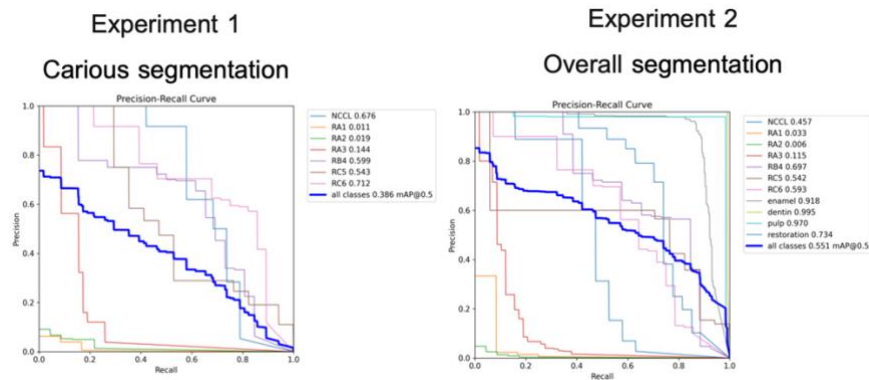


Figure 2.
Precision-recall (PR) curves of the YOLOv8 image segmentation performance for the carious segmentation (RA, RB, RC, and NCCL) and overall segmentation.

The experiment results at mAP0.5 for carious segmentation revealed that RA1 had the lowest score at 1.1% and RC6 had the highest score at 71.2%, with an overall average of 38.6% across all classes. For overall segmentation under mAP0.5 setting, RA2 had the lowest score at 0.6% and dentin had the highest score at 99.5%, resulting in an overall average of 55.1% across all classes.

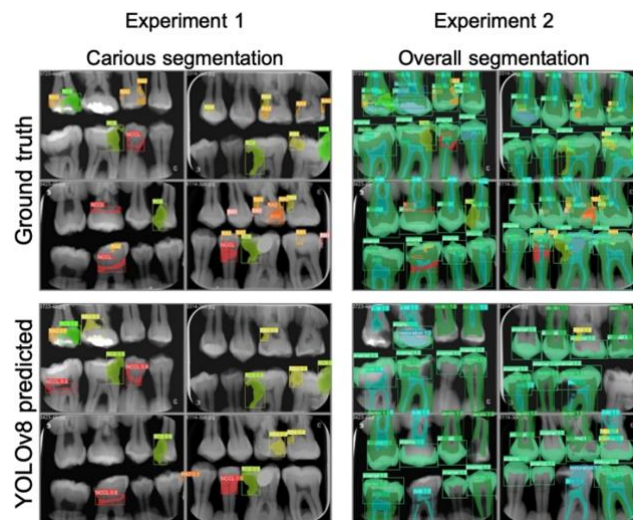


Figure 3.
YOLOv8 segmentation results compared to ground truth.

Discussion

The CNN-based YOLO is a real-time detection algorithm capable of predicting multiple bounding boxes and their associated class probabilities. YOLO trains on complete images and

directly focuses on optimizing detection performance. During both training and testing, YOLO processes the full image, inherently capturing contextual information about the classes and their appearances. Redmon et al. compared YOLO with R-CNN for object detection. They discovered that YOLO can simultaneously predict bounding boxes and class probabilities for multiple objects across various classes in an image. When comparing real-time detection capabilities, they found that while Fast R-CNN is more accurate, it does not perform as well in real-time scenarios. In contrast, YOLO demonstrated both high accuracy and strong real-time detection performance⁽²³⁾. In 2023, Yilman et al. conducted a study on tooth classification performance in panoramic films using YOLOv4 and Fast R-CNN. The YOLOv4 method proved to be more effective than the Faster R-CNN method in classifying teeth, with higher recall, precision, and F1 scores. Furthermore, in terms of computation time, the YOLOv4 method was found to be approximately four times faster than Faster R-CNN for tooth classification⁽²⁴⁾. As such, these YOLO systems are particularly useful for detecting and classifying the stages of carious lesions in dental radiographs, which is crucial for dentists to accurately diagnose and assess the extent of caries for effective treatment. This study was interested in YOLOv8, the latest version of YOLO by Ultralytics, which has the performance to appropriately detect and segment carious lesions in bitewing radiographs compared to cross-sectioned teeth.

This research was designed by having radiographs read by three experienced dentists to establish a robust reference standard where cross-sectioned teeth were used for comparison. However, it was discovered that interpreting the results of cross-sectioned teeth in half and then interpreting the results presented several limitations, leading to disagreements during the readings. For instance, extracted teeth were sometimes incomplete or with some enamel being chipped, making them appear radiopaque on radiographs similar to the appearance of carious lesions. Additionally, the coloration of teeth with brown stains could be mistaken for carious lesions. Teeth embedded in self-cured clear acrylic before being sectioned could only be visually examined, and not with surface tactile tools, which caused debates about the extent of carious lesions. Moreover, when sectioning teeth, only the single most prominent position was chosen, which made it difficult to clearly observe lesions that gradually move towards buccal or lingual/palatal aspects, such as NCCL. In the study by Devito et al.⁽²⁵⁾, extracted teeth were sectioned and examined microscopically, with histologic examination serving as the gold standard. However, limitations that arose due to dichotomization led to disagreements among examiners about classifying white or brown stains as carious lesions. Thus, based on the researcher's perspective, experimental designs with human subjects encounter limitations in detecting carious lesions. This aspect still requires further development to establish stronger standards.

Evaluating the model's image segmentation performance using mAP at IoU 50 revealed the performance of the caries segmentation. Carious lesions have small and more variable shapes and positions, resulted in low scores. Due to limitations in how YOLO learns to predict bounding boxes from data, it struggles to generalize objects with new or unusual aspect ratios or configurations. While a small error in a large box is usually minor, the same error in a small box significantly impacts the IoU⁽²³⁾. This study is similar to the findings in Lee et al. study⁽²⁶⁾, which used U-net by separating the model into distinct tests for caries and anatomy. They observed that with a small training dataset, the segmentation of dental structures performed quite accurately for anatomical regions, deferent from carious regions.

From the above tests conducted within separate classes, we proceeded to test the overall segmentation. It was anticipated that the performance of caries detection would improve due to the addition of anatomical groups, which would help further distinguish between caries and

anatomical structures. However, it was found that the number of detected caries instances decreased compared to testing in separate classes. This suggests that the algorithm, at this stage, still cannot fully replicate the human brain's capabilities. Therefore, this area requires further development in the future. Another noteworthy observation is that the algorithm did not mistakenly identify the pulp as a carious lesion, which is a positive outcome.

The parameters used to evaluate the model's performance include precision, recall, and F1-score. In the tests for caries detection, the values were low in both in the caries segmentation and the overall segmentation, the values were low. An interesting observation is that for RA1, the precision was 1, but recall and F1-score were both 0. A precision of 1 indicates that all identified positions for RA1 were true positives ($FP = 0$), but a recall of 0 means that the model did not correctly identify any true positive locations ($TP = 0$) or missed all positive locations ($FN > 0$). For RA2, the precision, recall, and F1-score were all 0. This indicates that the model did not identify RA2 as a true positive and failed to detect any positive locations. The F1-scores were 0 is due to the harmonic mean of precision and recall, leading to RA1 and RA2 having an F1-score of 0. Therefore, while the model is effective in detecting carious lesions, further development is needed for the RA1 and RA2 models.

This study is a pilot study that demonstrates the efficacy of YOLOv8 in accurately detect and segment carious lesions in bitewing radiographs, using training label-data from cross-sectioned teeth. The test results show that the classification of caries is at an acceptable level. In the future, YOLOv8 will be further developed to improve its effectiveness in classifying all types of carious lesions, aiming for higher and more consistent results. Additionally, the model will be tested in various scenarios to assess its efficiency, with the goal of validating YOLOv8's effectiveness in detection and segmentation the different levels of carious lesions.

Conclusion

This study aimed to assess the YOLOv8's segmentation performance using training data from cross-sectioned teeth. Performance evaluations, including precision, recall, F1-score, and mAP at an IoU of 50, revealed that YOLOv8 was effective in detection and segmentation the stages of carious lesions in bitewing radiographs at an acceptable level.

Reference

1. Frencken JE. *Br Dent J.* 2017;223(3):183-9.
2. Ismail AI, Pitts NB, Tellez M, Banerjee A, Deery C, Douglas G, et al. *BMC Oral Health.* 2015;15 Suppl 1(Suppl 1):S9.
3. Kidd EA, Fejerskov O. *J Dent Res.* 2004;83 Spec No C:C35-8.
4. Chu CH, Chung BT, Lo EC. *Int Dent J.* 2008;58(5):265-8.
5. Carvalho JC, Mestrinho HD, Guillet A, Maltz M. *Caries Res.* 2020;54(2):154-64.
6. Diniz MB, Rodrigues JA, Hug I, Cordeiro Rde C, Lussi A. *Community Dent. Oral Epidemiol.* 2009;37(5):399-404.
7. Roongruangsilp P, & Khongkhunthian, P. *J Osseointegr.* 2022;14(3):166–73.
8. Schwendicke F, Golla T, Dreher M, Krois J. *J Dent.* 2019;91:103226.
9. Dayo AF, Wolff MS, Syed AZ, Mupparapu M. *Dent Clin North Am.* 2021;65(3):427-45.
10. Cantu AG, Gehrung S, Krois J, Chaurasia A, Rossi JG, Gaudin R, et al. *J Dent.* 2020;100:103425.
11. Terven J, Córdova-Esparza D-M, Romero-González J-A. *Mach.* 2023;5(4):1680-716.
12. Schwendicke F, Samek W, Krois J. *J Dent Res.* 2020;99(7):769-74.

- 13.Schwendicke F, Cejudo Grano de Oro J, Garcia Cantu A, Meyer-Lueckel H, Chaurasia A, Krois J. *J Dent Res*. 2022;101(11):1350-6.
- 14.Aydın B, Pamir T, Baltacı A, Orman MN, Turk T. *Eur J Dent*. 2015;9(2):262-6.
- 15.Schropp L, Alyass NS, Wenzel A, Stavropoulos A. *Dentomaxillofac Radiol*. 2012;41(8):686-90.
- 16.Soltani P, Devlin H, Aydın U, Tafti KT, Baghaei K. *Oral Radiol*. 2024;40(2):109-23.
- 17.Subramanyam R, Prasad KP, Anuradha B. *Int J Eng Res Appl*. 2014;4(7):173-7.
- 18.Russell BC, Torralba A, Murphy KP, Freeman WT. *Int. J. Comput. Vis*. 2008;77(1):157-73.
- 19.Safari S, Baratloo A, Elfil M, Negida A. *Emerg (Tehran)*. 2015;3(3):87-8.
- 20.Baeyens J-P, Serrien B, Goossens M, Clijsen R. *Arch. Physiother*. 2019;9(1):4.
- 21.Tharwat A. *Applied Computing and Informatics*. 2020.
- 22.Panyarak W, Wantanajittikul K, Charuakkra A, Prapayasadok S, Suttapak W. *J Digit Imaging*. 2023;36(6):2635-47.
- 23.Joseph R. SKD, Ross B. G. ,Ali F.. CoRR. 2015;abs/1506.02640(In proceeding of 2016 IEEE Conference on Computer Vision and Pattern Recognition):779-88.
- 24.Yilmaz S, Tasyurek M, Amuk M, Celik M, Canger EM.. *Oral Surg Oral Med Oral Pathol Oral Radiol*. 2024;138(1):118-27.
- 25.Devito KL, de Souza Barbosa F, Felipe Filho WN. *Oral Surg Oral Med Oral Pathol Oral Radiol Endod*. 2008;106(6):879-84.
- 26.Lee S, Oh SI, Jo J, Kang S, Shin Y, Park JW. *Sci Rep*. 2021;11(1):16807.

SP13-HARNESSING DIGITAL SCIENCE AND ENGINEERING FOR
ENVIRONMENTAL SUSTAINABILITY



CARBON DIOXIDE EFFICIENCY ANALYSIS OF ADSORPTION AND DESORPTION USING K_2CO_3/Al_2O_3 SORBENT UNDER VARIOUS OPERATING PARAMETERS WITH AVRAMI KINETIC MODEL

Kaung Sat Han,¹ Ratchanon Piemjaiswang,² Benjapon Chalermssinsuwan,^{3, *}

¹International Postgraduate Program in Hazardous Substance and Environmental Management, Chulalongkorn University, 9th floor, CU Research Building, Phayathai Road, Wang Mai, Pathum Wan, Bangkok 10330, Thailand

²Environmental Research Institute, Chulalongkorn University, 2nd floor, Institute Building 2, Phayathai Road, Wang Mai, Pathum Wan, Bangkok 10330, Thailand

³Department of Chemical Technology, Faculty of Science, Chulalongkorn University, Phayathai Road, Wang Mai, Pathum Wan, Bangkok 10330, Thailand

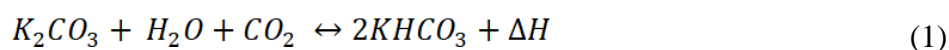
*e-mail: benjapon.c@chula.ac.th

Abstract:

Global carbon dioxide emissions from fossil fuels and industry totaled 37.15 billion metric tons in 2022. Therefore, it is a priority to consider a method or a solution for reducing CO₂ emission while the global energy sector is still dependent on hydrocarbon fuels. Among carbon capturing concepts, there are a lot of recent studies on the application of reversible gas-solid adsorption of CO₂ on potassium carbonate based on alumina (K_2CO_3/Al_2O_3) with reliable efficiency and reusability. The adsorption and desorption capacities of the sorbent are influenced by the operation parameters such as temperature, pressure, water vapor and flow patterns. There have been several research on reaction kinetics of K_2CO_3/Al_2O_3 which mostly focused on adsorption or regeneration. The study of operating parameters' effects on K_2CO_3/Al_2O_3 with kinetic models including adsorption and regeneration is still demanding in this field. Subsequently, it becomes vital to comprehend the intricacies of reaction kinetics in order to analyze operational variables without requiring several experiments. In most of the studies, reaction kinetics were investigated with the experimental approach by setting variable parameters. The reaction kinetic models can simulate the experimental results with mathematical equations expecting to minimize the number of tests. Mostly, pseudo kinetic models are selected for gas-solid adsorption, but Avrami model has better accuracy. In this study, the effects of multiple operating settings were analyzed on the adsorption and regeneration efficiency of K_2CO_3/Al_2O_3 with Avrami model. The effects of the flow patterns such as fixed bed, bubbling, turbulence and fast fluidization on CO₂ adsorption capacity were investigated to explore the changes in cumulative adsorption efficiency. Moreover, the effects of temperature and water vapor were also studied with various settings. For the desorption, the effects of pressure and temperature were investigated on the regeneration efficiency with Avrami desorption model. According to the obtained model, the flow patterns were found to have significant impacts showing the great gap between turbulent fluidization, which was the highest capacity and the lowest which was fast fluidization. For temperature, the sorbent reached the highest adsorption capacity at 333K then declined gradually from 343K to 363K because the adsorption is an exothermic reaction. Then, the sorbent showed increasing capacity along with the rise of water vapor percentage (7%, 12.5%, 18.5%) until it reached 22.5% where was the lowest as the water droplets took over in the pores of the sorbent particles. For desorption kinetics, Avrami model demonstrated that the temperature of 573K and 0.2 bar of pressure were the optimum condition providing the highest regeneration efficiency.

Introduction:

Due to industrialization, the use of fossil fuel has significantly increased for the purpose of high energy demand. So, greenhouse gases emission (carbon dioxide) become a major environmental issue which can lead to global warming, a very harmful effect on human, animal life and the environment. Nowadays, carbon capturing technologies are developing regarding CO₂ removal such as chemical and physical adsorption, membrane application and biological process. Mostly, post combustion capture has been used in coal power plants and other high CO₂ emission industries. The CO₂ adsorbing solid sorbents (K₂CO₃/Al₂O₃) are promising by showing low cost of raw material, low toxicity and conventional regeneration [6]. In theory, CO₂ and H₂O deposit on porous surface of sorbent particles and then react with active sites forming a layer on the sorbents during gas-solid reaction [3]. As the reaction keeps on, the layer becomes thicker reaching the sorbent adsorption limit. In regeneration stage, full capacity sorbents release adsorbed CO₂ by applying specific temperature or pressure. The fine powder like sorbents with defined particle diameters have high CO₂ capturing capacity and regeneration ability under desired operational conditions such as pressure, temperature and velocity of injected gas [1]. This gas-solid reaction with K₂CO₃/Al₂O₃ and CO₂ is a reversible exothermic reaction as in equation (1) during adsorption progress in turn regeneration is endothermic as it requires heat to adsorb CO₂.



In recent years, there have been a lot of studies on gas-solid adsorption on K₂CO₃/Al₂O₃ sorbent. There are methods to carry out the adsorption and regeneration of K₂CO₃/Al₂O₃ such as pressure swing adsorption (PSA) and temperature swing adsorption (TSA). In general PSA process, the desorption stage is completed by decreasing pressure, so the adsorption capacity of sorbent was reduced, and CO₂ is released [7]. TSA is a process that the adsorption temperature is maintained 333K to 373K and the regeneration is done by heating the sorbent to desorption temperature 393K-473K then the sorbent is cooled down to adsorption temperature and circulated back to carbonator [8]. The flow diagram of TSA concept is shown in Fig. 1. This study of operation parameters was then based on the TSA concept.

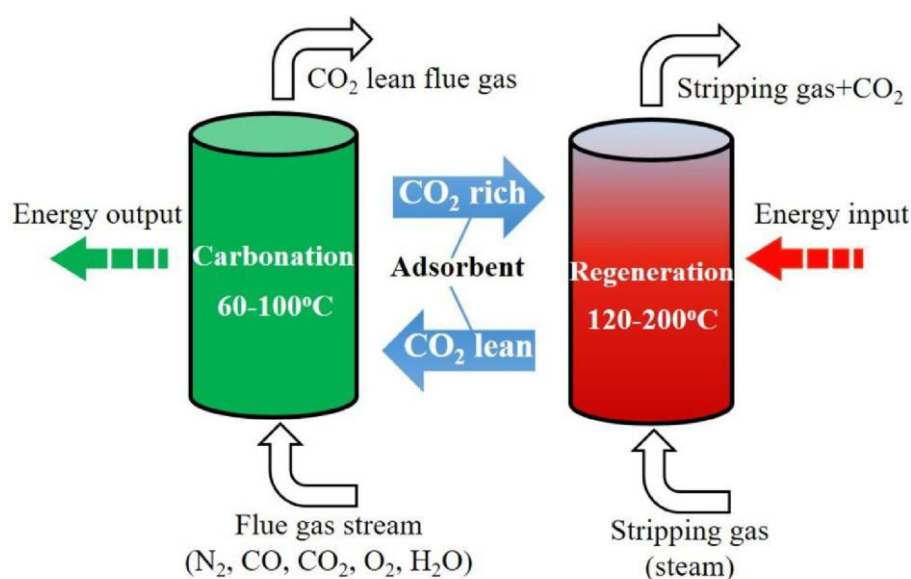


Figure 1. General flow diagram of temperature swing adsorption [8].



The reaction kinetics study of gas-solid adsorption is generally based on the concept of shrinking core model frameworks as the formation of solid product layer covering the surface of solid with the distinctive interface between reactant and product layer [4]. Pseudo first order model is mainly applied for adsorption process only controlled by surface diffusion then second order follows up on the Langmuir adsorption isotherm equation which is considered that the chemical reaction is the rate controlling step of the adsorption process [3]. Both models are suitable for gas solid reaction on the porous adsorbents even though the results obtained from the pseudo first order and second order model may have some limitation. The main reason of the selection of Avrami fractional model on gas solid adsorption study is that the model is designed for the phase transition rate and the crystallization phenomena of materials allowing to investigate the reaction kinetics with shrinking core concept then it can predict the adsorption kinetics of CO₂ with solid adsorbents [9]. In a recent study of kinetic characteristics of silicon adsorbent for carbon capturing at different CO₂ concentrations and temperature, it was found that Avrami model fits the CO₂ isothermal adsorption curve with reliable accuracy [5]. Moreover, the other models were compared to the results of Avrami model. There were three settings of temperature (303K, 323K and 343K) and five parameters of CO₂ concentration in that study proving the fact that Avrami model predicted with a better accuracy than other models [5].

The effects of operating parameters on efficiency of sorbent have been studied in recent years with different models, flow patterns, reactors and methods. For desorption, it was found that total sorption capacity was not completely influenced by regeneration time or number of cycles but highly impacted by regeneration pressure showing 0.2 atm was better than 0.8 atm [10]. In some studies, combination of a specific flow pattern and various operating parameters like temperature and pressure can make certain impacts in adsorption and regeneration efficiency. The objectives of this study are to understand sorbent efficiency under different operating parameters and to validate the point that Avrami model can predict the experimental values along with parameter changes. It is challenging to acquire all input data of Avrami model equation from referenced studies and find similar research with same sorbent and concept of capturing methods eligible for Avrami model.

Methodology:

In this study, Avrami kinetic model was used to calculate the cumulative adsorption and desorption capacity of K₂CO₃/Al₂O₃ sorbent under various operating conditions (flow patterns, temperature and water vapor and pressure) by simulating the CO₂ kinetics data from experimental study of Jongartklanga et al. 2016 [1] and desorption kinetics from Angkanawisan et al. 2022 [2]. In general, the adsorption values were calculated by collecting experimental data from reference research then Avrami equation was applied again to fit with actual experimental data in each parameter. The mathematical calculation of cumulative adsorption capacity of sorbent for experiment with time was governed by the following equation.

$$q = \frac{1}{m} \int_0^t Q (C_{in} - C_{out}) dt \quad (2)$$

According to equation (2), the inlet and outlet concentration of CO₂ were required, and these values were dependent on the outlet fraction (*F*) of CO₂. The inlet concentration was provided from experimental data so the outlet fraction plots of respective parameters from the experiment were analyzed to get outlet fractions of each 3 mins of reaction time and these were inserted into equation (3) along with *C_{in}* to find *C_{out}*.

$$F = \frac{C_{in}}{C_{out}} \quad (3)$$

The reaction time was 30 minutes, and the cumulative adsorption values were calculated for every 3 mins. The adsorption column with the internal diameter of 0.025 m and 0.8 m height was applied. The operation parameters of this study and related input data are mentioned in Table 1. The applied temperature range is the suitable operating temperature opt for sorbent adsorption while water vapor range represents actual flue gas coming out of coal combustion containing 6-12% H₂O and coal gasification process with 2-28% H₂O [11].

Table 1.

Applied parameters with respective mass loading and inlet gas velocity

| | Parameters | Mass loading (g) | Inlet velocity (m/s) |
|---------------------|------------------------|------------------|----------------------|
| Flow patterns | Fixed bed | 60 | 0.01 |
| | Bubbling fluidization | 60 | 0.20 |
| | Turbulent fluidization | 60 | 1.02 |
| | Fast fluidization | 300 | 2.64 |
| Temperature | 323K | 60 | 0.01 |
| | 333K | 60 | 0.01 |
| | 343K | 60 | 0.01 |
| | 353K | 60 | 0.01 |
| | 363K | 60 | 0.01 |
| Water vapor content | 7% | 60 | 0.01 |
| | 13.5% | 60 | 0.01 |
| | 18.5% | 60 | 0.01 |
| | 22.5% | 60 | 0.01 |

By inserting input data from experiment to equation (2), the cumulative adsorption capacity of each parameter variation for 30 mins were obtained and these results were be used to find the required equivalent cumulative capacity, reaction constant and exponent embedded in Avrami equation. MATLAB program was used to identify the reaction constant (k), equivalent capacity and Avrami exponent (n) by fitting the curves of the obtained cumulative adsorption capacity from previous calculations with time (min) in curve fitting tool with Avrami kinetic model [3] as mentioned below.

$$q = q_e \left(1 - e^{-\frac{(kt)^n}{n}} \right) \quad (4)$$

The following exponents and constant were inserted in Avrami equation again to calculate the cumulative adsorption capacity for compromising the simulated results of Avrami model with the experimental values. For desorption kinetics, the experimental desorption data of the research focused on regeneration of K₂CO₃/Al₂O₃ sorbent were simulated using Avrami desorption model [2]. In this case, the pressure and temperature were only focused as operating parameters to study regeneration capacity of potassium carbonate sorbent. The governed equation for regeneration was the same as adsorption. In general, the calculation procedures of adsorption and regeneration capacity are nearly the same only differ in variation parameters. The experimental results on regeneration with temperature variation 423K, 473K, 523K and 573K were simulated as well as pressure parameters 0.2 bar, 0.4 bar,



0.6 bar and 0.8 bar. The reaction time was set for 30 mins for each case and desorption capacity values were collected for every 5 mins. The required k and n values were identified in same manner as adsorption kinetic with the use of MATLAB program along with the equation (4). Then, the regeneration capacity values obtained from the desorption model were fitted with actual experiment results for both modified and unmodified type in the purpose of validating the Avrami model capability.

Results and Discussion:

Effect of adsorption flow patterns

The four categories of flow patterns on gas-solid reaction with K_2CO_3/Al_2O_3 sorbent and CO_2 were studied to investigate the changes in cumulative adsorption capacity of sorbent. According to the Avrami model calculation, the capacity of the sorbent was 8500 mmol/g which was the highest in turbulent fluidization condition compared to other patterns. The fast fluidization provided the least value of capacity, only 25 mmol/g while the bubbling and fixed bed were in second and third. In theory, due to moderate velocity of 1.02 m/s and non-circulating turbulent flow patterns, the solid sorbent provides greater surface area to react with the injected gas promoting the adsorption capacity. In the case of fast fluidization, the efficiency of sorbent adsorption can be lower because of the high inlet velocity giving sorbent a bit amount of time to react with CO_2 . Following the procedures to simulate the experimental data with Avrami equation, the Avrami exponent (n), equivalent adsorption capacity and reaction constant (k) were obtained by fitting the equation (4) in MATLAB curve fitting tool and the results are described in Table 2. The changes in adsorption capacity influenced by flow patterns are shown in Fig. 2 where the simulated data from Avrami model were compared with experimental results.

Table 2.

Fitting parameters of Avrami model under different flow patterns

| Flow pattern | k (1/min) | n | q_e (mmol/g) (Avrami model) |
|------------------------|-------------|-----|----------------------------------|
| Fixed bed | 0.097 | 2.5 | 952 |
| Bubbling fluidization | 0.175 | 1.7 | 4723 |
| Turbulent fluidization | 0.306 | 1.8 | 8500 |
| Fast Fluidization | 0.083 | 1.6 | 25 |

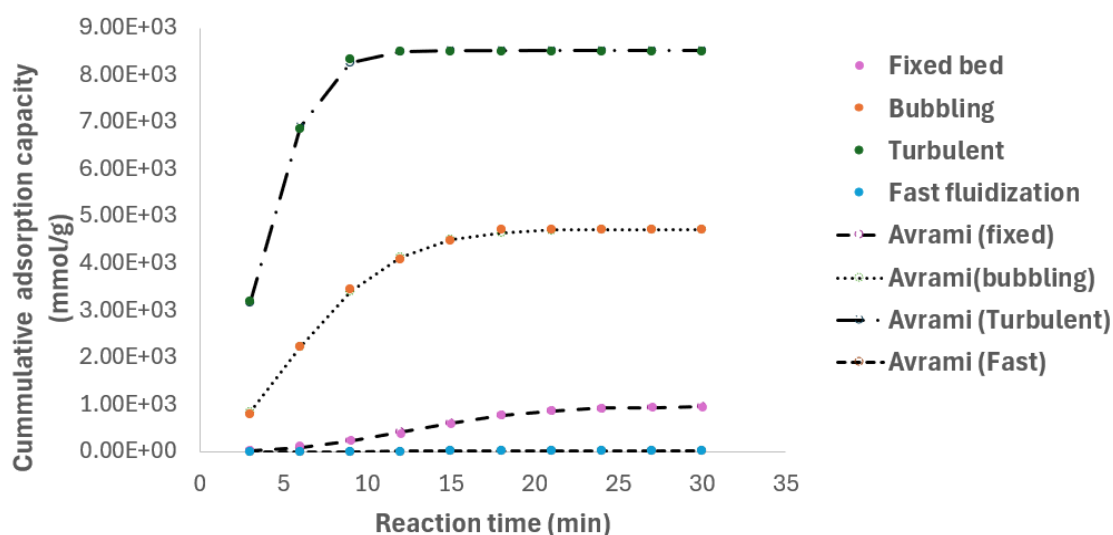


Figure 2. Effect of different flow patterns on CO₂ cumulative adsorption capacity and Avrami model fitting with experimental data

Effect of adsorption temperature

With temperature variation, the five cases of temperature parameter mentioned in Table. 1 were run with the same 0.01 m/s inlet velocity and 60 g of mass loading for all cases. It was investigated that the cumulative adsorption capacity increased along with temperature (323K- 333K) showing 1209 mmol/g of capacity in 333 K but it was found decreased in the next setting of temperature (343K - 363K). The calculation steps were carried out in same manner as Avrami model then k and n values of each temperature setting are expressed in Table 3 respectively. The comparison plots between model results and experimental outcomes are also described in Fig. 3.

Table 3.

Fitting parameters of Avrami model under different temperature

| Temperature (K) | k (1/min) | n | q_e (mmol/g) (Avrami model) |
|-----------------|-------------|-----|----------------------------------|
| 323 | 0.131 | 2.3 | 519 |
| 333 | 0.084 | 2.5 | 1209 |
| 343 | 0.063 | 2.4 | 1009 |
| 353 | 0.181 | 1.9 | 256 |
| 363 | 0.631 | 2.4 | 128 |

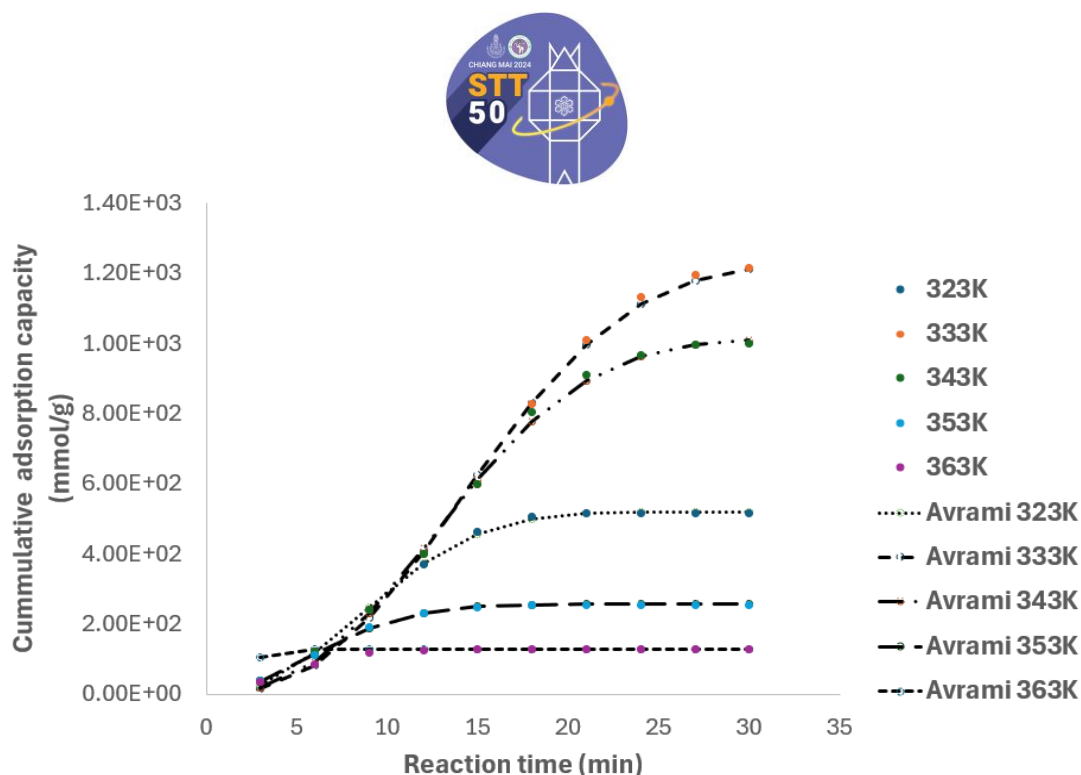


Figure 3. Effect of different temperature on CO₂ cumulative adsorption capacity and Avrami model fitting with experimental data.

Effect of adsorption water vapor content

Four settings of water vapor content were investigated in this study to determine the effects of humidity in gas/solid adsorption reaction. By analyzing the calculated results from experimental data, the adsorption capacity was promoted due to the existence of water vapor in the system. Theoretically, it was found that water vapor can help solid sorbent to promote the adsorption capability on carbon dioxide. The parameter of 18.5% water vapor gave a significant amount of cumulative capacity nearly two-fold the second highest 13.5%. It was investigated that the highest water vapor setting 22.5% gave the lowest value of capacity among the others. The detailed outcomes of Avrami kinetics model and experimental results are described below.

Table 4.

Fitting parameters of Avrami model under different water vapor content

| Flow pattern | k (1/min) | n | q_e (mmol/g) (Avrami model) |
|--------------|-------------|-----|----------------------------------|
| 7 | 0.269 | 1.5 | 104 |
| 13.5 | 0.128 | 2.3 | 559 |
| 18.5 | 0.083 | 2.5 | 1112 |
| 22.5 | 0.195 | 1.7 | 94 |

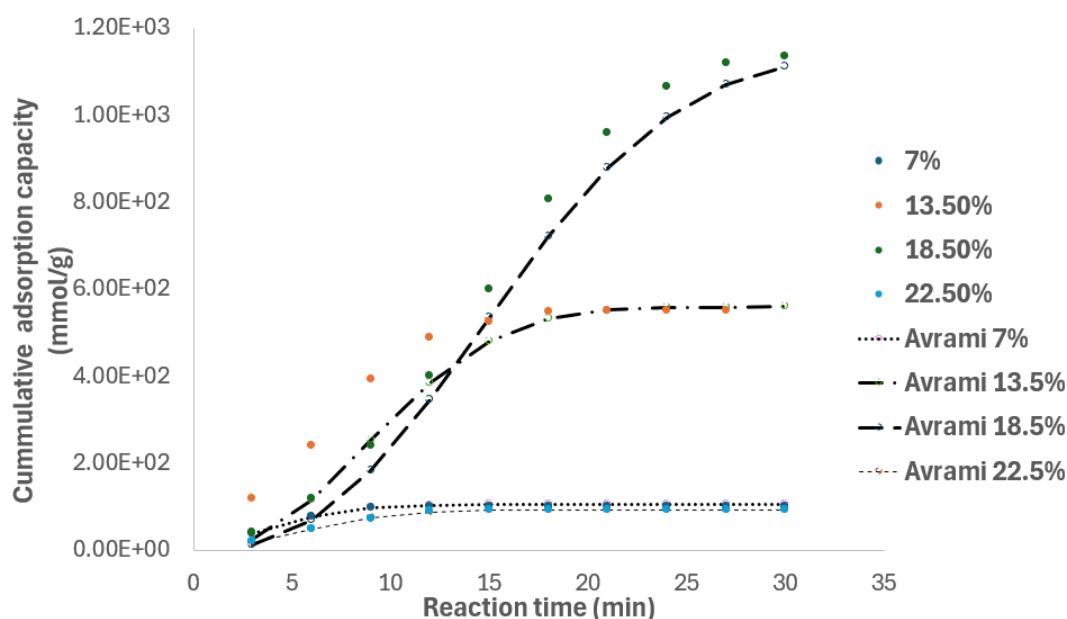


Figure 4. Effect of water vapor content on CO₂ cumulative adsorption capacity and Avrami model fitting with experimental data

Effect of regeneration pressure and temperature

For the study of desorption kinetics, four parameters of pressure were investigated by using Avrami desorption model. Then, it was investigated that the candidate sorbent preferred low pressure in desorption stage giving the highest 41 mg at 0.2 bar which was the lowest pressure setting. For the pressure above 0.2 bar, it was found that regeneration capacity declined drastically. The simulated desorption capacity results from Avrami equation compared to experimental data shown in Fig. 5 (a) and fitting parameters in Table 5.

Table 5.

Fitting parameters of Avrami model under different temperature and pressure

| Parameters | k (1/min) | n | q_e (mg CO ₂) (Avrami model) |
|------------|-------------|-----|---|
| 423K | 0.088 | 2.9 | 204 |
| 473K | 0.175 | 1.7 | 291 |
| 523K | 0.306 | 1.8 | 441 |
| 573K | 0.083 | 1.6 | 735 |
| 0.2 bar | 0.152 | 1.1 | 42 |
| 0.4 bar | 0.083 | 4.6 | 34 |
| 0.6 bar | 0.103 | 3.9 | 12 |
| 0.8 bar | 0.062 | 2.4 | 6 |

As the regeneration reaction of potassium carbonate sorbent is an endothermic reaction, temperature changes have a significant impact on the desorption efficiency. The experiment was carried out on four different temperatures as described in Table. 5. Following the calculation data, it was investigated that the desorption capacity increased with the rise of operating temperature. At the highest point 573K, sorbent gave 740 mg of regeneration capacity. Avrami equation was used following the same manner as calculating pressure parameters to simulate the experimental data then Avrami desorption model fit well as shown in Fig. 5 (b).

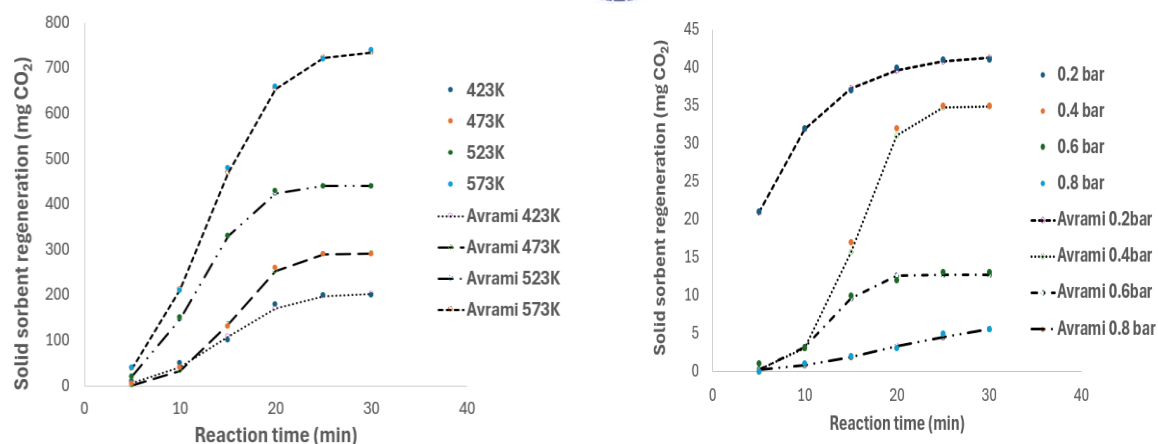


Figure 5. Effect of operating conditions on CO₂ regeneration capacity and Avrami model fitting with experimental data (left) temperature and (right) pressure.

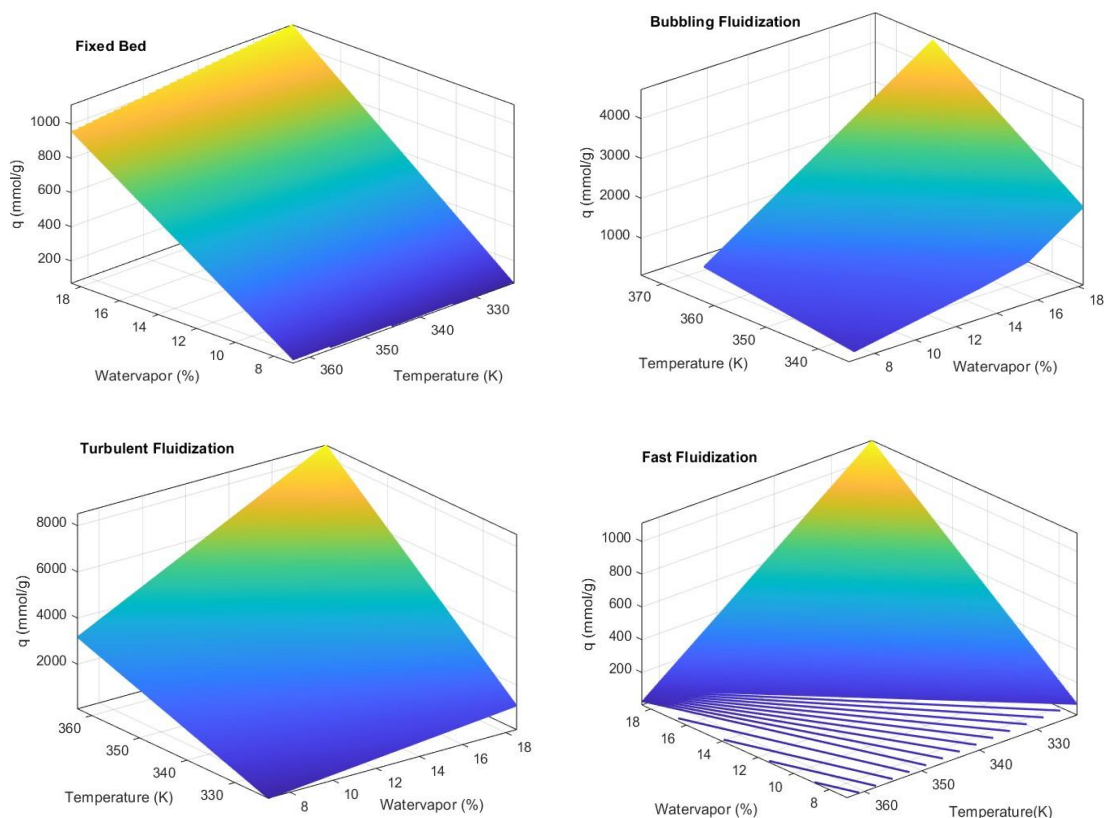


Figure 6. 3D surface interactions between operation parameters and adsorption capacity

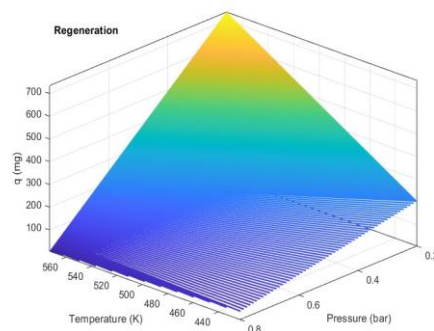


Figure 7. 3D surface interaction between operation parameters and regeneration capacity

The 3D surface interactions studies for applied parameters and capacity in adsorption and desorption were carried out using MATLAB program. For optimum operating temperature and water vapor, it was found that the range of 330K- 340K and 18.5% of water vapor content gave highest points in respective flow patterns as in Fig. 6. In regeneration, the capacity increased along with the rising temperature, but it declined drastically after 0.2 bar. According to Fig. 7, 560 K and 0.2 bar were the optimum conditions for regeneration. The results of 3D surface interactions were found to be similar with the model results explained above showing 8000 mmol/mg range of q in turbulent and 0.2 bar was the best option in regeneration pressure variation.

Conclusion:

Reaction kinetics of selected potassium carbonate sorbent were studied in this work with the application of Avrami model. The adsorption and regeneration are the most critical parts of the gas-solid reaction in carbon capturing and Avrami model approach can simplify the experiment study under various operating conditions with mathematical equations minimizing cost and high amount of time. Model validation is needed to verify the fact that the Avrami model is eligible for the desired scope. In this study, Avrami kinetic model showed reliable results between experimental data in both desorption and regeneration. Mostly, the simulation of model will not be the same as experiment so the values can be adjusted lower or higher to get the possible outcomes. In carbon capturing by solid adsorbent, the effects of operation parameters on the reaction kinetics will not give a complete determination of adsorption and regeneration because there are some remaining parameters such as gas velocity and reactor designs affecting on sorbent efficiency. The studies of reaction kinetic model on solid sorbent for the purpose of carbon capture are still demanding and future research on finding optimal operation parameters is recommended to promote the efficiency of solid sorbent.

Acknowledgements:

This study was financially supported by the Research Fund of master's degree from International Postgraduate Program in Hazardous Substance and Environmental Management (IPHSM), Graduate School, Chulalongkorn University. In addition, this research is funded by National Research Council of Thailand / Chulalongkorn University for providing the Mid-Career Research Grant ([N42A660438](#)).

Nomenclature

| | |
|-------|---|
| q | = adsorption capacity (mmol/g or mg CO ₂) |
| q_e | = equivalent adsorption capacity (mmol/g) |
| t | = time (min) |



| | |
|-----------|--|
| m | = mass of solid loading (g) |
| Q | = flowrate (kg/m^3) |
| C_{in} | = initial CO_2 concentration (mmol) |
| C_{out} | = outlet CO_2 concentration (mmol) |
| F | = outlet fraction of CO_2 |

References:

1. Nathphatsorn Jongartklanga, Saowaluck Chanchairoekb, Pornpote Piumsomboona, Benjapon Chalermssinsuwan, Correlations of kinetic parameters with various system operating conditions for CO_2 sorption using $\text{K}_2\text{CO}_3/\text{Al}_2\text{O}_3$ solid sorbent in a fixed/fluidized bed reactor, Journal of Environmental Chemical Engineering, Volume 4, Issue 2, Pages 1938-1947, June 2016.
2. Sasitron Angkanawisan, Pornpote Piumsomboon, Benjapon Chalermssinsuwan, Regeneration of modified potassium carbonate with monoethanolamine sorbent supported on gamma-alumina in CO_2 capture, Energy Reports, Volume 8, Supplement 1, Pages 171-177, April 2022.
3. Baihe Guo, Yanlin Wang, Jingnan Guo, Xiaolei Qiao, Man Zhang, Yan Jin, Experiment and kinetic model study on modified potassium-based CO_2 adsorbent, Chemical Engineering Journal, Volume 399, November 2020.
4. Zhenshan Li, General rate equation theory for gas-solid reaction kinetics and its application to CaO carbonation, Chemical Engineering Science, Volume 227, December 2020.
5. Sheng Xu, Jingrou Huang, Xiaozhu Wei, Yilan Chen, Minyi Liu, Junjie Wu, Yamin Liu, Preparation of amine functionalized micro-mesoporous silicon adsorbent from fly ash and its kinetic characteristics of CO_2 adsorption/desorption process, Ceramics International, Volume 50, Issue 14, Pages 25150-25160, July 2024.
6. Jeong Ho Choi, Young Eun Kima, Sung Chan Nama, Sung Youl Parka, Il Soo Chuna, Yeo Il Yoona, Jung-Hyun Lee, Promoter characteristic study on the K_2CO_3 absorbents for CO_2 capture: Mass transfer according to functional group and chain length of promoter, Energy Procedia 114 898 – 90, 2017.
7. Rafael M. Siqueira, Geovane R. Freitas, Hugo R. Peixoto, Jailton F. do Nascimento, Ana Paula S. Musse, Antonio E.B. Torres, Diana C.S. Azevedo, Moises Bastos-Neto, Carbon Dioxide Capture by Pressure Swing Adsorption, Energy Procedia, Volume 114, Pages 2182-2192, July 2017.
8. Yafei Guo, Jian Sun, Ruilin Wang, Weiling Li, Chuanwen Zhao, Changhai Li, Jiaqing Zhang, Recent advances in potassium-based adsorbents for CO_2 capture and separation: a review, Carbon Capture Science & Technology, Volume 1, December 2021.
9. Saeed Nazari Kudahi, Ali Reza Noorpoor, Niyaz Mohammad Mahmoodi, Determination and analysis of CO_2 capture kinetics and mechanisms on the novel graphene-based adsorbents, Journal of CO_2 Utilization, Volume 21, Pages 17-29, October 2017.
10. Sutthichai Boonprasop, Benjapon Chalermssinsuwan, Pornpote Piumsomboon, Effect of operating parameters of potassium carbonate supported on gamma alumina ($\text{K}_2\text{CO}_3/\text{Al}_2\text{O}_3$) on CO_2 capture capacity using depressurized regeneration, Journal of the Taiwan Institute of Chemical Engineers, Volume 88, Pages 215-225, July 2018.
11. Zahra Ghanbarpour Mamaghani, Kelly A. Hawboldt, Stephanie MacQuarrie, Adsorption of CO_2 using biochar - Review of the impact of gas mixtures and water on

adsorption, Journal of Environmental Chemical Engineering, Volume 11, Issue 3, June 2023.



CELLULAR AUTOMATA BASED MODEL TO PREDICT WILDFIRE SMOKE DISPERSION

Sirawit Yokyong*, Nattapat Chantarojsiri, Phuwadech Prayurathanes,
Pranee Disrattakit, Laokhwan Ngamprasit
Mahidol Wittayanusorn School, Thailand.
*e-mail: sirawit.yok_g32@mwit.ac.th

Abstract:

Wildfire is a significant global disaster, causing extensive damage to ecosystems and human residences alike. Despite the immediate effects of the fire itself, the smoke poses a critical threat to air quality and public health, contributing to respiratory diseases and environmental pollution. In this study, we aim to develop a model simulating the dispersion of wildfire and smoke to understand better and mitigate their impact. In our model, the cellular automata algorithm and the probability method were used to construct an equation conditioning the state changes of neighboring cells, then the spread of wildfire and smoke dispersion was investigated. The model was validated by integrating data on wind vectors, landscape elevation, and fuel characteristics of past wildfire events, using it on the model. Evaluation of the model's performance has an accuracy of 83% in simulating wildfire behavior compared to real-world observation. Through this computational approach, our study contributes to wildfire management strategies by providing a tool for predicting and understanding the dynamics of wildfire and smoke dispersion, ultimately aiding in the developing more effective mitigation and response measures.

Introduction:

Wildfire is a disaster that causes extensive damage in many ways. The fire from wildfire causes critical damage to many living factors, such as agricultural products or habitats of living organisms. In 2019, a wildfire in Australia was widely spread over 40,000 square kilometers and killed 20 people. Despite the damage from the fire, 25% of PM 2.5 is caused by wildfire, poses a critical threat to air quality and public health, contributes to respiratory diseases and can lead to heart attack.¹

Methodology:

This study uses Cellular Automata to develop a computational model capable of simulating the dispersion of wildfire and smoke. The proposed model was constructed using a combination of the cellular automata algorithm and a probabilistic approach. This hybrid method was chosen to effectively capture the dynamic and stochastic nature of wildfire propagation and smoke behavior in diverse landscapes.

In the proposed model, the simulation map is divided into a 2D array of squares of the same size called a cell. All cells obey a simple rule regarding its eight neighboring cells. All changes from the rules of the entire array will be applied simultaneously in another transition. The duration between each transition is called a time step. Each cell in our model consists of four information layers: Geographical & Climate, Vegetation Types, Wildfire, and Dust.

Geographic & Climate Layer and Vegetation Types Layer

The Geographic & Climate layer includes terrain elevation and wind for each cell. The elevation data are kept as a number in each cell representing its average elevation. However, the wind data are kept as two numbers: wind speed, and its angle with respect to the x-axis. This data is needed since wildfire tends to propagate upwards and along the wind.

Vegetation Types layer includes vegetations in each cell and its propagation constants P_{veg} describing fire propagation and dust emission rate in each vegetation type. Since fire spreads faster among small plants such as grasses and shrubs than among large trees. Each type also has a different dust emission rate.^{2,3}

Both layers are inputted by users, and in this model, we assume that these values in both layers do not evolve over time.

Wildfire Layer

The wildfire evolves over discrete time and space according to rules which is based on probabilities and other geographical properties. For each individual cell, we define variables for x-axis wind speed as w_x , y-axis wind speed as w_y , and terrain height as H_{ij} . For which there are three states for each cell in this layer:

- 1) Has fuel & has not burnt.
- 2) Burning
- 3) Fully burnt, no fuel, or can't be burnt.

All cells start in either state 1) or state 3) in the initial state. Then, we ignite some of the cells, change their states to state 2), and simulate the wildfire.^{4,5}

For this layer, the model uses a probabilistic approach. Each cell c_{ij} will consider all its 8 neighboring cells. The probability P that a fire spreads from cell c_{ij} to its neighbor is described by:

$$P = P_{veg}P_{wind}P_{slope} \quad [1]$$

Here, P_{veg} represents probabilistic factor from vegetation types. P_{wind} represents factor from wind, and P_{slope} represents factor from elevation slope.

P_{veg} is a constant which can be inputted and adjusted in the vegetation type layer, while P_{wind} and P_{slope} are described below.²

$$P_{wind} = e^{V(c_{w1}+c_{w2}(\cos \theta_w-1))} \quad [2]$$

$$P_{slope} = e^{c_s \theta_s} \quad [3]$$

Where V represents wind speed, c_{w1} , c_{w2} and c_s represent adjustable constants. θ_w and θ_s are wind angle and slope angle respectively. All parameters' units in this model are independent from those of in the real world and the values of each parameter need to be calibrated before being used.

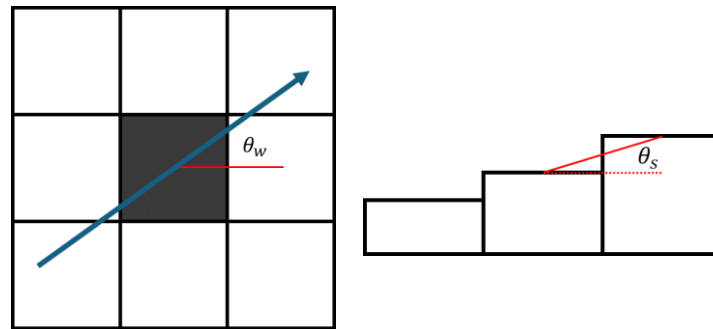


Figure 1. Visualization of wind angle θ_w (left) and slope angle θ_s (right)

Dust Layer

The proposed model uses gaussian plume dispersion equation described by:⁶

$$C = \frac{Q}{2\pi u \sigma_y \sigma_z} \exp\left(-\frac{1}{2} \frac{y^2}{\sigma_y^2}\right) \times \left\{ \exp\left(-\frac{1}{2} \frac{(z-H)^2}{\sigma_z^2}\right) + \exp\left(-\frac{1}{2} \frac{(z+H)^2}{\sigma_z^2}\right) \right\} \quad [4]$$



Where, σ_y and σ_z are horizontal and vertical coefficients, C is concentration at given (x, y, z) point from the emission point, and Q is rate of emission.

For which our model assumes $H = 0$ and $z = 0$

σ_y and σ_z are based on wind stability in 4 states (extremely unstable, moderately unstable, slightly unstable, and neutral) where they are described by

$$\sigma_y = ax^b \quad [5]$$

$$\sigma_z = cx^d + f \quad [6]$$

where, the a , b , c , d , e and f constants depend on the stability class and on the distance, i.e. they may be different for x values smaller or greater than 1 km.⁷ The proposed model assumes a Neutral wind stability and downwind distance > 1 km but can be changed as we need.

Results and Discussion:

The proposed model is tested with a small and uncomplicated initial dataset at first to verify the accuracy of model's predictions and refine the values until it performs correctly.

Results analysis is calculated by:

$$accuracy = \frac{S_{sim} \cap S_{real}}{S_{sim} \cup S_{real}} \times 100\% \quad [7]$$

Where, S_{sim} is the number of cells that has caught fire in the simulation, and S_{real} is the number of cells that has caught fire in the picture.

Model Functionalities

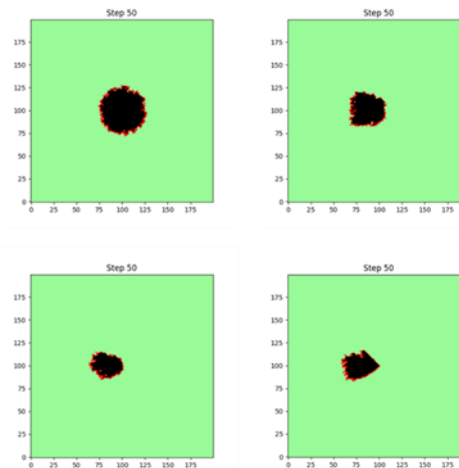


Figure 2. Influence of wind speed on fire spread
(Top left → Top Right → Bottom Left → Bottom Right)
From Low to High

In Figure 2, the wind is simulated to come from the right side of the simulation field, resulted in a fire direction going more into the left side.

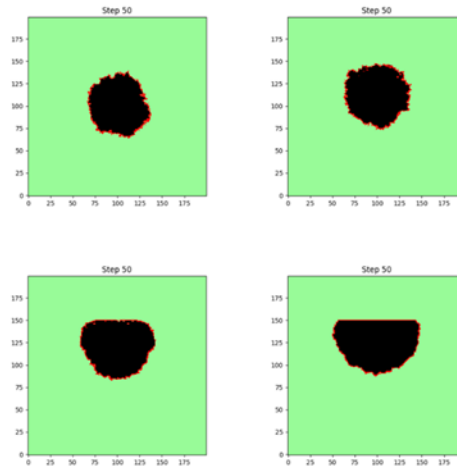


Figure 3. Influence of elevation slope on fire spread
(Top left → Top Right → Bottom Left → Bottom Right)
From Low to High

In Figure 3, the slope angle is set to be higher in each simulation resulted in a more defined border of fire front from being a curve to a straighter line like.

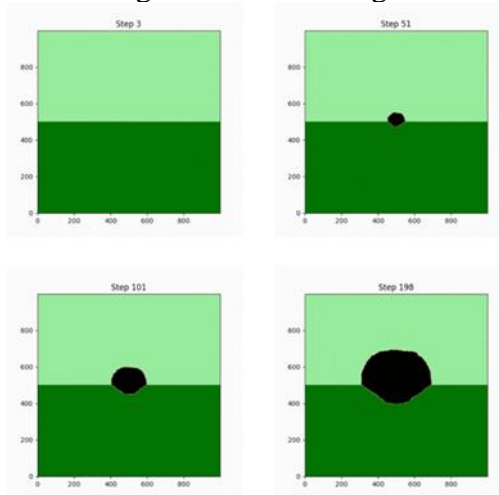


Figure 4. Influence of vegetation type on fire spread

In Figure 4, dark green part has a slower rate of burning from a lower we set. This results in a less spread of the fire on the dark green part compared to light green.

Results

For the verification of the fire spreading module, a wildfire case from satellite image of GISTDA-SENTINEL2 were used [Chiang Mai, Doi Inthanon, 2020] (Figure 5.) which we mapped (Figure 6.) the vegetation types and input the corresponding coefficient into the model.

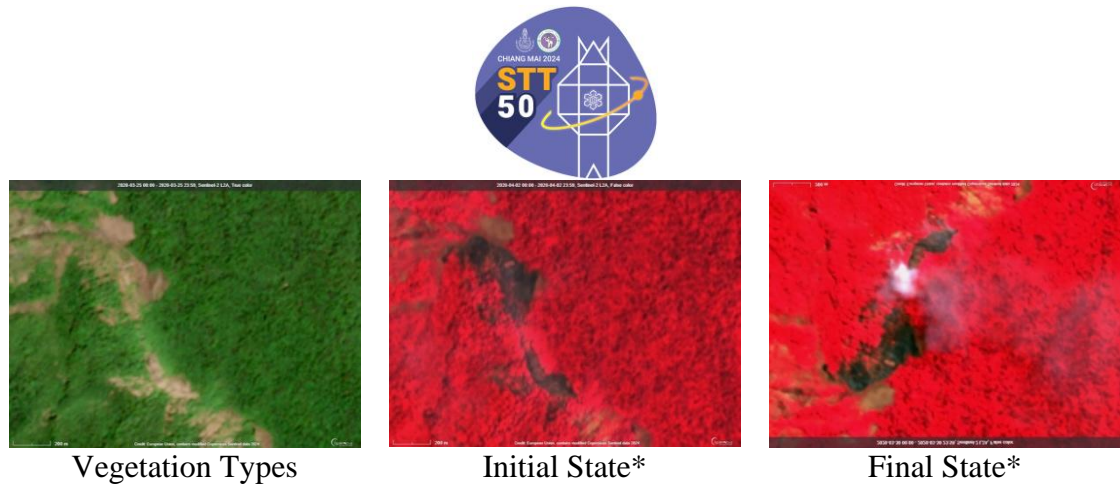


Figure 5. Wildfire case used in the model
(*red filtered)

GISTDA-SENTINEL 2 [Chiang Mai, Doi Inthanon, 2020]



Figure 6. Mapped image

The input is simulated until the final timestep is reached and compared to real final state. See below.

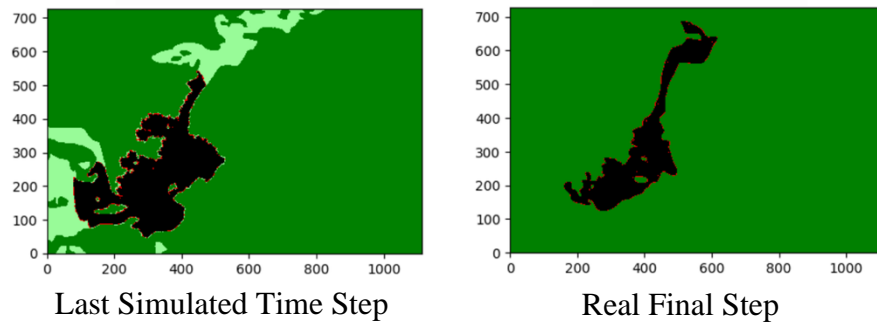


Figure 7. Comparison between Simulated and Real event

Optimizing the run time of the model is one of our top priorities. We ran the model for some size of map (cells * cells) and graph out the run time. See Figure 8.

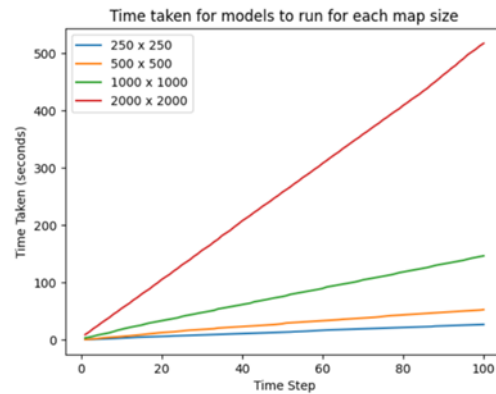


Figure 8. Time taken for model to run for each map size

Time taken to simulate 100-time steps

- 250 x 250 - 27 s
- 500 x 500 - 53 s
- 1000 x 1000 - 146 s
- 2000 x 2000 - 517 s

And on average

- 250 x 250 - 0.27 s
- 500 x 500 - 0.53 s
- 1000 x 1000 - 1.46 s
- 2000 x 2000 - 5.17 s

The model can work quickly enough for forecast forest fires, and the time it takes depends on the number of cells on the map.

For dust concentration module, result from gaussian plume dispersion equation implemented into the model is as shown.

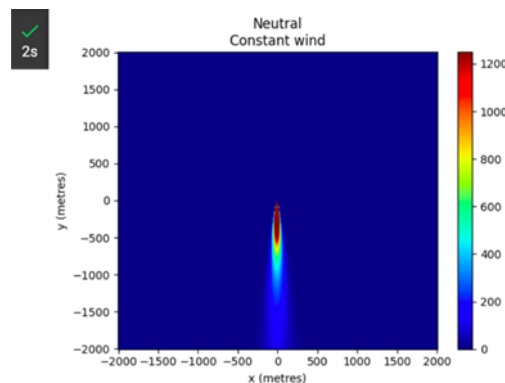


Figure 9. Result from dust particles simulation

To verify the accuracy of the model, we used NOAA's READY model inputted with the same initial variables condition.

The variables used for both simulation:

- Q (Gas emission rate)
- H (Origin of dispersion height, m)
- v (Downwind velocity, m/s)
- wind direction (wind_dir, degrees)
- r (radius)
- t (generation time frame, hours)

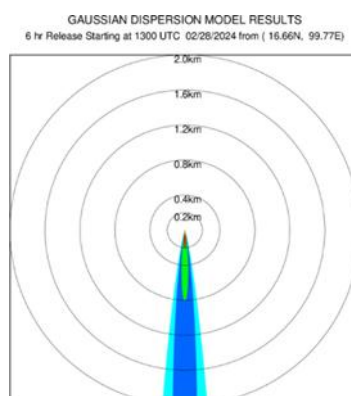


Figure 10. Simulation Result from READY model

The results are similar to those generated by the READY model were obtained. Additionally, the time required to produce concentrations in the proposed model was significantly reduced.

Conclusion:

The proposed wildfire model consists of three adjustable variables: wind, elevation, and vegetation type. It can work quickly depending on the number of cells in the map. When the model was tested on real-life samples, it was 83 percent accurate in predicting wildfires. The inaccuracy was caused by; Sample's satellite image resolution, terrain and wind information that wasn't detailed enough, and few vegetation types.

For dust layer, the model uses gaussian plume dispersion model which is close to NOAA's READY Model using the same initial conditions.

To be fully able to use the model, we need to integrate our currently two separate modules of fire and dust to one single model with two layers. An interface for inputting initial state parameter can also be further developed.

Suggestions

- More factors should be taken into consideration, such as humidity, temperature, and more types of vegetation.
- The model should be implemented into other programming languages and optimized for faster execution.
- A more efficient and accurate input method for scenarios should be implemented.
- Calculations in this model should be given an appropriate size for faster execution.
- All variables and constants in the model must be calibrated before execution.

Acknowledgements:

This project is supported by Mahidol Wittayanusorn School. Additional support was provided in data and model by GITSDA sentinel-2 satellite, Thai Meteorological Department (TMD), and National Oceanic and Atmospheric Administration (NOAA).

References:

1. Burke M, Driscoll A, Heft-Neal S, Xue J, Burney J, Wara M. Proc Natl Acad Sci U S A. 2021;118(2).

2. Freire JG, DaCamara CC. *Nat Hazards Earth Syst Sci.* 2019;19(1):169–179.
3. Trucchia A, D’Andrea M, Baghino F, Fiorucci P, Ferraris L, Negro D, Gollini A, Severino M. *Fire.* 2020;3(3):26.
4. Alexandridis A, Russo L, Vakalis D, Bafas GV, Siettos CI. *Int J Wildland Fire.* 2011;20(5):633.
5. Ntaimo L, Hu X, Sun Y. *SIMULATION.* 2008;84(4):137–155.
6. Rjoub D, Alsharoa A, Masadeh A. *Electronics.* 2023;12(5):1239.
7. Lotrecchiano N, Sofia D, Giuliano A, Barletta D, Poletto M. *Int J Safety Secur Eng.* 2020;10(4):431–439.



DEVELOPMENT OF AMINE-MODIFIED NaY ZEOLITES FROM RICE HUSK WASTE FOR EFFICIENT DIRECT AIR CO₂ CAPTURE.

Kanchana Phianchana,¹ Pacharapol Nokpho,² Benjapon Chalermnsinsuwan,^{2*}

¹Program of Petrochemistry and Polymer Science, Faculty of Science, Chulalongkorn University, 254 Phayathai Road, Wangmai, Pathumwan, Bangkok 10330, Thailand

²Department of Chemical Technology, Faculty of Science, Chulalongkorn University, 254 Phayathai Road, Wangmai, Pathumwan, Bangkok 10330, Thailand

*e-mail: benjapon.c@chula.ac.th

Abstract:

Rice Husk Silica (RHS) in amorphous phase was extracted through leaching of hydrochloric acid and calcination from rice husk, which is a byproduct from rice milling process. This RHS was then employed as an effective silica source (97.96%) for synthesizing zeolites. Zeolites are well-known for their unique structural features and are particularly valued for their CO₂ capture capabilities. The cations within zeolites are crucial in attracting CO₂ molecules into their pores. While zeolites inherently possess good CO₂ adsorption capacity, their performance can be further enhanced through surface modifications that increase CO₂ uptake. Zeolites with the FAU structure are extensively researched due to their stable crystal formations and expansive pore volumes. Amine functionalization has been widely used to increase CO₂ adsorption in these zeolites for effectively enhancing their CO₂ capture capacity. In this study, NaY zeolite was synthesized from local Thai rice husk waste to become silica and subsequently modified on its surface with various types of amines. The results demonstrated that high-purity silica was successfully extracted from the rice husk waste, providing an adequate silica base for zeolite synthesis. The synthesized NaY zeolites were characterized by XRD to confirm the zeolite structure and FT-IR to determine functional groups. Furthermore, the amine-modified zeolites exhibited enhanced CO₂ capture efficiency across multiple adsorption-desorption cycles.

Introduction:

Air pollution is emitted from industries and power plants that burn fossil fuels such as coal, oil and natural gas. This emitted air pollution known as a greenhouse gas, including carbon dioxide (CO₂), is the major contributor to global warming and continually rising global temperatures [1]. The growing demand for energy and the reliance on fossil fuels in urban and industrial activities have led to an excessive production of greenhouse gases. Prioritizing the capture of CO₂ is crucial for environmental protection. One approach is to reduce fossil fuel usage and increase the use of renewable energy sources. Other solutions include separating and converting CO₂ into valuable fuels. Currently, absorption and adsorption are the most commonly used methods for CO₂ capture [2]. Various materials, including zeolite-based catalysts, are used for CO₂ conversion [3].

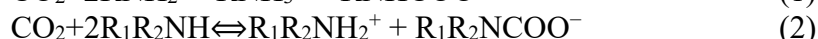
Solid adsorbents such as silica [4], zeolite [5], MOF (Metal Organic Framework) [6], activated carbon [7], alumina [8], metal oxides [9] and organic polymers [10] are used in adsorption application. Zeolites are preferred adsorbents for CO₂ due to their high surface area, appropriate pore size, and thermal and chemical stability, especially at low temperatures.

Rice husk, which is often considered as a solid waste from rice milling, contains approximately 70% of organic compounds and 30% of hydrate silica (SiO₂) [11]. When rice husk is leached with mineral acid and then calcined in air, it produces white powder rice husk

silica (RHS). RHS, with its high silica purity, is an excellent source for producing inorganic materials like silicon carbide and silicon nitride. Additionally, RHS has been used as a silica source for synthesizing microporous materials such as zeolites and mesoporous silica.

Zeolites are microporous crystalline aluminosilicates composed of tetrahedral TO_4 units ($\text{T}=\text{Si}$ or Al) linked together by sharing oxygen atoms. The general formula of zeolites is $\text{M}^{n+}[\text{Si}_x\text{Al}_y\text{O}_z]\cdot m\text{H}_2\text{O}$ where M^{n+} is extra-framework cation, $[\text{Si}_x\text{Al}_y\text{O}_z]$ is zeolite framework, and $m\text{H}_2\text{O}$ is water molecules in sorbed phase. NaY zeolite, the main focus in this work, is in the faujasite (FAU) family with a framework containing double 6-rings linked through sodalite cages, creating supercages with an average pore diameter of 7.4 Å [12]. Among the FAU structure zeolites, 13X and NaY are the most widely used for the adsorption and storage of CO_2 [13]. The efficiency of NaY zeolites in CO_2 adsorption is attributed to their high surface area, robust crystal structure, and extensive three-dimensional pore network. Cations in zeolites play a critical role in CO_2 capture because they can attract CO_2 into zeolite.

Amine modification of zeolites enhances CO_2 adsorption by introducing amine groups onto the zeolite surface. This modification can activate aluminum sites, increase surface area, reduce pore size, and improve porosity, stability, and regeneration properties. Monoethanolamine (MEA) and diethanolamine (DEA) are commonly used to boost the adsorption capacity and selectivity of zeolites. Equations (1) and (2) illustrate the reactions of different amines with CO_2 : Equation (1) represents the reaction between CO_2 and primary amines, while Equation (2) shows the reaction between CO_2 and secondary amines [2].



In this study, NaY zeolite was synthesized from local Thai rice husk waste to become silica and subsequently modified on its surface with various types of amines include: Monoethanolamine (MEA), Diethanolamine (DEA), 2- amino-2-methyl-1-propanol (AMP), N-methyl-4-piperidinol (MPDL) and Methyldiethanolamine (MDEA). The results demonstrate that high-purity silica was successfully extracted from the rice husk waste, providing an adequate silica base for zeolite synthesis. The amine-modified zeolites exhibited enhancement of CO_2 capture efficiency across multiple adsorption-desorption cycles.

Methodology:

1. Silica extraction from Rice husk

Rice husk (local rice mill, Thailand) was washed thoroughly with water to remove the adhered soil and dust and dried at 100 °C overnight. The dried rice husk was refluxed in 3M HCl solution (37%wt HCl, Merck) for 3 h, filtered and washed repeatedly with water until the filtrate was neutral (pH 5-7). After the acid treatment, the rice husk was dried at 100 °C overnight and pyrolyzed in a furnace muffle (Carbolite) at 600 °C for 5 h to remove the organic contents [12]. The obtained product, RHS was characterized by X-ray Fluorescence (XRF), Fourier-transform infrared spectroscopy (FTIR) and X-ray Diffractometer (XRD).

2. Synthesis of NaY Zeolite using silica extracted from Rice husk

The zeolite NaY was synthesized from a seed gel and feedstock gel with a procedure modified from that described elsewhere [14]. The major difference between seed gel and feedstock gel is that the feedstock gel was prepared and used immediately without aging. The first part, the seed gel (solution 1) with a molar ratio of $10.67\text{Na}_2\text{O} : \text{Al}_2\text{O}_3 : 10\text{SiO}_2 : 180\text{H}_2\text{O}$ was prepared by adding Na_2SiO_3 solution to the solution of NaAlO_2 (Cernic international CO., LTD.). The mixture was stirred until homogeneous and transferred into a polypropylene (PP) bottle, capped, and aged at room temperature for 24 h. The feedstock gel (solution 2) with molar ratio $4.30\text{Na}_2\text{O} : \text{Al}_2\text{O}_3 : 10\text{SiO}_2 : 180\text{H}_2\text{O}$ was prepared in similar fashion to that of the seed gel except that it was used immediately without aging. The NaY synthesis in which



the seed gel and the feedstock gel were mixed and aged at room temperature for 24 h and crystallized at 90 °C at 24 h. After the crystallization, the samples were cooled down to room temperature. The solid product was separated by filtration, washed thoroughly with distilled water, and dried at 110 °C. The obtained product was characterized by X-ray Fluorescence (XRF), X-ray Diffractometer (XRD), Surface area and Pore size analyzer: BET and CHN analyzer.

3. Preparation of the amine/zeolite sorbents

A non-modified solid sorbent, Amines was loaded on support NaY zeolite by impregnation method. The 3 g of NaY zeolite and 30% Amines with 70 ml of de-ionized water were mixed on stirrer at the speed of 220 rpm for 24 h. Then, the mixture was filtrated and dehydrated in oven at 100 °C for 24 h. To study the effect of preparation method, the preparation parameters affecting the CO₂ adsorption capacity of solid sorbents were explored. There are parameters to study including: solid sorbent modification using MEA (supplied by Chemipan company), DEA (supplied by KEMAUS), AMP (supplied by Myskinreceipt), MPDL and MDEA (supplied by Hebei Guanlang biotech).

4. CO₂ capture experiment

The experimental apparatus utilized for the CO₂ capture process is shown in Figure 1. To initiate CO₂ adsorption, a 1 g sample of the sorbent was loaded into a fixed bed reactor. The sorbent was then regenerated by heating the reactor to 120°C for 45 minutes with N₂ gas (supplied by Thai-Japan company). The flow rate of the N₂ gas was controlled by a mass flow controller set at 150 mL/min. The adsorption process was began by introducing the ambient air, which contains CO₂ at a concentration of approximately 400 ppm at feed flow rate maintained at 150 mL/min. The CO₂ concentration in the outlet gas was continuously monitored using a CO₂ sensor. The process continued until the sorbent reached saturation, as indicated by the sensor readings showing CO₂ levels around 400 ppm.

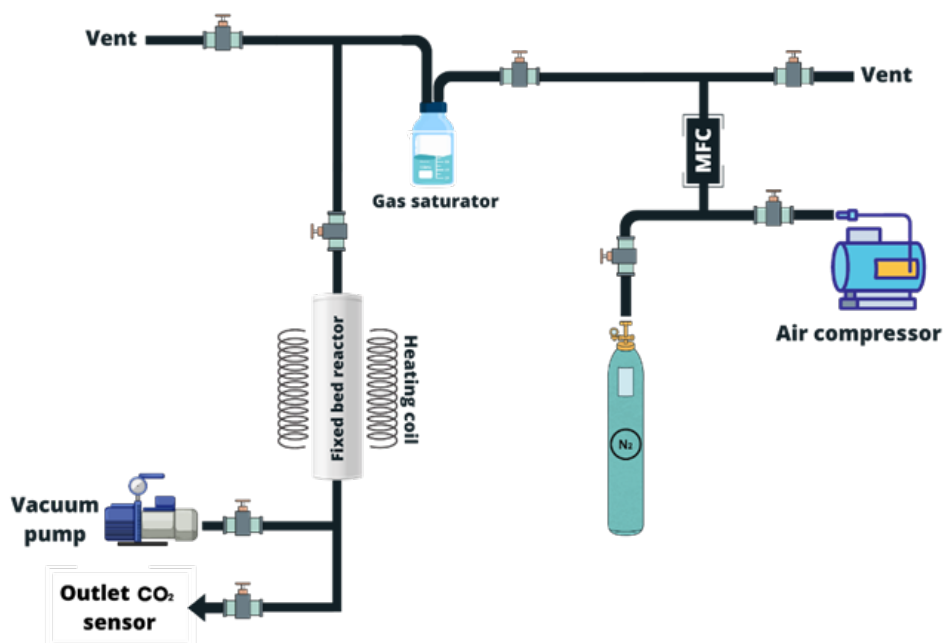


Figure 1. Schematic diagram of CO₂ capture process in fixed bed reactor

Results and Discussion:

1. RHS characterization

The chemical compositions of RHS in the form of stable oxides are shown in Table 1. The major component was SiO_2 with purity approximately 98%wt along with small amounts of other inorganic oxides. The silica purity of the RHS from acid-leached rice husk was sufficient to use as a silica source for the synthesis of NaY zeolite.

Table 1. Chemical components of RHS determined by XRF.

| Component | %wt. |
|-------------------------|------|
| SiO_2 | 98 |
| Al_2O_3 | 0.6 |
| CaO | 1 |
| K_2O | 0.4 |

1.1 Fourier-transform infrared spectroscopy (FTIR)

Characterization was carried out to examine the functional group characteristics of the silica synthesized from RHS. The spectra were obtained at wavenumber $400\text{--}2000\text{ cm}^{-1}$, and the results are shown in Figure 2. The result showed that the appearance of the synthesized silica by hydrochloric acid indicates asymmetric stretching vibration of the siloxane bonds (Si–O) at 1058.73 cm^{-1} and symmetric stretching vibration 803.69 cm^{-1} . The peaks appearing at 441.14 cm^{-1} can be attributed to Si–O–Si bending vibration [15].

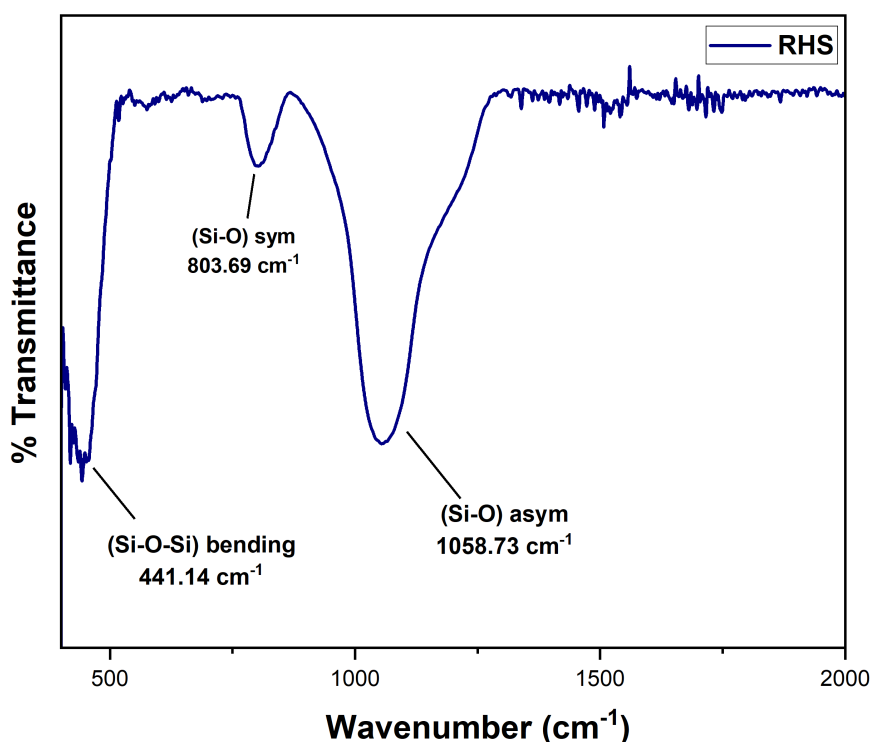


Figure 2. FTIR spectra of RHS.

1.2 X-ray Diffractometer (XRD)

XRD pattern of RHS in Figure 3, only a broad peak with 2θ at 22° , which is a characteristic of a high purity amorphous silica (SiO_2), was observed. This assumption



correlates well with the result from elemental compositions from XRF as demonstrated in Table 1. Moreover, the obtained silica in the amorphous phase could be beneficial for zeolite synthesis because it can be dissolved easily in NaOH solution to produce sodium silicate (Na_2SiO_3) for NaY zeolite synthesis [12].

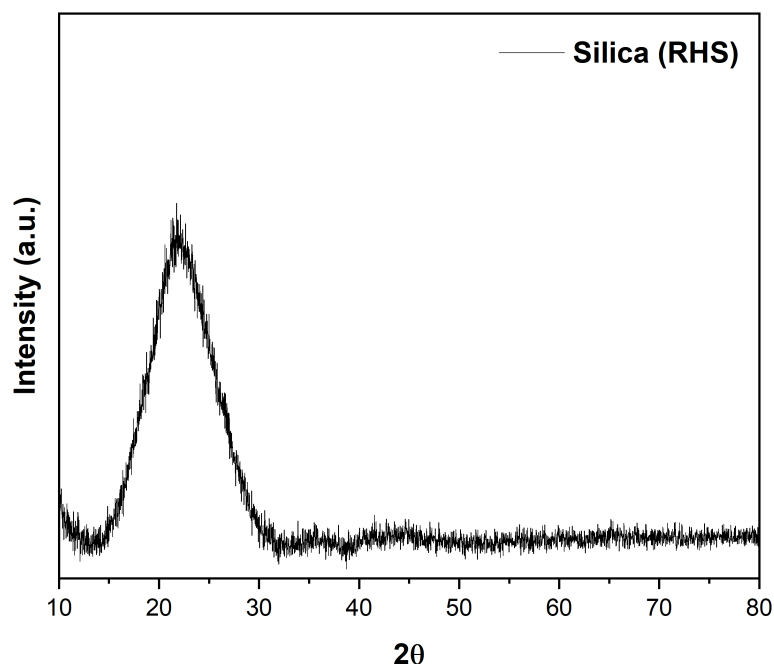


Figure 3. XRD pattern of RHS.

2. NaY zeolite characterization

2.1 X-ray Fluorescence (XRF)

The chemical compositions and $\text{SiO}_2/\text{Al}_2\text{O}_3$ ratio of NaY zeolite were analyzed by energy dispersive XRF. The results are shown in Table 2. The SiO_2 and Al_2O_3 were the predominant oxides with a mass ratio of 2.47. The Si/Al ratio of NaY zeolite is the ratio of silicon (Si) to aluminum (Al) atoms in the framework, which is directly related to the $\text{SiO}_2/\text{Al}_2\text{O}_3$ ratio. In NaY zeolite, the typical Si/Al ratio is between 2 and 3, with a common value of around 2.5 [16].

Table 2. Chemical components of NaY zeolite.

| Component | %wt. |
|--|------|
| SiO_2 | 58.5 |
| Al_2O_3 | 23.7 |
| Na_2O | 15.8 |
| $\text{SiO}_2/\text{Al}_2\text{O}_3$ ratio | 2.47 |

2.2 X-ray Diffractometer (XRD)

The XRD patterns of NaY zeolite are shown in Figure 4. The products from synthesized NaY zeolite were characterized by XRD compared with the pattern of standard

NaY. As shown in Figure 4, synthesized NaY zeolite gave an XRD pattern characteristic of NaY, and all peaks were similar to those of the standard NaY. In addition, the NaY zeolite whose peaks are at 2-Theta of 5°, 10°, 11°, 15°, 19°, 20° and 24°. The process with an aging time of 24 hours was sufficient to produce NaY in its pure phase, confirming the successful synthesis of pure NaY zeolite from silica extracted from RHS [17].

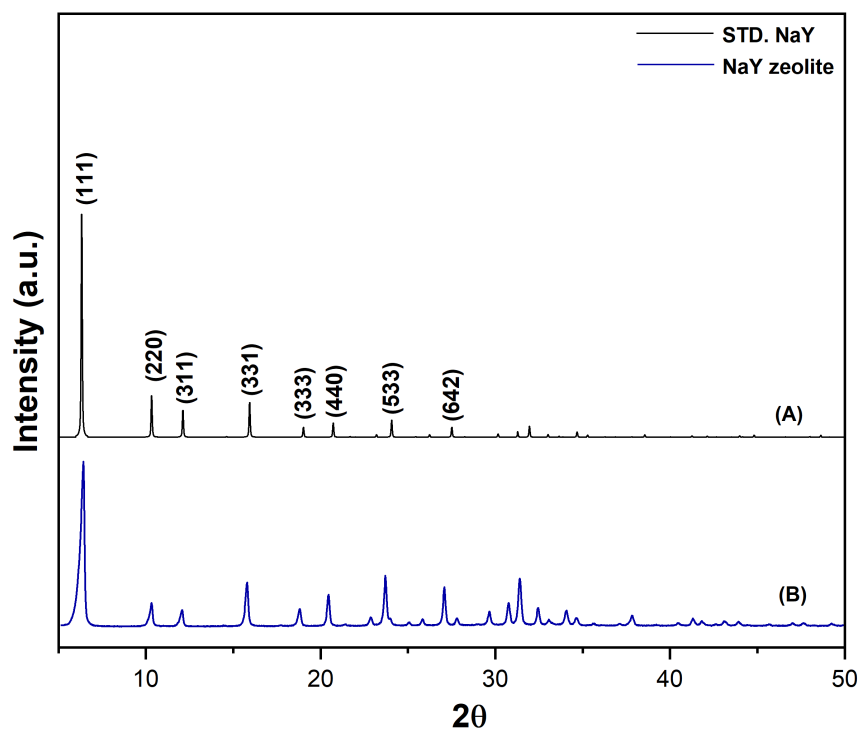


Figure 4. XRD spectrum of (A) standard NaY zeolite and (B) NaY synthesis.

2.3 Surface area and Pore size analyzer: BET

The N₂ adsorption–desorption isotherms of NaY zeolite at 77 K in Figure 5. are of a typical type IV isotherm, which indicate the mesoporous feature of the adsorbents. The pore characteristics of the adsorbents are listed in Table 3 [16]. The BET surface area was measured to be 616.9 m²/g, closely matching values reported in other studies [12][18] on NaY zeolite synthesis, this is evidence that crystallization for 24 h allowed a more complete formation of NaY zeolite and the high surface area highlights its effectiveness as an amine support.

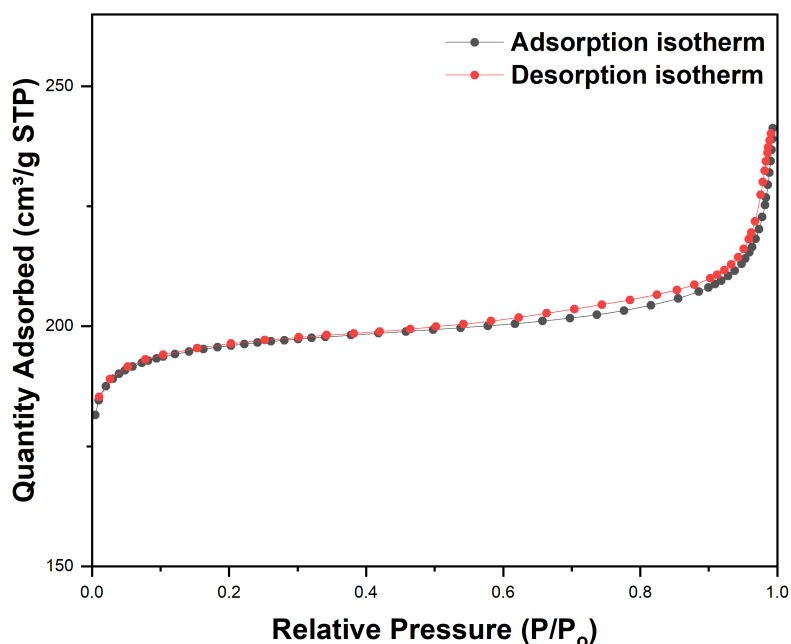


Figure 5. N₂ adsorption–desorption isotherms of NaY zeolite.

Table 3. The BET surface areas, pore volumes, and average pore diameters of NaY zeolite.

| Sample | BET surface area (m ² /g) | Pore volume (cm ³ /g) | Pore diameter (nm) | Ref. |
|-------------|---|-------------------------------------|-----------------------|-----------|
| NaY zeolite | 616.9 | 0.37 | 2.47 | This work |
| NaY zeolite | 625.1 | 0.32 | 2.55 | [12] |
| NaY zeolite | 691.5 | 0.43 | 2.55 | [18] |

2.4 CO₂ adsorption capacity

In order to examine the CO₂ adsorption capacity on solid absorbent, the repeated CO₂ adsorption–desorption runs were carried out. In this recycle test, the value of maximum CO₂ adsorption capacity was steady at each run due to complete removal of CO₂ from the synthesized adsorbent in the process of desorption. The maximum capacities of MEA/NaY, DEA/NaY, MPDL/NaY, AMP/NaY and MDEA/NaY were 14.31, 10.19, 10.73, 3.28 and 2.66 mgCO₂/g adsorbent, respectively (Table 4 and Figure 6).

Table 4. CO₂ adsorption capacity of non-modified and amine-modified NaY zeolites.

| Sample | CO ₂ Adsorption Capacity (mgCO ₂ /g sorbent) |
|--------------|---|
| NaY zeolites | 1.67 |
| MEA/NaY | 14.31 |
| DEA/NaY | 10.19 |
| MPDL/NaY | 10.73 |
| AMP/NaY | 3.28 |
| MDEA/NaY | 2.66 |

Effect of the amine types

As mentioned above, the average pore diameter of NaY zeolite is 2.46 nm, which renders it mesoporous and therefore suitable for amine loading. The CO₂ adsorption capacity was studied by impregnated amine to the solid sorbent. MEA/NaY had higher CO₂ adsorption capacity than DEA and MPDL modified sorbents. This may be attributed to the functional group R-NH₂ of amines should be the active sites for CO₂ adsorption.

The interaction of CO₂ with amines can be governed by several different mechanisms. Primary and secondary amines can react directly with CO₂ to produce carbamates through the formation of zwitterionic intermediates. The mechanism for the reaction of CO₂ with primary, secondary, and tertiary amines, the first step proceeds with the lone pair on the amine attacking the carbon from CO₂ to form the zwitterion. Free base then deprotonates the zwitterion to form the carbamate. Tertiary amines react with CO₂ through a different mechanism. Instead of reacting directly with CO₂, tertiary amines catalyze the formation of bicarbonate. In this mechanism, CO₂ does not bind with tertiary amines without H₂O (under dry condition). In this study, the CO₂ adsorption test was carried out under dry conditions, and this cannot serve the role of the CO₂ capturing. This leads lower adsorption capacity than theoretical value. Adsorbed amount of CO₂ on MDEA/NaY and AMP/NaY was very low for the adsorption test under the dry condition, and the adsorption of CO₂ on tertiary amines may be due to electrostatic and van der Waals forces [19].

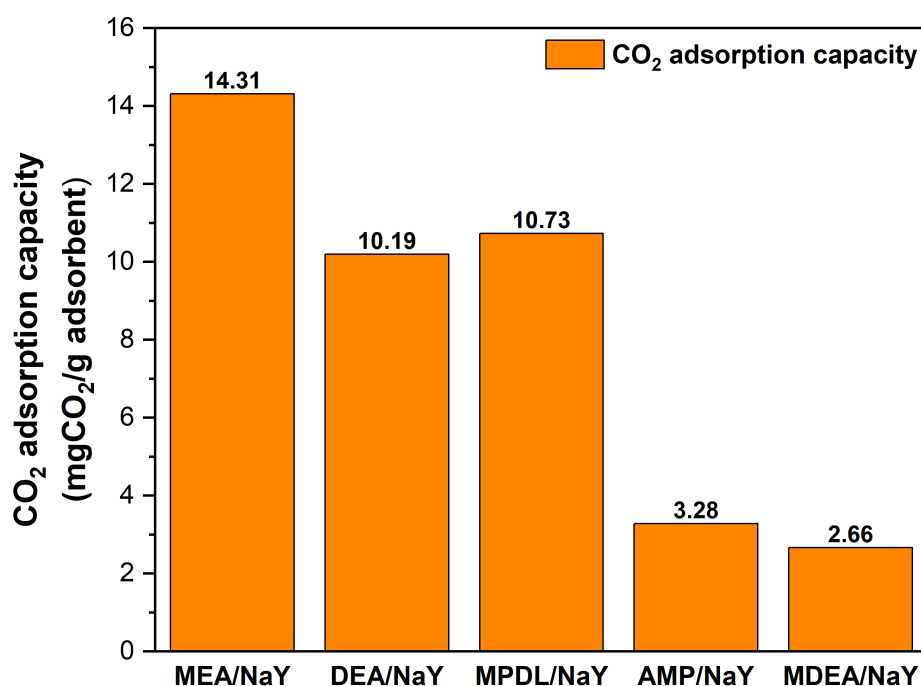


Figure 6. CO₂ adsorption capacity of amine-modified NaY zeolites.

Conclusion:

The development of an alternative silica extraction from Rice husk waste and utilization in NaY zeolite synthesis was accomplished by leaching in 3M HCl solution. The SiO₂ purities obtained from the Rice husk (RHS) 98wt%. NaY zeolite was successfully synthesized from RHS. NaY zeolite as supports for amine-based adsorbents and used for adsorbing CO₂ in fixed bed reactor. The loading of the five amines (MEA, DEA, MPDL, AMP and MDEA) on the NaY zeolite was investigated, and the adsorbent loaded by MEA was found to have the highest CO₂ adsorption capacity 14.31 mgCO₂/g adsorbent. The



functional -NH_2 group of the amines was found to be the active site and chemical adsorption be the primary mechanism for CO_2 adsorption.

Acknowledgements:

This research project was supported by The Second Century Fund (C2F), Chulalongkorn University. In addition, the National Research Council of Thailand / Chulalongkorn University for providing the Mid-Career Research Grant (N42A660438) was partially acknowledged.

References:

1. Tobaramseekul P, Sangsuradet S, and Worathanakul P. *Atmosphere*. 2022;**13**(2).
2. Bahmanzadegan F and Ghaemi A. *Case Studies in Chemical and Environmental Engineering*. 2024;**9**:100564.
3. Al-Qadri AA, et al. *Journal of Energy Chemistry*. 2023;**79**:418-449.
4. Taheri FS, et al. *Energy and Fuels*. 2019;**33**(6):5384-5397.
5. Khajeh Amiri M, Ghaemi A and Arjomandi H. *Iranian Journal of Chemical Engineering(IJChE)*. 2019;**16**(1):54-64.
6. Mondino G, et al. *Industrial and Engineering Chemistry Research*. 2020;**59**(15):7198-7211.
7. Lee KM, et al. *Industrial & Engineering Chemistry Research*. 2012;**51**(3):1355-1363.
8. Nokpho P, et al. *Energy Reports*. 2022;**8**:134-140.
9. Ma X, et al. *AIChE Journal*. 2023;**69**(1).
10. Maleki F, Ghaemi A, and Mir Mohamad G. Sadeghi. *Environmental Progress and Sustainable Energy*. 2023;**42**(1).
11. Park BD, et al. *Biomass and Bioenergy*. 2003;**25**(3):319-327.
12. Wittayakun J, Khemthong P, and Prayoonpokarach S. *Korean Journal of Chemical Engineering*. 2008;**25**(4):861-864.
13. Walton KS, Abney MB, and Douglas LeVan M. *Microporous and Mesoporous Materials*. 2006;**91**(1):78-84.
14. Robson HE. 2nd rev. ed. 2001: Amsterdam ; New York : Elsevier.
15. Dhaneswara D, et al. *International Journal of Technology*. 2020;**11**(1):200-208.
16. Banaei M, Anbia M, and Kazemipour M. *Journal of Ultrafine Grained and Nanostructured Materials*. 2018;**51**(2):174-182.
17. Association SC.o.t.I.Z. *Database of Zeolite Structures*. 2017;Available from: https://europe.iza-structure.org/IZA-SC/pow_pat.php?ID=99.
18. Feng L, et al. *Adsorption*. 2020;**26**(7):1101-1111.
19. Ko YG, Shin SS, and Choi US. *Journal of Colloid and Interface Science*. 2011;**361**(2):594-602.



EXPLORING MICROWAVE-ASSISTED ZEOLITE 13X REGENERATION FOR EFFECTIVE DIRECT AIR CO₂

Paka-on Amornsinsin,¹ Pacharapol Nokpho,¹ Pornpote Piumsomboon,¹

Benjapon Chalermssinsuwan^{1,*}

¹ Department of Chemical Technology, Faculty of Science, Chulalongkorn University,
254 Phayathai Road, Wangmai, Pathumwan, Bangkok 10330, Thailand

*e-mail: benjapon.c@chula.ac.th

Abstract:

Since the beginning of the industrial revolution, there has been an unprecedented increase in heavy pollution released from industries such as the combustion of fossil fuels including coal, crude oil, and natural gas which contributes to global warming and climate change, resulting in global average temperatures rising by 0.8-1.2°C. In 2020, the average yearly CO₂ level in the atmosphere has increased by about 50% and reached its highest value of 420 ppm. An interesting CO₂ capture technology is direct air capture (DAC) by solid adsorbent. A suitable solid adsorbent should have high CO₂ adsorption capacity, selectivity, and stability during several adsorption/desorption cycles. Zeolite 13X is one of the most interesting adsorbents due to the features listed above. However, utilizing the conventional heating approach to regenerate zeolite 13X consumed a lot of energy during the regeneration process. Another fascinating option is to use microwave radiation because it is easy to operate and use less time to regenerate. This study then investigated the effect of microwave oven power and regeneration time of zeolite 13X. Moreover, the ANOVA analysis was applied in this study to evaluate the suitable condition in term of regeneration efficiency.

Introduction:

Global climate change is an immediate and pressing issue that requires urgent global attention. The average global temperature has risen by 0.8 to 1.2°C. Additionally, CO₂ levels have risen by 50% since the Industrial Revolution, with the highest recorded value of 412.5 ppm in 2021. [1] This elevated level of CO₂ contributes to the greenhouse effect by trapping excess heat in the atmosphere, thereby driving global warming. Extensive research indicates that, in addition to industrial emissions, which are primarily caused by fuel burning, human daily activities significantly contribute to the increase in atmospheric CO₂ levels. [2, 3] Consequently, technologies for capturing CO₂ directly from ambient air at low concentrations have been developed to address this issue [4], as only industrial CO₂ capture is insufficient to eliminate excess CO₂ emissions. The use of liquid amine-based to capture CO₂ is a conventional method for capturing CO₂ directly from the air. However, this strategy has drawbacks. First, the amine solution has a corrosive effect on the equipment. Second, the amine degrades when it is used over multiple adsorption/desorption cycles. Finally, it takes a lot of energy to regenerate. [5] Given these considerations, using solid adsorbents for direct air CO₂ capture is a promising alternative due to the low energy requirement for regeneration, relatively fast kinetics, reasonable stability over multiple adsorption/desorption cycles, and high CO₂ equilibrium loading compared to liquid amine-based CO₂ capture method. [6,7]

Generally, silica, zeolite, MOF (Metal Organic Framework), activated carbon, graphene, metal oxides, alumina, and organic polymers are some of the most widely used solid adsorbents for CO₂ adsorption. Among these, zeolites are particularly notable due to their high surface area, well-defined pore sizes, and commendable thermal and chemical stability, which results in high CO₂ adsorption capacity. Specifically, zeolite 13X has been identified as the

most effective zeolite for CO₂ capture due to its suitable silica to alumina ratio. Moreover, zeolite 13X has a more complex FAU structure and a larger pore size than other zeolites. Due to the larger pore size, zeolite 13X can accommodate larger molecules, such as CO₂, which results in a greater CO₂ adsorption capacity. [8]

Zeolite 13X with a limited thermal conductivity presents significant challenges for its regeneration. Conventional heating methods, also known as temperature swing adsorption (TSA), are energy-intensive and time-consuming. Furthermore, it also has a disadvantage in terms of heat loss due to conduction, convection, and radiation, which is a mechanism that occurs during the heating process for regeneration. [9] As a result, microwave regeneration is a novel technique that uses microwave radiation to directly heat the sorbent by inducing molecular vibrations within the sorbent and releasing captured CO₂ without first heating the reactor walls. Moreover, Microwave regeneration offers potential advantages, including quick start-up and stopping, non-contact heating, reduced energy consumption, and shorter regeneration times compared to conventional methods. [10, 11] Elison et al. reported that microwaves have reduced CO₂ desorption times by 50% compared to conventional regeneration due to the fast heat rates caused by microwave irradiation. Furthermore, the energy required for microwave desorption was estimated to be approximately 16-18 kJ/mol, which is less than half of the energy needed for conventional thermal desorption, which is around 41.5 kJ/mol. [12] Similarly, Nokpho et al. investigated the regeneration of gamma-alumina sorbent modified with potassium carbonate and monoethanolamine using microwave radiation. Their study reported that the microwave regeneration approach not only increases efficiency but also the sorbent's reusability. [13]

The factors discussed above motivate this study, which focused on the microwave regeneration of zeolite 13X by capturing CO₂ directly from the air using a fixed-bed column. The objective of this study is to evaluate the effects of microwave power and time on the regeneration efficiency of the adsorbent over multiple adsorption/desorption cycles. In addition, the ANOVA analysis was applied in this study to evaluate the suitable condition in term of regeneration efficiency.

Methodology:

Materials

The CO₂ capture adsorbent used in this study is a commercial zeolite 13X in the shape of spherical pellets provided by Jiangxi OIM Chemical CO., LTD, China. The particle size ranged from 1.6-2.5 mm, with a bulk density ≥ 0.64 g/ml. The purity of N₂ used was 99.99% was supplied by Thai-Japan company and CO₂ ~ 400 ppm adsorbed from ambient air.

CO₂ adsorption experiment

The experimental setup comprises three primary sections, as illustrated in Figure 1. This schematic diagram depicts the CO₂ capture process within a fixed-bed reactor and includes the following components: gas preparation, CO₂ adsorption, and CO₂ analyzer. For the gas preparation step, the ambient air which contain CO₂ about 400 ppm was pumped from the ambient air using an air compressor and N₂ came from the gas tank.

In the CO₂ adsorption part, N₂ gas was introduced at a flow rate of 1 L/min. This gas was purged through the column for approximately 30 minutes to eliminate all volatile gases from the reactor and associated pipelines. Then, CO₂ from the gas preparation section was fed into the fixed-bed column at a flow rate of 5 L/min. The operating temperature and pressure of this experiment were 30°C and 1 bar, respectively.

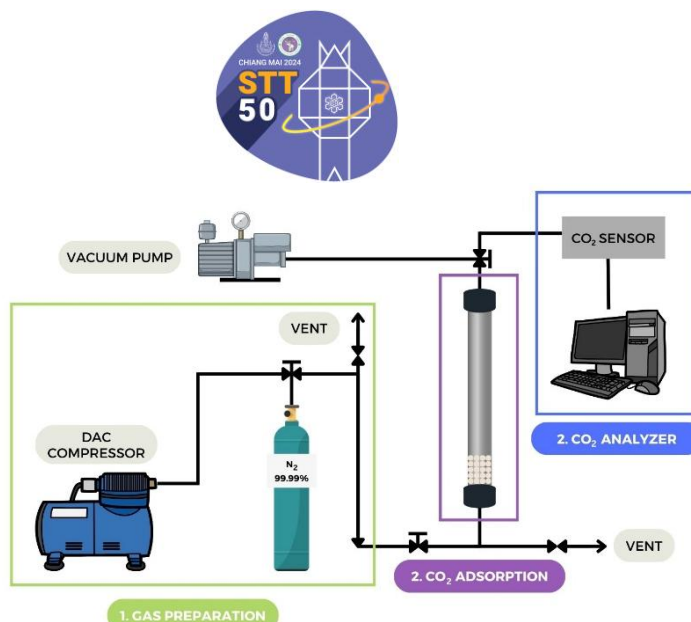


Figure 1. Schematic diagram of CO₂ capture process in a fixed-bed reactor.

Equilibrium in the system was attained when the CO₂ concentration of the gas at the outlet matched that of the gas at the inlet, where the outlet CO₂ concentration was monitored continuously by a CO₂ sensor (with error limits of ± 0.01 %vol CO₂) in the CO₂ analyzer section. Then, the amount of CO₂ adsorbed per unit mass of solid sorbent (q_{eq}) was calculated using equation (1) [13].

$$q_{eq} = \frac{1}{m} \int_0^t Q(C_{in} - C_{out}) dt \quad (1)$$

where q_{eq} is the amount of CO₂ adsorbed per unit mass of solid sorbent at equilibrium (mgCO₂/g-sorbent), m is mass of solid sorbent (g), Q is mass flow rate of gas (mg/min), C_{in} is mass concentration of CO₂ in inlet gas (%CO₂), C_{out} is mass concentration of CO₂ in outlet gas (%CO₂) and t is adsorption time (min).

Microwave regeneration of zeolite 13X

To reuse the sorbent, a regeneration process was applied. Regeneration was performed under conventional microwave oven by using 2 factors including: microwave power and regeneration times according to the 2^k factorial design method, where ‘2’ represents the two levels of each factor under consideration (‘high’ and ‘low’ levels), while ‘k’ enumerates the different influencing factors subjected to the test. [13, 14] In the systematic evaluation of these factors, two levels were tested for each parameter. Microwave power was examined at 300 W and 600 W, while regeneration time was assessed at 5 minutes and 15 minutes. The test range for the regeneration of zeolite 13X adsorbent is based on research that recommends a wide regeneration temperature range of 90°C to 250°C. [9, 15, 16] To determine the optimal regeneration conditions, this study adjusted the microwave power and regeneration time, converting these parameters to temperature values using an infrared thermometer. Consequently, the optimum range for microwave power and regeneration time was established, as detailed in Table 1.

Table 1. Experiment range and level of the regeneration operating parameters.

| Operating parameter | Symbol | Unit | Level | | |
|---------------------|--------|--------|-------|--------|--------|
| | | | Lower | Middle | Higher |
| Microwave power | A | watt | 300 | 450 | 600 |
| Regeneration time | B | minute | 5 | 10 | 15 |

To assess CO₂ capture capacity and regeneration efficiency, the regeneration efficiency was calculated using Equation (2). The adsorption and desorption processes were conducted across 5 cycles.

$$REG (\%) = \frac{q_{avg,reg}}{q_f} \times 100 \quad (2)$$

where REG is the regeneration efficiency of the sorbent (%), $q_{avg,reg}$ is CO₂ adsorption capacity, averaged over five cycles (mgCO₂/g-sorbent), q_f is CO₂ adsorption capacity of 1st cycle (mgCO₂/g-sorbent).

Results and Discussion:

CO₂ capture capacity

Figure 2 illustrates a comparison of CO₂ adsorption capacity of the adsorbent across 5 CO₂ adsorption-desorption cycles under various experimental conditions. The results indicate that case 5 (600 W, 15 min) provided the adsorbent with notable stability in CO₂ adsorption. Particularly, the adsorption capacity in the 5th cycle under this condition was 14% lower than that in the 1st cycle. In contrast, under experimental cases 1, 2, 3, and 4, the CO₂ adsorption capacities in the 5th cycle were reduced by 76%, 72%, 60%, and 70%, respectively, compared to the 1st cycle. The data suggest that increasing microwave power and regeneration time generally improves the stability of zeolite 13X in CO₂ adsorption. Additionally, the CO₂ adsorption capacities under cases 1, 2, 3, and 4 exhibited a similar trend, with a notable increase in capacity observed between cases 4 and 5. These findings highlight the need for further investigation into the regeneration efficiency and ANOVA analysis, to better understand the effects of regeneration conditions on adsorption performance.

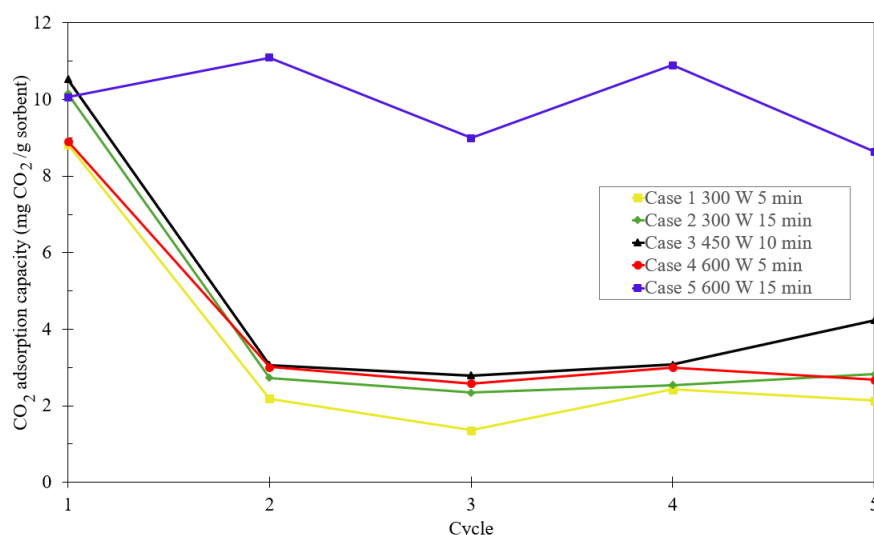


Figure 2. CO₂ adsorption capacity of zeolite 13X at 5 adsorption-desorption cycles in different regeneration conditions.

Regeneration performance

Figure 3 presents the regeneration efficiency, calculated using Equation (2). For case 5, which involved a microwave power of 600 W and a regeneration time of 15 min, the regeneration efficiency was 98.41%, surpassing that of the other conditions. This higher efficiency can be attributed to the greater energy input and extended duration provided in this case. Increasing microwave power and regeneration time causes molecular vibrations within



the adsorbent to remain in the microwave field for a longer duration, causing the temperature of the adsorbent to rise. This increases the kinetic energy of the CO₂ molecules, thereby overcoming the adsorption energy barriers and facilitating their release from the zeolite structure. This phenomenon not only promotes the release of adsorbed CO₂ but also enhances the efficacy of the adsorbent in subsequent cycles of the CO₂ adsorption process. [17]

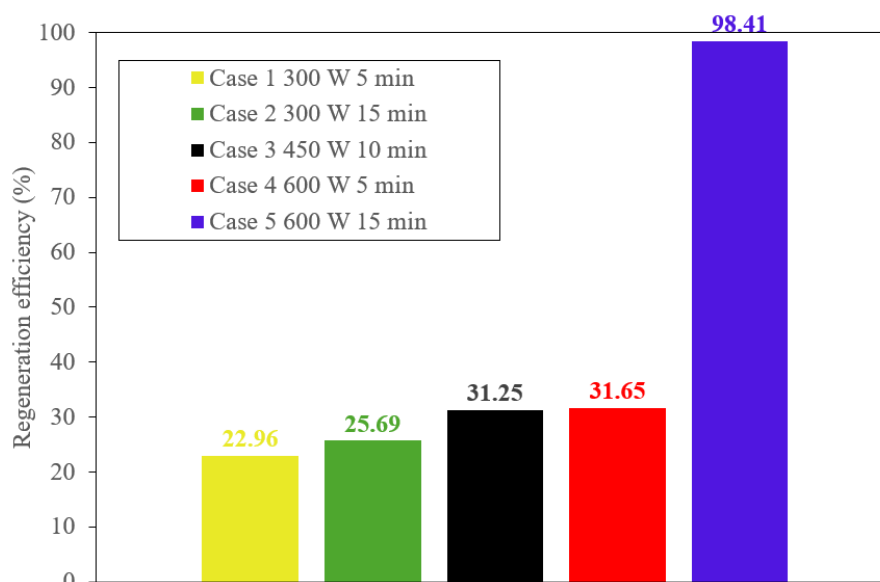


Figure 3 The regeneration efficiency of zeolite 13X with different regeneration conditions

Statistical analysis

The experimental results presented above are based on a 2^k factorial design experiment approach to investigate the simultaneous effects of process variables. This method is effective for investigating the interactions and influences of several factors on the experimental outcome of interest. The statistical analysis was applied to assess the effects of the factors under investigation, including microwave power, regeneration time, and regeneration cycle. The ANOVA method, also known as Analysis of Variance, was used as a statistical technique comparing the means of two or more groups to determine if they are significantly different from each other. [18] The results were analyzed with the findings presented in Table 2.

Table 2 ANOVA analysis table.

| Source | Sum of Squares | df | Mean Square | F-value | p-value |
|---|----------------|----|-------------|---------|---------|
| Model | 6434.75 | 4 | 1608.69 | 69.88 | 0.0027 |
| 1. Microwave power | 2664.14 | 1 | 2664.14 | 115.73 | 0.0017 |
| 2. Regeneration time | 2043.84 | 1 | 2043.84 | 88.78 | 0.0025 |
| 3. Regeneration cycle | 38.68 | 1 | 38.68 | 1.68 | 0.2856 |
| 4. Interaction of Microwave power-Regeneration time | 1688.10 | 1 | 1688.10 | 73.33 | 0.0033 |
| Residual | 69.06 | 3 | 23.02 | | |
| Cor Total | 6503.81 | 7 | | | |

The factors analyzed in Table 2 were chosen through statistical methods, with a Model F-value of 69.88 indicating significant results. Key variables affecting regeneration efficiency are microwave power, regeneration time, and their interaction, which significantly impact efficiency with p-values of 0.0017, 0.0025, and 0.0033, respectively. Microwave power is the most influential variable, supported by the highest F-value of 115.73. However, the regeneration cycle variable did not significantly affect efficiency due to a p-value of 0.2856.

Figures 4 and 5 illustrate 2D and 3D interaction between study variables and regeneration efficiency, respectively. The result show that increasing of microwave power and regeneration time improve efficiency, enhancing molecular vibrations and prolonging the zeolite 13X adsorbent's microwave exposure. This leads to higher temperatures, facilitating more CO₂ release and thus better regeneration efficiency. Optimal conditions were identified as 600 W of microwave power and 15 minutes of regeneration time. The number of regeneration cycles did not significantly alter efficiency, suggesting that the study's conditions were inadequate for complete CO₂ desorption.

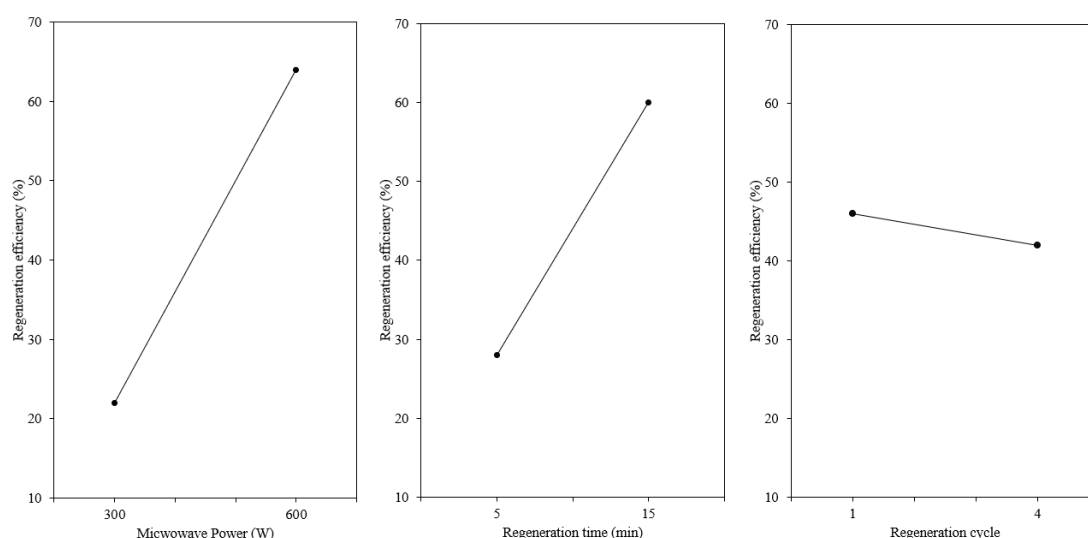


Figure 4. Interaction between study variables and regeneration efficiency.

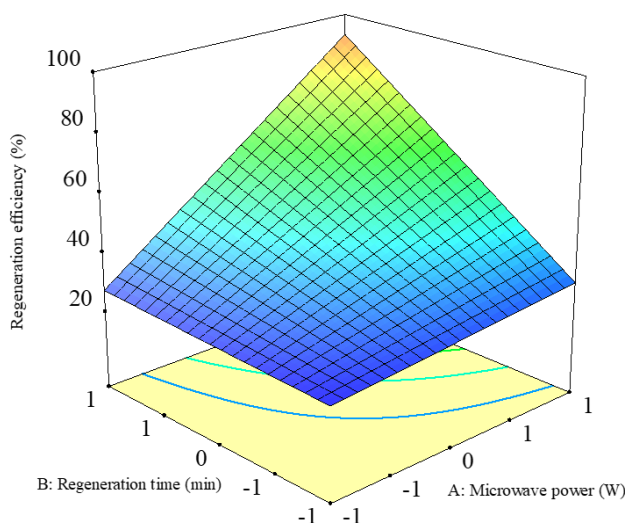


Figure 5. 3D surface interaction between study variables and regeneration efficiency.



Conclusion:

This study evaluated the effects of microwave regeneration operating variables including microwave oven power, regeneration time, and regeneration cycle affected the regeneration efficiency of zeolite 13X solid sorbent by using a 2^k factorial design experiment to identify optimal conditions. ANOVA was employed to investigate the interactions and influences of these factors on regeneration efficiency.

In the investigation of the adsorbent regeneration process, it was observed that microwave-assisted regeneration emerged as an innovative method that yielded results exceeding expectations and demonstrated practical applicability under suitable regeneration conditions. Analysis of the effects of operating variables revealed that increasing both microwave power and regeneration time improved the regeneration efficiency of the adsorbent. This enhancement is attributed to the increased microwave power and regeneration time enhances molecular vibrations within the adsorbent, allowing it to remain in the microwave field for a longer duration, causing the temperature of the adsorbent to rise. This increases the kinetic energy of the CO₂ molecules, thereby overcoming the adsorption energy barriers and facilitating their release from the zeolite structure. This phenomenon not only promotes the release of adsorbed CO₂ but also enhances the efficacy of the adsorbent in subsequent cycles of the CO₂ adsorption process. The optimal conditions for achieving maximum regeneration efficiency in this study were identified as a microwave power level of 600 W and a regeneration time of 15 minutes, in contrast, the regeneration cycle did not have a statistically significant impact.

In conclusion, this research introduces a novel approach for the regeneration of CO₂ capturing adsorbents, which offers potential cost savings for the process. Notably, microwave regeneration can significantly reduce both the regeneration time and energy consumption, contributing to more sustainable environmental practices.

Acknowledgements:

This research project was supported by The Second Century Fund (C2F), Chulalongkorn University. In addition, the National Research Council of Thailand / Chulalongkorn University for providing the Mid-Career Research Grant (N42A660438) was partially acknowledged.

References:

1. Dziejarski B, Serafin J, Andersson K, Krzyżyńska R. *Materials Today Sustainability*. 2023;24:100483.
2. Veselovskaya JV, Derevschikov VS, Kardash TY, Stonkus OA, Trubitsina TA, Okunev AG. *International Journal of Greenhouse Gas Control*. 2013;17:332-340.
3. Derevschikov VS, Veselovskaya JV, Shalygin AS, Yatsenko DA, Sheshkovas AZ, Martyanov ON. *Chinese Journal of Chemical Engineering*. 2022;46:11-20.
4. Kong Y, Shen X, Cui S. *Microporous and Mesoporous Materials*. 2016;236:269-276.
5. Gjernes E, Helgesen LI, Maree Y. *Energy Procedia*. 2013;37:735-742.
6. Mao H, Zhou D, Hashisho Z, Wang S, Chen H, Wang H. *Journal of Industrial and Engineering Chemistry*. 2015;21:516-525.
7. Van Schagen TN, Van der Wal PJ, Brilman DWF. *Chemical Engineering Journal Advances*. 2022;9:100187.
8. Bahmanzadegan F, Ghaemi A. *Case Studies in Chemical and Environmental Engineering*. 2024;9:100564.

9. Erguvan M, Amini S. Carbon Capture Science & Technology, 2024;11:100189.
10. Yassin MM, Biti S, Afzal W, Martín CF. Journal of Environmental Chemical Engineering. 2021;9:106835.
11. Gomez-Rueda Y, Verougstraete B, Ranga C, Perez-Botella E, Reniers F, Denayer J. Chemical Engineering Journal. 2022;446:137345.
12. Ellison C, Hoffman J, Shekhawat D. International Journal of Greenhouse Gas Control. 2021;107:103311.
13. Nokpho P, Amornsri P, Boonmattoon P, Wang X, Chalermssinsuwan B. Materials Today Sustainability. 2024;26:100728.
14. Boonprasop S, Chalermssinsuwan B, Piumsomboon P. Journal of the Taiwan Institute of Chemical Engineers. 2017;78:282-289.
15. Jacobs JH, Deering CE, Sui R, Lesage KL, Marriott RA. Chemical Engineering Journal. 2023;451 (4):139049.
16. Sayılğan SC, Mobedi M, Ülkü S. Microporous and Mesoporous Materials. 2016;224:9-16.
17. Balraj A, Premalalitha PP, Ramamoorthy SV, Mayilvahanan SA, Venkatesan S, Annadurai L, Subramanian G, Srinivasan V, Vetrivelvan S. Chemical Engineering and Processing - Process Intensification. 2022;17:109000.
18. Rueda AMP. Academic Press. 2023:157-160.

AUTHORS INDEX

- Achara Kleawkla, 822
Akkarapong Jaidej, 678
Anakhaorn Srisaipet, 829
Anawat Ajavakom, 330
Anawat Pinisakul, 603
Apichart Suksamrarn, 355
Apichat Imyim, 255
Asma Yafad, 518
Aussara Panya, 51, 183
Bannarat Jaroendee, 687
Benjapon Chalermainsuwan, 876, 896, 905
Chadaporn Keatmanee, 475
Chanoknon Kongkanta, 781
Chanya Thawonsuk, 759
Chatchadaporn Pinthong, 423
Cherlynn Van Beem, 62
Chidchanok Meechaisue, 649
Chompunoot Wangboon, 72
Chonchanok Muangnapoh, 36
Chongdee Buranachai, 277
Janjira Panchompoo, 239
Jitnapa Sirirak, 442
Kanit Mukdasai, 476, 513
Kanyarat Kwansirikul, 655
Kasidit Nootong, 86
Khamron Mekchay, 554
Kittimasak Naijit, 463
Mantana Jamklang, 140, 192
Marina Mani, 707
Mayuramas Wilai, 321
Mongkol Phaengphech, 204
Nattaya Tawichai, 728
Netnapa Chana, 101
Nipada Ruankaew Disyatat, 44
Niramol Juntarachai, 292
Onnida Wattanarat, 505
Orawan Khantamat, 120
Orawan Kritsunankul, 263
Panita Kongsune, 447
Pannee Leeladee, 283
Pathrapol Lithanatudom, 146
Pattarasuda Chayapakdee, 167
Phetlada Kunthadee, 270
Pitiwat Wattanachai, 859
Pongchai Dumrongrojwathana, 130
Pornpen Werawatganone, 363
Pornthep Sompornpisut, 454
Pornthip Tongying, 346
Preecha Kasikamphaiboon, 615
Preenapa Saengaroon, 249
Puey Ounjai, 154
Rachanon Thiratrakulchai, 430
Rasryne Hirankalyakorn, 488
Ratchadaporn Puntharod, 11
Ratinan Boonklurb, 582
Ruangdaj Tongsri, 639
Ruchanok Tinikul, 209
Ruttachuk Rungsiwiwut, 92
Saoowapa Chotisuwan, 744
Sarawut Kumphune, 26, 109, 835, 843, 850
Sarawut Rimdusit, 772
Sarita Paisansuthichol, 226
Sathit Prasomphan, 496
Sirawit Yokyong, 888
Siriporn Sakboonyarat, 546
Siwaporn Saewan, 526, 594
Sorawat Siangpipop, 623
Sunita Chamyuang, 198
Supason Wanichwecharungruang, 379
Supattara Phokaeo, 81
Sutthipong Taweelarp, 698
Tanatorn Khotavivattana, 386
Teera Chewonarin, 790
Thanakorn Lowasri, 753
Thanawat Kongrak, 574
Thaned Kangsamaksin, 175
Thawichai Traiporm, 1
Thitiphan Chimsook, 735
Tirayut Vilaivan, 369
Torsak Luanphaisarnnont, 401
Tuangrat, 231
Uthumporn Kankeaw, 416
Vimoltip Singtuen, 664, 671
Vorarat Champattanachai, 18
Wachirachai Pabuprapap, 314
Waewdaw Rupean, 767
Wanpen Naklua, 409
Warinthorn Chavasiri, 298, 339, 393
Watchara Kaewsuwan, 217
Watcharaphong Ariyakriangkai, 867
Wetchasart Polyiam, 161
Wilai Mayuramas, 305
Wimon Sukplum, 630
Wiramsri Sripochanart, 796
Worarat Srisurat, 532
Yupa Thasod, 716
Yuree Wandee, 805, 813



<https://stt50.scisoc.or.th>



www.science.cmu.ac.th



Faculty of Science, Chiang Mai University



VidyaGram CMU (@sci_cmu)



SCI CMU (@sci_cmu)



Science CMU Official



SCI CMU Info. Center @scicmu